

INTERNATIONAL CONFERENCE ON ENGINEERING TECHNOLOGIES

October 26-28, 2018

Konya/TURKEY

PROCEEDINGS

Editor
Prof. Dr Ismail SARITAS

E-ISBN: 978-605-68537-3-9





International Conference on Engineering Technologies

**International Conference, ICENTE
Konya, Turkey, October 26-28, 2018**

Proceedings

**Editor
Prof. Dr. Ismail SARITAS**

**International Conference on Engineering Technologies, ICENTE'18
Konya, Turkey, October 26-28, 2018**



International Conference on Engineering Technologies

International Conference, ICENTE
Konya, Turkey, October 26-28, 2018

Proceedings

Editor
Prof. Dr. Ismail SARITAS

E-ISBN: 978-605-68537-3-9

Saday Mühendislik Sertifika No: 35542



www.saday.com.tr

Saday Mühendislik

Kürden Mh. Temizciler Sk. No:5 Meram / KONYA
Tel: 0.332 323 07 39

October – 2018

EDITOR :

Prof. Dr. Ismail SARITAS

Selcuk University, Turkey

Department of Electrical and Electronics Engineering, Faculty of Technology

Alaeddin Keykubat Campus 42031 Konya, Turkey

isaritas@selcuk.edu.tr

ASSISTANT EDITORS :

Dr. Ilker Ali OZKAN

Selcuk University, Turkey

Department of Computer Engineering, Faculty of Technology

Alaeddin Keykubat Campus 42031 Konya, Turkey

ilkerozkan@selcuk.edu.tr

Dr. Murat KOKLU

Selcuk University, Turkey

Department of Computer Engineering, Faculty of Technology

Alaeddin Keykubat Campus 42031 Konya, Turkey

mkoklu@selcuk.edu.tr

PREFACE

International Conference on Engineering Technologies (ICENTE'18) was organized in Konya, Turkey on 07-09 October, 2018.

The main objective of ICENTE'18 is to present the latest research and results of scientists related to Electrical and Electronics, Biomedical, Computer, Mechanical, Mechatronics, Metallurgical and Materials Engineering fields. This conference provides opportunities for the delegates from different areas in order to exchange new ideas and application experiences, to establish business or research relations and to find global partners face to face for future collaborations.

All full paper submissions were double blind and peer reviewed and they were evaluated based on originality, technical and/or research content/depth, correctness, relevance to conference, contributions, and readability. Selected papers that were presented in the conference will be published in the Journal of Selcuk Technic if their content matches with the topics of the journal.

At this conference, there were 303 paper submissions from 16 different countries and 128 universities. Each paper proposal was evaluated by two reviewers. And finally, 163 papers from 12 different countries were presented at our conference.

In particular, we would like to thank Prof. Dr. Mustafa SAHIN, Rector of Selcuk University; Prof. Dr. Abdullah Uz TANSEL, City University of Newyork; Prof. Dr. Ahmet Fahri OZOK, Okan University; Assoc. Prof. Dr. Ayhan EROL, Afyon Kocatepe University; Journal of Selcuk Technic. They made crucial contribution towards the success of this conference. Our thanks also go to the section editors and colleagues in our conference office.

Prof. Dr. Ismail SARITAS
Editor

PROGRAMME COMMITTEES

HONORARY CHAIR :

Mustafa Sahin, Rector of Selcuk University, Turkey

CHAIR :

Ismail Saritas, Selcuk University, Turkey

CO-CHAIR :

Necmettin Tarakcioglu, Selcuk University - Turkey

Alla Anohina Naumeca, Riga Technical University – Latvia

Silyan Sibinov Arsov, Rousse University, Bulgaria

Mehmet Cunkas, Selcuk University - Turkey

Fatih Basciftci, Selcuk University - Turkey

Murat Ciniviz, Selcuk University - Turkey

PUBLICATION CHAIR :

Ilker Ali Ozkan, Selcuk University, Turkey

Murat Koklu, Selcuk University, Turkey

INTERNATIONAL ADVISORY BOARD

Adem Alpaslan Altun, Turkey

Ahmet Fenercioglu, Turkey

Ahmet Yonetken, Turkey

Ahmet Afsin Kulaksiz, Turkey

Alexander Sudnitson, Estonia

Alina Ivan Dramogir, Romania

Alla Anohina Naumeca, Latvia

Almoataz Youssef Abdelaziz, Egypt

Amar Ramdane Cherif, France

Anca Loana Andreescu, Bulgaria

Anne Villems, Estonia

Antonella Reitano, Italy

Antonio Mendes, Portugal

Arif Gok, Turkey

Aristomenis Antoniadis, Greece

Artan Luma, Macedonia

Asrun Matthiasdottir, Israel

Bahattin Karakaya, Turkey

Biagio Lenzitti, Italy

Binod Kumar, India

Boris Akanaev, Kazakhstan

Dimitris Dranidis, Greece

Domenico Tegolo, Italy

Eisha Akanksha, India

Elinda Kajo Mece, Romania

Engin Ozdemir, Turkey

Erdal Bekiroglu, Turkey

Erdinc Kocer, Turkey

Erol Turkes, Turkey

Ertugrul Durak, Turkey

Gabriel Luna Sandoval, Mexico

Hakan Isik, Turkey

Hamit Saruhan, Turkey

Hamza Bensouilah, Algeria

Hasan Gokkaya, Turkey

Hayri Arabaci, Turkey

Heinz Dietrich Wuttke, Germany

Howard Duncan, IE

Hulusi Karaca, Turkey

Humar Kahramanli, Turkey

Huse Fatkic, Bosnia and Herzegovina

Ibrahim Uyanik, Turkey

Ihsan Korkut, Turkey

Ilker Ali Ozkan, Turkey

Ivan Jelinek, Czech Republic	Natasa Hoic Bozic, Croatia
Jaharah A Ghani, Malaysia	Nihat Yildirim, Turkey
Jan Vom Brocke, Liechtenstein	Nikolaos Blasis, Greece
Janis Grundspenkis, Latvia	Novruz Allahverdi, Turkey
Janusz Jablonowski, Poland	Pantha Ghosal, Australia
Jiri Srba, Denmark	Pino Caballero Gil, Spain
Kadir Gok, Turkey	Saadetdin Herdem, Turkey
Karl Jones, United Kingdom	Sakir Tasdemir, Turkey
Laurentiu Cristian Deaconu, Romania	Shahabuddin Memon, Pakistan
Luca Lombardi, Italy	Silyan Sibinov Arsov, Bulgaria
M Ugras Cuma, Turkey	Spiridon Cretu, Romania
Mahdi Shahbakhti, United States	Stavros Christodoulakis, Greece
Majida Ali Abed Meshari, Iraq	Stavros Nikolopoulos, Greece
Marco Porta, Italy	Tahir Sag, Turkey
Mehmet Akbaba, Turkey	Tatjana Dulinskiene, Latvia
Mehmet Akif Sahman, Turkey	Temel Kayikcioglu, Karadeniz Technical University, Turkey
Mehmet Cengiz Kayacan, Turkey	Thomas Engel, Luxembourg
Mehmet Turan Demirci, Turkey	Tugce Demirdelen, Turkey
Mirjana Ivanovic, Serbia	Ulvi Seker, Turkey
Miroslav Neslusan, Slovakia	Virginio Cantoni, Italy
Muciz Ozcan, Turkey	Yuri Pavlov, Bulgaria
Muhammad Zia Ur Rehman, Pakistan	Zarifa Jabrayilova, Azerbaijan
Mumtaz Mutluer, Turkey	
Murat Koklu, Turkey	

ORGANIZING COMMITTEE

Alla Anohina Naumeca, Latvia	Fatih Basciftci, Turkey
Silyan Sibinov Arsov, Bulgaria	Mehmet Cunkas, Turkey
Angel Smrikarov, Bulgaria	Hayri Arabaci, Turkey
Lilia Georgieva, United Kingdom	Polyxeni Arapi, Greece
Ismail Saritas, Turkey	Suleyman Neseli, Turkey
Necmettin Tarakcioglu, Turkey	Ibrahim Uyanik, Turkey
Haci Saglam, Turkey	Ayhan Erol, Turkey
Murat Ciniviz, Turkey	

TECHNICAL COMMITTEE

Ilker Ali Ozkan, Turkey	Harun Sepet, Turkey
Esra Kaya, Turkey	Burak Tezcan, Turkey
Eyub Canli, Turkey	Murat Koklu, Turkey

CONTENTS

ANKLE FOOT ORTHOSIS A CONTROL STRATEGY	1
ZAIN SHAMI, M NABEEL ANWAR	
THEORETICAL NBO AND TD DFT ANALYSIS OF GLYOXYLDIUREIDE	5
NIHAL KUS, SALIHA ILICAN	
ELICITATION OF BIOMATERIALS FOR MIMICKING MICROPHYSIOLOGICAL SYTEMS ON A CHIP	9
ECEM SAYGILI, OZLEM YESIL CELIKTAS	
HYBRID ORBITAL LOCALIZATION OF E CROTONIC ACID USING NBO ANALYSIS	12
SALIHA ILICAN, NIHAL KUS	
FABRICATION OF DIFFUSION AND INTERNAL GELATION BASED ALGINATE SILICA HYBRID HYDROGELS FOR ENZYME IMMOBILIZATION	16
RABIA ONBAS, OZLEM YESIL CELIKTAS	
OPTIMIZATION OF CONCENTRATION AND SAND THICKNESS FOR AGAR ASSISTED SAND HARDENING PROCESS BY MICROBIAL BIOCALCIFICATION	19
ALPCAN ARIC, BURAK TALHA YILMAZSOY, IREM DENIZ CAN, TUGBA KESKIN GUNDOGDU	
DESIGN OF A HOME HEALTH CARE DATABASE IN MONITORING CHRONIC RESPIRATORY DISEASES	22
ILAYDA HASDEMIR, GOKHAN ERTAS	
A NEW APPROACH FOR FEATURE EXTRACTION FROM FUNCTIONAL MR IMAGES	26
GUZIN OZMEN, SERAL OZSEN	
A CLUSTERING PROBLEM WITH GAUSSIAN MIXTURE MODEL BASED ON EXPECTATION MAXIMIZATION	30
EBRU PEKEL, ERDAL KILIC	
AN APPLICATION OF HYBRID SUPPORT VECTOR MACHINE AND GENETIC ALGORITHM TO CLASSIFICATION MODEL	34
ZEYNEP CEYLAN, EBRU PEKEL	
SMARTPHONE BASED ACTIVITY RECOGNITION USING K NEAREST NEIGHBOR ALGORITHM	37
ALMONTAZER MANDONG, USAMA MUNIR	
A NEW MULTI OBJECTIVE ARTIFICIAL BEE COLONY ALGORITHM FOR MULTI OBJECTIVE OPTIMIZATION PROBLEMS	41
ZULEYHA YILMAZ ACAR, FIKRI AYDEMIR, FATIH BASCIFTCI	
PREDICTION OF SEPSIS DISEASE BY ARTIFICIAL NEURAL NETWORKS	45
UMUT KAYA, ATINC YILMAZ, YALIM DIKMEN	
E TRANSACTIONS SECURITY ANALYSIS	55
TAHAR MEKHAZANIA	

SPIRAL SEARCH OPTIMIZATION ALGORITHM APPLIED TO IIR DIGITAL FILTER DESIGN	61
OUADI ABDERRAHMANE, BENTARZI HAMID, ZITOUNI ABDELKADER	
AUTOMATIC LEARNING OF SEMANTIC RELATIONSHIPS FOR THE ONTOLOGY CONSTRUCTION APPLICATION ON ARABIC TEXT	66
BENABDALLAH ALI	
OBJECT RECOGNITION SYSTEM BASED ON ORIENTED FAST AND ROTATED BRIEF ORB FEATURES	71
AHMED MOHAMMED AHMED BAYATI, ERSIN KAYA	
ACTIVATION FUNCTIONS IN SINGLE HIDDEN LAYER FEED FORWARD NEURAL NETWORKS	75
ENDER SEVINC	
TEMPORAL EXTENSIONS TO RDF	81
DI WU, ABDULLAH UZ TANSEL	
ECG ARRHYTHMIAS CLASSIFICATION USING SVM CLASSIFIER	86
MUSTAFA ALGBURI, ERSIN KAYA	
TWO DIMENSIONAL MEASUREMENT SYSTEM FOR PVC PROFILES VIA IMAGE PROCESSING	89
MURAT AKDOGAN, SULEYMAN YALDIZ	
MAPPING LOCATION OF A SUSPECT BY USING FORENSIC IMAGES TAKEN WITH THEIR OWN MOBILE PHONE	93
KERIM KURSAT CEVIK, FARUK SULEYMAN BERBER, ECIR UGUR KUCUKSILLE	
REGISTRATION AND AUTHENTICATION CRYPTOSYSTEM USING THE PENTOR AND ULTRAPENTOR OPERATORS	97
ARTAN LUMA, BESNIK SELIMI, BLERTON ABAZI	
COMPARISON OF MATURITY MODEL FRAMEWORKS IN INFORMATION SECURITY AND THEIR IMPLEMENTATION	102
ARTAN LUMA, BESNIK SELIMI, BLERTON ABAZI, MENTOR HAMITI	
COMPARATIVE STUDY ON AUTOMATIC SPEECH RECOGNITION	105
ARZO MAHMOOD, ERSIN KAYA	
PROJECT DEVELOPMENT WITH SERVICE ORIENTED ARCHITECTURE	109
RIDVAN SARACOGLU, EMINE DOGAC	
ULTRA LOW COST WIRELESS SENSOR NETWORK NODE DESIGN FOR EDUCATIONAL USE	112
AYHAN AKBAS	
PROVIDING CONTEXT AWARE SERVICES TO DEMENTIA PATIENTS AND CAREGIVERS	115
OZGUN YILMAZ	
THE EFFECT OF BALANCING PROCESS ON CLASSIFYING UNBALANCING DATA SET	121
SAMARA JWAI, ERSIN KAYA	
COMPARISON OF AGILE SOFTWARE DEVELOPMENT AND TRADITIONAL SOFTWARE DEVELOPMENT IN TURKEY	125
CIHAN UNAL, FATIH BASCIFTCI, CEMIL SUNGUR	

PERFORMANCE ESTIMATION OF SORTING ALGORITHMS UNDER DIFFERENT PLATFORMS AND ENVIRONMENTS	130
MENTOR HAMITI, ELISSA MOLLAKUQE, SAMEDIN KRRABAJ, ARSIM SUSURI	
MODEL DEVELOPMENT FOR ESTIMATION OF TRAFFIC ACCIDENTS WITH METAHEURISTIC ALGORITHMS	134
AHMET OZKIS, TAHIR SAG	
CLASSIFICATION OF EEG SIGNALS BY USING TRANSFER LEARNING ON CONVOLUTIONAL NEURAL NETWORKS VIA SPECTROGRAM	137
AHMET ESAD TOP, HILAL KAYA	
GAS ROBOT IMPLEMENTATION AND CONTOL	143
ALI MARDAN HAMEED QUTUB, ISMAIL SARITAS	
EXAMINATION OF MACHINE LEARNING METHODS IN HAND POSTURE ESTIMATION	146
MUHAMMED FAHRI UNLERSSEN, MURAT KOKLU, KADIR SABANCI	
MONITORING ANDROID USERS ACTIVITIES KEYLOGGER APP	149
AHMET CALISKAN, SAKIR TASDEMIR	
ARTIFICIAL NEURAL NETWORK AND AN APPLICATION IN BUSINESS FIELD	153
ISMAIL AHMET KURUOZ, SAKIR TASDEMIR	
FUSION OF SMARTPHONE AND SMARTWATCH SENSORS FOR SMOKING RECOGNITION	158
SUMEYYE AGAC, MUHAMMAD SHOAIB, OZLEM DURMAZ INCEL	
EPILEPTIC SEIZURE CLASSIFICATION USING SUPPORT VECTOR MACHINES	163
BURAK TEZCAN, ILKER ALI OZKAN, SAKIR TASDEMIR	
GERMAN CREDIT RISKS CLASSIFICATION USING SUPPORT VECTOR MACHINES	166
BURAK TEZCAN, SAKIR TASDEMIR	
MODIFIED GREY WOLF OPTIMIZATION THROUGH OPPOSITION BASED LEARNING	170
TAHIR SAG	
RECOGNITION OF SIGN LANGUAGE USING CONVOLUTIONAL NEURAL NETWORKS	173
MUCAHID MUSTAFA SARITAS, ILKER ALI OZKAN	
FEASIBILITY STUDY OF A PASSIVE HOUSE ANKARA CASE	177
GUL NIHAL GUGUL	
COSTS AND CO BENEFITS OF PASSIVE HOUSES ANKARA RESIDENTIAL SECTOR	184
GUL NIHAL GUGUL	
A FUZZY CONTROL SYSTEM DESIGN ACCORDING TO THE DEVELOPMENT PERIODS OF THE CULTIVATED MUSHROOMS	190
VILDAN EVREN, ABDULKADIR SADAY, ILKER ALI OZKAN	

FUZZY LOGIC BASED CONTROLLER DESIGN FOR CONTROL OF VENTILATION SYSTEMS	194
ILKAY CINAR, ILKER ALI OZKAN, MURAT KOKLU	
PYRAMID SHAPED NET ZERO ENERGY DORMITORY BUILDING DESIGN	200
MUSTAFA ALTIN, GUL NIHAL GUGUL	
INVESTIGATION OF DIFFERENT REINFORCED CONCRETE FLOORING AND DIFFERENT BUILDING FOUNDATION SYSTEM SOLUTIONS IN TERMS OF BUILDING COST	204
MUSTAFA ALTIN	
A NEW APPROACH WITH FUZZY LOGIC BASE FOR PHOTOVOLTAIC PANEL SURFACE CLEANING	208
MUMTAZ MUTLUER, ABDURRAHIM ERAT	
PMUS PLACEMENT OPTIMIZATION FOR FAULT OBSERVATION IN POWER SYSTEM	212
BENTARZI HAMID, ZITOUNI ABDELKADER, RECIUI ABDELMADJID	
OPEN SOURCE CODED REMOTE MONITORING OF RENEWABLE ENERGY SYSTEMS	218
ERDAL KAPLAN, AHMET YONETKEN	
REGENERATIVE BRAKING BEHAVIOR ANALYSIS OF A L7 CATEGORY VEHICLE IN DIFFERENT DRIVE CYCLES	223
DILARA ALBAYRAK SERIN, ONUR SERIN	
LIFE PREDICTION OF ALUMINUM ELECTROLYTIC CAPACITORS USED IN TWO LEVEL INVERTERS	228
VOLKAN SUEL, HALIL ALPER ONAY, MUHAMMET KENAN AKINCI, TAYFUN OZGEN	
AN INVESTIGATION OF THE PV MAXIMUM POWER POINT TRACKING MPPT SYSTEMS	233
MUMTAZ MUTLUER, KUBRA ORKUN	
CLASSIFICATION OF SNORE SOUNDS BASED ON DEEP SPECTRUM FEATURES	237
GULSEVIN KODALOGLU, FIKRET ARI, DOGAN DENIZ DEMIRGUNES	
DRONES AND THEIR APPLICATION IN AMBIENT ASSISTED LIVING	242
RADOSVETA SOKULLU, ABDULLAH BALCI, EREN DEMIR	
CORRELATIONS BETWEEN COLOR FEATURES OF VITREOUS AND NON VITREOUS DURUM WHEAT KERNELS WITH LINEAR REGRESSION	248
ESRA KAYA, ISMAIL SARITAS	
PERFORMANCE COMPARISON OF 2 D ZALMS AND BM3D ALGORITHMS FOR IMAGE DENOISING	252
GULDEN ELEYAN, MOHAMMAD SALMAN	

WIND PV HYBRID SYSTEM POTENTIAL SITES AND ELECTRICITY GENERATION POTENTIAL ANALYSIS IN WESTERN PROVINCE OF ZAMBIA GIS BASED ANALYTIC APPROACH II	256
MABVUTO MWANZA, KORAY ULGEN, MANUEL F ARIZA TABA, ALAIN C BIBOUM, KAKOMA MWANSA	
TACKLING CLIMATE CHANGE GLOBAL EFFORTS AND ENERGY PREFERENCES	264
HAYRIYE SAGIR, AKIN AKYIL	
IMPLEMENTING PEAK CURRENT MODE CONTROL OF INTERLEAVED SEPIC CONVERTER	274
ONUR KIRICIOGLU, MURAT UNLU, SABRI CAMUR	
THE IMPORTANCE OF THE DIVERSITY FACTOR	278
MEHMET FAHRI YAPICIOGLU, HASAN HUSEYIN SAYAN, HAKAN TERZIOGLU	
CONTROL OF SPWM APPLIED 15 LEVEL INVERTER WITH ARM PROCESSOR	282
ABDULVEHHAB KAZDALOGLU, BEKIR CAKIR, TARIK ERFIDAN, MEHMET ZEKI BILGIN	
PERFORMANCE EVALUATION OF P O IC AND FL ALGORITHMS USED IN MAXIMUM POWER POINT TRACKING SYSTEMS	286
FUAD ALHAJ OMAR, GOKSEL GOKKUS, AHMET AFSIN KULAKSIZ	
RAYLEIGH BASED OPTICAL REFLECTOMETRY TECHNIQUES FOR DISTRIBUTED SENSING APPLICATIONS	290
KIVILCIM YUKSEL	
ESTIMATION OF POWERLINE ROUTE FROM AIRBORNE LIDAR	293
MUSTAFA ZEYBEK	
APPLICATION OF VARIOUS BANDWIDTH ENHANCEMENT METHODS ON SELJUK STAR MICROSTRIP ANTENNA	298
DILEK UZER, SEYFETTIN SINAN GULTEKIN, RABIA TOP, MEHMET YERLIKAYA, OZGUR DUNDAR	
DESIGN AND SIMULATION OF A NEW SINGLE PHASE MULTILEVEL INVERTER STRUCTURE	301
ERSOY BESER, BIROL ARIFOGLU	
SIMULATION OF MULTI LEVEL INVERTER FED PERMANENT MAGNET SYNCHRONOUS MOTOR PMSM	305
ESRA KANDEMIR BESER, ERSOY BESER	
STATISTICAL FEATURE EXTRACTION AND ANN BASED CLASSIFICATION OF TEMPORAMANDIBULAR JOINT SOUNDS	311
UGUR TASKIRAN, SALIMKAN FATMA TASKIRAN, MEHMET CUNKAS	
DESIGN AND ANALYSIS OF GRID TIED PHOTOVOLTAIC PV SYSTEMS UNDER UNCERTAIN WEATHER CONDITIONS	315
UMAIR YOUNAS, BAYRAM AKDEMIR, AHMET AFSIN KULAKSIZ	
A STUDY ON THE EFFECT OF DAYLIGHT IN ENERGY EFFICIENCY	321
AYKUT BILICI, ISMAIL SARITAS	

OVERVIEW OF POTENTIAL OF RENEWABLE ENERGY SOURCES IN ARTVIN PROVINCE	325
MEHMET CUNKAS, ENES HALIT AYDIN	
AN OVERVIEW ON FIRE DETECTION SYSTEMS	330
MEHMET CUNKAS, VACIP DENIZ	
A NOVEL PASSIVE FILTER TO ELIMINATE HARMONICS IN STAND ALONE DFIG WITH NON LINEAR LOADS	336
CAGATAY KOCAK, MEHMET DAL, KAZIM TOPALOGLU, MUSTAFA YEGIN	
AN APPLICATION IN THE AUTOMOTIVE SECTOR WITH THE PURPOSE OF INVESTIGATION AND PREVENTION OF EDGE CRACK PROBLEM AT 980 MPA AND ABOVE LEVEL STEEL MATERIALS	342
EBRU BARUT, BAHADIR KUDAY, ORCUN YONTEM	
A CALORIMETRIC INVESTIGATION OF CO ₂ N ₂ AND AR ADSORPTION	350
FEHIME CAKICIOGLU OZKAN, ASLI ERTAN	
EFFECT OF REACTION TEMPERATURE ON THE AMOUNT OF CARBON NANOTUBES BY CHEMICAL VAPOR DEPOSITION IN FLUIDIZED BED	355
MEHMET GURSOY, DUYGU UYSAL ZIRAMAN, OZKAN MURAT DOGAN, BEKIR ZUHTU UYSAL	
ESTIMATION OF DRINKING WATER PROPERTIES FILTERED WITH GRAPHENE OXIDE MATLAB BASED FUZZY LOGIC MODELING	359
OZGE BILDI CERAN, INCI SEVGILI, HALUK KORUCU, BARIS SIMSEK, OSMAN NURI SARA	
COMPRESSIVE BEHAVIOR OF GLASS CARBON EPOXY 55 FILAMENT WOUND HYBRID PIPES CONFINED COMPOSITE CONCRETE WITH EXPANSIVE CEMENT	363
LOKMAN GEMI, MEHMET ALPASLAN KOROGLU, MERVE CALISKAN	
EXPERIMENTAL INVESTIGATION OF BEHAVIOR OF HYBRID GFRP BOX BEAM SECTIONS	367
MEHMET ALPASLAN KOROGLU, LOKMAN GEMI, MEHMET YARIMOGLU	
CHEMICAL RECYCLING OF POLYETHYLENE TEREPHTHALATE PET BOTTLE WASTES WITH ALCOHOLYSIS TRANSESTERIFICATION OF SHREDDED PET WITH 2 ETHYLHEXANOL TO PRODUCE DIOCTYL TEREPHTHALATE DOTP	370
VEDAT ARDA KUCUK, BARIS SIMSEK, TAYFUN UYGUNOGLU, MEHMET MUHTAR KOCAKERIM	
THEORETICAL CALCULATIONS ON STRUCTURAL PROPERTIES OF 1 4 DIAMINOBTANE	373
AYSUN GOZUTOK, AKIF OZBAY	
THEORETICAL STUDIES OF N N TETRACHLORO 1 4 DIAMINOBTANE AND N N TETRABROMO 1 4 DIAMINOBTANE	377
AYSUN GOZUTOK, AKIF OZBAY	
EVALUATING THE STABILITY AND HEAT TRANSFER PERFORMANCE OF CARBON BASED AQUEOUS NANOFUIDS	380
TUGCE FIDAN ASLAN, MEHMET OZGUR SEYDIBEYOGLU, ALPASLAN TURGUT, ELIF ALYAMAC SEYDIBEYOGLU	

PTAU ALLOY NANOPARTICLES AS AN ELECTROCHEMICAL SENSOR FOR HYDROGEN PEROXIDE OZLEM GOKDOGAN SAHIN	386
EFFECT OF PROCESS CONTROL AGENT ON THE CHARACTERISTICS OF 316L POWDERS PREPARED BY MECHANICAL ALLOYING ROUTE CIHAD NAZIK, NECMETTIN TARAKCIOGLU	389
EFFECT OF MILLING TIME ON PROPERTIES OF AA7075 POWDERS ENHANCED BY MECHANICAL ALLOYING METHOD EMRE CAN ARSLAN, CIHAD NAZIK, NECMETTIN TARAKCIOGLU, EMIN SALUR	393
INVESTIGATION OF LOW VELOCITY IMPACT BEHAVIOURS OF NANOSILICA FILLED AND BASALT FIBER REINFORCED NANOCOMPOSITES AT SEA WATER CORROSION CONDITION IBRAHIM DEMIRCI, NECATI ATABERK, MEHMET TURAN DEMIRCI, AHMET AVCI	397
REMOVAL OF PHOSPHORUS USING MG AL LAYERED DOUBLE HYDROXIDES HASAN KIVANC YESILTAS, TURAN YILMAZ	400
MODELLING OF HARDNESS VALUES OF AISI 304 AUSTENITIC STAINLESS STEELS NECIP FAZIL YILMAZ, AYKUT BILICI, MUSA YILMAZ	404
DESIGN AND DYNAMIC MODELLING OF AN ANKLE FOOT PROSTHESIS FOR TRANSFEMORAL AMPUTEES SELIN AYDIN FANDAKLI, HALIL IBRAHIM OKUMUS, AHMET FURKAN ERDEM	409
MEASUREMENT OF WALL THICKNESS OF EXTRUDED PVC PROFILES USING IMAGE PROCESSING METHODS MURAT AKDOGAN, SULEYMAN YALDIZ	415
NUMERICAL INVESTIGATION AND MODELLING OF CONFINED TURBULENT RECIRCULATING FLOWS TAHIR KARASU	419
DYNAMIC ANALYSIS AND CONTROLLING OF A 2 DOF ROBOT MANIPULATOR USING FUZZY LOGIC TECHNIQUES BEKIR CIRAK, SAMI SAFA ALKAN, FATIH IRIM	434
USABILITY OF FUZZY LOGIC CONTROL FOR PERFORMANCE OF DUAL AXIS SOLAR TRACKING SYSTEM BEKIR CIRAK, FATIH IRIM, SAMI SAFA ALKAN	438
INVESTIGATION OF CONCRETE SLAB CRACK WHEN PLACED DIRECTLY ON CLAY AHMED ABDULLAH	446
INVESTIGATION OF WEAR OCCURRED IN DRY CLUTCH DISK WORKING UNDER VARIOUS TORQUES AND ROTATION SPEEDS IBRAHIM SEVIM, MUHAMMED EMIN TOLU, NURULLAH GULTEKIN, MURAT MAYDA	452
ENERGY CONSUMPTION OPTIMIZATION FOR HEAT PUMP DOMESTIC HEATER EMRE SAGLICAN, OZDEN AGRA	459

INVESTIGATION OF THE EFFECTS OF WALNUT BIODIESEL ON A DIESEL ENGINE EXHAUST EMISSIONS	465
A ENGIN OZCELIK, HASAN AYDOGAN, MUSTAFA ACAROGLU	
HEAT RECOVERY OPTIMIZATION	469
CEYDA KOCABAS, AHMET FEVZI SAVAS	
DYNAMIC CHARACTERIZATION OF THE TORSIONAL VIBRATION DAMPER USING QUASI STATIC TORQUE LOADING TEST	473
OMER FARUK UNAL, HASAN ANIL ERKEC, CIHANGIR KAPLAN, YUKSEL CETINKAYA, TUNCAY KARACAY	
EMISSION CHARACTERISTICS OF BIODIESEL BLENDS IN COMMON RAIL DIESEL ENGINE	477
HASAN AYDOGAN, A ENGIN OZCELIK, MUSTAFA ACAROGLU	
RISK ANALYSIS AND MANAGEMENT IN CONSTRUCTION PROJECTS	
AYMAN H AL MOMANI	
TOOL WEAR BASED SURFACE ROUGHNESS PREDICTION VIA NEURAL NETWORK IN FACE MILLING	481
HACI SAGLAM, MUSTAFA KUNTOGLU	
CFD CASE STUDY ON A NOZZLE FLOW LITERATURE REVIEW THEORETICAL FRAMEWORK TOOLS AND EDUCATIONAL ASPECTS	486
ALI H ABDULKAREEM, EYUB CANLI, ALI ATEŞ	
STRENGTH AND COMPACTION CHARACTERISTICS OF RECYCLED CONCRETE AGGREGATES	490
EKREM BURAK TOKA, MURAT OLGUN	
A COMPUTATIONAL STUDY FOR PLAIN CIRCULAR PIPE FLOW	494
ALI H ABDULKAREEM, EYUB CANLI, ALI ATEŞ	
THE RELATIONSHIP BETWEEN TIRE MECHANICS AND ENERGY	498
EYUB CANLI, SERAFETTIN EKINCI	
THE DESIGN OPTIMIZATION OF A GRIPPER MECHANISM USING THE BEES ALGORITHM	502
OSMAN ACAR, METE KALYONCU, ALAA HASSAN	
COMPARISON OF EMPIRICAL AND EXPERIMENTAL RESULTS OF TEMPERATURE ON CUTTING TOOL HARDNESS DURING ROUGH TURNING	507
MUSTAFA KUNTOGLU, HACI SAGLAM	
ANALYSIS OF EXERGY DESTRUCTION RATES IN THE COMPONENTS OF THE ORC SYSTEM USING N PENTANE FLUID	513
ALI KAHRAMAN, REMZI SAHIN, SADIK ATA	
POTENTIAL EVALUATION OF SCALING AND SIMILARITY FOR TRACTOR TIRES	519
EYUB CANLI, SERAFETTIN EKINCI	
MATHEMATICAL MODELING OF THERMOELECTRIC GENERATOR BY REGRESSION ANALYSIS	523
ABDULLAH CEM AGACAYAK, HAKAN TERZIOGLU, SULEYMAN NESELI, GOKHAN YALCIN	

INTERN ENGINEERING APPLICATION STATISTICS	528
EYUB CANLI, AHMET ALI SERTKAYA	
VARIATION OF FRACTURE TOUGHNESS OF RESISTANCE ON SPOT WELDED SHEET STEELS WITH HARDNESS	533
IBRAHIM SEVIM, MUHAMMED EMIN TOLU	
EFFECT OF RED MUD AS A NANOFLUID ON COOLING PERFORMANCE	538
AHMET ALI SERTKAYA, EYUB CANLI	
CRITICISM ON APPLIED TRAINING REVIEWS RENEWABLE ENERGY FIELD CASE	542
EYUB CANLI, SELAHATTIN ALAN	
STRENGTH AND MODAL ANALYSIS OF 8 MEMBERED WALKING MECHANISM	547
ALI FEYZULLAH, KORAY KAVLAK	
NUMERICAL SIMULATION OF THE COALESCING OIL WATER SEPARATOR	553
SEDAT YAYLA, MEHMET ORUC	
ELECTRICAL ENERGY HARVESTING WITH PIEZOELECTRIC	558
SEDAT YAYLA, MEHMET ORUC	
FATIGUE TESTER DESIGN AND FRAME ANALYSIS FOR ESTIMATION OF FATIGUE LIFE OF HELICAL COMPRESSION SPRINGS	563
GOKHAN YALCIN, SULEYMAN NESELI, HAKAN TERZIOGLU, ABDULLAH CEM AGACAYAK	
DETERMINATION OF BASIC CONSTRUCTION PARAMETERS OF KNITTING MACHINES	567
DUYGU ERDEM, GABIL ABDULLA	
INVESTIGATION OF THE ENERGY PROFILE OF KARAMAN	570
BEKIR CIRAK, MEHMET ONUR OGULATA, SEZGIN ESER, YASIN UNUVAR	
APPLICATIONS OF 3D PRINTING TECHNOLOGY IN DENTISTRY	578
BEKIR CIRAK, MEHMET ONUR OGULATA, SEZGIN ESER, YASIN UNUVAR	
COMPARISON OF VARIOUS MACHINE LEARNING METHODS ON WART TREATMENT PERFORMANCE OF CRYOTHERAPY	583
KADIR SABANCI, MURAT KOKLU, MUHAMMED FAHRI UNLERSEN	
FLAME RETARDANT FINISH FOR COTTON FABRIC USING BORON HYBRID SILICA SOL	586
ESRA GELGEC, SULTAN ARAS, FATMA FILIZ YILDIRIM, PERINUR KOPTUR, SABAN YUMRU, MUSTAFA COREKCIOGLU	

Ankle Foot Orthosis: A Control Strategy

Z. SHAMI¹ and M. N. ANWAR²

¹School of Mechanical & Manufacturing Engineering (SMME),
National University of Sciences & Technology (NUST), Islamabad, Pakistan, zainshami@hotmail.com

²School of Mechanical & Manufacturing Engineering (SMME),
National University of Sciences & Technology (NUST), Islamabad, Pakistan, nabeel@smme.nust.edu.pk

Abstract - There have been efforts intending to help rehabilitation of patients and athletes with tendon injuries for their mainstreaming in daily life. It had recently been discovered that reducing inflammation of the injury is not effective on its own therefore the use of Orthosis to revive the muscle function becomes a necessity. In this paper efforts have been made to develop an active control system for a supportive Orthosis device for such people. A thorough related literature review was carried out to identify the technological gaps in the recent developments in control of ankle-foot Orthosis and to conceptualize a novel design and plan a theoretical framework. The control system is an integration of electronic and mechanical components. The proposed working principle of this Orthosis is that a partially paralyzed muscle when activated produces a weak raw Electromyographic (EMG) signal that is picked up by the surface EMG electrodes. This signal is pre-processed, rectified and smoothed and then fed to Control Module to control the mechanical parts and assist the ankle movement.

Keywords: EMG, Orthosis, Muscle activation, Motor action, Active Control System

I. INTRODUCTION

THE alignment, stabilization, as well as assistance of muscles can be carried out using assistive devices called Orthoses. These Orthoses are different from prosthetics as they do not serve as a replacement for lost limbs but in fact target limb impairment in extremities by supplementing lost muscle function. There are three categories for lower extremity Orthosis, knee-ankle foot Orthosis (KAFO), ankle-foot Orthosis (AFO) and foot Orthosis (FO). Orthoses can be further categorized based on other characteristics such as the design and power source. The categories based on design are hinged and solid, and the categories based on power source are active, semi-active and passive. [1]

Based on motion, AFOs can be classified into two categories, static and dynamic. Static Orthoses are used to stop movement of bones to align them correctly while Dynamic Orthoses provide articulation of joints to amplify the weak muscle function. Dynamic Orthoses can be manually operated or automated using a control system with active feedback. [2]

The control strategies that had been implemented vary substantially in accordance with the intended application and functionality of the Orthosis device and the structure and scope of the control scheme with the instrumentation necessary for sensing the state of the human-robot system. Various sensor modalities were highlighted for tapping into the user's physiological control system. The chosen

modalities must be appropriate for the user's physiological condition and personal preferences. The high-level controller is responsible for perceiving the user's locomotive intent, which consists of activity mode recognition or direct volitional control. Advancements in machine learning techniques and the recent proliferation of wearable sensor technologies is likely to fuel developments in this area. Coordinated sharing of the load between the human and an Orthosis may also be necessary to realize rehabilitative outcomes. It is at this level of control that the device's kinematics and dynamics are taken into account and used to compute the set of actuator inputs to achieve the desired states in a dynamic, yet stable manner. [3]

This research intended to cater to these existing deficiencies in the control systems and to produce a control system for an ankle Orthosis existing in the form of ordinary footwear to efficiently recover lost motor muscle function through rehabilitation exercise or physiotherapy while providing physical and psychological comfort to the user- patients and athletes.

II. METHODOLOGY

The methodology in the project comprised of the following steps:

A. Conceptualization

1) Dynamic model of Ankle

The dynamic model of a foot is given in the figure below:

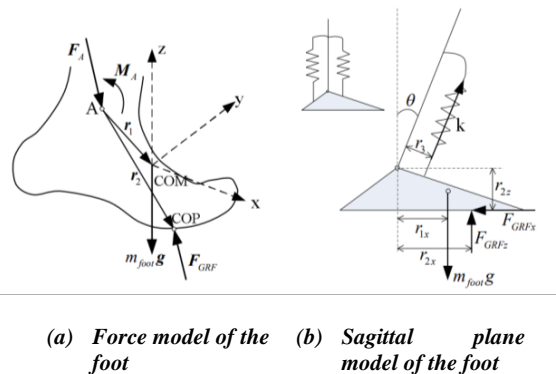


Figure 1: Dynamic Model of Foot [4]

F_A is the ankle reaction force, F_{GRF} is the ground reaction force, m_{foot} is mass of foot, a_{foot} is the foot linear acceleration vector, g is the acceleration due to gravity, k is the stiffness coefficient of the muscle and I is the mass moment of inertia of the foot.

Taking forces in the x-axis and making F_{GRFx} the subject and the foot is in static equilibrium $a_{foot}=0$, the ground reaction force in the x-axis is found to be:

$$F_{GRFx} = F_{Ax} + \sin\Theta \cdot kr_3 \left| \Theta \right| \quad (1)$$

Taking forces in the z-axis and making F_{GRFz} the subject and the foot is in static equilibrium $a_{foot}=0$, the ground reaction force in the z-axis is found to be:

$$F_{GRFz} = F_{Az} + m_{foot}g - \cos\Theta \cdot kr_3 \left| \Theta \right| \quad (2)$$

Taking anticlockwise moment positive, the moment along the ankle in (b) the following equation is acquired:

$$\Sigma M_{ankle} = M_A + r_{1x} \cdot m_{foot}g + r_{2x} \cdot F_{GRFz} - r_{2z} \cdot F_{GRFx} + kr_3^2 \Theta = I\ddot{\Theta} \quad (3)$$

Combining equation (1) and (2) with (3) and making M_A the subject of the equation [4]:

$$M_A = (r_{1x} - r_{2x})m_{foot}g - r_{2x} \cdot F_{GRFz} + r_{2z} \cdot F_{GRFx} + (r_{2x}\cos\Theta + r_{2z}\sin\Theta) kr_3 \left| \Theta \right| - kr_3^2 \left| \Theta \right| + I\ddot{\Theta} \quad (4)$$

When walking at a pace of 1 m/s, the Ground Reaction Force in the x-axis, F_{GRFx} , is 0.8 times the body weight and the Ground Reaction Force in the z-axis, F_{GRFz} , is the body weight [5], the mass of the foot is 1.38 % of the entire body mass [6], the foot makes an angle of 45° during plantar flexion and 20° during dorsiflexion, the mass moment of inertia of the foot, $I = 0.0042 \text{ kgm}^2$ [7], the distance r_3 between the centers of the soleus muscle and the ankle is approximately 0.25 m and the angular acceleration, $\ddot{\Theta} = 500 \text{ rad/s}^2$ during plantar-flexion and $\ddot{\Theta} = 1500 \text{ rad/s}^2$ during dorsiflexion [8].

2) Example of moment calculation

a) Example No. 1

The ankle moment for a short person with the following parameters had been calculated:

$$r_{1x} = 0.0455 \text{ cm}, r_{2x} = 0.082 \text{ cm}, r_{2z} = 0.065 \text{ cm}, m = 63 \text{ kg}$$

At this mass of person the elastic force of the muscle required is 862.09 N during plantar-flexion and 648.5 N during dorsiflexion.

The moment of ankle during plantar-flexion:

$$M_A = (0.0455 - 0.082)(0.0138 \times 63)(9.81) - (0.082)(63)(9.81) + (0.065)(0.8)(63)(9.81) + (0.082\cos(45^\circ) + 0.065\sin(45^\circ))(862.09) - 862.09(0.25) + 0.0042(500)$$

$$M_A = 142.6 \text{ Nm}$$

And moment of ankle during dorsiflexion:

$$M_A = (0.0455 - 0.082)(0.0138 \times 63)(9.81) - (0.082)(63)(9.81) + (0.065)(0.8)(63)(9.81) + (0.082\cos(20^\circ) + 0.065\sin(20^\circ))(648.5) - 648.5(0.25) + 0.0042(1500)$$

$$M_A = -114.6 \text{ Nm}$$

b) Example No. 2

The ankle moment for a tall person with the following parameters had been calculated:

$$r_{1x} = 0.068 \text{ cm}, r_{2x} = 0.123 \text{ cm}, r_{2z} = 0.07 \text{ cm}, m = 82 \text{ kg}$$

At this mass of person the elastic force of the muscle required is 1122.1 N during plantar-flexion and 844.2 N during dorsiflexion.

The moment of ankle during plantar-flexion:

$$M_A = (0.068 - 0.123)(0.0138 \times 82)(9.81) - (0.123)(82)(9.81) + (0.07)(0.8)(82)(9.81) + (0.123\cos(45^\circ) + 0.07\sin(45^\circ))(1122.1) - 1122.1(0.25) + 0.0042(500)$$

$$M_A = 181.4 \text{ Nm}$$

And moment of ankle during dorsiflexion:

$$M_A = (0.068 - 0.123)(0.0138 \times 82)(9.81) - (0.123)(82)(9.81) + (0.07)(0.8)(82)(9.81) + (0.123\cos(20^\circ) + 0.07\sin(20^\circ))(844.2) - 844.2(0.25) + 0.0042(1500)$$

$$M_A = -147 \text{ Nm}$$

Thus the moment or torque provided to the ankle of an average person should be the average of the magnitudes which comes out to be 162 Nm for plantar-flexion and 121.2 Nm for dorsiflexion.

B. Designing Control System

1) DC High Torque Servo Motor (30 N-m peak torque)

The recommended motor is a high torque metal servo capable of generating a peak torque of 30 N-m. The maximum torque requirement for the ankle joint is 180 N-m during gait, thus a gear system or belt and pulley drive of 1:6 can be incorporated into the design to amplify the torque 6 times. A servo motor is used instead of a stepper motor due it being able to maintain high torque during change in dynamic loading as is in the case of gait.

2) EMG Sensor

Measuring muscle activity by detecting its electric potential, referred to as electromyography (EMG), has traditionally been used for medical research. Sensor board V3.0 captures, filters, rectifies and amplifies the electrical activity; depending on the amount of activity in the selected muscle outputting between zero volts to the voltage of the power source.

This signal is then input to the Arduino Uno Controller. The output is an analogue signal, therefore the sampling rate depends on the measurement hardware not the sensor. [9]

3) Microcontroller board

Arduino Uno is a microcontroller board based on the ATmega328P. It has 14 digital input/output pins (of which 6 can be used as PWM outputs), 6 analog inputs, a 16 MHz quartz crystal, a USB connection, a power jack, an ICSP header and a reset button. It contains everything needed to support the microcontroller; it requires a connection to a computer with a USB cable or power it with a AC-to-DC adapter or battery to get started. The maximum sampling frequency of Arduino Uno is 10 kHz and the maximum sampling rate is 10,000 per second. [10]

4) Orthosis Circuit Diagram

The Circuit Schematic Diagram is shown above with the servo getting an external DC Power Supply equivalent to its

peak torque rating which is 24V and 3A and the Muscle Sensor V3.0 getting a DC Power Supply from two 9V batteries. The Muscle Sensor acquires the raw EMG signal that it processes and supplies to the Microcontroller Board, which uses the processed EMG signal to rotate the motor shaft at the desired angles.

5) Control System

The Orthosis works using the control system shown in Figure 2, the mid muscle, end muscle and reference electrodes provide a raw EMG signal to the Muscle Sensor V3.0, the signal is rectified and smoothed by the Muscle Sensor V3.0. The Arduino Uno reads the EMG signal from the Muscle Sensor V3.0 from analog port A0, this signal can be displayed on the computer using the serial port on the Arduino user interface. The Arduino can be used in three modes, **follow mode**, **opposite mode** and **automated mode**. In **follow mode**, the values of the signal which correspond to plantarflexion and dorsiflexion are used for a healthy subject. The Arduino Uno is coded such that if the values read are for plantarflexion, the motor provides the torque required for plantarflexion thus moving the foot to the plantarflexed position and if the values read are for dorsiflexion, the motor provides the torque required for dorsiflexion thus moving the foot to the dorsiflexed position. In **opposite mode**, the opposite of follow mode occurs i.e. if values are read for plantarflexion, the motor torque provided is for dorsiflexion. In **automated mode**, a weak EMG signal is read from a patient suffering from partial paralysis and the motor starts to provide the torque for plantarflexion then dorsiflexion after regular intervals in a loop mimicking the movement of a normal foot during walking.

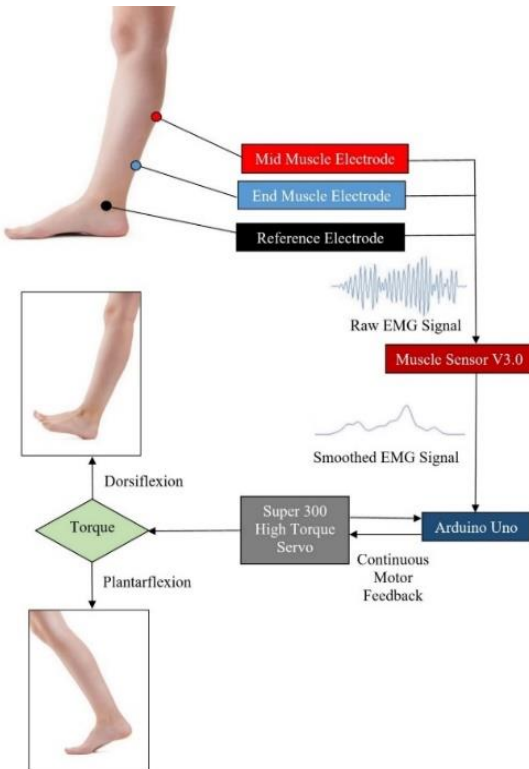


Figure 2: Control System of Orthosis

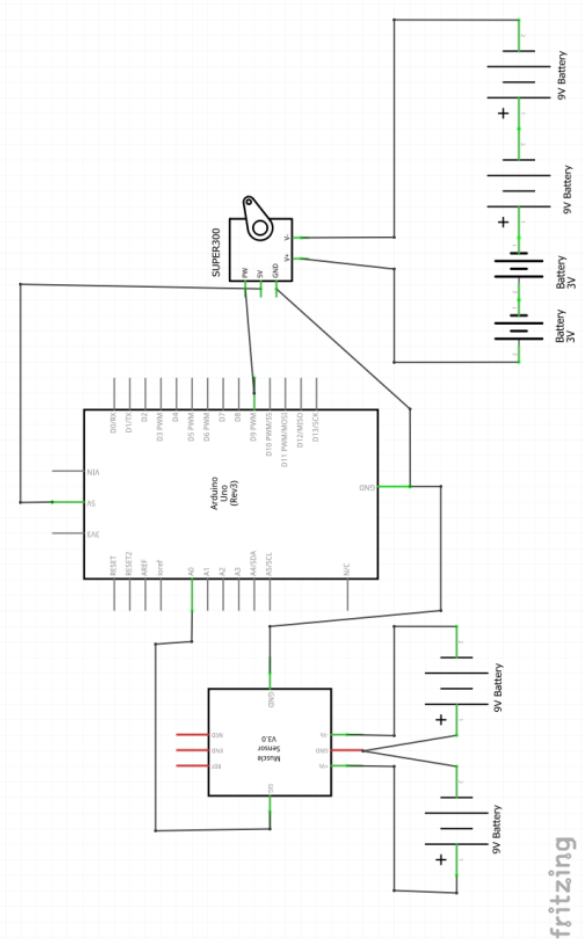


Figure 3: Circuit Schematic Diagram for Orthosis

III. CONCLUSION

Based on the findings of the model following are the major conclusions:

- This is an active control system allowing use in real-time applications such as active physiotherapy and gait assistance. It can produce precise foot movements and uses Electromyography (EMG) as its only input.
- The control system made using the muscle sensor v3.0, Arduino Uno and high torque servo can be easily integrated into an ankle foot Orthosis.

REFERENCES

- [1] E. S. Arch and S. J. Stanhope, "Orthosis Device Research," in Full Stride, New York, NY, Springer, 2017, pp. 99-116.
- [2] "Orthosis," American Orthopaedic Foot & Ankle Society, 2013. [Online]. Available: www.aofas.org/footcaremd/treatments/Pages/Orthosis.aspx.
- [3] M. R. Tucker, J. Olivier, A. Pagel, H. Bleuler, M. Bouri, O. Lambercy, M. J. R., R. Riener, H. Vallery and R. Gassert, "Control strategies for active lower extremity prosthetics and Orthosis: a review," Journal of neuroengineering and rehabilitation, vol. 12, no. 1, 2015.

- [4] Y. Bai, F. Li, J. Zhao, J. Li, F. Jin and X. Gao, "A powered ankle-foot orthoses for ankle rehabilitation," in IEEE International Conference on Automation and Logistics (ICAL), 2012.
- [5] J. Nilsson and A. Thorstensson, "Ground reaction forces at different speeds of human walking and running," *Acta Physiologica*, vol. 136, no. 2, pp. 217-227, 1989.
- [6] "ExRx.net : Home", Exrx.net, 1999. [Online]. Available: <https://exrx.net/>. [Accessed: 02- Feb- 2018].
- [7] Y. S. Narang, V. M. Arelekatti and A. G. Winter, "The effects of prosthesis inertial properties on prosthetic knee Moment and hip energetics required to achieve able-bodied kinematics," *IEEE Transactions on Neural Systems and Rehabilitation Engineering*, vol. 24, no. 7, pp. 754-763, 2016.
- [8] N. Okita and H. Sommer, "Angular acceleration of the foot during gait using an IMU," in Annual Meeting of American Society of Biomechanics (ASB), 2013.
- [9] SparkFun, "Muscle Sensor v3," SEN-13027, [Online]. Available: www.sparkfun.com/products/retired/13027.
- [10] Arduino, "Arduino Uno Rev3," [Online]. Available: store.arduino.cc/usa/arduino-uno-rev3.

Theoretical NBO and TD-DFT Analysis of Glyoxyldiureide

N.KUS¹ and S. ILICAN²

¹Eskisehir Technical University, Eskisehir/Turkey, nkus@anadolu.edu.tr

²Eskisehir Technical University, Eskisehir/Turkey, salihailican@gmail.com

Abstract - Glyoxyldiureide (also known as allantoin 2,5-dioxo-4-imidazolidinyl urea or the diureide of glyoxylic acid) is a product of purine metabolism and known for a long time ago to exist in nature, such as, in allantoinic and amniotic fluids, in fetal urine and in many plants and bacteria. In this study, Natural Bond Orbital (NBO) calculations were performed with the Gaussian 09 suit of programs at the density functional theory with (B3LYP)/6-311++G(d,p) level of approximation. Electron density HOMO-LUMO surface level energy was found for most stable conformer. Stabilization energies for selected NBO pairs obtained from Fock matrix. TD-DFT (B3LYP) calculations were carried out and the results were evaluated.

Keywords - Glyoxyldiureide, Time Dependent-Density Functional Theory (TD-DFT), Natural Bond Orbital (NBO).

I. INTRODUCTION

Glyoxyldiureide (GDU) is a product of purine metabolism and known since long ago to exist in nature, for example, in allantoinic and amniotic fluids, in fetal urine and in many plants and bacteria. GDU is active in skin-softening and rapid skin cells regeneration. It removes corneocytes by loosening the intercellular kit or the desmosomes (protein bridges) that maintain the adhesion of corneocytes to each other. It then exfoliates dry and damaged cells and boosts the radiant appearance of the skin, whose surface becomes smoother and softer. Due to these properties, GDU has been used in cosmetic industry in several forms (e.g., lotions, creams, suntan products, shampoos, lipsticks, and various aerosol preparations), as well as in topical pharmaceutical preparations for treatment of skin diseases for many years. states of disease [1,2].

Hence, in the present investigation, natural bond orbital (NBO) and time dependent density functional theory (TD-DFT) analysis of GDU at the B3LYP(6-311++G(d,p) level have studied for the first time in available literature.

II. COMPUTATIONAL DETAILS

The theory of density function, which has been developing since 1980s, and the electronic structure approaches of atoms and molecules, has started to be used in recent years. It is a very important result to determine the basic condition

characteristics of the system. An incorrect density gives the energy that is right on the energy. One of the best-known functions is the Becke3 (B3) hybrid change function. This function is usually used in conjunction with Lee-Yang-Parr (LYP) correlation. Becke has adjusted these three parameter values in B3LYP function according to experimental data such as atomization energy, ionization potential, proton affinity. In electronic structure calculations, basic sets use linear combinations of gaussian functions to form molecular orbitals in a molecule. The basic set of 6-311G gives more accurate results than the minimal base set for both energies and molecular properties. The triple split valence basic sets (such as 6-311G) define three basic functions for each of the valence orbitals. Such basic sets are useful in the identification of interactions between electrons in electron correlation methods. This basic set adds functions d to heavy atoms and functions p to hydrogen atoms. In this study, TD-DFT and DFT calculations has been performed using Gaussian 09 program at the B3LYP with the 6-311++G(d,p) basis set [3-5]. The relative stability of the conformers was explained using the natural bond orbital (NBO) was performed according to Weinhold and co-workers, using NBO3 as implemented in Gaussian 09 [6].

III. RESULTS AND DISCUSSION

The optimized geometries, energies of the possible conformers of glyoxyldiureide (known as, allantoin, 2,5-dioxo-4-imidazolidinyl urea or the diureide of glyoxylic acid) calculations were achieved with the Gaussian 09 suit of programs at the DFT level of theory, using the 6-311++G(d,p) basis set. The three-parameter hybrid density functional which is called B3LYP, includes Becke's gradient exchange correction and the Lee, Yang and Parr and Vosko. Glyoxyldiureide has a chiral center with R and S enantiomers being conformationally and spectroscopically equivalent. In NBO and TD-DFT studies, we considered only S enantiomers form (Fig.1). According to the calculations electronic energy difference (ΔE_e) between the conformer I and II, III and IV are 10.9, 13.68 and 17.90 kJ mol⁻¹, respectively. These results agree with the previous report [7]. Energies of the low-energy excited states were calculated using the TD-DFT at the B3LYP/6-311++G(d,p) level.

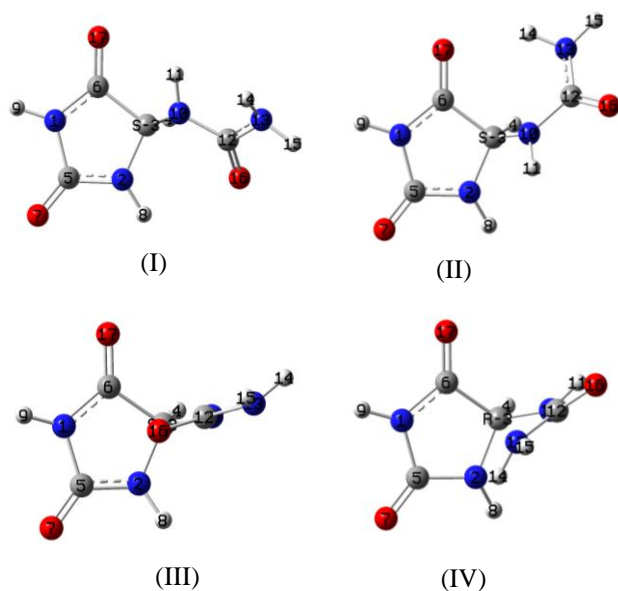


Figure 1: Conformers of Glyoxyldiureide.

Table 1: Energy of vertical absorption (ΔE) and oscillator strength (f) calculated using the TD-DFT(B3LYP) method at the ground state equilibrium geometry of most stable conformer (I).

State	Type	ΔE (eV)	f	Excitation wavelength (nm)
S ₀		0.00		
S ₁	LP(1)- π^*	5.2646	0.0009	235.51
S ₂		5.9462	0.0309	208.51
S ₃		5.9507	0.0196	208.35
S ₄		5.9743	0.0045	207.53
S ₅		6.1312	0.0010	202.22
T ₁		4.8301		256.69
T ₂		5.1513		240.68
T ₃		5.3486		231.81
T ₄		5.6838		218.14
T ₅		5.8272		212.77

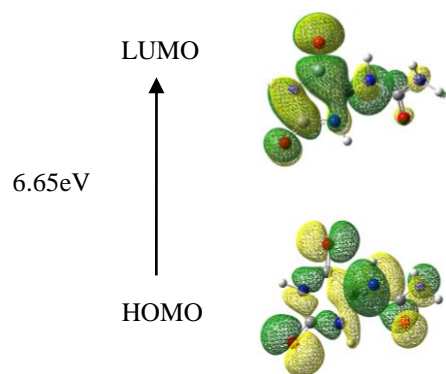


Figure 2: Electron density HOMO-LUMO surfaces of energy for GDU-I

TD-DFT results of the singlet states of GDU-I calculated at the B3LYP/6-311++G(d,p) level of theory as functions of the dihedral angle C-N-C=O =168°. When we excited the molecule with 5.26 eV (235.51 nm) energy it increased to the S₁ state and transition is LP(1)→ π^* . We need to more energies for excited to the S₂, S₃, S₄ and S₅ states see in Table 1.

The energy difference between the HOMO and LUMO for GDU-I is 6.65 eV and plotted in Figure 2.

Table 2: Stabilization energies for selected NBO pairs for GDU-I obtained from the B3LYP/6-311++G(d,p) calculations^a.

Pair	DonorNBO (i)	AcceptorNBO (j)	E(2) kJ/mol	E(j)-E(i) au	F(i,j) au
A	LP (1)N1	$\pi^*(C5-O7)$	182.88	0.29	0.102
B	LP (1) N1	$\pi^*(C5-O7)$	243.15	0.28	0.117
C	LP (1) N2	$\pi^*(C6-O17)$	241.90	0.28	0.116
D	LP (1) O7	Ry*(1) C5	77.12	1.84	0.165
E	LP(2) O7	$\sigma^*(N1 - C5)$	124.06	0.62	0.123
F	LP(2) O7	$\sigma^*(N2 - C5)$	103.41	0.70	0.120
G	LP (1) N10	$\pi^*(C12-O16)$	185.47	0.30	0.107
H	LP (1) N13	$\pi^*(C12-O16)$	195.21	0.31	0.112
I	LP (1) O16	Ry*(1) C12	73.82	1.77	0.158
J	LP (2) O16	$\sigma^*(N10 - C12)$	99.94	0.68	0.116
K	LP (2) O16	$\sigma^*(C12 - N13)$	98.02	0.68	0.115
L	LP (1) O17	Ry*(1) C6	74.24	1.67	0.154
M	LP (2) O17	$\sigma^*(N1 - C6)$	109.98	0.71	0.124
N	LP (2) O17	$\sigma^*(C3 - C6)$	92.38	0.60	0.105

^a See atom numbering in Figure 1. LP, lone electron pair orbital, Ry*, Rydberg orbital

A more detailed and powerful analysis of the electronic-type interactions within a molecule can be performed using NBO approach. According to this method, orbital interaction energies, $E(2)$, between filled (donor) and empty (acceptor) NBOs (including non-lewis extra valence Rydberg orbitals) are obtained from the second-order perturbation approach,

$$E(2) = \Delta E_{ij} - q_i \frac{F_{ij}^2}{\varepsilon_j - \varepsilon_i}$$

where F_{ij}^2 is the Fock matrix element between the i and j NBO orbitals, ε_j and ε_i are the energies of the acceptor and donor NBOs, and q_i is the occupancy of the donor orbital [8]. The most relevant NBO interactions for GDU-I are listed in Table 2 and plotted in Figure 3. NBO interaction energies are 243.15 and 241.90 kJ mol⁻¹ for B and C pairs, respectively. These interactions correlate with the electronic charge back-donation from the Nitrogen 1 and 2 lone electron pairs to the C5-O7 and C6-O17 π -anti bonds [9].

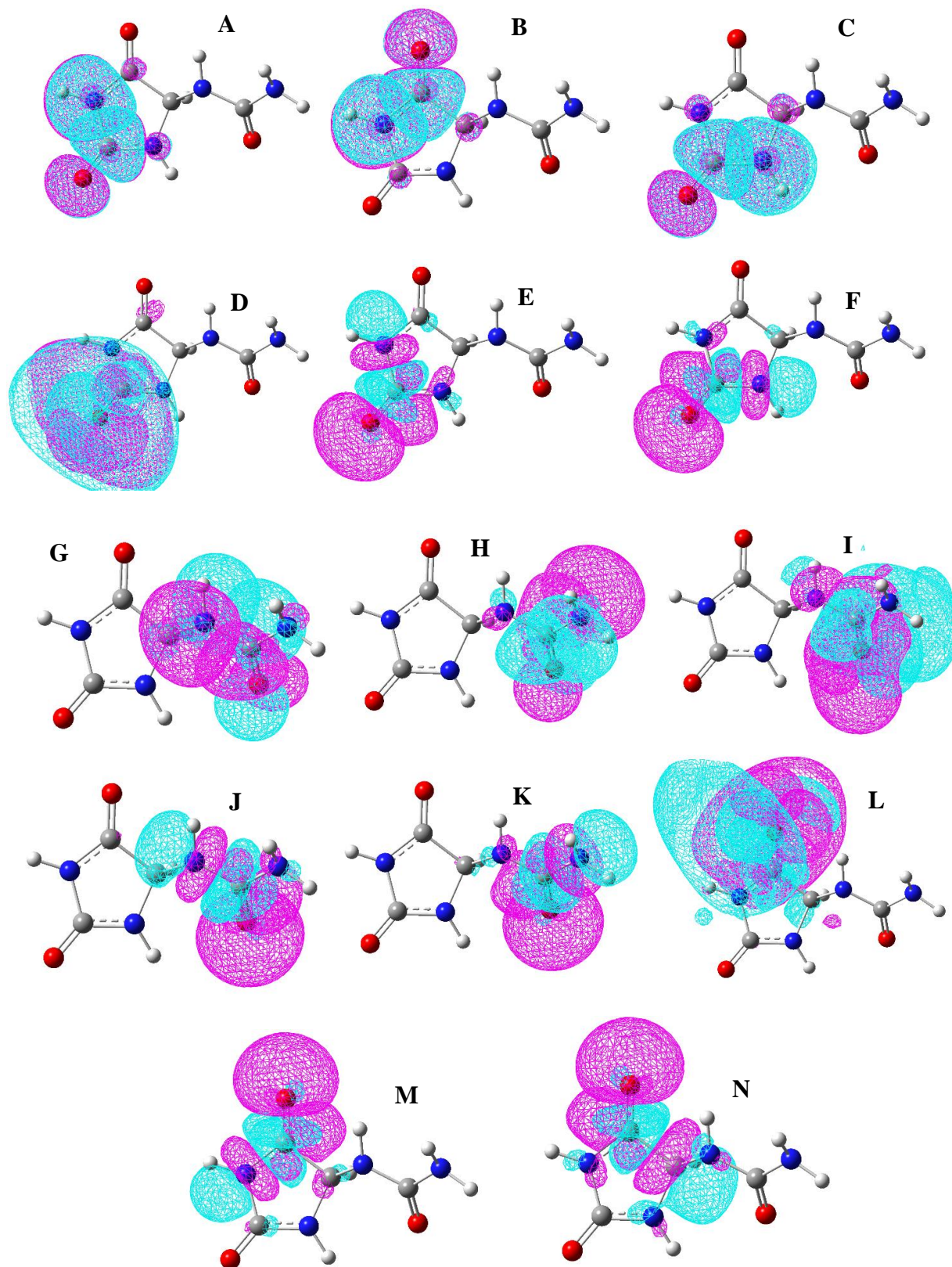


Figure 3: Electron density surfaces of selected NBOs for GDU-I calculated at the B3LYP/6-311++G(d,p) level of theory showing the dominant orbital interactions (see Table 2). Isovalues of the electron densities are equal to 0.02 e. Magenta and cyan colors correspond to negative and positive wave function signs. Color codes for atoms: red, O; gray, C; white, H; dark blue N.

The NBO charges for the GDU-I are shown in Table 3. The general trends regarding the charges on atoms in conformer I are identical. As anticipated, the N1-H9 bond is considerably polarized, whereas the C3-H4 bond is nonpolarized. For example in the molecule, the charges on N1 and H9 are -0.651 and +0.423e, whereas on C3 and H4 are +0.091 and +0.217 e [10].

Table 3: Natural Bond Orbital (NBO) atomic charges^a in GDU-I, obtained from B3LYP/6-311++G(d,p) calculations^b.

Atom	NBO charges
N1	-0.651
N2	-0.652
C3	0.091
H4	0.217
C5	0.812
C6	0.686
O7	-0.597
H8	0.430
H9	0.423
N10	-0.674
H11	0.402
C12	0.802
N13	-0.822
H14	0.384
H15	0.400
O16	-0.665
O17	-0.584

^a In units of electron; $e = 1.60217646 \times 10^{-19}$ C.

^b See in Figure 1 for atom numbering.

IV. CONCLUSION

The NBO and TD-DFT of Glyoxyldiureide (GDU) were studied using quantum chemical methods. The GDU-I conformer of the molecule was calculated to be the most stable form in the ground electronic state, being more stable than the other conformers 10.9, 13.68 and 17.90 kJ mol⁻¹, respectively. The relative stability of the GDU-I was explained using the NBO method. Stabilization energies for selected NBO pairs calculated and electron density surfaces were plotted. TD-DFT results helped us to find excited energy levels and HOMO-LUMO energy.

REFERENCES

- [1] A. V. Shestopalov, T. P. Shkurat, Z. I. Mikashinovich, I. O. Kryzhanovskaia, M. A. Bogacheva, S. V. Lomteva, V. P. Prokofev, E. P. Guskov, "Biological functions of allantoin", *Izv. Akad. Nauk.: Ser. Biol.*, vol. 5, pp. 541-545, 2006.
- [2] C. Thornfeldt, "Cosmeceuticals containing herbs: fact, fiction, and future", *Dermat. Surg.*, vol. 31, pp. 873-880, 2005.
- [3] M.J. Frisch, G.W. Trucks, H.B. Schlegel, G.E. Scuseria, M.A. Robb, J.R. Cheeseman, G. Scalmani, V. Barone, B. Mennucci, G.A. Petersson, H. Nakatsuji, M. Caricato, X. Li, H.P. Hratchian, A.F. Izmaylov, J. Bloino, G. Zheng, J.L. Sonnenberg, M. Hada, M. Ehara, K. Toyota, R. Fukuda, J. Hasegawa, M. Ishida, T. Nakajima, Y. Honda, O. Kitao, H. Nakai, T. Vreven, J.A. Montgomery, J.E. Peralta Jr, F. Ogliaro, M. Bearpark, J.J. Heyd, E. Brothers, K.N. Kudin, V.N. Staroverov, R. Kobayashi, J. Normand, K. Raghavachari, A. Rendell, J.C. Burant, S.S. Iyengar, J. Tomasi, M. Cossi, N. Rega, J.M. Millam, M. Klene, J.E. Knox, J.B. Cross, V. Bakken, C. Adamo, J. Jaramillo, R. Gomperts, R.E. Stratmann, O. Yazyev, A.J. Austin, R. Cammi, C. Pomelli, J.W. Ochterski, R.L. Martin, K. Morokuma, V.G. Zakrzewski, G.A. Voth, P. Salvador, J.J. Dannenberg, S. Dapprich, A.D. Daniels, O. Farkas, J.B. Foresman, J.V. Ortiz, J. Cioslowski, D.J. Fox, Gaussian 09, Revision A.0.2, Gaussian, Inc., Wallingford CT, 2009.
- [4] R. Bauernschmitt, R. Ahlrichs, "Treatment of electronic excitations within the adiabatic approximation of time dependent density functional theory", *Chem. Phys. Lett.*, vol. 256, pp. 454-464, 1996.
- [5] R. E. Stratmann, G. E. Scuseria, M. J. Frisch, "An efficient implementation of time-dependent density-functional theory for the calculation of excitation energies of large molecules", *J. Chem. Phys.*, vol. 109, pp. 8218-8224, 1998.
- [6] A. E. Reed, L. A. Curtiss, F. Weinhold, "Intermolecular interactions from a natural bond orbital, donor-acceptor viewpoint", *Chem. Rev.*, vol. 88, pp. 899-926, 1988.
- [7] N. Kus, S. Haman Bayarı, R. Fausto, "Thermal decomposition of allantoin as probed by matrix isolation FTIR spectroscopy", *Tetrahedron*, vol. 65, pp. 9719-9727, 2009.
- [8] F. Weinhold, C. R. Landis, *Valency and Bonding. A Natural Bond Orbital Donor-Acceptor Perspective*. Cambridge University Press: New York, 2005.
- [9] J. B. Moffat, *Theoretical Aspects of Heterogeneous Catalysis*. Springer Science & Business Media, 2013.
- [10] R. P. Gangadharan and S. S. Krishnan, "Natural Bond Orbital (NBO) Population Analysis of 1-Azanaphthalene-8-ol", *Acta Physica Polonica A* vol, 125, pp. 18-22, 2013.

Elicitation of biomaterials for mimicking microphysiological systems-on-a-chip

Ecem SAYGILI and Ozlem YESIL CELIKTAS

Ege University, Izmir/Turkey, ecem.sygl@gmail.com
Ege University, Izmir/Turkey, ozlem.yesil.celiktas@ege.edu.tr

Abstract - As the cell culture based *in vitro* assays have a vital role in biomedical field, there is an increasing demand for tissue analogues to screen and functionalize tissue/organ models via microfluidic platforms. Depending on the desired application, the material selection and design of microchannels must be compatible to meet the demands. Thus, the materials for microfluidic platforms should present the appropriate properties. This study presents some of the advantages and challenges of using thermoplastics, thermosets and elastomers for microfluidic systems.

Keywords – polymers, microfluidics, cell culture, tissue models

I. INTRODUCTION

The increasing demand for tissue analogues in the medical field creates *in vivo* requirements such as screening, miniaturization and robust tissue and organ models. *In vitro* experiments are an important research tool for tissue engineering. Despite routine practice, current methods of analysis remain insufficient to demonstrate the physiological response of cellular microenvironment to external factors and cells *in vitro* function. Microfluidic applications, such as organs-on-chip systems, aims to overcome this problem and mimic the basic functions of organs with microengineering technology [1–3]. Polymers are necessary materials that offer a new perspective on 3D cell culture models via microfluidic technology. They enable nutrients and other soluble components to effectively reach and diffuse into 3D tissue structures. Compared to other materials, polymers have low mechanical strength, low melting point and high electrical resistance. The greatest advantage is that they can be designed or synthesized with the desired properties according to the intended function. Furthermore, surface modifications can be made to improve the properties of many polymers such as biocompatibility, solvent resistance, surface chemistry. Polydimethylsiloxane (PDMS) has been used as a traditional polymer for cell culture studies owing to its features such as transparency, auto-fluorescence and its gas permeability. However, it is known that PDMS absorbs solvents and analytes and it swells when in contact with a range of liquids [4, 5]. Thus, off-stoichiometry thiol-ene-epoxies (OSTE+) with a two-stage curing process and polysulfone (PFS) polymers, which are a hard and processable thermoplastic

polymers, can be used alternatively to elastomer-based polymers such as PDMS because they have low surface adsorption and no small molecules bulk adsorption [6, 7].

II. METHODS

A. PDMS Based Microplatforms

PDMS, the most investigated polymer in microfluidic, is a cheap, non-toxic and optically permeable material. It belongs to a broader class of polymers, commonly known as silicon or polysiloxane, characterized by a siloxane skeleton of silicon and oxygen atoms. It can also remain chemically stable in very different environments. Though PDMS can swell in solvent, some additives have been shown to reduce this swelling. Since PDMS is a transparent material and provide very good permeability to gases, it can be used in live cell imaging studies. Because of its features, PDMS is the most widely used polymer in microfluidic applications like organs-on-a-chip systems [4]. For instance, in the study conducted by Grosberg et al. (2011), a heart-on-a-chip system was obtained using a musculus thin film platform. This platform was formed by planting cells on an elastic thin film and the PDMS surface was covered with fibronectin to align the cells [8]. In the study, the PDMS surface was covered with fibronectin to align the cells. Similarly, Punde et al. (2015) chose to use PDMS as the membrane interface in their work to mimic the lung microenvironment. The only microfluidic applications in which PDMS and similar materials are used are not organs-on-chip systems. It is stated that using microfluidics for enzymatic reactions provides a few advantages such as decreased consumption of valuable catalysts and reagents, controllable reaction conditions [9]. Yildiz-Ozturk et al. (2017) fabricated a S-shaped PDMS microplatform to determine the dispersion coefficient of the model substrates, 4-Nitrophenyl- β -D-glucopyranoside (pNPG₁) and 4-Nitrophenyl- β -D-glucuronide (pNPG₂) for β -glucosidase and β -glucuronidase [10].

According to the general production method of PDMS-based microplatforms; well-mixed uncured PDMS solution is prepared in the rate of 10:1 sylgard 184/sylgard 184 curing agent. Then, vacuum is applied to the mixture to remove air bubbles and then PDMS heated to be cured for 1.5 hours at 80 °C (Figure 1).

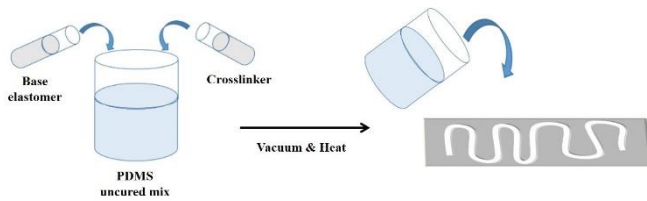


Figure 1. PDMS-based microfabrication.

In general, mold is used to have the desired microchannel shape on to the PDMS material. Thus, solutions are poured to the mold and then left to be cured. Lastly, obtained microchannels are covered to be supported by slides such as glass or PMMA sheets (Figure 2).

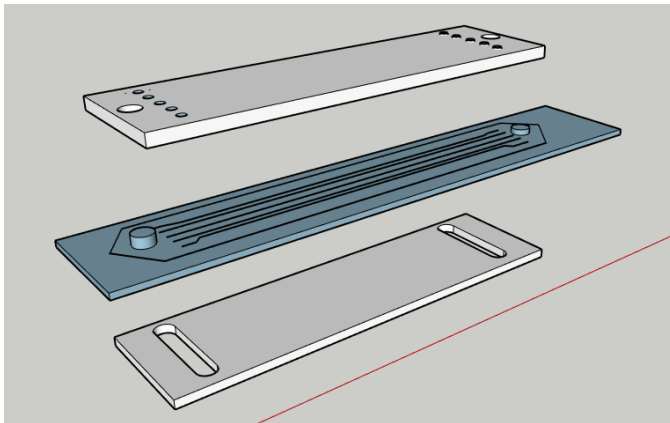


Figure 2. Supporter materials for microplatforms.

B. OSTE+ Polymerization

Off stoichiometry thiol-ene-epoxy (OSTE), an UV-curable polymer, has tunable mechanical properties can be achieved according to proportion of available thiol and ene monomers. Also, it has been showed in many studies that OSTE-based platform removes a few disadvantages of PDMS while preserving PDMS-related qualities and manufacturing convenience. Sticker et al. (2015), conducted a study to assess the biocompatibility of OSTE as a suitable cell culture material. In this study, viability, cell adhesion characteristics and morphology of epithelial, fibroblast and mesenchymal stem cells were investigated [6]. Although OSTE systems have advantages in microfluidic platforms, they have some disadvantages, such as the presence of unreacted monomers that induce cytotoxicity and cause a change in glass transition temperature. To solve this problem, a third epoxy component is added to the present OSTE prepolymer and the newly synthesized epoxy-containing polymer is named "OSTE +" where "+" represents the added epoxy component. OSTE + is also suitable for biological analysis thanks to its transparency and double curing process. This material not only solves the problems related to OSTE, but most importantly it brings the material into the field of bioanalysis with its customizable

surface feature. These features have allowed OSTE to take its place in cell culture applications. However, Fredrik et al. (2015), observed in their study in which they developed an OSTE + polymer-based neural probe that OSTE + was cytotoxic on cells. But, they also report that when OSTE + incubated in with water for a week, the cytotoxicity was not exist [11].

In general, there is a two-step development process including heat and UV stages for OSTE + material. Depending on the application, the order of the steps can be changed (Figure 3).

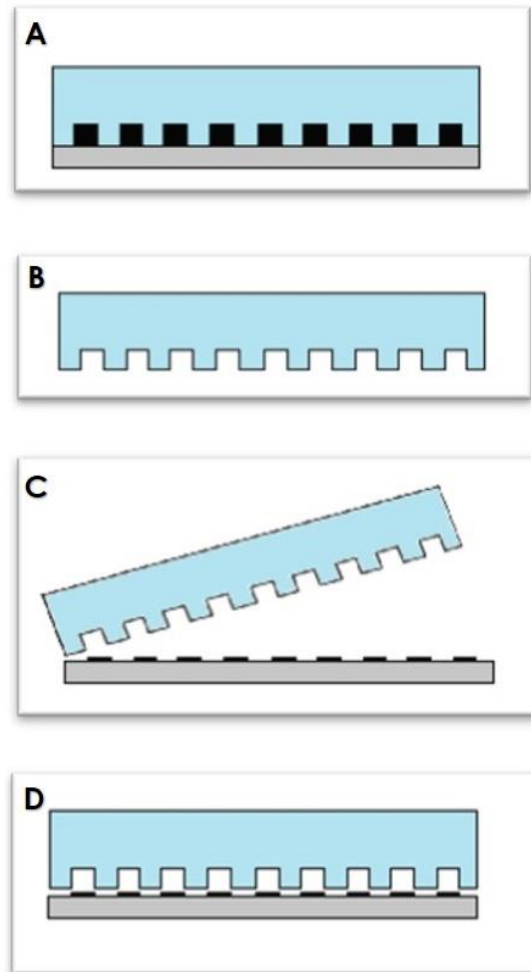


Figure 3. OSTE and mold bonding via UV application (A); peeling of semi-cured OSTE material from mold (B); bonding semi-cured OSTE material to the desired slide (C,D).

C. A Thermoplastic Polymer: Polysulfone (PSF)

The production process of thermoplastics such as poly (methyl methacrylate) (PMMA), polystyrene, polysulfone (PSF) and polycarbonate is a cost effective process. Besides, materials are, biocompatible and possess excellent optical properties. For the production of thermoplastics, metal or silicone molds are generally used which have high temperature resistance. Thus, it is possible to produce high amounts and at low cost.

As the surface properties of the thermoplastics are not similar to PDMS's, to contact with the other materials, thermoplastics needs surface modifications like coating [12].

As an autoclavable thermoplastic material, PSF is resistant to various chemicals. Due to its thermoplastic polymer properties it is widely used for medical devices. Researchers used polysulfone as one of the layer of their multi-layered *in vitro* platform [7]. They used a rigid and machinable PSF to construct the platform's fluid handling section (Figure 4). In a similar study, Tsamandouras et al. (2017) used polysulfone as fluidic plate instead of using PDMS. Same researchers reported the absence of non-specific binding to PSF by using LiverChip™ [13].

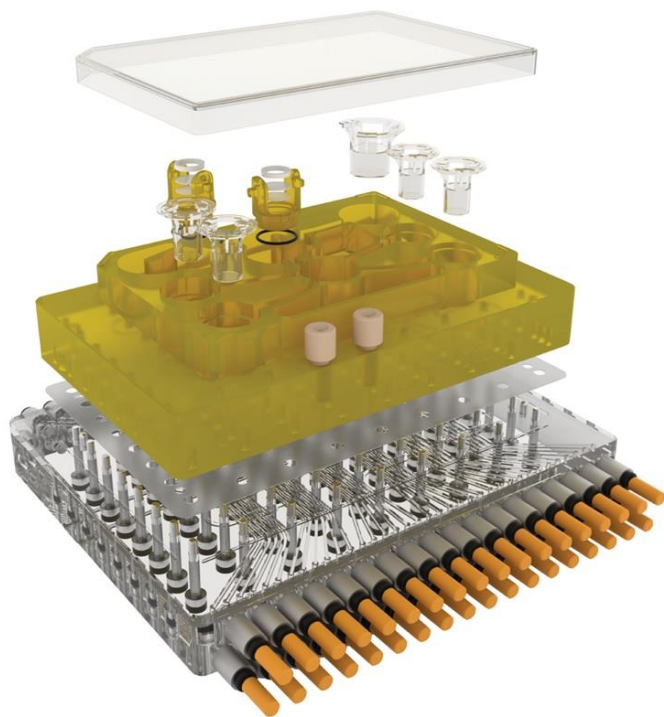


Figure 4. Polysulfone (PSF) based fluid handling section [13] Printed with permission from Nature Publishing Group.

III. CONCLUSION

In this paper, we have presented a research in regards to the most popular polymer types and their usage parameters for microfluidic platforms. Considering the current literature, it is clear that PDMS has many excellent physical properties, which make it useful in microfluidic applications. However, its ability to absorb hydrophobic small molecules is a disadvantage for many applications. Recent studies show that using OSTE, OSTE + and PSF polymers can overcome this undesired outcomes. Compared to PDMS, it is known that both OSTE and PSF materials have more rigid structures and neither of those absorb hydrophobic materials. Besides, their excellent bonding properties, OSTE polymers are ideal materials for microfabrication of cell-based assays. However, the fact that OSTE polymers are not as biocompatible as

PDMS should be considered.

IV. REFERENCES

- [1] C. Luni, E. Serena, and N. Elvassore, "Human-on-chip for therapy development and fundamental science," *Curr. Opin. Biotechnol.*, vol. 25, pp. 45–50, 2014.
- [2] A. Polini, L. Prodanov, N. S. Bhise, V. Manoharan, M. R. Dokmeci, and A. Khademhosseini, "Organs-on-a-chip: a new tool for drug discovery," [Http://Dx.Doi.Org/10.1517/17460441.2014.886562](http://dx.doi.org/10.1517/17460441.2014.886562), pp. 335–352, 2014.
- [3] S. N. Bhatia and D. E. Ingber, "Microfluidic organs-on-chips," *Nat. Biotechnol.*, vol. 32, no. 8, pp. 760–772, 2014.
- [4] B. J. van Meer *et al.*, "Small molecule absorption by PDMS in the context of drug response bioassays," *Biochem. Biophys. Res. Commun.*, vol. 482, no. 2, pp. 323–328, 2017.
- [5] M. W. Toepke and D. J. Beebe, "PDMS absorption of small molecules and consequences in microfluidic applications," *Lab Chip*, vol. 6, no. 12, pp. 1484–1486, 2006.
- [6] D. Sticker, M. Rothbauer, S. Lechner, M. T. Hehenberger, and P. Ertl, "Multi-layered, membrane-integrated microfluidics based on replica molding of a thiol-ene epoxy thermoset for organ-on-a-chip applications," *Lab Chip*, vol. 15, no. 24, pp. 4542–4554, 2015.
- [7] C. D. Edington *et al.*, "Interconnected Microphysiological Systems for Quantitative Biology and Pharmacology Studies," *Sci. Rep.*, vol. 8, no. 1, pp. 1–18, 2018.
- [8] A. Grosberg, P. W. Alford, M. L. McCain, and K. K. Parker, "Ensembles of engineered cardiac tissues for physiological and pharmacological study: Heart on a chip," *Lab Chip*, vol. 11, no. 24, pp. 4165–4173, 2011.
- [9] T. H. Punde *et al.*, "A biologically inspired lung-on-a-chip device for the study of protein-induced lung inflammation," *Integr. Biol. (United Kingdom)*, vol. 7, no. 2, pp. 162–169, 2015.
- [10] E. Yildiz-Ozturk, S. Gulce-Iz, M. Anil, and O. Yesil-Celiktas, "Cytotoxic responses of carnosic acid and doxorubicin on breast cancer cells in butterfly-shaped microchips in comparison to 2D and 3D culture," *Cytotechnology*, vol. 69, no. 2, pp. 337–347, 2017.
- [11] F. Ejserholm *et al.*, "Biocompatibility of a polymer based on Off-Stoichiometry Thiol-Enes + Epoxy (OSTE+) for neural implants," *Biomater. Res.*, vol. 19, no. 1, pp. 1–10, 2015.
- [12] D. Sameoto and A. Wasay, "Materials selection and manufacturing of thermoplastic elastomer microfluidics," vol. 9320, p. 932001, 2015.
- [13] N. Tsamandouras, W. L. K. Chen, C. D. Edington, C. L. Stokes, L. G. Griffith, and M. Cirit, "Integrated Gut and Liver Microphysiological Systems for Quantitative In Vitro Pharmacokinetic Studies," *AAPS J.*, 2017.

Hybrid Orbital Localization of E-Crotonic Acid using NBO Analysis

S. ILICAN¹ and N. KUŞ²

¹Eskisehir Technical University, Eskisehir/Turkey, salihailican@gmail.com

²Eskisehir Technical University, Eskisehir/Turkey, nkus@anadolu.edu.tr

Abstract - E-crotonic acid (ECA, C₄H₆O₂) is the smallest carboxylic acid which has three conformers with planar C₁ symmetry and one conformer with nonplanar C_s symmetry. All conformers were optimized using Density Function Theory (DFT) level using the 6-311++G(d,p) basis set and the B3LYP functional. The second-order Fock matrix was used to evaluate the donor-acceptor interactions in the Natural Bond Orbital (NBO) basis. The bond polarization and hybridization effects in wave functions associated with formation of the conformers. All calculations are performed by using Gauss-View molecular visualization program and Gaussian 03 program package. HOMO-LUMO energy value of ECA-I calculated and found to be about 6.15eV. Molecular Electrostatic Potential (MEP) surfaces of all the conformers were mapped.

Keywords – E-crotonic acid, DFT, NBO, HOMO-LUMO energy, MEP.

I. INTRODUCTION

Unsaturated carboxylic acid, one of them is crotonic acid (CA), has special chemical structure, can be used in the chemical industry, for example pharmaceutical intermediates materials, surface coating, plasticizer, preparation of fungicides and resin [1-3]. Molecules which are containing carboxylic acid are absorbing blocks for more complex raw chemicals, on the other hand they are not economically competitive [4, 5]. CA was thought to be important due to these disclosures and it deserved to be researched.

CA has two different isomers (E- and Z-) [6]. In our study, E- form (E-crotonic acid, ECA) was computed and analyzed. The results of natural bond orbital (NBO) analysis have been investigated the hybridization, charge distribution and electrostatic potential density for atoms of ECA. Donor and acceptor interactions were determined with selected stronger stabilization energy (>10%) using second-order perturbation equation (Fock matrix). Strongest electron donation formed from lone pair oxygen to anti-bonding C-O.

II. COMPUTATIONAL DETAILS

All calculations were carried out with the Gaussian 03 package programme [7]. The calculations of systems containing C, H, and O are defined by the standard 6-311++G(d,p) basis set function of B3LYP density functional

theory (DFT) [8-10]. The relative stability of the conformers was performed by the natural bond orbital (NBO) method level of theory, according to Weinhold and co-workers, using NBO 3 program under Gaussian 03 programme [11].

III. RESULTS AND DISCUSSION

The potential energy surface was scanned with the Gaussian 03 suit of programs at the DFT level of theory, using the 6-311++G(d,p) basis set, it found four minimum of ECA (Fig. 1). It was observed that three of the conformers were planar, while the other one was non-planar. In this study, only planar conformations were analyzed. DFT calculation results gave rise that ECA-I was the most stable form.

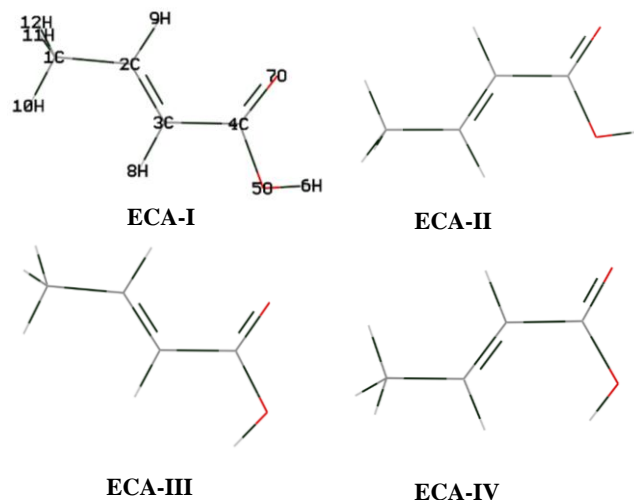


Figure 1: Conformers of E-crotonic acid.

NBO method plays a major role in intermolecular orbital interactions in the compound. According to this method, orbital interaction energies, $E(2)$, between filled (donor) and empty (acceptor) NBOs (including non-Lewis extra valence Rydberg orbitals) are obtained from the second-order perturbation approach,

$$E(2) = \Delta E_{ij} - q_i \frac{F_{ij}^2}{\varepsilon_j - \varepsilon_i}$$

where F_{ij}^2 is the Fock matrix element between the i and j NBO orbitals, ε_j and ε_i are the energies of the acceptor and donor NBOs, and q_i is the occupancy of the donor orbital [12]. The most relevant NBO interactions for three conformers (ECA-I, ECA-II and ECA-III) are listed in Table 1 and plotted in Figure 2. The higher NBO interaction energies are 175.80, 173.54 and 167.72 kJ mol⁻¹ for ECA-I, ECA-II and ECA-III, respectively. These interactions correlate with the electronic charge back-donation from the O5 to the anti-bonding C4-O7 for all conformers (see Fig. 2: ECA-I.b, ECA-II.b and ECA-III.b pairs).

Table 1: Stabilization energies for selected NBO pairs for ECA-I, ECA-II and ECA-III obtained from the B3LYP/6-311++G(d,p) calculations^a.

Pair	Donor NBO (i)	Acceptor NBO (j)	$E(2)$ kJ/mol	$E(j)-E(i)$ au	$F(i,j)$ au
ECA-I.a	$\pi(C2-C3)$	$\pi^*(C4-O7)$	86.29	0.29	0.072
ECA-I.b	LP (2) O5	$\pi^*(C4-O7)$	175.80	0.35	0.110
ECA-I.c	LP (1) O7	Ry*(1)C4	70.72	1.77	0.154
ECA-I.d	LP (2) O7	$\sigma^*(C3-C4)$	71.43	0.70	0.100
ECA-I.e	LP(2) O7	$\sigma^*(C4-O5)$	140.51	0.60	0.129
ECA-II.a	$\pi(C2-C3)$	$\pi^*(C4-O7)$	85.33	0.29	0.071
ECA-II.b	LP (2) O5	$\pi^*(C4-O7)$	173.54	0.35	0.110
ECA-II.c	LP (1) O7	Ry*(1)C4	65.15	1.80	0.149
ECA-II.d	LP (2) O7	$\sigma^*(C3-C4)$	67.58	0.70	0.097
ECA-II.e	LP(2) O7	$\sigma^*(C4-O5)$	140.80	0.60	0.128
ECA-III.a	$\pi(C2-C3)$	$\pi^*(C4-O7)$	79.80	0.31	0.071
ECA-III.b	LP (2) O5	$\pi^*(C4-O7)$	167.72	0.35	0.108
ECA-III.c	LP (1) O7	Ry*(1)C4	74.15	1.78	0.158
ECA-III.d	LP (2) O7	$\sigma^*(C3-C4)$	74.73	0.67	0.100
ECA-III.e	LP(2) O7	$\sigma^*(C4-O5)$	141.68	0.59	0.129

^a See atom numbering in Figure 1. LP, lone electron pair orbital, Ry*, Rydberg orbital.

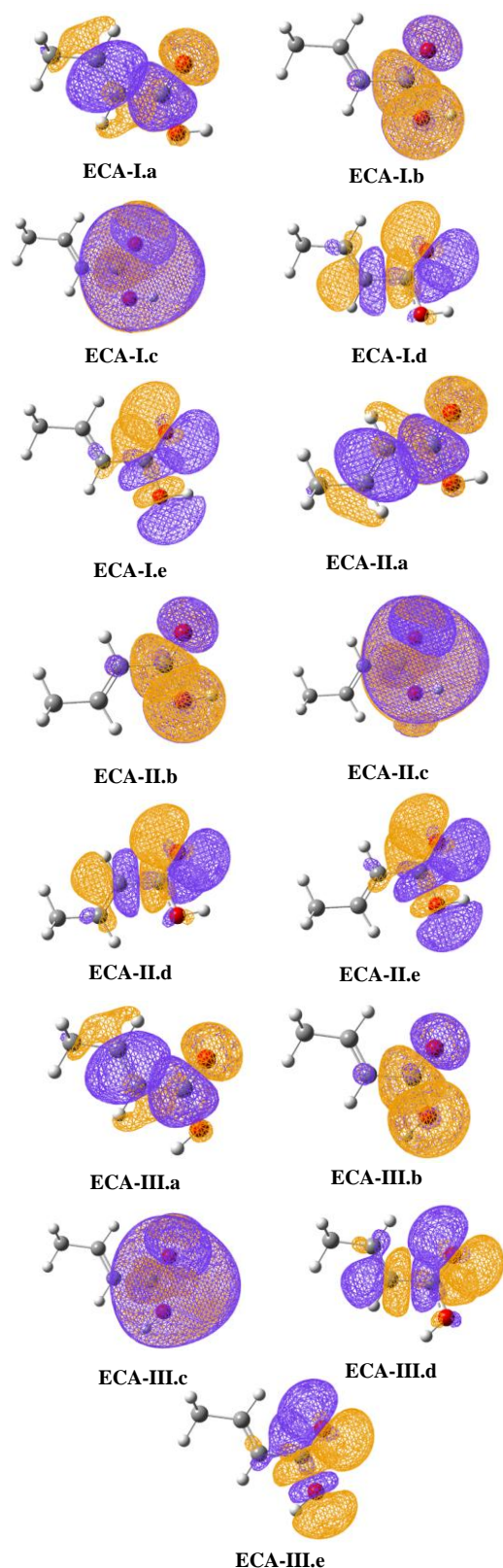


Figure 2: Electron density surfaces of selected NBOs for ECA-I, ECA-II and ECA-III calculated at the B3LYP/6-311++G(d,p) level of theory showing the dominant orbital interactions (see Table 2). Isovalues of the electron densities are equal to 0.02 e. Purple and yellow colors correspond to negative and positive wave function signs. Color codes for atoms: red, O; gray, C; white, H.

The highest occupied molecular orbital (HOMO) and lowest unoccupied molecular orbital (LUMO) are the main orbitals taking part in chemical reaction. The energy difference between the HOMO and LUMO for ECA-I is 6.15eV (Fig. 3).

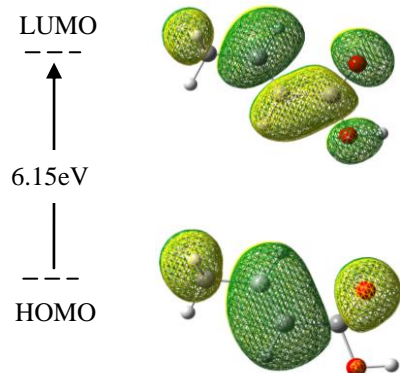


Figure 3: Electron density HOMO-LUMO surfaces of energy for ECA-I.

ECA-I	
H(0.220) H(0.220) C(-0.615)	H(0.207) (-0.066) O(-0.609) C(-0.334) C(-0.766) H(0.211) O(-0.666) H(0.482)
H(0.206)	
ECA-II	
H(0.207) C(-0.614) H(0.219) H(0.219)	H(0.213) O(-0.595) C(-0.323) C(-0.763) (-0.078) O(-0.700) H(0.485) H(0.204)
H(0.222) H(0.222) C(-0.615)	H(0.213) O(-0.573) (-0.063) C(-0.355) C(-0.763) H(0.189) O(-0.673) H(0.466)

Figure 4: NBO charges (Units of electron; $e=1.60217646 \times 10^{-19} \text{C}$) for ECA-I, ECAII and ECA-III, obtained from B3LYP/6-311++G(d,p) calculations (See in Figure 1 for atom numbering).

The NBO charges were calculated by methods B3LYP/6-311++G(d,p) for the all conformers and shown in Figure 4. The oxygens have a maximum negative charge about -0.69e and -0.61e in ECA-I, -0.70e and -0.60e in ECA-II and -0.67e and -0.57e in ECA-III. The hydrogen atom which bounded

with oxygen has maximum positive charge about +0.48e, +0.49e and +0.47e in ECA-I, ECA-II and ECA-III, respectively [13].

Molecular electrostatic potential (MEP) surface map illustrates the charge distributions of molecules three dimensionally, and it correlates the total charge distribution with dipole moment, electronegativity, and partial charges and site of chemical reactivity of a molecule. This map allows us to visualize variably charged regions of a molecule. In this study, mapping of the electrostatic potential onto the molecular surface was performed with GaussView5, and given in Figure 5. Different values of the electrostatic potential at the surface of a molecule appear with the different colors. The colors in Figure 5 were chosen such that regions of attractive potential appear in red and those of repulsive potential appear in blue. Negative electrostatic potential corresponds to an attraction of the proton by the concentrated electron density in the molecules. As a result, the maps of all the conformers showed that the oxygen atom carrying an electron already (O5) is not attractive to a negative test charge, while the opposite is exactly true for the other oxygen atom (O7).

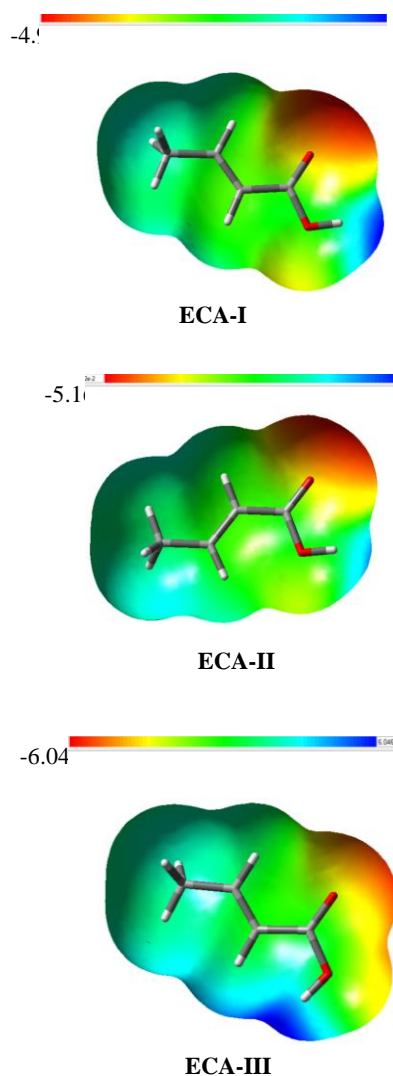


Figure 5: Molecular electrostatic potential surfaces for ECA-I, ECA-II and ECA-III.

IV. CONCLUSION

The NBO analysis for ECA conformers were studied using quantum chemical methods. The relative stability of the ECA conformers were analyzed using the NBO method. Stabilization energies for selected NBO pairs calculated and electron density surfaces were plotted. HOMO-LUMO energy of ECA-I was calculated and found to be about 6.15eV. MEP surfaces and NBO charges were determined for all conformers according to Schrödinger equation.

REFERENCES

- [1] E. Hack, D. Hümmer, M. Franzre, "Concentration of crotonic acid using capacitive deionization technology", *Sep. Purif. Technol.*, vol. 209, pp. 658-665, 2019.
- [2] R. Ulber, D. Sell (Eds.), *White Biotechnology-Advantages in Biochemical Engineering Biotechnology*, Springer Verlag, 2007.
- [3] J.A. Asenjo, *Separation Processes in Biotechnology*, Marcel Dekker Inc., New York, 1990.
- [4] I. J. Misiak, P.P. Wieczorek, P. Kafarski, "Crotonic acid as a bioactive factor in carrot seeds (*Daucus carota* L.)", *Phytochemistry*, vol. 66(12) pp. 1485-1491, 2005.
- [5] C. Castro, A. C. Promo, "Solid state cyanocobaltates that reversibly bind dioxygen: synthesis, structure and reactivity relationships", *J. Mol. Catal. A: Chem.*, vol. 117(1-3), pp. 273-278, 2002.
- [6] N. Kuş, R. Fausto, "Near-infrared and ultraviolet induced isomerization of crotonic acid in N₂ and Xe cryomatrices: First observation of two high-energy trans C–O conformers and mechanistic insights", *J. Chem. Phys.*, vol. 141, pp.234310, 2014.
- [7] Gaussian 03, Revision C.02, M. J. Frisch, G. W. Trucks, H. B. Schlegel, G. E. Scuseria, M. A. Robb, J. R. Cheeseman, J. A. Montgomery, Jr., T. Vreven, K. N. Kudin, J. C. Burant, J. M. Millam, S. S. Iyengar, J. Tomasi, V. Barone, B. Mennucci, M. Cossi, G. Scalmani, N. Rega, G. A. Petersson, H. Nakatsuji, M. Hada, M. Ehara, K. Toyota, R. Fukuda, J. Hasegawa, M. Ishida, T. Nakajima, Y. Honda, O. Kitao, H. Nakai, M. Klene, X. Li, J. E. Knox, H. P. Hratchian, J. B. Cross, V. Bakken, C. Adamo, J. Jaramillo, R. Gomperts, R. E. Stratmann, O. Yazyev, A. J. Austin, R. Cammi, C. Pomelli, J. W. Ochterski, P. Y. Ayala, K. Morokuma, G. A. Voth, P. Salvador, J. J. Dannenberg, V. G. Zakrzewski, S. Dapprich, A. D. Daniels, M. C. Strain, O. Farkas, D. K. Malick, A. D. Rabuck, K. Raghavachari, J. B. Foresman, J. V. Ortiz, Q. Cui, A. G. Baboul, S. Clifford, J. Cioslowski, B. B. Stefanov, G. Liu, A. Liashenko, P. Piskorz, I. Komaromi, R. L. Martin, D. J. Fox, T. Keith, M. A. Al-Laham, C. Y. Peng, A. Nanayakkara, M. Challacombe, P. M. W. Gill, B. Johnson, W. Chen, M. W. Wong, C. Gonzalez, and J. A. Pople, Gaussian, Inc., Wallingford CT, 2004.
- [8] P. C. Hariharan, J. A. Pople, "The influence of polarization functions on molecular orbital hydrogenation energies", *Theor. Chim. Acta*, vol. 28(3), pp. 213-222, 1973.
- [9] R. Bauernschmitt, R. Ahlrichs, "Treatment of electronic excitations within the adiabatic approximation of time dependent density functional theory", *Chem. Phys. Lett.*, vol. 256, pp. 454-464, 1996.
- [10] R. E. Stratmann, G. E. Scuseria, M. J. Frisch, "An efficient implementation of time-dependent density-functional theory for the calculation of excitation energies of large molecules", *J. Chem. Phys.*, vol. 109, pp. 8218-8224, 1998.
- [11] A. E. Reed, L. A. Curtiss, F. Weinhold, "Intermolecular interactions from a natural bond orbital, donor-acceptor viewpoint", *Chem. Rev.*, vol. 88, pp. 899-926, 1988.
- [12] F. Weinhold, C. R. Landis, *Valency and Bonding. A Natural Bond Orbital Donor-Acceptor Perspective*. Cambridge University Press: New York, 2005.
- [13] R. P. Gangadharana, S. S. Krishnan, "Natural Bond Orbital (NBO) Population Analysis of 1-Azanaphthalene-8-ol", *Acta Physica Polonica A*, vol. 25, pp. 18-22, 2014.

Fabrication of diffusion and internal gelation-based alginate-silica hybrid hydrogels for enzyme immobilization

Rabia ONBAS¹ and Ozlem YESIL CELIKTAS¹

¹ Ege University, Izmir/Turkey rabiaonbas@gmail.com

¹Ege University, Izmir/Turkey, ozlem.yesil.celiktas@ege.edu.tr

Abstract – The organic-inorganic hybrid materials have been preferred in various studies to immobilize biomolecules. The aim of this study was to compare two different synthesis methods in terms of enzymatic activity. Moreover, the new formulated internal gelation-based method was developed which yields homogenous gels with the possibility to control gelation rates. Thanks to these properties, this gel can be injected into microchannels, which allows the development of enzymatic microreactors to overcome limitations of immobilized enzymes in monoliths.

Keywords – diffusion gelation method, internal gelation method, alginate-silica hybrid gel, β -glucosidase

I. INTRODUCTION

Alginate is a naturally occurring anionic polymer typically obtained from brown algae that is comprised of α -L-guluronate (G units) and β -D-mannuronic acid (M units) residues. It is a very attractive biopolymer for researchers because it is biocompatible, low toxic and affordable [1, 2]. More importantly, it is capable of forming a soft gel with divalent cations in mild conditions. However, environmental changes (temperature, pH) result in enzyme leakage [3]. In order to overcome these difficulties alginate can combine with silica which provides various advantages such as good moldability, chemical resistance and mechanical stability. Due to these properties, it is possible to prevent enzyme denaturation [4, 5].

There are two methods to synthesize alginate-silica hybrid hydrogel which are known as diffusion/external and internal gelation-based methods by ionic cross-linking [6]. In diffusion-based method, divalent cations are generally formed by calcium diffusion into the alginate bead from outer CaCl_2 solution. Gelation occurs very fast which results in concentration gradient and inhomogenous structure. Also, very limited shapes can be obtained such as beads, fibres or films [7]. The internal gelation-based method uses CaCO_3 as a Ca^{2+} source, which provides uniform distribution in alginate. Acidic environment (GDL; D-glucono-d-lactone) leads to the release of Ca^{2+} ions that provide controllable and homogenous gelation. Moreover, molding of gels is possible in different shapes [8]. As gelation occurs by ionic cross-linking, there are

no toxic materials used in these methods which prevent enzyme denaturation.

II. METHODS

A. Free Enzyme Kinetics

The Michaelis–Menten constant (K_M) and maximal reaction rate (V_{max}) were determined for free enzyme. Enzyme amount of β -glucosidase was kept constant (4 μg) while pNPG concentration was between 1–100 mM for free enzyme.

B. Enzyme Immobilization with Diffusion Gelation Method

For enzyme immobilization, 5 mL preformed silicic acid sol (1.5 M) was adjusted to pH 5.1 (± 0.1) with NaOH 0.1 M and mixed with 5 g 3 wt% sodium alginate solution (alginic acid sodium salt, from brown algae, Aldrich) and 4 μg of β -glucosidase. This mixture was then dropped into an aqueous solution which has polydiallyldimethylammonium chloride (PDADMAC) (0.4 wt%) (20 wt% in H_2O , Aldrich) and CaCl_2 (20 mM). Then beads were incubated 3 h [7].

The Michaelis–Menten constant (K_M) and maximal reaction rate (V_{max}) were determined for immobilized enzyme in alginate silica hybrid beads. The amount of β -glucosidase was kept constant (4 μg) while pNPG concentration was between 1–40 mM for immobilized enzyme.

C. Enzyme Immobilization with Internal Gelation Method

Internal gelation method [9] was prepared by modification of the method reported by Desmet et al. (2014) [10]. About 0.1825 g CaCO_3/g sodium alginate and 5 g (2 wt %) sodium alginate solution were mixed and homogenized for 1 h [11]. Polydiallyldimethylammonium chloride (PDADMAC, 20 wt.% in H_2O) (30 μl) which catalyzes the polycondensation of the silica precursor was mixed with 5 ml (0.75 M) preformed silicic acid sol and the solution was adjusted to pH 4.8 (± 0.1) with NaOH (0.1 M). In order to release Ca^{+2} ions and trigger gelation 3 ml of 100 mM freshly prepared GDL was added to sodium alginate- CaCO_3 solution [12]. Then, silicic acid-PDADMAC solution and sodium alginate containing CaCO_3 solution were homogenized for a few minutes. Monoliths were

prepared in a syringe and left for 24 h aging.

The enzymatic activities of both free and immobilized enzyme were assayed with 4-nitrophenyl β -D-glucopyranoside (pNPG) was used as a substrate for the enzymatic activities of free and immobilized enzyme. The reaction medium comprised of buffer solution (50 mM Ca-Na acetate buffer, pH 4.8), 4 μ g β -glucosidase enzyme, and 20 mM pNPG (Sigma-Aldrich). The reaction condition was, 37°C rotating at 100 rpm for 15 min. After incubation, the reaction was stopped by adding 100 mM Na₂CO₃. UV-vis spectroscopy was used to detect the amount of 4-nitrophenyl (pNP) at 420 nm.

III. RESULTS

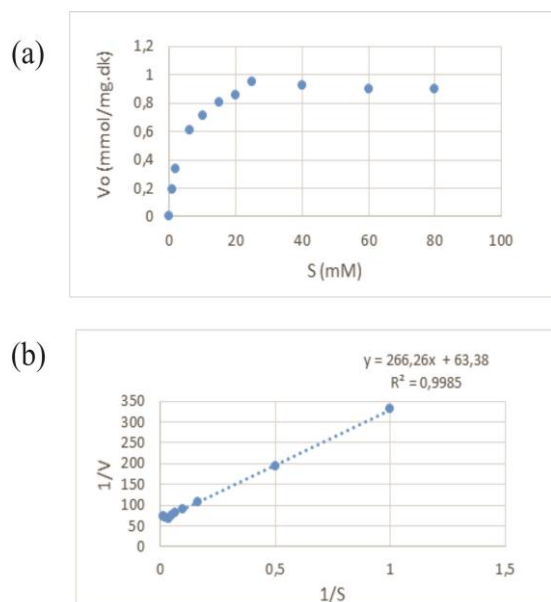


Figure 1: (a) Michaelis-Menten graphs for free enzyme; (b) Lineweaver-burk graph for free enzyme.

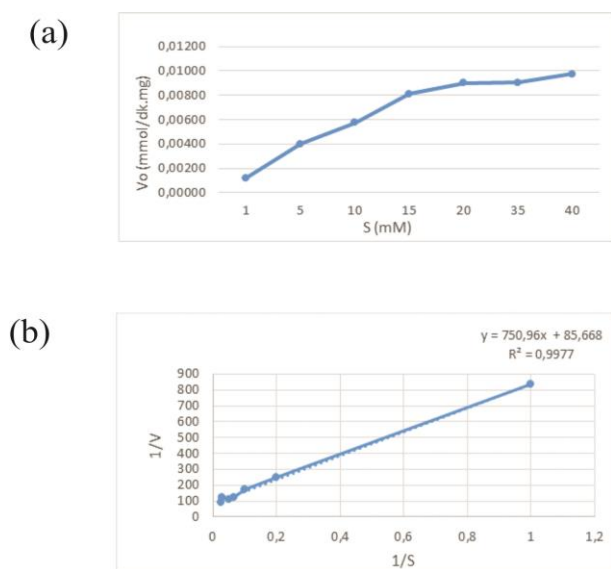


Figure 2: (a) Michaelis-Menten graphs for immobilized enzyme; (b) Lineweaver-burk graph for immobilized enzyme.

Table 1: Kinetic values of free enzyme and immobilized enzyme.

	Vmax (mmol mg ⁻¹ dk ⁻¹)	Km (mM)	Relative activity (%)
Free enzyme	0.016	4	100
Alginate-silica hybrid bead	0.012	9	73

Michaelis-Menten and Lineweaver-burk graphs for free enzyme and immobilized enzyme in alginate-silica hybrid beads were depicted in Figure 1 and Figure 2. As seen in Table 1, it is expected that Vmax value of free enzyme is higher than Vmax value of immobilized enzyme due to limitation of enzyme-substrate interaction. In other words, diffusion limitation occurs in polymer, which results in lower Vmax value. It is also expected that Km value of immobilized enzyme is higher than Km value of free enzyme. The reason for that is the formation of enzyme-substrate complex which is related to the diffusion of substrate through the pores of polymer. Relative activity was calculated by considering Vmax values. Relative activity value of immobilized enzyme indicated that limitation of diffusion has been overcome considerably [13].

Table 2: Enzymatic activity of alginate-silica hybrid monolith and beads.

	Relative activity (%)
Free enzyme	100
Alginate-silica hybrid monolith	73
Alginate-silica hybrid beads	69

Relative activities of alginate-silica hybrid monolith which is prepared based on internal gelation method and alginate-silica hybrid beads prepared by diffusion gelation method are very close to each other (Table 2). New formulated internal gelation method indicates it can overcome diffusion limitation.

IV. CONCLUSION

In this study, different gelation methods for fabricating alginate-silica hybrid gels were compared in terms of enzyme activity. Enzymatic activities were relatively close. Internal gelation-based monoliths are good candidates not only for enzyme immobilization but also for cell encapsulation and tissue engineering studies. Moreover, internal gelation-based method provides homogenous structure, controllable gelation rate and moldability, which is very important for microfluidic applications such as enzymatic microreactors.

ACKNOWLEDGMENT

This work was supported by the Scientific and Technological Research Council of Turkey, TUBITAK (113M050) and Ege University Research Fund (15-FBE-012). The grant from TUBITAK 2210-C National Graduate Scholarship Program is highly appreciated.

References

- [1] K.Y. Lee, and D.J. Mooney, "Alginate: properties and biomedical application," *Prog Polym Sci.*, vol. 37, pp. 106-126, 2012.
- [2] K.I. Draget and C. Taylor, "Chemical, physical and biological properties of alginates and their biomedical implications," *Food Hydrocolloids.*, vol. 25, pp. 251-256, 2011.
- [3] S.Y. Lim, K.O. Kim, D.M. Kim, and C.B. Park, "Silica-coated alginate beads for in vitro protein synthesis via transcription/translation machinery encapsulation," *J Biotechnol.*, vol. 143, pp. 183-189, 2009.
- [4] T. Coradin, N. Nassif, and J. Livage, "Silica-alginate composites for microencapsulation," *Appl Microbiol Biotechnol.*, vol. 61, pp. 429-434, 2003.
- [5] E.T. Hwang, and M.B. Gu, "Enzyme stabilization by nano/microsized hybrid materials," *Engineering in Life Sciences*, vol. 13, pp. 49-61, 2013.
- [6] L.W. Chan, H.Y. Lee, and P.W.S. Heng, "Mechanisms of external and internal gelation and their impact on the functions of alginate as a coat and delivery system," *Carbohydrate Polymers*, vol. 63, pp. 176-187, 2006.
- [7] Kurt Ingar Draget, G.S.k.-B., Olav Smidsrød, Alginate based new materials. *International Journal of Biological Macromolecules*, vol. 21, pp. 47-55, 1997.
- [8] K. Catherine, and P.X.M. Kuo, "Ionically crosslinked alginate hydrogels as scaffolds for tissue engineering: Part 1. Structure, gelation rate and mechanical properties," *Biomaterials*, vol. 22, pp. 511-521, 2001.
- [9] R. Onbas, O. Yesil-Celiktas, "Synthesis of alginate-silica hybrid hydrogel for biocatalytic conversion by β -glucosidase in microreactor," *Eng. Life Sci.* doi: 10.1002/elsc.201800124, 2018.
- [10] J. Desmet, C.F. Meunier, E.P. Danloy, and M.-E. Duprez, "Green and sustainable production of high value compounds via a microalgae encapsulation technology that relies on CO₂ as a principle reactant," *J. Mater. Chem. A.*, vol. 2, pp. 20560-20569, 2014.
- [11] Gurikov, P., Raman, S.P., Weinrich, D., Fricke, M. et al., A novel approach to alginate aerogels: carbon dioxide induced gelation. *RSC Adv.* 2015, 5, 7812-7818.
- [12] S. Akay, R. Heils, H.K. Trieu, I. Smirnova, O. Yesil-Celiktas, "An injectable alginate-based hydrogel for microfluidic applications," *Carbohydr Polym.*, vol. 161, pp. 228-234, 2017.
- [13] G. Demirel, G. Özçetin, F. Şahin, and H. Tümtürk, "Semi-interpenetrating polymer networks (IPNs) for entrapment of glucose isomerase," *Reactive and Functional Polymers*, vol. 66, pp. 389-394, 2006.

Optimization of Concentration and Sand Thickness for Agar Assisted Sand Hardening Process by Microbial Biocalcification

Alpcan Arıç¹, Burak Talha Yılmazsoy¹, Irem Deniz Can², Tuğba Keskin Gündoğdu¹

¹Ege University, Engineering Faculty, Bioengineering Department, 35100, Izmir, Turkey

²Celal Bayar University, Faculty of Engineering, Bioengineering Department, 45140, Manisa, Turkey

*Corresponding author: Tuğba Keskin Gündoğdu (keskin.tugba@gmail.com)

Abstract – This study presents a novel approach for microbial biocalcification process. Microbial biocalcification process was combined with sand hardening with *Sporosarcina pasteurii* grown on agar plates. The effect of different CaCl₂ concentrations (25 mM, 50 mM and 100 mM) and sand thickness (1mm, 5mm and 10 mm) was tested in duplicates. The agar assisted sand hardening was found as successful with optimum concentration of 50 mM CaCl₂ and optimum thickness with 10 mm.

Keywords – biocalcification, bio cement, agar, sand hardening

I. INTRODUCTION

Accommodation is a basic need of humanity and this need is largely eliminated by concrete structures. From raw material to final product, the cement industry is environmental pollutant. The production process of cement contains a large number of chemical and heat treatment processes. The heat treatment (1350-1450 °C) applied to the raw material during the production constitutes approximately 40% of the energy consumed during the cement production. Mostly, source of energy consists of fossil fuels and wastes for this process. For this reason, the cement production process includes all the negative consequences of the burning of fossils and wastes (Türkkan, 2015). In addition, the production emissions have a negative effect on human health from allergy to death. The biocalcification based concrete production technique has environmentally friendly production stages against these negativities. In the calcification process, essentially by adding a calcium crystal core into the appropriate solution in vitro, the solution is disturbed and small nuclei are formed by accumulation in molecules (nucleation) (Türkkan, 2015). Biocalcification consists of the biological pathways for the chemical pathways of classical concrete production and is fully compatible with nature. CaCO₃, which is produced in the biocalcification process, can form a hard, durable and long-lasting concrete alternative material by connecting the materials which are easily accessible in nature like sand and which are quite abundant in nature (Siddique and Chahal, 2011).

II. MATERIALS AND METHODS

A. Microorganism and Nutrient

In this study, the bacterium *Bacillus pasteurii* (DSM-33), also known as *Sporosarcina pasteurii*, was used. *S. pasteurii* is a gram-positive, facultative and non-pathogenic bacteria (Yoon et al, 2001). The bacterium provided in a lyophilized form from the DSMZ culture collection. For the DSMZ-DSM 33 culture, Medium 220 + Urea (20 g / l) was used as nutrient. The content of Medium 220 is 15.0 g / l peptone from casein, 5.0 g / l peptone from soymeal, 5.0 g / l NaCl, 15.0 g / l agar and 1000.0 ml distilled water.

B. Analytical Methods

B.1. Chemical CaCO₃ tests

Exothermic reaction occurs between HCl and CaCO₃ (CaCO₃ (s) + 2 HCl (l) = H₂O (l) + CO₂ (g) + CaCl₂ (aq)). The solid sample is incubated overnight in HCl, then dried and the mass loss determined. In the analysis, sand samples containing increasing amounts of CaCO₃ were used as standard sample series. R value of standards samples graph is 0.99.

B.2. ATR-FTIR Analysis

ATR-FTIR (Attenuated Total Reflection - Fourier Transformed Infrared Spectrometer) is used to examine the structure of solid liquid and powder samples. The device determines the vibration frequencies of the bonds in the molecules and defines the functional groups. Hardware features; DTGS detector, 4000 - 600 cm⁻¹ spectrum range, Laser diode and Spectrum 10 software.

ATR-FTIR device analysis is used in many analyzes because of its fast realization and practicality. Molecular groups give peaks in a certain spectrum and their presence can be observed. Like each molecule, CaCO₃ has a unique spectrum (Figure 1). CaCO₃ gives peaks at approximately 1480, 881 and 712 wave count (cm⁻¹) (Viravaidya et al. 2004). Values may vary depending on the characteristics of the device and the environment in which the analysis is performed. Due to the analysis costs, a limited number of samples were analyzed with the FTIR device.

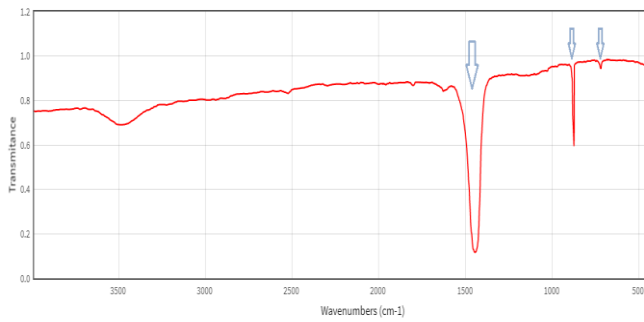


Figure 1. FTIR Spectrum of CaCO₃

C. Agar Assisted Sand Hardening

The agar assisted sand hardening process started with the revitalization of the lyophilized culture supplied from DSMZ (Germany). *Sporosarcina pasteurii* was grown on agar plates. After 24 h incubation non-sterilized sand was spread over agar plates and the 20 mL calcification medium with proper concentrations was added on sands and mixed gently (Figure 2). The Calcification medium consists DSM 33 medium, 20 g/L urea and CaCl₂. CaCl₂ concentrations was prepared as 25 mM, 50 mM and 100 mM. The thickness of the sand was adjusted to 1 mm, 5 mm and 10 mm.

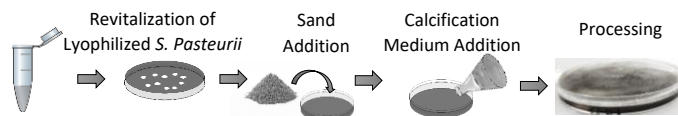


Figure 2. Experimental set-up of sand hardening process

III. RESULTS AND DISCUSSION

The sand hardening process depends on the bacteria concentration, sand thickness and CaCl₂ concentration. By growing bacteria on agar plates the bacterial concentration was assumed as constant. The sand thickness was changed as 1mm, 5mm and 10 mm; the CaCl₂ concentrations were 25 mM, 50 mM and 100 mM All experiments were performed in duplicates and all the parameters has control group without bacteria. The agar plates with bacteria and without bacteria were kept at different incubators at 30°C. After one week the sand hardening because of microbial biocalcification was completed. Solid basal medium is an elastic and sticky because of agar. At the end of the calcification process the agar and the sand was stacked together and cannot be separated from each other. At control group the sand that is close to agar surface was seemed as hardened but it was elastic (Figure 2A). The sand on agar plates with bacteria was found as hardened and stable (Figure 2B). The agar surface was thinner than the control group which shows that the bacteria also used the medium inside. The hardest sand was observed with 10 mm thickness and 50 mM CaCl₂ concentration.



Figure 3. Results of sand hardenin (A: Without inoculum; B: With inoculum)

The chemical CaCO₃ concentration tests was explained in Materials and Methods section. The difference of CaCO₃ formation was compared according to mass losses from the samples. The mass loss results were changed between 13 to 22% in the samples with inoculum and 14 to 18% in the samples without inoculum. The maximum difference was observed with samples with 50 mM concentration which was also found in previous study with liquid medium (Deniz Can et al. 2017). The maximum difference between the control samples and the samples with inoculum was found in 10 mm thickness (Figure 4).The 80% of the results showed that the calcification process was succesful with inoculum.

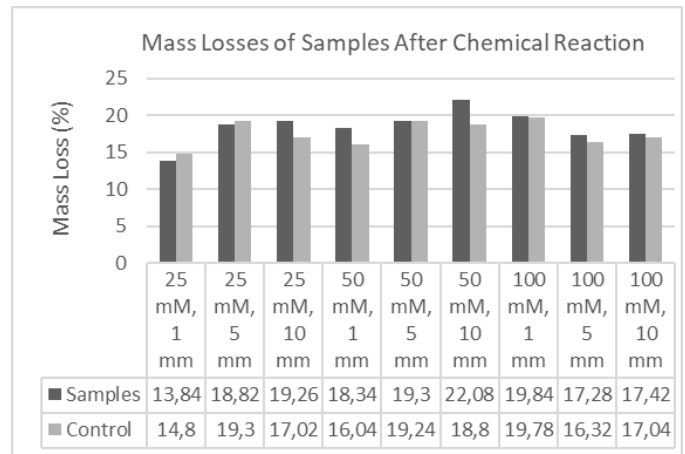


Figure 4. Results of chemical analysis

FTIR analysis was performed on 5 mm (25 mM, 50 mM and 50 mM Control) samples. When the analysis results were examined (Figure 5), all of the spectra were observed to have CaCO₃ peaks. On the other hand, the intensity of the peaks were different. The transmittance level of the samples containing bacteria (blue and orange lines) was lower than the control group. When the wavelength is around 1480 and 881, it was seen that the transmittance level in the 25 mM sample decreased more than the other two samples which means the amount of CaCO₃ was higher than other samples. As a result, the two samples containing bacteria have higher CaCO₃ concentrations

compared to the control group. The results of FTIR analysis are consistent with observational and chemical analysis results. In the 3 analysis methods, the majority of the bacteria containing samples contain higher levels of CaCO_3 .

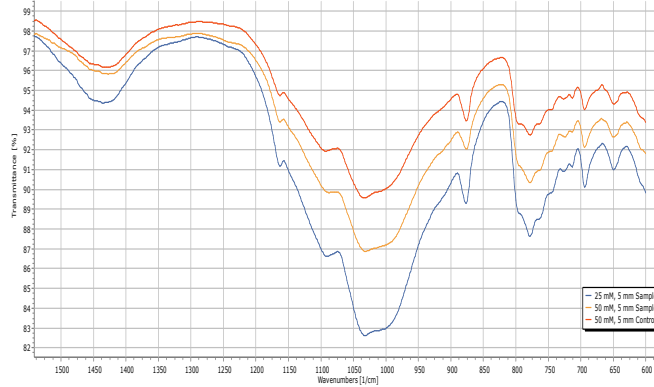


Figure 5. ATR-FTIR Results (red line: 50 mM CaCl_2 , 5 mm thickness, control, orange line: 50 mM CaCl_2 , 5 mm thickness, with inoculum; blue line: 25 mM CaCl_2 , 5 mm with inoculum)

4. CONCLUSION

The microbial biocalcification process can be used for sand hardening which can replace with cement-based construction. Agar assisted hardening process has the advantage of further design elements. The best concentration of CaCl_2 for microbial biocalcification is 50 mM and the thickness is 10 mm.

ACKNOWLEDGEMENT

This study was supported financially by TUBITAK with 2209 Bachelor Students Research Project grant. We also acknowledge Prof. Dr. Nuri AZBAR for using Environmental Biotechnology and Bioenergy Laboratory and TBT (Turkey Biodesign Team) for advisory support.

ACKNOWLEDGMENT

The authors wish to thank TUBITAK-2209A Student Project-2017 for financial support of this study.

REFERENCES

- [1] Türkkan, A. "Çimento Fabrikalarının Sağlık Etkileri." (2015): 1-36.
- [2] Siddique, R., Chahal, N.K., "Effect of ureolytic bacteria on concrete properties." *Constr. Build. Mater.* 25, (2011): 3791–3801.
- [3] Yoon Jung-Hoon, et al. "Sporosarcina aquimarina sp. nov., a bacterium isolated from seawater in Korea, and transfer of *Bacillus globisporus* (Larkin and Stokes 1967), *Bacillus psychrophilus* (Nakamura 1984) and *Bacillus pasteurii* (Chester 1898) to the genus *Sporosarcina* as *Sporosarcina globispora* comb. nov., *Sporosarcina psychrophila* comb. nov. and *Sporosarcina pasteurii* comb. nov., and emended description of th." *International Journal of Systematic and Evolutionary Microbiology* 51.3 (2001): 1079-1086.
- [4] Viravaidya C., Mei Lia A., Mann, S. "Microemulsion Based Synthesis of Stacked Calcium Carbonate (Calcite) SUPERstructures", *Chemical Communication*, vol 1, pp. 2182-2183, 2004
- [5] Deniz I., Keskin T., Yılmazsoy BT., Aric A., Andic-Cakir O., Sendemir A., Ayol Altun D., Tokuc A., Kokturk G., Avcı F., *ICONTEs 2017, International Conference on Technology Engineering and Science*, October 26-29, 2017, Antalya, Turkey, Abstract Book, p 166

Design of a Home Health Care Database in Monitoring Chronic Respiratory Diseases

İ. HASDEMİR¹ and G. ERTAŞ¹

¹ Department of Biomedical Engineering, Yeditepe University, İstanbul/Turkey, ilayda.hasdemir@gmail.com

¹Department of Biomedical Engineering, Yeditepe University, İstanbul/Turkey, gokhan.ertas@yeditepe.edu.tr

Abstract - For chronic respiratory diseases, continues monitoring of the vital physiological parameters of the patients taking home health care is very important. Information technology-based applications offer useful tools in improving the quality of home health care services. In this study, we have worked on a framework for patients with chronic respiratory diseases and designed a database for home health care.

Keywords – home health care, chronic respiratory disease, database.

I. INTRODUCTION

The delivery of health services in the world is changing rapidly, with advances in surgical and non-surgical treatments, increased elderly populations, accessibility of self-help facilities and private health care programs [1]. Increasing elderly population and associated chronic and degenerative diseases, a shortage of staff to provide home care services, changes in health problems, changes in patient potential and developments in medical technology require a new model for health services offered at home [2]. Home and community care covers the services of professionals in residential and community settings for the treatment of self-care, home care, long-term care, assisted life and substance use disorders and other health and social care services, as well as the primary and secondary facilities offered at the hospitals and the physicians' offices [3]. Home health care is a beneficial solution for patients who are suffering from chronic diseases and requiring continues monitoring of several physiological parameters. Among these parameters, respiration rate (or respiration pattern) and heart beat rate are the most common ones aimed to be monitored such as in the chronic respiratory diseases [4, 5].

Chronic respiratory diseases are one of the common causes of morbidity and mortality in the world. Treatment of these diseases targets to reduce symptoms, prevent acute attacks and worsening of respiratory function, improve if possible, prolong life and improve quality of life [6]. One of the most important problems limiting the daily life of people with chronic respiratory disease is the limitation of self-limitation, anxiety of shortness of breath and social isolation. However, this not only puts the person in a vicious circle, but also causes his

complaints to increase even more. The person acts less as he / she isolates, and accordingly, muscle weakness increases and shortness of breath is felt more [7]. For this reason, it is very important for patients with chronic respiratory diseases to continue their normal lives in their homes. Respiratory system diseases affect not only the patient but also the family and environment of the patient. For a more productive, happy, fulfilled and quality life, home care programs that take the patient with the respiratory system disease and the patient's environment as a whole are extremely important.

Information technology-based applications for home care services offer several beneficial tools to improve the quality of health care by creating cooperative environments between the patients, the physicians and the nurses [8]. With the use of these applications, a huge amount of data are generated [9]. These huge amount of data causes a lot of problems as accessing the data stored. To solve this problem, health monitoring systems with Internet-of-Things (IoT) technologies have been developed [10]. The framework studies of these developed systems need to be improved. Our study consists of both framework study and database. We have designed a database that can be used at home to improve the management of chronic respiratory diseases.

II. FRAMEWORK PROPOSED

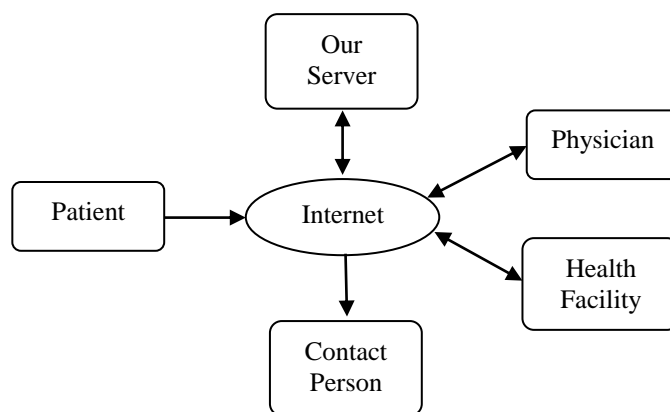


Figure 1: Our Framework Study

Our framework study focused on early detection of symptoms and patient follow-up to assist the patient. When

patient goes to the health facility for control, he is asked to use a device at home. The patient obtains this device from us. With this device, while performing the patient's normal daily activities, the physiological parameters of the patient such as heart rate and respiration can be monitored over the internet. The physiological data of the patient taken from the device can be accessed by the physician, health facility, our server and contact person via internet.

III. DATABASE DESIGNED

The database designed consists of eight tables considering different possible types of information: Patient related data (demographics and other), device related data (device details, calibration and maintenance data, measurement data, borrow data), physician's report data and facility related data. Figure 2 shows the relationship between these tables and the details of each table is as explained as follows. The design process is handled using Microsoft Access.

A. Patient Information Table

This table, Table 1, consists of unique patient identification number (PID) given automatically, patient name, surname, date of birth, place of birth, gender, blood group, nationality, unique nationality identification number, accommodation

address including zip code and phone number. The patient's insurance company and insurance number is also stored in this table to perform the insurance procedures easily with the insurance information of the patient when necessary. Also, admission date and registered facility ID are recorded. Thus, patients are followed up.

Table 1: Contents of the "Patient Information" table

Field Name	Data Type	Field Size
PID	AutoNumber	Long Integer
Name	Short Text	30
Surname	Short Text	30
DOB	Date/Time	
POB	Short Text	255
Gender	Short Text	1
Nationality	Short Text	2
NationalityID	Short Text	20
Adress	Short Text	150
ZipCode	Short Text	5
Phone	Short Text	20
Email	Short Text	30
InsuranceCompany	Short Text	50
InsuranceNumber	Short Text	30
BloodGroup	Short Text	3
AdmissionDate	Date/Time	Short Date
RegisteredFacilityID	Number	Long Integer

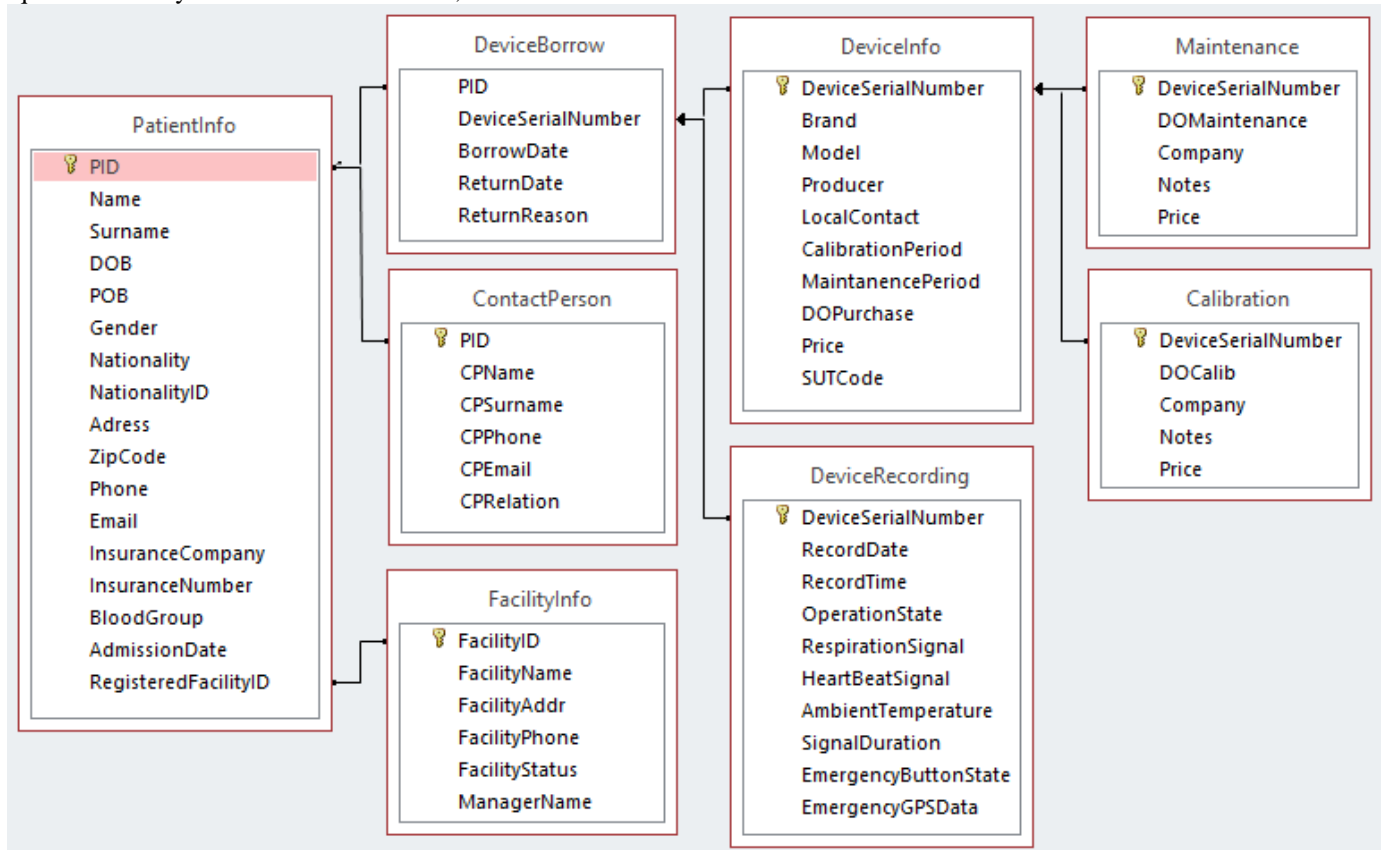


Figure 2: Database designed

B. Device Borrow Table

In this table, Patient ID, device serial number, borrow date, return date and return reason are recorded in Device Borrow

Table, Table 2. Thus, the records of the device used by the patient are kept. Patient ID states in Device Borrow Table has one-to-one relationship with the Patient ID states in Patient Information Table.

Table 2: Contents of the “Device Borrow” table

Field Name	Field Type	Field Size
PID	Number	Long Integer
DeviceSerialNumber	Short Text	20
BorrowDate	Date/Time	Short Date
ReturnDate	Date/Time	Short Date
ReturnReason	Short Text	200

C. Contact Person Table

Patient ID, Contact person’s information are recorded in Contact Person table, Table 3. In the case of emergency the contact person's information is used in that table. Patient ID states in Contact Person Table has one-to-one relationship with the Patient ID states in Patient Information Table.

Table 3: Contents of the “Contact Person” Table

Field Name	Data Type	Field Size
PID	AutoNumber	Long Integer
CPName	Short Text	30
CPSurname	Short Text	20
CPPhone	Short Text	30
CPEmail	Short Text	30
CPRelation	Short Text	1

D. Facility Information Table

Facility's ID, name, address, phone, status and manager name are recorded in Facility Information Table, Table 4. All information about the facility where the patient uses is available in this table. Thus, the health facility can reach their patient’s physiological parameters. Registered Facility ID states in Facility Info Table has many-to-one relationship with the Registered Facility ID states in Patient Information Table.

Table 4: Contents of the “Facility Information” Table

Field Name	Data Type	Field Size
RegisteredFacilityID	AutoNumber	Long Integer
FacilityName	Short Text	25
FacilityAddr	Short Text	75
FacilityPhone	Short Text	15
FacilityStatus	Short Text	1
ManagerName	Short Text	30

E. Device Recording Table

Device serial number, record date, record time, operation state, respiration signal, heart beat signal, ambient temperature, signal duration, emergency button state and emergency GPS data are recorded in Device Recording Table, Table 5. From this table the respiration and heart beat signals recorded by the device are reached. Information about the measurement made and the measured media are recorded. The patient can call for help with the emergency button. Device serial number states in Device Recording Table has one-to-one relationship with the Device Serial Number states in Device Borrow Table.

Table 5: Contents of the “Device Recording” Table

Field Name	Data Type	Field Size
DeviceSerialNumber	Short Text	20
RecordDate	Date/Time	Short Date
RecordTime	Short Text	255
OperationState	Short Text	255

RespirationSignal	Long Text	
HeartBeatSignal	Number	Byte
AmbientTemperature	Number	Decimal
SignalDuration	Number	Integer
EmergencyButtonState	Yes/No	On/Off
EmergencyGPSData	Short Text	30

F. Device Information Table

Device serial number, brand, model, producer, local contact, calibration period, maintenance period, date of purchase, price and SUT code are recorded in Device Information Table, Table 6. This table contains information about the device which patient used. Device serial number states in Device Info Table has one-to-one relationship with the Device Serial Number states in Device Borrow Table.

Table 6: Contents of the “Device Information” Table

Field Name	Data Type	Field Size
DeviceSerialNumber	Short Text	20
Brand	Short Text	10
Model	Short Text	10
Producer	Short Text	20
LocalContact	Short Text	50
CalibrationPeriod	Number	Byte
MaintenancePeriod	Number	Byte
DOPurchase	Date/Time	Short Date
Price	Currency	
SUTCode	Short Text	255

G. Maintenance Table

Device serial number, date of maintenance, company, notes about the device and maintenance price are recorded in Maintenance Table, Table 7. So, the device maintenance is checked. Device Serial Number states in Maintenance Table has one-to-one relationship with the Device Serial Number states in Device Information Table.

Table 7: Contents of the “Maintenance” Table

Field Name	Data Type	Field Size
DeviceSerialBumber	Short Text	20
DOMaintanance	Date/Time	Short Date
Company	Short Text	50
Notes	Short Text	255
Price	Currency	

H. Calibration Table

Device serial number, date of calibration, company, notes and price are recorded. The calibration information of the device is reached from this table where necessary. Device Serial Number states in calibration table has one-to-one relationship with the Device Serial Number states in Device Information Table.

Table 8: Contents of the “Calibration” Table

Field Name	Data Type	Field Size
DeviceSerialBumber	Short Text	20
DOCalib	Date/Time	Short Date
Company	Short Text	50
Notes	Short Text	255
Price	Currency	

I. CONCLUSION

Demand for home health services is increasing especially for patients suffering from chronic diseases. Continues monitoring of several physiological parameters of the patients are required by several setups. In this study, a framework has been introduced and a database has been designed for this purpose. The uses of the framework and the database would offer remarkable facilities for physicians, nurses, patients and care takers of the patients. Physicians can access to both personal and clinical information of the patients to create a personalized patient file record. The use of our database combines elements of various integrated care models that reflect the basic principles: promoting patient self-management, an effective response to the patient's needs, and shared accessible information.

The next step will be to evaluate our framework and database actually increase competence, adherence to treatment, actions and improves the health status of patients with chronic respiratory diseases. In addition, this study may provide a total report on the needs of patients in the home, as well as the needs for care of the medical supplies and the patient population status.

In the future, we plan to develop a portable and wearable device for use with the framework proposed that would allow widespread use of the database designed to help both healthcare workers and planners to improve the management of chronic respiratory diseases.

REFERENCES

- [1] Durrani, H. (2016). Healthcare and healthcare systems: inspiring progress and future prospects. *Mhealth*, 2.
- [2] Jiang, Z., Lu, L., Huang, X., & Tan, C. (2011, September). Design of wearable home health care system with emotion recognition function. In *Electrical and Control Engineering (ICECE), 2011 International Conference on* (pp. 2995-2998). IEEE.
- [3] Ellenbecker, C. H., Samia, L., Cushman, M. J., & Alster, K. (2008). Patient safety and quality in home health care.
- [4] Appelboom, G., Camacho, E., Abraham, M. E., Bruce, S. S., Dumont, E. L., Zacharia, B. E., ... & Connolly, E. S. (2014). Smart wearable body sensors for patient self-assessment and monitoring. *Archives of Public Health*, 72(1), 28.
- [5] Sobnath, D. D., Philip, N., Kayyali, R., Nabhani-Gebara, S., Pierscionek, B., Vaes, A. W., ... & Kaimakamis, E. (2017). Features of a mobile support app for patients with chronic obstructive pulmonary disease: literature review and current applications. *JMIR mHealth and uHealth*, 5(2).
- [6] Celli, B. R., & Barnes, P. J. (2007). Exacerbations of chronic obstructive pulmonary disease. *European Respiratory Journal*, 29(6), 1224-1238.
- [7] Spathis, A., & Booth, S. (2008). End of life care in chronic obstructive pulmonary disease: in search of a good death. *International journal of chronic obstructive pulmonary disease*, 3(1), 11.
- [8] Carreiro-Martins, P., Gomes-Belo, J., Papoila, A. L., Caires, I., Palmeiro, T., Gaspar-Marques, J., & Neuparth, N. (2016). Chronic respiratory diseases and quality of life in elderly nursing home residents. *Chronic respiratory disease*, 13(3), 211-219.
- [9] Guan, K., Shao, M., & Wu, S. (2017). A Remote Health Monitoring System for the Elderly Based on Smart Home Gateway. *Journal of healthcare engineering*, 2017.
- [10] Anzanpour, A., Rahmani, A. M., Liljeberg, P., & Tenhunen, H. (2015, December). Internet of things enabled in-home health monitoring system using early warning score. In *Proceedings of the 5th EAI International Conference on Wireless Mobile Communication and*

Healthcare (pp. 174-177). ICST (Institute for Computer Sciences, Social-Informatics and Telecommunications Engineering).

A New Approach for Feature Extraction from Functional MR Images

G.ÖZMEN¹ and S. ÖZŞEN²

¹ Selcuk University, Konya/Turkey, gozmen@selcuk.edu.tr

²Konya Technical University, Konya/Turkey, seral@selcuk.edu.tr

Abstract - The functional MR images consist of very high dimensional data containing thousands of voxels, even for a single subject. Data reduction methods are inevitable for the classification of these three-dimensional images. In the first step of the data reduction, the first level statistical analysis was applied to fMRI data and brain maps of each subject were obtained for the feature extraction. The second step is the feature selection. According to the feature selection method used in the classification studies of fMRI and which is called as the active method, the intensity values of all brain voxels are ranked from high to low and some of these features are presented to the classifier. However, the location information of the voxels is lost with this method. In this study, a new feature extraction method was presented for use in the classification of fMRI. According to this method, active voxels can be used as features by considering brain maps obtained in three dimensions as slice based. Since the functional MR images have big data sets, the selected features were once again reduced by Principal Component Analysis and the voxel intensity values were presented to the classifiers. As a result; 83.9% classification accuracy was obtained by using kNN classifier with purposed slice-based feature extraction method and it was seen that the slice-based feature extraction method increased the classification accuracy against the active method.

Keywords - Classification, Feature extraction, fMRI, SPM

I. INTRODUCTION

fMRI, a special application of magnetic resonance imaging (MRI), is a noninvasive method. With this method, researchers record three-dimensional brain images while a subject performs a cognitive or sensory task in the MR device [1]. fMRI data analysis consists of image acquisition, pre-processing and statistical analysis. Due to its noisy structure, some preprocessing operations should be applied to fMRI images. These processes are realignment, slice-timing, co-registration, segmentation and spatial normalization [2]. The most common filtering method used after standard pre-processing steps applied to fMRI images is known as spatial smoothing. With the spatial smoothing, the intensity value of each voxel is replaced with the mean values of neighboring voxels. This process corresponds to the use of a low-pass filter

to suppress high-frequency signals in the frequency domain. Various filters are used to perform this operation. The most common spatial filtering method is the convolution of the image with the Gaussian filter [3].

Statistical analysis of pre-processed fMRI data can be used to detect activations in brain regions [4]. In the statistical analysis of fMRI data, the voxel intensity values can be determined in the brain regions by comparing the changes in the control state with the changes in the task state. The most commonly used method to evaluate the statistical significance of neural correlations in the brain is known as Statistical Parametric Mapping (SPM). SPM is a voxel-based and univariate approach based on the General Linear Model (GLM) [5]. Activation maps are the result of statistical analysis applied to functional MR images are evaluated as characteristics that characterize the brain functions of each subject. SPM [6] based analysis produces voxel values under the null hypothesis distributed according to a known probability density function. This is accomplished by obtaining the spm.T maps expressing the activation maps.

Functional MR data is composed of very high dimensional images containing thousands of voxels. These three-dimensional images need to be reduced for use in classification applications. The activation maps obtained as a result of analysis of fMRI data are one of the most important steps to reduce the size of fMRI. Because of the fact that fMRI consists of three-dimensional images, even the activation maps have quite a number of voxels for the classifier inputs. For this reason, the number of features should be reduced by applying feature selection processing to the reduced data. Many of the feature selection methods can be applied to spm.T maps obtained from fMRI data.

However, [7] emphasized that some special feature selection methods would yield better results. In this context, voxel-based and transformation-based feature selection methods are possible to use. In transformation-based feature extraction, data is transferred from the original high-dimensional coordinate system to a new low-dimensional coordinate system. Principal Component Analysis (PCA) is one of the transformation-based feature extraction methods. In PCA applications, vectors are found as eigenvectors of the estimated covariance matrix of the data. Thus, the original fMRI data matrix is converted into rows in a transformation matrix with these vectors.

Most often, the dimensionality of the data is reduced by eliminating the basic components with the lowest variance.

PCA is used to create a new feature space from the high-dimensional data. Each brain voxel is expressed in the new feature space with a vector [8]. Voxel-based feature extraction methods keep the data in the original coordinate system. However, all the voxels are sorted and used only as high-density valuable voxels as a result of feature extraction.

"The most active voxel method" is the most commonly used method in the voxel-based feature extraction. According to this method, voxels in the activation map are ranked from high to low according to their density values and the highest n voxels are selected as features. The disadvantage of this method is that it lost location informations of voxels. Another feature selection method which [7] suggested is "the most distinctive voxels" method. In this method, the accuracy of the selected voxels on the training data of the classifier is taken as a measure of the distinctive power of the voxel and the highest rated voxels according to this measurement are selected. Another feature selection method is "The most effective voxels according to their interest" method. This method is similar to the active method but allows a homogenous selection of voxels from all regions of interest (ROI) within the brain. This method applies the active method to each ROI and selects the most active voxels from each.

In this study, an alternative method against to active voxel method is proposed by using all brain voxels. With the proposed method which is called slice-based feature extraction, the density values of the active voxels in each slice of the three-dimensional image are evaluated according to sagittal slice. Thus, all voxels are used as features without losing the position information.

Support Vector Machines (SVM) [9, 10], k nearest neighbor (kNN) [11], Naive Bayes (NB) [12] and Random Forest (RF) [13] classifiers were used with Orange Canvas 3.4 to classify fMRI data. Classifier performances were evaluated by classifying accuracy (CA), Precision, Recall, F score, and area under ROC curves (AUC). In order to measure the performance of the classification process, training and test data were prepared by k-fold cross-validation method. When the classifier results were compared to the active voxel method and the slice-based method, it was seen that the slice-based method improves the classification results.

II. MATERIAL AND METHOD

In this study, fMR images, recorded from 20 healthy and 20 depression patients, were used. fMR images were obtained with positive and negative visual stimulus by block design recording procedure [14]. The processing steps applied to the recorded fMRI data are shown in Figure 1. In this study, re-alignment, slice-timing, co-registration, and spatial normalization operations were applied to the fMRI data with the SPM12. With re-alignment, the image's volumes are re-aligned to a single reference volume to correct errors due to head movements. Slice timing used to correct the timing difference between slices. The fMRI data does not provide a very clear image from the anatomical point of view. For this reason, the functional images were co-registered with

the structural images. After co-registration, high-resolution T1 images were normalized to a T1-weighted standard brain template by spatial normalization. With the last step which is called smoothing, the distorting effect on the image was eliminated.

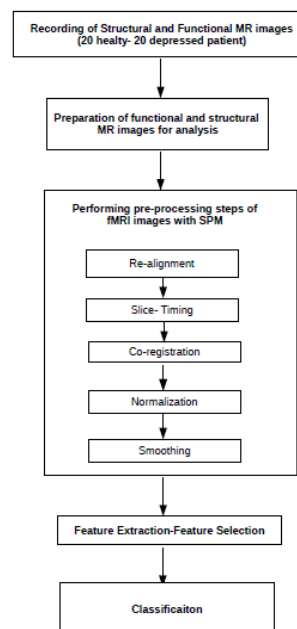


Figure 1. The workflow of study

Examples of the preprocessing steps performed in this study are shown in Figure 2 for a subject selected from the control group.

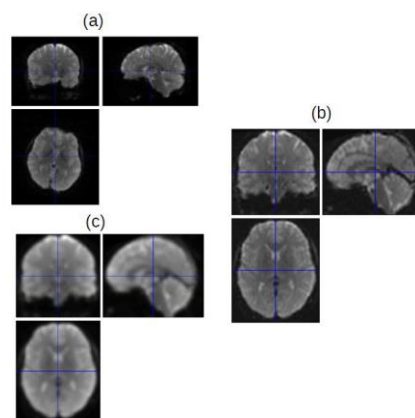


Figure 2. Preprocessing steps applied to a functional MR image of a subject selected from the control group a) Realignment b) Normalization c) Smoothing

In the next steps of this study are feature extraction, feature selection and classification of pre-processed fMRI data. The first operation of feature extraction is statistical analysis. In this study, fMRI data obtained from one subject contained $79 \times 95 \times 78$ voxels. The total number of data consists of 120 fMRI volumes recorded for 4 seconds each. There are a total of $79 \times 95 \times 78 \times 120$ voxels in 120 volumes. In such conditions, it

is impossible to use such high-size data that accommodate all brain voxels in classifier inputs. For this purpose, in order to reduce the size of fMRI data and also to obtain the density values of the voxels used as determinants of the classification problems, first level statistical analysis was applied to fMR images. As a result of this process, spm.T maps were created for all subjects. In this study, the first stage of feature extraction was completed for each subject by using spm.T maps. So that fMRI data with 79x95x78x120 dimension was reduced to 79x95x78 by using the spm.T map. This process was carried out for all 40 subjects. Figure 3 shows a spm.T maps of a healthy and a patient subject which are randomly selected.

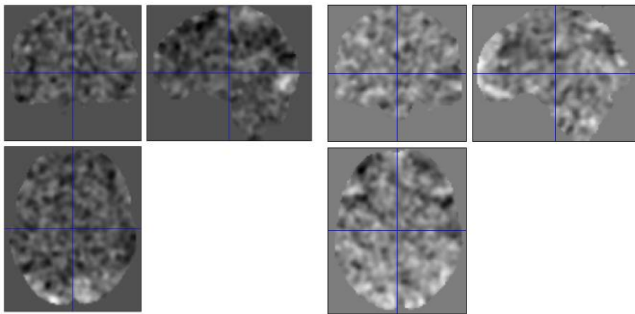


Figure 3 (a) Spm.T map of a subject from the control group (b) Spm.T map of a subject from the patient group

Figure 4 shows the colored map of the spm.T map of the control group given in Figure 3.

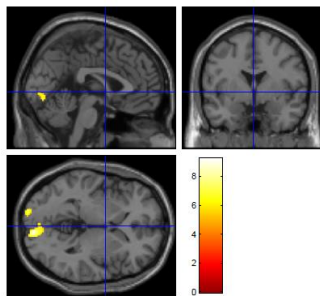


Figure 4. Color image of the activation map of a subject belonging to the control group

III. RESULTS

Evaluation of classifier results by active voxel feature selection method

In this study, a total of 585390 voxels were present in the activation map (79x95x78) of a subject. Primarily, all of these voxels were presented to the classifiers as features but the result was not obtained. Secondly, according to the active voxel method, voxels were ranked from the highest to the lowest value and the first 1000 voxels features were chosen. Thus, a total of 1000 features for one subject and 1000x40 for 40 subjects were presented to the classifiers. The classification results are shown in Table 1.

TABLE 1. Classification results for the active voxel method

	AUC	CA	F1	Precision	Recall
SVM	57,50	57,50	66,70	60,80	57,50
NB	57,50	55,00	57,10	55,10	55,00
kNN	57,50	62,50	66,70	63,30	62,50
RF	52,50	47,50	48,80	47,50	47,50

AUC given in Table 1 is expressed the area under the ROC curve. CA is the classification accuracy. Precision is the positive prediction success and Recall shows how successful the positive samples are estimated. F1; indicates the harmonic mean of precision and recall values. In order to measure the performance of the classification process, training and test data were prepared by k-fold cross-validation method. The highest classification accuracy for Table 1 was obtained by kNN with 62.5% and the lowest classification accuracy was obtained by RF with 47.5%.

Evaluation of classifier results by slice-based feature selection method

In this study, a new feature selection method that can be used for functional MR images is suggested as an alternative to the active voxel method.. With this method, the density values of the active voxels in each slice are evaluated according to the sagittal section. This method allows data transformation without losing voxels location information. According to the slice-based feature selection method, (79x95x78 \rightarrow 7505x78) voxels in 78 different sagittal slices were obtained for each subject. An important property of the slice-based method is that it increases the number of samples used for one person by using 78 slices for a subject. This method can be used to increase the number of samples in studies where the number of subjects is insufficient. In the method of slice-based feature selection, PCA was used to reduce the number of features after data transformation was completed. In this study, 20 principal component features were used . Thus, 20x78 features for one subject and 20x3120 for 40 subjects were presented to the classifiers. The classification results are shown in Table 2.

TABLE 2. Classification results for the slice-based method

	AUC	CA	F1	Precision	Recall
SVM	67,9	67,9	62,1	69,8	67,9
NB	75,7	67,8	67,0	67,9	67,8
kNN	92,7	83,9	83,9	83,9	83,9
RF	87,2	78,5	78,2	78,5	78,5

The highest classification accuracy for Table 2 was obtained by kNN with 83.9% and the lowest classification accuracy was obtained by RF with 78.5%. According to the feature selection method used in the classification studies of fMRI and which is called as the active method, the intensity values of all brain voxels are ranked from high to low and some of these

features are presented to the classifier. However, the location information of the voxels are lost with this method. Especially in the classification of psychiatric diseases, it is known that activations occur in different brain regions of healthy persons and patients due to mood changes. In this study, a new feature selection method is presented for use in classification studies using all brain voxels. According to this method, active voxels can be used as features by considering brain maps obtained in three dimensions as slice based. Since the functional MR images have a very large size of data, the selected features were once again reduced by Principal Component Analysis and the obtained voxel intensity values were presented to the classifier.

As a result, it was seen that the slice-based feature extraction method increased the classification accuracy against the active method.

IV. REFERENCES

- [1] N. Billor and J. Godwin, "Variable Selection for Functional Logistic Regression in fMRI Data Analysis," *Turkiye Klinikleri Journal of Biostatistics*, vol. 7, no. 1, 2015.
- [2] J. E. Chen and G. H. Glover, "Functional magnetic resonance imaging methods," *Neuropsychology review*, vol. 25, no. 3, pp. 289-313, 2015.
- [3] K. Friston, J. Ashburner, C. D. Frith, J. B. Poline, J. D. Heather, and R. S. Frackowiak, "Spatial registration and normalization of images," *Human brain mapping*, vol. 3, no. 3, pp. 165-189, 1995.
- [4] S. Francis and R. S. Panchuelo, "Physiological measurements using ultra-high field fMRI: a review," *Physiological measurement*, vol. 35, no. 9, p. R167, 2014.
- [5] R. H. Myers and D. C. Montgomery, "A tutorial on generalized linear models," *Journal of Quality Technology*, vol. 29, no. 3, p. 274, 1997.
- [6] K. J. Friston, A. P. Holmes, K. J. Worsley, J. P. Poline, C. D. Frith, and R. S. Frackowiak, "Statistical parametric maps in functional imaging: a general linear approach," *Human brain mapping*, vol. 2, no. 4, pp. 189-210, 1994.
- [7] T. M. Mitchell, "Learning to decode cognitive states from brain images," *Machine learning*, vol. 57, no. 1-2, pp. 145-175, 2004.
- [8] H. Suma and S. Murali, "Principal Component Analysis for Analysis and Classification of fMRI Activation Maps," *International journal of computer science and network security*, vol. 7, no. 11, pp. 235-242, 2007.
- [9] J. Mourão-Miranda, "Patient classification as an outlier detection problem: an application of the one-class support vector machine," *Neuroimage*, vol. 58, no. 3, pp. 793-804, 2011.
- [10] M. D. Sacchet, G. Prasad, L. C. Foland-Ross, P. M. Thompson, and I. H. Gotlib, "Support vector machine classification of major depressive disorder using diffusion-weighted neuroimaging and graph theory," *Frontiers in psychiatry*, vol. 6, p. 21, 2015.
- [11] M. Misaki, Y. Kim, P. A. Bandettini, and N. Kriegeskorte, "Comparison of multivariate classifiers and response normalizations for pattern-information fMRI," *Neuroimage*, vol. 53, no. 1, pp. 103-118, 2010.
- [12] L. I. Kuncheva and J. J. Rodríguez, "Classifier ensembles for fMRI data analysis: an experiment," *Magnetic resonance imaging*, vol. 28, no. 4, pp. 583-593, 2010.
- [13] E. E. Tripoliti, D. I. Fotiadis, M. Argyropoulou, and G. Manis, "A six stage approach for the diagnosis of the Alzheimer's disease based on fMRI data," *Journal of biomedical informatics*, vol. 43, no. 2, pp. 307-320, 2010.
- [14] G. ÖZMEN, "Fonksiyonel Mr Görüntülerini Filtrelemede Yeni Bir Yaklaşım Ve Depresyon Hastalarının Sınıflandırılması Üzerine Etkileri," *Electrical-Electronics Engineering*, Selcuk University, 2018.

A Clustering Problem with Gaussian Mixture Model Based on Expectation Maximization

E. PEKEL¹ and E. KILIÇ¹

¹ Ondokuz Mayıs University, Samsun/Turkey, ebru.pekel@gmail.com

¹ Ondokuz Mayıs University, Samsun/Turkey, erdal.kilic@gmail.com

Abstract - Progressive technology, the development of the industry and the lack of protective precaution, and the responsibility for the uneducated employees are the main causes of work accidents. In this study, work accidents are clustered by taking into consideration the types of injuries, the effects of the injuries on the body and types of the accidents via Gaussian Mixture Model (GMM). The Gaussian mixture model (GMM) is a clustering method based on the Bayesian approach. In this study, work accidents were divided into classes by GMM. GMM were constructed on a dataset from an international construction company. According to the experimental results, it's explicit that it is possible to distinguish three groups by considering their own characteristic similarities of the work accidents. To cluster work accidents will play an important role in creating a policy of prevention in a workshop.

Keywords - Gaussian mixture model, clustering, machine learning, accident

I. INTRODUCTION

Production and its competition have increased dramatically, with major developments in technology all over the world in recent years. Therefore, employees are exposed to the hazards they may encounter during working hours. This necessitated the adoption of occupational health and safety (OHS) measures to prevent work accidents at workplaces[1].

OHS is a discipline with a broad scope involving many specialized fields which are the social, mental and physical well-being of workers that is the “whole person”[2].

Successful occupational health and safety practice needs the collaboration of both employers and workers in health and safety programs, and involves the consideration of issues relating to occupational medicine, industrial hygiene, toxicology, education, engineering safety, ergonomics, psychology, etc[3].

While work accidents and the deaths, injuries and incapacity of work resulting from these accidents bring material and spiritual losses for our country, they also constitute a serious job security problem for those who do business. Today, as the economy of our country grows rapidly, and the number of employees and the number of employees increases, occupational safety becomes vital[4].

II. MOTIVATION

A prediction on the severity and effects of accidents was conducted in this study due to there was not enough papers on the prediction or the forecasting of the type and the effect of work accidents in the literature[5]. This study focused on an application of a machine learning technique which has been applied in the field of occupational health and safety. Gaussian mixture model (GMM) is employed as a machine learning algorithm in this study and work accident types are tried for clustering by using GMM.

There are very few Gaussian mixture model applications in the literature. At the same time, there is no application of gauss mixture model on occupational health and safety in the literature. For this reason, this section of this paper summarizes the application of the Gaussian mixture model in each area.

It has been proposed a novel volume exploration scheme that explores volumetric structures in the feature space by modeling the space using the Gaussian mixture model (GMM) in[6]. Their model demonstrated interactive performance and good scalability.

The performance of GMM is compared to three commonly used classifiers: a linear discriminant analysis, a linear perceptron network, and a multilayer perceptron neural network for multiple limb motion classification using continuous myoelectric signals in [7]. The classification with GMM demonstrates better accuracy and results in a robust method of motion classification with low computational load.

In [8], an efficient approach to search for the global threshold of image using Gaussian mixture model was proposed. Then to fit the Gaussian mixtures to the histogram of image, the expectation maximization (EM) algorithm is developed to estimate the number of Gaussian mixture of such histograms and their corresponding parameterization. Finally, the optimal threshold which is the average of these Gaussian mixture means was chosen. And their experimental results show that the new algorithm performs better.

In [9], it has been proposed a robust EM clustering algorithm for Gaussian mixture models to resolve the drawbacks of the EM, first creating a new way to solve these initialization problems. Their proposed model results the superiority and usefulness in application.

In [10], different methods were proposed to choose sensible starting values for the EM algorithm to get maximum likelihood parameter estimation in Gaussian

mixture models. Similarly, a mixture model composed of a large number of Gaussians was used to interpret the brain image in [11].

An Adaptive Gaussian mixture has been proposed for modeling nonstationary temporal distributions of pixels in video surveillance applications [12]. In [13], analyze the usual pixel-level approach by an adaptive algorithm using Gaussian mixture probability density again.

In [14], a system Gaussian Mixture Models classifier is proposed for audio fingerprints data. He achieved fast and automatic process of large audio databases.

In [15], it was handled a problem which require high identification rates using short utterance from unconstrained conversational speech and robustness to degradations produced by transmission over a telephone channel. They achieved 96.8% identification accuracy.

In [16], a graph-based method based on Gaussian Mixture Modeling (GMM) to classify agricultural products is proposed. Their model gave the accuracies of 91.8%.

In Chapter 2, theoretical information on Gaussian Mixture Model is given and information about the software that helps to implement GMM was given in this study. In Chapter 3, detailed information on the data used in the application was given. In the same section, some performance visuals of the analysis were shown. Evaluations of the results were made and some inferences about job accidents were made in Chapter 4.

III. GAUSSIAN MIXTURE MODEL (GMM)

In this study, multivariate Gaussian distribution was handled in the mixture. From these Gaussian, i^{th} Gaussian is as seen in Eq.(1)[17].

$$f_i(x) = f(x; \mu_i, cov_i) = \frac{1}{(2\pi)^{d/2}} \exp\left\{-\frac{(x - \mu)^T cov_i^{-1}(x - \mu_i)}{2}\right\} \quad (1)$$

x is the data point and μ_i, cov_i are unknown before clustering process. Let k be the number of cluster in Eq.(2), the mixture model;

$$f(x) = \sum_{i=1}^k f_i P(C_i) = \sum_{i=1}^k f(x; \mu_i, cov_i) P(C_i) \quad (2)$$

Maximum likelihood for all data as seen in Eq. (3);

$$L = \sum_{j=1}^n \ln f(x_j) = \sum_{j=1}^n \ln \left(\sum_{i=1}^k f(x; \mu_i, cov_i) P(C_i) \right) \quad (3)$$

For any parameter θ_i (so μ_i or σ_i), Eq.(4) can be written.

$$\sum_{j=1}^n \left(\frac{1}{f(x_j)} \cdot \frac{\partial}{\partial \theta_i} \left(\sum_{i=1}^k f(x; \mu_i, cov_i) P(C_i) \right) \right) \quad (4)$$

The parameter θ_i belongs to the i^{th} node (i^{th} Gaussian), and this parameter is assumed to be fixed according to the other clusters (partial derivative of them).

That is, the derivation of the log-likelihood function can

be written as in Eq.(5).

$$\frac{\partial L}{\partial \theta_i} = \sum_{j=1}^n \left(\frac{1}{f(x_j)} \frac{\partial}{\partial \theta_i} \left((2\pi)^{-1} |cov_i^{-1}|^{0.5} \exp[g(\mu_i, cov_i)] P(C_i) \right) \right) \quad (5)$$

To calculate the maximum-likelihood estimator for μ_i , It is need to obtain the derivative of logarithm relative to $\theta_i = \mu_i$. As we have seen in Eq.(6), the only term that depends on μ_i is $\exp[g(\mu_i, \sigma_i)]$.

$$\frac{\partial L}{\partial \theta_i} \exp[g(\mu_i, cov_i)] = \exp[g(\mu_i, cov_i)] \cdot \frac{\partial L}{\partial \theta_i} g(\mu_i, cov_i) \quad (6)$$

Using the above formulas, log derivation is based on μ_i is found as in Eq.(7)-(8).

$$\sum_{j=1}^n (w_{ij} \cdot cov_i^{-1}(x_j - \mu_i)) \quad (7)$$

That is,

$$w_{ij} = P(C_i | x_j) = \frac{f(x_j; \mu_i, cov_i) P(C_i)}{f(x_j)} \quad (8)$$

If the above formula is solved by taking derivative zero and is multiplied both sides by cov_i , Eq. (9) will be obtained.

$$\mu_i = \frac{\sum_{j=1}^n w_{ij} x_j}{\sum_{j=1}^n w_{ij}} \quad (9)$$

For calculation of cov_i , the partial derivative must be processed in Eq.(5). So, final equation will be found as in Eq. (10).

$$cov_i = \frac{\sum_{j=1}^n w_{ij} (x_j - \mu_i)(x_j - \mu_i)^T}{\sum_{j=1}^n w_{ij}} \quad (10)$$

It is needed to take the derivative in Eq. (5) according to $P(C_i)$ to calculate the mixture weights $P(C_i)$. Lagrange multipliers technique should be used in this step due to need to force the rule of $\sum P(C_a)=1$. The equation of the maximum likelihood of $P(C_i)$ is obtained as in Eq.(11) after all mathematical simplification operations.

$$P(C_i) = \frac{\sum_{j=1}^n w_{ij}}{n} \quad (11)$$

The expectation maximization algorithm can be used to determine the parameters of the Gaussian mixture model. Expectation maximization is an iterative optimization algorithm. It is assigned random values to parameters (θ_i) as the initial values. E-step and M-step continues until the parameters converge or the change is sufficiently small. In the E-step the probability that x_j belongs to each distribution as in Eq.(12), that is[18],

$$P(\theta_i|x_j, \theta) = \frac{P(x_j|\theta_i)}{\sum_{l=1}^k P(x_j|\theta_l)} \quad (12)$$

In the M-step, the parameters (θ_i) is adjust by maximizing the Expected likelihood $P(x|\theta)$ in Gaussian mixture model. This can be achieved by setting the formulas in Eq. (13)-(14),

$$\mu_i = \frac{1}{k \sum_{j=1}^n \frac{P(\theta_i|x_j, \theta)}{\sum_{l=1}^k P(\theta_l|x_j, \theta)}} \quad (13)$$

and

$$\sigma_i = \sqrt{\frac{\sum_{i=1}^n P(\theta_i|x_j, \theta)(x_j - u_i)^2}{\sum_{i=1}^n P(\theta_i|x_j, \theta)}} \quad (14)$$

IV. EXPERIMENTAL RESULTS AND DISCUSSION

The dataset was collected from a company which is headquartered in Turkey. The data set consists of approximately 4000 work accident reports. In order to cluster work accidents by considering type of injury, injured part of body and type of accident, GMM was conducted in Matlab 2014 program[19]. While there are 4 different types of injuries such as cuts / slits, foreign matter evasion, burns, poisoning, there are 5 different types of the injured areas of body as hands/ fingers, eyes, internal organs, head / skull, legs and there are 11 different type of accident as Environmental accident, accident with needed only first aid, non-work related mortality accident, accident with lost work days, accidents resulting in limited disability, accident related with goods / equipment , motor vehicle accident, fatal accident, accident with needed the medical intervention , get off cheap, fire as seen in Fig.(1).

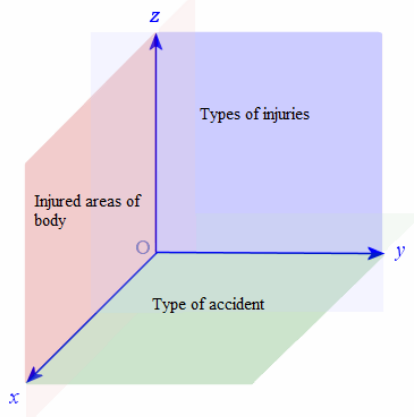


Figure 1: Variables

It is important to apply the legislative rules carefully to ensure occupational security. However, the adaptation of these legislation items to different work accidents would be healthier. Therefore, it is desired to cluster work accidents in different groups in this study. To cluster work accident into groups will be useful for taking more efficient measures in terms of occupational safety and

health. Different cluster numbers were analyzed with GMM and the graphs of likelihood and cluster groups are given in Fig. 1-4.

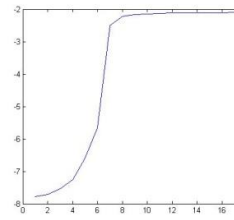


Figure 2.a: Data Likelihood for k=2

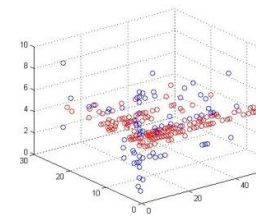


Figure 2.b: Cluster Groups for k=2

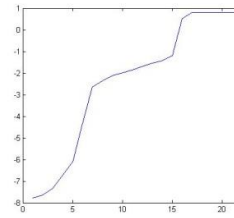


Figure 3.a: Data Likelihood for k=3

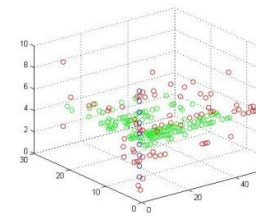


Figure 3.b: Cluster Groups for k=3

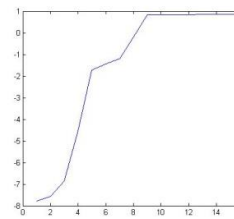


Figure 4.a: Data Likelihood for k=4

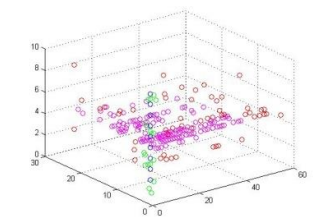


Figure 4.b: Cluster Groups for k=4

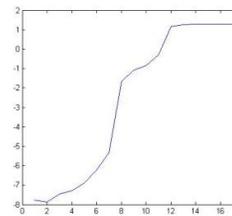


Figure 5.a: Data Likelihood for k=5

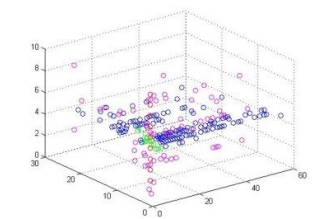


Figure 5.b: Cluster Groups for k=5

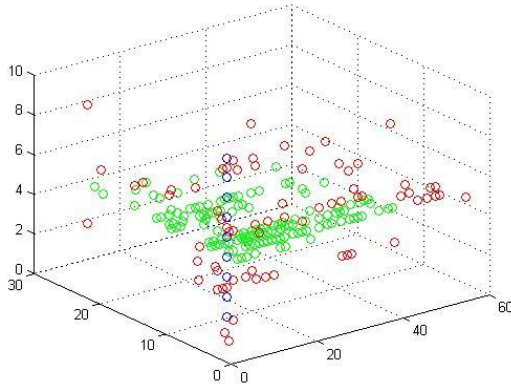
V. CONCLUSION

In this study, Gaussian mixture model based expectation maximization was proposed for clustering of job accidents. Because this study is the first clustering analysis which is performed on current data set, the actual cluster groups are not available as output data. Therefore, the accuracy rate is not calculated but the CPU times in different analyzes are given (Table I). Different cluster numbers (k) are considered in analyzes. The graphs obtained from analysis show that using the number of clusters of 3 or more in the proposed model is not a big influence on clustering results.

Table 1: CPU Times

	K=2	K=3	K=4	K=5
CPU Time (sn)	0.3029	0.3248	0.3949	0.3484

If CPU times and cluster graphs are taken into consideration, it would be more sensible to cluster work accidents by considering type of injury, injured part of body and type of accident with $k=3$ (Fig. 6).

Figure 6: Clustered work accidents with $k=3$

According to this study, it is possible to distinguish 3 groups by considering the injury characteristics and severity of work accidents. To propose measures of legislation for each of the three main groups of occupational accidents will create a more effective policy of prevention.

This application is performed for the first time in the literature and uncovers a path to discover to researchers. As the number of different papers on the same problem increases, it can be prepared the prevention of legislation specific to each cluster (so each work accident characteristics). It encourages the creation of a more flexible and preventive OHS.

ACKNOWLEDGEMENT

This study was partially supported by Rönesans Holding.

REFERENCES

- [1] Erginel, N. and Ş. TOPTANCI, *İŞ KAZASI VERİLERİNİN OLASILIK DAĞILIMLARI İLE MODELLENMESİ*. Mühendislik Bilimleri ve Tasarım Dergisi, 2017. 5(SI): p. 201-212.
- [2] LaDou, J., *Introduction to occupational health and safety*. 1986: National Safety Council.
- [3] Lay, A.M., et al., *The relationship between occupational health and safety vulnerability and workplace injury*. Safety science, 2017. 94: p. 85-93.
- [4] Ceylan, H. and M. Avan, *Türkiyede'ki İş Kazalarının Yapay Sinir Ağları ile 2025 Yılına Kadar Tahmini*. Uluslararası Mühendislik Araştırma ve Geliştirme Dergisi, 2012. 4(1): p. 46-54.
- [5] BARADAN, S., et al., *Ege Bölgesindeki İnşaat İş Kazalarının Sıklık ve Çapraz Tablolama Analizleri*. İMO Teknik Dergi, 2016. 7345(7370): p. 448.
- [6] Wang, Y., et al., *Efficient volume exploration using the gaussian mixture model*. IEEE Transactions on Visualization and Computer Graphics, 2011. 17(11): p. 1560-1573.
- [7] Huang, Y., et al., *A Gaussian mixture model based classification scheme for myoelectric control of powered upper limb prostheses*. IEEE Transactions on Biomedical Engineering, 2005. 52(11): p. 1801-1811.
- [8] Huang, Z.-K. and K.-W. Chau, *A new image thresholding method based on Gaussian mixture model*. Applied Mathematics and Computation, 2008. 205(2): p. 899-907.
- [9] Yang, M.-S., C.-Y. Lai, and C.-Y. Lin, *A robust EM clustering algorithm for Gaussian mixture models*. Pattern Recognition, 2012. 45(11): p. 3950-3961.
- [10] Biernacki, C., G. Celeux, and G. Govaert, *Choosing starting values for the EM algorithm for getting the highest likelihood in multivariate Gaussian mixture models*. Computational Statistics & Data Analysis, 2003. 41(3-4): p. 561-575.
- [11] Greenspan, H., A. Ruf, and J. Goldberger, *Constrained Gaussian mixture model framework for automatic segmentation of MR brain images*. IEEE transactions on medical imaging, 2006. 25(9): p. 1233-1245.
- [12] Lee, D.-S., *Effective Gaussian mixture learning for video background subtraction*. IEEE transactions on pattern analysis and machine intelligence, 2005. 27(5): p. 827-832.
- [13] Zivkovic, Z. *Improved adaptive Gaussian mixture model for background subtraction*. in *Pattern Recognition, 2004. ICPR 2004. Proceedings of the 17th International Conference on*. 2004. IEEE.
- [14] Herkiloğlu, K., *Gauss Karışım Modelleri Kullanılarak Ses İmzalarının Sınıflandırılması*. 2015, Fen Bilimleri Enstitüsü.
- [15] Reynolds, D.A. and R.C. Rose, *Robust text-independent speaker identification using Gaussian mixture speaker models*. IEEE transactions on speech and audio processing, 1995. 3(1): p. 72-83.
- [16] Ok, A.O., A.O. Ok, and K. Schindler. *Graph-based method based on Gaussian Mixture Modeling to classify agricultural lands*. in *Signal Processing and Communications Applications Conference (SIU), 2014 22nd*. 2014. IEEE.
- [17] Bilmes, J., *A gentle tutorial of the EM algorithm*. Tech. Rep. 97-021, Intl. Comp. Sci. Instit, Berkeley, 1997.
- [18] Han, J., J. Pei, and M. Kamber, *Data mining: concepts and techniques*. 2011: Elsevier.
- [19] Hunt, B.R., R.L. Lipsman, and J.M. Rosenberg, *A guide to MATLAB: for beginners and experienced users*. 2014: Cambridge University Press.

An Application of Hybrid Support Vector Machine and Genetic Algorithm to Classification Model

E. PEKEL¹ and Z. CEYLAN²

¹ Ondokuz Mayıs University, Faculty of Engineering, Computer Engineering Department, Samsun/Turkey, ebru.pekel@omu.edu.tr

² Ondokuz Mayıs University, Faculty of Engineering, Industrial Engineering Department, Samsun, Turkey, zeynep.dokumaci@omu.edu.tr

Abstract - Support Vector Machine (SVM) is one of the most popular machine learning algorithms in literature. It is a discriminative classifier formally defined by a separating hyperplane. In other words, SVM offers an optimal hyperplane which categorizes new examples in supervised learning. This paper presents a hybrid method that uses SVM and Genetic Algorithm (GA) together. Three different datasets obtained from UCI Machine Learning Repository were used to evaluate the performance of the proposed hybrid algorithm which were named as German, Messidor, and Pima Indian datasets. The numerical results showed that the hybrid GA-SVM algorithm provides a better prediction performance in improving the parameters compared to traditional SVM Algorithm. As a result, the accuracy rate with the GA-SVM algorithm increased from 76.4% to 77.1% in the German dataset, from 67.5% to 77.8 % in the Messidor dataset, and from 65.0% to 81.7% in the diabetes dataset.

Keywords - Classification, Genetic Algorithm, Machine Learning, Support Vector Machine

I. INTRODUCTION

Classification is a data mining technique that is used to produce the pattern in the dataset. The general process of the classification method is based on extracting patterns from the training set that consists of database objects, instances or class labels. The patterns are used to classify the class label of the testing objects where the values of the predictor features are known. Support Vector Machine (SVM), Decision Tree (DT) and Artificial Neural Network (ANN) are the most popular methods to construct a classification model.

SVM is a primarily classification method that is proposed by Vapnik, 1995 [1]. SVM can be used to learn classification, regression or ranking function. It is used in handwriting recognition, text categorization, image classification and in the sciences. SVM constructs hyperplanes in a multi-dimensional space that divides cases into different class labels. The working procedure of SVM is composed of a learning module (*SVM-learning*) and a classification module (*SVM-classification*). The training model takes the input file, target file to train the network. In the classification module, the

different class labels are given to learn and produce correct labels of the classes.

GA is a heuristic solution-search or optimization method. It is commonly used to solve complex linear and nonlinear optimization problems. It is inspired by natural by evolutionary processes such as mutation, crossover, and selection. Since, GA is an effective optimization approach, it is good candidate to find the optimal parameters of the SVM classifier [2].

The rest of the study was organized as follows: Section 2 gives brief information about the methodology of classical SVM and hybrid GA-SVM. In this section, the used datasets in this study were explained briefly. In section 3, the results of the algorithms were shown. The study was summarized and concluded in Section 4.

II. MATERIAL & METHOD

A. Dataset

In this study, a hybrid method (GA-SVM) that combines genetic algorithm and support vector machine was applied on 3 benchmark datasets obtained from the UCI machine learning repository [3]. These datasets;

German Credit Dataset includes 20 predictor variables (7 Numerical attributes and 13 Categorical or Nominal attributes) related to the information about demographic and credit status of people such nationality, credit history, age, job and etc. The dataset consists of 1000 credit applications. The goal is to classify each applicant into two categories which may be good or bad.

Messidor Dataset includes features derived from the Messidor image set in order to forecast whether an image contains signs of diabetic retinopathy or not. The dataset consists of 1151 images. Each image is labeled 0 or 1 (negative or positive diagnostic result). 540 instances are labeled 0; the remaining instances are labeled 1.

Pima Indian Dataset includes the diagnostic data of female patients who are at least 21 years old, are of Pima Indian heritage. The data contains 768 people with 8 input

parameters. The goal is to classify the people based on physiological measurements and medical attributes whether a patient has diabetes. Table 1 gives information about used datasets in this study.

Table 1: Dataset information

Dataset Name	Total Data	Attributes	Attribute Characteristics	Area
German Credit	1000	20	Categorical, Integer	Financial
Messidor	1151	20	Integer, Real	Life
Pima Indian	768	8	Integer, Real	Health

B. Method

Support vector machine is one of the supervised learning techniques with associated learning algorithms that analyze the data used for classification and regression analysis.

SVM maps the input data x into a higher dimensional feature space through a linear or nonlinear mapping. When each of the two categories is marked as belonging to one or the other of each category in training sample, SVM training algorithm creates a model that assigns new instances to a category or another by making it a non-probability binary linear classifier (Figure 1).

Each data item is plotted as a point in the n -dimensional space (where n is the number of variables in dataset) with the value of each property that is the value of a given coordinate. Then, classification is ended by finding hyper-plane which makes a very good distinction from two classes [4].

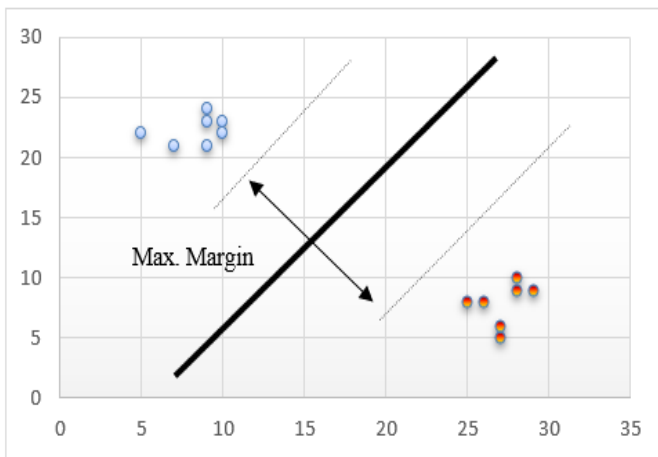


Figure 1: Classification in SVM [5]

The setting of parameters is important to obtain a good classification rate. Because, the selection of features and appropriate parameters setting can improve the accuracy of the SVM classifier [6,7]. Figure 2 shows the flowcharts of the hybrid GA-SVM algorithm.

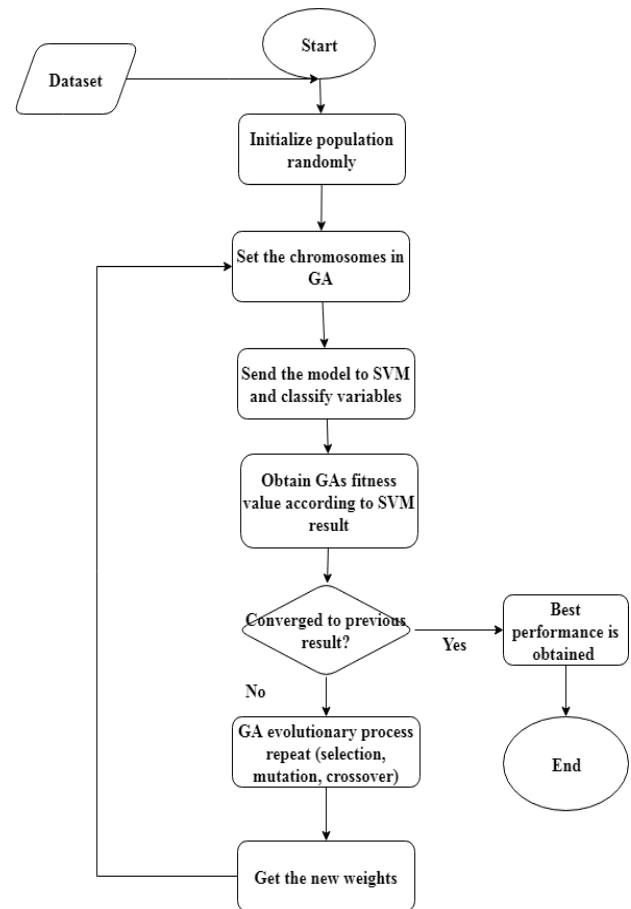


Figure 2: The flowchart of GA-SVM

III. RESULTS & DISCUSSION

The parameters of the SVM classifier are optimized with GA method to develop a more accurate result. The results are obtained from MATLAB 2017b software program.

Table 2 shows the ranges of parameter values used in the hybrid model. These parameters are selected based on the authors' experiences within a trial-and-error process. In-depth analysis and trials can be performed to find the appropriate set of parameters.

Table 2: Range of parameters of hybrid GA-SVM

Population size	Generation	Mutation	Crossover
100-200	100-200	0.10-0.20	0.60-0.70

At the same time, the classical SVM algorithm was applied on the same data set using WEKA software. The best performance was obtained on the diabetes data set.

As shown in Table 3, the conventional support vector machine achieved accuracy of 65.0%, while the hybrid (GA-SVM) provided an accuracy of 81.7%.

Table 3: Results of classical SVM and Hybrid GA-SVM

Dataset	Accuracy (%)	
	SVM	GA-SVM hybrid
German Credit Data	76.4	77.1
Messidor	67.5	77.8
Pima Indian	65.0	81.7

IV. CONCLUSION

Classification is an important technique in data mining and widely used in various fields. SVM is commonly used classification method in the literature. In this study, the genetic algorithm was integrated into the classical SVM method. The main aim of this study is to show that SVM can be used in classification studies with different hybrid models. The hybrid GA-SVM model was analyzed on three different datasets in terms of accuracy measurement. According to performance results, it was observed that the highest accuracy was obtained on diabetes data set of 81.7 %. In the future study, the proposed model can be operated with different parameter values on different datasets.

REFERENCES

- [1] Vapnik, V. (2013). *The nature of statistical learning theory*. Springer science & business media.
- [2] Lu, D., & Qiao, W. (2014, September). A GA-SVM hybrid classifier for multiclass fault identification of drivetrain gearboxes. In *Energy Conversion Congress and Exposition (ECCE), 2014 IEEE* (pp. 3894-3900). IEEE.
- [3] UCI Repository of Bioinformatics Databases [online] Available: <http://www.ics.uci.edu/~mlern/MLRepository.html>.
- [4] Huang, Y., Wu, D., Zhang, Z., Chen, H., & Chen, S. (2017). EMD-based pulsed TIG welding process porosity defect detection and defect diagnosis using GA-SVM. *Journal of Materials Processing Technology*, 239, 92-102.
- [5] Upadhyaya, S., & Ramsankaran, R. A. A. J. (2014). Support Vector Machine (SVM) based Rain Area Detection from Kalpana-1 Satellite Data. *ISPRS Annals of the Photogrammetry, Remote Sensing and Spatial Information Sciences*, 2(8), 21.
- [6] Tan, K. C., Teoh, E. J., Yu, Q., & Goh, K. C. (2009). A hybrid evolutionary algorithm for attribute selection in data mining. *Expert Systems with Applications*, 36(4), 8616-8630.
- [7] Temitayo, F., Stephen, O., & Abimbola, A. (2012). Hybrid GA-SVM for efficient feature selection in e-mail classification. *Computer Engineering and Intelligent Systems*, 3(3), 17-28.

Smartphone Based Activity Recognition using K-Nearest Neighbor Algorithm

Almontazer MANDONG^{1*}, Usama MUNIR¹

¹Karadeniz Teknik University, Department of Electrical and Electronics Engineering, Trabzon/TURKEY,

*Corresponding author: montazermandong@gmail.com

Abstract - Activity recognition of smartphone-based accelerometer sensor data using k-Nearest Neighbor (kNN) algorithm was studied. MATLAB is used in order to extract the data features (Mean, Median, Standard Deviation, Variance, Minimum Value and Maximum Value) and a sliding window algorithm with an overlap of 50% every 2.56 seconds. Data classification using kNN algorithm was done by using WEKA knowledge analysis software. An accuracy of 97.9769% was achieved by using kNN algorithm with k value of 3. A root mean squared error of 0.08, mean absolute error of 0.0101, and a relative absolute error of 3.6861% was also achieved during the process. kNN algorithm demonstrated to be an exceptional algorithm with high accuracy and low statistical error in predicting/classifying periodic daily activities such as walking, sitting, lying down and others.

Keywords – Activity Recognition, Machine Learning, Sensors, Machine Learning Algorithm, Data Analysis.

I. INTRODUCTION

SMARTPHONES became an integral part of our daily lives due to its numerous benefits for our everyday lives such as communications, research, social interactions and many others. Smartphones are devices that are able to run an Operating System which can perform numerous tasks that a personal computer can do such as running downloaded applications, surfing the internet and many other tasks. Smartphones evolved from having simple set of sensors into having sophisticated sensors such as GPS Navigation systems, Proximity Sensors, Accelerometers, Gyroscopes, Fingerprint sensors and many other features which can be used by users in many practical applications [1, 2].

With integrated sensors in smartphones and machine learning algorithms, recognition of various activities that we use in our daily lives through the use of various sensors can be used to create useful applications such as health monitoring system, fitness tracking, and many other applications which can help improve our quality of life. Tracking our daily activity can help us plan a more efficient and healthier lifestyle [1-5].

Numerous machine learning algorithms can be used to process and extract information from the raw data provided by various sensors. These algorithms can be generally categorized as supervised and unsupervised learning. Supervised algorithm is the most commonly used machine learning algorithm in the

industry today. Supervised machine learning algorithm needs set of known input and output values in order to predict the incoming data and extract information on it based on the known input and output data [5]. One of the commonly used supervised machine learning algorithm for identifying patterns or behavior of a data based on previously known data is k-nearest neighbor (kNN) algorithm. kNN can predict the classification of new data by searching for the most number of similar classified data in its neighbors [6].

In this paper, data is gathered using android smartphone with a built-in accelerometer sensor. 6 different types of activities are gathered independently and randomly appended with each other in order to produce a single file which is needed for training the data. A MATLAB code is used to process and extract data features by using different statistical tools and additional algorithms. After processing with MATLAB, another MATLAB code is used in order to convert the file into .arff file which is used in the data classification stage. After converting the file, WEKA knowledge analysis software by University of Waikato [8], a powerful standalone machine learning analysis software with numerous machine learning algorithms including kNN was used. Various statistical outcomes are generated and analyzed in order to obtain the desired information based on the raw data.

II. METHODOLOGIES

A. Data Gathering

Initially, raw data are gathered using Android based smartphone with a built-in accelerometer sensor. The original data set includes x, y and z axis values from the smartphone's accelerometer sensor. The raw data has a total length of 11072 samples. The raw data consists variations in x, y and z coordinates with respect to the location of the sensor in the smartphone with a frequency of 50Hz. Each activity is gathered independently in order to correctly classify each of them initially. The classified activities consisted of 6 common daily routines such as (1) walking, (2) walking upstairs, (3) walking downstairs, (4) sitting, (5) standing and (6) laying down respectively. Each activity is appended randomly with each other which resulted into a single file with x, y, z coordinates and their corresponding classifications. Figure 1. shows the different patterns of activities and their corresponding classifications.

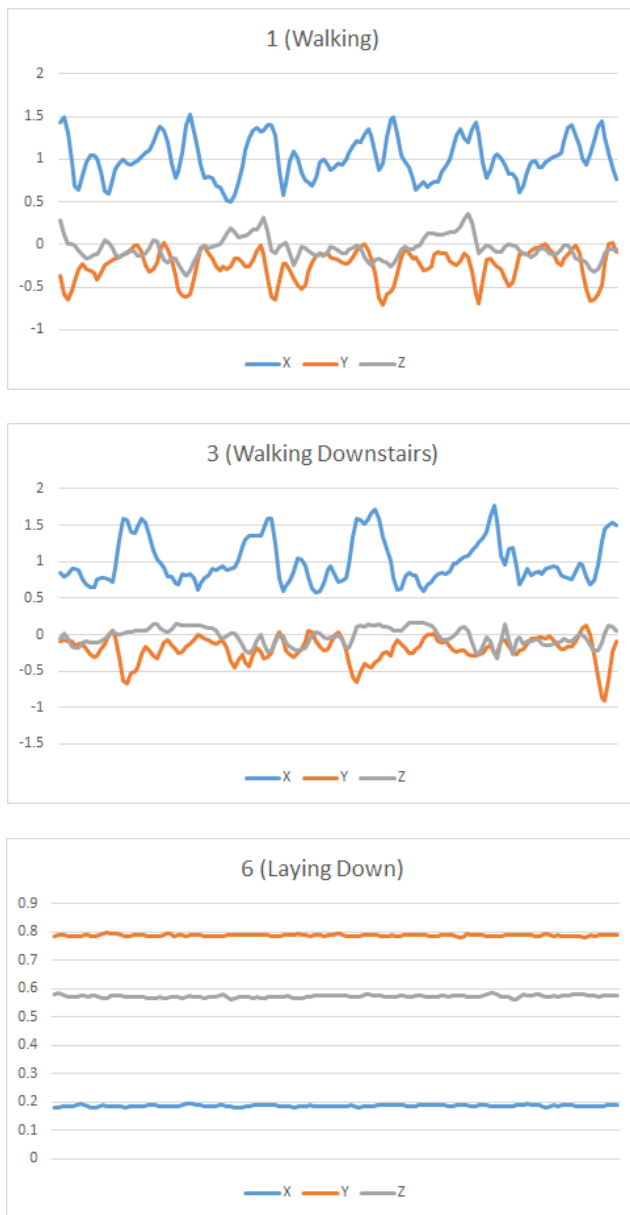


Fig. 1 – Data Patterns and Classification

B. Data Processing

After appending and formatting the raw data, the output data set will undergo data feature extraction using 6 different statistical tools which includes mean, median, standard deviation, variance, minimum value and maximum value using MATLAB. These statistical tools can help the machine learning algorithm to become more accurate in differentiating different types of data with minute difference in x,y and z values such as walking upstairs and walking downstairs.

Using a MATLAB code, a sliding window algorithm is used in order to segment the raw data. A sliding window of 2.56 seconds was used. For each window different data features were calculated, these features include mean, median, standard deviation, variance, minimum value and maximum value. Each window is overlapped by 50% with the next window. As a result, 6 new data sets with a length of 346 samples in each feature is achieved. After the process, Another MATLAB code is used to convert the data into a WEKA-compatible .arff

format file. After converting the data set into a format which the WEKA application recognizes, WEKA knowledge analysis software is used in order to classify the processed data set using kNN algorithm (*Itk in WEKA*).

Data classification is used in processing and organizing data from a known source and categorizing each of them in order to get essential information. It classifies data according to data set requirements for various objectives. A basic classification algorithm is shown in Fig. 2. A classifier is first trained using training set, so that classifier learns what was the connection or link between output and the observations. Then this classifier is evaluated using an unseen and unknown data, which is called test data, to check how accurate the classifier can classify the data [8].

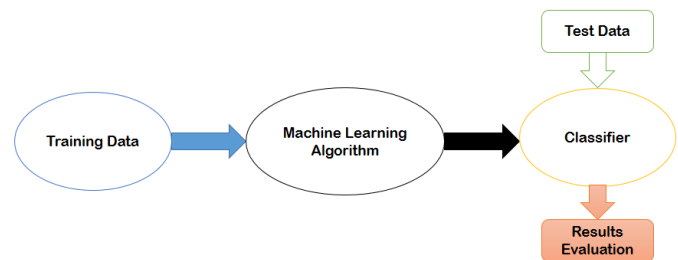


Fig. 2 – Basic Classification Algorithm

kNN is one of the best algorithm that can be used for such simple recurring activities. Figure 3. Shows how the kNN algorithm works, k-Nearest Neighbor algorithm classifies an unknown object by counting the number of its nearest neighbors based on the value of k. The unknown instance will be classified as the class which is most common among its k nearest neighbors. The value of k must be a positive odd integer in order to prevent having the same number of neighbor which will result to a confusion in classification. A cross-validation test option of 10 folds is used, which means that in every 100 instances, 10 known instances will be used in order to predict the other 90 instances. A k value of 3 is used which resulted in a prediction accuracy of 338/346 or 97.9769%.

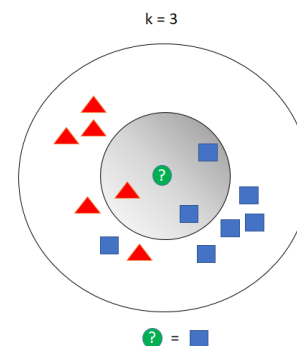


Fig. 3 – k-Nearest Neighbor Algorithm

III. RESULTS AND DISCUSSIONS

In order to effectively predict the activities from accelerometer data of a smartphone, kNN algorithm with k

value of 3 is used. Table 1 shows the classifier model (full training set). 339 out of 346 instances are correctly classified by the algorithm with a 97.9769% of accuracy. The algorithm also resulted in a kappa statistics of 0.9753 which shows that the result of data classification is almost in agreement with the desired data. A kappa statistics with a value of 1 is the best possible outcome which suggests that the predicted value is in agreement with the desired value [9]. The table also shows four different statistical error measurements which measures the degree of correlation between the predicted and actual values.

Table 1: Stratified Cross-validation Summary

Correctly Classified Instances	339	97.9769%
Incorrectly Classified Instances	7	2.0231%
Kappa Statistic	0.9753	
Mean Absolute Error	0.0101	
Root Mean Squared Error	0.08	
Relative Absolute Error	3.6861%	
Root Relative Squared Error	21.6485%	
Total Number of Instances	346	

Another important output parameters in WEKA is the confusion matrix. Confusion matrix shows the correctly and incorrectly classified instances. Table 2. shows the output confusion matrix of the data classification using kNN algorithm. The algorithm correctly classified 93 instances of activity a (walking), 51 of b (walking upstairs), 46 of c (walking downstairs), 47 of d (sitting), 52 of e (standing) and 50 of f (laying down). It also incorrectly classified 2 instances of c as a, 1 instance each of a and c as b, 2 instances of a as c and 1 instance of b as e.

Table 2: Output Confusion Matrix

a	b	c	D	e	f	
93	0	2	0	0	0	a=1
1	51	1	0	0	0	b=2
2	0	46	0	0	0	c=3
0	0	0	47	0	0	d=4
0	1	0	0	52	9	e=5
0	0	0	0	0	50	f=6

Each class(activity) has their own corresponding accuracy, Table 3 shows the detailed accuracy by class. Class 4 got the highest True Positive (TP) Rate of 1 which means that every activity with classification of 4 have been correctly predicted. The weighted average of 6 classes is 0.977 which also corresponds to a great overall accuracy. The False Positive (FP) rates of all 6 classes have a small value which is desired in any machine learning algorithm. Precision and Recall are important tools which tells us how the algorithm correctly predicts the relevant data. A precision and recall value nearer to 1 is desired, in this case both precision and recall have

0.977 weighted average. The F-Measure measures the harmonic mean of both recall and precision. Mathew's correlation coefficient (MCC) is a coefficient of the correlation between the actual (observed) and predicted value. MCC of +1 means that both actual and predicted data are strongly correlated. [10] Receiver Operating Characteristic (ROC) and Precision Recall Curve (PRC) Area are graphical representations that measures the performance between the correctly and incorrectly classified instances and used to measure the effectiveness of the classifier.

Table 3: Detailed Accuracy by Class

	TP Rate	FP Rate	Precision	Recall	Class
	0.979	0.012	0.969	0.974	1
	0.962	0.007	0.962	0.962	2
	0.938	0.007	0.957	0.947	3
	1.000	0.000	1.000	1.000	4
	0.981	0.000	1.000	0.989	5
	1.000	0.003	0.980	0.988	6
Average	0.977	0.006	0.977	0.977	

	F-Measure	MCC	ROC Area	PRC Area	Class
	0.974	0.964	0.975	0.945	1
	0.962	0.955	0.977	0.949	2
	0.947	0.939	0.967	0.904	3
	1.000	1.000	1.000	1.000	4
	0.990	0.989	0.994	0.985	5
	0.977	0.988	0.997	0.969	6
Average	0.977	0.971	0.984	0.957	

IV. CONCLUSION

Smartphone based accelerometer sensor was used for gathering raw data. Readings of the variations of x, y and z coordinates were obtained from the android application with a frequency of approximately 50Hz. 6 Different activities were independently gathered and randomly appended with each other in order to generate a single file for further processing. After appending all files, a MATLAB code was used in order to extract the data features and use sliding window algorithm which resulted into 6 data sets with 346 samples. Another MATLAB code is used in order to convert the file into a .arff files which is needed for data classification. WEKA knowledge analysis software with a built-in kNN algorithm is used in order to classify the processed data and generate statistical analysis of the data. kNN algorithm is used with a k value of 3 which resulted in 338/346 or 97.9769% correctly classified activities.

REFERENCES

- [1] T. Jeong, D. Klab, J. Starren, "Predictive Analytics Using Smartphone Sensors for Depressive Episodes", 2016
- [2] F. Concone, S. Gaglio, G. Lo Re, M. Morana, "Smartphone Data Analysis for Human Activity Recognition". Advances in Artificial Intelligence. AI*IA 2017. Springer, 2017

- [3] W. Kang, and Y. Han. "SmartPDR: Smartphone-based pedestrian dead reckoning for indoor localization." *IEEE Sensors journal* 15.5: 2906-2916, May 2015.
- [4] M. Ermes, J. Parkka, J. Mantjarvi and I. Korhonen, "Detection of Daily Activities and Sports With Wearable Sensors in Controlled and Uncontrolled Conditions," in *IEEE Transactions on Information Technology in Biomedicine*, vol. 12, no. 1, pp. 20-26, Jan. 2008
- [5] J. Brownlee, "Supervised and Unsupervised Machine Learning", Mar. 2016, retrieved from: <https://machinelearningmastery.com/supervised-and-unsupervised-machine-learning-algorithms/>
- [6] J. Brownlee, "K-Nearest Neighbors for Machine Learning", April 2016, retrieved from: <https://machinelearningmastery.com/k-nearest-neighbors-for-machine-learning/>
- [7] R. Gull, U. Shoaib, S. Rasheed, W. Abid, B. Zahoor, "Pre Processing of Twitter's Data for Opinion Mining in Political Context", *Procedia Computer Science*, 2016
- [8] E. Frank, M.A. Hall, and I. H. Witten. The WEKA Workbench. Online Appendix for "Data Mining: Practical Machine Learning Tools and Techniques", Morgan Kaufmann, Fourth Edition, 2016.
- [9] M.L. McHugh, "Interrater reliability: the kappa statistic.", *Biochemia Medica*, 22(3), 276-282, 2012.
- [10] W. Koehrsen, "Beyond Accuracy: Precision and Recall choosing the right metrics for classification tasks", Mar. 2016, retrieved from: <https://towardsdatascience.com/beyond-accuracy-precision-and-recall-3da06bea9f6c>

A New Multi-Objective Artificial Bee Colony Algorithm for Multi-Objective Optimization Problems

Z. YILMAZ ACAR¹, F. AYDEMIR² and F. BASCIFTCI¹

¹Selçuk University, Konya/Turkey, zuleyhayilmaz@selcuk.edu.tr

¹Selçuk University, Konya/Turkey, basciftci@selcuk.edu.tr

²Kuveyt Turk Participation Bank, Konya/Turkey, fikri.aydemir@kuveytturk.com.tr

Abstract - Since real-world problems have multi-objective optimization problems, algorithms that solve such problems are getting more important. In this study, a new multi-objective artificial bee colony algorithm is proposed for solving multi-objective optimization problems. With the proposed algorithm, non-dominated solutions are kept in the fixed-sized archive. It has benefited from the crowding distance during the selection of elite solutions in the archive. Moreover, the onlooker bees are selected from the archive members with the proposed algorithm. It is aimed to improve the archive members with this modification. To evaluate the performance of the proposed algorithm, ZDT1, ZDT2 and ZDT3 from ZDT family of benchmark functions were used as multi-objective benchmark problems and the results were compared with MOPSO and NSGA-II algorithms. The results show that the proposed algorithm is an alternative method for multi-objective optimization problems.

Keywords - Optimization, multi-objective optimization, artificial bee colony algorithm, swarm intelligence

I. INTRODUCTION

MANY of the problems in the real-world are defined as problems with more than one and often conflicting goals [1]. Since achieving these goals is an optimization process; such a problem is called a multi-objective optimization problem (MOP). A general MOP can be expressed by (1):

$$\begin{aligned} F(x) &= \{f_1(x), f_2(x), \dots, f_m(x)\}, \\ x &= (x_1, x_2, \dots, x_d) \ \& \ m > 1 \\ \text{Constraints:} & \\ h_i(x) &< 0 \ \text{for } i = 1, 2, \dots, I \\ g_j(x) &= 0 \ \text{for } j = 1, 2, \dots, J \end{aligned} \quad (1)$$

where x is decision vector with d dimensions; $F(x)$ is a set of objective functions; $h(x)$ and $g(x)$ are inequality and equality constraints of the problem.

Moreover, there are some concepts in multi-objective optimization:

Pareto-dominance: It is a method used to compare two solutions. To say that the solution a dominates the solution

b , the solution a must not be worse for all objective functions and be good from the solution b for at least one objective function.

Pareto-optimal: If there is no solution that dominates the solution a , the solution a is called pareto-optimal solution.

Pareto-optimal set: This set consists of pareto-optimal solutions.

In this process, optimization algorithms which provide many alternative solutions to decision-makers are used to solve these problems. In this study, artificial bee colony (ABC) algorithm is used to solve MOP. ABC algorithm is a popular algorithm proposed for numerical problems in 2005 [2]. Due to its easy applicability and low parameters, it has become a frequently used algorithm for solving optimization problems [3]. The ABC algorithm showed superior performances when compared with other algorithms known for solving single-objective problems. Along with single-objective problems, the literature suggests that the ABC algorithm is proposed for MOPs [4-10].

In this work, a new multi-objective ABC (MOABC) algorithm is proposed for MOPs. The proposed algorithm is applied on ZDT1, ZDT2 and ZDT3 from ZDT family benchmark functions and the results are compared with MOPSO [11] and NSGA-II [12] algorithms from other multi-objective optimization algorithms.

II. MULTI-OBJECTIVE ARTIFICIAL BEE COLONY ALGORITHM (MOABC)

ABC algorithm has been proposed by Karaboğa in 2005 [2]. This algorithm, which consists of three artificial bees, includes employed, onlooker and scout. The employed bees bring nectar to their hives from food sources and share the obtained information about the sources with the other bees in the hive. The onlookers select a food in the light of this information. In the algorithm, the exhaustion status of the sources is kept in the trial counter. If the counter of a source used by employed bee has reached the predetermined limit value, the employed bee is called as the scout bee and search for new source.

In the MOABC algorithm proposed in this work, initial solutions are generated firstly. Among these solutions, non-dominated solutions are kept in an archive. Improvement of

the current solutions is provided by employed bee stage. New solutions are found in (2):

$$v_{ij} = x_{ij} + \delta \times (x_{ij} - x_{kj}) \quad (2)$$

where x_{ij} is current solution, x_{kj} is neighbor solution ($i \neq k$) and v_{ij} is new candidate solution. δ is a random value in the range [-1,1].

A new solution is selected by applying greedy selection method between the candidate solution and current solution. If the selected solution is the current solution, the trial counter is incremented. If it is the new solution, the counter is reset to zero. The obtained solutions are compared with each AR member from the archive. and the archive is updated. This ensures that up-to-date solutions are retained in the archive. The employed bee stage and archive update procedure are shown by Algorithm 1 and Algorithm 2, respectively.

```

For  $i=1$  to  $PopulationNumber/2$ 
  Select randomly a dimension  $j$  and neighbor  $k$ 
  from the population ( $i \neq k$ )
   $v_{ij} = x_{ij} + \delta * (x_{ij} - x_{kj})$ 
  If  $v_i$  dominates  $x_i$ 
     $x_i = v_i$ 
     $trial_i = 0$ 
  Else if  $x_i$  dominates  $v_i$ 
     $trial_i = trial_i + 1$ 
  Else if  $v_i$  and  $x_i$  are non-dominated solutions
    If  $rand < 0.5$ 
       $x_i = v_i$ 
       $trial_i = 0$ 
    Else
       $trial_i = trial_i + 1$ 
    End If
  End If
   $UpdateArchive(v_i, AR)$ 
End For

```

Algorithm 1. Employed Bee Stage

```

For  $i=1$  to  $length(AR)$ 
  If  $v$  dominates  $AR_i$ 
    Add  $v$  to the archive
  Else if  $AR_i$  dominates  $v$ 
    Do nothing
  Else if  $AR_i$  and  $v$  are nondominated solutions
    Add  $v$  to the archive
  End If
End For

```

Algorithm 2. Archive Update Procedure

The onlooker bees in the MOABC are accepted as archive members in contrast to the basic ABC algorithm, and another archive member is used to improve an archive member. This process is represented by (3):

$$v_{ij} = AR_{ij} + \delta \times (AR_{ij} - AR_{kj}) \quad (3)$$

where the candidate solution v_{ij} in the onlooker bee stage is produced by using AR_{ij} which is an archive member, and AR_{kj} is a neighbor archive member ($i \neq k$). When a neighbor archive member is selected, the crowding distance (CD) values of all archive members are calculated [12] and the member AR_{kj} with the lowest CD value is selected. The δ is a random value in the interval [-1,1].

The current solution is an archive member and the candidate solution is produced by using the archive members as in (3). The archive update procedure shown in Algorithm 1 is used between these two solutions. Along with this process, it is aimed to increase the local search ability of the algorithm in the archive members. The onlooker bee stage is shown in Algorithm 3.

```

For  $i=1$  to  $length(AR)$ 
  Select randomly a dimension  $j$ 
  Select neighbor  $k$  from the archive ( $i \neq k$ ) according to
  crowding distance values
   $v_{ij} = AR_{ij} + \delta * (AR_{ij} - AR_{kj})$ 
   $UpdateArchive(v_i, AR)$ 
End For

```

Algorithm 3. Onlooker Bee Stage

A fixed-sized archive is used in the MOABC algorithm. When the archive is updated, the archive size is controlled. If the size reaches a predetermined value, elite archive members are kept in archive. CD values are used in the selection of elite members.

As in the basic ABC, in the MOABC algorithm, the trial counters of the food sources are controlled in the scout bee stage. If there is a food source that reaches the predetermined limit value, the new position is determined for that. There can be only one scout bee in every cycle. The stopping criterion is the number of evaluations. When the stopping criterion is satisfied, operation of the algorithm is terminated, and the current archive is returned as a result. The scout bee stage is represented by Algorithm 4:

```

Determine only one  $x_i$  solution with maximum
   $trial$  in the population
If  $trial_i \geq limit$ 
  Generate initial position for  $x_i$ 
   $trial_i = 0$ 
End If

```

Algorithm 4. Scout Bee Stage

III. EXPERIMENTS

The proposed MOABC algorithm is compared with MOPSO and NSGA-II algorithms based on the test functions using performance metric results.

A. Figures and Tables

In this study, ZDT1, ZDT2 and ZDT3 functions were used as test functions. ZDT test functions [13] are widely used in evaluating the performance of multi-objective optimization algorithms. The problems used are MOPs with unconstrained two objectives.

B. Performance Metric

The Inverted Generational Distance (IGD) [14] metric was used to evaluate the performance of the MOABC algorithm. With this metric, both the diversity and the convergence of the algorithm are examined. The metric calculates the distance between the true Pareto-front and the obtained Pareto-front by the MOABC algorithm. The low IGD value indicates the success of the algorithm. IGD value is expressed as (4):

$$IGD(OPF, TPF) = \frac{\sum_{i \in TPF} d(i, OPF)}{|TPF|} \quad (4)$$

where TPF is true Pareto-front, OPF is obtained Pareto-front by the MOABC algorithm. $d(i, OPF)$ is minimum Euclidean distance. $|TPF|$ is number of TPF solutions.

C. Parameter Settings

The decision variable number for the test functions is set to 30. The number of population is 50, and the maximum number of evaluations is $1.0E+5$. The results obtained 10 independent runs. Additionally, the limit value for the food sources is set to 5 in the MOABC algorithm. In this study, the results of the MOPSO and NSGA-II algorithms used for comparison were obtained from the PlatEMO platform (which can be downloaded from link: <http://bimk.ahu.edu.cn/index.php?s=/Index/Software>) [15].

IV. RESULTS AND DISCUSSION

The results obtained from the MOPSO, NSGA-II and MOABC algorithms proposed in this study for ZDT1, ZDT2 and ZDT3 test functions are shown in Table 1. Average IGD values and standard deviation values are included in the table.

Table 1: IGD and Standard Deviation Values for ZDT1, ZDT2 and ZDT3

Test Func.	Algorithms			
		MOPSO	NSGA-II	MOABC
ZDT1	Mean	4,96E+1	1,09E-2	7,63E-3
	Std	1,37E+1	6,65E-4	7,22E-4
ZDT2	Mean	6,18E+1	1,12E-2	1,05E-1
	Std	9,80E+0	8,67E-4	1,53E-1
ZDT3	Mean	5,59E+1	1,83E-2	9,50E-3
	Std	1,15E+1	1,15E-2	1,27E-3

Table 1 shows performance comparisons for MOPSO, NSGA-II and the proposed MOABC algorithms for ZDT1, ZDT2 and ZDT3 functions. As can be seen, the MOABC algorithm achieved better results than MOPSO and NSGA-II

algorithms for ZDT1 and ZDT3. For ZDT2, while the proposed MOABC algorithm yields better results than the MOPSO algorithm, the algorithm that achieves the best result is NSGA-II. The distributions of the solutions obtained by MOABC algorithm on the true Pareto-front are shown in Figures (1) – (3).

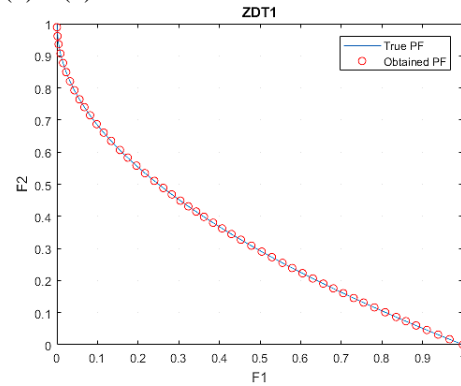


Fig. 1. Pareto-front of MOABC algorithm on ZDT1 function

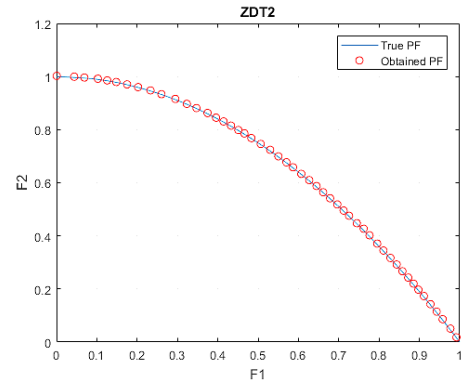


Fig. 2. Pareto-front of MOABC algorithm on ZDT2 function

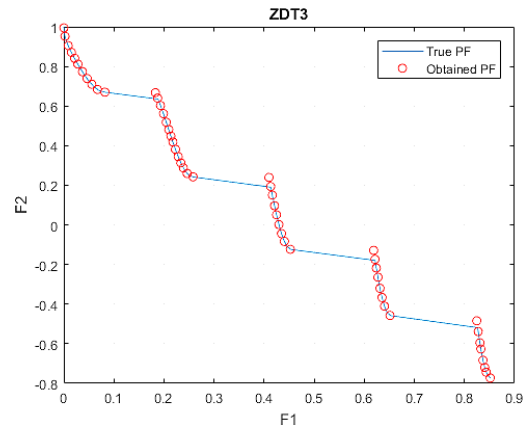


Fig. 3. Pareto-front of MOABC algorithm on ZDT3 function

As shown in Figs. (1) - (3), the MOABC algorithm showed a good distribution on the true Pareto-front with the solution variability. It seems that the non-dominated solutions obtained by the MOABC algorithm cover the true Pareto-front.

V. CONCLUSION

In this study, MOABC was proposed to solve MOPs. In the proposed algorithm, an improvement has been made in the onlooker be stage, and the results were compared with the MOPSO and NSGA-II algorithms. Three functions of the ZDT benchmark family were selected as the test function. IGD metric was used as performance metric. It is seen that the proposed MOABC algorithm is an alternative solution method to solve MOPs. In future works, the performance of MOABC algorithm can be evaluated in other test and engineering problems.

Forum]," *IEEE Computational Intelligence Magazine*, vol. 12, pp. 73-87, 2017.

REFERENCES

- [1] Konak, D. W. Coit, and A. E. Smith, "Multi-objective optimization using genetic algorithms: A tutorial," *Reliability Engineering & System Safety*, vol. 91, pp. 992-1007, September 2006.
- [2] D. Karaboga, "An idea based on honey bee swarm for numerical optimization," Technical report-tr06, Erciyes university, engineering faculty, computer engineering department, 2005.
- [3] D. Karaboga, B. Gorkemli, C. Ozturk, and N. Karaboga, "A comprehensive survey: artificial bee colony (ABC) algorithm and applications," *Artificial Intelligence Review*, vol. 42, pp. 21-57, 2014.
- [4] D. Gong, Y. Han, and J. Sun, "A novel hybrid multi-objective artificial bee colony algorithm for blocking lot-streaming flow shop scheduling problems," *Knowledge-Based Systems*, vol. 148, pp. 115-130, May 2018.
- [5] J. M. Sanchez-Gomez, M. A. Vega-Rodríguez, and C. J. Pérez, "Extractive multi-document text summarization using a multi-objective artificial bee colony optimization approach," *Knowledge-Based Systems*, November 2017.
- [6] Saad, S. A. Khan, and A. Mahmood, "A multi-objective evolutionary artificial bee colony algorithm for optimizing network topology design," *Swarm and Evolutionary Computation*, vol. 38, pp. 187-201, February 2018.
- [7] C. J. Pérez, M. A. Vega-Rodríguez, K. Reder, and M. Flörke, "A Multi-Objective Artificial Bee Colony-based optimization approach to design water quality monitoring networks in river basins," *Journal of Cleaner Production*, vol. 166, pp. 579-589, November 2017.
- [8] Kishor, P. K. Singh, and J. Prakash, "NSABC: Non-dominated sorting based multi-objective artificial bee colony algorithm and its application in data clustering," *Neurocomputing*, vol. 216, pp. 514-533, December 2016.
- [9] K. Dwivedi, S. Ghosh, and N. D. Londhe, "Low power FIR filter design using modified multi-objective artificial bee colony algorithm," *Engineering Applications of Artificial Intelligence*, vol. 55, pp. 58-69, October 2016.
- [10] M. Ding, H. Chen, N. Lin, S. Jing, F. Liu, X. Liang, *et al.*, "Dynamic population artificial bee colony algorithm for multi-objective optimal power flow," *Saudi Journal of Biological Sciences*, vol. 24, pp. 703-710, March 2017.
- [11] C. A. C. Coello and M. S. Lechuga, "MOPSO: a proposal for multiple objective particle swarm optimization," in *Evolutionary Computation, 2002. CEC '02. Proceedings of the 2002 Congress on*, 2002, pp. 1051-1056.
- [12] K. Deb, A. Pratap, S. Agarwal, and T. Meyarivan, "A fast and elitist multiobjective genetic algorithm: NSGA-II," *IEEE Transactions on Evolutionary Computation*, vol. 6, pp. 182-197, 2002.
- [13] E. Zitzler, K. Deb, and L. Thiele, "Comparison of Multiobjective Evolutionary Algorithms: Empirical Results," *Evolutionary Computation*, vol. 8, pp. 173-195, 2000.
- [14] E. Zitzler, L. Thiele, M. Laumanns, C. M. Fonseca, and V. G. d. Fonseca, "Performance assessment of multiobjective optimizers: an analysis and review," *IEEE Transactions on Evolutionary Computation*, vol. 7, pp. 117-132, 2003.
- [15] Y. Tian, R. Cheng, X. Zhang, and Y. Jin, "PlatEMO: A MATLAB Platform for Evolutionary Multi-Objective Optimization [Educational

Prediction of Sepsis Disease by Artificial Neural Networks

U.KAYA¹, A.YILMAZ² and Y. DİKMEN³

¹ İzmir Kavram Vocational College, İstanbul/Turkey, umut.kaya@kavram.edu.tr

²Beykent University, İstanbul/Turkey, atincyimaz@beykent.edu.tr

³İstanbul University, İstanbul/Turkey, ydikmen@istanbul.edu.tr

Abstract - Sepsis is a fatal condition, which affects at least 26 million people in the world every year that is resulted by an infection. For every 100,000 people, sepsis is seen in 149-240 of them and it has a mortality rate of 30%. The presence of infection in the patient is determined in order to diagnose the sepsis disease. If there is an infection in the patient, by using the results of various QSOFA and SOFA evaluations and measurements, it is determined whether the patient has sepsis or not. With the increased usage of artificial intelligence in the field of medicine, the early prediction of many diseases and the early treatment of the disease with these methods are provided. Considering the learning, reasoning and decision making abilities of artificial neural networks, which are the sub field of artificial intelligence are inferred to be used in predicting early stages of sepsis disease and determining the sepsis level is assessed. Therefore, in this study, it is aimed to reduce the patient losses by using multi-layered artificial neural network to early diagnose of sepsis. In constructed of artificial neural network model, feed forward back propagation network structure and Levenberg-Marquardt training algorithm are used. The input and output variables of the model are the parameters which doctors use to diagnose the sepsis disease and determine the level of sepsis. The proposed method aims to provide an alternative prediction model for the early detection of sepsis disease.

Keywords - Sepsis, artificial intelligence, artificial neural networks, sepsis risk prediction.

I. INTRODUCTION

Sepsis is a fatal condition, which affects at least 26 million people in the world every year that is resulted by an infection. For every 100,000 people, sepsis is seen in 149-240 of them and it has a mortality rate of 30%. In order to diagnose sepsis, it is determined whether there is an infection in the patient. For the diagnosis of infection in the patient, the presence of infection in the lungs, the detection of bacterial growth or bacterial infection in the hemoculture of the patient during bacterial screening, the presence of intraabdominal infection, new antibiotic therapy and other infections are investigated. In case of the determination of the infection, the patient's QSOFA criteria are considered. QSOFA is the scoring system, which consists of the respiratory rate in a minute, altered mental status and systolic blood pressure values. If QSOFA score is greater than or equal to 2, sepsis

suspicion occurs in the patient. To determine the diagnosis and severity of sepsis, a score named as SOFA is used, which are comprise of respiration, coagulation assessment for determination of coagulation level, liver evaluation, evaluation of cardiovascular system, evaluation of brain functions and renal function. While the decrease in SOFA score is an indication of a positive development in the case the patient, the increase of a SOFA score is expressed by the doctors as an approach to patient's death [1, 2, 3, 4].

3. International Sepsis and Septic Shock Consensus Definitions were reorganized by the American Medical Association [5]. In this new arrangement, the SIRS criteria determined by Bone et al. [6] were used. The occurrence of two or more of the following conditions according to the specified SIRS criteria leads to the SIRS syndrome:

- If the body temperature is lower than 36 degrees or higher than 38 degrees,
- If the patient has more than 90 heartbeats per minute
- If the patient has more than 20 breaths per minute,
- If the number of white blood cells in the patient is more than 12,000 or less than 4000 at 1 mm³, or if the number of immature neutrophils is greater than 10%, the patient is diagnosed with SIRS [5].

Key concepts used in the definition of sepsis are as follows [5]:

- Sepsis is the primary cause of death due to infection, especially if it is not noticed and is not treated immediately. This requires immediate intervention in case of recognition.
- Sepsis is a syndrome that is shaped by pathogenic factors and host factors that develop over time. What distinguishes the sepsis from infection is the presence of an abnormal or irregular host response and organ failure.
- There may be hidden organ failure due to sepsis; therefore, it should be considered to be present in any patient with an infection. However, unknown infection may be the cause of organ failure. Any unexplained organ impairment increases the likelihood of underlying infection.
- The clinical and biological phenotype of sepsis may be altered by pre-existing acute disease, prolonged ongoing additional disease, medications and interventions.
- Specific infections may result in local organ failure

without producing an irregular systemic host response.

The evaluation criteria used in determining the SOFA score are shown in Figure 1 [5].

- In a way that everyone can understand, Sepsis is a life-threatening condition that occurs when the body suffers damage to its tissues and organs during an infection reaction.

Patients with septic shock can be described by clinical Sepsis with persistent hypotension

requiring a mean arterial pressure of MAP \leq 65 mm Hg and a serum lactate level $>$ 2 mmol / L (18 mg / dL) despite adequate volume resuscitation. Hospital mortality exceeds 40% with these criteria.

- When SOFA is defined as consecutive or sequential organ impairment associated with Sepsis, QSOFA is expressed as rapid SOFA evaluation [5].

After these definitions, QSOFA (rapid SOFA evaluation criteria) are:

- The number of breaths per minute is equal to or greater than 22

- Changes in consciousness, i.e. mental activity

System	Score				
	0	1	2	3	4
Respiration					
PaO ₂ /FiO ₂ , mm Hg (kPa)	\geq 400 (53.3)	$<$ 400 (53.3)	$<$ 300 (40)	$<$ 200 (26.7) with respiratory support	$<$ 100 (13.3) with respiratory support
Coagulation					
Platelets, $\times 10^3/\mu\text{L}$	\geq 150	$<$ 150	$<$ 100	$<$ 50	$<$ 20
Liver					
Bilirubin, mg/dL ($\mu\text{mol/L}$)	$<$ 1.2 (20)	1.2-1.9 (20-32)	2.0-5.9 (33-101)	6.0-11.9 (102-204)	$>$ 12.0 (204)
Cardiovascular					
MAP \geq 70 mm Hg	MAP $<$ 70 mm Hg	Dopamine \leq 5 or dobutamine (any dose) ^a	Dopamine 5.1-15 or epinephrine \leq 0.1 or norepinephrine \leq 0.1 ^b	Dopamine $>$ 15 or epinephrine $>$ 0.1 or norepinephrine $>$ 0.1 ^b	
Central nervous system					
Glasgow Coma Scale score ^c	15	13-14	10-12	6-9	\leq 6
Renal					
Creatinine, mg/dL ($\mu\text{mol/L}$)	$<$ 1.2 (110)	1.2-1.9 (110-170)	2.0-3.4 (171-299)	3.5-4.9 (300-440)	$>$ 5.0 (440)
Urine output, mL/d			$<$ 500		$<$ 200

Figure 1: SOFA score evaluation criteria for sepsis [5].

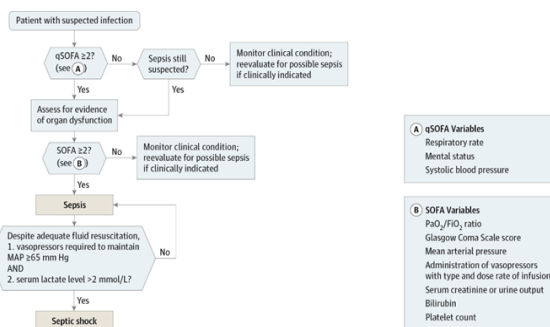


Figure 2: Sepsis and septic shock estimation algorithm using SOFA and QSOFA score criteria [5].

- The systolic blood pressure is equal to or greater than 100 mm Hg.

Figure 2 shows the application of clinical criteria to identify Sepsis and septic shock patients, and septic or septic shock conditions of patients are determined according to the SOFA and QSOFA criteria used in the algorithm [5].

These updated definitions and clinical criteria should clarify the long-term use of descriptors and drafts.

However, this should be an ongoing process. As with

Software and other encoder updates, the next work is to distinguish future iteration requirements.

The use of artificial intelligence methods in the field of medicine provides important contributions in the early diagnosis and treatment of diseases. The use of artificial neural networks for lung cancer risk analysis [7], prediction of cardiovascular disease risk with artificial neural networks [8] can be given as an example.

The cases of Sepsis are frequently observed in cancer patients and patients in intensive care are the leading cause of death in Turkey.

It is thought that this field will help doctors to reduce the number of death cases and to treat the disease by studies on the prediction of Sepsis disease using artificial intelligence methods. Artificial neural networks, one of the artificial intelligence methods that have the ability to learn and to decide, are tried to be obtained as an alternative early diagnosis method by using the anticipated risk of Sepsis.

II. RELATED STUDIES

The studies on Sepsis have been examined and the following studies in the literature have been given as examples.

Parente and colleagues have revealed that bio-labeling classifiers are useful for real-time diagnostic testing according to the characteristic roc curve in their study for rapid and accurate diagnostic testing of severe Sepsis cases using a nuclear classifier [9].

Ongenaes et al. added time series data to the medical database with semantic information by using ontology, and used machine learning technique for the automatic classification of this time series data. By machine learning technique, they have attempted to identify a complication that indicates clinical deterioration or to suggest a new pathological condition. While explaining uncertainty by adding this classification to ontology, they have associated it with prediction.

Baldini and colleagues benefited from biomarkers to diagnose sudden Sepsis. They tried to do Sepsis analysis with the devices they put in the bed. As a result, they observed that an integrated and portable device gave better results in a very short time [11].

Ward and colleagues used a machine learning method for the CPN scoring system, which they have manually defined to determine the severity of the systemic inflammatory response syndrome and to compare objective data with other severity scoring systems and to separate Sepsis and uninfected SIRS. They found that the area under the ROK curve was significant at 0.79 level in terms of predicting the 30-day mortality rate of the created Sepsis learning model. They have also shown that the model they produced have the ability to differentiate between Sepsis and non-infection-related SIRS [12].

Danner and colleagues studied on large data by evaluating records of 53313 emergency patients from January to June, 2015 and compared heart rate and pulse rate based on SIRS

criteria for Sepsis prediction with machine learning. Among the discharged patients, 884 patients had Sepsis, severe Sepsis or septic shock. In their study, they have indicated that heartbeat, pulse (systolic blood pressure ratio), and temperature variables are primary early determinants for preferential early Sepsis prediction with an (654/884) 74% accuracy value according to the 34% (304/884) SIRS criterion ($p < 0.0001$) in approved sepsis patients. They have emphasized the importance of physiologic-based prediction for an earlier, and more accurate diagnosis in Sepsis treatment [13].

Calvert and colleagues have resorted to machine learning with the purpose of developing high-performance early sepsis prediction technology for the general patient population by using the multi-parameter smart imaging data set (in the computer aided diagnosis and on the basis of clinical decision support systems) for the retrospective analysis of adults with non-sepsis and those who apply to intensive care unit. Sepsis predictions were made three hours before the first five-hour SIRS phase of the patient with the early Sepsis warning algorithm they developed. In a previously untried test case, the early warning algorithm showed 90% sensitivity and 81% specificity. It has gained an average area of 0.83 under the ROK curve for the estimated periods of up to three hours from a continuous SIRS event. They have shown that the use of multiple risk factors in Sepsis patient risk analysis is more important than the use of isolated individual risk factors. As a result, they have declared that the Sepsis prediction performed better than current standard practice [14].

Saraiva and colleagues have applied the results on bio marker lists to many transcriptomic (copying DNA itself in an RNA) studies for the diagnosis of Sepsis. They developed Support Vector Machine classifier based mixed integer linear programming and trained them separately with different sets of data, then combined them into common property constraints. As a result of this development they have achieved, the predictive success of bio markers in datasets has increased by 42% [15].

Morales and colleagues used the conditional independent mapping method (CIM) with the aim of verifying changes in the definition of Sepsis and investigating possible causal relationships between measured variables and survival outcome in their Sepsis diagnosis study. They tried to analyze one of the most useful multicenter Sepsis databases by applying this method. They have shown that the inflammatory response plays an important role in the diagnosis of Sepsis [16].

Vieira et al. have attempted to solve the problem of feature selection by using a particle swarm optimization method in a wraparound approach to artificial neural networks, fuzzy models, and assisted vector machines. The best particle flock optimization method which they tried to predict the outcomes of Sepsis patients was compared with the method of genetic algorithms. With accuracy it was shown that the best particle flock optimization method was similar to the method of

genetic algorithms, but that method needed a lower duration of simulation and fewer selected features [17].

Bui and his colleagues aimed to design and develop a remote imaging platform for Sepsis tracking indicators which they intended to increase the quality of outpatient treatment and reduce re-hospitalization and death rate. In this study which they conducted to expand outpatient criteria, they offered a remote monitoring solution solutions using high-frequency sensor devices such as temperature sensors for early detection of sepsis taking into account the difficulties of patient biometrics remotely using technology on the market [18].

Guillen and colleagues aimed to determine a new framework for estimating severe sepsis and identify early predictors using clinical laboratory values and vital findings collected from adult patients in ICU. They have attempted to explore models of logistic regression, support vector machines and logistic model trees methods by using vital findings, laboratory values, or a combination of vital findings and laboratory values. When the predictive support vector machine model, which uses vital and laboratory findings is applied to the retrospective cohort of intensive care patients, it has showed higher predictive power than the other two models with an accurate forecasting that there was severe sepsis developing in 339(%65) patients out of 3446. However, this model does not have the clinical transparency and interpretability of the other two models. Notwithstanding, the data before 24 hours to severe sepsis was used in this model and the data which was obtained just before two hours to severe sepsis was extracted to avoid misleading (prejudice). They have shown that the models on the basis of this framework and developed can be suggested for clinical decision support in intensive care unit and in non-intensive care environment [19].

Ghalwash et al. used the data mining technique which they in their previous studies for pattern recognition in the study of early diagnosis and the advantages of sepsis for blood cleansing treatment and they have shown that these patterns can be used to help doctor to make early diagnosis. In their study, they found that it is more likely for % 52 of patients with the combine of the blood cleansing treatment and early diagnosis to survive than % 32 of patients with the standard blood cleansing procedure.

In order to provide evidence of the classification of transient observations of patients, they first extracted time series from the original time series for early classification. Then, they have shown that the MSD method they used performed better than the other methods developed for time series and univariate time series. They have applied the MSD method which they constructed for an early diagnosis of septic patients. They have shown that the hybrid therapy they applied saved more patients than the standard approach [20].

Ghasemi and Raoufy compared the last 25 hours of heart rate dynamics of the sepsis patients who survived and unable to survive in the intensive care unit by using the time series

methods. Patients' RR (heart rate per millisecond) interval time series were calculated and impaired fluctuation analysis was applied to the data set every 30 minutes. For the analysis of heart rate variability, they have observed the sequential dependent fluctuation analysis algorithm (DFA) which is used for prediction of the sepsis mortality rate 9 hours before the death of sepsis patients. The exponential measurement parameter of the DFA algorithm is lower in dying patients. This parameter is more consistent in patients who survived and is closed to 1, whereas it is about 0.5 in patients who died. This parameter is further decreasing when approaching death. So, they have shown that this parameter can be used as a death alert (alarm) before 25 hours of death [21].

Jiang et al. presented the new graphical adaptive dynamic Bayesian network model which is a model calculation method as an evolutionary imaging approach that adapts spontaneously in determining the stage of sepsis for sepsis patients to provide medical knowledge and semantic deduction with clearly defined syntax. The system, which includes the clinical research and physician information, aims to provide the early caution of suspected infection patients who have gone through the sepsis stage by semantically extracting this information [22].

In study of ward patients' optimization of sepsis risk assessment by Mitchell et al. using the newly accepted definition of sepsis and developed predictive models, they related sepsis and non-intensive care ward patients more accurately and earlier. They have obtained the early detection which determines the ward patients at risk 12-24 hours before the onset of sepsis by using the physiological data and the multivariate logistic regression and laboratory data which can always be obtained from electronic health records in the area under the receiver operating characteristic curve (AUC) with a result of 74%. When this model was applied to a separate intensive care population, the receiver operating characteristic curve showed 56% success and the model performed poorly in this environment. This study was approved by the ethics committee of the University of Virginia. The primary data source was created from patient admissions at the Virginia Medical Center between September 2010 and August 2015 [23].

In the study of Gunnarsdottir et al.'s classification of Sepsis using demographic data and physiological characteristics of time series in intensive care unit. They established a generalized linear model for the probability of patients with intractable Sepsis (GLM) as a function of bedside measurements and demography. They selected physiologic variables are heart rate variability, respiratory rate, arterial oxygen saturation variance and low and medium frequency photoplethysmography, in addition to preselected demographic characteristics. The accuracy of the demographic model was tested as; 62.5% classification accuracy in the test data, 100% sensitivity throughout the patient group and 25% specificity. The classification accuracy of the physiological model is higher than the demographic model, which is 75%. Sensitivity

throughout the patient group was tested as 100% and specificity as 50% [24].

In their study, Marshall and colleagues used the discrete conditional survival model (DC-S), which is a classification component, to predict the patients' results, and survival component to predict the length of hospital stay. It was observed that the validation data included 773 infants and 9.8% (76) of them were late-onset Sepsis patients. The revealed model has the potential to accurately estimate the length of stay of the babies and, thus, to plan their stay. Logistic regression, Bayesian nets, and Navie Bayes classifier are the methodologies used to construct the discrete conditional survival model (DC-S). They introduced the combination of classification trees within the situational component of the discrete conditional survival model. They have demonstrated the suitability of these techniques for newborn care and emphasized that the capacity planning and resource management are key to newborn care. They expect that the development of statistical models will provide effective, accurate and easy-to-implement methods for newborn care management [25].

In their study of applied autoregressive Hidden Markov models for early detection of newborn sepsis, Stanculescu and colleagues viewed late-onset premature sepsis as one of the major clinical concerns when premature infants were under intense care. The model they applied can produce real-time estimates of the onset of infection and can work with incomplete data. They evaluated the efficacy of the autoregressive hidden Markov model for the diagnosis of Sepsis through data from the Newborn intensive care unit at the Edinburgh Royal Clinic [26].

In the study which Moutzouri and colleagues defended the additional effect of severe sepsis and diabetes mellitus on the red blood cell deformation, 40 patients suffering from severe Sepsis, 12 patients suffering from diabetes, and 24 patients with severe Sepsis were enrolled. The mean intensive care disease severity score in non-diabetic and diabetic septic patients was 23.5% and 26.8%, respectively. While the mortality rate was 22.5% in diabetic Sepsis patients; 34.3% in diabetic septic patients, septic shock rate was 15% in non-diabetic patients and 20.8% in diabetic patients. Patients with septic diabetes had a higher stiffness index (17.72 ± 6.31) compared to diabetic and non-septic patients (12.26 ± 2.28 , $p < 0.001$), and stiffness index in non-diabetic sepsis patients is (13.9 ± 2.86 , $p < 0.01$). They stated that the presence of diabetes in septic patients is effective in deformation of red blood cells and that this deformability may lead to severe micro-circulatory dysfunction in Sepsis patients [27].

In their study, Gültepe and colleagues report that Sepsis is a serious medical condition that is caused by an irregular immune response to infection. Early diagnosis of the Sepsis symptoms is important to prevent the progression of the disease to more severe stages that results in the death of one in every four individuals. 1492 Patient records with 233 Sepsis cases on electronic medical records were used in the clustering

analysis to identify features showing signs of sepsis. The Bayesian network that they used in their study was established using criteria for systemic inflammatory response syndrome (systolic), meaning arterial pressure and lactate level in patients with Sepsis. The acquire network reveals a clear correlation between lactate level and Sepsis. It has been shown that the lactate level may be a predictor of SIRS criterion [28].

Yanes et al. and intended to compare the tendency in Sepsis outcomes of people with or without type 2 diabetes T2DM in Spain between 2008 and 2012 and reported that there is conflicting evidence between sepsis mortality and T2DM patients. They used statistical analysis in the study by using the data from national hospital records. Type 2 diabetes was found to be less related to the mortality rate in the hospital (risk ratio = 0.88, confidence interval 95%, 0.86-0.90). They noted that the annual increase in the incidence of Sepsis was high in patients with type 2 diabetes in Spain, but they stated that the risk of death with Sepsis in admission was lower in patients with type 2 diabetes [29].

Schuh did a retrospective Sepsis and septic shock analysis study on 1674 patients selected from patients with intensive care heart and thoracic patients by using artificial neural networks. In his work he used the SIRS criteria [30] that Bone and his colleagues identified. In the model using multi-layer artificial neural network, he used sigmoid transfer function and logistic regression in the outcome. He used the Conjugate Gradient algorithm to train the artificial neural network. He stated that SIRS cases in 1544 patients, hypotensive SIRS cases in 1315(SAP<90mmHg or MAP<70 mmHg, % 78.6) and serious SIRS case in 1175 of all patients were seen [31].

The difference between the work done and the previous studies in the literature is the use of criteria determined according to the definition of new Sepsis made in 2016. In the definitions made in 2012 [32], the course of the disease is expressed as SIRS, Sepsis, severe Sepsis, septic shock. However, in 2016 [5] these definitions have been abandoned and SOFA and QSOFA scores have been found to be more successful than previous methods in diagnosing Sepsis disease and determining the level of Sepsis diseases.

It is aimed to obtain a better and more accurate Sepsis prediction by using this new Sepsis definition and the data set of SOFA and QSOFA scoring which are prominent in the diagnosis of the disease, together with other parameters. It is known that multilayer artificial neural network models are able to learn, generalize and deduce, as well as minimize error by using a back propagation algorithm and nonlinear problems are more successful in solution than other methods in the literature. Therefore, the best, most accurate, and least error-free prediction of the disease is targeted by using artificial neural network method with Levenberg-Marquardt training algorithm with multi-layer forward feedback propagation.

III. METHOD

By using the data on intensive care patients aged 18-65 years in Istanbul Data on intensive care patients aged 18-65 years in

Istanbul, the risk of catching Sepsis is being tried to be predicted with the help of artificial neural networks. The inputs and outputs of the patients placed in the intensive care unit and diagnosed as Sepsis are generated by the definition of Sepsis in 2017 and by examining the algorithms and variables used by the doctors were used in the modeling of the artificial neural network. The modeled inputs for the early diagnosis of Sepsis are the parameters used by physicians to diagnose Sepsis and the level of Sepsis. Input parameters were determined using the Sepsis definitions and criteria described in the Journal of the American Medical Association [5] published in 2016. All of the determined parameters were taught to network through multi-layered artificial neural networks by supervised learning which are never thought to be used in predicting Sepsis disease in Turkey and it was attempted to predict the outcome of death caused by disease or survival outcome.

A. Steps in Identifying Sepsis Disease and Sepsis Level

In order to determine the diagnosis and level of Sepsis disease, the following three steps are followed by doctors:

Stage 1: If the patient has SIRS or an infection, it means that infection is diagnosed.

Stage 2: If there is an infection diagnosis, the QSOFA score of the patient is calculated. If the QSOFA score is equal to or greater than 2, the patient is diagnosed with Sepsis.

Stage 3: To determine the level of Sepsis of the patient, the SOFA score, which consists of evaluation of respiration, coagulation, liver, cardiovascular system, brain function and kidney function is looked at. If the score is high, it means that the patient's Sepsis level is at advanced stages and the patient is close to death. If the SOFA score is low, it is concluded that the patient is recovering. Below are explanations of QSOFA the parameters that play a role in determining the data set used to diagnose Sepsis. Parameters used in prediction of Sepsis disease and data set formation are shown in below:

P = Patient

Tv = Temperature value at first hospitalization (°C)

Hv = Heart rate value at first hospitalization (min)

Bp = Number of breaths per minute (min)

PaCO₂ = Arterial partial carbon dioxide pressure of the patient (mmHg)

Leu = Leukocytes count in the blood of the patient (mm³)

Ne = Neutrophil count in the patient's blood (mm³)

Pn = Diagnosis of pneumonia in the patient (infection of the lung)

Bac = The presence of bacteria in the patient's blood

Iai = Presence of intra-abdominal infection

Oi = Presence of other infections in the patient

Nat = Presence of newly started antibiotic treatment in the patient

Ams = Altered mental status (turning on / off of consciousness)

Sbp = Systolic blood pressure value of the patient (mmHg)

PaO2 = Arterial partial oxygen pressure of the patient
 FiO2 = Percentage of oxygen in the air where the patient is breathing
 PaO2 / FiO2 = The ratio of the patient's oxygen partial pressure to the amount of oxygen in the air that the patient breathes
 Tro = The amount of thrombocyte in the blood of the patient
 Bil = The amount of bilirubin in the patient
 Epi = The amount of epinephrine in the patient
 Nor = The amount of norepinephrine in the patient
 Dob = Dobutamine supplementation to the patient
 Dop = dopamine supplementation to the patient
 MAP = Average arterial pressure
 GCS = Patient's Glasgow Coma Score
 Uri = The amount of urine output of the patient in 24 hours
 Cre = The amount of creatine in the patient
 Result = Diagnostic result indicating whether the patient has Sepsis.

Table 1, Table 2, and Table 3 contain examples of the parameters that make up the input of the artificial neural network model.

Parameters used in the diagnosis of Sepsis disease were normalized before they were used in the ANN model, and examples of the parameters forming the normalized ANN entries are shown in Table 4, Table 5 and Table 6.

Table 1: Input parameters of ANN used in the diagnosis of Sepsis

P	Tv	Hv	Bp	PaCO2	Leu	Ne	Pn	Bac	Iai	Oi	Nat	Ams	Sbp
1	37,6	105	16	36	12000	15500	Pos.	Neg.	Neg.	Neg.	Neg.	closed	60
2	37,8	140	20	32	7000	6000	Neg.	Pos.	Neg.	Neg.	Neg.	closed	110
3	35,7	112	40	25	10600	8400	Pos.	Neg.	Neg.	Neg.	Neg.	open	115
4	36,4	94	11	42	9200	6500	Pos.	Neg.	Neg.	Neg.	Neg.	closed	160
5	37,2	105	23	32	500	0	Neg.	Neg.	Neg.	Neg.	Pos.	closed	125

Table 2: Input parameters of ANN used in the diagnosis of Sepsis by electronically for review.

pao2	fiO2	pao2/fiO2	result pao2/fiO2	Tro	Bil	Epi	Nor	Dob	Dop	MAP	GCS
200	1	200	200	111000	0,2	0	0	Neg.	0	40	3
142	0,4	355	355	229000	0,6	0,5	0	Neg.	0	60	3
79	0,45	175,5555556	175,5	341000	0,49	0	0	Neg.	0	75	15
130	0,4	325	325	391000	0,7	0	0	Neg.	0	115	9
91	0,28	325	325	30000	37	0	0	Neg.	0	83	9

Table 3: Input parameters of ANN used in the diagnosis of Sepsis

Uri	Cre	Result
1200	1,54	Sepsis-death
1200	0,67	Sepsis-death (within 24 hours)
880	0,8	Sepsis-survival
1400	0,86	Sepsis-death
1100	2,04	Sepsis-death

Table 4: Normalized ANN sample input parameters.

P	Tv	Hv	Bp	paco2	Leu	Ne	Pn	Bac	Iai	Oi	Nat	Ams	Sbp
1	0,7 2	0,4	0,2	0,456	0,418	0,62	1	0	0	0	0	1	0
2	0,7 6	0,68	0,33	0,369	0,236	0,24	0	1	0	0	0	1	0,416
3	0,3 4	0,45 6	1	0,217	0,367	0,336	1	0	0	0	0	0	0,458
4	0,4 8	0,31 2	0,033	0,586	0,316	0,26	1	0	0	0	0	1	0,833
5	0,6 4	0,4	0,433	0,369	0	0	0	0	0	0	1	1	0,541

Table 5: Normalized ANN sample parameters

P	pao2/fiO2	Tro	Bil	MAP	Dop	Dob	Epi	Nor	Gcs
1	0,287	0,123	0,002	0,047	0	0	0	0	0
2	0,712	0,303	0,013	0,238	0	0	1	0	0
3	0,220	0,474	0,010	0,380	0	0	0	0	1
4	0,630	0,550	0,016	0,761	0	0	0	0	0,5
5	0,630	0	1	0,457	0	0	0	0	0,5

Table 6: Normalized ANN sample input parameters

P	Cre	Uri	Result
1	0,209	0,422	1
2	0,068	0,422	1
3	0,089	0,28	1
4	0,098	0,511	1
5	0,290	0,377	1

B. Artificial Neural Networks

Artificial neural networks are artificial intelligence methods in which the biological characteristics of nerve cells are imitated using mathematical models from the methods that enable machines to make deductions and decisions like a human being. In addition, these are structures with parallel and distributed processing capacity, in which the human brain is modeled on the working logic and each of these structures is bound with the weights of its own memory processing elements [33]. Artificial neural networks, which generalize by collecting information on samples and construct a structure that can deduce and make decisions based on information that

they have learned about in the past, have been used to solve complex problems in many fields [34]. The artificial neural networks, which are the basic building blocks of neurons, are made up of the model structures which use these neurons in the entrance, hidden layer and exit layers. The components of ANN are: input-hidden-output layer, activation function, bias weight values and learning and training algorithms. In this study, artificial neural networks were preferred because of their ability to deduce, make decisions and learn.

C. Feed Forward Back Propagation ANN

This network structure, which consists of two different algorithms, is a back propagation that determines whether the network, which is an advanced feed and supervised training method that expresses how the network works and remembers the patterns, can determine the desired output through inputs.

Errors are calculated by comparing the outputs obtained from the network with the desired output values in back propagation. The calculated error values are taken and the input threshold and weight values of the neural network are updated to try to reduce the error [35]. Figure 3 shows an example of this network structure.

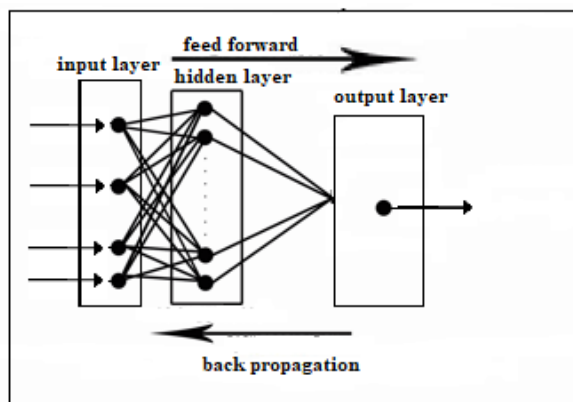


Figure 3: Feed forward back propagation artificial neural network model.

D. Artificial Neural Network Models Used for the Prediction of Sepsis Disease

P, Tv, Hv, Bp, PaCO₂, Leu, Ne, Pn, Bac, Iai, Oi, Nat, Ams, Sbp, PaO₂ / Fio₂, Tro, Bil, Epi, Nor, Dob, Dop, MAP, GCS, Uri and Cre from the normalized data are determined as input parameters and the Result parameter is determined as output parameter of the system.

Multilayer artificial neural network model was created in Matlab. Entries in the model consist of 24 parameters used in the diagnosis of Sepsis. As it can be seen from the figure, by using a feed forward network model and a back-propagation network model to minimize the network computation error, it is aimed to increase the performance of the network.

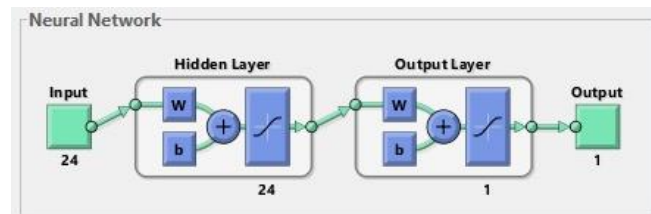


Figure 4: ANN model for Sepsis prediction.

Figure 4 shows the artificial neural network model. In the artificial neural network consisting of 24 inputs and 1 output, for the applicability in different data set successfully, data needs to be chosen randomly. Therefore, a random algorithm is chosen for training the data. For network training, The Levenberg-Marquardt algorithm which is most commonly used and known for its success in the literature is applied. For evaluation of performance, the mean square error algorithm (MSE), which is one of the most valid performance criterion used for many studies in the literature, is applied. Finally the default derivation algorithm is used for the derivative. As addition, the most commonly used hyperbolic tangent sigmoid function is used in the literature as a transfer function. The mean squared error performance graph (MSE) showing the training, test and verification values of the ANN network is shown in Figure 6, and it is seen that the training phase is terminated at epoch 8. At epoch 2 an increase in accuracy and at epoch 4 an increase in test value is seen. To increase the ANN performance, the training phase was repeated with the updated weights and the experiment is terminated with the lowest mean square error which gives the best result. The graphic in Figure 5 shows that the training phase is complete. The training graph of the ANN network is shown in Figure 6. The gradient, mu, and accuracy error values on the training graph were obtained as 3.6897e-8, 1e-11 and 6 at epoch 8, respectively.

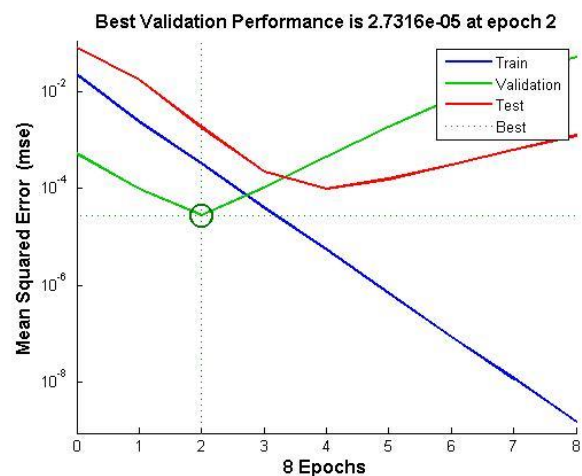


Figure 5: ANN performance graph.

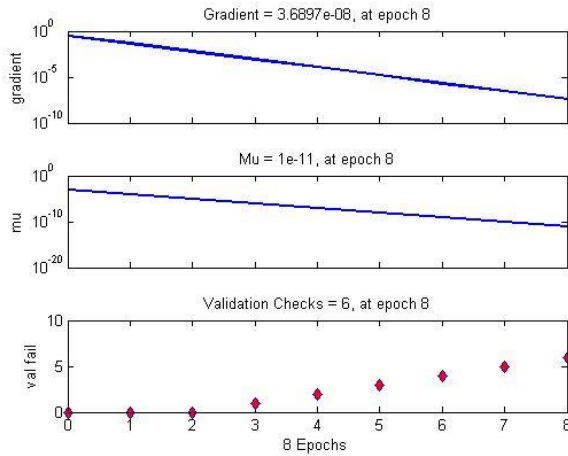


Figure 6: ANN training chart.

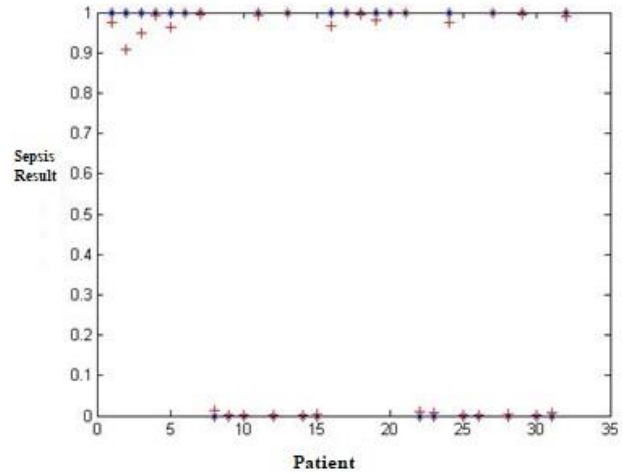


Figure 8: ANN output graph.

The regression graph of ANN network is shown in Figure 7. According to the regression graph, the ANN model has 99.95% education, 99.76% test, 99.99% accuracy and 99.93% performance in total.

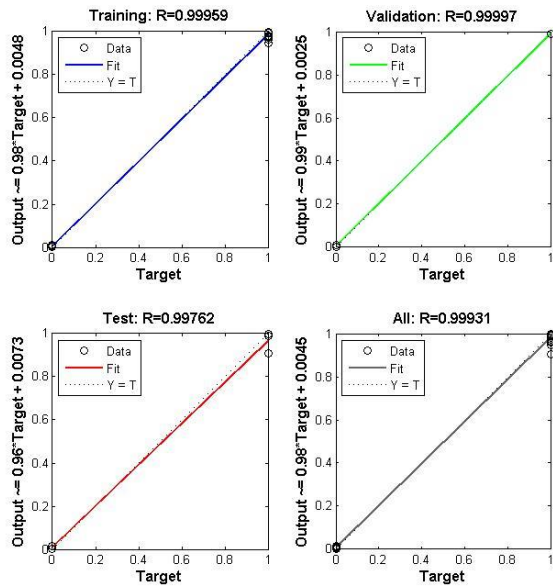


Figure 7: ANN regression graph.

The output graph of ANN network is shown in Figure 8. In this output graph (*), the actual output (+) refers to the output of the network. Accordingly, it is seen that the output obtained is close to the desired output.

IV. RESULT

24 different variables belonging to 32 patients were taken as inputs and 1 resultant variable was taken as output for the diagnosis of Sepsis by artificial neural networks. The regression graph shows that the system has reached an accuracy value of 0.99. In Table 7, the output values, error values and target values of the ANN are compared.

Table 7: Comparison of ANN sample output values, error values and target values.

Network output values	Target (Result Values)	Network Error Values
0,974	1	0,025
0,907	1	0,092
0,948	1	0,051
0,993	1	0,006
0,962	1	0,037

Table 8 shows the mean square error (MSE), root mean square error (RMSE), and root error sum (ESS) values for artificial neural network.

Table 8: ANN mean squared error, root mean squared error and root error sum values.

Mean square error(MSE)	Root mean square error(RMSE)	Error sum of squares(ESS)
5.0781e ⁻⁰⁴	0.0225	0.0162

V. CONCLUSION

New Sepsis definitions [5] that were done in 2017 were used for predictive modeling of Sepsis disease with artificial neural networks. According to the new definition of Sepsis, SIRS is now out of being a decisive criterion on its own, instead, it was observed that the presence of infection was investigated primarily by providing an infection diagnosis or SIRS criteria. It was expressed in new sepsis definition that Sepsis diagnosis should be determined by calculating QSOFA scores of patients who are diagnosed with infection, and the level of sepsis should be determined by calculating SOFA scores. Considering the increase in the use of artificial intelligence in medicine, artificial neural networks were used in this study to determine the level of the disease and to determine whether the patient died or survived from the disease. In this study, a 99% training, test and accuracy values were obtained by using a feed forward back propagation artificial neural network model constructed using the Levenberg-Marquardt training algorithm. Additionally, the mean squared error (MSE) value was $5.0781e-04$, the root mean square error (RMSE) value was 0.0225, and the root error sum (ESS) value was 0.0162 which were used to evaluate the performance of the artificial neural network in the literature. It is seen that the performance values obtained are better at satisfactory level when compared with the ones in literature. Why such a high accuracy level is reached can be explained by the fact that the number of patients was small according to the results obtained by expert evaluation. Besides, this interdisciplinary study was carried out according to the new sepsis criteria and it was aimed to be a pioneer in the work to be done thereafter. It is thought that this study using new definitions of Sepsis and artificial intelligence methods can guide doctors for the diagnosis of Sepsis. Furthermore, it is also expected to contribute to the reduction of the error possibility that may arise from the doctor error. In the next studies, it is thought that in the study, much larger patient data could be used to make improvements in predictive and intuitive modeling using different methods.

REFERENCES

- [1] Ç. Büke, "Yeni Rehberler Eşliğinde Sepsis", Türk Klinik Mikrobiyoloji ve Enfeksiyon Hastalıkları Derneği, Ege Üniversitesi Tıp Fakültesi, 2015 (in Turkish)
- [2] G. Aydın, "Sepsis ve Septik Şok", Akılcı Antibiyotik Kullanımı ve Erişkinde Toplumdan Edinilmiş Enfeksiyonlar, Sempozyum Dizisi No: 31, Kasım 2002; s. 131-140, İ.Ü. Cerrahpaşa Tıp Fakültesi Sürekli Tıp Eğitimi Etkinlikleri. (in Turkish)
- [3] D.C. Angus, W.T. Linde-Zwirble, J. Lidicer et al (2001) *Epidemiology of severe sepsis in the United States: analysis of incidence, outcome, and associated costs of care*. Crit. Care Med 29: 1303–1310.
- [4] Carcillo JA, Fields AI (2002) Clinical practice parameters for hemodynamic support of pediatric and neonatal patients in septic shock. Crit. Care Med 30: 1365–1378.
- [5] M. Singer, MD, FRCP; C. S. Deutschman, MD, MS; C.W. Seymour, MD, MSc; M. Shankar-Hari, MSc, MD, FFICM; D. Annane, MD, PhD; Michael Bauer, MD; R. Bellomo, MD; G. R. Bernard, MD; J.D. Chiche, MD, PhD; C. M. Cooper-Smith, MD; R. S. Hotchkiss, MD; M. M. Levy, MD; J. C. Marshall, MD; G. S. Martin, MD, MSc; S.M. Opal, MD; G. D. Rubenfeld, MD, MS; T.D. Poll, MD, PhD; J.L. Vincent, MD, PhD; D. C. Angus, MD, MPH.(February 23,2016), The Third International Consensus Definitions for Sepsis and Septic Shock (Sepsis-3), "Consensus Definitions for Sepsis and Septic Shock", American Medical Association, JAMA, Volume 315, Number 8, ppt 762-775. Copyright 2016 American Medical Association. (JAMA. 2016;315(8):801-810. doi:10.1001/jama.2016.0287.)
- [6] R.C. Bone, R. A. Balk, F. B. Cerra, et al. "Definitions for sepsis and organ failure and guidelines for the use of innovative therapies in sepsis." Chest 101, no. 6 (1992): 1644-55. <http://journal.publications.chestnet.org>.
- [7] E. Adetiba and O.O. Olugbara (2015). Lung Cancer Prediction Using Neural Network Ensemble with Histogram of Oriented Gradient Genomic Features. The Scientific World Journal, 2015.
- [8] J. Liu, Z.H. Tang, F. Zeng, Z. Li, L. Zhou (2013). "Artificial neural network models for prediction of cardiovascular autonomic dysfunction in general Chinese population". BMC Medical Informatics and Decision Making, 13, 80.
- [9] J. D. Parente, D. Lee, J. Lin, J. G. Chase and G. M. Shaw, "A fast and accurate diagnostic test for severe Sepsis using kernel classifiers", UKACC International Conference on Control 2010, Coventry, 2010, pp. 1-6.
- [10] F. Ongenaes, T. Dhaene, F. De Turck, D. Benoit and J. Decruyenaere, "Design of a probabilistic ontology-based clinical decision support system for classifying temporal patterns in the ICU: A sepsis case study," 2010 IEEE 23rd International Symposium on Computer-Based Medical Systems (CBMS), Perth, WA, 2010, pp. 389-394.
- [11] F. Baldini, A. Giannetti, C. Trono, L. Bolzoni and G. Porro, "The CAI instrument: A novel optical device for sepsis analysis for POCT applications," 2011 International Quantum Electronics Conference (IQEC) and Conference on Lasers and Electro-Optics (CLEO) Pacific Rim incorporating the Australasian Conference on Optics, Lasers and Spectroscopy and the Australian Conference on Optical Fibre Technology, Sydney, NSW, 2011, pp. 693-694.
- [12] L. Ward, M. Paul, S. Andreassen, Automatic learning of mortality in a CPN model of the systemic inflammatory response syndrome, Mathematical Biosciences, Volume 284, February 2017, Pages 12-20, ISSN 0025-5564, science direct.
- [13] O. K. Danner, S. Hendren, E. Santiago, B. Nye, P. Abraham, Physiologically-based, predictive analytics using the heart-rate-to-Systolic-Ratio significantly improves the timeliness and accuracy of sepsis prediction compared to SIRS, The American Journal of Surgery, Volume 213, Issue 4, April 2017, Pages 617-621, ISSN 0002-9610, science-direct.
- [14] J. S. Calvert, Daniel A. Price, U. K. Chettipally, Christopher W. Barton, Mitchell D. Feldman, Jana L. Hoffman, Melissa Jay, Ritankar Das, A computational approach to early sepsis detection, Computers in Biology and Medicine, Volume 74, 1 July 2016, Pages 69-73, ISSN 0010-4825, science-direct.
- [15] J. P. Saraiva, M. Oswald, A. Biering, C. Assmann, T. Klassert, M. Blaess, K. Czakai, R. Claus, Jürgen Löffler, Hortense Slevogt, Rainer König, *Integrating classifiers across datasets improves consistency of biomarker predictions for sepsis*, IFAC-Papers On-Line, Volume 49, Issue 26, 2016, Pages 95-102, ISSN 2405-8963, science-direct.
- [16] C. Morales, V. Ribas and A. Vellido, "Applying Conditional Independence Maps to Improve Sepsis Prognosis," 2016 IEEE 16th International Conference on Data Mining Workshops (ICDMW), Barcelona, 2016, pp. 254-260.
- [17] S. M. Vieira, L. F. Mendonça, G. J. Farinha and J. M. C. Sousa, "Meta-heuristics for feature selection: Application to sepsis outcome prediction," 2012 IEEE Congress on Evolutionary Computation, Brisbane, QLD, 2012, pp. 1-8.
- [18] T. Bui et al., "Remote patient monitoring for improving outpatient care of patients at risk for sepsis," 2016 IEEE Systems and Information Engineering Design Symposium (SIEDS), Charlottesville, VA, 2016, pp. 136-141.
- [19] J. Guillén et al., "Predictive models for severe sepsis in adult ICU patients," 2015 Systems and Information Engineering Design Symposium, Charlottesville, VA, 2015, pp. 182-187.
- [20] M. Ghalwash, V. Radosavljevic and Z. Obradovic, "Early Diagnosis and Its Benefits in Sepsis Blood Purification Treatment," 2013 IEEE

- International Conference on Healthcare Informatics, Philadelphia, PA, 2013, pp. 523-528.
- [21] P. Ghasemi and M. R. Raoufy, "Prediction of mortality in patients with sepsis using Detrended fluctuation analysis of Heart Rate Variability," 2016 23rd Iranian Conference on Biomedical Engineering and 2016 1st International Iranian Conference on Biomedical Engineering (ICBME), Tehran, 2016, pp. 150-154.
- [22] Y. Jiang, P. Tan, H. Song, B. Wan, M. Hosseini and L. Sha, "A Self-Adaptively Evolutionary Screening Approach for Sepsis Patient," 2016 IEEE 29th International Symposium on Computer-Based Medical Systems (CBMS), Dublin, 2016, pp. 60-65.
- [23] S. Mitchell et al. "Optimization of sepsis risk assessment for ward patients," 2016 IEEE Systems and Information Engineering Design Symposium (SIEDS), Charlottesville, VA, 2016, pp. 107-112.
- [24] K. Gunnarsdottir, V. Sadashivaiah, M. Kerr, S. Santaniello and S. V. Sarma, "Using demographic and time series physiological features to classify sepsis in the intensive care unit," 2016 38th Annual International Conference of the IEEE Engineering in Medicine and Biology Society (EMBC), Orlando, FL, 2016, pp. 778-782.
- [25] A. H. Marshall, K. Payne, K. J. Cairns, S. Craig and E. McCall, "Modelling the development of late onset sepsis and length of stay using discrete conditional survival models with a classification tree component," 2012 25th IEEE International Symposium on Computer-Based Medical Systems (CBMS), Rome, 2012, pp. 1-6.
- [26] I. Stanculescu, C. K. I. Williams and Y. Freer, "Autoregressive Hidden Markov Models for the Early Detection of Neonatal Sepsis," in IEEE Journal of Biomedical and Health Informatics, vol. 18, no. 5, pp. 1560-1570, Sept. 2014.
- [27] A.G. Moutzouri, G.A. Athanassiou, D. Dimitropoulou, A.T. Skoutelis, C.A. Gogos " Severe sepsis and diabetes mellitus have additive effects on red blood cell deformability", (2008) Journal of Infection, 57 (2) , pp. 147-151.
- [28] E. Gultepe, H. Nguyen, T. Albertson and I. Tagkopoulos, "A Bayesian network for early diagnosis of sepsis patients: a basis for a clinical decision support system," 2012 IEEE 2nd International Conference on Computational Advances in Bio and medical Sciences (ICCBMS), Las Vegas, NV, 2012, pp. 1-5.
- [29] J.M. de Miguel-Yanes, M. Méndez-Bailón, R. Jiménez-García, V. Hernández-Barrera, N. Pérez-Farinós, A. Lopez-de-Andrés, Trends in sepsis incidence and outcomes among people with or without type 2 diabetes mellitus in Spain (2008–2012), Diabetes Research and Clinical Practice, Volume 110, Issue 3, 2015, Pages 266-275, ISSN 0168-8227, science-direct.
- [30] R.C. Bone, R.A. Balk, F.B. Cerra, R.P. Dellinger, A.M. Fein, W.A. Knaus, R.M.H. Schein, W.J. Sibbald, J.H. Abrams, G.R. Bernard, J.W. Biondi, J.E. Calvin, R. Demling, P.J. Fahey, C.J. Fisher, C. Franklin, K.J. Gorelick, M.A. Kelley, D.G. Maki, J.C. Marshall, W.W. Merrill, J.P. Pribble, E.C. Rackow, T.C. Rodell, J.N. Sheagren, M. Silver, C.L. Sprung, R.C. Straube, M.J. Tobin, G.M. Trenholme, D.P. Wagner, C.D. Webb, J.C. Wherry, H.P. Wiedemann and C.H. Wortel (1992) American College of Chest Physicians Society of Critical Care Medicine Consensus Conference—Definitions for Sepsis and Organ Failure and Guidelines for the Use of Innovative Therapies in Sepsis. Critical Care Medicine 20, 864–874.
- [31] C. J. Schuh, "Sepsis and Septic Shock Analysis using Neural Networks," NAFIPS 2007 - 2007 Annual Meeting of the North American Fuzzy Information Processing Society, San Diego, CA, 2007, pp. 650-654.
- [32] R.P. Dellinger, M.M. Levy, A. Rhodes, D. Annane, H. Gerlach, S.M. Opal, J.E. Sevransky, C.L. Sprung, I.S. Douglas, R. Jaeschke, T.M. Osborn, M.E. Nunnally, S.R. Townsend, K. Reinhart, Kleinpell RM, Angus DC, Deutschman CS, Machado FR, Rubenfeld GD, Webb SA, Beale RJ, Vincent JL, Moreno R; Surviving Sepsis Campaign Guidelines Committee including the Pediatric Subgroup. Surviving sepsis campaign: international guidelines for management of severe sepsis and septic shock: 2012. Crit. Care Med. 2013 Feb; 41(2):580-637.
- [33] Ç. Elmas, 2003, *Yapay Sinir Ağları*, Seçkin Yayıncılık, Ankara, s. 21-39. (in Turkish)
- [34] H. Ergezer, M. Dikmen, E. Özdemir, 2003, *Yapay Sinir Ağları ve Tanıma Sistemleri*, Pivolka, s. 14-17. (In Turkish)
- [35] R. Dharwal and L. Kaur, (2016). *Applications of Artificial Neural Networks: A Review*. Indian Journal Of Science And Technology, 9(47).

E-Transactions security analysis

T. MEKHAZANIA

Larbi Tebessi University, Tebessa, Algeria, mekhaznia@yahoo.fr

Abstract - It is seems hard to proceed with an online transaction and, in the meantime, to keep an appropriate confidentiality of exchanged data. The problem becomes more complex when transmitting sensitive information such passwords, private documents or card indications via public networks. The security of electronic transactions is handled by various distinct protocols. Actually, the most widely used protocols are, the Secure Electronic Transaction, Secure Socket Layer, Internet Protocol Security and the 3D secure which are adopted by numerous participants in various economic, industrial and financial areas. The paper focuses on a comparison and analysis of such protocols characteristics, namely: privacy, authenticity, encryption algorithm uses, etc. We discuss also the advantages and shortcoming of these secure transaction mechanisms.

Keywords - *e-transaction; SET; SSL; IPSec; 3D-Secure.*

I. INTRODUCTION

SINCE the birth of the first server in 1983, the Internet keeps growing at an exponential rate; it has currently near two billion websites and more than three billion users¹. As a consequence of the convenience of such expansion, hundreds of thousands of Internet users are attracted in using electronic transaction, *e-transactions* in short, rather than physical exchanges especially in industrial or commercial areas; this means that such system has a very large potential for people since electronic documents has been substituted paper patterns. Such fact has reduced volume and weight. Moreover, e-transaction system brings the convenience in permanence of 24-hour a day. In addition, it may take few seconds to reach its destination and the receipt confirmation takes a similar period.

By another way, e-transactions involve multiple transfers of information between different entities. A lot of personal information, often confidential, travels during these processes through various stakeholders. It kept and used in general, for promotional purposes and users are rarely aware of the issues when they disclose such information. This fact constitutes a significant problem in terms of privacy and every web-user needs to be concern about his personal information swapped throw the network. It is therefore necessary to provide encryption tools and enable users to be aware of the use of open networks when transmitting sensible information such credit card numbers, passwords or confidential files.

In order to ensure the security of e-transactions involving sensitive information, various technology companies and financial organisations were implemented standards for the

Security of their transactions, especially financial operations over insecure networks. Such protocols allow involving transaction parties to exchange and verify their authenticity information without seeing such information. The most popular are the *Secure Electronic transaction (SET)*, *Secure Socket Layer (SSL)*, *Internet Protocol Secure (IPSec)* and *3-D Secure*. Such protocols constitute communication tools for securing credit card transactions and data exchange. They use blinding cryptographic algorithms that protect user information and preventing access to hackers and eavesdroppers.

The purpose of the paper is to investigate the characteristics of the mentioned protocols and their efficiency in real-life. The study discuss also the advantages and shortcoming of these secure transaction mechanisms.

II. E-TRANSACTIONS

A. Overview

An e-transaction is no more than exchanging information between parties involved in transaction. More precisely, it consists of a set of related interactions which describes the transfer of document, money, services or goods involving public and financial organisations and conducted over computer-mediated networks. In general, goods and services are ordered via networks using appropriate applications, but the delivery is accomplished offline. Given their importance, e-transactions are assured by well-defined business processes in terms of time and activity.

Since e-transactions are actually, the main tool of management between business and administration entities, its security from any type of threat seems the most important critical factor of its success [1].

B. Domains

In term of volume, the business and e-commerce processes dominate the e-transaction events, followed by instant messaging and social network activities and at last, scientific document exchange and companies management. Applications related to this area are spread over several mecanisms: online shopping and order tracking [2] [3], online banking [4][5], e-payment systems [6] [3], shopping cart applications [7], instant messaging [8], social networking services [9], teleconferencing [10] and others.

The reasons of the massive development of e-transactions are that companies can reach customers directly without intermediate and at all-time which reduces the service cost and increase the delivery speed in regard of private networks or traditional life services. Also, a customer has more opportunities and perspective to evaluate and compare

¹<http://www.internetlivestats.com/total-number-of-websites/>

products and services; it can also expand his investigation through international markets via network avenues.

E-transaction were also introduced in government services; they approved with the name of electronic administration or e-administration [11] [12] and refers to the mechanisms that translate traditional public services to electronic processes in order to convert document into digital form and create a paperless office. This fact improves productivity in sharing documents, keep more security to public information and reduce paper printing which helps the environment. It was recently introduced in public real-life services such the education [13] [14] and voting [15]; Its goal is the establishing of total transparency and accountability leading to better governance within people and organisations.

In health area, the electronic transaction were also used as a health record (EHR) which consists on the collection of patient health information such medical history, medication, laboratory test results, radiology images, vital signs, etc. [16] These statistics are stored on a unique database and shared across different health institutions [17]. This fact excludes the need to track down the patient's paper medical records, reduces the risk of data replication and facilitates the history searching.

Another recent area where e-transaction has taken place is the electronic authentication [18] which refers to the process of verifying a user or a machine identity based on several elements (password, PIN, IP, digital or biometric characteristics). The e-authentication is used to enable citizens to access government and society's services and reduce time people traveling, applying visas or licences, etc. More clearly, e-authentication is an important tool in achieving trust and online identity protection, which are vital to foster e-commerce and e-government.

III. PROTOCOLS

The Internet networks offers just a relative security to confidential and private information since such information moves through series of routing points before reaching the trust server. During its transportation, anyone of the network computers represents an opportunity to the information to be accessed or even updated. Therefore, the security of e-transaction must be accomplished by dedicated protocols, based on encryption algorithms, the most used are presented in following:

A. Secure Electronic Transaction

The Secure electronic transaction (*SET* in short) is denoted as a standard neural encryption protocol for ensuring the security of transactions via electronic avenues and preventing access to private details even from indiscrete eyes. The first release of SET was proposed in 1996 by the SET Consortium [19], It includes Visa and MasterCard in cooperation with Microsoft, Netscape, IBM and others; its goal is to develop a unified standard that combines incompatible protocols and resolves conflicts between the Secure Transaction Technology (STT) of Visa and the Secure Electronic Payment Protocol (SEPP) of MasterCard. The SET makes use of Netscape's Secure Sockets Layer (SSL), Microsoft's Secure Transaction Technology (STT) and Terisa System's Secure Hypertext

Transfer Protocol (S-HTTP). It uses certain aspects of a public key infrastructure (PKI). The SET employs a digital signature which enables sellers to verify customers' identity without seeing their card number. The standard process of SET is illustrates by figure 1 where step 1 concern the customer decision to purchase and step 2, when it sends order and payment information to merchant. Merchant forward customer information to its bank (step 3); the bank checks with issuer for payment authorisation (step 4); if no problems, it receives payment authorisation (step 5) which captures it and informs the merchant (step 6). Then, customer confirms the transaction (step 7); the merchant captures the confirmation and forward it to its bank (step 8). Finally, issuer sends credit card bill to customer (step 9).

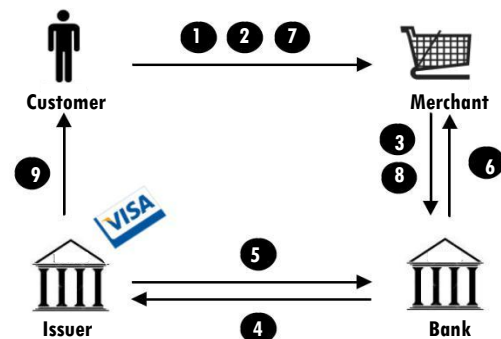


Figure 1: SET protocol description.

B. Secure Socket Layer

The Secure Socket Layer (*SSL* in short) is a standard suitable for conducting sensitive transactions. It was developed by Netscape in the 1990s [20] with the aim to provide connection security of transport of browsers to a Web servers and other applications such FTP and SMTP. The SSL certificate uses both a public and a private keys and enables the authentication of parties, the data integrity and prevents attacks over networks without the need for either end to meet to swap keys.

Since it works on the higher levels, the SSL has various limitations that concern the use of public keys which decrease the CPU performance and requires administrative maintenance related to system configuration and certificate management. The Transport Layer Security (TLS), an improved version of SSL, supports more secure algorithms, additional methods for exchanging keys and further configurable parameters.

The SSL process is accomplished in two phases: SSL handshake (key exchange) and the SSL data transfer via VPN. The figure 2 illustrates an SSL transaction which begins when a user requests a secure connection and presents a list of supported ciphers (step 1). The server picks the strongest cipher and a hash function and notify the user by its identification in the form of digital certificate (step 2). The user verifies the certificate (step 3) and then, generates a master secret and encrypted it with the server's public key and sends the result to the server (step 4). The server decrypts the master secret to set session keys which used to decrypt data (step 5). The step 6 concludes the handshake that allowed starting of secured data transfer via VPN (step 7).

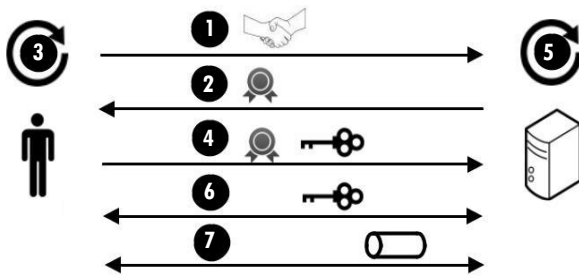


Figure 2. SSL transaction

C. IPSec

Proposed by the IETF in 1995 [21], The *IPSec*, an abbreviation of IP Security, is a framework of protocols (AH, ESP, IKE, ..) designed to provide various security services needed in business area. It supports facilities to encrypt and authenticate user's data (payload). If this done, an attacker can just locate the information destination despite that he can acquainted where it is going to. IPSec operates at the network layer of the OSI model and involves the VPN networks that allow the encapsulating security payload and permit to set up private groups through the Internet.

The advantage of IPsec concerns the security arrangements that can be handled without requiring changes to individual user computers; so, the identity of users can be protected and their IP masked with much security transparent functions.

By another way, the TPsec security concern just the IP layer; so, it is common that information may be visible to users in high layers, mostly when they are on the same system or they share the same IP address. Also, such protocol is characterised by its inherent complexity of implementation and interaction with the network processes.

The figure 3 shows the IPSec organisation. There are two situations:

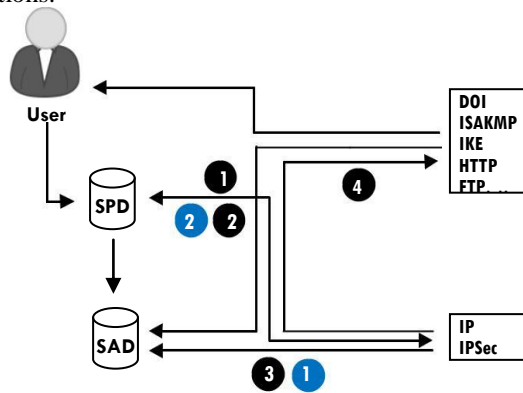


Figure 3. IPSec organisation model

- Outgoing traffic, illustrates by steps with black color: when the IPSec receives an outgoing data, it will consult the Security Policy database (SPD) about the way of processing data (step 1), the related characteristics are extracted from the Security Association Database (SAD) (step 2), if no characteristics are available, the IPSec layer consults the Internet Key Exchange (IKE) in order to develop a new SA according to received data (step 3).
- Incoming traffic, illustrated by steps with blue color: The

SPD is consulted about the directives of treatment of received data (step 1), the related characteristics are extracted from SPD (step 2).

D. 3-D Scheme

The 3-D secure is a based XML model developed by Visa and intended to endorse online credit card transactions, reduce the fraud and chargebacks, and isolate the responsibilities of the three parties (cardholder, seller and the communication between them) within the transaction continuum. It consists to tie the financial authorisation process with an online authorisation under the reference *Verified-by-Visa*. During the transaction, cardholders are usually asked to entering a PIN or a password after entering their card details. This fact reduces the likelihood of fraudulent usage of credit cards. The service has also been adopted by Mastercard, JCB and others. The figure 4 illustrates the 3D process; the step 1 concerns the validation of the shopping card and the choice of the payment method and card information including the secret PIN; such information is authenticated by the Verified-by-Visa system (step 2). Then, the payment platform requests the issuer authorisation (step 3); if accepted, the merchant receives the payment notification (step 4), otherwise, he received the rejection notification (step 5).

However, such system has drawn some reproach; it is appear hard to differentiate between the appropriate popup window *Verified-by-Visa* and an inline phishing frame since it is not served from a card issuing bank or a merchant site.

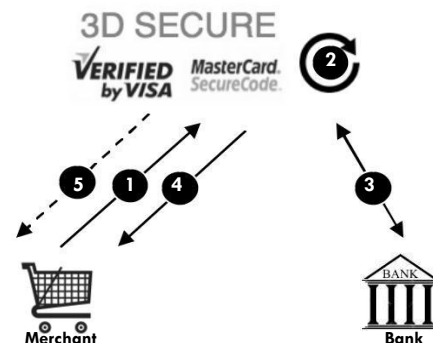


Figure 4. 3D Secure process

IV. E-TRANSACTION SECURITY

Attacks and threat against e-transactions can be classified into internal and external. Transaction systems are more exposed to internal threat (such sealing passwords of skimming cards) but companies are more concerned about the external ones. It is appears reasonable in the fact that companies can be controlled through internal corporate policies. So, they focus on unknown outside attackers who may gain unauthorised access to corporation sensitive assets.

By an external attack, an attacker, who has gain access to network, intercepts and analyses traffic; he tries to recover information about sessions by examining the unprotected packets attributes such TCP ports, IP source and destination and some identical information exchanged. This analysis allows in some cases to recover the identity of parties, personal relationship and with much luck, the related services.

The actual security troubles against public networks transactions include the following:

- *Steal information*: if networks are unprotected or if the encryption strength is not enough, the attacker extracts interesting information such credit card numbers, encryption keys or passwords intercepted from data stream. Such information is then used as a fake identity to obtain illegal benefits.
- *Denial of service*: An attacker monitors network traffic and maliciously, changes, distort or reroute some sensitive data in transit without the knowledge of the sender or the receiver. It can also sneak into the internal network and collect commercial or industrial secrets. Another attack involves the creation of errors in the computing applications causing wrong results or crash of the system. Such facts cause serious complications to business and tarnish the reputation of the company against its challengers.
- *Update online information*: a malicious act denoted by *Man-in-the-middle attack* and occurs when an eavesdropper is positioned between two users who believe communicating with each other. The eavesdropper intercepts, monitors, captures, controls the communication and possible alters it without the knowledge of the users. Such attack is used to intercept secret information related the negotiation encryption keys, access to Wireless point as a legitimate user or insert himself into a financial site between the login and authentication.
- *Cryptographic attack*: consists on the breaking of cryptosystem an revealing the transmitted data based on cryptanalytic methodologies such the *known plaintext attack* in which the attacker have access to a set of plain and cipher texts. By application of the encryption algorithm on plain texts, the result is compared to the available cipher texts. A statistical analysis allowed generating the encryption key which used later in decryption of intercepted information. The attacker can also performs similar attacks such *ciphertext only attack*, *chosen plaintext attack* or the *brute force* attack when the encryption key is less or equal to 64 bits.
- *Cross-Site scripting*: also known as XSS and consists on the injection of a malicious script in a regular page web site via web application. The script appears as a hyperlink with a malicious content. The XSS occurs when a user click on the link from another website, instant message or a web board; the malicious code is then access cookies, session tokens or data shared by the user's web page and the server; it can also rewrite the content of the HTML page. It can in some cases, used to display a factice form asking the user to insert personal information.

V. PROTOCOLS SECURITY ANALYSIS

The SET protocol uses a full public key infrastructure and signs messages which provides a high level of security and privacy for all transaction parties. Nerveless, it has objet of various criticisms, namely, the wide data amount of PKI

infrastructure [22], the key-pairs needed to establish each entity [23], the effort needed to obtain digital certificates [24], etc. By another way, SET transactions process is viewed as relatively slow [25]. Such complication prevents its large deployment and its success against other more efficient systems.

In practice and, when using a stolen credit cards to initiate a transactions, the merchant cannot reliably identify the cardholder in lack of a mechanism for user authentication. The authentication can be provided with the use of client certificates but they are rarely needed in authentication process. Furthermore, the client certificate is sometimes unlinked with his credit card.

Although, the SSL protocol offers a relatively web security traffic achieved by independent encryption keys of each direction of connection as well as for each instance; it provides a lot of known plaintexts that needs a strong encryption algorithm with no fail against known plaintext attacks or traffic analysis anyway. Also, SSL encrypts the connection, not data; so, the network security fails if connected machines are compromised. Such facts has been revealed in literature under various schemes related at most on MITM attack at the certificate chain validation level [26] [27] [28], to chosen plaintext attack [29] and other vulnerabilities [30].

Hence and, for full security, an implementation of a 1024-bit public key is required; in this case, software implementations may not be able to perform operations quickly enough; thus, signing, verifying and wrapping operations become expensive in resources. Also, large size certificates require wide bandwidth transmission. Moreover and, in hardware side, some difficulties appear when using smart cards with reduced computing capabilities. The implementation of cryptographic algorithms needs a processor extension which raises the card cost. By another way, the conduction of the e-transactions and, especially in e-commerce field, cardholders use the wireless handheld devices, such as cell phones or PDAs. In these situations, it seems difficult to support SET and, hardware accelerators may be required to endorse the bandwidth and processing power, that's increase the cost of the infrastructure

About 3D secure, the major problem concern the authentication of inline popup in which the cardholder introduces its password. It appears hard to distinguish between the legitimate verified-by-via frame and a fraudulent phishing popup since the 3D secure form hasn't an address and is part of neither the merchant site nor the cardholder issuing bank.

By another side, *Verified by Visa* label has been object of various critics, based that the pop-up window or frame is the card issuer propriety (unknown by the cardholder), still vulnerable to MITM attack when the cardholder cannot validates the SSL server certificate for the password page and some banks have also used the 3D Secure system to shift liability for fraud losses unfairly onto the cardholder. The 3D Secure has been also assessed negatively for requiring users to remember yet complicated password with the risk of lost or forgotten.

Table 1: SET, SSL, IPSEC and 3D secure characteristics comparison

	SET	SSL	IPSec	3D Secure
Certificate	All parties must have digital certificates	Client-Side certificate only and not strict identification	Mandatory for IPv6 implementation, optional in IPv4	Requires a SSL Certificate to be installed on web server
Authenticity	Ensured by the use of digital signatures and certificates of each transaction	One or two-way authentication using tokens and digital certificates	Two-way authentication via AH and ESP protocols by using tokens and digital certificates	Through password verification of cardholder
Privacy	<ul style="list-style-type: none"> Transaction information encrypted via DES key hashing code. Card information protected via RSA/3DES digital envelope hashing code. Information made available only when and where necessary 	<ul style="list-style-type: none"> Encryption via RC4, RC5, DES, IDEA and 3DES encryption keys. Protection through client-server and point to point architecture 	<ul style="list-style-type: none"> Uses Integrity check values with digital signatures on VP Networks Public keys encrypted by DH and Data by DES. 	Payment encrypted by SSL/TLS security protocols.
Integrity	Messages protection with Hash functions SH-1 and digital signature	<ul style="list-style-type: none"> Digital signature to ensure integrity SH-1 Symmetric cryptography Message checked by key MAC computation MD5 and SH-1 	<ul style="list-style-type: none"> Payload encrypted by 3DES, RC5, IDEA and others No confidentiality for user identity 	<ul style="list-style-type: none"> DH encryption for keys. Data transaction based on 3DES and AES encryption algorithms.
Non repudiation	Through content and receiver's digital signature of each transaction. It varies according of each country	Uses digital signature to ensures integrity	<ul style="list-style-type: none"> AH: Depends on cryptography algorithm. ESP: none 	Through relationships between three domains: acquirer, issuer, and interoperability domains
Cost	<ul style="list-style-type: none"> Slow response time: need to install digital wallet into customer computer. For the large and medium term e-commerce server application, support of SET requires additional hardware acceleration 	Expensive shop method relatively expensive	Moderate wide packet's size	<ul style="list-style-type: none"> Reduces operational expense by minimising chargebacks for unauthorised use. Charges depends of merchants websites
Security	Cryptographic attacks made against can render SSL insecure	Poor need to construct entirely open PKI	<ul style="list-style-type: none"> Low efficiency of key management. Vulnerable to DOS attacks, replay attacks, etc. 	Vulnerable to XSS and MIM attacks
Application	Built into the browser. No special software is needed	<ul style="list-style-type: none"> Web-enabled applications file sharing and email. No need of special. 	All IP - based services	Implementation left to individual banks and their contractors
Users	Business, marketing	Any secure communications, like credit card numbers	HR, Finance, IT Staff, Engineering, Operations	Payment
Scalability	Not widely used	<ul style="list-style-type: none"> Easily deployed Requires tight application integration 	Independent of applications	Incompatible with certain mobile browsers such frames and popups.

The IPsec architecture requires special purpose client software for remote user's workstations; it hence seemed as complicated in deploy and manage; therefore, VPN providers have to develop their own IPsec software clients based systems to work with their IPsec gateways. Such applications are usually considered as closed; so, they also are not commonly available for certain operating systems and presents incompatibility with vendors' products.

In spite of the fact that the IPsec VPN access is often tied to certain machine (desktop, PDA, ..) and perhaps for particular users; in practice, public users can only access the VPN using specific IPsec client; that limits the accessibility and mobility and requires the intervention of technical managers to proceed to manual configuration of parameters and rekeying intervals, that is appear hard to use for public users like sales personnel.

Overall and, while SSL seems inadequate in vulnerable machines, SET is inconvenient while better than SSL in security concern. 3D Secure based on SSL improves the shortcoming of SET and is more convenient in use while not so strict as SET concerning the security. The IPsec operates independent of the applications; it is hence suitable in use on reduced networks and LAN that, it takes longer to deploy on wide architectures.

The most characteristics of the cited protocols are summarised in table 1 above.

VI. CONCLUSION

The use of public networks for exchange documents and financial or business transactions is an essential tool in the people's real life. An efficient secure transfer mechanism can promote consumers' will and set their mind at ease to conduct the online transactions. Such fact is accomplished by various distinct protocols where a comparison between them seems a hard task given the complex environment of use and the involved heterogeneous factors. This paper investigates the mainstream of four major popular protocols, namely SET, SSL, IPsec and 3-D Secure. The study focused on their characteristics, domain and strategy of use and their encryption procedure. The comparison study shows the design issue of each one: its way of securing, authenticates parties, key exchange and the encryption methodologies.

While there are still lots of efforts focused on e-transactions security, it is not an easy decision to entrust public networks to exchange critical data such as credit card number, passwords, private document or any sensitive information unless using of VPN and pay the related expenses.

REFERENCES

- [1] D. Cameron, "Security Issues for the Internet and the World Wide Web," Computer Technology Research Corp., 1997.
- [2] S. Ha and L. Stoel, "Online apparel retailing: roles of e-shopping quality and experiential e-shopping motives," *J. Serv. Manag.*, vol. 23, no. 2, pp. 197–215, 2012.
- [3] L. Zhou, L. Dai, and D. Zhang, "Online Shopping Acceptance Model: Critical Survey of Consumer Factors in Online Shopping," *J. Electron. Commer. Res.*, vol. 8, no. 1, pp. 41–62, 2007.
- [4] R. Hernández-Murillo, G. Llobet, and R. Fuentes, "Strategic online banking adoption," *J. Bank. Financ.*, vol. 34, no. 7, pp. 1650–1663, 2010.
- [5] A. Y.-L. Chong, K.-B. Ooi, B. Lin, and B.-I. Tan, "Online banking adoption: an empirical analysis," *Int. J. Bank Mark.*, vol. 28, no. 4, pp. 267–287, 2010.
- [6] M. Al-Fayoumi, S. Aboud, and M. Al-Fayoumi, "Practical E-Payment Scheme," *Int. J. Comput. Sci. Issues*, vol. 7, no. 3, pp. 18–23, 2010.
- [7] M. F. Treutner, "Evolution of Standard Web Shop Software Systems: A Review and Analysis of Literature and Market Surveys," *Open Inf. Syst. J.*, vol. 5, pp. 8–18, 2011.
- [8] J. W. Rittinghouse and J. F. Ransome, *IM Instant Messaging Security*. 2005.
- [9] D. M. Boyd and N. B. Ellison, "Social network sites: Definition, history, and scholarship," *J. Comput. Commun.*, vol. 13, no. 1, pp. 210–230, 2007.
- [10] M. Billinghurst, A. Cheok, S. Prince, and H. Kato, "Real world teleconferencing," *IEEE Comput. Graph. Appl.*, vol. 22, no. 6, pp. 11–13, 2002.
- [11] J. C. Bertot, U. Gorham, P. T. Jaeger, L. C. Sarin, and H. Choi, "Big data, open government and e-government: Issues, policies and recommendations," *Inf. Polity*, 2014.
- [12] D. R. Mountain, "Disrupting conventional law firm business models using document assembly," *Int. J. Law Inf. Technol.*, vol. 15, no. 2, pp. 170–191, 2007.
- [13] B. Holmes and J. Gardner, *E-Learning: Concepts and Practice*, vol. 54, 2006.
- [14] R. E. Derouin, "E-Learning in Organizations," *J. Manage.*, vol. 31, no. 6, pp. 920–940, 2005.
- [15] a. Xenakis and a. Macintosh, "Procedural security in electronic voting," *37th Annu. Hawaii Int. Conf. Syst. Sci. 2004. Proc.*, vol. 00, no. C, pp. 1–8, 2004.
- [16] J. Starren, S. Sengupta, G. Hripsak, G. Ring, R. Klerer, and S. Shea, "Making grandma's data secure: a security architecture for home telemedicine," *Proc AMIA Symp*, pp. 657–661, 2001.
- [17] T. D. Gunter and N. P. Terry, "The emergence of national electronic health record architectures in the United States and Australia: Models, costs, and questions," *Journal of Medical Internet Research*, vol. 7, no. 1, 2005.
- [18] W. E. Burr *et al.*, "Electronic Authentication Guideline," *NIST Spec. Publ.*, vol. 800, p. 112, 2013.
- [19] M. S. . Merkow and K. L. Jim, Breithaupt; Wheeler, *Building SET Applications for Secure Transactions*. John Wiley, 1988.
- [20] D. Wagner and B. Schneier, "Analysis of the SSL 3.0 protocol," *Proc. 2nd Conf. Proc. Second USENIX Work. Electron. Commer. - Vol. 2*, p. 4, 1996.
- [21] S. Kent and K. Seo, "RFC 4301 Security Architecture for IP," *Ietf*, pp. 1–101, 2005.
- [22] A. Oram and J. Viega, *Beautiful Security*. 2009.
- [23] G. W. Treese and L. C. Stewart, *Designing Systems for Internet Commerce*, 2nd editio. 2003.
- [24] S. Lincoln D, *Web Security: A Step-by-Step Reference Guide*. Addison-Wesley, 1998.
- [25] W. Chou, "Inside SSL: Accelerating secure transactions," *IT Prof.*, 2002.
- [26] M. Marlinspike, "New tricks for defeating SSL in practice," *BlackHat DC, Febr.*, 2009.
- [27] M. Georgiev, S. Iyengar, S. Jana, R. Anubhai, D. Boneh, and V. Shmatikov, "The most dangerous code in the world," in *Proceedings of the 2012 ACM conference on Computer and communications security - CCS '12*, 2012.
- [28] S. Fahl, M. Harbach, H. Perl, M. Koetter, and M. Smith, "Rethinking SSL development in an appified world," in *Proceedings of the 2013 ACM SIGSAC conference on Computer & communications security - CCS '13*, 2013.
- [29] G. V Bard, "Vulnerability of SSL to Chosen-Plaintext Attack (Precursor to BEAST)," *Cryptol. ePrint Arch. Rep. 2004/111*, 2004.
- [30] P. G. Sarkar and S. Fitzgerald, "Attacks on ssl a comprehensive study of beast, crime, time, breach, lucky 13 & rc4 biases," *Internet https://www.isecpartners.com/media/106031/ssl_attacks_survey.pdf [June, 2014]*, 2013.

Spiral Search Optimization Algorithm Applied to (IIR) Digital Filter Design

A.OUADI¹, H. BENTARZI¹ and A. ZITOUNI¹

¹ Laboratory Signals and systems, University M'hamed Bougara Boumerdes, Algeria, lss@univ-boumerdes.dz

Abstract – The digital filters are more forward, give better, faster, less error in the output. They can perform different operations that highly difficult to be pursued by analog filters. The types of digital filters are Infinite duration impulse response (IIR) filter and Finite duration impulse response (FIR) filter. An IIR filter that is unlike FIR has feedback and gives better response with less compatible cost. The IIR filter is suitable for lower order filter and found more targeted than FIR. In designing IIR filter, the main difficulty may be faced in the higher order. Therefore, in this research work, the spiral search optimization technique may be used for designing higher order IIR digital filters. It is considered in the design providing unimodal error objective function. It can be noted that the spiral search optimization algorithm has succeeded to converge to only global optimum.

Keywords – Spiral Search Technique, Optimization, IIR digital filters, Unimodal error, Objective function.

I. INTRODUCTION

OVER the last few decades the field of Digital Signal Processing (DSP) has grown to important both theoretically and technologically. In DSP, there are two important types of Systems. The first type of systems performs signal filtering in time domain and hence it is known as Digital filters. The second type of systems provide signal representation frequency domain and are known as Spectrum Analyzer. Digital filtering is one of the most powerful tools of DSP. Digital filters are capable of performance specifications that would, at best, be extremely difficult, if not impossible, to achieve with an analog implementation. In addition, the characteristics of a digital filter can be easily changed under software control.

Digital filters are classified either as Finite duration impulse response (FIR) filters or Infinite duration impulse response (IIR) filters, depending on the form of impulse response of the system. In the FIR system, the impulse response sequence is of finite duration, i.e., it has a finite number of non zero terms. Digital infinite-impulse-response (IIR) filters can often provide a much better performance and less computational cost than their equivalent finite-impulse-response (FIR) filters and have become the target of growing interest [1,2]. However, because the error surface of IIR filters is usually nonlinear and multimodal, conventional gradient-based design methods may easily get stuck in the local minima of error surface [2,3]. Therefore, some researchers have attempted to develop design methods based on modern heuristic optimization algorithms such as

genetic algorithm (GA) [4], simulated annealing (SA) [5] etc.

Analytical or simple iterative methods usually lead to sub-optimal designs. Consequently, there is a need of optimization methods that can be used to design digital filters that would satisfy prescribed specifications.

In this research work, the application of the novel optimization technique called Spiral Search Optimization (SSO) to the design of digital filters is considered. The purpose is to design a filter that can satisfy the convergence to only global optimum [6].

II. DIGITAL IIR FILTER DESIGN ISSUES

The digital (IIR) filtering is an active area of research and has been considered for a variety of problems in signal processing and also in control field. Figure 1 illustrates the general structure and components of an IIR filter with input $x(k)$ and output $y(k)$. If an IIR filter is considered, the general input-output relationship is governed by

$$y(k) = \sum_{i=0}^L b_i x(k-i) - \sum_{i=1}^M a_i y(k-i) \quad (1)$$

Where $x(k)$ and $y(k)$ are the filter's input and output respectively, and $M \geq L$ is the filter order. The digital filter in a system identification configuration where the filter coefficients are the unknown system parameters and $d(k)$ that is simply the measured output of the system. The objective of the algorithm is to minimize a performance criterion that is based on the prediction error or estimation error, defined as follows:

$$e(k) = d(k) - y(k) \quad (2)$$

Where $d(k)$ and $y(k)$ are the desired and actual response of the filter, respectively. One commonly used term is the mean square error MSE, $J = E(e^2(k))$. This error which is usually expressed as the time averaged cost function defined by,

$$J(w) = \frac{1}{N} \sum_{i=1}^N (d(k) - y(k))^2 \quad (3)$$

Hence, the design of the filter can be considered as a minimization problem of the cost function $J(w)$ stated as $\min_{w \in W} J(w)$; where $w = [b_0, b_1, \dots, b_L, a_1, a_2, \dots, a_M]^T$ is the filter coefficient vector. The SSO technique may be used to minimize $J(w)$ for increasing filter coefficients.

III. SPIRAL SEARCH OPTIMIZATION ALGORITHM

Spiral search optimization method has been recently developed based on the analogy to spiral phenomena [7, 8].

Compared with traditional optimization techniques and other global optimizers, this method is easy to implement and very efficient in reaching optimum solutions.

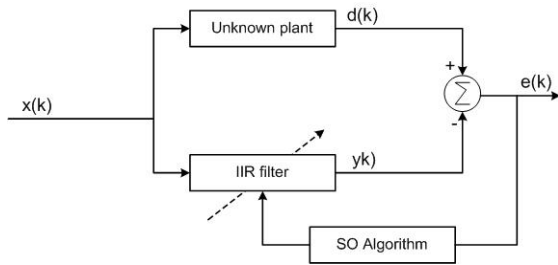


Figure 1 : Bloc diagram system identification design using spiral optimal algorithm

Patterns in nature are visible regularities of form found in the natural world. These patterns recur in different contexts and can sometimes be modeled mathematically. Natural patterns include symmetries, trees, spirals, meanders, waves, foams, arrays, cracks and stripes. Mathematics, physics and chemistry can explain patterns in nature at different levels. Patterns in living things are explained by the biological processes of natural selection and sexual selection. Studies of pattern formation make use of computer models to simulate a wide range of patterns.

Among the natural patterns, spirals are common in plants and in some animals. For example, in the nautilus (Figure 2), each chamber of its shell is an approximate copy of the next one, scaled by a constant factor and arranged in a logarithmic spiral.

The spiral phenomena occurring in nature are approximated to logarithmic spirals as in Fig. 2. Examples of natural spiral dynamics include whirling currents, low pressure fronts, nautilus shells and arms of spiral galaxies. Logarithmic spirals discrete processes to generate spirals that can form an effective behavior in metaheuristics. A two-dimensional algorithm has been first proposed [7], and then, a more generalized n-dimensional version has been recently suggested [8].

In the present work, the use of the spiral optimization technique is presented and used to identify the parameters of the digital IIR filter design. Thus, the spiral optimization algorithm aims at matching a desired magnitude response only which needs the two dimensional optimization. It is worth understanding the two dimensional optimization model.

2-D Spiral Model

Rotating a point x in 2-dimensional orthogonal coordinate system to the left around the origin by θ makes x' written as

$$x' = R_{1,2}^{(2)}(\theta)x \tag{4}$$

Where rotation matrix is $R_{1,2}^{(2)}(\theta) = \begin{bmatrix} \cos \theta & -\sin \theta \\ \sin \theta & \cos \theta \end{bmatrix}$

The rotation image is shown in Fig.3. Using this rotation matrix $R_{1,2}^{(2)}(\theta)$, we can formulate the following logarithmic spiral model which generates a point converging to the origin from an arbitrary initial point x_0 on the x_1 - x_2 plane while drawing a logarithmic spiral discretely.

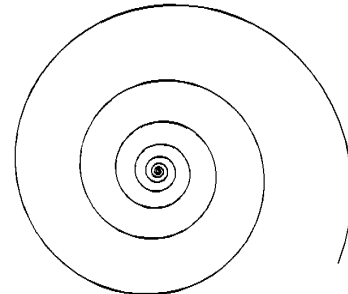


Figure 2: Logarithmic spiral

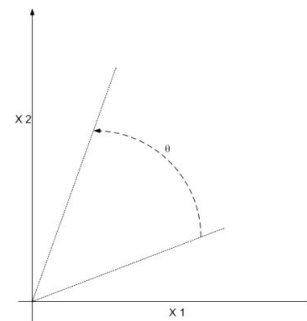


Figure 3: Rotation on 1-1 plane

$$\begin{bmatrix} x_1(k+1) \\ x_2(k+1) \end{bmatrix} = rR_{1,2}^{(2)}(\theta) \begin{bmatrix} x_1(k) \\ x_2(k) \end{bmatrix} = S_2(r, \theta) x(k), \quad x(0) = x_0 \tag{5}$$

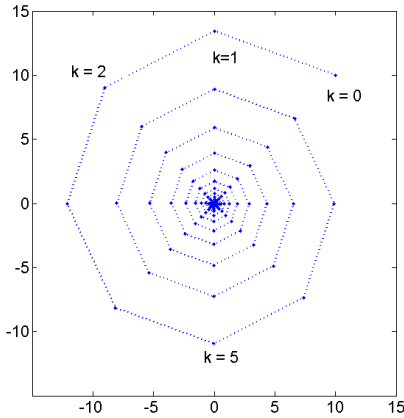
Where $0 < \theta < 2\pi$ is a rotation angle around the origin each k , $0 < r < 1$ is a convergence rate of distance between a point and the origin each k , and $S_2(r, \theta)$ becomes a stable matrix. Note that this spiral model has different expression that the parameter roles are clearer than the model used in [6] but they are essentially the same and have the same behavior.

Illustrations of Eq.(5) with parameters of Table I are shown in Fig.4. These figures indicate behavior of the spiral model and roles of two parameters.

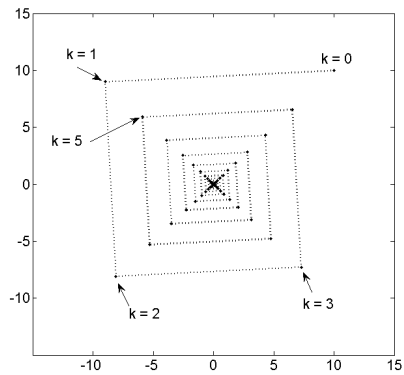
However, the spiral model Eq.(5) does not have enough flexibility for applications because has the center at only the origin. Thus, we enhance the spiral model Eq.(5) to have the center at an arbitrary point x^* as follows.

$$x(k+1) = S_2(r, \theta)x(k) - (S_2(r, \theta) - I_2)x^* \tag{6}$$

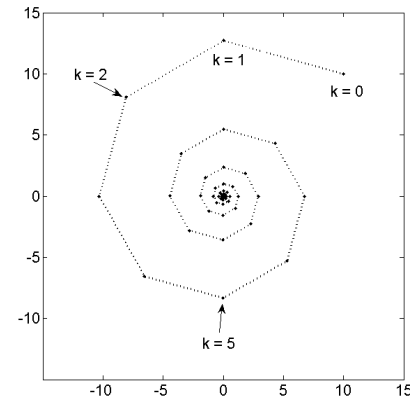
Which is derived by translating the origin of Eq.(5) toward an arbitrary point x^* . The convergence of the trajectory to x^* is confirmed from that Eq.(6) can be transformed into $e(k+1) = S_2(r, \theta)e(k)$ by using error variable $e(k) = x(k) - x^*$.



Case (a)



Case (b)



Case (c)

Figure 4: Illustrations of a 2D spiral search.

2-D Spiral Optimization Algorithm

Many methods in metaheuristics, such as GA, PSO and ACO, are multipoint searches with interactions. The representative interactions among search points are crossing in GA and using the best evaluation value in PSO. The search behaviors generated by the interactions contribute for achieving global and effective searches. Thus, making the spiral model Eq.(3)

Table 1: Parameters for 2D Illustrations.

Case	$r r =$	θ theta=
(a)	0.95	$\pi/4$
(b)	0.90	$\pi/4$
(c)	0.95	$\pi/2$

be a multipoint search model with a proper interaction is valid approach to construct a better metaheuristics.

The multipoint search model using Eq.(6) is formulated as follows:

$$x_i(k + 1) = S_2(r, \theta)x_i(k) - (S_2(r, \theta) - I2)x^* \quad (7)$$

$i = 1, 2, \dots, m$, with the common center x^* set as the best solution among all search points during a search. Namely, x^* becomes an interaction.

In this case, adopting the multipoint and adding the interaction have following meanings:

Interaction: Contribution to realize the intensification that should be done around a good solution.

Multipoint: Contribution to enhance both intensification and diversification of the spiral model.

In case of a minimization problem, the algorithm based on the multipoint model Eq.(7) is described as follows. The search points drawing spiral trajectories toward the common center x^* set as the best solution, which can naturally realize the strategy from diversification to intensification, can be expected to search a better solution.

The effectiveness of this method was confirmed by numerical experiments for 2-dimensional benchmark problems [7].

2-D Spiral Optimization Algorithm

Step 0: [Preparation] Select the number of search points $m \geq 2$, the parameters $0 < \theta < 2\pi$, $0 < r < 1$ of $S_2(r, \theta)$, and the maximum iteration number k_{max} . Set $k = 0$.

Step 1: [Initialization] Set the initial points $x_i(0) \in \mathbb{R}^2, i = 1, 2, \dots, m$ in the feasibility region and the center x^* as $x^* = x_{ig}(0), ig = \arg \min_i f(x_i(0)), i = 1, 2, \dots, m$.

Step 2: [Updating x_i]

$$x_i(k + 1) = S_2(r, \theta) x_i(k) - (S_2(r, \theta) - I2) x^*, \quad i = 1, 2, \dots, m.$$

Step 3: [Updating x^*]

$$x^* = x_{ig}(k + 1), \quad ig = \arg \min_i f(x_i(k + 1)), \quad i = 1, 2, \dots, m.$$

Step 4: [Checking Termination Criterion]

If $k = k_{max}$ then terminate. Otherwise, set $k = k + 1$, and return to Step 2.

IV. SIMULATION RESULTS AND DISCUSSION

Therefore, in this simulation study, IIR filters are designed for the system identification purpose. In this case the parameters of the filter are adjusted using the spiral search optimization

algorithm until the error between the output of the filter and the unknown system (Fig.1) is minimized.

Using this fitness function Eq.(6), the poles of the IIR filter being designed by algorithms are forced to move into the unit circle. The spiral optimization algorithm does not use gradient techniques and thus is appropriate for use in problems where the function to be optimized is non unimodal or non quadratic, such as the mean-squared error surface in a recursive adaptive filter. Computer simulations of the algorithm performance on two IIR filter examples will be illustrated hereafter.

Unimodal filter:

The first specific system identification design consists of a two-pole model shown in Fig.5. The plant or the unknown system has the following transfer function:

$$H_u(z) = \frac{1}{1-1.2Z^{-1}+0.6Z^{-2}} \tag{8}$$

Where $c_1 = -1.2$ and $c_2 = 0.6$ and the system to be identified having the two-pole transfer function given by:

$$H(z) = \frac{1}{1-b_1Z^{-1}-b_2Z^{-2}} \tag{9}$$

Assuming that the input signal is a white noise with unit power, the normalized error surface is a function of the filter coefficients b_1 and b_2 [2]. The minimum of the error occurs when $b_1 = c_1$ and $b_2 = c_2$. The stability region of this two pole filter model is the set of variable coefficients where:

$$\left\{ \begin{array}{l} -1 < a_2 < 1 \\ a_2 - 1 < a_1 < 1 - a_2 \end{array} \right\}$$

The set of points $\{a_1, a_2\}$ represents the search space that lie in the triangle of stable filter.

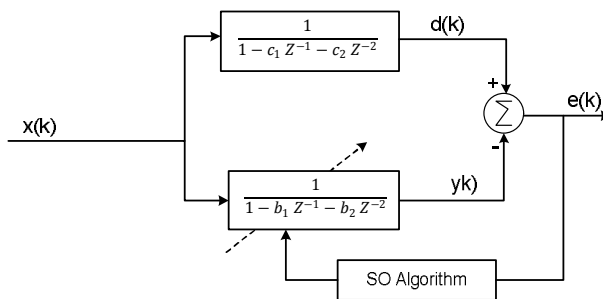


Figure 5: Two-pole plant model system identification.

Figure 6 represents contour plots which shows the points of equal normalized error in the b_1b_2 space from the configuration of Fig.5 where $c_1 = -1.2$ and $c_2 = 0.6$. The contour plot shows the uniformity of the error surface. Figure 7 shows the evolution of the mean square error (MSE) averaged over 11 runs of SOA. The presented results show that the optimization algorithm achieves and drives the filter coefficients toward the minimum squared error after few iteration steps.

V. CONCLUSION

The proposed spiral optimization algorithm has been clearly described. The spiral search optimization algorithm, for the first time to my best knowledge, is applied to designing digital recursive digital filters [6]. Second order IIR digital filter is considered in the design providing unimodal error objective function. The developed spiral search optimization algorithm has succeeded to converge to only global optimum in

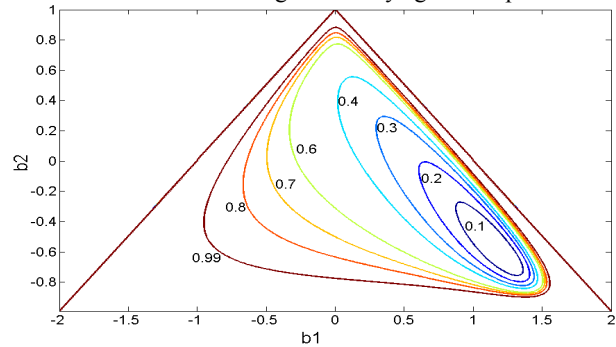


Figure 6: Surface Error of the system identification with second order filter

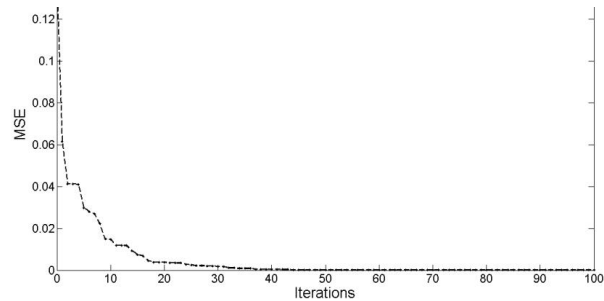


Figure 7: MSE evolution of this filter

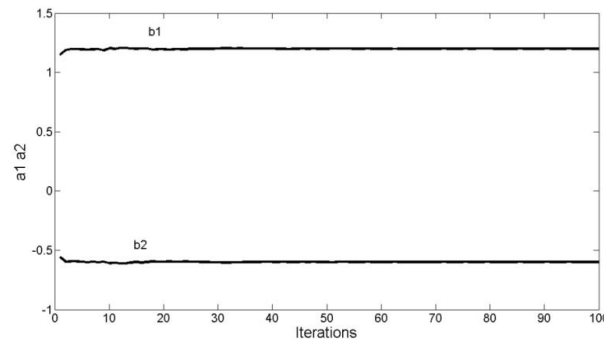


Figure8: Evolution of parameters of the second order digital IIR filter.

this case; conversely classical optimization algorithm can fail if starting point is not correctly chosen. The same steps can be applied to higher order IIR digital filters.

REFERENCES

[1] V. K. Ingle and J. G. Proakis, Digital Signal Processing Using MATLAB, Thomson Books, New Delhi, 2004.

- [2] L. Y. Cao, "Practical Issues in Implementing a Single-Pole Low-Pass IIR Filter," IEEE Signal Processing Magazine, pp. 114-117, 2010.
- [3] J. Skaf and P. B. Stephen, "Filter Design with Low Complexity Coefficients," IEEE Transactions on Signal processing, Vol. 56, No. 7,, pp. 3162-3170, 2008. doi:10.1109/TSP.2008.919386
- [4] X. Zhang and H. Iwakura, "Design of IIR Digital Filters based on Eigen Value Problem," IEEE Transactions on Signal processing, Vol. 44, No. 6, pp. 1325-1319, 1996.
- [5] N. Benvenuto and M. Marchesi, "Applications of Simulated Annealing for the Design of Digital Filters," IEEE Transactions on Signal Processing, Vol. 40, No. 2, pp. 323-331, 1992. doi:10.1109/78.124942
- [6] A. Ouadi, H. Bentarzi and A. Reoui, "Optimal multiobjective design of digital filters using spiral optimization technique", SpringerPlus 2013, Vol.2, pp.461-474, 2013.
- [7] K.Tamura, and K.Yasuda, " Primary study of spiral dynamics inspired Optimization", IEEJ Trans electrical Electron Eng, Vol. 6, Issue S1, pp.98-100, 2011.

Automatic learning of semantic relationships for the ontology construction

- Application on Arabic text-

Ali BENABDALLAH¹

Superior School of Management –Tlemcen (ESMT)
PoBox 119, Tlemcen 13000, Algeria

benabdallah.a13@gmail.com

Nour Elhouda BOUGHARI²

Department of Arabic literature, University Abou Bekr
Belkaid-Tlemcen

PoBox 119, Tlemcen 13000, Algeria

ali_tlemcen@yahoo.com

Abstract—The construction of an ontology from a textual corpus begins with the extraction of concepts constituting this ontology, and these concepts will be linked by semantic relationships. In this paper, we propose an extraction approach of the most important elements of the ontology, based first on a statistical method of extraction of the terms which is called “repeated segments method”, followed by the application of a weight filter to choose the most common terms. Then, in order to extract the semantic relationships linking the extracted concepts, we apply a machine learning technique based on a set of syntactic and semantic features of the sentences of the corpus. And finally we will discuss the results that can be obtained by applying our approach on a textual corpus of the Arabic language.

Keywords: *Extraction of semantic relations, Artificial Learning, ontology construction, syntactic and semantic features, Arabic Natural Language Processing.*

1-Introduction

The ontology construction from textual documents is a very important sub-domain of ontology engineering. The obtained ontology can be used in several domains of NLP (Natural Language Processing) such as semantic information retrieval, semantic annotation of resources, automatic indexing of documents, automatic summaries of texts, etc.

The use of texts in the process of ontologies construction is justified for two reasons: first, texts are often the bearers of knowledge stabilized and shared by communities of practice. Moreover, even if they do not replace them completely, texts are more readily available than experts who lack time to participate in the construction process

[Mon08]. But it should be noted that the use of experts is necessary especially in the validation of the ontologies obtained.

Such an ontology consists of a set of concepts that are both organized hierarchically and structured by relationships linking these concepts. Each ontology construction process must go through two important steps: one involves the extraction of concepts and the other concerns the extraction of semantic relations.

The objective of our approach is to construct an ontology from the Arabic texts in an automatic way. Beginning with the step of extracting the terms that will be the future concepts of ontology, the semantic relations will be extracted from the texts based on a set of syntactic and semantic features extracted from the sentences of text.

The next part is structured as follows: The first part focuses on our approach and the phases that constitute it and the methods used to prepare our corpus, and finally we will discuss the results that can be obtained by applying our approach on a sample of an Arabic textual corpus.

2- Preprocessing the corpus:

In a process of ontology construction from texts, the stage of constitution and preparation of the corpus is both primordial and delicate. Since, the corpus is the essential source of information for the entire construction process [Bou03].

The questions that arise in the design of any corpus include: the type of corpus (a "specialized" corpus is a corpus containing texts on a subject related to a domain of knowledge, for example, ('Computer science in Arabic'), the adequacy for the target project, the possibility of reusing this corpus, size (number of words), representativeness (that is, the variety of texts, Sources, etc.), the use of complete texts or samples, etc. [Mar03]

After collecting the corpus, it must be prepared to be ready for processing during the rest of the construction process. The usefulness of the corpus preparation is to remove the ambiguity, reduce the number of transactions and adapt the corpus to the objective of the next step "extraction of candidates-terms".

This preparation step is broken down into several sub-steps which are:

- Standardization: transforms the document into a more easily manipulated standard format. Before lemmatization, the document is standardized as follows: [Maz12]

- Delete special characters and digits, for example: ,٢,٣,٤,٥,(,٩...
- Deleting Latin words and characters: Latin characters are detected by their graphs.
- Removal of single letters: single-letter words in Arabic and abbreviations. (م: تاريخ), date abbreviations (الفقرة ب), (حروف) (ميلادي: هـ: تاريخ هجري "العلقة": او), etc.

- Deleting empty words: consists of eliminating all non-significant words, by comparing each recognized word with the elements of the list of empty words: "stop-list". (الضمائر المنفصلة), prepositions (حروف العطف), conjunctions (حروف الجر), etc.). Example: على في, أن, التي, عن, بلى, من, ... الذي مع, بعد, بين, هذه, هذا, انه, منذ, ما, لم

Generally, empty words that are very common (almost half the occurrences of a text) are not indexed because they are not informative [Ver04]

- Stemming:

It is a delicate task because Arabic is a flexional and highly differentiated language; The absence of diacritics creates ambiguity and therefore requires complex morphological rules, and capitalization is not used in Arabic, which makes it difficult to identify proper names, acronyms and abbreviations.

To solve the ambiguity, [Alj02] has shown that light stemming (based on deletion of suffix and prefix) surpasses that based on root detection in

the field of information retrieval. In our approach we considered the light stemming which consists of detecting whether prefixes or suffixes have been added to the word.

3- Extractions des candidats-termes :

After the preparation of the corpus, we proceed to the extraction step of the elements of the ontology. First, we begin to extract the terms by the method of the repeated segments, in the following one will apply a filtering to eliminate some terms that are not considered as concepts.

The method of "repeated segments" relies on the detection of strings consisting of words existing several times in the same text. It is a statistical technique for extracting information from texts. The repetition of the segments in a text indicates that these can be used to designate the concepts of the domain of the corpus. Segments of text can be separated by spaces or punctuation, and can be simple (single word) or complex.

The complex terms are identified in a window of four words in the same sentence (the number four is chosen according to the principle: a term designating a concept contains a maximum of four words [Maz12]).

The "repeated segments" method is based on the following proposition: "A relevant term is used several times in a specialized text". For this reason, we use the "weight filter" [Her06] to select terms with sufficient weight. The weight is measured by the total frequency of a term in the corpus. If this frequency is greater than a threshold: f_{min} (a threshold indicating relevance), the term will be kept for the next step in the construction process, otherwise this term will be ignored. (F_{min} is chosen empirically, and depends on the size of the corpus).

4-Extraction of semantic relations

Existing works in the field of extracting semantic relationships from text can be divided into two families: we usually distinguish works that are based on the frequency aspect of the corpus from which they extract the related concepts, and those who exploit structural indices to detect the linked elements, that is to say who follow a symbolic approach. [Vin04]

The symbolic methods of extracting lexical relations are based on indices collected on the context of an occurrence of related words to decide whether to acquire it or not; the symbolic classifier is therefore often a set of rules based on lexical, morphological, categorical, syntactic or other indices. These techniques can themselves be classified into two main families: [Vin04]

Language approaches in which structural indicators given previously are exploited (by a linguistic analysis for example).

- ❖ And approaches based on a notion of learning markers or relationships.

Our approach is based on a supervised learning method of semantic relations.

We first present the task of relation extraction as a classification task. For the sake of simplicity and clarity, we restrict our discussion to *binary* relations between two entities:

Given a sentence $S = w1, w2, \dots, e1, \dots, wj, \dots, e2, \dots, wn$

Where $e1$ and $e2$ are the entities, a mapping function $f_R(.)$ can be given as

$$f_R(T(S)) = \begin{cases} +1 & \text{If } e_1 \text{ and } e_2 \text{ are related according to } T(S) \\ -1 & \text{Otherwise} \end{cases}$$

Where $T(S)$ are features that are extracted from S . Essentially the mapping function $f_R(.)$ decides whether the entities in the sentence are in a relation or not. Put in another way, the task of entity relation extraction becomes that of entity-relation detection.

A labeled set of relationship pairs is prepared manually for learning. These pairs of relationships are extracted from external text resources, such as a dictionary or a lexical database. The function $f_R(.)$ is constructed as Perceptron classifier.

This classifier can be trained using a set of features selected after performing textual analysis of the labeled sentences. On the other hand, input to the classifiers can also take the form of rich structural representations like parse trees.

Given a set of positive and negative relation examples, syntactic and semantic features can be extracted from the text. These extracted features serve as cues for deciding whether the entities in a sentence are related or not.

Syntactic features extracted from the sentence include:

- ❖ (1) the entities themselves,
- ❖ (2) the types of the two entities,
- ❖ (3) word sequence between the entities,
- ❖ (4) number of words between the entities and
- ❖ (5) Path in the parse tree containing the two entities.

Semantic cues include

- ❖ The path between the two entities in the dependency parse.

Both the semantic and syntactic features extracted are presented to the classifier in the form of a feature vector, for training or classification. (Kambhatla, 2004) trains a log-linear model using the features described, for the task of entity classification.

On the other hand, (Zhao & Grishman, 2005) and (GuoDong et al., 2002) use SVMs trained on these features using polynomial and linear kernels respectively for classifying different types of entity relations.

5- Results and discussion

5-1 Text corpus:

In order to test our approach, we constructed a corpus of text from a set of Arabic textual documents containing definitions of technical words in electronics and computer science in Arabic, and these are the titles of some documents that constitute our corpus:

Title of document (in Arabic)	Title of document (in English)	Number of words
المعجم الموسوعي في الكمبيوتر والإلكترونيك	Encyclopedic dictionary in computer sciences and electronics	84 622
مصطلحات الحاسب والإنترنت	Terms of Computer and Internet	3 553
موسوعة مصطلحات الإنترنت والكمبيوتر	Encyclopedia of terms in Internet and computer sciences	16 490
...

Table 1: Titles of documents in our textual corpus

These documents are downloaded, selected and prepared manually (by deleting tables, diagrams, graphs, pictures ...), these documents are in "html" or "PDF" formats. The formats of these documents were converted into "txt" format. The total number of words in our corpus is about 304 665 words (size \approx 1 800 kb)

5-2 Extraction of "repeated-segments":

For extracting terms of our ontology we set the following parameters:

- Maximal Segment size = 4 words. It indicates the maximum size of a complex term. Example: بروتوكول نقل البريد البسيط (Simple Mail Transfer Protocol)
- Weighting threshold: The weight of a term is calculated by the total frequency, is the total number of occurrences in the corpus. Threshold weight of a simple word is = 40. Threshold weight of a complex term is = 10. These thresholds are selected relatively to the corpus size.

The following table shows a sample of selected segments:

Segment	Frequency
إنترنت	5278
كمبيوتر	3045
معلومات	2233
موقع	1624
...	...
الشبكة العالمية	203
البريد الإلكتروني	101
...	...

Table 2. Samples of selected segments.

5-3 Extraction de relations sémantiques :

By applying our relationship learning approach described earlier on our Arabic text corpus, our application can learn a set of semantic relations pairs based on a learning base containing pairs of relations chosen and filtered manually from two texts resources which are: a dictionary of synonyms and antonyms in Arabic and a lexical database of the Arabic language which is called Arabic WORDNET. And here are some examples of these pairs of relationships:

Relationship	Hypernym		Synonym		Antonym	
	Pairs	برنامج حاسوب (software)	شفرة (code)	حاسوب (Computer)	كمبيوتر (Computer)	جزئي (partial)
حاسوب (Computer)		آلة (Machine)	ابتكار (innovation)	اختراع (invention)	اقفال (lock on)	افتتاح (Opening)
آلة (Machine)		جهاز (Device)	ارتباط (correlation)	اتصال (connexion)	الإسراع (Accelerate)	التأخير (Delay)
جهاز (Device)		شيء مصنوع (Anything) (made)	عداد (Counter)	حاسب (Computer)	الممتلئ (Full of)	الفارغ (empty)
شيء مصنوع (Anything) (made)		جسم (Body)	إغلاق (Close)	اقفال (lock on)	التجميع (Assembly)	التقسيم (division)
...	

Table 3: List of relationship pairs [Benabdallah & al, 2017]

York, NY, USA, pp 340-347, ACM DL Digital Library, <http://dl.acm.org/citation.cfm?id=584848>.

6- Conclusion

In this paper we have proposed an automatic approach to extracting the most important elements of ontology which are semantic terms and relations. To do this, we used a corpus of texts in Arabic and two other text resources: a dictionary and a lexical database.

Our construction process begins with a preliminary step which is the preparation of the corpus going through normalization, the deletion of empty words and lemmatization. In order to extract the candidates-terms, we used a statistical method "repeated segments" followed by the application of a weight filter to choose the most frequent terms. And to connect the new extracted concepts an artificial learning method has been adopted based on a learning base containing a set of pairs of relationships.

References

Aljlal M, Frieder O (2002) On Arabic search: Improving the retrieval effectiveness via a light stemming approach. In: Proceedings of the eleventh international conference on information and knowledge management, ACM Press, New

Benabdallah, A., Abderrahim, M.A. & Abderrahim, M.EA. « Extraction of terms and semantic relationships from Arabic texts for automatic construction of an ontology », Int J Speech Technol (2017) 20: 289. doi:10.1007/s10772-017-9405-5

Bourigault D, Aussenac-Gilles N (2003) Construction d'ontologies à partir de textes. ATALA (Association pour le traitement automatique des langues) http://www.atala.org/taln_archives/TALN/TALN-2003/taln-2003-tutoriel-002.pdf.

GuoDong, Z., Jian, S., Jie, Z., & Min, Z. (2002). Exploring various knowledge in relation extraction. *Proceedings of the 43rd Annual Meeting on Association for Computational Linguistics* (pp. 419–444).

Kambhatla, N. (2004). Combining lexical, syntactic, and semantic features with maximum entropy models for extracting relations. *Proceedings of the ACL 2004*.

Marshman E (2003) Construction et gestion des corpus : Résumé et essai d'uniformisation du processus pour la terminologie, In: Observatoire de linguistique Sens-Texte (OLST). University of Montréal.

[http://olst.ling.umontreal.ca/pdf/terminotique/corpusentermi
no.pdf](http://olst.ling.umontreal.ca/pdf/terminotique/corpusentermi
no.pdf).

Mazari AC (2013) Vers une approche statistique pour l'extraction des éléments de l'ontologie à partir des textes arabes. In: RML (Revue Maghrébine des langues), ISSN: 2253-0673, 8th edition, Oran Algeria, pp 39-56.

Mondary T, Després S, Nazarenko A, Szulman S (2008) « Construction d'ontologies à partir de textes: la phase de conceptualisation », 19èmes Journées Francophones d'Ingénierie des Connaissances, Nancy, France, LIPN - UMR 7030 University of Paris 13 – CNRS.

Vergne J (2004) Découverte locale des mots vides dans des corpus bruts de langues inconnues, sans aucune ressource, 7eme Journées internationales d'analyse statistique des données textuelles, GREYC – University of Caen.

Vincent C, Pascale S,(2004) « Apprentissage semi-supervisé de patrons d'extraction de couples nom-verbe », TAL. Volume 45 - n° 1/2004, pages 153 à 182

Zhao, S., & Grishman, R. (2005). Extracting relations with integrated information using kernel methods. *Proceedings of the 43rd Annual Meeting on Association for Computational Linguistics* (pp. 419–426).

Object recognition system based on Oriented FAST and Rotated BRIEF (ORB) features

YRD.DOÇ.DR. ERSIN KAYA
AHMED MOHAMMED AHMED BAYATI

Abstract:

Recently, Object recognition systems become more exciting research subject because of its applications in vast fields of life. However, to build a prosperous object recognition system that requires a low power consumption, high performance, and low computation cost, the feature extraction algorithm is critical to achieving such results. Recent advances in computer vision field lead to many approaches. The systems that based on local point features has become a widely accepted and used method over the last years. In this research paper, we introduce an object recognition system based on ORB (Oriented FAST and Rotated BRIEF) algorithm which is a robust option to SIFT and SURF if we concerning the performance and cost.

Keywords: Object recognition, ORB, BRIEF , FAST , Features matching.

I. INTRODUCTION

Object recognition is an aggressive domain of research in the computer vision and images analysis applications. The fact can be evidenced by the presence of the immense volume of research conveyed in this area over the past three decades. Frequently, the task of object recognition is regarded as broadly covering of two sub-tasks; Object detection: Recognizing whether an example of the object class is in the image or not, and to localize the object in a given scene. The object recognition systems possess many challenges such as the appearance of an object in the image can have an extensive range of variety due to viewpoint changes, Scale, Orientation, Shape changes and illumination. Also, several views of the same object can give rise to widely different images. The feature extraction methods is a critical part of any object recognition system. However, over the past years, many approaches have been proposed such as SIFT (Scale-Invariant Feature Transform) and SURF(speeded up robust features). SIFT algorithm was introduced in 2004 by D.Lowe from University of British Columbia[1][3]. SIFT is feature extraction and description algorithm which converts an image into an extensive set of feature vectors each of which is rotation, scaling, invariant and partially invariant to illumination variations. Key locations are determined as maxima and minima of the result of DoG function performed in scale space to a set of flattened and resampled images. SIFT used a qualified k-d tree algorithm named best-bin-first search method[2] for features matching. The best-bin-first search method can recognize the nearest neighbors with great possibility using only an inadequate cost of computation. SURF algorithm is local feature

extraction and description method inspired by SIFT introduced in 2006 by Herbert Bay[4], and it is several times faster than SIFT. In SIFT, Lowe estimated Laplacian of Gaussian with Variation of Gaussian for obtaining scale-space. SURF goes a few more and estimates LoG among Box Filter. Figure 1 shows an illustration of such an approach.

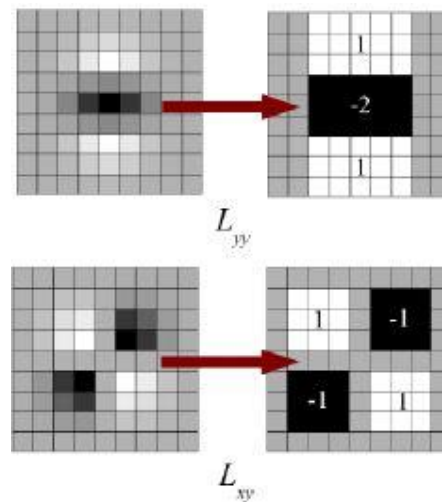


Figure 1: SURF Box filter.

One significant benefit of this conjecture is that convolution beside box filter can be efficiently determined among the help of integral images. Moreover, it can be done in parallel for several scales. Additionally, the SURF rely on the determinant of the Hessian matrix for both scale and location. For orientation distribution, SURF applies wavelet responses in horizontal and vertical direction for a neighborhood of size 6s. Satisfactory gaussian weights are also utilized to it. Later they are considered in space as given in Figure 2.

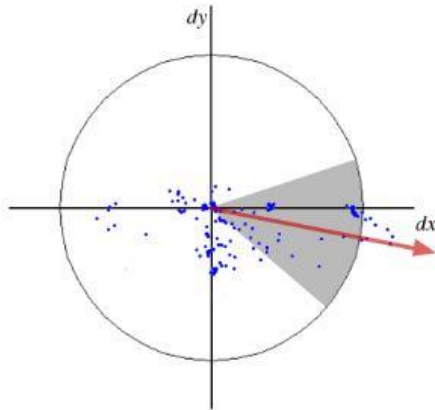


Figure 2 : SURF Orientation.

The general orientation is determined by measuring the total of all responses in a sliding orientation window of angle 60 degrees. The impressive point is that wavelet response can be observed out using integral images very quickly at any range. For numerous demands, rotation invariance is not required, accordingly no need of obtaining this orientation, which speeds up the method. SURF gives such a functionality named Upright-SURF or U-SURF. In this research paper, we proposed an object recognition system based on ORB(Oriented FAST and Rotated BRIEF) algorithm. ORB is a high performance and free option to SIFT and SURF introduced in 2011 by Ethan Rublee[5], and it is based on FAST corner detector and BRIEF binary descriptor.

II. METHODS

ORB is a local feature extraction algorithm introduced by Ethan Rublee in 2011[5]. ORB based on FAST corner detector algorithm[6,7] and BRIEF binary descriptor[8] with some qualifications to improve the performance. The authors of ORB modify the FAST algorithm to compute the orientation because of the original algorithm cannot measure the orientation of key points and called the new algorithm Oriented FAST(oFAST). oFAST computes the intensity centroid[9] of a located corner within the patch center; the orientation is the direction from the corner point to the centroid. Image moments are calculated with (X, Y) points which must be in a circular region of the patch to better the rotation invariance and given in this equation:

$$m_{pq} = \sum_{x,y} x^p y^q I(x, y),$$

The intensity centroid calculated using moments and given in this equation:

$$C = \left(\frac{m_{10}}{m_{00}}, \frac{m_{01}}{m_{00}} \right)$$

Then a vector from the corner point O to the centroid point C constructed. Moreover, the orientation of the patch given in this equation:

$$\theta = \text{atan2}(m_{01}, m_{10}),$$

ORB uses BRIEF(Binary Robust Independent Elementary Features) descriptor and modifies it to perform with the rotation. ORB rotate BRIEF according to the orientation of the key points. For any n, Features set. Binary tests at coordinates of pixels (xi,yi), define a matrix, 2xn which called S and contains the pixels locations. rBRIEF uses the patch orientation θ , to get the rotated version of S, S θ . Figure1 Show the rBRIEF performance comparing to SIFT, SURF and BRIEF.

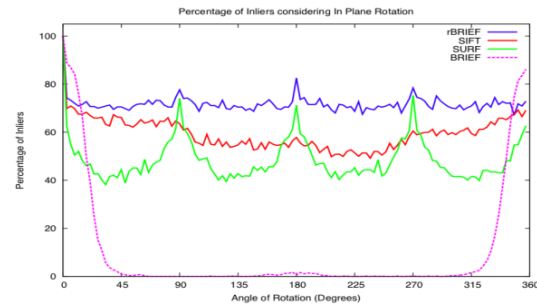


Figure 1 : rBRIEF performance compared to SIFT,SURF and BRIEF.

Figure 2 Show the ORB feature matching with Image and Rotated version of it.

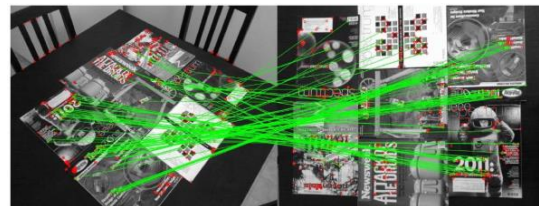


Figure 2: ORB Features matching with image and rotated version of it.

Figure 3 shows the proposed system flowchart firstly we extract features using ORB from the camera

video frame and the features of the object image then we used brute force knn matcher with $k=2$ to match two descriptors then calculate the distance between key points the lowest distance is the best. If good matches equal to or higher than the minimum points, the object will be recognized.

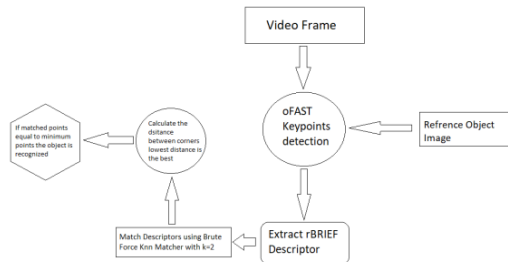


Figure 3: Proposed System Flow Chart.

III. RESULTS

We are tested our system using many objects in difference positions. Figure 4 show the matching results of object in any background. The proposed recognition system using a reference image of an object and detect its features then recognize the object in any scene or background. Figure 4 shows Konya stadium recognition using a template of it. The recognition can be done in any background. Firstly, the video frame is obtained from the camera in real-time and extract the features of the image using oriented FAST, and then we describe them using rBRIEF. In the matching process, we extract the key points and descriptor from the object reference image and using brute-force knn matcher with $k=2$ to get the better distances we perform filtering method on matches to get the matches with the lowest distance and check if the best matches equal or higher than the minimum.

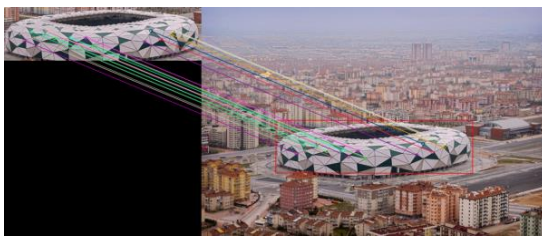


Figure 4 : Konya stadium Recognition using features from sample small image .

IV. CONCLUSION:

Object recognition systems are critical in wide of applications such as military, security, and surveillance. The existing systems face many challenges such as viewpoint variations, occlusion, illumination, scale, speed, and computation cost. In this research paper, we introduced an ORB-based system to recognize objects in a real-time with high performance and speed comparing to systems that based on SIFT and SURF methods.

REFERENCES

- [1] Lowe, David G. (1999). "Object recognition from local scale-invariant features" (PDF). *Proceedings of the International Conference on Computer Vision*. **2**. pp. 1150–1157. doi:10.1109/ICCV.1999.790410.
- [2] Beis, J.; Lowe, David G. (1997). "Shape indexing using approximate nearest-neighbour search in high-dimensional spaces" (PDF). *Conference on Computer Vision and Pattern Recognition, Puerto Rico: sn*. pp. 1000–1006. doi:10.1109/CVPR.1997.609451.
- [3] [U.S. Patent 6,711,293](#), "Method and apparatus for identifying scale invariant features in an image and use of same for locating an object in an image", David Lowe's patent for the SIFT algorithm, March 23, 2004.
- [4] [US 2009238460](#), Ryuji Funayama, Hiromichi Yanagihara, Luc Van Gool, Tinne Tuytelaars, Herbert Bay, "ROBUST INTEREST POINT DETECTOR AND DESCRIPTOR", published 2009-09-24.
- [5] Rublee, Ethan; Rabaud, Vincent; Konolige, Kurt; Bradski, Gary (2011). "ORB: an efficient alternative to SIFT or SURF". *IEEE International Conference on Computer Vision (ICCV)*.
- [6] E. Rosten and T. Drummond. Machine learning for highspeed corner detection. In European Conference on Computer Vision, volume 1, 2006. 1
- [7] E. Rosten, R. Porter, and T. Drummond. Faster and better: A machine learning approach to corner detection. *IEEE Trans. Pattern Analysis and Machine Intelligence*, 32:105– 119, 2010. 1
- [8] M. Calonder, V. Lepetit, C. Strecha, and P. Fua. Brief: Binary robust independent elementary features. In In European Conference on Computer Vision, 2010. 1, 2, 3, 5.
- [9] P. L. Rosin. Measuring corner properties. *Computer Vision and Image Understanding*, 73(2):291 – 307, 1999. 2.

Activation Functions in Single Hidden Layer Feed-forward Neural Networks

E.SEVİNÇ¹

¹ University of Turkish Aeronautical Association, Ankara/Turkey, esevinc@thk.edu.tr

Abstract – Especially in the last decade, Artificial Intelligence (AI) has gained increasing popularity as the neural networks represent incredibly exciting and powerful machine learning-based techniques that can solve many real-time problems. The learning capability of such systems is directly related with the evaluation methods used. In this study, the effectiveness of the calculation parameters in a Single-Hidden Layer Feedforward Neural Networks (SLFNs) will be examined. We will present how important the selection of an activation function is in the learning stage. A lot of work is developed and presented for SLFNs up to now. Our study use one of the most commonly known learning algorithms, which is Extreme Learning Machine (ELM). Main task of an activation function is to map the input value of a neural network to the output node with a high learning or achievement rate. However, determining the correct activation function is not as simple as thought. First we try to show the effect of the activation functions on different datasets and then we propose a method for selection process of it due to the characteristic of any dataset. The results show that this process is providing a remarkably better performance and learning rate in a sample neural network.

Keywords - Machine Learning, SLFN, ELM.

I. INTRODUCTION

NEURAL networks are widely used in many areas because of their powerful, fast and accurate learning capacities. Many new and different algorithms have been put forward and studies have been presented in Artificial Intelligence (AI). Additionally, many different types of machine learning methodologies are developing gradually. The purpose of our study is to present the role of activation function in a neural network. ELM is the one of the most popular learning methods used for such neural networks.

Despite many data and inputs available, AI mechanisms or smart systems are still lacking in powerful interpreter systems that can comment on these results. For example, in cancer detection cases, there might be a lot of data; however, there are still cases that you can encounter with false positives or true negatives. Generally it will not be so clear that which features you will use for better learning. Though there are lots of studies in this area, an optimization in this AI field seems to be valuable.

At this point, ELM capable of high and fast learning rate in neural networks can take part. The inputs and their selection methods are important; however related two topics come forward. The first one is the importance levels of the inputs.

Studies [2-5] can be examined on such a topic. This is so important that for example you might have 10 inputs for a case, and then if you select only third and fifth features of that dataset, learning rate might be more than the status which all features are involved.

The second topic is to get the *hidden neuron matrix* (\mathbf{H}) that is to evaluated due to the activation function. This matrix is required for mapping the inputs to the output nodes. After determining the weight matrix, an activation function is selected and all the values in that matrix are manipulated due to it. This means the learning capacity of the network is directly related with both weight matrix and the activation function.

Although the number of the hidden neurons is important for getting higher learning rates, activation function in SLFN has also a remarkable effect for achieving higher learning levels. We think that this work can be used for determining the activation function and can form a base for another work.

In this study, small and medium sized data sets from [1] will be used, and in order to get rid of the effect of hidden number of neurons on the experiments, a varying range of hidden neuron number will be used in the experiments. Thus within those ranges, the effect of different types of activation functions will be seen and observed at the same time.

In the 2nd part related works will be mentioned, in the 3rd section the activation functions and formulations will be discussed. Experimental studies will be presented in the 4th section and a method for determining the most appropriate one for any dataset will be proposed. Lastly, comments about future work and results will be discussed.

II. RELATED WORKS

Up to now, there are many examples of machine learning studies using ELM. The process starts with instantiating the links between the input and output layers. Initially, hidden neurons are randomly assigned; weight and biases are calculated due to inputs. Then this matrix is processed with the activation function, which is one of the important levels of the process. Then the output connections are set and found by reducing the cost function to a minimum through a linear system. Also mentioned in the related website [6], ELM is used for deriving learning methodologies in a similar way in many AI areas because of having low computational complexity, accurate results and being very fast. [2, 3, 5].

Especially effect of activation functions and saturation during training formulations are discussed in [7]. After making experiments with sigmoid, hyperbolic tangent functions and some other types, they declared that the logistic regression or conditional log-likelihood cost function worked better for any type of classification. It's also mentioned in the same study that classical neural networks with sigmoid or hyperbolic tangent functions, converge more slowly and apparently get stuck ultimately to a poorer local minima [7].

However, a new recurrent neural network with one-layer architecture and a discontinuous hard-limiting activation function for solving quadratic programming problems has been discussed in [8]. Study examining quadratic and nonlinear programming and SVM learning methods, puts forward the benefits of a recurrent neural network over a general one.

In the final study, a number of activation functions have been examined. It has been declared that most deep neural networks generally use non-periodic and monotonic activation functions. Neural networks with a single hidden layer using sinusoidal activation functions is declared to be used largely and by this, higher learning rates are more probable with the networks relying on the periodicity of the sinusoids [9].

Our study show and discuss all of the types of functions discussed in this part.

III. IMPLEMENTATION

A. Extreme Learning Machine (ELM)

The purpose of this study is to show the precise effect of hidden neurons in any neural network. We will also suggest a new method based on the nature of the data set to achieve a higher learning rate.

The problem solving technique here proposes a learning methodology for Single-hidden Layer Feedforward Neural network (SLFN)s. We will use a learning algorithm called *ELM* whose learning speed is much faster than traditional feedforward network learning algorithms like back-propagation (BP). For detailed information, studies [2-5] can be examined. However, for better understanding ELM will be explained briefly.

The output of SLFN having L number of hidden nodes is represented in (1) below;

$$f_L(x) = \sum_{i=1}^L \beta_i G(a_i, b_i, x), \quad x \in \mathbf{R}^n, a_i \in \mathbf{R}^n, \quad (1)$$

where a_i and b_i are learning parameters of hidden nodes and β_i is the weight connecting the i^{th} hidden node to the output node. $G(a_i, b_i, x)$ is the output of the i^{th} hidden node with respect to the input \mathbf{x} .

Given a standard SLFN with L hidden nodes and activation function $g: \mathbf{R} \rightarrow \mathbf{R}$ which is infinitely differentiable in any interval and the hidden layer output matrix \mathbf{H} of the SLFN is invertible and defined as in (2);

$$\mathbf{H}\beta = \mathbf{T} \quad (2)$$

\mathbf{H} is the output of hidden layer matrix of the neural network. The i^{th} column of \mathbf{H} is the i^{th} hidden node's output vector with respect to inputs x_1, x_2, \dots, x_N and the j^{th} row of \mathbf{H} is the output vector of the hidden layer with respect to input x_j . \mathbf{T} is the training error matrix in (2) and the smallest training error can be reached by this solution: i.e, $\min \|\beta\|$ and $\min \|\mathbf{H}\beta - \mathbf{T}\|$ a simple representation of the solution of the system in (2). This is also the target of the whole network and explained in detail in [2, 3].

B. Activation functions

In SLFNs, hidden neurons are modeled using an *activation function* for output. This function is important to implement and help to understand functional mapping between input and output nodes in a SLFN. By applying properties of the activation function to the neural network, the input signal is transformed to the output counterpart. For estimating the role of an activation function in a neural network, a sample illustration has been depicted in Figure 1.

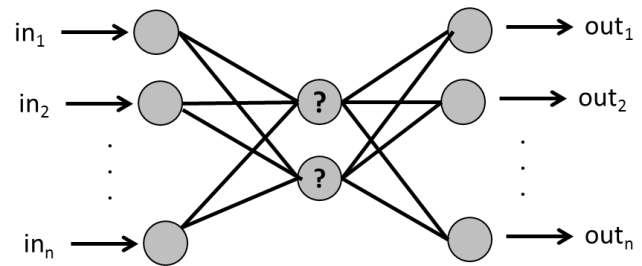


Figure 1: Role of activation function in a neural network

4 different types of activation function will be discussed in this study;

1) Sigmoid Function

Sigmoid is a non-linear, monotonic and S-shaped activation function that produces an output value in the range (0, 1). In this context, sigmoidal function is a special form of logistic function and is defined in (3);

$$\text{sig}(x) = \frac{1}{1 + e^{-x}} \quad (3)$$

A sigmoid function is a bounded differentiable real function that is defined for all real input values and has a positive derivative at each point. Sigmoid functions are known to be one of the most commonly used and major hidden layer output functions used in a neural network.

A wide variety of sigmoid functions have been used as the activation function of artificial neurons, including the logistic and hyperbolic tangent functions.

2) Tanh(hyperbolic tangent) Function

Tanh has a similar characteristic to that of sigmoid. It is nonlinear function and has a bound to range (-1, 1). Deciding between the sigmoid or *tanh* will depend on the requirement of gradient strength and is defined in (4);

$$\tanh(x) = \frac{e^x - e^{-x}}{e^x + e^{-x}} \quad (4)$$

Like sigmoid, *tanh* also has the vanishing gradient problem. This problem originates from multiplying many small numbers to compute gradients of the “front” layers in a neural network, ending in the gradient decreases exponentially. Since gradient is so small, computation is calculated down to limits of floating point data types and the system cannot learn any further or drastically degrade.

3) Sine Function

Sine is one of the commonly used nonlinear functions and has a bound to range (-1, 1). It is a periodic function and has rises and falls. However, the function saturated and its output converges to zero for large positive and negative inputs. These sinusoids are commonly defined as a generalized Fourier decomposition and have the potential to converge to a local minimum in their approximation capacity.

4) Hardlim Function

The hard limit transfer function forces a neuron to output a “1” if its net input reaches a threshold, otherwise it outputs “0”. This allows a neuron to make a decision or classification. It can say yes or no finally and is defined in (6);

$$\text{hardlim}(x) = \begin{cases} 1 & \text{if } x \geq 0 \\ 0 & \text{otherwise} \end{cases} \quad (6)$$

Hardlim is a neural transfer function that calculates a layer’s output from its net input.

IV. EXPERIMENTAL RESULTS

All experiments are done on a computer having 64-bit Windows 7 operating system, i5 4200u 1.6 Ghz. processor and 8 GB. RAM. Datasets are taken from UCI web page [1] which is commonly used and referenced in this field. An ascending order of datasets is presented due to the number of features and the instances in Table 1. Datasets will be referred with their IDs as shown from now on.

For each test, 10-fold cross validation method has been used for avoiding the effect of chance. This method, as mentioned in [10], whole data set is equally divided into defined fold number, i.e. 10 for our case. Then among 10 equal parts, the first 9 pieces are used for learning and the final part is used for testing. In this way all parts are subjected to the same process by turning one by one. Thus, all sub parts are rotated 10 times in the same way, i.e. 9 for learning 1 for testing, and then the averages of all runs are taken and the results are calculated.

Table 1: Used Datasets and Characteristics.

Dataset	ID	# instances	# features	# output
Iris	IRI	150	4	3
Monk1	MK1	432	7	2
Monk2	MK2	432	7	2
Monk3	MK3	432	7	2
Ionosphere	ION	351	34	2
WDBC	WDB	569	32	2
Pima Indian Dia.	PID	768	8	2
Wis.Bre.Cancer(Org)	WIS	699	10	2
Waveform	WAV	569	21	3
Spambase	SPM	4601	57	2

The test results are shown in Figure 2. All 10 datasets in Table 1 are put together and one whole figure is created. Each dataset has its own ID name on top of itself. Horizontal scale shows number of hidden neurons changing form 10% to 200%. This percentage is obtained by dividing the used number of hidden neurons to the number of instances in the dataset. Vertical scale shows the accuracy level achieved. It is between (0.0 - 1.0) as in (7).

$$\text{Accuracy} = \frac{\# \text{ truly_known_instances}}{\# \text{ all_instances}} \quad (7)$$

Figure 2 shows the learning rate of activation functions with respect to datasets. In the experiments the number of hidden neurons is also changing and inevitably has an effect on the learning rate of the system. In order to get rid of those effects, commonly used ranges are assigned and experiments are done due to these ranges, varying from 10% to 200% of the instance number of the dataset. All 10 datasets in Table 1 are included in Figure 2, and each dataset are applied with same hidden number of neurons and the same activation functions. Consequently, we will take the sample mean of all results and be able to see the real, purified effect of the activation function on the learning rate.

If we examine Figure 2, activation functions using sigmoid and sinusoid seem to be more successful for predicting the output. Another point to take attention is that the values tend to come closer after 40%-50%’s of horizontal scale, which means deviation gets smaller. Because the more hidden number of neurons you put in H matrix, the more accuracy you get.

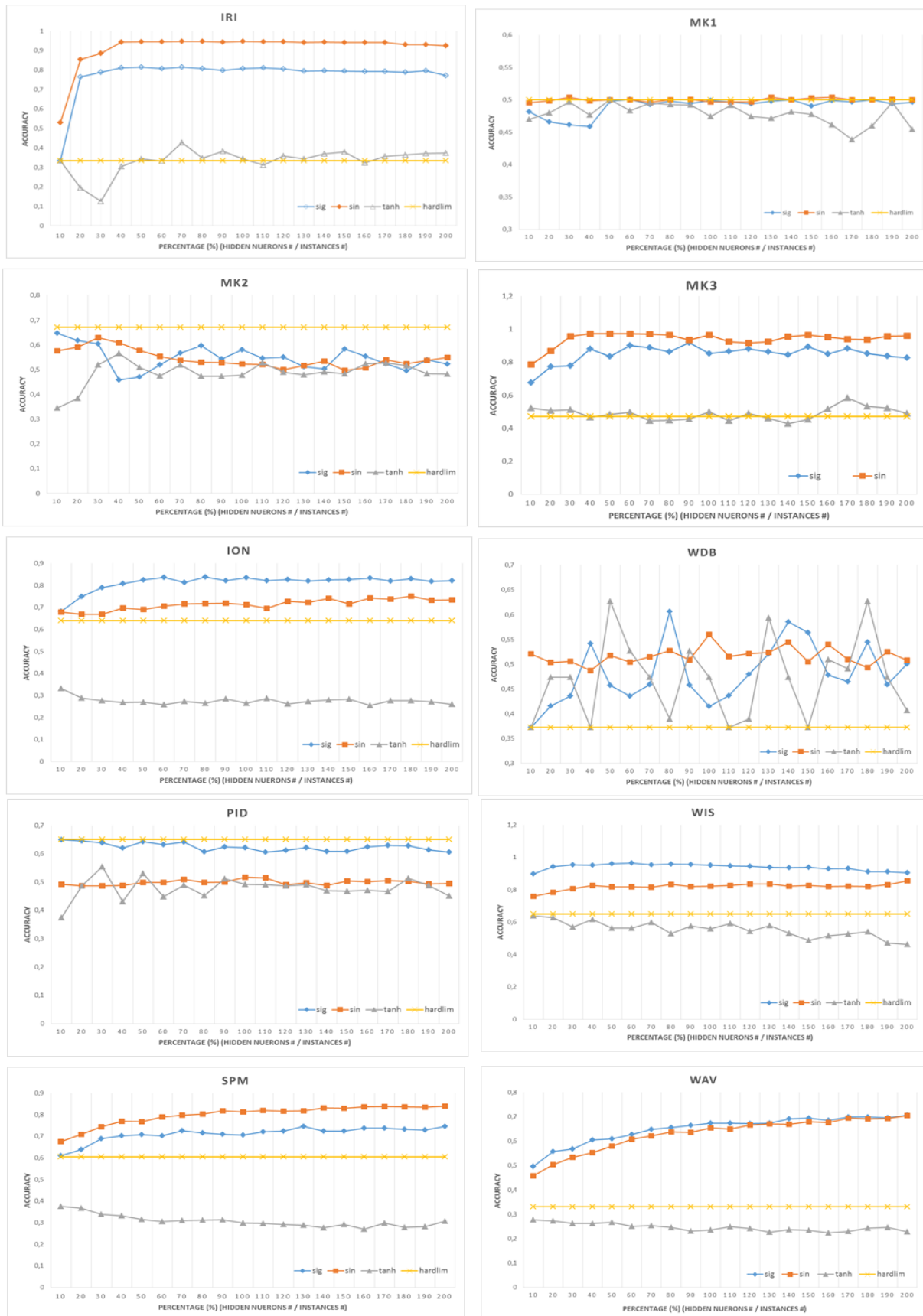


Figure 2: Results of activation functions with changing hidden neurons due to datasets.

As a result, this effect caused a variance of the distribution of the sample mean, and it can be clearly observed that values between 10% and 50% have more deviance and cause more error. Because of that, values greater than 60% will be taken into consideration and added to calculations to get the average. After taking the average of the values in Figure 2 as stated, we will get Figure 3. Here we can see the performance results of activation functions due to the datasets.

For example in Figure 3, WIS dataset shows the average of values of 4 activation functions of WIS dataset that are changing between 60% and 200% stated in Figure 2. Also we can observe which activation function has the most learning rate separately for that and the other datasets together.

If to talk about execution times of activation functions, they are almost close to each other, changing from 0.5 sec to 30 sec. In fact, the fundamental difference for execution times is originating from the size of dataset. The smaller dataset used, the shorter time to execute. It can be inferred that the effect of activation function is negligible for the execution times.

Now we can propose a method for the data used in the experiments. If we examine Figure 3, sigmoid activation function proves to be the most successful among others. Because many natural processes, such as those of complex system learning curves, exhibit a progression from small beginnings that accelerates and approaches a climax over time and a sigmoid function most probably best suits for such a case. Thus a mapping process of a sigmoid function might be most successful on such conventions.

Likewise when a detailed description or information is lacking, sigmoid function can often be used and is acceptable among others. [11]

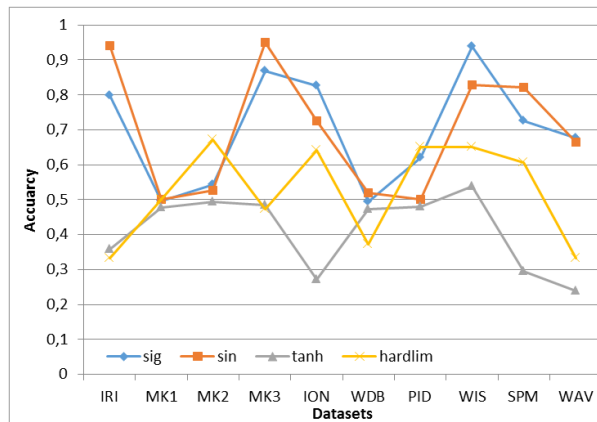


Figure 3: Dataset Performance due to Activation Functions.

On the other hand, *Sine* function has a similar learning capacity which is very close to that of sigmoid. This is mainly because of having the same origins. They are both non-linear, monotonic and have similar ranges for negative and positive infinity values.

Additionally back propagation relies on the use of a differentiable activation function and commonly use sigmoid. However, replacing it with another differentiable function such as sine does not affect the convergence so much and thus we

get similar results for these two functions.

Tanh function turns out that the logistic sigmoid that might “stuck” to a minimum during training. This is partially due to the fact that if a strongly-negative input is provided to the logistic sigmoid, it outputs values very close to zero that degrades learning. Because of that, *tanh* function has the worst performance among the others.

Hard limit (*hardlim*) transfer function forces a neuron to output a 1 if its net input reaches a threshold, otherwise it outputs 0. This allows a rough calculation for the output and lower performance is observed.

As seen in Table 2, general averages of 4 types of activation functions are given due to average performance value of accuracy levels of all datasets. The highest one is sigmoid and sinusoid functions respectively.

Table 2: General Performance of Activation Functions

Function Name	Learning Rate (%)
Sigmoid	69,86
Sine	69,75
Tanh	41,11
Hardlim	52,29

Table 2 shows the learning capabilities of the activation functions that form the goal of this study. Besides that, as the dataset sizes increase in terms of instances and feature numbers, sigmoid function seems to achieve better learning rates as seen in Figure 3. This result is also similar for sine function since they are similar. Consequently the most appropriate activation function for our study is either sigmoid or a sine function as seen in Table 2.

Finally, our method to propose is that if you don't have enough information about the characteristic of our data you can use sigmoid as activation function without any problem. If you have idea, for example if it is medium-sized or a huge dataset, you can prefer non-linear, monotonic and a derivative function that can smooth gradient of the data which is an important parameter.

V.CONCLUSION

In this study, we examined the effects of activation functions in a neural network. However, *sigmoid* function which is also called as standard logistic function is still very popular in classification problems and can be used on any occasion. On the other hand *sine* function is also acceptable.

One of the most probable future works might be to examine the effect of hidden neurons in neural networks. It is also observed in our experiments that any changes in this number might have a remarkable effect on the learning capacity of the system. An optimized point on this topic might be a promising future work.

REFERENCES

- [1] UCI Irvine Machine Learning Repository, Available: <http://archive.ics.uci.edu/ml/datasets.html>
- [2] Huang GB, Zhu QY, Siew CK, "Extreme learning machine, Theory and applications" *Neurocomputing* 70: 489-501, 2006.
- [3] Huang GB, Ding X, Zhou H, "Optimization method based extreme learning machine for classification" *Neurocomputing* 74: 155-163, 2010.
- [4] Feng G, Qian Z, Zhang X, "Evolutionary selection extreme learning machine optimization for regression" *Soft Computing* 16:1485-1491, 2012.
- [5] Huang GB, Zhou H, Ding X, "Extreme learning machine for regression and multiclass classification" *IEEE Transactions on Systems, Man, and Cybernetics, Part B (Cybernetics)* 42: 513-529, 2012.
- [6] ELM Classification web page, Available: http://www.ntu.edu.sg/home/egbhuang/elm_random_hidden_nodes.html
- [7] X. Glorot and Y. Bengio, "Understanding the difficulty of training deep feedforward neural networks", *Proceedings of the 13th International Conference on Artificial Intelligence and Statistics*, 2010.
- [8] Q. Liu and J. Wang, "A One-Layer Recurrent Neural Network With a Discontinuous Hard-Limiting Activation Function for Quadratic Programming" *IEEE Transactions On Neural Networks*, Vol. 19, No. 4, April 2008
- [9] G. Parascandolo, H. Huttunen, T. Virtanen, "Taming the Waves: Sine as activation function in deep neural networks", *ICLR 2017 conference submission*, 2017.
- [10] R.Kohavi. "A Study of Cross-Validation and Bootstrap for Accuracy Estimation and Model Selection", *Conference , International Joint Conference on Artificial Intelligence (IJCAI)*, 1995
- [11] Gibbs, M.N., "Variational Gaussian process classifiers". *IEEE Transactions on Neural Networks*. 11 (6): 1458-1464. (Nov 2000).

Temporal Extensions to RDF

Di Wu¹ and Abdullah Uz Tansel^{2,*}

¹ Department of Computer Science, Graduate Center, CUNY, USA

² Pattaya Campus, Thammasat University, Thailand

Abstract - The Semantic Web is based on Resource Description Framework (RDF) which is widely used in practice. RDF represents information by only binary predicates. This simple representation scheme is the basis of an elaborate layers of methodologies, called Semantic Web Layer Cake. Though simple, it is very powerful for modeling data and basic knowledge. However, it is very limited in representing their temporal variation. Reification is the method proposed in RDF for modeling temporal changes in data and knowledge. Moreover, reification is cumbersome since it requires at least four more triples to represent just one temporal fact. By their very nature, RDF repositories are large in general and reification causes them to explode in size. In this paper, we review Semantic Web techniques that are proposed for representing temporal data in RDF.

Keywords – Semantic Web, Temporal Data, Temporal Knowledge.

I. INTRODUCTION

THE “Semantic Web”, introduced by Tim Berners-Lee et al. in their 2001 article, is defined as “an extension of the current one [WWW], in which information is given well-defined meaning, better enabling computers and people to work in cooperation” [1]. Along with the wide spread expansion of Internet, Semantic Web is adopted by major search engines, governments, and big companies.

The Semantic Web has been proposed two decades ago; and its methodologies such as Resource Description Framework (RDF) being implemented in many domains, albeit slowly. Semantic Web allows sharing data and knowledge that are dispersed on servers connected via Internet not only by human users but also by computers. It enriches the web pages by semantic information that can be automatically processed by computers. The semantic information in RDF is represented by only binary predicates, i.e., triples in the form of (subject, predicate, object). This simple representation scheme is the basis of an elaborate layers of methodologies, called Semantic Web Layer Cake, to include more semantics that allow inferencing of new triples from the given ones. Though this simple representation is very powerful for modeling data and basic knowledge, it is very limited in representing their temporal variation. Reification is the method proposed in RDF for modeling temporal changes in data and knowledge. However, reification is cumbersome since it requires at least four more triples to represent just one temporal fact. By their very nature RDF repositories are large in general and reification causes them to explode in size. In this paper, we review various representative Semantic Web techniques that are proposed for representing temporal data in RDF, in an effort to lay the

foundation for developing a better solution for representing temporal knowledge in RDF.

The Semantic Web Layer Cake introduces conceptual structures and richness for enhanced semantic. The stack of conceptual tools in the Semantic Web Layer Cake are downward compatible. The bottom layer, Universal Resource Identifier (URI), provides a unique Id for every subject, object, and relationship thus makes linkage and integration among different knowledge bases possible [1]. Extensible Markup Language (XML) and XML Schema provide a standard for writing structured web documents with a user-defined vocabulary. RDF is a basic data model that includes a set of statements which are triples. RDF Schema (RDFS) is based on RDF, but provides modeling primitives for building hierarchy of objects. On top of RDF and RDFS, ontology vocabularies add more power for representing more complex relationships among objects. Web Ontology Language (OWL) is a logic-based language which allows more inferencing, so machine agents are able to exploit knowledge expressed in OWL. OWL 2 as the most current version includes structures as classes, properties, individuals, and data values. RDF/XML is the only mandatory syntax for RDF, RDFS, and OWL 2. Other notations are proposed for ease of use, such as OWL/XML, Functional Syntax, Manchester Syntax, and Turtle, etc. [8, 12]. The upper layer of Semantic Web Layer Cake, includes logic and proof, to derive information from the knowledge base represented by the bottom layers.

A temporal database has temporal data, and is able to deal with insertion, deletion, and query of temporal data. There are two major types of time: valid time and transaction time. Valid Time is a time period during which the data is true (valid) in the real world. Transaction Time is a time period during which the data is recorded in the database. Bitemporal Time covers both valid and transaction time. Based on the type of time support, temporal databases have three forms: historical databases that support only valid time, rollback databases that support only transaction time, and bitemporal databases that support both. Naturally, previous research in temporal databases provides a solid basis for adding temporality to Semantic Web.

RDF triples are statements without temporal attributes; and they are assumed to be true at present. However, many applications need temporal knowledge and data. To build a temporal extension for the Semantic Web, researchers proposed extending RDF with a temporal component. There are various proposals that extend RDF to express temporal knowledge. In this study, we review the major extensions to RDF to handle temporal knowledge. It is not comprehensive, however, we believe it is a satisfactory examination of the

*On leave from Department of Information Systems and Statistics, Baruch College and the Graduate Center, CUNY, USA

literature that would provide the reader sufficient background to understand temporal aspects of Semantic Web.

In the remaining of this paper, we first briefly explain the basic RDF model. Then we examine the proposals that add time dimension to RDF in detail. We summaries these proposals with a taxonomy that classifies these proposals to provide further insight into representing temporal knowledge.

II. RDF

RDF is a framework for expressing information about resources, which include documents, people, physical objects, and abstract concepts. RDF is designed for applications to process information that are included in the webpages by providing a common framework by which applications can exchange information without loss of meaning. The subject and object in an RDF triple represent two resources and the predicate represents the relationship between the subject and the object. This relationship is directional from the subject to the object, and is also called an RDF property. RDF triples can be represented as a directional graph that has nodes for subjects and objects and directed edges for predicates. These three elements in a triple can be Internationalized Resource Identifier (IRI), blank nodes, and literals.

An IRI is a Unicode string that can be used instead of Universal Resource Identifier (URI) to identify resources [4, 5]. For example, an IRI “http://example.com” denotes a website; “http://example.com/data” denotes a subcategory of the website; and “http://example.com/data/list.html” denotes a particular web page. IRIs have global scope and IRIs are absolute and may additionally have a fragment identifier (#). Two IRIs are equivalent only when they are equivalent strings. Thus, two IRIs may be not equivalent but refer to the same resource. For simplicity, namespaces are introduced to the syntax to represent repeated portion of the IRIs. In this paper, we use namespace “ex:” for “http://example.com/” and another useful namespace “rdf:” as “http://www.w3.org/1999/02/22-rdf-syntax-ns#”.

A blank node represents any resource that does not have an IRI but has meanings in triples if represents existential quantification. For example, if “a person has something to do”, although we cannot express that “something” with an IRI, but we can use a blank node as a place holder. Blank nodes have some unique characteristics: 1) Blank nodes have local scope and cannot be externally referenced; 2) Blank nodes are used to represent some resources that do not need or cannot be assigned with IRIs, i.e. existential quantifications; 3) Blank nodes have blank node identifiers that are local. In RDF, literals can appear only as object and predicate can only be an IRI [3, 12].

Consider the RDF triple:

ex:William ex:livesIn ex:NYC .

The subject is the IRI referring to a person “William”, and predicate is the IRI that refers to a relation “livesIn”, and the object is the IRI that refers to a city, NYC. This simple triple is represented in an RDF graph as below:

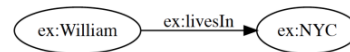


Figure 1: An Example RDF Triple

Note that this triple simply represents a true binary predicate: “William lives in NYC”, livesIn(William, NYC). There is no temporal information at all. We don’t have information about when this statement is recorded, nor when the statement becomes valid and expired. It is usually assumed to represent current (present) knowledge.

III. TEMPORAL EXTENSIONS TO RDF

A. Reification

Reification is a logic construct and is W3C working group recommendation [8, 12]. The RDF vocabulary, rdf:Statement, rdf:subject, rdf:predicate, and rdf:object, are used for reification purpose.

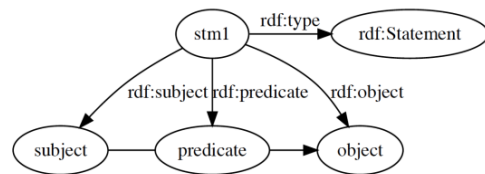


Figure 2: RDF Reification.

For example, In order to introduce the temporal information, that the triple ⟨ex:William, ex:livesIn, ex:NYC⟩ is valid in 2004, we need to create a blank node “_:x” representing a statement and 4 additional triples will be created to express the additional temporal information.

```
_:x rdf:type rdf:Statement .
_:x rdf:subject ex:William .
_:x rdf:predicate ex:livesIn .
_:x rdf:object ex:NYC .
_:x ex:isValid 2004 .
```

If there is another statement, “William lives in Boston in 2018”, using Reification approach, another blank node “_:y” and additional triples have to be created as well. Although “William” in “_:x” is the same “William” in “_:y”, we still have to create two separate triples. We can see from this example that Reification has a significant data redundancy problem. Not only we need to use four triples to express one temporal fact, but also the four triples are hard to be reused. Furthermore, if we need to express a bitemporal information, a second layer of reification has to be introduced and many more triples have to be added.

B. Temporal RDF

Gutierrez et al. propose “temporal RDF” to add temporal information into standard RDF [6]. Temporal RDF adopts the labeling solution to handle evolving RDF data. The definition of Temporal RDF starts with a Temporal Triple: $(s, p, o): [t]$, where (s, p, o) is an RDF triple, and t is the temporal label. In this definition, t is a natural number that represents a time point. To represent a time interval, the temporal triple is expressed as $(s, p, o): [t_1, t_2]$ as the union of all $(s, p, o): [t]$ where $t_1 \leq t \leq t_2$. A Temporal Graph is a set of Temporal Triples. This definition has several advantages: 1) It avoids

the complex format of time. A natural number is used to represent a time point, which is very simple and straightforward; 2) It integrates point-based and interval-based temporal information; 3) It combines an existing RDF triple with a temporal label so that modification is minimized; 4) The temporal label can be further extended for not only valid time, but also transaction time, even bitemporal time; 5) It is entirely within the standard definition of RDF.

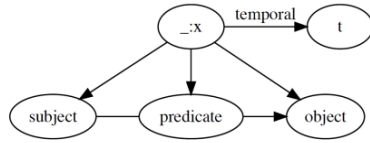


Figure 3: temporal RDF

Gutierrez et al. further extend the temporal RDF model to include implicit temporal labels (anonymous time) [7]. In their original paper, a temporal label t associates with either a time point which is a natural number, or a time interval that composed by two time points [6]. The advantages of having anonymous time are: 1) In the case that triples lack precise temporal information, anonymous time can specify them naturally. With anonymous time, RDF triples can easily be converted to a temporal graph. 2) Anonymous time itself has many uses. For example, a triple A occurs at time t_1 , and another triple B occurs at the same time as A does. Although we don't know the explicit time point of the "same time" that triple B occurs at, we can infer by both triples A and B that the "same time" is actually t_1 .

C. Named Graph

The named graph approach is developed by Carroll et al. [2] and Tappolet and Bernstein [13]. Carroll et al. define a named graph as an RDF graph with a URIref. Let U be URIs, B be Blank Nodes, L be Literals, then all nodes in an RDF graph are $V = U \cup B \cup L$. The set $T = V \times U \times V$ is the set of all RDF triples (or an RDF graph). The set of all RDF graphs G is the power set of T . A named graph ng is a pair (n, g) with $n \in U$ and $g \in G$ [2].

Named graph is adopted by W3C Recommendations in the RDF dataset definition as a standard RDF feature: The dataset is a default RDF graph (with no name) and some (zero or more) named graphs may also be included. Or more formally: An RDF dataset is a set of $\{G, (u_1, G_1), (u_2, G_2), \dots, (u_n, G_n)\}$ where G is the default graph, and (u_i, G_i) are named graphs where u_i s are URIref and G_i s are graphs. Each u_i is distinct [3].

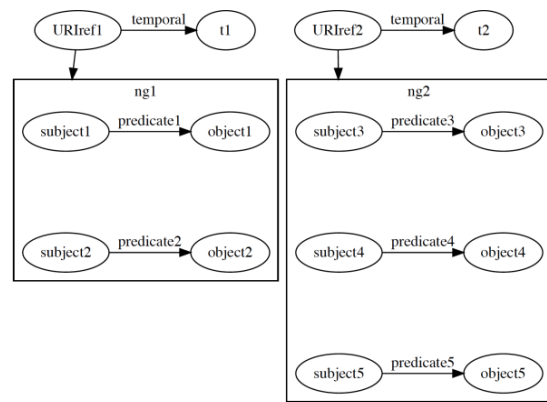


Figure 4: Named Graph

Tappolet and Bernstein adopt the named graph approach for adding temporal interval into RDF triples [13]. Because named graph is adopted as part of the RDF dataset definition, the difficulty of using this approach for adding temporal information is minimal. Since each named graph ng has a name which is a URIref and has a set of triples, the temporal information t can be attached to the URIref so that all the triples of that named graph share the same temporal information t .

D. 4D Fluents

McCarthy and Hayes define a fluent as a function that maps from objects and situations to truth [9]. Thus, fluents are relations that hold within some time interval and not in others. Welty and Fikes further develop the 4D Fluents approach to describe information changes over time [15]. The basic problem is how to logically account for the fact that "same" entity appears to be "different" at different times. 3D view distincts endurants that are wholly present at all times and perdurants that have temporal parts that only exist during the time the entities exist. 4D view (also called perdurantist view) maintains that all entities are perdurants. Thus, all entities have temporal parts and can be thought of intuitively as four dimensional.

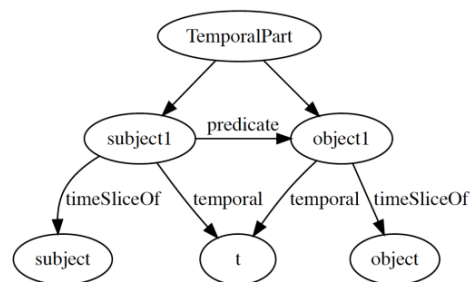


Figure 5: 4D Fluents

One consequence of a 4D approach is that time is "bundled in" with the temporal parts themselves and binary fluents can be represented as a simple binary relations between them. The time interval of a temporal part is defined to be the duration when a fluent holds. A single fluent in the 4D approach requires two extra objects, a temporal part and additional six triples, which is more than needed in reification. The most significant aspect of 4D Fluents approach is that it benefits the

defined capabilities of OWL, such as transitive, inversive etc.

E. RDF*

RDF* differs from RDF by allowing a triple in place of subject and object resources in a triple: such triples are called RDF* triples. Thus, the definition of an RDF* triple allows nesting: an RDF* triple may have another RDF* triple as its subject or object. The depth of the nesting is denoted as k . Thus, if $k = 0$, the triple is an ordinary RDF triple; and if $k > 0$, it is a nested RDF* triple.



Figure 6: RDF*

Since the definition of RDF* allows nesting, the unfolding process is defined recursively: If the unfolded RDF graph contains RDF* triples, then the transformation process will continue until all triples are ordinary RDF triples. Turtle* is provided by adding three additional terms: tripleX for an RDF* triple, subjectX and objectX for referring the subject and object of a tripleX. Also, the standard Turtle grammar is updated to include the definition of subject and object in tripleX. SPARQL* is also developed as a metadata extension of SPARQL. This extension enables querying for RDF* graphs. The specification of SPARQL* grammar has an embedded triple pattern as a new syntax element.

F. Singleton Property

Nguyen et al. [10] make a general extension to RDF by introducing singleton property. Temporality is one special kind of singleton property in this approach. The singleton property is based on the notion that “the nature of every relationship is universally unique”. A triple in RDF is considered as a relation that connects two entities. In every context, the relation is unique. There may be many relations between two entities, such as time, location, source, certainly, etc. The authors give examples to show how generic properties together with their sub-properties that represent different types of information about statements. For example, “isMarriedTo” relationship is considered as a generic property. All relevant information about “isMarriedTo” relationship is represented as its sub-properties. If there are two triples that have same “isMarriedTo” relationship between the same entities, then two sub-properties will be created, and each corresponding to its unique source. If there is temporal information, then it will be attached to the singleton property that represents the temporal relationship [10].

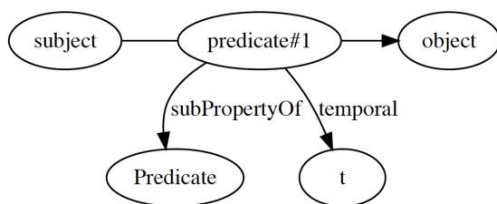


Figure 7: Singleton Property

Thus, by definition, for a triple (s, p, o) , p is a generic

property, and p has multiple sub-properties as singleton property, $p\#i$. Consequently, the relationship that connects s and o , is not p , but $p\#i$ and it defines a unique context. Each $p\#i$ defines multiple relationships for instantiating different values for i . It is important to keep the singleton property unique to avoid inconsistencies. Universally Unique Identifier (UUID) can be used to address this problem. UUID is supported by SPARQL and programming languages.

There are two types of queries: for data and for metadata that includes singleton properties. Querying for data basically follows standard RDF notation whereas querying metadata needs to include multiple triples in the query pattern. Nguyen et al. compare and evaluate five approaches: the Singleton Property, standard RDF reification, and three flavors of Provenance Context Entity (PaCE) in an experiment. In the comparison, three factors are considered: number of triples, query length, and time for query execution. The result shows the Singleton Property approach has better performance [10].

G. N-ary Relations

N-ary Relations approach addresses three major issues in RDF/OWL binary representation of relationships. Since a binary relation can only relate two individuals, then there are three issues that need to be addressed: 1) How to describe the relation itself; 2) How to relate more than two individuals; and 3) How to state the linked individuals are ordered. The sample scenarios for each problem are: 1) A patient with a disease and its probability; 2) A transaction that has buyer, seller, price, purpose, etc.; and 3) A flight that has multiple ordered airports on its route. The proposed solutions as n-ary relations for the three use cases are: 1) Introduce a new class of the particular relation, add the disease and probability as property of that class, then use an instance of that relation class to replace the old relation; 2) Introduce a new class of the product that has all other individuals as properties; 3) Use a list of arguments in a relation and use constraint on cardinality for arguments to represent city-on-the-road and destination [11].

Noy et al. distinguish n-ary relations and reification in RDF [11]. The most significant difference between these two is: reification focuses on the statement which has 3 parts (s, p, o) ; while n-ary relations focuses on the property, which is one part of the statement.

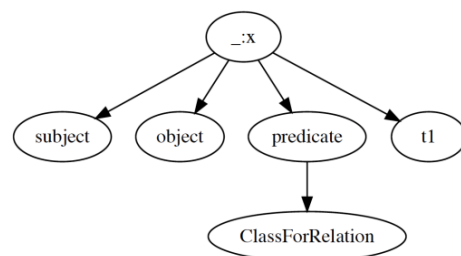


Figure 8: N-ary Relations

H. Annotated RDF

Udrea et al. develop the Annotated RDF (aRDF) as a generic extension to the standard RDF model. This approach uses aRDF as a single uniform framework to support various

extensions, such as uncertainty, pedigree, time, etc. [14]

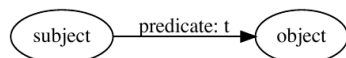


Figure 9: Annotated RDF

Annotated RDF, short for aRDF, has two parts. The first part is an ordinary RDF triple, (s, p, o) ; and second part is an annotation a from a partially ordered set A . An annotated RDF triple thus, is in the form of $(s, p:a, o)$. For a temporal extension, A can be a set of non-negative integers representing time instants. A can also be a pair of ordered integers x, y as time intervals [14]. In addition, the annotation is attached to the predicate p , not the entire triple (s, p, o) . Also, aRDF is similar to temporal RDF. In fact, we can consider temporal RDF as a variation of aRDF. However, temporal RDF uses arbitrary labeling t on ordinary RDF triples as $(s, p, o)[t]$ while aRDF uses annotations from a partially ordered set on predicates as $(s, p:a, o)$.

IV. TAXONOMY OF TEMPORAL EXTENSIONS TO RDF

We examine various approaches that extend standard RDF for temporal information. Since all of them extend the standard RDF model and they are developed with the goal of minimizing the needed modifications they have common aspects and also differences. These approaches convert one or more element of the triples into a meta resource to carry extra information. Depending on the element converted, we can categorize these approaches: graph, triple, or element level.

Graph level As an RDF dataset contains one or more RDF graphs, named graph approach uses the URIref of the named graph to carry temporal information. A named graph attaches the same time reference on all of its triples.

Triple level Triple level extensions treat an RDF triple as metadata and convert the triple into a resource to carry temporal information. Reification explicitly convert an RDF triple to a statement; and temporal RDF implicitly attach a temporal label to an RDF triple.

Element level 4D fluents converts the subject and object in a triple to be a timeslice of a fluent object to carry temporal information. Singleton Property converts the predicate in a triple and defines a unique sub-property that only exists in a temporal context. N-ary Relations creates a new class for the relation to carry temporal information. Annotated RDF attaches a partially ordered annotation to an RDF triple, and in terms of its syntax, the annotation is attached to the predicate. RDF* allows the subject and object in a triple to be metadata to form nested triples.

V. CONCLUSION

Standard RDF model is built upon the simple (s, p, o) triple structure and thus is limited in expressing only binary relationships. Along with the need to embed temporal information to standard RDF, scholars have developed various approaches. We examine these temporal extensions to RDF; and categorize them into three groups depends on how they extend the standard RDF model. Graph level extensions have Named Graph; Triple level extensions have Reification and temporal RDF; Element level includes 4D fluent,

Singleton Property, Annotated RDF, RDF* and N-ary Relations approaches. Naturally, each extension has performance differences in space and computation time. A detailed performance comparison of these extensions would be a beneficial study. We plan to explore this direction and also search for a better approach for handling temporal knowledge.

ACKNOWLEDGMENT

The research of second author is partially supported by the PSC CUNY Award, 60342-00-48.

REFERENCES

- [1] Tim Berners-Lee, Ora Lassila, and James Hendler. The semantic web. *Scientific American Magazine*, pages 29–37, May 2001.
- [2] Jeremy J. Carroll, Christian Bizer, Pat Hayes, and Patrick Stickler. Named graphs. *Web Semant.*, 3(4):247–267, December 2005.
- [3] Richard Cyganiak, David Wood, and Markus Lanthaler. Rdf 1.1 concepts and abstract syntax. W3C Recommendation, Feb 2014.
- [4] M. Duerst and M. Suignard. Internationalized resource identifiers (iris). <https://tools.ietf.org/html/rfc3987>. Accessed: 2018-06-16.
- [5] M. Dürst and M. Suignard. Internationalized resource identifiers (iris). RFC, page 832–843, 2005.
- [6] Claudio Gutierrez, Carlos A. Hurtado, and Alejandro Vaisman. Temporal RDF. In *Proceedings of Second European Semantic Web Conference*, pages 93–107, 2005.
- [7] Claudio Gutierrez, Carlos A. Hurtado, and Alejandro Vaisman. Introducing Time into RDF. *IEEE Trans. on Knowledge and Data Engineering*, 19:207–218, February 2007.
- [8] Frank Manola and Eric Miller. Rdf 1.0 primer. W3C Recommendation, 2004.
- [9] John McCarthy and Patrick J. Hayes. Some philosophical problems from the standpoint of artificial intelligence. In B. Meltzer and D. Michie, editors, *Machine Intelligence 4*, pages 463–502. Edinburgh University Press, 1969. reprinted in McC90.
- [10] Vinh Nguyen, Olivier Bodenreider, and Amit Sheth. Don't like rdf reification?: Making statements about statements using singleton property. In *Proceedings of the 23rd International Conference on World Wide Web, WWW '14*, pages 759–770, New York, NY, USA, 2014. ACM.
- [11] Natasha Noy, Alan Rector, Pat Hayes, and Chris Welty. Defining N-ary relations on the semantic web. W3C Working Group Note, 12:4, 2006.
- [12] Guus Schreiber and Yves Raimond. Rdf 1.1 primer. W3C Working Group Note, 2014.
- [13] Jonas Tappolet and Abraham Bernstein. Applied temporal rdf: Efficient temporal querying of rdf data with sparql. In Lora Aroyo, Paolo Traverso, Fabio Ciravegna, Philipp Cimiano, Tom Heath, Eero Hyvönen, Riichiro Mizoguchi, Eyal Oren, Marta Sabou, and Elena Simperl, editors, *The Semantic Web: Research and Applications*, pages 308–322, Berlin, Heidelberg, 2009. Springer Berlin Heidelberg.
- [14] Octavian Udrea, Diego Reforgiato Recupero, and V. S. Subrahmanian. Annotated rdf. *ACM Trans. Comput. Logic*, 11(2):10:1–10:41, January 2010.
- [15] Christopher Welty, Richard Fikes, and Selene Makarios. A reusable ontology for fluents in OWL. In *Proceedings of FOIS*, pages 226–236, 2006.

ECG arrhythmias classification using SVM Classifier

MUSTAFA HASAN NAJM.ALGBURI¹ and ERSİN.KAYA¹

¹ Konya Teknik University, Konya/Turkey, mhn_m93@yahoo.com

¹ Konya Teknik University, Konya/Turkey, ersinkaya@selcuk.edu.tr

Abstract - Heart diseases are the leading cause of death around the world About 610,000 people die of heart disease in the United States every year, that is 1 in every four deaths. ECG Arrhythmia classification plays a significant rule in heart disease diagnosis. In recent years, ECG feature extraction techniques have attracted researchers around the world, and numerous approaches have been developed for ECG signal analysis. The proposed methods were mostly based on Artificial neural networks. In this research paper, we present a heart arrhythmias recognition technique based on SVM(Support vector machines) compared to KNN classifier and ECG R-R interval variations. The paper focuses on three arrhythmias. Ventricular bigeminy, Ventricular tachycardia, and Ventricular trigeminy. The data used is from the MIT-BIH dataset and apply the Pan-Tompkins QRS detection algorithm for R-R variations calculation. The proposed approach using SVM reach 98% recognition accuracy and KNN is 97% accuracy. Our proposed work can be used as a smartphone application with a wearable ECG monitor.

Keywords – ECG, Ventricular bigeminy, Ventricular tachycardia, Ventricular trigeminy, SVM, KNN, Arrhythmias, Heart, ECG patch.

I. INTRODUCTION

ECG Signal is a representation of the heart electrical activity that generated by depolarization and repolarization of ventricles and atria, and it is used to diagnose numerous diseases. The ECG signal consists of a P-QRS-T Waves[1] Figure 1 shows the ECG signal waves. The ECG features that obtained from intervals and amplitudes is clinically relevant when developing algorithms for heart disease classification. Recent years, Researchers around the world presented many approaches for automated ECG features extraction especially for the examination of great recordings[2]. The ECG feature extraction methods depend on the ECG signal waves amplitude and intervals these features then applied for automatic analysis. Many techniques introduced to recognize these features[3][4][5]. One of the most ECG signal analysis used methods based on the time domain, but these methods are not always sufficient to learn all the features from ECG signal so to solve this issue the frequency representation of the signal is required. The ECG variations in the electrical patterns indicate various diseases[6]. ECG technology and since it is invented is responsible for monitoring and diagnosis of patients. The Features of the electrical activity that performed by heart is used to diagnosing the cardiac abnormalities.

However, The development of a precise and accurate method for automated ECG features extraction and recognition is a significant concern now. It is necessary that the ECG signal recognition system to be more accurate and the idea is to find the most critical properties within the waveform to allow the algorithm to learn how to recognize the cardiac abnormalities. Over the last years, academic researchers have proposed many methods to analyze and classify the ECG waveform[8]. These approaches include digital signal analysis, fuzzy logic[7], neural networks[9], Genetic algorithm, SVM, Hidden Markov model, Self-organizing map, the Bayesian[10] and other methods. Each of them presenting benefits and issues. In this research paper, We propose a heart arrhythmias detection method based on R- R interval variations. This research focuses on four arrhythmias which can be detected using variations of R-R interval the arrhythmias are Ventricular bigeminy, Ventricular tachycardia, and Ventricular trigeminy. Support vector machine(SVM) trained on a dataset collected from MIT-BIH ECG dataset. The SVM classifier compared to KNN classifier.

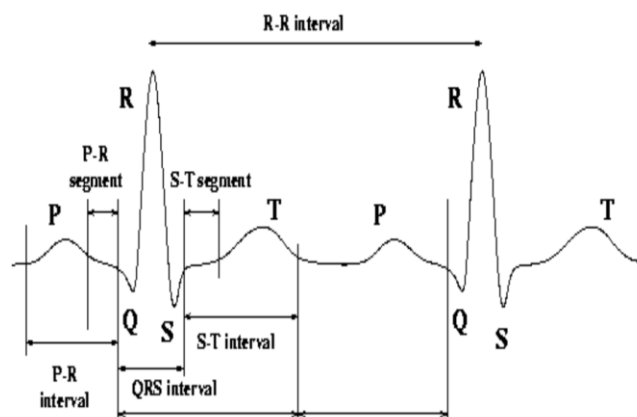


Figure 1: ECG signal waves

II. METHODS

II.1 Dataset:

The MIT-BIH dataset contains a half-hour ECG monitoring of two lead mobile ECG collected from 47 individuals suffering from some heart arrhythmias. These cases investigated by BIH arrhythmia laboratory during 1975 and 1979. The ECG records are obtained from the various state of inpatients about 60% and outpatients about 40% at Boston's Beth Israel hospital. The residual 25 records chosen is a clinically essential arrhythmia. However, we used the data to extract R-R intervals of four arrhythmias besides age and gender.

II.2 Support vector machines (SVM):

SVM is a supervised machine learning technique used in classification as well as regression tasks. It introduced by Vladimir N. Vapnik and Alexey Ya. Chervonenkis in 1963 and The first suggestion to use the kernel trick to maximum-margin hyperplanes was in 1992 by Bernhard E. Boser, Isabelle M. Guyon, and Corinna Cortes and Vapnik in 1993 proposed Vladimir N. Vapnik[10]. The modern conventional incarnation (soft margin) was introduced by Corinna Cortes and Vapnik in 1993[11]. Support vector machines, unlike other classifiers it is explicitly determined to obtain the greatest separating line. The support vector machine seeks for the nearest points, which it terms the "support vectors.". Once it has obtained the nearest points, the SVM models a line attaching them. It represents this connecting line by making vector reduction. The support vector machine then reveals the best separating line to be the line that divides the connecting line. The support vector machine is beneficial because when we get a new sample, we will have made a line that keeps, for example, points B and A as far apart from each other as possible, and so it is less likely that one will spillover over the line into the other's territory. In our paper, we used the SVM classifier with Linear kernel and trained it on the heartbeat variation dataset to classify whether it is normal or abnormal.

II.3 K-Nearest Neighbors:

KNN is the most straightforward machine learning approach that used in classification and regression[13]. In both cases regression or classification. The input contains the k closest feature training samples. If KNN used in classification the output is a group of classes. A majority of its neighbors classifies an object. The object is attached to its class if $k=1$ where k is a positive integer and usually is small.

III. RESULTS

We used the R-R intervals dataset to train an SVM classifier with a linear kernel. The train set is a 75% of the dataset and 25% for test set the SVM classifier reached a 98.6% accuracy. When using svm algorithm the error occurs in a normal state only and the total of errors is 10 errors. Figure 2 shows the Confusion Matrix of the SVM classifier. The SVM method compared to the KNN classifier which trained on the same

dataset and reaches a 98.3% accuracy. When using knn algorithm the error occurs in a normal state, Ventricular bigeminy and Ventricular trigeminy state and the total of errors is 12 errors. Figure 3 shows the Confusion Matrix of the KNN classifier.

Classifier	Accuracy	Precision	Recall
Linear SVM	98.6%	99%	99%
KNN	98.3%	98%	98%

Table 1: Classifiers Accuracy

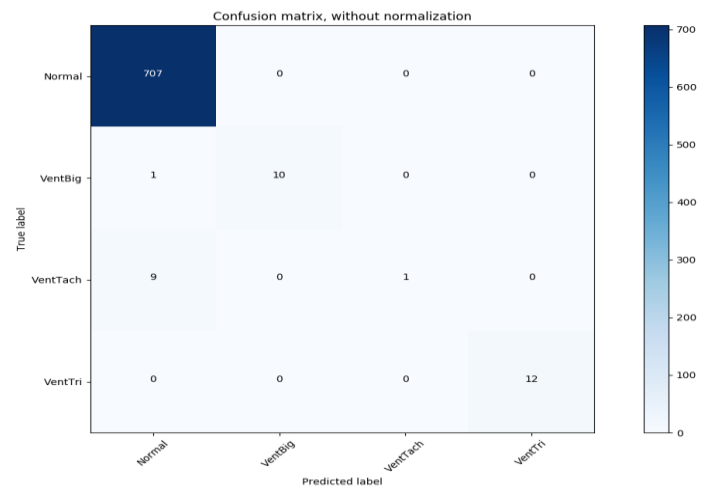


Figure 2: SVM classifier Confusion Matrix.

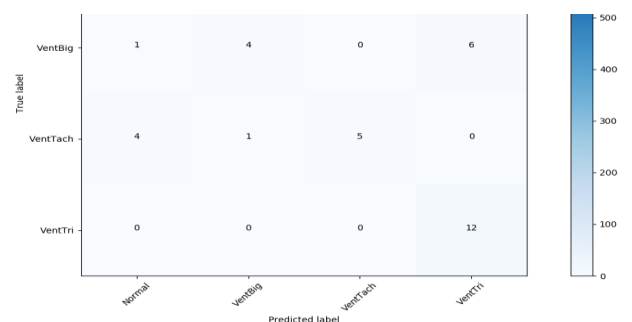


Figure 3: KNN Classifier Confusion Matrix.

IV. CONCLUSION

Heart disease is the leading cause of death around the world. Developing an accurate method of ECG signal analysis is critical to saving people lives. In this paper, We have used the SVM algorithm and the KNN algorithm and applied it to Data-MIT BIH to determine the type of disturbance that may occur in the heart and the result was the approximation between the two algorithms. We also used ad8232 to take the ECG signal from a particular person and convert it to R-R interval to compare the existing dataset and get the type of disturbance that might occur to the person. In short we introduced an accurate approach for Ventricular bigeminy, Ventricular tachycardia, and Ventricular trigeminy which can be used in various applications like wearable heart rate monitors. In the future we will develop this work that we take Dataset from people with heart disease and use a new non wire device to be more comfortable for the patient.

REFERENCES

- [1] Pan, Jiapu; Tompkins, Willis J. A Real-Time QRS Detection Algorithm. IEEE Transactions on Biomedical Engineering, vol. BME-22, pp. 230 – 236, March 2005.
- [2]S. Z. Mahmoodabadi, A. Ahmadian, and M. D. Abolhasani, "ECG Feature Extraction using Daubechies Wavelets," Proceedings of the fifth IASTED International conference on Visualization, Imaging and Image [23] Processing, pp. 343-348, 2005.
- [3]Juan Pablo Martínez, Rute Almeida, Salvador Olmos, Ana Paula Rocha, and Pablo Laguna, "A Wavelet Based ECG Delineator: Evaluation on [24] Standard Databases," IEEE Transactions on Biomedical Engineering Vol. 51, No. 4, pp. 570-581, 2004.
- [4]Krishna Prasad and J. S. Sahambi, "Classification of ECG Arrhythmias using Multi Resolution Analysis and Neural Networks," IEEE Transactions on Biomedical Engineering, vol. 1, pp. 227 231, 2003.
- [5]Cuiwei Li, Chongxun Zheng, and Changfeng Tai, "Detection of ECG Characteristic Points using Wavelet Transforms," IEEE Transactions on Biomedical Engineering, Vol. 42, No. 1, pp. 21-28, 1995.
- [6]C. Saritha, V. Sukanya, and Y. Narasimha Murthy, "ECG Signal Analysis Using Wavelet Transforms," Bulgarian Journal of Physics, vol. 35, pp. 68 77, 2008.
- [7] Goel, S., Tomar, P.,and Kaur, G. (2016). A Fuzzy Based Approach for Denoising of ECG Signal using Wavelet Transform. International Journal of Bio-Science and Bio-Technology, vol.8, no.2, pp. 143-156.
- [8] Sao, P., Hegadi, R., and Karmakar, S. (2015). ECG Signal Analysis Using Artificial Neural Network. International Journal of Science and Research, pp.82-86.
- [9] Jadhav, S., Nalbalwar, S.L. and Ghatol, A. (2012). Artificial Neural Network Models based Cardiac Arrhythmia Disease Diagnosis from ECG Signal Data, International Journal of Computer Applications, vol.44, no.15, pp. 8 13.
- [10] Gao, D., Madden, M., Schukat, M., Chambers, D., and Lyons, G. (2004). Arrhythmia Identification from ECG Signals with a Neural Network Classifier Based on a Bayesian Framework. Twenty-fourth SGAI International Conference on Innovative Techniques and Applications of Artificial Intelligence, vol.3, no.3, pp.390 409.
- [11] Boser, Bernhard E.; Guyon, Isabelle M.; Vapnik, Vladimir N. (1992). "A training algorithm for optimal margin classifiers". Proceedings of the fifth annual workshop on Computational learning theory.
- [12] Cortes, Corinna; Vapnik, Vladimir N. (1995). "Support-vector networks".
- [13]Altman, N. S. (1992). "An introduction to kernel and nearest-neighbor nonparametric regression." The American Statistician. 46 (3): 175–185.

Two Dimensional Measurement System for Pvc Profiles Via Image Processing.

M. AKDOĞAN¹ and S. YALDIZ²

¹Adil Karaagac Vocational and Technical Anatolian High School, Konya/Turkey, akdoganmurat@hotmail.com

²Selcuk University Technology Faculty, Mech. Eng. Department, Konya/Turkey, syaldiz@selcuk.edu.tr

Abstract—With technological advances in cameras and machine vision algorithms, many vision based measurement systems are now available in variety of industrial application [6]. Today, machine vision systems are widely used in the mass production. Image processing based computer vision applications use many different areas. In one of the works carried out for this purpose, digital image processing technology to measure geometrical size's of Pvc profile is used. Aiming at the problems in dimension measuring of extruded pvc profile, a real-time detection system is developed based on machine vision. The present work focuses on measurement of wall thickness of extruded pvc profiles through image processing technique. For this, a experimental setup has been prepared to hold digital camera in a fixed plane to capture the images of pvc profiles which help to get more accurate wall thickness results using image processing. This work has been done for measurement of up, down, left and right wall thickness of pvc profiles. The images are captured by using high resolution digital camera which are fixed in the experimental setup. OpenCV programming function was utilized in Python scripting language to perform image processing. So the high resolution captured images of profile are processed a sequential operations which are correcting defective images caused by working environment. And then developed image processing algorithms are applied to measurement of profile wall thickness. Finally, the geometrical sizes of profile are measured based on the calibration parameters information of the developed system. The acquiring results are compared with the results obtained by conventional systems. Dimension Control System decrease the non-standard profiles production and minimize the unnecessary consumption of raw materials.

Keywords— *Image Processing, Quality Control, Measurement.*

I. INTRODUCTION

In the mass production of pvc profile, in order to increase the product quality, it is required to measure the gasket gaps, wall thickness and internal and external sizes of extruded profile. The traditional method is to use electronic vernier calliper. This method is time-consuming and it is very easy to cause measurement error due to small tolerances. The development of manufacturing technology need higher requirements for the size measuring of profiles. Thus, researching and designing a system to measure the profiles

parameters rapidly have become the demand of the whole production industry. In recent years, digital signal processing and computer vision technology has become one of the effective methods to monitor the product quality and diagnose product faults as a brand new non-defective detection means gradually, which presents a powerful profile measuring technology. Compared with the traditional measurement methods, it has the advantages of noncontact, speed and high precision and can greatly reduce the cost.

In this paper, based on the actual profile, automatic size measurement system is developed. The acquired profile image is input to the computer and the all boundry edges are extracted and sizes measured according to improved image processing algorithm.

II. STRUCTURE OF MEASUREMENT SYSTEM

The hardware of the measuring system mainly consists of profile, industrial camera and its holder, lens, backlight source, computer and conveyor equipment. In the experimental setup camera (Elp-Usb 8MP 5-50 mm varifocal lens, Sony IMX179 sensor) are placed at the end of the conveyor, in such a position takes a cross-section image of profile just some seconds before their cutting. An illuminator (30W 5600/3200K Dimmable 396 Led video light lamp) lights up the profile sections in order to increase image contrast. It can ensure image clearer and brighter in case of dark condition. The overall structure of the system is shown in Figure 1.

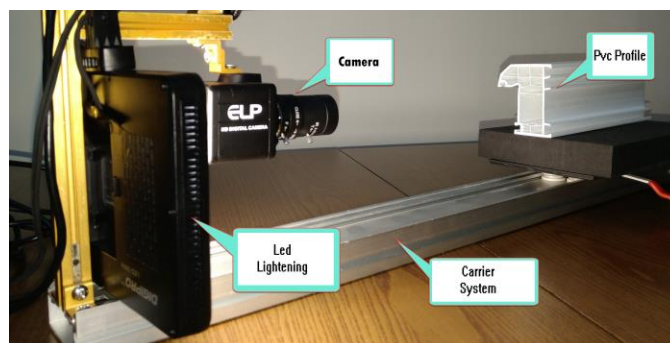


Figure 1: Experimental Setup

Its working process is that the profile to be measured is moved in front of the camera which is up to defined distance. Backlight source is placed back of the camera, so that each

profile can be lighted uniformly. The industrial camera that across the profile is equipped with lens which can acquire the profile image.

The software is installed in the computer with the operating system Windows 7. The development of the application program is based on Python programming language and OpenCV library. The image processing mainly includes the image acquisition, camera calibration according profile most outer sizes, grey level transformation, image filtration, edge extraction and contours finding. Developed algorithm for measuring profile sizes, applied on image which is included contours. In this system, camera calibration is carried out with the acceptance that the outer dimensions of the profile to be measured are invariant. Thus, pixel-mm conversion rates for the profile to be measured are determined according to the external dimensions. The structure of the software is as shown in Figure 2. The main task of this measuring system is to achieve the real-time measuring of the profile length, width, gasket gaps and wall thickness.

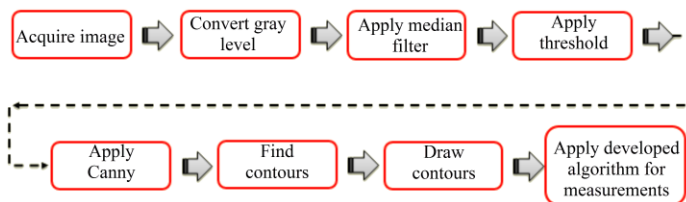


Figure 2: The flowchart of image processing in system

III. IMAGE PREPROCESSING

To find out useful information and data, this study getting image. Then, using some filters extract the noise removed images. This process is very important section before contour extracting step. Because, if wrong selected contour count of profile, next step is not success. In this step another important thing is lightening. Lightening is vital importance of well acquiring images.

1) *Image Thresholding*: One important approach in image segmentation is thresholding. The thresholding technique is used to separate an object from its background. Thresholding can be used to create binary images [1]. Figure 3. shows a thresholding view of profile image. For this operation used equation is shown (1).

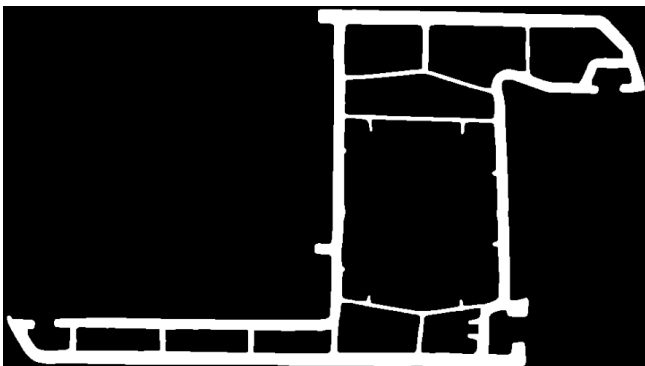


Figure 3: Threshed image of profile.

$$G_{x,y} = \begin{cases} 1, & f(x,y) \geq T(x,y) \\ 0, & f(x,y) < T(x,y) \end{cases} \quad (1)$$

2) *Median Filtering*: In image processing most suitable filter must be selected among the many filter [2]. Median filter is used some kind of noise reduction on an image. Median filtering is very widely used in digital image processing because, under certain conditions, it preserves edges while removing noise. Figure 4. (a) shows a not filtered view of profile image and Figure 4. (b) shows median filtered view of profile image.

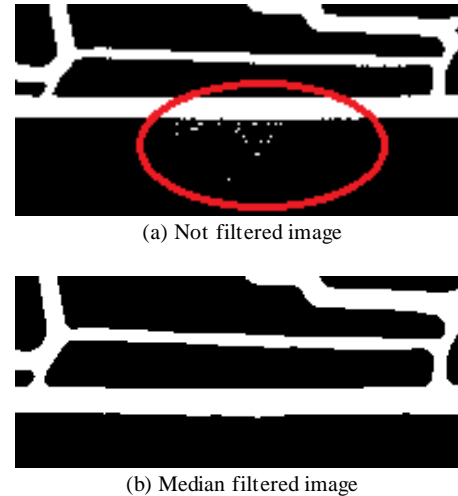


Figure 4: Median Filtering Operation

3) *Gaussian Filtering*: Gaussian filtering is used to blur images and remove noise but in our image not good result so not used in our system. The general mathematical expression of this filter used to eliminate the noises on the image is presented in Equation 2. Figure 5. shows a Gaussian filtered view of profile image after thresholding.



Figure 5: Gaussian Filtering Operation

$$G_{x,y} = \frac{1}{2\pi\sigma^2} \cdot \ell \frac{-(x^2+y^2)}{2\sigma^2} \quad (2)$$

4) *Edge Detection*: Edge detection is an image processing technique for finding the boundaries of objects within images. It works by detecting discontinuities in brightness. Edge detection is used for image segmentation and data extraction in areas. Canny edge detection algorithm is used in this study. For this operation used equation is shown (3) and (4). Figure 6. shows a Canny edge detection profile image after thresholding.

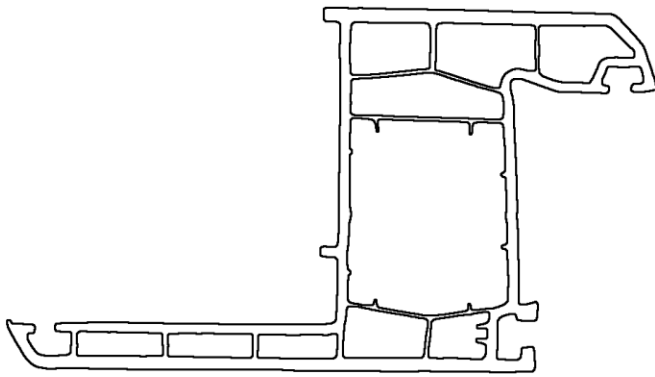


Figure 6: Canny edge detection image

$$G_x = \begin{bmatrix} -1 & 0 & 1 \\ -2 & 0 & 2 \\ -1 & 0 & 1 \end{bmatrix} G_y = \begin{bmatrix} -1 & -2 & -1 \\ 0 & 0 & 0 \\ 1 & 2 & 1 \end{bmatrix} \quad (3)$$

$$G = \sqrt{G_x^2 + G_y^2} \theta = \arctan\left(\frac{G_y}{G_x}\right) \quad (4)$$

5) *Contour detection:* Contour-based methods track the contour of the object rather than tracking all of the pixels that make up the object [7]. The well-known edge-based segmentation algorithm proposed by Canny [3]. First a Gaussian low pass filtering is carried out. The algorithm then searches for those points (at the edges) where the gradient of the grey level is maximum, since these are expected to correspond to the contour points that are of interest. A binary image that contains the object of interest. Figure 7. shows real image of product.

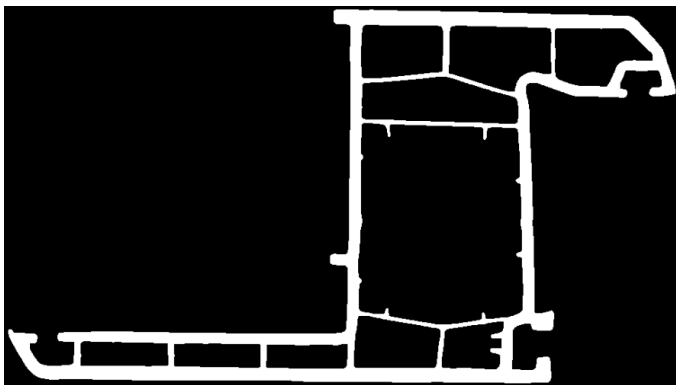


Figure 7: Real Image of Product

OpenCV uses the Suzuki algorithm to perform contour tracing [4]. In this algorithm, firstly the upper left contour pixel is found. Then, the neighborhood of the first pixel is checked in clockwise direction to find the next pixel of the contour. From now on, the search for the other pixels of the contour is done in anti-clockwise direction and ends when the first two pixels of the contour are found again. Polygonal representation performed and all contours described by a tree. This generates a collection of external contours.

Opencv command; cv2.drawContours (image, contours, x, (0,0,255),2). x is contour number. Figure 8. shows image contours.

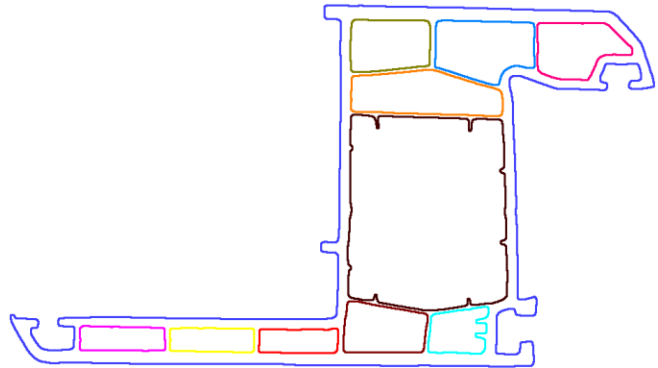


Figure 8: Image Contours

IV. TWO DIMENSIONAL MEASUREMENT

The standard dimensions of the pvc profile used in the study are given in Figure 9.

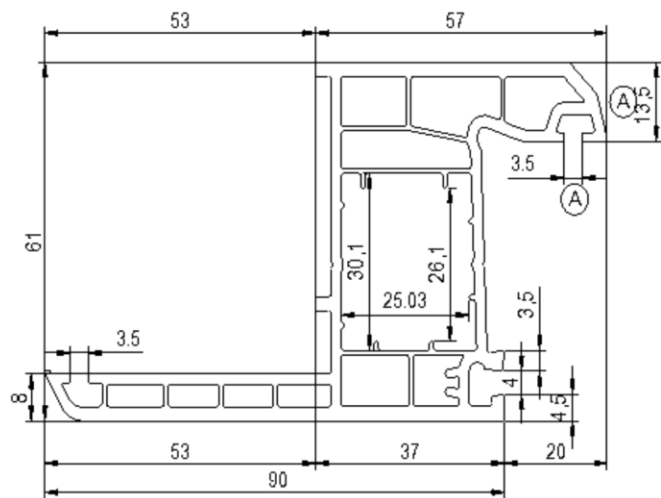


Figure 9: Technical Drawing of Product

With the algorithm developed in this study, the distance between two points on the contours is determined and displayed. Figure 10. shows image based measurement result of test sample profile.

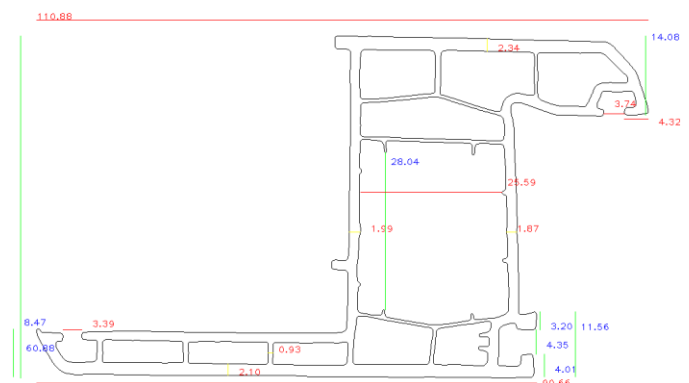


Figure 10: Measured image via image processing

Table 1, 2, and 3 shows image based measurement results of test sample and error percentage between image based result and standard values.

Table 1: Wall Thickness Measurements via Image Processing

	Wall Thickness			
	Top	Bottom	Right	Left
	<i>Std:2,50</i>	<i>Std:2,50</i>	<i>Std:2,00</i>	<i>Std:2,00</i>
	<i>Min:2,50</i>	<i>Min:2,50</i>	<i>Min:2,00</i>	<i>Min:2,00</i>
	<i>Max:----</i>	<i>Max:----</i>	<i>Max:----</i>	<i>Max:----</i>
Actual length (mm)	2,35	2,20	1,90	1,95
Measured length (mm)	2,34	2,10	1,87	1,99
% Error	0,42	4,54	1,57	2,05

Table 2: Height and Width Measurements via Image Processing

	Height and Width			
	Height	Bottom Width	Top Right Height	Bottom Right Height
	<i>Std:61,00</i>	<i>Std:90,00</i>	<i>Std:13,50</i>	<i>Std:12,00</i>
	<i>Min:61,30</i>	<i>Min:89,70</i>	<i>Min:13,30</i>	<i>Min:11,80</i>
	<i>Max:61,70</i>	<i>Max:90,30</i>	<i>Max:13,70</i>	<i>Max:12,20</i>
Actual length (mm)	61,25	90,10	13,75	12,00
Measured length (mm)	60,88	90,66	14,08	11,56
% Error	0,6	0,62	2,4	3,6

Table 3: Gasket Channel Measurements via Image Processing

	Gasket Channel Width		
	Bottom Left Width	Top Right Width.	Bottom Right Width
	<i>Std:3,50</i>	<i>Std:3,50</i>	<i>Std:4,00</i>
	<i>Min:3,30</i>	<i>Min:3,30</i>	<i>Min:3,80</i>
	<i>Max:3,70</i>	<i>Max:3,70</i>	<i>Max:4,20</i>
Actual length (mm)	3,40	3,80	4,25
Measured length (mm)	3,39	3,74	4,35
% Error	0,29	1,57	2,35

V. CONCLUSIONS

Today, Computer vision based systems are actively used almost entirely in manufacturing area. Especially contactless measurement is preferred because of its ability to provide high speed and precise measurement.

In this paper, computer vision has been performed for object measurement. This study presents a extruded products measurement method using image processing technics. The proposed method can measure all important sections of profile with a high accuracy. The experimental results show that the proposed measurement method is useful for measurement of pvc profiles. The experimental results show the algorithm is fast and requires minimum user interaction. This work is easily applicable for the companies that produce extrusion pvc products. When compared with the traditional measurement methods, the proposed approach has shown that the method can measure accurately, quickly and with high accuracy.

REFERENCES

- [1] Shapiro, Linda G. & Stockman, George C. (2002). "Computer Vision". Prentice Hall. ISBN 0-13-030796-3
- [2] Demigny D., On Optimal Linear Filtering for Edge Detection, IEEE Transactions On Image Processing, 2002, 11, 728-737
- [3] J.F. Canny, A computational approach to edge detection, IEEE Transactions on Pattern Analysis and Machine Intelligence PAMI-8 (6) (1986) 679-698.
- [4] Suzuki, S. and Abe, K., Topological Structural Analysis of Digitized Binary Images by Border Following. CVGIP 30 1, pp 32-46 (1985)
- [5] C. Liguori. A. Paolillo. A. Pietrosanto. "An on-line stereovision system for dimensional measurement of rubber extrusions". Measurement 35 (2004) 221-231
- [6] A.Hornberg (editor), Handbook of Machine Vision, WileyVCH, (2006).
- [7] Shaaban, K. M. and Omar, N. M., "3D information extraction using Region-based Deformable Net for monocular robot navigation," Journal of Visual Communication and Image Representation, vol. 23, pp. 397-408,2012.

Mapping location of a suspect by using forensic images taken with their own mobile phone

K.K. ÇEVİK¹, F.S. BERBER², E.U. KÜÇÜKSİLLE³

¹Akdeniz University, Antalya/Turkey, kcevik@akdeniz.edu.tr

²Süleyman Demirel University, Isparta/Turkey, farukberber@sdu.edu.tr

³Süleyman Demirel University, Isparta/Turkey, ecirkucuksille@sdu.edu.tr

Abstract - The location information of photos taken with today's mobile phones is stored in the same photo file with a structure called exif. With the software developed in this study, an analysis of the places where the suspect was in the past is carried out by reviewing location information on photos of suspects' mobile phones. With this process, suspect's location map is drawn based on dates. In addition, photos whose location information were deleted or modified using anti-digital forensic techniques or photos without location information can also be used to map the suspect's location. In this regard, an original study has been carried out. In this study, 1582 photographs with location information and 268 photographs without location information, which were obtained from a mobile phone and which were taken between 01.01.2018 and 31.06.2018 were used as data set. This data set was subjected to classification using CNN (Convolutional Neural Network) and it was determined that the same class images were taken at the same place. As a result of the information obtained, all the photographs are shown in application designed in this study by marking them on the map. The digital evidence examined by the software and findings obtained have been presented in this study.

Keywords - Digital forensics, anti-digital forensics, forensics software, exif, gps location, mapping, deep learning.

I. INTRODUCTION

Digital forensics can be defined as the process of transforming the findings obtained from digital media into judicial evidence using various technical hardware and software. This process consists of the steps of obtaining, storing, analyzing and reporting all the data such as pictures, photographs, videos, audio, texts, databases, emails, deleted data etc. stored on the information technology devices with digital evidence. Anti-Digital Forensics is the studies of making digital forensics processes partially or completely unsuccessful. Attempts by suspects to change or delete the contents of digital evidence obtained from the devices to be examined by forensic experts and to reduce the amount and quality of data are known as anti-digital forensics. In the process of forensic computing, the devices in which digital evidence is collected are also rapidly diversifying. Especially the widespread use of mobile phones allows to be accessed data which are important in the process of proving guilt or innocence in judicial cases from mobile phones. Elucidation of judicial incidents by accelerating the process of examining digital

evidence with the help of digital evidence collected from mobile phones of the suspect has been studied and continues to be studied in the literature.

Fan et al. proposed in their paper a novel technique to correlate statistical image noise features with three Exchangeable Image File format (EXIF) header features for manipulation detection.

By formulating each EXIF feature as a weighted sum of selected statistical image noise featured using sequential floating forward selection, the weights are then solved as a least squares solution for modeling the correlation between the intact image and the corresponding EXIF header. Image manipulations like brightness and contrast adjustment could affect these noise features and lead to enlarged numerical difference between each actual and its estimated EXIF feature from the noise features. By using the numerical difference as a manipulation indicator, they have achieved excellent performance in detecting common brightness and contrast adjustment. Based on cameras of different brands, their manipulation detection is also demonstrated to work well in a blind mode, where the camera brand/model source is unavailable. Several detection examples have suggested that their model can be applied in detecting real-world forgeries [1].

Safonov et al., the application of metadata from an EXIF-file for the estimation of the probability of defects existing in digital photos was considered. The following typical defects of photos were selected: exposure problems, noise, color cast, blur, JPEG artefacts, and the presence of red eyes. An extensive database of photographs captured using ten different cameras was collected, and the influence of various EXIF-tags on the presence of defects analyzed. An EXIF-based image enhancement pipeline was created which allows a reduction in the total time needed for automatic photo enhancement as a consequence of the estimation of the probability that several defects were presented in the corrected photo. The optimization of the image enhancement procedure was implemented by applying a specific classification based on the EXIF-tags contained in photographs, so that the number of cases for which a quality assessment was required is reduced [2].

Huang et al. studied in which techniques were described to decode location information in content accessed by a mobile electronic device and pass the decoded information to a native mapping application to provided an enhanced user experience. In an implementation, location information was decoded by

parsing a map link in content accessed by the mobile electronic device or from location information parameters were associated with a mapping application programming interface (API) call made by a mapping script embedded in the content. The decoded location information was passed to a native mapping application of the mobile electronic device. A map-related function then was provided by the mobile electronic device by accessing functionality of the native mapping application has been used the decoded location information [3].

Greenfeld said in his paper, GPS based navigation and route guidance systems were becoming increasingly popular among bus operators, fleet managers and travelers. To provided this functionality, one has been to have a GPS receiver, a digital map of the traveled network and software that could be associated (match) the user's position with a location on the digital map. Matching the user's location has to be done even when the GPS location and the underlying digital map had inaccuracies and errors. There were several approaches for solving this map matching task in Greengeld's paper. Some only match the user's location to the nearest street node while others were able to locate the user at specific location on the traveled street segment. In this paper a topologically based matching procedure was presented. The procedure was tested with low quality GPS data to assess its robustness. The performance of the algorithms was found to produce outstanding results [4].

McCloskey worked on an image forensics system estimates a camera response function (CRF) associated with a digital image, and compares the estimated CRF to a set of rules and compares the estimated CRF to a known CRF. The known CRF was associated with a make and a model of an image sensing device. The system was applied a fusion analysis to results were obtained from comparing the estimated CRF to a set of rules and from comparing the estimated CRF to the known CRF, and assesses the integrity of the digital image as a function of the fusion analysis [5].

Γεωργακίτσος has defined mobile device forensics which is the science of recovering digital evidence from mobile device under forensically sound conditions using accepted methods in his thesis. Mobile device forensics was an evolving specialty in the field of digital forensics and there was an increase in the number of mobile device forensics (MoDeFo) tools for proper recovery and speedy analysis of data present on mobile devices. Scope of his thesis was to provide an in-depth look into the technologies involved and their relationship to mobile device forensic procedures, the challenges associated while carrying forensic analysis and to elaborate various forensic analysis techniques and tools. This document also were discussed procedures for the preservation, acquisition, examination, analysis, and reporting of digital information on mobile devices as part of forensic analysis procedures [6].

Yao et al. defined that Computer-generated graphics (CGs) were images generated by computer software in their works. The rapid development of computer graphics technologies has made it easier to generate photorealistic computer graphics, and these graphics are quite difficult to distinguish from natural images (NIs) with the naked eye. In this paper, they proposed a method based on sensor pattern noise (SPN) and deep learning

to distinguish CGs from NIs. Before being fed into their convolutional neural network (CNN)-based model, these images—CGs and NIs—were clipped into image patches. Furthermore, three high-pass filters (HPFs) were used to remove low-frequency signals, which represent the image content. These filters were also used to reveal the residual signal as well as SPN introduced by the digital camera device. Different from the traditional methods of distinguishing CGs from NIs, the proposed method utilizes a five-layer CNN to classify the input image patches. Based on the classification results of the image patches, they deployed a majority vote scheme to obtain the classification results for the full-size images. The experiments have demonstrated that (1) the proposed method with three HPFs can achieve better results than that with only one HPF or no HPF and that (2) the proposed method with three HPFs achieves 100% accuracy, although the NIs undergo a JPEG compression with a quality factor of 75 [7].

With the software developed in this study, an analysis of the places where the suspect was in the past is carried out by reviewing location information on photos of suspects' mobile phones. With this process, suspect's location map is drawn based on dates. In addition, photos without location information or photos whose location information were deleted and/or modified using anti-forensic techniques can also be used to map the suspect's location. In this regard, an original study has been carried out.

II. MATERIAL AND METHOD

A. Material

Firstly, the image files found in the mobile phone of a person determined as suspicious (in the period between 01.01.2018 and 31.06.2018) were taken. A total of 1850 image files were identified as data sets. With the software developed in the C# programming language, those with and without the location information of these image files are distinguished. The file names of the files with the location information, the date of taking the images, the location information is stored in a database. Names and taking dates of non-location image files were recorded in the same database. For files that do not have a photo taken, the file creation date has been accepted as the taking date. A screenshot of the designed software is shown in Figure 1.

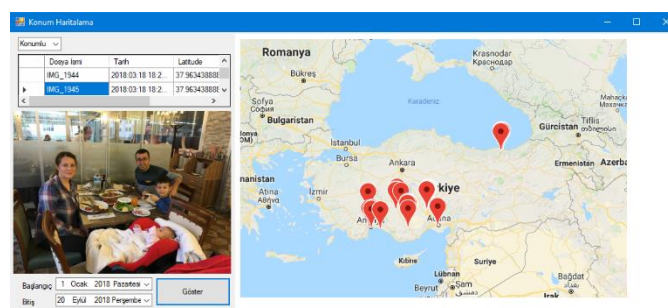


Figure 1. Designed software

Additional software has been developed to find the location information for image files that do not have location information. The application was performed using the Keras library in python programming language. In order to be used in the application, 1582 images with location information received from the mobile phone were used for training and validation purposes and these images were divided into 21 classes according to their location. These 21 classes are created by distinguishing the positions in the data set using a digit after the comma. For example, 36,8-59,6 class was used for 36,7785-59,57999. In addition, 268 images with no location information were also used for testing purposes. The ImageDataGenerator class was used when transferring all images. In this class, the ratio of rescale ratio was determined as 1/255, shear_range ratio was 0.2 and zoom_range ratio was 0.2. All images are again sized 64X64X3 with the help of the same class. First, a convolutional layer is created. In order to create this layer, the filters used in the Conv2D function were used as parameter 64, kernel_size parameter (3, 3) and relu (Rectified Linear Unit) as the activation function. Then the MaxPooling2D function is used to create the pooling layer and the pool_size parameter (2, 2) is given. Finally, the Dense function was used to create a fully-connected layer. This function has a value of 128 for the units parameter and relu is used as an activation function. Finally, the output layer is created using the Dense function again. This function has a value of 21 for units and softmax is used as an activation function. Then the model was compiled and 20 iterations were run for the training process.

B. Method

CNNs (Convolutional Neural Networks) are nurturing neural networks designed to recognize patterns from direct image pixels (or other signals) by combining feature extraction and classification, inspired by biological processes. A typical CNN consists of four layers: convolutional, activation, pooling and fully-connected. A convolutional layer is identified by sparse local connectivity and weight sharing. Each neuron of Layer connects to a small local area of the input. Different neurons respond to different local areas of the overlapping input to obtain a better representation of the image. Also, neurons of a convolution layer are grouped in feature maps that share the same weights. Thus, the entire procedure becomes equivalent to convolution, with shared weights that are the filters of each map. Weight sharing significantly reduces the number of network parameters, thus increasing productivity and preventing overfitting. Convolutional layers are usually followed by a non-linear activation layer to capture more complex properties of the input signal. Pooling layers are also used to sample the previous layer by collecting small rectangular value sets. The maximum or average pooling is usually applied by changing the input values with the maximum or average value, respectively. Pooling layers reduce the sensitivity of the output to small input values. Finally, one or more of the added dense layers are followed by an activation layer which produces the result of classification. The training of CNNs is performed by minimizing a loss function using gradient-based methods and back-propagation of errors, similar

to those of other ANNs. [8].

Figure 2 shows a typical CNN architecture.

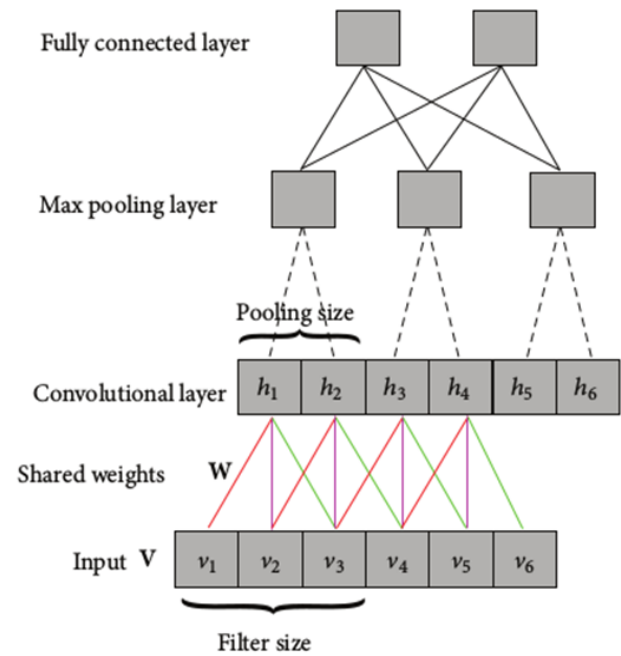


Figure 2: Typical CNN architecture [9]

III. RESULTS

In the data set, 1850 image files with location information and 268 files with no location information were used. With the designed C# software, files with location information and taking dates were received. This information is used in the program without changing the location mapping of the suspect. In addition, by using the CNN network, which was trained using these 1582 files, 268 images with no location information were classified for 21 different locations. The results are shown in Table 1.

Table 1. Classification result

CLASS	CORRECT	WRONG	TOTAL	SUCCESS
36.9-30.7	1	0	1	100
36.9-33.3	1	0	1	100
37.2-33.2	15	21	36	41.67
37.8-30.5	4	1	5	80
37.9-32.5	2	6	8	25
37.9-34.5	2	0	2	100
37.9-34.6	7	4	11	63.64
37-35.2	1	0	1	100
38-34.6	158	35	193	81.87
38-34.7	1	2	3	33.33
41-39.7	2	0	2	100
No location	5	0	5	100
Total	199	69	268	74.25

As a result of this classification, when the location information of 268 images were examined, it was determined that 199 were classified in the correct location and 69 were classified in the wrong location. In order to determine this accuracy, the person who was identified as suspicious and whose image was taken from his phone was used. As a result, the test success of CNN was determined as 74.25%.

IV. CONCLUSION

Using the data set created in the study, the location information of the suspect in the period between 01.01.2018 and 31.06.2018 has been tried to be reached. For this process, non-location image files have been categorized using CNN with files with location information in the data set. The overall success rate of the system was determined as 74.25%. When examining image files with wrong location information; it appears that the document image, the external media image, or only the people that do not contain the media object that includes them. Therefore, any document can be photographed in any environment. The objects in the photographs taken in the outside environment have a lot of similarities (tree, sea, vehicle, etc.). Because the photographs of the people only within their faces and bodies are independent of the spaces, they have little distinctive character. Performing these operations after extracting photos from suspicious photos of such situations can increase the success of the system.

Figure 1: This caption is centered.

REFERENCES

- [1] Fan, J., Cao, H., & Kot, A. C. (2013). Estimating EXIF parameters based on noise features for image manipulation detection. *IEEE Transactions on Information Forensics and Security*, 8(4), 608-618.
- [2] Safonov, I. V., Kurilin, I. V., Rychagov, M. N., & Tolstaya, E. V. (2018). Image Enhancement Pipeline Based on EXIF Metadata. In *Adaptive Image Processing Algorithms for Printing* (pp. 65-83). Springer, Singapore.
- [3] Huang, H., Kirouchenaradje, F. R., Palmer, D. K., Uribe, J. C., & Kale, C. V. (2011). U.S. Patent Application No. 12/724,210.
- [4] Greenfeld, J. S. (2002, January). Matching GPS observations to locations on a digital map. In 81th annual meeting of the transportation research board (Vol. 1, No. 3, pp. 164-173).
- [5] McCloskey, S. (2018). *U.S. Patent No. 9,934,434. Washington, DC: U.S. Patent and Trademark Office.*
- [6] Γεωργακίτσος, K. (2018). *Mobile device forensics: guidelines, analysis and tools* (Master's thesis, Πανεπιστήμιο Πειραιώς).
- [7] Yao, Y., Hu, W., Zhang, W., Wu, T., & Shi, Y. Q. (2018). Distinguishing Computer-Generated Graphics from Natural Images Based on Sensor Pattern Noise and Deep Learning. *Sensors*, 18(4), 1296.
- [8] Anthimopoulos, M., Christodoulidis, S., Ebner, L., Christe, A., & Mougiakakou, S. (2016). Lung pattern classification for interstitial lung diseases using a deep convolutional neural network. *IEEE transactions on medical imaging*, 35(5), 1207-1216.
- [9] Hu, W., Huang, Y., Wei, L., Zhang, F., & Li, H. (2015). Deep convolutional neural networks for 11hyperspectral image classification. *Journal of Sensors*, 2015.

Registration and Authentication Cryptosystem Using the Pentor and UltraPentor Operators

1st Artan Luma
Faculty of Contemporary Sciences and
Technologies
South East European University
Tetovo, Macedonia
a.luma@seeu.edu.mk

2nd Besnik Selimi
Faculty of Contemporary Sciences and
Technologies
South East European University
Tetovo, Macedonia
b.selimi@seeu.edu.mk

3rd Blerton Abazi
Faculty of Computer Science and
Engineering
University for Business and
Technology - UBT
Prishtina, Kosovo
blerton.abazi@ubt-uni.net

Abstract— *Any Internet banking system must solve the issues of authentication, confidentiality, integrity, and no repudiation, which means it must ensure that only qualified people can access an Internet banking account, that the information viewed remains private and can't be modified by third parties. However, this kind of approach does not involve image encryption and their safe storage for avoiding direct compromise of the data used for authentication and identification. Other work involves the definition of a strict authentication system by introducing a multi-level authentication technique that generates a password in multilevel instances for accessing and using cloud services inside of which, an e-mail cloud service can reside as well. In our research we will present a new approach on how the cryptosystems will validate the registration and authentication process using the mathematical pentor and ultrapentor operators. The paper will be followed by a concrete example of implementation with a detailed explanation through which we will defend our approach. In this section, you will briefly describe the project / dissertation based on which this manuscript has been prepared. You can mention the motivation that led you to take up this project and its objectives.*

Keywords— authentication; identification; cryptosystems; cryptography; pentor operator; ultrapentor operator; information security; cyber attacks

I. INTRODUCTION

User authentication and identification in e-mail clients have always represented a challenge in the Web. Email based user authentication and identification represent emerging techniques that appear as an alternative to the standard Public-Key-Infrastructure (PKI) and furthermore these approaches allow securing users from faulty impersonations and identity thefts [1]. However, the authentication and identification process in the web has not changed over the last twenty years and is mainly based on password identification and cookies [2]. The report from Google on email account security indicates that in 2011 and 2012 there is an increase in Google account blocking as a result of account hijacking and identity thefts [3]. The most widely used authentication strategy represents the text-based password scheme where users enter their login names and passwords. Despite their popularity, textual passwords suffer from several drawbacks. Although simple and straightforward textual passwords are easy to remember and maintain, they are mostly vulnerable to attacks. While complex and arbitrary passwords render the system substantially more secure, resisting the brute force search and dictionary attacks, they are difficult to guard and memorize [4].

Another aspect that advances the textual authentication is the graphical authentication which (compared to words) is easier to remember. Accordingly, it is difficult to formulate

and orchestrate attacks for graphical authentication considering that the password space of graphical authentication extends more than that of textual passwords and makes them harder to crack and brute force attack resistant. Still, graphical authentication suffers from the so-called shoulder-surfing which represents a hazard of intruder scrutinizing passwords by recording user sessions or directly supervising the users [5]. Some other related work regarding multilevel authentication is elaborated in [6] where the authors propose 3-level authentication based on textual, image based and one-time password fashion.

It has been proven that the e-banking, is a high-risk area with a potential for substantial economic loss. The high risk makes security a prime concern. The results indicate that U.S. victims of phishing attacks lost five times more money in 2006 than 2005. Although 80% of the victims in 2005 got their money back, in 2006 only 54% victims were refunded by their banks. In the U.K., online banking fraud increased by 55% during the first six months of 2006. It is reported that online attacks influenced nearly 30% of online banking users; more than 75% of those users logged in less frequently, and about 14% stopped paying bills online [16].

It is broadly known that the Internet has become an integral part of our lives, and the proportion of people who expect to be able to manage their bank accounts from everywhere is constantly growing. As such, the online system of e-banking has become a crucial component of any financial institution's multichannel strategy. It has been proven that information about financial institutions, their customers, and their transactions is, by necessity, extremely sensitive and doing such business via a public network introduces new challenges for security and trustworthiness.

Based on the above-mentioned research, it can be seen that the potential of becoming an internet victim is getting higher, and in this paper we will describe current authentications and we will propose a new solution for user authentication as well as how these solutions can be extended in the face of more complex future attacks.

II. RELATED WORK

Many encryption algorithms utilized today use proprietary methods to generate keys and therefore are useful for various applications. Here, we introduce details for some of these encryption algorithms. Strong side of these algorithms lies in the length of the key that is generated and used.

RSA algorithm [8, 9], for example, is based on the generation of two simple large numbers p and q , multiplied in the form $n = p \cdot q$. The algorithm also selects an encryption

exponent e , as $gcd(e, (p - 1) \cdot (q - 1)) = 1$ and the pair (n, e) is sent to the recipient. The recipient on the other side will now generate cryptic message in the form $c \equiv m^e \pmod{n}$. This encrypted message, then can be encrypted after the component d is found, which is easy considering that the sender has p and q from where it finds d as following $d \equiv 1 \pmod{(p - 1) \cdot (q - 1)}$. Decryption process is performed as $m \equiv c^d \pmod{n}$. The problem is that the algorithm is based on the generation of large prime numbers which is time consuming and computationally intensive.

Another approach that belongs to Online authentication is the TEA (Tiny Encryption Algorithm) [10–12]. This algorithm generates random numbers that will be sent to users that request authentication. From this random number together with user’s secret key, a ciphertext message is generated. After the server receives the encrypted message, it decrypts it using the random number sent earlier. The disadvantage of this approach is that the secret key is previously used for securing the communication line established between the user and the server rather than directly for authentication. Another aspect of this approach is that it is not clear in which way the secret key is sent or at least generated by the user.

In addition to the above mentioned, let us present two operators given as mathematical models called Pentor and Ultra Pentor [13]. These operators can easily be generated from any number and can be used for encryption purposes. The power of the proposed cryptosystem lies in the irreversibility trait that these two operators have during the authentication process. Once operators are generated, it is extremely difficult to find numbers from which these operators are derived. This irreversible feature is used to create online authentication scheme which uses exactly three steps of encryption algorithm. The power of the cryptosystem justifies the proposed approach for its potential application in online authentication systems. In the following section, their definitions and properties will be analyzed.

III. CRYPTOGRAPHY WITH PENTOR AND ULTRA PENTOR OPERATORS

In [14, 15] a mathematical definition for Pentor and Ultra Pentor is introduced. A Pentor of a number is given as an integer number with base n and for every natural and integer number n there exists one Pentor for the given base B . In order to represent this operator mathematically, we start from the modular equation for Pentor of an integer number n with base B that fulfills the condition $gcd(n, B) = 1$. From the aforementioned conditions the following was acquired [14]:

$$B^m \cdot P(n) \equiv 1 \pmod{n} \quad (1)$$

where B represents the base of the integer number n , $P(n)$ is the Pentor of the integer number, whilst n and m represent the order of the Pentor for the given integer number. The modular expression (1) was transformed to the equality expression of the form:

$$B^m \cdot P(n) \equiv 1 + n \cdot k \quad (2)$$

$$P(n) = \frac{1 + n \cdot k}{B^m} \quad (3)$$

where k is an integer number that fulfills the condition for the fraction to remain an integer number. For example, if we want

to find the Pentor of the first order than $m = 1$, the Pentor of the second order than $m = 2$ and so on [14].

Likewise, the UltraPentor of a number n with base B in which for every natural and integer number n there exists an UltraPentor for the given base B [14]. In order to represent this operator mathematically, we start from modular equation for UltraPentor of integer number n with base B that fulfills the condition $gcd(n, B) = 1$. Considering the above mentioned conditions, the modular equation for UltraPentor will look like:

$$B^m \equiv 1 \pmod{n} \quad (4)$$

where m is an integer number. The modular expression [1], was transformed to the equality expression by applying logarithmic operations on both sides and finding the UltraPentor as follows:

$$B^m = 1 + n \cdot l \mid \cdot \log_B \quad (5)$$

$$\log_B B^m = \log_B(1 + n \cdot l) \quad (6)$$

$$m \cdot \log_B B = \log_B(1 + n \cdot l) \quad (7)$$

where $\log_B B = 1$ and there is:

$$m = \log_B(1 + n \cdot l) \quad (8)$$

If $m = UP(n)$ then UltraPentor of an integer number n with base B can be written as:

$$UP(n) = \log_B(1 + n \cdot l) \quad (9)$$

where l is an integer number that fulfills the condition for $(1 + n \cdot l)$ to be written as B^a , where a is also an integer number [15]. The power of the above mentioned operators lie in their properties of irreversibility of retrieving the ID from the Pentor or UltraPentor itself which in our designed cryptosystem is kept secret on the user’s side.

IV. CRYPTOSYSTEM ALGORITHM FOR REGISTRATION (CERTIFICATION) AND AUTHENTICATION

At the beginning we will give some basic concepts for designing a new cryptosystem for registration (certification) and authentication. This cryptosystem will be based on mathematical operators known as Pentor and UltraPentor. As far as these two operators are concerned, we have clarified all the concepts for them at the previous section.

Now based on a scheme we will try to clarify the registration process (certification) of this new cryptosystem, as it is shown on the following figure:

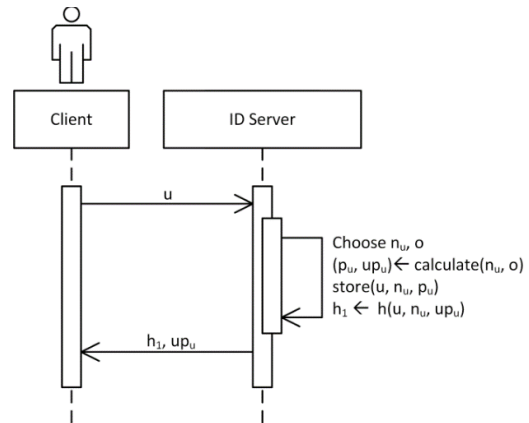


Fig. 1 Registration (certification)

From Fig. 1, it is clear that the client will be able to register (certify) by making a request to ID Server, where along with the request will also must enter the *username* that shortly we will make it with *u*. Then the ID Server will receive a random number from the list provided, which will also be the secret key of the client and we will mark it with n_u . In the same time, we define the order of Pentor and UltraPentor where we will mark it *o*. After we have defined n_u , now we can begin the calculations of the Pentor and Ultrapentor operators. Once these are calculated by ID Server on the server base they will be saved as *u*, n_u and u_p , where n_u and u_p are the secret key of the client. The ID Server will calculate the function $h(u, n_u, u_p)$ and will add the h_1 , with the couple of (h_1, u_p) (certificate) will be sent to the client.

Now these data, the client can be transferred/sent in various forms such as: certificate on USB, CD/DVD, etc. In this form the third party is not able to get information for the client. So, the registration process (certification) ends here.

Now we will explain the authentication process based on the following schema:

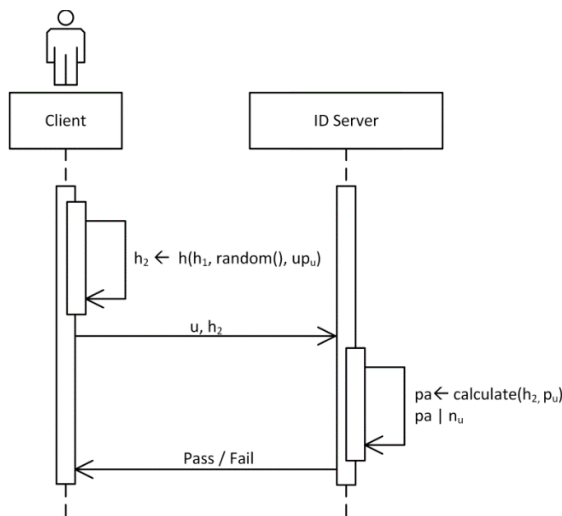


Fig. 2 Authentication

The client calculates the function $h(h_1, random(), u_p)$ and will add the h_2 , where during the calculation it takes a random number. Then, the client sends the couple of numbers (u, h_2) , to the Server ID, where the server ID will need to authenticate the client. Then it will happen an pentor attack with pentor operator p_u to the function h_2 and according to the pentor attach algorithm in the end of the process a value is gained which we will store at the *pa* variable. Now this value must be fulfilled with n_u , and if it is that the ID Server has authenticated the client and gives access to the system, otherwise if will be rejected.

V. CASE STUDY

Now we will show how the client's registration in the new cryptosystem will be realized. Now, the client will be able to register (certify) by making a request to ID Server, where along with the request will add also the *username* = *a.luma* that shortly we will mark it as *u*. This value will need to be converted based on ASCII code from text to number and we will have *username* = *a.luma* = 974610811710997, so *u* = 974610811710997. Then ID

Server will receive a random number from the list provided, which will also be the secret key of the client and we will mark it with n_u , ku $n_u = 13$. We also define the order of Pentor and UltraPentor where we will mark it with *o*, so $o = 1$. After we have defined n_u , now we can begin with the calculations of the Pentor and UltraPentor.

Calculation of Pentor is done based on the formula:

$$P_u = \frac{1 + n_u \cdot k}{B^o}$$

Where $n_u = 13$, B = 10 and $o = 1$.

Now, we'll count the client's Pentor:

$$P_u = \frac{1 + 13 \cdot 3}{10^1} = \frac{40}{10} = 4$$

So, the pentor of the client will be $P_u = 4$.

And UltraPentor calculations are made based on the formula:

$$UP_u = \log_B(1 + n_u \cdot l)$$

Where $n_u = 13$ and $B = 10$.

Now, we'll count the UltraPentor of the client:

$$UP_u = \log_{10}(1 + 13 \cdot 76923) = 6$$

So the client UltraPentor will be $UP_u = 6$.

Once Pentori and UltraPentor have been calculated they will be saved by ID Server on base as *u*, n_u and u_p , where n_u and u_p are the clients secret key. ID Server will make you calculate a function $h(u, n_u, u_p)$ and will add the h_1 , and the couple of (h_1, u_p) (certificate) and will sent all together to the client.

The function $h(u, n_u, u_p)$ will be calculated as in the following:

$$h(u, n_u, u_p) = h(974610811710997, 13, 6) = 974610811710997 \cdot 13 \cdot 6$$

$$h(u, n_u, u_p) = 76019643313457766$$

Now, when the UltraPentor has the value of $UP_u = 6$, then we function value we gained *h* we will divide by six digits from left to right as the following:

$$h(u, n_u, u_p) = 76019|643313|457766$$

Now we sum up these values as follows:

$$h(u, n_u, u_p) = 76019 + 643313 + 457766 = 1177098$$

As the result of the function *h* there are still more than six figures that we continue with his cutting, as follows:

$$h(u, n_u, u_p) = 1|177098$$

Now we sum up these values as follows:

$$h(u, n_u, u_p) = 1 + 177098$$

$$h(u, n_u, u_p) = 177099$$

Now from this value by shifting the figures we will get some combinations and the following:

- 177099
- 770991
- 709917
- 099177

where zero is replaced by $n_u = 13$ and we get 1399177

- 1399177
- 991770
- 917709

Now from all these combinations we choose one or random as a client function $h_1 = 177099$.

The client certificate will be from these parameters as follows:

$$(h_1, UP_u) = (177099, 6)$$

Now these data, the client can be sent in various forms such as: certificate on USB, CD/DVD, Cloud etc. In this form the third party is not able to get information for the client. So, the registration process (certification) ends.

Now we will explain the authentication process. The client calculates the function $h(h_1, random(), up_n)$ and will add the h_2 , where in the calculation take a random number.

The function $h(h_1, random(), up_n)$ will be calculated as in the following:

$$h(h_1, random(), up_n) = h(177099, 113, 6) \\ = 177099 \cdot 113 \cdot 6$$

$$h(h_1, random(), up_n) = 120073122$$

Now that UltraPentor has value $UP_u = 6$, then the value gained in the function h divide by six digits from left to right as the following:

$$h(h_1, random(), up_n) = 120|073122$$

Since it was the first digit of the value 073122 is zero then zero is replaced by $n_u = 13$ and we get the value of 1373122

$$h(h_1, random(), up_n) = 120|1373122$$

Now we sum up these values as follows:

$$h(h_1, random(), up_n) = \\ 120 + 1373122 = 1373242$$

As the result of the function h there are still more than six figures that we continue with his cutting, as follows:

$$h(h_1, random(), up_n) = 1|373242$$

Now we sum up these values as follows:

$$h(h_1, random(), up_n) = 1 + 373242 \\ h(h_1, random(), up_n) = 373243$$

Now from this value by shifting the figures we will get some combinations and the following:

373243
732433
324337
243373
433732
337324

Now from all these combinations we choose one whom we want or random as a client function $h_2 = 243373$.

Then, the client sends the the $(u, h_2) = (974610811710997, 243373)$, to the ID Server, where the ID Server will need to authenticate the client. The function h_2 will be have a Pentor Attack with the Pentor operator $p_u = 4$ and according to the Pentor Attack algorithm, in the end a value is gained to store on the variables pa .

The Pentor Attack will happen as following:

$$\begin{array}{r} 243373 \leftarrow 4 \\ + \quad 12 \\ \hline 24349 \leftarrow 4 \\ + \quad 36 \end{array}$$

$$\begin{array}{r} \text{---} \\ 2470 \leftarrow 4 \\ + \quad 0 \\ \hline 247 \leftarrow 4 \\ + \quad 28 \\ \hline 52 \leftarrow 4 \\ + \quad 8 \\ \hline 13 \leftarrow 4 \\ + 12 \\ \hline 13 \end{array}$$

So, the variable is $pa = 13$.

Now, this value must be fully versatile with $n_u = 13$, and if it is than the ID Server has authenticated the client and the client will gain access to the system, otherwise the system will reject the request.

In our concrete case we will have the following result:

$$n_u | pa \\ 13 | 13$$

which means that the ID Server has authenticated the client and gives access to the relevant client system.

VI. CONCLUSIONS

In this paper we have presented a completely new cryptographic algorithm as well as cryptosystem that use this algorithm for online user authentication. From the numeric examples it has been shown that the cryptosystem fully works and can be implemented in many applications where highly secured user transactions required.

Other important aspect is that the authentication does not need an encryption key for the process itself, but it can be used additionally for line security (encryption) considering that user might use regular unsecured internet line.

The future work would involve creating an online user authentication page that would use our proposed algorithm in real life applications. Some work has already started and results will follow soon.

REFERENCES

- [1] S.L. Garfinkel, E-mail based authentication and identification: an alternative to PKI. IEEE Comput. Soc. 1(6), 20–26 (2003).
- [2] M. Dietz, A. Czeskis, D.S. Wallach, D. Balfanz, Origin-bound certificates: a fresh approach to strong client authentication for the web, in Proceedings of the 21st Usenix Security Symposium, 2012.
- [3] M. Hern, An update on our war against account hijackers. The Google Blog (2013). Available via GOOGLE Online Security. <http://googleonlinesecurity.blogspot.com/2013/02/an->

- update-on-our-war-against-account.html of subordinate document. Cited 15 June 2013.
- [4] S. Balaji, Authentication techniques for engendering session passwords with colors and text. *Adv. Inf. Technol. Manage.* 1(2), 71–78 (2012).
- [5] H. Zhao, X. Li, S3PAS: a scalable shoulder-surfing resistant textual-graphical password authentication scheme, in 21st International Conference on Advanced Information Networking and Applications Workshops (AINAW 07) (2007), pp. 467–472.
- [6] S. Anand, P. Jain, Nitin, R. Rastogi, Security analysis and implementation of 3-level security system using image based authentication, in *Computer Modelling and Simulation (UKSim)* (2012), pp. 547–552.
- [7] H.A. Dinesha, V.K. Agrawal, Multi-level authentication technique for accessing cloud services, in *International Conference on Computing, Communication and Applications (ICCCA)* (2012), pp. 1–4.
- [8] R. Rivest, A. Shamir, L. Adleman, A method for obtaining digital signatures and public-key cryptosystems. *Commun. ACM* 21(2), 120–126 (1978).
- [9] D. Boneh, Twenty years of attacks on the RSA cryptosystem. *Not. Am. Math. Soc.* 46(2), 203–213 (1999).
- [10] D.J. Wheeler, R.M. Needham, TEA, a tiny encryption algorithm. *Lecture Notes in Computer Science (LNCS)* (Leuven, Belgium: Fast Software Encryption: Second International Workshop), vol. 1008 (1994), pp. 363–366.
- [11] J. Kelsey, B. Schneier, D. Wagner, Related-key cryptanalysis of 3-WAY, Biham-DES, CAST, DES-X NewDES, RC2, and TEA. *Lecture Notes in Computer Science (LNCS)* vol. 1334 (1997), pp. 233–246.
- [12] A. Bogdanov, M. Wang, Zero-correlation linear cryptanalysis with reduced data complexity. *Lecture Notes in Computer Science (LNCS)* (Fast Software Encryption 2012), vol. 7549 (2012), pp. 29–48.
- [13] A. Luma, B. Ismaili, B. Raufi, Multilevel user authentication and identification scheme for email clients. in *Proceedings of the world congress on engineering, WCE 2013, 3–5 July 2013. Lecture notes in engineering and computer science, London, UK* (2013), pp. 1221–1225.
- [14] A. Luma, B. Raufi, New data encryption algorithm and its implementation for online user authentication, in *International Conference on Security and Management, (CSREA Press, USA, 2009)*, pp. 81–85.
- [15] A. Luma, B. Raufi, Xh Zenuni, Asymmetric encryption decryption with Pentor and ultra Pentor operators. *Online J. Sci. Technol. (TOJSAT)* 2(2), 9–12 (2012).
- [16] M. Hertzum, J. N. Christian, N. Jørgensen and M. Nørgaard, Usable Security and E-Banking: ease of use vis-a-vis security *J. Australasian Journal of Information Systems.* 11, 2, 2004.

COMPARISON OF MATURITY MODEL FRAMEWORKS IN INFORMATION SECURITY AND THEIR IMPLEMENTATION

ARTAN LUMA¹, BLERTON ABAZI², BESNIK SELIMI³, MENTOR HAMITI⁴

¹ South East European University, Tetovo/Macedonia, a.luma@seeu.edu.mk

² UBT, Prishtina/Kosova, blerton.abazi@ubt-uni.net

³ South East European University, Tetovo/Macedonia, b.selimi@seeu.edu.mk

⁴ South East European University, Tetovo/Macedonia, m.hamiti@seeu.edu.mk

Abstract - Data is the key element of most businesses today and the volume of data continues to grow by 50% a year, along with an increase in server numbers by 20% a year. Data center grows in the same way, the risk of data manipulation opportunities increases. Rapid development of information technology and the transformation of society and digital businesses has made the need for data security to grow tremendously. Nowadays we face with more and more information security challenges. Information security ensures that within the enterprise, information is protected against disclosure to unauthorized users (confidentiality), improper modification (integrity), and non-access when required (availability). Companies that are responsible for information security, continuously develop systems and update the existing systems in order to provide secure solutions on the market and as well to have system readiness from eventual attacks. Risk assessment, however, assumes risk measurement without it is difficult for organizations to identify or measure the level of risk and as such its exposure would undermine the organization's security. Organizations that have an undefined status in relation to risk measurement are potentially vulnerable to possible attacks. Risk assessment is directly linked to the metrics. To protect the system in advance we need to identify what to protect, what should we protect and how to protect it. Information security assessment allows an organization to "recognize itself" about their risk exposures. Our main research goal on the paper is to provide a comparison and new approach to the frameworks of maturity model in the field of information security.

Keywords - information security, maturity model, confidentiality, risk assessment, framework.

I. INTRODUCTION

ALMOST all the software, that are launched in the market possess new and special features, but at the same time they carry with them several weaknesses that can be harmful. The above-mentioned problems cannot be fixed quickly, taking into account the complexity of such systems, where changes within the system structure need to be verified if it can affect some other part of the system. In recent years, we have

had a huge increase in the use of cloud services, which has made the gap between internal and external networks almost disappear.

Once security and risk requirements have been identified and risk management decisions have been taken, appropriate controls must be selected and implemented to ensure that risks are reduced to an acceptable level. The controls can be selected or can be designed to meet the specific needs of each case. The selection of security controls is dependent on organizational decisions based on the criteria for risk acceptance, risk treatment options, the overall risk management approach to be applied to the organization and should also be subject to all legislation and relevant national and international rules. Controls can be considered as guiding principles for information management security and are applicable to most organizations. Risk assessment, however, is a model of risk measurement without which for organizations is difficult to identify or measure the level of risk and as such its exposure would undermine the organization's security. For this reason, I consider that the first step to determining the necessary protection measures from the information system is the process of risk identification and controls, as processes that helps detect, correct and prevent cases of unauthorized attacks or attempts at the organization's information. Risk identification is an important step in risk management, to determine what could cause a potential loss, and to gain insight into how and why the loss might happen. Thus, if a corporation expects to perform risk assessment successfully, finding the appropriate threat and vulnerability pair of each asset is a crucial step. However, in the process of identifying threat and vulnerability pairs, it is difficult for the risk assessor, especially one who lacks information security competence, to recognize the feasible combinations [1].

The main data security objectives are structurally based on confidentiality, integrity and availability (see Figure 1 – CIA Triad Model.) [2]–[4]. Confidentiality means that the assets of a computing system are accessible only by authorized parties. The type of access is read-type access: reading, viewing,

printing, or even just knowing the existence of the information. Confidentiality is sometimes called secrecy or privacy. Integrity means that assets can be modified only by authorized parties or only authorized ways. In this context, modification included writing, changing, changing status, deleting and creating of the information. Availability means that assets are accessible to authorized parties. An authorized part should not be prevented from accessing objects to which he or she has legitimate access needs. A perfect system could preserve perfect confidentiality by preventing everyone from reading a particular information. However, this does not meet the requirement of availability for proper access. Availability is known by its opposite, denial of service [3].

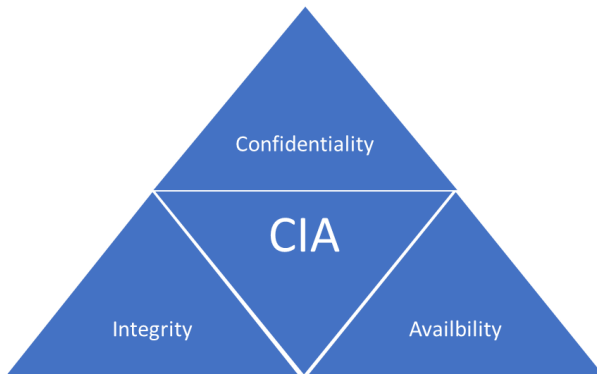


Figure 1 – CIA Triad Model.

II. MATURITY MODELS

Recently, we have seen a growing trend towards the collection personal data from the private and public sector [5]. This can be described also from the highly use of the social media networks through which people share many information's either from their private life, professional activities or other important events. Some organizations who operates with many services, thinks that using single sign-on (SSO) techniques as an authentication process service that permits a user to use one set of login credentials (e.g., name and password) to access multiple applications increases the efficiency and time on their daily operations. Using Single sign-On authentication (SSO) creates the ideal opportunity for your data to be easily distributed from one organization to another [6]. Additionally, the growing trend in cloud computing, which is seen as more secure for storage of data, creates the opportunity for everybody and organizations to extract information from their services or lives. In the technical aspect, the cloud platform is nothing more than storing data on another computer. However, it is challenging to create or use a security model if we do not have a method in advance to evaluate our needs in order to select the most suitable model for our organization. There are several maturity models for risk assessment in information security that could be adapted and implemented in any organization. Large organizations usually have in place several risk assessment processes at the same time. Those risk

assessment processes are decentralized from management and led by departments. For this reason, the need to create a centralized system of risk assessment across different processes and in this case in the field of information security is necessary. The centralization of the process enables the creation of more accurate reports through which we could identify potential threats and vulnerabilities within our system.

III. SECURITY MATURITY MODELS

Propose model for security maturity:

Model	Description of Levels	Focus areas
SSE-CMM	<ol style="list-style-type: none"> 0. Not performed 1. Performed informally 2. Planned and tracked 3. Well defined 4. Quantitatively controlled 5. Continuously improving 	Security engineering and software design
COBIT Maturity Model	<ol style="list-style-type: none"> 0. Non-existent 1. Initial / ad-hoc 2. Repeatable but intuitive 3. Defined process 4. Managed and measurable 5. Optimized 	Auditing of procedures
NIST Maturity Model	<ol style="list-style-type: none"> 1. Policy 2. Procedure 3. Implementation 4. Testing 5. Integration 	Checks level of Documentation

IV. SSE-CMM

The System Security Engineering – Capability Maturity Model (SSE-CMM) model is a security maturity model that adopts a context similar to the Capability Maturity Model Integration. SSE-CMM, like any other CMM tool, is designed to improve the process such as selecting contractors, etc. But, most importantly, it is oriented to bring a new approach on a cost-cutting solution. SSE-CMM has six maturity levels and is defined on three process areas with a number of processes / activities under each one. These process areas are the domain of the process of engineering and organization. It is worth identifying that the main focus of SSE-CMM is to improve system security engineering, especially during purchase process. It has barely considered some critical aspects of information security, such as human factor and ongoing risk management.

V. COBIT

According to [7] COBIT is considered as a risk-management based framework. COBIT is classified as an IT

Governance framework which consists of four main domain such as: Plan and Organize (PO), Acquire and Implement (AI), Deliver and Support (DS) and Monitor and Evaluate (ME). Each domain has different controls and for this reason organizations consider to use all the COBIT framework or in some cases to adapt specific controls which can fulfil their needs. Because COBIT controls are mainly related to the governance of business objectives, organizations usually point standards such as ISO 2700\0 to integrate it along with COBIT and maximize security controls [8].

VI. NIST

National Institute of Standards and Technology (NIST) maturity model focuses on documentation of procedures [9], [10]. This NIST framework is defined on five maturity levels such as: Policy, Procedure, Implementation, Testing and Integration in which the information security is considered as a risk that is managed through the enterprise risk management process. According to this we have identified the NIST framework as a risk-based framework [11]. The focus area of NIST maturity model is to check the level of documentation [12], [13]

VII. CONCLUSION

The results of this research clearly showed that there are metrics that can assess the security implementation in the organization. However, the use of a qualitative approach involves various disadvantages and is often criticized for being subjective and lacking criteria to judge the reliability and relevance of the results.

Future research needs to be undertaken to carry out best practices in security implementation using a qualitative and quantitative combined research. Quantitative work will be undertaken to demonstrate the effectiveness of the proposed model. A poll will be distributed to various organizations and the result will be published in the near future.

This best practice model can be considered a maturity model which implies a complete system with continuous improvement. The purpose of the proposed solution is to provide an organization with a way to conduct a self-study of its security implementation. There are five levels of compliance and each level consists of goals. An organization that constantly measures and controls its security implementation will reach the highest level and achieve security objectives.

Full compliance with the specified model is characterized by controlling the organization's security needs, monitoring the systems, being aware of threats and benchmarking by comparing the organization itself with other similar organizations and international standards.

REFERENCES

- [1] Y. C. Wei, W. C. Wu, and Y. C. Chu, "Performance evaluation of the recommendation mechanism of information security risk identification," *Neurocomputing*, vol. 279, pp. 48–53, 2017.
- [2] M. G. Solomon and M. Chapple, *Information Security Illuminated*. USA: Jones and Bartlett Publishers, Inc., 2005.
- [3] E. Maiwald et al., *Security Planning & Disaster Recovery*. 2002.
- [4] J. McCumber, *Assessing and Managing Security Risk in IT Systems: A Structured Methodology*, 1st ed. Boston, MA, USA: Auerbach Publications, 2004.
- [5] M. Talabis and J. Martin, *Information Security Risk Assessment: Risk Assessment*. 2012.
- [6] T. Bazaz and A. Khaliq, "A Review on Single Sign on Enabling Technologies and Protocols," *Int. J. Comput. Appl.*, vol. 151, no. 11, pp. 975–8887, 2016.
- [7] a Wiesmann, a Van Der Stock, M. Curphey, and R. Stirbei, "A guide to building secure web applications and web services," *The Open Web Application Security Project*, 2005. [Online]. Available: <http://scholar.google.com/scholar?hl=en&btnG=Search&q=intitle:A+Guide+to+Building+Secure+Web+Applications+and+Web+Services#2>.
- [8] M. Wolden, R. Valverde, and M. Talla, "The effectiveness of COBIT 5 information security framework for reducing cyber attacks on supply chain management system," *IFAC-PapersOnLine*, vol. 28, no. 3, pp. 1846–1852, 2015.
- [9] X. Y. Ge, Y. Q. Yuan, and L. L. Lu, "An information security maturity evaluation mode," *Procedia Eng.*, vol. 24, pp. 335–339, 2011.
- [10] A. Johnson, "Guide for Security-Focused Configuration Management of Information Systems," *Nist*, no. August, pp. 1–88, 2011.
- [11] NIST, "Framework for Improving Critical Infrastructure Cybersecurity," *Natl. Inst. Stand. Technol.*, pp. 1–41, 2014.
- [12] D. a. Chapin and S. Akridge, "How Can Security Be Measured?," *Inf. Syst. Control J.*, vol. 2, pp. 43–47, 2005.
- [13] S. Woodhouse, "An ISMS (Im)-Maturity Capability Model," in *2008 IEEE 8th International Conference on Computer and Information Technology Workshops*, 2008, pp. 242–247.

Comparative Study on Automatic Speech Recognition

A.MAHMOOD¹ and E. KAYA¹

¹ Konya Technical University, Konya/Turkey, janamohammed22@gmail.com

¹ Konya Technical University, Konya/Turkey, ersinkaya@selcuk.edu.tr

Abstract - Speech is a tool used as a means of communication between society. Along with the developing technology, various methods have been proposed to enable people to communicate and interact with the machines. In this study, Mel Frequency Cepstral Coefficients and Pitch Feature were obtained from the data set consisting of ten classes with different speakers. The obtained features were compared with classification achievements using k-Nearest Neighbor (KNN), Decision Tree (DT) and Quadratic Discriminant Analysis (QDA) classifiers. Furthermore, sensitivity of classifiers used with different numbers of training data is presented.

Keywords – Speech Recognition, Mel Frequency Cepstral Coefficients, k-Nearest Neighbor, Decision Tree, Quadratic Discriminant Analysis.

I. INTRODUCTION

SYSTEM development work for speech recognition with the machine started for the first time in the 1950s. In those years, various researchers put forward their first ideas on sound-dispersion and sound-science. A separate digit recognition system was developed for a single speaker at Bell Laboratories [1]. Another independent study was conducted at RCA Laboratories [2]. This study was a study of recognition of 10 different syllables belonging to a single speaker. In England, a speech recognizer was capable of recognizing 4 voices and 9 silences in the UCL was developed [3]. In this study, a spectrum analyzer and a pattern matcher were used to make the recognition decision. Another study was done at MIT Lincoln Laboratories [4].

In the 1960s, a number of basic ideas on speech recognition emerged and were published. The first study in was a voice recognition device in the Radio Research Laboratories [5]. In Japan, a vocal cognitive hardware was also implemented at Kyoto University [6]. One other approach that has been proposed as a speech recognition work with machine was dynamic monitoring of sound units, which is proposed for recognizing continuous sound fields [7]. At similar dates in the Soviet Union, dynamic programming methods for timing (fitting) on a pair of voice expressions were proposed [8].

In the 1970s, many successful and important studies were carried out, which could be considered turning points for speech recognition. Speech recognition studies were applied in

Russia [9] as a feasible technology and also in Japan [10] and in United States [11]. Russian researchers have helped to improve the use of pattern recognition in speech recognition, Japanese researchers have shown how successful dynamic programming methods can be applied to speech recognition, and US research has shown that Linear Predictive Coding (LPC) can be successfully applied for speech recognition it showed.

Many researches and studies related to speech recognition have been made in the literature. M. Karakaş, Mel Frequency Cepstral Coefficients and Dynamic Time Bending algorithms were used on MATLAB to obtain 88.5% average accuracy and 82% average accuracy with independent of the speaker using the "OPEN", "CLOSE", "START" and "STOP" classes [12]. Fezari et. al. used RSC 364 card for speech recognition and PIC 16F876 as microprocessor. Experiments with regular and irregular speech in the laboratory, with regular and irregular speech outside the laboratory, resulted in average success rates of 85%, 73%, 78% and 65%, respectively [13]. M. Hrnar developed a structure named EllaVoice using the zero crossing point and the improved dynamic time bending algorithms. Improved description of the Dynamic Time Bending structure means that the distance difference between the reference vector and the input vector is limited to the maximum value. Satisfactory accuracy value has been reported [14]. B. Öztürk and et. al. designed in MATLAB Simulink and installed on the C6713 DSK speech recognition board. Accuracy over 80% in the recognition of the letters "a", "e" and "i" has been achieved [15]. R. Phoophuangpairoj proposed multiple HMM voice recognition system. The system used consists of acoustic model, spelling dictionary, robot command grammar, recognition of robot command, and combining results of speech recognition algorithms. An average of 98% accuracy was achieved with a system developed using three different user groups, sex-linked, sex-independent, and sex-known [16]. Z. Jiang and et. al. applied Mel Frequency Cepstral Coefficients and Artificial Neural Networks algorithms in the security biometric recognition system. The recognition accuracy rate for 10 people in the simulation environment on MATLAB was found to be 99% [17]. G. Babui and et. al. implemented Mel Frequency Cepstral Coefficients and joint vector approach algorithms to design the navigator tool. Approximately 100% success has been achieved in working out the approximate results with the Hidden Markov Model

[18]. B. Bolat and et. al. used Square root mean error (RMS) and statistical neural networks algorithms. In experiments with 50 speech and 100 music data, an average success rate of 91% was achieved [19]. P. Leechor and et. at. designed Visual Basic 6 user interface used the Hidden Markov Model user kit. In a noisy environment, when a remote controlled car is controlled by speech commands, it achieves 98% accuracy success, while in a noisy room it is reduced by up to 44% [20]. V. A. Petrushin used Artificial Neural Networks algorithm for speech recognition. Based on the calls made to the call center in the study, 30 people tried to test 5 different emotions and achieved 70% success [21]. N. Öztürk and et. al. used Microsoft Visual Basic 6.0 programming editor. A robot design that can move through the voice command with the generated system has been successfully completed [22].

This paper begins with Introduction in Section I. In the section II, material and method are explained. Section III consists of experimental results. Finally, IV. In the section, the results obtained are evaluated.

II. MATERIAL AND METHOD

A. Mel Frequency Cepstrum Coefficients (MFCC)

Mel Frequency Cepstrum Coefficients (MFCC) is based on a known variation of the human ear's critical band frequency. With low-frequency linearly filters placed logarithmically at high frequencies, fractions containing phonetic characteristics of the voice can be captured. This is called the Mel Frequency Scale. MFCC is distributed as linearly in below 1 kHz and logarithmically in above 1 kHz.

B. k-Nearest Neighbor (KNN)

With today's surplus data size, it has become almost impossible for obtaining meaningful results in a short period of time. For this reason, a number of algorithms have been developed to automate the data evaluation process and discover the similarities of random raw data sets.

K-Nearest Neighbor (KNN) is a nonparametric and simple learning algorithm. As a result of having a nonparametric algorithm, it cannot be made no assumptions in the basic data distribution. This is an important advantage. Because, many of the practical data do not conform to the theoretical assumptions made. In addition, KNN does not use training data to generalize. Also, training phase is pretty fast. KNN maintains all training data and decides based on the training data set. KNN is based on the determination of distances between an unknown object and each object of the training set.

KNN assume data in feature space. Moreover, it evaluates data in metric space. The data are in the form of scalar or multidimensional vectors. Since points are in feature space, there is a concept of distance. Methods such as Minkowski, Euclidean and Manhattan are frequently used to calculate this distance.

Minkowski distance is a generalized distance calculation method. Mathematically expressed by Equation 1.

$$D_{Min}(x, y) = \left(\sum_{i=1}^n |x_i - y_i|^p \right)^{\frac{1}{p}} \quad (1)$$

Euclidean distance is a special case of Minkowski measure set to $p = 2$. Mathematically expressed by equation 2.

$$D_{L2}(x, y) = \sqrt{\sum_{i=1}^n (x_i - y_i)^2} \quad (2)$$

Manhattan distance is set by setting a special state of the Minkowski measure to $p = 1$. Mathematically expressed by equation 3.

$$D_{Man}(x, y) = \sum_{i=1}^n |x_i - y_i| \quad (3)$$

C. Decision Tree (DT)

Many decision trees in science of applied statistics have been developed under heading of machine learning algorithm. There are many learning methods that enable the decision tree to be formed by taking advantage of sample set.

It is very important to select algorithm for designing decision tree. The algorithm used depends on the tree structure. Therefore, different tree structures produce different rules while performing the classification process. Algorithms developed based on decision trees are separated from each other in terms of the root node and the other nodes, but they are similar or similar to each other in some points.

Decision trees use the best order by performing many tests to guess the target variant. The basic algorithm steps used in decision trees are similar. Initially, the root node is created. If all the instances belong to the same class, the node becomes a leaf, otherwise it is split and a branch is created. The branches cause other tests to take place and the test is terminated on leaves. The same algorithms are used in each section of the samples. Generally, categorical variables are used, if they are transformed into categorical.

D. Quadratic Discriminant Analysis (QDA)

Discriminant analysis is a statistical technique that allows a researcher to study the differences between two or more sample groups according to various variables at the same time. In general, some mathematical equations are used to group units. These equations, called the discriminant function, are used to determine the common characteristics of the groups, allowing them to identify the groups most similar to each other. The characteristics used to distinguish the groups are called discriminant variables. Briefly, discriminant analysis is the process by which discriminants of two or more groups are revealed by means of discriminant variables. It is a broad concept involving several statistical approaches closely related.

There are two basic functions of discriminant analysis such as linear discriminant analysis and quadratic discriminant analysis and classification (predictive discriminant analysis). It

is also necessary to first perform stepwise discriminant analysis in order to determine the variables that should be modeled to distinguish two (two group discriminant analysis) or more (multiple discriminant analysis) groups and which will contribute significantly to the discriminant.

E. Proposed Method

Initially, windowing was applied on speech data and then, MFCC features were extracted as in Figure 1.

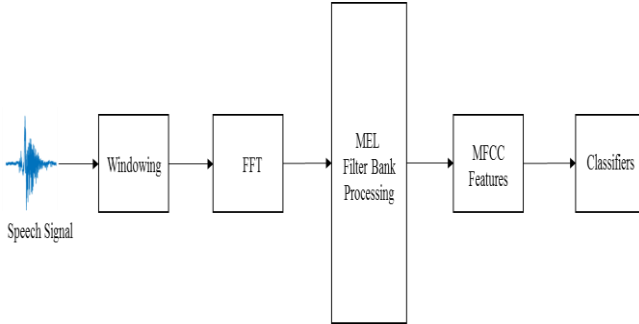


Figure 1: Proposed Method.

The purpose of feature extraction is to obtain a parametric symbol with a very small data size from the speech signal wave. This is often referred to as signal processing front-end. Speech signal changes in slow time rate. When examined in a sufficiently short period (5-100 ms.), characteristic is quite stable. However, when examined over long time periods (200 ms and higher), signal characteristic is beginning to include other speech sounds.

With windowing, the discontinuous parts of beginning and end of the signal are minimized. The main goal is to use the window to truncate parts without information at the beginning and end of the frames, thereby preventing spectral distortion. If the window $w(n)$, $0 \leq n \leq N-1$, N is accepted as the number of samples in each frame. Signal is windowed;

$$y_1(n) = x_1(n)w(n), \quad 0 \leq n \leq N-1 \quad (4)$$

Hamming Window used in proposed system is;

$$w(n) = 0.54 - 0.46 \cos\left(\frac{2\pi n}{N-1}\right), \quad 0 \leq n \leq N-1 \quad (5)$$

The next step is to apply Fast Fourier Transform (FFT) to transform the N samples of each frame into frequency domain from time domain. FFT is a fast algorithm for applying Discrete Fourier transform (DFT). Recent studies show that human perception of frequency content does not occur on a linear scale. Thus, a subjective scale called the "mel" scale is calculated for each sound of frequency f . 1 kHz sound which taken as a reference point is defined as 1000 mHz above the human hearing threshold.

One way to simulate this subjective spectrum is to use a uniformly placed filter bank on a mel scale. This filter bank is a bank that passes triangular band and is bounded by the interval and band width fixed mel frequency. The spread and bandwidth have a constant range of mel frequencies as in

Figure 2.

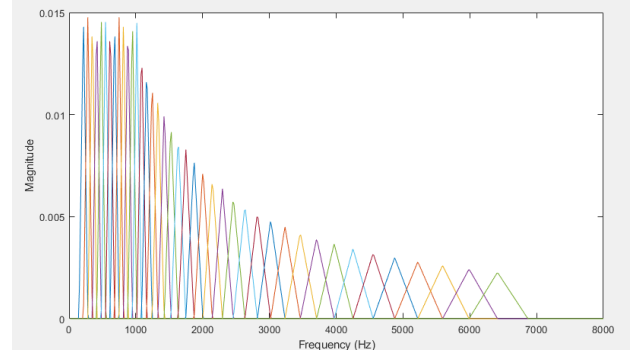


Figure 2: MEL Filter Bank.

Application of filter bank is implemented to frequency domain by FFT. Each filter in this mel transformer filter bank forms a histogram box in the frequency domain. At this last stage, the logarithmic mel spectra must be converted back to the time domain from the frequency domain. The result is called Mel Frequency Cepstrum Coefficients. In the analysis of the given frame, cepstral representation very well represents and depicts regional spectral features of signal. Since Mel Spectrum Coefficients and its logarithm are real numbers, it is possible to convert them into time domain by Discrete Cosine Transform (DCT). The result of the last step, mel power spectrum, can be expressed as S_k , $k = 1, 2, 3, \dots, K$.

Hamming Window used in proposed system is;

$$c_n = \sum_{k=1}^K (\log S_k) \cos\left[n\left(k - 0.5\right)\frac{\pi}{K}\right], \quad n=1, 2, 3, \dots, K \quad (6)$$

C_0 coefficient is not considered. Because it contains the average value of the input signal, it contains very little information about the identity of speaker. Briefly, a set of MFCCs is calculated for each speech frame superimposed on each other for a duration of 30 ms. Cosine transform of the logarithm of the short-term power spectrum defined in the Mel frequency scaling gives this result. This coefficient set is called an acoustic vector. That is, input audio signal is converted into acoustic vectors. The obtained MFCC acoustic vector classifiers are given as inputs. K-Nearest Neighbor, Decision Tree and Quadratic Discriminant Analysis are used as classifier.

III. EXPERIMENTAL RESULTS

In this study, speech dataset was obtained from CMU Audio Databases. 125 speech records of 5 female and 5 male with totally 10 different people were used. These records contain different letters, numbers and words belonging to related person.

MFCC feature extraction and classifiers run with Intel Core (TM) i7-7700 HQ CPU @ 2.8 GHz processors, and 4 GB RAM with 1 GB GDDR4 GeForce supported system memory with nVIDIA 1050 TI graphics card is used.

A different number of training and test data were used to perform sensitivity analysis of classifiers. Training and test data were divided into 10/115, 19/106, 29/96, 48/77 and 67/58 respectively. The main purpose of this analysis is to examine performance of classifiers and their behavior with many test data records. The results obtained are given in Table 1.

Table 1: Accuracy and Time Consumption Results of MFCC+Classifiers

Feature	Number of Training Records	Number of Test Records	KNN	DT	QDA
MFCC	10	115	%55.65	%54.78	%52.17
	19	106	%84.90	%79.24	%83.01
	29	96	%96.87	%86.45	%96.87
	48	77	%98.70	%94.80	%98.70
	67	58	%100	%89.65	%98.77
	Time Consumption (sec)		24.83	16.88	14.54

In Table 1, accuracy rates are generally increased with increase in total number of training records. In conclusion, it shows that classifiers accuracy is related to the number of training data. The highest classification accuracy belongs to KNN classifier with training / test Records (67/58) and 100%. After that QDA with 98.77% and DT with 89.65%. The lowest classification success belongs to QDA classifier with training / test Records (10/115) and 52.17%. When time consumption is taken into consideration, QDA has the lowest time consumption with 14.54 sec. KNN has the longest time consumption with 24.83 sec, although it has the highest classification accuracy rate.

IV. CONCLUSION

Classifiers are quite useful algorithms for speech and pattern recognition problems. This study shows that classifiers are highly useful in recognizing speech and have high recognition ability. The proposed classifiers based on statistical methods. In this study, KNN classifier have resulted in better speech recognition rates in our proposed three different classifiers. However, KNN classifier is slower in training and testing stages than other classifiers. Speech recognition has a lot of usage and application area and attracts many researchers. With this study, it is expected that the effects of the classifiers on the speech recognition can be seen and benefit the research groups working on Automatic Speech Recognition.

REFERENCES

[1] Davis, K. H., Biddulph, R. and Balashek, S. (1952) Automatic Recognition of Spoken Digits, Journal of the Acoustic Society of America, 24 (6): 637-642.
 [2] Olson, K. H. and Belar, H. (1956) Phonetic Typewriter, Journal of the Acoustic Society of America, 28 (6): 1072-1081.
 [3] Fry, D. B. (1959) Theoretical Aspects of Mechanical Speech Recognition, Journal of the British Institution Radio Engineers, 19 (4): 211-229.

[4] Forgie, J. W. and Forgie, C. D. (1959) Results Obtained From a Vowel Recognition Computer Program, Journal of the Acoustic Society of America, 31 (11): 1480-1489.
 [5] Suzuki, J. and Nakata, K. (1961) Recognition of Japanese Vowels-Preliminary to the Recognition of the Speech, Journal of Radio Research Lab., 37 (8): 193-212.
 [6] Sakai, T. and Doshita, S. (1962) The Phonetic Typewriter, Information Processing, Proceedings of IFIP Congress, Munich, s.445-450.
 [7] Reddy, D. R. (1967) Computer Recognition of Connected Speech, Journal of the Acoustic Society of America, 42: 329-347.
 [8] Vintsyuk, T. K. (1968) Speech Discrimination by Dynamic Programming, Kibernetika, 4 (2): 81-88.
 [9] Velichko, V. M. and Zagoruyko, N. G. (1970) Automatic Recognition of 200 Words, International Journal of Man-Machine Studies, 2: 223.
 [10] Sakoe, H. and Chiba, S. (1978) Dynamic Programming Algorithm Optimization for Spoken Word Recognition, IEEE Transactions on Acoustics, Speech and Signal Processing, ASSP-26 (1): 43-49.
 [11] Itakura, F. (1975) Minimum Prediction Residual Applied to Speech Recognition, IEEE Transactions on Acoustics, Speech, Signal Processing, ASSP-23 (1): 67-72.
 [12] M. Karakaş, "Computer Based Control Using Voice Input", Yüksek Lisans Tezi, Dokuz Eylül Üniversitesi, Eylül 2010.
 [13] M. Fezari, M.B. Salah, "A Voice Command System for Autonomous Robots Guidance", IEEE AMC-06 0-7803-9511, 2006.
 [14] M. Hrnčar, "Voice Command Control for Mobile Robots", Department of Control and Information Systems Faculty of Electrical Engineering University of Zilina, 2000.
 [15] B. Öztürk, T. Çakar, "Gerçek Zamanlı Ses Tanıma", Bitirme Projesi, İstanbul Üniversitesi Mühendislik Fakültesi Elektrik/Elektronik Mühendisliği Bölümü, Haziran 2007.
 [16] R. Phoophuangpaioj, "Using Multiple HMM Recognizers and the Maximum Accuracy Method to Improve Voice Controlled Robots", International Symposium on Intelligent Signal Processing and Communication Systems (ISPACS), December 2011.
 [17] Z. Jiang, H. Huang, S. Yang, S. Lu, Z. Hao, "Acoustic Feature Comparison of MFCC and CZT based Cepstrum for Speech Recognition", 2009 Fifth International Conference on Natural Computation, 2009.
 [18] G. Babui, H. Kumar, P.T. Vanathi, "Performance Analysis of Hybrid Robust Automatic Speech Recognition System", IEEE 978-1-4673-1318-6, 2012.
 [19] B. Bolat, Ü. Küçük, T. Yıldırım, "Aktif Öğrenen PNN ile Konuşma/Müzik Sınıflandırma", Akıllı Sistemlerde Yenilikler ve Uygulamaları Sempozyumu, ASYU-INISTA, 2004.
 [20] P. Leechor, C. Pompanomchai, P. Sukklay, "Operation of a Radio Controlled Car by Voice Commands", 2010 2nd International Conference on Mechanical and Electronics Engineering (ICMEE 2010), 2010.
 [21] V.A. Petrushin, "Emotion in Speech Recognition and Application to Call Centers", Andersen Consulting.
 [22] N. Öztürk, U. Ünözkan, "Microprocessor Based Voice Recognition System Realization", IEEE, 978-1-4244-6904-8/10, 2010.

Project Development with Service Oriented Architecture

R. SARAÇOĞLU¹ and E. DOĞAÇ²

¹ Van Yüzüncü Yıl University, Van/Turkey, ridvansaracoglu@yyu.edu.tr

¹ Van Metropolitan Municipality, Van/Turkey, emine.dogac@gmail.com

Abstract - In organizations that have more than one automation system, the modules / functions of the applications should be able to be used by other applications. The use of a service-oriented architecture (SOA) approach, which is designed to achieve this, is the focus of this study. It is important to simplify and standardize the automation services given to organizations. specific solutions to organizations should be modelled / analyzed easily. If more than one institution or organization is hosted in the same database, it is possible to reduce costs by using service-oriented architecture. It is ensured that the Information Technology (IT) departments of organizations increase their dominance over automation. In this way, the infrastructure will be created to support the production of new projects within the Corporation. With the programs of different companies within the institution and organization, it is ensured that integration opportunities are created in an independent manner.

Keywords - Information technology, service-oriented architecture, software development

I. INTRODUCTION

IN institutions and organizations, IT has long been perceived as a cost item, in which operating resources are transferred. Generally, the recycling of the investment was positive. Significant benefits have been achieved in terms of automating standard processes such as accrual, collection, order, workflow personnel and public relations, scaling and efficiency. The piles of paper and staff are replaced by high-capacity, regular and stable mainframe and servers. In a less or controllable environment, this was a problem without problems. On the other hand, in the institutions that wanted to adapt to the changing world and markets, large and accelerated changes started to push IT. Difficult to manage, using different technologies and company products, broken segments, functions, new data silos began to emerge. It is also difficult to access these new data silos within the new projects that IT will create, so for every new job, it must re-create rules engines, re-interface, re-analyze and re-create data silos. While the amount of investment in IT increases, recycling begins to decrease. IT creates a costly perception rather than a value-creating institution.

Flexibility and agility are the basic requirements for responding to changing needs within institutions and organizations and to have a true demand-based structure. These two vital features can find the first answer in the IT

world with the concept of SOA.

The communication between the automation of SOA-generated software and heterogeneous structures is ensured. Dynamic reconfigurable services are accessed individually. At the same time, demand-based solutions are created for unified business problems that come together with other services. With the automation of SOA technology, each thread is designed as the methods of a service. it can also be integrated into other projects of organizations. By converting small threads into services, a reusable structure is obtained. For this reason, maintenance costs are reduced to very low levels. The database layer is accessed only through the security protocols of the services to ensure maximum security. it allows IT to access the database and frees itself from large and independent data silos.

II. SERVICE ORIENTED ARCHITECTURE

Software architecture is one of the cornerstones of the software development process as it shows the main structure of a system and considers the needs of each stakeholder [1].

The basic idea of SOA is service. The service is defined as a discrete unit of the business functionality that can be done with the service agreement. The service agreement specifies the interaction between the service provider and the service user. These are:

- Service interface
- Interface document
- Service rules
- Quality of service (QoS)
- Performance [2].

A. Definition of SOA

SOA is an approach where different services are combined. In addition, by creating certain structures, it ensures the compatible operation of these services. So the service is in service.

Normally in multi-layered applications, one layer must always call another layer. In this approach, the hierarchy must be regular. To give a simple and classic example, let's assume that your project has a data layer and a business layer. The business layer calls the data layer, handles database operations, is unilateral and project-based. However, if you create the data layer as a service, it will not be single-sided and will allow use from anywhere. In this way, it does not matter where and / or

on which platform the application works. SOA eliminates dependencies in point-to-point integrations [3].

B. Purpose of SOA

In the long term, SOA aims to reduce the integration costs between the applications by using the services again and again by adopting the standards and increasing interoperability between the applications. It aims to create business processes using the services like lego stones and thus to realize their business needs faster when necessary [4].

C. Characteristics of SOA

Characteristics of SOA are follows:

- Services can be discovered.
- Services are self-contained and modular.
- Services can work together.
- Services are low dependent.
- Services have an addressable interface in the network.
- Services can be combined.
- SOA supports changes [5](Şenyurt, 2015).

III. RELATED WORKS

Beklen [6], in his work, has used a service-oriented architecture, implemented with his own rules in different fields such as finance, insurance and public. He stated that there is a need for detailed analysis and modeling to better identify the services. The fact that service-oriented architecture has been applied successfully for different sectors all over the world has also increased the maturity level of architecture. He stated that architecture has important advantages. because it uses methods-independent methods to solve problems with layers and uses platform-independent integration methods. Large scale software projects are developed by applying software engineering disciplines to solve different business problems in various sectors. However, each institution used different technologies and approaches in the infrastructure of applications. In some projects, applications were developed without using any architectural approach. Such situations cannot be integrated and integrated into one another, and are transformed into applications that are difficult to maintain, repeat, or connect to platforms. SOA, which aims to solve the application layers by isolating each other, examined the approach in sub-titles such as architecture, service and definition.

Channabasavaiah et al. [7], in their work, have put forward the idea that institution managers are pushing for more efficient use of corporate resources. They supported that SOA was one of the biggest solutions to this problem.

Üstündağ [8], in his study, to ensure the interoperability of existing enterprise applications and newly developed or purchased applications is one of the most invested areas of organizations. As a result of his work in the integration of systems with each other in a sample application developed with .Net and an existing SAP application. The number of applications that will interact with each other according to the size of the organization, the volume of business and the

complexity of its processes has increased. In view of this, it has been argued that the importance of developing such layers of integration as different layers can be better understood.

Srinivasan and Treadwell described the basic concepts, relationships and benefits of SOA as a new foundation for web services and service-oriented architecture [9].

Altınbaş [10], in his study, said that the purpose of service-oriented architecture is to combine the logical codes that can be used in common and open them to the use of other applications over a network in the service context. Naturally, in such a questioning, queries will be faster and more efficient. SOA is functionally located at the intersection of business processes and IT infrastructures. The importance of the work is to create access to design by using a service-oriented architectural approach. Because the use of service-oriented architecture in the project is that the Oracle platform can offer a complementary set of infrastructure services to service-oriented architecture. Similarly, the flexibility of business process automation as well as low cost and speed are among the advantages of this technology. In the same way, Oracle has been designed with a service-oriented architectural logic, and has advocated the convenience it provides for access to service-oriented architecture.

O'Brien [11], proposes the use of administrative activities, which are related to the scope, cost and effort estimation to be used in SOA projects during the management of an SOA project. In addition to technical, social, cultural and institutional aspects, the level of maturity as well as the experience of the organization were examined. The idea that the scope, cost and effort are tried to be taken into consideration by considering the types of SOA projects.

In another study that argues that a large SOA-based project is more successful with System Dynamics modeling methodology, it is aimed that SOA applications will benefit from this methodology [12]. System Dynamics is a methodology that examines and manages complex feedback environments such as business goals and social systems. In this study, various SOA scenarios were analyzed based on System Dynamics modeling. These different studies address the impact of SOA on the total impact of various factors and what kind of results they will give in the long term. They have identified two key features of SOA: rapid development and a high degree of reusability in many solutions textures and enhancements.

SOA is an architectural style for creating software applications using services offered in a network like web [13]. The applications in SOA are based on services. It encourages loose connection between services, so they can be reused. A service is an implementation of a well-defined business functionality, and such services can then be consumed by customers in different applications or business processes. Using SOA, businesses can achieve significant savings in development costs and can quickly adapt to changing business conditions by reusing and reusing existing services in the development of new applications. SOA has shown that it

provides better integration of enterprise IT resources, including previously isolated application silos and legacy systems.

For the flexibility and agility, the software desires, they need to be developed in a non-fragile, portable, uncomplicated, unnecessary repetition, easy to understand, regular and controllable structure [14]. SOA aims to minimize the impact of change. This structure is desirable to be applied very carefully and following a specific methodology after the objectives are thoroughly understood. Otherwise, it is thought that SOA may cause a used drug effect without being used. The useful parts of the old systems used in institutions before the transition to SOA were used in the newly developed SOA-based system. In this way, the old systems, which were obtained with great costs, were prevented from becoming completely useless. During the implementation of SOA, the importance of determining a choosing strategy is emphasized. After the determination of the conceptual services, it was decided to determine the strategies for the development of these services, to carry out technical and financial analysis among the strategies determined and to implement one of the strategies in line with these analyzes. It is argued that the likelihood of making mistakes in the decision stage is reduced. The importance of SOA management platform selection is emphasized while performing SOA-based service development and management.

Combining SOA and web services technology enables real enterprise application integration, because web services provide SOA applications with the ability to easily integrate applications written in a different programming language on a different operating system and placed on different hardware platforms.

As a result of all researches, it was seen that with SOA, more than one application can use the same layers over the same service. In this case, it is possible to make changes over a single service without interfering with client applications when a revision is required. The same infrastructure can be used for applications developed on different platforms. If an application has versions such as Windows, Linux, mobile, mac etc. the same infrastructure can be used for all of them. By hosting different layers of applications on different servers, easier management and performance can be ensured and the application development interface (API) can be created for the applications and the results can be integrated.

It is known that SOA facilitates the collection, organization and maintenance of enterprise solutions to respond quickly to changing requirements [15]. Re-usability is high in an application using SOA. Each service created can be re-used even in different projects. If there is a change in business requirements, the effect of this change on the application side is only available in this service. In other words, the relevant change is made only in this service and the applications using this service are not affected by the change much.

IV. CONCLUSION

In the long term, SOA helps to reduce integration costs between applications, shorten business processes and reduce economic costs. Most importantly, it prevents more code and write code again and again. Thanks to these features from the application principle of application virtualization, the information is delivered to the right users at the right time and speed. Thus, information security is also contributed very well.

By reducing the operating expenses to a great extent, the company will also have the opportunity to evaluate the savings it has made from there.

REFERENCES

- [1] B. Tekinerdoğan, *Software Architecture in Volume I. Computer Science Handbook*, 2nd Edition, CRC Press-Taylor and Francis Group, 2014.
- [2] T. Erl, *Service-Oriented Architecture: Concepts, Technology, and Design*, Prentice Hall PTR, ISBN: 0-13-185858-0, New Jersey, 2005.
- [3] K. Avci, SOA mimarisi nedir? Available: <https://www.kadir.xyz/yazi/60/soa-mimarisi-nedir/>, 2016
- [4] F. Hudayioğlu, SOA ve ESB nedir? Available: <http://turk-internet.net/portal/yazigoster.php?yaziid=14659/> 2006
- [5] S. B. Şenyurt, SOA Nedir? Available: <https://www.buraksenyurt.com/post/SOA-Nedir/>, 2015
- [6] A. Beklen, "Kurumsal Servis Odaklı Mimari Kavramı, Teknolojisi ve Tasarımı" Master Thesis, Science Institution, Maltepe University, İstanbul, 2009.
- [7] K. Channabasavaiah, K. Holley, M. T. Edward, "Migrating to a service-oriented architecture", *IBM Journal of Research Development*, 3-22, 2004.
- [8] S. Üstündağ, "Servis Odaklı Mimari", Master Thesis, Science Institution, Ege University, İzmir, 2006.
- [9] L. Srinivasan, J. Treadwell, "An Overview of Service-oriented Architecture, Web Services and Grid Computing", HP Software Global Business Unit, 2005.
- [10] S. Altınbaş, "Servis Odaklı Mimari Yaklaşımı Kullanılarak Ontoloji Temelli İlişkisel Veritabanlarına Erişim", Master Thesis, Science Institution, Ege University, İzmir, 2008.
- [11] L. O'Brien, A Framework for Scope, Cost and Effort Estimation for Service Oriented Architecture (SOA) Projects, *Australian Software Engineering Conference*, 2009.
- [12] JJ. Jeng, L. An, System Dynamics Modeling for SOA Project Management, *IEEE International Conference on Service-Oriented Computing and Applications (SOCA'07)*, 2007.
- [13] D. Çopur, "An Application of Service Oriented Architecture (SOA) Approach", Master Thesis, Science Institution, Başkent University, Ankara, 2011.
- [14] D. Herand, "Servis Odaklı Mimarinin (SOM) İş Süreçleri Üzerine Uygulanabilmesi için Bir Metodolojinin Geliştirilmesi", Master Thesis, Science Institution, Sakarya University, Kocaeli, 2013.
- [15] K. Dongsu, B. Doo-Kweon, Bridging Software Product Lines and Service-Oriented Architectures for Service Identification using BPM and FM, *9th IEEE/ACIS International Conference on Computer and Information Science*, 2010

Ultra-Low Cost Wireless Sensor Network Node Design for Educational Use

A.AKBAS¹

¹ University of Turkish Aeronautical Association, Ankara/Turkey, aakbas@thk.edu.tr

Abstract - Wireless Sensor Networks (WSN), as a popular hot topic, are attracting many researchers to investigate the challenges encountered during the deployment, operation or design phase of the wireless sensor networks. Hence, universities all around the world have already started undergraduate courses on WSNs and established WSN laboratories to practice the theoretical knowledge taught. In this paper, a design is proposed to meet the need for a WSN node for lab use, fulfilling design requirements of a wireless sensor node. Though WSN node designers usually focus on the energy efficiency to achieve maximum possible network lifetime, we have considered of secondary importance since the main goal is to achieve a WSN node design to practice the WSN strategies and protocols in lab environment at the lowest cost possible. In the paper, we present a novel WSN node design under \$10 for educational purposes employing ultra-low cost STM8S105C6 Microcontroller (MCU) of STMicroelectronics and Si4432 based RF transceiver.

Keywords - Wireless Sensor Networks, Sensor Node Design, STM8S105C6, Si4432, DRF4432F20

I. INTRODUCTION

WIRELESS Sensor Network is a group of dedicated sensor nodes spatially dispersed over a geographical region in large numbers to monitor and sense the physical or environmental conditions as temperature, humidity, pressure, light, vibration, pollution levels, wind speed and direction etc. [1]. Nodes operate autonomously to form an ad-hoc sensing network and collaboratively work to sense and send the data collected to sink node (i.e. base node where all data is gathered) directly or using neighboring nodes as hopping point to relay the data. Sink node further sends collected data via a gateway to control center. Control center may also query network by sending commands to base node to be broadcasted over the network [2].

II. RELATED WORK

There are a few number of WSN designs in the literature targeting educational purposes. Singh et al. [3] propose a solution suitable for use in educational environment to allow students to learn WSN basic concepts. This is an open source design based on 8051 architecture. Dikovic [4] et al. described their design criteria for educational usage, comparing a list of MCUs to be employed and discussed costs and complexities in their work. Though various designs and products are available in the market and literature [5-7], none of them have a goal to be used in labs for training and does not aim to be cost effective for total-cost of ownership.

III. NODE OVERVIEW

A typical WSN node (a.k.a. mote) consists of a microcontroller, a RF transceiver for communication and sensing circuitry and a power unit as illustrated in the Figure 1.

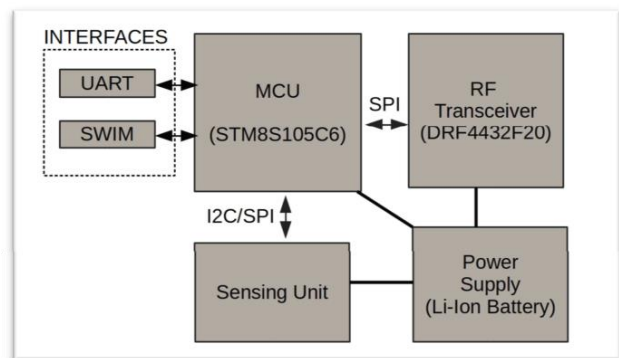


Figure 1: Internal connections of components.

As sensor nodes are deployed in large quantities, all WSN node designs focus on components to keep the costs low. For this reason, we have chosen components such that total cost of design will remain under \$10 USD. In the Figure 2, the WSN node designed is illustrated. Components are marked on the board in yellow. Units on the node are:

1. Microcontroller (STMicroelectronics STM8S105C6) [8]
2. SWIM Interface pins for software debugging and flash programming
3. RF Transceiver (DRF4432F20) [9]: SiLabs 4432 based RF transceiver module with 100mW output
4. Power Regulator
5. Honeywell HMC5883 Magnetic Sensor module [10]
6. Li-Ion Battery pack with 700mA capacity



Figure 2: WSN Node

The cost of materials used can be summarized on the Table 1.

Table 1: Bill of Materials

Unit	Description	Price
STM8S105C6	Microcontroller	0.80
DRF4432F20	RF Module	2.20
Power Supply	Li-Ion Battery Pack	2.00
Sensor	HMC5883 Magnetic Sensor module	2.00
Misc	PCB + Passive Components + Workmanship	2.00
	TOTAL (USD)	9.00

Prices given are FOB prices for 100+ pcs as sold at aliexpress.com.

IV. DESIGN CRITERIA

In the real world scenarios, harsh environments are considered for deployments that require many conditions to be met for the field usage but in the laboratory, we do not need to meet them all. WSN nodes are designed as energy-efficient battery-powered devices since it is usually neither possible nor practical to replace the batteries in deployed area. However, in lab, nodes will be re-used repeatedly and heavily, so we prefer to employ a widely available rechargeable cellular battery pack instead of disposable batteries to help prevent the environmental pollution. Moreover, these Li-ion batteries are even cheaper than standard AA-sized rechargeable batteries in addition to their higher capacity and relatively small size. For the selection of the processor to be employed in design, the widespread use and ultra-low cost of STM8S series taken into account. STM8S105C6 is 8-bit microcontroller device with up to 32 Kbyte Flash, integrated EEPROM, 10-bit ADC, and UART, SPI, I²C communication interfaces make it versatile for the WSN applications usage. 96-bit unique key for each device is ideal to identify nodes in the network. In addition, integrated EEPROM can be programmed with all the configuration information and application specific data. Flash program area is accessed via Single Wire Interface Module (SWIM) for easy programming. STM8S Discovery kits (sold at \$10) that STMicroelectronics has developed to help widespread use of STM8 devices have on-board ST-Link to use these kits as stand-alone programmers. Built-in SPI (Serial Peripheral Interface) and I²C (Inter-Integrated Circuit) buses help programmers to code easy and rapidly

with few lines of code. Furthermore, built-in buses run much faster than classical bit-banging style port driving. For the RF Unit, SiLabs 4432 based module has been chosen. Si4432 can be configured to operate at frequencies 315, 433, 868 and 915 MHz with choice of a few external components. Its built-in error recovery modes help error-free data transmissions. The module has 100mW RF power output capability that makes communication up to 1 km of outdoor distance possible.

V. HARDWARE DESCRIPTION

STM8S devices are designed to operate at voltage of 3.0V to 5.5V owing to on-chip power management that prevents the voltage drops to affect the mcu stability. Equipped with all necessary components as EEPROM, Flash program area, Analog-Digital Converter (ADC) on chip, STM8S105C6 saves valuable pin that leads to a smaller package size. Thanks to single pin SWIM interface that allows hardware debugging without any additional equipment and performs flash programming in seconds, STM8S really makes embedded code developing a breeze for everyone in lab environment. Sensor units can be connected to MCU via available I²C, UART or SPI buses. In the proposed design, HMC5883 based magnetic sensor is wired via I²C bus for illustration.

RF unit is connected to MCU over the built-in 4-pin synchronous SPI bus that simplifies the developers' job quite a lot. The high sensitivity (-121 dBm) and 20 dBm high power output make the module suitable for WSN applications. RF module has a Shutdown (SDN) input that setting SDN = 1 chip will be completely shut down the module in order to conserve power when the unit is idle waiting. Besides, MCUs are almost always idle, developer can code to force MCU to go into deep sleep mode and wake up by the interrupt from RF unit indicating that there is an incoming transmission to handle.

A. Firmware Description

The microcontroller on-board performs all the housekeeping duties including:

1. Collection and processing of the sensing data as received from sensor unit,
2. Processing and storing of data collected,
3. Transmission of generated data by the RF communication channel to sink node.

All data communication to and from the node is done via the DRF4432F20 RF transceiver unit. RF unit waits for incoming data when it is idle waiting and there is no ongoing transmission.

A base code template and library of sensor codes are prepared for students to use as guideline for their code developments. Basic codes have been implemented as library so that they are readily available to build up their projects with ease. Below pseudo-code from the library is given for illustration:

```

#define true 1
#define false !true

// set CPU registers etc.
initSystem();

// set RF baudrate registers, buffers etc.
initRF();

// set Sensor module reg. settings
initSensing();
// use Timer for periodic measurements
initTimer();
// run forever
while(True){
    // if buffer full, flag is set
    if(TXBufferFull== true){
        // send data
        RFUnitTX();

        TXBufferFull= false;
        // collect data
        collectData();
        //flag tx buffer full
        TXBufferFull= true;
        // re-configure Timer
        reLoadTimer();
        // re-start timer
        timeToSense= false;
    }
    if(RFUnitRXFlag== true){
        // receive the relayed data
        RFUnitRX();
        // save in TX buffer
        Rx2Tx();
        // send relayed data
        TXBufferFull= true;
    }
}
void interrupt RF() {
    // ready for Rx
    RFUnitRXFlag= true;
}
void interrupt Timer(){
    // time to collect data
    timeToSense= true;
}

```

VI. DEVELOPMENT TOOLS

In STM8 series devices, in-circuit debugging is managed through SWIM (single wire hardware interface) pin which also features ultra-fast in-circuit programming by means of freely available ST-Link software. STM8 microcontroller family is supported by a wide range of software tools both from ST and third-parties. C compilers are available from Cosmic, IAR and Raisonance, with free versions up to 32KB of code generation which is quite adequate for chosen STM8S105C6 MCU.

VII. CONCLUSION

STM8S105C6 MCU is ideal device for WSN applications due to their build-in features at incredibly low prices. Besides, easy debugging and fast flash programming via SWIM make it child play to develop code for everyone in Labs. Free C compilers and plenty of examples on the Internet make it more attractive to choose. Starting from the best MCU to fit for WSN node design, an ultra-low cost design with supplementary library is proposed for students to practice in the WSN labs.

REFERENCES

- [1] I.F. Akyildiz, W.Su, Y. Sankarasubramaniam and E. Cayirci. "A survey on sensor networks", IEEE Communications Magazine, vol. 40, pp. 102--114, November 2002.
- [2] E. H. Callaway, *Wireless Sensor Networks: Architectures and Protocols*. Auerbach publications, Boca Raton, 2004.
- [3] R. Singh, R. Uppal, G. Singh, Hod, B. Banda, S. Bahadur, E. College, F. Sahib, Punjab, C. Hod, B. Singh, B.E.g College. "Low cost open source based Sensor Node for Wireless Sensor Networks", National Conference on Virtual and Intelligent Instrumentation, Rajasthan, Pakistan. Nov 13-14, 2009.
- [4] A. Dikovic, G. Sisul, B. Modlic, "A Low Cost Platform for Sensor Network Applications and Educational Purposes", *Radioengineering*, Vol. 20, pp. 761--768, Dec 2011.
- [5] Y. Sun, X. Wang, F. Jia, J. Yu, "*Design of a Wireless Sensor Network node based on STM32*", *ICCSEE 2013 2nd International Conference on Computer Science and Electronics Engineering, 2013*.
- [6] Y.Tian, Y. Lv, L. Tong, "Design and application of sink node for wireless sensor network", (COMPEL) *The international journal for computation and mathematics in electrical and electronic engineering*, vol. 32, pp. 531--544, Mar 2013.
- [7] H. Li, O. Yong, Z. He, "The Design of Embedded Wireless Sensor Network Node", *IEEE 2010 2nd International Symposium on Information Engineering and Electronic Commerce*. 23-25 July 2010, Ternopil, Ukraine.
- [8] ST Electronics, STM8S105C4 8-bit MCU with 16 Kbytes Flash, Available: www.st.com/resource/en/datasheet/stm8s105c4.pdf.
- [9] Dorji~Applied~Technologies, DRF4432F20 - 20dBm Si4432 RF module, Available: www.dorji.com/docs/data/DRF4432F20.pdf
- [10] Honeywell , HMC5883 3-Axis Digital Compass IC Datasheet, Available: [http://aerocontent.honeywell.com/aero/common/documents/myaerospacecatalogdocuments/DefenseBrochuresdocuments/HMC5983\(3\) Axis\(Compass\)IC.pdf](http://aerocontent.honeywell.com/aero/common/documents/myaerospacecatalogdocuments/DefenseBrochuresdocuments/HMC5983(3) Axis(Compass)IC.pdf)

Providing Context-Aware Services to Dementia Patients and Caregivers

Özgün YILMAZ¹

¹ Ege University, Department of Computer Engineering, İzmir/Turkey, ozgun.yilmaz@ege.edu.tr

Abstract - As a result of increased human lifespan, dementia becomes a national public health and social care priority worldwide. Although, there is no cure for dementia, the wandering behavior of dementia patients can be managed by an ambient assisted living system. In this paper, Wandering Behavior Ontology (WBO) used for dealing with wandering behavior seen in early stage dementia patients is proposed. WBO is used in iCarus, which is an intelligent ambient assisted living system, for providing context-aware services to dementia patients and their caregivers. Knowledge sharing, knowledge reuse and logical reasoning are provided by using ontologies. iCarus aims to reduce the problems and financial burden associated with a wandering episode for the patients and their caregivers. It provides longer independent living for the elderly people and a cost-effective way of remotely monitoring them. The actions that are to be taken are determined by rule-based reasoning. These actions are sequential and they are defined in the developed ontology. These actions include warning the patient and informing the caregiver and the emergency service.

Keywords - Context-awareness, Rule-based reasoning, Ambient Intelligence, Ambient Assisted Living.

I. INTRODUCTION

As a result of increased human lifespan, dementia becomes a national public health and social care priority worldwide. World Alzheimer Report 2016 estimates that 47 million people live with dementia and that this number will rise to 131 million by 2050. Also, the total estimated cost of dementia has reached 818 billion US dollars worldwide, and by 2018, it will become a trillion dollar disease [1].

Dementia is the loss of cognitive functioning, resulting in impaired memory, difficulty in communication, and reduced cognitive ability. This affects the person's daily life and capabilities such as thinking, remembering and reasoning. Alzheimer's disease is progressive and gets worse over time. It destroys the brain slowly, while decreasing quality of life and finally leading to death [2, 3].

As a result of cognitive decline, people with early stage dementia may suffer from unpredictable wandering behavior. They have a tendency to leave their residences and get lost. This can result in malnutrition, sleep disturbances, accidents, injuries and in some cases death [4-6]. Studies show that approximately 67% of dementia patients may suffer from wandering behavior, and half of those not found within a day

suffer serious injuries or death. Wandering behavior might take place as a result of getting lost from spatial disorientation or getting lost due to goal-oriented behavior (e.g. a person trying to go to his old house or working place) [6, 7].

Dealing with this behavior requires continuous vigilance and being on alert all the time. The patient is a person and has the right to live autonomously as long as possible; however, the dignity of the patient should be preserved, but these are conflicting issues [6]. Caring for a dementia patient is very stressful, and the caregivers feel depression as a result of degenerating behavior of the patient [6, 8].

Although, there is no cure for dementia, the wandering behavior of dementia patients can be managed by using Information and Communications Technologies (ICT) [8]. ICT forms the basis of Ambient Intelligence (AmI) systems. AmI promotes an anthropomorphic human-centric computer interaction, where devices weave themselves into the fabric of everyday life, so that they are virtually invisible to humans [9-11]. Essential for AmI is the recognition of objects and their situational context, and the delivery of services that are personalized, adaptive and anticipatory [8, 12].

Ambient Assisted Living (AAL) is the application of AmI technologies in the health domain. AAL systems aim to enable people with specific needs (e.g. elderly or handicapped) to live independently for longer periods of time [12].

It is hard to think an AAL system without the context-awareness, since the context-awareness is a key factor in AmI and AAL systems [13-15]. Systems in these kinds of emerging fields need to have a higher understanding of the situations to deliver services or functionalities and to adapt accordingly [13]. Simply, the context-awareness means being aware of the current location and surrounding environment [15], and the it is crucial for delivery of personalized, adaptive, and anticipatory service in AmI and AAL systems [8, 12].

In this paper, Wandering Behavior Ontology (WBO), used for managing wandering behavior in dementia patients, is described. WBO is encoded in OWL (Web Ontology Language) and it is available online through a GitHub repository from [16]. WBO is used in iCarus, which is an intelligent ambient assisted living system, for providing context-aware services to dementia patients and their caregivers. Knowledge sharing, knowledge reuse and logical reasoning are provided by using ontologies. Ambient assisted living is provided through the ambient intelligence and

context-awareness paradigms. iCarus aims to reduce the problems and financial burden associated with a wandering episode for the patients and their caregivers. It provides longer independent living for the elderly people and a cost-effective way of remotely monitoring them. The actions that are to be taken are determined by rule-based reasoning. These actions are sequential and they are defined in WBO. These actions include warning the patient and informing the caregiver and the emergency service.

The system is rule-based and has expert system properties. The caregivers are able to compose their own rules and extend the functionality of the system with regards to their needs. Constructing new rules is accomplished by an innovative interface used by the caregivers. The users do not need to know the syntax of the used rule language. In this approach, the context reasoning is decoupled from the source code of the system. New functionalities can be added to the system without changing the source code. Thus, a flexible and extensible system is developed. WBO is used to provide the delivery of personalized, adaptive, and anticipatory services.

II. BACKGROUND

A. Ambient Intelligence (AmI)

Weiser [11] envisioned a paradigm in which computers disappear seamlessly embedded into the environment. AmI is built upon pervasive and ubiquitous computing paradigm where access to resources, data, and information is possible anytime and anywhere. Facilitated by the miniaturization of electronics, many mobile devices are available with sensing and computing capabilities, which takes the computational paradigm out of the desktop. These devices are portable, accessible, and affordable. This has flourished new opportunities while interacting with technologies, bringing them closer to people's daily life experiences [13].

AmI uses artificial intelligence to further enhance the use of surrounding, unobtrusive computing devices. AmI emerged to build intelligent environments such as smart homes, smart hospitals, and etc. AmI systems are expected to be sensitive, responsive, adaptive, transparent, ubiquitous, and intelligent. The context-awareness is a key factor in providing these features [14]. In iCarus, strong emphasis is placed on context and context-awareness.

B. Context-awareness

Different researchers have made different definitions of context in mobile computing. Dey [17] defines *context* as "any information that can be used to characterize the situation of an entity. An entity is a person, place, or object that is considered relevant to the interaction between a user and an application, including the user and applications themselves" [18].

Schilit and Theimer [19] refers to *context-aware computing* as software that "adapts according to its location of use, the collection of nearby people and objects, as well as changes to those objects over time" [17]. Thus, context-aware software

can be defined as software that adapts to its context and changes which occurs in this context [18].

Existing efforts to model context can be classified into three categories [20]: application-oriented approach, model-oriented approach and ontology-oriented approach. From these categories, in the application-oriented approach, no formalism and knowledge sharing between different systems are supported. Because it is not formal, it is specific to an application and lacks expressiveness. The model-oriented approach is formal, but knowledge sharing and the context reasoning are not supported. On the other hand, the ontology-oriented approach has the formal basis and the knowledge sharing in addition to supporting the knowledge reuse and the context reasoning [20]. In order to perform the reasoning over ontologies, we can use the rule-based reasoning and/or description logic reasoning.

In iCarus, the ontology-oriented approach is used because it has many advantages over the other approaches as it is mentioned earlier. WBO, used by iCarus, also includes metadata to improve certainty and accuracy of data similar to [21]. The software or hardware components used for sensing data are also modeled, and their precision and accuracy are included in WBO.

C. Ambient Assisted Living

One of the applications of AmI is in AAL domain which tries to exploit proper technologies to support citizens with specific needs (e.g. elderly or handicapped) to live in their preferred environment independently for a longer period of time. Thus, the costs of caring for the patient are reduced, and the quality of the patient's life is preserved [10].

AAL systems obtain knowledge about their surroundings with sensors, autonomously act on behalf of their users, or they interact with their users in an unobtrusive and intuitive manner. Especially, AAL systems should extend the time people spent in their homes, increase their autonomy, and mobility, help them maintain better life, enhance their security, and assist caregivers and families [22].

III. OVERVIEW OF ICARUS

In this section, iCarus is described briefly. For a detailed description of iCarus and its architecture, please refer to [23].

In iCarus, the patient's environment is partitioned into zones. Zones can be defined in both the spatial and temporal dimensions. Defining zones is caregivers' duty. There are 3 types of zones:

- 1. Green zone:** This is the safe zone. The patient's home may be considered as a green zone.
- 2. Red zone:** Areas that are dangerous for the patient are defined as red zones. An example of a red zone is a busy cross road.
- 3. Orange zone:** The orange zone is considered as a green zone, if the temporal constraint related to the zone is met. Otherwise it is considered as a red zone.

iCarus also supports considering other contextual information such as age, stage of dementia, weather, the proximity to the caregiver, stage of dementia, day of week, time spent in a zone, and other parameters. In addition, new zone types can be defined by caregivers according to their needs. A novel user interface can be used to construct rules without knowing the syntax of the rule language.

iCarus is a rule-based system. In case a wandering episode occurs, rule-based reasoning is used to decide on the actions. The situation's severity and the user preferences have an impact on the actions. The available actions are warning the patient by text and audio, helping the patients with navigation assistance for returning back to safe zone or home, notifying the caregiver, providing tracking mechanisms for the caregiver and emergency service, establishing voice communication and texting the caregiver and the emergency service.

The server receives the current location of the patient and the time stamp from the patient mobile application. Then, it specifies the zones where the patient is in, calculates speed and heading direction. This information is added to the ontology in order to construct the current context of the patient. Other dynamic context information is also added to the ontology. Then, rule-based reasoning is applied resulting in a sequence of actions. This sequence of actions includes a combination of the following actions:

- **Warning the patient:** The patient is requested to return back to the safe zone by text and audio notifications. In order to help the patients return back to the safe zone, audio, visual and text directions are presented on a map. If the patient does not comply in a certain amount of time, the application proceeds to the next action.
- **Sending alert notification to the caregiver(s):** An alert is sent to inform the caregiver of a wandering episode, to establish bidirectional communication, and to share the patient's location and navigation information. The caregiver can track the patient on a map, when an alert message is received. If the caregiver does not respond, the application proceeds to the next action.
- **Calling the caregiver with the speakers on:** The smart phone of the patient calls the caregiver with the speakers turned on. This action assumes that the patient will respond to a familiar voice.
- **Sending notification to an emergency service:** The patient application sends a message, notifying the authorities about the circumstance and navigation information of the patient through SMS or e-mail.
- **Calling an emergency service with the speakers on:** The patient application calls the emergency service with the speakers turned on. The caregiver can also command the patient's phone to call the emergency service.

The sequence of actions is sent to the mobile device of the patient, which in turn, the patient application processes the actions one by one sequentially. In the default setting, first the patient is prompted to return back to the safe zone. If the patient does not return to the safe zone, an alert is sent to the

caregiver. Alternatively, the patient can send an alert to the caregiver at any time if he/she is lost or there is an emergency. The caregiver can track the patient on a map through the caregiver mobile application, desktop application, or web application. The location, heading direction, and speed of the patient are shown to the caregiver. If the caregiver concludes that there is no danger for the patient, and the patient is not in a wandering episode, then the caregiver can cancel the alert. If the patient is located in the red zone and the caregiver does not respond, the application informs or calls the emergency service, because there might be a life danger.

If the caregiver concludes that there is a life danger, he can inform the emergency service or the police and give them a code which is valid for a limited amount of time. Now, the emergency personnel can track the patient on a web browser.

IV. WANDERING BEHAVIOR ONTOLOGY

As mentioned previously, WBO is encoded in OWL and it is available online through a GitHub repository from [16]. Domain ontologies are defined and shared across different platforms and people by using OWL. An ontology refers to a formal representation of a set of concepts in a domain and the relationships between those concepts [24, 25].

Protégé [26] ontology editor is used to develop WBO. A partial view of WBO from Protégé editor is shown in Figure 1. During the development, the best practices from other related work [20, 21, 25, 27-29] are adopted.

Providing knowledge sharing, knowledge reuse, and logical reasoning support are among the advantages of using ontologies. Jena [30] is used to manipulate ontologies and to perform logical inference. A general view of WBO depicting most important classes and the relationships between them is shown in Figure 2. Some of the classes are omitted in this figure, because there are a huge number of classes.

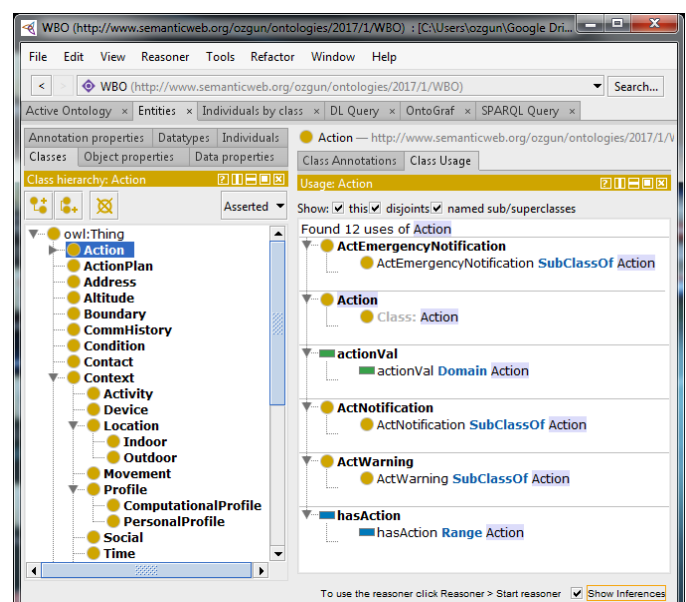


Figure 1: A partial view of WBO from Protégé editor.

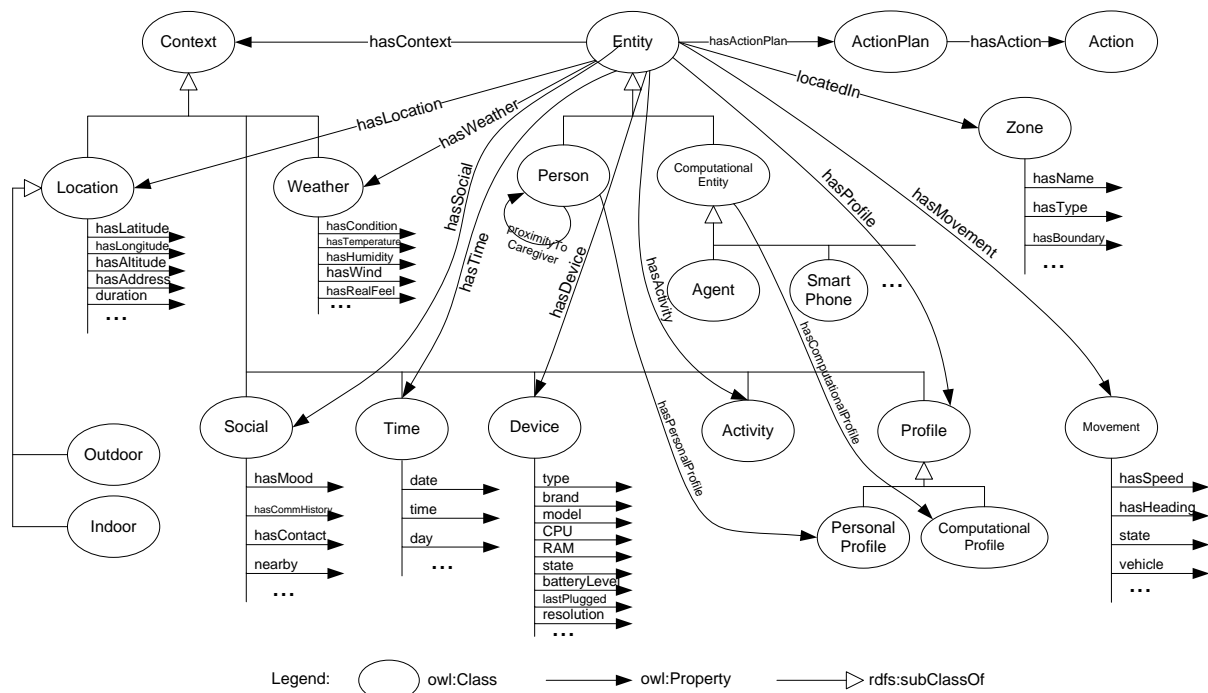


Figure 2: A general view of WBO.

WBO is modeled through classes, object properties, data type properties and restrictions. *Entity* class represents things that can be related to a context. *Entity* class has four subclasses: *Person*, *Place*, *Object* and *ComputationalEntity*. *ComputationalEntity* has many subclasses such as *Agent*, *SmartPhone*, *MobileDevice*, *Computer* and etc.

Entity is related to *Context* class. *Zone*, *location*, *time*, *weather*, *social situation*, *device*, *activity*, *network* and *profile* are subclasses of *Context* class.

Location is composed of *Latitude*, *Longitude*, *Altitude* and *Address* classes. Time spent at a place is stored in *duration* data type property. Time context consists of date, time and day of the week values. Device context includes device type, brand, model, CPU, memory, device state, battery level, last plugged time and screen resolution of the device. Network (not included in Figure 2) context models communication costs, network type, and other quality parameters such as network bandwidth, ping, packet loss rate, error rate, throughput, latency and jitter. *Profile* class stores entity ID, description, name and etc. *PersonalProfile* and *ComputationalProfile* are derived from *Profile* class. *PersonalProfile* models personal information such as name, surname, age, occupation, birthdate and other demographic information, whereas *ComputationalProfile* models computational information of a computational entity. *Person* class is associated with *PersonalProfile* class. Similarly, *ComputationalEntity* is associated with *ComputationalProfile* class. Every entity must have one and only one profile which is enforced by restrictions. All of these classes can be further extended to meet other requirements.

Weather class represents the current weather around an entity. Weather context is acquired from a third party web

service and consists of weather condition (such as sunny, cloudy, rainy, etc.), temperature, humidity, wind, and real feel temperature. Social context of the entity is composed of current mood, communication history, contacts, and nearby entities. *Movement* class models movement of the entity and it is associated with speed, heading, state and used vehicle.

In iCarus, individuals are created from the previously mentioned ontology classes, and the user specific context is constructed. Static context is composed of the user's personal profile and mobile device properties. Static context can be stored in a permanent storage. On the contrary, location, time, movement, and network parameters can change constantly in an application with mobile users and this information compose dynamic context. Dynamic context is handled on the fly programmatically. After the context is formed, the reasoning takes place. Reasoning is made over WBO to decide on the actions to take and the order of these actions.

ActionPlan class represents the action plan (interventions) composed of sequence of actions represented by *Action* class. As a result of the rule-based-reasoning, this class is linked to the context if there is a need to interrupt the patient. The OWL code for *hasActionPlan* and *hasAction* object properties is given in Figure 3.

Zone class represents the zone, the patient is currently located in. If the patient is not located in any one of the zones including user defined zones, then it is asserted that the patient is in the neutral zone, and this fact is added into the ontology. This serves as a syntactic sugar for better expressive power. WBO deals with quality of context similar to [20]. Physical sensors may produce incorrect or stale context data due to imperfect sensing and poor reliability. In WBO, quality is associated with a number of quality parameters, which capture

different dimensions of quality. Each parameter is linked to one or more appropriate quality metrics. A metric contains a value, a type and a unit. Three types of quality parameters are defined: accuracy, resolution and freshness. As a result, quality parameters can play an important role in rules defined to be used for reasoning.

```
<owl:ObjectProperty
rdf:about="./ozgun/ontologies/2017/1/WBO#
hasActionPlan">
  <rdfs:domain
rdf:resource="./ontologies/2017/1/WBO#Entity"/>
  <rdfs:range
rdf:resource="./ontologies/2017/1/WBO#ActionPlan"/>
</owl:ObjectProperty>

<owl:ObjectProperty
rdf:about="./ontologies/2017/1/WBO#hasAction">
  <rdfs:domain
rdf:resource="./ontologies/2017/1/WBO#ActionPlan"/>
  <rdfs:range
rdf:resource="./ontologies/2017/1/WBO#Action"/>
</owl:ObjectProperty>
```

Figure 3: The OWL code fragment for *hasActionPlan* and *hasAction* object properties.

A. Context Reasoning

By rule-based reasoning, high level context is obtained from low level context. Supplementary rules are shown in Table 1. For the essential rules, please refer to [23]. The caregiver can contact the system administrator to modify these rules or add new rules. In the consequents of the rules given in Table 1, an action plan is represented by *AP*, an individual which is created before reasoning. Similarly, *ActWarning*, *ActNotification* and *ActEmergencyNotification*, represents warning the patient, sending notification to the caregiver and to the emergency service, respectively.

Table 1: The supplementary rules used in reasoning.

Rule description	Rule
Speed limit	$(?p \text{ hasMovement } ?m) \wedge (?m \text{ hasSpeed } ?s) \wedge (\text{greaterThan}(?s, 50)) \Rightarrow (?p \text{ hasActionPlan } AP) \wedge (AP \text{ hasAction } ActWarning) \wedge (AP \text{ hasAction } ActNotification) \wedge (AP \text{ hasAction } ActEmergencyNotification)$
Hot and sunny weather	$(?p \text{ locatedIn } ?z) \wedge (?z \text{ hasType "NeutralZone"}) \wedge (?p \text{ hasWeather } ?w) \wedge (?w \text{ hasCondition "sunny"}) \wedge (?w \text{ hasTemperature } ?c) \wedge (\text{greaterThan}(?c, 35)) \Rightarrow (?p \text{ hasActionPlan } AP) \wedge (AP \text{ hasAction } ActWarning) \wedge (AP \text{ hasAction } ActNotification)$
Proximity limit	$(?p \text{ proximityToCaregiver } ?c) \wedge (\text{greaterThan}(?c, 20)) \Rightarrow (?p \text{ hasActionPlan } AP) \wedge (AP \text{ hasAction } ActNotification)$

The caregiver can activate or deactivate the supplementary rules, and he can also modify the limit values (speed limit, temperature limit and proximity limit) from the preferences.

The speed limit rule is for fast moving vehicles. If the patient is in a fast moving vehicle, he may end up far away from his home. If he takes an intercity bus, he may end up in

another city. For these reasons and for the fact that the dementia patients shouldn't and may not be able to drive, this rule may be necessary. Sending a notification to the emergency service is included in this rule because the patient's life might be in danger like the case with the red zone. Also, the caregiver may have difficulty catching up with the patient and faster action must be taken if the patient is moving fast.

The hot and sunny weather rule is for protecting the patients from heatstroke. The weather condition is acquired from online weather services. If the patient is in the neutral zone, the weather is sunny and the temperature is greater than 35 °C, then warning the patient and sending a notification to the caregiver actions will be taken.

The proximity limit rule is triggered when the distance between the patient and the caregiver exceeds the limit. The only action in the consequent is sending a notification to the caregiver and the emergency service is not notified.

V. RELATED WORK

In [20, 29], an OWL encoded context ontology (CONON) for modeling context in pervasive computing environments is proposed. Context reasoning is used to check the consistency and to derive high-level implicit context.

In [21], an ontology-based context model encoded in OWL is introduced. To assess the value of the context model, a scenario is described. In addition, a context ontology server is developed that manages and processes context information.

Rodriguez et al. [25] propose an ontological model to provide interventions for the wandering behavior. This model extends their Ambient Augmented Memory System (AAMS). AAMS provides the caregiver to define interventions based on the external memory aids to the patient provided by mobile devices. The ontology flexibility is demonstrated to personalize the AAMS system to support interventions for wandering through mobile devices. Context ontology and rule-based context reasoning is used.

In [27], the context model is composed of OWL encoded ontologies. The model consists of four related ontologies: users, devices, environment and services. The model supports logical inference to enhance the automatic context generation and the proactive behavior of some services.

In [28], ContextProvider, a framework that offers a unified and query-able interface to contextual data, is introduced. ContextProvider supports interactive user feedback, self-adaptive sensor polling, and minimal reliance on third-party platforms. ContextProvider also enables the rapid development of new context and bio-aware applications.

In this paper, wandering behavior in dementia patients is modeled by WBO which is an OWL encoded ontology. Context is also modeled as a subset of this ontology. Best practices from the related work are adopted about modeling context. Quality of context is modeled, because of sensing errors and inaccuracies. Logical reasoning, knowledge sharing and knowledge reuse are provided by using an ontology.

VI. CONCLUSION

As a result of increased human lifespan, dementia is a major health and social care challenge of today and the near future. Currently, there is no therapeutic solution for dementia. However, a solution for managing wandering behavior can be provided by using AmI. The context-awareness is a key factor in AmI, as it provides delivery of personalized, adaptive, and anticipatory services.

In this paper, WBO (Wandering Behavior Ontology), for dealing with wandering behavior in dementia patients, is described. WBO is encoded in OWL and by using ontologies, knowledge sharing, knowledge reuse and logical reasoning are facilitated. WBO is used by iCarus, which is an intelligent ambient assisted living system to provide context-aware services to dementia patients and their caregivers. The aim of iCarus is to provide independent living of the elderly people and a cost-effective way to monitor them in addition to reducing the adverse results and financial burden of a wandering episode for the patients and their caregivers. The interventions are deduced by rule-based reasoning. These interventions are sequential and they are defined in WBO.

In iCarus, the caregivers can construct new rules and extend the functionality of the system. Constructing new rules is accomplished by an innovative interface used by the caregivers. In this approach, the users do not need to know the syntax of the rule language and the context reasoning is decoupled from the source code. Without changing the source code, new functionalities can be added to the system. As a result, a flexible and extensible system is developed. By using WBO, the delivery of personalized, adaptive, and anticipatory services is achieved.

As a future work, it is planned to collaborate with dementia experts from other disciplines and use WBO in a real world setting.

REFERENCES

- [1] M. Prince, A. Comas-Herrera, M. Knapp, M. Guerchet, and M. Karagiannidou, "World Alzheimer Report 2016: Improving healthcare for people living with dementia: Coverage, quality and costs now and in the future," 2016.
- [2] Alzheimer's Disease Education and Referral Center, "Alzheimer's disease fact sheet," National Institutes of Health, Tech. Report NIH Publication No. 08-6423, 2010.
- [3] F. Sposaro, J. Danielson, and G. Tyson, "iWander: An Android application for dementia patients," in *2010 Annual International Conference of the IEEE Engineering in Medicine and Biology*, pp. 3875-3878.
- [4] D. L. Algase, D. H. Moore, C. Vandeweerd, and D. J. Gavin-Dreschnack, "Mapping the maze of terms and definitions in dementia-related wandering," *Aging Ment. Health*, vol. 11, pp. 686-698, 2007.
- [5] G. Cipriani, C. Lucetti, A. Nuti, and S. Danti, "Wandering and dementia," *Psychogeriatrics*, vol. 14, pp. 135-142, 2014.
- [6] J. Wan, C. A. Byrne, M. J. O'Grady, and G. M. P. O'Hare, "Managing Wandering Risk in People With Dementia," *IEEE T. Hum.-Mach. Syst.*, vol. 45, pp. 819-823, 2015.
- [7] J. Hoey, X. Yang, E. Quintana, and J. Favela, "LaCasa: Location and context-aware safety assistant," in *2012 6th International Conference on Pervasive Computing Technologies for Healthcare (PervasiveHealth) and Workshops*, 2012, pp. 171-174.
- [8] J. Wan, C. Byrne, G. M. P. O'Hare, and M. J. O'Grady, "Orange alerts: Lessons from an outdoor case study," in *2011 5th International Conference on Pervasive Computing Technologies for Healthcare (PervasiveHealth) and Workshops*, pp. 446-451.
- [9] P. Remagnino and G. L. Foresti, "Ambient Intelligence: A New Multidisciplinary Paradigm," *IEEE T. Syst. Man. Cy. A*, vol. 35, pp. 1-6, 2005.
- [10] J. Wan, C. Byrne, G. M. P. O'Hare, and M. J. O'Grady, "OutCare: Supporting Dementia Patients in Outdoor Scenarios," in *International Conference on Knowledge-Based and Intelligent Information and Engineering Systems*, 2010, pp. 365-374.
- [11] M. Weiser, "The Computer for the 21st Century," *The Computer for the 21st Century*, vol. 265, pp. 94-104, 1991.
- [12] T. Kleinberger, M. Becker, E. Ras, A. Holzinger, and P. Müller, "Ambient Intelligence in Assisted Living: Enable Elderly People to Handle Future Interfaces," in *International Conference on Universal Access in Human-Computer Interaction*, Berlin, Heidelberg, 2007, pp. 103-112.
- [13] U. Alegre, J. C. Augusto, and T. Clark, "Engineering context-aware systems and applications: A survey," *J. Syst. Software.*, vol. 117, pp. 55-83, 2016.
- [14] D. J. Cook, J. C. Augusto, and V. R. Jakkula, "Ambient intelligence: Technologies, applications, and opportunities," *Pervasive Mob. Comput.*, vol. 5, pp. 277-298, 2009.
- [15] D. J. Cook and S. K. Das, "How smart are our environments? An updated look at the state of the art," *Pervasive Mob. Comput.*, vol. 3, pp. 53-73, 2007.
- [16] Ö. Yılmaz. (2018, September). *Wandering Behavior Ontology* [Online]. Available: <https://github.com/ozgunyilmaz/WBO>
- [17] A. K. Dey, "Understanding and Using Context," *Pers. Ubiquit. Comput.*, vol. 5, pp. 4-7, 2001.
- [18] Ö. Yılmaz and R. C. Erdur, "iConAwa - An intelligent context-aware system," *Expert Syst. Appl.*, vol. 39, pp. 2907-2918, 2012.
- [19] B. N. Schilit and M. M. Theimer, "Disseminating active map information to mobile hosts," *IEEE Network*, vol. 8, pp. 22-32, 1994.
- [20] T. Gu, X. H. Wang, H. K. Pung, and D. Q. Zhang, "An Ontology-based Context Model in Intelligent Environments," in *Proceedings of Communication Networks and Distributed Systems Modeling and Simulation Conference*, pp. 270-275.
- [21] E. Kim and C. Jaeyoung, "An Ontology-Based Context Model in a Smart Home," in *International Conference on Computational Science and Its Applications*, 2006, pp. 11-20.
- [22] W. Kurschl, S. Mitsch, and J. Schönböck, "Modeling Situation-Aware Ambient Assisted Living Systems for Eldercare," in *2009 Sixth International Conference on Information Technology: New Generations*, pp. 1214-1219.
- [23] Ö. Yılmaz, "An ambient assisted living system for dementia patients," [Online]. Available: https://drive.google.com/file/d/1j9_64X3XKhzVV1E00QkRbFagTjQ2RH9/view, unpublished.
- [24] T. R. Gruber, "A translation approach to portable ontology specifications," *Knowl. Acquis.*, vol. 5, pp. 199-220, 1993.
- [25] M. D. Rodriguez, R. F. Navarro, J. Favela, and J. Hoey, "An Ontological Representation Model to Tailor Ambient Assisted Interventions for Wandering," in *AAAI Fall Symposium: Artificial Intelligence for Gerontechnology*.
- [26] Stanford Center for Biomedical Informatics Research. (2018, September). *Protégé* [Online]. Available: <http://protege.stanford.edu>
- [27] R. Hervás, J. Bravo, and J. Fontecha, "A Context Model based on Ontological Languages: a Proposal for Information Visualization," *J. Univers. Comput. Sci.*, vol. 16, pp. 1539-1555, 2010.
- [28] M. Mitchell, C. Meyers, A. I. A. Wang, and G. Tyson, "ContextProvider: Context awareness for medical monitoring applications," in *2011 Annual International Conference of the IEEE Engineering in Medicine and Biology Society*, pp. 5244-5247.
- [29] X. H. Wang, D. Q. Zhang, T. Gu, and H. K. Pung, "Ontology based context modeling and reasoning using OWL," in *Proceedings of the Second IEEE Annual Conference on Pervasive Computing and Communications Workshops*, pp. 18-22.
- [30] Apache Software Foundation. (2018, September). *Apache Jena* [Online]. Available: <https://jena.apache.org/>

The Effect Of Balancing Process On classifying Unbalancing Data Set

S.JASSIM¹ and E. KAYA¹

¹ Konya Technical University, Selcuk University, Konya/Turkey, samarajassim91@gmail.com

¹ Konya Technical University, Selcuk University, Konya/Turkey, ersinkaya@selcuk.edu.tr

Abstract - Unbalanced data indicates a situation where the number of monitoring is not the same for all categories in the label data set. In some fields, unbalanced data problems are very common. Some of machine learning classifiers failed to deal with unbalanced training data sets because they are sensitive to the proportions of different classes. As a result, these algorithms tend to favor the class with the largest proportion of observations known as the majority class, which may lead to misleading accuracy. Most of data sets are unbalanced because most of the data collected over the diseases are usually not disease. These data when used in the classification algorithm it gave un-well results, the data sets used in the training process must be balanced to increase this success. In this article, (SMOTE) synthetic minority over-sampling technique is used on data sets. K-Nearest Neighbors (K-NN), and Naïve Bayes (NB) classification algorithms are applied to classify the balanced datasets and according to the obtained classification results the balanced data sets achieved a better classification success.

Keywords – Unbalanced data, SMOTE, K-NN, NB, classification.

I. INTRODUCTION

In real-world unbalanced datasets are common problems, The data set is unbalanced if the classification classes are almost unequal. Recent years have brought increased interest in the application of automated learning techniques to difficult actual problems, many of which are described by unbalanced data. Moreover, the distribution of test data may vary from training data, and the error of classification may be unknown at the learning time [1]. These problems can be solved by re-sampling the dataset and make the dataset is balanced. Sampling is a method that handling the imbalance class in the training set by changing the minority and majority class size. A simple data-level approach to balancing classes includes repeated samples the main dataset, either by oversampling smaller number/classes or by undersampling the greater number/classes, as long as the class is almost the same. Both of these Strategies can be implemented in any learning system [2]. There are several disadvantages related to using undersampling. A disadvantage with undersampling is that it ignores potentially useful data. While with oversampling is that by making exact copies of present examples. The main disadvantage with oversampling is that by making exact copies of existing examples. the other disadvantage of oversampling is that it increases the number of training examples so that lead to an increase in learning time. Beside this, there is an

advantage of using sampling method, the clearest reason is there are not cost- sensitive application of whole learning algorithms, and therefore sampling is the only option for the wrapper-based process. The other reason for using sampling, the volume of the training set should be reduced in order to make the learning suitable. And the final reason is that misclassification costs are often unknown [3]. Also, there's several materials and methods that will be explained one by one in this article like K-NN, NAIVE BAYES, and SMOTE. At first, the K-NN will be explained briefly. (K-NN) K-nearest neighbor is one of the basal operations of different machine learning methods and it's the most used method. Used or classified or clustered and the regression in several research regions such as image interpolation and visible category recognition. The number of (k) is chosen according to the desirable limit of hit [4]. In this article, the researchers (R. J. Ramteke1, Khachane Monali Y.2) they provide a method that it works in two phases that based on image features and automatic abnormality detection, and this two-phase is normal and abnormal. The performance of K-NN is compared with kernel-based SVM classifier. The result shows that the K-NN gain is 80% classification rate which is more than the SVM. According to that results they tested this method on the number of real CT (Computed Tomography) scan brain images [5]. In the field of the conventional K-NN text classification algorithm, the researchers (Zhou Yong and Li Youwen and Xia Shixiong) they applied all training samples for classification process, consequently, it includes a massive issue of training samples and a high degree of calculation. The simulation results show that the suggested algorithm effectively improved the accuracy of K-NN [6]. The second material was naive bayes (NB) is the easier form of a Bayesian network, it's one of the most efficient and effective inductive learning algorithms for (ML) and (DM), also it does not affect on the classification. In this situation, (NB) yet is the optimal classifier [7]. In this paper, the researcher (I. Rish) aims to observe the data characteristics which impacts on the performance of (NB). So, a better understanding of the impact could be used to devise better techniques for learning efficiently [8]. In this paper, the researchers (Dr. Saurabh Mukherjeea, Neelam Sharma) they discussed the intrusion detection (ID) by using a Naive Bayes classifier with feature reduction, which (ID) is the operation of observation and analyzing the proceeding that being happened in a computer system in order to uncover marks of security problems [9]. While in this paper, the researchers (Andrew McCallum and Kamal Nigam) aims at clarifying the confusion by describing the differences and details of these two models. As a result,

they compared the theory and practice of two different first-order probabilistic classifiers [10]. Our final method is SMOTE, in this paper, they proposed an oversampling process in which the minority samples are taken by taking "synthetic" examples rather than taking redundant samples with replacement [11]. The researchers (Juanjuan Wang, Mantao Xu, Hui Wang, and Jiwu Zhang) shows a new way to improve the traditional SMOTE algorithm by integrating the local linear embedding algorithm (LLE). Experimental results explain that the underlying approach achieves an excellent performance to that of the traditional SMOTE [12].

II. BALANCING

The main problem of real-world application is the unbalanced dataset which that can cause an influence on the classification performance of ML algorithms. The dataset is named (unbalanced) if it held a larger number of samples the other of the classes. Datasets are imbalanced when fully one class is appeared by a small issue of training examples called a minority class while the other classes are the majority. So, to overcome this problem, a simple data methods for balancing the classes consist of resampling the main dataset, either by oversampling the minority class or by sampling the lower degree of majority until classes are almost evenly represented. Under-sampling is an effective process that is used to reduce the majority of class samples. In addition, the training process becomes faster and more balanced since a many majority class is ignored. The most popular re-processing mechanism is random majority under-sampling (RUS) [2] While in the oversampling method new samples are added to the minority category to balance the dataset. These process can be classified as a random and a synthetic oversampling. In the method of random oversampling, existing minority models are repeated to excess the size of the minority class. In the synthetic oversampling technique, artificial samples are produced for minority sample class. These new samples add basic information to the minority class and prevent its instances from the misclassification. There are several oversampling techniques, but the most used and popular one is SMOTE [13].

A. Synthetic Minority Oversampling Technique: SMOTE

There are a several of process available to resample a dataset applied in an ideal classification problem. The most popular mechanism is known as (SMOTE). is a process in which the minority class is over-sampled by taking each minority class by creating synthetic examples rather than by over-sampling with replacement. Neighbors are chosen from the nearest neighbors by random from the main SMOTE algorithm [2].

B. SMOTE Algorithm

Can show as the following bellow:

Algorithm SMOTE (T, N, k)

Input: Number of minority class samples T; Amount of SMOTE N%;
Number of nearest neighbors k.

Output: (N/100) * T synthetic minority class samples

1. (* If N is less than 100%, randomize the minority class samples as only random percent of them will be SMOTEd. *)
2. **If** N < 100
3. **Then** Randomize the T minority class samples
4. $T = (N/100) * T$
5. $N = 100$
6. **End if**
7. $N = (int)(N/100) * T$ (* The amount of SMOTE is assumed to be in integral multiples of 100. *)
8. $k =$ Number of nearest neighbors
9. $numattrs =$ Number of attributes
10. $Sample [] []$: array for original minority class samples
11. $newindex$: keeps a count of number of synthetic samples generated, initialized to 0
12. $Synthetic [] []$: array for synthetic samples
(* Compute k nearest neighbors for each minority class sample only. *)
13. **For** $i \leftarrow 1$ to T
14. Compute k nearest neighbors for i, and save the indices in the $nnarray$
15. $Populate (N, i, nnarray)$
16. **End for**
 $Populate (N, i, nnarray)$ (* Function to generate the synthetic samples. *)
17. **While** $N \neq 0$
18. Choose a random number between 1 and k, call it nn . This step chooses one of the k nearest neighbors of i.
19. **For** $attr \leftarrow 1$ to $numattrs$
20. Compute: $dif = Sample[nnarray][attr][attr] - Sample[i][attr]$
21. Compute: $gap =$ random number between 0 and 1
22. $Synthetic[newindex][attr] = Sample[i][attr] + gap * dif$
23. **End for**
24. $newindex++$
25. $N = N - 1$
26. **End while**
27. **Return** (* End of $Populate$. *)

End of Pseudo-Code [2].

III. CLASSIFICATION

In the machine learning (ML) the performance builds on the dimension and dataset. So, the classification is a logical way to select an effective machine learning algorithm that based on test and error experiments [14]. In problems and methods of classification had been looked like a key part of machine learning with a massive amount of applications that published lately. The concept of classification in machine learning (ML) has been traditionally treated in a broad sense, very often including supervised, unsupervised and semi-supervised learning problems [15]. The classification has some methods like NAÏVE BAYES, and K-nearest neighbor.

A. NAÏVE BAYES

(NB) is the simplest form of a Bayesian network, which one of the most efficient and effective inductive learning algorithms for machine learning and data mining. Also, it's competitive achievement in classification is amazing, because of the conditional independence the assumption on which it is based is not often true in real-world applications [7].

B. K-nearest neighbor

(K-NN) is one of the main operations of different (ML) methods and it's the most used method. Because of the simplicity of its application, different modified models of kNN such as weighted K-NN, kernel K-NN, and mutual K-NN, have been proposed. the relation of a request to a neighboring sample is basically measured by a similarity metric, such as Euclidean distance [4].

IV. DATASETS AND EXPERIMENTAL RESULTS

DATASETS

Hepatitis : The no. of attributes = 20 and the instance is 155, with 32 die, and 123 live.

Pima Indians Diabetes : The no. of attributes = 9 and the instance is 768, with 500 tested as negative, and 268 tested as positive.

EXPERIMENTAL RESULTS

In this framework, we used a WEKA program and we have been used two datasets (Hepatitis) and (Pima Indians Diabetes), at the first we implement the dataset without SMOTE. By taking the results of the classified instance, we found that the data is not balanced because there is a wide difference between correctly classified instances and incorrectly classified instances. To overcome this differ we implement the SMOTE oversampling algorithm on the same data and the (class value equal to 0), because it's oversampling technique and that working on increasing the minority class. When the experimental results are examined, the effect of SMOTE method is clearly seen on the data sets. The classification accuracy is increased after SMOTE operation is applied to the Hepatitis and Pima Diabetes data sets in the K-NN and NB classification algorithms. In the Hepatitis dataset, with K-NN and the classification algorithm (CA), mean of error, and F-measure it gave the results as showing in the table below. Then we applied SMOTE to the same data set with a parameter of k between 3-7 for each percentage 100,200,300 the best results were at 300% percentage and k-value equal to 5. Then we applied the same situation to the Pima data set, we also took the best result at the 300% percentage and the k-value equal to 3 as shown in the table below.

$$CA = (TP + TN) / (TP + TN + FP + FN) \quad (1)$$

$$MAE = TP / (TP + FP) \quad (2)$$

$$F\text{-Measure} = (2 * recall * Precision) / (recall + Precision) \quad (3)$$

Table 1: The results of Hepatitis and Pima data sets.

Dataset	K-NN classification algorithm					
	Without SMOTE			With SOMTE		
Hepatitis	CA	MAE	F-Measure	CA	MAE	F-Measure
		80.6452	0.1979	0.799	90.4382	0.1157
Pima Diabetes	NB classification algorithm					
	Without SMOTE			With SOMTE		
	CA	MAE	F-Measure	CA	MAE	F-Measure
	70.1823	0.2988	0.698	86.5776	0.1347	0.86

V. CONCLUSION

In this article, we have shown the effects of unbalancing data on classification accuracy. Ongoing work we focused on three directions. First, we explained the sampling strategy and the main algorithms of sampling. Second, what is SMOTE and the main work of this algorithm. Then we take a two dataset and we focused on how to make the data in balanced situation. Finally, we are extending our framework by implementing the K-NN in our data in addition of SMOTE to reach to the level of balancing. As a result from the table 1, the results show that the difference between correctly classified instances and incorrectly classified instances is being lower, that mean the data is reached to be balanced. That is the main effect of SMOTE's algorithm.

REFERENCES

- [1] Barua, S., Islam, M. M., Yao, X. ve Murase, K., 2014, MWMOTE--majority weighted minority oversampling technique for imbalanced data set learning, IEEE Transactions on Knowledge and Data Engineering, 26 (2), 405-425.
- [2] Ganganwar, V., 2012, An overview of classification algorithms for imbalanced datasets, International Journal of Emerging Technology and Advanced Engineering, 2 (4), 42-47.
- [3] Weiss, G. M., McCarthy, K. ve Zabar, B., 2007, Cost-sensitive learning vs. sampling: Which is best for handling unbalanced classes with unequal error costs?, DMIN, 7, 35-41.
- [4] Ertu'grul, Ö. ve Ta'gluk, M., 2017, A novel version of k nearest neighbor: Dependent nearest neighbor.
- [5] Ramteke, R. ve Monali, K., 2012, Automatic Medical Image Classification and Abnormality Detection Using K-Nearest Neighbour, 2, 1-7.
- [6] Yong, Z., Youwen, L. ve Shixiong, X., 2009, An Improved KNN Text Classification Algorithm Based on Clustering, 4.
- [7] Zhang, H., 2004, The Optimality of Naive Bayes, 1-6.
- [8] Rish, I., An empirical study of the naive Bayes classifier.
- [9] Mukherjee, D. S. ve Sharma, N., 2012, Intrusion Detection using Naive Bayes Classifier with Feature Reduction.
- [10] Mccallum, A. ve Nigam, K., A Comparison of Event Models for Naive Bayes Text Classification.

- [11] V. Chawla, N., W. Bowyer, K., O. Hall, L. ve Kegelmeyer, W. P., 2002, SMOTE: Synthetic Minority Over-sampling Technique, Journal of Artificial Intelligence Research 16.
- [12] Wang, J., Xu, M., Wang, H. ve Zhang, J., 2016, Classification of Imbalanced Data by Using the SMOTE Algorithm and Locally Linear Embedding, IEEE.
- [13] Shelke, M. M. S., Deshmukh, P. R. ve Shandilya, V. K., 2017, A Review on Imbalanced Data Handling Using Undersampling and Oversampling Technique.
- [14] Yucel, A., 2016, Predictive Text Analytics and Text Classification Algorithms.
- [15] Pérez-Ortiz, M., Jiménez-Fernández, S., A. Gutiérrez, P., Alexandre, E., Hervás-Martínez, C. ve Salcedo-Sanz, S., 2016, A Review of Classification Problems and Algorithms in Renewable Energy Applications.

Comparison of Agile Software Development and Traditional Software Development in Turkey

C.SUNGUR¹, F.BASCIFTCI² and C.UNAL³

¹ Selcuk University, Konya, Turkey, csungur@selcuk.edu.tr

² Selcuk University, Konya, Turkey, basciftci@selcuk.edu.tr

³ Selcuk University, Konya, Turkey, cihan_unal42@hotmail.com

Abstract - Agile approaches are the general name of the methods used to answer quickly to the need of change encountered late during the software development stages. Agile methodologies assist market demands faster by supporting various organizations and developing projects. Agile test strategy is the most suitable method for Information Technologies (IT). In this work, by focusing more on Agile software testing concept, agile software testing and traditional software methodologies are compared.

Keywords - Software development methods, agile software development, traditional software development, software industry implementations in Turkey.

I. INTRODUCTION

Agile methodology appeared towards the end of 1990s as a repetitive form of software development. Software industry became gradually more customer focused and as a result, it became the spine of highly dynamic modern business world. Thus, software industry and software quality assurance gained utmost importance. Strategy is invaluable for the growth and development of any organization [1]. Proper software planning and software test strategies became the main requirements for modern software development and functional, technical and maintenance expectations of the customer. Additionally, prioritization of executive targets and focusing on key test strategy options carry great importance for the correct and well-timed delivery of software. The needs of industry and customers are very dynamic. When a customer changes the coverage and the requirements throughout project stages, it causes a lot of new processes for the software developers. All project cost, time and effort become imbalanced. Furthermore, prioritization plays an important role in feature choosing and project cost because of the sector's dynamic structure and customer requirements. Factor behind this variation is lack of customers, directors, software developers and test users, synchronizing with every steps of Systems/Software Development Life Circle (SDLC) with integration. Dynamism of the sector, concentrated the clarity needs, focused directing periodization's and chosen supportive test strategy traits [2]. Agile software development circle is given at Fig. 1 below. After software is accepted, it will be proceeded to test stage. Otherwise circle continues.

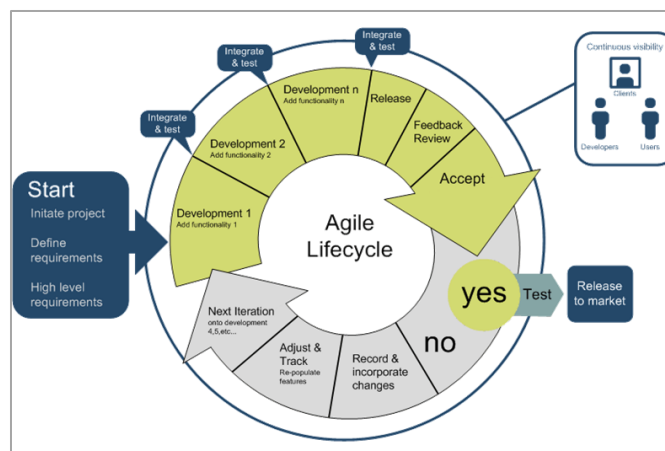


Figure 1: Agile Improvement Circle [3]

Projects are focused on quick software methodology due to how projects having a high risk of loss of money, time and resource lost and high risk of failure. The aim of the project is to research designating potential critic factors and indicators that could cause complications and research them thoroughly.

Because of how software became critical for business, economy and social activities, software development time and directing made the software development complicated and expensive. Software projects have high risk of failure. Portland Business Journal (2008) reported only a 65 to 80 percent of the IT projects were successful, and they couldn't succeed their goals and much delayed substantially or more expensive than planned.

According to the research made by Bloch at al. (2012), with the cooperation of Oxford University almost 45 percent of the IT projects (more than 15 million) passes exceed their budgets. Additionally, 7 percent of these projects have been cancelled and 56 percent of the delivered projects did not meet the expectations [4].

In Dr. Paul Dorsey's (2000) book called "This is a Disaster", he says "As an industry we are failing at our jobs". For this reason, we need to choose most suitable methodologies to improve software systems to prevent criticality, expenses, complication and high failure rates, errors [5].

This study consists of Literature Scanning, Material and Methods, Implementation and Conclusion chapters.

II. LITERATURE REVIEW

In a survey carried out between some of the best software companies at 2011, it has been seen only 5 percent of the projects are improved with Agile Technique. However, today 35-40 percent of the projects follow Agile Technique. This shows quick approach is closing in on traditional practices in sector. Improvement of the Agile systems have increased at every industry [6]. Moreover, manufacturing sector has developed suitable information systems to reduce cycling times and speeding up delivery times as well.

Dynamic software plays a highly important role in quality, planning and directing in industry. Adopting suitable test strategies and choosing correct software test methodology are highly important in today's software distribution and quality control. While Alleman (2002), were disputing over more suitable quick methods for project directing methods, he stated quick project directing methods are used for improving, delivering and obtaining knowledge technology systems in modern organizations. Despite the fact that agile methodology has existed for the last twenty years and used in practice in Information Technologies fields for almost ten years, professionals cannot still reach an agreement on which step of the which project it should be used on. Which features are important and software test and quality directing it can be implemented. In software quality guarantee field, in five SDLC stages Agile test method's most important features must be specified to the directors in an as open and understandable way in the same direction as the work priority and project goals. Understanding specific use cases completely in dept and suitability of specific software project categories to SDLC stages has become obligatory. Suitable agile test strategies and quick test method's inspection might ease the revising problem of IT projects. This allows for a larger field that needs a deeper programming. In this way, this work tries to analyze main Agile test qualities in an empiric way to make the IT projects about manufacturing sector marketing faster in niche context. There have been various studies about quick software improvement in Turkey and other countries. Summary of the studies in 2006-2017 about surveys about quick software improvement are listed in Table 1.

Table 1: Summary of Work about Quick Software Development [8]

Research Reference	Region / Survey Maker	Year	Participant Number	Target/Focus Area
[9]	Various Countries Digital Focus Company	2006	128 organizations 136 directors	The obstacles in front of the agile approaches and usages.
[10]	Various Countries Vijayasarathy and Turk	2008	98 participants	Adaptation and usage of agile software development
[11]	Europe Salo and Abrahamsson	2008	13 software organizations	Situation of agile methods - XP, SCRUM
[12]	Austurian Schindler	2008	Unreported	Situation of agile software development method and practices

[13]	35 different countries Azizyan, Magarian, Kajko-Mattson	2011	120 software organizations 121 participants	Agile approach methods and tools used with it
[14]	Unreported VersionOne	2013	Unreported	Agile methods and situation of software development
[15]	Holland, Indonesia Warma	2012	279 participants	Agile software development success
[16]	North Ireland Bustard, Wilkie, Gr eer	2010 2012	24 participants 30 participants	Changes in agile software development principle and practices implementation
[17]	Various countries Ambler	2010	108 participants	Success situation of the agile projects
[18]	Various countries Ambler	2014	114 participants	Agile software development adaptation
[19]	Turkey Baytam, Kalpsız	2011	30 participants	Agile methods- SCRUM
[20]	Turkey Agile Türkiye	2013	540 participants	Software productivity report
[21]	America Mali Senapathi, Meghann L. Drury-Grogan	2017	29 participants from 21 different companies	Development of a model for on going usage of agile methodology
[22]	Ireland, USA Meghann L. Drury-Grogan ve Kieran Conboy	2015	300 participants	Investigating decision features and hardships for agile software development
[23]	Germany Dr. Ines Mergel	2016	Unreported	Agile innovation methods in the state: A research agendum
[24]	Spain Agustin Yagüe, Juan Garbajosa, Jessica Diaz, Eloy González	2016	21 Software developers	Exploration study in Agile Global Software Development Communication

Total values of software wares, between 1997 and 2012 years, Gross National Product (GNP)'s grow from 1,7 percent to 2,6 percent and software directly contributed approximately 425 billion USA dollars to USA GNP. Employment at software industry also improved approximately by 40 percent (form 1,4 million to 2,3 million) in the same period, and average income of workers were almost three times higher than the amount of all other USA private sector workers.

III. MATERIAL AND METHOD

During the implementation phase of the study, quantities research methodology has been used with 5 software development methodology by failure factors taken into the account. 20 software developers residing in Ankara have been asked to evaluate 5 software development methodologies (Lean, Iterative, Agile, Ad-Hoc and Traditional) to make a survey. Results have been compared with literature and charted at Microsoft Excel settings. Table 2 shows failure factors and indicators analyzed in 4 aspects consisting of organizational, human, time and technique.

Table 2: Failure Factors and Indicator at Agile [26]

Proportions	Failure Factors	Sub Failure Factor		
Organizational	Management Commitment	1. Lack of sponsor or director 2. Lack of director support		
	Organizational Environment and Culture	3. Organization is regional and too large. 4. Organization policies are too political 5. Traditional or out dated organizational culture. 6. Traditional external pressure to watch over the waterfall process. 7. Unsuitable facility/working environment. 8. Local team gathering instead of collective ones. 9. Teams too large.		
		Knowledge and Experience	10. Lacking experience. 11. Lack of necessary talents. 12. Lack of project directive competence.	
			Team Work	13. No Team work 14. Team/Personal opposition 15. Poor customer relationship 16. Team member's / Team's low motivation.
				Requirements and Planning
		Customer Role		
			Monitoring Devices	21. Quick advancement observation methods/systems couldn't found. 22. Unsuitable technology or tools. 23. Straying from coding standards. 24. Lack of code observation/ observations. 25. Insufficient test cases / test scope
		Technique		Project, Technology and Tools

Lack of information and participation about Agile methods, company culture clashing with agile methodology, lack of director or director support, outside force to observe traditional waterfall stage, a larger organizational or communication error, teams unwillingness or inadequacy have been distinct reasons for the failure of the agile development.

IV. APPLICATION

Agile methodology is suggested for “Agile Manifesto” which consists of policies like persons, interaction with courses and tools, software working on extensive documents, customer cooperation on contract negotiation, resistance to change etc. Agile has become a software development based on flexible coding, adaptive planning, continuous delivery and testing, teamwork between personal and teams. Agile software

development teams aims at offering a working application in every sprint and showing it to customer and related person after every sprint. Relations and communication between team members are more important than a development tools or pre-determined timeline. Team spirit makes a project be successful according to an agile development course [27].

Agile method defends the importance of the relations between team and customer as much as it does with the relations between team members. Instead of intense documentation, agile software development prefers the periodically tested work code. Once a team member inserts their code top re-united code block, agile wants test procedures to start automatically. Thus, successful code blokes are prepared. The most important quality of agile software development cycle is that customer can make changes to their needs during the passage of project. Additionally, customer must join the project in all of its steps. Consequently, developers and customer must work together during every step of the project by giving feedbacks to each other.

Comparisons between agile software development and traditional (waterfall) plan oriented methodology are explained in the table 3 and details of agile software methodology are shortly explained.

Table 3: Planned methods and Agile methods [3]

Plan Based Methods	Agile Software Methods
Using tools and cycles	Focusing on people and relations
Completed documents	Functional software
Liaison meetings	Cooperation with customer
Plans must be followed	Changeable plan

According to the Ambysoft (2013) IT Project Success Rates Research by 173 participators, different software development paradigms have been compared. It's shown in Fig 2 that statistically failure rates between Average lean, agile and iterative approaches are almost the same and similarly, failure rates between traditional (waterfall) and ad-hoc (undefined cycle) are almost the same.

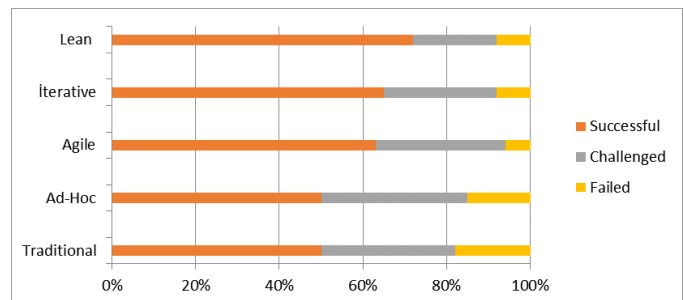


Figure 2: Comparing Software Development Paradigms: Ambysoft 2013 IT Project Success Rates Research [28]

20 Turkish programmers have been asked to rate 5 software development methodologies. Obtained data is given below at Table 4.

When work data was compared with Ambysoft (2013) IT

Project Success Rates Research, participators decided most successful software methodology list as follows; first place Lean, second place Agile, third place Iterative, fourth place Ad-Hoc and last place Traditional methods. While winning a third place at Ambysoft (2013) IT Project Success Rates Research according to our programmers, Agile has the success level of second place.

Table 4: Comparing Software Development Paradigms – Percentage and Frequency Table

	Failed		Challenged		Successful				Total			
	Complete Failure	Failure	Average	Successful	Definitely Successful	n	%	n	%			
										n	%	n
Lean	2	10%	3	15%	4	20%	5	25%	6	30%	20	100%
Iterative	3	15%	2	10%	6	30%	4	20%	5	25%	20	100%
Agile	1	5%	3	15%	6	30%	6	30%	4	20%	20	100%
Ad-Hoc	3	15%	3	15%	7	35%	4	20%	3	15%	20	100%
Traditional	4	20%	5	25%	6	30%	3	15%	2	10%	20	100%

According to the IT Project Success Rates Research made by 20 Turkish programmers, different software development paradigms are compared at Fig. 3. Failure rates between Average lean, agile and iterative approaches are statistically almost the same. Similarly, failure rates between traditional (waterfall) and ad-hoc (undefined cycle) are almost the same.

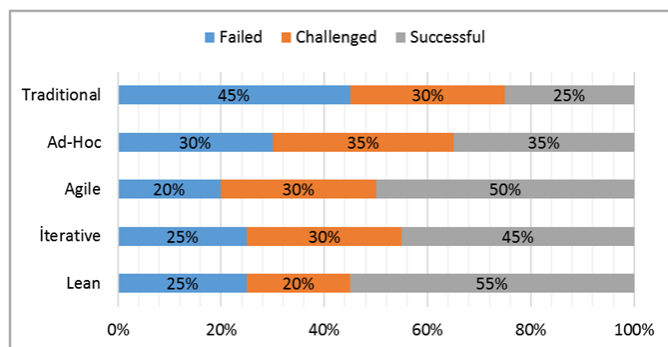


Figure 3: Comparison of Software Development Paradigms

Unlike traditional methodology, Agile methodology which consists of all the initialization of project, analysis, implementation, testing and maintenance step in a consecutive way, developer requires project plan to be carefully arranged and completed according to it before beginning these consecutive steps.

Agile test is completed with weekly and monthly sprints consisting of developers, project periodization before the next sprint, test running, describing and solving and customer feedback. At the same time it suggests a simple project designs for small units and way of starting and working.

V. CONCLUSION

Because of how high failure rates of software projects and project failures, money, time and money losses are vital importance in business life. In a study over agile software test cycles and factors effecting the cycle, failure factors and indicators can be observed over four dimensions (Organizational, Human, Time, Technique) and their sub categories which can contribute to software development methodologies especially Agile.

Within the scope of the study, 20 Turkish programmers have been asked to rate 5 software development methodologies. Gained data have been compared with Ambysoft 2013 IT Project Success Rates Research. Even though the results were mostly similar, the most distinct difference was that Ambysoft 2013 IT Project Success Rates Research put Agile Software Methodology third place, but it was a valuable and successful software development cycle deserving second place for Turkish programmers.

REFERENCES

- [1] Cohn, M., (2007). "Agile estimating and planning", 5th printing., Upper Saddle River, NJ: Prentice Hall PTR.
- [2] Mannila, J., (2013). "Key performance indicators in agile software development", s.57-58.
- [3] Yazılım Tasarım Danışmanları, (2011). "Uygulama geliştirme çevik", <http://sdc.net.au/services/application-development.aspx> [Visited Date : December 11 , 2017]
- [4] Bloch, M., Blumberg, S., and Laartz, J. (2012). "Delivering large-scale it projects on time, on budget, and on value", Retrieved from <http://www.mckinsey.com/insights/business-technology/> [Visited Date : December 11 , 2017]
- [5] Dr. Paul Dorsey (2000). "10 pagrindinių prietaisų kodėl IS projektai įlunga", <https://www.hks.harvard.edu/mrcbg/ethiopia/Publications/Top%2010%20Reasons%20Why%20Systems%20Projects%20Fail.pdf> [Visited Date : December 11 , 2017]
- [6] Schwaber, Carey, and Richard Fichera, (2005). "Corporate IT leads the second wave of agile adoption", Forrester Research, Inc.
- [7] Alleman, G.B., (2002). "Agile Project Management methods for IT Projects", Chapter X, pp(1-22), In: The Story of Managing Projects: A Global, Cross-Disciplinary Collection of Perspectives, Carayannis, E.G. and Kwak, Y.H. (Eds.), Greenwood Press / Quorum Books, CT.
- [8] Çetin, E., Durdu, P.O., (2014). "Türkiye'de Çevik Yazılım Geliştirme Üzerine Bir İnceleme", VIII. Ulusal Yazılım Mühendisliği Sempozyumu (UYMS 2014), KKTC.
- [9] Preuss, D.H.: "Digital Focus Unveils Market Survey Results at Agile 2006". <http://www.infoq.com/news/Digital-Focus-Unveil-Survey-2006> [Visited Date : December 11 , 2017]
- [10] Vijayasarathy, L. R., Turk, D., (2008). "Agile software development: A survey of early adopters", Journal of Information Management, 19 (2), pp. 1-8.
- [11] Salo, O., Abrahamsson, P., (2008). "Agile methods in European embedded software development organizations: a survey on the actual use and usefulness of Extreme Programming and Scrum", IET Software, 2 (1), 58-64.
- [12] Schindler, C., (2008). "Agile software development methods and practices in Australian IT industry: Results of an empirical study. In: International Conference on Computational Intelligence for Modelling Control & Automation", 321-326.

- [13] Azizyan, G., Magarian, M.K., Kajko-Mattson, M.,(2011). "Survey of agile tool usage and needs". In: Agile Conference 2011, 29-38.
- [14] VersionOne, "7th annual state of agile development survey", <http://www.versionone.com/pdf/7th-Annual-State-of-Agile-Development-Survey.pdf> [Visited Date : December 11 , 2017]
- [15] Warma, R.,(2012) , The Success of Agile Software Development, Yayınlanmamış Mezuniyet Tezi, Fontys University of Applied Sciences, Eindhoven.
- [16] Bustard, D., Wilkie, G., Greer, D.(2013), "The maturation of agile software development principles and practice: Observations on successive industrial studies in 2010 and 2012", In: 20th IEEE International Conference and Workshops on the Engineering of Computer Based Systems (ECBS), 139-146.
- [17] Ambler, S.(2010), "2010 Agile Project Success Rates Survey Results", <http://www.ambysoft.com/downloads/surveys/AgileSuccess2010.pdf> [Visited Date : December 11 , 2017]
- [18] Ambler, S.,(2014), "2014 Agile Adoption Mini-Survey", <http://www.ambysoft.com/downloads/surveys/AgileAdoption2014.pdf> [Visited Date : December 11 , 2017]
- [19] Baytam, V., Kalıpsız O.,(2011), "Scrum Yazılım Geliştirme Metodolojisi için Yönetim Sistemi Tasarımı ve Gerçeklenmesi", Yayınlanmamış Master Tezi, Yıldız Teknik Üniversitesi, İstanbul
- [20] Agile Türkiye, (2013), "2013 Software Productivity Report", <http://www.agileturkey.org/> [Visited Date : December 11 , 2017]
- [21] Mali Senapathi, Meghann L. Drury-Grogan, (2017), "Refining a model for sustained usage of agile methodologies", Communication & Media Management, Gabelli School of Business Fordham University, Hughes Hall, Rm. 513, 441 East Fordham Road, Bronx, NY 10458 USA.
- [22] Meghann L. Drury-Grogan ve Kieran Conboy, (2017). "Examining decision characteristics & challenges for agile software development", Journal of Systems and Software Volume 131, September 2017, 248-265.
- [23] Dr.Ines Mergel, (2016). "Agile innovation management in government: A research agenda", Government Information Quarterly, Volume 33, Issue 3, July 2016, 516-523
- [24] Agustin Yagüe, Juan Garbajosa, Jessica Díaz, Eloy González, (2016). "An exploratory study in communication in Agile Global Software Development", Computer Standards & Interfaces, Volume 48, November 2016, 184-197.
- [25] Shapiro, R.,(2014) . "The U.S. software industry as an engine for economic growth and employment",2
- [26] Chow, T. & Cao, D.,(2008). "A survey study of critical success factors in agile software projects", The Journal of Systems and Software, 81, 961-971.
- [27] Beck, K., Cockburn, A., Jeffries, R., and Highsmith, J., (2001). "Agile Manifesto", <http://www.agilemanifesto.org> , [Visited Date : December 11 , 2017]
- [28] Ambysoft Scott Ambler Associates, (2013). "IT Project Success Rates Survey", <http://www.ambysoft.com/surveys/success2013.html> [Visited Date : December 11 , 2017]

Performance Estimation of Sorting Algorithms Under Different Platforms and Environments

M.HAMITI¹, E. MOLLAKUQE², S. KRRABAJ² and A.SUSURI²

¹ SEE-University, Tetovo/R. Macedonia, m.hamiti@seeu.edu.mk

²University of Prizren, Prizren/R. Kosovo, elissamollakuqe@gmail.com,
samedinkrrabaj@gamil.com, arsimsusuri@gmail.com

Abstract - Sorting data is the ordering of data in a regular way, such as: from the largest value to the smallest value or vice versa. The research object is to implement five sorting algorithms on several computer platforms and specific environments, which will bring us some conclusions. The research object has been analyzed in terms of performance and are addressed in which computer architecture is most appropriate.

Keywords - sorting, sorting algorithms, performance, programming language, processor.

I. INTRODUCTION

Sorting data is data placement in a particular way, such as ups and downs. It is one of the most important computing applications. The Bank classifies all the checks made by the bank account number so that it can prepare individual bank statements at the end of each month, and so on. Sorting data is an intriguing problem that has attracted great research efforts. Algorithms sorting are effective algorithms that perform an important task by putting the elements of a list in a certain way or organized in a particular way. Sorting data is developed to adjust the values in different ways for a database. For example, solving a math problem will sort the numbers in a string, from the smallest to the largest or the largest to the smallest. Typically, sorting classifies and lists a set of data. Most sorting algorithms perform their work with three steps: compare, exchange and copy, continuing with execution over and over until the data is listed.

Algorithms of sorting are widespread in different branches of computer science, so in this research are analyzed such algorithms by seeing in what form these different algorithms are distinguished, how does the programming platform affect different sorting algorithms, how does the hintere in the performance of algorithms, and what are the advantages of using these algorithms.

II. PERFORMANCE OF ALGORITHMS IN DIFFERENT PLATFORMS

The concept of rankings is very important to understand because ranking allows people to better understand life in the surrounding world. Suppose someone tries to find a name on a phonebook or ask for an address on a table that contains hundreds of rows and columns, and so on.

But many branches of computer science depend on the concept of ranking, many commercial and non-commercial applications include data rankings, products, and extra units. Now, all sorting algorithms use different sorting methods, but they are distinguished by:

- simplicity / complexity of design
- speed
- behavior and
- The analytical properties they contain.

But analysis of algorithm performance is an issue we always have interest because algorithms are those computer parts that are often referred to as "smart in complex solutions." Therefore, their performance and accuracy is very important. The performance of algorithms is in fact dealt with in two aspects:

- According to time
- According to space

The Quick Sort algorithm is probably one of the most common sorting algorithms. It is characterized by an implementative simplicity, functional speed, and is efficient for classifications for different types of data. Moreover, Quick Sort has an internal ring, which means that it is fast in practice and in theory, which other sorting algorithms do not have.

Quick Sort uses the split method and the rule for sorting. It works by dividing a group into two subgroups, otherwise known as the MergeSort complement.

In computer science Merge Sort is another algorithm that is specified by the principle of divide and conquer. (Knuth, 2007). When invoking this algorithm to act on a n-string of data sets it first divides the string into two equal sequences, and then uses the recursiveness on the divisor made.

Bubble Sort is a simple rank order algorithm and at one and the same time too slow. Here, the ranking is done based on comparisons of the adjacent parties and elements change the place when it is noticed that they are not in the ranking. The name gets the idea "swim like a flush" from the bottom of the list on the other. (Niemann, 2015) Assuming that the order is top-down, higher values "swim" to the left, while lower values "swim" to the right. But what makes this algorithm inadequate is the lack of evidence when there is a large set of data that needs to be ranked.

Heap Sort is another sorting algorithm that is based on comparison, this can be assumed as an improved version of the Selection Sort algorithm. (PRINCETON EDU, 2017) The Heap Sort job is quite similar to the Selection Sort sort process, here entries are divided into two groups: the ranked and the ungrouped group, and linearly they will be ranked by drawing the largest element and by move it to the ranked group. What makes this algorithm unusual is the slow work it has, though in most cases Heap Sort replaces the Quick Sort algorithm

C# is an object-oriented programming language that is synonymous with JAVA programming language and is capable of running fast on computers. This programming language is capable of operating on many platforms, such as: Windows, Solaris, UNIX and LINUX. Setting up some sorting algorithms in one place is a bit difficult because we need to use some programming techniques. The C # programming language program is called "Sorting Analyzer", shown in the following chapters.

PYTHON is a programming language of the highest level with a general programming purpose. As a programming concept came in 1980 and the first implementations began in December 1989 by Guiso Van Rossum at Centrum Wiskunde & Informatica - CWI, Netherlands. Python is characterized by a design philosophy on code readability and a syntax that allows developers to display concepts in fewer rows compared to C ++ and JAVA programming languages.

The **PHP** code is placed within HTML or HTML5, or combined with templates, content management systems, or different webcams. The PHP code is usually processed through a PHP interpreter that is implemented as a module on the web server or as a Common Gateway Interface (CGI).

Java as an essential component of the Java platform was released in public in 1995. Java, although most of its syntax is derived from programming languages C and C ++, compared to these two languages it has a simpler object model such as and has less support for fair-by-fair work with system resources (such as memory). Java-written programs are usually compiled in bytes that are executed in a virtual Java machine (Java Virtual Machine) which is independent of computer architecture.

III. PERFORMANCE OF ALGORITHMS IN DIFFERENT COMPUTER ARCHITECTURE

The processor can be produced using different technologies:

- single-core processor
- multi-core processor

The development of processors runs in several generations: Core Solo, Core Duo, Core 2 Duo, Core 2 Quad, Core 2 Extreme, Core M, Core M3, Core i5, Core i7 and Core i7 Extreme Edition.

Intel Core i5 (TM) and Intel Core i7 (TM) processors are fast, more efficient and better equipped with flexibility for modern computing. They are housed in a large number of laptops and desktops. Technological enhancements have provided a wide range to get the processor that meets our needs. The Intel Core i7 (TM) processor offers a great speed and exceptional work start while the Intel Core i5 (TM) processor is closer to your daily needs. the Microsoft Equation

The performance of the sorting algorithms in the Intel Core i5 (TM) processor has been tested by analyzing data that has been divided into three categories:

- Unrecorded data
- Semi-sorted data
- Data sorted by repeated data.

Space complexity is not the only limitation that limits the speed of an algorithm. The total space is also important

The given graph, on the X axis, shows sorting algorithms while on Y axis provides the total memory needed in the byte.

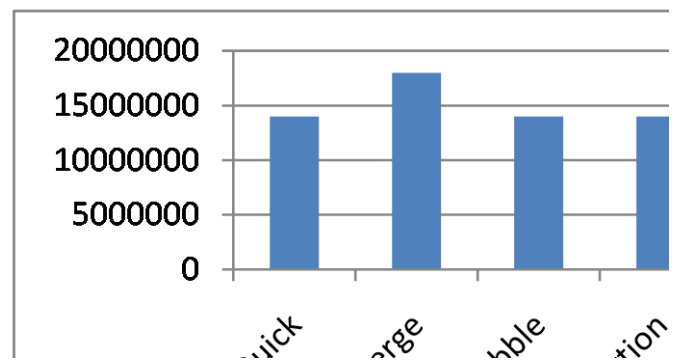


Figure 1: Memory in byte

Intel Core i7 (TM) is at the top of processor lists. (Zhislina, 2015) These processors are featured in Bridge Sandy models with larger amounts of cache (L3) and high-frequency workloads. Most of these models are very similar to Intel Core i5 (TM). The complexity of the space being not the only limitation of spatial algorithm performance, then the total space is:

- QuickSort: Using the stocks for this memory, the recursive depth has been added and 12 bytes to generate memory consumption.
- Merge Sort: The space consumed by Merge Sort is: $(100117 \times 4) +$ the size of the string declared in the program = 400492 bytes, so the variable size variables is $400492 - 400468 = 24$ bytes.
- Bubble Sort: The total space consumed depends on the declared variables, ie the complexity of the space $O(1)$.
- Insertion Sort: The total space consumed depends on the variables declared, ie the complexity of the space $O(1)$.
- Heap Sort: The total space consumed depends on the declared variables, ie the complexity of the O space (1) . (Nilsson, 2000)

IV. RESULTS

Using original programs written in specific programming languages (C #, JAVA, PYTHON and PHP) and Intel Core i5 (TM) processors, various analyzes have been carried out. To output results, a total of 100117 inputs (of type numbers) were analyzed, which are classified into three different files with the .xlsx extension. To get convincing results, they are categorized into three sets: unlisted data (un_sorted.xlsx), semi-sorted data (half_s.xlsx), and more sorted but repetitive file (sorted_rep.xlsx).

A. Implementing algorithms on the Intel Core i5 (TM) platform, 2.53GHz, 4GB of RAM in C #, Java, Python and PHP programming language

To analyze this sorting algorithm in C #, JAVA, PYTHON and PHP programming languages, there are provided auxiliary tools such as: the required memory of the device, a computer hardware that meets the required conditions (Intel Core i5 processor and 2.53 GHz workstation) and execution time.

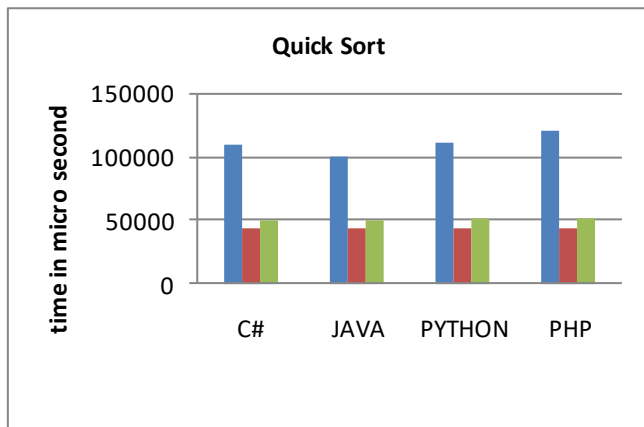


Figure 2: QuickSort on Intel Core i5(TM)

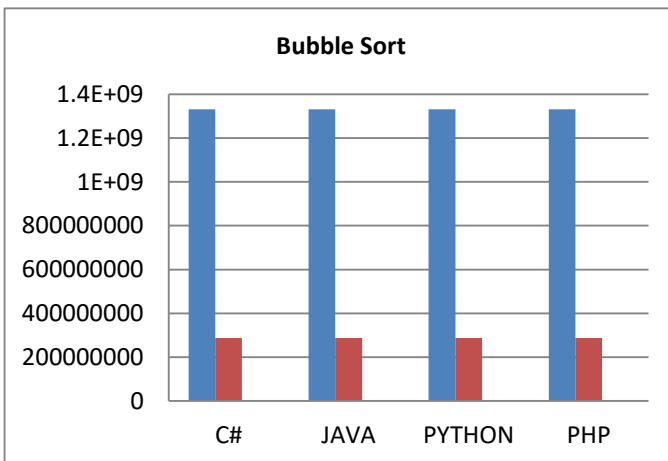


Figure 3: Bubble Sort on Intel Core i5(TM)

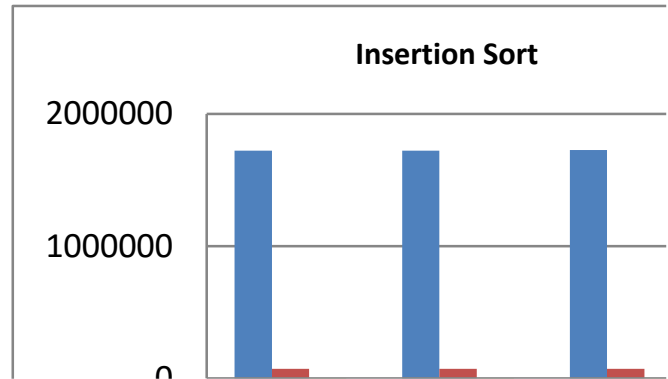


Figure 4: Insertion Sort on Intel Core i5(TM)

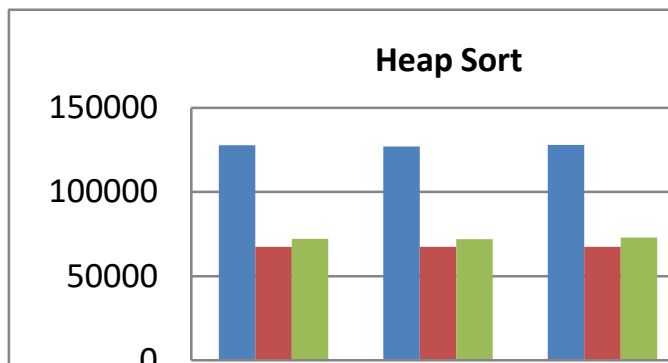


Figure 5: Heap Sort on Intel Core i5(TM)

V. CONCLUSION

In this study, there are analyzed sorting algorithms written on different programming platforms and in various execution environments, respectively execution in the Intel Core i5 (TM) processor. The results are generated by analyzing a data set of 100117, classified into three groups: half-sorted data, unlisted data and reclassified data. After the analysis of performance and time complexity for each sorting algorithm (Quick Sort, Merge Sort, Bubble Sort, Insertion Sort and Heap Sort), the following conclusions were generated:

- Sorting algorithms are good performance processor gauges
- All analyzed algorithms (QuickSort, MergeSort, BubbleSort, InsertionSort, and HeapSort) work faster in JAVA programming language, followed by C #, PYTHON, while PHP remains the slowest in algorithm performance.
- Sorting algorithms showed better performance on the Intel Core i7 (TM) processor, 3.10 GHz, 8GB RAM
- Quick Sort on the Intel Core i5 (TM) processor, 2.53GHz, 4GB of RAM, the average execution time for unrecorded data is 110122 microseconds, for semi-sorted data is 43702 microseconds, and for retrieved data is 50800 microseconds

- Merge Sort on the Intel Core i5 (TM) processor, 2.53 GHz, 4 GB of RAM, the average execution time for unrecorded data is 1152110 microseconds, for half-sorted data is 1118701 microseconds, and for retrieved data is 1032803 microseconds
 - Bubble Sort on the Intel Core i5 (TM) processor, 2.53 GHz, 4 GB of RAM, the average execution time for unrecorded data is 1332027302 microseconds, for semi-sorted data is 287687226 microseconds, while for replicated data is 1007 microseconds
 - Insertion Sort on the Intel Core i5 (TM) processor, 2.53 GHz, 4 GB of RAM, the average execution time for unrecorded data is 1723711 microseconds, for semi-sorted data is 73045 microseconds, and for retrieved data is 3521 microseconds
 - Heap Sort on the Intel Core i5 (TM) processor, 2.53 GHz, 4 GB of RAM, the average execution time for unrecorded data is 127848 microseconds, for semi-sorted data is 67462 microseconds, and for replicated data is 72566 microseconds
- [27] [http://onlinelibrary.wiley.com/journal/10.1111/\(ISSN\)1468-229X](http://onlinelibrary.wiley.com/journal/10.1111/(ISSN)1468-229X) (access 02/08/2017)
- [28] <http://libraries.pewinternet.org/2012/06/22/part-4-how-people-used-the-library-in-the-past-year/> (access 28/02/2017)
- [29] <http://www.libraries.psu.edu/psul/home.html>(access 22/03/2017)

REFERENCES

- [1] Cormen, T. H. *Introduction to Algorithms* . Cambridge. 2009
- [2] Demuth, H. *Electronic Data Sorting*. Stanford University. 2012
- [3] Granville Barnett, L. D. *Data Structure and Algorithms: Annotated Reference with Example*. Chicago: AWP, 2014
- [4] Lanne David & Williams Hugh, *Web Database Application with PHP and MySQL*, O'Reilly, United States of America, 2004
- [5] Nixon Robin, *PHP, MySQL, JavaScript & CSS*, O'Reilly, United States of America, 2012
- [6] Welling Luke & Thomson Laura, *PHP and MySQL Web Development*, Pearson Education, USA, 2008.
- [7] Ullman Larry, *PHP and MySQL for Dynamic Web Sites*, Peachpit Press, USA, 2012
- [8] Powers David, *PHP Solutions: Dynamic Web Design Made Easy*, Spring, UK, 2010
- [9] Gilmore W. Jason, *Beginning PHP and MySQL*, Apress, New York, 2009
- [10] Guna, A. *Fundamental Structure of Computer Science*. NY: AWP, 2013
- [11] Kim, P. S. *Theory and Applications of Models of Computation*. UK: LNCS 2008.
- [12] Knuth, D. E. *Early development of programming languages*. UK: AWP, 2007
- [13] Niemann, T. *Sorting and Search Algorithms*. NY: Pavel Dubner, 2015
- [14] Nilsson, S. *The Fastest Sorting Algorithm*. Dr Dobbs, 2000
- [15] Robert Sedgwick, K. W. *Algorithms* (4th Edition). Nã *Algorithms* (f. 480). Library of congress Cataloginig, 2016
- [16] Rosen, S. *Programming Systems and Languages*. McGraw-Hill, 2012
- [17] Sahn, E. H. *Fundamentals of Data Structures*. H. Freeman & Co, 2013
- [18] Sedgwick, R.. *Implementing Quicksort programs*. Comm. ACM, 2009
- [19] Thomas H. Cormen, C. E. *Introduction to Algorithms* (f. 1312). MIT Press, 2009
- [20] Wirth, N. *Algorithms & Data Structures*. NY: Prentice-Hall, 2010
- [21] Zhislina, V. (2015). *Why has CPU frequency ceased to grow*. 2014: Intel Corporate.
- [22] <http://www.cprogramming.com/tutorial/computersciencetheory/sortcmp.html>. (a.d.) (access 01/07/2017)
- [23] <http://algs4.cs.princeton.edu/25applications/> (access: 02/23/2017)
- [24] <http://www.tutorialspoint.com/php/>(access 15/08/2013)
- [25] <http://www.php-rocks.com/advanced.php>(access 15/08/2013)
- [26] <http://olabout.wiley.com/WileyCDA/Section/id-406100.html>(access 02/08/2017)

Model development for estimation of traffic accidents with metaheuristic algorithms

A.ÖZKIŞ¹ and T. SAĞ²

¹ Konya Technical University, Konya/Turkey, ahmetozkis@gmail.com

² Selcuk University, Konya/Turkey, tahirsag@selcuk.edu.tr

Abstract - In this study, mathematical models have been developed to estimate number of traffic accidents, injuries and fatalities occurred in Turkey between 2002 and 2014. In order to determine the appropriate values of three weight factors of these models, well-known metaheuristic algorithms, PSO and ABC, were used. Mean absolute errors (MAE) between the observed and estimated data were addressed as objective function and aimed to be minimize. The comparison of the obtained results show that the prediction successes of the ABC models are higher than that of the PSO models.

Keywords – Artificial bee colony, Estimation of traffic accidents, Nonlinear regression, Particle swarm optimization.

I. INTRODUCTION

Traffic accidents are a major problem in Turkey that causes financial losses, injuries and fatalities. According to statistical data about traffic accidents occurred in Turkey between 2002 and 2014 has given in Table 1, unfortunately, thousands of people die and hundreds of thousands of people are injured every year due to traffic accidents throughout the country [1].

Table 1: Numbers of injuries and fatalities from traffic accidents occurring in Turkey between 2002 and 2014

Year	Veh. No	Pop. (*1000)	Acc. No	Inj. No	Fat. No
2002	8 655 170	69 302	439 777	116 412	4 093
2003	8 903 843	70 231	455 637	118 214	3 946
2004	10 236 357	71 152	537 352	136 437	4 427
2005	11 145 826	72 065	620 789	154 086	4 505
2006	12 227 393	72 974	728 755	169 080	4 633
2007	13 022 945	70 586	825 561	189 057	5 007
2008	13 765 395	71 517	950 120	184 468	4 236
2009	14 316 700	72 561	1 053 346	201 380	4 324
2010	15 095 603	73 723	1 106 201	211 496	4 045
2011	16 089 528	74 724	1 228 928	238 074	3 835
2012	17 033 413	75 627	1 296 634	268 079	3 750
2013	17 939 447	76 668	1 207 354	274 829	3 685
2014	18 828 721	77 696	1 199 010	285 059	3 524

Veh. No: Number of vehicle
 Pop: Population
 Acc. No: Number of accidents
 Inj. No: Number of injuries
 Fat. No: Number of fatalities

Population growth and increasing the number of vehicles accordingly play an important role in traffic accidents. Therefore, these two parameters can be used to develop estimation models. Obtained estimations can contribute to improve traffic safety and to prevent future problems. In last two decades, numerous models have been proposed by using Artificial Neural Network (ANN) [2] which is an artificial intelligence technique, for transportation and traffic safety problems [3-7]. In addition to ANN, another method commonly used in model development is the metaheuristic approaches [8-11]. The successes of ANN and metaheuristic algorithms in modeling have also encouraged other researchers to work in this area. In this study, mathematical models that estimate number of accidents, injuries and fatalities occurred in Turkey between 2002 and 2014 have been developed using metaheuristic algorithms and obtained estimation results have been compared.

The article is organized as follows: the metaheuristic algorithms used in the study are briefly explained in section 2. The model pattern and normalization ranges of the parameters are given in section 3. Settings of the metaheuristic algorithms, developed models and experimental results are given in section 4. The conclusions and recommendations for future studies are given in section 5.

II. METAHEURISTIC ALGORITHMS

Classical mathematical approaches can have drawbacks in terms of calculation time and accuracy in solving complex problems. In order to overcome this situation, researchers have proposed metaheuristic algorithms which are inspired by nutrient-seeking behaviors of animal species and natural phenomena. There are numerous metaheuristic algorithms in the literature such as Genetic Algorithm, Ant Colony Optimization, Particle Swarm Optimization (PSO) [12], Artificial Bee Colony (ABC) [13] algorithm etc. In this study, a regression model was proposed by using PSO and ABC algorithms to estimate traffic accidents. Both algorithms are explained briefly as follows:

A. PSO Algorithm

The PSO is a swarm-based optimization algorithm proposed by Kennedy and Eberhart, inspired by food search behavior of birds and fishes. In the PSO algorithm, each individual in the

swarm is called a particle. The positions of the particles are updated using Eq. 1 and Eq. 2 according to the best position in their memory and the position of the best particle in the swarm. Thus, it is aimed to achieve a balance between local and global search.

$$v_{id}^{t+1} = wv_{id}^t + c_1 rand_{1d}^t (P_{id}^t - x_{id}^t) + c_2 rand_{2d}^t (P_{gd}^t - x_{id}^t) \quad (1)$$

$$x_{id}^{t+1} = x_{id}^t + v_{id}^{t+1}, \quad (2)$$

where, w is inertia weight, c_1 and c_2 are cognitive and social coefficients, $rand_1$ and $rand_2$ are random real numbers in range $[0, 1]$. t denotes number of the iteration and d denotes d . decision variable of the particles. P_i refers to the best position of i . particle and P_g refers to the best position of the swarm has found so far. Finally, v_i is the velocity vector of the i . particle.

B. ABC Algorithm

The ABC is an other swarm-based optimization algorithm proposed by Karaboga, imitating food foraging behaviors of honey bees. In the ABC algorithm, population consists of employed, onlooker and scout bees. Each employed bee is responsible for a food source and reports the amount of food in its source to the onlookers waiting in the hive. After all employed bees report their food amount, probability of selection for each source is assigned in proportion to the amount of their foods. The onlooker bees choose a food source by considering these selection probabilities. An employed bee turns into a scout bee and discovers a new food source if the existing source is exhausted (It means that existing source failed consecutively up to number of limits).

In ABC algorithm, the positions of the bees are updated using Eq. 3.

$$v_{ij} = x_{ij} + \phi_{ij}(x_{ij} - x_{kj}), \quad (3)$$

where, i denotes the i . solution, $k \in \{1, 2, \dots, MaxSourceNumber\}$ is randomly chosen index of neighbor solution provided that different from i , $j \in \{1, 2, \dots, D\}$ is randomly chosen decision variable, ϕ_{ij} is random real numbers in range $[-1, 1]$.

III. METAHEURISTIC-BASED MODELS

In this study, a linear model for accident estimation were proposed by using population (P), number of vehicles (V), accidents (A), injuries (I) and fatalities (F) for the years 2002-2014. These data has been obtained from website of the Turkish Statistical Institute [1]. Pattern of the used linear model is given in Eq. 4.

$$LinearModel = w_1 + w_2.V + w_3.P, \quad (4)$$

where w_1 , w_2 and w_3 are weighting factors and these factors must take appropriate values to successfully estimate A , I and F . Thus, PSO accident model ($PSOAM$), PSO injury model

($PSOIM$), PSO fatality model ($PSOFM$), ABC accident model ($ABCAM$), ABC injury model ($ABCIM$) and ABC fatality model ($ABCFM$) were developed separately. While developing models, the data of the first 9 years (2002-2010) were used for training and the last 4 years (2011-2014) were used for testing. Mean absolute errors (MAE) of the observed and estimated values have been addressed as the objective function to be minimized. The mathematical expression of the MAE is given in Eq. 5.

$$MAE = \frac{1}{DataNo} \sum |observed_j - estimated_j| \quad (5)$$

Please, note that variables used in models are normalized between 0.1 and 0.9. Normalization ranges are set 64.000.000 - 90.000.000 for P , 4.000.000 - 22.000.000 for V , 400.000 - 1.500.000 for A , 80.000 - 350.000 for I and 3.000 - 6.000 for F .

IV. COMPARISON OF THE MODELS

A. Parameter Settings of the Algorithms

For both algorithms, the population sizes and the number of iterations were set as 20 and 500 respectively to make a fair comparison. The cognitive and social coefficients (c_1 and c_2) of the PSO algorithm were both set to 2 and the inertia weight (w) was reduced from 0.9 to 0.2 during iterations. The limit value of the ABC algorithm was set to 100. The search space of the weighting factors is set to $[-5, 5]$.

B. Developed Models

The models developed by PSO and ABC algorithms are given in Eq. 6 – Eq. 11.

$$PSOAM = -0.249 - 0.744.V + 1.866.P, \quad (6)$$

$$PSOIM = -0.039 - 0.410.V + 1.167.P, \quad (7)$$

$$PSOFM = 0.353 - 0.395.V - 0.078.P, \quad (8)$$

$$ABCAM = -0.298 + 0.421.V + 1.125.P, \quad (9)$$

$$ABCIM = -0.217 + 0.179.V + 1.131.P, \quad (10)$$

$$ABCFM = 0.652 - 2.131.V + 1.035.P, \quad (11)$$

C. Experimental Results

The number of accidents, injuries and fatalities between 2011 and 2014 were estimated by using the developed models. The results and relative errors are given in Table 2-4.

Table 2: Comparison of the PSOAM and ABCAM models on the number of accidents

Year	Number of Acc. (Obs.)	PSOAM	PSOAM Relative Errors(%)	ABCAM	ABCAM Relative Errors(%)
2011	1 228 928	1 114 171	-9.38	1 087 055	-11.54
2012	1 296 634	1 193 383	-7.96	1 168 073	-9.91
2013	1 207 354	1 263 929	4.68	1 248 953	3.44
2014	1 199 010	1 332 972	11.17	1 328 449	10.79

When the estimated number of accidents and relative errors given in Table 2 are examined, it is seen that the PSOAM model estimated the observed number of accidents in 2011 and 2012 with fewer errors than the ABCAM model. In 2013 and 2014, the ABCAM model estimated fewer errors than the PSOAM model.

Table 3: Comparison of the PSOIM and ABCIM models on the number of injuries

Year	Number of Inj. (Obs.)	PSOIM	PSOIM Relative Errors(%)	ABCIM	ABCIM Relative Errors(%)
2011	238 074	224 709	-5.61	242 309	1.77
2012	268 079	237 398	-11.44	260 008	-3.01
2013	274 829	248 836	-9.45	277 321	0.90
2014	285 059	260 036	-8.77	294 325	3.25

When the estimated number of injuries and relative errors given in Table 3 are examined, it is seen that the ABCIM model estimates the observed number of injuries in all cases clearly with fewer errors than the PSOIM model.

Table 4: Comparison of the PSOFM and ABCFM models on the number of fatalities

Year	Number of Fatalities (Observed)	PSOFM	PSOFM Relative Errors(%)	ABCFM	ABCFM Relative Errors(%)
2011	3 835	4400	14.73	4 112	7.22
2012	3 750	4429	18.10	4 053	8.08
2013	3 685	4464	21.13	3 953	7.27
2014	3 524	4499	27.66	3 854	9.36

When the estimated number of fatalities and relative errors given in Table 4 are examined, it is seen that the ABCFM model estimates the observed number of fatalities in all cases with clearly fewer errors than the PSOFM model.

As a result, it was observed that the ABC-based models generally achieved more successful results than the PSO-based models.

V. CONCLUSIONS AND FUTURE WORKS

In this study, a regression model that predicts the number of traffic accidents, number of injuries and fatalities is proposed by using the data of traffic accidents that occurred in Turkey between 2002 and 2014. The weight factors in the model were re-determined by PSO and ABC algorithms for each estimation. As a result, it is seen that the model produced by ABC algorithm makes more successful predictions than the model proposed by PSO algorithm.

This study has shown that PSO and ABC are successful algorithms to develop estimation models. These algorithms can be used to estimate different problems such as energy estimation, population estimation etc. In addition, different mathematical models can be developed using the recently proposed different metaheuristic algorithms.

REFERENCES

- [1] Traffic Accidents Data of the Turkish Statistical Institute, in: http://www.tuik.gov.tr/PreIstatistikTablo.do?istab_id=1586
- [2] J.J. Hopfield, Neural networks and physical systems with emergent collective computational abilities, Proceedings of the national academy of sciences, 79 (1982) 2554-2558.
- [3] A.P. Akgüngör, E. Doğan, An artificial intelligent approach to traffic accident estimation: model development and application, Transport, 24 (2009) 135-142.
- [4] A. Manik, K. Gopalakrishnan, A. Singh, S. Yan, Neural networks surrogate models for simulating payment risk in pavement construction, Journal of Civil Engineering and Management, 14 (2008) 235-240.
- [5] X. Miao, B. Xi, Agile forecasting of dynamic logistics demand, Transport, 23 (2008) 26-30.
- [6] Y.S. Murat, H. Ceylan, Use of artificial neural networks for transport energy demand modeling, Energy policy, 34 (2006) 3165-3172.
- [7] F. Wang, Modeling traffic emissions with artificial neural networks and regressions, Geographical and Environmental Modelling, 2 (1998) 103-113.
- [8] T. Akiyama, Y. Kotani, T. Suzuki, The optimal transport safety planning with accident estimation process, in: Traffic and Transportation Studies (2000), 2000, pp. 99-106.
- [9] S. Jin, S.-Y. Park, J.-J. Lee, Driver fatigue detection using a genetic algorithm, Artificial Life and Robotics, 11 (2007) 87-90.
- [10] J.C. Jong, M.K. Jha, P. Schonfeld, Preliminary highway design with genetic algorithms and geographic information systems, Computer-Aided Civil and Infrastructure Engineering, 15 (2000) 261-271.
- [11] M. Nagai, M. Onda, T. Katagiri, Application of genetic algorithm to analysis of driver's behaviour in collision avoidance, International journal of vehicle design, 18 (1997) 626-638.
- [12] J. Kennedy, R. Eberhart, Particle swarm optimization, 1995 Ieee International Conference on Neural Networks Proceedings, Vols 1-6, (1995) 1942-1948.
- [13] D. Karaboga, An idea based on honey bee swarm for numerical optimization, in: Technical report-tr06, Erciyes university, engineering faculty, computer engineering department, 2005.

CLASSIFICATION OF EEG SIGNALS BY USING TRANSFER LEARNING ON CONVOLUTIONAL NEURAL NETWORKS VIA SPECTROGRAM

A.E. TOP¹ and H. KAYA²

¹Ankara Yildirim Beyazit University, Ankara/Turkey, aetop@ybu.edu.tr

²Ankara Yildirim Beyazit University, Ankara/Turkey, hilalkaya@ybu.edu.tr

Abstract - Previous studies on classifying Electroencephalography (EEG) sleep data generally use the signal itself. Many of these studies need series of pre-processing operations, manual feature extraction, complex and hard application processes. There is no need for lots of pre-processing stages in Convolutional Neural Networks (CNN) and features can be learned automatically instead of using manually extracted features. Also CNNs have better performance over most of other methods in visual classification.

The study presented in this paper is based on applying transfer learning with CNNs via spectrogram images, that were obtained by using Short-Time Fourier Transform (STFT), on ISRUC-Sleep dataset (ISRUC) for classifying EEG signals. AlexNet trained with 100 patient subjects from ISRUC was used as pre-trained CNN. For classifying sleep stages, single-channel EEG data, that was taken from 10 healthy people, was used as target domain. To reduce overfitting, we employed an image translation operation and images were augmented horizontally. The main purpose of using transfer learning method in this study is achieving better training duration and accuracy. Applying transfer learning increased the accuracy of the classification by 3.11%, when compared to the result of using non-pretrained AlexNet, which was trained from scratch.

For the evaluation of the proposed methodology, non-pretrained AlexNet and AlexNet trained with ImageNet were also performed on the same target domain and the results were compared. When the source domain of transfer learning was ImageNet, the accuracy was decreased by 2.73% compared to the result of training from scratch. Results showed that transfer learning increases the accuracy when target and source domains are similar, but it may decrease the accuracy when used on different domains (i.e., ImageNet includes images and ISRUC consists of signals).

Keywords - Electroencephalography (EEG), Convolutional Neural Network (CNN), transfer learning, spectrogram, Short-Time Fourier Transform (STFT).

I. INTRODUCTION

Convolutional Neural Networks (CNN) have been achieving state of the art results in many areas such as hand-written digit recognition and face detection since its beginning [1] in early 90's [2]. As Graphics Processing Units' (GPU) prices fall and their performances increase by time, Deep Learning (DL)

has become extremely popular in recent years. In last few years, a record breaking performance came by AlexNet [3] and then many papers have shown excellent results in visual classification [2, 4-8]. After AlexNet was introduced, Artificial Intelligence (AI) society that study on visual classification have focused much more on CNNs and they improved AlexNet's performance by changing some parameters or adding more layers, in other words, making it deeper [2, 5, 6].

When the data size is low, CNN trained from scratch gives terrible results. At [2], they trained a CNN from scratch with 3840 images of Caltech-256 [9] dataset and got 9.0% accuracy. But when they used same CNN architecture but pre-trained with ImageNet [10], they got 65.7% accuracy and beat state-of-the-art results at that time. The transfer learning approach is beneficial for smaller scale datasets. It increased the accuracy because target and source domains were similar (i.e. Caltech-256 is a similar dataset to ImageNet) in this study. When features are different, transfer learning is not much profitable.

Sleep stage has been classified from Electroencephalography (EEG) signal with various methods by using the signal itself in so many papers [11-15]. These methods come with some outcomes and requirements like pre-processing and feature extraction. On the other hand, there is no need for feature extraction in CNNs.

CNNs are more successful over so many techniques in visual classification. There are few examples of using visual representation of signals to classify sleep stages. Thus, the approach of this study, which is converting EEG signals into images that represent features of signal then constructing a CNN and making those images as the inputs of CNN, emerges.

A. Paper Organization

Section I contains the purpose and the scope of the research and also has an overview of related works. The second chapter includes proposed method, details about the data, and training details of the experimental study. In the final chapter, results obtained from experiments, comparison and discussion of the results are presented.

B. Related Work

This study covers image classification, sleep stage classification, convolutional neural networks, and transfer learning topics.

CNNs are so popular and they are getting state of the art results in the field of image classification. LeNet-5 [16] was proposed in 1998 by founding father of CNNs, Yann LeCun, and that had 7-level convolutional network. Since that time, CNNs have similar structure that consists of stacked convolutional layers, pooling layers sprinkled between convolutional layers, and one or more fully connected layers at the end of the stacked convolutional layers.

AlexNet [3] is a deep CNN that won ImageNet Large Scale Visual Recognition Challenge (ILSVRC) in 2012 with 63.3% accuracy [8]. This was a milestone for large scale object recognition. AlexNet has very similar structure to LeNet-5 and contains 5 convolutional layers initially and followed by three fully connected layers. It has a simpler design when compared to more complex designs that define state of the art results in image classification [17]. Recent improvements on performance is about increasing the number of layers [4-7], which makes the network deeper, changing the layer size [18] so the filter size such as Zeiler and Fergus decreased the filter size to 7*7 on ZF Net [2] or Simonyan and Zisserman decreased it to 3*3 on VGGNet [5] instead of 11*11 in [3] for large datasets like ImageNet.

For smaller datasets, deep learning is relatively harder to get good results such as Barnes et al. classified Tiny ImageNet and could only get 25.4% accuracy with AlexNet architecture. Then they improved by applying data augmentation, weight decay, and snapshot ensembling on different CNN architectures to get reliable results [17].

Transfer learning is a reasonable choice for small scale datasets if there is somehow similar source domain available. It transfers previously acquired knowledge to a new domain which helps solving new problems faster, better and more efficiently [19]. In [20] and [21], they used other categories as source domain to improve the performance on target categories and to reduce the need for number of training images. Their models were based on Support Vector Machines (SVM).

In [22], studied to learn visual world weights, that are learned from various datasets excluding their biases and have good generalization ability, then apply the learned visual world weights to new dataset with its bias that results in dataset specific model. Saenko et al. presented a study about domain adaptation, which they mapped the data from source domain to target domain, for object recognition [23]. In [22] and [23] both also used SVMs.

Similar to our work, following papers used AlexNet trained with ImageNet and transfer learning technique to their specific works. In [24], they trained AlexNet with ILSVRC 2012, then extracted features from the trained network and trained SVM and Logistic Regression classifiers. They outperformed state-of-the-art approaches that are using feature engineering. In [25], they trained AlexNet and model of [26] on ImageNet then used these pre-trained networks for emotion recognition. Shin et al. explored 3 different CNNs that are trained with ImageNet. CifarNet [27], GoogLeNet [6], and AlexNet are used as pre-trained networks and performed on 2 specific computer-aided detection problems. Wimmer et al. trained 4 different CNNs including AlexNet on ImageNet dataset. Then classified Celiac Disease by using them [28].

There are several studies on sleep stage classification. In [29]

and [30] Deep Belief Network (DBN) based feature extractors are used. Then a classifier algorithm such as Gaussian Mixture Model (GMM) is used by [29], Hidden Markov Model (HMM), K-Nearest Neighbors (KNN), and Support Vector Machine (SVM) are used all together by [30], and they got 91.31% accuracy. In [15], they used convolutional layers to extract features and softmax layer to classify multi-channel PSG recordings from MASS dataset [31]. Cui et al. used CNN combined with fine-grained segment [14]. They used multi-channel sleep signals from ISRUC-Sleep dataset (ISRUC) [32] and got 92.2% accuracy. All studies mentioned above used multi-channel signal.

Tsinalis et al. [13] used CNN based classification on single-channel EEG from Sleep-EDF database [33]. Supratak et al. implemented 2 step learning algorithm such as 2 different deep CNNs are utilized to extract features and a bidirectional recurrent neural network (RNN) is used to learn transition rules of 30s of the single-channel EEG signal [34].

Vilamala et al. applied transfer learning to Sleep-EDF [35]. Spectral images of each window of EEG was obtained and then trained on a pre-trained VGGNet. Gharbali et al. used pre-trained AlexNet with ImageNet on scalograms that are obtained from single-channel EEG signals by using Continuous Wavelet Transform (CWT) [36]. They used 10 healthy subjects from ISRUC on the study and got 84%.

II. PROPOSED METHOD

DL approaches need large amount of data and high performance hardware, mostly GPU, to get reliable success. As a subfield of DL, CNN has the same requirements. As the network goes deeper and number of parameters is increased, CNNs need more data and powerful resources.

When CNN was determined to be applied due to its advantages and good results are desired but there is a small scale dataset, this is a challenging task. One of the ways to overcome this issue is using transfer learning. Even there is a large scale dataset available, transfer learning may be still beneficial such as it can reduce the training duration.

In this study, EEG signals from ISRUC-Sleep dataset was used to classify sleep stages of healthy people. There are 10 healthy subjects in the dataset and their corresponding number of epochs is 8589. Each epoch is labeled to one of 5 sleep stages. Although it may not be considered as a very small dataset, transfer learning still improved its performance.

There is also a trade-off arisen about using CNN that ISRUC is a dataset that consists of signals, but CNNs are very successful in computer vision. CNNs became extremely popular in the visual recognition and most of the interest on CNNs are computer vision based. Also, there is not much example of using visual representation of signals to classify sleep stages. Therefore, signals were converted to spectrograms which visualize both frequency and amplitude of the signal.

A. Dataset

The target domain was the domain that has EEG signals that were collected from C3-A2 sensor placed on 10 healthy subjects of ISRUC-Sleep dataset. It has 8589 signals totally.

The source domain was the signals collected by the same sensor from 100 patient subjects of the dataset. Total number of

signals is 87187.

ISRUC consists of healthy subjects and patient subjects that have sleep disorders. EEG signals, that were used in the study, was sampled at 200 Hz. EEG signals were pre-processed by using a notch filter. Also they were filtered in the interval of 0.3 to 35 Hz. In this study, no further pre-processing was applied to reduce the noise or extract features.

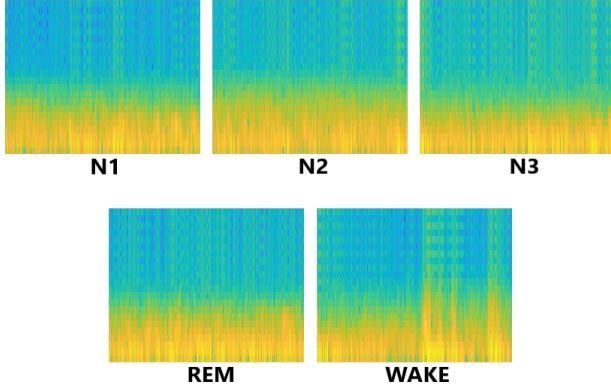


Figure 1: Generated spectrogram samples for each sleep stage

Spectrograms were used to represent the signals visually. Spectrograms can be generated by various ways. Most common one is using Fourier transform. Short-time Fourier Transform (STFT) was used to generate spectrograms from signals. STFT is a sequence of Fast Fourier Transform (FFT) of windowed data segments. The process is splitting the input signal into small chunks or frames equally along time axis then computing FFT for each chunk to calculate the magnitude of the frequency components. Hence each chunk gets its frequency distribution as a vertical line for the image. If the collection of all these frequency components are plotted, i.e., each chunk's corresponding vertical line is located according to its order in the sequence, then this forms the spectrogram image. The process explained above corresponds to computing the squared magnitude of the STFT of the signal $x[n]$, for a window width ω that can be expressed as:

$$\text{spectrogram}\{x[n]\}(m, \omega) = |\text{STFT}\{x[n]\}(m, \omega)|^2 \quad (1)$$

The formula of STFT is as following:

$$\text{STFT}\{x[n]\}(m, \omega) = \sum_{n=-\infty}^{\infty} x[n]w[n-m]e^{-j\omega n} \quad (2)$$

where $x[n]$ is the signal to be transformed, $w[n]$ is the windowing function, m is the time, ω is the frequency, n is the chunk.

Hamming window was selected as windowing function. Window width was specified as 22 in terms of samples. Number of points, that chunks are overlapping, was 11. Number of FFT points computed per chunk was 44. Resolution of generated images were 678*535 pixels in 'rgb' format and they were stored as '.png' files.

Example generated spectrogram images for each sleep stage are illustrated in **Figure 1** and the flowchart of how a spectrogram image was generated from a signal is given in **Figure 2**.

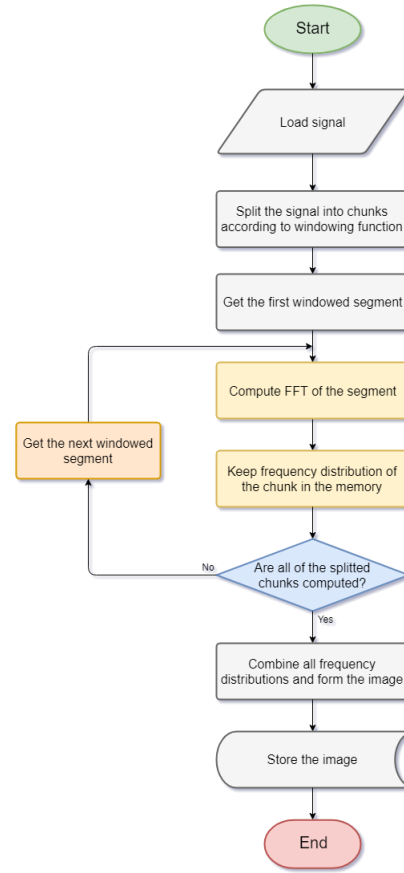


Figure 2: Flowchart of generating a spectrogram

B. Network Architecture

The study is based on using CNNs to make classification. Exactly the same architecture of AlexNet except the size of the last fully connected layer, which was changed to 5, was applied for all experiments. AlexNet's structure consists of 8 layers, which the first 5 are convolutional layers and the last 3 are fully connected layers. It used ReLU layers immediately after each convolutional layer and after each fully connected layer except the last one. Max pooling was also used in the network to reduce the spatial size of the representations. The input size was 227*227*3.

Size of the last fully connected layer was arranged as 5, due to sleep stage classification task as the data was labeled into 5 categories. The architecture of the used version is illustrated in **Figure 3**. All layers of the used architecture are listed in **Table 1**.

C. Pre-Training

Two different pre-training steps were performed to carry out transfer learning. The pre-trained CNNs were AlexNet trained with ImageNet (i.e. 1.2 million images from ImageNet, not all of the images that database contain, in fact it is ILSVRC-2012 data) and AlexNet trained with 100 patient subjects of ISRUC.

AlexNet trained with ImageNet is publicly available and thus obtained. Actual training phase was not performed for that network in this study. That was trained previously with 1.2 million images and validated with 50 thousand images.

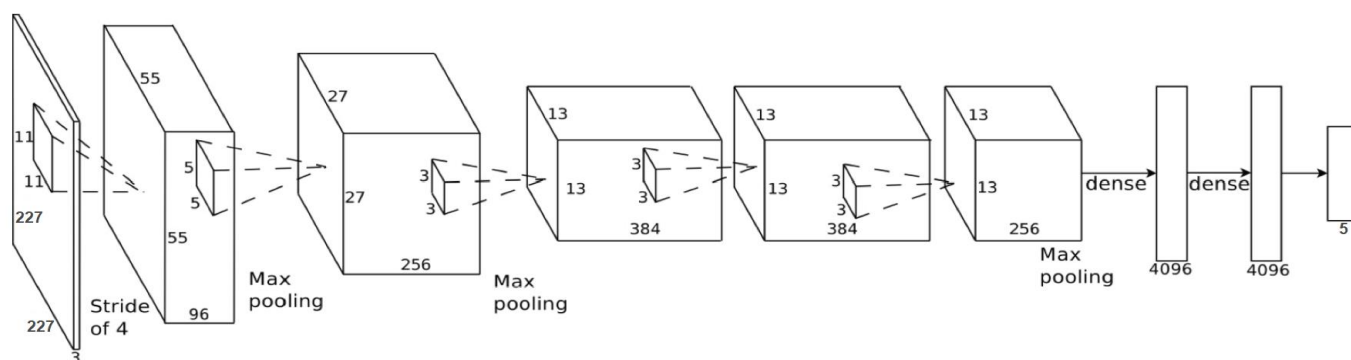


Figure 3: Architecture of the CNN [37]

Table 1: List of layers

Layer No	Layer Type	Details
1	Image Input	227x227x3 images
2	Convolutional	96 11x11x3 convolutions with stride [4 4] and padding [0 0 0 0]
3	ReLU	non-linear ReLU function
4	Cross Channel Normalization	cross channel normalization with 5 channels per element
5	Max Pooling	3x3 max pooling with stride [2 2] and padding [0 0 0 0]
6	Convolutional	256 5x5x48 convolutions with stride [1 1] and padding [2 2 2 2]
7	ReLU	non-linear ReLU function
8	Cross Channel Normalization	cross channel normalization with 5 channels per element
9	Max Pooling	3x3 max pooling with stride [2 2] and padding [0 0 0 0]
10	Convolutional	384 3x3x256 convolutions with stride [1 1] and padding [1 1 1 1]
11	ReLU	non-linear ReLU function
12	Convolutional	384 3x3x192 convolutions with stride [1 1] and padding [1 1 1 1]
13	ReLU	non-linear ReLU function
14	Convolutional	256 3x3x192 convolutions with stride [1 1] and padding [1 1 1 1]
15	ReLU	non-linear ReLU function
16	Max Pooling	3x3 max pooling with stride [2 2] and padding [0 0 0 0]
17	Fully Connected	4096 fully connected layer
18	ReLU	non-linear ReLU function
19	Dropout	50% dropout
20	Fully Connected	4096 fully connected layer
21	ReLU	non-linear ReLU function
22	Dropout	50% dropout
23	Fully Connected	5 fully connected layer
24	Softmax	softmax
25	Classification Output	cross entropy loss

Pre-training with ISRUC data was performed by using spectrograms generated from 100 patient subject. 95% of the signals were split out as training set, 5% of them was left out for validation. Mini-batch size was 64. Solver was chosen as stochastic gradient descent with momentum, where momentum was set to 0.9. It was used while updating weights and biases after forward pass. The learning rate was arranged as $1e-3$.

Image augmentation was held as only translating images from -60 pixels to 60 pixels randomly on x-axis. The reason behind only horizontal axis was used for augmentation is, spectrograms holds information about time on x-axis, while y-axis represents frequencies of the signal. Losing information from frequencies makes the image unpredictable. So, transformations that may distort the image vertically weren't used and making reflection on horizontal direction wasn't used either, even it is not affecting anything with y-axis. All images were resized from $678*535$ to $227*227$ pixels due to input size of the network.

Training was started with the parameters as described above. All weights and biases were initialized randomly. When the training was finished, the trained network with its final weights and biases was saved for using future purposes as in this study.

D. Training

Three different training were performed on the same target data which was spectrogram images generated from 10 healthy subjects of ISRUC. Two of them were used for transfer learning, while the other one was performed as training from scratch.

When the network explained in Section 3.C was trained and saved, it was ready for transferring its acquired knowledge. It was loaded to the training environment and its layers except the last fully connected layer were transferred with their weights and biases for the target task. The last 3 layers of the network were initialized freshly with random weights and biases.

10-fold cross validation was performed, which 9 folds were separated for training and 1 fold for validation, for all 3 training processes. For pre-trained CNNs, weights and biases of the transferred layers were updated with the learning rate of $1e-4$ while others were $2e-3$ and number of epochs it was trained all along was 16. Training from scratch one was trained in the same way with the same parameters as in Section 3.C, the only difference was applying 10-fold cross validation. Its number of epochs was 36. Image augmentation and resizing was also the same as in Section 3.C for both.

III. RESULTS

All experiments were performed in MATLAB with the hardware resources of one Intel Core i7-7820HQ CPU, 16 GB RAM, and a 4 GB NVIDIA Quadro M1200 GPU.

When all 10 trainings for each network were finished, average accuracy of them were calculated for evaluation. All results that are showed in this section for the same target domain which explained in Section 2. The overall accuracy of the proposed system is 81.05%. The final results are illustrated in *Figure 4*.

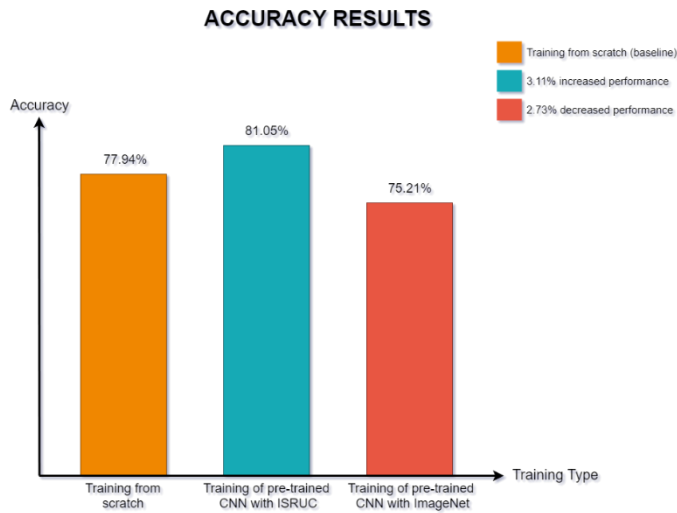


Figure 4: Accuracy results of 3 experiments

Training duration for both 16 epochs, that we applied transfer learning, was approximately 32 minutes, and for 36 epochs, which is training from scratch, was approximately 80 minutes.

Transfer learning was applied to achieve better performance. In the study, 2 different source domains were used for transferring the knowledge to the same target domain. First source domain was ImageNet, which has images of objects. It is relatively different than the target domain. Second source domain was ISRUC-Sleep data, which has signals of sleep stages. It is totally similar, even it is same dataset but different groups.

When both of the domains were similar, it increased the accuracy by 3.11% compared to the training from scratch. When they weren't similar, the accuracy was decreased by 2.73%. Results showed that transfer learning increased the accuracy when both of the domains are similar, but it decreased the accuracy when used on different domains. Number of epochs needed and so the training duration were decreased.

Future works can be established on fine-tuning the parameters of STFT that generates spectrograms or generating scalograms (that is generated by using continuous wavelet transform) from signals to train the network. Also, testing the proposed model on various signal datasets can be done.

APPENDIX

Appendix A: The results of each fold in detail as table
Appendix B: The outline of the process as flowchart

Table A: Results of every fold

	Training from scratch	Training of pre-trained CNN with ISRUC	Training of pre-trained CNN with ImageNet
Accuracy of 1. Fold	0.7662	0.8035	0.7430
Accuracy of 2. Fold	0.8039	0.8028	0.7593
Accuracy of 3. Fold	0.7546	0.7988	0.7416
Accuracy of 4. Fold	0.7680	0.8100	0.7470
Accuracy of 5. Fold	0.7720	0.8012	0.7511
Accuracy of 6. Fold	0.7846	0.8231	0.7402
Accuracy of 7. Fold	0.7762	0.8112	0.7400
Accuracy of 8. Fold	0.7965	0.8244	0.7732
Accuracy of 9. Fold	0.7864	0.8156	0.7641
Accuracy of 10. Fold	0.7860	0.8140	0.7614
Average Accuracy	77.94%	81.05%	75.21%

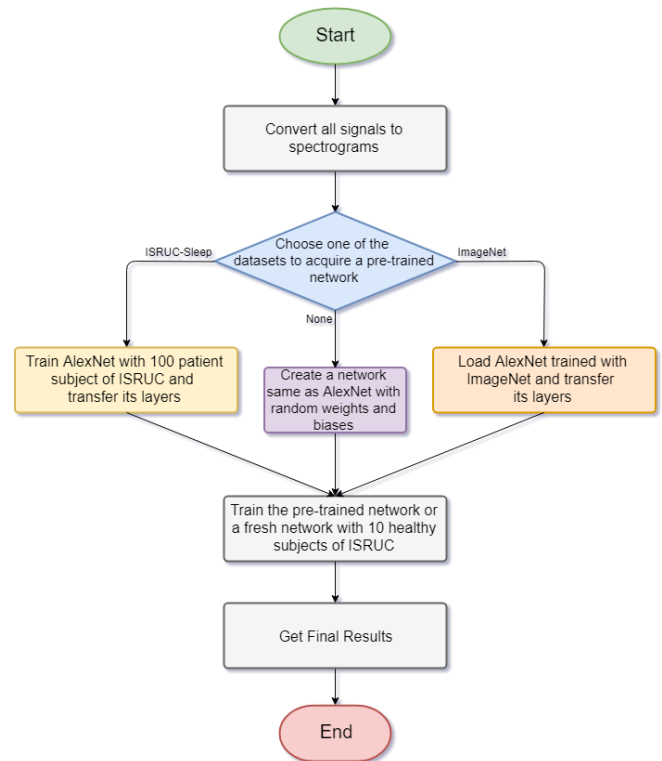


Figure B: Outline of trainings performed on the study as flowchart

REFERENCES

- [1] Y. LeCun, B. Boser, J. S. Denker, D. Henderson, R. E. Howard, W. Hubbard and L. D. Jackel, "Backpropagation Applied to Handwritten Zip Code Recognition," *Neural Computation*, vol. 1, no. 4, pp. 541-551, 1989.
- [2] M. D. Zeiler and R. Fergus, "Visualizing and Understanding Convolutional Networks," in *Computer Vision – ECCV 2014*, vol. 8689, Zurich, Switzerland, Springer, Cham, 2014, pp. 818-833.
- [3] A. Krizhevsky, I. Sutskever and G. E. Hinton, "ImageNet Classification with Deep Convolutional Neural Networks," in *Proceedings of the 25th International Conference on Neural Information Processing Systems - Volume 1*, Lake Tahoe, Nevada, Curran Associates Inc., 2012, pp. 1097-1105.
- [4] M. Lin, Q. Chen and S. Yan, "Network In Network," *CoRR, Abs/1312.4400*, 2013.
- [5] K. Simonyan and A. Zisserman, "Very Deep Convolutional Networks for Large-Scale Image Recognition," *CoRR, Abs/1409.1556*, 2014.
- [6] C. Szegedy, W. Liu, Y. Jia, P. Sermanet, S. Reed, D. Anguelov, D. Erhan, V. Vanhoucke and A. Rabinovich, "Going Deeper with Convolutions," in *2015 IEEE Conference on Computer Vision and Pattern Recognition (CVPR)*, Boston, MA, IEEE, 2015, pp. 1-9.
- [7] K. He, X. Zhang, S. Ren and J. Sun, "Deep Residual Learning for Image Recognition," in *2016 IEEE Conference on Computer Vision and Pattern Recognition (CVPR)*, Las Vegas, NV, IEEE, 2016, pp. 770-778.
- [8] O. Russakovsky, J. Deng, H. Su, J. Krause, S. Satheesh, S. Ma, Z. Huang, A. Karpathy, A. Khosla, M. Bernstein, A. C. Berg and L. Fei-Fei, "ImageNet Large Scale Visual Recognition Challenge," *International Journal of Computer Vision*, vol. 115, no. 3, pp. 211-252, 2015.
- [9] G. Griffin, A. Holub and P. Perona, "Caltech-256 object category dataset," California Institute of Technology, Los Angeles, CA, 2007.
- [10] J. Deng, W. Dong, R. Socher, L. J. Li, K. Li and L. Fei-Fei, "ImageNet: A Large-Scale Hierarchical Image Database," in *2009 IEEE Conference on Computer Vision and Pattern Recognition*, Miami, FL, IEEE, 2009.
- [11] S. F. Liang, C. E. Kuo, Y. H. Hu, Y. H. Pan and Y. H. Wang, "Automatic Stage Scoring of Single-Channel Sleep EEG by Using Multiscale Entropy and Autoregressive Models," *IEEE Transactions on Instrumentation and Measurement*, vol. 61, no. 6, pp. 1649-1657, 2012.
- [12] R. Sharma, R. B. Pachori and A. Upadhyay, "Automatic Sleep Stages Classification Based on Iterative Filtering of Electroencephalogram Signals," *Neural Computing and Applications*, vol. 28, no. 10, pp. 2959-2978, 2017.
- [13] O. Tzinalis, P. M. Matthews, Y. Guo and S. Zafeiriou, "Automatic Sleep Stage Scoring with Single-Channel EEG Using Convolutional Neural Networks," *CoRR, Abs/1610.01683*, 2016.
- [14] Z. Cui, X. Zheng, X. Shao and L. Cui, "Automatic Sleep Stage Classification Based on Convolutional Neural Network and Fine-Grained Segments," *Complexity*, vol. 2018, no. Article ID 9248410, 2018.
- [15] S. Chambon, M. N. Galtier, P. J. Arnal, G. Wainrib and A. Gramfort, "A Deep Learning Architecture for Temporal Sleep Stage Classification Using Multivariate and Multimodal Time Series," *IEEE Transactions on Neural Systems and Rehabilitation Engineering*, vol. 26, no. 4, pp. 758-769, 2018.
- [16] Y. Lecun, L. Bottou, Y. Bengio and P. Haffner, "Gradient-based learning applied to document recognition," *Proceedings of the IEEE*, vol. 86, no. 11, pp. 2278-2324, 1998.
- [17] Z. Barnes, F. Cipollone and T. Romero, "Techniques for Image Classification on Tiny-ImageNet," Stanford, CA, 2017.
- [18] P. Sermanet, D. Eigen, X. Zhang, M. Mathieu, R. Fergus and Y. Lecun, "OverFeat: Integrated Recognition, Localization and Detection using Convolutional Networks," in *CoRR, abs/1312.6229*, 2013.
- [19] S. J. Pan and Q. Yang, "A Survey on Transfer Learning," *IEEE Transactions on Knowledge and Data Engineering*, vol. 22, no. 10, pp. 1345-1359, 2010.
- [20] Y. Aytar and A. Zisserman, "Tabula rasa: Model transfer for object category detection," in *2011 International Conference on Computer Vision*, Barcelona, IEEE, 2011, pp. 2252-2259.
- [21] T. Tommasi, F. Orabona and B. Caputo, "Safety in numbers: Learning categories from few examples with multi model knowledge transfer," in *2010 IEEE Computer Society Conference on Computer Vision and Pattern Recognition*, San Francisco, CA, IEEE, 2010, pp. 3081-3088.
- [22] A. Khosla, T. Zhou, T. Malisiewicz, A. A. Efros and A. Torralba, "Undoing the Damage of Dataset Bias," in *European Conference on Computer Vision 2012*, Berlin, Springer, 2012, pp. 158-171.
- [23] K. Saenko, B. Kulis, M. Fritz and T. Darrell, "Adapting Visual Category Models to New Domains," in *European Conference on Computer Vision, ECCV-2010*, Berlin, Springer, 2010, pp. 213-226.
- [24] J. Donahue, Y. Jia, O. Vinyals, J. Hoffman, N. Zhang, E. Tzeng and T. Darrell, "DeCAF: A Deep Convolutional Activation Feature for Generic Visual Recognition," in *International Conference on Machine Learning, JMLR*, 2014, pp. 647-655.
- [25] H. W. Ng, V. D. Nguyen, V. Vonikakis and S. Winkler, "Deep Learning for Emotion Recognition on Small Datasets Using Transfer Learning," in *Proceedings of the 2015 ACM on International Conference on Multimodal Interaction*, New York, NY, ACM, 2015, pp. 443-449.
- [26] K. Chatfield, K. Simonyan, A. Vedaldi and A. Zisserman, "Return of the Devil in the Details: Delving Deep into Convolutional Nets," *CoRR, abs/1405.3531*, 2014.
- [27] A. Krizhevsky and G. Hinton, "Learning multiple layers of features from tiny images," University of Toronto, Toronto, 2009.
- [28] G. Wimmer, A. Vécsei and A. Uhl, "CNN Transfer Learning for the Automated Diagnosis of Celiac Disease," in *2016 Sixth International Conference on Image Processing Theory, Tools and Applications (IPTA)*, Oulu, Finland, IEEE, 2016, pp. 1-6.
- [29] M. Langkvist, L. Karlsson and A. Loutfi, "Sleep Stage Classification Using Unsupervised Feature Learning," *Advances in Artificial Neural Systems*, vol. 2012, no. Article No: 5 Article ID: 107046, p. 9, 2012.
- [30] J. Zhang, Y. Wu, J. Bai and F. Chen, "Automatic Sleep Stage Classification Based on Sparse Deep Belief Net and Combination of Multiple Classifiers," *Transactions of the Institute of Measurement and Control*, vol. 38, no. 4, pp. 435-451, 2016.
- [31] C. O'Reilly, N. Gosselin, J. Carrier and T. Nielsen, "Montreal Archive of Sleep Studies: an Open-Access Resource for Instrument Benchmarking and Exploratory Research," *Journal of Sleep Research*, vol. 23, no. 6, pp. 628-635, 2014.
- [32] S. Khalighi, T. Sousa, J. M. Santos and U. Nunes, "ISRUC-Sleep: A comprehensive public dataset for sleep researchers," *Computer Methods and Programs in Biomedicine*, vol. 124, pp. 180-192, 2015.
- [33] B. Kemp, A. Zwinderman, B. Tuk, H. Kamphuisen and J. Oberye, "Analysis of a Sleep-Dependent Neuronal Feedback Loop: the slow-wave microcontinuity of the EEG," *IEEE Transactions on Biomedical Engineering*, vol. 47, no. 9, pp. 1185-1194, 2000.
- [34] A. Supratak, H. Dong, C. Wu and Y. Guo, "DeepSleepNet: A Model for Automatic Sleep Stage Scoring Based on Raw Single-Channel EEG," *IEEE Transactions on Neural Systems and Rehabilitation Engineering*, vol. 25, no. 11, pp. 1998-2008, 2017.
- [35] A. Vilamala, K. H. Madsen and L. K. Hansen, "Deep Convolutional Neural Networks for Interpretable Analysis of EEG Sleep Stage Scoring," in *2017 IEEE 27th International Workshop on Machine Learning for Signal Processing (MLSP)*, Tokyo, IEEE, 2017, pp. 1-6.
- [36] A. A. Gharbali, S. Najdi and J. M. Fonseca, "Transfer Learning of Spectrogram Image for Automatic Sleep Stage Classification," in *International Conference Image Analysis and Recognition*, Cham, Springer, 2018, pp. 522-528.
- [37] A. Pedraza, J. Gallego, S. Lopez, L. Gonzalez, A. Laurinavicius and G. Bueno, "Glomerulus Classification with Convolutional Neural Networks," in *Annual Conference on Medical Image Understanding and Analysis*, Cham, Springer, 2017, pp. 839-849.

GAS ROBOT IMPLEMENTATION AND CONTROL

ALI MARDAN HAMEED QUTUB, Ismail SARITAS²

¹ Selcuk University, Konya/Turkey, akutub87@gmail.com

² Selcuk University, Konya/Turkey, isaritas@gmail.com

Abstract - Gas is one of the four basic forms of matter. A pure gas can be composed of individual molecules, simple molecules coming from a variety of atoms, or compound molecules coming from various atoms. The gas admixture may have a wide kind of clear gases, similar as air. What dividing gas and solid solid per unit of gas particles by large spaces. These separations is generally an invisible uncolored gas for the human viewer. In our daily life, both domestic and industrial gas usage is becoming widespread and becoming one of the indispensable sources of energy in our lives. Gas leakage means that native gas or different gases products leak of a pipelines or another container to the staying space either each another space where the gases shouldn't will be present. The fiery gases be possible make explode when submitted to fire and sparks, which is so risky for the public.

Keywords - Methan, Benzin, LPG, Gas robot, Control.

I. INTRODUCTION

Gas is one of the four basic states of matter. A pure gas may consist of individual molecules (eg, an inert gas such as neon), simple molecules of an atomic type (eg, oxygen), or compound molecules comprising a variety of atoms (eg, carbon dioxide). The electric and gravity areas within the interaction of the gas particles are considered to be negligible as indicated by the constant velocity vectors in the image. Gas state of matter is between liquid and plasma states [1]. Generally, a gas leak means that natural gas or other gaseous products leak from a pipeline or other coverage to the living area or to any area where the gas must not be present[2].

II. MATERIALS AND METHODS

2.1. The robot movement mechanism

In order to perform the gas measurement effectively, the robot has been developed. The robot's motion mechanism consists of four DC motors, motor drives to control these motors and an NRF module to control how they move. All elements of the movement mechanism are connected to the Arduino

development board in the developed robot. Also the movement of the movement mechanism is provided by the robot on the robot. The gas measuring robot is shown in Figure 1.

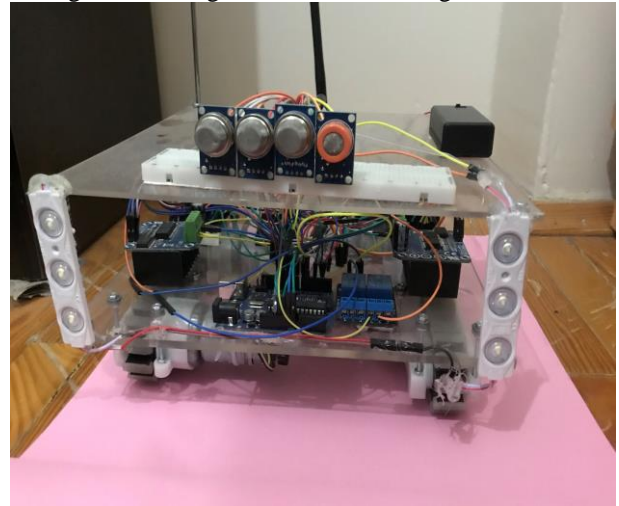


Figure 1: gas measuring robot.

2.2. Control Panel

A control panel has been developed to control the movement mechanism of the developed robot and to monitor the values taken from the gas sensors. The control panel includes the RF module for receiving data from the gas sensors, an LCD showing these data, the NRF module that sends control signals to the robot's motion mechanism, and the Arduino development platform to which all these electronic modules are connected. The display of the control panel is shown in Figure 2.



Figure 2 : Control Panel

III. REALIZATION OF GAS ROBOT

Detection of gas leaks is critical to ensure the safety of human life and equipment investments in large industrial sites and public places. Gas leaks can be detected by fixed gas sensors; however, however, manual determinations are much more effective. Trained personnel can inspect and scan a gas leak detector and gas equipment and pipes. A robot is designed for automatic mobile supervision of oil and natural gas infrastructure facilities and for remote sensing and isolation of gas leaks. When in automatic mode, the robot moves along a predetermined route and can remotely analyze gas density at a distance very close to potential leak points. Gas density measurement is performed using the Absorption Method and with multiple gas sensors. As the point measurement or room volume is used, the device is installed on a moving platform. The contribution of this project is twofold :

- 1- To propose a new hybrid method to develop fast and efficient employee search strategies.
- 2- Evaluate the proposed approach in simulation environment and real life. Then, it is to compare these results.

The methodology for designing the device for multiple uses depends on modifications in the industrial field in which the robot can be used; In addition, the portable gas sensor in this thesis is based on the mechanism built on it. The A set of all cells is divided according to the range of the radio frequency coverage sensor. When there is a gas leak in the pipe, the gas sensors operating depending on the algorithm shown below send data to the sequential monitor to record the values from the sensors and these values are saved to the memory cards and memory cards by exporting the values in the Excel sheet to compare the normal state and the abnormal condition.

IV. EXPERIMENTAL STUDIES AND DISCUSSION

4.1. Test Environment

The experiments were carried out in a closed room of approximately 16 m² with dimensions of 2m x 3m x 2.66m. The measurement room is empty. During the measurement, the temperature value is between 24-26 degrees and the humidity value is between 45-50%. After each measurement, the room was expected to return to normal conditions. LPG gas, methane gas and gasoline were used for the measurements. All measurements were made by the gas measuring robot developed in the thesis study. The gas measuring robot has 4 MQ series sensors. These sensors are located in the front of the robot and parallel to each other. The measurements were controlled from both the control panel and the arduino serial monitor. This is done both to check for a loss of data transmission and not to obtain an incorrect measured value due to a loss of data transmission.

4.2. Experimental Measurements

In the test environment, measurements are made separately for each gas by changing the distance value. In the gas measurements, the distance was increased from 5 cm to 100

cm by 5 cm and all measurement results are given in Table 1. Measurements of 5cm, 25cm, 50cm, 75cm and 100cm gases (LPG, Methane and Gasoline) were made.

Table 1 . Gas measurements at a distance of 5-100 cm.

V (m ³)	Sensor Distance (cm)	Perception Time (sec)	Gas flow Speed (m ² /s (Q = V/T))	MQ5 (LPG) (ppm)	MQ13 5 (Benzin) (ppm)	MQ4 (Methan) (ppm)
16	5	1	16,00	6146	673	1498
16	10	1,1	14,55	6032	647	1470
16	15	1,2	13,33	5530	593	1318
16	20	1,3	12,31	5198	547	1214
16	25	1,4	11,43	3757	527	1176
16	30	1,5	10,67	3264	467	1034
16	35	1,6	10,00	3083	423	986
16	40	1,7	9,41	2799	364	939
16	45	1,8	8,89	2325	325	882
16	50	1,9	8,42	1813	260	806
16	55	2	8,00	1690	227	759
16	60	2,1	7,62	1462	166	664
16	65	2,2	7,27	1329	151	598
16	70	2,3	6,96	893	138	541
16	75	2,4	6,67	751	115	465
16	80	2,5	6,40	684	86	275
16	85	2,6	6,15	618	61	209
16	90	2,7	5,93	267	49	190
16	95	2,8	5,71	153	38	161
16	100	2,9	5,52	106	31	95

As shown in Table 1, the sensitivity in the measurement decreases as the distance changes. While LPG gas measured a value of 5 cm at normal room conditions was 2251 ppm, LPG gas was measured as 8397 ppm when applied to the environment and it was seen that there was an increase of 273% in the gas measurement value. However, when the measurement distance was 100cm and LPG gas was applied to the environment, 2357 ppm was measured. The measured value between 5cm and 100cm decreased by 71%. Gasoline measured in the normal room conditions of 5cm and 156 ppm while the gasoline was measured as 829 ppm when applied to the environment and there is a 431% increase in gas measurement value. However, when the measuring distance was 100cm and applied to the gasoline environment, 187 ppm was measured. The measured value between 5cm and 100cm decreased by 77%. Methane gas was measured at 1712 ppm in normal room conditions, while methane gas was measured at 3210 ppm when applied to the environment and an increase in gas measurement value of 87% was observed. However, when the measurement distance was 100cm and the methane gas was applied to the medium, 1807 ppm was measured. The measured value between 5cm and 100cm decreased by 43%.

In addition, the detection time of the sensors increases with increasing distance. The sensing times and the sensitivity in the gas measurement vary depending on the flow rate of the gas. Flow rate change and gas measurement values by type of

gases (LPG, Methane and Gasoline) are shown in Figure 2,3 & 4.

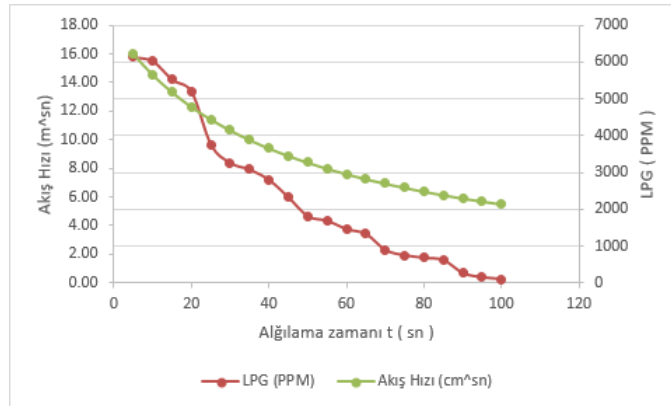


Fig. 2 : LPG and flow rate change graphic

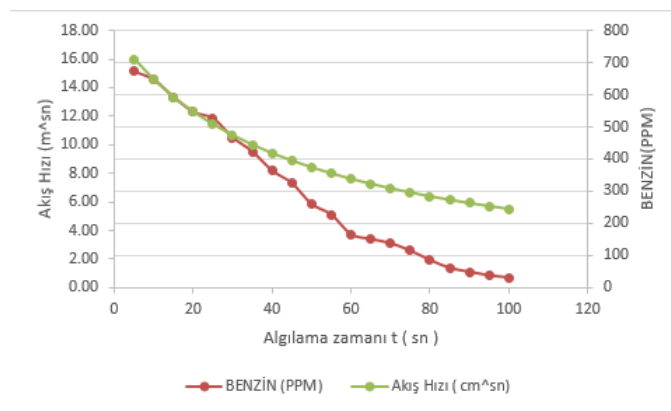


Fig. 3 : Gasoline and flow rate change graphic

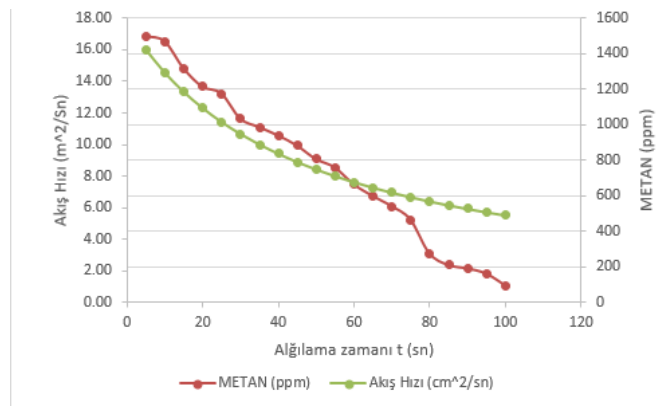


Fig. 4 : Methane and flow rate change graphic

(1)

V. CONCLUSIONS

The use of gas has now become a part of our lives. It helps us meet our vital requirements for warming, enlightenment and energy production. The use of gas has become a great need not only in industry but also in homes. The use of gas is an ecological choice because it creates less air pollution than fossil fuels and its use is encouraged.

Mistakes due to misuse of gas, gas leaks or carelessness, which is a fact of our lives, can cause many problems. These problems are briefly damage to property, loss of life and environmental damage.

Gas leak; The materials used in gas transportation (steel, PE pipe, valve chamber, tanks, regulator, etc.) are defined as the uncontrolled gas outlet arising from natural disasters or faults during use. The leakage of the gases mentioned in this definition cannot be seen by the eye but can be smelled. Sudden and correct interventions in gas leaks are vital.

Generally, gas leakage is done by hand-held gas measuring devices and fixed sensors. However, these devices are not used in any environment.

In this study, a gas measuring robot has been developed to detect gas leakages, to measure gas, to move, to be controlled by a control panel and to be able to view and direct images with an internal camera. With the gas measuring robot developed, the places where people can not reach easily can be controlled, gas-free environments that can harm human health very quickly and gas leaks can be determined. Furthermore, in this study, measurement accuracy of the gas measurement sensors at the unit distances has been studied and the results obtained have been evaluated.

REFERENCES

- [1] Deshmukh, L., Mujawar, T., Kasbe, M., Mule, S., Akhtar, J. ve Maldar, N., 2016, A LabVIEW based remote monitoring and controlling of wireless sensor node for LPG gas leakage detection, *Electronics and Smart Devices (ISESD), International Symposium on*, 115-120.
- [2] Kletz, T. A., 2001, Learning from accidents, 3, *OXFOR AUCKLAND BOSTON JOHANNESBURG MELBOURNE NEW DELHÍ*, Gulf Professional Publishing, p. 40-42.

Examination of Machine Learning Methods in Hand Posture Estimation

M. Fahri UNLERSEN¹, Murat KOKLU² and Kadir SABANCI³

¹ Necmettin Erbakan University, Konya, Turkey, mfunlensen@konya.edu.tr

² Selcuk University, Konya, Turkey, mkoklu@selcuk.edu.tr

³ Karamanoglu Mehmetbey University, Karaman, Turkey, kadirsabanci@kmu.edu.tr

Abstract – In this paper, a static hand posture identification is investigated. A dataset created by Vicon motion capture camera system is obtained from University of California, Irvine Machine Learning Repository. The dataset consists of unlabeled point sets which are reflective marker positions on the glove worn by a user. On each finger, there are 2 reflective points. And there is one more reflective point on the middle of the glove. Totally there are 11 reflective points on the glove. There is five hand posture in the dataset for different users. Totally there are 78095 records in the dataset. But in each posture, all of the reflective points' coordinates cannot be collected. So in the dataset, some coordinates are marked as unknown. In order to evaluate the machine learning methods, the number of attributes on each record needs to be equal. For this purpose, some manipulations are done on the dataset. For achieving the best estimation performance various machine learning methods are tested. The dataset is divided into two groups as training and testing with the ratio of %66 and %34 respectively. In the result of the test, the Random Forest method produced the best performance with 98.38% correctly classified instance. This success is followed by MLP and Knn Methods with success rates of 96.02% and 95.53% respectively.

Keywords - Machine Learning, Classification, Hand Postures, Remote sensing.

I. INTRODUCTION

ALTHOUGH, there are various important advances about Automatic speech recognition, automatic Sign Language Recognition (SLR) is still in its inception. Sign Language is a set of hand postures which are used during communication by people who had vocal and hearing disabilities [1], [2]. Nowadays, because of the absence of an automatic SLR system so, the obligation of experienced personnel employment for commercial translation services makes this services too expensive [2].

Automatic SRL proposes to identify a sequence of the produced signs by using various algorithms and methods [1]–[3]. In literature, there are various studies about SLR. Starner et.al in 1998 presented two real-time hidden Markov model-based systems for recognizing sentence-level continuous American sign language (ASL) using a single camera to track the user's unadorned hands. It is reported that these systems achieve the accuracy of 92% and 98% respectively [4]. Ravikiran et.al designed a system that can automatically capture, recognize and translate the sign language to speech. The system based on

detection of edges of fingers. The success rate is presented as 95% in the paper [5]. Bauer et.al in their study described the development of a video-based continuous sign language recognition system. The system is based on continuous density hidden Markov models (HMM) with one model for each sign. The accuracy of the system is reported as 91.7% [6]. Gardner et.al evaluated and compared several methods for the classification and recognition of static hand postures from small unlabeled point sets. It is reported that aggregate feature classifiers to be balanced across multiple users but relatively limited in maximum achievable accuracy [7].

As it is seen in the previous studies, automatic SLR is based on the perception of the hand postures. In this study, various machine learning methods are investigated about the ability of hand posture recognition by using unlabeled point sets.

II. MATERIAL AND METHODS

The estimation of hand posture based on machine learning is investigated in this study. For this purpose, a dataset is used in the examination of various machine learning methods. The dataset is created by using a Vicon motion capture camera system. The data is collected from a glove whose certain joints have infrared markers on. While the data collection procedure, the glove is worn by 12 different users. So the data become independent of users. The dataset is obtained from the University of California Irvine machine learning repository. On the back of the glove, a fixed arrangement of markers is used to provide a local coordinate system for the hand. There are 15 markers on the glove. The arrangement of markers is as follow;

- 3 markers were attached to the thumb with one above the thumbnail the other two on the knuckles.
- 2 markers were attached to each finger with one above the fingernail.
- The others (4) are attached to the joint between the proximal and middle phalanx.

The glove used in this study is presented in Figure 1. And also the infrared reflective markers are presented in Figure 1.



Figure 1: The infrared reflective markers on the glove.

There are 5 hand postures in the dataset. These postures are Grab (fingers curled as if to grab), Two finger pointing (point with pointer and middle fingers), Single finger pointing (point with pointer finger), Stop(hand flat) and Fist(with thumb out) as presented in Figure 2.

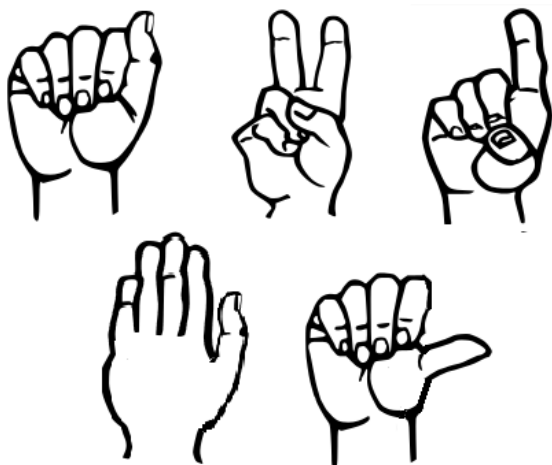


Figure 2: The 5 hand postures going to be estimated [8].

In the dataset, each visible marker has 3 coordinate value as X, Y and Z. So the number of attributes for each posture isn't equal. In order to achieve an equal number of attributes, the coordinates of markers who are invisible in the investigated posture are assumed as zero. The number of attributes and records in the dataset occurs as 36 and 78095 respectively. In this study various machine learning methods are investigated. First one is the *k-Nearest Neighbor Algorithm* (k-NN). The k-NN is a supervised learning algorithm that solves classification problems. The important point is the determination of the features of each category in advance. The most important optimization problems in the k-NN method are the identification of the number of neighbors and the method of distance calculation algorithm [9]. In the study, the identification of the optimum k number is performed with experiments, and the Euclidean Distance Calculations method is used as a distance calculation method.

The next one is *Multilayer Perceptron*. It is a feed forward type artificial neural network model which maps input sets onto appropriate output sets. A multilayer perceptron (MLP) is composed of multiple layers of nodes where each layer is

connected to the next. Each node is a processing element or a neuron that has a nonlinear activation function except the input nodes. It uses a supervised learning technique named back propagation and it is used for training the network. The alteration of the standard linear perceptron, MLP is capable of distinguishing data which are not linearly separable [10].

Another machine learning method, *Bayes Net* used in the study, is a probabilistic graphical model and a statistical model representing a group of random variables in addition to their conditional dependencies through a directed acyclic graph. For instance, a Bayesian network can represent the probabilistic relations between diseases and symptoms. When the symptoms are given, the network can calculate the probabilities of the existence of various diseases [11].

Random Forest is a supervised learning algorithm. It creates a forest and makes it somehow random. The random forest algorithm is used in a lot of different fields, like Banking, Stock Market, Medicine and E-Commerce [12], [13].

In statistics, the *logistic model* is a widely used statistical model that, in its basic form, uses a logistic function to model a binary dependent variable; many more complex extensions exist. In regression analysis, logistic regression is estimating the parameters of a logistic model; it is a form of binomial regression. Logistic regression was developed by statistician David Cox in 1958 [14], [15].

III. RESULTS

In order to investigate the mentioned methods, the dataset is divided into two groups as train and test, randomly. There is no common record in each part. The dividing ratio of train and test from the main datasets is 66% and 34% respectively.

Each machine learning methods is trained and tested by the datasets. The estimation success rates of mentioned methods are presented in Table 1.

Table 1: The results of machine learning methods.

Machine Learning Method	Success Rate %
Multilayer Perceptron	96.02
Random Forest	98.38
k-NN	95.53
Simple Logistic	83.98
Logistic	84.19
BayesNet	93.05

As seen in Table 1, the best performance in the estimation of hand posture is achieved with Random Forest method. Graphical representation of results is shown in Figure 3.

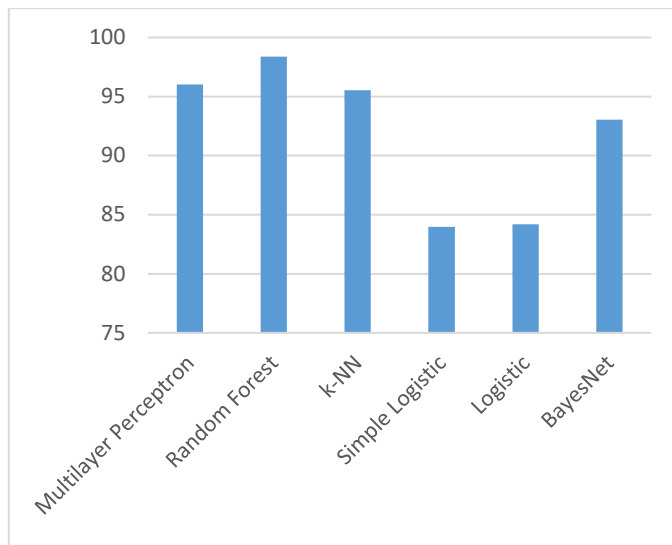


Figure 3: Estimation success rates

IV. CONCLUSION

Machine learning methods are investigated in this study in terms of ability to estimate hand posture. This can be used to the automatic recognition of the sign language. Today, it is compulsory to ask help from a professional to translate sign language into speech. So it is always expensive and hard to find a suitable person to translate. In a communication between a deaf and blind people a system used this machine learning methods can be useful. And it makes both blinds and deaf life easier. While the camera on the cell phone takes the live videos of signs and then converts the signs into voice, it is also possible to convert voices obtained from the microphone of the cell phone to sign language. We hope that this study will be useful for future studies.

REFERENCES

- [1] A. Kumar, K. Thankachan, and M. M. Dominic, "Sign language recognition," in *2016 3rd International Conference on Recent Advances in Information Technology (RAIT)*, 2016, pp. 422–428.
- [2] H. Cooper, B. Holt, and R. Bowden, "Sign Language Recognition," in *Visual Analysis of Humans*, London: Springer London, 2011, pp. 539–562.
- [3] Suharjito, R. Anderson, F. Wiryana, M. C. Ariesta, and G. P. Kusuma, "Sign Language Recognition Application Systems for Deaf-Mute People: A Review Based on Input-Process-Output," *Procedia Comput. Sci.*, vol. 116, pp. 441–448, Jan. 2017.
- [4] T. Starner, J. Weaver, and A. Pentland, "Real-time American sign language recognition using desk and wearable computer based video," *IEEE Trans. Pattern Anal. Mach. Intell.*, vol. 20, no. 12, pp. 1371–1375, 1998.
- [5] J. Ravikiran, K. Mahesh, S. Mahishi, R. Dheeraj, S. Sudheender, and N. V Pujari, "Finger Detection for Sign Language Recognition," in *Proceedings of the International MultiConference of Engineers and Computer Scientists*, 2009, p. 5.
- [6] B. Bauer and H. Hienz, "Relevant features for video-based continuous sign language recognition," in *Proceedings Fourth IEEE International Conference on Automatic Face and Gesture Recognition (Cat. No. PR00580)*, pp. 440–445.
- [7] A. Gardner, C. A. Duncan, J. Kanno, and R. Selmic, "3D hand posture recognition from small unlabeled point sets," in *2014 IEEE*

- International Conference on Systems, Man, and Cybernetics (SMC)*, 2014, pp. 164–169.
- [8] David Rakowski, "Sign Language," 1991. [Online]. Available: <http://lifeprint.com/as1101/topics/wallpaper1.htm>. [Accessed: 20-Oct-2018].
- [9] M. F. Unlarsen, K. Sabanci, and M. Ozcan, "Determining Cervical Cancer Possibility by Using Machine Learning Methods," *Int. J. Latest Res. Eng. Technol.*, vol. 3, no. 12, p. 6, 2017.
- [10] M. W. Gardner and S. R. Dorling, "Artificial neural networks (the multilayer perceptron)—a review of applications in the atmospheric sciences," *Atmos. Environ.*, vol. 32, no. 14, pp. 2627–2636, 1998.
- [11] E. Frank, M. A. Hall, and I. H. Witten, *The WEKA Workbench. Online Appendix for "Data Mining: Practical Machine Learning Tools and Techniques"*, Fourth. 2016.
- [12] N. Donges, "The Random Forest Algorithm," *SAP Mach. Learn. Found.*, vol. 5, pp. 18–22, 2018.
- [13] S. Dreiseitl and L. Ohno-Machado, "Logistic regression and artificial neural network classification models: a methodology review," *J. Biomed. Inform.*, vol. 35, no. 5–6, pp. 352–359, Oct. 2002.
- [14] D. B. Walker, S.H.; Duncan, "Estimation of the probability of an event as a function of several independent variables," *Biometrika*, vol. 54, no. 1/2, pp. 167–178, 1967.
- [15] D. R. Cox, "The regression analysis of binary sequences (with discussion)," *J Roy Stat Soc B.*, vol. 20, no. 2, pp. 215–242, 1958.

Monitoring Android Users Activities: Keylogger App

A. CALISKAN¹ and S. TASDEMIR¹

¹ Kuveyt Türk Participation Bank Research & Development Center, 41420 Kocaeli, Turkey, ahm.caliskan@outlook.com

²Selcuk University, Konya/Turkey, stasdemir@selcuk.edu.tr

Abstract – Nowadays the use of mobile devices has increased considerably. The increase in the number of mobile application users leads to increased interest in mobile application development. In this study, a keylogger application that to work on Android smartphones was developed for mobile security awareness. The device user's all keystrokes will be saved. These records can be monitored remotely on the admin device. There are currently similar apps on the Google Play Store. Many of these applications on Play Store perform keylogger function by using their own application keyboard instead of device keyboard. In this study, the new keyboard has not been developed. Keystrokes of the user these using the device keyboard are stored in the database on the server. This application on the administrator device allows remote monitoring.

Keywords - Android, Mobile, Keylogger, Spyware

I. INTRODUCTION

The use of mobile devices is increasing day by day. Increased use of mobile devices has resulted in the increased rate of mobile application development. There are many different apps in the Play Store such as health apps, cyber apps, and social network apps.

The use of mobile devices is of considerable importance for children and unqualified users. Parents want to know some information about children like which website they visit, people they communicate etc. for their own safety. Given the current need for safety and control and given the size of the targeted audience, monitoring and tracking app in this study is a matter of great importance.

There are many studies on malware applications in the literature.

In the study "Android Applications and Security Breach" [1] some types of cyber attacks and mobile threats that attackers perform to steal user information are described. In addition, the "Remote Access Trojan" example that called Dendroid was analyzed.

In the study that called "Keylogg -A Touch Based Key Logging Application" [2], Keylogger software risks in open source mobile operating systems are described. An application that records keystrokes for Android has been developed to draw attention to the potential security risks of open source mobile operating systems. The records the user's keystrokes (keylogger) in the device to the log file.

In the paper "Android Security: Permission Based Attack" [3], it is explained that the highest access privileges can be granted and thus access to resources in the user device and then some important user's data can be stolen.

In the study "Android Malware Detection & Protection: A Survey" [4], malware applications on Android are described.

In the paper that called "An Enhanced Security Framework for Reliable Android Operating System" [5], an increase in the number of applications installed as malware in the Android operating system has been mentioned.

In this study, Android keylogger application has been developed to perform user tracking/monitoring on smartphones and tablets etc. The information of the monitored user is stored in the database on the server. The keystrokes of the monitored device can be viewed remotely by retrieving the information on the server with the application belonging to the admin.

II. MATERIAL & METHOD

The software used in the study and the concepts used in the application development stage are given in this section.

A. Keylogger

A program that records user keystrokes on the device that called keylogger. Such software is not just software that records keystrokes. Depending on the choice of the developer, it enables the user activities to be viewed in more detail by taking screenshots of the device.

If the keylogger is not part of a trojan or rootkit, it requires installation locally, not remotely. If the system will be accessed remotely, trojan software with keylogger feature can be preferred [6].

B. Android Studio

Android Studio is the official Integrated Development Environment (IDE) for Android app development, based on IntelliJ IDEA. [7]

C. Android

Android is an open source operating system developed for mobile devices [8]. Android is Linux based and developed by Google.

1) Activity

The classes in which the user interacts are represented on Android devices. The activity classes that enable the

functionalities of the components (Button, TextView, EditText, ListView, etc.) on the screens designed by the developer.

Activity lifecycle is shown in Figure 1. [9].

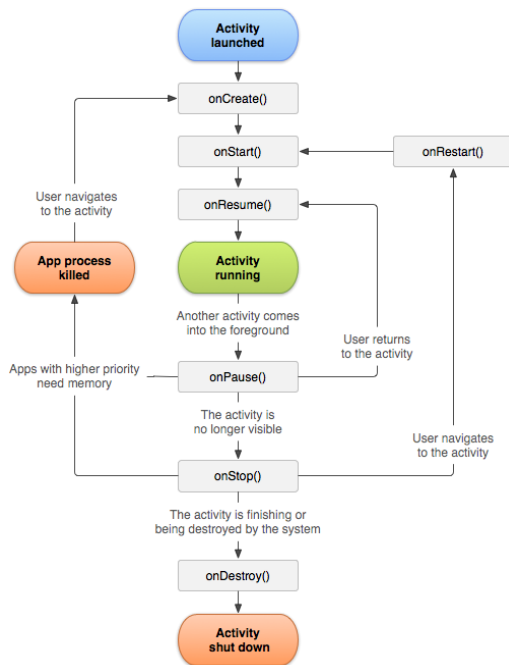


Figure 1: Activity Lifecycle

2) Layout

Layouts are XML files used to design the user interface on Android. Layout XML files in res/layout folder.

3) Service

Service is the classes that perform the background operations in Android applications. It does not provide a UI.

Service lifecycle is shown in Figure 2. [10]

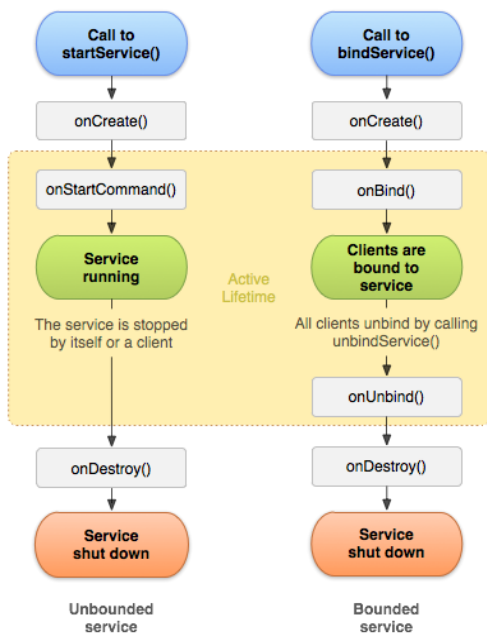


Figure 2: Service Lifecycle.

4) Intent

There may be more than one Activity or Service in Android applications. Intents are objects used in operations such as switching between activities, starting a new Activity or starting a Service.

5) SQLite

SQLite is an open source relational database management system used to perform database operations on Android devices.

6) Shared Preferences

Shared Preferences is used to store simple data in the Android operating system. It is more convenient to use Shared Preferences instead of using SQLite when need to store small size simple data.

7) AndroidManifest.xml

AndroidManifest is an XML file in the main directory of the project that keeps important information of the application and specifies the system permissions to be used in applications. This XML file is essential for running app.

8) AsyncTask

Android has its own AsyncTask thread class for Android developers. AsyncTask allows the main thread to be processed without interrupting and if UI update is required, it provides communication with the main thread.

9) Content Provider

Content Provider provides an interface built on a simple URI addressing model using the content:// scheme for transfer and publish data [11].

10) Android Mobile Devices and Hosting

Lenovo P2a42 (Android version 6.0.1) smartphones, Samsung Galaxy Tab A6 (Android version 5.1.1) and also web hosting (GoDaddy) were used in this project.

III. APPLICATION STUDY

Tested on Lenovo P2a42 (Android version 6.0.1) after application development. "Android adb terminal" was written on the monitored device for testing.

The screenshot is shown in Figure 3.

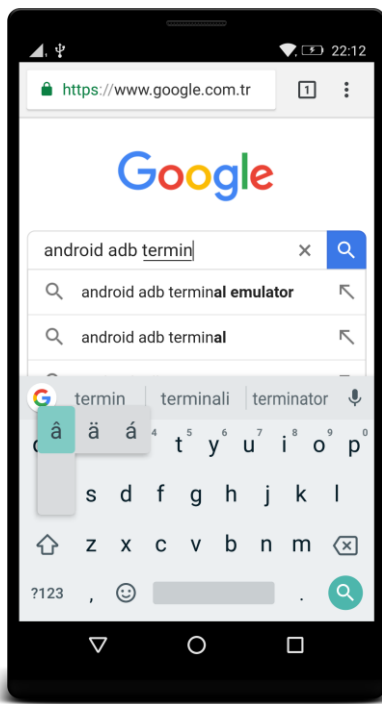


Figure 3: Keystrokes on the monitored device.

Keystrokes on the monitored device can be remotely reviewed on the administrator device. Keystrokes are recorded on an hourly basis for application performance. The date is selected in the administrator device. If there are keystrokes in that day, keystroke records are listed as hourly segments. Date selection and hour segments in the administrator application are shown in Figure 4 and Figure 5.



Figure 4: Date selection in the administrator app.

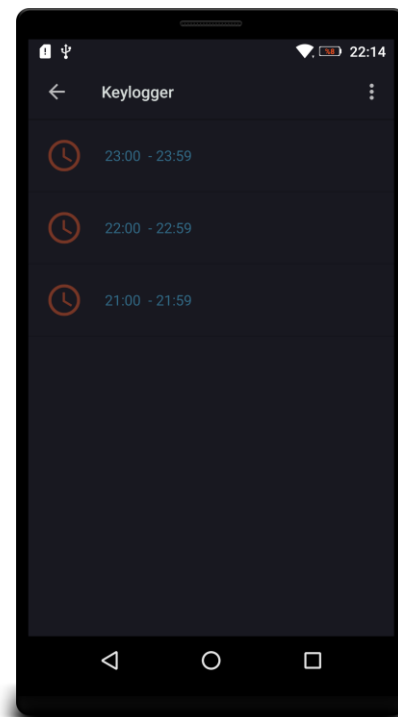


Figure 5: Hour segments in the administrator app.

The administrator can remotely display the keystrokes of the monitored device with the time information. Text entered in the monitored device can be reviewed on the administrator device. It is shown in Figure 6.

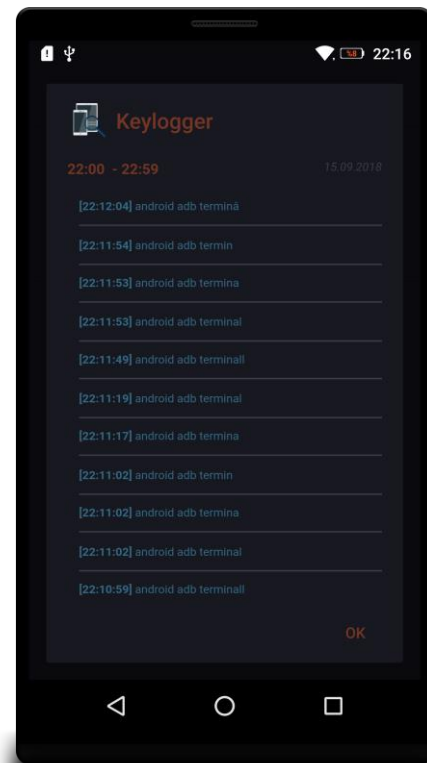


Figure 6: Reviewing keystrokes on the administrator device.

Android keylogger application works successfully, as shown in the figures.

The application on the administrator device allows the display of keystrokes on the monitored device. Most of the similar apps in Play Store perform keylogger with their own keyboard instead of the original system keyboard. In this study, a new keyboard has not been developed; the keylogger function is performed with the original keyboard. Furthermore, unlike other applications, these keystrokes are remotely reviewed on the administrator device.

IV. CONCLUSION AND RECOMMENDATIONS

Android was preferred in this study due to Android is the most used mobile operating system.

Applications similar to the developed keylogger app in this project are available on the Play Store. Unlike these applications, in this study, a new keyboard has not been developed for the keylogger feature. The original keyboard was used for keylogger feature.

As can be seen in the Application Study section and figures, the aim of paper has been achieved successfully. The keylogger feature can be used on the admin device.

This application can also be improved and developed as a desktop and web application.

Contrary to malicious spyware, such an application can be used especially for children controlling and monitoring by their parents. In that way, their surfing on the internet and texting can be controlled by their parents.

In addition, this study was carried out to guide application developers and researchers who will work ethically in this regard.

REFERENCES

1. Benítez-Mejía DGN, Sánchez-Pérez G, and Toscano-Medina LK. *Android Applications and Security Breach*. in *2016 Third International Conference on Digital Information Processing, Data Mining and Wireless Communications (DIPDMWC)*. 2016.
2. Bhosale P, et al., *Keylogg -A Touch Based Key Logging Application*. *International Journal of Research in Engineering and Technology*, 2016. **5**(4): p. 12-15.
3. Jain A and Prachi. *Android Security: Permission Based Attack*. in *2016 International Conference on Computing for Sustainable Global Development (INDIACom)*. 2016. Gurgaon/India.
4. Arshad S, et al., *Android Malware Detection & Protection: A Survey*. *International Journal of Advanced Computer Science and Applications*, 2016. **7**(2): p. 463-475.
5. Park JH, et al., *An Enhanced Security Framework for Reliable Android Operating System*. *Security Comm. Networks*, 2016. **9**: p. 528-234.
6. Elbahadır H, *Hacking Interface*. 2014, İstanbul: Kodlab Yayın Dağıtım Yazılım ve Eğitim Hizmetleri San. ve Tic. Ltd. Şti.
7. Android. 2018 [22.09.2018]; Available from: <https://developer.android.com/studio/intro/>.
8. Narman AE, *Android Programlama*. 2013, İstanbul: Kodlab Yayın Dağıtım Yazılım ve Eğitim Hizmetleri San. ve Tic. Ltd. Şti.
9. Android. 2018 [15.09.2018]; Available from: <https://developer.android.com/reference/android/app/Activity.html>.
10. Android. 2018; Available from: <https://developer.android.com/guide/components/services>.
11. Meier R, *Profesyoneller için Android ile Uygulama Geliştirme*, ed. Arslan turalı M. 2013, İstanbul: Pusula Yayıncılık.

Artificial Neural Network and An Application in Business Field

I. KURUOZ¹ and S. TASDEMIR¹

¹Selcuk University, Konya/Turkey, iakuruoz@gmail.com

¹Selcuk University, Konya/Turkey, stasdemir@selcuk.edu.tr

Abstract - *In today's world, information technologies are integrated into all vital and social elements. Besides, these technologies are attractive for the people of all ages. Each business has a life span like human beings and it is impossible for the businesses to adapt the competition and/or to survive by keeping away from the information technologies. The developments like artificial intelligence, expert systems and artificial neural networks (ANN), which provide future estimation to the businesses as well as aim the optimization of the conducted processes, are irreplaceable for these businesses. ANN, one of these techniques, has been started to be used frequently in business life thanks to its success in producing solutions. In this study, general information about ANN is given, general information about business and types of businesses are explained and an example of ANN application is performed after literature research. To exemplify ANN, TOPSIS (The Technique for Order of Preference by Similarity to Ideal Solution) method of participation banks is applied to ANN in order to predict 2017 4th quarter data and performance is sorted. Based on the results, chosen banks are affected by the factors such as crises, exchange rate etc. and thus, it is detected that their performances are depended on extrinsic factors.*

Keywords - *Business, Artificial Neural Network, Financial Failure Prediction*

I. INTRODUCTION

In globalizing world economy, it is essential to use resources effectively to maintain operations of business. Firm owners, employees, producers and consumers consistently look for ways to conduct their financial operations against rapidly changing economic conditions. Nowadays, ANN prediction technique is widely used in many areas. ANN methodology provides important advantages like learning mechanism, generalization, capable of working with infinite number of variables. ANN provides linear and non-linear modelling without dependency between input and output variables. Learning algorithm, organization of data set, estimation period etc. are influential on the performance of ANN. It is considered that a great number of trials and investigation would be helpful.

ANN is a method, which can be applied in various areas as portfolio management, stock market index, and price estimation of gold, currency or stock certificate. ANN has become preferred in prediction problems since it utilizes from previous information and experiences and it can learn the complex relationships between variables [1].

Research results show that most of the companies use financial failure prediction. In light of these findings, in this study, an application associated with financial failure prediction is done by means of ANN.

The studies that have attracted attention in the literature review are as follows: "Predicting bank failure: An improvement by implementing a machine-learning approach to classical financial ratios (Hanh Le ve Viviani, 2018)" [2], "Predicting failure risk using financial ratios: Quantile hazard model approach (Dong ve ark., 2018)" [3], "Artificial Neural Networks in Business (Tkac ve Verner 2016)" [4].

In the course of literature research, it is seen that businesses study on using all sources of statistics and technology to fulfill the required conditions since it is not easy to keep pace with current competition world. Otherwise, it very difficult to maintain their operations for the businesses.

When applications of ANN are examined, it is determined that the method has widespread application fields and obtains successful results [5]. If the studies are analyzed with respect to the sub-titles of business science, it can be realized that studies in marketing field mainly focus on demand estimation, price estimation, estimation of the prices of stock certificate, and sale estimations. The studies in management field concentrate on decision-making and process improvement. The studies in production field are mostly related to process monitoring, new product estimation and quality control. Lastly, it is noticed that the studies in finance field are generally focused on the estimation models and the comparison of the alternative models.

When the studies are investigated with regard to ANN models, it is seen that the researchers fundamentally concentrate on multilayered network method because this method provides intended skills. Besides, multilayered network method gives effective results in the applications in business field and the method is suitable with learning algorithms.

In this study, the future estimation of financial success of the participation banks across the country are done via TOPSIS method. As a results, it is inferred that the financial conditions of the chosen banks are depended on extrinsic factors rather than internal factors.

Data for the implementations are chosen from the ratio tables which are published on website (www.tkbb.org.tr-The Participation Banks Association of Turkey) for the years between 2010 and 2017. After forming decision matrix, the normalization procedure is applied to the data in order to make

them suitable for ANN method. Finally, 2017 4th quarter data are predicted.

II. ARTIFICIAL INTELLIGENCE

Artificial intelligence is a branch of science that deals with the ability of machines to produce solutions to complex problems like humans. To do this, in general, characteristics of human-brain are taught to the computer via algorithms or mathematical applications. Depending on the desired needs, more/less flexible or effective approaches can be presented with respect to the chosen mental attitudes. Albeit artificial intelligence is generally associated to the computer sciences, it has also close relationships with other science fields like mathematics, biology, psychology, philosophy etc. Combining of the information belonging to all these fields will eventually depend on the developments in artificial intelligence [6].

There are different approaches, which's trueness or wrongness have not been proved yet, on artificial intelligence. Though some of the approaches seem more useful compared to the others, the new alternatives are frequently produced. The researchers of artificial intelligence has focused on solving some problems for 50 years. Therefore, they have divided into subjects like progressive computation, planning etc. In this context countless solutions have been implemented efficiently and reliably.

A. Artificial Neural Network (ANN)

ANN models are the most known and used artificial intelligence models. ANN models are non-linear and has the ability of parallel processing and they are an artificial intelligence application which can match an input data with output data. ANN is used in solution of the problems within the scope of the prediction, classification and clustering types. If literature is reviewed it will be seen that ANN is used in finance, business and economy areas in the 80's.

The general properties that separates ANN's from other learning algorithms can be listed as follows [7].

- **Non-linear:** There is a relation between all outputs and inputs. In linear systems, if one of the inputs is changed corresponding to this change an output also changes but it is related only with this changed input. In non-linear systems input and output changes are connected with all the network.
- **Error tolerance:** Due to having parallel distributed parameters of the ANN every computation is an isolated island within its own region. Because of this, even if affected component is damaged the system would not stop. ANN system having an error tolerance means that information is distributed over the system.
- **Supervising process:** Neural network can solve complex problems owing to its ability to change its own parameters. In this case although valid parameters of the problem are unknown network can provide the solution by itself.
- **Learning process:** Output-input or only input data are required so that ANN can learn a problem. Learning

cluster has to have sufficient number of data. Learning process can be defined as a process which obtains weight data defining the relationship between input and output layers.

- **Generalization:** Neural network not only produces supervised data but also describes new data.
- **Memory:** In biological systems, data are dispersedly kept. In ANN, memory is distributed into multiple local sub-memories. Connections constants are ANN memory types. The values of weights represent the current information state of the network.

B. Structure and Working Principle of Artificial Neural Cells

The structure of the human brain convinced scientists to work on it because of the outstanding properties of it. By copying the neuro-physical structure of the brain, a similar mathematical model was tried to be extracted. Various artificial cells and network models have been developed to fully implement the brain structure and behavior. As a result of these studies, artificial neural networks have emerged as different branches of the algorithmic calculation method [8].

As in the neural cells of biological neural networks, artificial neural networks also have artificial neural cells. Artificial neural cells are also referred to as process elements in engineering science. As shown in figure 1, each process element has five basic elements. These are; inputs, weights, aggregation function, activation function and outputs.

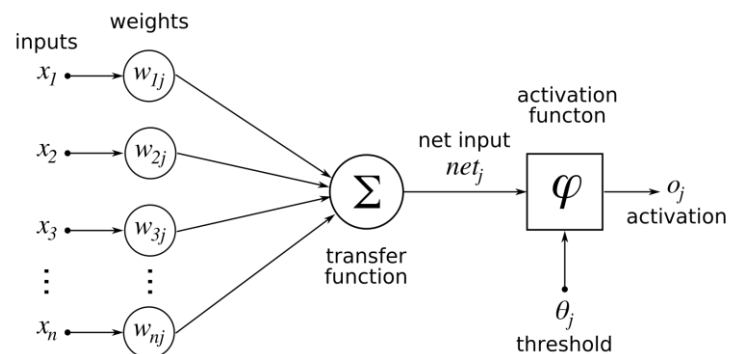


Figure 1: Artificial neural network cell

C. What is Business?

Business is the production units that brings together production factors in a planned and systematic way with the aim of producing service and profit [9].

Generally businesses have three goals:

- **Profit-making:** In addition to being used as a measure in evaluating and inspecting the success level of the business, it is also a tool that allows it to fulfill its legal obligations to the government such as tax to be paid etc. It appears as the main purpose of the businesses.
- **Service to the community:** Businesses give a part of their profits to the state as taxes, another part of the profit is distributed to the partners and employees to fulfill their responsibilities. Thus, the advantage of being more successful and long-lasting is obtained.

- Maintaining the business: Businesses must establish a consistent balance to achieve their goals of making a profit and serving the community. When this balance is established, the business will be long-lasting. If the business intends to generate excessive profits in a short time; it would either keep the price of the goods and services offered high or offer cheap quality goods, as a result of which the business would have to withdraw from the market after a certain period of time.

D. Financial Failure

If businesses have a difficulty fulfilling their financial obligations or never meet them, this is called financial failure. Not predicting financial failure or failing to make the right decisions while in it results in bankruptcy.

The technological developments and globalization tendency and the subsequent disappearance of the financial limits have increased the importance of estimation and decision making. Accurate and right decisions are substantial given this financial uncertainty. In this period, companies that made wrong decisions had to experience the financial failure. The concept of financial failure began to arise from the business literature in the 1960s and in 1970s with the oil crisis it is revealed that estimating financial failure is essential [1, 5].

III. APPLICATION

The TOPSIS method was introduced based on the studies of Chen and Hwang (1992) [10] and Demireli (2010) [11]. TOPSIS method is one of the decision making methods with decision matrices having multiple criteria. In the method, alternatives are processed according to the predetermined criteria and the results are compared between maximum and minimum values. The multi-criteria decision-making problem having n number of alternatives and m criteria can be represented by n-points in the m-dimensional space (Eleren and Karagül, 2008) [12]. Hwang and Yoon (1981) [13] constituted the TOPSIS method originates from the assumption that the solution alternative would be the shortest distance to the positive ideal solution point and the farthest distance to the negative ideal solution point.

This study covers the ratio data of a participation bank operating in Turkey. Data are published by Participation Banks Association of Turkey for the years between 2017 and 2010. It is thought that the study is influenced by the external factors since dataset incorporates the data of the 2010 international crisis and 2012 Euro crisis. These data are used to determine the financial performance of the company by being subjected to the decision matrix, normalization and weighting processes of TOPSIS method. The ratios and significance coefficients included in the process are shown in Table 1.

A significant portion of the determined ratios are shaped around the asset totals and profitability ratio. Another remarkable point is that the table includes the financial performance ratios of firms. These ratios indicate the financial success / failure of the companies.

Table 1: Decision matrix weight values

Criteria	Weight Vector	Input Parameters
Equity / Total Assets	0.1	X1
Total Loan / Total Assets	0.1	X2
Non-performing Loan / Total Loan	0.1	X3
Fixed Assets / Total Assets	0.1	X4
Liquid Assets / Total Assets	0.1	X5
Liquid Assets / Short Term Liabilities	0.1	X6
Net Profit For the Period / Total Assets	0.1	X7
Net Profit For the Period / Total Shareholders' Equity	0.1	X8
Net Profit Share Income After Specific Provisions / Total Assets	0.1	X9
Net Profit Share Income After Specific Provisions / Total Operating Income	0.1	X10

In this study, forward feedback multilayered propagation algorithm which is widely used for estimation is used. The generated ANN has 10 inputs and 1 output. Input parameters for this model; Equity / Total Assets (X1), Total Loan / Total Assets (X2), Non-performing Loans / Total Loan (X3), Fixed Assets / Total Assets (X4), Liquid Assets / Total Assets (X5), Liquid Assets / Short Term Liabilities (X6), Net Profit For the Period / Total Assets (X7), Net Profit For the Period / Total Shareholders' Equity (X8), Net Profit Share Income After Specific Provisions / Total Assets (X9), Net Profit Share Income After Specific Provisions / Total Operating Income (X10) and output parameter; Log (Total Assets) (Y) consists of 11 parameters. For the ANN training and test processes, a total of 352 data sets were used (32 from each parameter).

In practice, the model that the first procedure was chosen by considering the MSE (Mean Square Error) error rate which is considered to be the most suitable after many trainings. The formula used for the MSE calculation is given in Equation 1 [14].

$$MSE = \frac{1}{n} \sum_{i=1}^n (d_i - O_i)^2 \quad (1)$$

Here; d_i is the target or actual value (log (total assets)), O_i is output or estimated value (ANN), n is the number of output data.

26 of 352 data were used for training and 6 of it were used for testing. Levenberg-Marquardt (trainlm), Bayesian Regularization (trainbr), Gradient Descent Backpropagation (traingd) algorithms were used for training and testing, and the results were obtained. In order to determine the transfer function Hyperbolic Tangent Sigmoid (tansig), Logistic Sigmoid (logsig) and Linear (purelin) transfer function

developed in Matlab software was run with the program. In the training and testing process, the number of neurons in the hidden layer is 5, 10, 15, 20, 25, 27, 30, 33, 38, 40, 50 and the number of epoch is 5, 10, 15, 19, 21, 24, 28, 31, 35, 40, 50 and was run individually. The best result was obtained in the trainlm algorithm, logsig transfer function, 21 epoch 10-25-1 model. In this case, MSE were found 0.00004 and 0.00436 in training and the testing respectively.

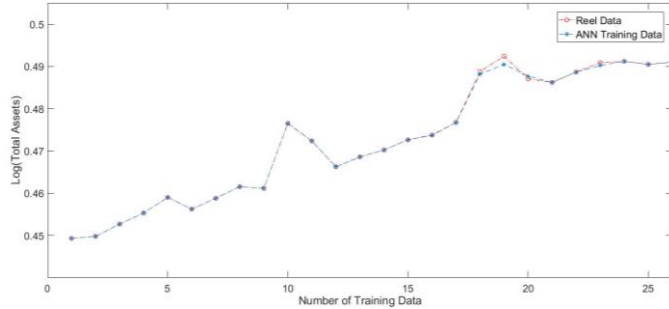


Figure 2: Comparative graph of actual data and results of training process with ANN (10-25-1 model)

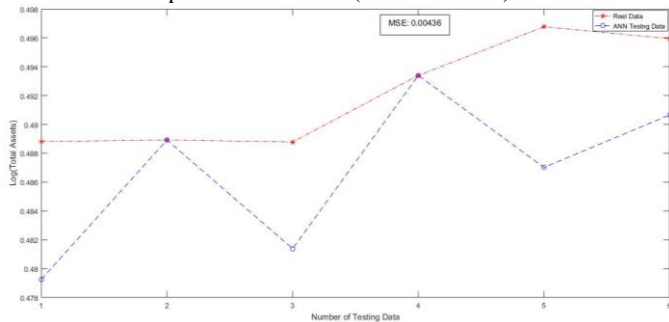


Figure 3: Comparative graph of actual data and testing results with ANN (10-25-1 model)

The importance of the variables used in the study is equal to each other. But as it is known, the most important factor, regardless of the sector, is profitability. Successful businesses generally continue to live with high profit margins. Another factor that concerns the profitability ratio is the debts and payment obligations. The costs and expenses of excessively indebted enterprises will increase and the business will not be able to continue their financial lifetime. Our results have supported the literature studies and industry. Turkish banking is seen to be highly affected by external variables such as international variables, economic crisis etc., especially in today's values. Figure 4 and Figure 5 show that the ANN model was successful in the training data not very good results in the test data. Correlation analysis; the correlation rate of the training output was 0.99598 and it was found to have a high rate. The correlation rate of the test outputs is 0.79525 and has a good rate, although not successful (Figure 4 and Figure 5). But it is not enough for the application.

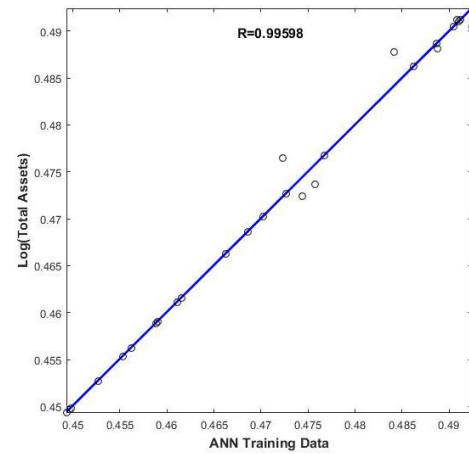


Figure 4: Graph of relationship between ANN training values

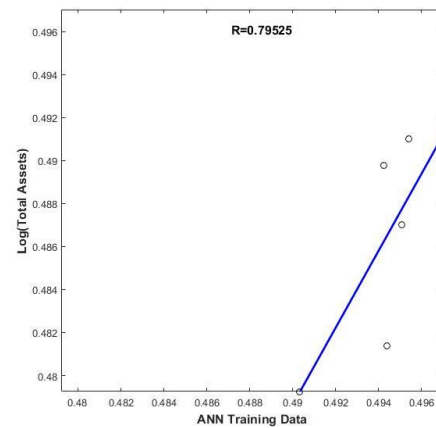


Figure 5: Graph of relationship between ANN test values

IV. RESULTS AND RECOMMENDATIONS

Rapid changes in the economic and social spheres all over the world especially after 1980 increased the necessity of financial growth and development of the countries and this led to the freedom of financial field. The risks and the number of risks faced by the businesses exposed to these developments have increased. Another result of economic freedom is globalization. The integration of financial systems together with globalization has increased the fragility of banks against external factors, shocks and crises.

Today's modern business structures must constantly change to adapt to new technologies and structures. Information technologies are included in business strategies as they provide conveniences and opportunities in international competition, flexibility in management and production of new products and services.

The developments in information technologies have increased the business intelligence in an accurate manner. The skills of the ANN, the obscurity in its structure, increased the work on this subject and kept it up to date.

The number of problems that the ANN cannot solve due to the applicability, generalization, accuracy, and predictive skills is very small. However, as it can be seen from the studies, success is directly proportional to the architecture and network structure for successful ANN applications. ANN is generally

used for estimation, data classification, data mapping, diagnosis and improvement. As a result of the literature reviews, ANN has been applied in finance, marketing, management and production fields with various subtitles and achieved high success. In addition, where the studies are applied; in terms of time, efficiency, process control, quality control, it has been found that it brings high gains to businesses.

In order to improve the test condition, especially in ANN, the network structure can be changed. Or different artificial intelligence techniques can be used as hybrids.

V. REFERENCES

- [1] A. Bayrakçı, *Hisse Senedi Fiyatının Tahmininde Yapay Sinir Ağı Yaklaşımı.*, Eskişehir, Osmangazi Üniversitesi, Fen Bilimleri Enstitüsü, 1997.
- [2] H. H. Le ve J.-L. Viviani, *Predicting Bank Failure: An Improvement by Implementing a Machine-learning approach to classical financial ratios*, 2018.
- [3] M. C. Dong, S. Tian ve C. W. Chen, *Predicting failure risk using financial ratios: Quantile hazard model approach*, 2018.
- [4] S. C. Rana ve J. N. Patel, *Selection of best location for small hydro power project using AHP, WPM and TOPSIS methods*, 2017.
- [5] M. Tkac ve R. Vernet, *Artificial Neural Networks in Business: Two Decades of Research, Applied Soft Computing*, pp. 788-804, January 2016.
- [6] Ş. K. Yılmaz, *Yapay Sinir Ağlarıyla Yapılmış İşletme Uygulamaları*, Uluslararası Sosyal Bilimler Sempozyumu, Elazığ, 2016.
- [7] N. Keleş. (2018, July). Yapay zeka nedir?. Available: <http://www.yazsum.sakarya.edu.tr/ndex.php/d%C3%B6k%C3%BCman/49-yapay-zeka-nedr.html?tmpl=component&prnt=1&layout=default>.
- [8] İ. Kaya, S. Oktay ve O. Engin, *Kalite Kontrol Problemlerinin Çözümünde Yapay Sinir Ağlarının Kullanımı*, no. 21, 2005.
- [9] E. Öztemel, *Yapay Sinir Ağları*, Papatya Yayıncılık, 2012.
- [10] T. Koçel, *İşletme Yöneticiliği*, İstanbul: Beta, 2014.
- [11] G. C. Akkaya, E. Demireli ve Ü. H. Yakut, *İşletmelerde finansal başarısızlık tahminlemesi: yapay sinir ağları modeli ile İMKB üzerine bir uygulama*, no. 10, 2010.
- [12] Shu-Jen ve C. L. Hwang, *Fuzzy Multiple Attribute Decision Making: Methods and Applications*, Berlin, Springer - Verlag, 1992.
- [13] C. L. Hwang ve P. Yoon, *Multiple Attribute Decision Making In: Lecture Notes in Economics and Mathematical Systems*, Springer-Verlag-Berlin, 1981.
- [14] Ş. Taşdemir, *Yüzey Pürüzlülüğünün Yapay Sinir Ağı Ve Regresyon Modelleri İle Belirlenmesi Ve Karşılaştırılması*, Teknik Bilimler Meslek Yüksekokulu Teknik-Online Dergi, 2011.
- [15] A. Eleren ve M. Karagül, *Türkiye Ekonomisi Performans Değerlendirmesi, Celal BAYAR Üniversitesi İktisadi ve İdari Bilimler Fakültesi Yönetim ve Ekonomi Dergisi*, cilt 15, no. 1, 2008.
- [16] E. Demireli, *Topsis Çok Kriterli Karar Verme Sistemi: Türkiye'deki Kamu Bankaları Üzerine Bir Uygulama*, Journal of Entrepreneurship and Development, cilt 1, no. 5, pp. 100-112, 2010.

Fusion of Smartphone and Smartwatch Sensors for Smoking Recognition

S. AĞAÇ¹, M. SHOAIB² and Ö. DURMAZ İNCEL¹

¹ Galatasaray University, İstanbul/Turkey,
sumeyye.agac@ogr.gsu.edu.tr, odincel@gsu.edu.tr

²University of Twente, Enschede/Netherlands,
m.shoaib@utwente.nl

Abstract - Human activity recognition using different types of sensors is used for many applications, such as well-being. Motion sensors integrated in smartphone and smartwatch devices are suitable platforms to recognize daily activities. In this paper, the objective is to recognize some activities where hand movements play an important role, such as smoking and eating. We use a dataset of 45 hours collected from 11 participants. The dataset includes both simple activities, such as sitting and standing, and complex activities, such as smoking while walking and drinking while standing. In total, we have ten different activities in our dataset and most of them have similar patterns. We use accelerometer and gyroscope sensors available on smart phones and smart watches, which are commonly used motion sensors. We first determine the high impact features in order to reduce the number of features and choose the most efficient ones, by applying feature selection algorithms. We use random forest classifier to determine the impact of using smartwatch sensors alone, smartphone sensors alone and the fusion of two on the recognition performance of activities. The results show that fusion of the sensors on the two devices increases recognition performance of the considered activities. By using sensors from both devices, we achieve an increase of 21%, 43%, 44% and 5% for smoking related, drinking related, eating and simple (sitting, standing and walking) activities respectively, compared to using only phone sensors.

Keywords - Activity recognition, wearable computing, motion sensors

I. INTRODUCTION

The use of smart devices such as smartphones and smartwatches is growing rapidly thanks to the technological advancements. Smartphone and smartwatch devices are equipped with various sensors, such as accelerometer, gyroscope, magnetometer and GPS. Accelerometer and gyroscope sensors can be used to capture movements and detect human activities. While smartphones are efficient to detect simple activities, such as walking and biking, the smartwatch is more convenient to recognize complex activities where hand-wrist movements play an important role, such as smoking or drinking. In real life, both complex and simple activities are performed together. Therefore, using smartwatch in addition to smartphone can have a positive impact on the overall performance of the recognition of daily activities.

As mentioned, using only a smartphone can be insufficient to detect complex activities and it can be difficult even for the simple activities if the user does not carry phone with him/her. In daily life, users smoke while standing or drink a coffee while standing. Besides, smoking, eating and drinking activities can be easily confused with each other as they have similar hand-wrist movements.

In this paper, we investigate the individual use of smartphone and smartwatch sensors as well as their fusion to recognize complex and simple human activities. For this purpose, we collected data from 11 participants for 10 different activities. The dataset includes both simple and complex activities: smoking while sitting (smokeSD), smoking while standing (smokeST), eating (eat), drinking while standing (drinkSD), drinking while sitting (drinkST), sitting (sit), standing (stand), smoking while walking (smokeWalk), walking (walk) and smoking in a group conversation (smokeGroup). As can be seen from the dataset, activities were performed both alone and in combination with each other and complex activities have similar patterns and this makes recognition of our activities more challenging.

In total, we extract 45 features from accelerometer (ACC) and gyroscope (GYR) sensors. We use four dimensions of sensors (x, y, z and magnitude) then we apply several feature selection algorithms to find the best features with the specific dimensions. Instead of using all the features, this method will decrease the number of features to extract, that in return decreases computational cost and removes unnecessary features from the feature list. The main highlights of the paper are as follows:

- We make an analysis using a smartphone and a smartwatch: we investigate the use of these two devices individually and in combination. Some activities such as standing were well recognized, but we want to observe the impact on devices for more complex activities.
- We analyse if using only a smartwatch will achieve a good enough accuracy for simple activities.
- We use feature selection algorithms to make a prudent selection of features to save more energy on battery limited devices.

The rest of the paper is organized as follows. We describe the related work in Section II, methodology for activity recognition in Section III, performance evaluation in Section IV and finally we present the conclusions in In Section V.

II. RELATED WORK

In recent years, recognition of daily human activities using sensors integrated in portable devices is extensively studied in the literature [1, 2, 3]. In most of them smartphone sensors are used to collect the data [4, 5, 6]. With the increase in the use of smartwatches, researchers try to recognize some activities using smartwatches which were difficult to recognize using only smartphones [7, 8].

In [8], researchers aim to detect 13 daily human activities using the fusion of smartwatch and smartphone sensors. However, instead of using a real smartwatch device, they attached a smartphone on the right wrist of participants. The second smartphone was in the pocket position. Their dataset has two different types of activities: simple activities, such as walking, jogging and sitting and complex activities, such as smoking, eating and typing. They use mean and standard deviation features that they chose manually for four dimensions (x, y, z and magnitude). Accelerometer and gyroscope sensors were used individually and in combination. They reported that fusion of smartwatch and smartphone sensors achieved a high accuracy for the complex activities which were difficult to recognize only with a smartphone in the pocket. Besides that, the fusion of two did not bring a significant difference for the simple activities.

Similarly, in [7], authors use fusion of smartphone and smartwatch sensors to increase the accuracy of activity recognition. However, their dataset contains only four activities which are walking, sitting, standing and driving. To collect driving data, they ask the participants to simulate the action of driving, it does not represent the real activity. They state that, particularly for driving activity, using only a smartphone can be insufficient. For example, being a driver can be easily confused with being a passenger using a smartphone located at the front pocket. They use data of accelerometer in three axes (x, y and z). As a feature set, they use mean, standard deviation and fusion of these two.

In [9], they indicate that during the human activity recognition process, feature selection (type and number of features) has an important effect on the computational complexity using wearable devices. In [10], researchers create an initial feature set using seven feature (in three dimensions) and apply three feature selection algorithm using Weka tool [11]. They aim to obtain most efficient features. While retaining a certain accuracy, this will increase the number of features by eliminating inefficient features automatically. Therefore, unnecessarily consumed energy will be saved. In addition, instead of taking all axis of chosen features at the beginning, this will allow finding the efficient dimension(s) of features.

In this study, our focus is on the comparison of the impact of smartwatch sensors on the recognition performance of complex activities in addition to smartphone sensors. For this purpose, our dataset contains several smoking variations and some other activities which have very similar hand-wrist movements as smoking, such as drinking and eating. Besides,

different from our previous works, we realize a prudent feature selection to determine the best features automatically. This will allow saving more resources which is very important particularly for smartwatches.

III. METHODOLOGY

A dataset of 45 hours was collected with eleven participants (9 male, 2 female), aged from 20 to 45. While collecting data, two devices which are smartphone (Samsung Galaxy S2 or S3) and smartwatch (LG Watch R, LG Watch Urbane or Sony Watch 3) are connected through Bluetooth. All participants carried smartphone in the right pocket of their pants and smartwatch on their right wrist to capture their hand-wrist movements directly. A sampling rate of 50 Hz was selected for this study as this is sufficiently higher to recognize these daily activities. Dataset contains smoking activities in different forms and some other activities which are very similar hand-wrist movements, such as eating. In total, there are ten different activities which are smoking while standing (smokeSD), smoking while sitting (smokeST), eating (eat), drinking while standing (drinkSD), drinking while sitting (drinkST), standing (stand), sitting (sit), smoking while walking (smokeWalk), walking (walk) and smoking in a group conversation (smokeGroup). Dataset includes readings from several sensors such as accelerometer, gyroscope, and magnetometer, but in this study, we are particularly interested in using accelerometer and gyroscope in three axes.

The short definitions of the two sensors used in this work are as follows:

- Accelerometer: The sensor measures the acceleration of the device. It is quantified in meters per second squared (m/s^2).
- Gyroscope: The sensor measures the orientation of device. It is quantified in radian per second (rad/s).

In this study, the following features are computed from the accelerometer and gyroscope readings over a time window:

- Mean: The average value of a set of numbers.
- Median: The middle value of sorted a set of numbers.
- Standard deviation (std): The square root value of the variance.
- Minimum (min): The lowest value in a set of numbers
- Maximum (max): The highest value a set of numbers
- Skewness: The measure of symmetry, or more exactly a lack of symmetry. A distribution or a set of numbers is symmetric if it is identical to the left and to the right of the central point [12].
- Kurtosis: The measure of if the data are in heavy tail or in light tail compared to a normal distribution. In the other words, a set of numbers in kurtosis raised tend to have heavy tails or absurd values. a set of numbers to weak kurtosis tend to have light tails, or lack of absurd values. A uniform distribution would be the extreme case [12].
- Range: The difference between the highest and lowest value in a set of numbers.

- Integration: The measure of the signal area under the data curve. The measure used to estimate speed and distance of a signal, particularly signal of accelerometer sensor. [13]
- Correlation: The measure used as a marker of exchange between each pair of axes.
- Root Mean Square (rms): The square root of the sum of each value in a set of numbers, known also as the quadratic mean.
- Absolute Difference: Sum of absolute differences between each set of number and the average of set divided by the length of the set of number.

Feature selection is investigated to determine the most predictive attributes (named also as features in the text). In Weka tool [11], feature selection is divided into two parts which are attribute evaluator and search method. Attribute evaluator is the technique which evaluates each attribute in the dataset. Search method investigates different feature combinations to observe a list of chosen features. Feature selection techniques used in this study are described below. The first seven belongs to the attribute evaluator and the rest to the search method. These brief definitions are taken from the online documentation of Weka [11].

- CfsSubsetEval: Evaluates the worth of a subset of attributes by considering the individual predictive ability of each feature along with the degree of redundancy between them.
- CorrelationAttributeEval: Evaluates the worth of an attribute by measuring the correlation (Pearson's) between it and the class.
- GainRatioAttributeEval: Evaluates the worth of an attribute by measuring the gain ratio with respect to the class.
- InfoGainAttributeEval: Evaluates the worth of an attribute by measuring the information gain with respect to the class.
- OneRAttributeEval: Evaluates the worth of an attribute by using the OneR classifier.
- ReliefFAttributeEval: Evaluates the worth of an attribute by repeatedly sampling an instance and considering the value of the given attribute for the nearest instance of the same and different class.
- SymmetricalUncertAttributeEval: Evaluates the worth of an attribute by measuring the symmetrical uncertainty with respect to the class.
- BestFirst: Searches the space of attribute subsets by greedy hillclimbing augmented with a backtracking facility.
- GreedyStepwise: Performs a greedy forward or backward search through the space of attribute subsets.
- Ranker: Ranks attributes by their individual evaluations.

During this study, except feature selection, python programming language with Scikit-learn [14] machine learning library was used. Feature extraction was made separately, one for the complex activities which are smokeSD, smokeST, drinkSD, drinkST, smokeWalk and smokeGroup, and one for the simple activities which are sit, stand and walk. Features are extracted from four dimensions of sensors: x, y, z and

magnitude (the sum square root of x, y and z axis). As the focus of using a gyroscope with accelerometer is recognizing complex activities, we extract both ACC (accelerometer) and GYR (gyroscope) features for the complex activities while extracting only ACC features for the simple ones. Then, we realize feature selection using the Weka tool. Using selected features, Random Forest algorithm was used for the classification because this algorithm is more efficient than a Decision Tree. By creating many trees different as possible, a weakly correlated population is obtained, and it gives results in a short time. For the evaluation method, 10-fold cross validation without shuffling was used. In this study, we investigate six sampling rates (1, 2, 5, 10, 25 and 50 Hz) with four window size (5, 10, 20, 30 seconds). We generate these lower sampling rates data from 50 Hz data. Due to the limited space, in the rest of the paper, we only report the best results which are obtained using 50 Hz with 20 seconds.

IV. PERFORMANCE EVALUATION

In this section, firstly, we present the results of feature selection and classification analysis.

We use Python programming language for feature extraction and classification. We used a Python-based machine library which is Scikit-learn [14] to realize the classification phase. We use Random Forest classifier with a number of eleven trees and as a validation method, we use 10-fold stratified cross-validation without shuffling. At each iteration, the validation method divides the dataset into ten equal subsets. Then, it uses nine parts for training one part for testing. We present f1-score as a performance metric and it ranges between zero and one. For the ease of reading, in the text, we present it in terms of percentages.

Firstly, we perform the feature selection phase. We try to find one feature set for the simple activities using accelerometer and one for the complex activities using the fusion of accelerometer and gyroscope sensor. After feature extraction as mentioned in Section III, we give two input files (one for the simple activities and one for the complex activities) consecutively to the feature selection algorithm on the Weka tool. Most of the algorithms' search method was based on the ranking features in a certain range. For example, OneRAttributeEval ranks features between approximately 17 and 45, and GainRatioAttributeEval ranks between 0.02 and 0.28 for complex activities. However, certain feature selection algorithms use other search methods such as BestFirst which is binary (0 for not selected and or 1 for selected features). These different score ranges of algorithms complicate understanding which features is more successful. To avoid this difficulty, we normalized data to 0-1 range, called as min-max normalization. For each feature such as ACCMEAN-X (mean of accelerometer's x axis) or GYRRMS-M (rms of gyroscope's m axis), we sum up the normalized scores given by each algorithm, which give us a total score for each feature. For the simple activities features total scores were between a range of 0 and 8.87 and for the complex, scores were between

0 and 8.78. We created three separate classes by dividing these intervals into three parts and put each feature in the appropriate class according to its total score. The names of classes are high impact, medium impact, and low impact features. For simple activities, 4 features from 45 and for complex activities, 9 features from 90 belong to the high impact group. The high impact features are presented in Table 1.

Table 1: High impact features

Simple Activities	Complex Activities
ACCMAX-X	ACCMAX-X
ACCMIN-X	ACCMEDIAN-X
ACCRMS-X	ACCRMS-X
ACCRMS-Z	ACCSTD-X
	ACCRANGE-X
	GYRSTD-Z
	GYRMEDIAN-M
	GYRMIN-Z
	GYRMAX-Z

By reducing the number of features from 90 to 11, the computational complexity is also reduced. In return, this directly affects the battery consumption of the smart devices. Once high impact features are selected, we realize the classification phase using only these features. To better understand the performance of our devices, we consider three different cases. In the first case, we evaluate performance of activities using only smartphone data, in the second only smartwatch data and in the end the fusion of smartphone and smartwatch data. Classification results using accelerometer and gyroscope sensors for three cases are presented in Figure 1. All activities are recognized with the highest f1-score using smartwatch-smartphone, except walking. For all activities, the smartwatch performs better than the smartphone.

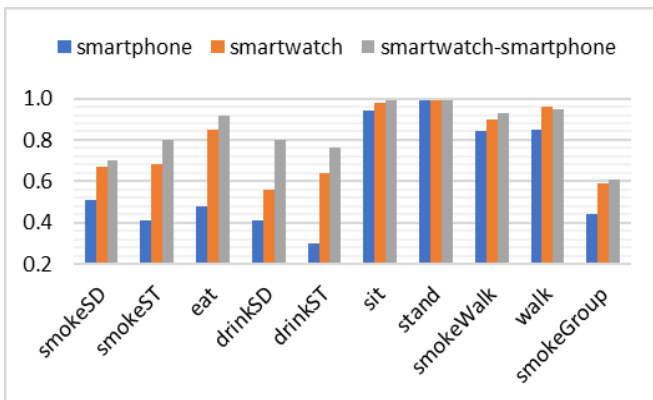


Figure 1: Recognition performance of activities using smartphone, smartwatch and smartwatch-smartphone in term of f1-score.

We observe the lowest performance for drinkST using only smartphone. For the simple activities (sit, stand and walk), both smartwatch, smartphone and smartwatch-smartphone achieve over an 85% f1-score. Therefore, simple activities do not necessitate the use of smartwatch sensors. However, complex activities are recognized within a range of 30%-51% which is relatively low. This is expected since the phone was

carried in the pocket and it is challenging to capture wrist movements. Thus, using smartwatch and smartphone together have an important impact on the recognition performance of complex activities. For example, for the drinkST activity which has the lowest performance in all, we could achieve a performance of 76% using the two devices together. Besides, for the simple activities since we already achieve the highest performance with the phone sensors, using the combination of the devices did not improve the performance, thus, only the smartphone would suffice. For example, stand activity has a performance of 99% in three cases.

Table 2: Confusion matrix using accelerometer sensors of smartwatch and smartphone.

		Predicted Class									
		smokeSD	smokeST	eat	drinkSD	drinkST	sit	stand	smokeWalk	walk	smokeGroup
Actual Class	smokeSD	647	7	0	57	0	0	4	3	0	225
	smokeST	6	716	18	29	115	4	0	0	0	13
	eat	0	27	829	6	80	0	0	0	0	0
	drinkSD	77	17	9	773	8	0	4	4	0	49
	drinkST	0	118	79	24	639	9	0	0	0	2
	sit	0	1	0	1	3	937	0	0	0	0
	stand	0	0	0	0	0	0	940	1	0	0
	smokeWalk	0	1	0	5	0	0	0	389	14	7
	walk	0	0	0	2	0	0	0	18	395	0
	smokeGroup	246	10	0	68	1	0	0	17	0	410

Table 3: Confusion matrix using accelerometer and gyroscope sensors of smartwatch and smartphone.

		Predicted Class									
		smokeSD	smokeST	eat	drinkSD	drinkST	sit	stand	smokeWalk	walk	smokeGroup
Actual Class	smokeSD	701	13	0	60	0	0	3	1	0	164
	smokeST	10	747	3	33	141	0	0	0	0	7
	eat	0	12	864	25	41	0	0	0	0	0
	drinkSD	89	11	5	775	17	0	6	2	0	36
	drinkST	6	113	64	29	699	7	0	0	0	3
	sit	0	0	1	0	4	937	0	0	0	0
	stand	0	0	0	0	0	0	940	0	0	1
	smokeWalk	0	0	0	2	0	0	0	395	16	3
	walk	0	0	0	3	0	0	0	21	391	0
	smokeGroup	253	5	0	64	1	0	0	10	0	419

We also investigate whether using only the accelerometer sensor would achieve a good score in comparison to using both accelerometer and gyroscope. The confusion matrices of the accelerometer and the fusion of accelerometer and gyroscope are given in Table 2 and 3, respectively. Particularly, smokeSD and smokeGroup activities are mostly confused with each other. The reason can be that some participants did not talk much in a group conversation. Accordingly, they did not or performed the hand-wrist movements less. Smoking and drinking while sitting are the second most frequently confused activities. However, they are confused almost half of times of smokeSD and smokeGroup confusions. As expected, sitting, standing and walking

activities are less confused. When we compare the results in Table 2 and 3, sit and stand activities achieve the highest recognition performance and adding the gyroscope sensor did not change the number of true predicted activities. However, it positively impacted the recognition of complex activities. But this effect is not remarkably high. Hence, if battery is a concern, then the use of only accelerometer may also be sufficient with an acceptable recognition rate.

V. CONCLUSION

In this paper, the main motivation was to evaluate the recognition performance of smoking activity by using motion sensors of smartwatch and smartphone devices. We investigated the impact of using only smartphone, only smartwatch and as well as their fusion. For this purpose, we used a dataset collected from eleven participants for ten different activities: smokeSD, smokeST, eat, drinkSD, drinkST, sit, stand, smokeWalk, walk, smokeGroup. Recognition of these activities is a challenging issue because most of activities involve similar hand movements, as in case of smoking while sitting and drinking while sitting or smoking while talking and smoking while standing. We used a dataset including 45 features (in x, y, z and magnitude axis) which are commonly used features in activity recognition domain for each two sensors. Instead of getting them as a single huge group of features or select some features manually, we applied feature selection algorithm to determine high impact features and created our feature set using only 9 features.

Considering the results, it seems that the activities are especially confused when they have similar patterns with drinking and smoking using data collected by the smartwatch. We can say that the better result is obtained using fusion of the accelerometer and gyroscope. It can be said clearly that the performance of fusion of the smartphone and smartwatch is better than the smartphone alone, except sit and stand activities which have already good performances. Besides, to better determine the best features with their efficient axes, feature selection algorithms are useful. We observe that the smartwatch is more precise for the recognition of the considered human activities. As a future work, battery consumption on a smartwatch and smartphone by applying the same methodology can be studied. Besides, additional sensors, such as linear accelerometer or magnetometer can be used.

ACKNOWLEDGMENT

This work is supported by Tubitak under Grant number 117E761 and by the Galatasaray University Research Fund under Grant Number 17.401.004. We thank Şilan Subaşı who helped us in the application of feature selection algorithms.

REFERENCES

- [1] Kawsar, Ferdaus Ahmed, Sheikh Iqbal Ahamed, and Richard Love. "Smartphone based multimodal activity detection system using plantar pressure sensors." *Proceedings of the 29th Annual ACM Symposium on Applied Computing*. ACM, 2014. Zheng, Lingxiang, et al. "A novel energy-efficient approach for human activity recognition." *Sensors* 17.9 (2017): 2064.
- [2] Zheng, Lingxiang, et al. "A novel energy-efficient approach for human activity recognition." *Sensors* 17.9 (2017): 2064.
- [3] Kwapisz, Jennifer R., Gary M. Weiss, and Samuel A. Moore. "Activity recognition using cell phone accelerometers." *ACM SigKDD Explorations Newsletter* 12.2 (2011): 74-82.
- [4] Ronao, Charissa Ann, and Sung-Bae Cho. "Human activity recognition with smartphone sensors using deep learning neural networks." *Expert Systems with Applications* 59 (2016): 235-244.
- [5] Bayat, Akram, Marc Pomplun, and Duc A. Tran. "A study on human activity recognition using accelerometer data from smartphones." *Procedia Computer Science* 34 (2014): 450-457.
- [6] Zhao, Kunlun, et al. "Healthy: A diary system based on activity recognition using smartphone." *Mobile Ad-Hoc and Sensor Systems (MASS), 2013 IEEE 10th International Conference on. IEEE, 2013.*
- [7] Ramos, Felipe Barbosa Araújo, et al. "Combining Smartphone and Smartwatch Sensor Data in Activity Recognition Approaches: an Experimental Evaluation." *SEKE*. 2016.
- [8] Shoaib, Muhammad, et al. "Towards detection of bad habits by fusing smartphone and smartwatch sensors." *Pervasive Computing and Communication Workshops (PerCom Workshops), 2015 IEEE International Conference on. IEEE, 2015.*
- [9] Seneviratne, Suranga, et al. "A survey of wearable devices and challenges." *IEEE Communications Surveys & Tutorials* 19.4 (2017): 2573-2620.
- [10] Khalifa, Sara, Mahbub Hassan, and Aruna Seneviratne. "Feature selection for floor-changing activity recognition in multi-floor pedestrian navigation." *Mobile Computing and Ubiquitous Networking (ICMU), 2014 Seventh International Conference on. IEEE, 2014.*
- [11] Weka website: Data Mining Software in Java, <http://www.cs.waikato.ac.nz/ml/weka/>
- [12] Groeneveld, Richard A., and Glen Meeden. "Measuring skewness and kurtosis." *The Statistician* (1984): 391-399.
- [13] Nambu, Masayuki. "Body surface mounted biomedical monitoring system using bluetooth." *Engineering in Medicine and Biology Society, 2007. EMBS 2007. 29th Annual International Conference of the IEEE. IEEE, 2007.*
- [14] Pedregosa, Fabian, et al. "Scikit-learn: Machine learning in Python." *Journal of machine learning research* 12.Oct (2011): 2825-2830.

Epileptic Seizure Classification Using Support Vector Machines

B. TEZCAN¹, I.A. OZKAN¹ and S. TASDEMIR¹

¹ Selcuk University, Konya/Turkey, btezcan@selcuk.edu.tr

¹ Selcuk University, Konya/Turkey, ilkerozkan@selcuk.edu.tr

¹ Selcuk University, Konya/Turkey, stasdemir@selcuk.edu.tr

Abstract – Epilepsy is one of the most common brain disorders affecting millions of people. Epileptic seizures can have many trigger factors such as genetics, brain damage etc. and can occur without warning. Epileptic people have spasms during the seizure that might result in serious injuries. Therefore, the detection of epilepsy and classification on seizure signals are carries an important role in neurology. Electroencephalogram (EEG) is widely used for diagnosis of epileptic seizures. In this work, Support Vector Machines (SVM) are used for the classification of epileptic seizures in EEG signals. The dataset is a highly popular epileptic seizure detection dataset from Bonn University. SVM performance highly depends on its parameters. Crow Search Algorithm (CSA) has been used for the parameter optimization of SVMs. CSA-SVM has achieved seizure detection rate of 98.69% accuracy.

Keywords – Support Vector Machine, Classification, EEG, Epilepsy, Metaheuristics

I. INTRODUCTION

A seizure is a sudden surge of electrical activity in the brain. Seizures affects how a person appears and acts. Lots of different things can happen during a seizure. People with epilepsy suffer from recurrent seizures at unpredictable times [1]. Frequent seizures can result in serious injuries or death.

Electroencephalogram (EEG) is widely used for diagnosis of epileptic seizures. EEG is the multi-channel recording of the brain's electrical activity. EEG activity associated with a seizure patient can closely resemble a benign pattern in another patient's activity. Because of the unpredictable epileptic seizures and complicated characteristics of EEG activity, classification of seizure data gains importance.

Support Vector Machines (SVM) is a highly used classification algorithm. However, he performance of the SVM depends on setting the appropriate parameters [2]. Wrong settings of parameters can decrease performance of the SVM and increase computational burden. In the last decade, meta-heuristic optimization algorithms are used frequently.

Crow Search Algorithm (CSA) is a new meta-heuristic optimization algorithm [3]. CSA has been developed considering the intelligent behaviors of crows. Crows are now considered to be among the world's most intelligent animals [4]. A crow flocks shows a behavior related to optimization processes. Crows hide some of their food in hiding places and use them when they need it. Some crows follow other crows to

steal from their hiding places. But it is hard to find a crow's hiding place. Because crows can detect that they are followed and avoid leading other crows to its hiding place.

II. SUPPORT VECTOR MACHINES

Consider $X = \{x_1, x_2, \dots, x_m\}$ as a training set. $y_i = \{-1, +1\}$ corresponds to class values. Function $f : X \rightarrow \{\pm 1\}$ must be solved to find classes.

Structural Risk Minimization based SVMs try to find most suitable hyperplane between classes. While doing this, SVMs try to establish balance between exploitation and exploration. A class of hyperplanes are defined in search space H in Eq. 1 where $w, x \in H, b \in R$.

$$\langle w, x \rangle + b = 0 \quad (1)$$

Eq. 2 represents decision function.

$$f(x) = \text{sgn}(\langle w, x \rangle + b) \quad (2)$$

Vapnik proposed a method for finding the optimal hyperplane so that error rate in training set can be minimized. Eq. 3 should be solved to find optimal hyperplane. Eq 3. has the constraints in Eq. 4.

$$\text{minimize } \tau(w) = \frac{1}{2} \|w\|^2 \quad (3)$$

$$y_i(\langle w, x_i \rangle + b) \geq 1 \quad \forall i \in \{1, \dots, m\} \quad (4)$$

Using the constraints in Eq. 4, for every $y_i = +1, f(x_i)$ becomes +1 and $y_i = -1, f(x_i)$ becomes -1. Detailed information about these formulas can be found in Scholkopf and Smola's work [5].

Upper method can only be applied to linearly separable spaces. Boser ve ark. [6] proposed a kernel-based approach for the non-linear spaces where maximal hyperplane is needed. It suggests changing scalar products in Eq. 4 with a non-linear kernel function (Eq. 5).

$$y_i(K(w, x_i) + b) \geq 1 - \varepsilon_i, \quad \forall i \in \{1, \dots, m\} \quad (5)$$

Most popular kernel functions are given below:

- Linear: $K(x_i, x_j) = (x_i \cdot x_j)$
- Polynomial: $K(x_i, x_j) = (\gamma x_i \cdot x_j + c)^d$
- Radial Basis Function (RBF):

$$K(x_i, x_j) = e^{-\gamma \|x_i - x_j\|^2}$$

Here, x_i, x_j represents examples, d represents polynomial degree ve γ represents gauss value.

III. DATA

The data set used in the study is the clinical EEG dataset provided by Bonn University [7]. It consists of different categories denoted as A, B, C, D and E.

- A - Eyes open, means when they were recording the EEG signal of the brain the patient had their eyes open
- B - Eyes closed, means when they were recording the EEG signal the patient had their eyes closed
- C - They identify where the region of the tumor was in the brain and recording the EEG activity from the healthy brain area
- D - They recorded the EEG from the area where the tumor was located
- E - Recording of seizure activity

Each category includes 100 single-channel EEG signals. Each signal is a recording of brain activity for 23.6 seconds.

IV. TWO CLASS PROBLEM: BETWEEN A, B, C, D VERSUS E

Although there are five classes, most studies work on binary classification, mostly category E versus others. Each category in the dataset contains 100 files, each representing a person. EEG signal of every row contains 4097 data points. Each data point is an EEG recording of brain activity at a point in time. This 4097 data point divided into 23 chunks, each containing 178 data points.

For this classification task, SVM algorithm is used. SVM is one of the best algorithms for binary classification. SVM performance highly depends on its parameters. There are two parameters we would like to optimize. One of them is the parameter C which determines the width of the SVM hyperplane. The other one is the γ which is used in RBF (Radial Basis Function) kernel. Kernels are used in SVM for mapping non-linear search spaces. RBF is the most used kernel function.

The optimization of SVM parameters were done using the CSA optimization algorithm. Every agent in the CSA algorithm represents the two SVM parameters. In each iteration of the CSA algorithm, these parameters fed into an SVM block and accuracy from this block used as fitness value. Best parameters

with highest accuracy in each iteration stored. When the iteration criteria is reached, best parameters fed into an SVM block with 10-fold cross validation and final results were gained.

CSA-SVM model has achieved 98.69% accuracy for binary classification of EEG data. This accuracy has been compared with literature in Table 1. As seen in Table 1., CSA-SVM achieved compatible results with literature.

Table 1: Literature comparison of CSA-SVM

Reference	Year	Classifier	Accuracy (%)
[8]	2013	KNN	98.20
[9]	2015	SVM	98.80
[10]	2017	ANN	98.72
[11]	2017	SVM	99.25
[12]	2017	RF	97.40
[13]	2017	RF	99.60

In Figure 1, ROC curve for the final 10-fold cross validation has been given. It draws a curve that is inside “the very good” part of the ROC curve.

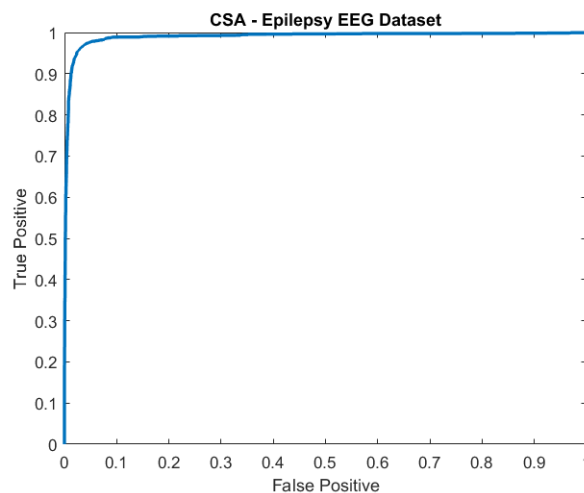


Figure 1: EEG dataset ROC curve

In Figure 2, boxplot for the final 10-fold cross validation has been given. It shows a balanced and narrow plot and includes a discrete value.

V. CONCLUSION

An important event in epilepsy disease is seizure. Epileptic seizure are unpredictable and different epileptic EEG data can show many resemblances. Therefore, classification of epileptic seizures in EEG data is important. In this study, binary classification of EEG data has done using CSA-SVM over a highly popular epilepsy benchmark dataset. CSA-SVM achieved 98.69% accuracy. Literature comparisons show that CSA-SVM achieves an accuracy rate comparable with literature.

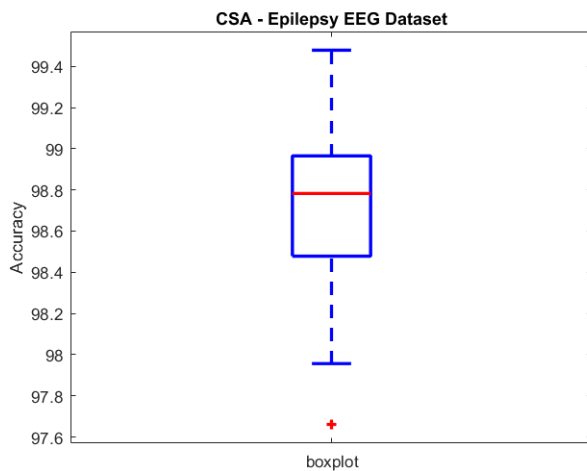


Figure 2: EEG Dataset Boxplot

REFERENCES

- [1] Shoeb, A. and J. Guttag, *Application of machine learning to epileptic seizure detection*, in *Proceedings of the 27th International Conference on International Conference on Machine Learning*. 2010, Omnipress: Haifa, Israel. p. 975-982.
- [2] Jiang, M., et al., *A Cuckoo Search-Support Vector Machine Model for Predicting Dynamic Measurement Errors of Sensors*. IEEE Access, 2016. **4**: p. 5030-5037.
- [3] Askarzadeh, A., *A novel metaheuristic method for solving constrained engineering optimization problems: Crow search algorithm*. Computers & Structures, 2016. **169**: p. 1-12.
- [4] Wikipedia contributors. "Corvus." *Wikipedia, The Free Encyclopedia*. 2018 [cited 2018 15.04.2018]; Available from: <https://en.wikipedia.org/w/index.php?title=Corvus&oldid=846865293>.
- [5] Scholkopf, B. and A.J. Smola, *Learning with kernels: support vector machines, regularization, optimization, and beyond*. 2001: MIT press.
- [6] Boser, B.E., I.M. Guyon, and V.N. Vapnik, *A training algorithm for optimal margin classifiers*, in *Proceedings of the fifth annual workshop on Computational learning theory*. 1992, ACM: Pittsburgh, Pennsylvania, USA. p. 144-152.
- [7] Andrzejak, R.G., et al., *Indications of nonlinear deterministic and finite-dimensional structures in time series of brain electrical activity: Dependence on recording region and brain state*. Physical Review E, 2001. **64**(6): p. 061907.
- [8] Kaleem, M., A. Guergachi, and S. Krishnan. *EEG seizure detection and epilepsy diagnosis using a novel variation of Empirical Mode Decomposition*. in *2013 35th Annual International Conference of the IEEE Engineering in Medicine and Biology Society (EMBC)*. 2013.
- [9] Fu, K., et al., *Hilbert marginal spectrum analysis for automatic seizure detection in EEG signals*. Biomedical Signal Processing and Control, 2015. **18**: p. 179-185.
- [10] Jaiswal, A.K. and H. Banka, *Local pattern transformation based feature extraction techniques for classification of epileptic EEG signals*. Biomedical Signal Processing and Control, 2017. **34**: p. 81-92.
- [11] Wang, L., et al., *Viologen-based conjugated ionic polymer for nonvolatile rewritable memory device*. European Polymer Journal, 2017. **94**: p. 222-229.
- [12] Mursalin, M., et al., *Automated epileptic seizure detection using improved correlation-based feature selection with random forest classifier*. Neurocomputing, 2017. **241**: p. 204-214.
- [13] Hussein, R., et al., *Robust detection of epileptic seizures based on L1-penalized robust regression of EEG signals*. Expert Systems with Applications, 2018. **104**: p. 153-167.

German Credit Risks Classification Using Support Vector Machines

B. TEZCAN¹ and S. TASDEMIR¹

¹ Selcuk University, Konya/Turkey, btezcan@selcuk.edu.tr

¹ Selcuk University, Konya/Turkey, stasdemir@selcuk.edu.tr

Abstract - Support Vector Machines (SVM) is one of the most popular classification algorithms. SVM penalty parameter and the kernel parameters have high impact over the classification performance and the complexity of the algorithm. So, this brings the problem of choosing the suitable values for SVM parameters. This problem can be solved using meta-heuristic optimization algorithms. Salp Swarm Algorithm (SSA) and Crow Search Algorithm (CSA) are new meta-heuristic algorithms. SSA is a swarm algorithm that is inspired from a mechanism salps forming in deep ocean called salp chain. CSA algorithm is inspired by the intelligent behavior of crows. In this paper, SVM parameter optimization is done using SSA and CSA. German Credit dataset from the UCI data repository is used for the experiments. All experiments results are gathered from a 10-fold cross validation block. Evaluation criteria determined as accuracy, sensitivity, specificity and AUC. SSA and CSA gave accuracy results of 0.72 ± 4.62 and 0.71 ± 3.53 respectively. Also, ROC curves and box plots of the algorithms are given. CSA algorithm draws better graphs.

Keywords – Support Vector Machines, Optimization, Parameter, Metaheuristics

I. INTRODUCTION

Support Vector Machines (SVM) is a learning methodology based on Structural Risk Minimization (SRM). SVMs can give good results on non-linear problems, but SVM performance highly depends on suitable parameters. Parameters directly affects the model performance. Therefore, Particle Swarm Optimization (PSO), Genetic Algorithm (GA) and Grid Search (GS) have been used numerously in parameter optimization of SVMs [1-3]. However, GS algorithm is time consuming and PSO and GA algorithms often stuck in local optimums. Therefore, SVM parameter optimization needs new methods.

Nowadays, optimization is used in many fields. Conventional methods are used for simple optimization problems, but computers are used for solving high level optimization problems. Many algorithms were developed for solving optimization problems. Each algorithm has advantages and disadvantages for any problem. Many different test problems are used in literature for testing performances of these algorithms. Because of the high usage of these problems, they became benchmarks. However, in real life situations, performances can be different from the ones achieved over benchmark problems.

Optimization is finding the best solution over all solutions in given conditions. Any problem with constraints involving

unknown parameter values can be called an optimization problem [4].

Sometimes, creatures that doesn't show any value by themselves can show great intelligence when they group up. Individuals belonging to a group make use of the behavior of the best individual or the all other individuals or their own experiences and use these as a tool to solve future problems. For example, an animal in a flock can react to a danger and this reaction moves in the flock to ensure all animals behave the same way against that danger. By observing these behaviors of animals, swarm intelligence algorithms are developed [5].

Salp Swarm Algorithm (SSA) is a recently developed meta-heuristic algorithm [6]. SSA has the advantages of few parameters and strong global search. In this study, SVM parameter optimization has done using SSA and CSA [7]. German Credit dataset from UCI repository used for the experiments.

Organization of the paper as follows: SVMs are defined, Swarm intelligence algorithms introduced, experiments and conclusion.

II. SUPPORT VECTOR MACHINES

Consider $X = \{x_1, x_2, \dots, x_m\}$ as a training set. $y_i = \{-1, +1\}$ corresponds to class values. Function $f : X \rightarrow \{\pm 1\}$ must be solved to find classes.

Structural Risk Minimization based SVMs try to find most suitable hyperplane between classes. While doing this, SVMs try to establish balance between exploitation and exploration. A class of hyperplanes are defined in search space H in Eq. 1 where $w, x \in H, b \in R$.

$$\langle w, x \rangle + b = 0 \quad (1)$$

Eq. 2 represents decision function.

$$f(x) = \text{sgn}(\langle w, x \rangle + b) \quad (2)$$

Vapnik proposed a method for finding the optimal hyperplane so that error rate in training set can be minimized. Eq. 3 should be solved to find optimal hyperplane. Eq. 3. has the constraints in Eq. 4.

$$\text{minimize } \tau(w) = \frac{1}{2} \|w\|^2 \quad (3)$$

$$y_i(< w, x_i > +b) \geq 1 \quad \forall i \in \{1, \dots, m\} \quad (4)$$

Using the constraints in Eq. 4, for every $y_i = +1$, $f(x_i)$ becomes +1 and $y_i = -1$, $f(x_i)$ becomes -1. Detailed information about these formulas can be found in Scholkopf and Smola's work [8].

Upper method can only be applied to linearly separable spaces. Boser ve ark. [9] proposed a kernel-based approach for the non-linear spaces where maximal hyperplane is needed. It suggests changing scalar products in Eq. 4 with a non-linear kernel function (Eq. 5).

$$y_i(K(w, x_i) + b) \geq 1 - \varepsilon_i, \quad \forall i \in \{1, \dots, m\} \quad (5)$$

Most popular kernel functions are given below:

- Linear: $K(x_i, x_j) = (x_i \cdot x_j)$
- Polynomial: $K(x_i, x_j) = (\gamma x_i \cdot x_j + c)^d$
- Radial Basis Function (RBF):

$$K(x_i, x_j) = e^{-\gamma \|x_i - x_j\|^2}$$

Here, x_i, x_j represents examples, d represents polynomial degree ve γ represents gauss value.

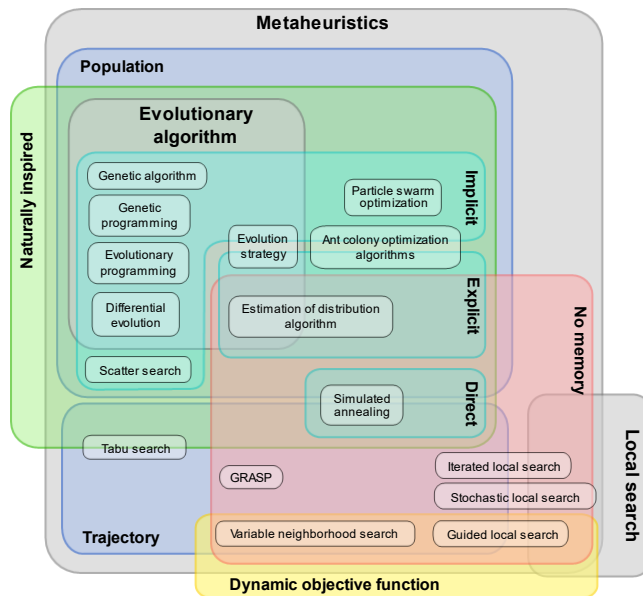


Figure 1: Euler diagram of the different classifications of metaheuristics [10]

III. OPTIMIZATION AND SWARM

Real time optimization problems are complicated and hard to solve. Generally, algorithms used in solving hard optimization problems have high computational burden and specifically design for a certain problem. Using these algorithms for different optimization algorithms is almost impossible. Therefore, heuristic algorithms are designed. Heuristic algorithms do not guarantee the best solution but works faster.

Heuristic algorithms evaluate the search space and finds a solution very close to the best. But they do not guarantee finding the best solution. When these types of algorithms are developed, they use some information about the problem they are developed for, so they have some problem specific features and called heuristic algorithms. A* search, hill climbing algorithm and best first search are a few of the heuristic algorithms.

Metaheuristic algorithms are not problem specific. 'Meta' mean higher level in Greek. Metaheuristic algorithms can be denoted as higher-level heuristic algorithms. Metaheuristics are generally nature inspired and can be used for many different problems. Metaheuristics act like a black-box because they do not need specific information about the optimization problem. Genetic Algorithm (GA), Ant Colony Optimization (ACO), Artificial Bee Colony (ABC) and Particle Swarm Optimization (PSO) are a few of the metaheuristic algorithms. Figure 1 shows the classification of metaheuristics.

Characteristic of metaheuristics can be given [11]:

- Metaheuristics are strategies that "guide" the search process.
- The goal is to efficiently explore the search space in order to find (near-) optimal solutions.
- Techniques which constitute meta-heuristic algorithms range from simple local search procedures to complex learning processes.
- Metaheuristic algorithms are approximate and usually non-deterministic.
- They may incorporate mechanisms to avoid getting trapped in confined areas of the search space.
- The basic concepts of metaheuristics permit an abstract level description.
- Metaheuristics are not problem-specific.
- Metaheuristics may make use of domain-specific knowledge in the form of heuristics that are controlled by the upper level strategy.
- Today's more advanced metaheuristics use search experience (embodied in some form of memory) to guide the search.

Swarm intelligence algorithms are flexible and solid method that are developed inspired by animals' swarm behaviors. ACO and PSO are two of the most used swarm intelligence algorithms. ACO algorithm mostly used in solutions of combinational optimization problems and PSO algorithm mostly used in continuous optimization algorithms. For example, routing problems (traveling salesman, vehicle routing etc.), assignment problems (graph coloring etc.), scheduling problems (open-shop scheduling etc.) can be solved using ACO and problems that needs function optimization in many different engineering fields can be solved using PSO.

Swarm can be defined as discrete individuals influencing each other. Individuals can be a human or an ant. In swarms, N individual work together to achieve a purpose. This easily observable "collective intelligence" arises from repetitive behaviors of individuals.

IV. EXPERIMENTS

In this study, SVM parameter optimization over German Credit data has done using SSA and CSA algorithms. The two algorithms compared with each other and the literature. RBF (Radial Basis Function) kernel function were used in SVM. Two parameters of SVM were optimized. These are balancing parameter between error rate and generalization called C and RBF kernel parameter γ . Every population member in the optimization algorithms are defined as a combination of C and γ . An SVM block were used as fitness functions of the optimization algorithms. Parameters that provide best SVM accuracy were stored in each iteration. Best parameters were given when the end criterion. These best parameters were fed into a 10-fold cross validation SVM block and results were gained.

German dataset classifies people described by a set of attributes as good or bad credit risks. It includes 1000 instances and 24 attributes. The original dataset, in the form provided by Prof. Hofmann, contains categorical/symbolic attributes. For algorithms that need numerical attributes, Strathclyde University produced a numerical file. This file has been edited and several indicator variables added to make it suitable for algorithms which cannot cope with categorical variables. Several attributes that are ordered categorical (such as attribute 17) have been coded as integer.

Table 1: SSA and CSA performance results

Algorithm	Performance Criteria	Results
SSA	Accuracy	0.72±4.62
	Sensitivity	0.41±0.03
	Specificity	0.97±0.02
	AUC	0.63±0.04
CSA	Accuracy	0.71±3.53
	Sensitivity	0.43±0.09
	AUC	0.70±0.05

In Table 1, accuracy, sensitivity, specificity and AUC values of SSA and CSA algorithms are given. SSA algorithm gave 72% accuracy rate and it's better than the CSA's 71% accuracy rate. Both algorithms gave low sensitivity values.

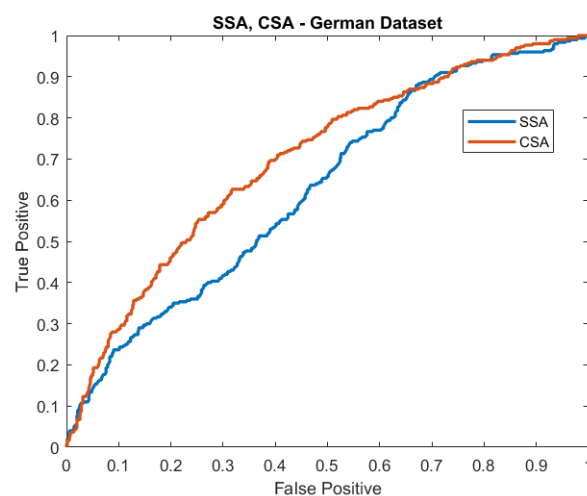


Figure 2: ROC curves of SSA and CSA

In Figure 2, ROC curves for SSA and CSA over 10-fold cross validation can be seen. CSA algorithm show a better ROC curve than SSA algorithm. CSA curve is in the area accepted as “normal” but SSA curve is close to the “bad” area. In Figure 3, boxplots of SSA and CSA can be seen. SSA boxplot draws a narrower box. CSA boxplot is higher than SSA boxplot. It can't be concluded for sure, but it can be said that there is a possibility CSA has better distribution than SSA.

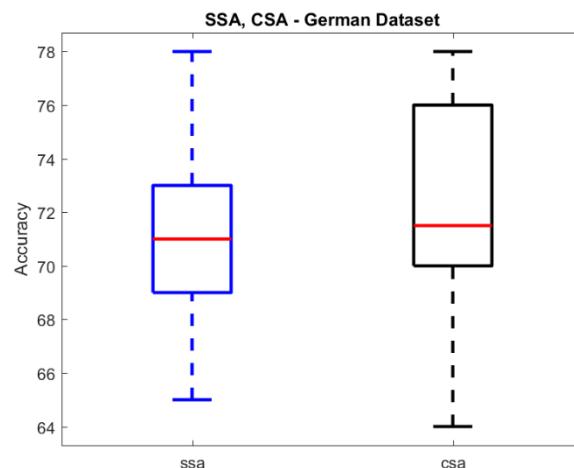


Figure 3: Boxplots of SSA and CSA

V. CONCLUSION

In this study, German credit risks classification has done using Support Vector Machines. SSA and CSA algorithms used for the parameter optimization of SVMs. RBF kernel function used in SVM experiments. C and γ parameters were optimized. 10-fold cross validation average accuracy values were used as fitness functions of optimization algorithms. Both algorithms achieved similar results, but CSA algorithm draws better ROC curve and boxplot. Experiments show that both algorithms can compete for SVM parameter optimization.

In future studies, we will consider different SVM kernel functions. Even though RBF is the most used kernel function, it can't always be better than other kernels like sigmoid, polynomial etc.

REFERENCES

- [1] Cheng, J., et al., *Temperature drift modeling and compensation of RLG based on PSO tuning SVM*. Measurement, 2014. **55**: p. 246-254.
- [2] Gencoglu, M.T. and M. Uyar, *Prediction of flashover voltage of insulators using least squares support vector machines*. Expert Systems with Applications, 2009. **36**(7): p. 10789-10798.
- [3] Li, X.Z. and J.M. Kong, *Application of GA-SVM method with parameter optimization for landslide development prediction*. Nat. Hazards Earth Syst. Sci., 2014. **14**(3): p. 525-533.
- [4] G. Murty, K., *Optimization for decision making. Linear and quadratic models*. 2009.
- [5] Akyol, S. and B. Alataş, *Güncel sürü zekası optimizasyon algoritmaları*. Vol. 1. 2012.
- [6] Mirjalili, S., et al., *Salp Swarm Algorithm: A bio-inspired optimizer for engineering design problems*. Advances in Engineering Software, 2017. **114**: p. 163-191.
- [7] Askarzadeh, A., *A novel metaheuristic method for solving constrained engineering optimization problems: Crow search algorithm*. Computers & Structures, 2016. **169**: p. 1-12.
- [8] Scholkopf, B. and A.J. Smola, *Learning with kernels: support vector machines, regularization, optimization, and beyond*. 2001: MIT press.
- [9] Boser, B.E., I.M. Guyon, and V.N. Vapnik, *A training algorithm for optimal margin classifiers*, in *Proceedings of the fifth annual workshop on Computational learning theory*. 1992, ACM: Pittsburgh, Pennsylvania, USA. p. 144-152.
- [10] *Metaheuristics classification.svg*, M. classification.svg, Editor. 2018, Wikimedia Commons, the free media repository.
- [11] Blum, C. and A. Roli, *Metaheuristics in combinatorial optimization: Overview and conceptual comparison*. ACM Comput. Surv., 2003. **35**(3): p. 268-308.

Modified Grey Wolf Optimization Through Opposition-Based Learning

T. SAĞ

Selcuk University, Konya/Turkey, tahirsag@selcuk.edu.tr

Abstract –OBL strategies have a growing research interest in the field of metaheuristic optimization since it can accelerate the convergence to optima without tackling to local extrema. On the other hand, GWO which is an outstanding algorithm, has been recently presented and it has gained a good place in literature owing to its performance. Three types of opposition-based learning (OBL) methods, known as Type-I, center based sampling, and generalized OBL, are adapted to Grey Wolf Optimization (GWO) algorithm. The proposed approaches are then applied to test functions in order to evaluate the performance. The effect of OBL methods on GWO algorithm is investigated in this study.

Keywords – OBL, GWO, optimization.

I. INTRODUCTION

OPPOSITION-Based Learning (OBL) is firstly introduced by Tizhoosh in 2005 [1]. It is used to improve existing performance of the algorithms by enhancing the convergence speed and avoiding local extrema. However, it does not work like a mutation operator depend on randomness generation. It tries to calculate the candidate solutions stated in the opposite directions of the current solutions. Thus, OBL methods provides a more effective exploration to optimization algorithms in the search space. So, many research efforts have been conducted in recent years [2, 3, 4].

Several metaheuristics involving genetic algorithms [1], differential evolutionary algorithm [5, 6], particle swarm optimization [7, 8], artificial bee colony optimization [9], harmony search [10], simulated annealing [11] and even multiobjective optimization techniques [12, 13] are exploit the searching capability of OBL methods and successfully applied on the optimization problems. In addition, researches have been proposed several types of OBL.

This study focuses on Grey Wolf Optimization (GWO) algorithm, which is inspired from the leadership hierarchy and hunting strategy of grey wolves in nature [14]. It has been reported that GWO achieved very competitive results compared to other well-known meta-heuristics. According to information from the web of science [15], GWO algorithm has been cited 718 times since it was proposed in 2014. However, a few studies about OBL with GWO have been presented in literature. Here, three different types of OBL methods called as Type-I, center based sampling, and generalized OBL, are combined with GWO algorithms. Afterwards, the performance of the proposed three approach and original GWO are compared with each other. For this purpose, three well-known benchmark

problem involving large-scale dimensions are used to test the methods for two different values of jumping rate. These are Rosenbrock, Rastrigin, and Powell functions.

The rest of the paper is organized as follows. The brief explanation of OBL and mathematical definitions of three types of OBL are given in section-II. The descriptions of original GWO algorithm and proposed methods are stated in section-III and section-IV, respectively. Then, benchmark functions are explained in section-V. The experimental results are demonstrated in section-VI. Finally, the conclusions and future works are briefly considered in section-VII.

II. OPPOSITION-BASED LEARNING

The concept of Opposition-Based Learning has been an attractive research field for the last decade. Considering the metaheuristic optimization problems, OBL calculates the oppositions of the candidate solutions so that it can explore the search space deeply. It can be easier to explain OBL by emphasizing the basic definition of the opposite number.

Definition of Opposite Number: Let $x \in [lb, ub]$ be a real number. The opposition number \tilde{x} is defined as in Eq.(1).

$$\tilde{x} = lb + ub - x \quad (1)$$

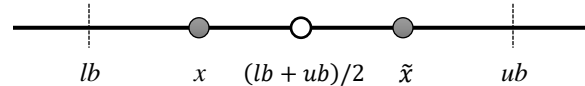


Figure 1: The demonstration of opposite number in one dimension.

With respect to the definition above, an opposite solution is obtained by calculating Eq.(1) for each dimension of the current solution. Several versions of OBL has been proposed in literature. In general, these methods can be classified in two groups: (i) the first one depends on a mapping function using decision variables and (ii) the second one uses the objective function value to search for solutions with opposite quality [3]. Three types of OBL consist of Type-I, center-based sampling and generalized OBLs, are used in this study. The descriptions of these are given below, respectively.

A. Type-I

In fact, this type is known as the basic form of OBL and it is mathematically defined in Eq.(2) [1].

$$\tilde{x}_i = lb_i + ub_i - x_i \quad (2)$$

where $x_i \in \mathbb{R}$ is the i.th candidate solution of an optimization problem with n-dimension and $x_i \in [lb_i, ub_i]$.

B. Center-Based Sampling (CBS)

CBS aims to calculate an opposite solution \tilde{x} which consists of parameters closer to the center of each variable [16]. It is defined as in Eq.(3).

$$\tilde{x}_i = rand_i(lb_i + ub_i - 2 * x_i) + x_i \quad (3)$$

where $rand_i$ is a uniformly distributed random number in the range of [0,1].

C. Generalized OBL (GOBL)

GOBL is another type of OBL which aims to obtain candidate solutions closer to the global optimum [17]. It is defined as in Eq.(4).

$$\tilde{x}_i = k * (lb_i + ub_i) - x_i \quad (4)$$

where $k \in [0,1]$ is a random number.

III. GREY WOLF OPTIMIZATION

Grey Wolf Optimizer (GWO) algorithm is inspired from the leadership hierarchy and hunting strategy of grey wolves in nature. Four types of grey wolves called alpha (α), beta (β), delta (δ), and omega (ω) simulates the leadership hierarchy. In accordance with the analogy of the social hierarchy of wolves, the fittest three solutions are named as α , β and δ , respectively. The rest ones are assumed to be ω . Further, the three main phases of algorithm consist of hunting, searching for prey, encircling prey, and attacking prey [14].

Encircling behavior of the wolves is modelled as the following Eq. (5).

$$\begin{aligned} \vec{D} &= |\vec{C} \cdot \vec{X}_p(t) - \vec{X}(t)| \\ \vec{X}(t+1) &= \vec{X}_p(t) - \vec{A} \cdot \vec{D} \\ \vec{A} &= 2\vec{a} \cdot \vec{r}_1 - \vec{a} \\ \vec{C} &= 2 \cdot \vec{r}_2 \end{aligned} \quad (5)$$

where t is the current iteration, \vec{A} and \vec{C} are coefficient vectors, \vec{X}_p is the position vector of the prey, \vec{X} is the position vector of a grey wolf. \vec{a} is linearly decreased from 2 to 0 during the iterations and \vec{r}_1, \vec{r}_2 are random vectors in [0, 1].

In the algorithm, hunting phase is modelled that all candidate solutions update their positions according to the position of the best three agents. Three different position values ($\vec{X}_1, \vec{X}_2, \vec{X}_3$) are calculated by using Eq. (5) for 3 times between (α, β, δ) and current solution in the population. Then current solution is updated by Eq. (6). This process is repeated for all solutions in an iteration.

$$\vec{X}(t+1) = (\vec{X}_1 + \vec{X}_2 + \vec{X}_3)/3 \quad (6)$$

The phase of searching for prey is adapted to algorithm by utilizing coefficient \vec{A} which equals to random values greater than 1 or less than -1 to oblige the candidate solution to diverge from the prey. While exploration satisfies by searching for prey, the exploitation is implemented by decreasing the value of \vec{a} as the phase of attacking prey.

IV. PROPOSED METHOD

Type-I, CBS and GOBL opposition-based learning methods are adapted to GWO algorithm. These three modified GWO approaches are called as Type1-GWO, CBS-GWO and GOBL-GWO. OBL is applied on the generating stage of initial population and also it is applied at the beginning of each iteration depending on the jumping rate.

For each OBL method, the opposite population (**OppPop**) is calculated according to Eq.(2), Eq.(3) or Eq.(4) separately after the random initial population (**Pop**) is generated. Then the fittest candidate solutions are selected from combined population consisting of **Pop** and **OppPop**. Fig-2 shows this procedure as pseudocode.

Generate initial population with N-sized as random (<i>Pop</i>)
Calculate Opposite Population (<i>OppPop</i>)
Select the fittest N solutions from <i>Pop</i> and <i>OppPop</i>

Figure 2: Pseudo-code of initial population with OBL

Same OBL procedure is applied in each iteration depending coefficient named JumpingRate that is in the range of [0,1]. The outlines of the OBL based GWO algorithm is shown in Fig-3.

Generate initial population according to Figure-2.
For iteration=1 to MaxCycle
If $rand(0, 1) < \text{JumpingRate}$
Calculate Opposite Population (<i>OppPop</i>)
Select the fittest N solutions from <i>Pop</i> and <i>OppPop</i>
End If
Run GWO algorithm with the obtained population
End For

Figure 3: Pseudo-code of proposed approaches with OBL

V. BENCHMARK FUNCTIONS

Three benchmark functions obtained from specialized literature is employed to evaluate the success of the algorithm. The problems called Rosenbrock, Rastrigin and Powell are minimization functions. The details of functions are given in this section.

Rosenbrock function is a test problem for gradient-based optimization. The function is unimodal, and the global minimum is a narrow parabolic valley. However, this valley is easy to find, but convergence to the minimum is difficult. The formulation is given in Eq. (8).

$$f(x) = \sum_{i=1}^{d-1} [100(x_{i+1} - x_i^2)^2 + (x_i - 1)^2] \quad (8)$$

$$f(x^*) = 0, \text{ at } x^* = (1, \dots, 1) \text{ and } x_i \in [-30, 30]$$

Rastrigin function has lots of local minima. It is highly

multimodal, but locations of the minima are regularly distributed. The formulation is given in Eq. (9).

$$f(x) = 10d + \sum_{i=1}^d [x_i^2 - 10 \cos(2\pi x_i)] \quad (9)$$

$$f(x^*) = 0, \text{ at } x^* = (0, \dots, 0) \text{ and } x_i \in [-5.12, 5.12]$$

Powell function is another popular test problem, which is usually evaluated on the hypercube. The formulation is given in Eq. (10).

$$f(x) = \sum_{i=1}^{d/4} [(x_{4i-3} + 10x_{4i-2})^2 + 5(x_{4i-1} - x_{4i})^2 + (x_{4i-2} - x_{4i-1})^4 + 10(x_{4i-3} - x_{4i})^4] \quad (10)$$

$$f(x^*) = 0, \text{ at } x^* = (0, \dots, 0) \text{ and } x_i \in [-4, 5]$$

VI. EXPERIMENTAL RESULTS

GWO and the proposed approaches Type1-GWO, CBS-GWO, GOBL-GWO was run 30 times on each benchmark function. The statistical results are given in Tables 1 and Table 2. The first rows show mean values and standard deviation places in the second row. All methods were run by using the control parameters with same values. The number of search agents is 30. Maximum number of cycles is 500. On the other hand, all methods were run for two different jumping rate values 0.1 and 0.5, separately. Table 1 shows the results for JR value 0.1 and Table 2 is for the JR value 0.5.

Considering the results obtained from the algorithms, it can be clearly said that OBL methods has a positive effect on GWO algorithm. Especially CBS-GWO was able to achieve better results for almost all functions and both jumping values. However, the results of the algorithms are close to each other since problems have large-scale dimensions.

Table 1: Results for JR value 0.1

	GWO	Type1-GWO	CBS-GWO	GOBL-GWO
Rosenbrock (30D)	27.3870 0.7123	26.8294 0.7501	27.0949 0.7291	26.9683 0.6637
Rastrigin (100D)	2.7735 3.9310	2.2204 3.4541	0.0 0.0	3.2985 6.0371
Powell (24D)	5.9621e-05 5.4483e-05	7.4653e-05 8.3454e-05	7.7654e-05 1.3035e-04	8.2047e-05 9.5353e-05

Table 2: Results for JR value 0.5

	GWO	Type1-GWO	CBS-GWO	GOBL-GWO
Rosenbrock (30D)	27.0438 0.8217	26.9242 0.7045	27.2153 0.8010	26.8606 0.8685
Rastrigin (100D)	2.1020 2.6243	0.7668 2.0901	0.0 0.0	0.1268 0.6943
Powell (24D)	1.2316e-04 1.6889e-04	7.3511e-05 6.2531e-05	9.2242e-05 1.8068e-04	4.7796e-05 8.3796e-05

VII. CONCLUSION AND FUTURE WORKS

This paper aims to investigate the capability of OBL methods on GWO algorithm. For this purpose, three types of OBL called Type-I, Center-Based Sampling and Generalized OBL were adapted to GWO. Three well-known test problems are used to measure the performance. All approaches and original GWO algorithms were run under the same conditions for 30 times. The results show that OBL methods can be applied to improve the performance of GWO. In particular, CBS method has been obtained superior values to others.

For the future works, this paper has presented an encouraging preliminary study for a comprehensive study to determine the most appropriate OBL technique for GWO by conducting a more sensitive JR evaluation on a larger benchmark set.

REFERENCES

- [1] H. Tizhoosh, "Opposition-based learning: A new scheme for machine intelligence", In Computational intelligence for modelling, control and automation 2005 and international conference on intelligent agents, web technologies and internet commerce, pp. 695–701, 2005.
- [2] S. Mahdavi, S. Rahnamayan, and K. Deb, "Opposition based learning: A literature review", Swarm and Evolutionary Computation, vol.39 pp.1–23, 2018.
- [3] N. Rojas-Morales, M.C. Riff Rojas, and E. Montero Ureta, "A survey and classification of Opposition-Based Metaheuristics", Computers and Industrial Engineering, vol. 110, pp. 424–435, 2017.
- [4] Q. Xu, L. Wang, N. Wang, X. Hei, and L. Zhao, "A review of opposition-based learning from 2005 to 2012", Engineering Applications of Artificial Intelligence, vol. 29, pp. 1–12, 2014.
- [5] S. Rahnamayan and G.G. Wang, "Solving large scale optimization problems by opposition-based differential evolution (ODE)", WSEAS Transactions on Computation, vol.7(10), pp.1792–1804, 2008.
- [6] M.A. Ahandani, and H. Alavi-Rad, "Opposition-based learning in the shuffled differential evolution algorithm", Soft Computations, vol.16(8), pp.1303–1337, 2012.
- [7] H. Jabeen, Z. Jalil, and A.R. Baig, "Opposition based initialization in particle swarm optimization (O-PSO)", In Proceedings of the 11th annual conference companion on genetic and evolutionary computation conference, pp.2047–2052, 2009.
- [8] W. Gao, S. Liu and L. Huang, "Particle swarm optimization with chaotic opposition-based population initialization and stochastic search technique", Communications in Nonlinear Science and Numerical Simulation, vol.17(11), pp.4316–4327, 2012.
- [9] X.J. Yang, Z.G. Huang, "Opposition-based artificial bee colony with dynamic Cauchy mutation for function optimization", Int. J. Adv. Comput. Technol. vol.4 (4), pp.56–62, 2012.
- [10] A. Banerjee, V. Mukherjee, and S.P. Ghoshal, "An opposition-based harmony search algorithm for engineering optimization problems", Ain Shams Engineering Journal, vol.5(1), pp.85–101, 2014.
- [11] M. Ventresca, H.R. Tizhoosh, "Simulated annealing with opposite neighbors", In: IEEE Symposium on Foundations of Computational Intelligence, Honolulu, USA, pp.186–192, 2007.
- [12] X. Ma, F. Liu, Y. Qi, M. Gong, M. Yin, L. Li, J. Wu, "MOEA/D with opposition-based learning for multiobjective optimization problem", Neurocomputing, vol.146, pp.48–64, 2014.
- [13] T. Niknam, M. Narimani, R. Azizpanah-Abarghoee, B. Bahmani-Firouzi, "Multiobjective optimal reactive power dispatch and voltage control: a new opposition-based self-adaptive modified gravitational search algorithm", IEEE Syst. J. vol.7 (4), pp.742–753, 2013.
- [14] S. Mirjalili, S.M. Mirjalili, and A. Lewis, "Grey Wolf Optimizer", Advances in Engineering Software, vol.69, pp.46–61, 2014.
- [15] Web of Science (available on 05.10.2018) http://apps.webofknowledge.com/Search.do?product=WOS&SID=E6E6naim6BGXJGY3Ynj&search_mode=GeneralSearch&prID=63f14c7d-b900-4697-a7b8-07fdd5e1f4d9.
- [16] S. Rahnamayan, and G.G. Wang, "Center-based sampling for population-based algorithms", In 2009 IEEE congress on evolutionary computation, pp.933–938, 2009.
- [17] H. Wang, Z. Wu, S. Rahnamayan, and L. Kang, "A scalability test for accelerated de using generalized opposition-based learning", In 2009 Ninth international conference on intelligent systems design and applications, pp. 1090–1095, 2009.

Recognition of Sign Language using Convolutional Neural Networks

M. Mustafa SARITAŞ¹ and İlker Ali ÖZKAN²

¹Selcuk University, Graduate School of Natural Sciences, Konya, Turkey

¹Selcuk University, Department of Computer Engineering, Konya, Turkey, ilkerozkan@selcuk.edu.tr

Abstract- Hearing impaired people use sign language consisting of hand gestures for communication. It is important that individuals with hearing impairments communicate effectively in order to ensure their participation in society and to improve their quality of life. Efforts are currently underway to develop effective communication tools to help the social interaction of hearing-impaired people. In this study, a convolutional Neural Network (CNN) based application has been proposed to recognize the sign language with numbers with maximum efficiency. Automatic feature extraction and classification was performed using this proposed CNN model. With the proposed model, a classification success of 97.63% was achieved with 5-fold cross verification.

Keywords – Deep Learning, CNN, Sign Language Recognition.

I. INTRODUCTION

SIGN language is a language used by people with hearing and speech disorders. People use sign language as non-verbal means of communication to express their thoughts and feelings. However, for those who do not know the sign language, it is extremely difficult to understand. Trained sign language interpreters are needed, especially in education, medicine and legal situations [1].

There have been several studies in the last decade related to sign language recognition using linear classifiers, neural networks, kNN etc [2-6].

Vivek et al. used Convolutional Neural Networks in their work to describe the pictures containing the American sign language alphabets and numbers [7]. The data used in the study consists of 25 pictures taken from five people. They applied data replication techniques on the images they obtained. With the techniques they applied, they increased their performance by 20%. In addition, background extraction techniques were applied on the pictures. In their study, they achieved a success rate of 82.5% in the alphabet classification and 97% in the number classification. [7].

Garcia et al. have developed a real-time sign language recognition system for American sign language. In the study, pre-trained GoogleNet architecture was used. Researchers achieved a classification success of 72% [8].

Pigou et al. developed a sign language recognition system in their study using Microsoft Kinect, convolutional neural networks (CNNs) and GPU acceleration. In this study using CNN, feature extraction was performed automatically. The study has a cross validation classification success of 91.7% [9].

The recent success of deep learning models in sign language recognition has made a major contribution to sign language researchers [10]. Therefore, studies in the field of deep learning to increase the accuracy and efficiency of sign language recognition system are important. In this study, it is aimed to develop a Convolutional Neural Network structure in order to provide automatic feature extraction and sign language recognition. For this purpose, a sign language dataset containing the numbers was used.

Detailed information about the data and CNN used in the study is given in section 2, the CNN network structure used in the study is given in section 3, and the results obtained at the end of 5-fold cross validation are given separately for each class for comparison purposes is given in section 4.

II. MATERIAL AND METHODS

A. Sign Language Dataset

In this study, the sign language data set containing the numbers from 0 to 9 is used [11]. This data set aims to increase the quality of life of hearing and speech-impaired individuals and to facilitate their participation in the society. For this purpose, it is aimed to classify the sign language and convert it to sound. From 218 different participants, 10 sample images were taken for each expression. Images in the data set are 100 × 100 pixels in size. The data set consisting of three channel (RGB) images includes 10 classes covering 0-9 numbers [11]. As a preprocessing operation of the images in the data set, the new dimension was resized to be 64 x 64 pixels and single-channel. Figure 1 shows sample images of the sign language data set containing the numbers.



Figure 1: Sign Language Number Dataset.

B. Convolutional Neural Networks

In order to establish a model identification or machine

learning system with the classical machine learning techniques, the feature vector must first be extracted. The extraction of the feature vector can be carried out by those skilled in the art. For this reason, these techniques cannot process raw data without pretreatment and without expert assistance. Deep Learning does the learning process on raw data in contrast to traditional machine learning and image processing techniques.[12].

CNNs, the most important architecture of deep learning networks, have been used successfully in many image classifications and forecasting problems. [13, 14]. Progress has been made in applications with deep learning for sign language identification. In recent years, deep learning-based approaches have been shown to perform better than hand-crafted-based feature applications [10]. CNN architecture consists of layers such as convolution and pooling. Specific features are obtained from images classified with these layers. The fully connected layer and classification layers are placed after the convolution and pooling layers. The basic structure of CNNs is given in Figure 2. [15].

1) Convolution Layer

This layer, known as the core layer of CNN architecture, has a group of learnable filters. In the CNN's training, each filter is screened along the width and height of the input volume in the forward pass. After convolution process, 2-dimensional activation maps of these filters are created [16-18].

2) Pooling Layer

The main goal of the pooling layer is to reduce the input size for the next convolution layer. This does not affect the depth dimension in the data. This reduction in size results in loss of information. Such a loss is beneficial to the network for two reasons. The adjustment process reduces the spatial size of the input, thereby reducing the amount of parameters and calculation in the network [17-19]. Also, this process prevents the memorization issue in the system (overfitting).

3) Full Connected Layer

After several layers of convolution and pooling, the classification process is realized in a fully connected layer. The neurons in the fully connected layer are fully linked to all the activations in the previous layer [16-18].

III. PROPOSED CONVOLUTIONAL NEURAL NETWORK STRUCTURE

Table 1 shows the CNN model consisting of convolution, ReLU, Pooling, and consequently softmax layers.

Table 1: CNN Model for the classification Sign Language

Layer	Characteristics
Input	64x64
Convolution	16 3x3x1, Stride 1 Padding 3 ReLU
Pooling	Max Pooling 2x2 Stride 2
Convolution	16 3x3x16, Stride 1 Padding 3 ReLU
Pooling	Max Pooling 2x2 Stride 2
Convolution	64 3x3x32, Stride 1 Padding 3 ReLU
Pooling	Max Pooling 2x2 Stride 2
Convolution	128 3x3x64, Stride 1 Padding 3 ReLU
Pooling	Max Pooling 2x2 Stride 2
Fully Connected	Neurons -2048 ReLU and Dropout (0.5)
Fully Connected	Neurons -10
Output	10 (0,1,2,3,4,5,6,8,9)

As shown in Table 1, the network consists of a total of 15 layers including 11 layers and 4 layers placed at intervals. This model has 3 convolution, ReLU, maxPool layer and 2 Full Connected layers. In the last layer of the prepared model numerical sign pictures are classified with softmax function. By using this model, sign language number images were tested and their performance was evaluated.

The CNN model is trained with a minimum batch size of 32, epoch size is set to a maximum of not more than 10 epochs and learning rate of 0.001. The training progress is shown in the Figure 3.

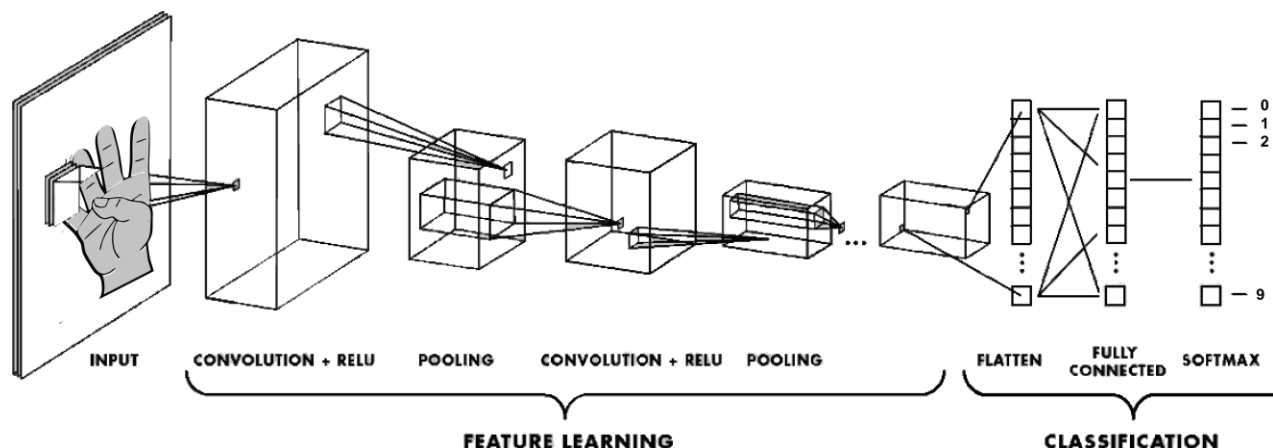


Figure 2: The basic structure of convolutional neural networks.

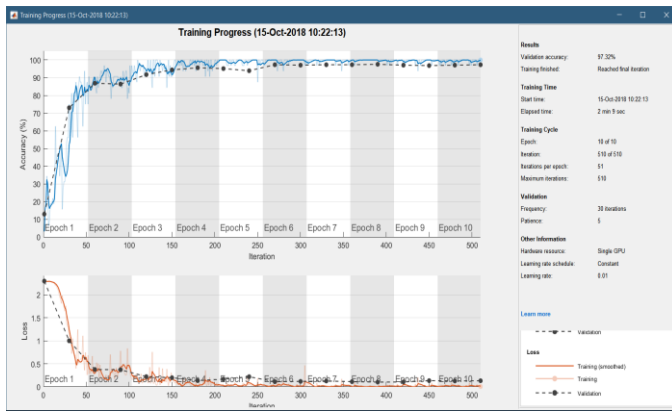


Figure 3: Sample training progress of the proposed CNN model

IV. RESULTS AND DISCUSSION

Sign language data is converted to digital data and processed in MATLAB [20]. The network is trained using the sign language digit images in Matlab R2017b on a Single NVIDIA GT 650M GPU with compute capability of 3.0.

In this study, 5-fold cross validation was performed to evaluate the ability of the proposed CNN to classify the number sign language. Initially, all segments are divided into five equal parts. The first four parts were used to train the CNN model and the other was used for testing. This process was repeated five more times considering the remaining segments for training and testing. The average classification results obtained from each of the five experiments were used to evaluate the performance.

During training, the weights of the neurons in the CNN are adjusted to minimize the error between the predicted and correct label of the sign language segments.

Convolutional neural networks use features to classify images. The network learns these features in the education process itself. Typically, a training period of 12.4 seconds was needed to complete the process. Later, developed CNN model was tested. Figure 4 shows the confusion matrix obtained as a result of the 5-fold cross verification.

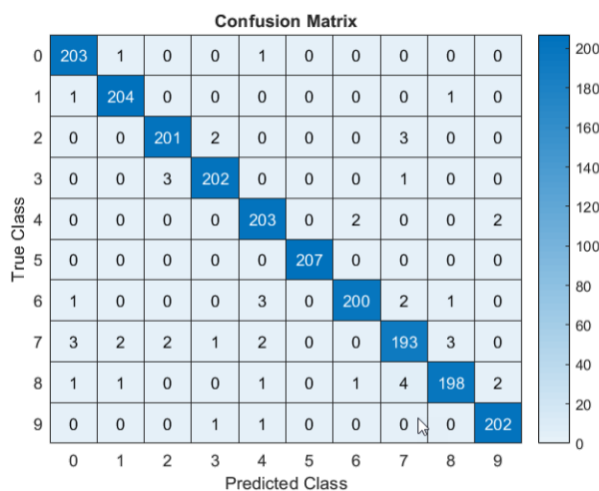


Figure 4: Confusion matrix across all 5 folds.

Precision, sensitivity and specificity analysis were performed to examine the reliability of the models in the test data. Precision tests whether the models produce reliable measurements. It is defined as the ratio of real positives to all positive results and can be calculated using Equation 1.

$$Precision = \frac{True\ Positives}{True\ Positives + False\ Positives} \tag{1}$$

Sensitivity is a measure of true positives which are correctly tested by a particular model. Sensitivity can be calculated using equation 2.

$$Sensitivity = \frac{True\ Positives}{True\ Positives + False\ Negatives} \tag{2}$$

Specificity measures the rate of correctly identified true negatives. Specificity can be calculated using Equation 3.

$$Specificity = \frac{True\ Negatives}{True\ Negatives + False\ Positives} \tag{3}$$

Precision, Sensitivity and Specificity analysis of the obtained model was performed. The results are given in Figure 5.

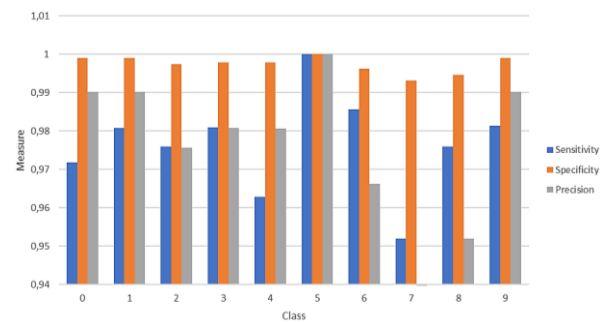


Figure 5: Precision, sensitivity and specificity analysis of the CNN model.

From Figure 5, it is observed that the highest sensitivity, specificity and precision values are recorded in the five digit class.

DeepDream to visualize images of features learned by the network that strongly activate its layers. These images allow exploration of the roles of various parts of the network. The deepdream presentation of fully connected layer features is given in Figure 6.

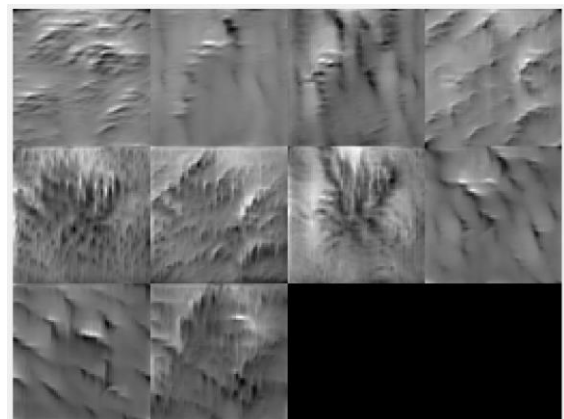


Figure 6: DeepDream feature visualization of last fully connected layer

As a result, sign language recognition systems created using artificial intelligence technologies are important to meet the unmet demand for professional translation services and to improve the quality of life of hearing impaired people. In this study, a CNN has been proposed for automatic feature extraction and classification in sign language containing numbers. Our results show that the model obtained was successful in classifying the sign language containing the numbers. Accuracy, sensitivity, specificity and precision values after 5-fold cross validation were found as 97.63%, 97.67%, 99.74% and 97.63% respectively.

References

- [1] W. contributors, "Sign language," https://en.wikipedia.org/w/index.php?title=Sign_language&oldid=860020963, [17 September 2018 20:19 UTC, 2018].
- [2] D. Aryanie, and Y. Heryadi, "American sign language-based finger-spelling recognition using k-Nearest Neighbors classifier."
- [3] T. Starner, and A. Pentland, "Real-time american sign language recognition from video using hidden markov models," *Motion-Based Recognition*, pp. 227-243: Springer, 1997.
- [4] H.-I. Suk, B.-K. Sin, and S.-W. Lee, "Hand gesture recognition based on dynamic Bayesian network framework," *Pattern recognition*, vol. 43, no. 9, pp. 3059-3072, 2010.
- [5] P. Mekala, Y. Gao, J. Fan, and A. Davari, "Real-time sign language recognition based on neural network architecture." pp. 195-199.
- [6] Y. F. Admasu, and K. Raimond, "Ethiopian sign language recognition using Artificial Neural Network." pp. 995-1000.
- [7] V. Bheda, and D. Radpour, "Using deep convolutional networks for gesture recognition in American sign language," *arXiv preprint arXiv:1710.06836*, 2017.
- [8] B. Garcia, and S. Viesca, "Real-time American sign language recognition with convolutional neural networks," *Convolutional Neural Networks for Visual Recognition*, 2016.
- [9] L. Pigou, S. Dieleman, P.-J. Kindermans, and B. Schrauwen, "Sign Language Recognition Using Convolutional Neural Networks," *Computer Vision - ECCV 2014 Workshops*. pp. 572-578.
- [10] L. Zheng, B. Liang, and A. Jiang, "Recent Advances of Deep Learning for Sign Language Recognition." pp. 1-7.
- [11] A. Mavi, and Z. Dikle, "Sign Language Digits Dataset," *Ayrancı Anadolu Lisesi, Ankara, Türkiye*, 2017.
- [12] I. Goodfellow, Y. Bengio, A. Courville, and Y. Bengio, *Deep learning*: MIT press Cambridge, 2016.
- [13] G. Litjens, T. Kooi, B. E. Bejnordi, A. A. A. Setio, F. Ciompi, M. Ghafoorian, J. A. W. M. van der Laak, B. van Ginneken, and C. I. Sánchez, "A survey on deep learning in medical image analysis," *Medical Image Analysis*, vol. 42, pp. 60-88, 2017/12/01/, 2017.
- [14] W. Liu, Z. Wang, X. Liu, N. Zeng, Y. Liu, and F. E. Alsaadi, "A survey of deep neural network architectures and their applications," *Neurocomputing*, vol. 234, pp. 11-26, 2017/04/19/, 2017.
- [15] MATLAB. "Convolutional Neural Network," <https://www.mathworks.com/solutions/deep-learning/convolutional-neural-network.html>.
- [16] Y. Akbulut, A. Şengür, and S. Ekici, "Gender recognition from face images with deep learning." pp. 1-4.
- [17] Y. LeCun, K. Kavukcuoglu, and C. Farabet, "Convolutional networks and applications in vision." pp. 253-256.
- [18] V. Sze, Y.-H. Chen, T.-J. Yang, and J. S. Emer, "Efficient processing of deep neural networks: A tutorial and survey," *Proceedings of the IEEE*, vol. 105, no. 12, pp. 2295-2329, 2017.
- [19] P. Sermanet, S. Chintala, and Y. LeCun, "Convolutional neural networks applied to house numbers digit classification." pp. 3288-3291.
- [20] M. U. s. Guide, "The mathworks," *Inc., Natick, MA*, vol. 5, pp. 333, 1998.

Feasibility study of a Passive House: Ankara Case

G. N. GUGUL¹

¹ Selcuk University, Faculty of Technology, Computer Engineering Department Konya/Turkey, gul.gugul@selcuk.edu.tr

Abstract - The amount of residential energy consumption has a significant share over final energy consumption in Turkey which is increasing parallel to the rapid increase in population, economic growth and the number of houses. For this reason, energy savings in residential sector is of great importance in Turkey. In this study, technical feasibility study of a single detached “Passive House” located in Ankara, Turkey is investigated using building energy simulation software. House is developed to draw advantage from sun in maximum level with convenient shape, color and window/wall ratio. Model house has high insulation level and low air tightness. According the simulations conducted minimum space heating demand of the 3 bedroom, 120 m² single detached house is estimated as 6,2 kWh/m²-year, overcompensating the “15 kWh/m²-year” Passive House target sufficiently. The primary energy demand is calculated as 30,8 kWh/m², marginally below the 120 kWh/m² target.

Keywords - Passive house, Low energy buildings, Building Energy Simulation

I. INTRODUCTION

ENERGY consumption of residential sector is effected by many components such as socio-economic levels, behavior's, number of electrical appliances, cultural construction traditions, climate, HVAC equipment and ventilation habits of the nation. While planning the energy demand of residential sector, these components should be taken into account according to regions traditions, energy sources and availability of equipment's. There are many types of residential buildings designed and constructed by taking into account these components and therefore consume less energy compared to traditional buildings. These residential buildings are studied in the literature in order to decrease, minimize, set to zero or raise to positive the energy consumption and associated emission.

A major part of these studies are conducted by developing the energy consumption model of buildings and applying scenarios to the developed model to calculate the energy savings by using building energy simulation software's such as DOE-2 [1], EnergyPlus [2], eQUEST [1], TRNSYS [3] and ESP-r [4].

According to the existing terminology, there are many terms used with the purpose of expressing low energy buildings [5]. Some of the terms used are Low Energy Buildings, Zero Energy Buildings, Net Zero Energy Buildings, Net Zero Off-

Site Energy Buildings, Net Zero Energy Cost Buildings, Net Zero Energy Emission Buildings, Zero Carbon Buildings, Approximately Zero Energy Buildings, Zero Emission House, Passive House, Plus Energy House, Net Positive Energy House and Hybrid Buildings. In newly built homes reaching passive house, net zero or net positive house standard get ahead of decreasing energy consumption. A newly built house should be designed with minimum energy demand, before energy of the home is provided by renewable resources.

Passive Houses allow heating and cooling related energy savings of up to 90% compared to typical building stock and over 75% compared to average newly constructed buildings. The aim of 'Passivehaus' organization established in Germany is to design the most energy efficient homes. Passive House Database is a common project of the Passive House Institute, the Passivhaus Dienstleistung GmbH, the IG Passivhaus Deutschland and the iPHA (International Passive House Association) and Affiliates. According to Passive House Database there are 3558 newly constructed passive houses in world one of which is in Turkey [10].

There are two Certified Passive house buildings in Turkey one of which is newly build, other one is EnerPHit Retrofit. Both of the passive houses that own “Passive House Certificate” in Turkey are in Gaziantep [11]. Detailed information about these buildings is given in Table 1.

Table 1: Passive Houses in Turkey

Location	Gaziantep 1	Gaziantep 2
Year	2015(<i>EnerPHit Retrofit</i>)	2011(<i>New build</i>)
Exterior wall	U:0,149 W/m ² K	U:0,092 W/m ² K
Basement floor	U:0,169 W/m ² K	U:0,111 W/m ² K
Roof	U:0,201 W/m ² K	U:0,101 W/m ² K
Frame	U _f :0,79 U _w :0,81 W/m ² K	U _w :0,96 W/m ² K
Glazing	U _g :0,56 W/m ² K g-value = 39 %	U _g :0,56 W/m ² K g-value = 39 %
Door	U:0,89 W/m ² K	U _d :0,74 W/m ² K
Heating installation	Air Sourced Heat Pump Vitocal	-
Domestic hot water	Solar panel system	-
Heating demand	20 kWh/m ² a	7,23 kWh/m ² a
Primary energy	79 kWh/m ² a	95,81 kWh/m ² a

As it is clear from Table 1 that annual heating demands per unit area of the buildings estimated by PHPP are 20 kWh/m²a and 7,23 kWh/m²a respectively. The PHPP is an easy to use planning tool for energy efficiency for the use of architects and planning experts.

Due to the low HDD (Heating degree day) of Gaziantep compared to Ankara [12] it is more possible to achieve passive house heating demands standard in Gaziantep whereas CDD (Cooling degree day) of Gaziantep is higher than Ankara that increases cooling demand.

In addition to constructed passive houses there are two theoretical studies conducted to develop a passive house in Turkey. In scope of a master's thesis completed at the Department of Architecture of Istanbul Technical University the application of passive house assessment for Turkey is investigated. In this thesis a model house is developed in computer software and the heating requirement provided for Ankara province is estimated as 13 kWh/m², the cooling requirement is 10 kWh/m², and the primary energy need is calculated as 54 kWh/m². Insulation thickness which provides the passive house standard boundary heating energy requirement is calculated as 27 cm for Ankara [13]. Another master's thesis is conducted in Izmir Katip Celebi University to evaluate passive building design parameters for Izmir city by modeling a 12 storey residential building in Ecotect Analysis and Revit software [14].

II. METHODOLOGY

In this section data used and methods followed during development of a passive house model in Ankara climate are described in detail.

In this study a single detached house with 120 m² heated area is planned to achieve passive house standard in which four people reside. Electricity consumption of the house is estimated based on mandatory electrical appliances required in a house. Heating demand of the house is estimated by energy demand model of the house developed in eQUEST building energy simulation software. Heat gains of the house are also calculated and subtracted from heating demand.

This research study uses simulation and theoretical data to achieve passive house status through envelope improvement and energy star appliances in Ankara, Turkey.

A. Model Development

Heating demand model of the house is developed in eQUEST building energy simulation software to estimate the energy consumed for heating and cooling by using climate data of Ankara, construction data of the building and internal heat gains.

A.1 Heat Gain

Heat gain from electrical appliances, lighting and people cause an increase in the ambient temperature therefore should be added to the model. Heat gain is classified as sensible, convective or latent. Sensible heat gain (SHG) is added directly to the conditioned space by conduction, convection,

and/or radiation (convective plus radiative). Latent heat gain (LHG) occurs when humidity is added to the space [15].

The sources of internal heat gains (IHG) include:

- People (SHG and LHG)
- Lighting (SHG)
- Electrical appliances
- Electrical plug loads (SHG)
- Processes such as cooking (SHG and LHG)

- People (SHG and LHG)

There are 4 people reside in house. Heat gain from people is calculated by using the heat gain activity in the ASHRAE catalog [15] given in Table 2 and equation (1).

$$HG_p = (HG_s \times N_p \times t) + (HG_l \times N_p \times t) \quad (1)$$

In this equation;

HG_p: Heat gain from people, Wh/day

HG_s: Sensible heat gain type, W

HG_l: Latent heat gain type, W

N_p: Number of people

t: Duration, hour

Table 2: Heat gain from people

Heat gain activity in the ASHRAE	Equivalent Activity	SHG (W)	LHG (W)
Theater seating	House seating	65	30
Sit at night in the theater	Sit at night in the house	70	35
Very light work	Very light work	70	45
Active business environment	Active business environment	75	55
Standing, light works, walking	Cleaning	75	55
Light bench work	Major cleaning	80	80

- Lighting (SHG)

In an experiment, the heat generated by the LED lighting was calculated as 78.1% of the supplied power to the LEDs, [16]. Therefore heat gain from the lighting is calculated by multiplying the power values of the lamps with usage durations in a day and 0,781.

- Electrical appliances (SHG and LHG)

Heat gain from some of the electrical appliances is both sensible and latent heat gain (tea machine, steam iron, etc. Power values of A+ energy star electrical devices are obtained from web. Power of the appliance is multiplied by usage duration and sensible and latent load fraction of the appliances [17]. Load fraction differs for each device and fractions for the appliances are given in Table 3.

Table 3: Load fractions of appliances

Appliance	Sensible Fraction	Convective Fraction	Latent Fraction
Miscellaneous loads (gas/electric house)	0,734		0,2
Television	1		
Microwave	1		
Stove and Oven gas	0,3		0,2
Refrigerator		1	
Washing Machine	0,4	0,6	0
Dish washer	0,51	0,34	0,15
Small Appliances	0,54	0,36	0,1
Lighting	0,78	0,1	

A.2 Climate Data

The normal climate data of Ankara is downloaded from the EnergyPlus weather data web site for Turkey in IWEC (International Weather for Energy Calculations) format. The IWEC data files are 'typical' weather files suitable for use with building energy simulation programs which are available for download in EnergyPlus weather format [18].

A.3 Physical Properties of the House

Materials used in construction of passive house and thermal properties of the materials are given in Table 5. In addition to the construction properties given in Table 5, window/wall ratio for each side, window blind materials and open/close durations of the blinds, exterior shades and door location of the house are decided according to simulations conducted for each option. Final physical shape of the house is also decided at the end of simulations conducted for different house shapes.

It's clear from Table 1 and Table 5 that U values of exterior wall and roof of the passive house in Ankara is half of the passive house in Gaziantep which means thermal resistance of the passive house in Ankara is double of the passive house in Gaziantep due to higher HDD of Ankara compared to Gaziantep. As it is shown in Table 5, polyisocyanurate is selected as insulation material due to the high energy savings obtained compared to polyurethane and polystyrene conducted in a study for cold climates [19]. In addition, Polyisocyanurate increases value of a building due to its high resistivity to fire and humidity. It's also economic, easy to install and environment friendly. Insulation installed in exterior wall is 33 cm and in roof is 30 cm. Window glazing of the house is selected as triple glazing filled with argon gas. Window frames are aluminum.

In model house all rooms are kept at 20°C during winter, at 26 °C during summer.

Normally the ACH value varies from 0,5 ACH for tight and well-sealed buildings to about 2,0 for loose and poorly sealed buildings. For modern buildings the ACH value may be as low as 0,2 ACH [20]. In this study, airflow into the house by natural ventilation (ACH) is assumed as 0,4.

III. RESULTS AND DISCUSSION

In this section results of heat gain and electricity consumption are given. Then model development and estimation by the simulation of the model are presented. Finally total energy demand of the house is given to show if the study reach passive house standard or not.

A. Heat Gain and Electricity Consumption

Before the development of model, heat gain and electricity consumption of the house is calculated by taking into account mandatory electrical appliances, equation [1] and Table 3. Daily heat gain from people is given in Table 5.

Table 4: Heat gain from people

Activity	Hour, h	SHG, Wh	LHG, Wh
House seating	0-8	2080	960
Active business environment	8-9	300	220
Nobody at house	9-18	0	0
Sit at night in the house	18-23	1400	700
Very light work	23-24	280	180
Total, Wh		4060	2060

is given in Table 5.

Table 4 shows that daily heat gain from people is 6,12 kWh/day. Daily electricity consumption and heat gain from appliances, lighting and people are given in Table 6.

A.1 Envelope Development

Model house is a highly insulated house as it is seen in Table 5. Firstly envelope constructions and climate data are inserted to the model and then heating and cooling demands are calculated. Then window/wall ratio between 5-45% for each side is applied to the model and most efficient window/wall ratio for each side is decided. Finally different basement shapes are applied to the model to determine most efficient architectural drawing. Also, model is run for different envelope colors and basement types (earth contacting, open crawl space, over garage).

B. Calculation of Total Energy Demand

Heating and cooling energy demand of the house is calculated by using heat gain data and simulation of the model of the house in building energy simulation software.

Electricity consumption of the house is calculated by multiplying usage durations of the electrical appliances by power values.

Model house is developed for Ankara climate. In a study conducted in Konya daily energy consumption for hot water demand of a house is calculated as 4 GJ/year, 1 GJ/year-person with a solar domestic hot water system [21]. Therefore, in this study energy demand for hot water is assumed to be the same as the study conducted in Konya due to similar climate of Konya to Ankara.

Table 5: Properties of constructions in passive house

Construction	Material (Ordered from outside to inside)	Thickness, mm	Thermal Conductivity, W/m-K	Thermal Resistance R_i , m^2K/W	Thermal conductivity U , W/m^2K
Exterior wall	Plywood	16	0,115	0,138	0,057
	Polyisocyanurate	305	0,020	15,11	
	E Wall Cons Material	NA	NA	0,980	
	Polyisocyanurate	25	0,020	1,254	
	GYPBd 1/2 in (GP01)	13	0,160	0,080	
	Total			17,48	
Roof (Ceiling)	Blt-Up Roof 3/8 in (BR01)	9	0,162	0,058	0,055
	Polyisocyanurate	305	0,020	15,11	
	Plywood	16	0,115	0,138	
	Roof Cons Mat 4	NA	NA	2,940	
	GYPBd 5/8 in (GP02)	16	0,160	0,099	
	Total	0	0,000	18,34	
Glazing	Glazing	6	1,000	0,006	0,557
	Argon gas	16	0,018	0,889	
	Glazing	6	1,000	0,006	
	Argon gas	16	0,018	0,889	
	Glazing	6	1,000	0,006	
	Total			1,796	
Door	Wood	40	0,220	0,027	36,667
	Light Soil, Damp 12 in	6	0,862	0,354	
Basement	Concrete	305	1,724	0,177	0,063
	Polyisocyanurate	305	0,020	15,11	
	Plywood 1 in (PW06)	305	0,115	0,220	
	Total	25		15,86	

Table 6: Heat gain and electricity consumption of the house

	Usage Duration, h/day	Number	House Heat Gain, W			Heat Gain, kWh/day	Electricity Consumption, kWh/day	Power, W
			SHG	CHG	LHG			
Refrigerator	24	1	38			0,91	0,90	38
Laptop	4	2	50			0,40	0,40	50
Charge App.	3	3	7			0,06	0,09	10
Vacuum Cleaner	0,10	1	840			0,08	0,12	1200
Washing Machine	0,50	1	166	250		0,21	0,21	416
Dishwasher	0,25	1	212	141	62,4	0,10	0,20	800
Cooking	1	1	1200			1,20	1,20	1200
TV	5	1	48			0,24	0,24	48
Lighting	6	5	19,5			0,59	0,75	25
People						6,12		
Total						9,92	4,11	

According to Table 6 daily total heat gain is calculated as 9,92 kWh/day, daily electricity consumption is calculated as 4,11 kWh (1500 kWh/year). Hourly heat gain is subtracted

from estimated hourly heating demand. Hourly heat gain is shown in Table 7.

Table 7: Hourly heating demand

Hour	Refrigerator	Laptop	Charge App.	Vacuum Cleaner	Washing Machine	Dish washer	Cooking	TV	Lighting	People	Total
1	38									380	418
2	38									380	418
3	38									380	418
4	38									380	418
5	38									380	418
6	38									380	418
7	38									380	418
8	38						600			380	1018
9	38										38
10	38										38
11	38										38
12	38										38
13	38										38
14	38										38
15	38										38
16	38										38
17	38										38
18	38									380	418
19	38	100	21				600	48	39	380	1226
20	38	100	21		208	88		48	39	380	922
21	38	100	21					48	39	380	626
22	38	100		84				48	39	380	689
23	38							48	39	380	505
24	38								39	380	457

B. Model development

Heating and cooling demand of the passive house is estimated by the model developed in software. Model house is a highly insulated house as it is seen in Table 5. After the insertion of constructions to the model, heating and cooling demands are estimated by simulations. Then window/wall ratio between 5-45% for each side is applied to the model and most efficient window/wall ratio for each side is decided. Most energy efficient exterior door and window/wall ratio for each side are given in Table 8.

Table 8 Energy efficient exterior door and window/wall ratio

Case	Side			
	North	South	East	West
Door Direction	-	1	-	-
Window Direction and Percentage	5%	45%	15%	15%

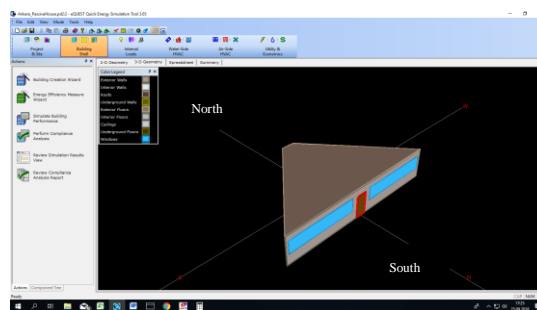
As it is clear from Table 8 45% of South wall, 15% of east and west walls and 5% of north wall are constructed of window. Most energy efficient window glazing type for Ankara climate is decided to be argon filled clear triple glazing. Low-E coated glazing may be effective in hot climates

but it increased heating demand in Ankara where cooling load is very low compared to heating load.

Also, model is run for different envelope colors and most efficient envelope color is decided to be light brown with absorptivity 0,8.

Construction of basement is another significant factor in decreasing energy demand. According to the basement shapes applied to the model, most efficient basement is concluded to be earth contacting basement.

Finally different architectural drawings are applied to the model by keeping heated area, constructions and window/wall ratio constant. As a result of these applications most energy efficient house shape is concluded to be triangle shape and the shape of the model house is shown in Figure 1.



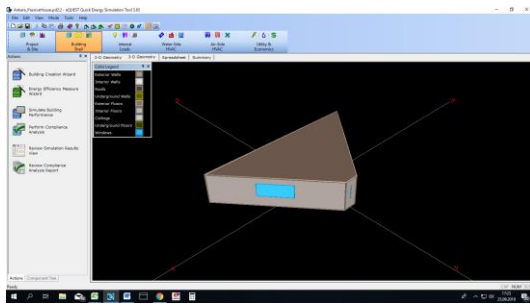


Figure 1: Most efficient house shape

Most efficient house shape shown in Figure 1 shows that as much as decreasing the wall on north side as possible decreases heating demand in cold climate due to the replacement the exterior wall in north side with the wall in east and west side. However an exact triangle shape is not always possible in real life. Heating demand for each building shape is given in Figure 2.

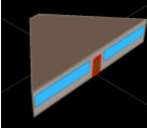
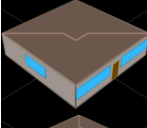
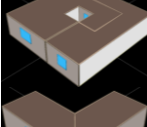
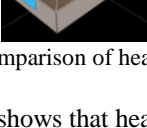
Shape	Heating demand, kWh/year
	819
	1049
	1094
	881
	1089

Figure 2: Comparison of heating demand of different building shapes

Figure 2 shows that heating demand for triangle shape house is 21% less than square shaped house.

C. Cooling Demand

After the construction, shape and color of the house are determined cooling and heating energy demand of the house is estimated hourly by simulation software. In model house all rooms are kept at 26 °C during summer. Cooling system has air cooled condenser and split system. In addition, house has exterior blinds as shown in Figure 3 which are closed during daytime of summer.

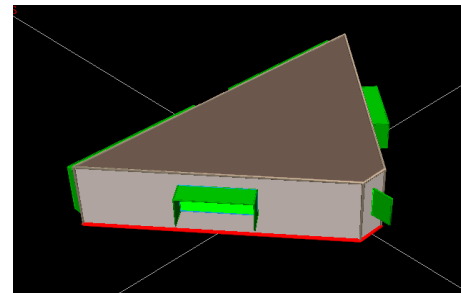


Figure 3 Exterior blinds of the house

Indoor blinds of the house are made of fabric drapes with light color. Indoor blinds are 60% closed when the house is occupied, 100% open when the house is not occupied. House is naturally ventilated during summer therefore heat gain is not taken into account. According to simulation results model house consumed 272 kWh/year energy for cooling between end of May and end of September. Daily simulation result is given in Figure 4.

D. Heating demand

Heating system of the house is designed as electric baseboard system and has air forced ventilation during winter. Total energy consumption of system is composed of Auxiliary end-use (pumps), heating end-use and ventilation fan end-use. Heating demand of the system is estimated as 1886 kWh/year. For each hour of the year, if the hourly heating demand is higher than heat gain, heat gain is subtracted from demand. If hourly heating demand is lower than heat gain, heating demand is assumed to be zero. By taking into account heat gains, net heating demand is calculated as 819 kWh/year. Daily heat gain, net heating demand and cooling demand are shown in Figure 4.

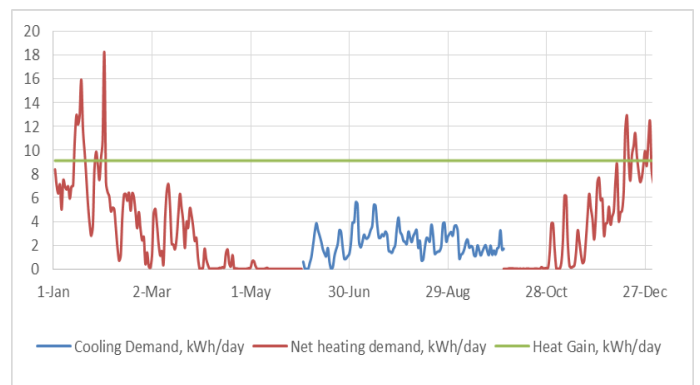


Figure 4: Daily heat gain, net heating demand and cooling demand, kWh/day

E. Total energy demand

According to the results shown in Figure 4 total heating and cooling demand of the house is estimated as 1092 kWh/day.

Electricity consumption of the house is calculated as 1500 kWh/year as given in Section III.A. Four people reside in the model house which results in consumption of 4 GJ/year (1111 kWh/year) energy for hot water demand. Finally primary Energy Demand of the house is calculated as 3703 kWh/year and 30,8 kWh/year-m². Heating Demand of the house is estimated as 819 kWh/year and 6,2 kWh/year-m² which overcompensate passive house standards.

Heating demand per unit area is half of the results obtained in a master's thesis completed at the Department of Architecture of Istanbul Technical University for Ankara climate which was estimated as 13 kWh/m². In master thesis primary energy need was calculated as 54 kWh/m² whereas it is calculated as 30,8 kWh/m² in this study which is also close to the half of the amount obtained in thesis. Main reason to obtain half of the results is to lower cooling demand by exterior blinds closed during summer and triangle shape of the house. Also insulation thickness is higher than the study conducted in Istanbul [13].

IV. CONCLUSION

This study is conducted to investigate the feasibility of a passive house in Ankara climate. In order to reach the passive house target, the residential building is planned to have high insulation and low air tightness.

Annual heating energy demand per unit area of the model house is calculated as 6,2 kWh/year-m² that overcompensate passive house standards in case of a triangle shape. Primary Energy Demand of the house is calculated as 3.703 kWh/year and 30,8 kWh/year-m² which shows its feasible and convenient to build passive houses in Middle Anatolian region to reduce energy consumption from building sector.

REFERENCES

- [1] DOE2. (2018, January) eQUEST Overview. Available: <http://www.doe2.com/download/equest/eQUESTv3-Overview.pdf>
- [2] USDOE. (2018, January) EnergyPlus Energy Simulation Software. Available: <http://www.energyplus.gov/>
- [3] TRNSYS. (2018, January) Available: <http://sel.me.wisc.edu/trnsys>
- [4] ESRU. (2018, January) ESP-r Overview. Energy Systems Research Unit. Available: http://www.esru.strath.ac.uk/Programs/ESP-r_overview.htm
- [5] H. Lee, S. Gurung and T. Brick. "Zero Energy Buildings. Helsinki" Thesis, Helsinki Metropolia University of Applied Sciences, 2012.
- [6] A. N. Bulut, (2018). Pasif Evler & Firsatlar. Available: http://www.imsad.org/Uploads/Etkinlikler/Adana/izocam_nuri_bulut.pdf
- [7] F. Wolfgang. "What Can be a Passive House in Your Region with Your Climate?", Darmstadt: Passive House Institute, 2015.
- [8] D. Tiwari. Passive House Concept: Standard and Case study. Metropolia University of Applied Sciences, 2018.
- [9] European Commission. (2014). Shares Tool Manual Version 2014.51008. pp. 1-27. Available: https://ec.europa.eu/eurostat/documents/38154/4956088/SHA_RES2014manual.pdf/1749ab76-3685-48bb-9c37-9dea3ca51244
- [10] Passive House Institute. (2018, March). Passive House Database. Available : https://passivhausprojekte.de/index.php#s_adfa73159c0f55f1b6b68ec8f21a28c1
- [11] Passive House Institute. (2018, March) Passive House Database-Turkey. 2018. Available: https://passivhausprojekte.de/index.php?lang=en#k_TURKEY
- [12] GDM-HDD. (2018, March). General Directorate of Meteorology Heating Degree Days. Available: <https://www.mgm.gov.tr/veridegerlendirme/gun-derece.aspx>.
- [13] B. Demirel, "Pasif Ev Uygulamasinin Türkiye İçin Değerlendirilmesine Yönelik Bir Çalışma," Yüksek Lisans Tezi, Mimarlık Anabilim Dalı, İstanbul Teknik Üniversitesi, İstanbul, 2013.
- [14] I. Güçü, "Evaluation of Passive Building Design Parameters for Izmir City," Master Thesis, Dept. of Urban Regeneration, Izmir Katip Celebi Univ., Izmir, Turkey, 2016.
- [15] T. Varkie. (2018, March). Internal heat gains (IHG). energy-models. Available: <http://energy-models.com/internal-heat-gains-ihg>.
- [16] B. Ahn, J. Park, S. Yoo, J. Kim, S. Leigh and C. Jang, "Savings in Cooling Energy with a Thermal Management System for LED Lighting in Office Buildings," *Energies*, Vol. 8, pp. 6658-6671, July 2015.
- [17] M. Cristina Escribá. "Heat Gains, Heating and Cooling In Nordic Housing," Aalto University Department of Electrical Engineering, 2015.
- [18] USDOE-Weather. (2018, January) EnergyPlus Energy Simulation Software-Weather Data Sources. USDOE. Available: https://energyplus.net/weather-location/europe_wmo_region_6/TUR//TUR_Ankara.171280_IWEC.
- [19] G. N. Gugul, "Energy Simulation Study of Efficient Construction Materials for Cold Climate Homes," in *Kiruna, Sweden The 9th International Cold Climate Conference Sustainable new and renovated buildings in cold climates.2018*
- [20] NPTEL. (2018, March). Cooling and Heating Load Calculations. National Programme on Technology Enhanced Learning. Available: <https://nptel.ac.in/courses/112105129/pdf/R&AC%20Lecture%2035.pdf>
- [21] G. N. Gugul, "Techno-Economic Analysis of Solar Domestic Hot Water System for Single Detached Dwellings in Konya," in *Konya, Turkey, International Conference on Engineering Technologies. 2017*, pp. 775-780.

Costs and co-benefits of Passive Houses: Ankara residential sector

G. N. GUGUL¹

¹ Selcuk University, Faculty of Technology, Computer Engineering Department Konya/Turkey,
gul.gugul@selcuk.edu.tr

Abstract – Residential sector is responsible for a significant share of final energy consumption in the world and Turkey. Constructing energy efficient homes is noteworthy for sustainability and energy transitions. Novel approaches show up to describe efficient homes such as net zero energy homes and passive houses. Passive design strategies are becoming common. Passive Houses are buildings with heating demand below 15 kW h/m² year, with comfortable indoor conditions. However, in order to achieve passive house target in addition to technical knowledge, cost and co-benefit analyses should be done to prove practicality. This paper investigates the economic feasibility and co-benefits of passive houses in Ankara climate. The cost analysis in this study is conducted for newly build homes and by using cutting edge technology.

Keywords - Passive house, Cost analyses, Residential energy

I. INTRODUCTION

TURKEY is situated in a geographical location where climatic conditions are quite temperate however there are significant differences in climatic conditions from one region to the other. While the coastal regions have milder climates, the Anatolia plateau has a dryer climate with hot summers and cold winters. In Turkey 82% of energy consumption in buildings is consumed for heating. Heating energy consumption of buildings constitutes 26% of the final energy consumption in our country. According to statistical information; energy consumption of a house with the same climatic conditions and the same usage area in Turkey is 2 - 3 times higher than in France, Germany, England and Sweden which indicates that the energy efficiency measures in Turkey are inadequate [1].

Residential buildings are studied in the literature in order to decrease, minimize, set to zero or raise to positive the energy consumption and associated emission. According to the existing terminology, there are many terms used with the purpose of expressing low energy buildings such as Low Energy Buildings, Passive Houses, Zero Energy Buildings, Net Zero Energy Buildings, Net Zero Energy Cost Buildings, Net Zero Energy Emission Buildings, Zero Carbon Buildings, Plus Energy House, Net Positive Energy House and Hybrid Buildings. In newly built homes reaching “passive house standard” passed ahead of decreasing energy consumption. A newly built house should be designed with minimum energy demand, before energy demand of the home is provided by renewable resources or new technologies.

The principle behind a Passive House is significantly

increasing the energy efficiency of a building, decreasing the associated emissions then the HVAC systems can be radically simplified on reaching a certain level of efficiency. CO₂ emissions from houses for each standard are given in Figure 1.

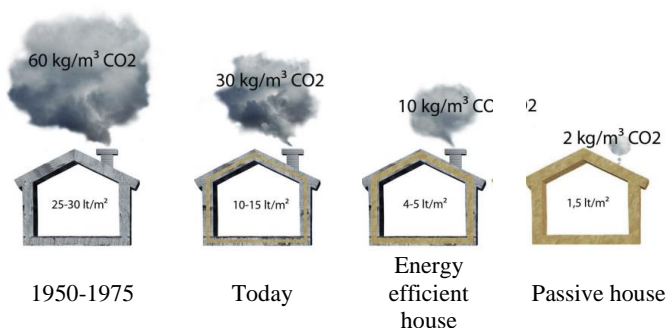


Figure 1: CO₂ emissions from houses for each standard [2]

In Passive Houses comfort should be at maximum level by keeping the passive house solution simpler than what is presently used in conventional buildings with affordable solutions. In passive houses it is sufficient to minimize energy use with simple systems from conventional sources. As a general rule, if the energy consumption is between 10% and 25% of current consumption levels, the savings obtained from conserved energy is enough to pay for the extra construction costs.

Insulation is highly recommended in all passive houses for all climates. Also shading is absolutely necessary in climates with high levels of solar radiation. Heat recovery is required in all climates especially if the external temperatures are often below 8°C or above 32°C. Ground may be used as a heat or cold buffer if an opportunity exists to use the ground to reduce heating and cooling loads [3].

There are many techniques to develop a passive house. In order to investigate these techniques for different climates many Passive house studies are conducted around the world. The Passive House Institute has developed several Passive House building techniques to suit the Central European climate which will be illogical to directly copy these techniques from the Central European example to other parts of the world. Instead, the details should be found to suit the climate and geographic conditions to develop a Passive House solution of each location [3]. A Passive House Specification developed for Germany and Finland is given in Table 1.

Table 1: Passive house Specification for Germany and Finland [4]

	Germany	Finland		
		South	Central	North
Heating Demand, kWh/m ²	≤ 15	≤20	≤25	≤30
Heating Demand, W/m ²	10		-	
Primary Energy Demand, kWh/m ²	≤120	≤130	≤135	≤140
Overheating hours/year Temperature>25°C, %	10		-	

The Central European definition is difficult to be reached in colder climates thus, *a country/region based approach* is required by taking into consideration the heating degree days (HDD) of the location. Climate condition areas of European countries and Turkey are given in Figure 2 with range of heating degree days.

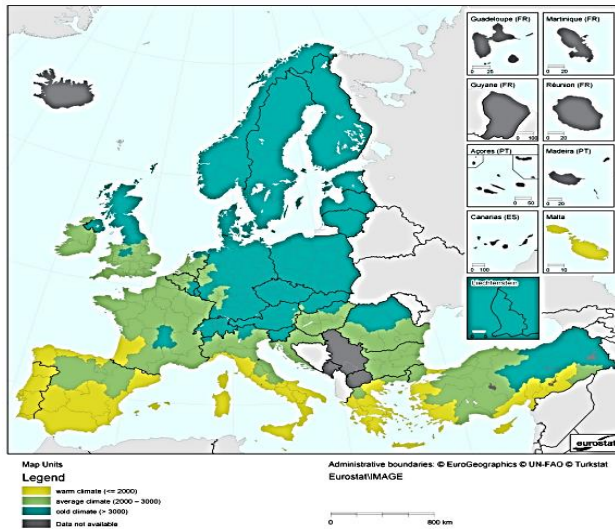


Figure 2: Climate condition areas of Europe [5]

As it is clear from Figure 2, Germany and Finland are in “cold climate” region with HDD greater than 3000. Ankara is in “average climate” region with HDD between 2000 and 3000. Therefore Passive house specifications of Germany and Finland cannot be applied to residential houses of middle Anatolian region of Turkey. Due to the warmer climate of Ankara compared to Germany, a lower level than 15 kWh/m²-yr should be obtained with a sensible cost.

The ‘Passivehaus’ organization established in Germany is developed in order to design the most energy efficient homes. Passive House Database is a common project of the Passive House Institute, the Passivhaus Dienstleistung GmbH, the IG Passivhaus Deutschland and the iPHA (International Passive House Association) and Affiliates. According to Passive House Database there are 4462 passive houses with passive house certificate in world of which 3558 are newly constructed and one of which is in Turkey. The buildings with

passive house certificate include all types of buildings and 2484 of 4462 buildings are single detached buildings [6].

There are two Certified Passive house buildings in Turkey [7] one of which is newly build, other one is EnerPHit Retrofit. Both of the passive houses that own “Passive House Certificate” in Turkey are in Gaziantep [6]. In addition to constructed passive houses there are two theoretical studies conducted to develop a passive house in Turkey one of which is conducted at the Department of Architecture of Istanbul Technical University and the heating requirement provided for Ankara province is estimated as 13 kWh/m², the cooling requirement is 10 kWh/m², and the primary energy need is calculated as 54 kWh/m² [8]. Another master's thesis is conducted to evaluate passive building design parameters for Izmir city by modeling a 12 storey residential building in Ecotect Analysis and Revit software [9].

Numbers of passive house certificated buildings show the inadequate tendency in Turkey to Passive houses. In order to increase the trend to passive houses in Turkey, this study aimed to investigate cost and co-benefits of passive houses for Ankara climate.

II. METHODOLOGY

In this study firstly a passive house model is developed for Ankara climate with heating demand lower than 15 kWh/m²-yr, then cost and co-benefits of the passive houses are investigated in scope of Ankara region.

A. Passive House Model Development

Heating demand model of the house is developed in eQUEST building energy simulation software by using climate data of Ankara. The climate data of Ankara is downloaded from the EnergyPlus weather data web site in IWEC (International Weather for Energy Calculations) format [10]. Construction properties of the house are decided according to the constructed passive houses in locations with similar HDD to Ankara. Some of the newly build single detached residential passive houses in world are shown in Table 2 according to their climate regions.

As it is clear from Table 2 that, Croatia Zagrebacka, Italy Emilia-Romagna, Romania Bucharest, Belgium Wijtschate, Bulgaria Varna and Bulgaria Sofia are in “average climate” region with HDD between 2000 and 3000 similar to Ankara, Turkey. Therefore, U values of the passive house model in Ankara are assumed to be the average values of U values of the passive houses in these regions.

Table 2: Some of the newly build single detached residential passive houses [6]

Climate Region	Country	ID	Year of construction	U-value, W/m ² K				Primary energy requirement, kWh/m ² -yr	Annual heating demand, kWh/m ² -yr
				Exterior wall	Basement	Roof	Glazing		
Cold Climate, HDD>3000	Belgium Torhout	421	2005	0,115	0,112	0,093	0,79		15
	Canada, BC, Nelson	2504	2013	0,097	0,091	0,047	0,50	119	14
	Finland Espoo	3902	2013	0,076	0,087	0,053	0,34	105	18
	Germany Bayern	5439	2017	0,117	0,125	0,108	0,50	38	13
	Hungary Budapest	2193	2010	0,093	0,124	0,100	0,51	93	13
	Netherlands Swalmen	1495	2009	0,100	0,140	0,100	0,70	65	15
	Norway Oslo	1060	2007	0,110	0,095	0,102	0,55	110	15
	Poland	4496	2015	0,086	0,121	0,078	0,53	83	13
	Sweden Halmstad	4182	2014	0,081	0,092	0,065	0,53	81	14
	UK Dunoon (Scotland)	1695	2009	0,095	0,150	0,094	0,80	99	21
Average Climate, 2000<HDD<3000	Croatia Zagreb	4886	2005	0,130	0,190	0,120	0,70	87	11,3
	Italy Emilia-Romagna	5194	2017	0,113	0,174	0,090	0,60	98	9
	Romania Bucharesti	4994	2016	0,124	0,178	0,224	0,50	84	14
	Belgium Wijtschate	4875	2006	0,110	0,117	0,090	0,60	121	13
	Bulgaria Varna	2021	2009	0,112	0,166	0,092	0,70	32	13
	Bulgaria Sofia	3892	2013	0,095	0,119	0,078	0,65	52	11
Warm Climate HDD<=2000	Cyprus	5222	2013	0,198	0,478	0,169	0,80	68	5
	Turkey Gaziantep	4976	2011	0,092	0,111	0,101	0,56	96	7,23
	Portugal Ilhavo	2402	2012	0,262	0,421	0,234	1,00	74	11
	Portugal Ilhavo	4744	2015	0,298	0,408	0,231	0,65	31	13

Averages of the U values of the passive houses in “Average Climate” region are shown in Table 3.

Table 3: Average of the U values of the passive houses in Average Climate region [6]

Country	U-value, W/m ² K				Heating demand, kWh/m ² -yr
	Ext. wall	Basement	Roof	Glazing	
Croatia	0,13	0,190	0,120	0,7	11,3
Italy	0,11	0,174	0,090	0,6	9
Romania	0,12	0,178	0,224	0,5	14
Belgium	0,11	0,117	0,090	0,6	13
Bulgaria	0,11	0,166	0,092	0,7	13
Bulgaria	0,09	0,119	0,078	0,65	11
Average	0,11	0,157	0,116	0,62	11,8

Detailed properties of the model of the developed passive house are given in Table 4.

Table 4: Detailed properties of the passive house model in Ankara

Heated area, m ²	100 m ² , 2 floors	
Roof area, m ²	100	
Exterior Wall area, m ²	100,5	
Window area, m ²	19,5	
Number of people	4	
Heating equipment	Electric heating (No cooling)	
Roof construction, cm	Blt-Up Roof	1
	Polystyrene	30

Exterior wall cons., cm	Concrete	20
	GypBd	2
	Polystyrene	30
Basement Cons., cm	Concrete	30
	GypBd	1
	Light Soil	30
Glazing Type	Argon filled triple, Fiberglass frame	
Window/wall ratio, %	S→40, N→5, W→10, E→10	
Door material	Steel, polyurethane	
Exterior doors	1 Door→South side	
Color of roof/walls	Brown, Abs=0,8	
Infiltration (ACH)	0,4	
Building operation	Daytime unoccupied, Typical use	
Interior light load	5,5 W/m ²	
Cooking load	0,5 W/m ²	
Electric equipment	3,5 W/m ²	
Domestic hot water	60 lt/person-day	
Interior light load	Supply water→= 45 °C	
Cooking load	Mains water→= Ground temp	
Electric equipment	Efficiency=0,95	
Thermostat set point	20 °C	

B. Heating and Primary energy requirement

After the development of model heating demand and total energy demand of the house is estimated by building energy simulation software. Then total demand is divided to the heated area of the house. Finally Heating and Primary energy requirement of the house is determined

C. Cost benefits

In order to calculate cost benefits, a traditional house model is developed and results of passive house and traditional house are compared. Differences of passive house and traditional house are given in Table 5.

Table 5 Differences of passive house and traditional house

Construction	Passive house	Traditional house
Roof Insulation	30 cm Polystyrene	2,5 cm Polystyrene
Exterior wall	30 cm Polystyrene	2,5 cm Polystyrene
Basement	30 cm Polystyrene	No insulation
Glazing Type	Argon filled triple gazing, Fiberglass frame	Air filled Double glazing, Fiberglass frame
Window/wall ratio, %	S→40, N→5, W→10, E→10	S→20, N→20, W→20, E→20
Infiltration (ACH)	0,4	0,75

Cost of extra insulation and glazing material is obtained from local firms ([11], [12]). Then energy saving is calculated and cost benefit of the passive house is compared with a traditional house.

C. Co- benefits

Main benefits of passive houses are decrease in heating demand and related greenhouse gas emission. The heat loss of a passive house is so small that a standard heating system is unnecessary. However passive houses have additional benefits. These benefits are investigated and presented.

III. RESULTS AND DISCUSSION

In this section energy demand of the house estimated by the software are given and in order to analysis cost benefits model is compared with a traditional house. Finally, co-benefits of the house are investigated.

A. Passive House Model Development

Model of the house is developed by using the detailed information given in section II-A. After the development of model, U values of the construction materials are found as given in Table 6.

Table 6: U values of the construction materials in passive house

Construction	U Value, W/m ² K
Roof	0,085
Exteriors Walls	0,091
Basement	0,180

When Table 3 and Table 6 are compared, U values of roof and exterior walls are smaller than the expected which means a better resistance. However U value of basement is found to be a bit larger than expected which means almost identical or slightly smaller resistance.

B. Heating and Primary energy requirement

Heating and primary energy demand of the house is estimated as 12 kWh/m²-yr and 54 kWh/m²-yr by the simulations conducted which shows that the model house reaches “passive house” standard. In case of 0,95 efficiency boiler is fired and higher heating value of the natural gas is taken as 9155 kcal/m³ (10,62 kWh/ m³) [13] 1,2 m³/m²-year NG is fired for heating which is lower than the “1,5 m³/m²-year” amount set by passive house institute [14].

Primary energy demand of the passive house is close to the primary energy demand of the passive house in Bulgaria Sofia.

Heating and primary energy demand of the traditional house is estimated as 81 kWh/m²-yr and 125 kWh/m²-yr by the simulations conducted which shows that the traditional house is in B energy class.

Ankara is in III. zone of Turkey according to heating degree-day zones. Reference Indicator (RI) According to Primary Energy (kWh/m²-yr) for III. zone of Turkey in “Regulations on Energy Performance in Buildings” is 285 kWh/m²-year for single detached homes. RI of an B energy class building is 0,6×RI. Therefore RI of Ankara is between 114 and 171 kWh/m²-yr for single detached homes in B energy class which shows the energy class of the traditional house is B.

Energy demands of passive and traditional house are given in Figure3.

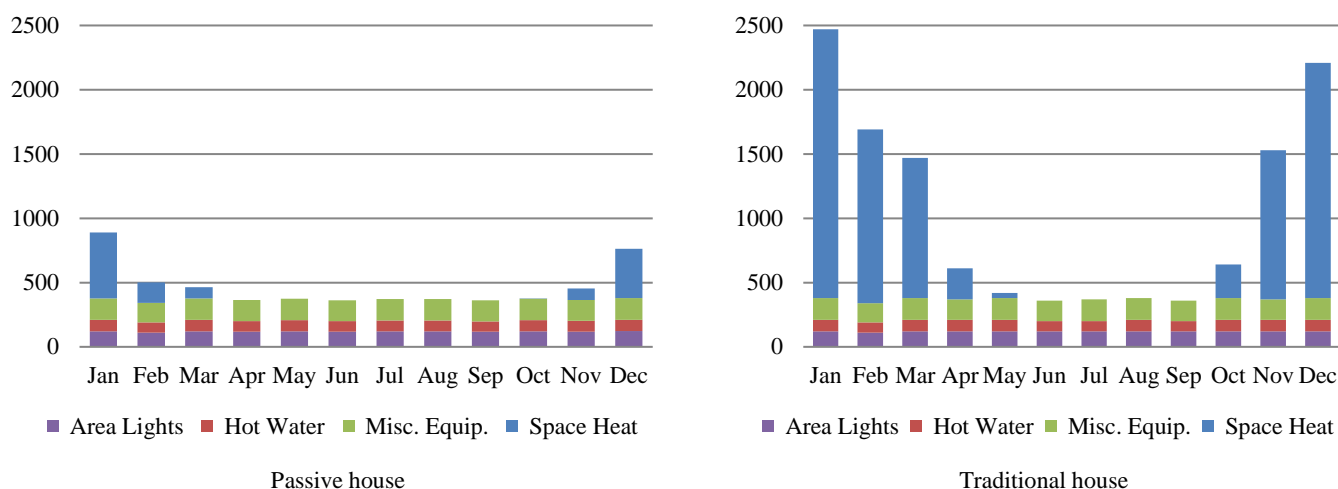


Figure3: Primary energy demand of the model passive and traditional house

C. Cost benefits

According to the results obtained in simulations heating demands of the passive and traditional house are estimated as 1.233 kWh/year and 8060 kWh/year respectively, difference of which is 6827 kWh/year. Main heating equipment operated in Ankara is Natural Gas (NG) fired boiler. In case of 0,95 efficiency boiler is fired and higher heating value of the natural gas is taken as 9155 kcal/m³ (10,62 kWh/ m³) [13] 698 m³/year NG is saved in passive house compared to traditional house. NG price in Ankara at October 2018 is 1,36 TL/m³ [13]. Therefore energy saving due to heating demand costs 951 TL/year. Construction costs of the materials given in Table 5 are tabulated in Table 7.

Table 7: Cost of different materials in passive house and traditional house

Construction	Passive house, TL/m ²	Passive house, TL	Traditional house, TL/m ²	Traditional house, TL
Roof Insulation	157	15.690	11	1.053
Exterior wall	161	16.130	10	1.040
Basement	161	16.050		0
Glazing Type	183	3.567	99	1.940
Total		51.437		4.033

Table 7 shows that reaching passive house target costs 47.404 TL more than traditional house. However energy saving due to heating demand costs 951 TL/year. Therefore final cost of passive house is 46.453 TL. Even if nominal interest and inflation are assumed to be zero payback period of the passive house is calculated as more than 40 years.

The most cost efficient exterior wall insulation material in [12] is Exterior Plate insulation (52) (Thermal Conductivity Value, $\lambda=0,035$ W/mK) which is used for heat, sound insulation and fire safety purposes. Both surfaces of Exterior

Plate insulation (52) are uncoated rockwool slabs. Tip 300 roof insulation (Thermal Conductivity Value, $\lambda=0,035$ W/mK) in [12] is also the most cost efficient roof insulation material. In case of using Exterior Plate insulation (52) and Tip 300 instead of Polystyrene insulation cost analyses is recalculated and results are given in Table 8.

Table 8: Cost of different materials in passive house and traditional house

Construction	Passive house, TL/m ²	Passive house, TL	Traditional house, TL/m ²	Traditional house, TL
Roof Insulation	36	3.570	11	1.053
Exterior wall	55	5.548	10	1.040
Basement	36	3.570		0
Glazing Type	183	3.567	99	1.940
Total		16.254		4.033

Final cost of passive house in this case is 11.271 TL. If nominal interest and inflation are assumed to be zero payback period of the passive house is calculated as nearly 10 years which is acceptable duration.

C. Co- benefits

Most significant benefits of passive houses are decrease obtained in heating demand and related greenhouse gas emission. The heat loss of a passive house is so small that a standard heating system is unnecessary. However passive houses have additional benefits. In passive houses temperature variations disappear between rooms providing thermal comfort compared to traditional houses. Passive homes are heated directly by the sun, unlike solar-powered houses, which use solar power indirectly by converting sunlight to electricity.

Also protections against external noise, additional safety, lower occurrences of respiratory illnesses, and improved

leasing potential or betterment are additional benefits of passive houses [15].

Excessive decrease in primary energy demand in passive houses promote and make easy to live in a net zero energy off-grid house which means no bills and not effected by energy cut-offs.

IV. CONCLUSION

This paper reports the cost analysis and co-benefits of a passive house located in Ankara, Turkey. The results have shown that an excessive insulation is necessary in Ankara climate, since the significant part of the year for the comfort is the cold season. The aim to reduce the annual heating energy consumption to 15 kWh/m² is passed by reaching 12 kWh/m² heating demand with the application of 30 cm insulation. This paper showed that the 15 kWh/m² target of passive house standard cannot be simply exported every country, even every city. It should be considered that the insulation thickness and the ventilation rate limits, put by the standard, may be different for each region of Turkey. The passive house studied in this paper, is found that a thickness of 30 cm (U = 0,035 W/m²K) with 0,4 ACH rate was sufficient to reach 12 kWh/m² annual heating demand with payback period of 10 years compared to a traditional B energy class house.

REFERENCES

- [1] GDRE. (2018, January). Heating and Insulation Available: http://www.yegm.gov.tr/verimlilik/b_en_ver_b_2.aspx
- [2] A. N. Bulut. (2018, January). Pasif Evler & Firsatlar, Available: http://www.imsad.org/Uploads/Etkinlikler/Adana/izocam_nuri_bulut.pdf
- [3] W. Feist. (2015, January). What Can be a Passive House in Your Region with Your Climate?, Passive House Institute, Darmstadt.
- [4] D. Tiwari. (2018, April). Passive House Concept: Standard and Case study, Metropolia University of Applied Sciences.
- [5] European Commission. (2014). Shares Tool Manual Version 2014.51008. pp. 1-27. Available: https://ec.europa.eu/eurostat/documents/38154/4956088/SHA_RES2014manual.pdf/1749ab76-3685-48bb-9c37-9dea3ca51244
- [6] Passive House Institute. (2018, March). Passive House Database. Available : https://passivhausprojekte.de/index.php#s_adfa73159c0f55f1b6b68ec8f21a28c1
- [7] A. Atmaca and N. Atmaca, "Energy and Buildings Life cycle energy (LCEA) and carbon dioxide emissions (LCCO2A) assessment of two residential buildings in Gaziantep, Turkey," *Energy and Buildings*, Vol. 102, pp. 417-431, September 2015.
- [8] B. Demirel, "Pasif Ev Uygulamasinin Türkiye İçin Değerlendirilmesine Yönelik Bir Çalışma," Yüksek Lisans Tezi, Mimarlık Anabilim Dalı, İstanbul Teknik Üniversitesi, İstanbul, 2013.
- [9] I. Güçü, "Evaluation of Passive Building Design Parameters for Izmir City," Master Thesis, Dept. of Urban Regeneration, Izmir Katip Celebi Univ., Izmir, Turkey, 2016.
- [10] USDOE. (2018, January) EnergyPlus Energy Simulation Software. Available: <http://www.energyplus.gov/>
- [11] Yasasan. (2018, January). Cam fiyat listesi. Available: <http://www.yasasan.com.tr/db/liste/Is%C4%B1cam.pdf>
- [12] Izocam. (2018, January). Fiyat Listesi. Available: http://www.izogun.com/excel/2018_izocam_fiyat_listesi.pdf
- [13] Başkent Doğalgaz. (2018, January). Doğalgaz Fiyatları. Available: <https://www.baskentdogalgaz.com.tr/DogalgazFiyatYeni.aspx>
- [14] Passive House Institute. (2018, January). What is a passive house?. Available: https://passivehouse.com/02_informations/01_whatisapassivehouse/01_whatisapassivehouse.htm
- [15] M. Jakob, "Marginal costs and co benefits of energy efficiency investments The case of the Swiss residential sector," *Energy Policy*, vol. 34, pp. 172–187, January 2006.

A Fuzzy Control System Design According to the Development Periods of the Cultivated Mushroom

Vildan EVREN¹, Abdulkadir SADAY², Ilker Ali OZKAN³

¹Selcuk University, Konya, Turkey, evrenvildannn@gmail.com

²Selcuk University, Konya, Turkey, abdulkadirsaday@gmail.com

³Selcuk University, Department of Computer Engineering, Konya, Turkey, ilkerozkan@selcuk.edu.tr

Abstract – Determination of the indoor air quality of the cultivation medium in the cultivation of mushroom affects the production efficiency of mushrooms. Ventilation systems in the cultivation of mushrooms are widely used to provide the desired temperature and humidity values. The optimal temperature and humidity values for cultivation vary depending on the period. In different periods, the optimum temperature and humidity values can be controlled by controlling the ventilation system for optimum cultivation and it is important to affect the production quality and efficiency. In this study, a fuzzy control system design was made according to two different development periods of the cultivated mushroom.

Keywords – cultivated mushroom cultivation, fuzzy expert system design, fuzzy control system

I. INTRODUCTION

The ecological requirements of the plants produced in the greenhouse is vary. The ambient conditions of the greenhouse areas should be adjusted according to the optimal values of the plants to be grown. If the temperature and humidity values do not have the optimum values, it is necessary to ventilate the plant for development. Deviations in the optimal value will quickly change the course of plant development and greatly affects the quality of product yield accordingly. [1, 2].

Cultivation mushroom should be grown in places where temperature and humidity can be kept under control, easy to ventilate and do not receive sunlight. Mushroom production in greenhouses isolated against light [2, 3].

Mushroom production and cultivation has been carried out in many countries for many years. In our country, cultivated mushroom cultivation has started to become widespread in recent years and many facilities have been established. However, in most of these facilities the ambient conditions are not adjusted to the optimal value. Therefore, this situation affects the production efficiency of the mushrooms [3-5].

Fuzzy logic is a method of artificial intelligence that deals with thinking like human beings and where the experience of experts can be included in the solution of problems. The advantage of the method is that, as in classical clusters, an element belonging to a set is not 0 or 1, but is represented by membership values ranging from 0 to 1 [6]. Since the

introduction of fuzzy set theory by A. Lotfi Zadeh in 1965, the method has been applied in many fields, particularly in the fields of engineering, medicine, biology, education and economics [6, 7]. In addition, functions such as decision support systems, classification, optimization, estimation and control in agricultural areas are used for different purposes in animal and vegetable production [8, 9].

In this study, a fuzzy expert system (FES) has been designed in the cultivation of the cultivated mushroom which controls the ambient ventilation according to the optimum temperature and humidity values in different development periods. The developed fuzzy expert system has two inputs and single output and the ventilation rate is determined according to temperature and humidity rate.

II. MATERIAL-METHOD

Mushroom cultivation is divided into two periods, the period of development of micelles and the period of hat formation. Mushroom is a very selective plant in terms of climatic requirements. Especially the temperature, humidity and ventilation requirements are different in different development periods. Optimal values in each development period are within very narrow limits. The optimal value of deviation can be rapidly changed in the course of the development and the quality of product yield is greatly affected accordingly [10].

For this purpose, a fuzzy expert system (FES) has been designed for the development period of the mushroom micelles and for the period of hat formation. Developed fuzzy expert system has two inputs and single output and the amount of ventilation is determined according to temperature and humidity rate. When watering in mushroom production, water drops may occur on the mushrooms depending on the humidity and temperature. Failure to perform ventilation results in bacterial growth on mushrooms.

The general structure of the fuzzy expert system, which is developed to provide optimum temperature and humidity levels for mushroom cultivation, is given in Figure 1.

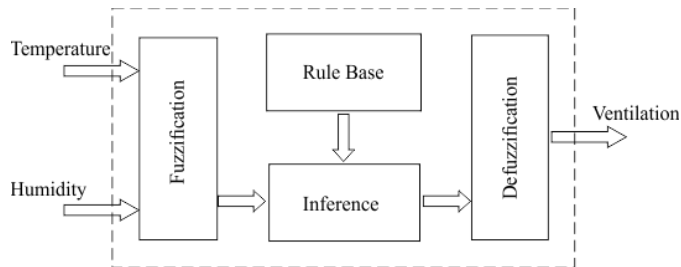


Fig 1: Developed fuzzy expert system structure.

The limit values of the parameters in the micelle development stage of mushrooms are as follows [1]:

- Temperature = [19-30 °C]
- Humidity = [50-110 %]

The best temperature for micelle development is between 23-25 °C. There is a regression in micelle development above and below these temperature values. Development stops at 28 °C and micelles die at 30 °C. For mushroom development, both soil moisture and air relative humidity must be high. Humidity is one of the most important reasons for the occurrence of mushrooms in nature in certain periods. Mushrooms usually become active in the periods when the soil and air are moist after the rains, and they start to develop and form hats. Proportional air humidity should be in the 70-90% range for the development of mushroom micelles. At a lower humidity rate, the compost loses water and slows the development of the micelle. At higher humidity, a favorable environment is created for the development of many diseases in the mushroom. [1, 5, 10].

The main purpose of ventilation is to remove the carbon dioxide accumulated in the atmosphere and replace with fresh air. Ventilation helps to maintain and regularly regulate the humidity and temperature level in the atmosphere. Normal growth is observed when the amount of carbon dioxide in the air is between 0.03% and 2%. As the ratio increases, the micelle development slows down. After 2%, the development stops [1].

The limit values of the parameters in the hat formation phase of mushrooms are as follows:

- Temperature = [12.5-17.5 °C]
- Humidity = [55-92 %]

In the second stage of development, the temperature demand of the mushroom is lower during the period of hat-forming. The optimum temperature at this stage should be in the range of 14-16 °C. When this temperature value falls below or exceeded, both production and quality are affected. The rise in temperature to 18 °C results a reduction in overall efficiency and may lead to various diseases [1].

The mushrooms should have 70-80% moisture during the hat formation period. The ventilation rate should be between 0.03% and 0.1%. Among these values, hat formation occurs normally. The ventilation affects the development of mushroom abnormally when rate is between 1.0% and 1.8%. The stems of the mushrooms become thinner and longer, the product quality decreases [1].

A fuzzy control system has been developed for both periods in the development of mushrooms. The developed fuzzy control systems have two inputs and single output and determine which stage and ratio of the ventilation fans, which provide fresh air to the environment according to the temperature and humidity

values in the development environment. Control speed of the ventilation fan is provided between [0-100] per minute.

In the developed fuzzy control system, linguistic expressions are determined as Low (L), Medium (M) and High (H).

The limit values and linguistic expressions of the input and output parameters of the control system are given in Table 1 and 2, respectively, for the micelle development period and the hat development period.

Table 1: Limits and linguistic expressions of the system parameters of micelle period.

Parameter	Linguistic Expression	Min	Max
Humidity	L, M, H	50	110
Temperature	L, M, H	19	30
Ventilation	L, M, H	0	100

Table 2: Limits and linguistic expressions of system parameters of hat period.

Parameter	Linguistic Expression	Min	Max
Humidity	L, M, H	55	95
Temperature	L, M, H	12	18
Ventilation	L, M, H	0	100

The linguistic expressions of the input and output variables of the control system were created using the Matlab Fuzzy Logic toolbox [11]. Temperature, humidity and ventilation fan parameters belonging to the micelle period are given in Figure 2-4. The membership functions of the hat period parameters were created similar to the micelle period.

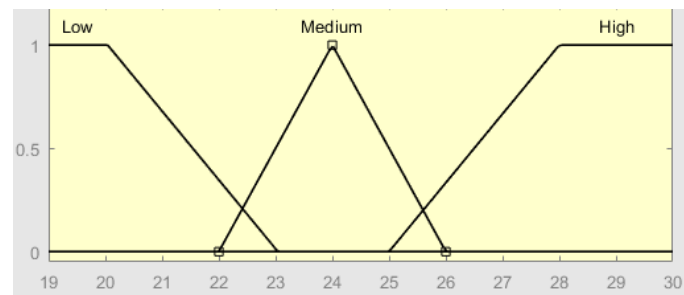


Fig 2: Membership functions of temperature.

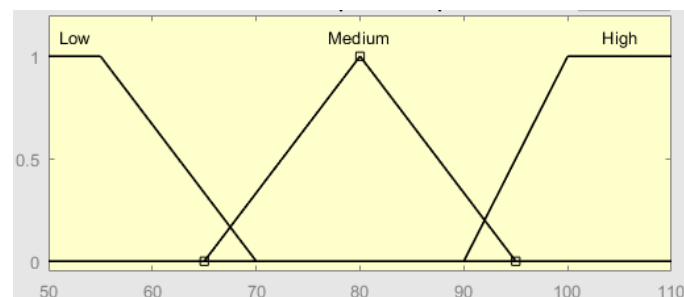


Fig 3: Membership functions of humidity.

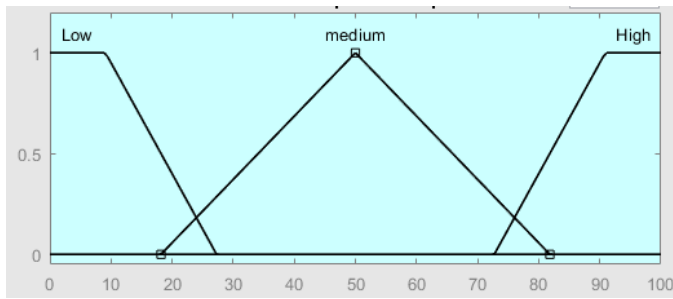


Fig 4: Membership functions of ventilation.

In the control system, Mamdani min-max is used as an inference mechanism. In our study, Centroid (Centroid) method was used to clarification process because of successful results in fuzzy control systems. [12]. In this method, the weighted averages of the membership functions of the fuzzy clusters that make up the output are multiplied by the maximum membership value they have [8]. The elution by weighted average method is given in Figure 5.

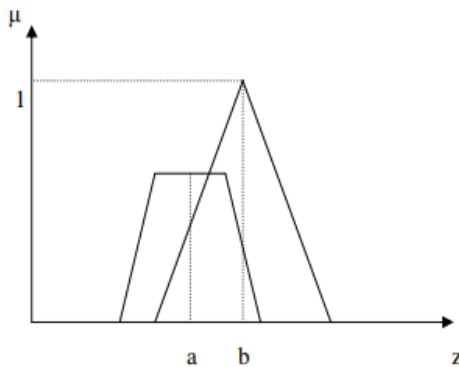


Fig 5: Clarification with weighted averaging method.

III. RESULTS

Cultivated mushrooms ecological requirements are vary according to the biological structure of the mushrooms. In accordance with these differences, the control of the environment directly affects the product efficiency. In order to increase product productivity, two different fuzzy expert system designs have been made in order to provide condition differences in micelle development and hat formation periods.

In the designed FES, temperature values are assigned as input parameters and ventilation values are assigned as output parameters. Cultivation conditions vary according to the type of mushrooms. In this study, the cultivated mushroom type is discussed. Cultivated mushroom cultivation were studied in two periods as micelle development period and the period after hat formation. For both periods, temperature, humidity and ventilation rates were determined separately.

According to the fuzzy rule base created, simulation graphs are created to determine the effect of the input parameters on the output systems. Charts created with Fuzzy Logic Toolbox Surface Viewer are shown in Figure 6 for micelle period and Figure 7 for hat period.

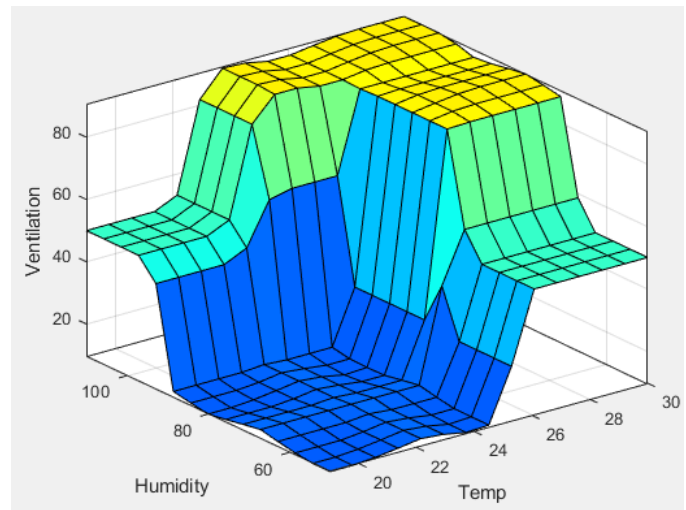


Fig 6. Humidity - temperature for ventilation (micelle period)

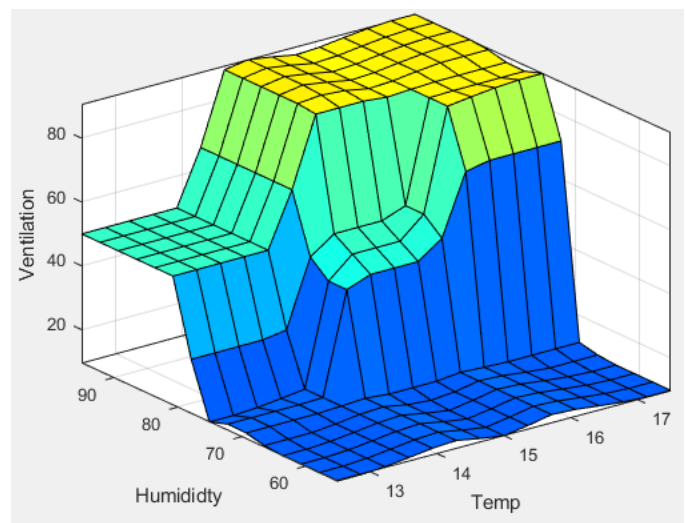


Fig 7. Humidity - temperature for ventilation (hat period)

For example, in a fuzzy expert system, an environment with a temperature of 24 °C and humidity of 80% in micelle period ventilation was 9.58. The result of the fuzzy expert system obtained for ambient values of 24 °C and humidity of 80% is given in Figure 8.

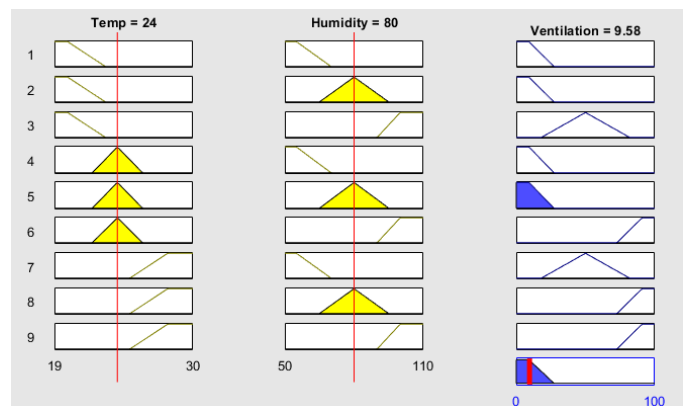


Fig 8: Fuzzy expert system result with Centroid rinse method.

The ventilation and temperature graph of the environment, which has 80% humidity, is given in Figure 9.

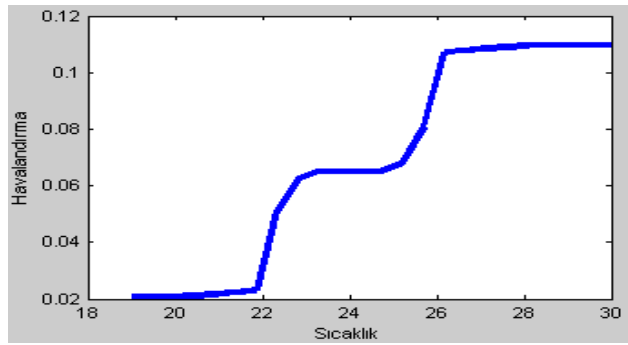


Fig 9: Micelle development period ventilation - temperature graph.

The amount of ventilation of an environment in which the temperature was 15 °C and the humidity was 71.2% was obtained as a value of 39.4 in the developed fuzzy expert system. The results of the fuzzy expert system obtained for these values are given in Figure 10.

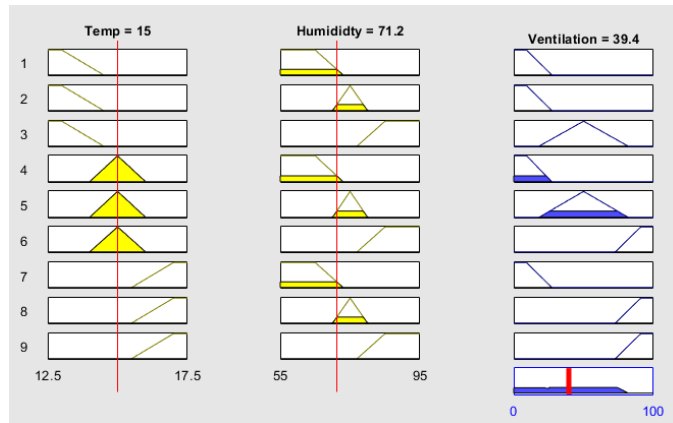


Fig 10: The result of the FES with the Centroid rinse method.

The ventilation and temperature graph of the environment, which has a humidity of 80% for the hat formation period is given in Figure 11.

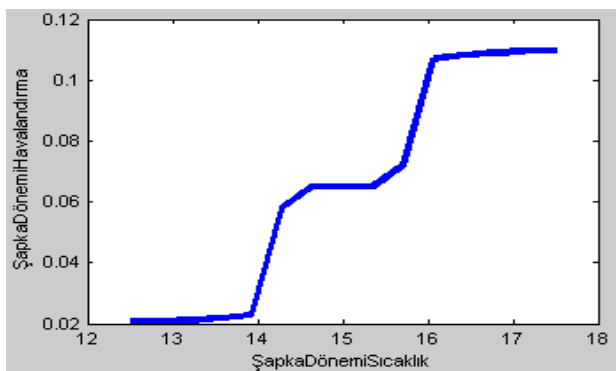


Fig 11: Ventilation - temperature graph of hat formation period.

When the control results obtained are examined, it can be seen that fuzzy control systems developed for different periods are such that they meet the needs of the development period of the cultivate mushroom. For example, in the period of micelle

ventilation works less at the 20 °C but during the period of hat development ventilation works with full capacity at the same temperature value.

In subsequent studies, the number of input and output parameters and membership functions can be increased for better efficiency. For example, it can be improved by adding parameter of irrigation amount as output parameter according to ambient conditions. Control of the amount of ventilation and irrigation according to the input parameters soil moisture and soil temperature values will help to achieve better results in efficient cultivation of the cultivated mushrooms.

REFERENCES

- [1] C. Özdemir. (2010). *Mantar Yetiştiriciliği*. Available: <http://traglor.cu.edu.tr/objects/objectFile/vLQG2sna-3122012-44.pdf>
- [2] Ş. Oluklu and B. Kibar, "Pleurotus eryngii Mantarının Optimum Misel Gelişim Koşullarının Belirlenmesi," *Iğdır Üniversitesi Fen Bilimleri Enstitüsü Dergisi*, vol. 6, pp. 17-25.
- [3] A. G. Özkul, "Kültür Mantarı İklimlendirme Tesisatı," presented at the IV. Ulusal Tesisat Mühendisliği Kongresi ve Sergisi, İzmir, Turkey, 1999.
- [4] N. C. E. Z. Dernek, "Alternatif Besin Mantar Üretim Ve Tüketimde Karşılaşılan Sorunlar Ve Çözüm Önerileri."
- [5] E. Eren and A. Pekşen, "Türkiye'de kültür mantarı üretimi, sorunları ve çözüm yolları. 1," *Ulusal Mikoloji Günleri (1-4 Eylül 2014) Özet Kitabı*, 2014.
- [6] G. Klir and B. Yuan, *Fuzzy sets and fuzzy logic* vol. 4: Prentice hall New Jersey, 1995.
- [7] C. W. De Silva, *Intelligent control: fuzzy logic applications*: CRC press, 2018.
- [8] U. Karadavut and A. Akkaptan, "Bitkisel üretimde bulanık mantık uygulamaları," *Türk Bilimsel Derlemeler Dergisi*, pp. 77-82, 2012.
- [9] S. Dubey, R. Pandey, and S. Gautam, "Literature review on fuzzy expert system in agriculture," *International Journal of Soft Computing and Engineering*, vol. 2, pp. 289-291, 2013.
- [10] E. Eren, M. Çetin, L. Türkler, and O. Öz, "Kültür mantarı yetiştiriciliğinde iklimlendirme ve otomasyonu," ed: İklim, 2011.
- [11] J. R. Jang, *MATLAB: Fuzzy logic toolbox user's guide: Version 1*: Math Works, 1997.
- [12] R. Mikail, "Tuzlu toprakların ıslahı için bir bulanık uzman sistem tasarımı," Selçuk Üniversitesi Fen Bilimleri Enstitüsü, 2007.

Fuzzy Logic Based Controller Design for Control of Ventilation Systems

Ilkay CINAR¹, Ilker Ali OZKAN² and Murat KOKLU²

¹ Selcuk University, Graduate School of Natural Sciences, Konya/Turkey, ilkay_cinar@hotmail.com

² Selcuk University, Konya/Turkey, {ilkerozkan, mkoklu}@selcuk.edu.tr

Abstract – The health and productivity of living things in closed areas is directly related to indoor air quality. In order to prevent the deterioration of indoor air quality, ventilation systems that enable the transfer of clean air to the inner environment or ventilation systems that enable the transfer the delivery of carbon dioxide gas to the outer environment are widely used. In cases where ventilation systems are inadequate, the increase in the amount of carbon dioxide and carbon monoxide in the inner environment can damage human health. In addition, obtaining the level of external environment with excessive ventilation can lead to unnecessary energy consumption. In this study, a system that absorbs air from the environment using carbon dioxide, oxygen and carbon monoxide values in ambient air and controls the operation of the ventilation system that gives fresh air to the environment is designed with fuzzy logic method. The overall purpose of the system is to achieve the ideal ventilation level. Two separate ventilation valves were controlled at the same time with the fuzzy control system designed in the study. The fuzzy control system was created with MATLAB Fuzzy Logic Toolbox and the operating structure of the control system had analyzed.

Keywords – Fuzzy logic control, ventilation systems, closed areas

I. INTRODUCTION

People are found in closed areas during their lives, both during work and rest. Depending on this, the simplest operation that can be done to ensure safe working environments and comfort conditions in these areas is ventilation. The ambient air is polluted by the gases and dust that occur in the working areas of the living things in the closed section due to respiration, heat dissipation and other reasons. [1].

The atmospheric air we breathe in our daily lives contains 79.04% nitrogen(n), 20.93% oxygen(O₂) and 0.03% carbon dioxide(CO₂) gases. The decrease in oxygen in closed environments is caused by the increase in the volume of other gases. If necessary measures are not taken, workers in these environments may face serious health risks. [2].

The oxygen needed to sustain our lives is colourless, odorless and tasteless. Lack of oxygen or decrease in the amount of oxygen creates difficulties in breathing.

The effect of oxygen amount in the air on human health is given in Table 1. As shown in the table, the amount of oxygen of less than 19% affects the health and efficiency of living things.

Table 1: The effect of the amount of oxygen on human [3]

O ₂ (%)	Possible impact
21	Normal breathing.
19	Almost normal breathing
17	Acceleration and strain in breathing
15	Dizziness, blurred vision, dizziness
9	Fainting or loss of consciousness
6	Decrease in breathing, then stop of the heart
0	Convulsion, contraction and death in a short time

Carbon dioxide is an odorless and colorless suffocating gas. It's heavier than air, and that's why it collapses into the ground. It occurs during breathing and when a substance containing carbon burns. (coal, oil, wood etc.). The effect of carbon dioxide amount in the air on human health is given in Table 2.

Table 2: The effect of the amount of carbon dioxide on human [3]

CO ₂ (%)	Possible impact
1	There's no perceivable effect.
3	It gets harder to breathe.
5-6	Frequent and difficult breathing - headache
10	Severe pain
15	Partial loss of consciousness due to narcotic effect
18	Drowning and death
25	Death in a short time

Carbon monoxide gas, such as carbon dioxide, is another dangerous gas that is constantly spreading to the environment after the combustion process. It is impossible for carbon monoxide gas to be detected by human senses due to its odorless, colorless and tasteless properties [4, 5]. In addition, the typical first symptoms of carbon monoxide poisoning can be easily confused with these diseases because of their similarity to flu-like diseases. This situation makes it difficult for carbon monoxide to be detected and saved of humans from this situation. [6]. Because of this feature, it is a very dangerous gas called "insidious killer" in occupational safety. Table 3 shows the different concentrations related to levels of carbon monoxide gas, which has a legal limit of 50ppm, in our country.

Table 3: The effect of the amount of carbon monoxide on human [5]

Concentration In The Air (ppm)	CO Levels in the blood (%)	Symptoms and finds
35	0-10	No effect.
200	10-20	Mild headache, skin vein enlargement
400	20-30	Headache, throbbing pain in the temple
800	30-40	Severe headache, nausea, vomiting
1600	40-50	In addition, heart rate and respiration increase
3200	50-60	Coma, tachycardia
6400	60-70	Coma, respiratory depression, death
12 000	70-80	Weak pulse, respiratory failure and death

As can be seen from the tables given above, when we consider oxygen, carbon dioxide and carbon monoxide in working environments, they have different effects on people at certain intervals. When we look at Table 1, while the oxygen value increases, the positive effects on human beings, while Table 2 and Table 3 when we look at the value of carbon dioxide and carbon monoxide increases, the negative impact on human health is increasing. These values show how important ventilation systems are to keep the Specified Gas volumes at an ideal level. The air conditioning system that provides fresh air to the environment and the ventilation system that absorbs dirty ambient air to remove carbon monoxide and carbon dioxide from the environment can be controlled separately so the internal air quality can be adjusted. In this study, we aimed to design a fuzzy expert system that controls ventilation systems according to carbon dioxide, oxygen and carbon monoxide values.

In the literature, there are various studies on fuzzy logic control of ventilation systems and on fuzzy logic control of air conditioning systems. [7-10]. However, in the scanning, there was no found studying on control of ventilation systems using the values of carbon dioxide, oxygen and carbon monoxide concentration in ambient air with related to fuzzy logic.

II. MATERIAL METHOD

A. Fuzzy Logic

Fuzzy logic is a mathematical discipline based on fuzzy set theory that allows us to achieve the structure we use every day and interpret our behavior. The basis of fuzzy logic is a set of fuzzy set theory, in which the values "true" and "false" are determined. Here again, as in the traditional logic, there are values "1" and "0". However, fuzzy logic is not only confined oneself to these values but also uses their intermediate values (values between 0 and 1). Fuzzy logic says that a distance is not only close or distant, but also how close or how far away it is. Fuzzy set theory is a mathematical theory aimed at expressing uncertainty in the form of "less cold" or "close to cold" between the "warm" and "cold" statements, for example. There is also a non-clear numerical value behind these linguistic values [11-13].

This approach was first introduced in 1965 under the name of

fuzzy logic or fuzzy set theory in an article published by Lotfi Zadeh from the University of California at the United States. [12].

B. Fuzzy Logic Control

Fuzzy Logic Control focuses on gaining an intuitive understanding of how to best control the process or plant. Fuzzy logic control is not a mathematical process model. As a matter of fact, it is the rule that the input and output sizes are processed on the basis of formulation of the sizes belonging to the grammatical structure [14-16].

As seen in Figure 1, the fuzzy logic control system consists of fuzzification, inference mechanism and defuzzification.

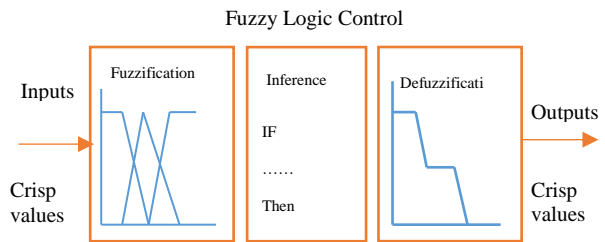


Figure 1: Fuzzy logic control system [17].

1) Fuzzification

Fuzzification is the process of converting control input information received from the system to symbolic values that are linguistic qualifiers.

Membership functions are mathematical models that are used to solve fuzzy problems more easily and to calculate them easily. The most important of these functions are triangular, trapezoid, gaussian, bell curve and sigmoidal membership functions [11, 15].

In this study, triangular and trapezoidal membership functions were used for linguistic expressions given in equations 1 and 2 respectively.

$$Triangular(x; a, b, c) = \begin{cases} a \leq x \leq b & \Rightarrow \frac{x-a}{b-a} \\ b \leq x \leq c & \Rightarrow \frac{c-x}{c-b} \\ x < a \text{ and } x > c & \Rightarrow 0 \end{cases} \quad (1)$$

$$Tramp(x; a, b, c) = \begin{cases} a \leq x \leq b & \Rightarrow \frac{x-a}{b-a} \\ b \leq x \leq c & \Rightarrow \frac{c-x}{c-b} \\ x < a \text{ and } x > c & \Rightarrow 0 \end{cases} \quad (2)$$

2) Fuzzy Rules

The fuzzy rule base consists of a combination of several rules that can be changed proportionally according to the complexity of the application. The rules are usually represented in the structure "IF necessary-THEN action". Each rule connects an input data to an output data. Operations on this volume are performed on fuzzification data [18].

Fuzzy membership degrees from the fuzzification unit are evaluated according to verbal rules and results are obtained.

The rule-based inference mechanism created by the experts according to the verbal rules constitutes the most important part of the fuzzy logic controller design. Each rule within this structure provides a control that corresponds to a certain part of the system to be inspected. By using all rules together, a rule base expressing the whole system model is revealed [19].

In our study, Mamdani method was used for inference mechanism. Figure 2 is shown the structure of Mamdani inference method.

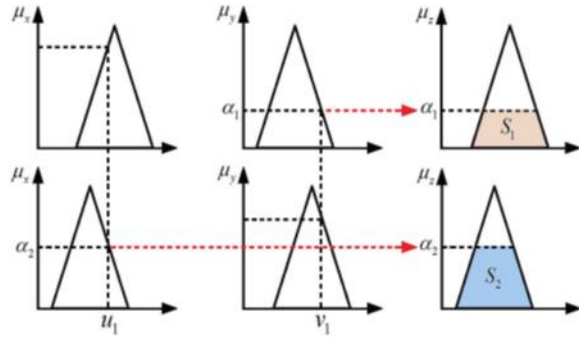


Figure 2: The structure of Mamdani fuzzy inference method [19].

In the Mamdani inference method, the membership levels from the blur unit are associated with the output membership function using the minimum relationship operator.

3) Defuzzification

It is the unit in which fuzzy output values are converted to a problem-specific scale at the input. Centroid method, which is the most widely used defuzzification method was used in our study. Centroid method is given in Equation 3 [20].

$$x^* = \frac{\int \mu(x)dx}{\int \mu(x)dx} \tag{3}$$

Where X* represents the defuzzification value.

III. FUZZY CONTROL SYSTEM DESIGN

Developed fuzzy control system has three inputs and two outputs. hvf_1, which attracts polluted air in the environment according to the oxygen and carbon dioxide percentages and carbon monoxide values in the working environment, is hvf_2 ventilation fans that provide fresh air to the environment. Thanks to the fuzzy logic system developed, it has been determined at which stage and at which rate will operate of the ventilation fans. The fuzzy expert system structure developed is shown in Figure 3.

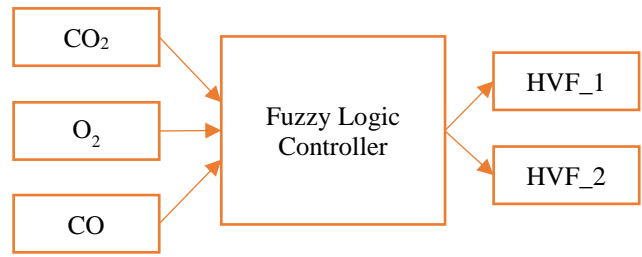


Figure 3: Developed Fuzzy Expert System Structure.

As indicated in Table 2, carbon dioxide gas has a death effect on human health after 18% and therefore, the carbon dioxide parameter was determined as limit value [0-18]. The effects of oxygen gas on human health are important at rates below 21%, so the oxygen parameter [0-21] was determined. As shown in Table 3, since carbon monoxide gas has a fatal effect of 3200 ppm and above, the carbon monoxide parameter is determined as [0-3200].

The control of speed of revolutions per minute of the hvf_1 and hvf_2 parameters had been provided between [0-2000]. Linguistic expressions in the fuzzy control system developed were determined as normal (N), Low danger (LD), Danger (D), very danger (VD) in carbon dioxide, oxygen and carbon monoxide parameters. The linguistic expressions of the output parameters were determined as very low(vl), low(l), medium (m), high (h), and very high (VH).

The limit values and linguistic expressions of the input and output parameters of the control system are given in Table 3.

Table 3: The limit values and linguistic expressions of system parameters.

Parameter	Linguistic Expression	Min	Max
CO ₂ (%)	N,LD,D,VD	0	18
O ₂ (%)	N,LD,D,VD	0	21
CO (ppm)	N,LD,D,VD	0	3200
HVF_1 (min ⁻¹)	VL,L,M,H,VH	0	2000
HVF_2 (min ⁻¹)	VL,L,M,H,VH	0	2000

Linguistic expressions of input and output variables of the control system were created using Matlab Fuzzy Logic toolbox. The membership function graphs of the parameters of carbon dioxide, oxygen, carbon monoxide, hvf1, hvf2 are given in Figure 4-8.

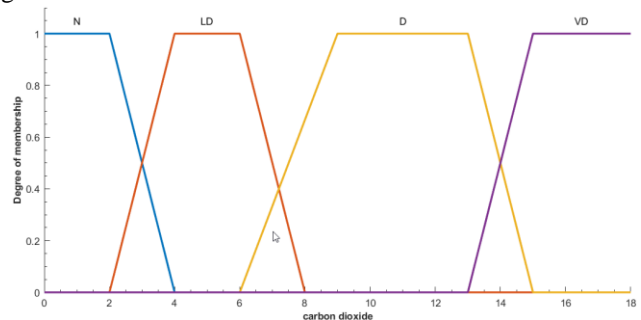


Figure 4: Membership functions of carbondioxide.

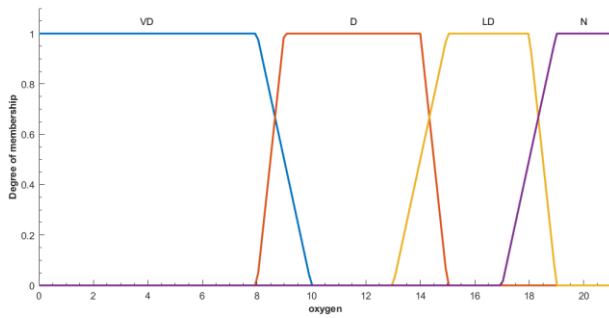


Figure 5: Membership functions of oxygen.

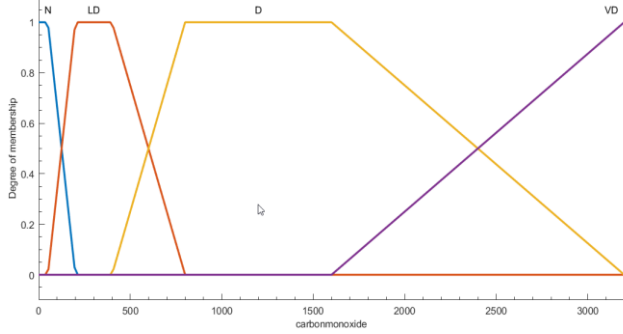


Figure 6: Membership functions of carbonmonoxide.

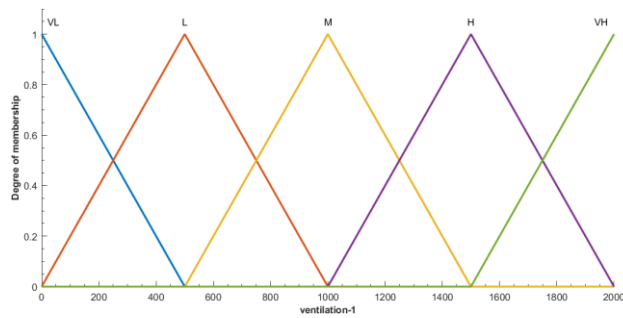


Figure 7: Membership functions of ventilation -1.

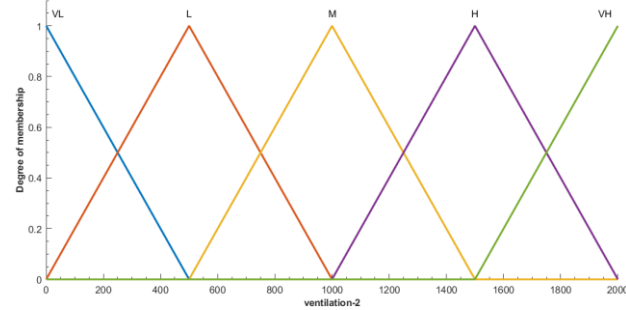


Figure 8: Membership functions of ventilation -2.

Rules for the determination of the working levels of ventilation fans hvf_1 and hvf_2 according to the carbon dioxide, oxygen and carbon monoxide values in the working environment have been prepared with the help of an occupational safety specialist. A total of 64 rules were created to cover all combinations of input variables. In the control system, Mamdani min-max as an inference mechanism has used. In our study, the Centroid method was used for defuzzification because it provides successful results in fuzzy control systems [21].

IV. RESULTS

According to the fuzzy rule base created, simulation graphs created to determine the effect of the input parameters on the output systems. The graphs created with Fuzzy Logic Toolbox Surface Viewer are given in among Figure 9-12.

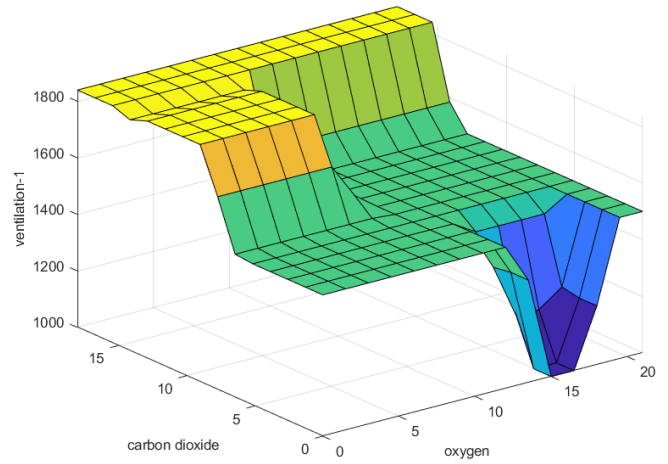


Figure 9: carbondioxide - oxygen for ventilation-1.

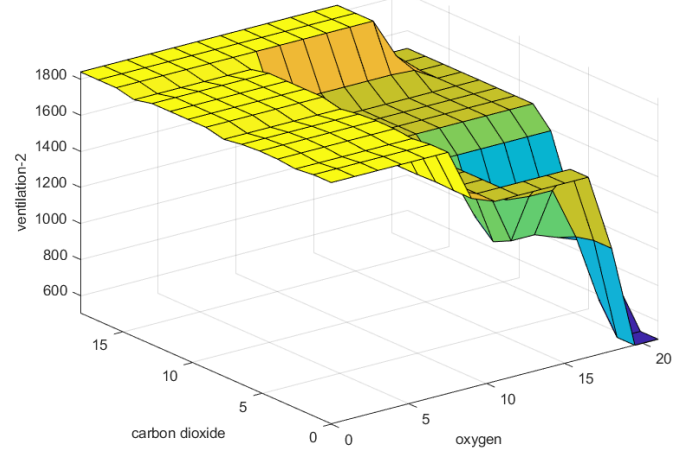


Figure 10: carbondioxide - oxygen for ventilation-2.

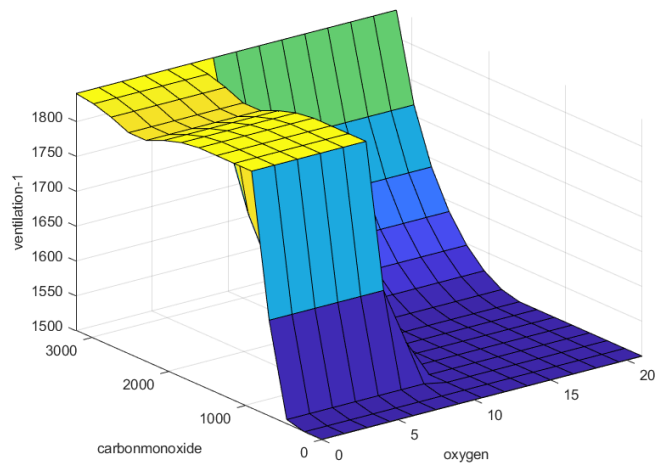


Figure 11: carbonmonoxide - oxygen for ventilation-1.

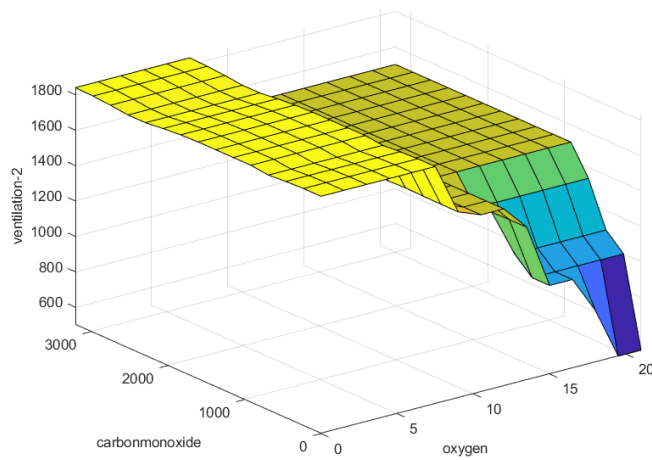


Figure 12: carbonmonoxide- oxygen for ventilation-2.

To test the proposed fuzzy control based ventilation system, carbon dioxide 3%, oxygen 13.7% and carbon monoxide 30 ppm signal values were used. Fuzzy rules have been calculated according to the signal values defined. In defuzzification, R05, R09, R21, and R25 rules are fired. At the end of the process, the output speed of ventilation 1 and ventilation 2 has been rinsed. As shown in Figure 13, 1040 min^{-1} controller output values for ventilation-1 435 min^{-1} ventilation-2 were obtained for the given signal values.

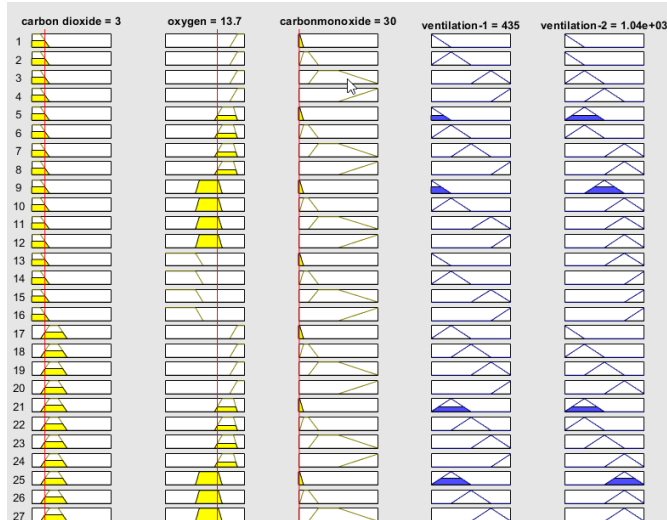


Figure 13: Fuzzy rule viewer.

In order to verify the fuzzy Model, 10 test data pairs and the resulting simulation outputs has given in Table 4.

Table 4: Test outputs of fuzzy control.

Simulation No	CO ₂ (%)	O ₂ (%)	CO (ppm)	HVF_1 (min^{-1})	HVF_2 (min^{-1})
1	5	18	80	621	448
2	7	16	45	926	705
3	6	14	56	529	1071
4	2	18	85	338	447
5	16	18	45	1840	1292
6	16	18	356	1840	1500
7	2	18	3100	1680	1250
8	2	20	65	254	162
9	7	8	45	926	1810
10	14	20	65	1560	822

When the test result outputs are analyzed, it is seen that CO₂% and CO ppm change in the environment is the most effective parameters on ventilation- 1 which draws polluted air from the environment. In the simulation 4,while the HVF_1 is 338 min^{-1} for CO₂ value 2, in the simulation 5, the HVF_1 reaches 1840 min^{-1} value for CO₂ value 16. At the same time, In the simulation 4, while the HVF_1 is 338 min^{-1} for CO value 85, in the simulation 7, the HVF_1 reaches 1680 min^{-1} value for CO value 3100.

The most effective parameter in ventilation-2 is the O₂ % values . For example, In simulation 2, while the HVF_2 is 705 min^{-1} for O₂ value 16, in simulation 9, the HVF_2 rises to 1810 min^{-1} value for O₂ value 8.

In addition, the change in carbon monoxide values in simulation 5 and 6 and the change in carbon dioxide values in simulation 8 and 10 can be seen that effects on HVF_2.

V. CONCLUSIONS

In this study, fuzzy ventilation control system was performed in order to ensure indoor air quality. Carbon dioxide, oxygen and carbon monoxide variables in the indoor environment are also affected by the ventilation system. Despite this interaction, a complex ventilation system with fuzzy logic approach has been successfully checked. In addition, in order to design an optimum system, an intuitive knowledge of input and output parameters has been sufficient.

In later studies, other gases which may be present in the ambient air can be added to the system and a more effective control result can be obtained by increasing the input and output parameters in the fuzzy expert system. It will also help to achieve more successful results by increasing the number of membership functions.

REFERENCES

- [1] I. Ekmekçi, "The importance of ventilation in the perspective of OSH in chemistry sector," *Istanbul Commerce University, Journal of Science*, vol. 16, no. 32, pp. 65-76, 2017.
- [2] A. R. ERGUN, and İ. Sağlığı, "YERALTI MADEN İŞLETMELERİNDE GAZ VE TOZ PATLAMALARI VE ÖNLEMLER."
- [3] M. DURŞEN, and B. YASUN, "Yeraltı Madenlerinde Bulunan Zararlı Gazlar ve Metan Drenajı," 2012.
- [4] S. Metin, Ş. Yıldız, T. Çakmak, and Ş. Demirbaş, "2010 Yılında Türkiye'de Karbonmonoksit Zehirlenmesinin Sıklığı," *TAF Preventive Medicine Bulletin*, vol. 10, no. 5, 2011.

- [5] F. T. Sönmez, "Karbon Monoksit Zehirlenmesi: Klinik Bulgular, Sonuçlar, İzlem, Zehirlenme Tanısı ve Tedavisi," *Konuralp Tıp Dergisi*, vol. 7, no. 3, 2015.
- [6] "GAZLARLA İLGİLİ ZARARLI ORTAMLAR VE GAZ GÜVENLİĞİ," 2018; http://www.maden.org.tr/genel/bizden_detay.php?kod=8735.
- [7] R. Gates, K. Chao, and N. Sigrimis, "Identifying design parameters for fuzzy control of staged ventilation control systems," *Computers and Electronics in Agriculture*, vol. 31, no. 1, pp. 61-74, 2001.
- [8] J. Schäublin, M. Derighetti, P. Feigenwinter, S. Petersen-Felix, and A. Zbinden, "Fuzzy logic control of mechanical ventilation during anaesthesia," *British journal of anaesthesia*, vol. 77, no. 5, pp. 636-641, 1996.
- [9] H. Guler, and F. Ata, "The comparison of manual and LabVIEW-based fuzzy control on mechanical ventilation," *Proceedings of the Institution of Mechanical Engineers, Part H: Journal of Engineering in Medicine*, vol. 228, no. 9, pp. 916-925, 2014.
- [10] S. Yordanova, D. Merazchiev, and L. Jain, "A two-variable fuzzy control design with application to an air-conditioning system," *IEEE Transactions on fuzzy systems*, vol. 23, no. 2, pp. 474-481, 2015.
- [11] K. Tanaka, "An introduction to fuzzy logic for practical applications," 1997.
- [12] R. Mikail, "Tuzlu toprakların ıslahı için bir bulanık uzman sistem tasarımı," Selçuk Üniversitesi Fen Bilimleri Enstitüsü, 2007.
- [13] M. M. Adnan, A. Sarkheyli, A. M. Zain, and H. Haron, "Fuzzy logic for modeling machining process: a review," *Artificial Intelligence Review*, vol. 43, no. 3, pp. 345-379, 2015.
- [14] A. Kaur, and A. Kaur, "Comparison of fuzzy logic and neuro-fuzzy algorithms for air conditioning system," *International journal of soft computing and engineering*, vol. 2, no. 1, pp. 417-20, 2012.
- [15] C. W. De Silva, *Intelligent control: fuzzy logic applications*: CRC press, 2018.
- [16] C.-C. Lee, "Fuzzy logic in control systems: fuzzy logic controller. I," *IEEE Transactions on systems, man, and cybernetics*, vol. 20, no. 2, pp. 404-418, 1990.
- [17] Ö. Karal, "JAVA ortamında bulanık mantık kontrol: Kamyon yükleme-boşaltma uygulaması," Pamukkale Üniversitesi Fen Bilimleri Enstitüsü, 2004.
- [18] N. Güner, and E. Çomak, "Investigating Mathematics Attitude for High School Students by Using Fuzzy Logic Method," *Pamukkale University Journal of Engineering Sciences*, vol. 20, no. 5, pp. 189-196.
- [19] S. Ünsal, and I. Aliskan, "Performance Analysis of Fuzzy Logic Controllers Having Mamdani and Takagi- Sugeno Inference Methods By Using Unique Software and Toolbox," in *Electrical, Electronics and Biomedical Engineering (ELECO), 2016 National Conference 2016*.
- [20] İ. Ertuğrul, "AKADEMİK PERFORMANS DEĞERLENDİRMEDE BULANIK MANTIK YAKLAŞIMI," *Atatürk Üniversitesi İktisadi ve İdari Bilimler Dergisi*, vol. 20, no. 1, 2006.
- [21] D. Saletic, D. Velasevic, and N. Mastorakis, "Analysis of basic defuzzification techniques." pp. 7-14.

Pyramid Shaped Net Zero Energy Dormitory Building Design

M. ALTIN¹ and G. N. GUGUL²

¹Konya Technical University, Higher School of Vocational and Technical Sciences, Konya/Turkey,
maltin@ktun.edu.tr

²Selcuk University, Faculty of Technology, Computer Engineering Department, Konya/Turkey,
gul.gugul@selcuk.edu.tr

Abstract -

Pyramid shaped buildings take advantage of solar radiation and day light further more compared to traditional buildings. In this study a pyramid shaped net zero energy passive dormitory building is designed and system requirements of the building is calculated. Heating, electricity and hot water demand of the dormitory building is supplied by PV/T panels integrated on exterior wall of the building. Electricity consumption of the dormitory is estimated as 286 kWh/day whereas heating demand is calculated as 62 MWh/year. The PV/T system to raise this building to net zero energy building standard is calculated as nearly 34 kW system composed of 135 PV panels with an area of 338 m² coated on exterior wall. One side of building on where panes can be mounted is 350 m². Therefore, only south façade of the building is enough for panel installation and this system raises dormitory to net zero energy passive building standard.

Keywords – Pyramid building, net zero energy, passive house, PV/T

I. INTRODUCTION

PYRAMID shaped buildings are considered as the most convenient symbol of green buildings due to their sustainable structural system, rely on natural ventilation and light and harmony with their surroundings [1]. Pyramid shaped buildings are more stable however cost more to construct compared to square shaped buildings. The inclined external walls tend to gain more solar energy and daylight through windows installed on the external walls which results in an increase in the efficiency of solar panels installed on the external walls. In addition to energy efficiency, the presence of windows and daylight will improve physiological responses (decrease blood pressure and heart rate and increase oxygen saturation and body temperature), reduce sleepiness and improve mood, increase the frequency of communication and social interaction and improve performance [2].

There are many buildings built in pyramid shape in recent years in the world. The Muttart Conservatory is a botanical garden located in Edmonton, Alberta, Canada which consist our feature pyramids for display of plant species found across three biomes, with the fourth pyramid hosting as a seasonal display [3]. A solar power system installed on a pyramid-shaped office building in Scotland, U.K., has been shortlisted in the Solar

Power Portal Award under the category "Most Innovative System Design" [4]. VIA 57 West is a pyramid shaped high-rise residential building offering 709 residential units with a lush garden at the heart of the building in New York [5].

The aim of this research work is to develop a net zero energy passive dormitory building design incorporating with Photovoltaic hybrid collectors as a source of renewable energy.

II. METHODOLOGY

In this section methods followed during development of the architecture and construction properties, final energy demand and demand model of the dormitory building in Konya climate are described in order to satisfy net zero energy and passive building standards.

A. Architectural plan

Architectural plan of the dormitory building is developed in pyramid shape in order to take advantage of sunlight in maximal level. Dormitory building is designed as four floors. Detailed information about area and number of people can reside are given in Table 1.

Table 1: Detailed information about building area

	Area, m ²	Intended purpose	Number of people
Basement	2560	Garage	-
Ground floor	1860	Dormitory	72
1 st floor	1400	Dormitory	46
2 nd floor	1000	Dormitory	38
3 rd floor	650	Dormitory	30
4 th floor	375	Conference room and cafeteria	-

B. Construction materials

Construction materials of the building are decided according to a developed passive house model in building simulation software environment for Konya climate and given in Table 2.

Table 2: Construction materials of the building

Construction	Material (Ordered from outside to inside)	Thickness (mm)	Thermal Conductivity, W / m-K	Thermal Resistance, Ri (m ² K / W)	Thermal conductivity coefficient, U, (W / m ² K)
Exterior wall	Polywood	16	0,115	0,138	0,057
	Polyisocyanurate	305	0,020	15,110	
	E Wall Cons Material 2	NA	NA	0,980	
	Polyisocyanurate	25	0,020	1,254	
	GYPBd 1/2 in (GP01)	13	0,160	0,080	
	Total			17,482	
Roof (Ceiling)	Blt-Up Roof 3/8 in (BR01)	9	0,162	0,058	0,055
	Polyisocyanurate	305	0,020	15,110	
	Polywood	16	0,115	0,138	
	Roof Cons Mat 4	NA	NA	2,940	
	GYPBd 5/8 in (GP02)	16	0,160	0,099	
	Total	0	0,000	18,345	
Glazing	Glazing	3	0,800	0,004	1,135
	Argon gas	12	0,028	0,435	
	Glazing	3	0,800	0,004	
	Argon gas	12	0,028	0,435	
	Glazing	3	0,800	0,004	
	Total		0,000	0,881	
Basement	Light Soil, Damp 12 in	305	0,862	0,354	0,063
	Concrete	305	1,724	0,177	
	Polyisocyanurate	305	0,020	15,110	
	Polywood 1 in (PW06)	25	0,115	0,220	
	Total			15,860	

C.2 Heat Gain

The increase in the ambient temperature due to the heat gain from electrical appliances, lighting and people cause an increase in internal temperature and heat gain are taken into account in heat demand calculation.

There are 166 student reside in dormitory. In addition to students, number of staff is assumed to be 10. Heat gain from people is calculated by using the heat gain activity in the ASHRAE catalog [6] given in **Hata! Başvuru kaynağı bulunamadı.** and equation (1).

$$HG_p = (HG_s \times N_p \times t) + (HG_l \times N_p \times t) \quad (1)$$

In this equation;

HG_p : Heat gain from people, Wh/day

HG_s : Sensible heat gain type, W

HG_l : Latent heat gain type, W

N_p : Number of people

t : Duration, hour

C.3 Electricity Demand

Electricity demand of the building is calculated by using the electrical appliances in building, their power values and usage durations.

C.3 Electricity Production

In this study hybrid photovoltaic/thermal (PV/T) collector systems is used as renewable energy source to supply electricity, heating and hot water demand of the students due to

PV/T's solar energy conversion into electricity and heat with a single device [7]. In addition to production of electricity and hot water at the same time from one panel, another advantage of PV/T is to supply extra electricity production of at least 25% per year with cooled PV cells [8].

A study conducted to show the heat transfer performance in a hybrid photovoltaic thermal solar collector from experimental data and observed that lower cell temperature is resulting in a significant increase in the electrical performance of the system such as electrical and thermal efficiency [9].

III. RESULTS

In this section architectural drawing and energy consumption of the building are given.

A. Architectural plan

Dormitory building is developed in pyramid shape. Dormitory building is developed in light of information given in Table 1 and cross section drawings of each floor are shown in Figure 1.

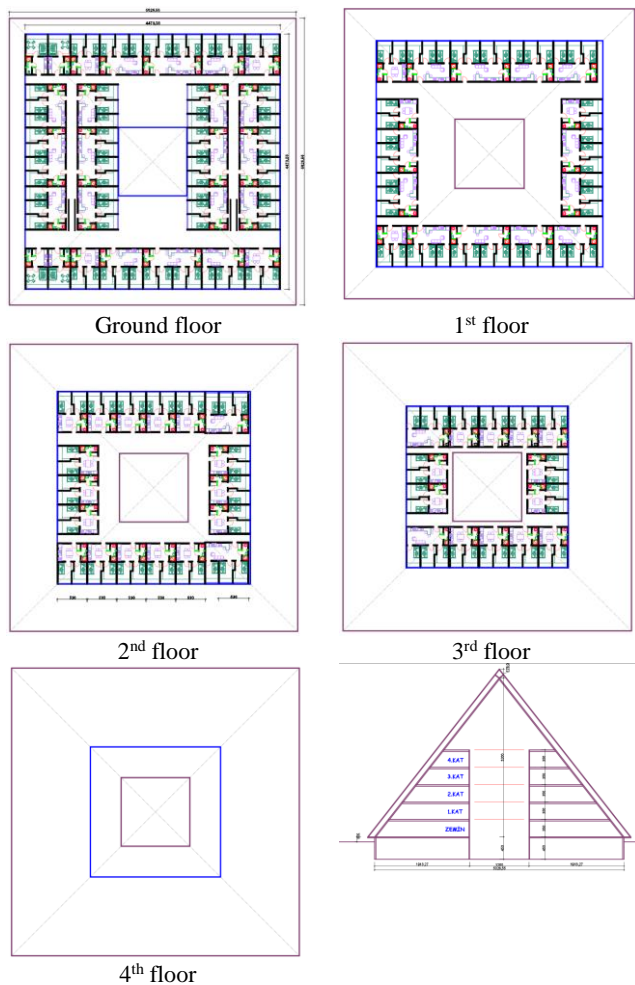


Figure 1: cross section drawing of each floor

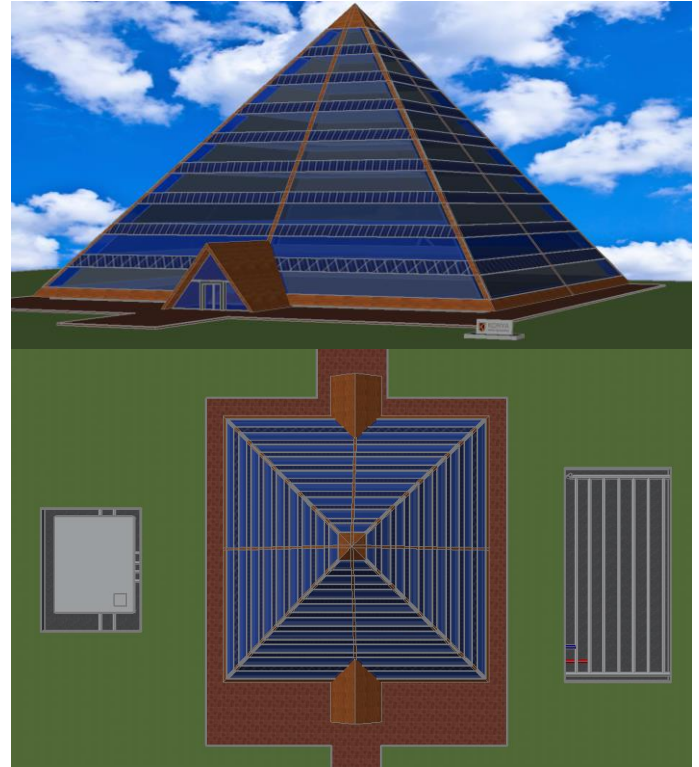


Figure 2: Exterior view of the building

B. Heat Gain and Electricity Consumption

Heat gain and electricity consumption of the dormitory are calculated by taking into account mandatory electrical appliances and shown in Table 3.

Exterior view of the building is given in Figure 2.

Table 3: Heat gain and electricity consumption

	Usage Duration, h/day	Number	Heat Gain, W			Heat Gain, kWh/day	Electricity Consumption, kWh/day	Power, W
			SHG	CHG	LHG			
Refrigerator	24	74	38			67	66	38
Laptop	15	170	50			127	127	50
Charge App.	3	170	7			3	5	10
Vacuum Cleaner	5	5	840			21	30	1200
Washing Machine	5	10	166	249		8	20	416
TV	5	74	48			17	17	48
Lighting	6	120	19			14	18	25
People	15	170	65		30	242		65
Total						501	286	

Heat gain and electricity consumption of the dormitory is calculated as 501 kWh/day and 286 kWh/day as given in Table 3.

C. Renewable system Capacity

Electricity demand of the dormitory building is supplied by PV/T panels integrated on exterior wall of the building. Electricity consumption of the dormitory is calculated as 501 kWh/day as given in Table 3.

Total heated area of the dormitory is 5.285 m², as given Table 1. Therefore, daily heat gain per unit area of the dormitory is calculated as “501/5285=0,094” kWh/day-m².

Konya is located in Average Climate region, with heating degree day (HDD) between 2000<HDD <3000. According to Passive House Institute, annual heating demand of passive houses in Average Climate region [10] are nearly 12 kWh/m². Therefore, annual heating demand of the dormitory building

is assumed as 12 kWh/m² and total demand is calculated as 63,4 MWh/year. Nearly 200 days of a year heating system is operating in Konya. So daily heating demand is 317 kWh/day which is lower than heat gain. This result shows that there is no requirement for heating system.

Electricity consumption of the building is 286 kWh/day. PV/T panels produce 15% more electricity compared to PV panels which reduces electricity requirement to 243 kWh/day. Sunshine hours of Konya is nearly 7,2 h/day. Power of PV panels that can provide electricity demand is so 34 kW. Power value of each panel used is 250 W which shows number of required panels is 135. One panel cover 2,5 m² area. Finally, necessary area for PV/T panels is calculated as 338 m².

Total exterior wall area of the building on where PV/T can be mounted is 1400 m² in all sides, 350 m² in one side. Therefore, only south façade of the building is enough for panel installation.

IV. CONCLUSION

In this study a pyramid shaped net zero energy passive dormitory building is designed and system requirements of the building are determined. Electricity demand of the dormitory building is supplied by PV/T panels integrated on exterior wall of the building in all sides.

Daily heating demand of the dormitory is calculated as 317 kWh/day which is lower than heat gain. This result shows that there is no requirement for heating system. A simple air condition system can be installed for peak cold days.

Electricity consumption of the building is 286 kWh/day. PV/T panels produce 15% more electricity compared to PV panels which reduces electricity requirement to 243 kWh/day. PV system capacity that can provide electricity demand is so 34 kW composed of 135 panels which cover 338 m². One side of building on where pane can be mounted is 350 m². Therefore, only south façade of the building is enough for panel installation and this system raises dormitory to net zero energy passive building standard.

REFERENCES

- [1] M. A. El-Demirdash, The Green Pyramid Rating System, Ministry of Housing, Utilities and Urban Development, Giza, 2011.
- [2] R. S. Zadeh, M. M. Shepley, G. Williams ve S. S. E. Chung, The Impact of Windows and Daylight on Acute-Care Nurses' Physiological, Psychological, and Behavioral Health, cilt 7, no. 4, pp. 35-61, 2014.
- [3] Edmonton, Muttart Conservatory, 2018. Available: https://www.edmonton.ca/attractions_events/muttart-conservatory.aspx.
- [4] I. CLOVER, Scottish solar pyramid nominated for Solar Power Portal Award, 2013.
- [5] archdaily, VIA 57 West / BIG, 2016. Available: <https://www.archdaily.com/794950/via-57-west-big>.
- [6] IBPSA-USA, ASHRAE Standard 62.1-2007, Atlanta, 2009.
- [7] V. Tyagi, S. Kaushik ve S. Tyagi, Advancement in solar photovoltaic/thermal (PV/T) hybrid collector technology,

Renewable and Sustainable Energy Reviews, cilt 16, no. 3, pp. 1383-1398, 2012.

[8] Solimpeks-PV/T, powervolt, 2018. Available:

<http://www.solimpeks.com/product/volther-powervolt/>.

[9] A. Khelifa, K. Touafek, H. B. Moussa, I. Tabet, H. B. c. E. hocine ve H. Haloui, Analysis of a Hybrid Solar Collector Photovoltaic Thermal (PVT), Energy Procedia, cilt 74, p. 835 – 843, 2015.

[10] Passive House Institute, Passive House Database, 2018.

Available:

https://passivhausprojekte.de/index.php#s_adfa73159c0f55f1b6b68ec8f21a28c1.

Investigation of Different Reinforced Concrete Flooring and Different Building Foundation System Solutions in Terms of Building Cost

Mustafa ALTIN¹

¹ Konya Technical University, Higher School of Vocational and Technical Sciences

Selcuklu, Konya/TURKEY

maltin@ktun.edu.tr

Abstract - Computer Aided Design (CAD) programs have entered a very rapid improvement process with support of artificial intelligence. The development of computer hardware systems also affects CAD programs. Development of computer hardware provides to get fast and safe results, to present economic solutions, to prepare as many alternatives as possible and most significantly to calculate the optimum cost for designed projects. The most essential subject in stage of preparation of the design is to prepare the safest, economical and aesthetic system without making concessions. The choice of construction system for construction in the project stage, preparation of projects according to different production systems and obtaining the most cost-effective materials by preparing the quantities are the priority subjects for the producer companies. In this study, commonly used CAD program in Turkey the IdeCAD Structural ver. 8.62 was used and for a light weighted workshop both architectural and reinforced statics project was prepared. Three different flooring systems are considered for the reinforced statics project. These are normal flooring, ribbed (filler-joist floor) flooring and Beamless flooring. Continuously and Spread foundation preferences were evaluated as the building basement system. Separately reinforced concrete static projects were prepared in accordance with current regulations. For all alternatives, concrete, mold and reinforcement quantities were prepared very quickly with the CAD program and cost analyzes were made at the current unit prices. All prepared alternatives have been compared and construction of the building by using normal flooring system and Spread foundation is decided as the most appropriate choice and recommendations are made.

Keywords - Reinforced Concrete Flooring, Building Foundation System, Building Cost, Computer Aided Design

I. INTRODUCTION

ONE of the most important elements for building a constitute is the sources of funding and the most accurate use of the financing provided. A building that is decided to construct is expected to provide both aesthetic and safety and the most economical solutions. It is expected that a building to be constructed will be prepared in accordance with all the of the current regulations and will ensure the safety of living creatures. Cost savings and aesthetic concerns guide us when providing safety. Cost analyses are discussed in the project phase and the most ideal analyses are made. When the most economical analyses are made, it is also imperative that the construction be issued according to earthquake-resistant construction rules [1].

Some of the mandatory requirements of the line of business where lightweight workshops, commercial factories such as commercial plants and warehouses where simple machinery are used, take special measures in project design. Because of the different request of the working area and floor heights of the machines to be used may cause some irregularities in the buildings, it requires more precise analysis of the project to be applied. Economic, aesthetic and safety concerns make us obliged to select the most suitable project by developing alternative projects. The foundations are the first carrier structural elements of the building, taking all the loads that are riding on it and transferring it to the floor. These are the legs which carry the loads from the column and the reinforced partition at the structure and transfer them to the building floor. Building foundations; which is constructed with various materials such as stone, concrete, reinforced concrete, wood and steel are constructed by considering the ground studies, building loads, building shape and appropriate construction rules. Must be strong of the foundation structure, good examination of ground for lay of subtraction, ultimate bearing capacity calculated well. As flooring systems, the normal flooring, ribbed (Filler-joist floor) flooring, cassette flooring, Beamless are produced with alternatives such as flooring system is decided according to the best solution and requests. Computer Aided Design Programs (CAD) are widely used in the construction sector, as in other sectors, and are among the indispensable because of the rapid and alternative results.

In this study, alternative studies were carried out to prepare an economical, safe and aesthetic building in the pre-construction stage of a light-weight workshop which is planned to be built in Konya Karatay industrial zone. The building has a 500 m² residence area and consists of basement, ground floor, 1st floor and penthouse.

II. MATERIAL AND METHOD

The purpose of the light weight workshop is intended as spice processing, packaging and ready-to-use products. The building, which is the basis of the study, is in the industrial district of Konya. In order to find the most ideal cost during the design phase, all the necessary analyzes were prepared considering the 3 alternative floorings as normal, ribbed (filler-joist floor) and beamless flooring in the building conveyor system and 2 different foundation as, strip and spread foundation. The building has a 500 m² basement area. Basement floor is used as storage area. The ground floor is

designed as factory sales center, manufacturing and packaging, manager, accounting and food engineer, WC-sinks. On the 1st floor, product packaging, dust separation and product separation, on the roof floor drying and storage usage area is decided to be made. Figure 1 shows the ground floor plan of the light-weighted workshop and Figure 2 shows the building's front façade.

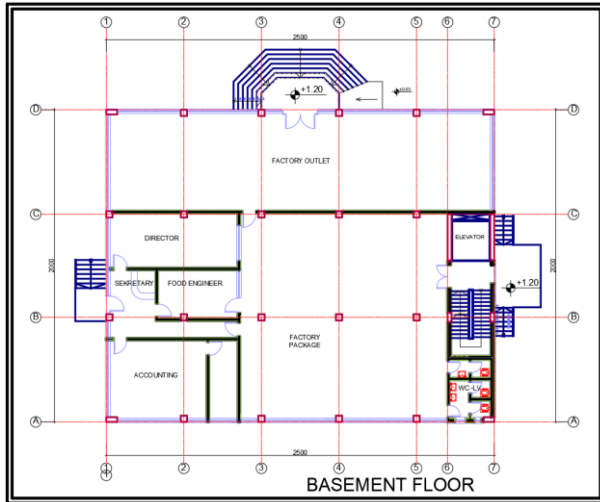


Figure 1: Basement floor plan of the building

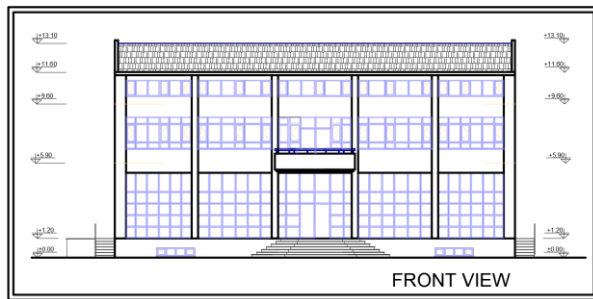
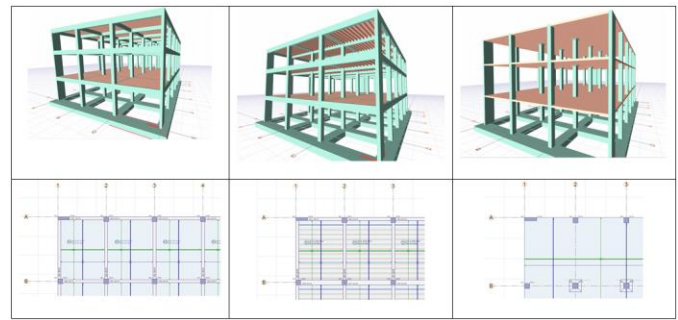
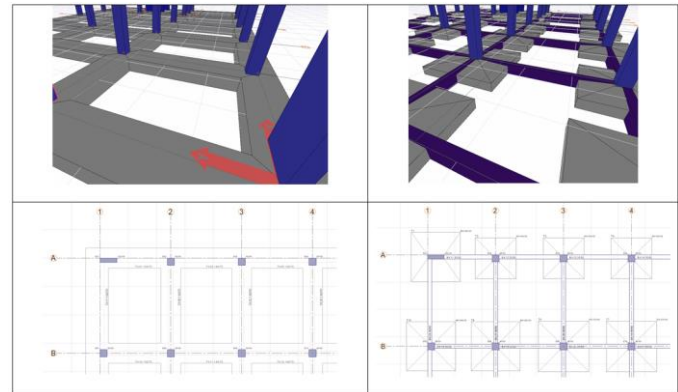


Figure 2: Front façade of the building

The lightweight workshop building is individually designed as a normal flooring, ribbed (filler-joist floor) flooring and beamless and these designs were analyzed according to both the strip foundation and spread foundation rules. System analysis are conducted for account acceptance, according to 2007 Turkish Earthquake Regulation [6], TS 498 [7] and TS 500 [8]. In the analyzes, calculations have been made by taking into consideration the earthquake-resistant construction principles and all projects are designed to be submitted to the approval of the official institution in the form of an implementation project. Both perspective and plan images of flooring types are given in Figure 3, and both perspective and plan images of foundation types are given in Figure 4.



a. Normal Flooring b. Ribbed Flooring c. Beamless Flooring
Figure 3: Flooring Types



a. Strip Foundation b. Spread Foundation
Figure 4: Foundation Types

One of the biggest advantages of the CAD program is that after the necessary analysis calculations are made, all drawing sheets of the project that are produced automatically by the program are taken automatically and made necessary arrangements and ready for approval. It is important for the time and accuracy of CAD program to give Project drawing sheets and is economical [1,9]. As a CAD program, the widely used in IdeCAD Reinforced Concrete Ver. 8.62 was used. All Structure General Information which is based on the calculations of the prepared Soil investigation reports and commercial area project are given in Table 1.

Table 1. Building general information

Building Location Information	
Building City	Konya
Building District	Karatay
Building Geometry Information	
Number of floors	3
Building Height	12.90 m
Max. Floor Height	4.70m
Max. Beam Span	6.40m
Earthquake Parameters	
Building importance coefficient/factor [I]	1.00
Load-bearing system behavioural coefficient [X/Y]	7.00
Eccentricity ratio	0.05
Earthquake Region	4
Effective ground acceleration coefficient	0.10
Soil Parameters	
Soil Type	Z3

Spectrum Characteristic Periods	Ta:0.15, Tb:0.60
Allowable bearing value	15.00 tf/m ²
Coefficient of soil reaction	2000.00 tf/m ²
Soil Group	A
Material Science	
Column	C20 - S412
Beam	C20 - S412
Slab	C20 - S412
Foundation	C20 - S412
Rules and Regulations	
TS500 (February 2000)	
DBYBHY (2007)	

The quantities of both projects were automatically taken from the CAD program and the prices of formwork, concrete and steel were determined according to the list of unit prices published annually by the 2018 Ministry of Urbanism and Environment, and according to the quantities obtained Costs are found. Table 2 shows the poz number, definitions and unit prices of 2018 in the relevant unit prices [10]. Table 3 show that Strip Foundation quantity values, Table 4 show that Spread Foundation quantity values.

Table 2. List of Unit Prices of Related Manufactures

Poz Number	Description	Price (₺)
Y.16.050/04	Concrete loss (including concrete transplantation) in C 20/25 pressure resistance class produced or purchased in concrete plant, printed with concrete pump	179.65
Y.21.001/03	Flat surface reinforced concrete formwork with plywood	48.50
Y.23.014	Y.23.014 Ø 8- Ø 12 mm ribbed concrete steel stick, cutting, bending and replacing of rods (Thick bars are considered in the same pose)	3548.84

Table 3: Quantity of quantities determined by the CAD program on the continuous foundation

Material Type	Carrier System Type Strip Foundation			Unit
	Normal Flooring	Ribbed Flooring	Beamless Flooring	
Concrete (Y.16.050/04)	628.64	605.00	623.00	m ³
Formwork (Y.21.001/03)	3234.00	2972.00	2604.00	m ²
S412 Steel (Y.23.014)	60.992	69.973	80.366	Ton

Table 4: Quantities determined by the CAD program of the spread foundation

Material Type	Carrier System Type Spread Foundation			Unit
	Normal Flooring	Ribbed Flooring	Beamless Flooring	
Concrete (Y.16.050/04)	628.64	605.00	623.00	m ³
Formwork (Y.21.001/03)	3234.00	2972.00	2604.00	m ²
S412 Steel (Y.23.014)	60.992	69.973	80.366	Ton

According to the quantities and unit prices, the related costs of the light weight Workshop building are calculated separately by using the construction forms. Table 5 shows the Strip foundation, Table 6 shows the Spread foundation cost and results.

Table 5: Strip foundation cost calculation of light weight workshop building

Material Type	Carrier System Type Strip Foundation						
	Price (₺)	Normal Flooring	Total (₺)	Ribbed Flooring	Total (₺)	Beamless Flooring	Total (₺)
Concrete (Y.16.050/04)	179.65	628.64	112935.18	606.87	109024.20	623.00	111921.95
Formwork (Y.21.001/03)	48.5	3234	156849.00	2972.00	144142.00	2604.00	126294.00
S412 Steel (Y.23.014)	3548.84	60.992	216450.85	70.612	250590.69	80,366	285206.08
Total			486235.03		503756.89		523422.03

Table 6: Spread foundation cost calculation of light weight workshop building

Material Type	Carrier System Type Spread Foundation						
	Price (₺)	Normal Flooring	Total (₺)	Ribbed Flooring	Total (₺)	Beamless Flooring	Total (₺)
Concrete (Y.16.050/04)	179.65	602.00	108149.30	633.39	113788.50	575.00	103298.80
Formwork (Y.21.001/03)	48.5	3257.00	157964.50	3660.00	177510.00	2608.00	126488.00
S412 Steel (Y.23.014)	3548.84	54.69	194086.10	66.751	236888.60	72.402	256943.10
Total			460199.90		528187.10		486729.90

III. CONCLUSION

CAD programs have become indispensable in the construction technologies today. Official institutions have made it mandatory for the projects to be prepared with the CAD programs. Nowadays, most government projects are installed with e-signatures on the system in the Internet environment and if there are errors in the project, they request changes in the project when all project information is complete, the license is prepared with e-signature. All projects

are stored in electronic environment and projects can be accessed by e-signature at any time. While the light weighted workshop building project is under design, it has been subjected to cost analysis in three different types of flooring systems and two types of foundation systems and cost calculations were made based on current unit prices with only concrete, formwork and steel quantities. In this study, which is made to decide the most economical, safest and aesthetic building system;

a. The cost of normal flooring system is 486.235.03 ₺ if it is made as strip foundation and 460.199.90 ₺ if it is based on spread foundation. 26.053.13 ₺ spread foundation will be given an advantage.

b. The cost of ribbed (filler-joist floor) flooring system is 503.756.89 ₺ if it is made as strip foundation and 528.187.10 ₺ if it is based on spread foundation. 24.430.21 ₺ strip foundation will be given an advantage. No assessments have been made for the filler-joist floor material in the calculations and must be taken for the ribbed flooring as an additional cost for the material and workmanship to be selected. An additional cost of approximately 30,000 ₺ will be required in a cost analysis to be made using filler-joist floor bricks.

c. The cost of beamless flooring system is 523.422.03₺ if it is made as strip foundation and 486.729.90 ₺ if it is based on spread foundation. 36.692.13 ₺ spread foundation will be given an advantage. In this study, the project, designed as ribbed (filler-joist floor) and spread foundation, comes at the highest cost with 528.187.10 ₺, the lowest costs of normal flooring and the project designed as spread foundation are cost 460.199.90 ₺. The difference is 67.987.20 ₺. When the material and workmanship are added, the approximate difference is 100.000.00 ₺. This also shows us that the projected project will be made more economical, such as about 17.8%.

Because of CAD supported analyses, the design of normal flooring and spread foundation has given the most appropriate values. It can be said that different results may be achieved in other different studies. Normal flooring system is not preferred in some parts of our country. In our developing country, it is aimed to create awareness in this study prepared to prevent the high-cost systems from being preferred. It should not be overlooked that spread foundation applications can yield economic results in buildings such as industry, workshop factories, and may not provide appropriate results in residential constructions. Using the advantages that CAD programs have given us, this work has been revealed that very fast and economical designs can be made, and appropriate costs can be found without compromising the safety principle.

REFERENCES

- [1] ALTIN MUSTAFA, TAŞDEMİR ŞAKİR (2014). The Cost Analysis of An Education Building Through Computer Aided Design According to Different Flooring Systems. International Conference on Advanced Technology & Sciences (ICAT'14) 12-15 August 2014, Antalya, Turkey., 386-389.
- [2] Yapı Teknolojisi (2016), AÇIKEL D. A., ALTIN M., DORUM A., Nobel Yayın Dağıtım, Ankara,
- [3] Topcu A. (2018), Reinforced Concrete II Lecture Notes, Eskisehir Osman Gazi University,
- [4] ALTIN M., (2010). "Contribution of Computer Aided Design Programs to the Perceptions of the Students of Construction Lessons in Construction Project Drafting and Techniques at Vocational Higher Schools", International Conference on New Trends in Education and Their Implications 11-13 November 2010, 461-467
- [5] <http://www.idecad.com/default.asp>
- [6] Turkish Earthquake Code (TEC). Regulations on structures constructed in disaster regions. Ankara: Ministry of Public Works and Settlement; 2007.
- [7] TS 498, (1997), "Design Loads for Buildings", TSE, Ankara.
- [8] TBC-500-(2000). Requirements for design and construction of reinforced concrete structures. Ankara: TSE; 2000.
- [9] Mustafa ALTIN and Şakir TAŞDEMİR, "Design and Construction of an Overpass with Computer-Aided Design Software and its Use in Construction Technology Education", Academic Journal of Science, ISSN: 2165-6282, Volume 01, Number 02 (2012), pp:15-20 <http://universitypublications.net/ajs/0102/html/FIR576.xml>
- [10] <http://www.birimfiyat.com>

A New Approach with Fuzzy Logic Base for Photovoltaic Panel Surface Cleaning

M. MUTLUER¹ and A. ERAT²

¹Necmettin Erbakan University, Department of Electrical and Electronics Engineering, Konya/Turkey, mmutluer@konya.edu.tr

²Konya/Turkey, a.rahim_erat@outlook.com

Abstract - Today, electricity is generated by solar energy through photovoltaic solar cells and the efficiency of the systems developed in this direction is being investigated. The efficiency of the photovoltaic panels used to transform solar energy into electricity is utmost importance. Dusting, equipment used (DC conductors, inverter, panel interior design, etc.), shadowing, amount of radiation and many other factors have affect to the efficiency of photovoltaic solar panels. Recent studies have shown that dust and dust derived particles on the panel surfaces have a very serious effect on the efficiency and so photovoltaic panel surfaces must be kept clean to absorb more effective solar radiation for increase the efficiency of photovoltaic panels. The surface cleaning of the photovoltaic panels can be done manually or by intelligent systems. However, when the enormous expansion areas of solar power plants are considered, the use of automated intelligent systems will be more rational. Thanks to an intelligent panel surface cleaning system, very serious photovoltaic efficiency gains will be achieved. In this declaration, it is planned to design an intelligent system with a fuzzy logic base that can automatically clean the panel surfaces.

Keywords - Arduino, Fuzzy Logic, PV Panel Surface Cleaning System, PV Panel Efficiency

I. INTRODUCTION

The most important source of energy for the Earth is the sun. The fact that most of the ecological problems due to the use of traditional energy sources are not found in generating energy from solar energy makes solar energy source alternative to traditional energy sources. The sun, which consists of the H and He gases, is a medium-sized planet. The distance between the earth and the sun is 150 million km. The sun's energy which comes from to the world is 20,000 times the energy consumed in a year in the world. The temperature increases towards the center of the sun and reaches 20×10^6 °C. The temperature on the surface is 6000°C [1].

Solar cells are semiconducting materials that directly convert the sunlight coming to their surface into electrical energy. The areas of solar cells whose surfaces are square, rectangular and circular are generally 100cm² and their thickness changes between 0,1-0,4mm. The solar energy is converted into electric energy with an efficiency of 5% to 30% depending on the structure of the solar cell and the semiconductor material used. In order to increase the electrical energy obtained, a large

number of solar cells are connected in parallel or in series and mounted on a surface. This structure is called the solar cell module or the photovoltaic module in Figure 1 [2].

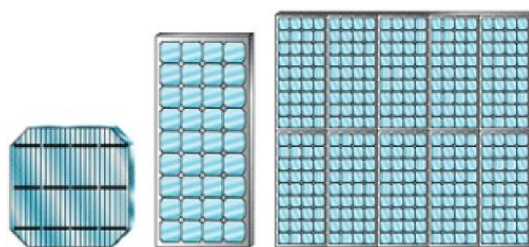


Figure 1: Photovoltaic solar cell.

The photovoltaic effect is a physical process by which a photovoltaic cell converts solar radiation to electricity. As seen in Figure 2 [3] photons strike the surface of semiconductor materials such as silicon to release electrons from atoms. Some of the photons on the photovoltaic cell are absorbed by the cell, a part is reflected, and the leftover is transferred through the cell to the electron in the atom of the semiconductor material. Thanks to this newly acquired photon energy, the electron gains the ability to be freed its normal position for a single atom in a semiconductor material to be part of the current in an electric circuit [2].

Today, studies for photovoltaic panel surface cleaning are mostly industrial applications. Unfortunately, these studies are far from any scientific innovation and inefficient. So they are just doing primitive cleaning and the efficiency of working in this direction is low. Nevertheless, although panel cleaning is considered in academic work, these studies focus on the mechanical or chemical cleaning of the system and are therefore not at the desired level in terms of overall system efficiency [4-6]. In this case, it is necessary to utilize artificial intelligence and it is thought that the efficiency of the system will increase and the operating costs will decrease. This is also the result of such a prediction.

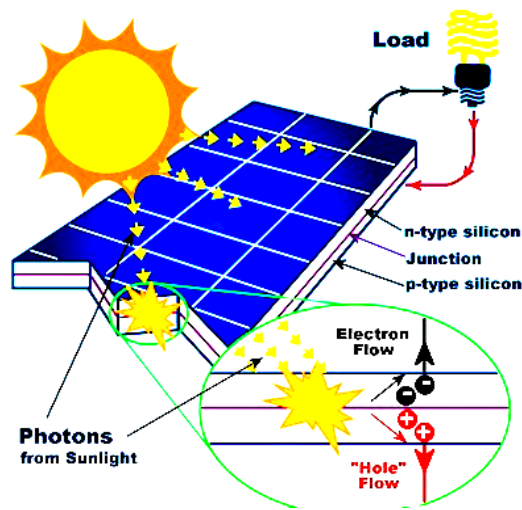


Figure 2: The operation principle of the solar cell.

II. PHOTOVOLTAIC PANELS EFFECTIVE FACTORS

The efficiency of photovoltaic solar panels are determined under standard test conditions of $1000\text{W}/\text{m}^2$ radiation, 25°C temperature and 1.5 mass air ratio (Air Mass). The energy obtained from a photovoltaic system depends on many factors. Some of these are the nominal characteristic values of the components making up the PV system (Figure 3) [7], the structure of the system, the geographical position of the system, dusting, radiation, temperature, and structures around the installation site and faults that may occur during operation [8].

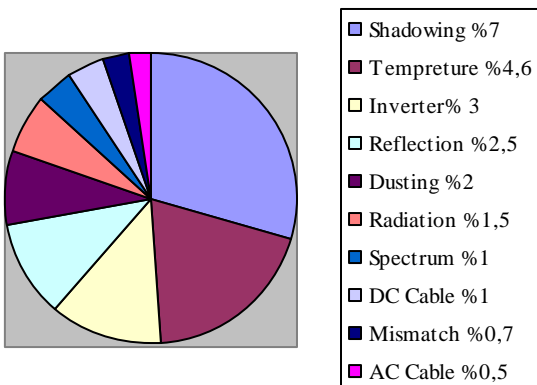


Figure 3: Losses in PV system.

The pollution effect is the accumulation of dust or other dust derivative particles on the photovoltaic panels. Contamination on the panel surface can seriously affect the energy production efficiency of the photovoltaic panel. Investigations on the effect of dust on the efficiency of PV panels show that, especially in low rainfall areas, the efficiency is over 15% of the dust related losses [9]. The way to avoid this large losses of efficiency is to keep the modules clean [10].

III. INTELLIGENT SYSTEM DESIGN FOR CLEANING PHOTOVOLTAIC PANEL SURFACE

In the photovoltaic systems, the surfaces of the photovoltaic panels must be kept clean to absorb effective solar radiation in order to obtain a useful output power. The panel surface cleaning can be done manually in small photovoltaic areas. However, for the spread of photovoltaic fields in large areas, very serious work is needed to clean the surface of the modules. Intelligent systems should be preferred for cleaning panel surfaces to avoid this serious work load and time losses. With the choice of these intelligent systems, efficiency gains are achieved in large proportions.

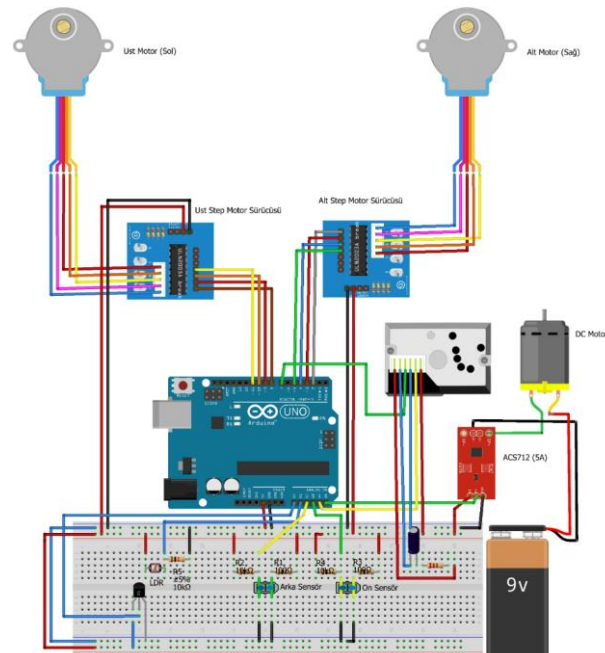


Figure 4: Architecture of the cleaning system.

In this declaration, the design of an intelligent system that is based on arduino and fuzzy logic is envisaged. For the design, arduino microcontroller card and fuzzy logic system will be preferred and the circuit was shown in Figure 4. The temperature, panel output current, pollution and shading factors affecting the panel efficiency will be selected as input data for the fuzzy logic system. For correct solution of fuzzy logic, the input data is first refined. Afterwards, this data will be blurred and the correct decision grade will be obtained so that the intelligent system can move on the panel surface.

A. Fuzzy Logic Structure of the PV System

In this design, an artificial intelligence method based on the fuzzy logic system was used. As system inputs, the temperature, panel surface pollution (dusting), panel exit current and shading data which are affecting the efficiency of the photovoltaic panel were chosen. As shown in Figure 5, for the most accurate solution of the fuzzy logic problem these four data are designed as inputs to the fuzzy logic system.

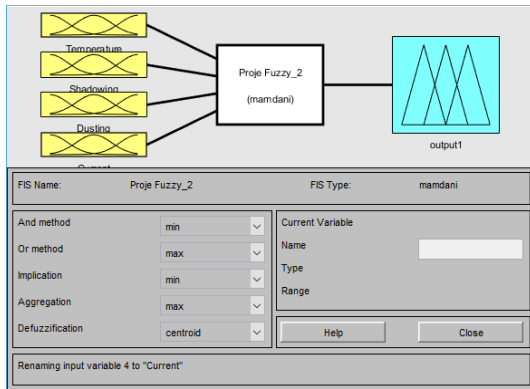


Figure 5: Inputs and output of the PV system.

B. Membership functions of the PV System

For the temperature input, two membership functions are defined as normal and high temperature (h.temperature). Figure 6 shows graphs of these membership functions in triangular membership format and the specified temperature ranges.

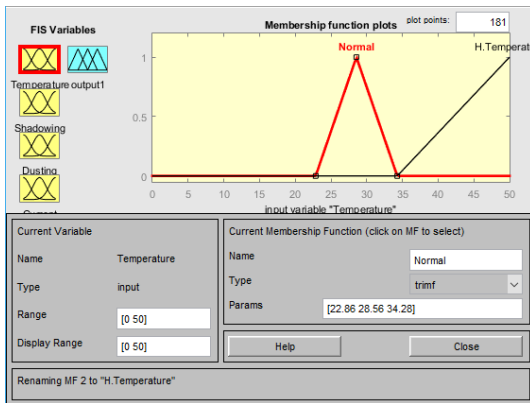


Figure 6: Graphs of membership function for temperature input

Two membership functions are defined for shadowing input as shadowy and normal. Figure 7 shows graphs of these membership functions in triangular membership format and the specified shadowing intervals.

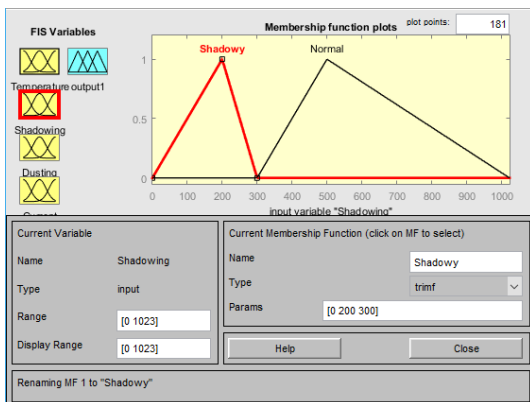


Figure 7: Graphs of membership function for shadowing input

Two membership functions are defined for pollution entry

as clean and dirty. Figure 8 shows graphs of the triangular membership format of these membership functions and the determined pollution intervals.

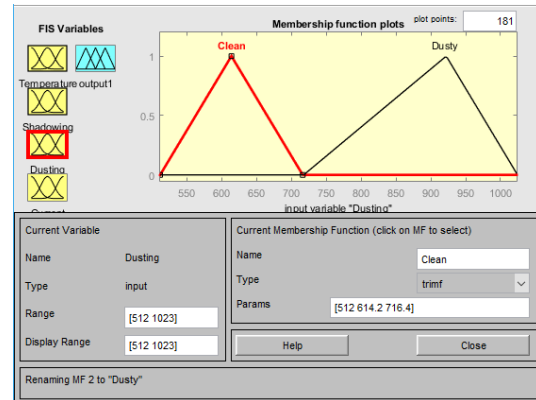


Figure 8: Graphs of membership function for pollution input

For current input, two membership functions are defined as low current (l.current) and normal current (n.current). Figure 9 shows graphs of these membership functions in triangular membership format and the determined current ranges.

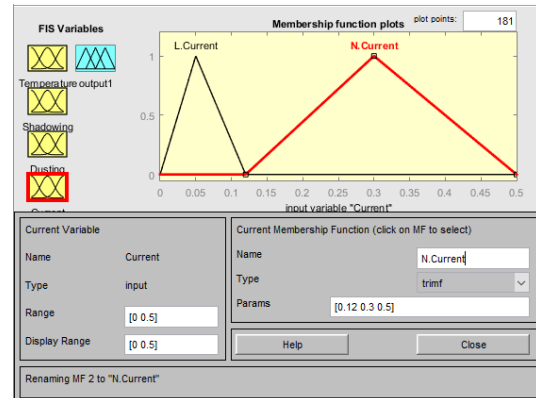


Figure 9: Graphs of membership function for current input

C. The operating rules of the PV system

For the correct solution of a fuzzy problem the rules are defined according to the inputs data. The purpose of creating these rules is to get the most accurate solution of the system. Figure 10 and Figure 11 show the rules of the fuzzy logic system.

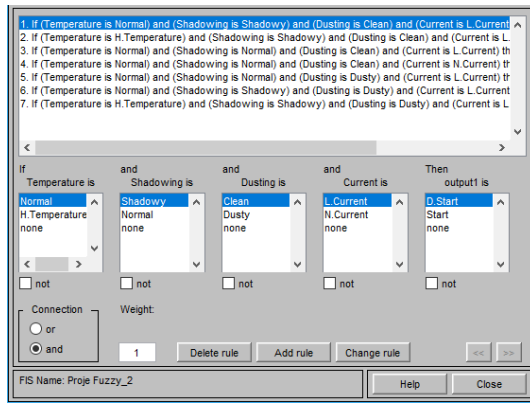


Figure 10: Determination of fuzzy system rules



Figure 11: Demonstration of fuzzy system rules

As a result of the specified input data firstly blurring and then defuzzification, a decision outcome of the system is obtained. The designed system starts to clean the surface of the panel by moving on the panel surface according to the degree of this decision. Having achieved this exit decision, the value ranges of the membership functions of the inputs of the system are determinative.

IV. RESEARCH RESULTS AND CONCLUSION

In order to obtain the electricity efficiency of the solar cells with high efficiency from the solar panels, the photovoltaic panel surfaces must be kept clean for more effective sunlight absorption. Although energy conversion efficiency in solar panels changes according to the panel structure, the average efficiency is around 20%. This efficiency is also reduced with the accumulation of dust, dirt, pollen and various dust particles on the panel over time. Located in a dirty and dusty geography, especially solar power plants installed in the desert the efficiency depending on the dust shows a decline of around 30%. It is aimed to design an intelligent cleaning system based on fuzzy logic to avoid these efficiency losses due to the pollution of the surfaces of the solar panels. This system, which will be designed, will be able to clean the panel surface by acting as a fuzzy logic base, and prevent 15-20% efficiency losses due to dust pollution.

REFERENCES

- [1] E. Öztürk, "Fotovoltaik panellerin verimine modül sıcaklığının etkisinin deneysel olarak araştırılması", Master Thesis, Karabük University, Institute of Science, Karabük, 2014.
- [2] A. Erkul, "Monokristal, polikristal, amorf silisyum güneş panellerinin verimliliğin incelenmesi ve aydınlatma sistemine uygulanması", Master Thesis, Gazi University, Institute of Science, Ankara, 2010.
- [3] <http://www.kuark.org/2014/12/gunes-pilleri-nasil-calisir>, Aug. 2018.
- [4] M. Kegeleers, "The development of a cleaning robot for PV panels", Master Thesis, Faculty of Engineering Technology, Technology Campus De Nayer, 2015.
- [5] S. T. Mobin, "Design and development of solar panel cleaning system", Master Thesis, Mechatronics and Automation, National Institute of Technology, Rourkela, 2015
- [6] J. J. John, "Characterization of soiling loss on photovoltaic modules, and development of a novel cleaning system", Department of Electrical Engineering, Indian Institute of Technology, Bombay, 2015.
- [7] S. Ekici and M. A. Kopru, "Investigation of PV system cable losses", International Journal of Renewable Energy Research, Vol.7, No.2, 2017.
- [8] F. Demirci, "Fotovoltaik güneş pillerinin çalışmasını etkileyen dış faktörlerin incelenmesi", Master Thesis, Sakarya University, Institute of Science, Sakarya, 1996.
- [9] M. Piliouline, J. Carretero, M. Sidrach-de-Cardona, D. Montiel, P. Sanchez-Friera, "Comparative analysis of the dust losses in photovoltaic modules with different cover glasses", Proceedings of 23rd European Solar Energy Conference, 2008.
- [10] S. Ghazi, "Dust effect on flat surfaces – a review paper", Renewable and Sustainable Energy Reviews 33, pp. 742–751, 2014.

PMUs Placement Optimization for Fault Observation in Power System

H. BENTARZI¹, A.ZITOUNI¹ and A. RECIOU¹

¹Laboratory Signals and systems, Université M'hamed Bougara Boumerdes, Algeria, lss@univ-boumerdes.dz

Abstract – This paper presents a new approach for obtaining the optimal placement of the phasor measurement units (PMUs) in smart power grids to achieve full network observability under fault conditions. The proposed modeling framework is implemented using the binary teaching learning based optimization (BTLBO) technique. It is proposed for the objective function and constraints alike. The proposed approach is applied to the IEEE 14-bus benchmark system. The simulation results demonstrate that the proposed framework can give a fine-tuned optimal solution with a simple model and acceptable solution characteristics compared with previous works in the literature.

Keywords - Binary teaching learning technique, optimization, PMUs placement, fault, observability.

I. INTRODUCTION

IN order to make the electrical power systems more reliable, stable, and controllable; state estimation of the transmission network is necessary [1]. The Phasor Measurement Unit (PMU) is a tool for measuring the voltage and current those are synchronized by using the global positioning system (GPS) satellite [2]. The power station including the Phasor Data Concentrator (PDC), which is used for analyzing the PMU data, can receive the synchronous data from each PMU in real time [3].

State estimation of power network may allow the scheduling generation and interchange; monitoring outages and scheduling alternatives; supervising scheduled outages; scheduling frequency and time corrections; coordinating bias settings; and emergency restoration of system [4]. This can be achieved either by state estimation algorithms [5] or by means of PMUs with extreme precision, time synchronization, and excellent performance. Measuring state estimation is achieved through complex bus voltages [6] that enable the estimation of the neighborhood bus voltage magnitudes and angles by using the line flow measurement (both real and reactive power). The static and dynamic behaviors of the power grid may be obtained from the information gathered by PMUs.

Faults that occur in the transmission line may be either permanent or temporary [7, 8]. Permanent fault may lead to a broken transmission line or a power generator malfunction; this causes different signals during the pre-fault and post-fault. This can be easily detected and located. However, the temporary fault may cause insulator flashover, which may lead to full insulator breakdown if it occurs frequently. This emphasizes the importance of PMU-based fault location technique [9-11].

Nowadays, Wide Area Monitoring System (WAMS) that is considered the most advanced system to detect disturbances and avoid a bulk blackout is based on the PMUs. It aims to maintain the dynamic stability in the whole power network [11]. This is implemented by synchronizing and recording the acquired data from systems in distributed locations through new computing and communication technologies. Upon their delivery to the central control station, these data are measured and analyzed from any point of the power network. In addition to its ability to monitor the static stability of the network (as traditional SCADA), WAMS enables the controllers to recognize unusual activities within the power network such as instability in the network voltage, to analyze the network oscillation, and to detect fault localization. Thus, using the data provided by PMUs installed in some appropriate buses of a power grid, one can construct a new type of measuring system to improve the observability and the precision of the power system state estimator. The observability depends on the type, the number and the geographic distribution of measurements [12]. Several methods [13-17] were considered when formulating the optimal placement of monitoring devices for fault location.

In this research work, a binary teaching learning based optimization (BTLBO) algorithm for the optimal placement of phasor measurement units (PMUs) is proposed. The optimal PMU placement problem is formulated to minimize the number of PMUs installation subject to full network observability at the power system buses during the fault. The effectiveness of the proposed method is verified by the simulation of IEEE14-bus.

II. FAULT ANALYSIS USING PMU

PMU-based fault location technique is achieved through monitoring the synchronized fault voltages, calculating the line currents between these buses, and forming bus injection currents at two terminals of the faulted line. Thus, calculation of fault locations can be indirectly investigated.

A PMU placed at a given bus of the network can measure both the phasor voltages and phasor currents of all lines incident to that bus. Thus, the entire parameters of a bus can be made observable by placing judiciously PMUs at specific buses of the network. As shown in Fig.1, most power transmission networks may consist in general of five different sub-network configurations or types [18]. In this figure, for each of the five sub-networks, the placed PMUs obey to what is called the “one bus spaced deployment strategy”.

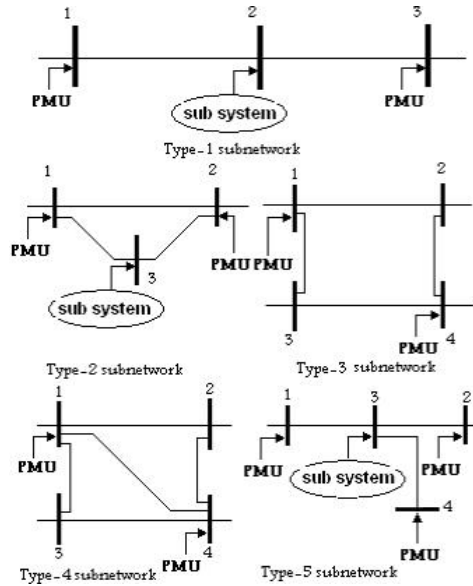


Figure 1: The five possible sub-network configurations.

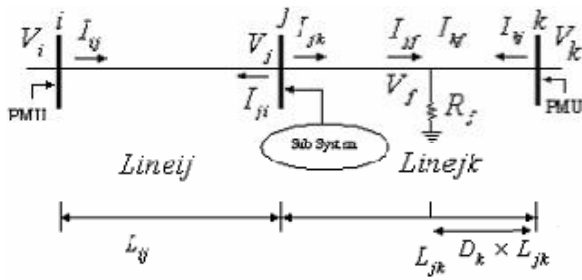


Figure 2: Faulty type-1 sub-network

Whatever is the considered sub-network type, it is always possible to make the fault location problem of that sub-network similar to the fault location problem of type-1 sub-network [19]. A faulty type-1 sub-network is shown on Fig.2. In this figure, a fault occurs in line jk between bus j and bus k . The fault location problem consists thus, of finding the parameter D_k .

By using the voltage phasor of bus i and the parameters of line ij , the voltage phasor of bus j will be determined as:

$$V_j = V_i - (I_{ij} - V_i - L_{ij} Y_{ij}/2) L_{ij} Z_{ij} \quad (1)$$

In addition,

$$I_f = I_{kf} + I_{jf} \quad (2)$$

Where the line parameters Z_{ij} and Y_{ij} are relative to the Π line model. Current phasor I_{jk} however, cannot be deduced with the similar way as no PMU is connected at bus j . Therefore, the problem consists of finding two unknown variables I_{jk} and D_k . Using the basic electrical networks theory and assumption constraints, the two sets of equations of the two unknown variables can be derived:

- Network equations, derived from equations (1) and (2)

$$F_1(I_{jk}, D_k, \theta) = 0$$

- Constraints equations, assuming pure resistance fault impedance or $Arg(I_{ij}) = Arg(V_{ij})$

$$F_2(I_{jk}, D_k, \theta) = 0$$

Where θ represents the known variables, such as V_i, V_j, V_k , etc. In Table 1 are summarized the two groups of equations for fault location detection of three phase faults.

solving numerically these sets of equations leads to the unknown parameter D_k , that is the location of the fault on the line between bus j and bus k .

III. PROBLEM FORMULATION

It is not economical to install a PMU at each bus of a wide-area power network. Thus, the problem of optimal PMU placement (OPP) concerns with where and how many PMUs should be implemented in a power system to achieve full observability at minimum number of PMUs [4].

A PMU placement optimization problem, for n -bus system, may be defined as:

$$\text{Objective function: } J = \text{Min} \sum_{i=1}^n x_i$$

$$\text{such that: } f(X) \geq \hat{i} \quad (3)$$

Where x is a binary decision variable vector, whose entries are given as:

$$x_i = \begin{cases} 1 & \text{if Bus } i \text{ has a PMU} \\ 0 & \text{otherwise} \end{cases} \quad (4)$$

$f(X)$ is a vector function, whose entries are non-zero if the corresponding bus voltage can be obtained by using the given measurement set, otherwise zero. Entries of a vector \hat{i} are all equal to two or more.

Table 1: Summary of the two groups of equations for fault location detection.

Group 1: Network equation ($n=0,1,2,$)	
$V_{jn} = V_{kn} - (I_{kfn} - V_{kn} \times Y_{kfn} / 2) \times Z_{nfn}$	
$I_{jkn} = (V_{jn} - V_{fn}) / Z_{jfn} + V_{fn} \times Y_{jfn} / 2$	
$I_{fn} = (V_{kn} - V_{fn}) / Z_{kfn} - V_{fn} \times Y_{kfn} / 2 + (V_{jn} - V_{fn}) / Z_{jfn} - V_{fn} \times Y_{jfn} / 2$	
Group 2: Constraint equation	
a-g fault	$Re(I_{f0} + I_{f1} + I_{f2}) \times Im(V_{f0} + V_{f1} + V_{f2}) = Im(I_{f0} + I_{f1} + I_{f2}) \times Re(V_{f0} + V_{f1} + V_{f2})$
b-c-s fault	$Re(I_{f1} - I_{f2}) \times Im(V_{f1} - V_{f2}) = Im(I_{f1} - I_{f2}) \times Re(V_{f1} - V_{f2})$
b-c-g fault	$V_{f1} = V_{f2}$
a-b-c-g fault	$Re(I_{f1}) \times Im(V_{f1}) = Im(I_{f1}) \times Re(V_{f1})$

Constraints

In order to form the constraint set, entries of the binary connectivity matrix A are defined as follows:

$$A_{k,m} = \begin{cases} 1 & \text{if } k = m \\ 1 & \text{if } k \text{ and } m \text{ are connected} \\ 0 & \text{if otherwise} \end{cases} \quad (5)$$

According to the knowledge that by placing a PMU on one bus, the voltage phasors of neighboring buses may be determined by:

$$f = A \times X \quad (6)$$

Constraint functions defined by Equations (3), (4) and (5) may satisfy full network fault observability even with optimization of the number of PMUs.

The method for making the constraint equations (vector function $f(X)$) can be discussed for the following cases:

- Neither PMU measurements nor conventional (flow and injection) measurements exist,
- Only flow measurements exist,
- Both flow and injection measurements (they may be zero or measured injections) exist or PMU and conventional flow or injection measurements exist.

To verify the proposed method, it has been tested using IEEE 14-bus grid shown in Fig.1.

IV. BTLBO OPTIMIZATION ALGORITHM

A new method that is binary version of TLBO has been used in this paper [20]. The algorithm of this binary version can be discussed as:

Step 0: define an optimization problem, the objective function: Minimize (objective function) $y = f(x_1, x_2, \dots, x_{n-1}, x_n)$ such that: $x_1, x_2, \dots, x_{n-1}, x_n$ can take only two values: either a "1" or a "0".

choose the number of students will be used or the population size, elite size and the number of generation. It can be considered that the minimization problem; the maximization is similar.

Step 1: initialization: propose a population (that will be made to attain the final solution) or students randomly according to the following equation:

$$x_{(i,j)}^1 = randi([0,1],1) \quad (7)$$

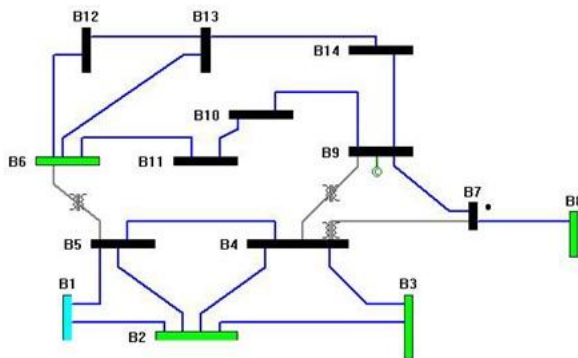


Figure 3 : IEEE 14-bus system.

i : refer to student number, so there are i^{th} student, $i=1, 2, \dots, P$
 j :refer to the course number, $x_{(i,j)}$ is the level of the i^{th} student at the j^{th} course, $j=1, 2, \dots, D$

The small number 1 refers to the generation number that is the first generation.

After the manipulation of the above equation $P \times D$ times, we obtain a $P \times D$ matrix which represents our population:

$$\text{population}^1 = \begin{bmatrix} x_{(1,1)}^1 & \dots & x_{(1,D)}^1 \\ x_{(2,1)}^1 & \dots & x_{(2,D)}^1 \\ \vdots & \ddots & \vdots \\ x_{(P,1)}^1 & \dots & x_{(P,D)}^1 \end{bmatrix} \quad (8)$$

Choose the teacher: the best student is the one which has the minimum fitness function.

Step 2: teacher phase

Every student tries to be as his teacher, so he makes his design variables as those of the teacher, of course not all of them otherwise he will be exactly as his teacher. Thus, the student copies some components of teacher and replaces his components by copied ones. The number of copied components depends on the ability of teacher and the student; that is represented by one random number h . The number h that is between 0 and D is given by:

$$h = randi(D,1) \quad (9)$$

This number determines how many courses that student i will learn from his teacher.

The location of these courses in the teacher vector can be specified according to the following equation:

$$\text{Course} = randi(h,[1,h]) \quad (10)$$

These randomly selected courses are now ready to be transmitted from teacher to student:

$$X_{i,new} = X_i$$

$$X_{i,new}(\text{course}) = X_{\text{teacher}}(\text{course})$$

$$\text{if } f(X_{i,new}) < f(X_i) \text{ then } X_i = X_{i,new} \text{ else do nothing} \quad (11)$$

Execution may make duplicate solutions; consequently one more step is required.

Step 3: remove duplicate solutions by mutation on randomly selected dimensions.

Step 4: learner phase

The interaction between students in binary interpretation will be as follows:

Select for a student i another one j , if j is better than i then i will learn from j by trying to change components that are different from those of j , in order to be similar to him; otherwise he will change some components that are similar to those of j . This can be done as follows:

For $i = 1:P$ do

Select another student j and record where they are similar and where they are different in a vector,

$$q = [q_1 \ q_2 \ \dots \ q_D] \text{ such that } q_k = 1 \text{ if } x_{i,k}^g = x_{j,k}^g \text{ else } q_k = 0; \quad k = 1, \dots, D$$

The vector $h = randi(D,1)$ states how many courses student i will learn from j if he is better than him or change them in other case.

The vector $\text{course} = \text{randi}(h, [1, h])$ gives the location of courses which will be learnt or changed.

Now the learning process can be implemented:

$X_{i,\text{new}} = X_i$, the new student is the old one with some modifications.

if $f(X_i^s) < f(X_j^s)$ then $X_{i,\text{new}}(\text{course}) = X_j(\text{course}) \times \text{not}(q(\text{course}))$
 else if $f(X_i^s) \geq f(X_j^s)$ then $X_{i,\text{new}}(\text{course}) = \text{not}(X_j(\text{course})) \times q(\text{course})$ (12)

Equation (12) shows that some components where i and j differs will be copied from j (the highest learned one between the two) to i otherwise (j is inferior to i) some of similar component in i will be changed from 0 to 1 or 1 to 0. Now, check if the new student is better than the old:

if $f(X_{i,\text{new}}) < f(X_i)$ then $X_i = X_{i,\text{new}}$ else do nothing (13)

After the implementation of the process for all the population, a new teacher will be determined.

Step 5:-Remove duplicate solutions.

-replace bad solutions by elite solutions and again remove duplicate solutions.

Step 6: if $g \neq$ number of generation then go to step2 else stop.

Using the binary teaching learning based optimization explained previously which is based on the problem formulation pointed out in previous section; an algorithm for the optimal placement problem is given as follows:

1. Construct the binary connectivity matrix using the one line diagram and constraint modification when injection, flow measurements or already installed PMUs.
2. Define the optimization parameters; the population size (pop_size), the design variables (N_buses), and the number of generation (N_gen), the (elite size).
3. Generate random solutions within boundaries of the system.
4. Check that random solutions satisfy the inequality constraint of buses $f(x) = (A * X) \geq i$,
5. Modify those are not satisfying the constraints.
6. Calculate the fitness of each solution using the objective function of expression,
7. Set the best solution as teacher of the population,
8. For each student, apply teacher phase, replace x by x_{new} if it gives better fitness function (less) otherwise keep the old one.
9. If the duplicate solutions exist then modify the duplicate solutions for avoiding the trapping in the local optima. In the present work, duplicate solutions are modified by mutation on randomly selected dimensions of the duplicate solutions before executing the next generation without losing the observability.
10. For each student apply learner phase, replace x by x_{new} if it gives better fitness function (less) otherwise keep the old one.
11. Again, remove duplicate solutions keeping the constrained satisfied (observability).
12. Replace (elite_size) bad solutions by (elite_size) elite solutions.

13. Again, remove duplicate solutions keeping the constrains satisfied (observability), then determine the teacher.

14. Repeat from step 7 for maximum number of iterations.

15. Put the best solution x_{teacher} as the final solutions.

The flowchart for the optimal placement algorithm is shown in Figs.4 and 5.

V. SIMULATION RESULTS AND DISCUSSION

The proposed PMU placement optimization algorithm has been implemented using MATLAB® on the IEEE 14-bus network shown in Fig.3. Network data is given in Table 1. The used parameters in the optimization are: The maximum iteration number in BTLBO is set at 1000 with the population size of 100. In this simulation, the best solutions of the binary TLBO is obtained after 20 runs of the algorithm. The simulations have been carried out on a PC Intel i5 (2.40 GHz) with 4 GB RAM. It may be mentioned that the required number of PMUs is not necessarily unique. Since heuristic algorithms, such as TLBO, are based on a random search in the search space of the problem, and the result of each execution of these algorithms might be different from another one. Therefore, they must be run several times to ensure that the optimal point of the problem can be attained. However, from the observability point of view, there is no difference between different configurations with the same number of PMUs, so only one configuration has been presented.

Two sets of simulations have re carried out on the IEEE 14- bus system, which are initially assumed to have no flow measurements and no previously existed PMUs. In the first set of simulations, zero injection is simply ignored while in the second set, it is used as existing measurement.

The IEEE 14 bus test system has only one zero-injection bus. The output of the BTLBO algorithm is 8 PMUs. The information of the system and zero injections are given in Table.2.

The global solution may be obtained after a few iterations (between 5 and 10) and population size (10). Seven PMUs can be installed in order to fully observe the IEEE14 bus system. However, when injection is ignored, different configuration of PMUs installation is obtained, whereas, considering injection gives only one set (1, 2, 4, 6, 9, 10 and 13). It can be noted that the number of PMUs required for system fault observability reduces by 1, if the system observability is to be maintained after considering zero injection buses.

The number of PMUs calculated by the proposed approach is given in Table 3. The number of PMUs that guarantees full observability of power system during any failure that can occur; each bus is observable by at least two PMUs.

VI. CONCLUSION

The obtained simulation results are in agreement with the previous research work results [13, 14, 16, and 17]. Moreover, the results show that full network observability can be achieved under fault conditions using more than 50% PMUs installation; however, under normal conditions, approximately 30% PMUs installation is required.

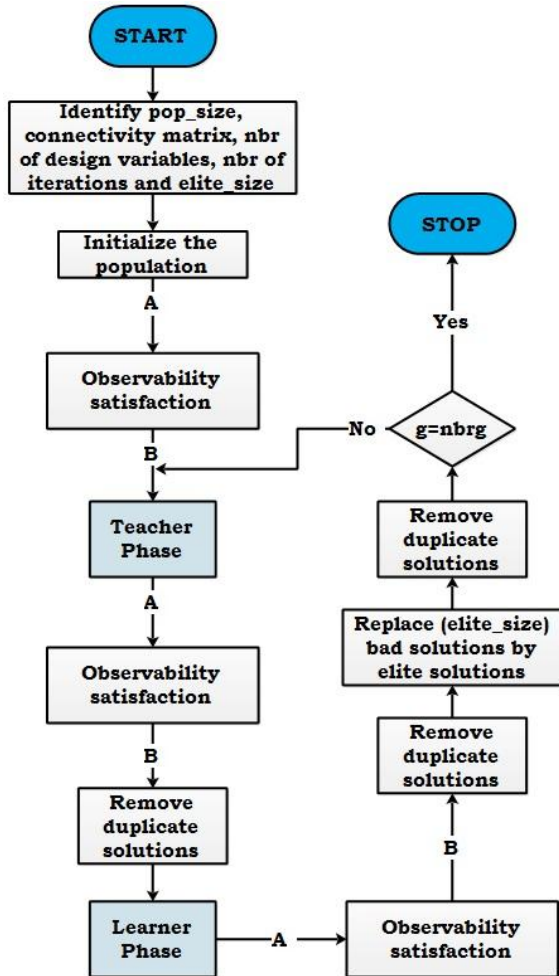


Figure 4 : Flow chart of BTLBO algorithm applied to the optimal PMU placement.

Finally, the proposed work represents a potential tool to monitor power systems, and it will help the operators in a smart grid environment.

REFERENCES

[1] K.J. Karimi, Power system static state estimation with phasor measurements. Cornell Univ., Ithaca, NY (USA), 1986.
 [2] A.G. Phadke, Synchronized phasor measurements in power systems. *IEEE Computer Applications in power*, 6, pp 10-15, 1993.
 [3] A. Ouadi, H. Bentarzi and J. C. Maun, Phasor Measurement Unit Reliability Enhancement Using Real-Time Digital Filter, *International Journal of Circuits, Systems and Signal processing*, 5, pp 1-8, 2011.
 [4] A.G.Phadke, and J.S. Thorp, *Synchronized phasor measurements and their applications*. Vol. 1.: Springer, 2008.
 [5] J. Allemong, L. Radu, and A. Sasson, A fast and reliable state estimation algorithm for AEP's new control center. *IEEE Transactions on Power Apparatus and systems*, 4, pp 933-944, 1982.
 [6] N.H. Abbasy, and H.M. Ismail, A unified approach for the optimal PMU location for power system state estimation. *IEEE Transactions on Power Systems*, 24, pp 806-813, 2009.
 [7] H. Yin, and L. Fan. PMU data-based fault location techniques. in *North American Power Symposium (NAPS)*, . IEEE, 2010.

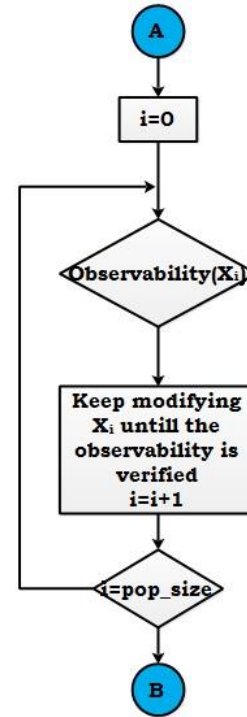


Figure 5 : Observability subroutine.

Table 2: System information of IEEE 14-bus system.

System	Num. of branches	Num. of zero injections	Zero injection buses
IEEE 14-bus	20	1	7

Table 3. Optimum number and location of PMU

System	Num. of PMUs	Location of PMUs
IEEE 14-bus with Zero injection buses	7	1,2,4,6,9,10,13
IEEE 14-bus with injection buses	8	1,2,4,6,9,10,13, 14

[8] Y.-H. Lin, C.-W. Liu, and C.-S. Chen, A new PMU-based fault detection/location technique for transmission lines with consideration of arcing fault discrimination-part I: theory and algorithms. *IEEE Trans. on power delivery*, 19, pp 1587-1593, 2004.
 [9] Y.-H. Lin, C.-W. Liu, and C.-S. Chen, A new PMU-based fault detection/location technique for transmission lines with consideration of arcing fault discrimination-partII: performance evaluation. *IEEE Trans. on power delivery*. 19, pp 1594-1601, 2004.
 [10] A. Ibe, and B. Cory, A travelling wave-based fault locator for two-and three-terminal networks. *IEEE Trans. on power delivery*, 1, 283-288, 1986.
 [11] T. Takagi, et al., Development of a new type fault locator using the one-terminal voltage and current data. *IEEE Transactions on Power apparatus and systems*, 8, 2892-2898, 1982.
 [12] Xu Bei, Yeo Jun Yoon and Ali Abur, Optimal placement and utilization of phasor measurements for state estimation, Texas A&M University, 2008.

- [13] S. Chakrabarti, E. Kyriakides, Optimal placement of phasor measurement units for power system observability, *IEEE Trans. Power Syst.* 23, 1433–1440, 2008.
- [14] H.H. Müller, C.A. Castro, Genetic algorithm-based phasor measurement unit placement method considering observability and security criteria, *IET Gener. Transm. Distrib.* 10, 1, 270–280, 2016.
- [15] N.H. Abbasy, H.M. Ismail, A unified approach for the optimal PMU location for power system state estimation, *IEEE Trans. Power Syst.* 24, 806–813, 2009.
- [16] M. Hajian, et al., Optimal placement of PMUs to maintain network observability using a modified BPSO algorithm, *Int. J. Electr. Power* 33, 28–34, 2011.
- [17] A. Mahari, S. Heresh, Optimal PMU placement for power system observability using BICA considering measurement redundancy, *Electr. Power Syst. Res.* 103, 78–85, 2013.
- [18] Kai-Ping Lien, Chih-Wen Liu, Chi-Shan Yu, and Joe-Air Jiang, “Transmission Network Fault Location Observability With Minimal PMU Placement,” *IEEE Transaction on Power Delivery*, Volume 21, Issue 3, July 2006 Page(s):1128 – 1136.
- [19] S. S. Geramian, H. Askarian Abyane, Member IEEE, K. Mazlumi, “Determination of Optimal PMU Placement for Fault Location Using Genetic Algorithm”, 13th International Conference on Harmonics and Quality of Power, ICHQP 2008, Wollongong, NSW, Australia.
- [20] A. Recioui, H. Bentarzi and A. Ouadi, Application of a Binary Teaching Learning-Based Algorithm to the Optimal Placement of Phasor Measurement Units, Book chapter, *Progress in Clean Energy*, 1, 817-830, 2015.

Open Source Coded Remote Monitoring of Renewable Energy Systems

E.KAPLAN¹ and A. YONETKEN¹

¹ Kocatepe University, Afyon/Turkey, erdalkaplan77@gmail.com

¹Kocatepe University, Afyon/Turkey, yonetken@aku.edu.tr

Abstract - Renewable energy systems have become one of the preferred electricity generation methods because of their environmental friendliness and low cost of operation. This system, which can be used in almost every area, has become very popular with innovative building applications. Remote monitoring of the renewable energy systems are being sold in the developing countries such as our country in high cost ready equipments. The remote monitoring of the energy generated from the production center will be designed and the system will be provided with the use of open source code development.

Keywords – Remote Monitoring of Solar, Reducing Cost in Remote Monitoring of Solar Systems, Renewable Energy Remote Monitoring

I. INTRODUCTION

The smart revolution which has started with smart phones continues in cars and electronic equipments by developing them inside. Smart revolution is now going on with the thing of internet. And a part of this remote monitoring of renewable systems, which are likely to be energy of the future, will provide great convenience to those using these systems. It is aimed to design a system which will be beneficial for all users using renewable energy systems. At first, ready-made boards are programmed and data communication with closed circuit wifi is monitored, then data is transferred via internet.

II. UNDERSTANDING MEASURING AC POWER

A whole house energy monitor measures the energy used by appliances connected to the house mains. To understand how it does this, it is useful to know something about how appliances interact with the electrical system.

Not all appliances interact with the electricity system in the same way. This article will first discuss resistive loads and how the power they use is calculated. It then goes on to discuss reactive loads, and a bit about non-linear loads. Finally, it will show how we measure the direction of power flow, which is important if energy is generated as well as consumed.

A. Resistive Loads

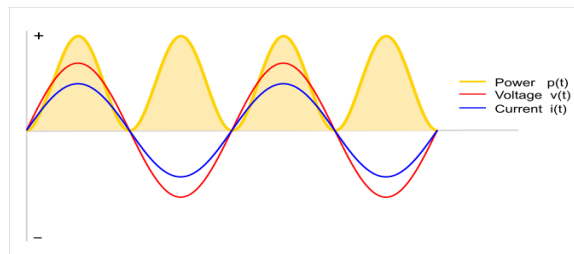


Figure 1: Voltage and current phase relationships in a resistive load

The yellow line is power at a given time (at any given instant it's called **instantaneous power**) which is equal to the product of the voltage and current at a given time. Notice the power is always positive. In this case, the positive direction is energy flowing to the load.

B. Partially Reactive Loads

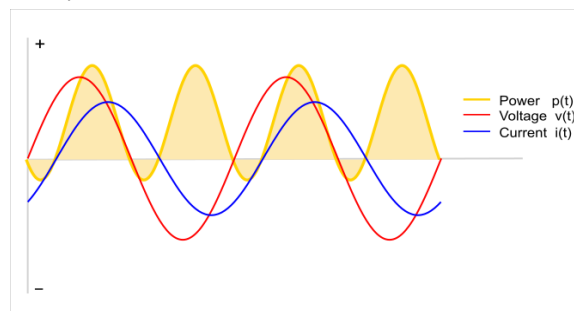


Figure 2: Voltage and current phase relationships in a partially reactive load

Now yellow line goes negative for a period of time, the positive bit is energy flowing to the load and the negative bit is energy flowing back from the load.

The other thing to consider is that the voltage and current waveforms have been shifted apart. Imagine charging a fairly large capacitor with a resistor in series (so that it can't charge instantly): To start with, the capacitor is discharged. The supply voltage rises, and is higher than the voltage on the capacitor, so current flows into the capacitor (the positive direction on the graph), which causes the capacitor voltage to rise. The supply voltage falls. Now, the voltage across the charged capacitor is higher than the supply voltage. Current starts to flow back in the direction of the supply (the negative direction on the graph). This causes the current waveform to appear as if it is shifted, as depicted in the graph. (This is referred to as phase shift).

III. ARDUINO MATH

Real power is the average of instantaneous power. The calculation is relatively straightforward.

A. Real Power

$$P = \frac{1}{T} \int u(t) \times i(t) dt \equiv U \times I \times \cos(\varphi) \quad (1)$$

Equation 1. Real Power Definition.

U - Root-Mean-Square (RMS) voltage.

I - Root-Mean-Square (RMS) current.

$\cos(\varphi)$ - Power factor.

B. Real Power Definition In Discrete Time

$$P \equiv \frac{1}{N} \sum_{n=0}^{N-1} u(n) \times i(n) \quad (2)$$

Equation 2. Real Power Definition in Discrete Time.

$u(n)$ - sampled instance of $u(t)$

$i(n)$ - sampled instance of $i(t)$

N - number of samples.

Real power is calculated simply as the average of N voltage-current products. It can be shown that this method is valid for both sinusoidal and distorted waveforms.

C. Voltage RMS Calculation in Discrete Time Domain.

$$U_{rms} = \sqrt{\frac{\sum_{n=0}^{N-1} u^2(n)}{N}} \quad (3)$$

Equation 3. Voltage RMS Calculation in Discrete Time Domain.

RMS current is calculated using the same equation, substituting voltage samples, $u(n)$, for current samples, $i(n)$.

IV. INTERFACING ARDUINO WITH SENSORS

1. The CT sensor and burden resistor
2. The biasing voltage divider ($R1$ & $R2$)

For example if we choose 100A as our maximum current;

$$\text{Primary peak-current} = \text{RMS current} \times \sqrt{2} = 100 \text{ A} \times 1.414 = 141.4 \text{ A} \quad (4)$$

$$\text{Secondary peak-current} = \text{Primary peak-current} / \text{no. of turns} = 141.4 \text{ A} / 2000 = 0.0707 \text{ A} \quad (5)$$

$$\text{Ideal burden resistance} = (\text{AREF}/2) / \text{Secondary peak-current} = 2.5 \text{ V} / 0.0707 \text{ A} = 35.4 \Omega \quad (6)$$

$$\text{Burden Resistor (ohms)} = (\text{AREF} * \text{CT TURNS}) / (2\sqrt{2} * \text{max primary current}) \quad (7)$$

(Aref = Arduino Analog Resistance Voltage)

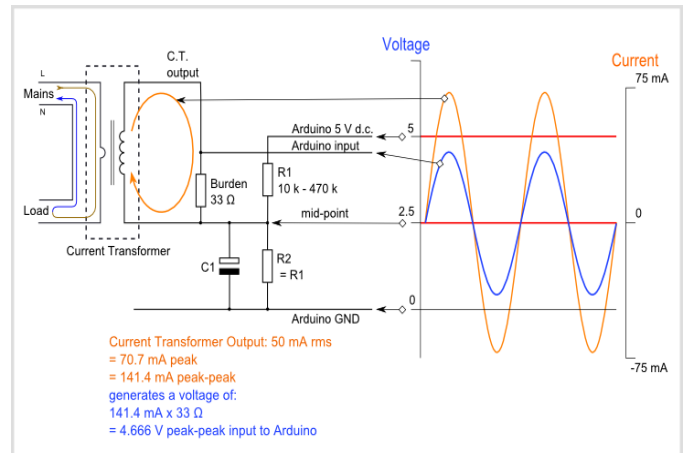


Figure 3: Interfacing Arduino with Current Transformer & Sensors

V. SET UP ARDUINO YUN SYSTEM

The Arduino Yun is basically two independent systems on one board. There is a 8bit AVR micro controller and a Linux system based on the Atheros AR9331. The Atheros runs a Linux distribution based on OpenWrt named OpenWrt-Yun (Aka Linino). We used the AVR controller for the measurement of currents, voltage, current and light. This data is then transferred to the Atheros system which performs the communication part to distribute the data. The communication between the AVR and the Atheros is done by a serial connection and a software called the "bridge". There are several tutorials on the web that explains how the two systems communicate with each other using the "bridge".

VI. INTERFACING ARDUINO WITH YHDC

The Arduino Yun can be used via USB like a regular Arduino board, we'll be using it via WiFi. Our sketches and other materials uploaded via WiFi, after the Yun is configured.

After your Yun is connected to the WiFi, we can start to work on our sketch. As you know, an Arduino Sketch has a .ino extension, that must be contained in a folder with the same name.

Basically the Arduino IDE does the job for us, by copying the content of the www folder on the SD card. If your sketch is called "mysketch", the www folder will be created on the SD card in: SD/arduino/www/mysketch. You can also do this manually, but if you upload using WiFi, the IDE will do the job.

VII. CIRCUIT DESIGN AND PROGRAMMING

A. Circuit Design

For current measurement we used 2 (CT) sensors. One is for measuring produced solar power, the other for consumed. We used 100A type (YHDC SCT-013-000). As our currents are not reaching 100A. The main line we used a 165 Ohm burden resistor, which allows a maximum measurement of 20A which is more than enough for our house consumption. For the solar panels we chose a 330 Ohm burden, which allows a maximum of 10A, which is more than enough for a 1kW system that we have used for this project.

List Of Electronic Equipments We Used In This Project

D1	1 LED White
U2	1 Arduino Y'un
C1,C2,C3	3 Capacitor Electrolytic 100uF
CON2,CON3,CON4	3 2pin wire terminals
CON1	1 4pin wire terminals
R8	1 Resistor, 100k
R9	1 Resistor, 10k
R12	1 Resistor, 1k
R1,R4,R5	3 Resistor, 330k
R10,R11,R2,R3,R6,R7	6 Resistor, 470k
6 pin headers to connect sensor shield to Arduino	3 pieces
Prototype PCB for sensor connection shield	1 piece
220V to 9V voltage transformer	1 piece
YHDC SCT013-000 current sensor	2 pieces

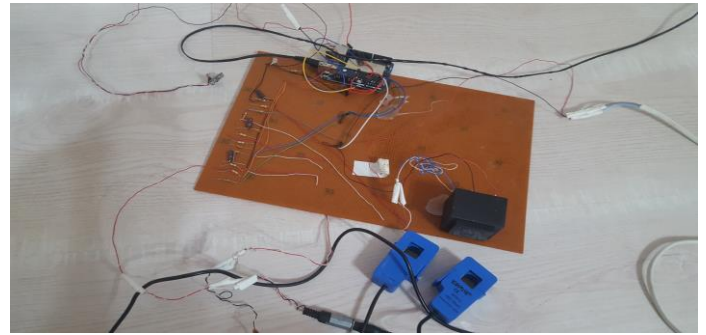


Figure 4: Designed Circuit Board in Home

B. Programming Part

1. PHP Scripts

The PHP pages to access the data from a local network or to display the data in a web browser. There are 2 php pages that we used. One is index.php for categorizing and indexing measured results to viewer, the other query.php collects measured results from Arduino then writes them to database.

2. Arduino

We firstly prepared arduino yun like a local web server,

- opkg update
- opkg install openssh-sftp-server
- opkg install php5 php5-cgi php5-mod-gd php5-mod-json php5-mod-pdo php5-mod-pdo-sqlite php5-mod-sqlite
- opkg install libsqlite3 sqlite3-cli

located php scripts to www folder, created a database in /mnt/sda1 ,then uploaded an arduino sketch for measuring the produced and consumed power. Arduino sketch collects calculating values and making a calculation with libraries. These values are like below, you can get values with <http://IP/DATA/GET> and change them in Arduino sketch.

```
{
  "value":
  {
    "c": "3.56",
    "L": "0",
    "sv": "218.75",
    "cv": "214.12",
    "cp": "0.86",
    "sa": "140.11",
    "ca": "150.57",
    "cr": "345.78",
    "C": "621.05",
    "s": "0.35",
    "S": "0.00",
    "sp": "0.40",
    "I": "0",
    "sr": "0.00"
  },
  "response": "get"
}
```

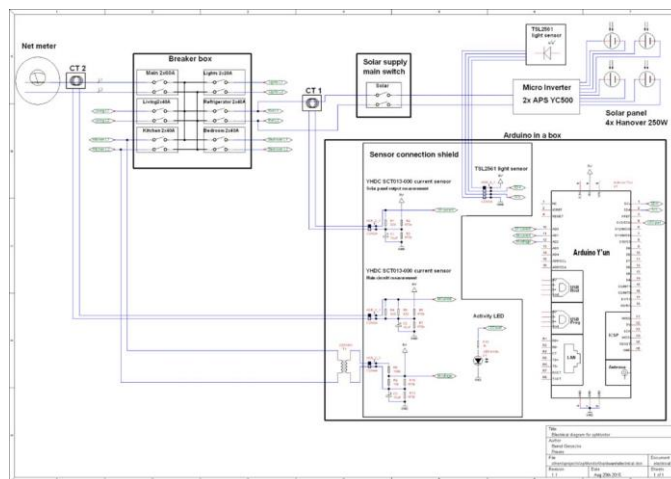


Figure 5: Circuit Design

3. Libraries We Have Used On This Project

Adafruit Sensor library

-- Link: https://github.com/adafruit/Adafruit_Sensor

-- License: Apache License, Version 2.0

Adafruit TSL2561 library

-- Link: https://github.com/adafruit/Adafruit_Sensor

-- License: BSD License

OpenEnergyMonitor CT sensor library

-- Link: https://github.com/adafruit/Adafruit_Sensor

-- License: Licence GNU GPL V3

Arduino uses emoncms library to calculate consumed and produced power.

```
/** Instance to Linino process */
Process emonCMS;

dataString += String ( solar );

dataString += ",c:";

dataString += String ( cons );

dataString += ",l:";

dataString += String ( light );

dataString += "}\\"";

emonCMS.runShellCommand ( dataString );
```

4. Calibration

There is a special url that we would use from a web browser to get the necessary data;

<http://ARDUINO-YUN-IP/data/get>

(we have to replace the ARDUINO-YUN-IP with the IP of our Arduino YUN) will send you something like

```
{ "value": { "c": "3.91", "L": "0", "sv": "217.65", "cv": "217.73", "cp": "1.01", "sa": "67.30", "ca": "850.28", "cr": "859.75", "C": "850.17", "s": "0.31", "S": "0.00", "sp": "0.19", "l": "0", "sr": "0.00", "response": "get" }
```

In this data we can see the values that we need for calibration:

- sr and sa which are the real and apparent power of the solar panel
- s which is the measured current of solar panel
- cr and ca which are the real and apparent power of the mains supply
- c which is the measured current of mains

you will need these 4 values for the calibration. You can ignore the other values but here are their meanings:

- L is the measured light value if you have a TSL2561 attached and enabled the software for it

- l is the same as above

- sv is the measured voltage from solar panel

- sp is the pShift1 value the Yun is using

- S is the power measured from the solar panel

- cv is the measured voltage from mains supply

- cp is the pShift2 value the Yun is using

- C is the power measured from mains supply

Now for the calibration:

vCal:

You have to measure the main's voltage and adjust vCal to the average value you measure

iCal1:

You have to measure the current on the solar panel supply and adjust iCal1 until the current you measure and the current (value s) send by the Yun are the same

iCal2:

You have to measure the current on the main supply and adjust iCal2 until the current you measure and the current (value c) send by the Yun are the same

pShift1:

You can change the value until the real power (value sr) and apparent power (value sa) measured from the solar panel are identical

pShift2:

You can change the value until the real power (value cr) and apparent power (value ca) measured from the mains supply are identical

It is a little bit difficult to calibrate the iCal and pShift values, but with some patience you would get the correct values.

You have to start with vCal, because until this is correct the other values will never match!

VIII. RESULTS

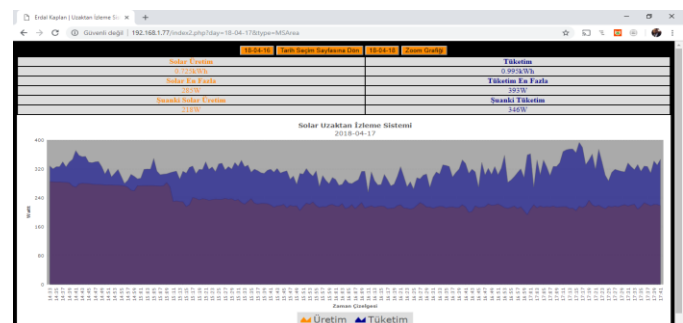


Figure 6: Display Results on 16.04.2018 14:33 between 17:41

16.04.2018 remote view record shows us;
 Produced Solar Power: 0,725kwh
 Solar Max Produce: 285 watts
 Instant Solar Power: 218 watts
 Consumed Power: 0,995kwh
 Max Consumed Power: 393 watts
 Instant Consumed Power: 346 watts

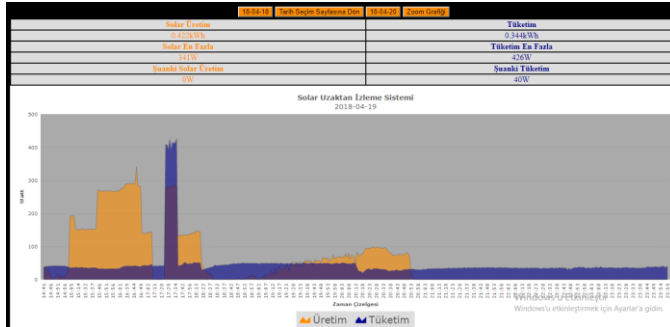


Figure 7: Display Results on 19.04.2018 14:41 between 23:59

19.04.2018 remote view record shows us;
 Produced Solar Power: 0,422kwh
 Solar Max Produce: 341 watts
 Instant Solar Power: 0 watts
 Consumed Power: 0,344kwh
 Max Consumed Power: 426 watts
 Instant Consumed Power: 40 watts

We have got these results with 500 watts solar panel, 800 watts inverter and 500 watts computer for consumed power.

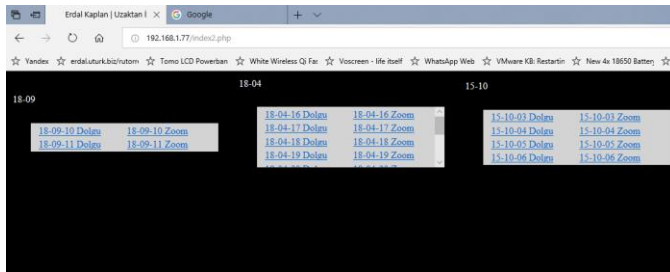


Figure 8: Monthly list of produced and consumed power

The results are not % 100 accurate but they are close for about % 10 - % 15, Project is still in development.

REFERENCES

- [1] An Open-Source Monitoring System for Remote Solar Power Applications Nikolas Wolfe, Computers and Society (2015)
- [2] Remote Sensing Letters 5 (1) Abingdon: Taylor & Francis,2014, 10-18
- [3] A server database system for remote monitoring and operational evaluation of renewable energy sources plants, Elsevier, 2005.
- [4] International Journal of Electrical, Electronics and Data Communication, Vol 2, Iss 9, Pp 1-5 (2014)
- [5] Journal of Solar Energy , Vol 2017 (2017)
- [6] Engineering Science & Technology, an International Journal; 2013, Vol. 16 Issue 4, p145-151, 7p
- [7] Establishment of a remote monitoring system for renewable energy, Kai-chun Hunag (2008)
- [8] OpenEnergyMonitor, (www.openenergymonitor.org)

Regenerative Braking Behavior Analysis of a L7 Category Vehicle in Different Drive Cycles

D. ALBAYRAK SERİN¹ and O. SERİN²

¹ Sabancı University, Istanbul/Turkey, dilaraalbayrak@sabanciuniv.edu

² Kocaeli University, Kocaeli/Turkey, serinonur@gmail.com

Abstract – Electric vehicles came into scene of automotive industry in early 1800s. At those times electric vehicles were seen as more reliable than internal combustion engines. But with decrease in price of oil and faced obstacles in cell chemistry and related components interest in electric vehicle area shifted towards vehicles with internal combustion engines until mid-1950s. With increased carbon gasses and global warming threads, automotive industry accelerated their researches on electric vehicles. When it comes to powering electric vehicles and maximization of energy utilization, regenerative braking phenomenon is one of the most crucial concepts in electric vehicle subject. Hence this study aims to observe behavior of regenerative braking over a L7 category vehicle in different cycles and discuss possible ways of making best of regenerative braking in this type of vehicles.

Keywords – Electric vehicles, modeling, regenerative braking, simulation.

I. INTRODUCTION

Since the beginning of 20th century, the field of electric vehicles has been a popular area of research and development. It is a known fact that most of the vehicles driven in daily life is powered by fossil fuels. Unfortunately, usage of vehicles with internal combustion engines lead to excessive release of carbon gasses such as SO_x (sulfur oxides), NO_x (nitrogen oxides) and other harmful gasses. Due to aims about decreasing amount of harmful gasses inside the atmosphere and providing a greener environment, studies on electric vehicles and hybrid electric vehicles have been supported vastly in recent years. But firstly electric vehicle concept should be explained in detail. Electric vehicles are road vehicles that embody electric propulsion and act suitable to green environment necessities [1]. Basic goals of electric vehicle technology can be given as high reliability, robustness, high efficiency and low cost [2]. It is stated that usage of electric power for vehicle propulsion is one of the best solutions proposed to fight fuel crisis and global warming [1]. The philosophy behind electric vehicle researches can be summarized with 5Cs concept which are cleanness, convenience, connection, cleverness and cost effectiveness [3]. Due to global warming and increasing prices of fossil fuels, usage of internal combustion engines are no longer fully desired. On the contrary, researches and developments in the

field of electric vehicles have been rising in years. It is supported that, electric vehicles will replace usage of internal combustion engines in the future [4]. So it can be emphasized that, when it comes to producing vehicles with zero emissions and leaving no carbon prints, electric vehicles can be seen as one of the best solutions for preserving the environment.

The aim of this paper is to analyze regenerative braking behavior of a L7 category electric vehicle in different drive cycles. With this study, effect of regenerative braking phenomenon over various drive cycles is observed and outcomes are compared to each other. Regenerative braking concept can be emphasized as a motor acting like generator during braking of the vehicle and converting the kinetical energy of the vehicle into electrical energy. This electrical energy returns to battery to be stored and to be re-used [5]. This concept can also be emphasized as a way of enhancing energy saving and reaching a higher level of energy efficiency [6].

This study is formed by multiple chapters. Section II, Material and Method is used to present both vehicle and drive cycle modeling processes. Detailed vehicle and drive cycle information can be seen in this section. Section III, Results stands for outcomes found from simulations which are done with the help of created models. Results of each and every cycle simulation is represented as graphs. In Section IV, Discussion outputs presented in Results section are compared, commented and interpreted. Moreover, these meanings are compared to sample papers from related literature. In the last section a conclusion is done by presenting an overall evaluation of the study along with faced problems and possible future studies will be briefly introduced.

II. MATERIAL AND METHOD

For this paper, a L7 category electric vehicle along with multiple drive cycles are modelled on MATLAB/Simulink software. A L7 vehicle is a heavy quadricycle type of car with four wheels. The scientific reason behind selection of this vehicle is the increasing share of these vehicles among total transport options and less amount of legal framework when compared to M₁ category passenger cars. Unladen mass of L7 category vehicles cannot exceed 550 kg [7]. Renault Twizy can be given as an industrial example to this type of vehicle (Figure 1).



Figure 1. Renault Twizy [8]

The vehicle used in this study has approximately 480 kg of unladen mass and 13 kW maximum motor power. All these properties apply with L7 category vehicle requirements [7]. Load model, battery model and other sub-systems are configured on MATLAB/Simulink and their combination provides the whole vehicle model. Overall vehicle model is presented in Figure 2, below.

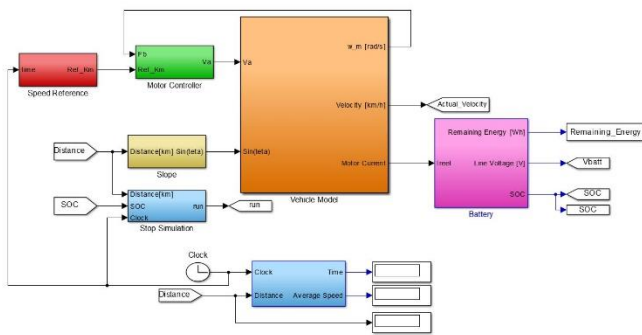


Figure 2. Vehicle Model

In addition to vehicle model, multiple route options are also modelled which the vehicle is simulated to be driven such as NEDC, Japanese, WLTC, UDSS drive cycles. NEDC stands for new European drive cycle which is a regulative drive cycle used for vehicle certification [9]. WLTC represents worldwide harmonized light duty test cycle and it is used to monitor drive ability of the vehicle [10]. UDSS stands for urban dynamometer driving schedule. It is mostly utilized for light duty vehicles [11] hence this cycle is very useful for this study due to characteristics of the modelled vehicle.

NYCC drive cycle stands for New York City cycle along with its traffic features [12]. Japanese drive cycles benefitted in this study is JP 10-15, this cycle explicitly belongs to Japan [13]. Apart from regulative cycles, a route from Turkey is added to this study by researchers. This route corresponds to toll road between Istanbul and Ankara, two of the most well-known cities of Turkey. Analysis results of these cycles are represented in Section III, Results.

III. RESULTS

At the first simulation the modelled vehicle is tested on Japanese drive cycle. In Figure 3, alteration of vehicle velocity during Japanese cycle, JP 10-15 is given.

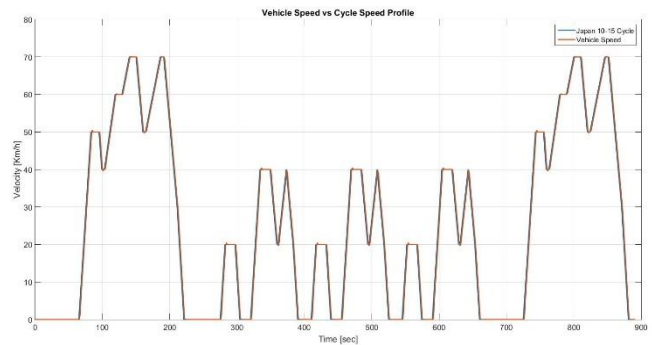


Figure 3. Japanese Drive Cycle Velocity Alteration

From above it can be seen that, velocity profile of the modelled vehicle is 100% compatible with velocity profile of the Japanese Drive Cycle. After this step, the vehicle is tested on NEDC drive cycle in order to observe speed changes in this route. Related graph is given in Figure 4.

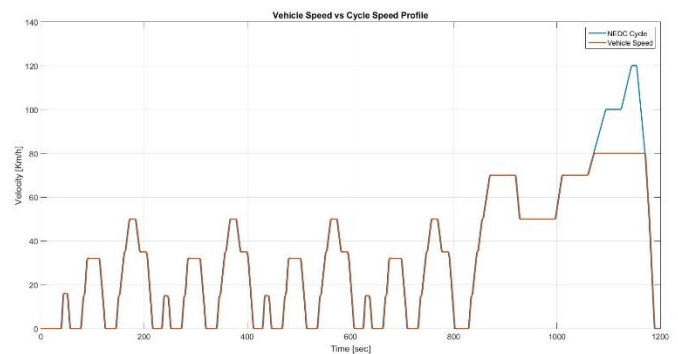


Figure 4. NEDC Drive Cycle Velocity Alteration

In Figure 4 it can be observed that at one point in NEDC drive cycle velocity reaches 120 km/h but since maximum velocity the modelled vehicle can reach is 80 km/h it can only cover that distance with 80 km/h. Following simulation is carried out in WLTC drive cycle and acquired graph is presented in Figure 5.

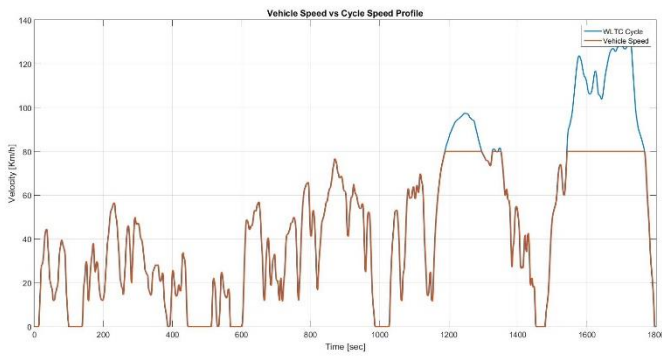


Figure 5. WLTC Drive Cycle Velocity Alteration

Again in this drive cycle there are two sections where velocity exceed maximum velocity value of the modelled vehicle thus it can only cover these areas with 80 km/h. UDDS cycle is also run in this paper and simulation results are given in Figure 6. UDDS cycle represents Los Angeles city driving conditions hence there is a vast variation gap in velocity graph.

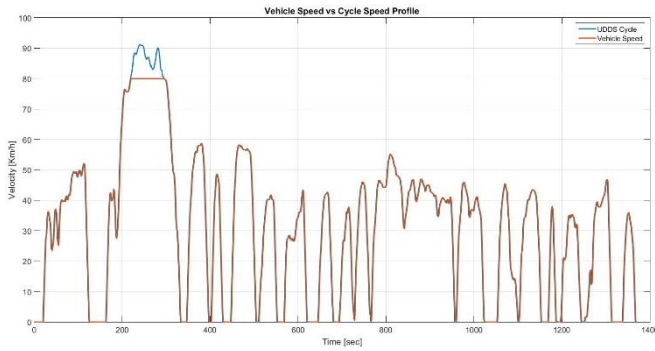


Figure 6. UDDS Drive Cycle Velocity Alteration

At some point UDDS velocity profile goes beyond 80 km/h, these intervals are covered with the maximum velocity value of the vehicle. New York City cycle, NYCC is also driven in simulations and related graph is given in Figure 7.

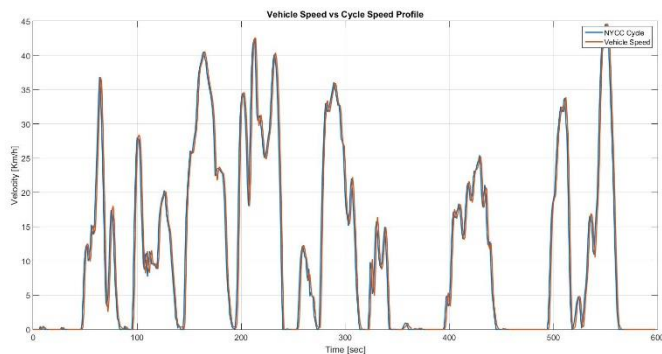


Figure 7. NYCC Drive Cycle Velocity Alteration

Since velocity profile in NYCC drive cycle is quite low, the vehicle can easily adapt to these values. To elaborate, as given in Figure 7, velocity profiles fit almost perfectly. After testing the vehicle in these multiple regulative cycles, information

retrieved about regenerative braking is gathered on a single graph, Figure 8.

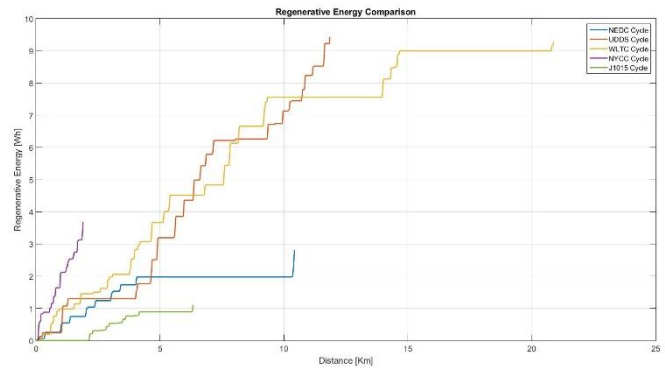


Figure 8. Regenerative Braking Comparison in Regulative Cycles

As the result of simulation of each drive cycles with modelled L7 category vehicle it is seen that driving this vehicle in different drive cycles does not have any major effect of regenerative braking behavior of the vehicle since there is no slope alterations. At this point it is important to emphasize that slope is a crucial entity for regenerative braking and in case of no slope during the route, there can be no notable impact of regenerative braking.

For further analysis of regenerative braking phenomenon over L7 category vehicle, an additional route between Istanbul and Ankara with 450 kilometers along with various slopes, is created and the vehicle is driven in this route. Elevation data of the route is retrieved from Google Earth [14] and slope data is calculated accordingly. Related elevation graph is given in Figure 9.

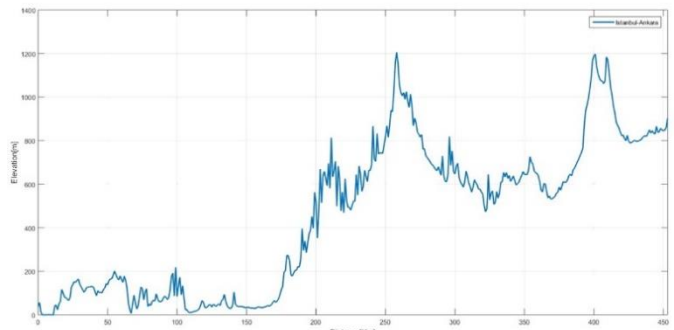


Figure 9. Elevation Alteration between Istanbul and Ankara.

As stated earlier, this route is tested via different constant velocity values. Graphs obtained with gathering of each velocity values are presented in Figure 10 and Figure 11. Explicit examination over regenerative braking between Istanbul and Ankara is done between 250 and 350 kilometers, this distance corresponds to Bolu Mountain, due to high elevation alterations which is an important effect over regenerative braking. With this application finding the answer to possible behavior change of regenerative braking over a distance with constant speed question is aimed.

From the graph it can be interpreted that with increase in slope of the descended hill, amount of retrieved energy from regenerative braking also increases.

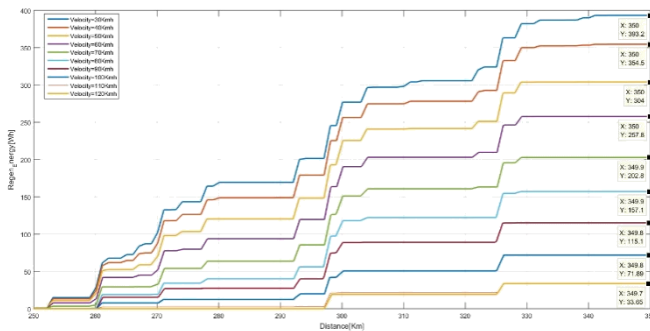


Figure 10. Energy Retrieved From Regenerative Braking

The graph stands for velocity alteration from 30 km/h to 120 km/h, by increasing the speed by 10 km/h. It can be interpreted that with increase in average velocity, recovered amount of energy from regenerative braking also decreases.

The relation between velocity and regenerative energy retrieval is also applicable for percentage graph depicted in Figure 11. From this figure, it can be interpreted that while the vehicle is cruising with 80 km/h velocity through 100 kilometers distance, it recovers 2% of its battery capacity.

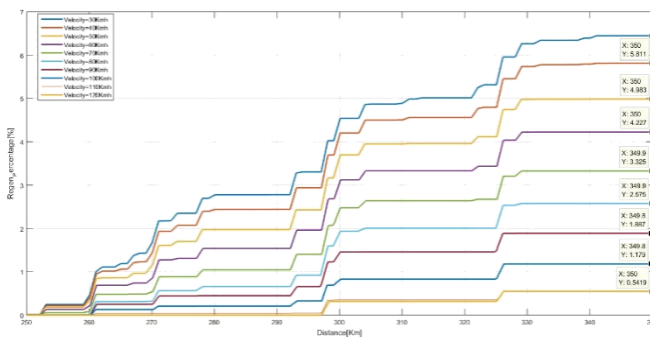


Figure 11. Percentage of Regenerative Energy Retrieval

IV. DISCUSSION

In this section, comparing results which are acquired from this study to sample papers from literature is held. The first paper from literature is done by Yoong et al. [6] in 2010 about regenerative braking concept in electric vehicles. In this paper forming a regenerative braking circuit system via different components such as MOSFETS, DC-DC converters, ultracapacitors is aimed. As the result of this study, it is stated that regenerative braking is a vital concept for electric vehicles since it yields a better energy consumption efficiency in stop-and-go traffic conditions and more control over braking. Additionally it is commented that usage of flywheels through the vehicle wheels provide power recovery enhancement during regenerative braking.

Second example from literature is a study held by Perbowo and Purwadi [15] in 2013. In this paper, researchers aim to

observe performance analysis over an electric vehicle which is converted from an internal combustion engine vehicle named GANG car. During analysis, performance of regenerative braking over GANG car is held over NEDC cycle and a custom modelled route named Sabuga downhill. Researchers model Sabuga downhill road characteristics by retrieving elevation data of the road from Google Earth [14]. It is explained that, downhill has an average slope of -9.5% and total length of the track is 311 meters. It can be interpreted from the paper that, NEDC does not have a notable relation with regenerative braking enhancement. On the other hand this situation alters vastly over analysis on Sabuga downhill with enhancement of regenerative braking effect over vehicle during cruise over the downhill. These outcomes are quite supportive for the results acquired for this new study.

Third study is done by Choi et al. [16] in 2014 in order to observe regenerative braking behavior over an electric bus. For this research multiple drive cycles such as UDDS, Busan and others are utilized in terms of drive characteristics. As the result, it is mentioned that aggressiveness and regenerative braking phenomenon are directly proportional.

The last sample from literature is held by Duong et al. [17] in 2017 for holding a control simulation to observe regenerative braking system operation over altered drive cycles. For this study researchers select regulative cycles such as NEDC, EUDC, ECE R15 and FTP-75 cycles. Modelled vehicle of this paper is a Toyota Hiace. This research states that recovering energy from regenerative braking system alters from one drive cycle to another, yet recovered energy is rather small when compared to spent energy amount. Nevertheless, it is given in the paper that energy recovery is also related to other factors like control algorithms and efficiency of energy storage systems.

In this novel study it is retrieved from simulation results is that, effect of regenerative braking over international and regulative cycles is very low. Additionally with increase in slope of the downhill, that the vehicle is cruising on, recovered energy from regenerative braking increases respectively.

V. CONCLUSION

As conclusion this paper can be summarized as analysis of a modelled light weight electric vehicle with the help of MATLAB/Simulink. For further analysis multiple drive cycles such as NEDC, UDDS along with a custom modelled route is used. Amount of recovered energy is calculated according to simulation results and compared to one another. The results retrieved from this study are solely based on simulation results and computing. For further studies, researchers aim to model vehicles from other categories and compare results of different vehicles over different drive cycles in terms of recovered energy with the help of regenerative braking.

REFERENCES

- [1] C. C. Chan, "The State of the Art of Electric, Hybrid, and Fuel Cell Vehicles," *Proceedings of the IEEE*, vol. 95, no. 4, pp. 704-718, 2007.
- [2] K. T. Chau, C. C. Chan and C. Liu, "Overview of Permanent-Magnet Brushless Drives for Electric and Hybrid Electric Vehicles," *IEEE Transactions on Industrial Electronics*, vol. 55, no. 6, pp. 2246-2257, 2008.
- [3] C. Maini, K. Gopal and R. Prakash, "Making of an 'all reason' Electric Vehicle," in *Electric Vehicle Symposium and Exhibition (EV57)*, Barcelona, Spain, 2013.
- [4] S. M. B. Billah, K. K. Islam and S. Hossain, "Experimental Verification of Regenerative Braking Characteristics by Applying Different Motor Armature Voltage," in *International Conference on Innovations in Science, Engineering and Technology (ICISSET 2016)*, Kumira, Malaysia, 2016.
- [5] M. Toll, "Regenerative braking: how it works and is it worth it in small EVs?," 24 04 2018. [Online]. Available: <https://electrek.co/2018/04/24/regenerative-braking-how-it-works/>. [Accessed 19 08 2018].
- [6] M. K. Yoong, G. D. Gan, C. K. Leong, Z. Y. PHuan, B. K. Cheah and K. W. Chew, "Studies of Regenerative Braking in Electric Vehicle," in *2010 IEEE Conference on Sustainable Utilization and Development in Engineering and Technology*, Kuala Lumpur, Malaysia, 2010.
- [7] The Commission of the European Communities, "Commission Directive 2001/116/EC," The Commission of the European Communities, 2001.
- [8] R. UK, "TWIZY features," 2018. [Online]. Available: <https://www.renault.co.uk/vehicles/new-vehicles/twizy/features.html>. [Accessed 15 08 2018].
- [9] B. Degraeuwe and M. Weiss, "Does the New European Driving Cycle (NEDC) really fail to capture the NOX emissions of diesel cars in Europe?," *Environmental Pollution*, vol. 222, pp. 234-241, March 2017.
- [10] M. Tutuianu, A. Marotta, H. Steven, E. Ericsson, T. Haniu, N. Ichikawa and H. Ishii, "Development of a World-wide Worldwide harmonized Light duty driving Test Cycle (WLTC)," Development of the Harmonized driving Cycle (DHC) Sub-group, 2014.
- [11] U. S. E. P. A. (EPA), "Vehicle and Fuel Emissions Testing Dynamometer Drive Schedules," 31 01 2017. [Online]. Available: <https://www.epa.gov/vehicle-and-fuel-emissions-testing/dynamometer-drive-schedules>. [Accessed 15 08 2018].
- [12] "EPA New York City Cycle (NYCC)," [Online]. Available: <https://www.dieselnet.com/standards/cycles/nycc.php>. [Accessed 15 08 2018].
- [13] R. Nicolas, "The different driving cycles," 01 05 2013. [Online]. Available: <http://www.car-engineer.com/the-different-driving-cycles/>. [Accessed 19 08 2018].
- [14] "Google Earth," 2017. [Online]. Available: <https://www.google.com/earth/index.html>. [Accessed 15 09 2017].
- [15] W. Parbowo and A. Purwadi, "Regenerative Braking Performance Analysis on GANG CAR Electric," in *International Conference on Information Technology and Electrical Engineering (ICITEE)*, 2013.
- [16] J. Choi, J. Jeong, S. W. Cha and Y. Park, "Analysis of Regenerative Braking Effect for E-REV Bus According to Driving Cycle Based on Simulation," in *IEEE Vehicle Power and Propulsion Conference (VPPC)*, Coimbra, Portugal, 2014.
- [17] T. T. Duong, D. Van Do and T. T. Nguyen, "Research on Using PID Algorithm to Control Simulation Model of Regenerative Braking System Based on Driving Cycles," in *International Conference on System Science and Engineering (ICSSE)*, Ho Chi Minh City, Vietnam, 2017.

Life Prediction of Aluminum Electrolytic Capacitors Used in Two-Level Inverters

V. SUEL¹, H. A. ONAY², M. K. AKINCI³ and T. OZGEN⁴

¹ Akim Metal Research and Development Center, Istanbul/Turkey, vsuel@akimmetal.com.tr

² Akim Metal Research and Development Center, Istanbul/Turkey, haonay@akimmetal.com.tr

³ Akim Metal Research and Development Center, Istanbul/Turkey, mkakinci@akimmetal.com.tr

⁴ Akim Metal Research and Development Center, Istanbul/Turkey, tozgen@akimmetal.com.tr

Abstract - Aluminum electrolytic capacitors (AL-CAPs) are widely used in two-level inverter applications with having prominent features such as high capacitance – high voltage ratings, energy storage capability and good voltage regulation performance at low-cost. Reports show that Al-CAPs play a critical role on determining a power electronics system's life performance. With increasing safety concerns brought by standards, it is crucial to deeply analyze Al-CAPs life performance in advance. For this reason, this paper focuses on the life estimation of Al-CAPs used in two-level inverters. In order to do this, a prototype is implemented and a practical and easy to understand method is suggested for selection and life estimation of Al-CAPs based on measurements on prototype. Life improvement methods are also discussed in the scope of the work.

Keywords - Aluminum electrolytic capacitor, dc link capacitor, life estimation, equivalent series resistance, fast fourier transform.

I. INTRODUCTION

AL-CAPS are widely used in a great number of power electronics applications such as uninterruptable power supplies, photovoltaic systems, wind turbines, electric vehicles, led drivers, motor drivers and etc. When price/performance characteristics are evaluated in such applications requiring high capacitance and high withstand voltage ratings, AL-CAPs stand out as the most preferred capacitor type. On the other hand, according to the research results shown in Figure 1, AL-CAPs hold the maximum distribution of long-term possible failures, which is more than 50%, compared to other power electronic devices [1, 2]. It is widely accepted that the life of a power electronics system is equal to the life of the used AL-CAPs [3]. For these reasons, the selection of AL-CAPs and its life estimation play a critical role on long-life system design.

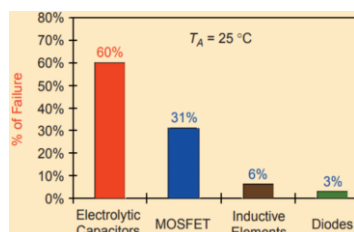


Figure 1: Distribution of failure for each power component [2]

In this study, primary wear-out mechanisms for AL-CAPs are investigated in Section 2. Life determinant factors for AL-CAPs are explained in Section 3. Based on the measurements on prototype, recommended life prediction method is provided step by step in Section 4. Results are evaluated and life increment methods are discussed at the end of the paper.

II. ROOT CAUSES OF WEAR-OUT FAULTS

AL-CAPs used in power electronics systems are expected to operate under electrical, thermal and mechanical stresses. AL-CAPs operating under harsh environment conditions start to wear out over time and they are unable to maintain their datasheet properties. The main factor that causes AL-CAPs wearing out mechanism is the evaporation of the electrolyte liquid in the internal structure shown in Figure 2. With the decline of the electrolytic liquid over time, the equivalent series resistance (ESR) of the capacitor increases, the increased ESR causes capacitor power losses to increase and hence internal temperature which further accelerates in the evaporation rate of the electrolytic liquid [4].

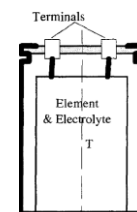


Figure 2: Mechanical construction of aluminum electrolytic capacitor [4]

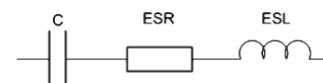


Figure 3: Equivalent model of aluminum electrolytic capacitor

The change in ESR according to the amount of electrolytic liquid in the internal structure of AL-CAP is shown in Figure 4. An old rule of thumb says that the reduction in the electrolytic liquid from 30% to 40% causes the ESR to increase 2-3 times from its initial value [4].

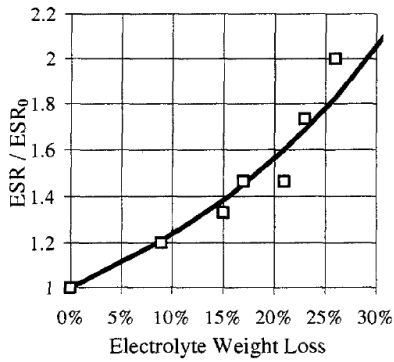


Figure 4: ESR dependence on the amount of electrolytic liquid [4]

In general terms, AL-CAPs have three distinct indicators of the completion of its useful life. Standard [5] suggests that if any of these three conditions begin to occur, AL-CAPs should be considered as failed and they should be considered as unusable:

- 20% decrease in capacitance below its initial value
- 2-3 times increase in ESR over its initial value
- Considerably increase in leakage current

After completing AL-CAPs useful life, the power system will not be able to provide the expected hold up time. Voltage fluctuations on AL-CAPs will become so high that its average value will fall significantly, especially at low line. The switching elements in the inverter structure (IGBTs, MOSFETs, etc.) will start to produce more and more heat over time and total system efficiency will deteriorate significantly. Eventually, power system will be unusable in a very short of time [6].

According to the above mentioned critical points, it is obvious that AL-CAPs directly affect the whole system's life performance. For these reasons, selection and life estimation of AL-CAPs are very important for a reliable and long life design. In the literature, capacitor life estimation methods are generally based on capacitance and ESR monitoring, which are seem to be impractical, rather complex, time-consuming or quite expensive [1, 7, 8]. In this study, a practical and easy to understand method is suggested to estimate the life of the selected AL-CAPs used in two-level inverters. By implementing the suggested life estimation method, the information on replacing time of the capacitors are provided for the users before aforementioned situations occur.

III. LIFE CALCULATION PARAMETERS

The simplest AL-CAP life calculation method is based on the assumption that life is doubled with every decrease of temperature by 10°C [6]. Life estimation formula based on this assumption is given by equation (1):

$$L_{\text{estimated}} = L_0 * 2^{(T_{\text{rated}} - T_{\text{operated}})/10} \quad (1)$$

- $L_{\text{estimated}}$: Estimated life
- L_0 : Rated life
- T_{rated} : Maximum operating temperature
- T_{operated} : Case temperature under working conditions

Equation (1) is a practical way to get an idea of life, whereas it gives an erroneous result since it is lack of the information of current harmonics and operating voltage. In this study, a life estimation method is presented by considering current harmonics, temperature and operating voltage effects to get more reliable and accurate result.

A. Effect of Current Harmonics on AL-CAPs life

In all two-level inverter structures shown in Figure 5, the dc bus faces with high frequency ripple current due to high frequency pulse-width modulation (PWM) switching of the inverter side and low frequency ripple current from the source side [9]. For this reason, dc bus capacitor current frequency spectrum consists of low frequency (100 Hz and its multiplies) and high frequency ($2*f_{\text{sw}}$, its multiplies and side-bands) components. All harmonic contents have an effect on capacitor power dissipation and its life. Therefore, capacitor life estimation methods without considering the effects of current harmonics are not so accurate [10].

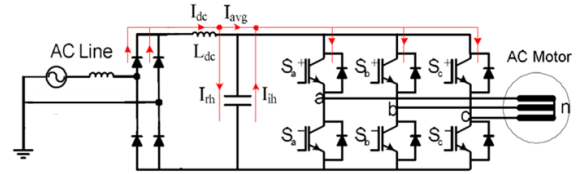


Figure 5: General structure of two-level inverters [9]

In order to examine the current harmonics effect on life, the first step is to obtain all 100 Hz referred values of each harmonic contents via the datasheet graph shown in Figure 6. Thereafter, total 100 Hz equivalent rms current value should be calculated using equation (2). The ripple current factor, RCF, is then calculated using equation (3).

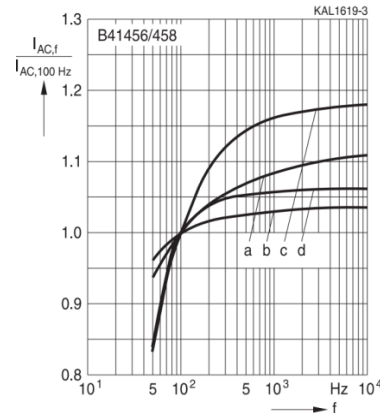


Figure 6: Frequency factor of permissible ripple current [10]

$$I_{AC,100Hz} = \sqrt{\sum_1^n (I_{1,100Hz}^2 + I_{2,100Hz}^2 + \dots + I_{n,100Hz}^2)} \quad (2)$$

$$RCF = \frac{I_{AC,100Hz}}{I_{\text{rated}}} \quad (3)$$

B. Temperature Effect on AL-CAPs life

According to the Arrhenius Law, the life of the aluminum electrolytic capacitor is calculated based on the assumption that it is doubled with every decrease of temperature by 10°C. [3]. In order to apply this assumption, the rms value of the current flowing through the capacitor in any operating conditions must be smaller than the ripple current rating. The ripple current ratings are usually given in the datasheets at the maximum ambient temperature (85°C or 105°C). The temperature multipliers are needed, as shown in Figure 7, to find the maximum permissible rms current value for the working conditions. If the calculated rms current value under operating conditions does not exceed the ripple current rating, the capacitor life cycle according to the Arrhenius Law can be applied to get an idea of life for the selected capacitor [6].

Table 1: Example of Temperature Multipliers [11]

Temperature [°C]	40	60	85
Multiplier	1.89	1.67	1.0

In this study, as a worst case, capacitor core temperature is recommended as a reference temperature value to make life calculations more accurate [6].

C. Operating Voltage Effect on AL-CAPs life

Generally, operating voltage has a less effect on AL-CAPs life cycle performance compared to the current harmonics and core temperature effects. It is generally considered that operating voltage does not effect the life for small size radial type capacitors. On the other hand, operating voltage has an effect of capacitor life cycle for medium and large size snap in and screw type capacitors [12]. When investigating the operating voltage effect on AL-CAPs life, it is necessary to find the K_v coefficient by equation (4):

$$K_v = \left(\frac{U_R}{U_X} \right)^n \quad (4)$$

- K_v : Voltage factor
- U_R : Rated voltage
- U_X : Operating voltage
- n : Exponent

$$1.00 \leq \left(\frac{U_R}{U_X} \right) \leq 1.25 \quad \rightarrow \quad n = 5$$

$$1.25 < \left(\frac{U_R}{U_X} \right) \leq 2.00 \quad \rightarrow \quad n = 3$$

$$2.00 < \left(\frac{U_R}{U_X} \right) \quad \rightarrow \quad n = 1$$

IV. APPLICATION EXAMPLE

In this section, for an easy understanding of the recommended AL-CAP life estimation method, step by step calculation is examined based on the input parameters for a two-level inverter application in Table 1.

Table 2: Two-level inverter design inputs

Selected DC bus capacitor	1500 μ F 400 V
Supply Voltage	220 V-rms, 50 Hz
AL-CAP Operating Voltage	320 V-dc
Inverter switching frequency	10 kHz
Control Method	Space Vector PWM (SVPWM)
Cooling	Natural Cooling

Selected DC bus capacitor is 1500 μ F, 400 V aluminum electrolytic capacitor with screw terminals of part number B43455 from EPCOS [13]. For the life calculations, measurement setup in Figure 8 is established. The schematic view of the measurement setup is also shown in Figure 9. The used equipments are listed in Table 2.

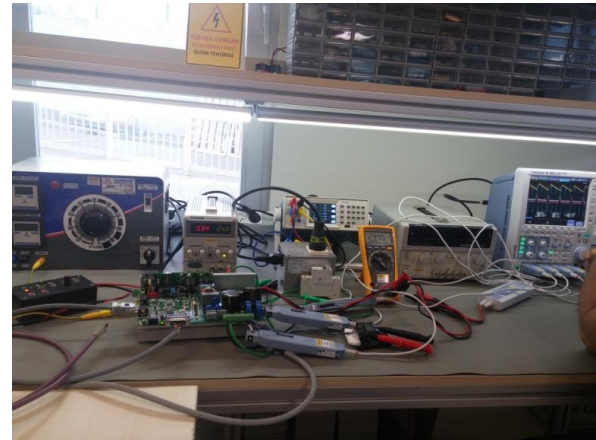


Figure 7: Test setup

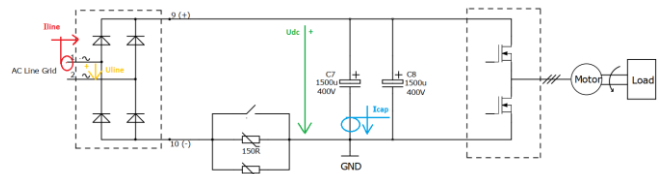


Figure 8: Schematic view of test setup

- CH1: Line voltage, U_{line}
- CH2: DC bus capacitor voltage, U_{dc}
- CH3: Line current, i_{line}
- CH4: DC bus capacitor current, i_{cap}

Table 3: Equipment list

Input source	AC Grid; 220 V _{AC} , 50 Hz
Oscilloscope	Yokogawa / DLM2034 / 350 MHz Oscilloscope
Voltage Probe	Yokogawa / 701927 / 150 MHz High Voltage Differential Voltage Probe
Current Probe	Yokogawa / 701928 / 50 MHz Current Probe

In order to measure dc bus capacitor current accurately, the current probe should be demagnetized before measurement. In addition, the current path length should be as short as possible. The recommended connection for dc bus capacitor current measurement is shown in Figure 10.



Figure 9: Measurement connection of dc bus capacitor current

An oscilloscope view of the measurement is shown in Figure 11. Harmonic spectrum of the dc bus capacitor current is also shown in Figure 12. According to the Figure 12, current harmonics frequency spectrum is well coincided with theory, which consists of low frequency harmonics (100 Hz and its multiplies) coming from the input side and high frequency harmonics (20 kHz and its multiplies) coming from the inverter side [9].

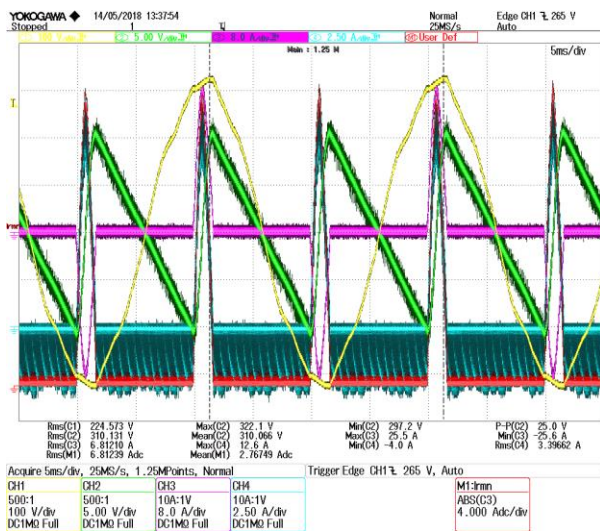


Figure 10: Oscilloscope view of measurement setup

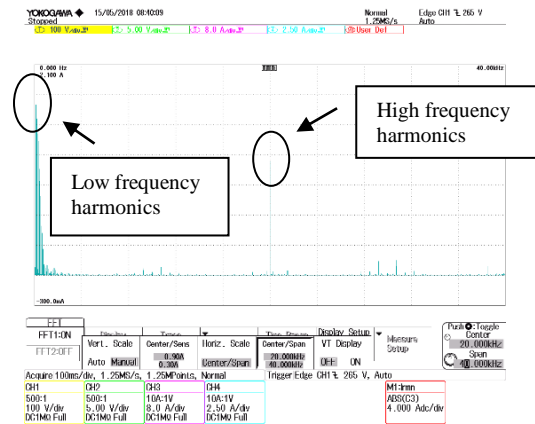


Figure 11: Harmonic spectrum of dc bus capacitor current

Equivalent 100 Hz values for each harmonic current are calculated by using frequency factors in Figure 13. Total rms current value referred to 100 Hz is calculated as 2.90 A_{rms} via equation (2). Thereafter, ripple current factor is obtained as 0.54 via equation (3). Finally, the voltage factor is calculated as 3.05 according to Table 3 values and equation (4).

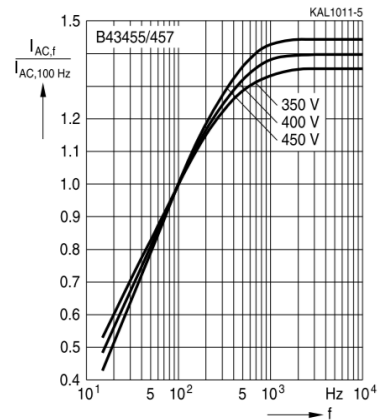


Figure 12: Frequency factor of permissible ripple current

Table 4: Measured and calculated values for current harmonics

Harmonic Frequency [Hz]	RMS Current Value [mA-rms]	100 Hz Referred Coefficients	100 Hz Referred RMS Current Values [mA-rms]
100	1750	1,00	1750
200	1600	1,15	1391
300	1390	1,25	1112
400	1135	1,30	873
500	840	1,33	632
600	590	1,38	428
700	360	1,40	257
800	175	1,42	123
20.000	1200	1,45	828
40.000	250	1,45	172
60.000	230	1,45	159
80.000	150	1,45	95
100.000	80	1,45	55

EPCOS provides useful life curves in capacitor datasheets [10]. By entering calculated ripple current factor value to the vertical axis of Figure 14, the nominal life can be obtained for various core temperatures. As a result, the life of the selected capacitor is obtained by multiplying voltage factor and nominal life value which is given in Table 4.

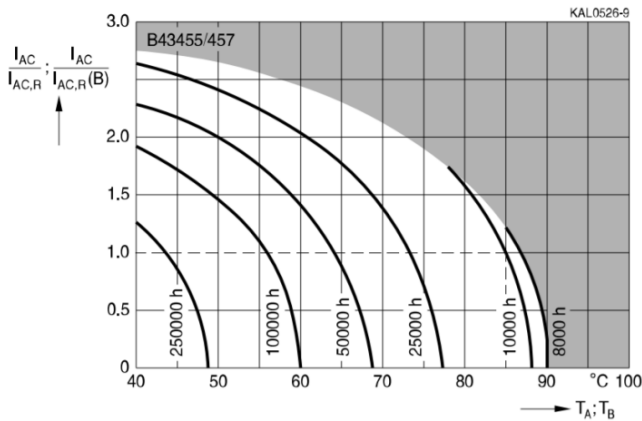


Figure 13: Useful life curve of selected AL-CAP [13]

Table 5: Life calculation results

Operating Core Temperatures [°C]	Life Prediction [k-hours]
70	114
80	60
90	24

V. EVALUATION OF THE RESULTS

In this study, instead of the complex and costly life estimation methods of dc bus capacitor in the literature, a practical and easy to implement method using the information of capacitor current harmonics, core temperature and operating voltage is presented. For this purpose, the life estimation of a selected AL-CAP used in a two-level inverter application is performed. According to the results, the most dominant factors for determining the life are observed as current harmonics and core temperature. In the future studies, input line filter effects to reduce current harmonics and forced cooling method (fan, heatsink etc.) to reduce core temperature on AL-CAP life will be investigated to improve the life performance of AL-CAPs.

REFERENCES

- [1] Lahyani, A., Venet, P., Grellet, G. and Viverge P. J., "Failure Prediction of Electrolytic Capacitors During Operation of a Switchmode Power Supply", *IEEE Trans. Speech and Audio Proc.*, 13(6):1199-1207, 1998.
- [2] Venet, P., Perisse, P., El-Husseini, M. H. and Rojat, G., "Realization of a Smart Electrolytic Capacitor Circuit", *IEEE Industry Applications Magazine*, Jan. | Feb., 2002.

- [3] Sun, B., Fan, X., Yuan, C. A., Qiang, C. And Zhang, G., "A Degradation Model of Aluminum Electrolytic Capacitors for LED Drivers", *16th International Conference on Thermal, Mechanical and Multi-Physics Simulation and Experiments in Microelectronics and Microsystems*, 2015.
- [4] Gasperi, M. L., "Life Prediction Method for Aluminum Electrolytic Capacitors", *IEEE Industry Applications Conference*, 1996.
- [5] Venet, P., Darnand, H. and Grellet, G., "Detection of faults of filter capacitors in a converter. Application to predictive maintenance," in *Proc. Int. Telecommun. Energy Conf.*, 1993, pp. 229–234.
- [6] Maniktala, S., "Troubleshooting Switching Power Converters".
- [7] Jano, R. and Pitica, D., "Accelerated Ageing Tests for Predicting Capacitor Lifetimes", *IEEE 17th SIITME*, 2011.
- [8] Kai, Y., Wenbin, H., Weijie, T., Jianguo, L., and Jingcheng, C., "A Novel Online ESR and C Identification Method for Output Capacitor of Buck Converter", *IEEE ECCE*, 2014.
- [9] Hava, A. M., Ayhan, U. and Aban, V. V., "A DC Bus Capacitor Design Method for Various Inverter Applications", *IEEE ECCE*, 2012.
- [10] "Aluminum Electrolytic Capacitors", EPCOS Data Book, 2017.
- [11] Lelon, MKR Series Aluminum Electrolytic Capacitor Datasheet.
- [12] Jianghai Application Note, Life Time Estimation.
- [13] EPCOS, B43455 Series Aluminum Electrolytic Capacitor Datasheet.

An Investigation of the PV Maximum Power Point Tracking (MPPT) Systems

M. MUTLUER¹ and K.ORKUN²

¹Necmettin Erbakan University, Department of Electrical and Electronics Engineering, Konya/Turkey, mmutluer@konya.edu.tr

²Konya/Turkey, orkun.kubra@gmail.com

Abstract - Solar systems are silicon structures that convert solar energy directly into electrical energy and have an important place in electricity generation. There are disadvantages such as high cost of investment, efficiency in energy conversion not being at desired level, although it is beneficial such as not polluting the environment, making no noise, not needing fuel. For these reasons, efforts to improve the efficiency of systems powered by solar energy have gained importance. Recent research and developments in the field of power conversion systems have led solar systems to gain momentum in recent years. The three most important factors directly affecting electricity generation from solar panels are solar radiation, ambient temperature and panel voltage. If the power transferred from the solar panel to the load is not optimal, the power obtained from the photovoltaic panel is inefficient. Maximum Power Point Tracking (MPPT) is used to maximize the efficiency of solar energy systems. However, users generally do not know which maximum power point tracking method should be used. In this study, we investigated the most efficient MPPT system design for solar panels and the most common MGN methods in the literature.

Keywords - PV Solar Tracking Systems, Maximum Power Point Tracking (MPPT)

I. INTRODUCTION

Solar energy is the transformation of solar rays on the earth into heat and electricity through solar panels. Photovoltaic (PV) batteries convert solar radiation from the surface into electrical energy. A PV power generation system consists of components such as cells, control unit and battery unit. With the light of the sun striking photovoltaic cells act like a forward-facing diode, on a wide surface with photo-voltage and photo current. The expression of the resulting stream of sunlight falling on the cell is given in.

$$I = I_{PH} - I_S \cdot \left[\exp \left[\frac{q}{A \cdot k \cdot T} \cdot (V + I \cdot R) \right] - 1 \right] - \frac{V + I_S \cdot R_S}{R_{SH}} \quad (1)$$

Here, I_{PH} represents the photon current, I_S saturation current, R is the load resistance, R and V are the series and parallel resistances, V is the load voltage, I is the load current.

In recent years, many R&D studies have been undertaken to maximize the use of the sun and to increase the efficiency of PV systems. Some of these are related to the use of Maximum

Power Point Tracking (MPPT), Solar Tracking (ST) and non-transformable inverters.

II. MAXIMUM POWER POINT TRACKING (MPPT)

The maximum power point tracking (MPPT) technique is an electronic hardware that monitors the voltage and current values of the PV system and controls the output voltage with an algorithm structure rather than physical hardware or mechanical structure.

The vast majority of studies on PV systems involve increasing productivity. Keeping the power from the PV system at the maximum level directly affects and increases the efficiency of the PV system [1]. Three methods are used to maximize the power obtained in medium and large power PV systems. These include mechanically mechanized solar tracking, maximum power point tracking (MPPT) and both. For smaller PV systems, pulse width modulation (PWM) and maximum power point tracking (MPPT) are preferred for charging systems due to economic reasons.

Linear voltage regulation in the battery charging system allows 15%-30% of the obtained energy to be transferred to the battery, while the efficiency using the DC-DC converter is between 75% and 95%. The MPPT technique is actually an improved structure of the PWM method and is controlled by PWM with the help of the MPPT algorithm [2].

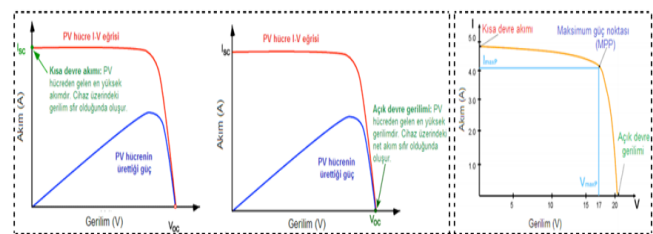


Figure 1: The current-voltage curve of a Photovoltaic cell [8]

As shown in Figure 1, the PV panel characteristic is defined as the I-V characteristic. Important points on the characteristic; the first point short circuit current I_{SC} and the second point open circuit voltage V_{OC} . In these two points the PV panel power is zero. The system's maximum power point is where the slope is zero in the I-V characteristic curve. The current and voltage values at this point constitute the maximum power value [2].

The $dP / dV = 0$ or $dP / dI = 0$ points, where the curve of the characteristic curve shown in Figure 2 is zero, is defined as the maximum power point (MPP). PMPP, VMPP, and IMPP values represent the power, voltage, or current axis trace deviations of the maximum power point [2].

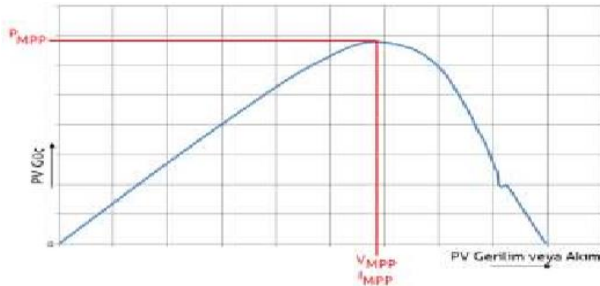


Figure 2: PV panel power curve [2]

The MPPT technique relies on the principle of finding the VMPP voltage value, IMPP current values, to obtain PMPP maximum power output from the PV panel under a given solar radiation (Figure 2). Depending on external influences (solar radiation, panel temperature or load), the voltage or current value that will produce the maximum power point may vary. Therefore, it is necessary to continuously monitor the voltage and current parameters and compare them to the previous situation [3-4].

III. MAXIMUM POWER POINT TRACKING METHODS

A. Constant Voltage Method

The simplest is the maximum power point tracking method. In this method, the panel voltage is set equal to the specified reference voltage value, and the maximum power point is set in sync with the fullness ratio setting [5]. The flow diagram of the constant voltage method is given in Figure 3.

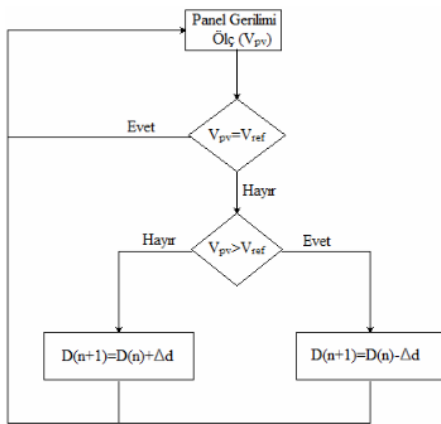


Figure 3: Constant voltage method flow diagram [5]

B. Method of Change and Observation (C&O)

In this method, firstly the voltage and current values of the solar panel are measured and the panel power P1 in the first case is calculated. In the second step, a power (P2) calculation is made again taking into account slight changes in the tension or the void space ratio (D). When P1 and P2 are compared, if P2 is greater than P1, the motion on the power curve continues

in P2 direction. If the opposite is the case, the movement on the power curve will also be in the opposite direction. At this point the maximum power point of the panel (PMPP) is present, so that the voltage value (VMPP) corresponding to that point can be found.

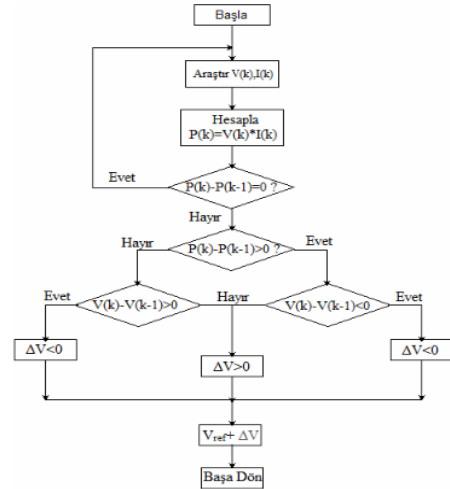


Figure 4: Method of Change and Observation flow diagram [5]

C. Increased Conductivity Method

It can be said that if the equation (2) is solved by the knowledge that the derivative of the force is equal to zero at the maximum power point, the maximum power point will be equal to zero, the positive values will be to the left of the maximum power point and the negative values to the right of the maximum power point. In this method, the maximum power point is obtained by comparing the voltage and current values with the previous voltage and current values [5]. For a photovoltaic system, the strain derivative of the output power can be expressed as:

$$\frac{dP}{dV} = \frac{d(I \cdot V)}{dV} = I + V \frac{dI}{dV} = I + V \frac{\Delta I}{\Delta V} \tag{2}$$

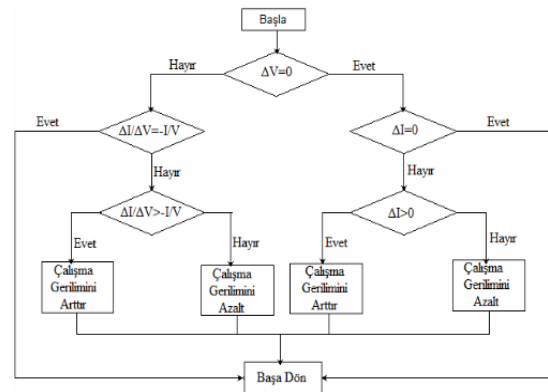


Figure 5: Increased conductivity method flow diagram

D. Open-Circuit Voltage Method

In open circuit voltage method, the relationship between open circuit voltage (VOC) and maximum power point voltage (VMPP) is examined under various environmental conditions.

$$V_{MPP} = K V_{OC} \tag{3}$$

The K value in this equation is a constant value that varies according to the characteristics of the solar panel. This constant is obtained based on VMPP and VoC measurements under various environmental conditions. It is difficult to select the most suitable value for K constant. However studies have been reported to have a value of 0.73 to 0.80 in the polycrystalline solar panel for this constant [6]. The main disadvantage of this method is that it cannot generate electricity as a result of the test cell being deactivated and thus the power loss is experienced.

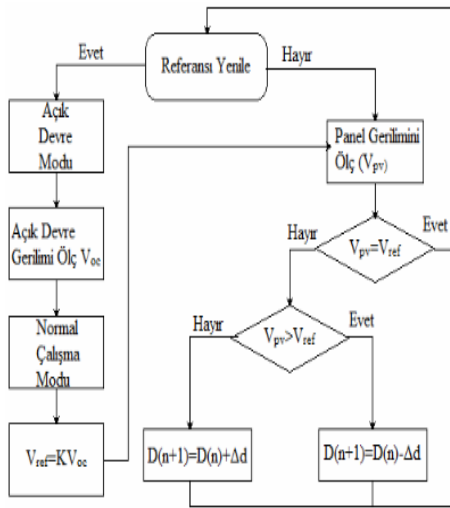


Figure 6: Open circuit voltage method flow diagram [6]

E. Short-Circuit Current Method

Short circuit current method and open circuit voltage method are similar methods. In this method, there is a linear relationship between the short circuit current of the solar panel and the maximum power point current. This relationship can be expressed as;

$$I_{MPP} = K I_{OC} \tag{4}$$

Although the short circuit current method is more accurate and effective than the open circuit voltage method, the application cost of the short circuit current is higher than the open circuit voltage because it is measured [6]. The main disadvantage of the short circuit current method is that the load is cut off from the power source while measuring the short-circuit current. The flow diagram for this method is given in Figure 7.

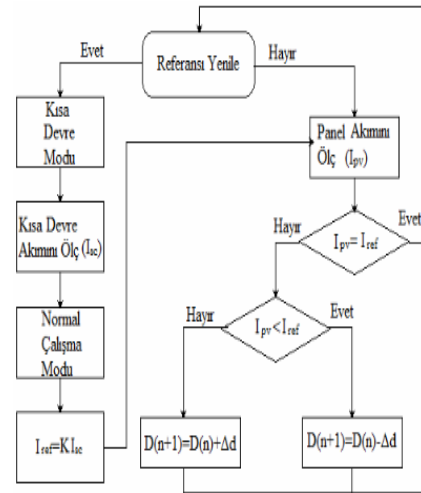


Figure 7: Short circuit current method flow diagram

F. Memory Table Method

In this method, the maximum power points of the photovoltaic panel are determined for various environmental conditions that are likely to occur and the maximum power points are loaded on the memory device in the control system. During operation, the appropriate maximum power point is determined by the present sensors and applied via in the system [6].

G. Single-Loop Control Method

The single cycle control method is a nonlinear maximum power point tracking method. This method involves the use of a single level inverter whose output current can be adjusted according to the photovoltaic panel voltage to obtain maximum power. The optimal calculation of the L and C parameters is necessary for the single cycle control method to work properly. The single cycle control system is shown in Figure 8 [7].

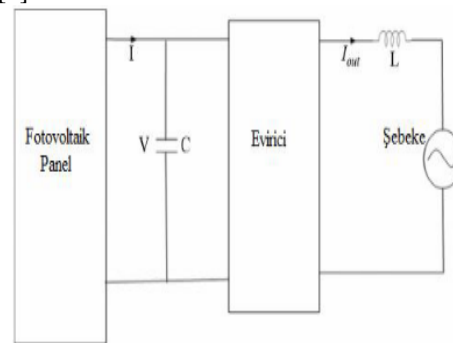


Figure 8: Single-loop control method [7]

H. Differentiation Method

In this method, the maximum power point is obtained by solving the following relation.

$$\frac{dP}{dt} = \frac{d(IV)}{dt} = I \frac{dV}{dt} + V \frac{dI}{dt} = 0 \tag{5}$$

This method needs to be solved quickly in real time so that it can work perfectly. But this is quite difficult, because at least, eight calculations and measurements of the current and voltage are required. Some of those; dV , dI , dV/dt , $V \cdot dI/dt$ and $I \cdot dV/dt + V \cdot dI/dt$ for a dt time. This method requires powerful and costly equipment to achieve a faster maximum power point tracking [7].

IV. CONCLUSION

A number of maximum power point monitoring methods have been developed to take advantage of the maximum power from solar energy. In this study, several methods of maximum power point monitoring are examined, flow diagrams of methods are given, and the advantages of methods over each other are theoretically compared and examined. All methods are successful at capturing the maximum point. However complexity, cost and application difficulty are effective in determining which method to choose. Some of the methods have very easy topologies, while others are quite complex. Again some methods operate with current or voltage information alone, while others require both. Constant voltage, open circuit voltage, short circuit current, single-loop control and memory table methods take attention with simple topological structures and low costs. Change and observation, increased conductivity and differentiation methods are separated from others by their cost, complexity, and their ability to be controlled by voltage or current parameters. The MPPT technique is actually an improved structure of the PWM method and the DC-DC converter is controlled by PWM with the help of the MPPT algorithm, and the efficiency of these systems is between 75% and 95%. Considering this data, it is aimed to select a simple, high efficiency maximum power point tracking system at the lowest possible cost and feasibility that would be possible according to the preference of the users in order to avoid the productivity losses due to not working at maximum power in solar energy systems. This system, which will be designed, will move the installed solar energy system to the maximum power point, there by preventing the loss of efficiency in the system and ensuring maximum efficiency.

REFERENCES

- [1] A.P.K. Yadav, S. Thirumaliah International Journal of Advanced Research in Electrical, Electronics and Instrumentation Engineering 1(1) (2012) 18-23.
- [2] Ercan KURAK, Volkan ERDEMİR, Bahtiyar DURSUN Düzce Üniversitesi Bilim ve Teknoloji Dergisi , PV Sistemin İçin Maksimum Güç Noktası İzleyicisi Tasarımı ve Uygulaması
- [3] B. Das, A. Jamatia, A. Chakraborti, P.Rn. Kasari, M. Bhowmik International Journal of Advances in Engineering & Technology 4(1) (2012) 579-591.
- [4] H. Abouobaida, M. El Khayat, M. Cherkaoui Journal of Electrical Engineering 14(4) (2014) 1-6.
- [5] Dolara A., Faranda R., Leva S., Energy Comparison of Seven MPPT Techniques for pv systems, Journal of Electromagnetic Analysis & Applications, 2009, 3, 152-162
- [6] Eram T., Chapman P. L., Comparison of photovoltaic array maximum power point tracking techniques, Energy Conversion, 2007, 22, 439-449.
- [7] Ali A. N. A., Saied M. H., Mostafa M. Z., Moneim T. M. A., A survey of maximum power point tracking of photovoltaic systems, Energytech, 2012, DOI:10.1109/Energytech.2012.6304652.
- [8] Sharma, S.K., Im, H., Kim, D.Y., Mehra, R.M., 2014. Review on Seand S-doped hydrogen a tedamorphous silicon films. Indian J. PureAppl. Phys., 52, pp. 293– 313.

Classification of Snore Sounds Based On Deep Spectrum Features

G.KODALOĞLU¹, F.ARI² and D.D.DEMİRGÜNEŞ³

¹ Department of Electrical and Electronics Engineering, Ankara University, Ankara, Turkey, kkodaloglu@ankara.edu.tr

² Department of Electrical and Electronics Engineering, Ankara University, Ankara, Turkey, fari@eng.ankara.edu.tr

³ Biomedical and Clinical Engineering Center, Gülhane Training and Research Hospital, Ankara, Turkey, ddemirgunes@gmail.com

Abstract - In this paper, we proposed a method to automatically extract features from snore sound signals to diagnose sleep apnea. It was observed that post apneic snore sounds starting points change abruptly, with the use of this information snore sounds' change points were detected. Different sub-datasets were obtained, spectrograms were calculated from them and Convolutional Neural Network (CNN) was used as a feature extractor. Two different machine learning algorithms were used as classifiers which were CNN and Support Vector Machine (SVM) respectively. As can be seen from the results, the feature vectors obtained with time reference to the starting points of the snore segments gave better results in apnea diagnosis as expected.

Keywords - Sleep apnea, Snore sound, Abrupt change detection, Spectrogram, CNN, SVM.

I. INTRODUCTION

THERE are many different definitions of snoring in the literature and one of them is the mechanism of snoring saying that snoring is vibration of anatomical structures through the pharyngeal airway [1]. According to the World Health Organization (WHO), Obstructive Sleep Apnea Syndrome (OSAS) is a clinical disorder marked by frequent pauses in breathing during sleeping usually accompanied by loud snoring [2]. Polysomnography is still the gold standard for diagnosis of OSAS but Home Sleep Apnea Tests are alternatively used [3]. In both cases, snoring sounds are important parts of diagnosis. Studies have shown that methods based on snoring voice analysis can reach up to 90% sensitivity and specificity and reach up to 80% accuracy rates for OSA detection [4]. Even if worked with small populations (generally between 5 and 60 subjects) [4], the results are promising.

Researchers have developed various methods for OSAS diagnose in the snore sound signal. These traditional methods use hand crafted features both in time and frequency. Azarbazin used high order statistic features like skewness, kurtosis, first formant frequency and energy to detect apnea [5]. Qian, used spectrogram pattern, intensity (dB), fundamental frequency (F_0), formant frequencies (F_1 , F_2 and, F_3) to analyse snore sound data [6]. Kızılkaya used chaotic

features of snore sounds [7]. Amiriparian proposed a method for extracting deep spectrum features for classification and localization from pretrained networks. Different type of machine learning classifiers could be used while classifying deep spectrum features [8]. Some of snore sound works related with deep learning were interested in snore source [6, 8, 9].

In this work, we proposed a method which detected snore sound s' start and end points and then spectrograms were created from these episodes. Convolutional Neural Network (CNN) was used for extracting deep spectrum features. CNN and SVM were used for classification. The two different spectrogram databases and classifiers were compared according to their classification specificity and sensitivity.

II. MATERIALS AND METHODS

System block diagram of detecting change points, extracting features and classification respectively may be seen in Fig 1.

A. Database

The data used for this study were collected from the sleep laboratory of the patients who applied to the Gülhane Military Academy Ear Nose Throat department. 4-channel Biopac Systems, Inc. brand MP35 model was used as the Biomedical Data Collection System. The records consist of snoring sounds ranging from 6 to 9 hours, blood oxygen saturation and upper airway airflow data. A microphone was connected to the first channel of this data collection unit as it should be 20 cm above the head of the patient which can record sound at a frequency of 60 - 12000 Hz [10]. The dataset was transferred to MATLAB as a text file and then saved as an audio file (fs = 2000 Hz).

B. Detection of Snore Sounds Change Points

The change point estimation of snoring segments was done by Gustafsson's multi-model approach via parallel filter [11]. The first criterion in the detection of change points is the accurate prediction of unknown change points and locations. The best way to achieve this is to estimate the regression model for each possible segment and find the values that minimize the optimization criterion [12].

According to Gustafsson, low order models usually preferred in change detection and also while selecting model

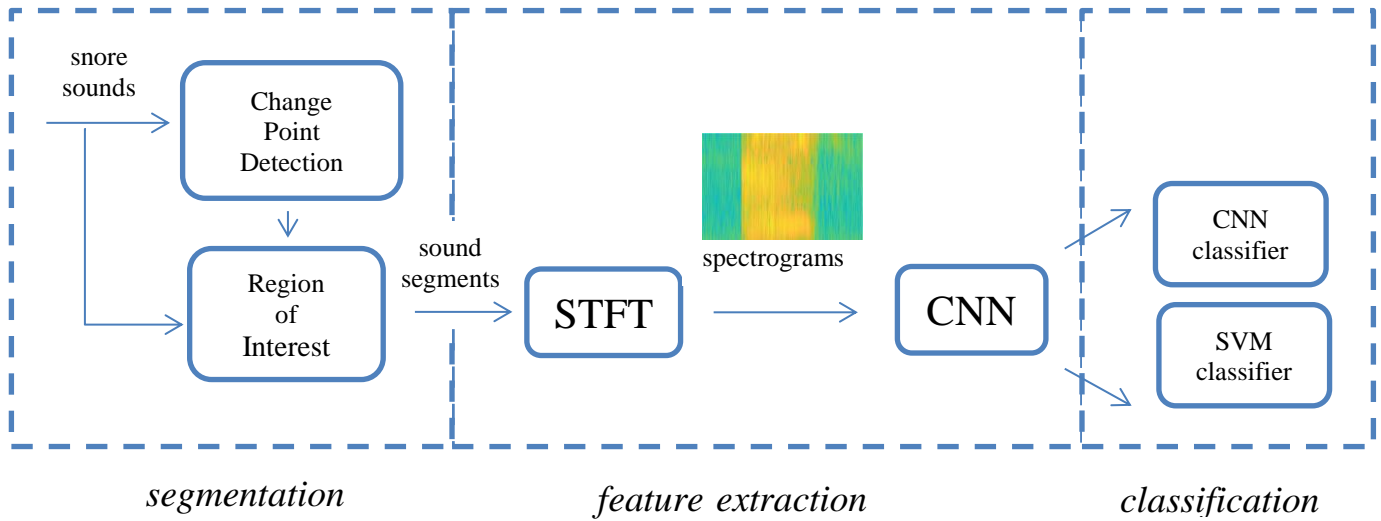


Fig. 1. Design of our proposed system

order increase the model order until the loss function (V) doesn't decrease significantly. The approach was used for an EEG signal and the loss function decreases(not significantly) second order AR model to fourth order AR model [11]. The same approach was used by Bassevi le and Nikiforov for speech signal segmentation using second order AR model [12]. As a model order, according to loss function (V), a fourth order AR model was used for each segment separately.

For each segment model was defined based on changing regression with piecewise constant parameters according to Eq. (1).

$$y_t = \varphi_t^T \theta(i) + e_t \quad (1)$$

In this formula e_t is measurement noise, φ_t (2) is auto-regression, θ_t (3) is parameter vector and i is the segment number. For AR models φ_t and θ_t are defined as below.

$$\varphi_t^T = (y_{t-1}, y_{t-2}, \dots, y_{t-n}) \quad (2)$$

$$\theta_t^T = (a_t^1, a_t^2, \dots, a_t^{n_a}) \quad (3)$$

After every possible segmentation of data was examined separately, the best model was computed and model parameters (θ_t) and their covariances (R_t) for each segmentation were estimated via least square estimation. The expectation of measurement noise square formula is given below.

$$E(e_t^2) = \lambda(i)R_t \quad (4)$$

$\lambda(i)$ is a possibly segment dependent scaling of the noise.

Estimate of θ , it's covariance and system residuals (ε) were computed;

$$P(i) = (\sum_{k_{i-1}+1}^{k_i} \varphi_t R_t^{-1} \varphi_t^T)^{-1} \quad (5)$$

$$\hat{\theta}(i) = P(i) \sum_{k_{i-1}+1}^{k_i} \varphi_t R_t^{-1} y_t \quad (6)$$

$$\varepsilon_t = y_t - \varphi_t^T \hat{\theta}_{t-1} \quad (7)$$

The test statistics V (sum of squared residuals), D (- log determinant of the parameter vectors' covariance matrix) and N (number of the data in each segment) was calculated from 5, 6 and 7.

$$V(i) = \sum_{k_{i-1}+1}^{k_i} (y_t - \varphi_t^T \theta(i))^T R_t^{-1} (y_t - \varphi_t^T \theta(i)) \quad (8)$$

$$D(i) = -\log \det P(i) \quad (9)$$

As optimality criteria, statistical criteria which was maximum likelihood was chosen. The likelihood for data y^N is denoted $p(y^N | k^N, \theta^N, \lambda^N)$. For eliminating the parameters θ^N and λ^N marginalized likelihood was used.

$$p(y^N | k^N) = \int_{\theta^N, \lambda^N} p(y^N | k^N, \theta^N, \lambda^N) p(\theta^N | \lambda^N) p(\lambda^N) d\lambda^N d\theta^N \quad (11)$$

Using these equations estimated change time sets were calculated with maximum a posteriori estimation.

$$\widehat{n, k^N} = \arg \max_{n, k^N} p(y^N | k^N) p(k^N) \tag{12}$$

According to noise scalings $\lambda(i)$ which was assumed unknown but constant possible change times were calculated as below.

$$\widehat{k^N} = \arg \min_{n, k^N} \sum_{i=1}^n D(i) + (Np - nd - 2) \log \sum_{i=1}^n \frac{V(i)}{Np - nd - 4} + 2n \log \frac{1 - q}{q} \tag{13}$$

Here, q is change probability at time n, p is measurement vector's (y_t) and d is regression vector's (φ_t) dimensions respectively.

For multiple segments different filters run in parallel, the likelihood determines which one is the best. Because of the computational complexity, a local tree search algorithm was used which is a recursive local search scheme. Generally, the global maximum can be found only by searching through the whole tree. Tree algorithm jump branches may be seen in Fig 2. With this algorithm, each branch is divided into two at time t, one of these branches expresses a jump. The historical data does not contain information about what happens after the jump. The algorithm uses some rules to keep the fixed number of sequences.

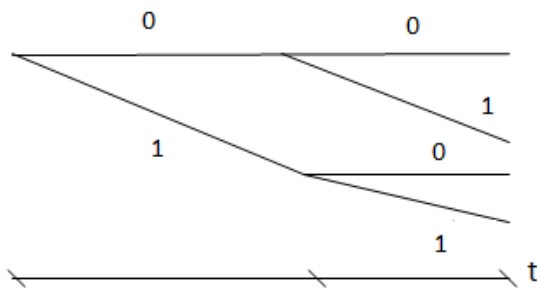


Fig. 2. Tree of jump sequences (0 corresponds no jump, 1 corresponds jump at time t)

The cut off sequences were decided according to the number of filters and sequence's lifelengths (ideally minimum lifelength should be 0). The least probable sequence was cut off until the only number of filters are left and if it was older than a minimum lifelength. The output of the algorithm at time t is a parameter estimate of the most probable sequence.

C. Visualization Method: Spectrogram

Two main datasets were calculated from snore sounds. The first one was calculated for whole snore sound segments taking around 1 sec before and after the start point. Second dataset was calculated for time durations between 50 ms

before the start point to 50 ms, 100 ms, 150 ms, 200 ms, 300 ms and 350 ms after start point respectively.

Spectrograms (log magnitude of short time Fourier transforms) were created from datasets using Short Time Fourier Transformation (STFT). Then frequency-time spectrograms were plotted by calculating power spectral densities. A snore sound after apnea, its change points may be seen in Fig 3(a) and its spectrogram may be seen in Fig 3(b).

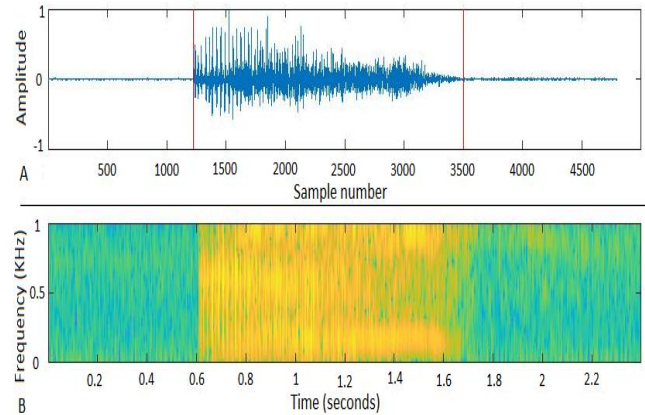


Fig. 3. (a) Example of a snore sound after apnea segmentation and (b) its spectrogram

D. Analysis Method: CNN

CNNs are a kind of machine learning algorithms which are commonly used for classification, recognition or detection. CNN learns features from inputs so the user doesn't need to extract features manually anymore. As is known, CNN inputs can be used with images, videos or such in this work visual representations of audio signals [13]. CNNs run a small window over the spectrogram so that the weights of the network that looks through this window can learn from various features of the input data. The used CNN architecture model is seen in Fig 4.

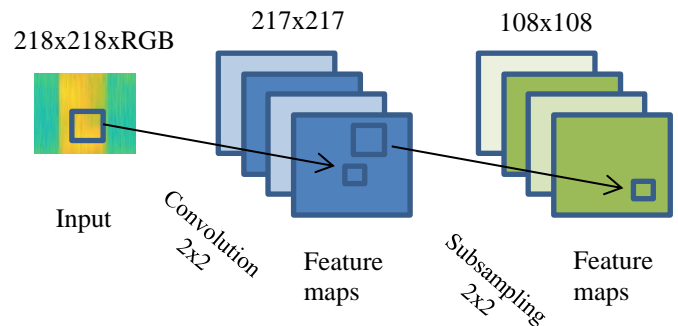


Fig. 4. Feature extraction with CNN system

The first layer is the input layer which is our spectrograms, then comes convolution layer to convolve filters (kernels) according to stride size. Third layer uses ReLU (rectified linear unit) as an activation function as,

$$f(x) = \begin{cases} x; & x \geq 0 \\ 0; & x \leq 0 \end{cases} \quad (14)$$

it makes output zero if the input is less than zero and if the input is greater than zero, the output is equal to the input. ReLU has more advantage the convergence of stochastic gradient descent compared to the other activation functions (e.g. sigmoid, tangent) [16].

The fourth layer is dropout layer, our goal in implementing this layer is to prevent overfitting making by the probabilities of half of the samples as zero. Afterward comes max-pooling layer, it takes the maximum of the value in the 2x2 matrix dimensions and again with the 2 strides it applies to the whole matrix. The output of the max-pooling layer flattened to feed the fully connected layer.

E. Classification

In this study, feature vectors which feed two different machine learning classifiers were obtained by CNN and CNN was used as one of the classifier. The other classifier was SVM which is used in previous snore sound classification works [8, 9] also.

CNN uses feature vectors as an input after implementing a softmax activation function. The function allows each output to scale from zero to one and at the same time divides each of them resulting in the sum of the outputs being equal to one. The output of the softmax function is equivalent to the probability that any of the classes are true. Using cross-entropy we could measure the performance of classification model.

SVM was used for binary (apnea or simple snoring) classification in this work. Given a training sample, the SVM constructs a hyperplane as the decision surface in such a way that the margin of separation between positive and negative examples [14]. The best hyperplane maximizes the margin between two classes using support vectors which are the closest data point to the hyperplane. The linear kernel was chosen as kernel function because of their advantages on using linearly separable data and fast solution.

III. EXPERIMENTAL RESULTS

Nine of the patients used in this study were diagnosed with apnea, the other nine were the patients diagnosed with simple snoring, and the diagnoses were made by a physician [10]. In total, 746 segments were used, of which 644 were simple snoring and the rests (102) were apnea. For classification, 5 fold cross-validation was implemented to whole data segments and the results were calculated by averaging each fold results.

It was noted apnea in adults scored when there is a drop in the peak signal excursion by $\geq 90\%$ of pre-event baseline using a sensor which could be oronasal thermal, pulse oximeter etc for ≥ 10 seconds [15].

Apnea/Hypopnea Index (AHI) was used as an apnea criteria, so if $AHI > 5$ patient scored as apnea for this work. Body mass index (BMI) was calculated as a statistic measure. Age, AHI and BMI statistics for this work may be seen in

Table I.

At this stage, the multi-model approach was used with matched filters. AR model order was chosen as 4 and 12 parallel filters were used to calculate model parameters. After this step, obtained datasets was used to calculate the STFT (20 ms Hamming window with 50% overlaps). The obtained spectrogram images were recorded in 218x218 pixel dimensions.

TABLE I. PATIENT'S STATISTICS

Diagnose	Age (mean±std. dev.)	AHI (mean±std. dev.)	BMI (mean±std. dev.)
OSAS (n=9)	43.25±17.52	25.00± 11.11	28.05± 9.46
Simple Snorer (n=9)	42.55±11.97	8.54± 5.11	27.81± 1.61

Obtained spectrograms were normalized by subtracting mean images of the training sets. After that 8 filters in 2x2x3 dimensions are used in Convolution layer. The ReLU is then followed. Then dropout and max-pooling were applied respectively. It took the maximum of the value in the 2x2 filter dimensions and again with the 2 strides it applies to the whole matrix.

The fully connected layer activations were used as features. Softmax function was used as an activation function. Then, CNN and SVM classifiers were used to score apnea and simple snorers. Here in Fig 5 obtaining features for labeling apnea (obtained from one datasets' test segments) which are fully connected layer neuron activations may be seen.

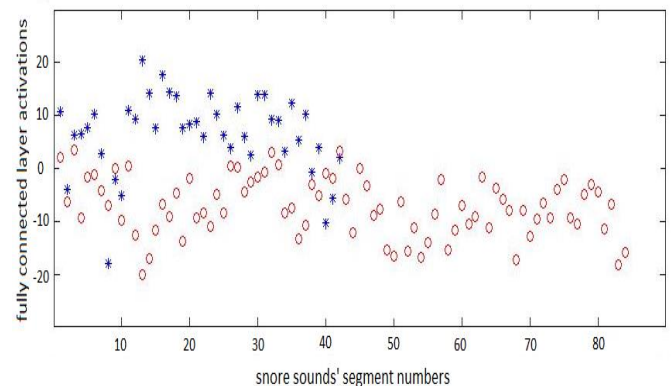


Fig. 5. The activations of the fully connected layer for each neuron (blue * dots are for snore after apnea, red o dots are for simple snore).

According to CNN and SVM classification results, specificity and sensitivity calculated. CNN 5 fold cross validation classification results may be seen in Table II and SVM 5 fold cross validation classification results may be seen in Table III. "All" meanings that the dataset which is snore segment 1sec before and after taking.

TABLE II. RESULTS OF SNORE SEGMENTS' CLASSIFICATION ACCORDING TO CNN CLASSIFIER

	Segment duration (ms)							
	100	150	200	250	300	350	400	All
Spec (%) (mean±std. dev.)	67 ± 7	76 ± 5	78 ± 7	80 ± 6	83 ± 8	73 ± 9	75 ± 5	72 ± 6
Sens (%) (mean±std. dev.)	90 ± 3	91 ± 2	90 ± 2	93 ± 2	91 ± 1	94 ± 3	92 ± 2	91 ± 2

TABLE III. RESULTS OF SNORE SEGMENTS' CLASSIFICATION ACCORDING TO SVM CLASSIFIER

	Segment duration (ms)							
	100	150	200	250	300	350	400	All
Spec (%) (mean±std. dev.)	71 ± 6	79 ± 5	82 ± 6	85 ± 4	80 ± 5	74 ± 6	73 ± 4	76 ± 4
Sens (%) (mean±std. dev.)	90 ± 2	92 ± 1	95 ± 2	91 ± 1	93 ± 3	92 ± 2	90 ± 2	91 ± 2

IV. CONCLUSION

In this study, it is thought that the sudden change at the starting points of the snoring sound signals carries meaningful information in order to classify simple snorer-apnea. For this reason, the segments obtained by the start points of the snoring sounds and the segments obtained entirely from the snore segment were applied as inputs to obtain CNN's feature vectors as two separate databases. It was observed that the classification results obtained from the start-point segments were meaningful. The features obtained from the spectrogram images were tested with two different classifiers and it was observed that the performance of the SVM better classification accuracy according to CNN.

ACKNOWLEDGMENT

The authors would like to thank Prof. Dr. Osman Eroğul allowing us to use the polysomnography records in this study.

REFERENCES

- [1] D. Pevernagie, R. M. Aarts, M. De Meyer, "The acoustics of snoring", *Sleep Medicine Reviews* 14 ,pg 131–144, 2010.
- [2] World Health Organization, [://www.who.int/respiratory/other/Obstructive_sleep_apnoea_syndrome/en/](http://www.who.int/respiratory/other/Obstructive_sleep_apnoea_syndrome/en/).
- [3] Rosen I.M. , Kirsch D.B. , Chervin R.D., Carden K.A., Ramar K., Aurora R.N., Kristo D.A., Malhotra R.K., Martin J.L., Olson E.J., Rosen CL., "Clinical Use of a Home Sleep Apnea Test: An American Academy of Sleep Medicine Position Statement", *J Clin Sleep Med.*, pg1205-1207 , 2017.
- [4] A. Roebuck et al., "A review of signals used in sleep analysis," *Physiological b Meas.*, vol. 35, no. 1, pp. R1–R57, 2014.
- [5] Azarbarzin A., "Snoring Sounds Analysis: Automatic Detection, Higher Order Statistics, and its Application for Sleep Apnea Diagnosis", Ph. D. thesis, University of Manitoba, Department of Electrical and Computer Engineering, Winnipeg, 2012.
- [6] Qian K., Janott C., Pandit V., Zhang Z., Heiser C., Hohenhorst W., Herzog M., Hemmert W., Schull, "Classification of the Excitation Location of Snore Sounds in the Upper Airway by Acoustic", *IEEE Transactions on Biomedical Engineering*, vol. 64, no 8, 2017.
- [7] Kızılkaya M., Arı F., Demirgüneş D. D. , "Detection of Sleep Apnea with Chaotic Sound Features", *Signal Processing and Communications Applications Conference (SIU)*, Haspolat, Turkey, 2013. s.l. : IEEE, 2013.
- [8] Amiriparian S., Gerczuk M., Ottl S., Cummins N., Freitag M., "Snore Sound Classification Using Image-based Deep Spectrum Features".
- [9] New T. L., Tran D. H., Ng W. Z. T., "An Integrated Solution for Snoring Sound Classification Using Bhattacharyya Distance based GMM Supervectors with SVM, Feature Selection with Random Forest and Spectrogram with CNN", *Interspeech*, Stockholm, Sweden 2017.
- [10] Demirgüneş D. D.; "Analysis and Comparison of Physiological Signals From Simple Snorers and Obstructive Sleep Apnoea Ayndrome (OSAS) Patients," Ankara University, Graduate School of Natural and Applied Sciences Department of Electronic Engineering, Ankara, 2009.
- [11] Gustafsson F., *Adaptive Filtering and Change Detection*, West Sussex:John Wiley and Sons, Ltd.,2000.
- [12] Basseville M., Nikiforov I., "Detection of Abrupt Changes: Theory and Application ", Prentice-Hall, 1993.,
- [13] Lim W., Jang D., Lee T., "Speech Emotion Recognition using Convolutional and Recurrent Neural Networks", *Signal and Information Processing Association Annual Summit and Conference (APSIPA)*, Jeju, South Korea, 2016.
- [14] Haykin S., "Neural networks and learning machines ", 3rd edition, Pearson Education, 2009.
- [15] Berry B. R., Budhiraja R., Gottlieb D., Gozal D., Iber C., Kapur V. Marcus C., Mehra R., Parthasarathy S., Quan S., Redline S., Strohl K., Ward Davidson S., Tangredi M., "Rules for Scoring Respiratory Events in Sleep: Update of the 2007 AASM Manual for the Scoring of Sleep and Associated Events", *Journal of Clinical Sleep Medicine*, Vol. 8, No. 5, 2012
- [16] Dev D., "Deep Learning with Hadoop", Packt Publishing, 2017

Drones and Their Application in Ambient Assisted Living

Radosveta Sokullu¹, Abdullah Balci¹, Eren Demir¹

¹Ege University, Izmir/Turkey, radosveta.sokullu@ege.edu.tr

¹Ege University, Izmir/Turkey, abdullah.balci@ege.edu.tr

¹Ege University, Izmir/Turkey erendemir33@gmail.com

Abstract – Extending lifespan and increased aging population in many countries around the world present a considerable challenge for healthcare services and systems. The two main options – personal care at home or in care in a nursing facility – are very human labor demanding and place a huge financial burden both for the elderly and their relatives, and the healthcare system. Many IoT based applications ensure continuous monitoring of the patient and his surroundings, providing assessment and triggering assistance when necessary. AALS is a growing area of research where new enabling technologies help add new features and solve new challenges. Unmanned aerial vehicles (UAVs), commonly known as drones, are one such technology. For years they have been indispensable for many military applications, but recently they have claimed their place in our everyday lives as well. From weather probing and gaming, to photography and transportation, drones have quickly become the new disruptive force in our society. Could they also add something new to AALS? How will the conservative elderly accept these flying mini robots? There are numerous questions that can come to one's mind.

This work presents an overview of existing drone based applications for ambient assisted living followed by a critical analysis and evaluation of drone related technologies and their possible applications in AALS for the elderly.

Keywords – unmanned aerial vehicles, drones, Internet of Things, elderly, dementia, Ambient Assisted Living

I. INTRODUCTION

As an important area of research, Ambient Assisted Living Systems (AALS) and applications have been discussed and evaluated in many comprehensive review papers. A very recent work in this area is [1] where the authors investigate approaches for developing AALS and identify current practices and directions for future research. They define ambient assisted living as the provision of sustainable care for the growing number of elderly in their homes or selected living environments, personalized care based on their profile and surrounding context, which will allow them to extend their independent existence. Considering the main functionality of the system, four major aspects of AAL systems can be defined: health monitoring aspect, safety related aspect, daily activities and routines aspect, social connectedness aspect. Each new technology contributes new features and enhances the applications that allow the elderly to remain self-sufficient for a longer time. After the boom of wireless sensor networks, cellular based applications and

Internet of Things (IoT), it seemed there is not much to be added. However, very recently many researchers have turned their attention to the “drones” and the possible applications they can fit in as related to AALS. Drones have for years been associated with military and civil, predominantly outdoor and surveillance applications. Can they be the new generation “flying pets” which will make life easier, safer and more pleasant for the elderly?

In this paper we first present a very brief characteristic of the drones, followed by a summary of existing applications in AALS incorporating drones. The study is concluded by a critical evaluation and discussion of the advantages and disadvantages of using drones in ambient assisted living system for the elderly.

II. AMBIENT ASSISTED LIVING SYSTEMS FOR THE ELDERLY

Aging population in many countries poses a large financial and human burden on providing adequate health care services increased even further by the neurological complications caused by increase life span. As people tend to live longer, dementia, Alzheimer and related conditions force them to rely on the help of other, relatives or caregivers in order to continue their existence. However, the disproportion of the number of people above 65, which is estimated to be 1 in 5 in 2030 and to reach 2.1 billion in 2050, providing home or nursing facility care becomes more and more difficult and unsustainable. A study presented in [1] reports the number for people above 65 per 100 children under the age of 15 in different parts of the world. While in the 1950 there were about 48 elderly per 100 children, in America and Europe, their number is predicted to rise to 230 for every 100 children by the year 2050.

In search of viable solutions, that will ensure the wellbeing of the elderly, the most recent technological achievements are considered. Wireless sensor networks, cellular networks and IoT are among the major technologies employed. Based on them, the so called Ambient Assisted Living systems have become a major research topic in the last ten – fifteen years. Advances in telecommunications, computer systems and sensor miniaturization, combined with the ubiquity of mobile and connected devices allow continuous monitoring, usually in real-time, assessment and triggering assistance in an event-driven intelligent way thus creating a more secure, more

reliable environment for the elderly and allow them longer independent living. These systems in general are known as Ambient Assisted Living systems. Most of them so far have focused on the monitoring, assessment and prevention of hazardous situations, in considerably static and closed environments restricting both the physical and socio-cultural inclusion of the elderly. Even though, there are many highly enhanced applications, a major issue with most of the existing solutions is that they are static systems or wearable solutions which can easily be damaged or destroyed.

A new technological wave, promising to address some very niche application cases has appeared in the form of small flying robots, known as drones. In this study we investigate and summarize some of the most recent applications of AALS that incorporate drones.

From here on the paper is structured as follows: in section III we present details related to the structure and functionality of the drones. In section IV a short overview and most popular definitions of Ambient Assisted Living systems are presented followed by a detailed and critical description and evaluation of AAL related systems which are incorporating the use of drones. The main contribution of this paper is the summary of drone based applications which can be used for extending the independent life of the elderly in their selected living environment as well as the critical evaluation of how much this new technology can contribute to the existing AAL systems and how its acceptance and usefulness can be evaluated.

III. UNMANNED AERIAL VEHICLES

Unmanned aerial vehicles (UAVs), commonly known as “drones” are cost-efficient and reliable small aerial vehicles, which can fly both autonomously or remotely controlled and are equipped with a number of sensors to serve a plethora of civil applications. Used for many years in military applications, in the last decade these small devices have become the choice for commercial applications as well due to their ease of deployment, low acquisition and maintenance costs, high-maneuverability and ability to hover. Such vehicles are being utilized in a number of areas from environmental and disaster monitoring, to search and rescue and even construction operations. Their main advantages are small size and high operability in different environments, but on the flip side their batteries are short-lived and their operation requires precise localization, usually based on a strong GPS signal. A general functional diagram based on the main building blocks of an UAV is given in Figure 1 below.

The set of different sensors comprises the first main block. Some of the most important ones are; a barometer, a pitot tube, a current/voltage sensor, an IMU (inertia measurement unit), distance, and temperature and magnetometer sensors. The second major block is the autopilot, which interprets the information from the sensors and all the other components, keeps the aircraft in balance and allows it to fly. It sends

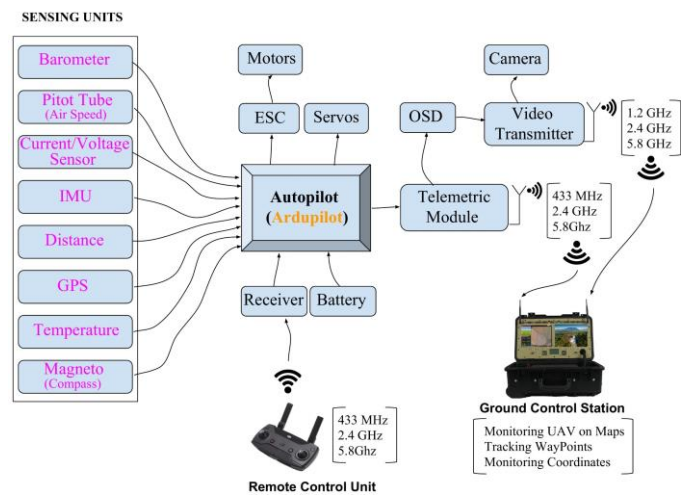


Fig. 1. Major functional blocks of an UAV

commands to the electronic speed controller (ESC) to ensure the flight of the drone. On the other hand, it receives commands from the remote controller (RC) and according to the information received it controls the servos and other motors. The third main block is the communication unit which comprises the remote controller module, the telemetric module and the video transmitter. Finally, there is the Ground Control Station (GCS) which displays real time data for the UAVs location and performance. It is also used to monitor live stream data generated by the UAV camera. The fifth and last main component is the battery; usually a Lithium polymer (LiPo) offering high capacity with low weight and high discharge rates.

Drones are usually classified based on their structure and on their specific flight capabilities. The first criteria characterize the drones as “fixed wing”, “flap wing” or “multi rotor”, while the second defines HALE (High Altitude Long Endurance vehicles, that can fly over 9000 meters), MALE (Medium Altitude Long Endurance vehicles, up to 9000m) and VTOL (vehicles which have the ability of Vertical Take-Off and Landing).

IV. AAL APPLICATIONS INCORPORATING DRONES

Ambient assisted living is a hot research topic, however there are quite many and varying definitions of what it actually covers. In its most general sense, the term AAL refers to intelligent systems of assistance for a better, healthier and safer life in the preferred living environment. It covers concepts, products and services that interlink and improve new technologies and the social environment. The authors of a major recent work [1], which investigates the approaches for developing AALS and identifies current practices, provide a more detailed definition of ambient assisted living as “the provision of sustainable care for the growing number of elderly in their homes or selected living environments, personalized care based on their profile and surrounding context, which will allow them to extend their independent

existence". Considering the main functionality of these systems, four major aspects of AALS can be defined:

1. Health monitoring aspect
2. Safety related aspect
3. Daily activities and routines aspect.
4. Social connectedness aspect.

Historically the health monitoring aspect was the first to draw researchers' attention and today there are many elaborate solutions spanning from monitoring of vital signs and chronic diseases to active telemedicine solutions like remote interaction with patients and assessment of health records. Projects related to this aspect and involving use of drones are discussed in sub-section A.

Safety of the elderly, whether living alone or in a nursing facility has always been a prime concern. Reduced mobility together with increased instability is a common reason for fatal falls and traumas. Emergencies like wandering away and getting lost are also related to the personal safety of the elderly. Fall detection also prompts a number of possible response actions especially for elderly living alone [2,3,4]. However, there are some additional points that triggered very innovative solutions involving drones which are summarized in sub-section B.

With increased age people tend to become less active and more detached, even following simple routine daily activities can become a burden. Scientists from the medical and the engineering community have joined efforts to enhance the living environments in a way to help and motivate the elderly to continue an active daily life. This is much easier in nursing facilities, where more options exist and patients are more easily motivated for physical activities. For people living alone at home even routine physical exercises can become a considerable issue. Some suggestions on how robots or drones can become the new era pets for the elderly and help motivate them for physical activities are considered in sub-section C.

Most of the existing AAL projects address these first three aspects. However, the last one, social inclusion and connectedness is most often overlooked. A major reason stems from the fact that the aging population is less accustomed to the new emerging technologies and the acceptance rate at this late stage can be very low. Being usually physically restricted, unnoticeably leads to social isolation, which in its turn further reduces the motivation for physical activities and starts a vicious downward cycle of exclusion. Some proposed solutions in this direction which involve drones in very unusual roles are discussed in sub-section D.

A. Drone aided health monitoring systems

According to an extensive study in the USA [5] the cost of chronic diseases (heart disease, diabetes, arthritis and obesity) is an overwhelming component for overall healthcare expenses. Annual medical cost for treating chronic diseases depending on the number of chronic diseases is presented in Figure 2 below.

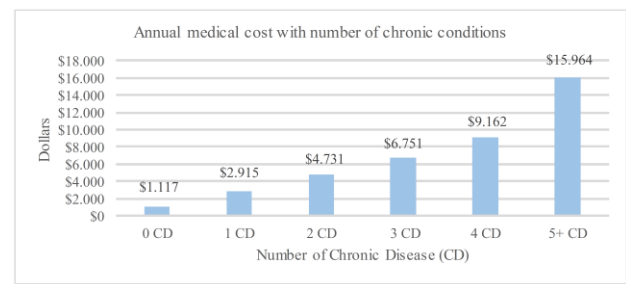


Fig. 2. Annual medical cost for different number of chronic conditions [6]

Chronic disease patients are required to visit medical facilities on a regular basis for routine checkups and medicine replenish. Community solutions combining healthcare with homecare delivery are extremely expensive especially for remote and rural areas. Difficulties in visiting medical centers and lack of transportation are major reasons for falling out with regular medication intake. In their work [7], the authors propose to use drones in order to overcome such problems in rural areas and for elderly living in remote areas.

Drones can be used to deliver routine test kits, medication refills and even pick up standard blood and urine tests. Such an application will immensely reduce travel time and workloads of caregiver and medical personnel. Drones are more competitive when time-sensitive tasks and goods are considered and are also independent of the ground roads and terrain. The authors propose and detail the concept of drone-aided aerial healthcare delivery and pickup service for chronic disease and elderly people in remote/rural areas. The main architecture of the system is given in Figure 3 below.

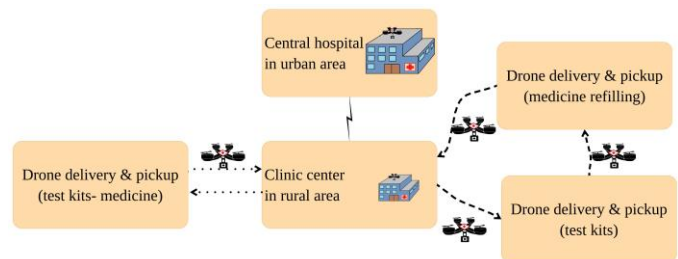


Fig. 3. Concept of drone-aided healthcare delivery and pickup service in rural area

The study shows that as simple as it is, this idea is actually not easy to realize due to both strategical and financial limitations. Thus they propose, simulate and investigate the feasibility of two different models for drone based healthcare services in rural and isolated environments: the strategic and the operational model. The strategic model allows deciding on the optimal location of drone centers and how many centers would be required for a given area, with a specific population and geographical terrain limitations. The operational model on the other hand determines the optimal number of drones for each center as well as the optimal drone flight schedule for each center. The schedules are defined taking into consideration real life limitations like specific demands of the patients in terms of flying times and restrictions as well as the

cost-benefit ratio to help provide an economically viable healthcare solution.

A major health problem that might lead to death especially in elderly people is cardiac arrest. An interesting niche application addressing distribution and delivery of AEDs (Automated External Defibrillators) which incorporates drones is discussed in the thesis work of J. Lennartson [8]. When a cardiac arrest happens outside of a hospital the survival rate is very low, because the person has to be shocked with a defibrillator within minutes of the attack. The survival rate is said to be 74% if the patient is shocked within 3 min of the arrest [9] and is reduced to 50% after 5 min [10]. As a rule, defibrillators are carried in all ambulances and recently, in Sweden, there are AEDs placed in some public areas. However, as the study in [8] points out the average time for an ambulance to reach the patient in Stockholm is around 13 min. Even worse, there are many islands, where ambulances have difficulty to reach. In such situations, the authors propose the use of drones. Their study provides some very interesting results and insights. Despite some limitations of the study, the results show that drones have larger possibilities of being faster than the ambulance especially when the high-survival-rate 3 min interval is considered (Figure 4 below).

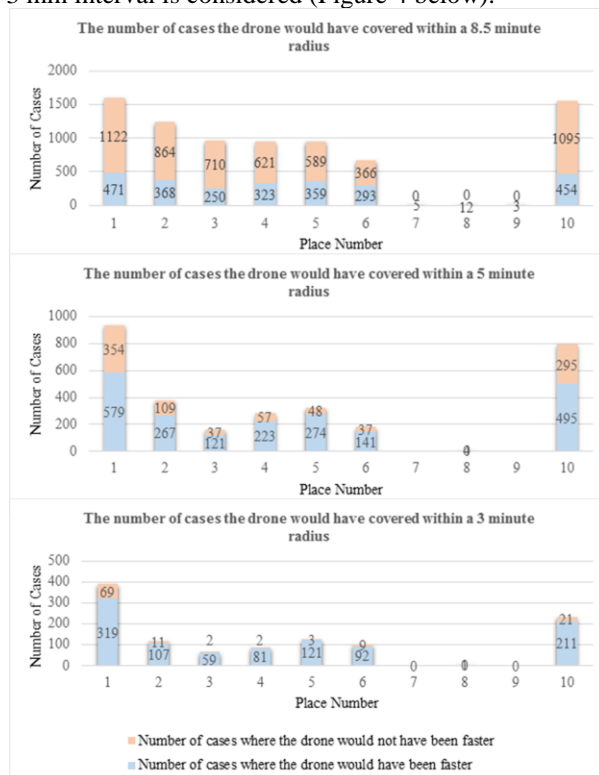


Fig. 4. The number of cases covered by drone/ambulance within 8.5, 5 and 3 minutes radius for inner Stockholm area

B. Drone aided safety related applications

A common safety hazard for the elderly, especially people in early stages of dementia, is getting lost or wandering off. An interesting drone based application has been proposed that can help in cases of wandering dementia patients [11]. A team from Toronto University describes 3 different experiments involving the use of UAV for the purpose of locating a

wandering person with dementia. The exact experiments are performed on test subjects simulating individual lost patients with dementia (PwD) employing drones together with Search and Rescue (SAR) operational methods for their rescue. Specific algorithms to determine the drones' paths are proposed and tested. Performance metrics include the time needed to detect the lost person and the complete duration of each mission. Furthermore, the authors provide a differential longitude and latitude analysis from an initial parting point (IPP) and for that calculate the time to find the test subject and the battery life of the drone.

These experiments bring light on several very important issues related to the use of drone for tracking and locating wandering elderly people in outdoor areas. First of all, the authors are optimistic that the suggested approach allows locating the missing person within the first 10 min which is considered as the lower limit for safety independent of the terrain. Second, they point out many major hurdles that have to be overcome before such operations can be considered of practical value. In order to use drones for these purposes models based on underlying algorithms of wandering that can be technically implemented to automate the search process are required. Another important issue is that drones can help locate the person but monitoring battery usage as well as longitude and latitude is crucial for success. And last but not least, a major problem exists with the specific regulations and restrictions for flying drones in different countries which have to be clarified before drone-based search and localization can become a practically feasible option.

C. Drone aided daily activities and routines

Drones are generally used in outside applications, but some researchers suggest that they can also be quite useful inside.

The first application is a UAV for indoor patient care - a customized quadcopter, called Healthbuddy, whose main goal is to facilitate independent living for the elderly in their living quarters [12]. The application can help people suffering from long hours of isolation, both elderly, or cancer patients or patients with depression. Healthbuddy is designed to navigate around the house at regular intervals trying to detect the person/patient using image, sonar and voice recognition (VR) strategies. Health based queries requiring simple yes/no responses; VR strategies to classify speech responses extracted from surrounding noise are utilized by the server to provide patient analysis. Finally, the Healthbuddy system as a whole determines what the most appropriate line of action in the given situation is. The functional block diagram of HealthBuddy is given below in Fig. 5.

A more evolved work on indoor drone application is presented in "QuadAALper - The Ambient Assisted Living Quadcopter", as the PhD thesis of Ricardo Miguel Gradim Nascimento from the University of Porto [13,14,15]. The work presents the design of a drone that can autonomously navigate inside the house and recognize a person lying on the floor. An original method for flying the drone indoors without GPS information is proposed which is based on QR code detection using a smartphone mounted on top of the drone.

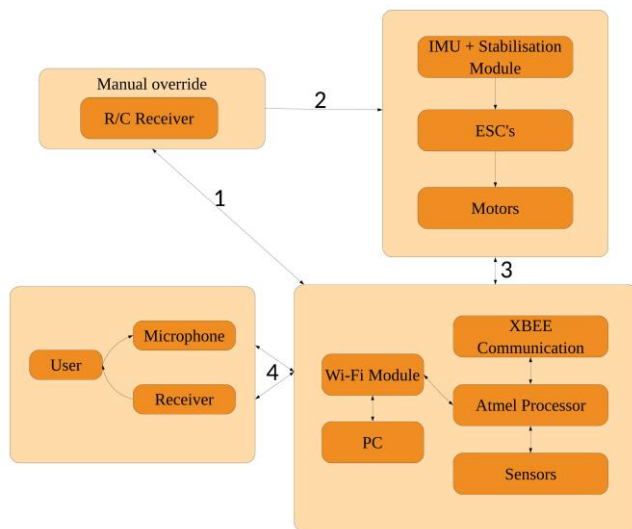


Fig. 5. The block diagram of Healthbuddy

The QR codes, 20 x 20 are placed on the ceiling. The drone is a Arducopter, controlled by an open source controller Pixhawk. This very innovative work is a first step and prototype in the realizing a “flying helper” in the house.

D. Drones for better social inclusion

Many people can argue that computer games and virtual reality are one of major reason for social isolation among the younger generation. Obviously there is also the other camp which points out the positive effects of this modern pastime as well as its potential for enhancing both visual and motor skills.

One group of researchers from Singapore has put these opinions to a test, not with children or adolescents, but with elderly citizens in a nursing facility, with ages ranging from 56 to 92 years [16]. They carried out an intervention project using Nintendo Wii to explore the long-term physiological effects of video games on the elderly. This and some other similar studies [17,18,19] inspired a group from the Polytechnic Institute of Leiria, Portugal together with a group from Ecuador, (Universidad de las Fuerzas Armadas Espe) to develop a drone based VR application for the elderly [20,21]. Their work makes use of different wireless technologies, wearable and inertia measurement unit (IMU) sensors to generate a body area network that scans arm movement and sends information through Bluetooth Low Energy (BLE) to control a virtual UAV (Unmanned Aerial Vehicle) remotely. The developed system consists of a 3D simulator using VR glasses for immersive visualization and Raspberry Pi devices with Sense HAT board for hand controls. As a result, it emulates the control of a drone in a simulated environment. The general architecture of the system is given in the Figure 6 below.

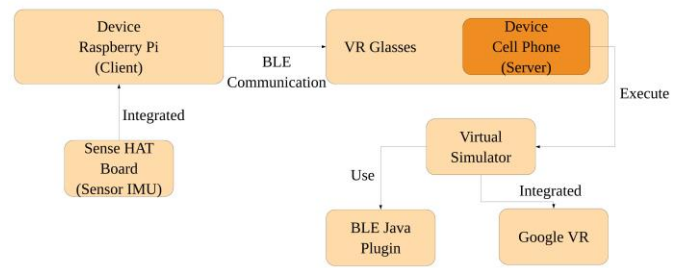


Fig. 6. General architecture of drone-based VR application

The application helps the elderly to preserve and/or develop better cognitive skills (eye-hand coordination) and improve mental and physical state. The researchers performed tests with a group of elderly in a nursing facility and observed that their skill level increased when they used the system for a period of time, progressing from easy to difficult level.

V. EVALUATION AND RESEARCH CHALLENGES

All of the discussed drone projects address a specific niche application and provide an interesting non-traditional solution. Since most of the projects are either in their initial state or first prototype it is very difficult to evaluate the effect they will have on the elderly and enhancing their lives as a component of future AAL systems.

Considering the technical requirements, it can be pointed out that such systems have several very important features in common. They should definitely be designed with high failure possibility in mind, should possess high degree of dynamism and adaptability to different specific conditions, should allow for ease of deployment and most of all should be able to ensure a desired level of privacy and confidentiality.

For evaluating the performance of these drone-based AALS the following parameters used in previous research can be considered useful.

- usability – defines the extent to which a specific technological product can be used by the specified user group to achieve the specified goal
- acceptability – defines the degree of users predisposition to use the system/tool
- efficacy – defines the capability of users to effectively complete a task using the system/tool
- utility – defines the belief of the users that using the system/tool will enhance their performance
- obtrusiveness – defines how much the users consider the system/tool as an encumbrance

At the current stage the proposed systems can be evaluated as singular, niche applications which if proven fiscally viable can pave the road to enhancing the AALS even further. Drones can fill in gaps where other technologies cannot (delivery functions), can extend scope of existing applications (localization and rescue of wandering PwD), or can enrich in content existing systems (virtual reality and gaming) and make them more appealing and easily acceptable for the elderly.

However, on the flip side, the drone technology is still not

mature and feasible enough to be easily deployed on an everyday scale. There are a number of challenges to be overcome. While technical and technological challenges are handled with ease and ingenuity with each new project or application, there are challenges outside the technical realm which can take much longer to overcome. Roughly they can be divided into two groups: regulational and ethic challenges.

Regulational challenges relate to the lack of clear nationwide and international regulations related to how, when and where drones can be flown and this is quite an important challenge. At the same time more research is required looking into existing (even though scatted and quite limited) regulations and how they have to be altered. As drones become more sophisticated and powerful questions of their proper management become even more important not only within the single countries but also internationally. Thus regulations have to be created and implemented at a much larger scale.

The second major aspect is the ethical aspect. Since the concepts of personal space and immediate environment gain completely new meanings it becomes even more difficult and elusive to define the borders of what is "good" and what is "bad". Currently there is a lot of research and standardization work going on in this area. Because this paper is focused more on the technologically related aspects we will not go in details on the ethical aspect. However, a very good evaluation on this subject can be found in [22,23].

VI. CONCLUSION

In this paper we focused on summarizing how a new emerging technology, the unmanned aerial vehicles (UAVs), commonly known as drones, can be utilized to enhance the ambient assisted living systems, ensuring longer, more independent and more safe life of the increasing growing elderly population in the world. A short description of the main functional blocks of a drone was presented followed by a concise overview of AALS and their characteristics. The main focus of the paper is the summary of very recent niche applications which feature the use of drones for creating enhanced AALS. The paper is concluded by an evaluation section, which proposes several performance metrics to be used in evaluating the drone-based AAL solutions. Finally, the open research issues and challenges are discussed.

REFERENCES

- [1] Al-Shaqi, R., Mourshed, M., Rezgwi, Y., "Progress in ambient assisted systems for independent living by the elderly", Springerplus 5 (624), pp. 1-20, 2016
- [2] Rakhman, A. Z., Kurnianingsih, Nugroho, L. E., Widyawan, "u-FAST: Ubiquitous fall detection and alert system for elderly people in smart home environment.", Makassar Int. Conf. on Electrical Engineering and Informatics, pp. 136-140 (2014).
- [3] Kong, X., Meng, L., Tomiyama, H., "Fall detection for elderly persons using a depth camera." Int. Conf. on Advanced Mechatronic Systems., pp. 269-273, (2017)
- [4] Bhati, N., "mHealth based ubiquitous fall detection for elderly people." 8th Int. Conf. on Computing, Communication and Networking Technologies, pp. 1-7, (2017).
- [5] Epping-Jordan, J., Pruitt, S., Bengoa, R., Wagner, E., "Improving the quality of health care for chronic conditions." Qual. Saf. Health Care 13(4), 299-305 (2004) [Ward, B.W.: Multiple chronic conditions among us adults: A 2012 update (2014)]
- [6] Gerteis, J., Izrael, D., Deitz, D., LeRoy, L., Ricciardi, R., Miller, T., Basu, J., "Multiple chronic conditions chartbook", Agency for Healthcare Research and Quality, (2014).
- [7] Kim, S. J., Lim, G. J., Cho, J., Cote, M. J., "Drone-Aided Healthcare Services for Patients with Chronic Diseases in Rural Areas." Journal of Intelligent and Robotic Sys 88, pp. 163-180, (2017).
- [8] Lennartsson, J., "Strategic Placement of Ambulance Drones for Delivering Defibrillators to Out of Hospital Cardiac Arrest Victims." Stockholm, KTH Royal Inst. of Tech, 2015.
- [9] Valenzuela, T.D., Roe, D.J., Nichol, G., Clark, L.L., Spaite, D.W., Hardman, R.G., "Outcomes of rapid defibrillation by security officers after cardiac arrest in casinos." The new England Journal of Medicine 343 (17), pp. 1206- 1209, (2000).
- [10] Hjärtstartarregistret, <https://www.hjartstartarregistret.se/#faktasida/1>, last accessed 2018/08/31.
- [11] Hanna, D., Ferworn, A., Lukaczyn, M., Abhari, A., Lum, J., "Using UAVs in Locating Wandering Patients with Dementia." IEEE/ION Position, Location and Navigation Symposium, (2018)
- [12] Todd, C. et al., "A proposed UAV for Indoor Patient Care, in Technology and health care" Official Journal of the European Society for Engineering and Medicine, (2015).
- [13] Nascimento, R.M.G., "QuadAALper- The Ambient Assisted Living Quadcopter", Porto, (2015).
- [14] NMEA Data, <http://www.gpsinformation.org/dale/nmea.htm>, last accessed 2018/08/31.
- [15] MAVLink Micro Air Vehicle Communication Protocol - QGroundControl GCS, <http://qgroundcontrol.org/mavlink/start>, last accessed 2018/08/31.
- [16] Jung, Y., Li, W., Gladys, C., & Lee, K. M., "Games for a Better Life: Effects of Playing Wii Games on the Well-Being of Seniors in a Long-Term Care Facility." Proceedings of the Sixth Australasian Conference on Interactive Entertainment, pp. 1-6, (2009).
- [17] IJsselsteijn, W., Nap, H.H., de Kort, Y., Poels, K., "Digital Game Design for Elderly Users." The proceeding of Future Play, pp. 17-22, Toronto (2007).
- [18] Cota, T. T., & Ishitani, L., "Motivation and benefits of digital games for the elderly: a systematic literature review." Revista Brasileira de Computação Aplicada, 7(1), pp. 2-16, (2014).
- [19] De Schutter, B., & Brown, J. A., "Digital Games as a Source of Enjoyment in Later Life." Games and Culture, 11(1-2), pp. 28-52, (2016).
- [20] Crespo, A.B., "Development a virtual reality model simulation in order to control a drone using a wearable device in a 3d environment" Leiria, (2017).
- [21] Crespo, A.B., Idrovo G.G., Rogrigues, N., Pereira, A., "Development of a virtual reality model simulation to control a drone by using wearable devices in a 3D environment." 1st International Conference on Technonology and Innovation in Sports, Health and Wellbeing, (2016).
- [22] Cavallo, F., Aquilano, M., Arvati, M., "An Ambient Assisted Living Approach in Designing Domiciliary Services Combined with Innovative Technologies for Patients with Alzheimer's Disease: A Case Study." American Journal of Alzheimer's Disease&Other Dementias 30 (1), pp. 69-77, (2015).
- [23] Novitzky, P., "Ethics of ambient assisted living technologies for persons with dementia." Dublin, (2016).

Correlations Between Color Features of Vitreous and Non-vitreous Durum Wheat Kernels With Linear Regression

Esra KAYA*, İsmail SARITAŞ

* *Electrical and Electronics Engineering, Faculty of Technology
Selcuk University, Alaeddin Keykubab Yerleskesi Selcuklu, Konya, 42075 Turkey*
esrakaya@selcuk.edu.tr
isaritas@selcuk.edu.tr

Abstract—The vitreousness of durum wheat is an indicator of the wheat kernel protein content thus its quality and color characteristics of durum wheat kernels can give us an idea about the vitreousness of durum wheat. In this study, linear regression analysis was applied in order to compare the color characteristics of vitreous and non-vitreous durum wheat kernels and to see if there is a linear relationship between them. The results were presented as a series of correlation confusion matrices and fit function graphs.

Keywords— Color Features, Correlation, Durum Wheat, Linear Regression Analysis, Vitreousness

I. INTRODUCTION

Durum wheat is the type of wheat which is preferred for the production of pasta because of its firm structure and its provision of the necessary color characteristics to the end product [1]. Good quality durum wheat has high semolina yield, which is in direct proportion with the color of pasta, and low flour rate and also has lower dry matter loss compared with bread wheat [1, 2]. Good quality wheat also has a glassy appearance which is defined as vitreousness [2]. On the contrary, non-vitreous durum wheat has low semolina yield and high flour rate and also has a somewhat opaque appearance caused by starchy spots which indicates the existence of flour [2, 3]. While vitreous durum wheat has firm structure, the structure of non-vitreous durum wheat is soft [3].

II. RELATED WORKS

There are only a handful of studies about vitreousness and the majority of them are about microscopic analysis for determining the structure of wheat kernels, or the classification of vitreous and non-vitreous wheat kernels. However, there is not a single study that evaluates the relationship between the color features of vitreous and non-vitreous durum wheat kernels.

In 2006, Neethirajan et al. classified vitreous and non-vitreous durum wheat kernels with different moisture contents [4]. The kernels' images were obtained under the influence of soft X-rays and transmitted light [4]. Gray level distribution, textural and shape moments were used as features [4]. As a result, they observed that the moisture content does not influence the classification accuracy and that the transmitted light is more advantageous for the classification accuracy [4].

In another study, Venora et al. classified vitreous, starchy, piebald and shrunken wheat kernels using a machine vision system with transmitted light illumination in 2009 [5]. Linear Discriminant Analysis (LDA) and on-line Bayesian classifier was used for the classification [5]. High overall classification percentages were found satisfying.

On the other hand, Serranti et al. used hyperspectral imaging for image acquisition and classified vitreous, yellow berry and Fusarium-damaged wheat by using Partial Least Squared Discriminant Analysis (PLS-DA) in 2013 [6]. The results were satisfactory.

Finally, the study realized by Chichti et al. in 2018 was more different than the other example studies given. In this study, similar vitreous wheat grains with different hardness which grows in two different environments were inspected for understanding the endosperm microstructure [7]. Light transmission was applied through longitudinal cross sections of wheat grains to investigate the endosperm structure and it is found that central region of grains have greater compactness compared to other regions [7].

As can be seen, there is not a single study related to the relationship between the color features of vitreous and non-vitreous durum wheat, not only in the example studies given, but in the literature in general.

III. MATERIAL AND METHOD

A. Durum Wheat Data

The durum wheat data used in this study was obtained for a previous study of ours [8]. Normalized red, green and blue color values of vitreous and non-vitreous wheat kernels were extracted from images taken as features, after the application of image preprocessing [8]. There were 3000 durum wheat kernel samples for each of vitreous and non-vitreous wheat kernels [8]. The durum wheat species was Type-1252 durum wheat [8].

B. Correlation and Linear Regression Analysis

Correlation means the dependency of two random variables to each other [9]. Our study deals with linear dependency of red, green and blue color features with each other and also the linear dependency of color features of vitreous and non-vitreous wheat kernels. Thus, in this study all linear dependencies were measured by using Pearson's correlation

coefficient and it takes the values between -1 and 1 [10]. If the correlation coefficient is close to -1, then the variables have a negative linear relationship [10]. If it is close to 1, it means that the variables have a positive linear relationship [10]. Finally, 0 value means no linear relationship [10].

But the term correlation is somewhat superficial and not really gives the exact relationship between the variables. At this point, regression analysis comes into play. Regression analysis means describing the dependence of a response variable in terms of a predictor variable, thus a response variable Y can be explained as a conditional distribution of a set of predictor variables $x = (x_1, \dots, x_p)^T$ [11, 12]. This is actually named as multiple linear regression analysis because there is more than one predictor variable. There are many scientific application areas which takes advantage of linear regression analysis for its estimation and prediction abilities [12]. For estimation purposes, regression analysis tries to estimate the effect of a predictor variable on the response variable while controlling or adjusting the other predictor variables to enhance the relationship of predictor and response variable [12]. For prediction purposes, regression analysis tries to predict response values of unobserved variables based on a estimated regression model of observed predictor values and their responses [12]. Linear regression analysis investigates the linear relationship between predictor and response variables and fit a linear model that describes the linear dependency between these variables.

In this study, correlations between various variables were investigated and linearity fit function between the variables was found based on the correlation results which gives a linear relationship.

IV. RESULTS AND DISCUSSIONS

It was found from the correlation results that red, green, and blue color features of vitreous wheat kernels were in linear correlation with each other. Table 1 shows the correlation confusion matrix belonging to red, green and blue color features of vitreous wheat kernels. The diagonals all have the value of "1" and it is a natural result because all colors are linearly correlated to themselves. Also, the other values are all close to "1", so we can conclude that red, green, and blue color features of vitreous wheat kernels are in linear correlation with each other. Linearity relationship is listed in descending order as follows: red-green, green-blue and red-blue. Similarly, red, green, blue color features of non-vitreous wheat kernels are also linearly related and the order of the linearity relationship is also similar with different correlation coefficients. Table 2 shows the correlation of non-vitreous wheat kernel color features.

The relationship between the color features of vitreous wheat kernels and non-vitreous wheat kernels is also an object of curiosity. When the correlation was investigated, it was observed that red color features of vitreous and non-vitreous wheat kernels were not linearly related because the correlation coefficients were close to "0". Same situation can also apply to other color features; the relationship between green color features of vitreous and non-vitreous wheat kernels and the relationship between blue color features of vitreous and non-

vitreous wheat kernels. The correlations belonging to these non-linearity situations are shown in Table 3, Table 4 and Table 5.

Table 1. Confusion matrix showing the linear correlation of vitreous wheat color features

Vitreous Wheat Color Correlation Confusion Matrix	Red	Green	Blue
Red	1,0000	0,9473	0,8023
Green	0,9473	1,0000	0,9112
Blue	0,8023	0,9112	1,0000

Table 2. Confusion matrix showing the linear correlation of non-vitreous wheat color features

Non-vitreous Wheat Color Correlation Confusion Matrix	Red	Green	Blue
Red	1,0000	0,9882	0,8777
Green	0,9882	1,0000	0,9240
Blue	0,8777	0,9240	1,0000

Table 3. Confusion matrix showing the nonlinearity relationship between red color features of vitreous and non-vitreous wheat kernels

Red Color Correlation Confusion Matrix	Vitreous Wheat	Non-vitreous Wheat
Vitreous Wheat	1,0000	0,0074
Non-vitreous Wheat	0,0074	1,0000

Table 4. Confusion matrix showing the nonlinearity relationship between green color features of vitreous and non-vitreous wheat kernels

Green Color Correlation Confusion Matrix	Vitreous Wheat	Non-vitreous Wheat
Vitreous Wheat	1,0000	0,0154
Non-vitreous Wheat	0,0154	1,0000

Table 5. Confusion matrix showing the nonlinearity relationship between blue color features of vitreous and non-vitreous wheat kernels

Blue Color Correlation Confusion Matrix	Vitreous Wheat	Non-vitreous Wheat
Vitreous Wheat	1,0000	0,0033
Non-vitreous Wheat	0,0033	1,0000

We have seen that the color features of vitreous wheat kernels have a linear relationship among eachother. The linearity relationship is also true for the color features of non-vitreous wheat kernels. After proving the linear relationship, it is possible to formulate the linearity by using multiple linear regression analysis. The results obtained after linear regression analysis are shown in Figure 1 and Figure 2 for both vitreous and non-vitreous durum wheat kernels, respectively. The R^2 statistic, which is known as the coefficient of determination and indicates the closeness of the data to the fitted regression line or in this study's case regression plane, is 0.8669 for vitreous wheat and it is close to 1. Thus, it is an indicator that there is significant linear regression relationship. Also, there is strong linear regression relationship between the color features of non-vitreous wheat because the R^2 statistic is 0.9066. The statistics for both linear regression analysis is shown in Table 6.

We have also compared the regression analysis fit functions by showing them together in one plot which is Figure 3. It can be seen clearly that the planes differ from eachother by some slope value which can be expressed as linear relationship. The linearity relationship between the fit functions can also be seen from the correlation confusion matrix which is shown in Table 7.

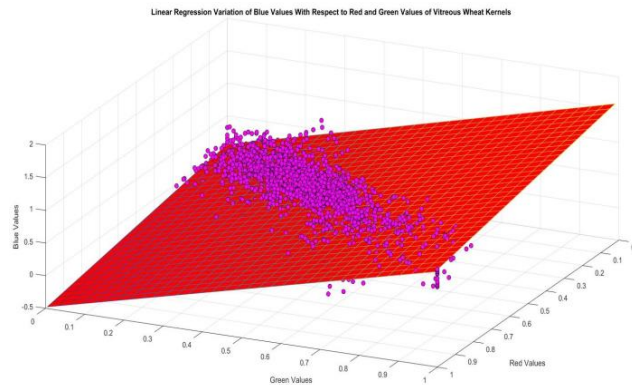


Figure 1. The Linear Regression Plane as The Fit Function for Color Features of Vitreous Wheat Kernels

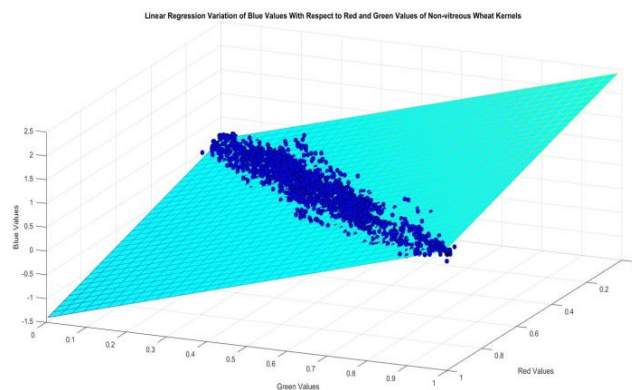


Figure 2. The Linear Regression Plane as The Fit Function for Color Features of Non-vitreous Wheat Kernels

Table 6. Statistics for linear regression analysis belonging to color features of vitreous and non-vitreous wheat kernels

Linear Regression Analysis Statistics	R^2 Statistic	F-Statistic	P-value	Error Variance
Vitreous Wheat	0,8669	6,504E+03	0	0,0064
Non-vitreous Wheat	0,9066	9,70E+03	0	0,0055

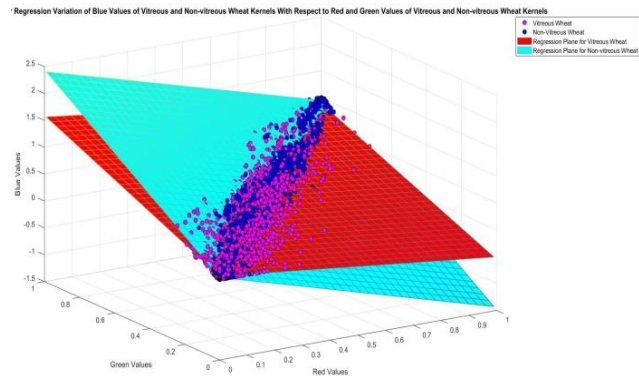


Figure 3. The Linear Regression Planes for Color Features of both Vitreous and Non-vitreous Wheat Kernels

Table 7. Confusion matrix showing the linear correlation between the regression planes of both vitreous and non-vitreous wheat color features

Regression Fit Function Correlation Confusion Matrix	Vitreous Wheat Fit Function	Non-vitreous Wheat Fit Function
Vitreous Wheat Fit Function	1,0000	0,9877
Non-vitreous Wheat Fit Function	0,9877	1,0000

V. CONCLUSION

As it is seen from the study, red, green and blue color feature combination is linearly related for both vitreous and non-vitreous durum wheat kernels. On the contrary, when we compare red to red, green to green and blue to blue color features for vitreous and non-vitreous durum wheat kernels, it can be seen that there does not exist a linearity relation. After formulating the linear dependency of blue color features to red and green color features for both vitreous and non-vitreous durum wheat kernels by using multiple linear regression analysis, we have obtained linearity fit functions which is a plane. Although red, green and blue color features of vitreous wheat kernels are not related to their equivalents of non-vitreous wheat kernels, their linearity fit function planes are linearly related to eachother which we have shown in Figure 3 and Table 7. This situation can provide us with the ability of separating durum wheat kernels as vitreous and non-vitreous

mathematically and thus, we can use a more exact model for classification problems.

ACKNOWLEDGMENT

Appreciations to Selcuk University Scientific Research Projects Unit (BAP) and Selcuk University Instructor Training Program Unit (OYP) for its support of this project.

REFERENCES

- [1] A. Torbica, M. Drašković, J. Tomić, D. Dodig, J. Bošković, and V. Zečević, "Utilization of Mixolab for assessment of durum wheat quality dependent on climatic factors," *Journal of Cereal Science*, vol. 69, pp. 344-350, 2016.
- [2] A.-N. Sieber, T. Würschum, and C. F. H. Longin, "Vitreosity, its stability and relationship to protein content in durum wheat," *Journal of Cereal Science*, vol. 61, pp. 71-77, 2015.
- [3] J. Dexter, B. Marchylo, A. MacGregor, and R. Tkachuk, "The structure and protein composition of vitreous, piebald and starchy durum wheat kernels," *Journal of cereal Science*, vol. 10, no. 1, pp. 19-32, 1989.
- [4] S. Neethirajan, C. Karunakaran, S. Symons, and D. Jayas, "Classification of vitreousness in durum wheat using soft X-rays and transmitted light images," *Computers and electronics in agriculture*, vol. 53, no. 1, pp. 71-78, 2006.
- [5] G. Venora, O. Grillo, and R. Saccone, "Quality assessment of durum wheat storage centres in Sicily: evaluation of vitreous, starchy and shrunken kernels using an image analysis system," *Journal of cereal science*, vol. 49, no. 3, pp. 429-440, 2009.
- [6] S. Serranti, D. Cesare, and G. Bonifazi, "The development of a hyperspectral imaging method for the detection of Fusarium-damaged, yellow berry and vitreous Italian durum wheat kernels," *Biosystems engineering*, vol. 115, no. 1, pp. 20-30, 2013.
- [7] E. Chichti, M. Carrère, M. George, J.-Y. Delenne, and V. Lullien-Pellerin, "A wheat grain quantitative evaluation of vitreousness by light transmission analysis," *Journal of Cereal Science*, vol. 83, pp. 58-62, 2018.
- [8] E. Kaya, İ. Sarıtaş, and İ. A. Özkan, "Detection of Impurities in Wheat and Classification of Durum Wheat Vitreousness in a Dynamic System," in *4th International Conference on Advanced Technologies & Sciences (ICAT Rome)*, Rome, ITALY, 2016.
- [9] R. A. Fisher, *Statistical Methods for Research Workers*. Oliver and Boyd, 1950.
- [10] (20.09.2018). *Correlation Coefficient*. Available: <https://ch.mathworks.com/help/matlab/ref/corrcoef.html>
- [11] D. J. Olive, "Multiple linear and 1D regression," *David J. Olive*, 2010.
- [12] G. M. Fitzmaurice, "Regression," *Diagnostic Histopathology*, vol. 22, no. 7, pp. 271-278, 2016.

Performance Comparison of 2-D ZALMS and BM3D Algorithms for Image Denoising

Gülden ELEYAN¹ and Mohammad SALMAN²

¹ Electrical & Electronics Engineering Department, Avrasya University, Trabzon/Turkey,
gulden.eleyan@avrasya.edu.tr

² Electrical & Electronics Engineering Department, American University of the Middle East, Kuwait,
mohammad.salman@aum.edu.kw

Abstract - In this study, a performance comparison was performed using our recently proposed two-dimensional zero attracting least mean square (2D ZA-LMS) algorithm and the popular block-matching and 3-D filtering (BM3D) algorithm for image denoising problem. Different experiments were carried out using different noise types such as Gaussian, Salt&Pepper and Speckle. Experimental results show that the ZA-LMS algorithm has a better performance for both sparse and non-sparse images.

Keywords – least mean square, image denoising, sparse signals, adaptive filters

I. INTRODUCTION

Image denoising is an important preprocessing step for cleaning the images exposed to noise in many areas of the image processing applications such as, satellite images, medical images and so on. There are several different state-of-the-art algorithms previously proposed that clean the noise in images. In the last couple of decades researchers have paid more attention to algorithms that use the sparsity feature as an advantage.

In [1], the first two-dimensional adaptive filtering algorithm which can be applied as an adaptive line enhancer is presented. It is a direct extension of the one-dimensional (1-D) LMS algorithm [LMS]. Researchers in [2] proposed the use of a 2-D Adaptive Wiener filtering driven by metaheuristic algorithm for the denoising of satellite images contaminated with Gaussian noise. One of the popular filtering algorithms, the block-matching and 3-D filtering method (BM3D) was proposed in 2006[3]. In this algorithm the sparsity is achieved by grouping similar 2D image blocks into 3D data arrays.

In system identification and communication applications, the system may be in sparse nature [4] such as acoustic echo cancellation and network cancellation applications. Channel impulse response is frequently sparse due to high-speed data transmission, which will be dominated by a small number of high elements or taps [5,6].

Another research based on sparse signals was presented in [7]. The algorithm is transform-based and used the real and complex valued sparse image denoising idea. For the complex domain implementation, a nonlocal BM3D filter was used.

In this paper, we are implementing our recently proposed two-dimensional zero attracting least mean square (2D ZA-LMS) [8] for image denoising problem. Our algorithm is compared with the BM3D algorithm for sparse and non-sparse images using different noise types.

The paper organized as following: Section 2 includes review of the 2-D ZA-LMS and BM3D algorithms. In Section 3 simulations and discussions about the performance comparison of the two algorithms are presented. At last section, conclusions are drawn.

II. FILTERING ALGORITHMS

A. 2-D ZALMS

One-dimensional version of the algorithm is as follows:

$$\begin{aligned} \mathbf{w}(n+1) &= \mathbf{w}(n) - \mu \frac{\partial L_1(n)}{\partial \mathbf{w}(n)} \\ &= \mathbf{w}(n) - \rho \operatorname{sgn}[\mathbf{w}(n)] + \mu e(n) \mathbf{x}(n), \end{aligned} \quad (1)$$

The update equation of the 2-D ZA-LMS algorithm can be written based on Eq (1) as:

$$\begin{aligned} \mathbf{w}_{n+1}(m_1, m_2) &= \mathbf{w}_n(m_1, m_2) - \rho \operatorname{sgn}[\mathbf{w}_n(m_1, m_2)] \\ &\quad + \mu e(n) \mathbf{x}(n_1, n_2) \end{aligned} \quad (2)$$

The dimension of the weight matrix $\mathbf{w}_n(m_1, m_2)$ is $N \times N$, where $m_1 = 0, 1, \dots, N-1$ and $m_2 = 0, 1, \dots, N-1$. Where the parameter $\rho = \mu\gamma$ and it controls the zero-attraction term. The filter weights and the input data matrix can be rewritten and converted to one dimensional case as a $N^2 \times 1$ column vector.

$$\mathbf{w}_n(m_1, m_2) = \begin{bmatrix} \mathbf{w}_n(0,0) \\ \vdots \\ \mathbf{w}_n(0, N-1) \\ \vdots \\ \mathbf{w}_n(N-1,0) \\ \vdots \\ \mathbf{w}_n(N-1, N-1) \end{bmatrix} \quad (3)$$

and

$$\mathbf{x}(n_1, n_2) = \begin{bmatrix} \mathbf{x}(n_1, n_2) \\ \vdots \\ \mathbf{x}(n_1, n_2 - N + 1) \\ \vdots \\ \mathbf{x}(n_1 - N + 1, n_2) \\ \vdots \\ \mathbf{x}(n_1 - N + 1, n_2 - N + 1) \end{bmatrix}. \quad (4)$$

B. BM3D ALGORITHM

BM3D is one of the state-of-the art algorithms that have been used in image denoising which is based on the idea of sliding the image windows and searching the blocks includes a similarity with the processed one at that moment in three-dimensional transform domain. The algorithm has two basic steps: The first one is about estimating the denoised image by hard thresholding and the second one is based on Wiener filtering where it is used for the original degraded image and the estimated version that handled from the initial step [9].

III. SIMULATION RESULTS

To test both 2D ZA-LMS and BM3D algorithms, different images were used for this comparison. Standard test images which are 8-bit 256×256 grayscale sparse and non-sparse images corrupted with different types and different degrees of noise were used. In all experiments, 2D ZA-LMS had a step size parameter as $\mu=0.001$, zero attraction term $\rho=10^{-4}$ and $\varepsilon=10$. The original images were degraded by additive white Gaussian noise (AWGN), salt & pepper, and speckle noises.

The Circuit image which is shown in Figure 1(a) is used for first test. It is degraded by an additive white Gaussian noise (AWGN) with zero mean and different variances (0.0001, 0.001, 0.02, 0.2, 0.4, 0.8) as seen in Fig 2(a). In Figure 1(c) the noisy images were filtered with BM3D algorithm and in Figure 1(d) the noisy images were filtered with ZA-LMS algorithm. We see that ZA-LMS significantly outperforms the BM3D. If we pay attention to the most degraded images while the

variance is 0.8, we see that ZA-LMS filtered the noise very efficiently.

From Figure 2(d), the ZA-LMS denoising results show that we with high variance values such as 0.8, our algorithm still capable of denoising the images in a much better way than BM3D algorithm.

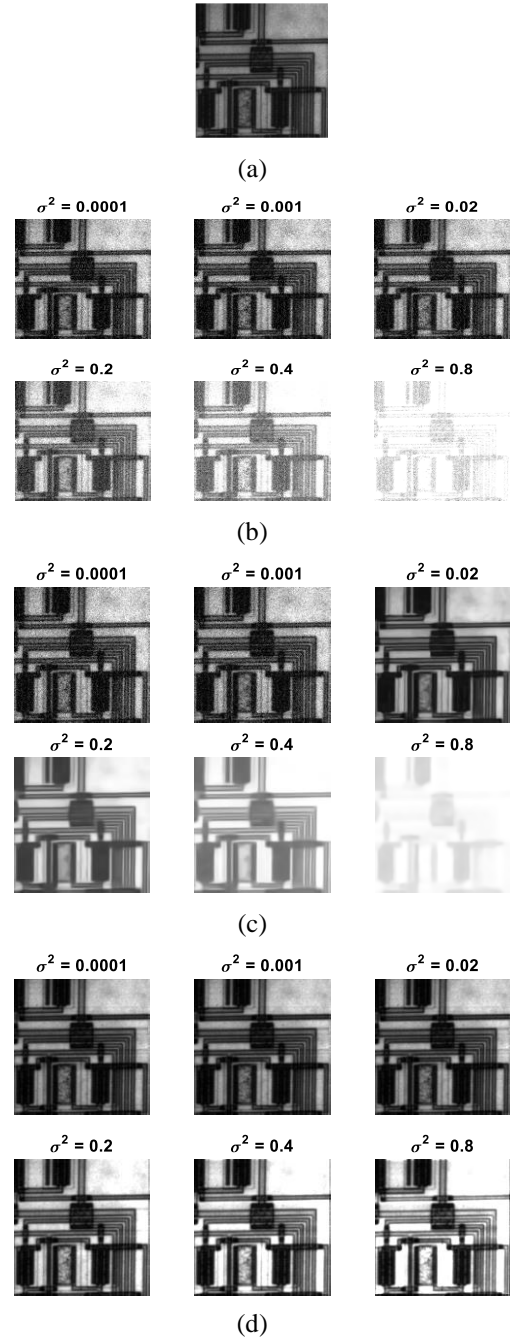


Figure 1: (a) The original image “Circuit”, (b) Degraded image with different (AWGN), (c) BM3D algorithm denoising results (d) ZA-LMS algorithm denoising results

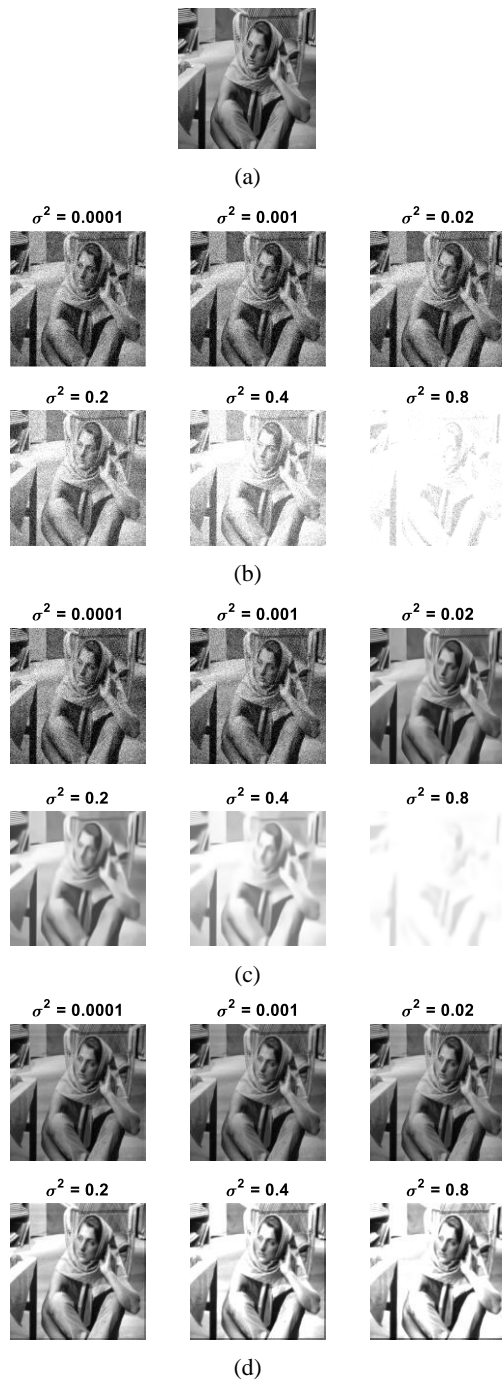


Figure 2: (a) The original image “Barbara”, (b) Degraded image with different AWGN noises (c) BM3D algorithm denoising results (d) 2D ZA-LMS algorithm denoising results

In Figure 3, another experiment with different types of noise under same variance (0.2) was conducted. The first one, AWGN with zero mean. The second one is speckle noise with zero mean and the third one is salt & pepper noise with

probability of 0.2. It was noticed that BM3D is giving good results with AWGN while it gave blurry results with other noise. On the other hand, ZA-LMS gave good results with the three noise types with almost no blurring effects. In general, 2D ZALAMS algorithm managed to denoise images that was affected with noise of various variance values successfully.

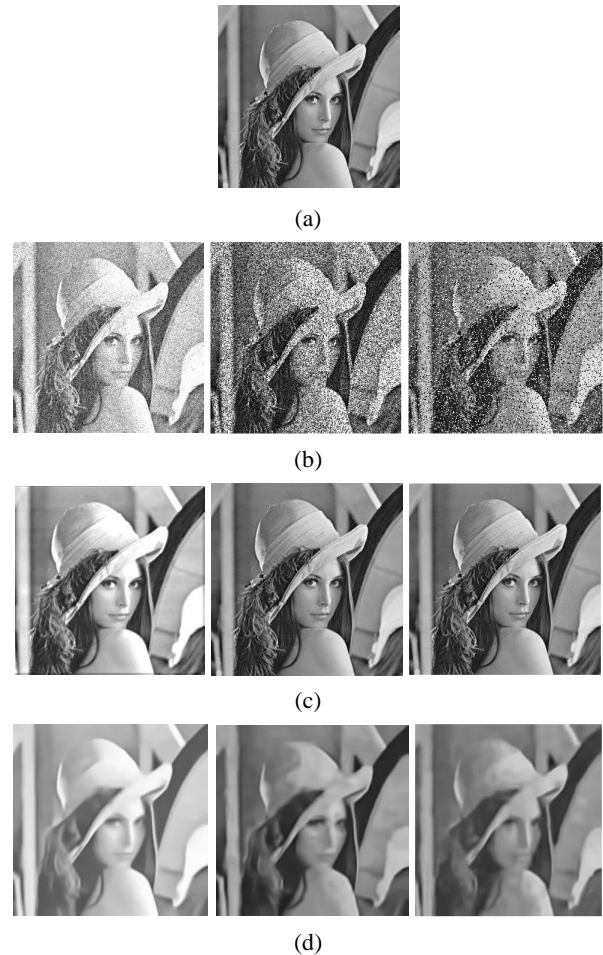


Figure 3: (a) The original image “Lena”, (b) Degraded image with different noise, namely AWGN, Speckle and Salt&pepper, respectively. (c) 2D ZA-LMS algorithm denoising results (d) BM3D algorithm denoising results

IV. CONCLUSION

In this paper extensive experiments were conducted to compare our recently proposed ZALMS algorithm and BM3D algorithm for image denoising. From the experiment results show that ZALMS algorithm is much better than BM3D algorithm under different noise environments. Another advantage is that ZALMS algorithm gave a good performance for both sparse and non-sparse images compared to BM3D algorithm.

REFERENCES

- [1] M.M. Hadhoud and D.W. Thomas. "The two-dimensional adaptive LMS (TDLMS) algorithm". *IEEE Transactions on Circuits and Systems*, vol. 35, no. 5, pp. 485–494, 1988.
- [2] S. Suresh and S. Lal. "Two-dimensional CS adaptive FIR Wiener filtering algorithm for the denoising of satellite images," in *IEEE Journal of Selected Topics in Applied Earth Observations and Remote Sensing*, vol. 10, no. 12, pp. 5245-5257, Dec. 2017.
- [3] K. Dabov, A. Foi, V. Katkovnik, and K. Egiazarian. "Image denoising with block-matching and 3D filtering," *Proceeding of SPIE Electronic Imaging '06*, no. 6064A-30, San Jose, California, USA, January 2006.
- [4] J. Wright, Y. Ma, J. Mairal, G. Sapiro, T.S. Huang, S. Yan. "Sparse representation for computer vision and pattern recognition". *IEEE Proceedings*, vol. 98, no. 6, pp. 1031–1044, 2010.
- [5] N. Czink, X. Yin, H. Ozelik, M. Herdin, E. Bonek, B. Fleury. "Cluster characteristics in a MIMO indoor propagation environment". *IEEE Transactions on Wireless Communications*, vol. 6, no. 4, pp. 1465–1475, 2007.
- [6] L. Vuokko, V.M. Kolmonen, J. Salo, P. Vainikainen. "Measurement of large-scale cluster power characteristics for geometric channel models". *IEEE Transactions on Antennas and Propagation*, vol. 55, no. 11, pp. 3361–3365, 2007.
- [7] K. Dabov, A. Foi, V. Katkovnik, and K. Egiazarian. "Image denoising by sparse 3D transform-domain collaborative filtering", *IEEE Trans. Image Process.*, vol. 16, no. 8, pp. 2080-2095, August 2007.
- [8] G. Eleyan, M. S. Salman and C. Turan, "Two-dimensional sparse LMS for image denoising", *2015 Twelve International Conference on Electronics Computer and Computation (ICECCO)*, Almaty, 2015, pp. 1-4.
- [9] M. Lebrun, "An analysis and implementation of the BM3D image denoising method", *Image Processing On Line*, vol. 2 (2012), pp. 175-213.

Wind/PV Hybrid System Potential Sites and Electricity Generation Potential Analysis in Western Province of Zambia: GIS Based Analytic Approach II

¹M. MWANZA, ¹M.F. TABA, ¹A.C. BIBOUM, ²M. KAOMA, ¹K. ÜLGEN

¹Solar Energy Institute, Department of Energy Technology, Ege University, Izmir/TURKEY

²School of Engineering, Department of Agriculture Engineering, University of Zambia, Lusaka/ZAMBIA

Abstract- Wind and Solar energy is clean, free, and renewable energy sources which is increasingly used in the world for electricity generation in many countries. However, just like any other alternative energy source option, wind/PV hybrid systems development is not free from imposing negative impacts on both the environmental and the society. Thus, these potential impacts can hinder or delay hybrid energy technology deployment in wind/solar potential sites. Hence, in order to address these negative issues and increase social acceptability and environmental sustainability of wind/PV hybrid system deployment in Zambia, a bottom up approach using GIS and analytical methods has been used in this study for analyzing the potential sites for wind/PV hybrid system development and electricity generation potential in these sites for Western Province of Zambia. The potential sites are categorized into four levels depending on the wind speed value. The total feasible potential site suitable for development of wind/solar hybrid systems is found to be approximately 7.80% (9859.24km²) of the total surface area of Western Province representing wind/solar PV hybrid electricity generation potential of 208.96TWh/year at a hub height of 90m. The electricity generation potential is nine (9) times more than the projected 2030 energy consumption for the entire country. The study is very important to help guide in deployment of mini off-grid and grid-tied wind/PV hybrid energy technology across the province with increased public acceptability and reduced environmental impacts.

Keywords: Wind Energy, Solar Energy, Sustainability, Potential Site, Wind availability

I. INTRODUCTION

The share of wind and solar energy in the electricity industrial across the world has increased recently due to among other reasons the reduced investment costs of wind and solar energy technologies[1], maturity of the technology, the widely availability of the resource, and increasing environmental concerns [2, 3]. In addition, due to reduced reserves and increased price of fossil fuel and global warming issues which are considered as serious threats to the world by many countries and researchers across the global [2].

Wind and solar energy is one of the mostly used among the renewable energy sources for electricity generation due to its ability to increase electricity industrial sustainability [4] and increase energy security in many countries [2,5]. The total installed capacity of wind and solar power across the

global have tremendously increased, for instance the total install capacity of wind power across the world increased from 369.553MW in 2014 to 392GW in the mid of 2015 [6, 7], with China taking a lead in the total cumulative installed capacity which was estimated at 129GW contributing about 32.91% to the total installed capacity in 2015 [7,8]. According to [9] wind and solar energy is one of the renewable energy resources that are expected to contribute a huge amount to the electricity industrial across the global by 2030. The wind power capacity is projected to reach 1000GW by 2020, representing about 12% of the total electricity generation in the world [10].

Hence, despite having the ideal plateau landscape with good potential of wind and solar energy in some parts of the country, wind and solar energy has continued to play minor role in the electricity generation mix (less than 1%) in Zambia due to various reasons such as lack of availability of wind and solar energy potential site maps and information on the electricity generation potential of both wind and solar energy technology. Nonetheless, the government of Zambia in the National Energy Strategy 2008-2030 intends to include wind and solar energy in the national electricity generation mix [11]

However, just like any other alternative energy supply option, solar PV/wind hybrid systems development at utility scale is not free from imposing negative impacts on both the environmental and society [12]. These potential impacts can hinder or delay hybrid energy technology deployment in potential sites [12] Therefore, for sustainable hybrid systems development and optimal utilization of wind and solar energy, hybrid systems sitting is a very crucial step [13]. According to literature, Sustainable energy system is defined as a system able to provide the energy needs of the current population equally for all without compromising the safety of the environment for the future generations[14]. Hence, various factors that affect the deployment of wind/solar energy technology have to be taken into consideration when selecting the potential sites for hybrid system development and assessing the available solar and wind energy potential [14]; such as wind speed characteristics, solar radiation, avian interaction effect on the migrating birds, visual impact and noise to the public,

electromagnetic interference effect of wind turbine on TV or communication systems, land use which tends to be huge for wind and solar farms and many other impacts and parameters such as cost and accessibility of hybrid systems sites to mention but a few [14-16].

Recently various studies have been conducted across the world to assess the suitable sites for wind and solar farm deployment in various countries using solar radiation data and wind speed data measured at different height above the ground level [2, 17]. Hence, Geographical Information System (GIS) analytic approach have been/is widely applied method for evaluating wind and solar farm suitability analysis i.e. identifying potential sites and optimal location for land, solar farm, and wind farm development and also for potential analysis of both solar PV and wind systems in many studies, [18], for instance Yanwei Sun et al used this same approach to analysis potential of solar PV generation for Fujian Province of China [18]. Justin Robert Brewer applied this approach to evaluate the solar power potential and suitable locations for utility scale systems for the South West Region of U.S.A [19], Imtiaz Ahmed Chandio et al in their study used the approach to analyze and locate highly suitable using land suitability analysis for sustainable hillside development in Malaysia[20]. J.M.Sanchez et al used the approach combined with Fuzzy multi criteria decision making method to select the site for onshore wind farm in Southeastern Spain [21]. Beata Sliz-Szkliniarz and Joachim Vogt evaluated the wind energy potential for Kujawsko-Pomorskie Voivodeship using the similar approach [22] just to mention but a few. Thus, in this study the GIS analytic approach has been adopted for analyzing the potential site for deployment of wind/PV solar hybrid systems (mini off-grid and grid interactive hybrid systems).

According to the results of the rapid resource assessment that was undertaken in 2005 by USAID and the wind/solar dataset obtained from NASA using online system across Zambia, the Western Province has been identified as the windiest region in the country with wind speed as shown in Table 1[23]. Therefore, based on USAID studies and data collected from NASA the analysis of the potential site for sustainable wind/PV solar hybrid systems development in Western province of Zambia has been conducted in this study using the GIS analytic approach.

Table 1: Districts in Western Province with their Locations and annual average wind speed at 10m

District	Altitude (m)	Wind Speed(m/s)		Coordinate	
		MDZ	NASA	Lat.(°S)	Long. (°E)
Kalabo	1063	4.90	4.83	14.950	22.700
Kaoma	1132	4.80	4.12	14.800	24.800
Mongu	1065	5.90	4.45	15.250	23.170
Senanga	1025	3.30	4.56	16.120	23.270
Sesheke	989	-	4.11	17.474	24.296
Lukulu	1092	-	4.30	14.408	23.259
Shangombo	1024	-	4.68	16.323	22.104

MDZ-Meteorological Department of Zambia

NASA- National Aeronautics and Space Administration

II. THE STUDY AREA

The analysis of the potential site and electricity generation potential of hybrid energy technology is applied for the study area which is located between the latitude of 13.5°S and 18°S and longitude of 22°E and 25.5°E in the western part of Zambia with average elevation of 1056 meters and total land area of 126,386km². The province has a total population of about 1,007,900 people with electrification rate of about 3.21%[23,24].The province has low electrification rate, despite having good wind speed and higher solar radiation. Fig. 1 shows the location of the study area and the main districts in the province which are Sesheke, Kaoma, Lukulu, Mongu, Senanga, Shang'ombo, and Kalabo having average wind speeds at height of 10m as 4.11, 4.12, 4.30, 4.45, 4.56, 4.68, 4.83m/s respectively[NASA]. The province has installed fossil fuel (diesel) based power plant of 88MW, Kaoma (2.62MW), Lukulu (0.512MW) contributing to greenhouse gas emissions in Zambia [24].

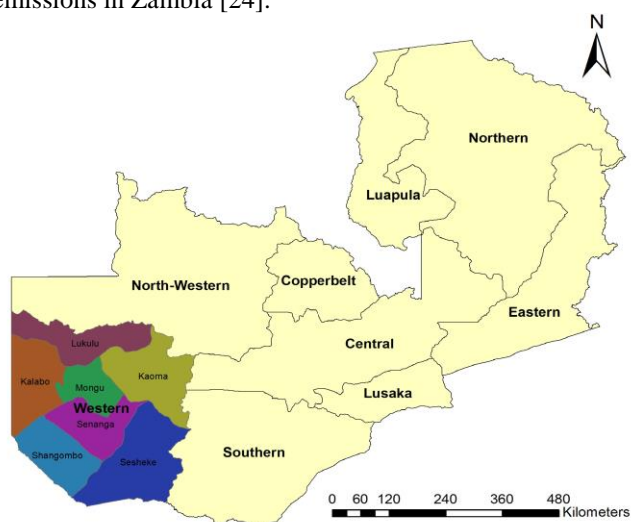


Fig. 1: Location of Western Province in Zambia [ArcGIS]

III. ANALYSIS METHODOLOGY

The approach used in this study for analyzing potential site for wind/PV solar hybrid systems development and evaluating the electricity generation potential involves a number of steps, as summarized in fig.2 below.

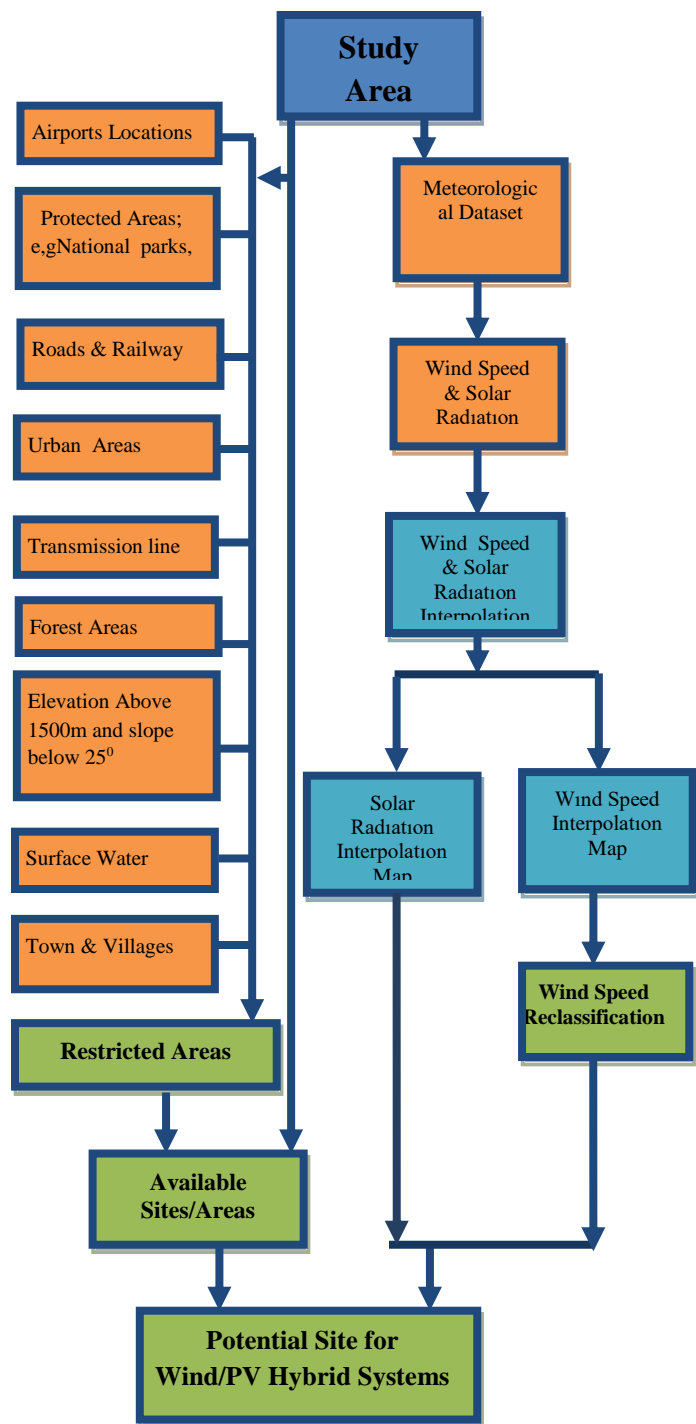


Figure 2. Hierarchy Diagram for Wind/PV Hybrid System Potential Sites Analysis

A. Data Collection and Processing

The wind speed and solar radiation data used in this study has been collected from NASA Surface Meteorology and Solar Energy which is based on three-hours intervals averaged for a period of 10years. The data has been extracted from at least ten (10) locations in each district for wider coverage of the province and to improve the quality of interpolation.

The approach used in this study is a combination of the proposed methodologies used in various studies carried out

previously in many countries with some adjustment to suit the study area. The approach have four main steps, firstly the available areas for renewable energy technology deployment has been evaluated considering both environmental sustainability and social acceptability, i.e exclusion of all factors that are considered potential hindrance or that may restrict deployment of renewable energy technology as shown in fig.2. However, not all the available areas are suitable for wind energy technology deployment, thus in order to pinpoint the feasible potential sites, the wind speed characteristics have been considered. The second step involved gathering of meteorological data that is, wind and solar dataset from the study area: wind speed, solar radiation, ambient air temperature, air pressure, and land elevations which are important for estimation of speed and solar characteristic and wind/solar energy electricity generation potential. Then the wind speed for the study area has been extrapolated to a new height using eq.1 given below and the power exponent used has been estimated using eq.2. After that, interpolation of wind speed and solar radiation horizontally in order to create a layer of continuous surface for wind speed/solar radiation and predict the wind speed/ solar radiation in other location where the data was lacking has been carried out using spatial analysis in GIS software. The wind speed reclassifications were done in order to classify the wind speed according to their potential thus, four wind speed bins were considered as follows: $>4.75\text{m/s}$ extremely suitable, $>4.5\text{m/s}$ strongly suitable, $>4.0\text{m/s}$ moderately suitable, and $<4\text{m/s}$ not suitable. The annual average wind speed for potential site was restricted to above 4m/s at 10m height based on the previous studies [25]. In the third step, the reclassified wind speed and solar radiation layers were overlaid with the layer of available areas for wind/PV solar hybrid system deployment in order to determine the feasible potential site for hybrid systems. In the final step, evaluation of the total available area from the feasible potential site according to wind speed bin has been carried out.

B. Potential Site Selection

The economics of using wind and solar energy sources for electricity generation are mainly dependent on the local weather conditions and the capacity of wind turbines and PV solar technology to effectively extract energy over a wide range of wind speeds and solar radiation respectively [26,27].

a) Wind speed Extrapolation

Estimating the wind speed V_r at hub height H_r is vital since the wind speed varies with height above the surface [28-30]. The power law is one of the common method used to predict the wind speeds at a wind turbine hub height H_r using wind speed measured at reference height e.g 10m (H_{ref})[22,31]. The wind speed at the hub height has been estimated using eq. 1[31-34].

$$V_r = V_{ref} \left(\frac{H_r}{H_{ref}} \right)^\alpha \tag{1}$$

Where, V_r is wind speed at wind turbine hub height H_r , V_{ref} is wind speed at measurement height H_{ref} , and α is wind shear exponent or ground surface friction coefficient.

b) Wind Speed & Solar Radiation Interpolation

After the extrapolation of the wind speed data to 50m and 90m height above ground level using excel spreadsheet. The data were uploaded into the GIS software for interpolation using spatial analysis in order to determine the distribution of the wind speed across the study area. The same was done for solar radiation. There are various interpolation methods that can be used to interpolate meteorological data [35-36]. However, the accuracy of the output does not only depend on the method applied but also on the distribution of data sample used in the analysis [22]. In this study Inverse Distance Weighting (IDW) has been used to carry out interpolation analysis. After interpolation analysis, the wind speed and solar distribution maps for Western Province of Zambia at 10m height were created as shown in fig 3 and 4. These maps have been used for wind speed reclassification which was used to evaluate the potential sites. The wind speed bin has been used as the main factor for locating the potential site for hybrid system since solar radiation is available throughout the province while wind energy is limited to some locations.

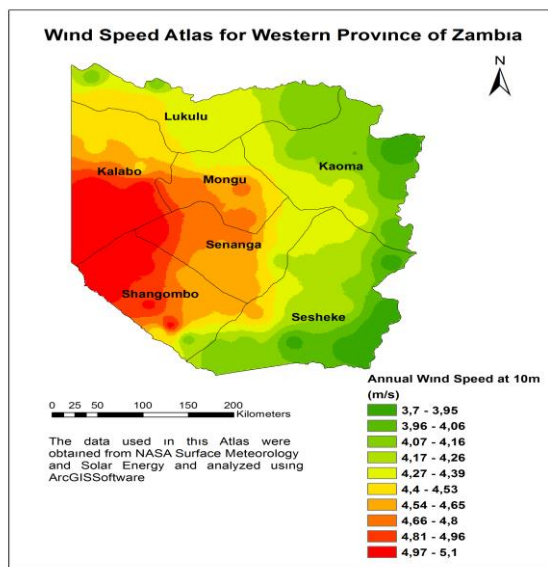


Figure 3: Wind Speed Distribution in Western of Zambia at 10m Height

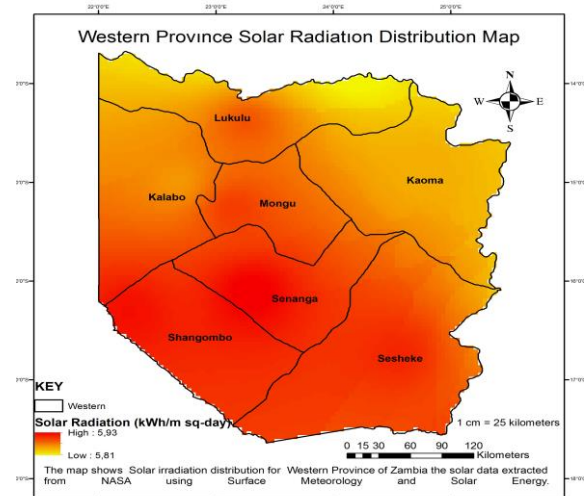


Figure 4: Solar Radiation Distribution in Western Province

c) Available Area Analysis

In order to assess the alternative available areas based on the restrictions summarized in fig. 2, different types of map layers for restrictions have been gathered from various sources. These maps included elevation maps (DEM), land use/cover layer, Town and village location map, Airport location map, National parks maps, surface water bodies maps, roads and railway map, study area boundaries, and transmission line maps [14, 21-22, 37-39].

After creating buffers, and change some features from vector to raster and reclassification, spatial analysis has been used to evaluate the available areas for solar RETs development as shown in fig.4.

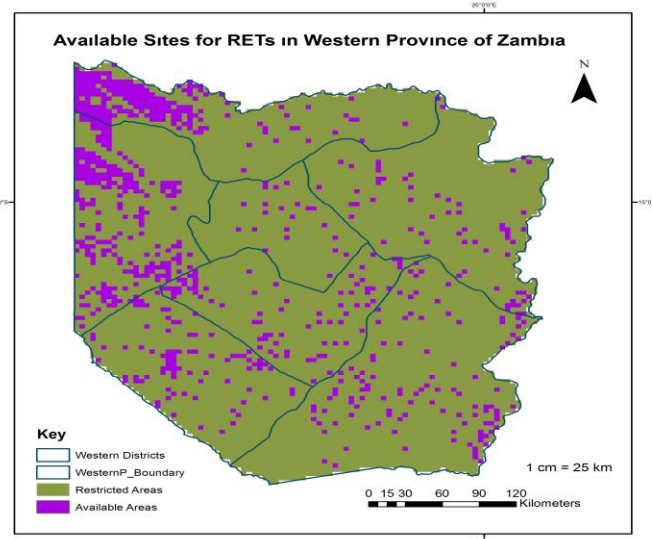


Figure 4. Available Areas for Solar RETs in Western Province

However, as early stated not all these areas are suitable for wind systems, thus in order to pinpoint the most feasible potential sites for hybrid wind/PV system, the reclassified wind speed surface area layer were overlaid on available surface area layer using spatial analysis.

C. Electricity Generation Potential

a) Wind Electricity Generation Potential

The wind power density estimated at reference height can also be vertically interpolated to tower hub height [Ahmed Belhamadia, et al, 2013]. Since power produced by wind turbine is directly proportion to cube of wind speed, the power density at hub height has been evaluated using eq.2 given below [37-40].

$$P_r = P_{ref} \left(\frac{H_r}{H_{ref}} \right)^{3\alpha} \quad (2)$$

Where P_r (W/m²) is the power density at tower hub height H_r , and P_{ref} (W/m²) is the power density at reference height H_{ref} . The electricity output per wind turbine annually has been estimated using eq. 3.

$$E_{WT} = P_r \times A_{WT} \times CF \times T_a \quad (3)$$

Where A_{WT} is wind turbine swept area (m²), CF is wind turbine capacity factor, T_a is the total hours for the time period of wind data (for month or year or years) 8760hours for this study. Therefore, total electricity generation potential E_{EG} from potential sites for a wind energy technology considering minimum area required (10D x 10D(D-rotor diameter)) for a stand-alone wind turbine with a wind farm array efficiency of 90% has been evaluated using eq. 4.

$$E_{EG} = E_{WT} \eta_A \left(\frac{A_i}{A_{WT}} \right) \quad (4)$$

Where η_A is array efficiency of wind farm, A_i is the total area of potential sites (m²), and A_{WT} is the required area around each wind turbine (m²) calculated considering diameter of 10D.

b) Solar PV Electricity Generation Potential

Considering the estimated area of potential sites and the area required by wind turbines and technical characteristics of PV generation systems to convert the solar energy to electrical energy, the potential sites available technical solar energy potential considering the available areas between the wind turbines has been estimated as using eq 5 below[41,42]:

$$E_T = A_{ADS} \cdot P_{PD} \cdot CF \cdot T_{TSH} \quad (5)$$

Where E_T is Solar electricity generation Potential (MWh/year), A_{ADS} is Suitable Area between wind turbines of potential sites (km²), P_{PD} is suitable area Power Density (MW/km²), CF is Capacity factor of PV module considered in suitable areas (%), and T_{TSH} -8760(hours/year)]

IV. RESULT AND DISCUSSION

In this study the feasible potential site for wind/PV solar hybrid systems have been classified according to wind speed levels as extremely suitable for wind speed above 4.75m/s, strongly suitable for above 4.50m/s, and moderately suitable for those wind speed above 4.0m/s at 10m height, while the rest of the areas with wind speed below 4.0m/s have been considered not suitable for wind/PV Solar Hybrid Systems. Fig.5 shows the potential sites for hybrid system development according to suitability levels (Wind speed level). The analyzed results indicates that the extremely suitable sites cover an area of 3311.502km² representing about 2.62% of Western Province's total surface area, while strongly suitable sites cover an area of 3311.501km² representing 2.62% of total surface area of Western province, the moderately suitable site has been estimated to cover an area of 3236.240km² representing approximately 2.56% of the total surface are of Western province and while unsuitable areas has been estimated to be 92.20% of Western province's total surface area. Hence, the total surface area with the potential for wind/PV Hybrid system development, which will support environmental sustainability and increase social acceptability, has been found to be approximately 7.80% of Western province's total surface area.

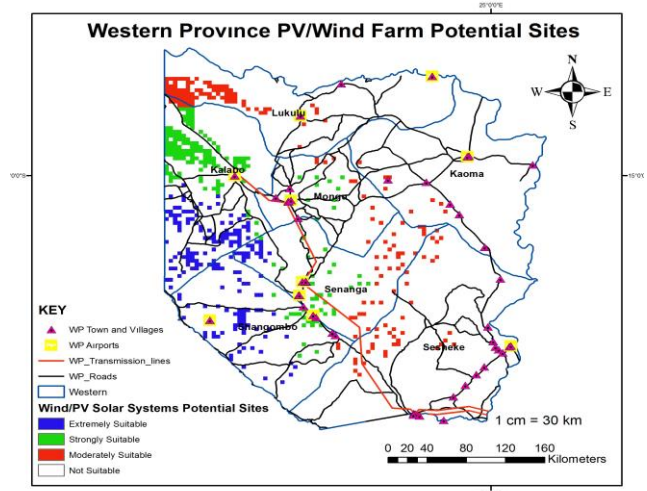


Figure 5. Wind/Solar PV Hybrid Systems Potential Sites in Western Province

Although, most of parts in the country do not have wind energy potential for electricity generation, estimate shows that the Western province has good wind resource potential for electricity generation. Fig. 5 shows wind-belt regions and wind/solar PV hybrid system potential sites of Western Province of Zambia. The wind energy resource of this region has remained untapped for electricity generation in Zambia. As it can be seen most locations in the Western Province are not covered by the Transmission line and there is no wind farms in the province, as such, stand-alone hybrid wind/PV solar systems may be the best alternative for electrification of the province and increasing the electrification rate from the current levels which is below 10%.

Fig 5 further shows that the extremely suitable areas are mostly located in Sha'ngombo and Kalabo districts, meaning that these districts are extremely suitable location for development of hybrid systems in province and nation. With the lack of grid in these areas, wind/PV solar hybrid mini off grid system maybe the best option for electrification of these regions and improving access to electricity and improving the living standards for the rural populations. Currently the Sha'ngombo district is using diesel generator for supplying electrical energy to the districts, hence, use of this type of systems for energy generation that is hybrid systems can reduce these burdens the company and province is currently facing of higher operation costs and greenhouse gas emissions. In addition, it can be observed that most part of the province have potential sites for hybrid system development which the government can tap in for energy mix for the country. This can further help improve the grid system performance by reducing energy transporting distances from far hydropower stations and improve voltages at the customer end. This can also help reduce much dependent on the hydro sources and improve energy diversification and energy security in the province and nation.

It is also worth to note that the energy potential for extremely suitable areas is three times more than the focused national energy demand for the fiscal year 2030. This gives the government more options to include into the national energy mix to the current hydro energy sources.

The solar radiation for the seven districts and wind speed characteristics for the seven districts covering the three

Table 2b: Solar Radiation Characteristics

District	Jan	Feb	Mar	Apr	May	Jun	Jul	Aug	Sep	Oct	Nov	Dec	Annual Average (kWh/m ² -day)	Yearly Solar Radiation (kWh/m ²)
Lukulu	5,52	5,5	5,71	6,07	5,75	5,57	5,86	6,34	6,56	6,35	5,91	5,57	5,89	2149,85
Kalabo	5,57	5,52	5,63	5,98	5,77	5,59	5,87	6,33	6,42	6,17	5,83	5,62	5,86	2138,90
Mongu	5,73	5,65	5,78	6,02	5,63	5,44	5,72	6,25	6,51	6,44	5,98	5,75	5,90	2153,50
Kaoma	5,42	5,44	5,66	6,03	5,76	5,53	5,87	6,32	6,6	6,38	5,82	5,41	5,85	2135,25
Senanga	5,95	5,91	5,83	5,92	5,56	5,32	5,56	6,13	6,47	6,46	6,07	6,06	5,93	2164,45
Sesheke	5,77	5,8	5,79	5,92	5,56	5,32	5,6	6,23	6,54	6,53	6,08	5,86	5,91	2157,15
Shang'ombo	5,98	5,88	5,84	5,88	5,58	5,32	5,56	6,06	6,4	6,45	6,06	6,05	5,92	2160,80
Provincial	5,71	5,67	5,75	5,97	5,66	5,44	5,72	6,24	6,50	6,40	5,96	5,76	5,89	2151,41

Table 2b: Wind Speed Characteristics

District	Jan	Feb	Mar	Apr	May	Jun	Jul	Aug	Sep	Oct	Nov	Dec	Annual Average (m/s)
Lukulu	3,2	3,65	3,29	4,29	4,19	4,46	4,96	5,14	6,02	4,34	3,98	3,82	4,27
Kalabo	3,2	3,81	3,4	4,56	4,47	4,76	5,32	5,5	6,45	4,44	4,08	3,93	4,49
Mongu	3,3	3,95	3,58	4,76	4,66	4,97	5,54	5,74	6,74	4,68	4,30	4,09	4,69
Kaoma	3,2	3,49	3,18	4,01	3,92	4,16	4,59	4,79	5,59	4,23	3,89	3,72	4,06
Senanga	3,3	3,86	3,59	4,68	4,55	4,82	5,36	5,63	6,6	4,76	4,38	4,08	4,63
Sesheke	3,3	3,53	3,41	4,18	4,01	4,21	4,65	4,98	5,83	4,62	4,26	3,9	4,24
Shang'ombo	3,3	4,19	3,78	5,18	5,08	5,43	6,07	6,29	7,38	4,9	4,51	4,26	5,03
Provincial	3,24	3,76	3,44	4,48	4,37	4,64	5,16	5,39	6,31	4,55	4,18	3,95	4,45

Table 3: Wind Speed Characteristics at 10m Height

Description of Suitability Levels	Height H _r (m)	Mean Wind speed v _{av} (m/s)	Variance σ (m/s)	Scale Factor c(m/s)	Shape Factor k	Most Probably Wind Speed (m/s)	Max. Wind Speed (m/s)	Power Density P _{av} (W/m ²)	Yearly Energy Density E _{av} (kWh/m ²)
Extremely	10	4.75	2.77	5.34	1.795	3.39	8.10	142.58	1249,001
Strongly	10	4.50	2.54	5.07	1.865	3.36	7.49	114.96	1007,050
Moderately	10	4.00	2.19	4.51	1.939	3.10	6.50	76.55	670,5780

different suitable wind/PV hybrid system potential sites at 10m heights are summarized in Table 2a and 2b respectively. It can also be noted that the province have good solar energy potential which can be used for electricity generation for the province and the nation. This good solar energy potential combined with wind energy potential provides a great opportunity for the development of hybrid systems in the province. Table 3 summarises the wind speed characteristics at 10m height

Table 4 shows the wind turbine details and electricity generation potential for the two types of wind turbines considered in the study at manufacturers standard hub heights assuming each larger and medium sized wind turbines require (at 10D diameter around wind turbine) 1.16km² area (for Goldwind turbine) and 0.23km²area (for DWT54 wind turbine) for installation with 90% wind farm array efficiency. Due to lower wind speed in Zambia, hence, medium (250kW) and larger (2500kW) sized wind turbines with higher hub height of 50m and 90m and lower cut in and rated wind speed have been considered in this study. These wind turbines have been considered due to their lower cut-in and rated wind speed and high capacity factor greater than 40%. The results presented in table 4, shows that wind turbines with lower cut-in and rated wind speed have higher capacity factors compared to those with higher cut-in and rated wind speed. Therefore, the wind turbines with lower cut-in and rated wind speed are more suitable for hybrid system application in Western province of Zambia, due to the availability of lower wind speed regime in the province and the entire Zambia.

Table 4a: Wind Turbines Details and Capacity Factor in Extremely Suitable Potential Sites

Wind Turbine Model	Hub Height Hr (m)	Rated Capacity (kW)	Wind Sped (m/s)			Rotor Details		Capacity factor CF (%)	Energy Generation Eg(MWh/a)
			Cut-in	Rated	Cut-Out	Diamter (m)	Swept Area (m ²)		
Goldwind GW 121	90	2500	3,00	9,30	22,00	121	11595	50	24876,11
DWT54	50	250	3,00	8,00	25,00	54	2277,40	51	3594,02

Table: Wind and Solar Electricity Generation Potential in Extremely Suitable Potential Sites

Description of Energy Source	Hub Height (m)	Swept Area (m ²)	Power Potential	Capacity factor	Energy Potential
			(GW)	CF (%)	(TWh/a)
Wind	90	11595	7.14	50	63.94
	50	2277.40	3.65	51	47.03
Solar	Active PV Area(m ² /MW)				
	18000		73.58	22.5	145.02

In addition, it should be noted that wind turbines with higher hub heights and larger swept areas have higher electricity generation potential despite having same or lower capacity factor to those at lower hub height and having smaller swept area. This is due to higher wind speeds at higher hub heights as compared to lower hub heights.

Table 4a shows that Goldwind GW121/2.5MW wind turbine with hub height 90m and cut-in and rated wind speed of 3.0m/s, 9,30m/s, and cut-out wind speed of 22m/s has the highest wind electricity generation potential despite having the lower capacity factor of 50%, 42% and 40% for extremely, strongly and moderately suitable areas respectively.

At hub height of 50m, DWT54/52 250kW wind turbines have the high capacity factor of 51%, 44%, and 41% as compared to Goldwind turbine at 90m hub height. However, due to higher wind speed at higher hub height Goldwind turbine have the highest electricity generation potential for the three wind farm potential sites.

V. CONCLUSION

This study has assessed and analyzed the potential sites for hybrid systems considering wind speed characteristics as the main deciding factor. It can be concluded that Western Province has a huge potential sites for hybrid systems development which can contribute tremendously to the national energy mix. From the analysis it was found that about 2.62% of the province is extremely suitable for wind/PV hybrid system development. With Shan'gombo and Kalabo being the extremely suitable sites for such type of projects due to the presence of good wind speed characteristics.

Furthermore, the analysis shows that at 90m height and using Goldwind GW 121/2.5MW turbine in the extremely sites more electricity generation can be achieved enough to meet the national daily energy needs.

Therefore, it can be concluded that Kalabo, Shangombo, Mongu, and Senanga are the main districts having the

potential site for wind/solar PV hybrid system development. However, thorough studies on the ground are necessary for wind energy. The potential sites are categorized into four levels depending on the wind speed value. The total feasible potential site suitable for development of wind/solar hybrid systems is found to be approximately 7.80% (9859.24km²) of the total surface area of Western Province representing wind/solar PV hybrid electricity generation potential of 208.96TWh/year at a hub height of 90m. The electricity generation potential is found to be nine (9) times more than the projected 2030 energy consumption for the entire country. The study is very important to help guide in deployment of mini off-grid and grid-tied wind/PV hybrid energy systems across the province with increased public acceptability and reduced environmental impacts

REFERENCES

- [1] Li Meishen, Li Xianguo, 2005 "Investigating of wind characteristics and assessment of wind energy potential for Waterloo region, Canada". *Energy Convers Manag.* 2005; 46(18-19): 3014-33.
- [2] Farivar Fazelpour, Nima Soltani, Sina Soltani, Marc A. Ardabil, 2015 "Assessment of wind energy potential and economics in the north-western Iranian Cities of Tabriz and Ardabil" *Renewable and Sustainable Energy Reviews* 45 (2015) 87-99, ScienceDirect.
- [3] Sultan Al-Yahyai, Yassine Charabi, 2015, "Assessment of large-scale wind energy potential in the emerging city of Duqm (Oman)", *Renewable and Sustainable Energy Reviews* 47 (2015) 438-447, ScienceDirect.
- [4] Mostafaiepour A. 2010, "Productivity and development issues of global wind turbine industry," *Renew Sustain Energy Rev* 2010; 14:1048-58.
- [5] Sahin AD. 2004 'Progress and recent trends in wind energy' *Energy Combust* 2004; 30: 501-43.
- [6] Global Wind Energy Council(GWEC), 2015'Global Wind Statistics 2014'10-2-2015.
- [7] World Wind Energy Association (WWEA), 2015 "Worldwide wind market booming like never before: Wind capacity over 392Gigawat" September 9, 2015: Press Releases Statistics. <http://www.windea.org/hyr2015/>
- [8] Changyi Liu, Yang Wang, Rong Zhu, 2016, 2Assessment of the economic potential of China's onshore wind electricity," *Resources, Conservation and Recycling* (2016), ScienceDirect. <http://dx.doi.org/10.1016/j.resconrec.2016.10.001>.
- [9] Ahmed Belhamadia, Muhamad Mansor, Mahmoud A. Younis, 2013 "Assessment of Wind and Solar Energy Potentials in Malaysia" 2013 IEEE Conference on Clean Energy and Technology (CEAT).
- [10] FromWikipediathefreeencyclopedia,Windpower.Aavailableat:o(http://en.wikipedia.org/wiki/Wind_power)4 [accessed 20.03.17].
- [11] National Energy Strategy: 2008-2030 (Zero Draft)
- [12] USA Office of Energy Efficiency & Renewable Energy www.energy.gov

- [13] Sahin A.Z, Aksakal A., 1998, " Wind Power Energy Potential at the Northeastern Region of Saudi Arabia," *Review Energy* 1998; 14: 435-40.
- [14] Nazli Yonca Aydin, Elcin Kentel, Sebnem Duzgun, 2010, " GIS-based environmental assessment of wind energy systems for spatial planning: A case study from Western Turkey,"*Renewable and Sustainable Energy Reviews* 14 (2010) 364-373, ScienceDirect.
- [15] Kaoshan Dai, et al, 2015, "Environmental issues associated with wind energy-A review,"*Renewable Energy* 75(2015) 911-921, ScienceDirect.
- [16] Shifeng Wang, Sicong Wang, 2015, "Impacts of wind energy on environment: A review,"*Renewable and Sustainable Energy Reviews* 49 (2015) 437-443, ScienceDirect.
- [17] Kasra Mohammadi, Ali Mostafaipoor, Majid Sabzpooshani, 2014 'Assessment of solar and wind energy potentials for three free economic and industrial zones of Iran' *Energy* 67 (2014) 117-129, ScienceDirect.
- [18] Yan-wei Sun, et al, 2013, " GIS-based approach for potential analysis of solar PV generation at the regional scale: A case study of Fujian Province,"*Energy Policy* 58(2013) 248-259, ScienceDirect.
- [19] Justin Robert Brewer, 2014, " Solar PV Site Suitability: Using GIS analytics to Evaluate Utility-Scale Solar Power Potential in the U.S. South West Region", Master Thesis, Brigham Young University. Available online at https://ceen.et.byu.edu/sites/default/files/snrprojects/692-brewer_justin-20143-dpa.pdf.
- [20] Intiaz Ahmed Chandio, et al, 2014, "GIS-based land suitability analysis of sustainable hillside development,"*Procedia Engineering* 77(2014)87-94, ScienceDirect, available online at www.sciencedirect.com.
- [21] J.M.Sanchez-Lozano, M.S. Garcia-Cascales, M.T. Lamata, 2016,"GIS-based onshore wind farm site selection using Fuzzy Multi-Criteria Decision Making methods. Evaluating the case of Southeastern Spain,"*Applied Energy* 171 (2016) 86-102, ScienceDirect.
- [22] Beata Sliz-Szkliar, Joachim Vogt, 2011, " GIS-based approach for the evaluation of wind energy potential: A case study for the Kujawsko-Pomorskie Voivodeship," *Renewable and Sustainable Energy Reviews* 15 (2011) 1696-1707, ScienceDirect.
- [23] United States Agency for International Development, 2005 'Zambia Rural Electrification Master Plan: Phase 1: Rapid Resource Assessment' Final Report December 30, 2005.
- [24] Central Statistical Office, 2013, www.city population.de/Zambia-Cities.html, Central Statistical Office of Zambia, 2013, "2010 Census of Population and Housing: Population and Demographic Projections 2011-2035," Report, July 2013. www.zamstats.gov.zm
- [25] Central Statistical Office, 2007, *Environment Statistics in Zambia: Energy Statistics*, Republic of Zambia Central Statistical Office report, 27 March 2007, www.zamstats.gov.zm
- [26] Monique M. Hoogwijk, 2004,"On the global and Regional Potential of Renewable Energy Sources," ISBN: 90-393-3640-7, PhD Thesis (2004), University of Utrecht, Netherland, .
- [27] Wiser, R., Z. Yang, M. Hand, et al, 2011: *Wind Energy*. In IPCC Special Report on Renewable Energy Sources and Climate Change Mitigation [O. Edenhofer, R. Pichs-Madruga, Y. Sokona, K. Seyboth, P. Matschoss, S. Kadner, T. Zwickel, P. Eickemeier, G. Hansen, S. Schlömer, C. von Stechow (eds)], Cambridge University Press, Cambridge, United Kingdom and New York, NY, USA, pp. 542
- [28] Azadeh Kamjoo, Alireza Maheri, Ghanim Putrus, Arash Dizqah, 2011, "Optimal Sizing of Grid Connected Hybrid Wind-PV systems with Battery bank Storage", Northumbria University, Newcastle, UK.
- [29] Binayak Bhandari, Kyung-Tae Lee, Gil-Yong Lee, Young-Man Cho, Sung-Hoon Ahn, 2015"Optimization of Hybrid Renewable Energy Power Systems: A Review", *International Journal of Precision Engineering and Manufacturing-Green technology* Vol. 2, No. 1, pp 99-112Hhhfarm, and Busin
- [30] Sunanda Sinha,S.S. Chandel, 2015, "Review of recent trends in optimization techniques for solar photovoltaic-wind based hybrid energy systems",*Renewable and Sustainable Energy Reviews* 50 (2015) 755-769, ScienceDirect
- [31] Paul Gipe, 2004,"Wind Power: Renewable Energy for Home, Farm, and Business", 2nd Edition 2004, White River Junction,VT: Chelsea Green Pub. Co.,c1993, ISBN 978-1-931498-14-2, pp 36-38.
- [32] Amir Dabbaghiyan, Farivar Fazelpour, Mohamadreza Dehghan Abnavi, Marc A. Rosen, 2016' Evaluation of Wind energy potential in province of Bushehr, Iran'*Renewable and Sustainable Energy Reviews* 55 (2016) 455-466, ScienceDirect.
- [33] Pham Quan, Thananchai Leephakpreeda, 2015 'Assessment of wind energy potential for selecting wind turbines: An application to Thailand'*Sustainable Energy Technologies and Assessments* 11 (2015) 17-25, ScienceDirect.
- [34] Tabios G, Salas J. A comparative analysis of techniques for spatial interpolation of precipitation. *Water Resources Research* 1985:365–80.
- [35] Collins F, Bolstad P. A comparison of spatial interpolation techniques in temperature estimation. In: *Third international conference/workshop on integrating GIS and environmental modeling*. Santa Barbara, CA: National Center for Geographic Information Analysis (NCGIA); 1996.
- [36] Luo W, Taylor MC, Parker SR. A comparison of spatial interpolation methods to estimate continuous wind speed surfaces using irregularly distributed data from England and Wales. *International Journal of Climatology* 2008:947–59, doi:10.1002/joc.1583.
- [37] Rob van Haaren, Vasilis Fthenakis, 2011, "GIS-based wind farm site selection using spatial multi-criteria analysis (SMCA): Evaluating the case for New York State,"*Renewable and Sustainable Energy Reviews* 15(2011)3332-3340, ScienceDirect.
- [38] Joss J.W. Watson, Malcolm D. Hudson, 2015, " Regional Scale wind farm and solar farm suitability assessment using GIS-assisted multi-criteria evaluation,"*Landscape and Urban Planning* 138 (2015) 20-31, ScienceDirect.
- [39] B.Dursun, B.Alboyaci, 2011, "An Evaluation of Wind Energy Characteristics for four Different Locations in Balikesir", *Energy Sources, Part A*, 33:1086-1103, (2011).
- [40] Satyanarayana Gaddada, Shiva Prashanth Kumar Kodicherla, 2016,"Wind energy potential and cost estimation of wind energy conversion (WECSs) for electricity generation the selected locations of Tigray region Ethiopia,"DOI 10.1186/s 40807-016-0030-8, Gaddada and Kodicherla *Renewables* (2016):10, Renewables, Wind, Water, and Solar, Springer Open.
- [41] Anthony Lopez, Billy Roberts, Donna heimiller, Nate Blair, Gian Porro, 2012,"U.S Renewable Energy Technical Potentials: A GIS-Based Analysis" Technical Report NREL/TP-6A20-5146, July 2012.
- [42] Yan-wei Sun, Angela Hof, Run Wang, Jian Liu, Yan-jie Lin, De-wei Yang, 2013"GIS-based approach for potential analysis of solar PV generation at the regional scale: A case study of Fujian Province" *Energy Policy* 58 (2013) 248-259, ScienceDirect.

Wind Turbines Data Sources;

- [43] www.aweo.org/windodols.html
- [44] http://www.thewindpower.net/turbine_en_28_vestas_1650.php
- [45] http://www.thewindpower.net/manufacture_en_14-vestas.php
- [46] <http://www.vestas.com>
- [47] http://www.academia.edu/16835378/Suitable_Wind_Turbine_Identifier_Using_Capacity_Factor_and_Economic_Feasibility
- [48] <http://en.wind-turbine-models.com/turbines/111-enron-750i>
- [49] <http://www.ewtdirectwind.com/wind-turbines/dw5254-250kw.html>
- [50] <https://www.senvion.com/global/en/wind-energy-solutions/wind-turbines/mm/mm92/>
- [51] <http://www.enercon.de/en/products/ep-1/e-53/>
- [52] <http://www.goldwindamericas.com/solutions>

Tackling Climate Change: Global Efforts and Energy Preferences

H. SAGIR¹ and A. AKYIL²

¹ Selcuk University, Konya/Turkey, hayriyesamur@selcuk.edu.tr

² Selcuk University, Konya/Turkey, aakyil@selcuk.edu.tr

Abstract - Humanity has been in interaction with its surroundings since its existence. Humanity uses environment for improving life standards and make changes on the surroundings by means of developing technology. The change has been exponentially increasing after industrial revolution. Effective usage of energy has utmost importance in the present day, during which exponentially increasing energy demand and sharply decreasing fossil resources are at stake. The ratio of the fossil fuels in compensating energy need of the world is about 80-85% recently. Utilization of alternative energy sources will become indispensable considering the depleting fossil fuel resources. Additionally, fossil fuels harm environment and humanity in an irreversible manner. Especially, increasing consciousness about environment has been leading countries to renewable energy sources starting from 1980s. In order to process renewable energy sources, problems that are related with technical and economical resources should be solved. It is expected that renewable energy sources will become the primary energy sources in the second part of 21th century after these aforementioned problems will be overcome. Important studies from the literature about global tackling of climate change and determination of sustainable environmental policies are reviewed in this work. Also the potentials and utilization rates of energy sources that pose importance in tackling climate change are investigated specifically to Turkey.

Keywords - Climate change, Energy, Fossil fuels, Paris agreement, Renewable energy sources.

I. INTRODUCTION

ENERGY is one of the indispensable elements in sustaining life for individuals and states. It has strategic importance in a lot of field such as heating, illuminating, transportation, military defense, communication, transmission, etc. The need for energy will be continuously growing as time passes according to this context. Energy need should be compensated in a continuous, safe, economic and ecologic manner. It is the same for Turkey. The energy need of Turkey that had started to increase significantly in 1990s will continue to rise in an increasing manner according to the projections. Technological advancements and digital world incen world population to a more energy consuming daily life. One of the principal facts of the recent world is that the life without energy seems not realizable and supplying energy is one of the most strategic topics among the states.

It is possible to group energy sources available in the world

into three groups which are; renewable, non-renewable and nuclear energies. The basic property of the renewables is that these sources don't have a limited reserve. In other words, there won't be any changes in their reserves even if they are utilized in energy generation or not. Non-renewable energy sources, on the other hand, are petroleum, natural gas and coal. They are called fossil fuels because they are originating from the fossils of livings from millions of years before. Their resources are limited because they rely on the limited plant and animal fossils. They will be extinct in the future.

Another dimension of the topic is constituted by the relationship between energy and environment. Activities of humanity have important effects on the environment. These so called effects reach to an extent that the era that we live is called as antroposen era by some scientific groups. Human activities harm natural environment so much that sensitive balances of ecosystem such as water cycle, carbon cycle are damaged seriously. Humanity spoils mentioned sensitive balances by its activities. The most prominent one of those damages is the climate change due to global warming. Climate change that is currently being experienced is one of the serious problems that we face today and threatens whole world. A global effort is needed in order to solve this problem. The present position of the global solution search for climate change problem is the Paris Climate Change Agreement signed in New York 2016, which can be regarded as a continuing work of 1992 United Nations Climate Change Frame Contract.

A. Global Climate Change

If there wouldn't be any atmosphere that can keep heat and temperature at a certain level, most of the livings couldn't find a space for living. However earth atmosphere is heated more due to intensive usage of fossil fuels, destruction of forest and plant fields, rapid and improper urbanization and climate change is being experienced accordingly [1] (Samur, 2005; 19). The greenhouse gases that are emitted due to intensive use of fossil fuels because of rapid population growth of the world led to heating of the atmosphere. This situation which is called greenhouse effect occurs as a result of the accumulation of greenhouse gases in the atmosphere and atmosphere is unable to absorb them. Earth atmosphere was harmed due to human activities by utilization of fossil fuels intensively, especially just after industrial revolution [1] (Samur, 2005; 32). These harms turned into and revealed as climate change; as a reaction

of the natural environment.

Global climate change is the general name for designating the change in the climate as a result of rising average temperatures due to the greenhouse gases such as carbon dioxide and methane which are emitted from human activities [4] (Şahin vd.,2017). Greenhouse gases do not prevent solar irradiation to reach earth surface but they block some of the reflection from going back to space and thus they prevent excessive cooling of the earth surface. Excessive amounts of greenhouse gases in the atmosphere lead to more heat conserved in the atmosphere and global warming occurs. Intensive utilization of fossil fuels, destruction of forests, soil and oceans after industrial revolution interrupted balance of greenhouse gases [6] (Köse,2018:57). Carbon dioxide in the atmosphere has no direct harm on human health but it has greenhouse gas effect on the atmosphere. According to reported studies, carbon dioxide amount excess 400 ppm limit permanently, however it is known that the amount was below 300 ppm for about 800 thousand years and it was about 280 ppm even before the industrial revolution [4] (Scrippsm Instution of Oceanography, 2017; Şahin vd.,2017). As a result of all of these, temperatures have risen 0.85 degrees comparing to a century before according to the 5. Evaluation report of IPCC [16] (IPCC,2013). Our concern towards the depletion of fossil fuels is not lesser than our concern towards global climate change. Nevertheless, it should not be inferred that states and countries are completely reckless to global climate change.

The problems due to energy usage originating from fossil fuels can be listed as; increasing global average temperatures and dependently increasing global climate change; increasing regional and domestic air pollution and extinction in biological species types in plant and animal populations; increasing health spendings; increasing safety risks at national and international levels; depletion of fossil fuels; continuing inequality; effected developing and underdeveloped countries; emerging climate refugees due to harmed environment of people and their increasing number; more frequent extreme air incidents.

As a conclusion, the changes affect whole world globally more or less. Tackling climate change makes global efforts a must at the same time. Because, the important point in global warming is to reduce greenhouse gases in the atmosphere. In other words, all countries should deal with the problem more or less. A planet that is feasible for human life has not been discovered yet. Countries should solve the problem by making meetings and in solidarity.

B. Historical Development of Climate Regime

Although it is known that carbon dioxide and other gases are the reasons of increasing earth average temperatures for about a century, considering this as a problem started at the second half of 1980s. There are reasons about countries that are not cooperating to tackle down the global climate change. Some of the reasons are; discrimination between developed and developing countries; freeloading; concerns towards

sovereignty rights of countries due to boundless climate change problem; and absence of knowledge about the amount and quality of the possible gains. Despite all these, United Nations Climate Change Frame Contract was open to signature in 1992 United Nations Environment and Development Conference in order to find a solution for climate change at global level. It was aimed to reduce greenhouse gases to a level that wouldn't affect the climate system by the contract. The contract imposes obligations to developed and developing countries at different weights. Turkey was included in Appendix-1 and Appendix-2 lists of the contract because of that it is a OECD country. At first, Turkey didn't signed the contract, however the contract that was realized by 194 countries was signed by Turkey in May 2004 [7] (Çakmak vd,2016,898).

Climate change was defined as a common concern of humanity in the 1992 United Nations Climate Change Frame Contract and reducing greenhouse gas emissions below 1990 levels totally and separately took place in the agreement. However this contract does not contain any binding clauses for the countries. Climate Change Parties Conference that is designated as COP shortly takes place each year in order to evaluate and assess the actions of the countries against climate change. No decrease in the emission amount in the atmosphere was detected until 3rd COP meeting. Therefore parties in the 3rd meeting in 1992 constituted a text with several binding clauses and solid targets and put the agreement named as Kyoto Protocol to signature.

It was aimed to compose a protocol and legal regulation in order to reduce greenhouse gas emissions under 1990 levels during the studies in 3rd Parties Conference [8] (Türkeş,2003:3). The protocol put heavier loads on developed countries and put some binding obligations to them for reducing emissions by satisfying the discrimination between parties in terms of liabilities according to "common but discriminated obligations principle" of the agreement. Quantitative emission limits or reduction obligations, which are also known as emission targets, were determined for the Appendix-I parties that take place in protocol Appendix-B list. Appendix-I parties that take place in Appendix-B list of the protocol consist of 38 industrialized countries and European Union. The protocol also put a total target or maximum that projects total greenhouse gas emissions 5% below the 1990 levels in the first obligation period between 2008-2012 for developed country parties that are listed in Appendix-B list. Individual Appendix-I party countries emission targets are defined as "assigned amount" and it is shown in Appendix-B [7] (Çakmak vd 2017:898). Emission Trade, Partner (collaborator – mutual) Application Mechanism and Clean Development Mechanism are the regulations that took place in the Kyoto Protocol, that were applied during the realization of the protocol. Emission trade is a regulation or application for trading emissions between countries. According to this regulation, each country has a quota for emissions. A country that exceeds its emission quota has the right to purchase

additional emission quota from the quota of another country. Partner Application Mechanism, on the other hand, is an economical incentive mechanism that makes a country having obligations of reducing emissions to realize its obligation by funding the emission reduction projects. Clean Development Mechanism is an application that is formed for making developed countries to support emission reducing projects of developing countries economically considering the cooperation between developed and developing countries [7] (UNFCCC, 2017; cited by Çakmak vd,2017:899).

Kyoto Protocol is an agreement that caused a lot of debates when it was opened to signature. Solid binding points for the countries, serious liabilities especially for developed countries are the leading points that cause debates. In 2015, countries gathered in 21th Climate Change Conference in Paris in order to determine their road map for the period after Kyoto Protocol.

21th Parties Conference which is also known as Paris Climate Summit was held on the dates between 30 November-15 December 2015. 187 countries including Turkey that emit the 96% of the total global emissions gathered. 195 countries including Turkey signed the Paris Agreement after intensive negotiations. According to the agreement, endeavor is needed for keeping the increase in global average temperature below 2°C, restricting temperature increase with 1.5 °C. It is asked from the developed parties to support countries starting from the underdeveloped states and small island states, in terms of economy, technology and capacity. In order to Paris Agreement to be inured, at least 55 countries that form the 55% of the global green house gas emissions should become part of the agreement and the agreement came to force and inured at 4 November 2016. 166 countries were voted the agreement in their parliaments. 25 out of 29 countries that didn't vote the agreement in their parliament are the countries out of Appendix-I. The remaining four countries are Turkey, Czechia, Russia and Sweden in Appendix-I [7,9] (UNFCCC, 2017;cited by Çakmak vd,2017:901).

It can be said that Paris Conference had been accepted in an easier manner than Kyoto Protocol by the countries if the decisions and agreement process of the Paris Climate Conference is compared to the Kyoto Protocol. The most prominent reasons for this easier acceptance are the effects of global climate change that are more obvious and apparent and a global consensus on the climate change due to human activities. Today, nature force humanity to change comparing to the first years of 2000s. Environmental disasters originating from the climate are experienced in each country more or less and developments that are emerging related to the process are realized much more rapidly comparing to the projections. Alongside of these, there is an increasing ratio of awareness related to the climate change in the society. Non-Governmental Organizations (NGO) and environmentalist civil society foundations play a significant role in promoting such awareness. Thus, global society has reached a level that is higher in terms of awareness relating to global climate change

comparing to 1990s. Another important factor in this higher awareness issue is the role of technology in communication which aids humans by enabling information to be passed and transmitted without borders of time and space [4] (Şahin,2017:81).

II. GLOBAL ENERGY USAGE

It wouldn't be wrong to say that the biggest share in energy utilization belongs to fossil fuels and this situation will continue in the close future if an assessment and evaluation of the current situation is done in respect of the global energy utilization. The share of the renewable energy will increase constantly for each year in the future though fossil fuels will be estimated to be dominant over them.

Estimations of Outlook for Energy for the period till 2040 are given as follows (DEKTMK; 2018);

1. Global energy need will increase with a rate of 25 % due to the effect of countries different than OECD countries. In order to compensate this energy need increase, utilization of all energy sources will become indispensable.

2. Energy consumption in every portion of the industry will increase. A 20% increase is foreseen in industrial energy demand between the years of 2016-2040.

3. Share of low carbon resources and renewable energy will increase in global scale. The share of coal energy will be replaced by the renewable energy sources in numerous places in the world. Especially solar and wind energy systems will increase at a rate of about 400%. Therefore their share in global energy supply will increase tri fold. The CO₂ emissions originating from electricity generation will decrease about 30% because of the mentioned increase.

4. Natural gas will be the most preferred energy source. Natural gas demand will exhibit a 40% increase and will be the most demanded energy resource among all resources. As a result, natural gas will compensate 26% of the world energy need till 2040.

5. Transportation sector will play a significant role in the future of energy. It is expected that the share of transportation in the global energy demand increase will be about 30%. The leading position of petroleum in transportation and modern transport will continue in the future. Alongside of these projections, a strong wave of development in the electric vehicles is in the projections due to the decreasing battery costs, increasing model options and political incentives.

6. The increase in energy efficiency by the technological developments will empower carbonless energy struggles. Tendency towards low carbon energy sources, energy efficiency and doubled world economy until 2040 will lead to a 45% reduction in carbon emissions. Nevertheless, energy sourced carbon emissions in global scale will be 10% more comparing to year 2016 and it will experience its peak in 2040.

7. Tackling emissions will be more convenient and easy thanks to the technological development. Global CO₂ emissions increase about 40% though there are reductions

about 10% in Europe and North America. The basic reason of this increase is the global GNP increase at a rate of 55%. The share of China in this increase is about 60%. In the process towards 2040, global GNP will decrease about 45% by the energy efficiency studies and more green resources, and CO₂ emissions will see its peak value by increasing 10 % comparing to 2016 level. Emissions of Europe and North America will decrease about 15% between years 2016-2040; the countries other than North America, Europe and China will constitute half of the global emissions.

The average green house gas effect of fossil fuels in atmosphere is 57% while products that are used in agriculture has 19%, destruction of forests has 17% and industrial waste has 8%. US and Canada have a share of 47% in green house gas emissions while West Europe Countries follow them with a share of 24%. US that have so high impact on global climate change decided to withdraw its signature from the Paris Agreement in June 2017 [6] (New York Times,01/06/2017;:cited by Köse 2018:60). This deeply influence the Paris Agreement that came into force in a time that is less than one year and that was signed by 195 countries, in a negative manner.

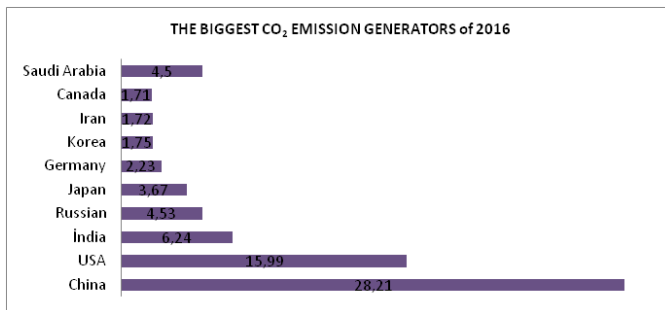


Figure 1: The 10 countries that generate the highest CO₂ emissions [4].

The highest CO₂ emitting country is China in 2016 as it can be seen in Figure 1. While China was in the last part of the list during the period before 2000, its CO₂ emission volume had increased with the increase in their economical growth in accordance with their development targets. China is followed by US with its 15.99 emission volume. India also increased rapidly in this list similar to China.

A. Situational Assessment and Evaluation in Respect of Turkey for the Energy Policies Focusing on Climate Change

Although Turkey plays a significant role in tackling climate change, it avoids undertaking an emission reduction target that poses a liability on it before 2020 [6] (Kivilcim,2013:18 cited by ;Köse,2018: 66). This behavior led to negativeness in international relationships though the average emission amounts are lower than the values of developed countries. It is one of the rare countries that didn't vote the agreement in its parliament though it is one of the parties of the agreement. However the reason of Turkey for this attitude is clear. Because, Turkey is

accounted for Appendix-I countries since it is a member of OECD countries and this poses emission reduction liabilities on our country. Signing the agreement is not evaluated as a right choice by the policy makers since such a liability would negatively affect development of the country.

It is foreseen that temperatures will rise about 1 or 2 degrees in Turkey according to the calculations till 2050. It is estimated that volume of the streams will reduce at a rate of 5 to 25% by the reduction in precipitation rates due to the 2 to 3 degrees increase in temperature if the green gas emission ratio exceeds two folds in the next 60 years. Draught and insufficient water sources will be experienced in upcoming future when all of aforementioned facts are considered. It is seen that Turkey will be one of the countries that will be negatively affected from the global warming and climate change. Turkey will face water shortage (scarcity) in the end of a 30 years except Karadeniz region according to UN water report [6] (The UN World Water Development Report 2016:19 cited by Köse,2018:67).

Turkey should consider climate change for all policies that it will apply for aforementioned directions. In a more accurately expression, all policies and regulations that are in effect should be evaluated in terms of climate change and their disadvantages and advantages would be laid down. The road maps related to the public policies should be prepared considering climate change.

Energy policies are the most prominent ones among the policy fields that contribute about this topic. As it is mentioned earlier, energy source to be used has an important role on the tackling with the climate change. Alongside of this, energy sources should be preferred by picking the least risk bearing option and proper prices, if a situational evaluation would be done in respect of the energy security. It is necessary for Turkey to convey energy diversity and to harness its natural sources as much as it can. Turkey should increase the share of its self resources in energy generation as much as possible.

B. Renewable Energy Sources and Situation of the World

It is possible to classify energy sources of the world into renewable and non-renewable energy sources. If the reserve of the energy source is decreasing or limited after the utilization of the energy source, then this energy source is regarded as non-renewable energy source. If the resource that is used for harnessing energy has no change in amount and energy generation from that resource can be done unlimitedly, subject resource is regarded as renewable energy. Alongside of this, if the energy source is used without any additional processes, it is regarded as primary energy source. If the energy source becomes available for energy generation after some processes, this energy source

is regarded as secondary energy source. Coal, petroleum, natural gas, nuclear energy and renewable energy sources are primary energy sources [2] (Sağır &Doğanalp, 2016; 236). Renewable energy can be expressed as renewable energy sources that can be regarded as it can be obtained without a production process that takes time, not originating from fossil resources, having less impacts on environment comparing to conventional energy sources, continuous and ready to use [3] (Urgun, 2015:3; cited by Yurdadoğ,Tosunoğlu 2017:2). Renewable energy is the energy that is obtained from natural sources such as sun, wind, renew itself rapidly after it is used and not depleting due to its usage according to International Energy Institute. Although renewable energy sources that are regarded as clean energy sources cause some destruction in the environment at an acceptable level, they have a structure such that do not cause pollution, and they are sensitive to environment [3] (Ağaçbiçer, 2010: 48;cited by Yurdadoğ,Tosunoğlu 2017:2).

These energy resources are named as clean energies or green energies because they do not emit hazardous/harmful gases during their utilization or after their utilization. "Alternative energy sources" title, on the other hand, is another title that is given to these energy sources. Renewable energy is an energy type that is obtained from self national sources of a country. Therefore these energy sources help domestic and regional development. Renewable energies are consist of energy sources such as solar energy, wind energy, geothermal energy, hydraulic energy (except big scale dams; because methane is emitted from the degrading plant and animal residues that are remained under the big water mass in those dams. Methane gas is another type of gas that leads to global warming), biomass energy, hydrogen energy (hydrogen is a gas that is not found in the nature as a free agent. Therefore countries use various processes to generate hydrogen. It is possible to obtain hydrogen from coal, wind, water. Hence, the source we use to obtain hydrogen determines the cleanness of the energy whether it is clean or not). Although these aforementioned clean energies have some negative impacts on the environment, those negative effects are very limited comparing to the negative impacts of fossil fuels. As a conclusion, there will be a negative effect regardless of the energy source that is chosen in respect of the environment. The important thing here is the qualification of the impact in terms of compensability [2] (Sağır&Doğanalp, 2016; 237).

Importance of the energy had been become more realizable after the first petroleum crisis in 1973 by the all countries in the world. After this date, countries took steps towards diversifying their energy sources and tended towards alternative energy sources. Especially, countries

those were dependent to abroad search for policies in order to make their energy sources sustainable. The search for alternative energy sources gained acceleration when it came to 2000s and studies on renewable energy sources increased [9] (Karagöl,Kavaz 2017:9). The share of renewable energy in global energy consumption in 2014 was realized as 19.2%. This share exceeded 20% levels in 2015 and 2016. The share of fossil fuels is about 79% and nuclear energy is about 2.5% (Figure 2). This figure shows that one out of five consumed energy in the world comes from renewable energy sources. Technological developments, economical events and newly emerging markets make the solar and wind electricity generation systems less cost bearing systems. Especially wind and solar power stations that would be established in the shores are become competitive comparing to stations with fossil fuels in terms of economical cost [9] (Amin,2016;cited by Karagöl,Kavaz 2017:10).

When the investments in 2016 are examined, it is seen that China had a leading point. China is followed by US, Japan, India and Germany. United Kingdom that was in the fourth place in the report of previous year lost one rank (Table 1).

Table 1: The first five countries in annual investments, net capacity increase and biofuel production in the renewable energy field.

Source: REN 21,2018:25

Investment to renewable energy and fuels (hydraulic energy is not included) (above 50 MW)	China	USA	Japan	India	Germany
Geothermal power capacity	Indonesia	Turkey	Chile	Iceland	Honduras
Hydroelectric capacity	China	Brazil	India	Angola	Turkey
Solar photovoltaic capacity	China	USA	India	Japan	Turkey
Concentrated solar energy systems capacity	South Africa	-	-	-	-
Solar Thermal Capacity	China	Turkey	India	Brazil	USA
Wind Energy Capacity	China	US	Germany	United Kingdom	India
Biodiesel production	USA	Brazil	Germany	Argentina	Indonesia
Ethanol fuel production	USA	Brazil	China	Canada	Thailand

The rate of utilization of the renewable energy sources in total electricity generation of countries are shown in Figure 2. Denmark compensates 57% of its total electricity need from renewable energies, especially using wind energy. Uruguay and Germany follow Denmark by 30% and 28% respectively. It is worth to mention that Uruguay, Honduras

and Nicaragua also take place in the figure though mostly developed countries constitute the figure.

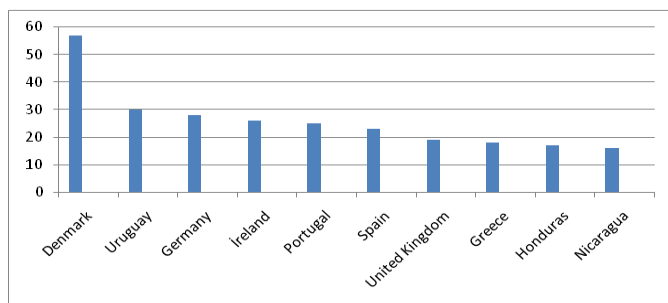


Figure 2: Electricity generation share of renewable energy; First 10 countries, 2017 [REN 21,2018:43].

C. Hydraulic Energy

Hydraulic energy is a type of energy that is obtained by the flow and falling speed of water. By another expression, it is the conversion of the hydraulic energy into electrical energy. It is the most widespread renewable energy type because of its advantage over remaining energy sources in terms of cost [9] (Karagöl&Kavaz,2017:13). Especially countries that are located in regions that have rough and watery terrains have advantage in terms of hydraulic energy potential. Global hydraulic electricity plant capacity reached to 1.267 GW installed power by the 21.9 GW increase in 2016 according to the 2018 Hydroelectricity Status Report published with the Hydroelectricity and Future Energy Systems Beijing Forum. China reached the biggest hydraulic energy generator position in the world by its 9.1 GW installed power capacity. China is followed by Brazil (3.4 GW), India (19. GW), Portugal (1.1 GW) and Angola (1 GW) (<http://www.yenienerji.info>). The first ten countries when the hydroelectricity capacities are checked in the world are shown in Table 2 according to the data of IHA 2017 (Hydropower Status Report).

According to the table, China has a capacity that is nearly equal to the total of remaining countries in respect of hydroelectricity capacity. It increases the gap by its investments in this field.

Hydraulic energy is also an important energy source in respect of Turkey. There is a hydraulic energy capacity that can compensate 20% to 30% of the energy need of the country after 2020. Hydroelectricity potential of Turkey corresponds to 1% of the world total and 16% of the total of the Europe. It is the most used renewable energy source of Turkey in electricity generation. The hydroelectricity potential of Turkey exhibits an increase by the newly established hydroelectricity plants (Figure 3).

Table 2: Hydroelectric capacity in country level; First ten countries
Source: IHA,2017

Rank	Country	Hydraulic Capacity (MW)
1	China	331,110
2	USA	102,489
3	Brazil	98,015
4	Canada	79,323
5	India	51,975
6	Japan	49,905
7	Russia	48,086
8	Norway	31,626
9	Turkey	26,249
10	France	25,405

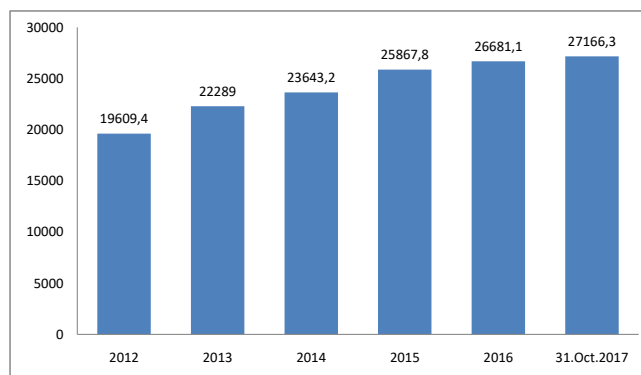


Figure 3: Hydroelectric energy development between 2012-2017 (MW) Source: TEİAŞ 2017.

D. Solar Energy

Solar energy is one of the most abundant renewable energy types on the world and this sourced is used in order to harness electricity and heat out of it. Only 0.04 of the solar energy that reaches to earth surface can be used by humanity because obtaining energy from photovoltaic panels is expensive comparing to fossil fuels [9] (Mohtasham,2015:1289-1297;cited by Karagöl Kavaz,2017:13). The principal problem about solar energy is the cost of photovoltaic cells. If the cost can be lowered, then solar energy will be the most preferred renewable energy type. An increase more than 50% especially in 2014 is visible in solar energy market though it is more expensive comparing to the energy generation from fossil fuels. The production amount that was 303 GW in 2016 had reached to 402 GW in 2017 (Figure 4).

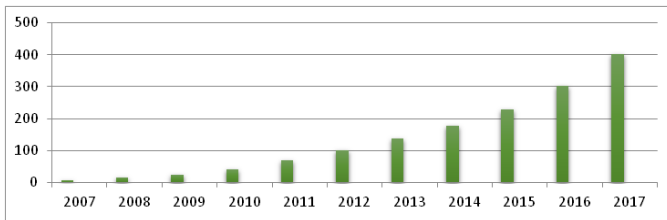


Figure 4: Solar PV global capacity and annual additions, 2007-2017 Source: REN21,2018:90.

It is observed that gradually more energy is generated from solar energy that is the most abundant renewable energy source, when it is examined in yearly basis. The biggest share in solar energy is attributed to China as it can be seen for the other sources, if the ten countries that generate the highest amount of electricity out of solar energy (Figure 5).

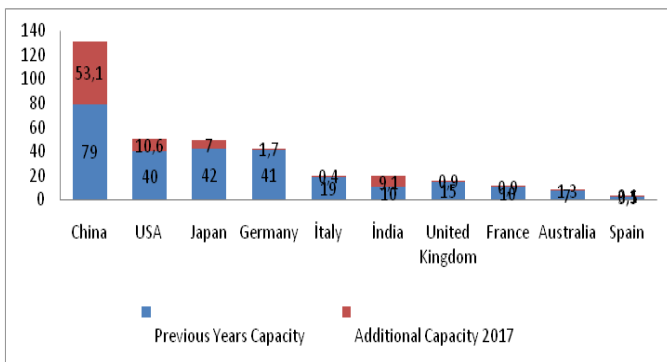


Figure 5: Solar energy generation capacity; First 10 countries, 2017 Source: REN 21, 2018:91.

China almost doubles its capacity of installed power of solar energy in 2017 according to the figure. US, Japan and India increased their installed power capacity substantially as it is understood from the figure.

Turkey has 2737 hours of total insolation period and 1527 kWh/m² yearly average solar energy according to the Solar Energy Potential Atlas (GEPA). It has daily 7.5 hours of average insolation period. Decreasing cost of photovoltaic panels and increasing efficiencies boost investments to solar energy. Electricity generation from solar energy was realized as 2060 MW after ten months of 2017 and comparing to 2014 in which the total amount was only 40 MW, this is a significant increase (Figure 6).

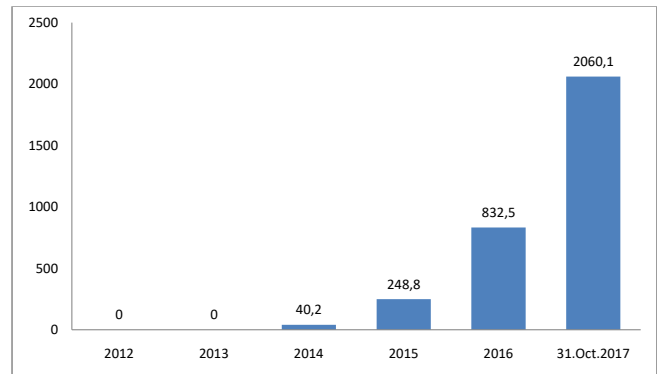


Figure 6: Solar energy development between 2012-2017 (MW) Source: TEİAŞ 2017.

Realization of 3 thousand MW electricity generation from solar energy in 2019 and then making this number to reach 5 thousand MWs in 2023 is aimed according to the estimations of Ministry of Energy and Natural Sources [9] (Karagöl,Kavaz,2017:22)

E. Geothermal Energy

It can be defined as hot water or vapor that contains more mineral and gases in its content comparing to underground and surface streams/waters, having a stable temperature, located in the deep earth crust and heated by the internal heat energy of the earth . Geothermal energy that is mostly utilized in hot water tourism in general is started to be used in energy generation by the investments in recent periods. Although it is not widespread as other renewable energy sources, it strengthens its position among those energy sources due to the facts that it is not affected by the climate conditions and it possesses continuity. Installed plant power for electrical energy generation in the world at the end of 2016 was 13.3 GW [5] (Onat,2018:14). This capacity increased 1.4 GW in 2017 (REN 21 2017:81). US have the first place in terms of geothermal energy capacity in the world. US are followed by Philippines, Indonesia and Turkey (Figure 7).

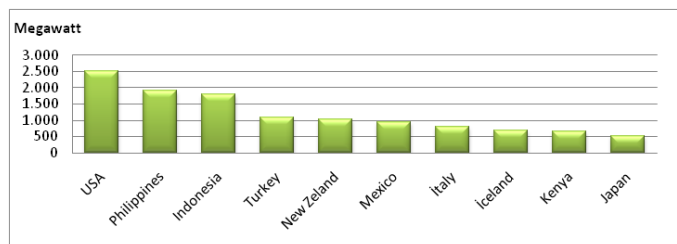


Figure 7: Geothermal power capacity, First 10 countries, 2017 Source: REN 21,2018:80.

The percentage increase in 2017 in respect of capacity increase of geothermal energy is given in Figure 8.

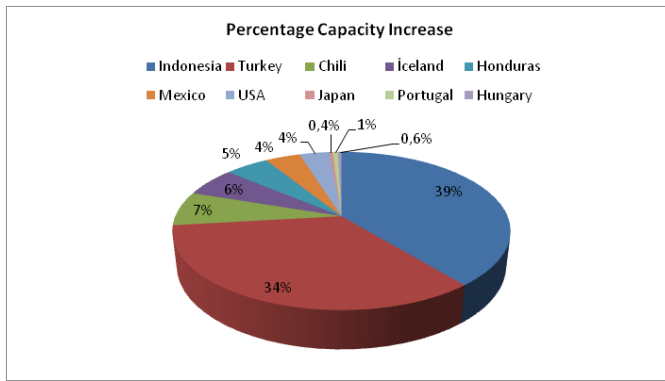


Figure 8: Geothermal Power Capacity – Global Capacity Additions; Percentage Increase in Countries Level; 2017 Source: REN 21,2018:79.

Indonesia is in the first place with 39% capacity increase. Turkey, Chile, Iceland, Honduras and Mexico follow it respectively.

Turkey is a high geothermal capacity country because of its characteristic of being on the Alpine-Himalayan zone. Its geothermal capacity is theoretically 31.5 GW. Geothermal installed power capacity had reached to 821 MW at the beginning of 2017 from 114 MW by the increasing investments starting from 2012[5](Onat,2018:14).

F. Wind Energy

Wind energy is one of the leading sources in worldwide in respect of the renewable energy capacity. Energy obtained from only wind energy in Denmark in 2014 corresponded to 39.1% of the total consumption. The country that has the highest installed power of wind energy is China with 36% value. Countries that follow China in this field are US and Germany (Figure 9).

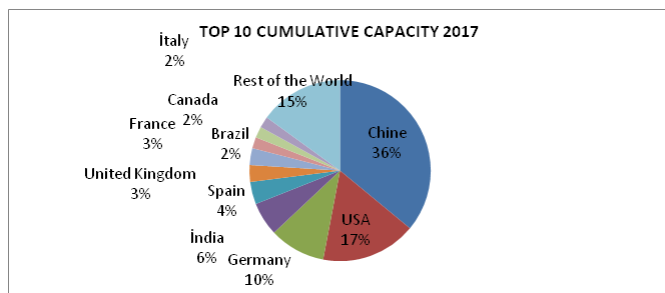


Figure 9: Percentage distribution of world wind energy total capacity: 10 countries Source: GWEC,2018:3.

Countries gradually increase their investments on electricity generation from wind energy in yearly basis and make investments in this field. 18% of the electricity is estimated to be generated by means of wind energy in 2050 according to the data of IEA[19] (IEA 2013). Newly installed capacity ratios as 2017 are shown in Figure 10.

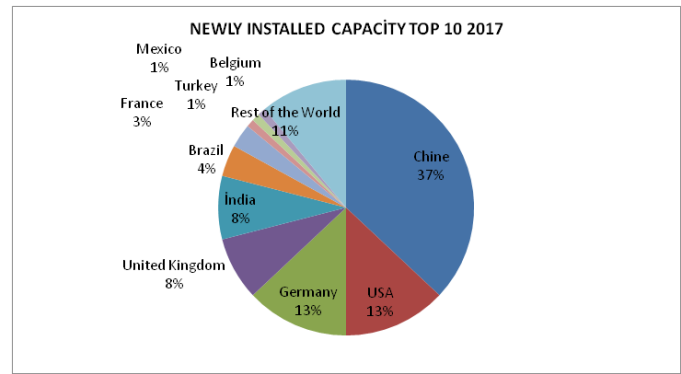


Figure 10: World Wind Energy 2017 - Increase in newly installed capacity: 10 countries Source:GWEC,2018:3.

China, US, Germany and United Kingdom exhibited advancement in this field by adding on their capacities when newly installed capacity ratios are viewed according to the figure.

Turkey forms 1% by its newly installed capacity in 2017. The calculated wind energy potential of Turkey is 88 thousand MW. Turkey is at the first rank among the OECD countries with this calculated rate. Although Turkey has 7 fold higher potential comparing to Germany, its installed capacity is 8.5 fold lower than Germany. The 2260.5 MW wind energy installed power capacity in 2012 of Turkey reached to 6353.8 MW level in 2017 (Figure 11).

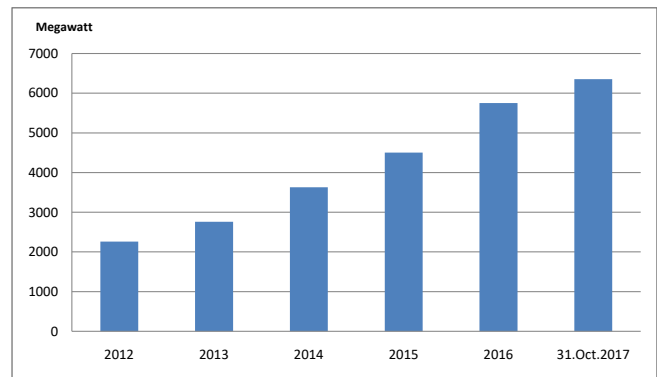


Figure 11: Change of wind energy in installed power capacity (2016-2017) Source: TEİAŞ 2017.

G. Biomass Energy

Plant and animal origin matters that have carbohydrate compounds as their basic compounds are defined as biomass energy source and energy obtained from those sources are defined as biomass energy. The capacity of global bioelectricity (electricity generation from bioenergy) exhibited 7% increase between 2016 and 2017, and it increased to 122 gigawatts. This energy that is used in numerous fields such as heating, energy and transportation

constitutes 14.1% of the total consumed energy according to 2017 data [13] (REN21,2018:71).

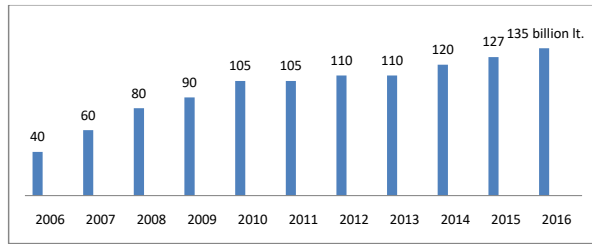


Figure 12: Global trends in ethanol, biodiesel and HVO production, 2006-2016 Source: REN 21,2018:72.

Ethanol, biodiesel and HVO production that was 40 billion liters in 2006 showed an increase more than 3 folds and reached to 135 billion liters when it came to 2016.

The high potential of Turkey in biomass energy is left behind comparing to the other renewable energy options. The biomass energy installed power of Turkey is about 467 MW level as the end of 2016. This rate is projected to be at 2 thousand MW in the 2023 targets.

III. CONCLUSION

Energy constitutes one of the most important needs of modern world. Thus, it is strategically important for every country. Energy sources in the world are classified in 2 groups as renewable and non-renewable energy sources. Non-renewable energy sources that are also named as fossil fuels are the most common energy type.

The dependency on non-renewable fossil fuels is at very high levels. Petroleum has the first rank as the energy source that has the highest utilization rate among fossil fuels. It is estimated that natural gas will replace petroleum according to the projections while petroleum will continue to its dominant behavior. There are two principal reasons for this: the first thing is the estimation that petroleum sources will deplete till 2050; and second, natural gas is an energy source that is relatively less harmful to the environment comparing to the petroleum. Nevertheless, it seems that dependency on fossil fuels will continue for long times if there won't be radical changes in the global energy sector. However, a lot of countries exhibited more demand on renewable energy sources as time passes. Increasing the shares of renewable energy sources in utilization is in the strategies that have priority, especially in the policies for tackling climate change. The basic goal by sustainable development, on the other hand, is achieving the development without taking the rights of future generations. In other words, the principal point to be taken into consideration as a criterion is treating both the future generations and present generations in a fair manner [2]

(Sağır&Doğanalp, 2016; 238).

Energy causes various numerous harms on environment during its generation, usage, transportation and storage. Hence, relationship between energy and environment is regarded as an important factor in environmental protection policies. The reason of global climate change that is given as the most prominent global problem of our day is the gases that are named as green house gases and are emitted due to intensive utilization of fossil fuels. The realization of effective tackling the climate change is depending on the reduction of fossil fuel usage as far as it can be. Alongside of these, tackling climate change necessitates a global cooperation. International community strives in order to develop this cooperation in the leadership of UN since 1990s. The final point after the process that was started with UN Climate Change Frame Contract is the Paris Climate Conference that was realized in 2015. Some of the scientific groups is considering the cooperation sense that was realized in a relatively short time as a significant success while others propose that decisions of the conference will be insufficient for tackling the climate change. The degree of success of the taken decisions will be seen in time.

We must make significant changes in our energy habits as individuals and governments if we want to live in a sustainable future and if we want to inherit a more healthy life quality and higher environment for our future. Using energy with a more efficient manner, reducing energy usage as much as we can do are the activities that we can do as individuals. An energy policy focusing to environment would be the most appropriate option for a sustainable future if we consider the problem in respect of the governments. For this, it is necessary to increase the share of renewable energy and incentive mechanisms for renewable energy topic. Renewable energy will provide sound benefits to country economy in terms of both energy security and national development since it is an energy type that can be obtained from self sources of the countries.

REFERENCES

- [1] H. Samur, "Küresel İklim Değişimi ve Beklenen Küresel Felaketi Önleme Stratejileri", Master Thesis, Selcuk University Social Sciences Institute, Konya, Turkey, 2005.
- [2] H. Sağır, B.Doğanalp, "Bulanık Çok Kriterli Karar Verme Perspektifinden Türkiye İçin Enerji Kaynakları Değerlendirmesi", Kastamonu Üniversitesi İktisadi ve İdari Bilimler Fakültesi Dergisi, , Sayı.11, ss.233-256, Ocak 2016.
- [3] V. Yurdadoğ, Ş. Tosunoğlu, Türkiye'de Yenilenebilir Enerji Destek Politikaları, Eurasian Academy of Sciences Eurasian Business & Economics Journal, , Sayı 9, Nisan 2017.
- [4] Ü. Sahin, "Uluslararası Çevre Rejimleri", *Dora Basım Yayım*, İstanbul, Turkey, 2017.
- [5] N. Onat, Türkiye'de Yenilenebilir Kaynaklardan Elektrik Enerjisi Üretimi: Mevcut Durum Ve Gelecek Beklentileri, akıllı Ulaşım sistemleri ve Uygulamaları Dergisi, Cilt 1, Sayı 1, 2018.

- [6] İ. Kose, “İklim Değişikliği Müzakereleri: Turkey'nin Paris Anlaşması'nı İmza Süreci”, *Ege Stratejik Araştırmalar Dergisi*, vol. 9, iss. 1, pp. 57-81, 2018.
- [7] E.G. Cakmak, T. Dogan, B. Hilmioglu, Bilgin, “İklim Değişikliği sürecinde Paris anlaşmasının Rolü ve Turkey'nin Konumu”, *VII. Ulusal Hava Kirliliği ve Kontrolü Sempozyumu*, Antalya, Turkey, November 2017.
- [8] M. Türkes, G. Kılıç, “Avrupa Birliği'nin İklim Değişikliği Politikaları ve Önlemleri” TMMOB Çevre Mühendisleri Odası V. Ulusal Çevre Mühendisliği Kongresi, 2003
- [9] E.Karagöl Tanas,İ. Kavaz, Dünyada ve Türkiye'de Yenilenebilir Enerji, SETA, Sayı 197, Nisan 2017.
- [10] Dünya Enerji Konseyi Türk Milli Komitesi (DETMK)(2018), 2018 Enerji Görünümü: 2040'a Bakış, <https://www.dunyaenerji.org.tr/2018-enerji-gorunumu-2040a-bakis/>, E.T.: 05/08/2018.
- [11] Global Wind Statistick 2017, Global Wind Energy Council, 2018.
- [12] Hidropower Status Report 2017 (İHA),2018.
- [13] Renewables 2018 Global Status Report(Ren 21),2018.
- [14] <https://www.statista.com/statistics/271748/the-largest-emitters-of-co2-in-the-world/,2018>
- [15] <https://enerjigunlugu.net/icerik/11658/danimarka-ruzgr-elektrigini-tuketecek-yer-ariyor.html>
- [16] <https://assets.kpmg.com/content/dam/kpmg/tr/pdf/2018/02/sectorel-bakis-2018-enerji.pdf>
- [17] <http://www.ipcc.ch/report/ar5/>
- [18] <http://www.yenienerji.info/haberler/kuresel-hidroelektrik-gucu-2017-de-rekor-kirdi>
- [19] International Energy Agency,World Energy Outlook 2013.

Implementing Peak Current Mode Control of Interleaved SEPIC Converter

O.KIRCIOĞLU¹, M. ÜNLÜ² and S.ÇAMUR³

¹Kocaeli University, Kocaeli/Turkey, onur.kircioglu@kocaeli.edu.tr

²Kocaeli University, Kocaeli/Turkey, muratunlu@kocaeli.edu.tr

³Kocaeli University, Kocaeli/Turkey, scamur@kocaeli.edu.tr

Abstract - The SEPIC converter can operate both as a step down and as a step up and widely used in photovoltaic applications, power factor correction circuits and LED drivers. In this study, interleaved two phase SEPIC converter with peak current control is designed and peak current mode controller implemented. The open-loop and closed-loop responses (duty ratio to output voltage and inductor current to output voltage) of the converter are obtained. The simulation results show that the converter has good dynamic response in the case of input voltage and load changes.

Keywords - SEPIC converter, peak current mode control, interleaved converters, frequency responses, coupled inductors.

I. INTRODUCTION

THE SEPIC converter can operate both as a step down and as a step up. They have advantages such as having a continuous input current and positive output voltage when compared to other buck-boost DC-DC converter topologies. But it has four passive elements (two inductors and two capacitors), thus it is a fourth order system and its control is difficult. In the SEPIC converter, two inductances can be used separately, or a coupled inductor wound on the same can may be used [1]. Using coupled inductors saves printed circuit board (PCB) space, increases power density, reduces cost, and also reduces the ripple inductor current by half [2]. It also improves the dynamic response of the system by reducing the effective degree of the system [1].

The power of the SEPIC converter is limited to a few hundred watts. Multiple converters can be connected in parallel to design a converter for high power. Interleaving technique is a frequently used method for parallel operation. In this method, each converter connected in parallel is controlled by shifting the phase by $(360/n)$ relative to each other. In this expression, "n" refers to the number of parallel connected converters. The main advantages of the interleaving technique are;

- Reduce input current ripple.
- Reduces the size of passive elements [3].
- Since the current stresses of the circuit elements are reduced, the power losses are reduced and the efficiency of the system is increased [4, 5].

- Thermal management is easier because power losses are reduced.

- Ensures the system is modular.
- The reliability of the system increases.

In most applications, it is desirable that the output voltage of the DC-DC converters remain constant at the desired value. But the output voltage also changes when the input voltage and the load resistance change. For this reason, DC-DC converters must have a feedback control system for a regulated output. DC-DC converters frequently have two types of control methods, voltage mode and current mode control [6]. In the current mode control, the inductor current or the switch current is used to control the output voltage. The current mode control method for DC-DC converters is done in three basic ways [7]; Hysteresis band control, Constant off time control and Peak current mode control.

Peak current mode control is the most commonly used current mode control method. This method has many advantages over the voltage mode control method. These advantages can be listed as follows:

- Protects the system against short-circuit conditions and improves system reliability by removing the risk of deterioration of the switching elements [6].
- It is not affected by the change of input voltage and there is no transient regime in the system [8, 9].
- Improves the dynamic response of the system. In addition, since the output voltage is controlled by the inductance current, the system's degree is reduced and the controller design becomes easier.
- In multiphase DC-DC converters, it ensures that the current sharing of parallel-connected converters is equal [7].

The disadvantage of the current mode control method is that the system cost is higher and the complexity is more complicated if additional current information is needed.

II. TWO PHASE INTERLEAVED SEPIC CONVERTER WITH COUPLED INDUCTOR

An ideal inductor in which each inductor is tightly coupled with the same number of windings on a single core; the mutual inductance causes current to be evenly divided between the two connected inductors. In practice, the inductors do not have

equal inductance and their ripple currents will not be exactly equal. However, for a desired ripple current value, it is estimated that the required inductance in the coupled inductor is half needed if there were two separate inductors. The inductor L_{11} is coupled with L_{12} and the inductor L_{21} is coupled with inductor L_{22} . In this way, the predefined input current ripple can be accomplished with smaller inductance compared to uncoupled inductors. The mutual inductances for the upper phase inductors (M_1) and the bottom phase inductors (M_2) are calculated as in (1);

$$M_1 = k_1\sqrt{L_{11}L_{12}} \text{ and } M_2 = k_2\sqrt{L_{21}L_{22}} \quad (1)$$

A two-phase interleaved SEPIC converter is constructed by paralleling two classic SEPIC converters. It consists of two pair of the coupled inductors, a pair of the capacitors, diodes and power switches. The block diagram of interleaved SEPIC converter with coupled inductor is shown in Fig. 1.

A controller generates two PWM control signals with 180° out of phase for the two power switches (S_1 and S_2). The input current of this converter (i_{in}) is the sum of each current of the inductors i_{L11} and i_{L21} , and their waveforms are shown in Fig. 2. The inductor values have been chosen to enable operation in CCM mode. The designed SEPIC converter in CCM includes four operating intervals. The equations of these intervals vary depending on which mode the SEPIC is operating (the buck ($D < 0.5$), boost ($D > 0.5$) and $D=0.5$ modes).

In Mode I: The switch S_1 is ON, while the switch S_2 is OFF. On the contrary, the diode D_1 is OFF, and diode D_2 is ON. In this mode, the voltages across inductors L_{11} is V_{in} , while the voltage across inductor L_{12} is V_{C1} . Therefore, the inductor currents i_{L11} and i_{L12} increase. The equations for this mode are as follows;

For the upper phase;

$$\begin{aligned} L_{11} \frac{di_{L11}}{dt} + M_1 \frac{di_{L12}}{dt} &= V_{in} \\ L_{12} \frac{di_{L12}}{dt} + M_1 \frac{di_{L11}}{dt} &= V_{C1} \\ C_1 \frac{dv_{C1}}{dt} &= -i_{L12} \end{aligned} \quad (2)$$

For the bottom phase;

$$\begin{aligned} L_{21} \frac{di_{L21}}{dt} + M_2 \frac{di_{L22}}{dt} &= V_{in} - V_{C2} - V_{C3} \\ L_{22} \frac{di_{L22}}{dt} + M_2 \frac{di_{L21}}{dt} &= -V_{C3} \\ C_2 \frac{dv_{C2}}{dt} &= i_{L21} \end{aligned} \quad (3)$$

And equation of the output capacitor is obtained as follow,

$$C_3 \frac{dv_{C3}}{dt} = i_{L21} + i_{L22} - \frac{V_{C3}}{R_L} \quad (4)$$

In Mode II: The switch S_1 is OFF, while the switch S_2 is ON. Inversely, the diode D_1 is ON, and diode D_2 is OFF. In this mode, the voltages across inductors L_{21} is V_{in} , while the

voltage across inductor L_{22} is V_{C1} . The equations for this mode are as follows;

For the upper phase;

$$\begin{aligned} L_{11} \frac{di_{L11}}{dt} + M_1 \frac{di_{L12}}{dt} &= V_{in} - V_{C1} - V_{C3} \\ L_{12} \frac{di_{L12}}{dt} + M_1 \frac{di_{L11}}{dt} &= -V_{C3} \\ C_1 \frac{dv_{C1}}{dt} &= i_{L11} \end{aligned} \quad (5)$$

For the bottom phase;

$$\begin{aligned} L_{21} \frac{di_{L21}}{dt} + M_2 \frac{di_{L22}}{dt} &= V_{in} \\ L_{22} \frac{di_{L22}}{dt} + M_2 \frac{di_{L21}}{dt} &= V_{C2} \\ C_2 \frac{dv_{C2}}{dt} &= -i_{L22} \end{aligned} \quad (6)$$

And equation of the output capacitor is obtained as follow,

$$C_3 \frac{dv_{C3}}{dt} = i_{L11} + i_{L12} - \frac{V_{C3}}{R_L} \quad (7)$$

In Mode III: The switches S_1 and S_2 are OFF, while the diodes D_1 and D_2 are ON. This mode of operation occurs when the converter operates as a buck ($D < 0.5$). The currents of the all inductors ramp down linearly by flowing through the diodes D_1 and D_2 . The both phases have the same equations as given (2) and (4) in this interval. But for output voltage (V_{C3}) equation is as in (8);

$$C_3 \frac{dv_{C3}}{dt} = i_{L11} + i_{L12} + i_{L21} + i_{L22} - \frac{V_{C3}}{R_L} \quad (8)$$

In Mode IV: The switches S_1 and S_2 are ON, while the diodes D_1 and D_2 are OFF. This mode of operation occurs when the converter operates as a boost ($D > 0.5$). The currents of the all inductors ramp up linearly by flowing through the diodes D_1 and D_2 . The both phases have the same equations as given (1) and (5) in this charge interval. But for output voltage (V_{C3}) equation is as in (9);

$$C_3 \frac{dv_{C3}}{dt} = -\frac{V_{C3}}{R_L} \quad (9)$$

For a desired inductor current ripple, L_{11} , L_{12} , L_{21} and L_{22} inductor values are calculated as shown in (10):

$$L_{11} \cong L_{12} \cong L_{21} \cong L_{22} \geq \frac{1}{2} \frac{V_{in(\min)} \times D(\max)}{\Delta I_L \times f_{sw}} \quad (10)$$

III. CONTROLLER DESIGN OF THE CONVERTER

The designed system consists of two parts as power stage and control stage as can be seen from Figure 1. In order to control the output voltage, the error voltage is generated by taking the feedback from the output voltage. The error voltage

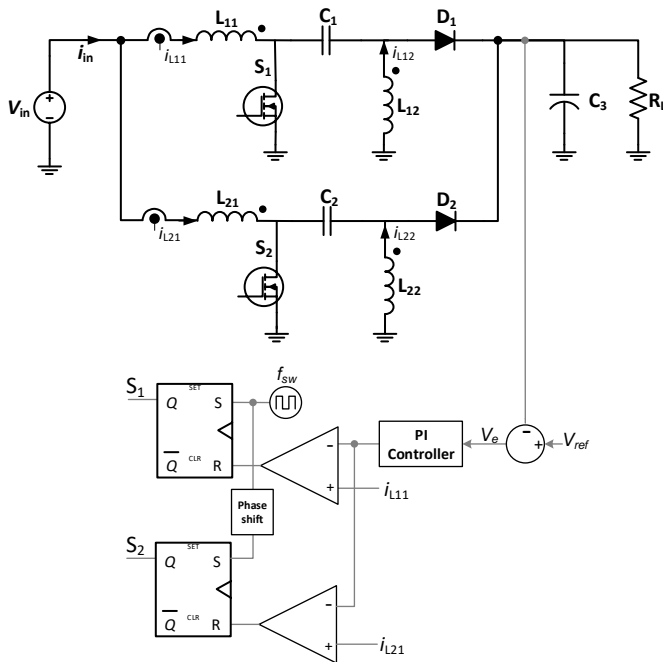


Figure 1: Peak Current Mode Controlled SEPIC Converter block diagram.

is applied to the PI controller to obtain the reference current for the peak current mode control block. In peak current mode control, when the duty cycle is greater than 0.5, subharmonic oscillations occur. In order to avoid this situation, slope compensation technique is used [10].

The circuit parameters used in simulation studies are shown in Table 1. The frequency responses of the interleaved SEPIC converter were obtained using the AC sweep mode in the PSIM software. The open loop frequency response and step response of the converter without the peak current mode controller are shown in Figure 2.a and 3.a, respectively. The responses of the peak current mode-controlled converter are shown in Figure 2.b and Figure 3.b.

Table 1. Parameters of the SEPIC converter

Parameter	Value
$C_1 = C_2$ (Coupling Capacitor)	340 μF
C_3 (Output Capacitor)	1200 μF
$L_{11} = L_{21}$	500 μH
$L_{12} = L_{22}$	$\sim 500 \mu\text{H}$
k (Coupling Coefficient)	0.99
Switching Frequency (fsw)	40 kHz

The PI controller was designed to control the output voltage of the converter, and the converter's closed loop operation was performed. The frequency and step response of the voltage mode-controlled converter are shown in Figure 4.a and Figure 5.a, respectively. The responses of the peak current mode-controlled converter are shown in Figure 4.b and Figure 5.b. In the simulation studies, the K_p and K_i coefficients of the PI controller were chosen to 0.05 and 0.005, respectively.

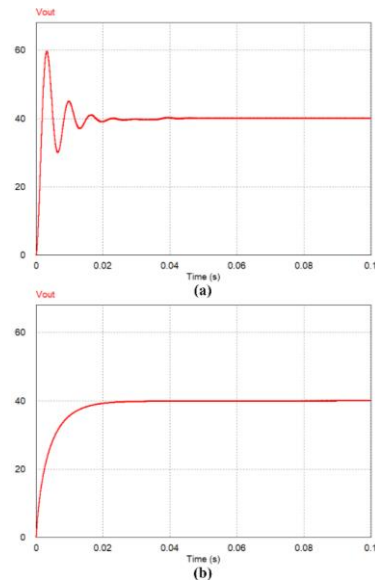


Figure 3: Step responses of the open loop system: Duty ratio to output voltage (a) inductor current to output voltage (b).

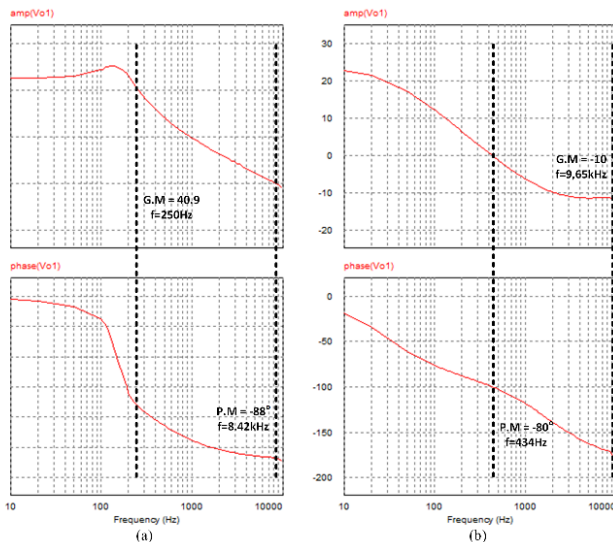


Figure 2: Bode diagrams of the open loop system: Duty ratio to output voltage (a) inductor current to output voltage (b).

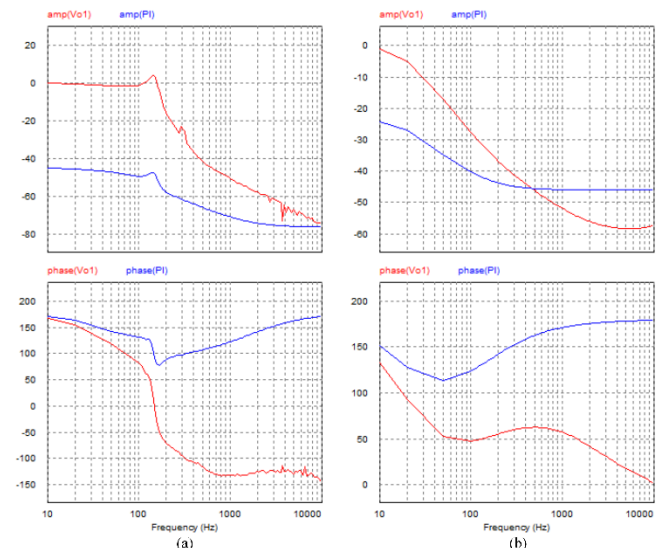


Figure 4: Bode diagrams of the closed loop system: voltage mode control (a) peak current mode control (b).

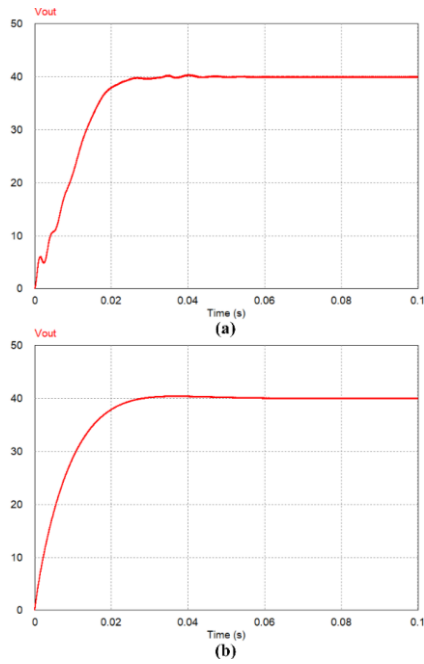


Figure 5: Step responses of the close loop system: voltage mode control (a) peak current mode control (b)

In order to test the performance of the designed controllers, input voltage and load change cases are discussed. In the 0.1s of the simulation, the input voltage was increased from 20V to 30V. Then the output current was doubled in the 0.2s. The output voltage of the voltage mode controlled and current mode-controlled converters operating under this scenario is shown in Figure 6.a and Figure 6.b respectively.

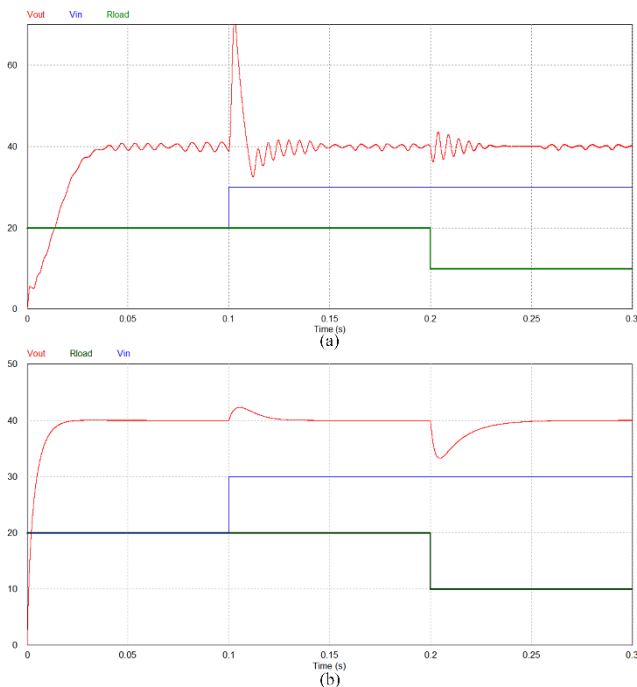


Figure 6: Dynamic response in the case of input voltage and load changes (a) voltage mode control (b) peak current control

IV. CONCLUSION

The frequency and step responses of open-loop system and closed-loop system of the designed SEPIC converter have been obtained. Moreover, it has been obtained the frequency and step responses of the SEPIC with peak current controller (V_o/i_L) and without peak current controller (V_o/D). The dynamic responses of the designed SEPIC converter with peak current controller (V_o/i_L) and without peak current controller (V_o/D) are demonstrated in Fig. 6. From results, it can be deduced that the designed SEPIC converter with peak current mode controller has better response; it is fast to changes in load and input voltage and can successfully maintain the output voltage.

REFERENCES

- [1] G. Di Capua and N. Femia, "A critical investigation of coupled inductors SEPIC design issues," *IEEE Trans. Ind. Electron.*, vol. 61, no. 6, pp. 2724–2734, 2014.
- [2] N. Pragallapati and V. Agarwal, "Distributed PV Power Extraction Based on a Modified Interleaved SEPIC for Nonuniform," *IEEE J. Photovoltaics*, vol. 5, no. 5, pp. 1442–1453, 2015.
- [3] C. Chang and M. a Knights, "Interleaving technique in distributed power conversion systems," *Circuits Syst. I Fundam. Theory Appl. IEEE Trans.*, vol. 42, no. 5, pp. 245–251, 1995.
- [4] C. Shi, A. Khaligh, and H. Wang, "Interleaved SEPIC Power Factor Preregulator Using Coupled Inductors In Discontinuous Conduction Mode With Wide Output Voltage," *IEEE Trans. Ind. Appl.*, vol. 52, no. 4, pp. 3461–3471, Jul. 2016.
- [5] C. Yang, Y. Liu, P. Tseng, T. Pan, H. Chiu, and Y. Lo, "DSP-Based Interleaved Buck Power Factor Corrector With Adaptive Slope Compensation," *IEEE Trans. Ind. Electron.*, vol. 62, no. 8, pp. 4665–4677, 2015.
- [6] Mohan, N., Robbins, W. and Undeland, T. (2007). *Power electronics: Converters, Applications, and Design*, Hoboken, NJ: Wiley.
- [7] J. Li, "Current-Mode Control: Modeling and its Digital Application," Virginia Polytechnic Institute and State University, 2009.
- [8] A. K. G. Uma, "Comparative study between peak current mode and hysteric current mode control of a single – ended primary inductance converter," *IET Power Electron.*, vol. 5, no. June 2009, pp. 1226–1235, 2012.
- [9] F. Taeed and M. Nymand, "High-performance digital replica of analogue peak current mode control for DC–DC converter," *IET Power Electron.*, vol. 9, no. 4, pp. 809–816, 2016.
- [10] C. C. Fang and R. Redl, "Subharmonic Instability Limits for the Peak-Current-Controlled Boost, Buck-Boost, Flyback, and SEPIC Converters with Closed Voltage Feedback Loop," *IEEE Trans. Power Electron.*, vol. 32, no. 5, pp. 4048–4055, 2017.

THE IMPORTANCE OF THE DIVERSITY FACTOR

M.F. YAPICIOĞLU¹, H. H. SAYAN² and H. TERZİOĞLU³

¹ Enerjisa Başkent Electricity Distribution Inc. , Çankırı/Turkey, mehmetfahri.yapicioglu@eedas.com

²Gazi University, Ankara/Turkey, hsayan@gazi.edu.tr

³Selcuk University, Konya/Turkey, hterzioglu@selcuk.edu.tr

Abstract – Electrical installation requirements of all structures are specified in the Electrical Internal Installation Project, necessary design and calculations; Electrical Internal Facilities Regulation, Electrical Installation Project Preparation Regulation, Measurement and Details of Cable Chimney and Energy Room and Application Areas and related local circulars are prepared by reference, controlled and approved by responsible Electricity Distribution Companies. The concurrent power mal calculations performed in the Electrical Internal Installation Project directly affect the selection of the materials related to the electrical facilities of the structures. Simultaneous power (at the same time the power drawn) is obtained by multiplying the coefficient of synchronization with the installed power. Therefore, synchronous coefficient plays an important role in the electrical internal installation projects in order to determine the electrical materials of the buildings at ideal values. In the present case; Synchronization coefficients in the Electrical Internal Installation Projects are made by reference to the synchronization coefficients specified in the a.2 subparagraph of the 57.MADDE of the Electrical Internal Facilities Regulation, which was prepared many years ago and cannot respond to the developments in today's conditions and the constantly renewed technology. In parallel with the evolving living standards and current technology, this simultaneous power spending account will increase the reliability of all structures in terms of performance and cost of the electrical installations. In this article, the concurrency coefficient; I will try to explain what impacts and how they affect risk, performance, cost and reliability. Thus, the importance of the coefficient of synchronization will be emphasized.

Keywords – Installed power, simultaneous power, diversity factor, Electrical Internal Installation Project.

I. INTRODUCTION

Developing technologies, changing living conditions and expectations of today's people increase expectations in all plans and projects. It is not possible to ignore "energy efficiency de in our world where energy is limited and expensive. Plans and projects that will be prepared by accepting expectations and energy efficiency focus will be projects with high performance. The data of the installed power shall be determined in the electrical internal installation project. [1] Especially in projects such as construction, mechanical and electrical projects with high cost and risk, pre-made simulations, designs and calculations are of great

importance to reduce both productivity and risks. [2] [3] [4] [5] In many projects, the sensitivities taken into account during design contribute to performance and efficiency, while simultaneous power calculations in Electrical Internal Installation Projects contribute to the electrical quality, performance and efficiency of the structures. Material selection and design in electrical facilities; It is made by reference to the zaman demand power / simultaneous power "calculated in the Electricity Internal Installation Projects. Simultaneous power (at the same time the power drawn) is obtained by multiplying the coefficient of synchronization with the installed power.

Installed power; The sum of the rated power of the electrical energy consumers in a facility [7] is determined by need and is not likely to be saved in this regard. Simultaneous power / Requested maximum power: The maximum value Concurrency coefficient: The ratio of the maximum demand power of a group of consumers or electrical devices at a given time interval to the sum of the maximum individual demand forces within the same time interval (Value less than 1 or 1). [7]

As it directly affects the cost, safety and performance of the electrical installations, it is important to determine the simultaneous power and the simultaneity coefficient [7]. Simultaneity coefficient plays an important role in the electrical internal installation projects in order to determine the electrical materials of the buildings at ideal values. The development of the simultaneous power spending account in parallel with the evolving living standards and the current technology will improve the reliability of all structures in terms of performance and cost. For information on how to use the coefficients of concurrency, please refer to the Electrical Internal Facilities Regulation.

In this study, the importance of the coefficient of synchronization which is effective in the selection of materials and equipment used in electrical facilities is explained by examples. It is explained in this example that the current regulation needs to be updated.

structures are very important factors that should be taken into consideration in the calculation of the simultaneous power. Also called mechanical load of places such as hotels, hospitals, plaza; Since the forces such as kitchen load, heating-cooling loads can be activated at full capacity at the same time, the simultaneous power must be considered equal to the installed power, in other words, the coefficient of synchronicity must be taken 1. Similarly, even in dwellings; When the high-power heater / cooler, electric water heater etc. is activated, the powers of the special electrical equipment which can operate at full capacity should be calculated by reference to the installed power when calculating the simultaneous power. The simultaneous power calculation of the mechanical loads which are not possible to be activated at the same time is calculated by taking the power into account. For example, in buildings with a central heating-cooling system, since both systems cannot be activated at the same time, the power synchronization coefficient of the system having great power is calculated by taking 1 and added to simultaneous power.

III. MATH

The detected concurrency coefficients are multiplied by the respective installed forces to determine multiple simultaneous power.

$$\text{Simultaneous power} = \text{Installed power} \times \text{Diversity factor} \quad (1)$$

$$\text{Diversity factor} = \text{Simultaneous power} / \text{Installed power} \quad (2)$$

$$I = P / (V \times \sqrt{3} \times \text{Cos}\theta) = P / (380 \times 1,73 \times 0,8)$$

$$I = P / 526 \quad (1)$$

We will make a sample calculation;

For a building with 5 floors and 4 apartments on each floor; The lift power of is 7.5 kW, the lighting power of the stair is $12 * 75W = 900W$, the hydrophore is 2.5 kW.

The load profiles of the apartments are as follows.

	Piece	Total power (W)
Lighting	25	2500
Plugs	14	4200
Washing machine	1	2500
Dishwasher	1	2500
Electric Heater	1	2000
Total		13700 W

Building Board Power;

Apertments	13700 W x 20	= 274000 W
Lightings	900 W x 1	= 900 W
Lift	7500 W x 0,55	= 4125 W
Hydrophore	2500 W x 1	= 2500 W
Total		281525 W

For an apartment.

Installed Power: 13700 W

Diversity factor: 60% for the first 8 kW,
40% for the emaining power.

The demand power of an apartment

$$8000 \times 0,6 = 4800 \text{ W}$$

$$13700 - 8000 = 5700 \text{ W}$$

$$5700 \times 0,4 = 2280 \text{ W}$$

$$4800 + 2280 = 7080 \text{ W}$$

The demand power of an apartment: 7080 W

The demand power of Building:

Apertments	7080 W x 20 x 0,39	= 55224 W	[10]
Lightings	900 W x 1	= 900 W	
Lift	7500 W x 0,55	= 4125 W	
Hydrophore	2500 W x 1	= 2500 W	

Total **62749 W**

As can be seen from the example; simultaneous forces obtained according to the purpose of use and type of load were collected and total concurrent power was found.

Total simultaneous power; In fact, this means the presence of electrical installation elements, electrical protection elements, electrical transmission elements. Because the current calculation is made with reference to the simultaneous power, the current value obtained in this way; It affects the selection of electrical circuit elements such as meter, thermal magnetic switch, current transformer, conductor.

IV. MATERIAL AND METHOD

The importance of the coefficient of synchronicity is explained by a facility with a hospital.

The data regarding the installed power and the investments made in line with this power are calculated by taking into consideration the installed capacity of a facility which is intended for use as a hospital.

Purpose of: Hospital

Installed Power: 4611,6 kW

Demand Power: 2876,7 kW [are calculated with reference to the existing coefficients]

Selected TR: 2X1600 kVA TR

The hospital has been operating for about 5 years and the largest simultaneous power recorded in the memory of the electronic meter in the hospital within 5 years, in other words, the load or demant power that is activated at the same time is 1954,08 kW. In this case, the required transformer power; It would be 2X1000 kVA or 2000kVA.

It is not only the transformer facility cost, but also the facility hospital because of the fact that not only the cost of the simultaneous power calculation is made in the projecting phase, therefore, the generator facility should be built with the capacity to back up all transformer power. This will also increase the size of the problems that may occur if the simultaneous power is not optimally calculated.

In another example, I would like to share the details of a facility that is used for school purposes.

Purpose of: Government offices (school)

Installed Power: 1175 kW

Demand Power: 804 kW [are calculated with reference to the existing coefficients]

Selected TR: 1000 kVA TR

The maximum synchronous power value recorded by the electronic meter of a long-time facility is only 252.54 kW, at almost a quarter of the calculated simultaneous power. If this situation could be predicted, in the simplest way, the cost would be reduced by 1/4.

It would not be right to read the concurrent power calculation as an effect that would only reduce the cost. Many facilities are due to this prediction error after a certain time; they need to make additional facilities or plant changes by offering revised projects under the name of renovation, power increase. The revised forces, which are not planned during the project phase, are expected to be a potential risk with the activation of the plant, due to the special conditions of some devices (a motor that attracts excessive current at the time of development) or the voltage drops due to distance. In case of any of these problems, there will not be any problem of additional facilities with the renovation projects, and the problems that the plant is experiencing with the electricity will bring along business, production.

V. RESULT

In this study, the importance of the coefficient of synchronization is explained. It is explained by the examples that the value of the coefficient of synchronicity in the current regulation needs to be updated. As a result of this, it is understood that the required coefficient of simultaneity of the studies should be updated again. By providing the necessary data for the following work, optimization studies and concurrency coefficients can be re-determined.

REFERENCES

- [1] TMMOB ELECTRICAL ENGINEERS ROOM, Electrical Internal Facilities Regulation. ANKARA, 1954.
- [2] A cellular automaton based model simulating HVAC fluid and heat transport in a building. Modeling approach and comparison with experimental results A.Saiza.J.F.UrchueguiabJ.Martos <https://doi.org/10.1016/j.enbuild.2010.03.024>
- [3] Semi-automatic approach for thermographic inspection of electrical installations within buildings A.S.Nazmul HudaSoibTaibaMohd ShawalJadinbDahamanIshaka <https://doi.org/10.1016/j.enbuild.2012.09.014>
- [4] Energy performance building evaluation in Mediterranean countries: *Comparison between software simulations and operating rating simulation Lamberto Tronchin *, Kristian Fabbri DIENCA-CIARM, University of Bologna, Viale Risorgimento 2, I-40136 Bologna, Italy Received 17 July 2007; received in revised form 3 October 2007; accepted 9 October 2007*
- [5] Benchmarking Productivity Indicators for Electrical/Mechanical Projects Awad S. Hanna, M.ASCE; Pehr Peterson; and Min-Jae Lee, S.M.ASCE [https://ascelibrary.org/doi/abs/10.1061/\(ASCE\)0733-9364\(2002\)128:4\(331\)](https://ascelibrary.org/doi/abs/10.1061/(ASCE)0733-9364(2002)128:4(331))
- [6] Framework of Success Criteria for Design/Build Projects Albert P. C. Chan; David Scott; and Edmond W. M. Lam [https://ascelibrary.org/doi/abs/10.1061/\(ASCE\)0742-597X\(2002\)18:3\(120\)](https://ascelibrary.org/doi/abs/10.1061/(ASCE)0742-597X(2002)18:3(120))
- [7] Regulation of electrical internal facilities <http://www.resmigazete.gov.tr/eskiler/2003/12/20031203.htm>
- [8] Measurement and Details of Cable Chimney and Energy Room http://www.emo.org.tr/genel/bizden_detay.php?kod=59703&tipi=2&sube=16
- [9] Baskent Electricity Distribution company data.
- [10] Simultaneity coefficient for 20 apartments should be taken 0.39.[1]

Control of SPWM applied 15 level inverter with ARM Processor

Abdulvehhab KAZDALOGLU¹, Bekir CAKIR², Tarik ERFIDAN³, M. Zeki BILGIN⁴

¹Electrical Engineering Department, Kocaeli University, vahap@kocaeli.edu.tr

²Electrical Engineering Department, Kocaeli University, bcakir@kocaeli.edu.tr

³Electrical Engineering Department, Kocaeli University, erfidan@kocaeli.edu.tr

⁴Electrical Engineering Department, Kocaeli University, bilgin@kocaeli.edu.tr

Abstract- In multi-level inverters, it is desirable that the output voltage is sinusoidally close and the total harmonic distortion is low. For this purpose, different methods and applications are applied to control multilevel inverters. In this study, matlab / simulink supported ARM processor and control system were used to control multilevel inverters (MLI). Thus, the control circuit is easily designed using the simulation circuit generated by matlab / simulink. With this method, any changes to the matlab / simulink control circuit algorithm can be easily applied. The control of the 15-level inverter circuit designed in this study was done with ARM processor and the results were evaluated.

Keywords - Multilevel inverter, Simulation, ARM processor

I. INTRODUCTION

In recent years there have been intensive researches on the control of MLI s. In inverter topologies, while trying to achieve the most efficient result with the least number of switching elements, the control method used in the switch is at least as effective as the topology. There are many different applications of pulse width modulation (PWM) that are commonly used to control inverters. Although one of these methods, sinusoidal pulse width modulation (SPWM), is more flexible than conventional PWM signals, it is not sufficient in terms of modulation and harmonic components. It is seen as an advantage that SPWM can be produced numerically, and that there is no need for serious mathematical calculations in design. [1].

SPWM also affects the inverter output voltage of carrier wave changes. In order to minimize the harmonic distortion, carrier waves are generated according to different amplitude and different frequency values and PWM signals, which control the power switches of the inverter, are obtained by comparing with reference sinusoidal signals [2].

Processor performance and capacity are also important for SPWM implementation. Depending on the number of levels of the inverter, the increasing number of carrier signals makes the control process difficult.

In recent years, along with the development and progress of technology, the development of control systems has also accelerated [3]. Microprocessors are now used in all areas of our lives. Most of the microprocessors we use are used in electronic devices that we use in our daily lives. The ARM

processor is one of these microprocessors. ARM is an abbreviation for Advanced RISC Machine, and RISC (Reduced Instruction Set Computer) refers to computer processors designed in accordance with the processor architecture. Low cost, and low power consumption, the ARM processor is used in many applications [4]. Most of the processor cores used in modern mobile devices, such as Tablets and Smart Phones, are a derivative of ARM or ARM architecture.

The STM32F4 kit produced by STMicroelectronics, high performance, low cost, programmers and debugging units on the kit are becoming increasingly widespread in their control circuits [5].

II. 15 LEVEL INVERTER DESIGN

In this study, different from the literature examples, asymmetric-fed multilevel inverter to the supply voltage levels are analyzed in case of using the Fibonacci sequence. For the Supply voltage levels the first terms of the Fibonacci sequence 1-1-2-3 levels that were selected. Inverter topology consists of two modules. The first module is called the leveling module, and the second module is called the polarity module. 15-level inverter topology is given in figure 1.

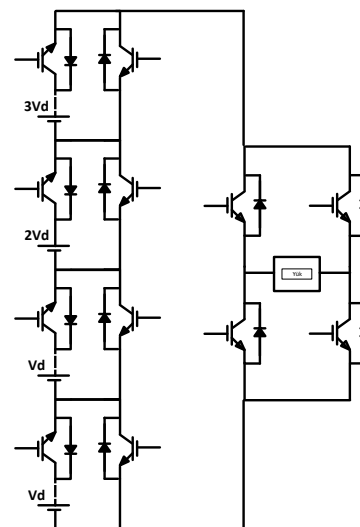


Figure 1. 15-level inverter topology [6]

In the level module, 1V-1V-2V-3V voltage sources are used. Positive alternating voltage levels are obtained at 0V-1V-2V-3V-4V-5V-6V-7V levels at the level module output. In the polarity module, these voltage levels are switched in such a way that the output at the mains frequency is obtained so that + and - alternating voltages are obtained.

In this study, to obtain the driving signals of the switching elements, instead of calculating the angle, an algorithm was written to generate the driving signals, the switching signals to follow the sinusoidal function. For example, for a 15-level circuit, the positive alternative would be 7, because a positive sine function would be selected. This function; $f(x) = 7 \sin wt$

An algorithm is then written to run the required switching elements at each integer value of this function. Figure 2 shows a schematic diagram of the $f(x) = 3 \sin wt$ algorithm for 3 levels required for a 7-level output.

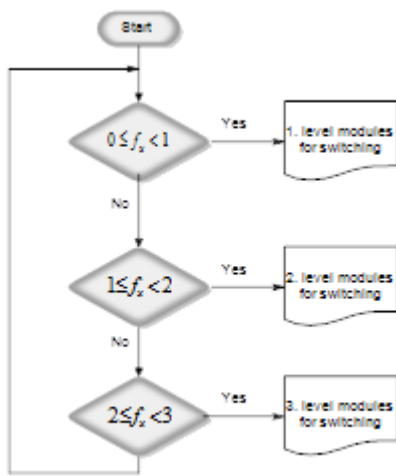


Fig. 2. Principle diagram of the switching algorithm

Designed inverter; IGBT have been chosen instead of MOSFET since the switching frequency does not go up to high levels and the inverter model to be designed can then be used in high power applications. While IGBT is selected, IGBT Modules which are suitable for topology have been chosen. The CM150DY-24A 1200V 150A IGBT module was selected from MITSUBISHI's IGBT series .

For the CM150DY-24A model 1200V 150A IGBT module from MITSUBISHI IGBT series, it is better to use the IGBT specific drive circuits recommended by the manufacturer. For this reason, CONCEPT has selected 2SC0108T model driver circuit, which removes the possibility of a short circuit, while allowing 2 IGBTs to remain at the same time with the possibility of giving dead time in the same way.

The drive can be operated in either half bridge mode or two independent IGBT drive modes. When a value resistor is connected between the MOD input and the GND input, the half bridge mode is selected. In this case, a dead time needs to be set so that the two IGBTs are not active at the same time. The dead time interval can be changed according to the resistance value to be connected. According to the resistance value, a value

between 0.5 μ s and 3.8 μ s can be set. For this, a formula is given in the driver's technical document.

$$R[K\Omega] = 33 \cdot T_d[\mu s] + 56,4$$

$$0,5 \mu s < T_d < 3,8 \mu s$$

According to this formula; 73K Ω <R <182K Ω must be selected [7].

In this study, the STM32F4 discovery kit was used to control the inverter circuit. The STM32F4 development kit is built using the ARM processor and has a 168 MHz microcontroller with a Cortex-M4 base. ARM processors are very fast compared to 8-bit processors, thanks to the 32-bit architecture. It is communicated to the computer via the USB ports on the card. The input - output and power pins of the card are supplied with two 2 - pin 50 - pin male connectors for ease of operation. With 4 different color LEDs, users can control their software easily. Figure 3 shows the STM32F4 Discovery development kit.



Figure 3. STM32F4 Discovery Development Kit

In this study, 6 PWM channels were used to generate IGBT drive signals. 5 channels are set to 50Hz and multiples, and 1 channel is set to 10kHz PWM. The Duty rates (D) of the PWM signals are obtained by the matlab simulink program and are recorded in series (6x200 data) and the processor is programmed. For a 10kHz maximum PWM frequency, one normal timer, Timer6, was used to generate this frekans interrupt. When the Timer6 interrupt comes, the D values are updated to the new value. In Figure 4 , if the circuit designed in MATLAB / Simulink te is made suitable for ARM processor, the following circuit is obtained..

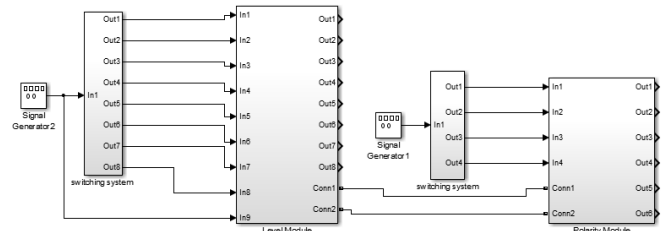


Figure 4. Block circuit of 15-level inverter

The Matlab / Simulink model obtained for the switching signals is shown in Figure 5

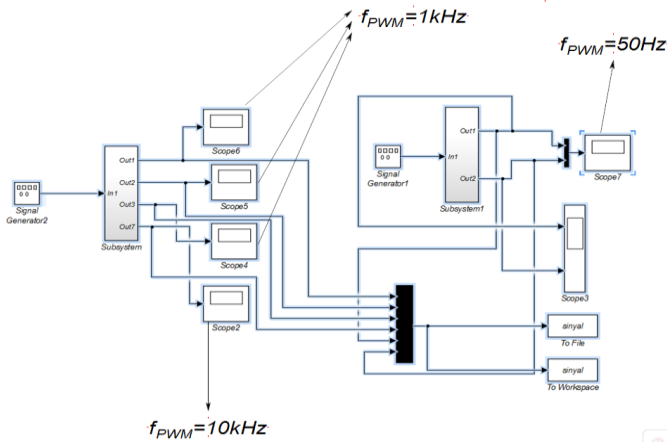


Figure 5. Matlab / Simulink model for switching signals

The 15-level inverter circuit is shown in Figure 6. Level module consisting of 4 IGBT modules in section 1, in section 2, IGBT driver cards, in section 3, consisting of 2 IGBT modules, the polarity module, in section 4, the STM32F4 discovery kit is available.

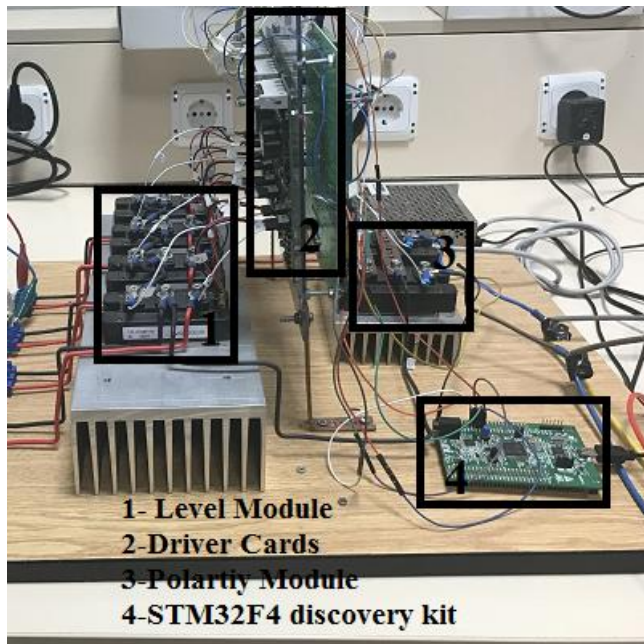


Figure 6. 15-level inverter circuit

The experimental study was tested under pure ohmic load. 3kw power and 12 192 ohm resistance sets were used in the laboratory. In the experimental study, the 5 resistances on the set were connected in parallel and the measurement was taken for the ohmic load value of 38.4 ohms.

The current and voltage waveforms at the inverter output are shown in Fig. 7.

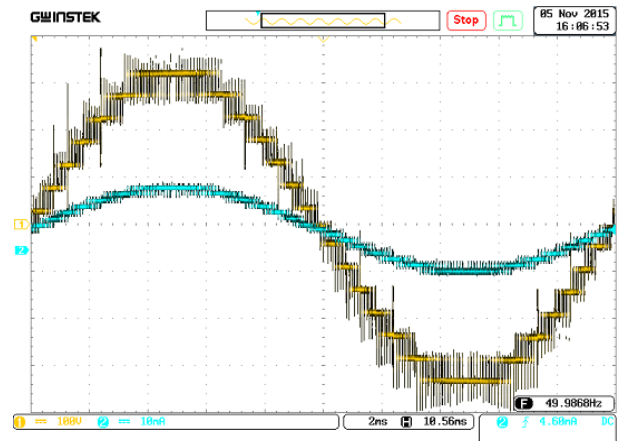


Figure 7. Pure Ohmic (R) load for 1-1-2-3 (5-5-10-15), R = 38 ohms

Graphs of total harmonic distortion of the current and voltage at the inverter output are given in Figures 8 and 9. The minimum THD value was 5.08%.

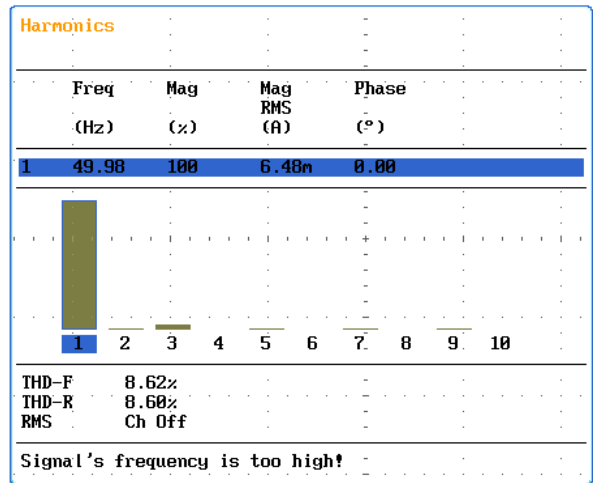


Figure 8. THD analysis result (max. Value)

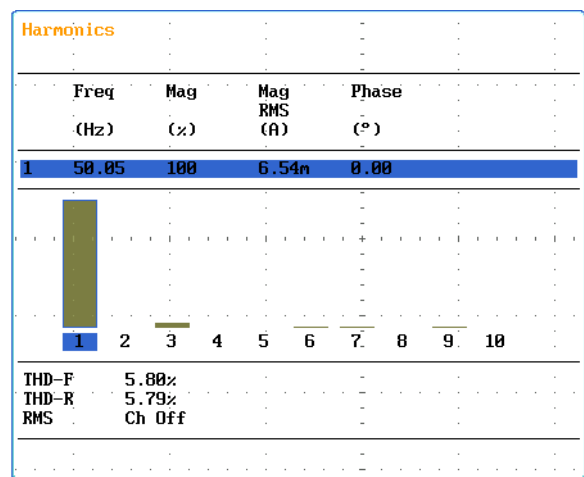


Figure 9. THD analysis result (min. Value)

III. CONCLUSION

In this study, the ARM based control system was implemented using Matlab / Simulink software to control multilevel inverters. First of all, 15 level inverter circuit is simulated in matlab / simulink program. The control circuit was then made available to the ARM and the control signals were applied to the actual circuit via the STM32F4 discovery kit.

With the STM32F4 discovery kit, the control of the inverters can be done easily via matlab / simulink. STM32F4 cards are widely used because of their low cost and easy programming. ARM based processors will be very useful for academic work and will be very useful for quickly turning simulation exercises into practice.

REFERENCES

- [1] Colak I, Kabalci E, "A Review on Inverter Topologies and Developments, " *International Conference on Electrical and Electronical Engineering*, ELECO, pp. 1-5, 2008.
- [2] S. Tuncer, " *The Examination of the Effect of Carrier Waveform Variations on Output Voltage of Multilevel Inverters*, "Gazi Üniv. Muh. Mim. Fak. Der, Vol. 24, , pp. 613-628, 2009.
- [3] Kuo, B. C., " *Automatic Control Systems*", Prentice Hall, 7th Edition, 1995.
- [4] Sandeep Raj, T. C. Krishna Phani, Jyotirmayee Dalei "Power quality analysis using modified S-transform on ARM processor", *Embedded Computing and System Design (ISED)*, 2016 Sixth International Symposium on, 15-17 Dec. 2016, India
- [5] T. Yaren, V. Süel, Y. Yeniaydin, B. Sakaci and S. Kizir, "Development of Simulink Based Control Training Applications with STM32F4 Kit," Turkish Automatic Control National Meeting, pp. 868-873, 11-13 Sept., Turkey, 2014.T
- [6] E. Beser, "Design of a single phase multilevel inverter by performing switching element number and harmonic optimization," Ph D Dissertation, Kocaeli University, Turkey, 2009
- [7] https://gate_driver.power.com/sites/default/files/product_document/application_manual/2BB0108T_Manual.pdf

Performance Evaluation of P&O, IC and FL Algorithms used in Maximum Power Point Tracking Systems.

F. ALHAJ OMAR¹, G. GOKKUS² and A. AFSIN KULAKSIZ³

¹ Selcuk University, Konya/Turkey, fuad.omar@selcuk.edu.tr

² Nevsehir Haci Bektas Veli University, Nevsehir/Turkey, gokselgokkus@nevsehir.edu.tr

³ Konya Technique University, Konya/Turkey, afsin@selcuk.edu.tr

Abstract - Solar energy is the most viable alternative source; furthermore, the implementation of solar energy technologies can reduce the problems of environmental pollution and electricity production costs besides securing the demands of electrical power. This research addresses the evaluation of three algorithms used in maximum power point tracking systems (MPPT). These algorithms are Perturbation & Observation (P&O), Incremental Conductance (IC) and Fuzzy Logic (FL). They are considered as the most used in MPPT due to their simplicity and ease of realization. Based on Matlab/Simulink environment, the mathematical models of the three algorithms are designed and tested under various weather conditions. Collected simulation results illustrated the effectiveness of Fuzzy logic algorithm to draw more energy, decrease oscillation and provide a fast response under variable weather condition. The final simulation results show the fuzzy logic algorithm exhibits a better performance compared to both perturbation & observation and Incremental conductance algorithms.

Keywords – Photovoltaic, MPPT, Incremental Conductance, Perturbation & Observation, Fuzzy Logic.

I. INTRODUCTION

The continued dependency on fossil fuels for energy production is leading to the continued rise in carbon emissions giving rise to atmospheric changes. Furthermore, continual daily increases in global energy use are depleting the supplies of oil and gas.

However, renewable energy sources are more viable alternatives since they are clean, pollution-free and non-exhaustible. Among all renewable energy systems, the solar energy system has received the most attention due to its ease of implementation and cost reduction. Despite all the advances in PV technology, the solar cells have some drawbacks such as the energy conversion efficiency is low and the characteristic curve of a solar cell is nonlinear and depends on the irradiance level and ambient temperature (Fig. 1) [1]. To increase the efficiency of the solar cell and optimize the power obtained from PV system, many maximum power point tracking techniques (MPPT) have been proposed, amongst these techniques, perturbation & observation, Incremental

conductance and Fuzzy logic. The Maximum Power Point (MPP) is the point on the current-voltage (I-V) curve (Fig. 1) which corresponds to the maximum possible power output for the given PV panel (P_{max}), and the Maximum Power Point Tracker (MPPT): A device that continually finds the MPP under variable weather conditions [2]. A typical diagram of the MPPT in a PV system is shown in (Fig. 2).

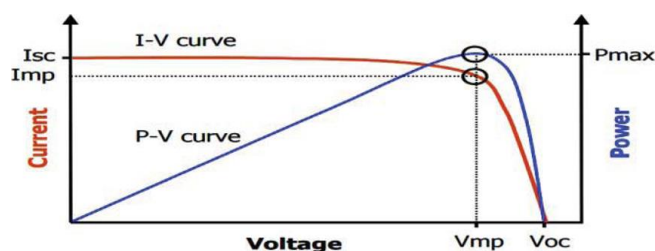


Figure 1: P-V & I-V characteristics of a solar panel.

In this study, a simulation test set up to evaluate the performance of the three mentioned MPPT algorithms. For performance evaluation, the mathematical models of the P&O, IC and FL algorithms are designed in Matlab/Simulink, and simulation results are obtained under different irradiation.

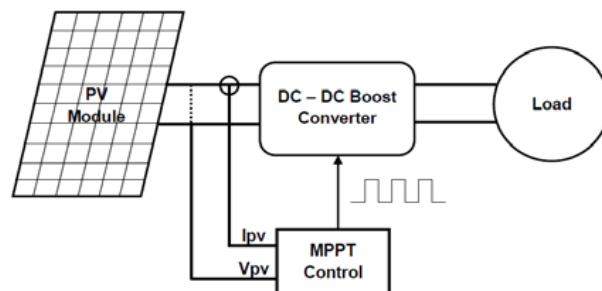


Figure 2: Typical diagram of MPPT in a PV System.

II. MAXIMUM POWER POINT TRACKING TECHNIQUES

A. Perturbation & observation (P&O):

This technique depends on changing duty cycle (perturbation) and measuring the output power (observation). First, if the change in duty cycle is positive and change in

power is positive, this means the operating point would be on the left of the MPP and the next perturbation would be positive. On the other hand, if the change in power is negative, this means the operating point would be on the right of the MPP and the next perturbation would be negative. If the change in the duty cycle is negative and the change in power is positive, that means the operating point would be on the right of the MPP and the next perturbation would be negative. On the other hand, if the change in the duty cycle is negative and the change in power is negative, that means the operating point would be on the left of the MPP and the next perturbation would be positive [3]. The basic principle of the P & O algorithm is summarized in Table 1.

Table 1: The basic principle of the P & O algorithm.

Perturbation	Change in power	Next perturbation
positive	positive	positive
positive	negative	negative
negative	positive	negative
negative	negative	positive

B. Incremental conductance (IC):

This technique depends on the fact that the differential of the PV power with respect to PV voltage is zero at the MPP, positive on the left of the MPP, and negative on the right of the MPP [4], as given by:

$$\frac{dP_{PV}}{dV_{PV}} = 0, \text{ at MPP.}$$

$$\frac{dP_{PV}}{dV_{PV}} > 0, \text{ left of MPP.}$$

$$\frac{dP_{PV}}{dV_{PV}} < 0, \text{ right of MPP.}$$

By using the measured values of V_{pv} and I_{pv} at different instants, the MPP can be reached as shown in (Fig. 3).

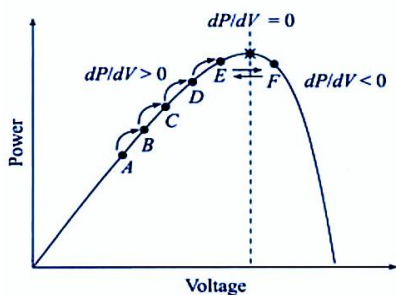


Figure 3: The principle of the IC algorithm.

C. Fuzzy Logic (FL):

Generally fuzzy logic control consists of three stages: fuzzification, rule base table lookup, and defuzzification [5]. In the fuzzification stage and based on a membership function, shown in (Fig. 4), numerical input variables are converted into linguistic variables. Where five fuzzy levels are used: NB

(Negative Big), NS (Negative Small), ZE (Zero), PS (Positive Small), and PB (Positive Big).

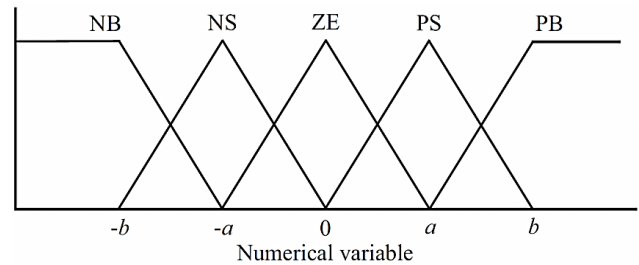


Figure 4: The proposed membership function for inputs and output of fuzzy logic algorithm.

For more accuracy seven fuzzy levels can be used. In (Fig. 4), a & b represent the range of the numerical variable values. Usually, the inputs to a MPPT fuzzy logic controller are an error E and a change in error ΔE . The user has the flexibility of choosing how to compute E and ΔE .

$$E(n) = \frac{P(n) - P(n-1)}{V(n) - V(n-1)}$$

And

$$\Delta E = E(n) - E(n-1)$$

After calculating E and ΔE they will be converted to the linguistic variables, the fuzzy logic controller output, which is a change in duty cycle ΔD of power converter, can be found in the proposed rule base which is shown in Table 2.

Table 2: The proposed fuzzy logic rule base.

ΔE E	NB	NS	ZE	PS	PB
NB	ZE	ZE	NB	NB	NB
NS	ZE	ZE	NS	NS	NS
ZE	NS	ZE	ZE	ZE	PS
PS	PS	PS	PS	ZE	ZE
PB	PB	PB	PB	ZE	ZE

The change in duty cycle ΔD for the different combinations of E and ΔE is determined according to the power converter being used and the knowledge of the user.

During the defuzzification stage, the linguistic variables, namely the output of the fuzzy logic controller, are converted to numerical variables depending on the proposed membership function which is shown in (Fig. 4). This generates an analog signal that will control the power converter to the MPP.

III. MODEL OF THE SYSTEM

Based on the general mathematical equation of the PV cell, the model of the PV panel was built in Matlab/Simulink. The maximum output power of the modeled PV panel according to the Irradiance level are shown in Table 3.

I-V and P-V characteristics of the PV panel are obtained in several irradiance levels and constant temperature which are shown in (Fig. 5, Fig. 6). It is obvious that there is a maximum power point in every P-V curve in a specific irradiance.

Table 3: The MPP value according to the Irradiance level.

Irradiance level	Maximum power
700 w/m ²	28 Watt
900 w/m ²	38 Watt
1100 w/m ²	46 Watt

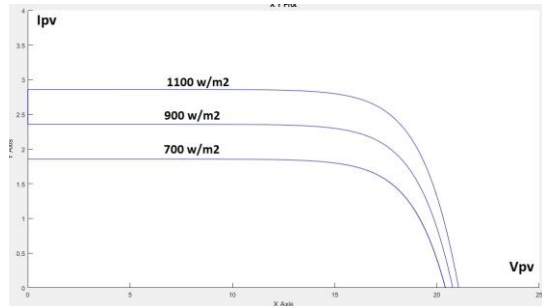


Figure 5: I-V characteristic of modeled PV panel.

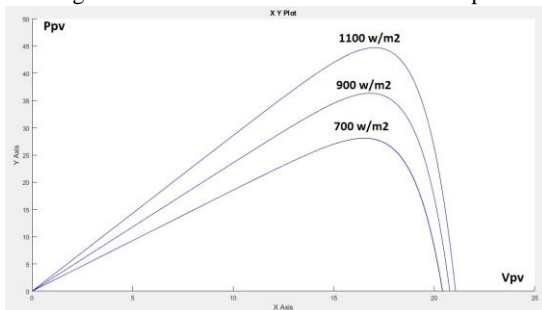


Figure 6: P-V characteristic of modeled PV panel.

A DC-DC boost convertor is utilized in the simulation. By controlling the duty cycle of the switching elements, the PV terminal voltage will be kept at the point that maximum power is obtained, and also the output voltage of PV panel will be matched with the desired load voltage. Input-output DC-DC boost converter equation is:

$$V_{pv} = V_o(1 - D)$$

Where V_{pv} is PV panel output voltage, V_o is DC-DC boost converter output voltage, and D is duty cycle [6].

The proposed system has been modeled and simulated using MATLAB/Simulink. (Fig. 7) shows our proposed Simulink model. In the simulation study, the three mentioned MPPT techniques are simulated and evaluated under the operating condition assuming the constant temperature and variable irradiance.

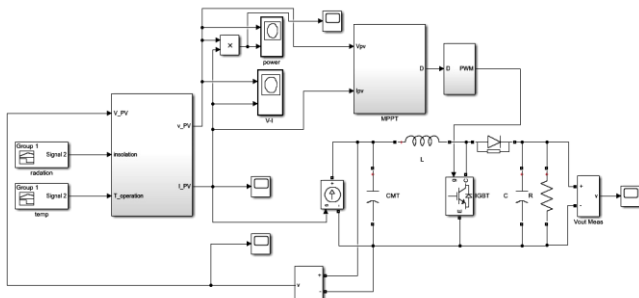


Figure 7: Diagram of the proposed system.

IV. SIMULATION RESULTS AND VALIDATION DISCUSSIONS

With a view to evaluate and analyze the maximum power point tracking techniques, an offline simulation has been tested in Matlab/Simulink for every algorithm.

Different levels of solar irradiance 700W/m², 900W/m² and 1100W/m² were applied as shown in (Fig. 8), while the temperature was constant at 25 degree Celsius.

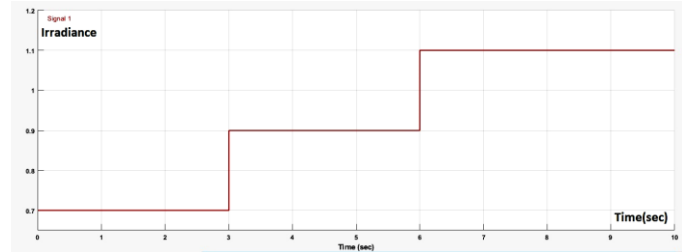


Figure 8: Solar irradiance: 700 W/m², 900 W/m² and 1100 W/m².

The withdrawn power from the PV panel was plotted with respect to time, refer to (Fig. 9, Fig. 10 and Fig. 11). Also the output voltage of the DC-DC boost converter for every algorithm was plotted, as illustrated in (Fig. 12, Fig. 13 and Fig. 14)

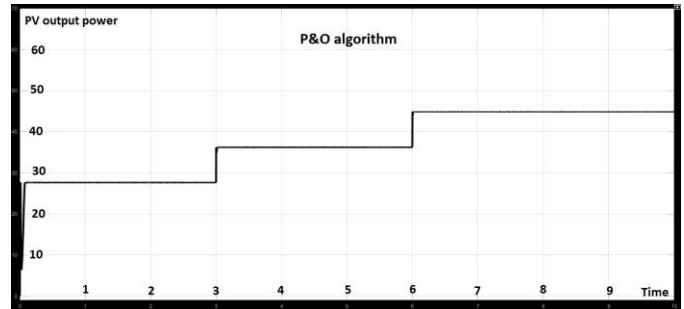


Figure 9: output power of solar panel with P&O algorithm.

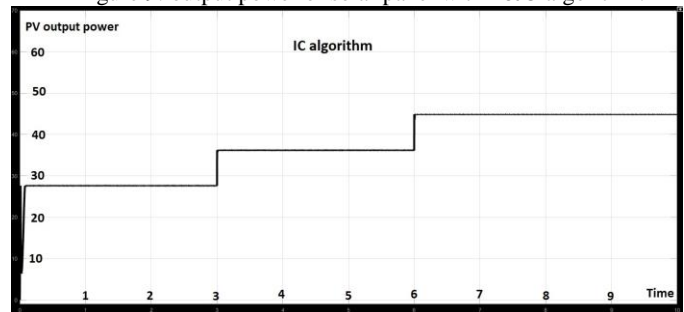


Figure 10: output power of solar panel with IC algorithm.

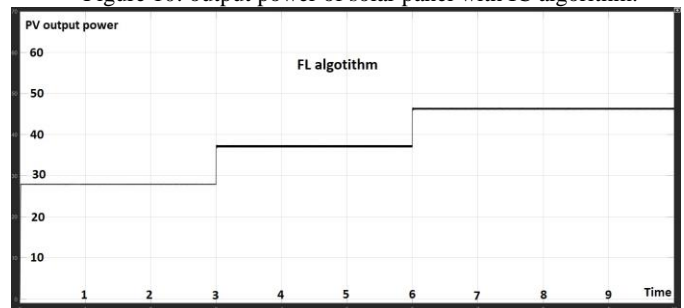


Figure 11: output power of solar panel with FL algorithm.

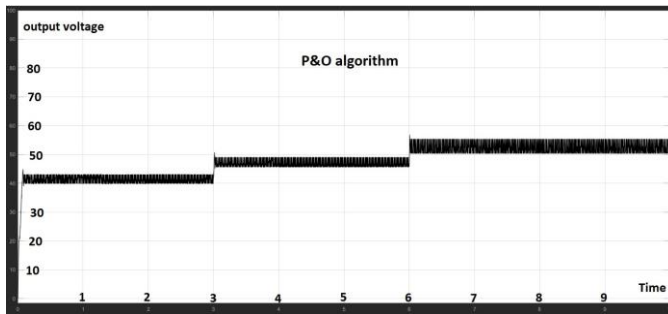


Figure 12: output voltage of boost converter with P&O algorithm.

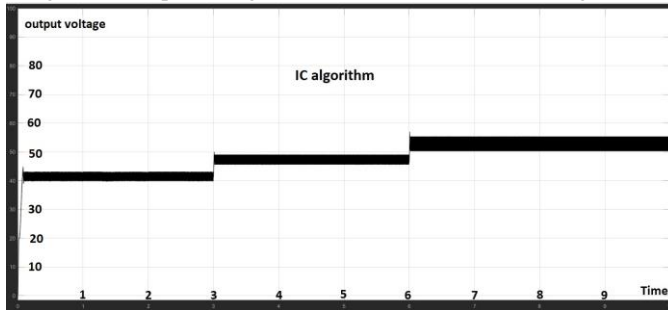


Figure 13: output voltage of boost converter with IC algorithm.

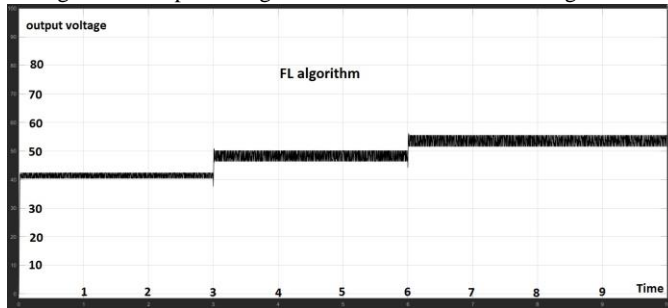


Figure 14: output voltage of boost converter with FL algorithm.

Through the collected simulation results, we can notice that all the tested algorithms were able to find and track the maximum power point despite the instantaneous change in the irradiance. It is also obvious that both algorithms, P&O and IC, were able to make the operating point of the system near the MPP, while FL algorithm made the operating point exactly at the MPP. Thus, the withdrawn energy from the solar panel using the FL algorithm was greater than the produced energy using the other algorithms, as shown in the Table 4.

Table 4: The withdrawn energy by using each algorithm.

Irradiance level	Withdrawn energy by P&O	Withdrawn energy by IC	Withdrawn energy by FL
700 W/m ²	27 watt	28 watt	28 watt
900 W/m ²	36 watt	36 watt	37 watt
1100 W/m ²	44 watt	44 watt	46 watt

Observing (Fig. 9 and Fig. 10), the P&O and IC algorithms show good dynamic performance, but larger steady state oscillations at the MPP, which makes the MPPT accuracy low.

The simulation results indicate that the steady state oscillation at the maximum power point is less when using the FL algorithm, (Fig. 11), resulting in lower energy loss and

increased system efficiency.

Finally, with the view to optimizing the power production from solar panels, the results have showed that Fuzzy Logic technique has proven to exhibit superior performance in terms of efficiency than conventional techniques, (P&O and IC).

V. CONCLUSION

In this paper, a performance evaluation of Perturbation & Observation, Incremental conductance and Fuzzy logic used in maximum power point tracking system is presented. In order to verify the performance of the three maximum power point tracking techniques, the algorithms models were built in Matlab/Simulink and simulation results were collected. It is shown that the Fuzzy logic technique has better tracking achievement, is able to obtain maximum power in terms of variable irradiance, and is preferable in comparison with the conventional techniques. A fuzzy logic algorithm also reduces the steady state oscillation at the MPP resulting in decreased power losses.

Future efforts will be directed towards implementing of fuzzy logic algorithm by using STMicroelectronics-32 bit ARM and will be tested in the real PV system. Experimental results will be obtained to demonstrate the accuracy and effectiveness of the Fuzzy logic algorithm to increase the efficiency and yield of the solar generation system.

ACKNOWLEDGMENT

The research underlying this paper was supported by The Council for At-Risk Academics (CARA), United Kingdom.

REFERENCES

- [1] S. Mulel, R. Hardas, and N. Kulkarni, "P&O, IncCon and Fuzzy Logic Implemented MPPT Scheme for PV Systems using PIC18F452," in *IEEE WiSPNET Conference*, 2016.
- [2] P. Takun, S. Kaitwanidvilai, and C. Jettanasen, "Maximum Power Point Tracking using Fuzzy Logic Control for Photovoltaic Systems," in *International Multi conference of Engineers and Computer Scientists, Vol II, Hong Kong, March 2011*.
- [3] N. Karamia, N. Moubayedb, and R. Outbibe, "General review and classification of different MPPT Techniques," in *Renewable and Sustainable Energy Reviews*, pp. 1–18, 2017.
- [4] A. Safari and S. Mekhilef, "Simulation and Hardware Implementation of Incremental Conductance MPPT with Direct Control Method Using Cuk Converter," *IEEE Transactions On Industrial Electronics*, Vol. 58, No. 4, April 2011.
- [5] M. Kumar, S. Kapoor, R. Nagar, and A. Verma, "Comparison between IC and Fuzzy Logic MPPT Algorithm Based Solar PV System using Boost Converter," *International Journal of Advanced Research in Electrical, Electronics and Instrumentation Engineering*, Vol. 4, Issue 6, June 2015.
- [6] S. Soltani, and M. Kouhanjani, "Fuzzy Logic Type-2 Controller Design for MPPT in Photovoltaic System," *22nd Electrical Power Distribution Conference*, April, 2017.

Rayleigh-based Optical Reflectometry Techniques for Distributed Sensing Applications

K. YÜKSEL ALDOĞAN¹

¹ İzmir Institute of Technology, İzmir/Turkey, kivilcimyuksel@iyte.edu.tr

Abstract - In this paper, we discuss the operation principles, sensing mechanisms, challenges and application areas of the optical reflectometry techniques exploiting Rayleigh scattering phenomenon, considering both time- and frequency-domain schemes. Among various distributed optical fiber sensor (DOFS) systems interrogated by optical reflectometry techniques, a special emphasis was given, in this paper to distributed acoustic sensor (DAS) interrogation methods. Recent progresses obtained through our research collaborations are also presented.

Keywords – Rayleigh scattering, optical reflectometry, fiber optic sensors, distributed sensing.

I. INTRODUCTION

OPTICAL fibers have revolutionized the modern telecommunications. Communication industry is not the unique domain benefiting from the advantages of the optical fibers. Owing to high capacity (low loss, high bandwidth), and by the advent of the optoelectronic devices, optical fiber technology has also been studied as a potential way of realizing innovative sensor implementations.

The requirements of today's science and technology such as optimal efficiency, productivity, reduced energy consumption, and high safety level can be addressed by novel smart sensing systems based on optical fibers. The increasing demand for data-based decision-making and accurate automation & control systems further increases the need for advanced sensor systems that are capable of monitoring variations of the physical and chemical parameters in a spatially distributed manner along various structures. For this purpose, distributed optical fiber sensors (DOFS) represent a powerful class of alternative technologies to the conventional electrical sensors due to their unprecedented features such as low-weight, small dimensions and immunity to electromagnetic interferences [1].

Many successful demonstration of DOFS have been benefiting from these advantages across multiple sectors. Historically, oil & gas industry (i.e. well and pipeline monitoring) was the pioneer in terms of commercial adoption of distributed temperature sensing systems based on Raman and Brillouin scattering. Nowadays, many other successful implementations of DOFS can be listed, particularly in the domains of manufacturing, power & energy, transportation, aerospace, medical, and security.

The major factor driving the growth of DOFSs is their remote sensing capability in difficult operating conditions and

challenging surroundings, where for instance, the sensing fiber can be placed along a long and/or inaccessible spaces while the interrogator unit is kept at a safe distance. The single-mode optical fiber used as sensing element is usually same as the fiber used in telecom cables.

The intrinsic Rayleigh scattering, observed in the optical spectrum from 800 to 1750 nm, is the primary source of attenuation in modern telecommunications [2]. The structure of the optical fiber material is, by nature, disordered by density variations giving rise to random fluctuations of the refractive index on a smaller scale than the optical wavelength. When the optical wave encounters these discontinuities, it scatters in every direction, a small part of which is re-captured by the fiber and propagates back towards the source (called Rayleigh backscattered signal) [2]. This backscattering effect in the optical fiber has been exploited in various sensor systems where the interrogation units make use of the optical reflectometry techniques to perform spatially-resolved measurements of Rayleigh backscattered signal (RBS) [2].

The interrogator schemes fall into two main categories depending on their operational mode: Optical Time-Domain Reflectometry (OTDR) and Optical Frequency-Domain Reflectometry (OFDR) families (cf. Table 1 for comparative analysis of the performance parameters and applications [2]).

Both OTDR and OFDR are deployed for measuring a wide variety of parameters, ranging from temperature, strain, acoustic/vibration, magnetic field, 3D shape to refractive index, and chemical composition.

Among all the Rayleigh-based distributed sensing applications, distributed vibration or acoustic sensing (DAS) has become extremely popular research area and experiencing the fastest transition into commercialization due to the great potential in adapting and utilization of this technology in real-life applications such as seismic, oil well, and railway trackside monitoring systems [3].

A. Optical Time-Domain Reflectometry-OTDR

An OTDR launches short optical pulses (probe signal) into the sensing fiber. The returning light (test signal) is separated from the probe signal and is fed into the receiver where the optical power of the test signal is measured as a function of time. The power evolution with time of the detected (backscattered and reflected) signal provides the distributed information of position and magnitude along the fiber under test.

The key parameters of the dynamic range (or sensing range) and the spatial resolution in OTDR need to be balanced [4].

Conventional OTDR which is the most common maintenance and troubleshooting tool for optical fiber communication networks, has been evolving into several variants, principally to serve as an interrogating system for quasi-distributed and distributed sensors. The following can be listed in the OTDR family: ν -OTDR (Photon-counting OTDR) [5,6], POTDR (Polarization OTDR) [7,8], ϕ -OTDR (Phase OTDR or coherent-OTDR) [9-11], and λ -OTDR (Wavelength tunable-OTDR) [12].

B. Optical Frequency-Domain Reflectometry-OFDR

Instead of working in the time domain as OTDR, OFDR operates in the frequency domain (or *Fourier* domain), covering both incoherent- and coherent types [13].

Optical frequency domain reflectometer (OFDR) providing millimeter resolution over medium to long measurement ranges has also been attracting great attention as an interrogating tool for several sensor systems. It can be considered as a competing technique to OTDR family, especially for acoustic sensing applications.

In the basic configuration of ν -coherent- OFDR, the optical carrier frequency of a tunable laser source is swept linearly in time without mode hops. Then, the frequency-modulated continuous-wave signal (*probe signal*) is split into two paths, namely the *test arm* and the *reference arm*. The former includes the sensing fiber whereas a reference reflector (also called *local oscillator*) is placed in the latter. The test signal (containing Rayleigh backscattering and Fresnel reflections) coherently interferes at the coupler with the reference signal. Superposition of the interfering signals is converted into electrical domain by the detector which yields the beat terms that are related to the optical amplitude and phase responses of the reflection sites in the sensor fiber.

In an OFDR, the narrow linewidth, mode-hop free tunable laser source whose frequency can be chirped linearly in time, is the key technology for improving the sensing range and the spatial resolution [14]. OFDR and P-OFDR have been implemented in temperature [15-17], strain [18], and vibration [19] measurements.

Table 1: Comparison of Rayleigh-based distributed sensors.

	OTDR	ν -OTDR	ϕ -OTDR	OFDR
Spatial resolution	1-10 m	1-10 cm	1-10 m	5mm-10cm
Measurement range	10s km	100 m	A few km	100s m
Complexity	moderate	high	high	high
Applications	Fire Leak Load SRI Loss	Strain SRI Current	Intrusion Strain Vibration	Strain Temperature Vibrations Magnetic field (POFDR)

II. DISTRIBUTED ACOUSTIC SENSING

Distributed acoustic sensing (DAS) (also known as distributed vibration sensing, DVS) is a fiber-optic sensing technique based on the detection of RBS light in optical fibers using ϕ -OTDR (Phase OTDR), that has been a field of intensive research for more than ten years [20]. ϕ -OTDR is based on a pulsed laser source that must be highly coherent, contrary to conventional OTDR systems. Among all the vibration sensing techniques, ϕ -OTDR has been given growing attention because of its ability in the realization of distributed measurements that are capable of both characterizing and localizing a vibration or acoustic phenomenon present along a long-distance optical fiber [3, 21].

ϕ -OTDR schemes can be divided into two main categories according to the detection method employed; namely, direct detection and coherent detection ϕ -OTDR. The straightforward direct detection scheme relies on the measurement of local changes in the backscattered signal's power over time. With coherent detection (homodyne or heterodyne), the backscattered signal is mixed with a reference signal, and the amplitude as well as the phase component of the backscattered signal can be extracted (cf. Figure 1) [21]. The backscattered signal power is not linearly related to the magnitude of the vibrations. Therefore, direct detection schemes provide information only about the frequency content of the vibration. Nevertheless, the extraction of phase can be used to deduce both the magnitude and frequency of external vibrations.

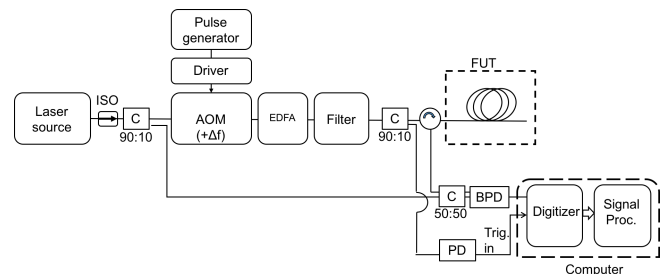


Figure 1. Implementation of the coherent ϕ -OTDR system (heterodyne detection).

ISO: isolator, FUT: Fiber Under Test, AOM = acousto-optic modulator, EDFA = fiber amplifier, C = Coupler, BPD = balanced photo-receiver

A typical ϕ -OTDR trace recorded by the experimental setup is shown in Figure 2. It consists of two sections; the first part is the Rayleigh backscattered signal up to the end of FUT having an exponentially decaying speckle pattern as expected, the second part represents the receiver noise (thermal noise and shot noise).

When a local perturbation applied, relative positions of the scattering centers in the perturbed zone change, resulting in a change on the measured intensity from that zone. Therefore, subtracting the amplitude traces from the first trace, clearly points out the position of the applied vibration.

In order to improve the signal to noise ratio (SNR) and provide high-precision dynamic strain measurement capability, recent research has focused on the implementation of weak fiber Bragg gratings (FBGs) as artificial scattering

centers (having known reflectivity and position) rather than the Rayleigh backscattering signal as realized in a standard Φ -OTDR system.

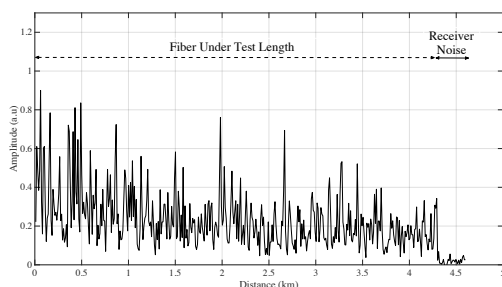


Figure 2. A typical single Φ -OTDR trace recorded by the experimental test setup.

Efforts have been made using so-called frequency sweep [22] and passive 3x3 coupler [23] demodulation schemes. A sensor scheme based on equally-spaced, low reflectivity FBGs interrogated by direct detection Φ -OTDR has been recently demonstrated (cf. Figure 3) [24], where the tradeoff between the maximum number of gratings and grating reflectivity has been analyzed by simulations.

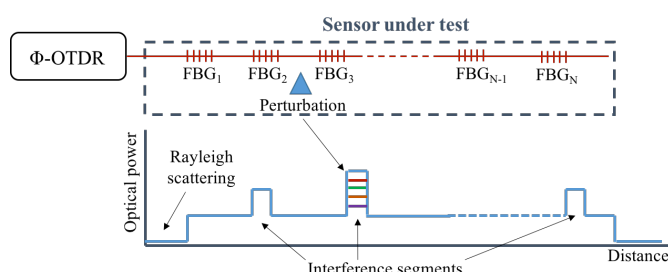


Figure 3. Schematic diagram of the FBG array system interrogated by Φ -OTDR [24]. FBG: Fiber Bragg Grating.

III. CONCLUSION

In this paper, optical reflectometry methods used for DOFS systems are categorized and general background information is provided. Motivations, challenges and requirements of DOFS interrogation schemes are discussed.

Results obtained by different research groups in terms of performance characteristics and future perspectives together with the recent progresses obtained via our collaborative research will be elaborated in the presentation.

ACKNOWLEDGMENT

The author gratefully acknowledges financial support from the TÜBİTAK (BİDEB-2219-1059B191600612).

REFERENCES

- [1] A. Hartog. *Distributed fiber-optic sensors: principles and applications*. Kluwer Academic Publishers. Chapter 4 of *Optical fiber sensor technology* (K.T.V. GRATTAN and B.T. MEGGITT, Editors), 2000.
- [2] M. Wuilpart. *Rayleigh scattering in optical fibers and applications to distributed measurements*. EPFL Press / CRC, Chapter 8 of *Advanced fiber optics: concepts and technology* (L. THÉVENAZ, Editor), pp. 223-278, 2011.
- [3] Y. Liu *et al.*, "Distributed fiber optic sensors for vibration detection", *Sensors*, vol. 16, no.8, 1164, 2016.

- [4] K. Yüksel, V. Moeyaert, M. Wuilpart, and P. Mégret, "Optical layer monitoring in passive optical networks (PONs): A review" (Invited). *Transparent Optical Networks*, 2008. ICTON 2008. 10th Anniversary International Conference on, pp.92-98.
- [5] M. Wegmüller, F. Scholder, and N. Gisin, "Photon-counting OTDR for local birefringence and fault analysis in the metro environment", *Journal of Lightwave Technology*, 22(2):390-400, February 2004.
- [6] D. Kinet, C. Caucheteur, M. Wuilpart, and P. Megret, "Quasi-distributed measurement of surrounding refractive index using photon-counting time domain reflectometry", In *Proceedings IEEE Sensors 2011*, Limerick, Ireland, October 2011.
- [7] M. Wuilpart and M. Tür, *Polarization effects in optical fibers*. EPFL Press/CRC, 2011. Chapter 8 of *Advanced fiber optics: concepts and technology* (L. THÉVENAZ, Editor).
- [8] M. Wuilpart, P. Megret, M. Blondel, A.J. Rogers, and Y. Defosse, "Measurement of the spatial distribution of birefringence in optical fibers", *IEEE Photonics Technology Letters*, 13(8):836-838, August 2001.
- [9] Z. Wang *et al.*, "Novel railway-subgrade vibration monitoring technology using phase-sensitive OTDR", *Proc. SPIE* 10323, 103237G, 2017.
- [10] C. Wang *et al.*, "Distributed acoustic sensor using broadband weak FBG array for large temperature tolerance", *IEEE Sensors Journal*, vol. 18, no.7, 2796-2800, 2018.
- [11] X. Zhang *et al.*, "A High performance distributed optical fiber sensor based on -OTDR for dynamic strain measurement", *IEEE Photonics Journal*, vol. 9, no.3, 6802412, 2017.
- [12] C. Crunelle, M. Wuilpart, C. Caucheteur, and P. Megret, "A quasi-distributed temperature sensor interrogated by a wavelength-sensitive optical time-domain reflectometer", *Measurement Science and Technol.*, 20:027001, 2009.
- [13] K. Yüksel, M. Wuilpart, P. Megret, "Optical frequency domain reflectometry: roadmap for high-resolution distributed measurements," *Proceedings of the IEEE Laser and Electro-Optics Society Symposium-Benelux*. 2007, pp. 231-234.
- [14] K. Yüksel, M. Wuilpart, and P. Megret, Analysis and suppression of nonlinear frequency modulation in an optical frequency-domain reflectometer," *Optics Express*, 17(7):5845-5851, March 2009.
- [15] K. Yüksel, P. Megret, and M. Wuilpart, "A quasi-distributed temperature sensor interrogated by optical frequency-domain reflectometry," *Measurement Science and Technology*, 22:115204 (9 pages), 2011.
- [16] K. Yüksel, V. Moeyaert, P. Megret, and M. Wuilpart, "Complete analysis of multireflection and spectral-shadowing crosstalks in a quasi-distributed fiber sensor interrogated by OFDR," *IEEE Sensors Journal*, 12(5):988-995, May 2012.
- [17] C. Crunelle, M. Legre, M. Wuilpart, P. Megret, and N. Gisin, "OFDR measurements for characterization of the beat length dependence on temperature," *Optical Fiber Measurements Conference (OFMC)*, Teddington, UK, October 2007, pp. 115-118.
- [18] K. Yüksel, D. Pala, "Analytical investigation of a novel interrogation approach of fiber Bragg grating sensors using Optical Frequency Domain Reflectometry," *Optics and Lasers in Engineering* 81, 119-124, 2016.
- [19] S. Wang, X. Fan, Q. Liu, Z. He, "Distributed fiber-optic vibration sensing based on phase extraction from time-gated digital OFDR," *Optics Express*, 13 (26), 2015.
- [20] Miah, K., Potter, D. K., "A Review of Hybrid Fiber-Optic Distributed Simultaneous Vibration and Temperature Sensing Technology and Its Geophysical Applications," *Sensors*, 17, 2511. 2017. doi:10.3390/s17112511
- [21] J. Jason, K. Yüksel, and M. Wuilpart, "Laboratory evaluation of a phase-OTDR setup for railway monitoring applications," *IEEE Photonics Society, 22nd Annual Symposium*, Delft, The Netherlands, 2017, pp. 18-21
- [22] F. Zhu *et al.*, "Improved Phi-OTDR sensing system for high-precision dynamic strain measurement based on ultra-weak FBG array," *Journal of Lightwave Technology*, 33(23), 2015.
- [23] C. Wang *et al.*, "Distributed acoustic sensor using broadband weak FBG array for large temperature tolerance," *IEEE Sensors Journal*, vol. 18, no.7, 2796-2800, 2018.
- [24] K. Yüksel, J. Jason, VDM Soto, M. Lopez-Amo, P. Megret, and M. Wuilpart, "Performance evaluation of Phase-OTDR sensing system based on weak fiber Bragg grating array," (*accepted*). *IEEE Photonics Society, 23rd Annual Symposium*, Brussels, Belgium, 2018.

Estimation of Powerline Route from Airborne LiDAR

M.ZEYBEK¹

¹ Artvin Coruh University, Geomatics Engineering Department, Artvin/Turkey, mzeybek@artvin.edu.tr

Abstract – In this study, powerline extraction investigated from aerial LiDAR data. Powerline transmission line is important task to inspect. LiDAR data include millions of points with geospatial data information. However, it requires processing to obtain useful information from these point clouds. Automatically extraction of powerlines is a crucial task for powerline managements. Here we propose an automatic planimetric (2D) powerline extraction from aerial LiDAR data. Results are showed that the automatic fitting methods are sufficient to extract powerline from LiDAR data.

Keywords – Powerline, Airborne LiDAR, Segmentation.

I. INTRODUCTION

Powerline inspection is an important task in order to recognize risks and dangerous events for energy management planning. Traditional ways from field study is an intense labor, difficult to get idea of powerline situation and also high cost. Latest researches were focused on remotely sensed data sources involving to the inspection power lines, containing synthetic aperture radar (SAR) and satellite optical images. Powerline corridors are planned mostly long and including different field types. Small scale field studies generally inadequate to inspect all powerline with high precision. Airborne LiDAR (ALS) has the potential of acquisition 3D point cloud on the power line corridors on large areas include power lines, vegetation and buildings. It makes difficult to extract the power line points accurately and efficiently. Therefore, recent developments of studies focused on classifying powerlines with efficient and automated way from airborne LiDAR point cloud data.

LiDAR system is basically used for the generation of high resolution and detailed digital terrain models (DTMs), but also increasingly useful for surveying of different mapping applications such as, tree detection road detection, road management, railway surveys, archaeological surveys and more [1-6].

The power line extraction methods from 3D LiDAR point cloud could be grouped into two categories. One is supervised classification using classifiers and the other is unsupervised classification. Supervised methods can achieve mostly higher accuracy than unsupervised techniques for small areas. Supervised methods usually depend on the train classification samples. Developments of unsupervised methods can process for different areas without any training data need. The classification accuracy of these methods reaches to 90%. Due

to it is complicated extraction of feature of linearity, a slight research has been completed over forest and rural areas using airborne LiDAR data.

According to advantages of LiDAR technology, it has fastest and highest accuracy way to collect spatial data. Thus, it has crucial role to inspection and mapping of the powerline more than other traditional surveying tools.

Xu, et al. [7], is proposed the LiDAR as a high-speed digital grid construction and management surveying technique for China. They achieved optimized route, less remove, environment protection, less labor work, process increase quality guarantee and completed LiDAR technology to powerline construction.

Voxel-based Piece-wise Line Detector (VPLD) is proposed by Jwa, et al. [8]. They developed new method, VPLD, for automatic reconstruction of powerline model using only point cloud data without any other spatial information.

Shen, et al. [9], is proposed powerline extraction algorithm can effectively detect of transmission lines for various terrain type around 95%.

Unmanned Aerial Vehicles (UAVs) has also great potential for inspection of powerlines [10]. It has a great potential for detecting of powerlines from UAVs captured images. Generally, Hough transformation is the basic tool for line detection on images.

In this study, our main aim is to develop high precision and fast unsupervised power line route extraction method that works over rural point clouds. The main contribution of the presented pipeline clearance powerline detection method utilizing LiDAR data. This proposal investigates a power line point cloud extraction algorithm combining 3D point cloud processing analysis with 2D image processing that detects the powerlines, resulting in a usable, practical and automatically detection solution for geospatial inspection in the power line management.

The pipeline of the paper is organized as follows: Section 2 point out the proposed method for power lines detection ALS LiDAR point clouds. In section 3, experimental studies demonstrated the reliability of proposed detection method on real point cloud data. Section 4, the advantages and disadvantages of the proposed method are debated and conclusions are drawn.

II. MATERIAL AND METHODS

The basic principle of LiDAR system is calculation the pulse how long takes those pulses to return and how much of the

energy comes back to sensor and record both information. The coordinates and orientation of the airplane and the sensor have to be recorded at high precision for the LiDAR point cloud for using georeferenced data from GNSS/GPS (Global Navigational Satellite Systems/Positional Systems) inertial navigation system (INS) and integrated software (Figure 1).

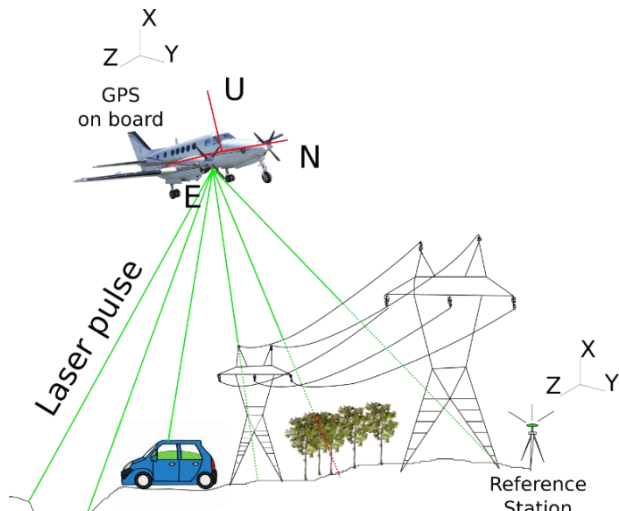


Figure 1 Airborne LiDAR scanner collection of data on simplified figure

The volume of the LiDAR data is key issue to process on computer. To complete this goal, we proposed a two-step progress as follows: (i) non-ground point classification, which was to pre-process the point cloud and remove the points that were surely belonging to the ground, and (ii) power line density-based classification, which was to divide each of the line within each corridor of point's neighborhood and determine whether the point is from power lines connected or not connected based on these density features.

The first step was slow, but it can accurately locate the ground points and remove them from raw point clouds. The second step was designed to detect each power line points, but it was relatively fast. The combination of these steps is accurate and rapid to classify power line points.

A. Pre-processing Point Cloud

Interested area from LiDAR point cloud clipped manually (Figure 2). Raw point cloud data consist of outlier points. In order to process point cloud with high accuracy, noise and outlier points have to be removal. Statistical outlier removal (SOR) algorithm used for this process [11].

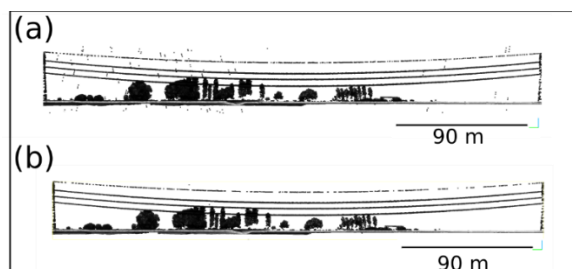


Figure 2 Pre-processing raw point cloud, a) before SOR filtering b) after noise removal and manual clipping powerlines between poles

B. Ground and Non-Ground point filtering

The ground point extraction is the key step for generating digital terrain model (DTM). In literature many studies have been developed. Ground filtering for rural areas is relatively easier than urban areas due to low detail. Vegetations can be separated easily with interpolation-based method.

We implemented our surface-based prototype in MATLAB programming language (MathWorks Co. Ltd.) script. Firstly, split the whole area to small patches which is called also tile the point clouds. Then detect the lowest height point. After all patches lowest point ground candidates used for produce the ground surface. The surface model estimated from polynomial function.

C. Edge Detection

In this section, the 2D height deviation image which represents the point cloud is processed to detect the powerlines instead of dealing with an irregular 3D point cloud. Two-dimensional processing includes useful methods for 2D edge detection, and also decreases the computational time due to the regular representation of data into a standard raster grid [12]. The proposed 2D approach starts with gridding the point cloud into a regular lattice, then a standard edge detection technique is applied to find the powerline candidates, finally the detected edges are filtered to remove the non-powerline edges with the next section mentioned Hough transformation.

In an image, an edge is a curve that follows a path of rapid change in image intensity. Edges are often associated with the boundaries of objects in a scene. Edge detection is used to identify the edges in an image. The implemented function searches for places in the image where the intensity changes rapidly [13].

This approach provides a powerful edge detection that enables to extract edges by Canny method [14].

This method of edge detection method differs greatly from other detectors due to it includes two kind of thresholds and detects weak edges which connected to strong edges

D. Line Detection

The *hough* function from Matlab implements the Standard Hough Transform (SHT) [15]. The Hough transform is designed to detect lines, using the parametric representation of a line,

$$\rho = x*\cos(\theta) + y*\sin(\theta) \quad (1.1)$$

where, ρ is the distance from the origin to the line along a vector perpendicular to the line. θ is the angle between the x-axis and this vector. The *hough* function generates a parameter space matrix whose rows and columns correspond to these ρ and θ values, respectively.

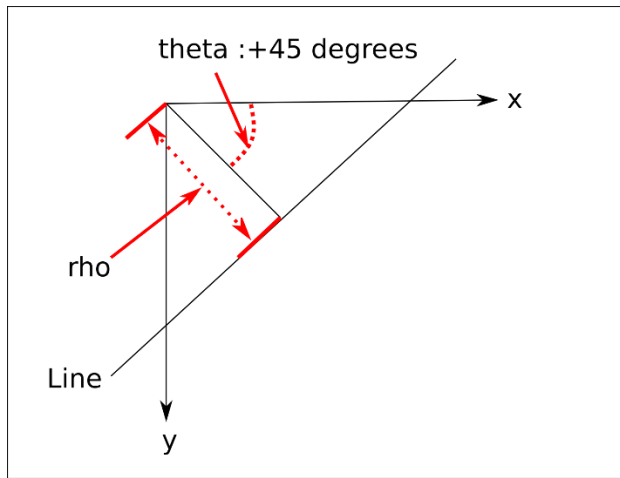


Figure 3. SHT parameter space

The SHT is a parameter space matrix whose rows and columns correspond to *rho* and *theta* values respectively.

The classical Hough Transform has been widely used in the image analysis field for a various of applications including shape detection and object recognition. This method also improved its application for detecting lines in three dimensional point clouds [16, 17]. However, here it has been used for raster 2D data from above ground level (AGL) information.

III. EXPERIMENTS AND ANALYSIS

In this section we were analyzed to validate the strength and accuracy of the proposed algorithm for the powerline detection using single point cloud datasets captured by ALS LiDAR system [18]. The region of interested area is common featured large farm areas and flat morphology.

Our study site includes complex rural area surrounding the Bergama province Izmir at Turkey.

For the LIDAR systems used in the production of map and map information, within the scope of implementation of the LiDAR test flight during 2014-2015 by the General Command of Mapping between October 23-November 6, the two different heights in the test Bergama (1200m and 2600m) Optech company of Pegasus HA-500 and Riegl firm LMS-Q1560 LiDAR system of Turkey representative NIK construction and SEZA of Electronic Ltd.Co. Lidar airborne through data flights were carried out. Lidar data was obtained at two different flight heights and different densities and the data was processed in LMS (LIDAR Mapping Suite) and RiProcess (Riegl Process) software and recorded in *las* format. In this test study, the power line was extracted by using the point clouds obtained from Optech company at a height of 1200 m. The point density of LiDAR datasets is 18 points/m², and 23 cm point spacing [18]. For the dataset, ground truth is not available. Thus, quantitative metrics have not calculated for the power line class.

At first, ground and non-ground filtering carried out due to powerline cables which locates above ground. Point cloud data from ALS has include quite a lot of detail 3D scene. Ground seed points evaluated for continuous ground surface as presented in Figure 4. There seed sampling rates tested for quality of the surface goodness of fit. The implemented

algorithm removes the outlier points. It generates quite high accuracy, reliable and robust surface (Table 1).

The root means square error (RMSE) statistic is also known as the fit standard error and the standard error of the regression. It is an estimate of the standard deviation of the random component in the data, and is defined as

$$RMSE = S = \sqrt{\frac{(y_i - \hat{y}_i)^2}{v}}$$

where, *v*, degree of freedom, *y*, residuals.

As a result of low ground surface candidates which belongs to seed points, the results were as expected of the RMSE increasing.

Table 1. Ground surface accuracy assurance

Ground Seed Rate	10	30	50
RMSE (m)	0.32	0.15	0.11

Non-ground points compared distances through surface normal to the ground surface and above ground levels calculated. As a result, non-ground points add new characteristic information (Figure 5).

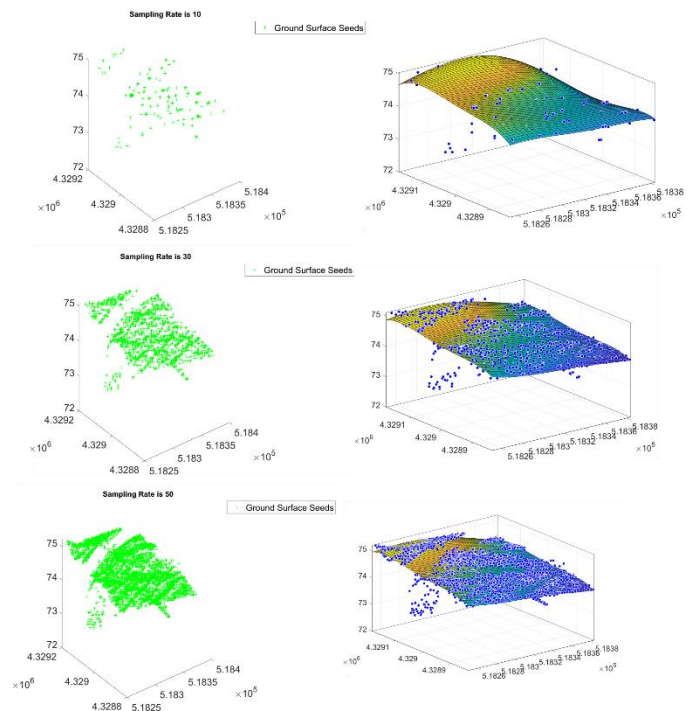


Figure 4. Ground Seeds (left) and Ground surface (right), varied sampling rate parameters range from 10-50 and polynomial surface fitting

Local maximum function is performed for high AGL cable points which is picking in point cloud by thresholding (Figure 7).

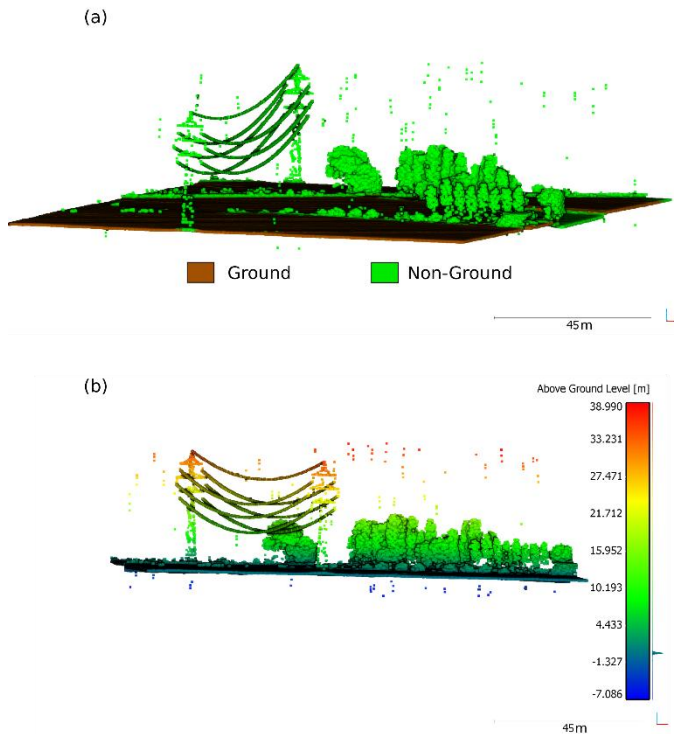


Figure 5 Filtered ALS data a) Ground and Non-ground data, b) Non-ground data distance to ground

Gridding point cloud data with AGL information is mandatory for edge detection. Mesh gridded data resulted as Figure 6a. Powerline AGL data has a feature when XY plane projected point cloud. This feature is a significant to detect of transmission route and useful for remove other edges such as tree, building etc.

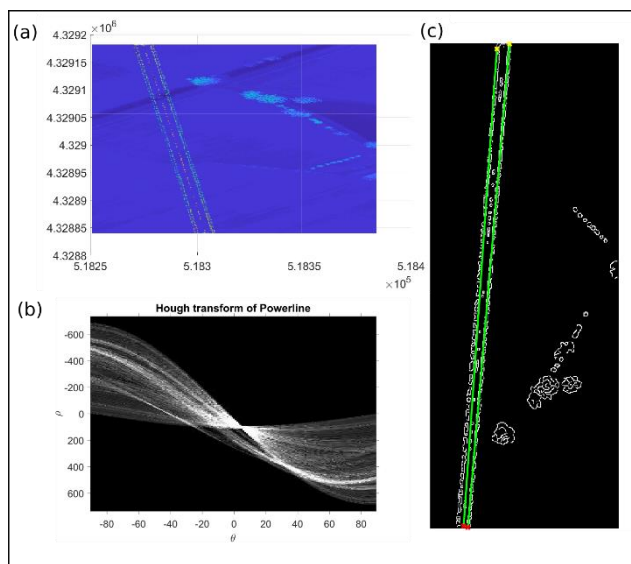


Figure 6 a) AGL rasterized grid, b) Hough space, c) extracted lines (green).

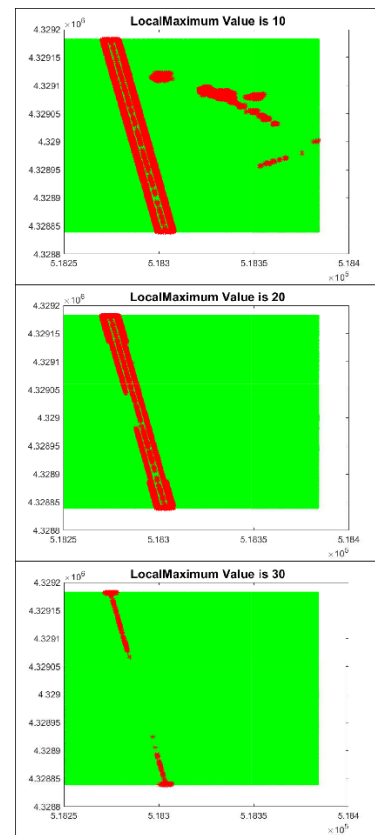


Figure 7. Local maximum value for cable candidates from AGL data, threshold value 10-30 m according to AGL presents the filtered points from top to down

As a result of an image processing methods, powerline route extracted from rasterized AGL information. Further studies may continue with buffer the segments and detect individual cables of powerline.

In this study, two pole power line cables detected from raw point cloud data. Accuracy metrics evaluated at ground filtering process. Quality checks were made visually thus, proposed method detects the cable route. However, accuracy of the segmentation point cloud in these segments should be done in more detail. According to our results, ALS LiDAR data include high detail and consists of measurement errors, noisy points thus these points should be removed from point clouds. And also, it requires the high computational systems and computer equipment's.

IV. CONCLUSION

In this research a pipeline for powerline segmentation from 3D unorganized point cloud acquired from airborne LiDAR system has been proposed. The workflow is split down into 4 main parts. First the point cloud is organized and the ground filtering procedures are employed. After that, the segmented non-ground is normalized with ground points and AGL calculated. Furthermore, the non-ground AGL values rasterized and edge detection have been employed. Finally, powerlines have been extracted using Hough transform approach based on 3D segmentation and 2D image processing methodologies respectively.

In the future, urban and forest data sets will be tested in order

to evaluate the applicability of the proposed pipeline in detecting powerline cables in different terrain. Adding computed point character information such as eigen values to the point cloud will be analyzed. For instance, the linearity information can be used to label powerline candidate points in complex point clouds. This can lead to improve extraction of powerlines. Future work will be focusing on how to automatically get the 3D powerlines without any user parameter or thresholds for the different data sets.

ACKNOWLEDGMENT

I am so grateful to General Command of Mapping for providing me the LiDAR Bergama test data required for this study.

REFERENCES

- [1] R. S. Wang, J. Peethambaran and D. Chen, "LiDAR Point Clouds to 3-D Urban Models: A Review", *Ieee Journal of Selected Topics in Applied Earth Observations and Remote Sensing*, vol. 11, pp. 606-627, 2018.
- [2] Z. Chen, B. Gao and B. Devereux, "State-of-the-Art: DTM Generation Using Airborne LIDAR Data", *Sensors (Basel)*, vol. 17, pp. 2017.
- [3] N. Masini and R. Lasaponara, "Airborne Lidar in Archaeology: Overview and a Case Study", 2013.
- [4] C. Thiel and C. Schmillius, "Comparison of UAV photograph-based and airborne lidar-based point clouds over forest from a forestry application perspective", *International Journal of Remote Sensing*, vol. 1-16, 2016.
- [5] S. A. Gargoum, K. El-Basyouny and J. Sabbagh, "Assessing Stopping and Passing Sight Distance on Highways Using Mobile LiDAR Data", *Journal of Computing in Civil Engineering*, vol. 32, pp. 2018.
- [6] M. Arastounia, Automatic Classification Of Lidar Point Clouds In A Railway Environment, 2012.
- [7] Z. Xu, F. Yang, Y. Huang, Z. Wang and Y. Liu, "Lidar Applications In The Electrical Power Industry", *The International Archives of the Photogrammetry, Remote Sensing and Spatial Information Sciences*, vol. XXXVII Part B4, pp. 2008.
- [8] Y. Jwa, G. Sohn and H. B. Kim, Automatic 3d Powerline Reconstruction Using Airborne Lidar Data, 2009.
- [9] X. Shen, C. Qin, Y. Du, X. Yu and R. Zhang, "An automatic extraction algorithm of high voltage transmission lines from airborne LIDAR point cloud data", *Turkish Journal of Electrical Engineering & Computer Sciences*, vol. 26, pp. 2043-2055, 2018.
- [10] C. Chen, B. Yang, S. Song, X. Peng and R. Huang, "Automatic Clearance Anomaly Detection for Transmission Line Corridors Utilizing UAV-Borne LIDAR Data", *Remote Sensing*, vol. 10, pp. 2018.
- [11] R. Radu Bogdan and C. Steve "3D is here: Point Cloud Library (PCL)", *Shanghai, China*, pp. 2011.
- [12] S. El-Halawany, A. Moussa, D. D. Lichti and N. El-Sheimy, *International Archives of the Photogrammetry, Remote Sensing and Spatial Information Sciences, Calgary, Canada*, pp. 2011.
- [13] W. Renkjumong, Singular Value Decomposition And Principal Component Analysis In Image Processing, 2007.
- [14] J. Canny, "A computational approach to edge detection", *IEEE Trans Pattern Anal Mach Intell*, vol. 8, pp. 679-98, 1986.
- [15] MathWorks, "Image processing Toolbox: User's Guide (R2015a).", 2015.
- [16] C. Dalitz, T. Schramke and M. Jeltsch, "Iterative Hough Transform for Line Detection in 3D Point Clouds", *Image Processing On Line*, vol. 7, pp. 184-196, 2017.
- [17] M. Jeltsch, C. Dalitz and R. Pohle-Fröhlich, "Hough Parameter Space Regularisation for Line Detection in 3D", *VISIGRAPP (4: VISAPP)*, pp. 345-352, 2016.
- [18] A. Kayı, M. Erdoğan and O. Eker, "OPTECH HA-500 ve RIEGL LMS-Q1560 ile Gerçekleştirilen LiDAR Test Sonuçları", *Harita Dergisi*, vol. 42-46, 2015.

Application of Various Bandwidth Enhancement Methods on Seljuk Star Microstrip Antenna

D.UZER¹, SS. GÜLTEKİN¹, R. TOP², M. YERLİKAYA² and Ö. DÜNDAR³

¹ Konya Technical University, Konya/Turkey, dilek_uzer@selcuk.edu.tr, sgultekin@selcuk.edu.tr

²Karamanoğlu Mehmetbey University, Karaman/Turkey, rabiator@kmu.edu.tr

³Necmettin Erbakan University, Konya/Turkey, ozdundar@konya.edu.tr

Abstract - In the study, antenna performance is analyzed on Seljuk star geometry microstrip patch by applying various bandwidth enhancement methods one by one or together. Antenna parameters and methods that give the best results are determined by trying every design made in simulation media. Therefore, it is indicated that desired improvements of antenna performance can be obtained by applying more than one method together.

Keywords – Seljuk star, antenna, bandwidth, HFSS.

I. INTRODUCTION

MICROSTRIP antennas are one of the antenna types which are preferred for nowadays wireless communication applications due to their applicability on different communication equipments easily at the same time they are produced, have small and modular natures, and other useful antenna parameters. They have simple structure that on a dielectric material between two conductive surfaces [1-4].

They are resonant antennas and radiate at certain frequencies they are designed but the most known disadvantage is narrow bandwidth. For this purpose, there are lots of studies and methods to enhance the impedance bandwidth of these antennas like etching slots on patch [6,8-10], shorting pin and shorting wall additions [5,7,9,12-13], choosing the optimum patch geometry [5-10], using various impedance matching methods [4,7-9], multilayer multi patch designs and using more than one method together [3-9,14-19].

In the study, etching slots and shorting pin addition methods are applied to Seljuk star shaped microstrip antenna (SSMSA) first one by one, then both together, for various positions-dimensions combinations. These combinations are obtained by trial-and-error method in simulations by HFSS [23] and chosen the optimum parameters that given the nearest results to theoretical ones. In the next sections these bandwidth enhancement methods (BEM) combinations on Seljuk star patch are explained.

II. SELJUK STAR MICROSTRIP ANTENNA

Seljuk star; one of the basic symbols of Seljuk and Turkish - Islam geography and has eight corners [9, 20- 22]. As seen from Figure 1, all geometrical features of this shape can be

calculated easily. When it is compared to a circular patch with same dimensions of SSMSA, the circumference of star patch is larger but the total surface area of the patch decreases [9]. This decrease reduces the copper losses and then total dimension of the patch. Due to the circumference increase, resonant frequency and bandwidth of the antenna can be varied. Again, by applying various BEM's, this new patch geometry has a better performance [9,11,12].

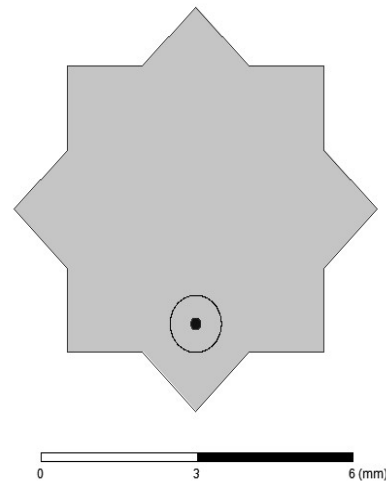


Figure 1: Seljuk Star Microstrip Patch Antenna.

III. ANTENNA DESIGN

In the study, effects of the pins and slot dimensions on bandwidth are investigated by etching circular (O) slots, adding various copper shorting pins with different positions and numbers on Seljuk star patch designed on Duroid 5880LZ material. At first, a basic design is tried for determining the optimum feed point x_b and ground plane dimensions L_{Top} . BEM combinations can be seen from Figure 2. The study is started with one pin (P) addition and the pin position is chosen at the opposite of the feed point. A radius of 0.5 mm, pin position “ p ” is changed with systematically steps from corner

to the center of the patch until the determination of the optimum result. Later, results of two, three and six pins combinations are analyzed, respectively, given in Figure 2. Then, a circular slot is etched on the patch and the slot radii " v_d " is varied between 1 and 25 mm. The optimum v_d value is found as 1mm with a resonant frequency of 5810 MHz. But any of designs that use slot and 1 pin together give good results. For this reason, pin addition designs are continued with the second-best result as $v_d = 20$. For all pin combinations given in Figure 2, p values are swept, again. At the end, from all results obtained, the pin and slot dimensions and combinations of optimum resonant frequencies and bandwidths are determined and given in Table 1.

IV. RESULTS

For the basic antenna design, return loses values are under -10 dB for the aimed resonant frequency, so there are not calculated any bandwidth values. By using more than one BEM' s together, as seen from Table 1, simulation results became closer to the theoretical values. Also, it was determined which method and which parameters effect the results and how. It was obtained for designs with slots. Although with various v_d values, return loses were obtained under -10dB but at this time resonant frequencies shifted from the desired values more and these simulations were not considered. The desired frequency and a bandwidth of %5.852 that two times of the aimed value, were obtained in addition with one shorting pin. After, by using slot etching and pin addition together, for different number of pins and position combinations, more than one combination gave successful resonant frequencies and bandwidths. The best results and their parameters are given in Table 2. Here,

BEM ; Bandwidth Enhancement Method applied on the antenna,

v_d ; radius of circular slot,

p ; pin position,

f_{rSim} ; Resonant frequency from simulation,

BW_{Sim} ; Calculated bandwidth from simulation,

Z_{Sim} ; Antenna impedance from simulation.

In this manner, it is shown that it is possible to acquire the frequencies with a bandwidth of about four times of the desired values as %9.450 by the usage of more than one BEM as optimum combinations.

V. CONCLUSION

In this study, effects of various bandwidth enhancement methods applied on Seljuk star shaped microstrip patch are investigated. Designs with slot addition, pin addition and applying both methods together are simulated by HFSS. Slot dimensions and number of pins with their optimum positions are obtained for optimum resonant frequencies and bandwidths closer to theoretical values. Using more than one method together, it is showed that better performances can achieved.

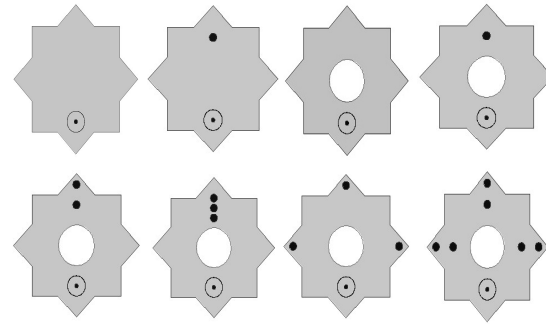


Figure 2: Chosen Pin and Slot Combinations.

Table 1: Design parameters and simulation results.

BEM	v_p (mm)	p (mm)	f_{rSim} (MHz)	BG_{Sim} (%)	Z_{Sim} (Ω)
-	-	-	5800	-	98,018
Circular Slot (CS)	1	-	5810	-	98,570
1 pin (1P)	-	-12	5810	5,852	83,189
1P+CS	1	-11	5800	5,172	84,540
2P+CS	20	-30	5780	8,651	78,939
3P+CS	20	-32	5840	8,390	80,746
3x2P+CS	20	-30	5800	8,966	78,402
3x1P+CS	20	-29	5820	9,450	78,692
$(h=4,75\text{mm}, \epsilon_r=1,96)$					

REFERENCES

- [1] K.R. Carver K.R. and J.W. Mink, "Microstrip Antenna Technology", *IEEE Trans. Antenn Propag.*, 29, 1, 2-24, 1981.
- [2] C.A. Balanis, *Antenna theory and design*, 1997.
- [3] Z.N. Chen, M.Y.W. Chia, *Broadband planar antennas: design and applications*, John Wiley & Sons. 2006.
- [4] R. Garg, P. Bhartia, I. Bahl, A. Ittipiboon, *Microstrip Antenna Design Handbook*, Boston, London, Artech House, p. 73-126, 2001.
- [5] K.C. Gupta, *Broadbanding techniques for microstrip patch antennas-a review*. Electromagnetics Laboratory/Th MIMICAD Research Center. Paper 118, 1998.
- [6] R. Bhalla, L. Shafai, "Resonance behavior of single U-slot microstrip patch antenna", *Microw. Opt. Techn. Let.*, 32, 5, 333-5, 2002.
- [7] S. Dey, R. Mitra, "A compact broadband microstrip antenna", *Microw Opt Techn Let.*, 11, 6, 295-7, 1996.
- [8] G. Kumar and K.P. Ray, *Broadband microstrip antennas*, Artech House, 2002.
- [9] D. Uzer, "Geniş Band Mikroşerit Yama Antenler için Uygun Yöntemlerin Araştırılması" (PhD thesis), Selçuk Üniversitesi, Fen Bilimleri Enstitüsü, Telekomünikasyon A.B.D., 2016.
- [10] D.B. Garima, J.S. Saini, V.K. Saxena, L.M. Joshi, "Design of broadband circular patch microstrip antenna with Diamond shape slot", *Indian Journal of Radio and Space Physics*, 40, 275-81, 2011.
- [11] D. Uzer, S. S. Gültekin, "A New Seljuk Star Shape Microstrip Antenna Design", *Progress in Electromagnetic Research PIERS 2012*, 27-30 Mar 2012, Kuala Lumpur, Malesia.
- [12] D. Uzer, S.S. Gültekin, Ö. Dündar, E. Uğurlu, R. Çalışkan, "Bandwidth Enhancement of Equilateral Triangle Microstrip Patch Antenna with Slot Loading and Dielectric Superstrate", *2nd International Conference on Computational and Experimental Science and Engineering*, (ICCESN-2015), 14-19 October 2015, Antalya- Turkey.
- [13] E. Aydın, S.Can, "Operating frequency calculation of a shorting pin loaded ETMA", *Microw. Opt. Techn. Let.*, 54, 6, 1432-5, 2012.

- [14] K.F. Lee, W. Chen, R.Q. Lee, K.M. Luk, K.F. Tong, "Microstrip Antennas with Multidielectric Layers", *Microw Opt Techn Let*, 9, 3, 149-53,1995.
- [15] P. Khotso, R. Lehmsiek, R.R. Van Zyl, "Circularly Polarized Circular Microstrip Patch Antenna Loaded with Four Shorting Posts for Nanosatellite Applications", *Microw Opt Techn Let*, 54, 1, 8-11, 2012.
- [16] M. Khodae, M. Akbari, S. Zarbakhsh, "A Novel Antenna With Dual Band-Notched Characteristics using Shorting Pin and Z-Shaped Slot on Conductor Backed", *Applied Computational Electromagnetics Society Journal*, 28, 9, 809-14, 2013.
- [17] D. Uzer, S.S. Gültekin, "An Investigation of Shorting Pin Effects on Circular Disc Microstrip Antennas", *International Journal of Applied Mathematics, Electronics and Computers (IJAMEC)*, Vol 3, No 3, 2015.
- [18] R. Chair, C.L. Mak, K.F. Lee, K.M. Luk, A.A. Kishk, "Miniature wide-band half U-slot and half E- shaped patch antennas", *IEEE Transactions on Antennas and Propagation*, 53, 8, 2645-52, 2005.
- [19] A.A. Deshmukh, G. Kumar, "Various slot loaded broadband and compact circular microstrip antennas", *Microw Opt Techn Let*, 48, 3, 435-9, 2006.
- [20] S.K. Yetkin, 1965. İslam Mimarisi, Ankara, Ank. Uni. İlah. Fak. Turk ve İslam San. Tar. Ens. Yay.
- [21] G. Oney, U. Erginsoy , 1992., Anadolu Selçuklu Mimari Süslemesi ve El Sanatları, Ankara, Türkiye İis Bankası Kultur Yay.
- [22] M. Büyükcanga, Türk Mimarisinde Sekiz Köşeli Yıldız Motifleri. 6th of International Turkish World Congress of Social Sciences. Calalabat, Kyrgyzstan: 1230- 4, 2008.
- [23] www.ansys.com/HFSS, 2015.

Design and Simulation of a New Single-Phase Multilevel Inverter Structure

E.BESER¹ and B. ARIFOGLU¹

¹ Kocaeli University, Kocaeli/Turkey, ebeser@kocaeli.edu.tr

¹ Kocaeli University, Kocaeli/Turkey, barif@kocaeli.edu.tr

Abstract - Inverters have become an indispensable element for many industrial applications today. Several types of inverters have been developed and multilevel inverter systems have also been introduced in the literature. Multilevel inverters produce voltage with low harmonic distortion. In this study, a new single-phase multilevel inverter design was given. The principles of proposed inverter structure were explained in detail. In addition, the simulation results of the developed design were included and the total harmonic distortion was calculated for the simulated cases. Level number of output voltage can be easily increased in the proposed inverter and output voltages with low harmonic content can be obtained. In the study, multilevel inverter structures in the literature were examined and compared with the proposed inverter structure. When the designed inverter structure is compared with similar structures in the literature, it is seen that when the same number of switching elements are used, it produces the highest number of output level. This shows that the output voltage with the lowest THD value can be obtained when the same number of switching elements is used.

Keywords - Single-phase, multilevel inverter, total harmonic distortion, half bridge cascaded multilevel inverter

I. INTRODUCTION

INVERTERS have become an indispensable element for many industrial applications today. Inverters are widely used in systems such as electrical motor drives, fuel cells, solar batteries, wind turbines or micro turbines feeding a load or grid [1]. A common feature in systems where inverters feed a load or grid is that the harmonic levels of the inverter output voltage are very low. Several types of inverters have been developed in the direction of this demand and multilevel inverter systems have been introduced in the literature.

Multilevel inverters produce voltage with low harmonic distortion due to creating stepped voltage at the inverter output.

As the level number of output voltage increases, the variation of the inverter output voltage becomes more similar to the sinus signal, the harmonic of output voltage decreases and its quality increases. Serial-connected level modules reduce the dv/dt voltage stress on each switch. Thus, the use of multilevel inverters make suitable for high voltage and/or high power applications.

Multilevel inverters can produce output voltage with sinusoidal form as well as output voltage with desired harmonics. Due to this feature, multilevel inverters are used in

active power filter applications. In addition, multilevel inverters are also used in compensation applications because they have the ability to generate voltages at desired amplitude, frequency and phase angles [2-4].

Multilevel inverters in the literature can be classified in three main groups as diode clamped inverters, flying capacitor inverters and cascaded inverters. Cascaded inverters are included in the literature as cascaded H-bridge inverters [5, 6], cascaded half H-bridge inverters [7-9] and cascaded transformers [10].

In this study, a new single-phase multilevel inverter design was given. The principles of proposed inverter structure were explained in detail. In the study, multilevel inverter structures in the literature were examined and compared with the proposed inverter structure. The simulation results of the proposed structure were included and the total harmonic distortion is calculated for the simulated cases.

II. PROPOSED INVERTER STRUCTURE

The proposed multilevel inverter is based on level modules and a source with opposite polarity as compared to independent sources in level modules. In Figure 1, the principle scheme of 8-level inverter with three level modules is shown. As can be seen from the principle scheme, the level modules can be connected to each other by cascaded. Thus, the system can be easily expanded and level number of output voltage can be increased. When the number of level modules is increased, the level number of the proposed multilevel inverter increases exponentially. The level number is an odd number in multilevel inverters generally, whereas, the level number is an even number in the proposed structure. This is due to the fact that the proposed inverter has no zero level.

The level number (n) varies depending on the number of level modules (m) in the inverter structure. The level number of the inverter can easily be found depending on the level module using Equation (1). The number of levels is scaled in power of 2 depending on the number of level modules.

$$n = 2^m \quad (1)$$

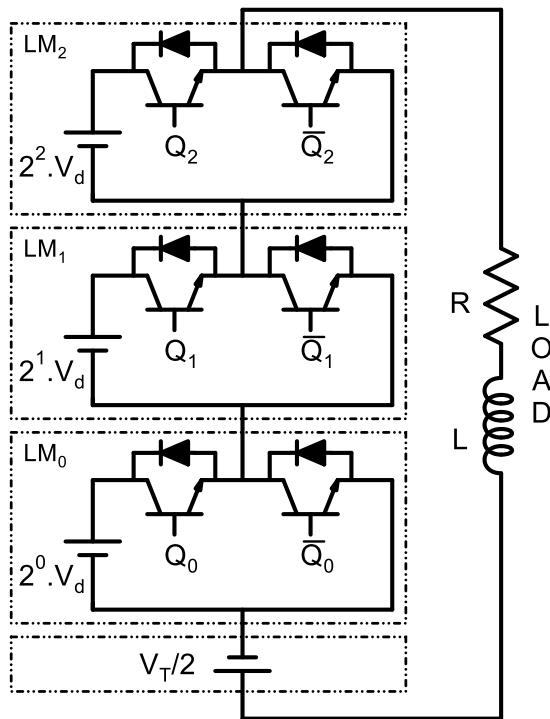


Figure 1: Principle scheme of 8-level inverter structure.

The level module consists of two switching elements and one independent DC source. In case the number of levels and the amplitude of the output voltage are known, the voltage (V_d) of the source to be used in the first level module can be found by using Equation (2). The value of the voltage source to be used in each level module to be connected after the first level module must be 2^k times of the first level module voltage.

$$V_d = \frac{2 \cdot V_{\max}}{n-1} \quad (2)$$

In the proposed inverter structure, there is a need for an

Table 1: Level number of output voltage, number of switching elements and number of sources depend on level modules.

Level Module	LM 0	LM 1	LM 2	LM 3	LM 4	LM m
Source Value	V_d	$2 \cdot V_d$	$4 \cdot V_d$	$8 \cdot V_d$	$16 \cdot V_d$	$2^{(m)} \cdot V_d$
Level Number	2	4	8	16	32	$2^{(m)}$
Number of Source	2	3	4	5	6	$m+1$
Number of Swit.Ele.	2	4	6	8	10	$2m$

The number of switching elements (r) and the number of sources used in inverters (s) can be computed with Equation (5) and (6) depending on the number of level modules.

$$r = 2m \quad (5)$$

$$s = m + 1 \quad (6)$$

independent source that is connected in series to the level modules and is opposite polarity as compared to independent sources in level modules. The voltage of this source is equal to half the sum of the voltage sources used in the level modules ($V_T/2$).

Each level module used in the proposed inverter requires an independent source. This is the disadvantage of the proposed inverter. This disadvantage can be overcome in two ways. First, a transformer with multi secondary winding is wound to obtain multiple AC sources. The alternating voltage in the secondary winding is rectified by a bridge rectifier and a capacitor to obtain the desired number of DC sources. The other way is that the inverter structure can be operated with solar cells from renewable energy sources. In this way, the solar batteries to be used in the system are grouped into the appropriate voltages and capacities and more than one voltage source is obtained.

The number of level modules (m) to be used depending on the number of levels can be found by using Equation (3).

$$m = \lfloor \log_2(n) \rfloor \quad (3)$$

The voltage of the source in each level module is obtained as $2^{(k)}V_d$. k is defined as

$$k = 0,1,2,3,\dots,m \quad (4)$$

where m is the module number.

Depending on the number of level modules (m), level number of output voltage (n) is calculated by using Equation (1). Table 1 shows the number of switching elements, the number of sources used in the multilevel inverter and the output voltage levels, depending on the number of level modules. The number of output voltage levels given in Table 1 shows the highest number of levels that can be achieved with m modules.

In this study, multilevel inverters have been examined in the literature. A comparison was made between existing multilevel inverters in the literature and the proposed inverter in Table 2 considering levels of output voltage (n), the number of level modules (m), switching elements (r) and independent sources (s).

In Table 2, the proposed inverter was compared with 4 different multilevel inverters in the literature. In the comparison, the maximum number of levels per switching element is obtained by the proposed inverter. For example, when 8 switching elements are used; 16 levels are obtained with the proposed inverter but 9 levels are obtained maximally in the examined multilevel inverters. The advantage of the proposed

structure is to achieve the highest level number using fewer switching elements.

As the level number of inverter increases, the output voltage (V_o) is more similar to the sinusoidal voltage and the Total Harmonic Distortion of the output voltage (THD) decreases.

Table 2: Comparison of the proposed inverter with multilevel inverters in the literature.

Multilevel inverters in the literature	LM = 1			LM = 2			LM = 3			LM = 4			LM = 5		
	n	r	s	n	r	s	n	r	s	n	r	s	n	r	s
Cascaded H-Bridge inverters ⁽¹⁾	3	4	1	5	8	2	7	12	3	9	16	4	11	20	5
Cascaded H-Bridge inverters ⁽²⁾				9			27			81			243		
Cascaded transformer inverters ⁽³⁾	5	8		11	12	1	29	16	1	83	20	1	243	20	1
Cascaded half H-Bridge inverters ⁽⁴⁾	3	6		7	8	2	15	10	3	31	12	4	63	14	5
Proposed inverter	2	2	2	4	4	3	8	6	4	16	8	5	32	10	6

- (1) Isolated dc sources in each H-Bridge are equal
- (2) Isolated dc sources in H-Bridges are scaled in power of 3
- (3) Turn ratio of the transformers are scaled in power of 3
- (4) Isolated dc sources in H-Bridges are scaled in power of 2

III.SWITCHING STRATEGY OF THE PROPOSED INVERTER

In order to obtain the switching signals of the proposed inverter, it is necessary to define the reference voltage. This reference voltage comes from a sine term and a fixed term. The reference voltage (V_{ref}) is defined in Equation (7).

$$V_{ref}(t) = \frac{(2^m - 1)}{2} (1 + \sin 2\pi ft) \tag{7}$$

Switching signals are generated for each instantaneous value of the reference voltage signal (V_{ref}). The equations of the switching signals for the switching elements used in the proposed inverter are given below.

$$Q_0(t) = V_{ref}(t) \text{ mod } 2 \tag{8}$$

$$Q_1(t) = \frac{V_{ref}(t) (V_{ref}(t) \text{ mod } 2)}{2} \text{ mod } 2 \tag{9}$$

Equations (9) can be generalized depending on the level module number. The generalized equation of the switching signal is given in Equation (10).

$$Q_{(k)}(t) = \frac{V_{ref}(t) (V_{ref}(t) \text{ mod } 2^{(k)})}{2^{(k)}} \text{ mod } 2 \tag{10}$$

By using Equation 10, switching signals used in the level modules of the proposed inverter can easily be obtained. Due to this signals, the output voltage in Figure 2 is achieved. As the level number increases, the output voltage is more like sinusoidal voltage.

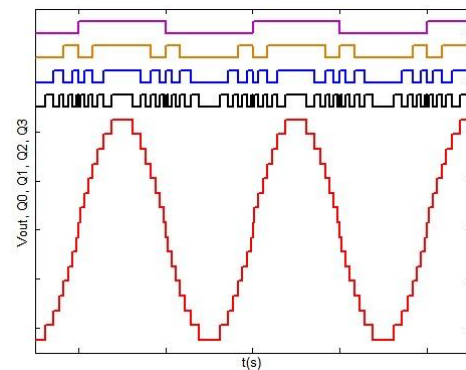
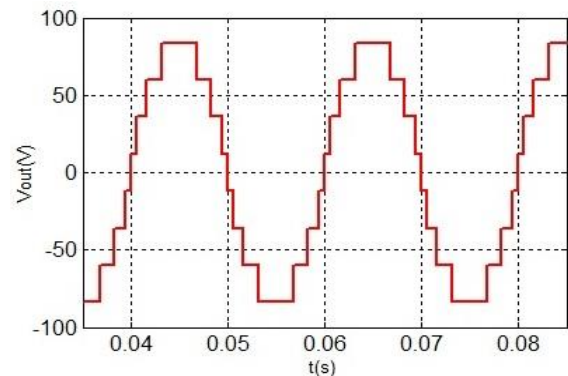


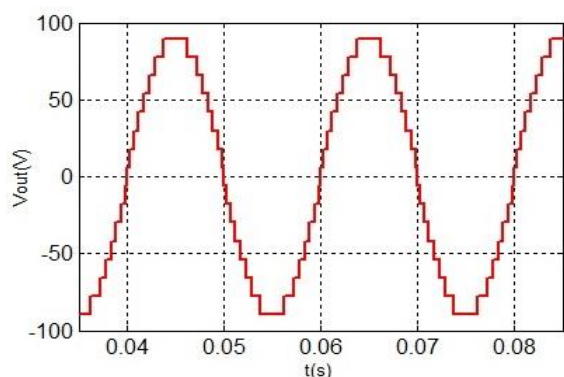
Figure 2: Switching signals and output voltage of the proposed inverter for 4 level modules.

IV.SIMULATION STUDY

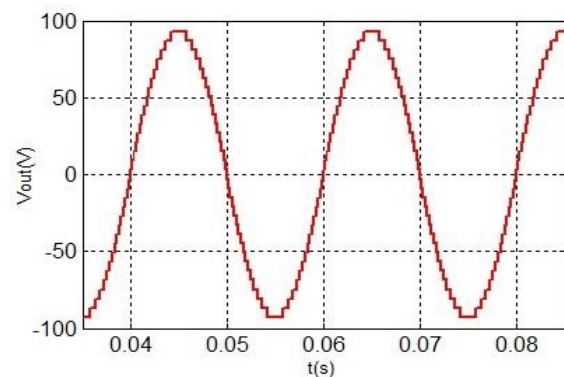
Proposed inverter was simulated for 8, 16, 32 and 64-level by using 3, 4, 5 and 6 level modules. Change of output voltage versus time is given for 8, 16, 32 and 64-level situations in Figure 3.



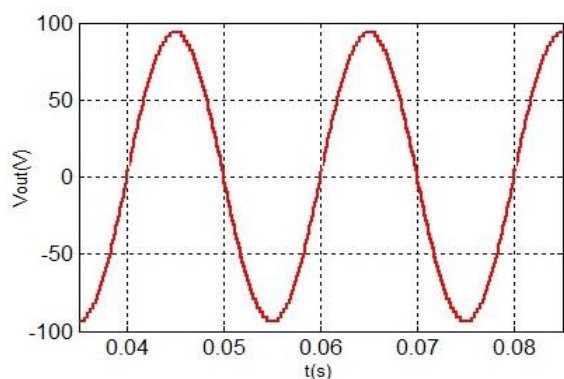
(a)



(b)



(c)



(d)

Figure 3:

- a) Output voltage wave of 8-level inverter for 3 level modules
 b) Output voltage wave of 16-level inverter for 4 level modules
 c) Output voltage wave of 32-level inverter for 5 level modules
 d) Output voltage wave of 64-level inverter for 6 level modules.

THD value of output voltage was calculated for five situations. In Table 3, calculated THD values depending on module and level number are given for the simulated cases.

It is seen from Table 3 that level number increases exponentially as the level module number increases. Besides THD value of the output voltage decreases linearly as the level module and level number increases. For instance, a comparison can be made between the inverter including 2 and 6 level modules. By increasing the level module number from 2 to 6, level number increased by 16 times, while THD value decreased from 23.45 % to 1.6%. In other words, it decreased by 14.65 times.

Table 3: THD values depending on level number.

Number of Level Module (m)	Level Number (n)	Total Harmonic Distortion (%)
2	4	23.450
3	8	12.210
4	16	6.180
5	32	3.170
6	64	1.600

V.CONCLUSION

In this study, existing multilevel inverter structures in the literature were investigated and a new multilevel inverter design was improved. First, basic structure of the proposed inverter was introduced. Proposed inverter is quite modular since it includes level modules, so it is convenient for expanding. The way of increasing the level number is explained in detail. The proposed inverter was simulated for four different level modules and results were given. THD values were also calculated for each simulation conditions. THD value decreased as the level number increased. It was calculated as 1.6% for 64-level inverter. When the proposed inverter is compared with the similar ones in the literature, it can be seen that it produces the highest level number at the output voltage for the same switching element number. This also means that the output voltage with the lowest THD value can be obtained if the same number of switching elements is used.

REFERENCES

- [1] B. Ozpineci, L.M. Tolbert, J.N. Chiasson, "Harmonic Optimization of Multilevel Converters Using Generic Algorithms", *IEEE Power Electronics Letters*, vol.3, no.3, pp.92-95, 2005.
- [2] M. Ortuzar, R. Carmi, J. Dixon, L. Moran, "Voltage Source Active Power Filter, Based on Multi-Stage Converter and Ultra Capacitor DC-Link", *The 29th Annual Conference of the IEEE Industrial Electronics Society (IECON 2003)*, vol.3, pp.2300-2305, 2003.
- [3] C. Junling, L. Yaohua, W. Ping, Y. Zhizhu, D. Zuyi, "A Closed-Loop Selective Harmonic Compensation with Capacitor Voltage Balancing Control of Cascaded Multilevel Inverter for High Power Active Power Filters", *IEEE Power Electronics Specialists Conference (PESC 2008)*, pp.569-573, 2008.
- [4] T.H. Abdelhamid, J.Y. Madouh, "Advanced Static VAR Compensator Using a New Topology of Multilevel Inverters Energized from Non-Equal DC Sources", *Power and Energy Society (PES 2008)*, pp.1-8, 2008.
- [5] B. Ozpineci, L.M. Tolbert, J.N. Chiasson, "Harmonic Optimization of Multilevel Converters Using Generic Algorithms", *35th Annual IEEE Power Electronics Specialists Conference*, pp.3911-3916, 2004.
- [6] C. C. Hua, C.H. Wu, C.W. Chuang, "Control of Low-Distortion 27-Level Cascade Inverter with Three H-Bridge Inverter Modules", *IEEE International Conference on Industrial Technology*, pp.277-282, 2006.
- [7] E. Beşer, "Anahtarlama Elemanı Sayısı ve Harmonik Optimizasyonu İle Bir Fazlı Çok Seviyeli Evirici Tasarımı", Kocaeli Üniversitesi Fen Bilimleri Enstitüsü, 2009.
- [8] E. Beser, B. Arifoglu, S. Camur, E. Kandemir Beser, "A Novel Design and Application of a Single Phase Multilevel Inverter", *International Review of Electrical Engineering (IREE)*, vol. 4 n.1, February 2009, pp. 7 – 13.
- [9] E. Beser, B. Arifoglu, S. Camur, E. Kandemir Beser, "A Novel Approach for Harmonic Optimization of A Single Phase Multilevel Inverter", *International Review of Electrical Engineering*, vol.4, no.4, July-Aug 2009.
- [10] F.S. Kang, S.J. Park, S.E. Cho, C.U. Kim, T. Ise, "Multilevel PWM Inverters Suitable for the Use of Stand-Alone Photovoltaic Power Systems", *IEEE Transactions on Energy Conversion*, vol.20, no.4, pp.906-915, 2005.

Simulation of Multi-Level Inverter Fed Permanent Magnet Synchronous Motor (PMSM)

E.KANDEMİR BESER¹ and E. BESER¹

¹ Kocaeli University, Kocaeli/Turkey, esrakandemir@kocaeli.edu.tr

¹Kocaeli University, Kocaeli/Turkey, ebeser@kocaeli.edu.tr

Abstract – In this study, a three-phase multi-level inverter topology is proposed for a permanent magnet synchronous motor (PMSM). PMSM model was formed in terms of a,b,c phase variables. The proposed inverter and switching strategy was introduced. The multi-level inverter was simulated together with PMSM and results were given. The inverter has a switch number advantage over the topologies in the literature and it exhibits a convenient feature for the sinusoidal machines as PMSM since it possesses sinusoidal voltage and current waveforms by increasing the level number.

Keywords - Three-phase, multilevel inverter, half bridge cascaded multilevel inverter, permanent magnet synchronous motor (PMSM)

I.INTRODUCTION

Permanent magnet synchronous motor (PMSM) is a type of synchronous machine. The most important feature that distinguishes PMSM from the conventional synchronous machine it has permanent magnets on the rotor instead of rotor field winding [1]. So the magnetic field is created by permanent magnets. It brings some advantages to PMSM such as high power density, ease of control, high torque to inertia ratio, low noise, low size and weight [1].

PMSM machines are generally fed by conventional pulsewidth-modulated (PWM) inverters. This action causes high voltage stress (dv/dt) across the motor terminals. Also in this case of using PWM inverters, the voltage harmonics are quite high although the current harmonics are low. To overcome this problem switching frequency can be increased but it increases the switching losses and dv/dt stress which become especially significant at high voltage and high power applications [2-4]. A filter can be placed between the inverter and motor, which brings additional weight [2]. Multi-level inverters (MLI) can be proposed as a good solution for the above problems. They produce higher levels on the output voltage with low dv/dt stress [5]. Harmonic distortion in the output voltage is reduced by increasing the number of levels [4]. They also have an advantage of lower switching frequency compared to PWM inverters [2]. Existing multi-level structures can be classified as diode clamped MLI, flying capacitor MLI, cascaded H-bridge MLI, and hybrid MLI topologies [6].

Some studies exist in the literature that uses multi-level inverter topologies for driving a PMSM. A seven-level is proposed in [1] and PMSM is controlled by field oriented

control. In [5], a comparative study between the two-level inverter and five-level inverter is made to convert super capacitive energy for PMSM load. A five-level diode clamped inverter is used to feed a PMSM and a fast space vector PWM algorithm is simulated in [7]. The permanent magnet synchronous motor (PMSM) is fed by a 4 leg asymmetric cascaded H-Bridges multi-level inverter in [8].

In this study, a PMSM is simulated by a different multilevel inverter topology which is not included in the literature. The switching signals of the proposed inverter are produced very simply. The inverter has a significant advantage over the topologies in the literature in terms of the number of switching elements.

II.PROPOSED THREE PHASE MULTI-LEVEL INVERTER

Proposed three-phase inverter consists of three numbers of single-phase multi-level inverter. Each single-phase inverter basically includes level modules (LMs) and a dc source having an opposite polarity according to dc sources in LMs [9].

In the proposed inverter, level number (n) for one phase varies dependent to the number of LM (m) in one phase. The level number of the inverter can be found related to LMs by Equation (1). Level number of the line voltage (N) can also be obtained by Equation (2).

$$n = 2^m \quad (1)$$

$$N = 2n - 1 = 2^{m+1} - 1 \quad (2)$$

By increasing LMs, level number can be increased exponentially. Due to this feature, the proposed structure is very convenient to be expanded. In multi-level inverters, level number is generally an odd number; however the levels of the proposed inverter change as an even number as the proposed structure has no zero level. In Figure 1, the principle scheme of three-phase 4-level inverter consisting 2 LMs in each phase is shown. As it can be seen from Figure 1 that the system can be easily expanded and level number can be risen by making a cascaded connection between LMs.

Each level module comprises of two switching elements and a dc source. The value of dc source in the first module can be found using level number and magnitude of the output voltage by Equation (3). The value of the other sources changes as $2^{(k)} V_d$. Here, k is the module number.

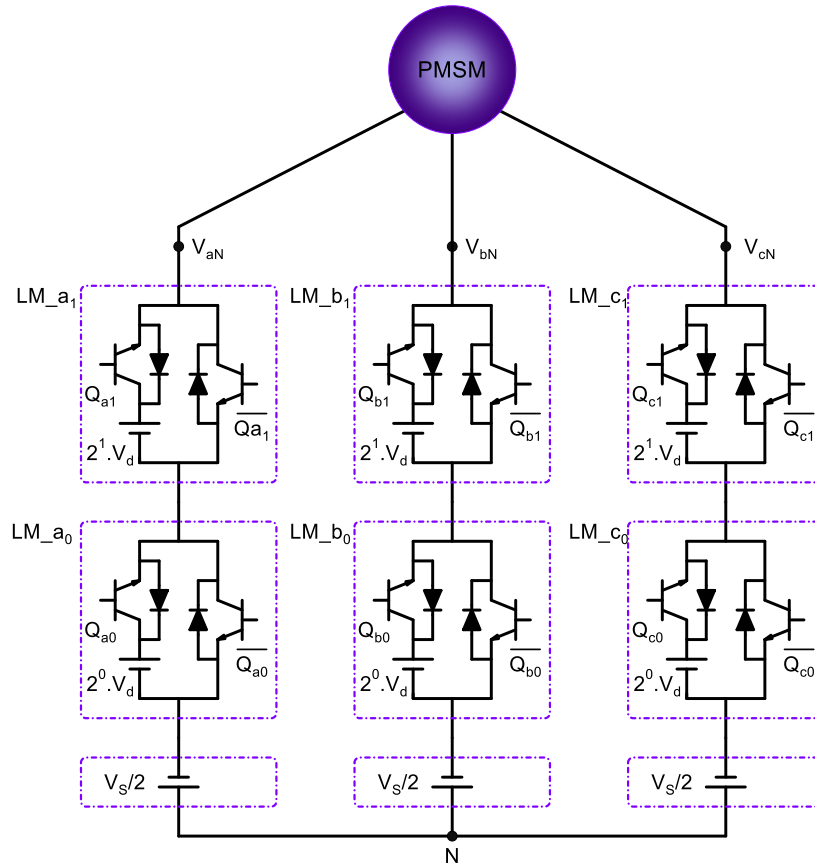


Figure 1: Principle scheme of three phase 4-level inverter structure feeding a PMSM.

$$V_d = \frac{2.V_{max}}{n-1} \tag{3}$$

In the proposed inverter, an additional dc source is required. This source is connected series with the LMs and has an opposite direction in comparison with the dc sources LMs. The voltage of the source is equal to the one half of the sum of dc source voltages in LMs. ($V_s/2$).

In Table 1, switching elements and dc source numbers and level number of the output voltage is given for one phase depending on LM number. Level number of the output voltage in Table 1 shows the maximum number of levels that can be obtained by m modules.

Table 1: Output voltage levels, switching elements number and source number depending on LMs in the proposed inverter.

Level Module Number	1	2	3	...	m
Level Number of Phase Voltage (n)	2	4	8		2^m
Level Number of Line Voltage (N)	3	7	15		$2n-1$
Total Source Number (S)	6	9	12	...	$3m+3$
Total Switching Element Number (R)	6	12	18		$6m$

Switching element and source numbers (r) and (s) can be calculated by using Equation (4) and (5) as in the following for one phase.

$$r = 2m \tag{4}$$

$$s = m + 1 \tag{5}$$

$$M = 3m \tag{6}$$

$$R = 2M \tag{7}$$

$$S = M + 3 \tag{8}$$

III.PMSM MODEL AND MULTI-LEVEL MOTOR DRIVE

Total module number (M) in the system can be calculated by Equation (6). Total switching elements and source numbers (R) and (S) can be found by Equation (7) and (8)

Mathematical model of the PMSM can be formed in terms of a,b,c phase variables. The voltage equations of the PMSM can be expressed in matrix form. The voltage equations of the

machine can be written as,

$$[V]_{a,b,c} = [R]_{a,b,c}[I]_{a,b,c} + \frac{d}{dt}[\lambda]_{a,b,c} \quad (9)$$

$$[\lambda]_{a,b,c} = [L]_{a,b,c}[I]_{a,b,c} + [\lambda_m]_{a,b,c} \quad (10)$$

The inductances are generally constant, they do not change by the rotor position in PMSM. So self-inductances can be accepted as $L_{aa} = L_{bb} = L_{cc} = L$ and mutual inductances can be taken as $L_{ab} = L_{ac} = L_{bc} = M$. Voltage equations can be arrange as in the following.

$$[V]_{a,b,c} = [R]_{a,b,c}[I]_{a,b,c} + \frac{d}{dt}\{[L - M][I]_{a,b,c} + [\lambda_m]_{a,b,c}\} \quad (11)$$

$$[V]_{a,b,c} = [R]_{a,b,c}[I]_{a,b,c} + [L - M] \frac{d}{dt}[I]_{a,b,c} + \frac{\partial}{\partial \theta}[\lambda_m]_{a,b,c} \frac{\partial \theta}{\partial t} \quad (12)$$

$$[V]_{a,b,c} = [R]_{a,b,c}[I]_{a,b,c} + [L - M] \frac{d}{dt}[I]_{a,b,c} + e_{a,b,c} \quad (13)$$

According to the voltage equations equivalent circuit of PMSM in terms of a,b,c phase variables can be obtained as in Figure 2.

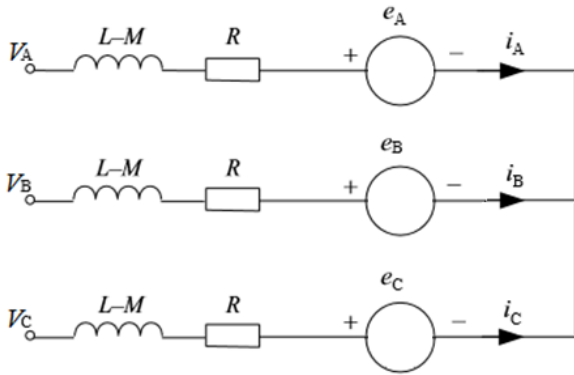


Figure 2: Equivalent circuit of PMSM in terms of a,b,c phase variables.

The electromagnetic torque and mechanical equations can also be written as,

$$T_e = p \left\{ [I]_{a,b,c}^T \frac{\partial [\lambda_m]_{a,b,c}}{\partial \theta_r} \right\} \quad (14)$$

$$T_e - T_l = \frac{d\omega_r}{dt} \frac{J}{p} \quad (15)$$

As it can be seen from Figure 1 that the proposed inverter is used for feeding a PMSM. V_a , V_b and V_c motor terminals are connected to the multi-level inverter output and multi-level voltage waveform is applied to the motor.

When a PMSM is fed by a conventional inverter, current harmonics is quite low. However, voltage harmonics is very high since the machine is driven by PWM methods. By using multi-level inverters, both voltage and current harmonics are quite low. By increasing the level number, total harmonic distortion (THD) value in voltage and current decreases further even though an output filter is not used. The importance of multi-level inverters becomes evident particularly in the case of feeding high-power PMSMs. Using PWM methods in high voltage values is not convenient considering voltage stress.

In order to obtain multi-level voltage at the inverter output for feeding a PMSM, first, switching signals are constituted [9].

For this purpose reference voltages should be defined as in Equation (16).

$$V_{a_ref}(t) = \frac{(2^m - 1)}{2} (1 + \sin 2\pi f t)$$

$$V_{b_ref}(t) = \frac{(2^m - 1)}{2} [1 + \sin(2\pi f t + 2\pi/3)] \quad (16)$$

$$V_{c_ref}(t) = \frac{(2^m - 1)}{2} [1 + \sin(2\pi f t - 2\pi/3)]$$

Switching signals are produced for each instantaneous value of V_{ref} . Equations of switching signals are given in the following.

$$Q_{abc_0}(t) = V_{abc_ref}(t) \bmod 2 \quad (17)$$

$$Q_{abc_1}(t) = \left(\frac{V_{abc_ref}(t) (V_{abc_ref}(t) \bmod 2)}{2} \right) \bmod 2 \quad (18)$$

These equations can be generalized depending on LM number. Generalized equation of switching signal is shown in Equation (19).

$$Q_{abc_k}(t) = \left(\frac{V_{abc_ref}(t) (V_{abc_ref}(t) \bmod 2^{(k)})}{2^{(k)}} \right) \bmod 2 \quad (19)$$

$$k = 0, 1, 2, 3, \dots, m \quad (20)$$

After generating switching signals multi-level output voltage is applied to PMSM and the motor is operated with a low voltage stress.

IV. SIMULATION STUDY

After completing PMSM and inverter models, PMSM was driven with the proposed three-phase multi-level inverter in the simulations and results were included in this Section. The PMSM parameters considered in simulation is shown in Table 2.

Table 2: Simulation parameters of PMSM.

Parameter	Symbol (Unit)	Value
Stator resistance	R (Ω)	0.57
Stator self inductance	L (mH)	4.25
Stator mutual inductance	M (mH)	0.25
Inertia	J (kgm^2)	0.00208
Friction	B (Nms)	0.0039
Number of poles	2p	4
PM Flux	$\partial \lambda_m / \partial \theta$ (Wb)	0.512

Motor phase voltage, line voltage, line current, electromagnetic torque and speed curves are shown in Figure 3 and Figure 4 in case of using a 16-level and 64-level inverter.

It is seen from Figure 3 and Figure 4 that the motor voltage and current is approaches to a sinusoidal form by increasing the level number of the inverter.

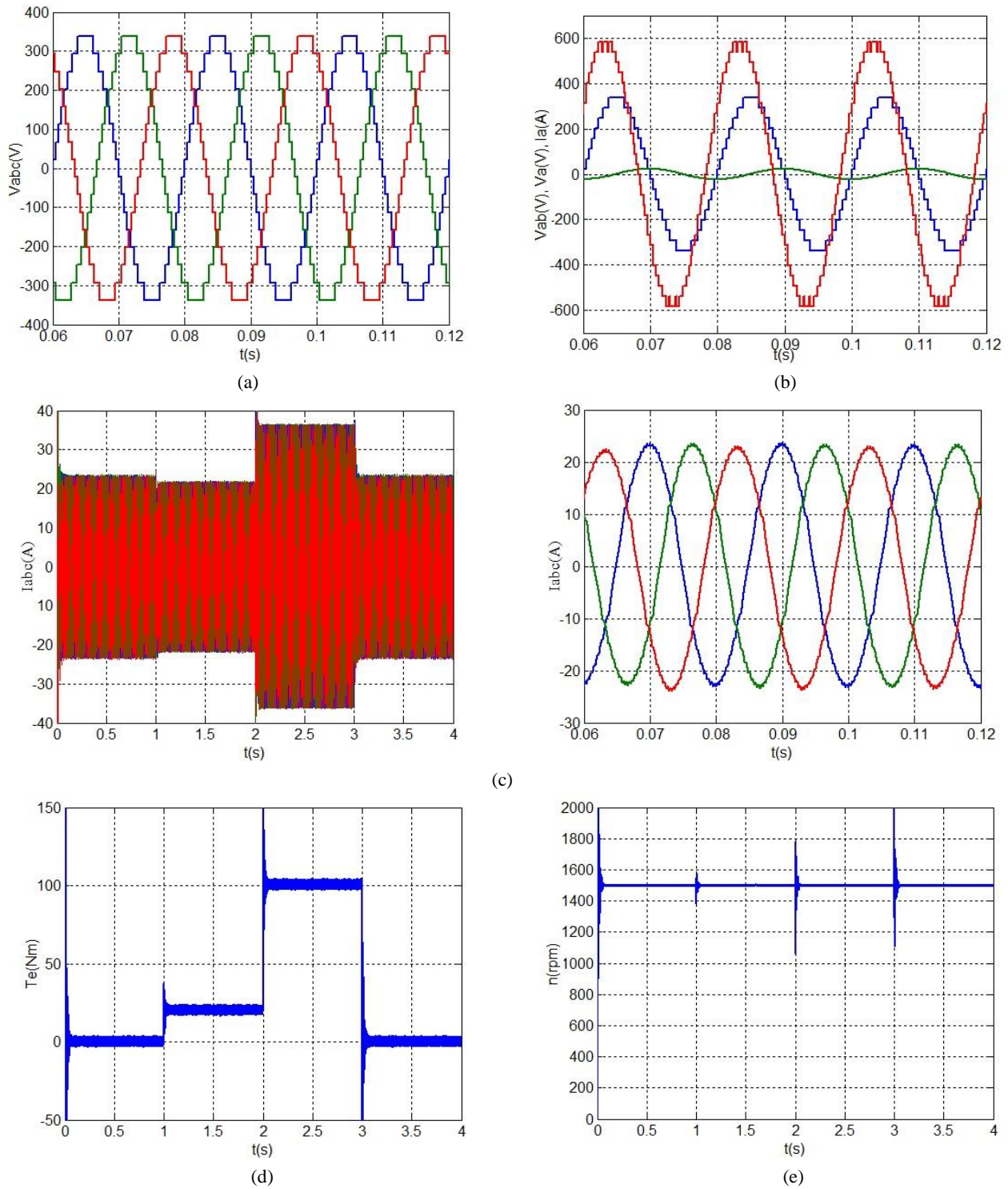


Figure 3: Simulation results of 16-level multi-level inverter fed PMSM

(a) Phase voltages, (b) Phase voltage, Line voltage and Line current (c) Phase currents (d) Electromagnetic torque, (e) Speed

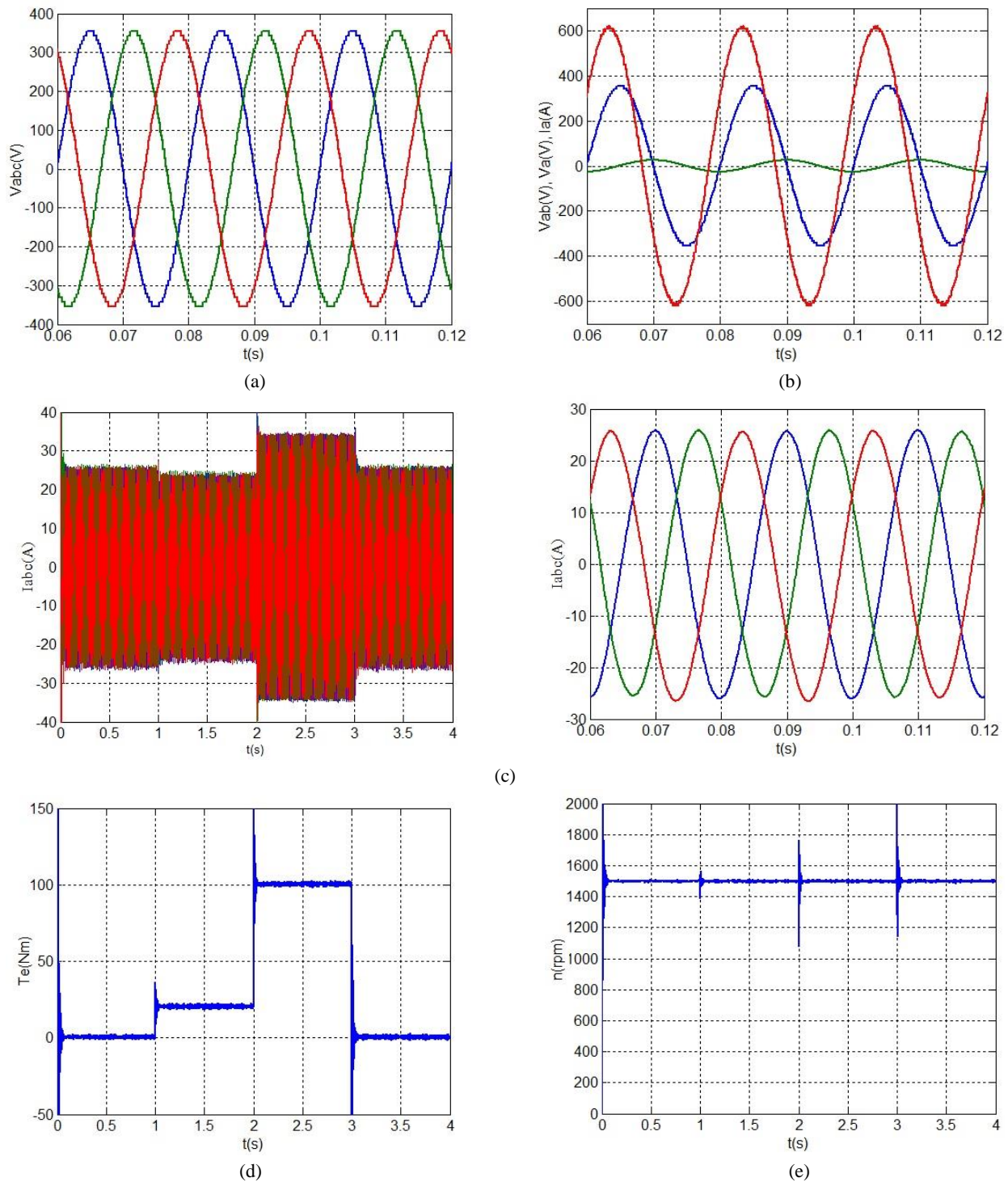


Figure 4: Simulation results of 64-level multi-level inverter fed PMSM

(a) Phase voltages, (b) Phase currents, (c) Phase voltage, Line voltage and Line current (d) Electromagnetic torque, (e) Speed

The THD values were also calculated and the results were given for the phase voltage, line voltage and phase current in Table 3 in case of 16-level, 32-level and 64-level. The THD values decrease by the increasing level number. Especially it is evident that the voltage harmonics is quite low compared to conventional PWM inverters.

Table 3: THD values of phase voltage, line voltage and phase current depending on level number.

Level Number (n)	Total Harmonic Distortion (%)		
	V _a	V _{ab}	i _a
16	5.15	4.10	3.00
32	2.54	2.05	1.40
64	1.26	0.93	0.35

V.CONCLUSION

The proposed three-phase inverter generates multi-level output voltage waveform with low dv/dt voltage stress. By increasing level number, total harmonic distortion in voltage and current waveforms decreases. It needs no output filter and it has an advantage of lower switching frequency compared to PWM inverters. Consequently, the proposed inverter is very suitable for using in sinusoidal machines as PMSMs since the voltage and current waveforms can be formed as sinusoidal. Especially it is convenient for high-voltage applications due to having low dv/dt voltage stress.

REFERENCES

- [1] J.Jacob, A.Chitra,"Field oriented control of space vector modulated multilevel inverter fed PMSM drive", *Energy Procedia*, vol.117, pp. 966-973, 2017.
- [2] N. P. Schibli, T.Nguyen and A. C. Rufer, "A three-phase multilevel converter for high-power induction motors", *IEEE Transactions on Power Electronics*, vol. 13, no. 5, pp. 978-986, September 1998.
- [3] K. A. Corzine, "A hysteresis current-regulated control for multi-level drives", *IEEE Transactions on Energy Conversion*, vol. 15, no. 2, pp. 169-175, JUNE 2000.
- [4] V. Nair R, A. Rahul S, R. S. Kaarthik, A. Kshirsagar, and K. Gopakumar, "Generation of higher number of voltage levels by stacking inverters of lower multilevel structures with low voltage devices for drives", *IEEE Transactions on Power Electronics*, vol. 32, no. 1, pp. 52-59, January 2017.
- [5] S.Jana, P.K.Biswas, U.Das, "A Comparative study of two-level and five-level inverter to convert supercapacitive energy for PMSM load", *IEEE Calcutta Conference (CALCON)*, 2017, pp.352-356.
- [6] V. Naumanen, J. Luukko, T. Itkonen, O. Pyrhönen and J. Pyrhönen, "Modulation technique for series-connected H-bridge multilevel converters with equal load sharing", *IET Power Electronics*, vol. 2, iss. 3, pp. 275–286, 2009.
- [7] E.Prasad, A.Sudhakar, V.Kumar, "Simulation of five-level inverter fed PMSM based on fast SVPWM", *IEEE International Conference on Power Electronics, Drives and Energy Systems (PEDES)*, 2012, pp.1-5.
- [8] K.Saleh, M.Sumner, "Sensorless control of a fault tolerant multi-level inverter PMSM drives in case of an open circuit fault", *International Symposium on Power Electronics, Electrical Drives, Automation and Motion (SPEEDAM)*, 2018, pp. 883-888.
- [9] E. Beser, E.Kandemir Beser, "A new three phase multi level inverter topology" 7 th International Conference on Advanced Technologies (ICAT'18), 2018.

Statistical Feature Extraction and ANN Based Classification of Temporomandibular Joint Sounds

U. TAŞKIRAN¹, S. F. TAŞKIRAN², M. ÇUNKAŞ³

¹Selcuk University, Konya/Turkey, utaskiran@selcuk.edu.tr

²Konya Technical University, Konya/Turkey, salimkanfatma@gmail.com

³Selcuk University, Konya/Turkey, mcunkas@selcuk.edu.tr

Abstract - In this study, a statistical feature extraction method is used to classify the Temporomandibular Joint (TMJ) sound. Temporomandibular Disorder (TMD) is the problems arising from or related to disorder of TMJ which is commonly known as jaw bone joint. TMD is a recurrent disorder related to jaw joint and common problem among the population. In fact TMD is so frequent that more than two third of population have some kind and level of TMD. TMJ sound listening is the easiest and quickest diagnose methods used by the clinic dentists. In the study, statistical features of TMJ sounds are extracted. Then extracted statistical features are applied to ANN for training and testing. Mean classification success rate of 87% to 89% is obtained in the study.

Keywords - TMJ, TMD, sound classification, statistical feature extraction, ANN based classification

I. INTRODUCTION

Temporomandibular joint (TMJ) disorder is any health problem arising from or related to TMJ. Temporomandibular joint lets jaw movements and it is the joint between the condyle of the mandibula known as lower jaw or jawbone and mandibular fossa of the temporal bone which are either of a pair of bones which form part of the side of the skull on each side and enclose the middle and inner ear. There is an articular disc between these two bones which allows complex jaw movements.

TMJ disorder (TMD) is very common in general population. In some populations, TMD diagnose percentage can be as high as 75%. At least 33% of population shows one more symptoms of the TMD [1]. According to Özan at all, TMD diagnose frequency in Turkey is even higher than the general disorder ratios around the world [2]. The main symptom of the disorder appears as reflected pains which appear to be not emanating from TMJ. Symptoms sometimes appear as face pains, outer ear pains, face muscle pains, migraine type aches, even strains in the eyes etc. For which, generally patients do not come for treatment to dental institutes in the first place. Additionally, jaw movement loss, deviations and deflections of mandibula and sounds and aches during the opening and closing of the jaw and even in extreme cases jaw locks can be observed [1].

Many studies aiming to classify the TMJ sounds are published in literature. Especially Widmalm and his colleagues published several papers on the subject. They first have tried to classify the sounds known as clicking and crepitation among dentist [3] and by using Reduced Interference Distribution (RID) they have defined as many as five different sound types [4]. Widmalm and his colleagues continued their research using amplitude and wave spectrum, pattern recognition to classify the TMJ sounds [5, 6, 10].

Many different researchers and academician including the some of the authors of this paper [14], Ghodsi at all [7] and Akan at all [8] [9], published papers on classification of TMJ sounds using different classification techniques including time based sample reduction, spectrum based techniques, time-frequency analysis, discrete evolutionary transform. Took at all have focused on differentiating sound from left and right joints based kurtosis and click sounds [11 ,12]. Knee joint sound classification study of Kim at all have showed similar studies based on joint sounds can be used to diagnose joint disorders similar to TMJ.

The importance of sound based diagnose already have known by dentist because clinic dentists frequently use TMJ sounds to diagnose of TMD which much simpler and cheaper than sending the patient for MR imaging. Clinical consultant through a stethoscope listen the sound of TMJ while opening and closing of the jaw. TMD related sounds are generally categorized as crepitation, clicking, popping, popping clicking etc by dental community. The experience of clinical dentist is obviously important to diagnose the disorder correctly. Many times sound misinterpretation may occur resulting from noisy clinical environment, in-familiarity of sounds and/or inexperience in field.

The objects of the study classify the chosen TMJ sounds by using statistical feature extraction and artificial neural networks (ANN). The data has been collected in real clinical environment with supervisory of experienced dentist. Sound data is the same as the records used in the paper of Taşkıran at all [14]. Data extraction and collection process are narrated in detail in reference [14].

Statistical feature extraction is used to train ANN and test the results. Statistical features are used some studies like [15] to classify the sounds originated from human body. The method presented in following section is given fairly good results even without preprocessing of the data. In future studies, further classification methods are intend to be tested and an on-line diagnostic machine and software is planned to develop.

II. MATERIAL AND METHOD

Data sets are borrowed from the previous work of the authors. Detailed description of the data recording processes and tools are given in reference [14]. Every data in data sets is 24 bit resolution, 5 seconds, 51200 KHz sample rate sound records making total of 256000 samples. Aforementioned sound data sets recorded during a clinical diagnose session while patients first open then close their mouth. Specially designed sound recording tool and software are used to record the sound of the jaw movement. TMJ sounds are recorded with data and time stamps and their respective tags whether if record belongs to a TMD patient or not.

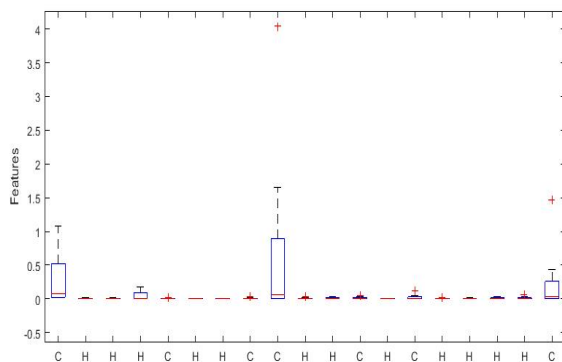


Figure 1: Statistical box plot of basic data classes (C: for click, H: for Healthy)

Statistical box plot of the data as seen in the Figure 1 gives somewhat clear visual difference between the healthy and unhealthy patient data. Further from above point, statistical properties of data are decided to be used for classification of the state of the patient. Using sampled data basic statistical features extracted from TMJ recordings:

- mean value
- standard deviation
- variance
- maximum and minimum difference of sampled data

For each record, using samples from right and left joint, 8 features obtained. All feature extraction process is realized by using MATLAB software.

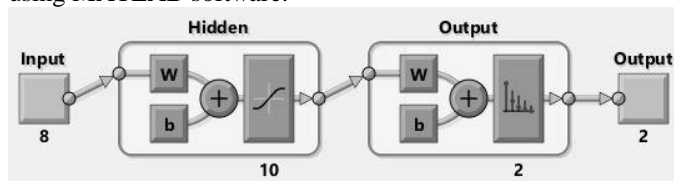


Figure 2: A multi layered feed forward ANN diagram used by MATLAB

After required features extracted, MATLAB ANN tool is used. In classification part artificial neural networks are chosen as classifier because of their efficiency in overall classifying problems.

A multi layered feed forward neural network as seen in the Figure 2 created using MATLAB’s neural pattern recognition application. MATLAB’s neural pattern recognition tool uses sigmoid function in hidden layers and a softmax layer before output. There are 10 hidden layers in neural classifier though lower number of hidden layers also gave the desired results.

Table 1: Healthy and TMD patient data distribution

	Number of features
TMD Patient	28
Healthy Person	48
Total	76

Then network is trained with the statistical features created before. 54 of total 76 features used to train neural network, remaining 22 are divided equivalently for validation and testing.

Table 2: Feature distribution for each step

	Number of features used
Training	54
Validation	11
Testing	11

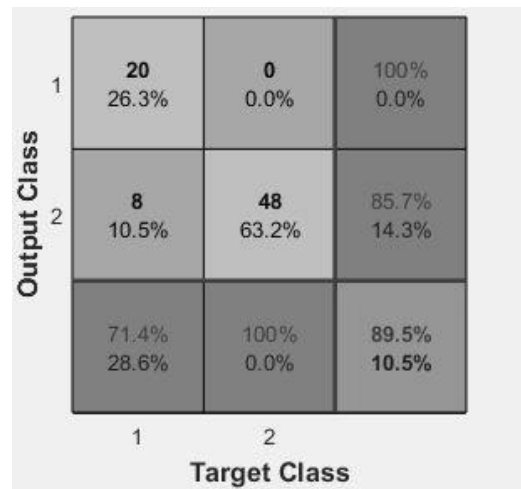


Figure 3: Confusion matrix

Because for each train process features are randomly divided, different results obtained each time. Confusion matrix in Figure 3 summarizes one of the most common results for training in which class 1 indicates TMD patient, class 2 means it is healthy person data:

- Rows of the matrix correspond to predicted classes by neural network and columns correspond to their real classes.
- Diagonal line shows percentage and amount of correctly classified features. The bottom cell of it shows overall accuracy and misclassification rate.

- The last column shows percentage of correctly or incorrectly classified predictions.
- The bottom row shows percentage of correctly or incorrectly classified features, true positive and false negative rate.

So it can be interpreted as; in 1st column 20 of 28 TMD patients correctly classified as TMD patients, 8 of them wrongly classified as healthy. In 2nd column all 48 feature classified correctly. Or all 20 class 1 predictions are correctly classified, 8 of 56 class 2 predictions are incorrectly classified and 48 of them correctly classified.

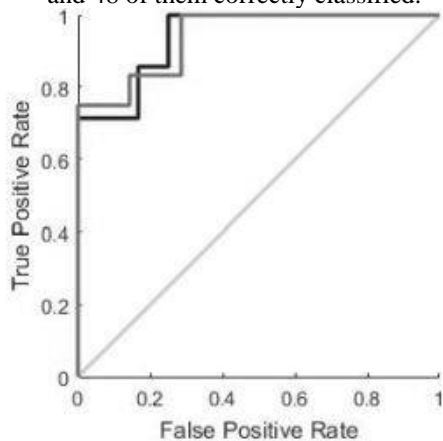


Figure 4: ROC Curve

As seen in the receiver operating characteristic curve Figure 4, trained network is pretty accurate since graph approaches to true positive rates which mean high probability of detecting TMD patients.

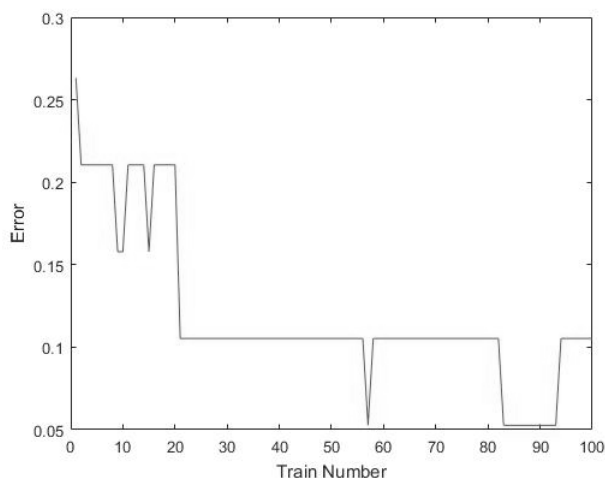


Figure 5: Error percentage for 100 trains of ANN

Overall results are obtained by running training and testing process many times. Typically classification and testing process is repeated 100 times and results are noted. The reason for repeated training sessions is to get realistic results for ANN model. It is known that some ANN models can perform unrealistically well because randomly chosen data by training algorithm may not represent full data spectrum but represent small amount of ideal conditions. Repeated training and testing process eliminates unrealistic ANN models and give the more realistic models and results in the long run.

A typical 100 run error percentages for ANN results are given in Figure 5. Note that some results have unrealistically low error percentages. To acquire better results network has trained multiple times and average of their success rate is considered as overall success rate which is approximately 87-89%.

III. RESULTS AND CONCLUSION

This study aims to explore and to determine if a person has TMD, using raw data obtained from TMJ sounds. Sound based classification is used many application especially medical diagnose. Listening sound of the patient body is greatly used in many medical areas and one of the main diagnostic tools. But listening many times requires expert ears for correct diagnostic. Consequently, study tries, at minimum, to help medical personnel for correct diagnosing of the disorders. Data is used in this study obtained from the previous study of the author.

ANN is used for classification of data by training the network first. Although there is no sound data preprocessing, results are promising. To validate the results training sessions repeated 100 times per run and correct classification rate saved. After 100 times repetition the mean of the correct classification rate is calculated around 87% to 89%. The rate is fairly high and better than the previous study of the authors.

Future study may include the more data. The methods like statistical digital signal processing, data preprocessing, noise filtering are planned further and better classification rate. Future study will include different type of disorder sound classification, identification of unhealthy joint, using deep learning and similar results.

REFERENCES

- [1] *Temporomandibular Disorders, Guidelines for Classification, Assessment and Management*, The American Academy of Orofacial Pain, Edited by C. McNeil. Quintessence Books, Illinois 1993.
- [2] F. Özan, S. Polat, İ. Kara, D. Küçük, H. B. Polat, "Prevalence Study of Signs and Symptoms of Temporomandibular Disorder in a Turkish Population", *The Journal of Contemporary Dental Practice*, vol. 8, no. 4, May 2007.
- [3] S. E. Widmalm, W. J. Williams, B. S. Adams. "The Waveforms of Temporomandibular Joint Sound Clicking and Crepitation." *Journal of Oral rehabilitation* 23; 44-49, 1996.
- [4] S. E. Widmalm, W. J. Williams, R. L. Christiansen, S. M. Gunn, D. K. Park. "Classification of Temporomandibular joint sounds based upon their reduced interference distribution." *Journal of Oral rehabilitation* 23; 35-43, 1996.
- [5] Sano T., Widmalm S. E., Westesson P. L., Takahashi K., Yoshida H., Michi K., & Okanao T., "Amplitude and frequency spectrum of Temporomandibular joint sounds from subjects with and without other signs/symptoms of Temporomandibular disorders", *Journal of Oral rehabilitation* 26; 145-150, 1999.
- [6] Djurdjanovic D., Widmalm S. E., William J. W., Christopher K. H. Koh, and Kok Pin Yang. "Computerized Classification of Temporomandibular Joint Sounds", *IEEE Transactions on Biomedical Engineering*. Vol. 47, No. 8, August 2000.
- [7] Ghodsi M., Hassani H., Sanei S., Hicks Y., "The use of Noise Information for detection of Temporomandibular disorder". *Biomed. Signal Process. and Control*. vol. 4, 79-85, 2009

- [8] Akan A., Başar Ünsal R., "Time-frequency analysis and classification of Temporomandibular sounds". *Journal of The Franklin Institute*, 337 (2000) 437-451, 2000.
- [9] Akan A., Ergin A., Yildirim M., Öztaş, E., "Analysis of Temporomandibular joint sounds in orthodontic patients". *Computers and Electrical Engineering* 32 (2006) 312-321, 2006.
- [10] Zheng C., Widmalm S. E., Williams W. J., "New Time-Frequency Analyses of EMG and TMJ sound signals." *IEEE Engineering in Medicine & Biology Society* 11th Annual International Conference. 1999.
- [11] Took C. C., Sanei S., Chambers J., & Dunne S., "Underdetermined blind source separation of Temporomandibular joint sounds". *IEEE Transactions on Biomedical Engineering* vol. 53, No. 10 Oct 2006
- [12] Took C. C., Sanei S., Rickard S., Chambers J. & Dunne S., "Fractional delay estimation for blind source separation and localization of Temporomandibular joint sounds". *IEEE Transactions on Biomedical Engineering*. Vol. 55No. 3, Mar 2008.
- [13] Kim, K. S., Seo J. H., Kang J. U. & Song C. G., "An enhanced algorithm for knee joint sound classification using feature extraction based on time-frequency analyses". *Computer Methods and Programs in Biomedicine* 94, 198-206, 2009
- [14] U. Taşkıran, S. Herdem, M. Çunkaş, F. Aykent, T. Y. Savaş, H. E. Koçer, "A Sample Reduction and ANN Based Classification of Temporomandibular Joint Sounds" *International Research Journal of Electronics and Computer Engineering*, Vol 1 No 3 (2015). (A pressed version of paper presented at Third International Conference on Science, Technology, Engineering and Management (3rd ICSTEM 2015)
- [15] S. Altunkaya, S. Kara, N. Görmüş and S. Herdem, "Statistically Evaluation of Mechanical Heart Valve Thrombosis Using Heart Sounds" *Proceedings of the World Congress on Engineering* 2010 Vol I WCE 2010, June 30 - July 2, 2010, London, U.K.

Design and Analysis of Grid-Tied Photovoltaic (PV) Systems under Uncertain Weather Conditions

U. YOUNAS¹, B. AKDEMIR¹ and A. A. KULAKSIZ¹

¹Konya Technical University / Turkey, umair.citad@gmail.com

¹Konya Technical University / Turkey, bayakdemir@selcuk.edu.tr

¹Konya Technical University / Turkey, afsin@selcuk.edu.tr

Abstract – Considering the rapid growth in global energy demand, renewable energy resources (RERs) particularly solar PV is the prominent need of modern power systems to mitigate the global energy crisis. PV is considered as one of the most useful RER, since it is inexhaustible, abundant, and clean. Besides, the power efficiency of Solar PV is highly affected by variations of solar irradiance and temperature of the solar cells. Hence, Maximum Power Point Tracking (MPPT) controller is used to control the switching duty cycle of the power converters which ultimately maximize the output power of the PV array. In this paper, case study of 240-kw solar PV array is performed in MATLAB/Simulink environment. Simulation is performed on ‘SunPower SPR-400E-WHT-D’ PV array which is comprised of 88 parallel strings and 7 series connected modules per string. The impact of variable weather conditions (irradiance and temperature) is analysed. Moreover, the 240 kw PV array is connected to 20 KV grid using boost converter and Voltage Source Converter (VSC). In this way, the inverted AC output power is coupled with AC grid. This bidirectional output power with unity factor can be utilized by industrial / commercial consumers to fulfil their energy demands.

Keywords - Renewable Energy, Solar PV system, MPPT, DC-DC Boost Converter, and Voltage Source Converter.

I. INTRODUCTION

THIS rising energy demand and environmental footprints divert the attention of the modern researchers towards Renewable Energy Resources (RERs). Therefore, the deployment of RERs particularly; the integration of solar photovoltaic (PV) is growing rapidly due to its flexible applications. Solar PV is clean and viable alternate energy resource with flexible off-grid and on-grid applications that are either in stand-alone (water pumping, electric vehicle charging or battery charging, and home energy supply system) or grid-connected configuration (power can be fed to the grid) [1]. Although, solar PV system has few limitations like its installation cost and power conversion losses in its electronic circuitry. Nevertheless, in the last 20 years, the demand of solar energy is still increasing from 20 % – 25% annually [2]. Besides, solar PV system is easy to install, less operational cost, noiseless, and environmental friendly energy resource that have capability to be deployed for large-scale grid-connected applications [3].

The key elements used in solar PV system are; PV module, DC-DC converter, battery bank, DC-AC converter,

and grid. The factors disturbing the power efficiency of PV plant are; (a) the efficiency of PV panel is low that is 8-15 %, (b) the power conversion losses are high, and (c) one-time higher installation cost of PV plant. The PV panel output power is highly affected with variable weather conditions (irradiance and temperature). However, the maximum power efficiency of PV plant can be achieved by means of an adequate Maximum Power Point Tracking (MPPT) controller and power conversion topology that can track the maximum power for available solar irradiance and temperature of the solar cells [4]. Although, the major contribution of the article is to analyse the impact of variable weather conditions on performance of PV array. Hence, it is important to be familiar with basic knowledge of PV array.

A single PV array is composed of various PV modules. While, each PV module have different IV characteristics. A single MPPT controller can be used if all the PV modules have the same characteristics. Due to partial shading, variable temperature, and irradiance, the behaviour of PV modules may vary. Hence, separate MPPT controller is required for each PV module to operate under the maximum power conditions. In literature, various MPPT controller techniques have been used to maximize the power efficiency of solar plant. These are; perturb & observe [5], incremental conductance [6], and artificial intelligence-based control algorithms [7], [8] have been proposed. These algorithms have benefits as well as limitations in terms of computational time, complexity, and implementation cost. In addition to available control technique, the objective of the research is to cope with the fluctuating weather conditions. The authors in [9] explained briefly that the temperature of the solar PV highly affect the voltage while, Irradiance of solar PV have huge impact on current. Hence, Irradiance and temperature particularly disturb the power quality of Soar PV array.

In this paper, the key elements of grid-connected solar PV plant are discussed. First, the mathematical model of PV cell is designed and analysed. Moreover, PWM based MPPT controller is designed which monitor the current and voltage of PV module and control the duty cycle of switch of DC-DC converter. This converter boosts the output voltage of the solar PV module. Furthermore, DC-AC VSC is employed to convert boosted DC to AC voltage. This inverted AC is further coupled with the grid. The rest of the paper is organized as follows:

Section 2 presents the detailed model of solar cell, DC-DC converter modelling and operation, overview of MPPT, and working mechanism of VSC. The performance evaluation of the proposed model in the form of various simulation results is performed in section 3. Finally, the paper is concluded with the summary of the future work for further improvement of current work.

II. MODEL DESIGN OF COMPONENTS OF SOLAR PV

The key elements used in Grid-Tied PV system are; solar panel, DC-DC boost converter, MPPT controller, DC-AC inverter, and coupling transformer that connect inverted AC to the grid. The system modelling is performed as follows:

A. Solar PV Model

The working of PV Cell is like a p-n junction diode. It works only in day time and at night it only produces 'diode current' which is also called as 'dark current'. PV array is composed of various PV modules. While, PV cells are the building blocks for the PV modules. The equivalent model for PV Cell is presented in Figure 1.

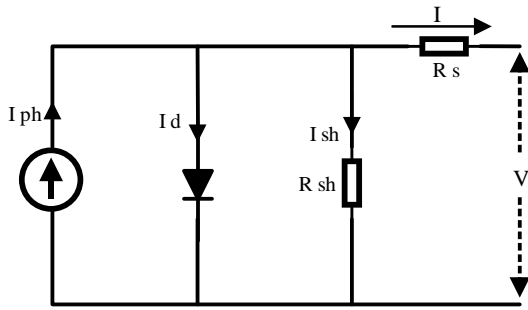


Figure 1: Equivalent model of PV cell

The equivalent model of PV cell is modelled with I_{ph} the photo current, I_d diode current, I_s shunt current passing through R_{sh} shunt resistance, and total output current (I) flowing through R_s series resistance. R_s is connected in series with parallel combination of R_{sh} and diode [10]. R_{sh} represents the intrinsic behaviour of the semiconductors while, R_s shows the resistance between neighbour PV cells as explained by the authors in [11]. However, net current equation obtained using Kirchhoff Current Law;

$$I = I_{ph} - I_d - I_{sh} \quad (1)$$

After substituting the values of diode and shunt current, we obtained,

$$I = I_{ph} - I_0 \left\{ \exp \left[\frac{q(V + IR_s)}{AKT} \right] - 1 \right\} - \left\{ \frac{(V + IR_s)}{R_{sh}} \right\} \quad (2)$$

In Eq. (2), the values of the constants are written as follows:

I_0 is diffusion current of diode junction, q is the electronic charge which is $1.602 \times 10^{-23} C$, K is Boltzmann constant that is $1.38 \times 10^{-23} J/K$, T is the temperature of p-n junction, and A is the ideality factor which is considered as 1 in proposed model not disturbing maximum power point of PV cell. Eq (2) can be further simplified by neglecting the value of R_{sh} .

$$I = I_{ph} - I_0 \left\{ \exp \left[\frac{q(V + IR_s)}{AKT} \right] - 1 \right\} \quad (3)$$

The maximum power equation of PV cell becomes,

$$P_{max} = V_{max} I_{max} = V_{max} \left[I_{ph} - I_0 \left\{ \exp \left(\frac{qV_{max}}{AKT} \right) - 1 \right\} \right] \quad (4)$$

The Eq. (4) is the desired equation to achieve the maximum power point. The main objective of this paper is to analyse the impact of unpredictable weather conditions (variable solar irradiance and flexible temperature) on the maximum power performance of the PV system. The PV characteristics of the proposed PV model are demonstrated in Figure 2.

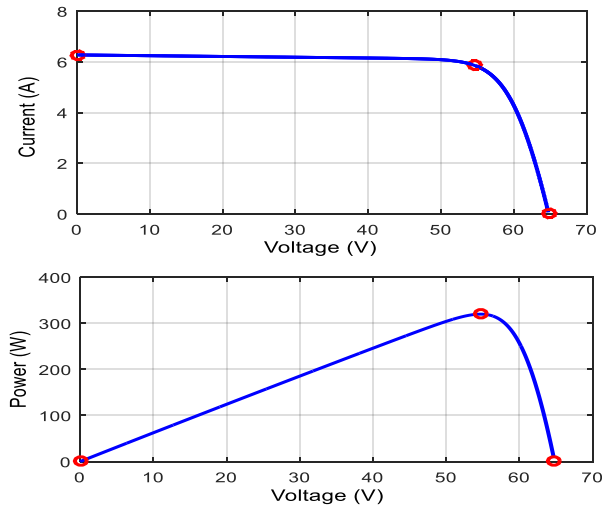


Figure 2: IV and PV characteristics of the proposed PV model

In Figure 2, the IV and PV characteristics are performed for the proposed model. These non-linear characteristics shows that the variations with temperature of the PV array are comparatively less but are highly sensitive to the variations of solar irradiance for net power of PV array.

B. Boost Converter Model

In the proposed model, the boost converter is configured to boost up the level of PV voltage and the circuit model is presented in Figure 3. Although, the PV generator voltage is not so high due to variable solar irradiance. Therefore, boost converter is employed to boost the voltage level up. The boosted voltage level is totally dependent on the switching duty cycle of the power switch (IGBT). The total time duration T of the switch is comprised of;

$$T = T_{on} + T_{off} \tag{5}$$

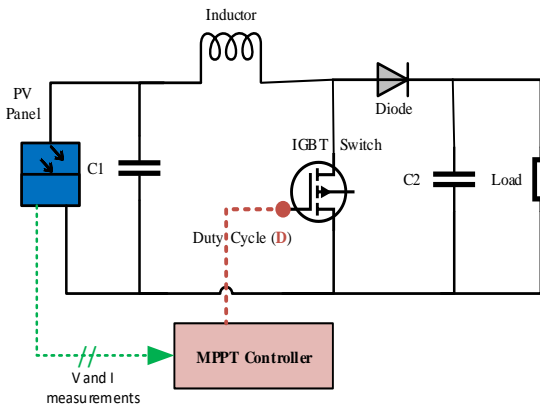


Figure 3: Model design of Boost Converter

The duty cycle (D) is the ratio of the ON-Time of the power switch. With respect to total time. This can be modelled as,

$$Duty\ Cycle, D = (T_{on}/T) \tag{6}$$

The final equation of output voltage of boost converter can be written as [12]:

$$V_o = \left(\frac{1}{1-D}\right) V_{pv} \tag{7}$$

As the value of D fluctuate between (0 & 1). Therefore, it is obvious from Eq. (7) that the minimum boosted output will be equal to V_{pv} when $D=0$. While, by increasing the value of D , the output voltage will increase by scalar multiple of V_{pv} .

C. Proposed PV Array Model Design

The proposed model comprised of all the necessary components required for PV panel as presented in Figure 4.

The objective of the case study is for the residential level. This PV array provide maximum of 240 kw that is applicable to fulfil the normal residential load. The model use *SunPower SPR 400E-WHT-D* PV array. This PV array comprised of 88 parallel strings and 7 PV modules are series-connected in each string. While, in each module total 128 cells are present. The other important components used in the system are; boost converter, MPPT controller, voltage source inverter, transformer and the grid.

The PV array is operated under different conditions of temperature and irradiance. The comparative analysis is performed in performance evaluation section with temperature ranges from 25 – 45 C^0 and irradiance vary slowly from 1000 – 200 w/m^2 and the respective impact on PV array output power is evaluated.

The PV array provide maximum of 240 kw at 1000 w/m^2 solar irradiance with temperature 45 C^0 . The output capacitor is used to smooth the output of PV array. 5 k-Hz boost converter is implemented which convert normal 273 V DC to 500 V DC voltage. Built in incremental conductance MPPT controller is used to control the power switch used in boost converter. MPPT measure the values of current and voltage from PV array and adjust the width of the pulses to generate desired maximum power from the PV array.

The VSC (3 level bridge DC-AC inverter) is incorporated which convert 500 V DC to AC voltage. In simulation model, the built-in inverter control block is used that have two main control loops; external control loop and internal control loop. As, total input to the VSC is 500 V DC hence, external control loop regulates the DC voltage between positive and negative 500 V and internal loop deals with grid currents.

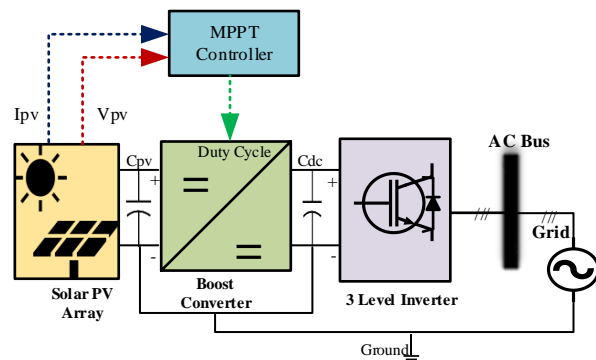


Figure 4: Proposed model design of Grid-Connected PV

To keep the unity power factor, the reactive current is kept zero. Moreover, the active and reactive voltages which are the signals from current controller are converted to three modulating signals. MPPT PWM generator use these modulating signals as reference and generate the desired output voltage.

III. PERFORMANCE EVALUATION

In the proposed research, the simulation analysis is performed on *SunPower SPR 400E-WHT-D* PV array having 400 kW of maximum power generation capacity. In this section, the analysis of current, voltage, solar power, solar irradiance/isolation and temperature of the solar PV cells will be performed.

A. Analysis of PV and IV Characteristics

In this research, we considered only 240 kW of the maximum power generation. The PV and IV characteristics of the proposed array are demonstrated in Figure 5. This is the exact response of the proposed PV array. The PV and IV characteristics are analysed based on variation in temperature. Normally, the temperature varies between $25C^0$ to $45C^0$. In this simulation environment, the simulation performed on $25C^0$ to $45C^0$ respectively. It is clear from the Figure 5 that huge variation in temperature have less effect on power of PV array. While, PV power is highly sensitive to change in irradiance due to change in current of PV array.

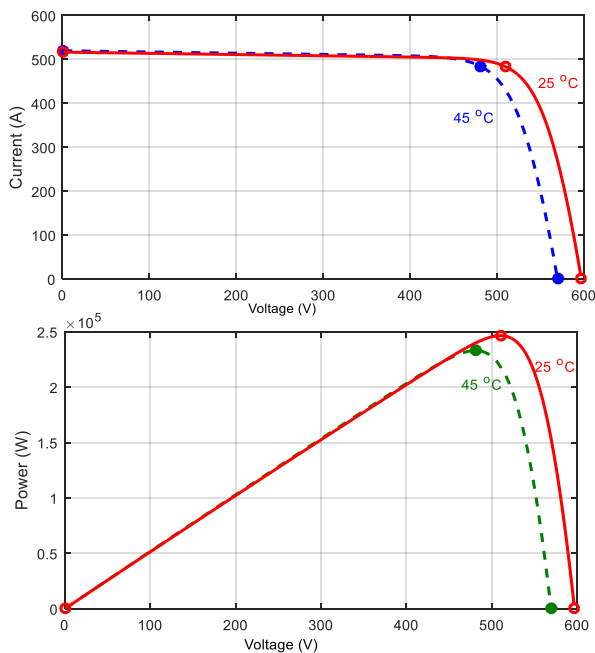


Figure 5: PV and IV characteristics of the PV array

B. Analysis of Voltage and Current of PV Array

The proposed PV array is executed to accomplish 240 kW of the power. However, the simulation results presented in Figure 6 shows the (490 v) voltage and (485 A) current capacity of PV array. This product of voltage and current gave rise to 238 kw which is quite close to desired 240 kw of power that is extracted from the PV array.

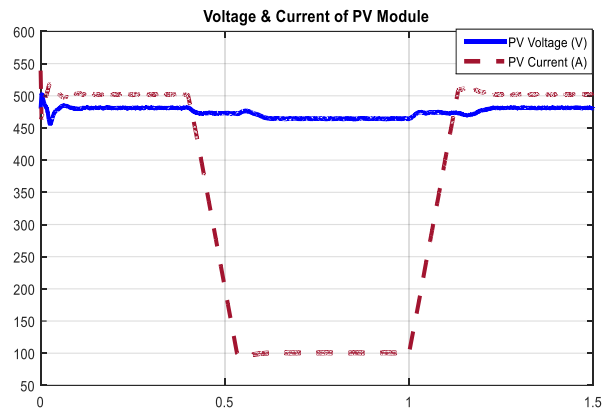


Figure 6: Voltage and Current of the PV array

The key factors under consideration are temperature and irradiance. As it is obvious from the results of Figure 7 that the change in irradiance highly disturb the current that in turns change the power generation of PV array. Therefore, simulation results are mostly based on the impact of irradiance on PV performance.

C. PV analysis of Array with respect to Irradiance

In MATLAB / Simulink directory, initially the behaviour of PV voltage and PV power is analysed at $1000 w/m^2$ and the temperature is kept constant that is $40 C^0$. In this case, we achieve almost stable PV voltage and achieved 240 kW which is the desired maximum power of proposed PV array. Later, irradiance is slightly decreased, and huge reduction in PV power is noticed respectively. Again, increase in output power is examined when irradiance actor is increased. Finally, the maximum power (240 kW) appeared when irradiance value approaches to $1000 w/m^2$. The simulation results related to voltage and power of the PV array under irradiance fluctuations are depicted in Figure 7.

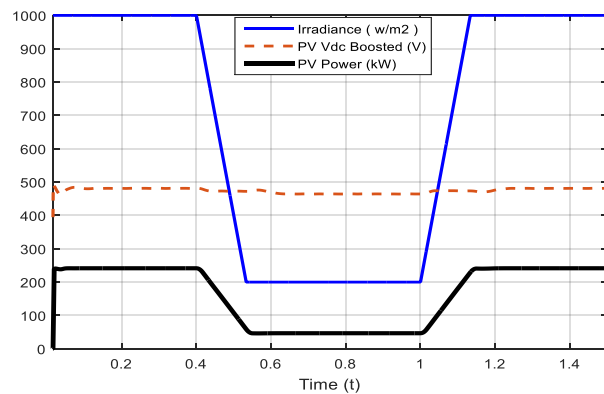


Figure 7: Impact of irradiance on PV characteristics of solar array

D. Three Level DC-AC Inverter Analysis

The DC-AC converter is the most important electronic element which converts boosted DC voltage to AC voltage [13]. In grid-connected PV system, consumer have the right to use grid power to satisfy load demand and can sell power to grid at the time of peak load demand. However, it is important to sustain the quality of the inverted signals in PV system. In proposed model, the single-phase grid voltage and inverted AC voltage and current are analyzed that are demonstrated in Figure 8 and Figure 9 respectively.

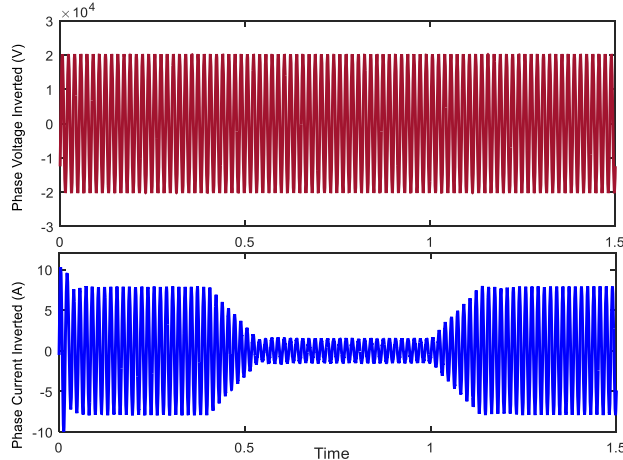


Figure 8: Single phase AC voltage and respective current

The inverted voltage is connected to three-phase 20 KV grid. Like boost converter, the power switching device of DC-AC inverter plays crucial role to reduce the power losses. In this model, 3 level inverter and IGBT is used as a power switch. The switching frequency is set high (3.7 kHz) to minimize the output power losses.

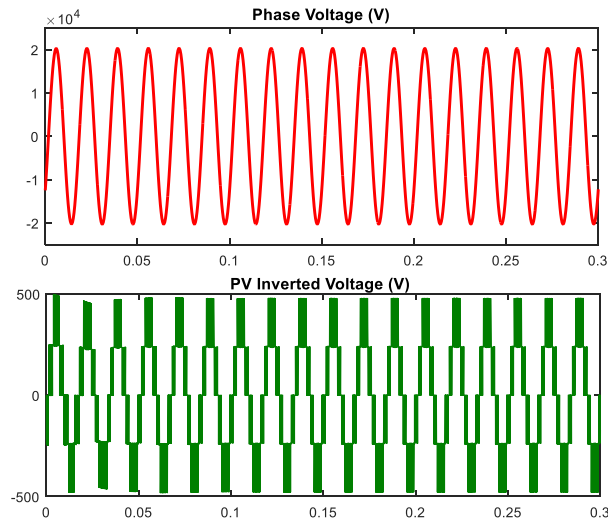


Figure 9: Grid and Inverted AC Voltage

The output of 3 level inverter converts boosted DC voltage to desired AC voltage. As stated earlier, in this case study the built-in model of inverter is used. Although, the AC voltage is recovered but still have ripples as plotted in Figure 10. By increasing the levels of inverter (multi-level inverters) the ripples and harmonics in the output signal can be minimized to a significant level. Although, the major focus of the research

is on the analysis hence, to improve grid synchronization of grid-tied PV systems the levels of inverter must be improved to achieve more quality results [14].

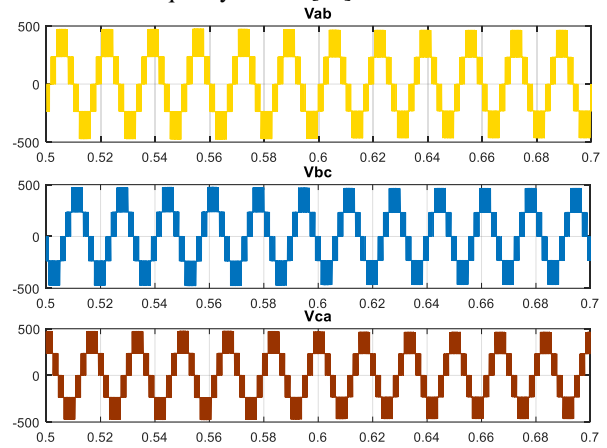


Figure 10: Three phases of inverted voltage

After inverting the voltage, transformer is used to step the voltage level up. This AC power transmitted through a transmission line to couple with grid voltage through AC bus. The AC voltage and current graphs are depicted in Figure 11. The three-phase grid voltage and current at AC are plotted for analysis. The voltage level is kept constant to 20 kV while, the value of current is varied with respect to the change in solar irradiance.

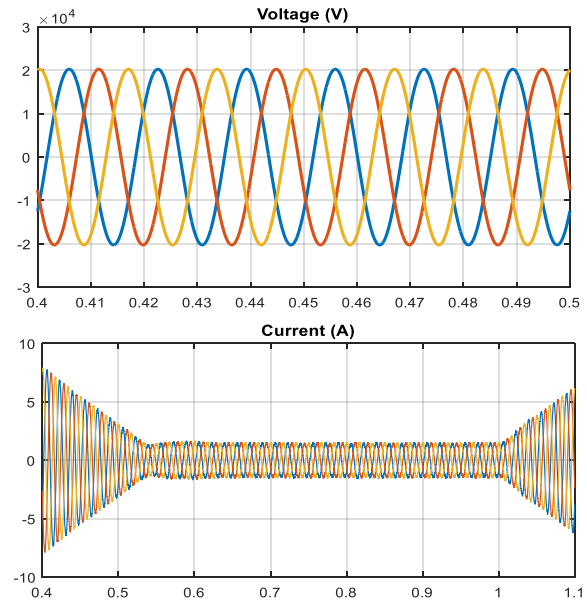


Figure 11: Inverted 3 phase voltage and currents

IV. CONCLUSION

The main motivation of the paper is to analyze the performance of PV system under the influence of variable weather conditions like temperature and irradiance of solar cells. The simulation is performed in MATLAB/Simulink directory on SunPower SPR 400E-WHT-D PV array, the simulation is performed to get 240 kW PV power at 1000 w/m² solar irradiance and 45 C⁰ temperature of solar

array. The analysis on boost converter, MPPT converter, 3 level bridge inverter and role of MPPT is explained. The simulation study might help the installation of PV array with feasible solar irradiance and reduce the maximum power fluctuations during rapid weather changing conditions. Moreover, the inverted voltage and current results are not considered too efficient for large scale practical applications of PV installations. Therefore, by incorporating the suggestions of future work, performance of PV array can be further improved.

In future work, the objective is to extend this work by introducing hybrid power system with Solar PV, Wind energy, and battery banks will be the active participants. Moreover, adaptive / intelligent MPPT controller will be designed to improve maximum power tracking of PV, and PLL will be employed to enhance grid synchronization.

ACKNOWLEDGMENT

Umair Younas would like to show his gratitude to the Konya Technical University that offered him funded PhD position. Moreover, he is thankful to Department of Electrical and Electronics Engineering and special thanks to Assoc. Prof. Ahmet Afsin Kulaksiz for his valuable guidance, motivation, and financial support for ICENTE'18 conference.

REFERENCES

- [1] O. Ellabban, H. Abu-Rub and F. Blaabjerg, "Renewable energy resources: Current status, future prospects and their enabling technology," *Renewable and Sustainable Energy Reviews*, vol. 39, pp. 748-764, 2014.
- [2] J. M. Carrasco et al., "Power-electronic systems for the grid integration of renewable energy sources: A survey," *IEEE Transaction on Industrial Electronics*, vol. 53, no. 4, pp. 1002-1016, 2006.
- [3] T. K. Roy and M. A. Mahmud, "Active power control of three-phase grid-connected solar PV systems using a robust nonlinear adaptive backstepping approach," *Solar Energy*, vol. 153, pp. 64-76, 2017.
- [4] T. Eswam and P.L. Chapman, "Comparison of Photovoltaic Array Maximum Power Point Tracking Techniques," *IEEE Transactions on Energy Conversion*, vol. 22, no. 2, pp. 439-449, 2007.
- [5] M. A. Aredes, B. W. França, L. G. B. Rolim and M. Aredes, "P&O method controls applied to grid connected PV systems," in *IEEE 24th International Symposium on Industrial Electronics (ISIE)*, Buzios, Brazil, 2015.
- [6] M. Al-Dhaifallah, A. M. Nassef, H. Rezk and Kottakkaran Sooppy Nisar, "Optimal parameter design of fractional order control based INC-MPPT for PV system," *Solar Energy*, vol. 159, pp. 650-664, 2018.
- [7] M. Dhimish, V. Holmes, B. Mehrdadi and Mark Dales, "Comparing Mamdani Sugeno fuzzy logic and RBF ANN network for PV fault detection," *Renewable Energy*, vol. 117, pp. 257-274, 2018.
- [8] K. Zeb, W. Uddin, M. A. Khan, Z. Ali and H. J. Kim, "A comprehensive review on inverter topologies and control strategies for grid connected photovoltaic system," *Renewable and Sustainable Energy Reviews*, vol. 94, pp. 1120-1141, 2018.
- [9] D. H. Daher, L. Gaillard, M. Amara and Christophe Menezo, "Impact of tropical desert maritime climate on the performance of a PV grid-connected power plant," *Renewable Energy*, vol. 125, pp. 729-737, 2018.
- [10] M.G.villalva, J.R.Gazoli and E.R.Filho, "comprehensive approach to modeling and simulation of photovoltaic arrays," *IEEE Transactions on Power Electronics*, vol. 24, no. 5, pp. 1198-1208, 2009.
- [11] A. K. A. K. D. Chatterjee, " Identification of photovoltaic source models," *IEEE Transaction on Energy Conversion*, vol. 26, no. 3, pp. 883-889, 2011.
- [12] T.-F. Wu and Y.-K. Chen, "Modeling PWM DC/DC Converters Out of Basic Converter Units," *IEEE TRANSACTIONS ON POWER ELECTRONICS*, vol. 13, no. 5, 1998.
- [13] H. X. Wang, M. A. Muñoz-García, G. P. Moreda and M. C. Alonso-García, "Optimum inverter sizing of grid-connected photovoltaic systems based on energetic and economic considerations," *Renewable Energy*, vol. 118, pp. 709-717, 2018.
- [14] G. Revana and Venkata Reddy Kota, "Closed loop artificial neural network controlled PV based cascaded boost five-level inverter system," in *International Conference on Green Energy and Applications (ICGEA)*, 2017.

A Study On The Effect Of Daylight In Energy Efficiency

A. BILICI¹, I. SARITAS²

¹ Gaziantep University, Gaziantep/Turkey, aykutbilici@gantep.edu.tr

²Selcuk University, Konya/Turkey, isaritas@selcuk.edu.tr

Abstract – There has been many researches on the efficiency of the lightening from manual switching to the automatic opening and closing by using motion sensors. Even though microprocessor systems have begun to be investigated as a trend, it is thought that these studies in which the adjusted/measured brightness of the environment do not provide sufficient resources.

Unlike other researches in this study, measuring the light intensity of the environment and setting the brightness level autonomously ensures that saving in electrical energy. While this autonomous system is being realized, microprocessors are programmed using PWM (Pulse Width Modulation) method and a high efficiency system has been created with LED lighting products.

In conclusion, this system ensures that the correct and efficient lighting level by providing the same brightness in the lighting systems continuously. At this point, a strong view will be obtained with the system that is produced and occupational safety and low error cost will be mentioned. It is believed that the system will protect eye health and increase work efficiency.

Keywords – Led, microprocessor, intelligent, lighting, energy.

I. INTRODUCTION

In recent years, efforts to self-regulate energy have reached a high level with the works done in our country. In order to minimize foreign energy dependence, there have been carried out many researches and investigations like, research on local coal resources, natural gas and oil deposits, government supports to increase production in renewable energy sources and construction of new hydroelectric power plants.

51% of total electricity production (Natural Gas+imported coal) is obtained from imported sources.

While efforts were being made to reduce dependence on foreign energy, the efficient use of produced electricity has also been an important issue.

As far as the total electrical energy produced in our country is concerned, the share of electrical energy consuming in all lighting areas is close to %20 [1]. (Figure 1)

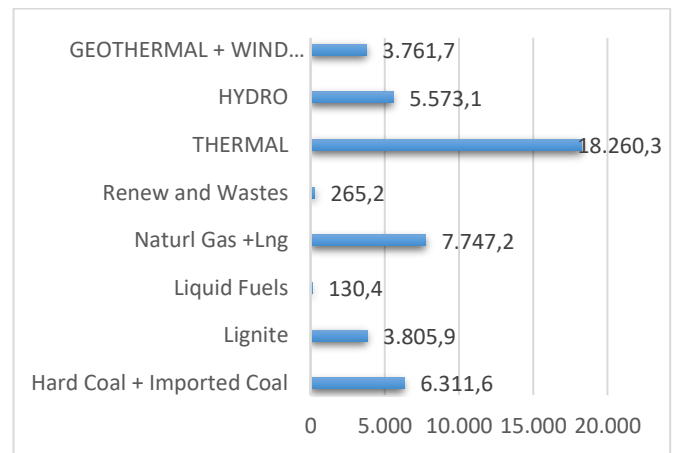


Figure 1 : Monthly Distribution of Turkey 's Gross Electricity Generation by Primary Energy Resources (GWh) - August 2018

At about 29% of electricity consumption is spent on lighting in household usage (Figure 2)

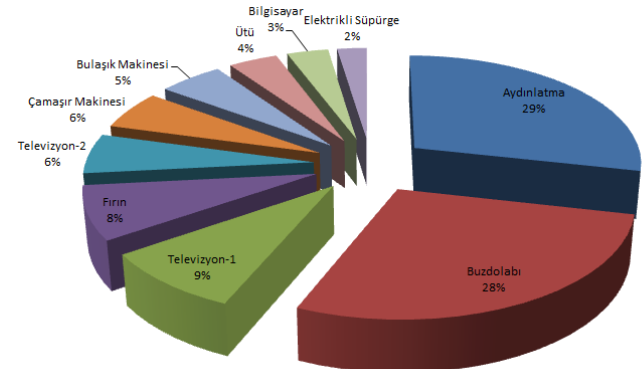


Figure 2 : Consumption distribution of home subscribers

By means of energy efficiency in lighting, budgetary and visual relief will be provided. The energy efficiency in lighting could be achieved by providing minimum luminous

intensity with necessary visual comfort. Therefore, the high-efficient light sources should be used instead of low ones[2].

Within this scope; instead of incandescent lamps, compact fluorescent lamps usage has become widespread that is 80% more efficient.

The use of LED lighting products should be encouraged in order to increase the efficiency of consumption. LED lamps are preferred because of efficiency, color, size, opening-closing time, dimming, long life, shock resistance and focusing features [3].

Many different studies have been conducted for more efficient use of the electrical energy used in lighting over the years.

Studies related to the lighting are divided into motion sensitive systems, time-adjusted systems, light intensity controlled systems.

In motion sensitive systems, the lighting devices works according to movement in the lighting area. If there is no movement during the specified period, the lighting device is closed[4]. Although it is not suitable for use in intensive work environments or offices, it is used in public areas where lighting is not used very often.

In time-adjusted systems, the on/off time of the lighting elements are determined. It shall not take into account any changes that may occur in the lighting environment during these periods, and shall only be on or off during the specified hours.

In light intensity controlled systems, studies have been done to make maximum use of daylight and to provide continuous lighting at the same level [5].

In studies making changes of the lighting devices' brightness levels with the sensors enabling to determine brightness level; the system is controlled by using a microcontroller or a microprocessor.

II. MATERIAL AND METHOD

Based upon the lighting usage information generated by this study, the lux value (light intensity value) should be determined and in accordance with the determined value, the lux value and lighting should be measured and made. Therefore, the daylight should be also used as a factor in lighting.

According to investigations made in different geographic regions of the United States; it was observed that the buildings which have windows with light passing rate fewer than 50%, has not so much positive impact to energy saving connecting to daylight by increasing windows. It is revealed that the factor that makes real impact to energy saving is daylight transmittance and the area of the window. It has been indicated that the windows of buildings with the types mentioned above will be more effective by making the area of window more daylight transmittance. In other words, increasing daylight transmittance by means of window area would make a major impact to energy saving through daylight-dependent dimmable lighting control systems [6].

According to a study made in Malaysia, it has been observed that approximately 30% lighting energy savings

could be possible annually by using lighting control systems connected to the daylight. [7].

The System is aimed to reach the most efficient light intensity by means of turning on/off or dimming the light with LED Panels in accordance with day light intensity.

In this system, the area to be set up will be constantly in the same light intensity will be provided by means of the software to be built into the microprocessor. Therefore, the different brightness levels at different times of the day would be prevent.

III. APPLICATION OF MAIN PARTS

Two basic elements have been identified for the establishment of the system;

1- System Unit

- A lux meter circuit to measure light intensity,
- GY-30 BH1750FVI Light Sensor Module that can measure light brightness from 0 to 65535lx
- An electronic circuit that uses a microprocessor to provide dimming and lighting in the direction of information from the lux meter,
- Software to be made with PWM Method, which enables the autonomous decision of the electronic circuit,

2- Environmental Components

- Led Panels to provide lightening,
- Power supply to provide electrical feeding of Led Panels

A circuit was designed that measures the light intensity of the environment so as to get the maximum benefit from the daylight and in that circuit "GY-30 BH1750FVI" light sensor module was used (Figure 3).



Figure 3: GY-30 BH1750FVI Light Sensor Module

Arduino Nano was used to control the lighting devices according to the measured brightness intensity. Arduino Nano (Figure 4) is an "Atmega328" based microcontroller card. It has 14 digital input / output pins (6 can be used as PWM output), 8 analog inputs, 16 MHz crystal, USB socket, ICSP connector and reset key.

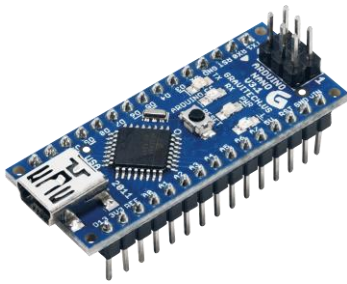


Figure 4: Microprocessor (Arduino Nano)

LED lighting devices working 12V-24V with Arduino microprocessor, lighting intensities setting, optimizing the environment of this technology will be maintained the luxury value.

PWM (Pulse Width Modulation) inverter power supplies have been widely used in recent years for the economic and easy control of electric motors. PWM stimulation is a discrete waveform derived from the logic comparison of reference and carrier waveforms at different frequencies [8].

The block diagram of the designed system is given in Fig.5

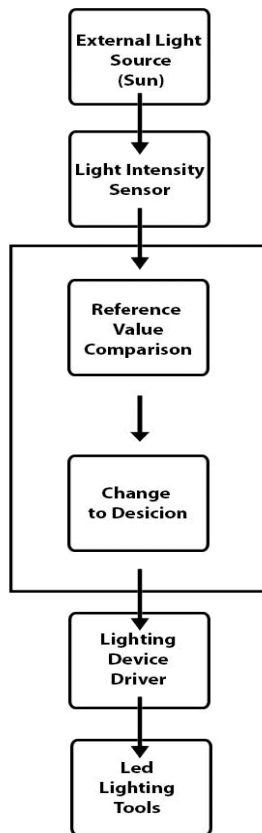


Figure 5. Block Diagram

IV. RESULT AND DISCUSSION

With the use of LED lighting devices and the daylight, the desired lighting intensity has been achieved with minimum energy. By this way, it was observed that there was a 70% improvement in electricity consumption compared with the

constantly open lighting of conventional lighting devices [9] (Fig. 6).



Figure 6: Daylight intensity-time chart

The study, which is considered to be open for 12 hours in the working environment, showed that although the weather, physical conditions and seasons are different, due to the use of daylight, an average savings of around 50% was observed (Figure 7).

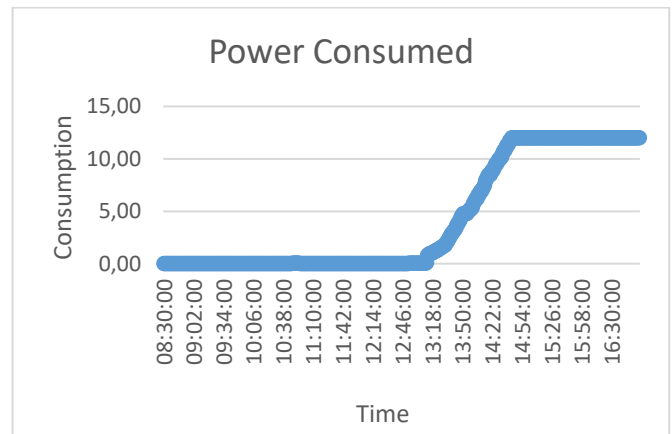


Figure 7: Consumption Graph by Methods

As a result, the use of daylight as an element of lighting and keeping the intensity of the ambient light continuously at the same levels ensure that the environment is healthier and more comfortable [10].

As a result, while the daily use of electricity was 6KW on average, thanks to this study, it was reduced to about 2KW.



Figure 8: Total power consumed

Besides the project's contribution to energy efficiency, providing the same amount of light intensity continuously will lead to;

- 1- Motivation/Serenity
- 2- Increase in employees' performance, occupational safety, more products and operations and competitive power of businesses by means of efficient visuality.

V. REFERENCES

- [1] PERDAHÇI C., HANLI U., "Aydınlatmada Enerji Verimliliği, Sanayi Enerji Yöneticisi Eğitimi", Kocaeli, 2010
- [2] Enerji Verimliliği Derneği, Available: "http://www.enver.org.tr/tr/icerik/aydinlatma/17", December, 2017.
- [3] GÖÇMEN E., "Aydınlatma Aygıtlarının Enerji Verimliliği Ve Güç Kalitesine Etkileri", pp.27-18, Kocaeli, 2014
- [4] ATIF, M.R., GALASIU, A. D., 2003, Energy performance of daylight-linked automatic lighting control systems in large atrium spaces (report on two fieldmonitored case studies, Energy and buildings 35, 5, pp. 441-461)
- [5] YUCEL U., AYAZ M., GUVEN A., BURÇ C., "2nd International Energy & Engineering Conference", akademikpersonel.kocaeli.edu.tr/uyucel/bildiri/uyucel23.10.2017_14.56.51bildiri.pdf
- [6] Elektrik Mühendisleri Odası, Available: https://www.google.com.tr/url?sa=t&rct=j&q=&esrc=s&source=web&cd=1&ved=0ahUKEwiJ29yb__LXAhWEVxoKHb0nCdCQFggnMAA&url=http%3A%2F%2Fwww.emo.org.tr%2Fekler%2F2cf8d98dca2b9de_ek.xls%3Ftipi%3D34&usq=AOvVaw28RIXaxkGicI259I0694b3 December, 2017.
- [7] KRARTI, M., ERICKSON, P.M., HILLMAN, T.C., A simplified method to estimate energy savings of artificial lighting use from daylighting, Building and environment, 40, 6, pp. 747-754, 2005
- [8] MAHLIA, T.M.L., SAID, M.F.M., MASJUKI, H.H., TAMJIS, M.R., Costbenefit analysis and emission reduction of lighting retrofits in residential sector, Energy and buildings, 37, 6, pp. 573-578, 2005
- [9] DEMİRBAŞ M., "Güneşiğine Bağlı Aydınlatma Kontrolü Ile İç Aydınlatmada Enerji Tasarrufunun Görüntü İşleme Yöntemleri Kullanılarak Gerçekleştirilmesi", pp. 51, Sakarya, 2015.
- [10] NABIL, A., MARDALJEVIC, J., "Useful daylight illuminance: a new paradigm for assessing daylight in buildings, Lighting research and technology", 37, 1, pp. 41-59, 2005.

Overview of Potential of Renewable Energy Sources in Artvin Province

E.H. AYDIN¹ M. ÇUNKAŞ²

¹ Artvin Çoruh University, Vocational High School, Artvin/Turkey, eneshalid@artvin.edu.tr

²Selcuk University, Electrical-Electronic Engineering Department, 42075, Konya/Turkey, mcunkas@selcuk.edu.tr

Abstract- In this study, Turkey's Black Sea located to the east of and having a fairly rugged terrain Artvin province's potential for renewable energy sources is investigated. The current map data of the General Directorate of Renewable Energy and the solar radiation quantities and wind velocity potentials of the Provincial Directorate of Artvin Meteorology is used. Weibull and Rayleigh distributions are calculated by using hourly wind velocity data of the meteorological station 17045 in Artvin province. Monthly wind power density is determined between June 2017 and September 2018 for this station. As a result of the calculations, the predictive power of the Weibull and Rayleigh distributions are compared and although the results are close, the weibull distribution is seen to produce more stable results.

Keywords- Renewable Energy, Solar Energy, Wind Energy, Artvin

I. INTRODUCTION

DESPITE the strong increase in renewable energy sources to investments done last year, when Turkey's energy potential is considered still it cannot say that reached the desired level. Turkey's 2023 use of renewable energy sources up to 30% and among the world's 10 largest economies, as well as a strategic sector for the 2071 target in line with the energy and boosting investment in nuclear technology; the use of these resources which are clean and domestic energy, is very important. Considering that we are a country rich in solar and wind energy potential, the efficient use of these energies can significantly eliminate our dependence on foreign energy. Turkey's electricity installed capacity is 87,138.7 MWh with the date 10/07/2018. 26,2% of this installed power belongs to natural gas, 23,3% to hydroelectric power plant, 21,9% to fossil fuels, 7,6% to wind and the rest to other energy production sources. In addition, there are currently no licensed solar power plants. The share of unlicensed wind, solar, thermal and hydroelectric power plants in production is 5.7% The installed capacity is measured as 85,200 MWh compared to the same month of the previous year. 26.4% of this installed power belongs to natural gas, 23.1% to hydroelectric power plant, 21.7% to fossil fuels, 7.6% to wind and the rest to other energy generation sources. The share of unlicensed wind solar thermal and hydroelectric power plants in production is 3.4% [1] In other words; an increase of 1.9% in electricity installed capacity compared to the previous year and a 2.3% increase in the contribution of renewable resources to production have been observed. According to the data of TEİAŞ dated August 2018, the domestic rate in electricity generation is 48.97%.

Considering that the electricity consumption of our country is increasing day by day (5,1% increase compared to the previous year), it is one of the steps that should be taken to increase the domestic rate in production as soon as possible.

Artvin province is a province of the Black Sea Region, with a surface area of 7367 km², located between 400 '35' and 410 32 'north latitudes and between 410 07' and 420 00 'east longitude. Province of Turkey's land area (783 577 km²) is up 0.9%. It is adjacent to Ardahan to the east, Erzurum to the south, Rize to the west and Georgia to the north. The north-west is Black Sea and the coastline is 34 km. Artvin is the province with the most variation in the climate of the Eastern Black Sea Region. In the area where the coastline and Cankurtaran mountain range take place, the typical Black Sea Climate is observed every season [8].

In this study, the potential of solar energy and wind energy from renewable energy sources in Artvin province was investigated. The solar energy potential was determined using the latest data from The Ministry of Forestry and Water Affairs and the Artvin Meteorological Provincial Directorate Station. The wind energy potential was measured by the wind measurement mast with a height of 10 meters from the measuring point located at an altitude of 680 meters at the station number 17045. These measurements were taken hourly. The wind speed data were taken from June 2017 to September 2018. The hourly wind velocity data were analyzed using two-parameter Weibull and Rayleigh distributions. The monthly wind power density for the station was estimated. The performance of the Weibull and Rayleigh distributions were also analyzed and shown on the graph after review.

II. SOLAR ENERGY

Turkey, in terms of solar energy potential is advantageous in many countries around the world. In Turkey, the average annual sunshine time of 2640 hours (7.2 hours per day total), the average annual solar radiation of 1311 kWh / m²-year (daily total of 3.6 kWh / m²) is known to be. Annually, an average of 110 days in space solar power, Turkey has a high energy potential. Southeastern Anatolia Region of Turkey with annual 2993 hours of sunshine duration is the most sunlight. This region is followed by the Mediterranean, Eastern Anatolia, Central Anatolia, Aegean and Marmara regions, respectively [6]. The black sea region exposes to at least solar energy in Turkey. However, even the Black Sea region receives more sunshine than many European regions that are

located in the north and which generate electricity from solar energy [2].

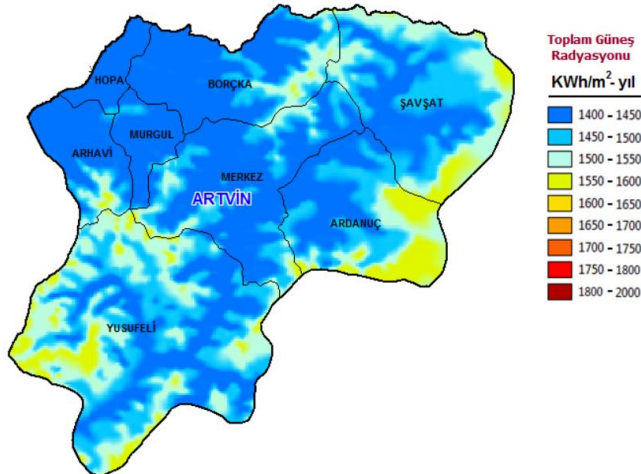


Figure 1: Atlas of Artvin solar energy potential [2]

Artvin is located in 1450-1500 KWh / m²-year band in terms of total solar radiation. Ardanuç and Şavşat, whose districts are located in a high band, are not suitable for establishing a solar power plant (SEP) in these areas due to their geographical location.

Table 1 presents monthly global radiation values and sunshine times for Artvin. The sunshine duration of the average of Turkey for According to April, May, June, July, August and September is over. Turkey average annual sunshine duration is 7,498 hours / day. However, there is no SEP currently established in Artvin. Although it is not very rich in terms of solar energy radiation value in Artvin province, it will be advantageous for system installation in case increasing to benefit from the sun with developing technologies.

Table 1: Global Radiation Values and Sunshine Duration for Artvin [2]

	Global Radiation Value (KWh/m ² -day)	Sunbathing Time (hrs)
January	1.79	4.11
February	2.5	5.22
March	3.87	6.27
April	4.93	7.46
May	6.14	9.10
June	6.57	10.81
July	6.50	11.31
August	5.81	10.70
September	4.81	9.23
October	3.46	6.87
November	2.14	5.15
December	1.59	3.75

III. WIND ENERGY

Turkey's top wind power producing areas are located near the mountain top, coastline, high ridges, or open space. Turkey's wind energy potential is about 48,000 MW,

according to the research. When compared to regions, wind energy potential can be listed as Marmara, Southeastern Anatolia, Aegean, Mediterranean, Black Sea and Eastern Anatolia. Wind turbine installed capacity in the world is around 486,661 MW as of June 2017 and it is increasing day by day. The wind turbine installed capacity in Turkey is 4718.3 MW. The provinces with the highest installed capacity are Balıkesir (767,3 MW), İzmir (613,6 MW), Manisa (393,9 MW), Hatay (277MW) and Osmaniye (185 MW) so on. In Turkey, the wind energy potential in the 50 m altitude areas is 48.000 MW, while the available wind energy power is only 10% of that of 4.718.3 MW. According to these figures, it is possible to conclude that especially the domestic wind turbines should be produced in order to fully utilize the wind energy potential in our country [3]. In Table 2, the wind is mainly in the northwest direction. According to 2017 data, annual average wind speed in Artvin was measured as 1,85 m / s[5].

Tablo 2: Monthly Average Wind Speed And Wind Direction for Artvin [5]

	Monthly average wind speed (m / s)	Wind direction
January	1.3	SE
February	1.6	SE
March	1.8	SSE
April	2.0	NNW
May	1.7	SSB
June	2.2	NW
July	2.6	NW
August	2.7	NW
September	1.9	NW
October	1.6	NW
November	1.3	SSE
December	1.5	NW

IV. WEIBULL DISTRIBUTION

Frequency distributions are used to determine the power potential of a particular region. If this is not possible, the wind speed can be found with other analytic distribution functions. One of the functions we can show the wind speed distribution is the Weibull distribution function. Weibull distribution is generally accepted in wind energy analysis because it is suitable for wind speed data.

In addition, Weibull distribution is a high (low error margin) distribution with respect to other distributions. This distribution contains two parameters. The parameter in equation (1) is called the scale parameter (c) which has the same unit as the wind speed. The scale parameter varies depending on the average speed. That is, if the average speed is high, the scale parameter is also high. In the equation (2), the dimensionless shape parameter (k) is the parameter expressing the frequency of the wind blowing. If the wind speed in a zone is blowing at a constant speed (the speed value is low or high), the shape parameter (k) is of great value. If the

wind speed does not blow at a constant speed, the shape parameter is small [4].

The scale parameter is calculated as follows.

$$c = \left(\frac{\sum_{i=1}^n (v_i)^k}{n} \right)^{\frac{1}{k}} \tag{1}$$

The shape parameter is calculated as follows.

$$k = \left(\frac{\sum_{i=1}^n v_i^k \ln(v_i)}{\sum_{i=1}^n v_i^k} - \frac{\sum_{i=1}^n \ln(v_i)}{n} \right)^{-1} \tag{2}$$

V. RAYLEIGH DISTRIBUTION

Another statistical approach used to calculate the distribution of wind velocity is Rayleigh distribution. In the Rayleigh distribution, the Weibull distribution shape parameter is assumed to be constant “2” Ray. In this case, Rayleigh density function can be defined by equation (3).

$$f_R (v) = \left(\frac{2v}{c^2} \right) \exp \left(- \left(\frac{v}{c} \right)^2 \right) \tag{3}$$

Rayleigh cumulative distribution function

$$F_R (v) = 1 - \exp \left(- \left(\frac{v}{c} \right)^2 \right) \tag{4}$$

Can be expressed in the form.

The average wind speed and power density for the Rayleigh distribution are given below. [7]

$$v_m = c \sqrt{\pi/4} \tag{5}$$

$$P_R = \frac{3}{\pi} \rho v_m^3 \tag{6}$$

VI. WIND VELOCITY DATA ANALYZE ACCORDING TO WEIBULL AND RAYLEIGH DISTRIBUTION

Data used for estimation of shape and scale parameters which are the parameters of Weibull distribution, were taken from station no 17045 between June 2017 and August 2018. The data obtained in Artvin Central Station within 16 months is shown in Table 3 and Table 4. For this study, a total of 10659 measurements were performed, ie calculations were done using the 10659 parameter [5].

Table 3:Hourly wind speed data for Artvin 17045 station for 2017

2017	Measured hourly data
June	689
July	678
August	658
September	578
October	704
November	622
December	648
Total	4577

Table 4: Hourly wind speed data for Artvin 17045 station for 2018

2018	Measured hourly data
January	692
February	649
March	728
April	698
May	730
June	695
July	744
August	726
September	420
Total	6082

Weibull power density and parameter calculations are given in Table 5 for 2017 and 2018. Rayleigh power density and parameter calculations of the same year and month are given in Table 6. All calculations were made by using hourly wind data. In the Rayleigh distribution, the value of (k) is considered to be 2 and the value in Table 6 is not specified. As the parameter, mean velocity (vm), standard deviation (σ), wind velocity Weibull and Rayleigh probability (iw (v)), wind velocity Weibull and Rayleigh cumulative (Fw (v)), wind possible velocity, the maximum value contributing to energy density (Vmax E), and the average energy density (P / A) for Weibull and Rayleigh distribution were calculated. These calculations were performed using Matlab codes. In addition, the mean energy density is used as ρ = 1.226.

Weibull and Rayleigh statistical analysis was used to determine which model was better for modeling. This criterion is expressed by the equation (7). The obtained results are shown in Table 7.

If the power density in the weibull and rayleigh distribution results obtained in Table 5 and Table 6 is above 50 W / m2, the wind turbine can be installed in that region. However, it should be kept in mind that the measurements received from the meteorological stations are done at a height of 10m, and therefore, this should be taken into account when evaluating the calculated power densities.

$$R^2 = \frac{\sum_{i=1}^n (y_i - z_i)^4 - \sum_{i=1}^n (y_i - z_i)^2}{\sum_{i=1}^n (y_i - z_i)^2} \tag{7}$$

Where yi, is wind speed, xi is the data estimated from the Weibull or Rayleigh distribution. N and zi represent the total number of data and the mean value, respectively. In this equation, R² is between 0 and 1.

Fig. 2 shows the comparison of the Weibull and Ryleigh distributions for 2017 and 2018 data. The values in Fig. 2 are very close to each other. However, Weibull distribution gave better results. It means good results in case the distribution of functions with the fluctuation is 1 and the fluctuation is least.

Table 5: Velocity and Power Prediction of Artvin Stations for the Years 2017-2018 according to Weibull Distribution

Months	k	c	V_m (m/s)	σ (m/s)	fw(v)	Fw(v)	$V_{enolasi}$ (m/s)	V_{maxE} (m/s)	P/A (w/m2)
June 2017	1,1188	2,3138	2,2205	1,9881	0,1852	0,6152	0,3116	5,7849	6,7110
July 2017	1,2572	2,8587	2,6591	2,1290	0,1732	0,5987	0,8091	6,0958	11,5253
August 2017	1,1732	2,8567	2,7034	2,3119	0,1593	0,6083	0,5595	6,6708	12,1114
September 2017	1,1325	2,0042	1,9161	1,6954	0,2172	0,6134	0,3015	4,9213	4,3125
October 2017	1,5023	1,8219	1,6444	1,1150	0,3323	0,5757	0,8786	3,2005	2,7258
November 2017	1,4622	1,5212	1,3778	0,9578	0,3865	0,5790	0,6920	2,7430	1,6032
December 2017	2,3960	1,8296	1,6218	0,7209	0,5232	0,5272	1,4603	2,3569	2,6150
January 2018	1,4968	1,7415	1,5725	1,0698	0,3463	0,5761	0,8336	3,0698	2,3838
February 2018	1,6023	1,7417	1,5614	0,9978	0,3721	0,5680	0,9458	2,8878	2,3334
March 2018	1,4565	1,9790	1,7933	1,2511	0,2959	0,5795	0,8923	3,5821	3,5353
April 2018	1,2163	1,9814	1,8575	1,5346	0,2402	0,6032	0,4791	4,4075	3,9287
May 2018	1,1847	1,6470	1,5545	1,3171	0,2797	0,6069	0,3431	3,7950	2,3027
June 2018	1,1174	2,0625	1,9801	1,7750	0,2074	0,6154	0,2745	5,1661	4,7588
July 2018	1,4085	3,0544	2,7812	2,0016	0,1848	0,5837	1,2685	5,7202	13,1877
August 2018	1,3606	3,0755	2,8164	2,0933	0,1765	0,5882	1,1584	5,9777	13,6938
September 2018	1,3213	2,4849	2,2877	1,7477	0,2113	0,5920	0,8521	4,9921	7,3391

Table 6: Velocity and Power Prediction of Artvin Stations for the Years 2017-2018 according to Rayleigh Distribution

Months	c	V_m (m/s)	σ (m/s)	fw(v)	Fw(v)	$V_{enolasi}$ (m/s)	V_{maxE} (m/s)	P/A (w/m2)
June 2017	2,8854	2,5571	0,9732	0,0449	0,9844	2,0403	4,0805	19,5751
July 2017	3,3005	2,9250	1,1133	0,0142	0,9957	2,3338	4,6676	29,2975
August 2017	3,3961	3,0098	1,1455	0,0106	0,9969	2,4014	4,8029	31,9195
September 2017	2,4179	2,1428	0,8156	0,1300	0,9462	1,7097	3,4194	11,5186
October 2017	2,0234	1,7932	0,6825	0,2612	0,8709	1,4308	2,8615	6,7506
November 2017	1,6220	1,4375	0,5471	0,4353	0,7316	1,1469	2,2938	3,4773
December 2017	1,7075	1,5132	0,5759	0,3974	0,7672	1,2074	2,4148	4,0567
January 2018	1,9356	1,7153	0,6529	0,2974	0,8464	1,3687	2,7373	5,9091
February 2018	1,8280	1,6200	0,6166	0,3438	0,8119	1,2926	2,5852	4,9777
March 2018	2,3107	2,0478	0,7794	0,1601	0,9307	1,6339	3,2678	10,0537
April 2018	2,4653	2,1848	0,8316	0,1181	0,9521	1,7432	3,4865	12,2101
May 2018	2,1715	1,9244	0,7324	0,2055	0,9054	1,5355	3,0709	8,3439
June 2018	2,6906	2,3845	0,9075	0,0721	0,9732	1,9025	3,8051	15,8725
July 2018	3,1702	2,8095	1,0693	0,0208	0,9934	2,2417	4,4834	25,9637
August 2018	3,1060	2,7526	1,0477	0,0250	0,9920	2,1963	4,3925	24,4168
September 2018	1,9596	1,7367	0,6610	0,2873	0,8534	1,3857	2,7714	6,1324

Figure 2: The Comprasion of Weibull and Rayleigh Forn 2017-2018

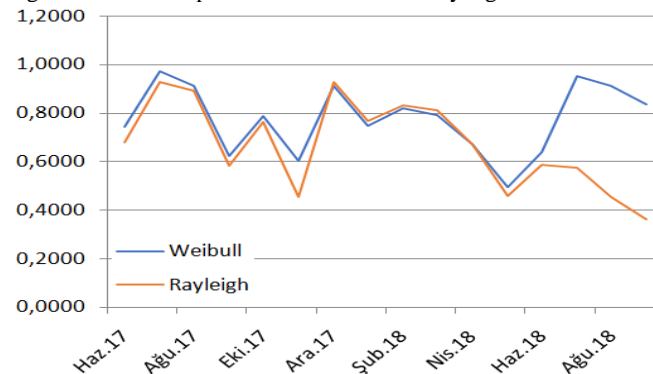


Table 7: The Comparison of Weibull and Rayleigh Distributions According to Determination Coefficient

Months	Weibull	Rayleigh
June 2017	0,7444	0,6797
July 2017	0,9706	0,9280
August 2017	0,9106	0,8938
September 2017	0,6213	0,5845
October 2017	0,7874	0,7662
November 2017	0,6038	0,4566
December 2017	1,4113	1,1281
January 2018	0,7474	0,7676
February 2018	0,8187	0,8342
March 2018	0,7916	0,8100
April 2018	0,6703	0,6708
May 2018	0,4951	0,4612
June 2018	0,6385	0,5896
July 2018	1,0504	0,5758
August 2018	1,0097	0,4538
September 2018	0,8361	0,3633

- [7] M. Kurban, F.O. Hocaoglu, and Y.M. Kantar, "A Comparative Analysis of Two Different Statistical Distributions Used in Forecasting Wind Energy Potential" Pamukkale University Faculty of Engineering, Engineering Sciences Journal, Denizli, 106, 2007.
- [8] Artvin Governorent, <http://www.artvin.gov.tr/> [Visit Date: 25 August 2018], 2018
- [9] Enerji Atlası, <http://www.enerjiatlası.com/gunes/> [Visit Date: 10 August 2018], 2018
- [10] Enerji Atlası, <http://www.enerjiatlası.com/ruzgar/> [Visit Date: 10 August 2018], 2018

VII. CONCLUSIONS

The study has presented a research on the potential of renewable energy sources in Artvin province. The sunshine duration on April, May, June, July, August and September for Artvin province is above the average of Turkey. But, it cannot be said that it has great potential in terms of solar energy. The studies on the utilization of this energy are still insufficient. The wind energy potential of the region was investigated by using Weibull and Rayleigh distributions. The meteorological data are measured at a height of 10 meters. If the measurements are done at 70 meters or higher, the wind potential will be higher and the power density will be changed with this result. weibull and Rayleigh distributions were compared and the weibull distribution is seen to produce more stable results. The expansion of investments in renewable energy sources of Artvin province and the realization of new investments will contribute much for the region's energy supply chain.

REFERENCES

- [1] Teias, <https://www.teias.gov.tr/en/elektrik-istatistikleri> [Visit Date: 15 August 2018], 2018.
- [2] Yegm, <http://www.yegm.gov.tr/MyCalculator/pages/8.aspx> [Visit Date: 10 August 2018], 2018.
- [3] Ekolojist.net, <http://ekolojist.net/ruzgarin-potansiyeli-ne/> [Visit Date: 18 August 2018], 2018.
- [4] Z. Demirkol, M.Cunkas "Renewable Energy Potential of Afyonkarahisar Province ", Eng. Science and Technology. Journal, c.2, p.1, v.2, n.1, 2014 ISSN: 2147-9364, 2014.
- [5] Mgm, <https://www.mgm.gov.tr/dataevaluation/il-ve-ilceler-statistic.aspx?M=ARTVIN> [Visit Date: 18 July 2018], 2018
- [6] K.B. Varınca, M.T. Gönüllü, "solar energy potential and the use degree of potential in Turkey, Management and Prevalence A Study on the" First National Solar and Hydrogen Energy Congress, Eskisehir, 270-274, 2006.

An Overview on Fire Detection Systems

V. DENİZ¹ and M. ÇUNKAŞ²

¹ Selcuk University, Graduate School of Natural Sciences, 42075, Konya/Turkey, vacipdeniz@hotmail.com

² Selcuk University, Electrical-Electronic Engineering Department, 42075 Konya/Turkey, mcunkas@selcuk.edu.tr

Abstract –Unfortunately, thousands of fires occur all around the world every year and of course the fire is a great disaster. These fires cause loss of lives, emotional depressions and loss of labor force in places that affect, additional for huge financial losses. That's why; human beings have constantly developed fire detection and prevention systems. Today, there are many effective and modern systems for fire detection. In this study, methods and techniques commonly used in fire detection are investigated. In addition, the advantages and disadvantages of the examined systems according to experiment and test results are discussed.

Keywords – Fire, fire detection, optic camera, wireless sensor networks, sensor node.

I. INTRODUCTION

Heat, flammable material and oxygen are required for fire to occur. The trees, bushes, dry grasses or many other objects in nature are flammable. If sufficient heat and oxygen come together in an environment where flammable materials are present, fire may occur. After the fire has started, flammable substances in the environment cause the fire to increase more and more. As the fire increases, it becomes increasingly difficult to interfere with the fire. The known rule for intervention when the fire starts is: 1 minute - 1 liter of water, 2 minutes - 100 liters of water, 10 minutes - 1000 liters of water. Therefore, interfering with the fire as soon as possible will significantly prevent the loss of life and property.

Fires occur due to carelessness, frayed materials, arson, natural events etc. For whatever reason, fires destroy thousands of lives, houses, forests etc. every year. Even after the fire is extinguished, it continues to threaten nature and human beings with harmful gases which it has released. For example, 30% of carbon dioxide in the atmosphere comes from forest fires [1]. This causes air pollution, global warming, extinction of rare species and so on.

Many methods have been developed to minimize the effects of fire in the short and long term. In the first phase, the location of fire must be determined precisely and as soon as possible. Today, there are many methods used for this purpose. Some of these are fire detection sensors, unmanned aerial vehicles, satellites, cameras, patrols and watchtowers. A lot of study is underway to perform fast and reliable fire detection systems.

In this article, we examine the most commonly used optical camera and wireless sensor networks for fire detection. We also evaluate these systems in terms of efficiency, accuracy, flexibility, and practical testing

The rest of the paper is organized as follows. After the introduction in section 1, information about Fire Detection and

Alarm Systems is given in Section 2. The Optical Sensor and Digital Camera is deal with in Section 3. The Wireless Sensor Networks are explained in Section 4. It concludes with results and discussion.

II. FIRE DETECTION AND ALARM SYSTEMS

A. Conventional Systems

These systems are fire alarm systems that operate by comparing the values detected by the detectors and the values already set by the manufacturer. They alarm when the threshold value is exceeded. Systems are installed places called "zone" on a single line. Since the alarm works in the zone where it installed, only the zone can be detected. It is not known which detector gives an alarm. A circuit is installed in each zone to identify the fire location. 20-30 detectors or switches can be placed in a zone. The number of zones should be increased to more easily determine the location of the fire. Conventional Systems are inexpensive and do not require programming. But in these systems are used more cables than advanced systems. As Conventional Systems do not take into account the negative effects such as pollution, dusting, drift compensation etc, they are likely to give false alarms over time [23,24].

B. Digital Addressable Systems

The decision-making and alarming characteristics of digital addressable systems are similar to conventional systems. The only difference of these systems from conventional systems is that they provide the address of the alarm information source. By this means, the location of the fire is determined as a point. Point or zone detection can be done using a software. Digital addressable systems use less cable than conventional systems. The system works by comparing the data from the sensor to the initial set value, and cannot make drift compensation. Also there are no maintenance warning elements [23, 25,27].

C. Analog Addressable Systems

In analog addressable systems, sensors are used as end components. Sensors send the data to the panel analogly. According to these data, the panel detects fire, fault, sensor maintenance (dirt, sensitivity, etc.). The system can adjust the sensor sensitivity when there is dirt. If the pollution threshold value is exceeded, it gives a warning of maintenance. The system can automatically adjust sensor sensitivities based on user request or location of sensors. In these systems, the components in the field work like a sensor and obtain data. Since this data carries analog values, it provides great flexibility in processing, deriving data. By using time-

dependent functions, different detectors in the system can be activated at different thresholds. In this way, more precise and error-free detection functions can be obtained [23,26,28].

D. Other Systems

Although there are no standards or certificates in the market, there are many systems that are called intelligent, multi-sensing, fuzzy logic based, interactive, algorithm based etc. Some organizations classify these systems as “distributed intelligence” or “distributed processing”. In Distributed Intelligent Addressable Systems, transactions are performed directly in the detector. A microprocessor located in the detectors determines the fire according to the fire algorithms. In this way, fire detection is made in a shorter time. Multi-sensing systems are systems that detect fire by comparing multiple different sensor data. When the system detects a change in value in any sensor, it also controls the values of other sensors. Monitoring multiple sensor values reduces the possibility of false alarms. This kind of systems; Photoelectric + Temperature + Ionization, Photoelectric + Temperature, Photoelectric + CO₂ + Temperature sensors are used more. Sometimes the sensors may not reach the threshold value in case of fire. Therefore, algorithms have been developed that give alarm by scanning the process even if the threshold value is not reached [23, 29-32].

III. OPTICAL SENSOR AND DIGITAL CAMERA

Most of the optical systems used for fire detection works according to the logic of recognition of smoke and flame. In these systems, the camera regularly sends the image data to the system. The system algorithm scans the smoke and flame shape of the images and determines if there is a fire. If there is fire in the environment, it informs the authorities by alarm, message etc. It also offers remote surveillance by using a simple monitor.

Many systems have been developed that use visual sensors to eliminate limitations such as the necessity to go to fire location [2-5].



Figure 1: Fire 100%, Normal 0% [6].

The Convolutional Neural Networks Method is one of the most effective methods used to process visual data.

Muhammed et al. [6] developed an early fire detection system using The Convolutional Neural Network Method for effective disaster management. When fire as soon as started with the small size, they detected at the high rate. To this aim, they trained their model with 10,319 images. The 5258 images comprise fire and 5061 images don't comprise fire. After fine tuning, they had fire detection with 94.39% accuracy. Figure 1 and 2 show some images related to the tests. As it is known, each color is formed by combinations of 3 main colors. There are many different colors forming of these colors on a picture. These 3 main colors usually form the color space of a picture. However, different color spaces are used to make the colors more live or bright.



Figure 2: Fire 5.19%, Normal 94.81% [6].

Vipin [7] has introduced a new approach to detect forest fires using image processing technique. The algorithm is developed for this system utilizing RGB and YCbCr color space. YCbCr color space is used because YCbCr color space separates brightness better than the RGB space. The system is tested using fire images and images similar to fire. With the developed algorithm, 99% flame detection rate and 14% false alarm rate have been obtained. Figure 3 shows some examples of experimental pictures.

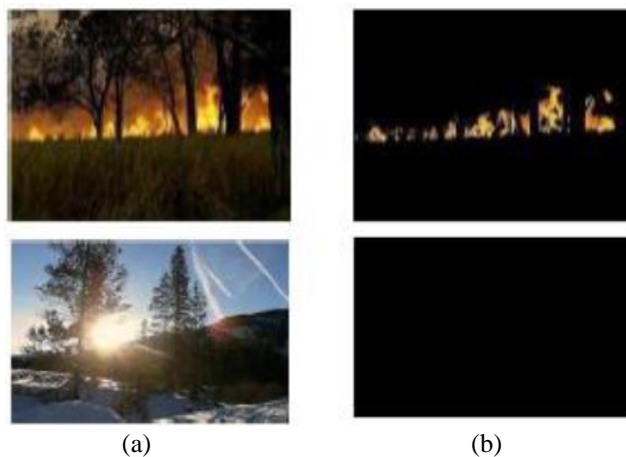


Figure 3: Experimental Results (a) Input images, (b) corresponding output images [7].

Fire detection using the optical camera is mostly used in forest areas. For this purpose, many countries have developed systems to detect forest fires. EYEFi forest fire detection

system having the following features was developed Australia[11].

- Camera having colorful during the day and ultra-light grayscale at night,
- Weather station,
- Lightening detection sensor,
- Communication unit(0.25 Mbps),
- Power system.

In addition, thermal or pan tilt zoom cameras can be included in the system. When the system detects smoke, it obtains images for the authorities and determines the location of the fire using the GIS map. In order to get a more accurate result, a lighting detector and a weather station are installed to system [8,9].

The ForestWatch is an optical camera sensor system which produced by Enviro-Vision Solutions in South Africa provides semi-automatic fire detection A tower camera makes a fire flame scan during the night, smoke through the day. Fire detection can be in the range of 16-20 km. and then fire status can notify with 0.25Mbps 3G or microwave connection. [9].

The ForestWatch have the following features [10,11].

- A Pan tilt camera for a 360° rotation and +33 to -83 tilt from horizon, with 24x optical zoom,
- Image sampling engine,
- Communications system such as 3G, microwave, or satellite,
- ForestWatch software.

FireWatch [11] is an automatic smoke detection system capable of detecting smoke in the range of 10-40 km. Since 1992, Germany has worked on this system. It currently is produced by the German Aerospace Institute. Operational FireWatch systems are used in Germany (178 towers, 22 control rooms), Estonia (5 towers, 1 control room), Cyprus (2 towers, 1 control room) and Mexico (1 tower, 1 control room). Pilot scale systems (1 or 2 towers) are used in the Czech Republic, Portugal, Spain, Italy, Greece and the USA. [9,34].

With the improved IQ FireWatch technology, smoke plumes up to 60 km can be detected in excellent weather conditions and visibility. In foggy and cloudy weather, this distance decrease to 15 km. Therefore, it is reliable up to 15 km.

A project is conducted to compare EYEfi, ForestWatch, FireWatch systems and human tower observer. The results of the research by Mathews et al. are shown in Table 1.

Table 1: New South Wales tests [9].

Test Type	Number of Reported Fires			
	Eyefi	Forest Watch	Fire Watch	Tower Observer
Six research fires ignited in Tumut	0	0	1	6
Six stationary fires including 2 at night	0	3	3	-

The results show that a well-educated individual performs better fire observation. These systems can be used to help with

fire detection. It is difficult for human to see a fire smoke at night but it can be easier to detect smoke with the help of these systems. Systems with camera or optical sensors in the indoor or open areas are affected by light, daylight, moving clouds, vegetation, shadow, etc. conditions. For this reason, fine-tuning should be done very well.

Burnett and Wing [34] investigated the effectiveness of a near-infrared (NIR) camera in a transformed record for fire detection. To compare their performance, eleven burning oblique stakes are simultaneously visualized with both NIR and camera-sensitive red, green, and blue (RGB) lights. Numerical differences in the contrast and flame size of the image from the fire are compared between paired NIR and RGB images. Quantitative analysis is performed with the Maximum Likelihood Classifier in ENVI, and the differences between contrast ratios and flame dimensions are statistically evaluated using the randomization test. The authors argue that the results are statistically significant in terms of contrast ratio and flame size in all NIR images, and also state that this technology can be evaluated as an alternative to the proven thermal sensors and can fill an important gap in fire detection.

Çelik [39] presented a computer-based fire detection algorithm to eliminate false alarms of conventional fire detection systems. In order to eliminate false alarms, the algorithm consisting of two main parts, fire color modeling and motion detection, can be utilized simultaneously with conventional fire detection systems. It can also be used as a standalone system for the detection of fire using video frames obtained through a video capture. To identify fire pixels, the fire color model is developed in the CIE $L^*a^*b^*$ color area and tested with ten different video sequences, including different types of fire. The moving pixels are separated from non-moving pixels using a background extraction algorithm with a frame differentiation algorithm on the frame buffer filled with successive frames of the input video. The mobile pixels, also perceived as fire pixels, are analyzed in successive frames to raise a fire alarm. The fire color model is tested in ten video images with various imaging conditions and achieved a success rate of 99.88%.

Şahin and İnce [40] developed a fire detection system based on remote temperature measurements and thermal perceptions of a particular forest area by using the radio-acoustic sounding (RASS) system. Unlike conventional systems based on smoke detection, the high resolution RASS technique can measure air temperature profiles directly and continuously. An alternative method for detection of forest fires is presented thanks to remote thermal mapping of a particular forest region.

IV. WIRELESS SENSOR NETWORKS

Sensor networks that collect and distribute environmental data are wireless networks of small, low-cost sensors. The wireless sensor networks make it easier to monitor and control physical environments with better accuracy than remote locations. [13]. There are applications in various fields such as environmental monitoring, indoor climate control, medical diagnostics, disaster management, emergency response, ambient weather monitoring and collection of sensing

information in areas where it is difficult to live. [14-17]. Wireless sensor networks use the IEEE 802.15.4 ZigBee communication protocol. The ZigBee protocol is a technology developed to operate wireless sensor networks at low power and low cost. The wireless sensor networks are also used in fire detection systems due to their flexible usage characteristics. First, the wireless sensors are placed in the fire detection zone. These sensors can communicate with each other and to the system center. They report the fire situation by calculating according to their algorithms when there is a fire sign.

Sensors placed in the data collection area have their own batteries, circuits, receivers and transmitters. Since it is not always possible to charge the batteries regularly, the systems with low power consumption have been developed.

Zhan et al [35] proposed a wireless sensor network method using a ZigBee for forest fire detection. The wireless sensor network structure for forest fire detection is designed in real-time using the CC2430 chip in the hardware of the network node. Environmental parameters such as temperature and humidity can be monitored in real time in the forest region. They say that fire-fighting or prevention can be done quickly according to the information obtained.

Luis et al. [18] designed a low-power wireless smoke alarm system. The system includes smoke, carbon monoxide and temperature sensors to reduce false alarms. In order to save power, the sensors work only when collecting data. In sleep mode, the transceiver is canceled, but thanks to the protocol developed, messages are not lost. The average energy consumption of the system is 36 μ Ah. Thus, 6 3V @ 1600 mAh (CR123 type) the battery when used can run for about 5 years. False alarms are decreased thanks to various sensors (temperature, smoke and CO) used. This increases the reliability of the system. In addition, the system can be controlled by an application on the mobile phone and detect fire status. A general structure is shown in Figure 4.

Son et al. [19] presented the Forest-Fires Surveillance System (FFSS) using wireless sensor networks for forest fires. Sensors in the system detect humidity, temperature and light. For less energy consumption, each node chooses the shortest path and reaches Sink. For providing this they used the Minimum Cost path Forwarding (MCF) protocol. In addition fire status is followed by a Web application.

Yu et al. [20] proposed a real-time forest fire detection using a wireless sensor network. The neural network method is used to process data in the network. System performance is tested by simulation. Five simulation scenarios having different number of nodes and different field sizes are tested. Thanks to this method, the communication load is reduced. So the reduction of the communication load will also reduce energy consumption.

Bouabdellahaet al. [36] discussed in detail the Canadian and Korean fire detection methods employed in hardware schemes and applied algorithms and compared using a real experimental approach. A sensor test bed is based on the MICA-Z plate form of Crossbow™ Company. Experimental studies were carried out in the forests of the city of Oran in the western part of Algeria, especially during the summer season.

According to the results, it was found that the Canadian approach was better in terms of energy consumption and execution speed.

Hartung et al. [21] developed a portable FireWxNet system to monitor weather conditions in uneven wild terrain. 3 sensor networks and 2 webcams in the system collected data for 1 week. Tests are carried out in areas where there is no access to electricity and internet. Abnormal changes are observed in the weather data obtained by the system when a fire broke out. With this data, fire direction and fire direction can be determined more easily. In addition, the weather data of the region where the system is located can be used for different purposes.

Díaz-Ramírez et al. [37] proposed two algorithms based on fusion techniques for forest fire detection. The first algorithm determines the fire alarm according to the threshold values by using the data from the temperature, humidity and light sensors. The second algorithm utilizes the data from the temperature and humidity sensors to determine the fire alarm with the help of the Dempster Shafer theory. Authors say that both methods can effectively detect the forest fires.

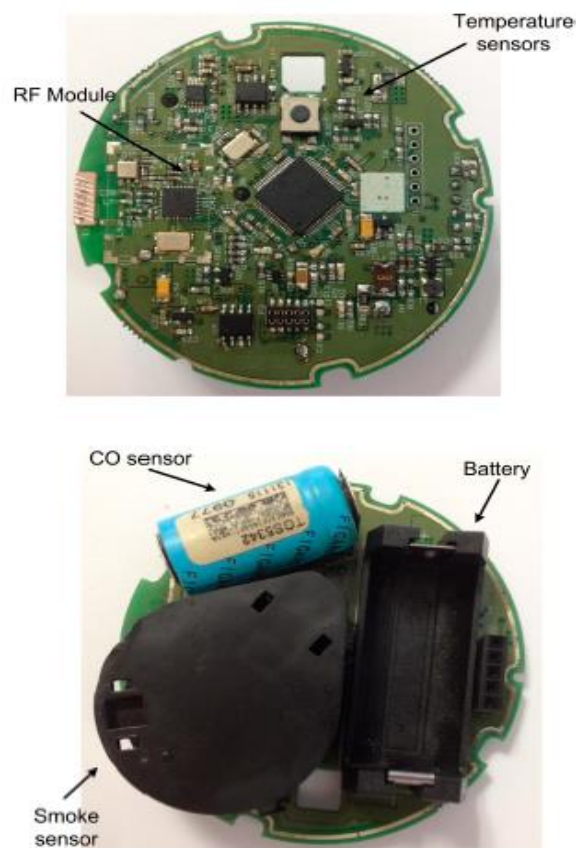


Figure 4: Main board of the fire sensing device [18].

Yazar [22] designed a fire warning system using wireless sensor networks. There is one sensor node in the system. Only the temperature sensor is used in the node. The critical status message appears on the LCD display when the sensor temperature is 40-60 ° C. If the temperature is 60 ° C and above, the LCD screen will display the fire alarm status message and the latitude and longitude information. With an interface program developed, the fire place can be observed on

the map. Although the added hardware (LCD display) provides ease of use, the false alarm rate will increase because only the temperature sensor is used.

Dener et al. [37] discussed the working procedures of the fire systems formed by wireless sensor networks by an exemplary application. First of all, the sensor networks, which are gateway and coordinate nodes, have been installed in the system's installment zones. The user then enters the system and can observe the data from the wireless sensor networks. The markings containing the temperature information are placed according to the information of the coordinates from the nodes. Thus, color changes were made by taking into account the temperature conditions of all the regions added. Then, it was determined in which area there is fire through the temperature data from the regions and the coordinate information from the nodes

V. DISCUSSION

In this section, properties of optical cameras and wireless sensor networks used in fire detection are discussed.

The features of the optical cameras are given as follow:

- It works only using visual data.
- Systems in open areas and wild terrain are affected by many factors, such as trees, weather conditions, slope, distance, height, etc.
- Since existing systems are mostly designed to observe long distances in forested areas, it is difficult to detect fires in distant areas as soon as they start.
- Since it is very affected by light, its sensitivity should be adjusted well. Otherwise the false alarm rate is increasing.
- When used in houses, feeling of constant monitored by cameras may disturb people.
- The system cost is high.
- Cameras can be used for security purposes by monitoring the environment.

The features of the wireless sensor networks are given as follow:

- Data can be obtained from many different sensors.
- It can be placed in hard-to-reach places.
- The system can connect for many different devices.
- Since the network can be expanded, it can be applied to very large areas.
- Fire localizing accuracy is high.
- They can collect many physical data from environment. These data can be used in different scientific fields.
- Cost is medium.
- They don't consume much energy.

VI. CONCLUSION

In this study, optical camera and wireless sensor networks are discussed as fire detection systems. The studies in the literature have been examined and a comparison has been done on fire detection systems. Optical camera systems when compared to Wireless Sensor Networks are more expensive and are less sensitive due to environmental conditions. The Wireless Sensor Networks detection systems are characterized by the fact that energy consumption is more economical and the Network can be expanded to any size or any place.

REFERENCES

- [1] An Inconvenient Truth, "Directed by Davis Guggenheim about former United States Vice President Al Gore's campaign [Documentary]," Los Angeles, NY, USA, 2006.
- [2] T. Qiu, Y. Yan, G. Lu, "An autoadaptive edge-detection algorithm for flame and fire image processing," *IEEE Trans. Instrum. Meas.* 61 1486–1493, 2012.
- [3] C.-B. Liu, N. Ahuja, Vision based fire detection, in: *Proceedings of the 17th International Conference on Pattern Recognition, ICPR 2004*, pp. 134–137, 2004.
- [4] T. Celik, H. Demirel, H. Ozkaramanli, M. Uyguroglu, Fire detection using statistical color model in video sequences, *J. Vis. Commun. Image Represent.* 18 176–185, 2007.
- [5] B.C. Ko, S.J. Ham, J.Y. Nam, Modeling and formalization of fuzzy finite automata for detection of irregular fire flames, *IEEE Trans. Circuits Syst. Video Technol.* 21 1903–1912, 2011.
- [6] K. Muhammad, A. Jamil, and S.W. Baik, "Early fire detection using convolutional neural networks during surveillance for effective disaster management." *Neurocomputing* 288 : 30-42, 2018.
- [7] V. Vipin, "Image processing based forest fire detection." *International Journal of Emerging Technology and Advanced Engineering* 2.2 : 87-95, 2012.
- [8] *EUFOFINET Project Detection Synthesis of Good Practices*, National Forest Centre, Zvolen, Slovakia.
- [9] S. Mathews, P. Ellis, and J. H. Hurle, "Evaluation of Three Systems." *Australia: Bushfire Cooperative Research Centre*, 2010.
- [10] K. Hough, "Vision Systems for Wide Area Surveillance: ForestWatch—a long-range outdoor wildfire detection system." *TASSIE Fire Conference Proceedings*, <https://doi.org/10.1017/CBO9781107415324>. Vol. 4. 2007.
- [11] A. A. Alkhatib "A Review on Forest Fire Detection Techniques". *International Journal of Distributed Sensor Networks*, Article ID 597368, 12 pages, 2014. <https://doi.org/10.1155/2014/597368>.
- [12] FireWatch, "Why FireWatch", 2018 Available: <https://www.iq-firewatch.com/technology>
- [13] H. Karl, and Andreas Willig. *Protocols and architectures for wireless sensor networks*. John Wiley & Sons, 2007.
- [14] D. Culler, D.Estrin, and M. Srivastava, "Guest editors' introduction: Overview of sensor networks." *Computer* 37.8 : 41-49, 2004.
- [15] K. Martinez, J.K. Hart, and R. Ong, "Environmental sensor networks." *Computer* 37.8 : 50-56, 2004.
- [16] A. Mainwaringet, D. Culler, J. Polastre, "Wireless sensor networks for habitat monitoring." *Proceedings of the 1st ACM international workshop on Wireless sensor networks and applications*. Acm, 2002.
- [17] I.F. Akyildiz, D. Pompili, and T. Melodia, "Underwater acoustic sensor networks: research challenges." *Ad hoc networks* 3.3 : 257-279, 2005.
- [18] J. A. Luis, J. A. G. Galán, and J. A. Espigado. "Low power wireless smoke alarm system in home fires." *Sensors* 15.8 : 20717-20729, 2015.
- [19] B. Son, Y. Her, and J.G. Kim. "A design and implementation of forest-fires surveillance system based on wireless sensor networks for South Korea mountains." *International Journal of Computer Science and Network Security (IJCSNS)* 6.9 : 124-130, 2006.
- [20] L. Yu, N. Wang, and X. Meng. "Real-time forest fire detection with wireless sensor networks." *Wireless Communications, Networking and Mobile Computing, 2005. Proceedings. 2005 International Conference on*. Vol. 2. IEEE, 2005.

- [21] C. Hartung, R. Han, C. Seielstad, S. Holbrook, "FireWxNet: A multi-tiered portable wireless system for monitoring weather conditions in wildland fire environments." *Proceedings of the 4th international conference on Mobile systems, applications and services*. ACM, 2006.
- [22] M. Yazar, "Fire warning system with wireless sensor networks," master's thesis, Yildiz Technical University Institute of Science and Technology, Istanbul, 2015.
- [23] T. Ataylar, "Conceptual Separation of Fire Detection Systems and Basic Differences Between Systems" Available: http://www.emo.org.tr/ekler/c9e5d0c06befbe4_ek.pdf
- [24] S.-W., Jee, et al., "Development of a Traceable Fire Alarm System Based on the Conventional Fire Alarm System. *Fire Technology*", 2014. 50(3): p. 805-822.
- [25] J. Cheon , J. Lee , I Lee, Y. Chae, Y. Yoo, G. Han " A single-chip CMOS smoke and temperature sensor for an intelligent fire detector". *IEEE Sens J* 9(8):914–921,2009
- [26] CT Kim, SK Hong, YS Yoo, HS Jung "A study on design and implementation of an analog addressable detector and a fire alarm system". *J Korean Inst Fire Sci Eng* 24(4):1–11, 2010.
- [27] G Jiang, F Shang, F Wang, X Liu, T Qiu "A combined intelligent fire detector with BP networks". In: *Proceedings of the 6th world congress on intelligent control and automation*, pp 5417–5419, Jun 2006
- [28] SK Kim, SW Jee, CH Lee, SH Yang, JJ Lee, PY Kim. " A study on the necessity of addressable fire detector. In: *Proceedings of 2010 autumn annual conference, Korean Institute of Fire Sci &Eng*, pp 175–179.
- [29] Xihuai W, Jianmei X, Minzhong B (2000) Multi-sensor fire detection algorithm for ship fire alarm system using neural fuzzy network. In: *Signal processing proceedings, 2000. WCCC-ICSP 2000. 5th international conference, vol 3*, pp 1602–1605
- [30] O Gunay, K Tasdemir, B. Ugur Toreyin, A Enis. "Fire detection in video using LMS based active learning". *Fire Technol* 46(3):551–577, 2010.
- [31] Y Qiongfang, Z Dezhong, F Yongli, D Aihua . "Intelligent fire alarm system based on fuzzy neural network". In: *ISA 2009. International Workshop*, pp 1–4
- [32] SL Rose-Pehrsson, SJ Hart, TT Street, FW Williams, MH Hammond, DT Bottuk, MT Wright, JT Wong. " Early warning fire detection system using a probabilistic neural network". *Fire Technol* 39(2):147–171, 2003.
- [34] J. D. Burnett and M. G. Wing. "A low-cost near-infrared digital camera for fire detection and monitoring", *International Journal Of Remote Sensing*, 39(3), 741–753, 2018.
- [35] J Zhang, W Li, N Han, J Kan "Forest fire detection system based on a ZigBee wireless sensor network". *Frontiers of Forestry in China* 3(3):369-374, 2008.
- [36] K. Bouabdellaha , H. Noureddine, S. Larbi "Using Wireless Sensor Networks for Reliable Forest Fires Detection" *Procedia Computer Science*, 19, 794–801, 2013.
- [37] M. Dener, Y. Özkök, C. Bostancioglu. "Fire Detection Systems in Wireless Sensor Networks". *Procedia - Social and Behavioral Sciences* 19, 1846–185, 2015.
- [38] A. Díaz-Ramírez, L.A. Tafoyaa , J.A. Atempaa , P. Mejía-Alvarez. "Wireless Sensor Networks and Fusion Information Methods for Forest Fire Detection", *The Iberoamerican Conference on Electronics Engineering and Computer Science*, May 16-18, Guadalajara, Mexico, 2012.
- [39] T. Çelik "Fast and Efficient Method for Fire Detection Using Image Processing" *ETRI Journal*, 32(6),881-890, 2010
- [40] Y.G. Sahin,. and T. Ince. "Early Forest Fire Detection Using Radio-Acoustic Sounding System." *Sensors* 9(3), 1480-1498, 2009.

A Novel Passive Filter to Eliminate Harmonics in Stand-alone DFIG with Non-linear Loads

Ç. KOÇAK¹, M.DAL², K. TOPALOĞLU³, and M.YEĞİN⁴

Kocaeli University, Kocaeli/Turkey, cgykck105@gmail.com¹

Kocaeli University, Kocaeli/Turkey, mdal@kocaeli.edu.tr²

Aktif Group, Istanbul/Turkey, kazim.topaloglu@aktif.net³

Kocaeli University, Kocaeli/Turkey, Kocaeli/Turkey, emy@kocaeli.edu.tr⁴

Abstract - In this study, a novel design approach proposed for a single-tuned passive filter is presented. The design approach based on a trial and error method aims to improve suppression capability of single-tuned filters group for specific harmonics originating from non-linear loads. Both the proposed single-tuned filter and the standard one are tested through comparative simulations for a stand-alone wind power generation system integrated with doubly-fed induction generator (DFIG) with non-linear loads. The simulation results derived using PLECS verify that the proposed method is more effective than the single-tuned filter which is used traditionally in power system applications.

Keywords –Harmonic elimination, doubly fed induction generator, harmonic filter, and energy quality.

I. INTRODUCTION

THE energy quality, which is described broadly in [1-2], became a more critical issue, and nowadays in power generation systems due to global increase in diversification of energy productions and their imperfect impact with the power electronics converters to national grid network. On the other hand, since the last two decades, the doubly fed induction generator (DFIG) has been used as one of popular choices for modern variable speed wind power generation systems due to its beneficial factors such as the size and cost associated with PWM back-to-back power electronic converters. However, harmonics generated by the back to back power converters and non-linear loads connected at the point of common coupling (PCC) are the most important factors in power quality worsening. In practical applications several types of single-tuned filters are usually used to eliminate the effects of these undesired harmonics in power generation systems. Among these filters, the single-tuned filter is one of the most popular passive filter used for the purposes of compensate the reactive power and to reduce the current harmonics [3].

In this study, a novel design approach based on trial and error method of a single-tuned filter is proposed to eliminate high magnitude harmonics generated by non-linear balanced loads. In order to adopt the proposed single-tuned filter to wind power systems, operational analyzes of a stand-alone DFIG under non-linear load are focused in terms of energy quality improvement. A design procedure which is commonly used for the standard single-tuned filters in power systems applications is adapted to the proposed filter design. However, in order to augment the capability of the proposed filter in

elimination of high magnitude harmonics several novel empiric formulas are introduced which can be used to determine the filter parameters of L , C , and L_s . The analysis of harmonics is carried out using fast Fourier transform (FFT) to evaluate the total harmonic distortion (THD) of the load currents with and without filters. The PLECS is used for simulation tests, which is one of the well-established and recognized simulation software for the power electronics systems [4].

This paper is organized as follows: Section II summarizes harmonic reduction techniques used for a stand-alone DFIG based wind power system. Section III, explains the proposed filter design procedure, and describes structure of stand-alone DFIG system shortly. Comparative simulation tests and obtained results are presented in Section IV. In the conclusion section the effectiveness of the proposed filter respect to the standard passive filters is concluded in terms of harmonic reduction capability.

A. Harmonic reduction techniques

In stand-alone operated DFIG based wind power generation systems, load types and demanded power connected to the stator of DFIG are normally unpredictable. Therefore, in these systems, reactive power compensation and harmonic reduction is a serious requirement for improvement of the power quality and consumers' satisfaction. Harmonic reduction techniques that are suggested for the stand-alone operated DFIG can be categorized into three different methods:

- Passive filters (L , LC , and LCL) are commonly used to eliminate especially harmonics generated by the PWM converters that are taken place at the rotor side (RSC) and the load side (LSC) and loads. Overview of the methods associated to harmonic filter design for renewable energy systems can be found in [5-7], and the references therein. However, there are also some alternative suggestions aimed to eliminate harmonics generated by non-linear loads that directly connected to the stator of the DFIG [8-9].
- The control based harmonic elimination technique considers reducing load harmonics by establishing a separate current control loop of the RSC for each harmonic component, but, this technique complicates the rotor side current control structure [10-11].

- Active parallel filters are aimed to inject opposite harmonics through the RSC into the rotor winding to compensate undesired harmonics. This method increases the losses and noise in the machine and also the rating of the RSC converter [12-14].

B. Stand-alone DFIG with Non-linear Loads

For proper operation of a stand-alone DFIG, constant stator voltage and constant frequency are required for local consumers. However, under non-linear load conditions the stator current and voltage waveforms of the DFIG are badly influenced with contents of undesired harmonics. In order to examine behavior of the stand-alone DFIG under the non-linear load conditions, a three-phase six-pulse diode rectifier with resistive load can be considered. In this case, non-linear loads connected to the DFIG deteriorate the stator voltage quality due to occurred current harmonics. Especially 5th and 7th harmonics are the most harmful once for overall the system and directly affects the performance of other loads connected to the PCC of the same power system. In power systems, the current and voltage THD factor should be acceptable in the limits of international standards according to IEC 519-1992, where the accepted limits are 3.08% for the voltage and 5% for the current at PCC (the point of common coupling) [15]. Therefore, passive filters are commonly used for eliminating undesired harmonics in power systems.

II. PROPOSED PASSIVE FILTER

The passive filters consisting of capacitors, inductors and/or resistors as shown in Fig.1 can be classified into two major types: tuned filters and high-pass filters. They are used traditionally in power system applications connecting in parallel with the non-linear loads, aiming to compensate the reactive power of the system and rejecting undesired dominant frequencies of voltage and current signals. For designing these filters, there are different approaches focusing to minimize the filter power losses, and to reduce the voltage and current distortions. Comparison of these design approaches is summarized in [6-7].

The proposed filter structure in this study is similar with the single-tuned one, which is the most popular in power system applications. However, the proposed filter is aimed to improve capability of suppressing high magnitude harmonics distortions. To achieve this goal with the proposed filter, compared to the standard filters, a larger sized inductance and a capacitance are required for the LC filter. In this case it's possible that the filter capacitors can receive a high magnitude capacitive current at rated frequency from the grid, and therefore, unnecessarily an over reactive power compensation can occur. In order to prevent the proposed filter from these undesired phenomena, it is suggested to combine LC filter elements with a star connected shunt inductance, L_s as shown in Fig.2.

A. Single tuned filter design procedure

The single-tuned filter (which is also called low-pass filter (LPF)) and the high-pass filter are most preferred ones in power systems applications, because the simplest to design and the lowest cost to implement. They are generally used as

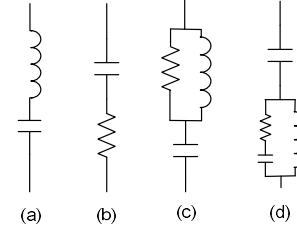


Figure 1: Proposed filter structure, a) single tuned, b) 1st-order high-pass, c) 2nd-order high-pass, 3rd-order high-pass

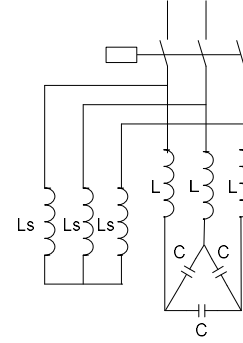


Figure 2: Proposed filter structure

group filters; for example, a group of single tuned filter is used to eliminate 5th, 7th, 11th, and 13th harmonic and the second order high-pass filter for 17th, 23th and 25th harmonics [3].

For the single tuned filter, the impedance of LPF is given by:

$$Z = R + j(2\pi \cdot f_n \cdot L) - \frac{1}{2\pi \cdot f_n \cdot C} \quad (1)$$

The reactive power requirement Q_{cn} for a specific harmonic is given by

$$Q_{cn} = \frac{Q_{net} \cdot u_{cn}^2 \cdot (f_r^2 - f_g^2)}{u_n^2 \cdot f_r^2} \quad (2)$$

where, Q_{net} is net reactive power required by the grid and f_r is harmonic number. The inductance and capacitance of the filter for specific harmonic frequencies are obtained from the following equations:

$$X_c = \frac{V_{ph}^2}{Q_{cn} \cdot f_n}, \quad X_L = \frac{X_c}{f_n^2} \quad (3)$$

However, in the most of applications, the standard values of these parameters are determined for a certain frequency of 189Hz as follows

$$L = \frac{f_g \cdot u_{cn}^2}{2\pi \cdot f_r^2 \cdot Q_{cn} \cdot 10^3}, \quad C = \frac{Q_{cn} \cdot 10^9}{2\pi \cdot f_g \cdot u_{cn}^2 \cdot 10^3} \quad (4)$$

A group of single-tuned LC filters with these values is used together for suppression of the dominant harmonics.

B. The design procedure of the proposed filter

The design procedure of the proposed filter requires the measurements of current and voltage, and the harmonic content of power system should be analyzed first according to these measurement results. Then using the Fourier series expansion for both the measured current and voltage, the peak values of each current harmonics and voltage harmonics are determined. In the next step, using the current and voltage peak values (V_p and I_p), obtained from Fourier series, The load current I_{rms} value and voltage V_{rms} value, and harmonic apparent power S_h are calculated for each identified dominant harmonic which has to be suppressed. In order to calculate filter parameters L , C , and L_s using the measured data, few empirical formulas are introduced in this study:

The load current and voltage *rms* values are given by

$$V_{rms} = \sqrt{V_1^2 + V_3^2 + V_5^2 + V_7^2 + V_{11}^2 + \dots + V_{19}^2} \quad (5)$$

$$I_{rms} = \sqrt{I_1^2 + I_3^2 + I_5^2 + I_7^2 + I_{11}^2 + \dots + I_{19}^2} \quad (6)$$

The total harmonic power

$$s_h = I_5V_5 + I_7V_7 + I_{11}V_{11} + \dots + I_{19}V_{19} \quad (\text{VA}) \quad (7)$$

The voltage across the filter capacitor

$$u_c = \left(\frac{f_g - 5}{f_g + 5} + \frac{5}{f_g} \right) V_{rms} \quad (8)$$

The shunt reactance

$$L_s = \frac{u_c^2 \cdot S_h \cdot (f_m^2 - f_g^2)}{2 \cdot \pi \cdot f_g \cdot f_m^2 \cdot I_{pn} \cdot V_{pn} \cdot I_{rms} \cdot V_{rms} \cdot \sqrt{3}} \quad (H) \quad (9)$$

The filter L-C parameters

$$L = \frac{u_c^2 \cdot S_h \cdot f_g}{2 \cdot \pi \cdot f_m^2 \cdot I_{pn} \cdot V_{pn} \cdot I_{rms} \cdot V_{rms} \cdot \sqrt{3}} \quad (H) \quad (10)$$

$$C = \frac{I_{pn} \cdot V_{pn} \cdot I_{rms} \cdot V_{rms} \cdot \sqrt{3} \cdot 10^6}{S_h \cdot 6 \cdot \pi \cdot f_s \cdot u_c^2} \quad (\mu F) \quad (11)$$

where f_g is the rated frequency (50 Hz) of the grid, $f_m (= f_n - n)$ active harmonic frequencies, n is order of harmonic, f_n is n^{th} harmonic frequency, and I_{pn} and V_{pn} are the peak value of n^{th} harmonic current and n^{th} harmonic voltage.

At the calculations stage, when designing a filter for any harmonic component, a low symbolic internal R resistance was added to represent the internal ohmic resistance of the capacitor and reactor groups for the internal R resistance of the filter. The short-circuit current (I_{sc}) and the demand current (I_{rl}) of the current source must be determined in the system [15]. It is determined when the outputs of the power source are shortened and the star point is grounded. Then, the largest demanded current, drawn from the source to the loads, is measured and the ratio I_{sc}/I_{rl} is used to determine the THD of the current harmonics as given in Table 1.

Table 1: Harmonic level depends on ratio, I_{sc}/I_{rl}

I_{sc}/I_{rl}	<11	11≤h<17	17≤h<23	23≤h<35	35≤h	THD
<20°	4.0	2.0	1.5	0.6	0.3	5.0
20°<50	7.0	3.5	2.5	1.0	0.5	8.0
50°<100	10.0	4.5	4.0	1.5	0.7	12.0
100°<1000	12.0	5.5	5.0	2.0	1.0	15.0
>1000	15.0	7.0	6.0	2.5	1.4	20.0

III. SYSTEM STRUCTURE AND SIMULATIONS

A. Structure of stand-alone DFIG system

A stand-alone DFIG system structure used in the simulation tests is depicted in Fig.3. As shown in the figure, a prime mover machine (i.e. in applications) a wind turbine or

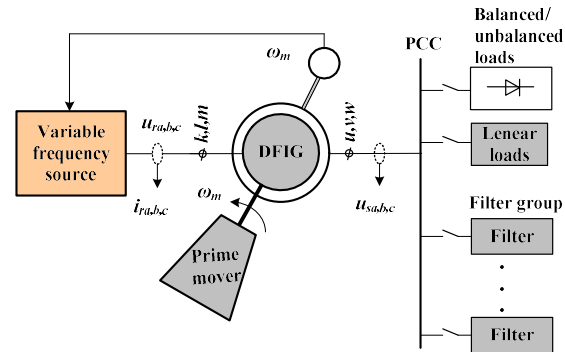


Figure 3: System structure used in simulations

combustion engine rotates the DFIG rotor shaft, and a variable frequency source supplies the rotor winding; the voltage applied to the rotor winding is adjusted depending on rotor shaft speed, so that the magnitude and frequency of the voltage on the stator terminal can be automatically regulated to the rated values. Local loads (linear or non-linear) are directly connected to the stator. Normally, the back-to-back converters are necessary required component of the DFIG based wind power systems. However, in this study, it is disregarded to simplify the system structure. The parameters of the DFIG used in the simulation are listed in Table.2.

A stand-alone DFIG system model with non-linear load is built using PLECS software, as shown in Fig. 4. It is considered to analyze the harmonics originating from the loads, and to evaluate the total harmonic distortion (THD) of the load currents with/without filters.

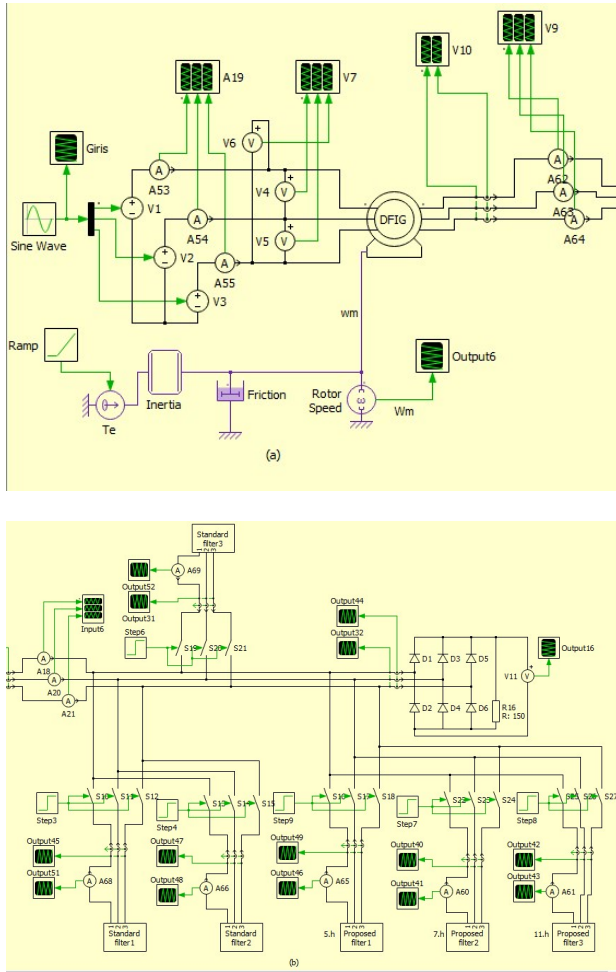


Figure 4: a) PLECS model of DFIG and power source used simulation, and b) model of a non-linear load and filters.

Both the standard single-tuned filter and the proposed filter with shunt reactance are shown in Fig. 5. The parameters of both filters used in simulation model are calculated using the following data: The voltage pick value, V_{peak} 534V (phase-phase), I_{peak} is 3.56A, the phase angle 360, and $\text{Cos}(\varphi)=0.80$.

B. Simulation results

The first simulation test is carried out running the DFIG system without filter in order to measure the voltage and current peak values, which are listed in Table 3. In this case, the effect of the harmonics on the load current waveform is observed for a non-linear load and then a phase current waveform and its harmonics spectrum are shown in Fig.6.

A second simulation test is carried out with/without filters for the same non-linear load. First, a standard filter is examined in terms of harmonic elimination capability, and secondly the proposed filter tested with the same non-linear load.

Table 2. The DFIG parameters

Stator voltaji	380 V
Rotor voltaji	190 V
Ölçülen hız (50 Hz)	1447 r.p.m.
Stator direnci	0.325 ohm
Rotor direnci	0.275 ohm
Manyetizma endüktansı	0.0664 H
Stator kaçak endüktansı	0.00264 H
Rotor kaçak endüktansı	0.00372 H
Eylemsizlik moment (inertia)	0.07 Kg.m ²

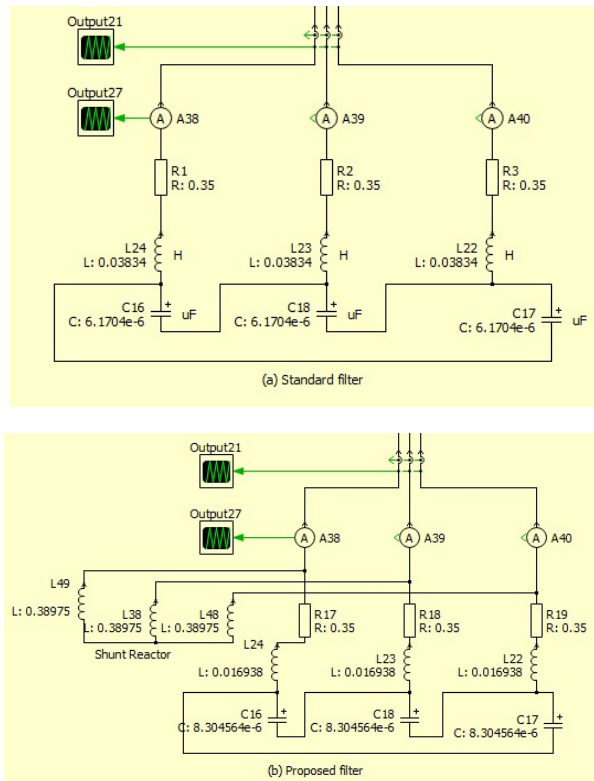
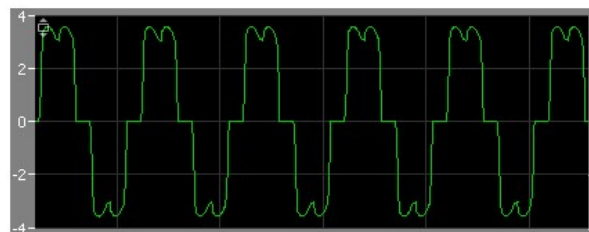


Figure 5: PLECS model of filters for 5th, a) standard, and b) proposed

Table3: Harmonic components peak values

Harmonic order (without filter)	1	5	7	11
I _{peak}	3,67	0,852	0,344	0,304
V _{peak}	534,09	13,675	10,868	10,895



(a) A phase-load current

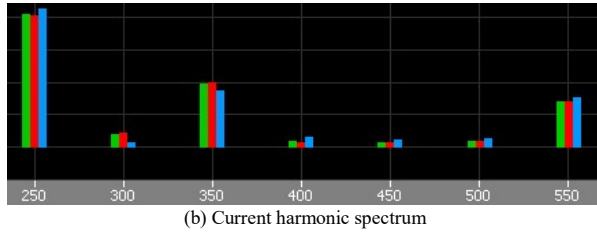


Figure 6: a) Harmonic current waveform obtained without filter for a non-linear load, b) harmonic bar graphs for each frequency.

Comparative results obtained from the second test are plotted in Fig.7 and Fig.8. From these figures, it can be observed that three filters are activated (attached to PCC) sequentially with small time spaces and in each step, it seems that load current increases when the standard filters are used, however this is not the case when the proposed filters are used.

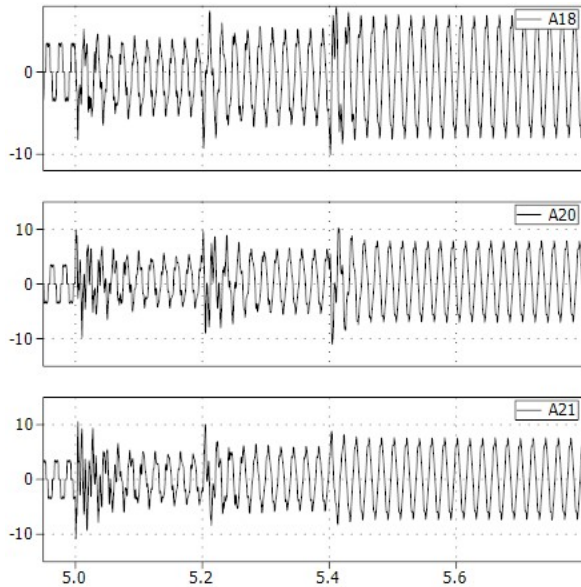


Figure:7. Simulation result obtained with the first-tuned filter for load phase current waveforms

The comparative results obtained for THD factor of the load current are also listed in Table 4. In the last test an example of usual application in the market are compared and obvious difference is explored for a specific frequency. For example, the performance of the standard filter and the proposed filter are compared for 5th harmonic which is one of the most harmful one at 250 Hz frequency, and obtained results are shown in Fig. 9. Here, it should be noted that the proposed filter's parameters L , C and L_s are calculated for frequency of 189Hz which a usual dominant frequency used for the standard filter design in practical applications.

The main purpose is to be as close to the relevant harmonic frequency as possible and to install the most suitable filter. So the goal is to attach the filter designed according to the value of 245 Hz for the 250 Hz value which corresponds to the 5th harmonic.

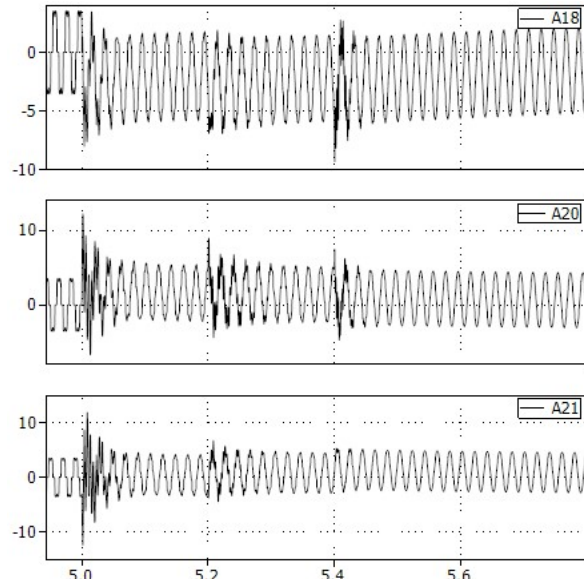


Figure:8. Simulation result obtained with proposed filter for load phase current waveforms

Finally, simulation results show that the proposed filter gives better result respect to the standard ones in terms of improvement of current waveform shape and also less power consumption. This can be seen from the Fig. 7, Fig.8 and Fig.9.

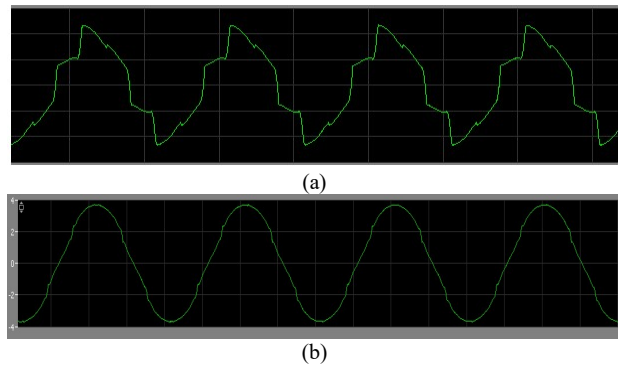


Figure: 9. A phase current waveforms with a) standard filter commonly used in markets, and b) proposed filter.

Table:4 THD factor of standard filter and proposed filter

Current THD (%)			Voltage THD (%)		
Without Filter	Standart Filter	Proposed Filter	Without Filter	Standart Filter	Proposed Filter
26,12	18,7	3,88	4,65	3,7	0,72

Benefit		
Standart Filter	Proposed Filter	
28,41%	85,15%	

Benefit		
Standart Filter	Proposed Filter	
20,43%	84,52%	

VI. CONCLUSION

In general, the filters in markets are designed for the frequency of 189Hz and these filters as a group are installed in parallel to grid depending on number of the dominant harmonics. However, this kind of application with the standard filters provides an inadequate performance for harmonics reduction and absorbs additional more power from the grid.

However, the proposed filter having an additional shunt reactance exhibits a better performance with respect to the standard single-tuned filters in terms of harmonic reduction and low power consumption from the power source. In a future study this approach will be tested in real applications aiming to suppress high magnitude harmonic currents with less reactive current consumption.

ACKNOWLEDGMENT

This study is carried out under a joint research project supported within the context of the cooperation between the TUBITAK-Turkey and BMBF-Germany. Turkish side of the project is funded by TUBITAK with grant number 115E006.

REFERENCES

- [1] Arrillaga J., Bradley D. A., and Bodger P. S., "Power system harmonics", New York: Wiley, 2003, ISBN 0-470-85129-5.
- [2] B. Singh, A. Chandra, K. Al-Haddad, Power Quality: An Introduction, in: Power Qual. Probl. Mitig. Tech., John Wiley & Sons Ltd, 2015.
- [3] Sik.Cho Y., Cha H., "Single-tuned passive harmonic filter design considering variances of tuning and quality factor," Journal of Inter. Council on Electrical Eng., vol.1, no. 1, 2011, pp. 7-13.
- [4] Analysis of wind turbine driven DFIG using PLECS software package IJEECT Vol. 6, Issue 2, April - June 2015.
- [5] L. S. Czarnecki. "An overview of methods of harmonic suppression in distribution systems", in Proc. of the IEEE Power Engineering Society Summer Meeting, vol. 2, pp. 800-805, 2000.
- [6] Shodhganga,-,"Design and simulation of passive filter" <http://shodhganga.inflibnet.ac.in/bitstream/10603/chap3.pdf>
- [7] Mboving C.S.A., Hanzelka Z., Klempka R. "Different approaches for designing the passive power filters" Przegląd elektrotechniczny, ISSN 0033-2097, v. 91, no. 11, 2015.
- [8] M. Malinowski, M.P. Kazmierkowski, W. Szczygiel, and S. Bernet, "Simple sensor less active damping solution for three-phase PWM rectifier with LCL filter;" In Industrial Electronics Society, 2005. IECON 2005. 31st Annual Conference of IEEE, page 5pp., 6-6 Nov. 2005.
- [9] Khatounian F., Monmasson E., Berthereau F.,Louis J.P. "Design of an output LC filter for a doubly fed induction generator supplying non-linear loads for aircraft applications" IEEE ISIE Inter. Symposium on Ind. Electron. 4-7 May 2004 Ajaccio, France.
- [10] V.T. Phan and H.H. Lee, "Control strategy for harmonic elimination in stand-alone DFIG applications with nonlinear loads" IEEE Trans. On Power Electron, vol. 26, no. 9, Sept. 2011.
- [11] Devshukla R., Tripathi R.K. "A novel voltage and frequency controller for standalone DFIG based wind energy conversion system" Elsevier Renewable and Sustainable Energy Reviews, no. 37, pp.69-89, 2014.
- [12] A. Jain and V. Ranganathan, "Wound rotor induction generator with sensorless control and integrated active filter for feeding nonlinear loads in stand-alone grid," IEEE Trans. Ind. Electron., vol. 55, no. 1, pp. 218–228, Jan. 2008.
- [13] Phan V.T. and Lee H.-H., "Performance Enhancement of stand-alone DFIG systems with control of rotor and load side converters using resonant controllers" IEEE Trans. on industry appl. vol. 48, no. 1, pp.199-210, Jan/Feb. 2012.
- [14] Liserre M., Blaabjerg F., Hansen S., "Design and control of an LCL-filter based three-phase active rectifier," IEEE Industry Application conference, Chicago, IL, USA, vol. 1, 2011, pp. 299-307.
- [15] Recommended practice and requirements for harmonic control in electrical systems. IEEE Std. 519-1992.

An Application in the Automotive Sector with the Purpose of Investigation and Prevention of 'Edge Crack' Problem at 980 MPa and Above Level Steel Materials

E.BARUT¹, B.KUDAY¹, O.YONTEM¹

¹ Toyotetsu Turkey Inc., R&D Center, Kocaeli, Türkiye, barute@toyotetsu.com.tr

¹ Toyotetsu Turkey Inc., R&D Center, Kocaeli, Türkiye, kudayb@toyotetsu.com.tr

¹ Toyotetsu Turkey Inc., R&D Center, Kocaeli, Türkiye, yontemo@toyotetsu.com.tr

Abstract -Automotive industry; is a dynamic sector which is constantly developing in line with the increasing demands in our country and in the world. Thanks to the issue of reducing greenhouse gas emissions from the subjects that have been studied in recent years, vehicle lightening studies for the automotive sector have been one of the important issues concerning the world. In this respect, due to the high strength values in the vehicles, the need for lightening of the steels used in high amounts has also arisen. It is aimed to develop high strength low density steels and to obtain steels with mild but desired strength values.

The strength of the steel materials is determined by the phases they contain. The austenite phase in the structure when high temperatures are reached during the shaping of the steel material; high-strength steels are obtained by converting to ferrite and martensite phases with rapid cooling. Due to the martensite phase embedded in the ferritic matrix, the high strength steels also have high hardness values. When shaping high-strength steel materials; One of the main problems encountered is the formation of edge cracks. Formation of edge cracks; The microstructure of the material varies depending on the parameters such as the mechanical properties and edge quality, and the edge cracks can be analyzed with the Hole Expansion Ratio test.

In the present study; deformations occurring in high-strength steels and macroscopic and microscopic studies have been conducted to understand the edge cracking problem. In this context, it was aimed to examine the effects of steel composition on edge cracking by selecting steels with different strength values and different compositions. The ratios of alloying elements forming the chemical composition were compared and their effects on hardenability were evaluated. Within the scope of the study, the control of the chemical composition for the samples was made by Optical Emission Spectrometer (OES) and Light Microscopy (IM) and Scanning Electron Microscopy (SEM) were used for the determination of phase distributions and structural phases of the samples. At the same time, crack propagation and fracture mechanisms were also investigated by using Scanning Electron Microscopy (SEM) and all results were evaluated.

Keywords - Advanced High Strength Steel (AHSS) Sheets, DP980(Dual Phase), Failure Analysis, Edge Crack.

I. INTRODUCTION

Modern high strength steels are the main choice of steels while automotive industry is concerned with minimization of vehicle's weight and energy conservation. Although the microstructures of these steels (DP, TRIP, HSLA, complex and partial martensitic steels etc.) vary, it is possible to design a high strength and shapeable matrix. Figure 1 shows the distributions of materials that can be used

for ULSAB-AVC (Ultra Light Steel Auto Body Advanced Vehicle Technology) of ultra-light steel [1].

As can be seen from Figure 1, dual-phase (DP) steels are widely used steels because of their high strength and easy formability in the automotive industry. In the simultaneous development of strength and ductility of these steels, it is aimed to form a ferritic matrix buried martensitic structures taking into consideration all the metallurgical elements (for example, alloy design and processing), (Figure 2). Especially, such a mixture microstructure is formed by annealing in a two-phase zone containing austenite-ferrite and then rapidly quenching, and tensile strength values in the steel range from 400 to 1200 MPa. In this respect, homogeneous distribution of ferrite and martensite in the matrix, as well as the carbon content, the dimensions and morphology of the phase components and the volumetric ratio of these phases must be controlled in the improvement of strength and ductility [2-5].

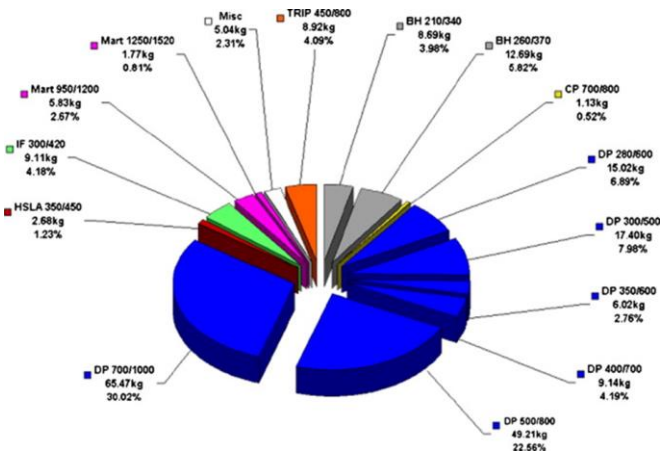


Figure 1: Distribution Diagram of High Strength Steels Preferably Used in the Automotive Industry (PNG-Class) [1]

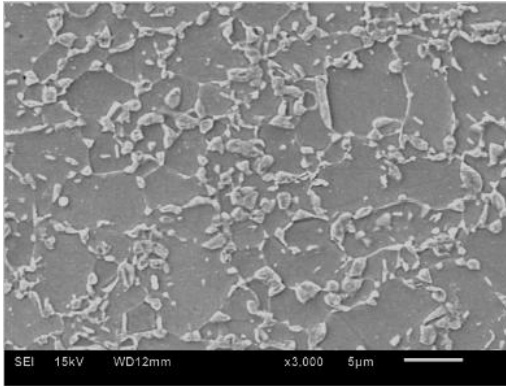


Figure 2: SEM Micrograph of DP780 Core; The microstructure contains the islet-appearing martensitic zones embedded in the ferritic matrix [2].

For example, in DP600 steel the matrix may contain 25-30% martensite and 75-70% ferrite [2]. Improved mechanical properties with increased martensite content can also cause significant losses in ductility.

The fact that the microstructure of DP steels can often be designed with different alloying elements and variable heat treatment conditions allows such steel group to be preferred over other high strength steels. Such a microstructural design refers to the distribution of the martensitic bulk within the matrix as a percentage. The effect of alloying elements is high, while both ferrite and martensite are to be determined [6].

Today's modellings are at a level that will contribute to the microstructural and mechanical design of such steels. It is possible to design alloys and heat treatment processes of high strength steels without going into production phase using thermodynamic principles and diffusion methods [6-9]. At the same time, by using the finite element method, it is able to determine the micro-mechanical processes which are subjected to the desired metallurgical properties and high strength steel, both in production and in use [4, 9].

One of the main problems encountered by the high strength steels preferably used for the automotive industry is the formation of edge cracks during forming (Figure 3). Such a problem can occur depending on the microstructure, mechanical properties and edge quality of the material [10, 11]. As is known, the edge tension performance of steel sheets is often determined by 'hole-expansion ratio' tests.

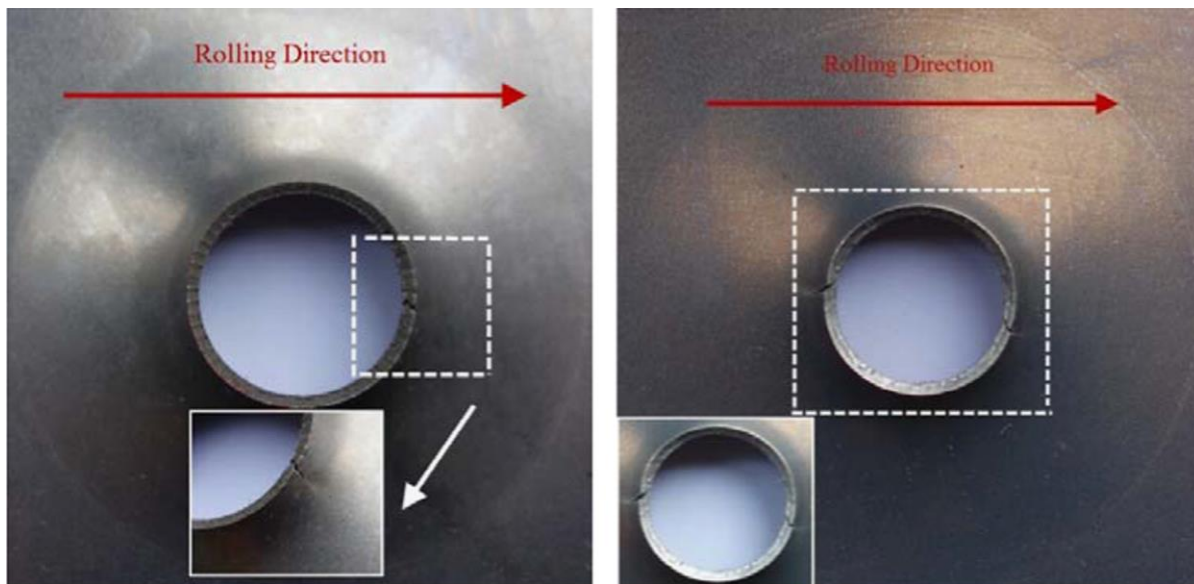


Figure 3: Edge Cracks Macro Views [10]

The edge cracks occur in the radial direction from the hole corner. Such cracking exists as an extension of microstructure nucleation due to shear mechanisms in the in situ deformation process[10].

From this point of view, it is necessary to characterize the elastic-plastic behavior of the matrix components of high-strength steels under loading conditions.

At low deformation rates (strain rate $<1 / s$), the martensitic zones exhibit an elastic behavior while the ferrite phase preferably deforms plastically. Plastic deformation of martensite occurs partly due to further deformation of ferrite and strain nonconformances at ferrit-martensite interface.

However, the increase in local strain and strain discrepancies between ferrite and martensite causes dislocations to accumulate within the ferrite grains. At the same time, these conflicts inevitably lead to pit formation at the interface as previously mentioned.

In this case macro and micro level fracture mechanisms will be introduced in the course of the deformation [5, 12-14].

Fracture behaviors of dual-phase steels can be inspected at the macroscopic and microscopic level (Figure 4).

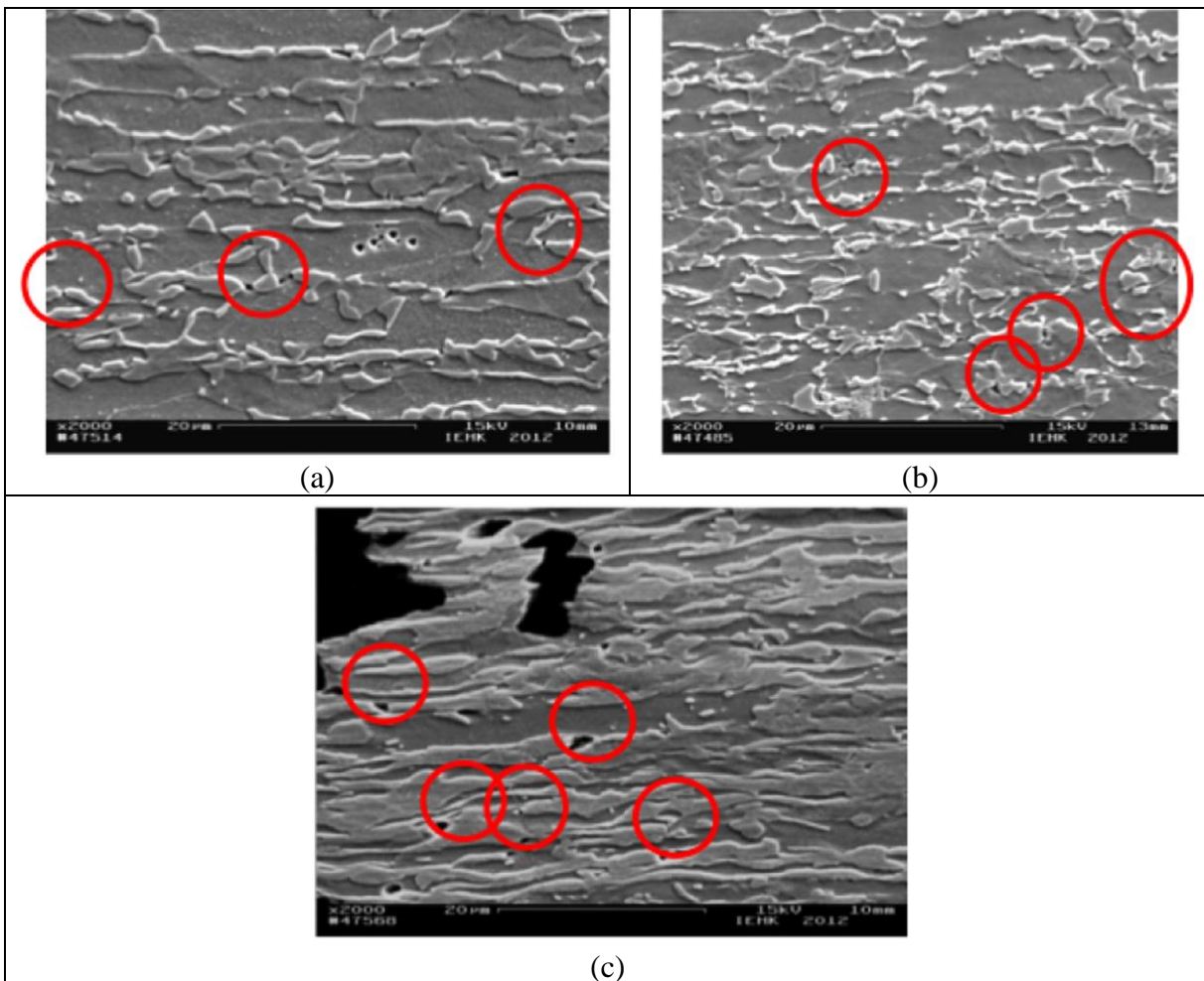


Figure 4:

SEM Micrographs of Tensile Testing of Industrial Produced DP Steels; (a) DP500, (b) DP800 and (c) DP1000 Steel. Cracked Starting Locations in Martensitic Regions Displayed in Red Circle.

At the macroscopic level, three main stages are observed, mostly involving pit nucleation, pit growth and pit consolidation. At the microscopic level, three basic modes of failure, which are in demand with each other, have been identified. These modes include;

- (i) crack nucleation in martensitic regions and brittle fracture as a result,
- (ii) decohesive decomposition at ferrite / martensite interfaces and
- (iii) the supernatant fracture of the ferritic matrix [9, 15-17].

Many studies have shown that the matrix on the development of fracture at the macroscopic and microscopic level has a direct effect on the amount of martensite (V_m). It is generally accepted that crack nucleation and progression are active in martensitic regions in dual phase steels containing martensite in a higher volume ratio and in which decohesive twinning occurs at the ferrite-martensite interface at intermediate martensite content ($V_m < 0.32$). On the final fracture, not only the effect of martensitic volumetric effect but also the effect of martensite morphology was revealed. A coarse martensitic structure of elongated shape and large size, geometrically distributed at the ferrite grain boundaries, limits the plastic flow of the ferrite grains and allows for the formation of high stress agglomerates. Thus, crack nucleation and progression in martensitic regions are facilitated. Besides all these phenomena, cracks starting from martensitic regions with the increase of plastic deformation show a transition towards the ferrite-martensite interface decay. In microstructures containing fine-grained martensite, the pits that cause damage occur at the ferrite-martensite interface [9, 18, 19].

II. MATERIAL AND METHOD

In order to understand the "edge crack" problem, which is the subject of this research, studies are being carried out as given in the following sequence.

- (i) the microstructural characterization of the DP980 material, the determination of the matrix in a ferritic-martensitic structure, the determination of the martensite bulk in the damaged part being twice as much as the undamaged fraction,
- (ii) the determination of the Ni and Mo elements in the chemical composition of the damaged part as being higher than that of the undamaged elements, and that it is possible to increase the hardenability due to the increase of these two elements,

- (iii) Assessment of "post uniform-%" and "HER" (hole expansion ratio) values of damaged and undamaged materials,
- (iv) Obtaining the values of "post uniform-%", "HER", and "YP / TS" by taking into account the maximum Ni and Mo values in the material composition and eliminating the possibility of tearing with this optimization.

Optimization study output was evaluated by the academic advisor and analysis / tests detailed in the below-mentioned laboratories of Kocaeli University Metallurgical and Materials Engineering were carried out.

- (i) control of chemical composition by optical emission spectrometry (OES) in damaged and undamaged parts,
- (ii) Performing light (IM) and scanning electron microscope (SEM) studies on damaged and undamaged parts, determination of structural phases in steel other than ferrite-martensite phases, determination of segregation / deformation bands, determination of residue and amount, type and distribution of these residues,
- (iii) SEM studies on the damaged part Interpretation of fractographs obtained by making, determination of surface, subsurface and matrix components contributing to crack formation,
- (iv) To perform the cross-sectional examination of the injured area and to support the findings obtained from the fractographs.

II. I. Damage Analysis Studies - Advanced Characterization

The macro shown in Figure 5 shows the visual damaged part. In all tests / analyzes applied to damaged (edge cracked) and undamaged (sheet metal) samples the technical equipment / equipment / equipment used is defined below.

- (i) Foundrymaster, optical emission spectrometer
- (ii) Microtest sample surface preparation equipment
- (iii) Olympus BX41RF-LED model light microscope
- (iv) JEOL JSM 6060 patterned scanning electron microscope.

II. I. I. Detection of Chemical Composition

Table 1 gives the chemical composition (wt%) values of the damaged and undamaged particles. According to the data given, the damaged material was found to contain some high Mo compared to the undamaged material. The compositional change for both materials is not only in the wt .-% Mo content but also in the microalloy (wt .-% Nb + Ti) elements.

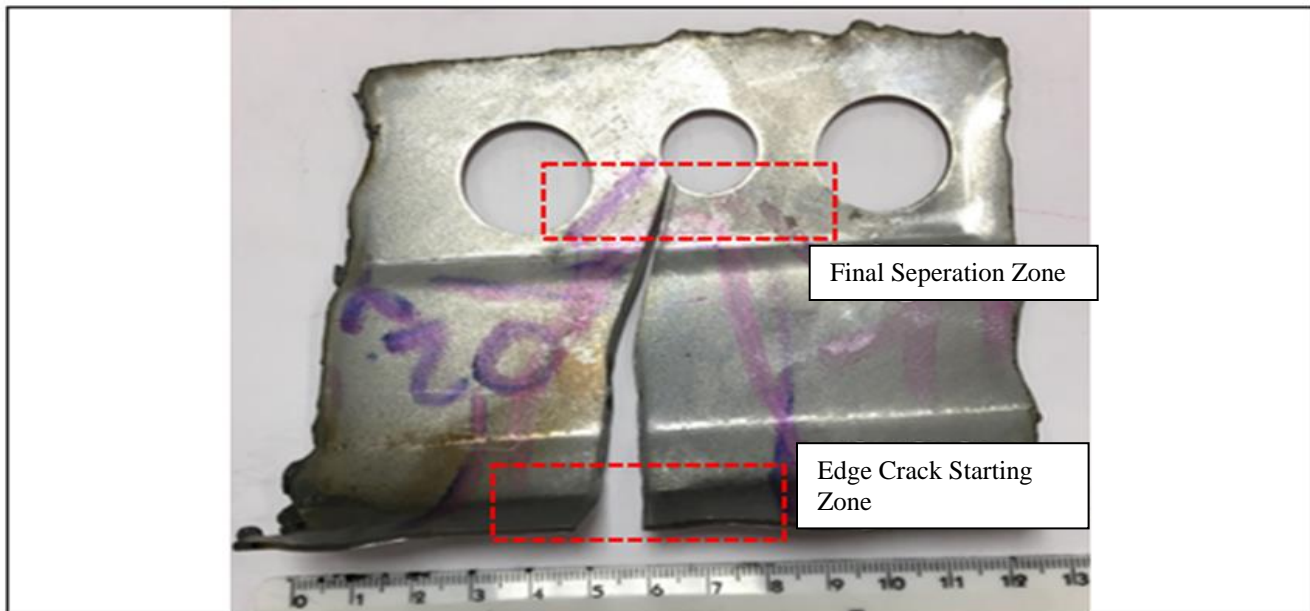


Figure 5: A Macro Image of a Damaged (Edge Crack) Fragment.

Table 1: Chemical Composition of Damaged and Uninfected Parts (wt-%).

Material	C	Mn	Si	Ni	Al	Cr	Mo	Nb	Ti	P	S	Fe
Undamaged	0.174	2.130	0.157	0.058	0.145	0.379	0.007	0.028	0.001	0.038	0.017	balance
Damaged	0.197	2.120	0.214	0.025	0.160	0.370	0.095	0.042	0.019	0.054	0.027	balance

The total microalloy element is 0.061% for the damaged material and 0.029% for the undamaged material.

II. I. II. Microstructural Characterization

Figures 6 and 7 show IM and SEM micrographs of undamaged and damaged fragments.

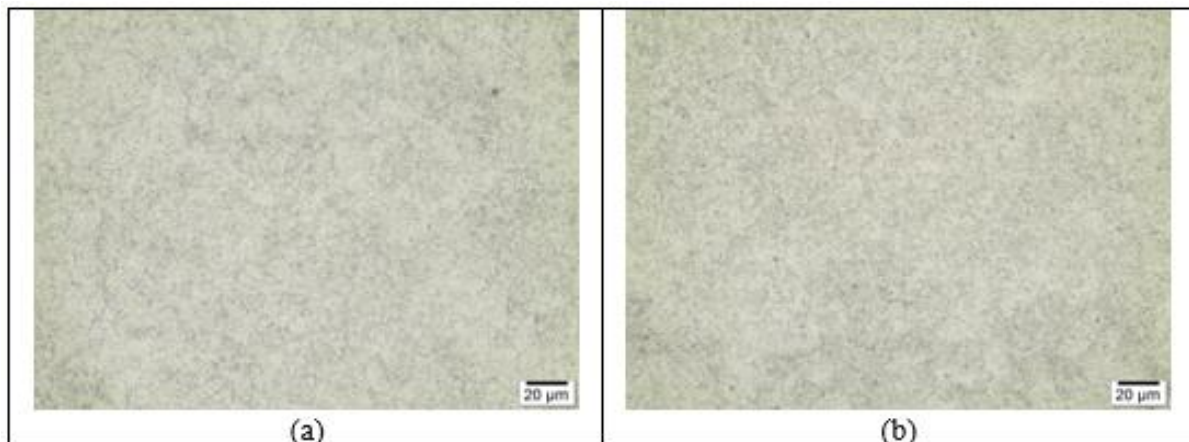


Figure 6: IM Micrographs of Undamaged and Damaged Steels

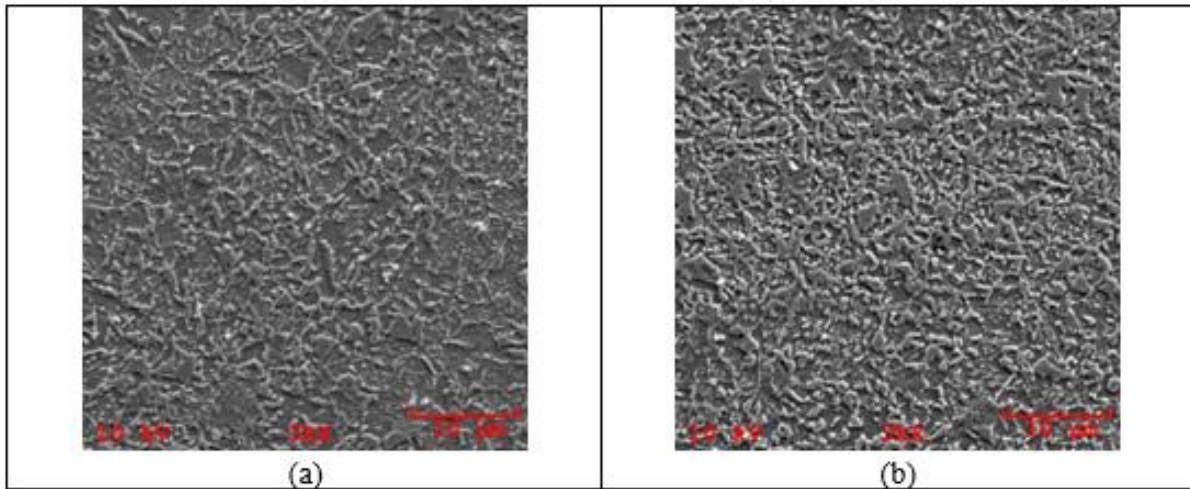


Figure 7: SEM Micrographs of Undamaged and Damaged Steels

The micrographs given in Figures 6a and b show that the steel matrix is of a similar character and that there are martensite islets embedded in the ferritic matrix.

SEM micrographs given in Figure 7 show that the ferritic and martensitic areas are higher and the damaged matrix contains a more intense martensite than the undamaged matrix.

II. I. III. Fractographic Study

Figure 8a shows the SEM micrograph of the fracture general surface taken from the tearing initiation zone. The cracks nucleated in the direction of roughness on the surface proceeded to cause tearing in the section (Figure 8b and c). Fractographic studies on the entire cross-sectional surface have been found to damage the matrix in the typical ductile breakage (Figure 8d), and the mechanism of microbubble fusion as described previously in the formation of such damage is effective (Figure 8d).

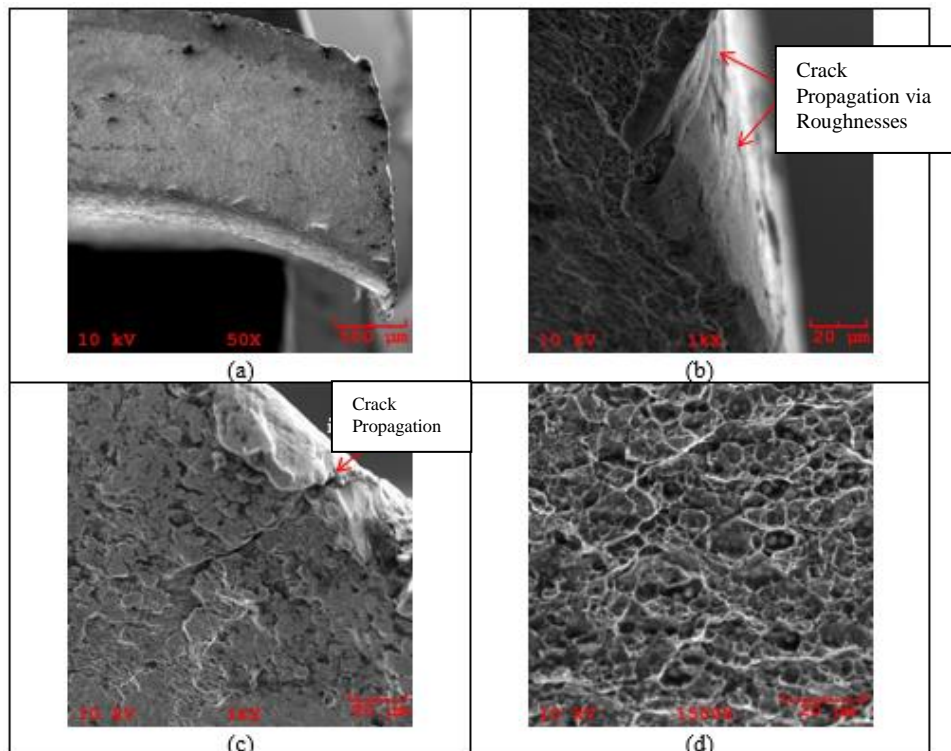


Figure 8:

Fractured Surface SEM Micrographs of the Tearing Initiation Region; (a) General Fractured Surface, (b and c) Surface Inward Crack Propagation, (d) Ductile Rupture Zone Over the Entire Section.

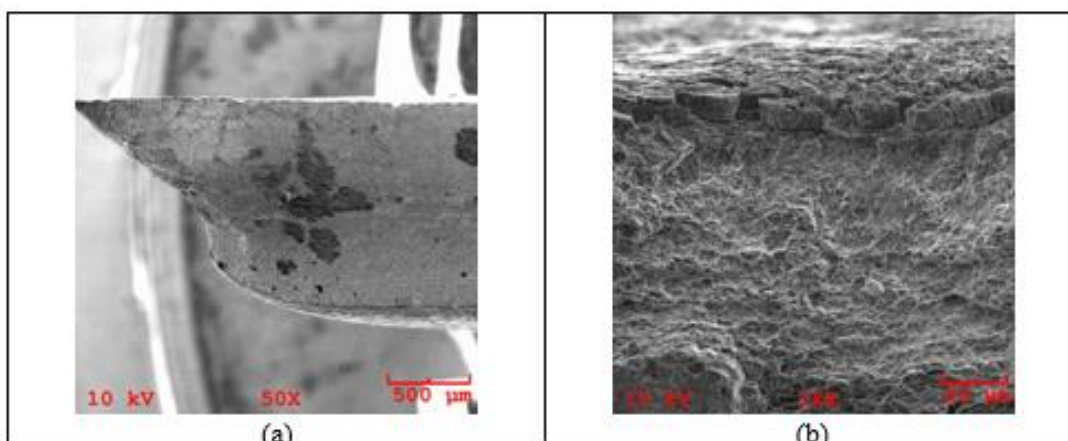


Figure 9: Broken Surface SEM Micrographs of the Ultimate Tearing Zone; (a) General Fractured Surface, (b) Sectioned Ductile Tearing Zone.

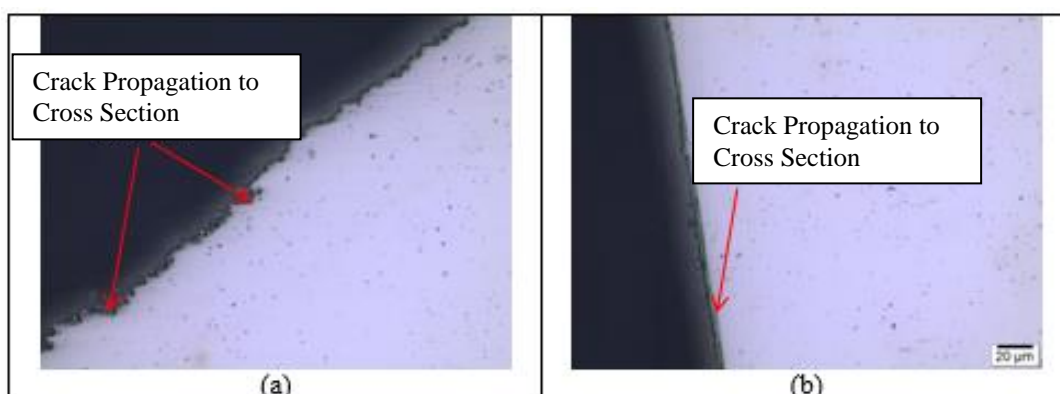


Figure 10: IM Micrographs in Shaded Location of the Broken Surface Cross-section; (a) Tearing Start and (b) Ultimate Tearing Zone.

The SEM micrograph shown in Figure 9a shows the ultimate tearing zone and the cause of ductile failure due to the matrix microbubble coupling mechanism being active (Figure 9b).

II. I. IV. Microscopic Investigation of Damaged Sections

Figure 10 shows IM micrographs of the damaged part in the polished position of the tearing initiation and final tearing sections. In both images, it was determined that cracks were directed inward from the surface.

III. RESULTS AND DISCUSSION

In this study; fracture mechanisms and edge crack formation at the macroscopic and microscopic level were investigated for high strength steels with different strength values. Therefore, undamaged parts and damaged parts are compared with each other.

Firstly; Chemical composition analysis by Foundrymaster Optical Emission Spectrometer (OES) is given in Table 1. According to Table 1, the total amount of microalloy element was measured as 0.029% by weight on the undamaged material, despite the damage of 0.061% by weight.

In this case, due to the the fact that the martensite ratio is higher due to the the fact that the martensite ratio is higher due to the alloying elements, it is seen that the parts having higher hardness are damaged parts. Alloy elements have shown that damaged parts have been cracked and broken.

The microstructural characterization of the parts was made with the Olympus BX41RF-LED model light microscope and the JEOL JSM 6060 scanning electron microscope and the results were evaluated. When the images obtained are examined, it can be mentioned that the martensite phase embedded in the ferrite matrix in high strength steels for all parts. However, the martensite ratio of the damaged parts is higher than the non-damaged parts, and it can be shown as evidence that martensite hardness increases the formation of cracks and causes cracking and edge cracking.

Thanks to the surface surveys performed by the SEM device; it was observed that the matrix carried out a typical ductile breakage and that such damage was caused by the association of microbubing.

When the results are examined; it is thought that several different parameters may be effective in the formation of edge cracking and the results of this study will be a predictor for future studies.

ACKNOWLEDGEMENT

We would like to thank Dr Hakan Atapek, assistant professor of the Department of Metallurgy and Materials Engineering, Kocaeli University, who supported and interpreted this study academically.

REFERENCES

- [1] V. Uthaisangskuk, U. Prael, W. Bleck, "Modelling of damage and failure in multiphase high strength DP and TRIP steels", *Engineering Fracture Mechanics*, 78, 469-486, 2011.
- [2] N. Saeidi, F. Ashrafzadeh, B. Niroumand, F. Barlat, "EBSD study of micromechanisms involved in high deformation ability of DP steels", *Materials and Design*, 87, 130-137, 2015.
- [3] H. Ghadbeigi, C. Pinna, S. Celotto, "Failure mechanisms in DP600 steel : initiation, evolution and fracture", *Materials Science and Engineering A*, 588, 420-431, 2013.
- [4] N. H. Abid, R. K. A. Al-Rub, A. N. Palazotto, "Micromechanical finite element analysis of the effects of martensite morphology on the overall mechanical behavior of dual phase steel", *International Journal of Solids and Structures*, 104-105, 8-24, 2017.
- [5] A. Das, M. Ghosh, S. Tarafder, S. Sivasprasad, D. Chakrabarti, "Micromechanisms of deformation in dual phase steels at high strain rates", *Materials Science and Engineering A*, 680, 249-258, 2017.
- [6] L. Schemmann, S. Zaefferer, D. Raabe, F. Friedel, D. Mattissen, "Alloying elements on microstructure formation of dual phase steels", *Acta Materialia*, 95, 386-398, 2015.
- [7] J. Rudnizki, B. Böttger, U. Prael, W. Bleck, "Phase-field modeling of austenite formation from a ferrite plus pearlite microstructure during annealing of cold-rolled dual-phase steel", *Metallurgical and Materials Transactions A*, 42(8), 2516-2525, 2011.
- [8] Y. Mazaheri, A. Kermanpur, A. Najafzadeh, "A novel route for development ultrahigh strength dual phase steels", *Materials Science and Engineering A*, 619, 1-11, 2014.
- [9] A. Ramazani, M. Abbasi, S. Kazemiabnavi, S. Schmauder, R. Larson, U. Prael, "Development and application of a microstructure-based approach to characterize and model failure initiation in DP steels using XFEM", *Materials Science and Engineering A*, 660, 181194, 2016.
- [10] X. Yu, J. Chen, J. Chen, "Interaction effect of cracks and anisotropic influence on degradation of edge stretchability in hole-expansion of advanced high strength steel", *International Journal of Mechanical Sciences*, 105, 348-359, 2016.
- [11] K. I. Mori, Y. Abe, Y. Suzui, "Improvement of stretch flangeability of ultrahigh strength steel sheet by smoothing of sheared edge", *Journal of Materials Processing Technology*, 210(4), 653-659, 2010.
- [12] R. G. Davies, "Influence of martensite composition and content on the properties of dual phase steels", *Metallurgical Transactions A*, 9, 671-679, 1978.
- [13] X. Sun, K. S. Choi, A. Soulami, W. N. Liu, M. A. Khaleel, "On key factors influencing ductile fractures of dual phase (DP) steels", *Materials Science and Engineering A*, 526(1-2), 140-149, 2009.
- [14] D. A. Korzekw, D. K. Matlock, G. Krauss, "Dislocation substructure as a function of strain in a dual-phase steel", *Metallurgical Transactions A*, 15, 1221-1228, 1984.
- [15] M. Sarwar, R. Priestner, "Influence of ferrite-martensite microstructural morphology on tensile properties of dual-phase steel", *Journal of Materials Science*, 31(3), 2091-2095, 1996.
- [16] Y. L. Su, J. Gurland, "Strain partition, uniform elongation and fracture strain in dualphase steels", *Materials Science and Engineering A*, 95, 151-165, 1987.
- [17] E. Ahmad, T. Manzoor, K. L. Ali, J. I. Akhter, "Effect of microvoid formation on the tensile properties of dual-phase steel", *Journal of Materials Engineering and Performance*, 9(3), 306-310, 2000.
- [18] X. J. He, N. Terao, A. Berghezan, "Influence of martensite morphology and its dispersion on mechanical properties and fracture mechanisms of Fe-Mn-C dual phase steels", *Journal of Metal Science*, 18(7), 367-373, 1984.
- [19] M. Calcagnotto, Y. Adachi, D. Ponge, D. Raabe, "Deformation and fracture mechanisms in fine- and ultrafine-grained ferrite/martensite dual-phase steels and the effect of aging", *Acta Materialia*, 59(2), 658-670, 2011.

A Calorimetric Investigation of CO₂, N₂ and Ar Adsorption

F.ÇAKICIOĞLU-ÖZKAN¹ and A. ERTAN²

¹ Izmir Yüksek Teknoloji Enstitüsü, İzmir/Turkey, fehimeozkan@iyte.edu.tr

²Hayat Kimya, İstanbul/Turkey, aertan@hayat.com.tr

Abstract - Calorimetric properties of CO₂, N₂ and Ar gases on synthetic zeolites namely, 5A and 13X, natural zeolite from Gördes/Bigadiç region and its acid (using HCl and H₃PO₄) treated forms were investigated by using a Tian-Calvet calorimeter, Setaram C80 at 25 oC. The zero coverage heat of adsorption values of CO₂, N₂ and Ar on the zeolites were determined. CO₂ adsorption on the adsorbents yielded the highest heat of adsorption values due to high quadrupole moment of CO₂ and hence formed strong specific interactions with the adsorbent. Ar adsorption exhibited the lowest zero coverage heat of adsorption values. Among the acid treated natural zeolites the one treated with 1.1 M H₃PO₄ solution was determined to have the highest heat of adsorption at zero coverage which has a close adsorption heat with the natural zeolite (about 80 kJ/mole) for CO₂ adsorption.

Keywords: adsorption heat, calorimetry, acid treatment, natural zeolite, gas adsorption

1. INTRODUCTION

Zeolites are porous crystalline aluminosilicates. The framework of the zeolite consists of an assemblage of SiO₄ and AlO₄ tetrahedra, joined together in various regular arrangements through shared oxygen atoms to form an open crystal lattice containing pores of molecular dimensions into which molecules can penetrate. The negative charge created by the substitution of an AlO₄ tetrahedron for a SiO₄ tetrahedron is balanced by exchangeable cations (e.g., Na⁺, K⁺, Ca²⁺, Mg²⁺), which are located in large structural channels and cavities throughout the structure.

Clinoptilolite, which is a member of the heulandite group, is the most abundant of the natural zeolite mineral. Compositions and purity vary widely among the many deposits found throughout the world. Gördes and Bigadiç (Turkey Western Anatolia) are the most known regions as clinoptilolite reserves. Clinoptilolite deposits are commercially important because their tuffs are often rather pure and can be mined with simple techniques.

Clinoptilolite rich zeolitic tuff can be modified with several methods such as acid treatment, ion exchange, silanation etc to make it appropriate for different industrial applications. The greater degree of acid treatment increases the strong Bronsted sites so that the electrostatic interactions between the adsorbent surface and the adsorbate molecules are high due to higher Si/Al ratio. The cation density which is an

important parameter in adsorption studies and is also controlled by acid treatment which generally leads to a higher degree of energetic homogeneity. Through acid treatment, removal of the aluminum and cations from the zeolite framework alters the local electric fields and field gradients and consequently reduces the strength of electrostatic interaction between adsorbate molecule and adsorbent (zeolite) surface. Clinoptilolite rich zeolitic tuff in chemically modified forms are studied for a wide variety of catalytic [1] and separation applications [2,3]. The performance of the application is limited by the adsorption characteristics of the zeolitic tuff. The success of the modification process is largely dependent upon understanding the interactions between the zeolite structure and the adsorbates. In order to determine the interaction characteristics of the adsorbate gases with the adsorbents the most frequently used system is Tian-Calvet type microcalorimeter. There are several parameters affecting the adsorption characteristics, hence being reflected on the heat of adsorption in microcalorimetry studies. In fact, molecular weight, molar volume, polarizability, size, strength of the adsorbate molecule and the temperature at which the adsorption takes place are important parameters and have to be carefully considered when performing adsorption in microcalorimetry [4]. The small molecules such as CO₂, N₂, CO, NH₃, and Ar are preferably used as adsorbate and are called as probe molecules. The adsorption of the probe molecules provides a powerful tool for characterizing zeolites and providing information on their nature and accessibility [5]. In a study performed by Bolis et al. [6] and Ozkan and Ulku [7] state that carbon dioxide is one of the most suitable probe molecules to reveal and characterize the surface interactions of the zeolites.

The aim of this study is to determine the effect of the acid treatment of natural zeolites on the calorimetric properties of CO₂, N₂ and Ar adsorption. Besides, synthetic zeolites are used for comparison with the natural zeolites.

2. EXPERIMENTAL

2.1. ADSORBENTS AND ADSORBATES

The zeolitic tuff obtained from Gördes-Fındıcak (Manisa, Turkey) region was used throughout this study. The zeolitic tuff was quantitatively analyzed by reference intensity ratio (RIR) method and it was determined that approximately 55 ± 5 % of the zeolitic tuff was clinoptilolite. The zeolitic tuff

with a particle size of 2000-850 μm was treated with different concentrations of acids such as HCl and H_3PO_4 solutions in the previous study [8]. The acid treated natural zeolites and also synthetic zeolites (5A and 13X) were used as the adsorbents. The code of the adsorbents and the treatment conditions are given in Table 1.

Table 1. Adsorbents used in the study

Zeolite Code	Definition	Treatment Conditions
NCW	Natural zeolite tuff washed with distilled water	2 hours at 60°C
C1-6h	Treated with 1 M HCl Solution	3 hours at 60°C
C3-3h	Treated with 3 M HCl Solution	3 hours at 60°C
C5-6h	Treated with 5 M HCl Solution	6 hours at 60°C
P1	Treated with 1.1 M H_3PO_4 Solution	6 hours at 60°C
5A	Synthetic zeolite-Aldrich (Lot # 04224HA)	No treatment was applied
13X	Synthetic zeolite-Aldrich (Lot # 04603BR)	No treatment was applied

The impurities present in the zeolitic tuff detected by XRD analysis were quartz and cristoballite. The chemical compositions of the clinoptilolite which has the same crystalline structure as heulandite is characterized by remarkable changes in the Si/Al ratio as well as in the composition of exchangeable cations. The chemical composition of the zeolitic tuff (NCW) washed with water was detected by EDX analysis (as oxide %; 14.1% Al_2O_3 , 64.2% SiO_2 , 1.8% MgO , 1.7% Na_2O , 5.3% K_2O , 1.0% CaO , 1.8% Fe_2O_3 and 10.3% H_2O). The zeolitic tuff used in this study is classified as low silica clinoptilolite [8]. CO_2 , N_2 and Ar molecules are used as adsorbates in this study.

2.2. CALORIMETRIC STUDIES

Throughout the study, Setaram C80 type microcalorimetry was used. Prior to calorimetric experiments the zeolite (~0.50g) was outgassed with a heating rate of 1°C/min and the temperature was ramped from 25 °C to 275°C. Once 275°C was reached, it was kept at this temperature for 5 hours. Afterwards, it was cooled down to experiment temperature, 25 °C, with the same rate.

This calorimeter allowed differential heats of adsorption and standard gas isotherms to be collected so differential heats of adsorption could be plotted as a function of surface coverage. Gas adsorption microcalorimetry which is of Tian-Calvet type provided information regarding the change of the heat of adsorption with the surface coverage along with the total amount of gas adsorbed. Besides, the adsorption took place by repeatedly sending doses of gas onto the initially

outgassed solid while recording the heat flow signal and the concomitant pressure evolution. The initial dose sent to the system was 50 mbar. At each dose, the equilibrium pressure was added to the sending incremental dose. Afterwards, the dose amount was increased to 300 mbar and the procedure was repeated until no further pressure change was observed. The heat evolved by each dose was measured and the corresponding amount adsorbed was obtained by the pressure change in the known volume of the apparatus. This was determined in previous calibration by allowing a known amount of gas to expand from the measure section into the vessels section formerly evacuated. For each dose, thermal equilibrium was attained before the pressure, the adsorbed amount and the integral heat evolved were measured. The adsorption experiments were concluded when a relatively high pressure was reached without the significant evolution of heat and the adsorbed amount became negligible.

3. RESULTS AND DISCUSSION

The representative calorimetric peaks of CO_2 , N_2 and Ar adsorption on zeolite NCW are given in Figure 3. The intensity of the peaks gradually decreases until no further adsorption takes place. The CO_2 peaks have the highest intensity whereas the lowest ones belong to Ar gas.

Figures 1-5 show the change in differential heat of adsorption (q_{diff}), calculated by using the area under each peak obtained for CO_2 , N_2 and Ar adsorption on the zeolites studied. As can be seen from the figures, the heat of adsorption decreased with increasing the amount adsorbed. However, for all the zeolites the heat of adsorption values of Ar (Figures 5 and 6) are lower than N_2 (Figures 3 and 4) and CO_2 (Figures 1 and 2). The main reason for that can be explained as Ar gas doesn't have a quadrupole moment and hence the interaction of Ar with the zeolites is not expected to be specific for the acidic sites, but involves only a nonspecific interaction dominated by dispersive forces. In addition to these acidic sites characterizing the acid treated zeolite, the physical properties of the adsorbate molecule contributes significantly to the heat of adsorption. Therefore, adsorption heat is greatly dependent on the nature of these adsorbate molecules. For instance, the heat of adsorption values for N_2 and Ar are significantly lower than that of CO_2 for all the samples due to the non-specific and weak interactions of the molecules with the zeolite surface.

Comparison of the figures also show that initially, the differential heat of CO_2 adsorption decreases rapidly, however, this sharp decrease was not observed for N_2 and Ar adsorption. After the initial region of the curves a continuous decrease in heat of adsorption points out to the presence on the zeolite of strong sites not belonging to the same energetic sites [9]. Such a strong energetic heterogeneity of the zeolites was detected by only CO_2 molecules.

The value of differential heat of adsorption evolved as a result of first gas dose can be comprehended as a measure of the strength of the strongest active sites in the structure [10]. For this aim the differential heats of adsorption curve was

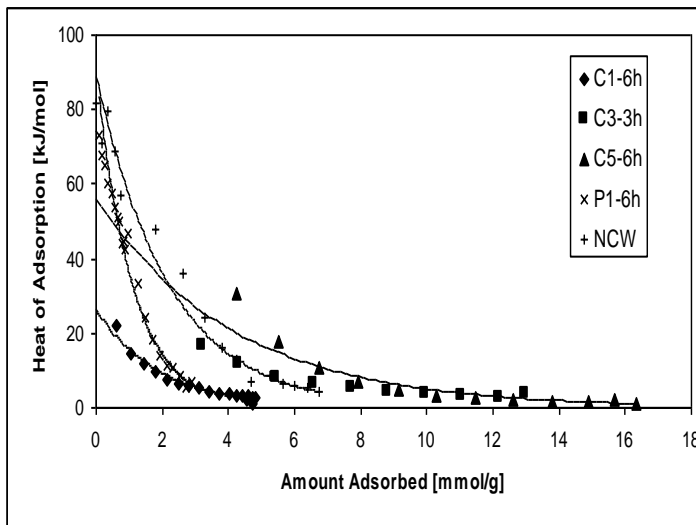


Figure 1: Differential Heat of Adsorption of CO₂ for acid treated natural zeolites

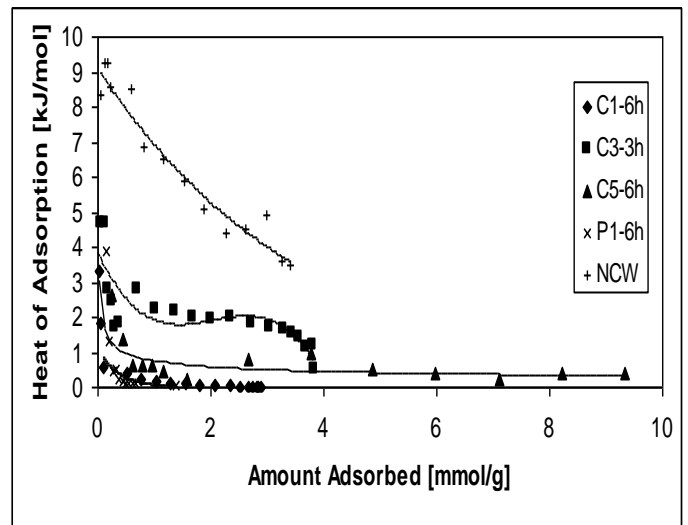


Figure 3: Differential Heat of Adsorption of N₂ for acid treated natural zeolites

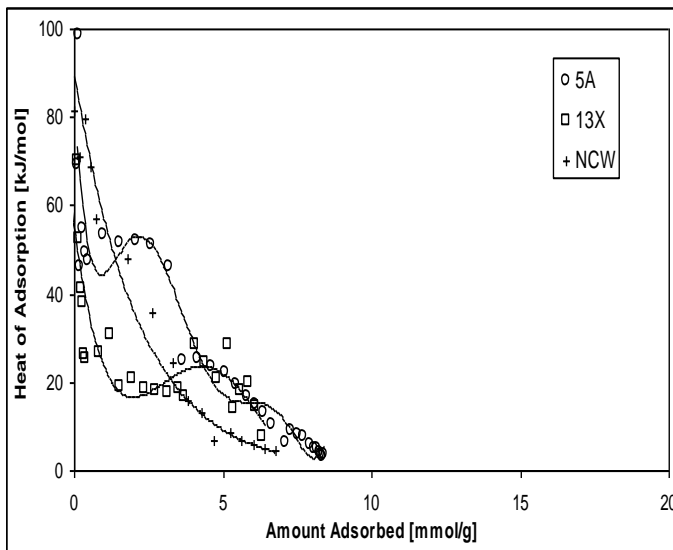


Figure 2: Differential Heat of Adsorption of CO₂ for natural and synthetic zeolites

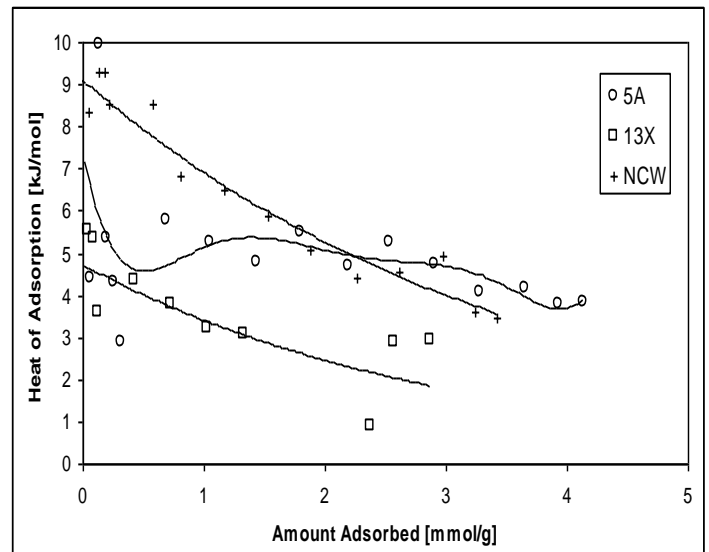


Figure 4: Differential Heat of Adsorption of N₂ for natural and synthetic zeolites

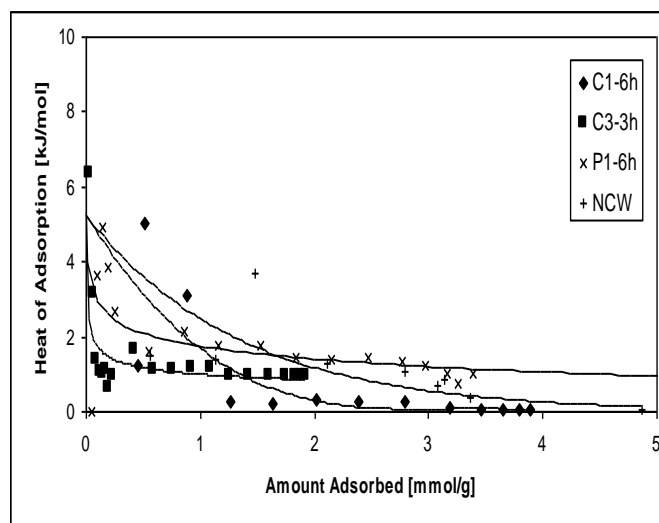


Figure 5: Differential Heat of Adsorption of Ar for acid treated natural zeolites

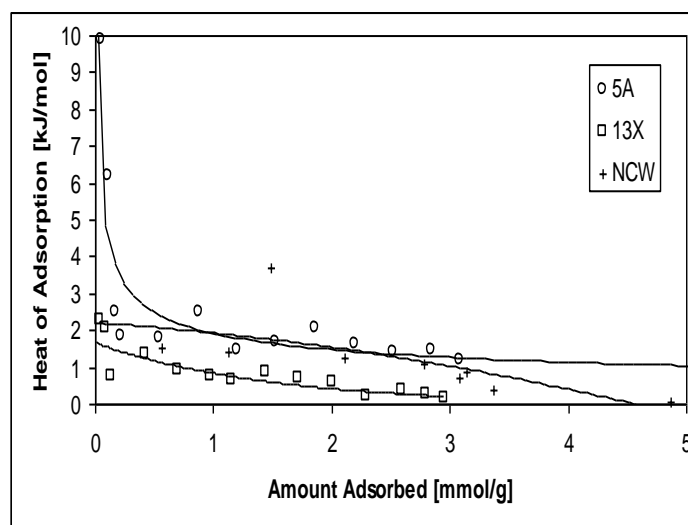


Figure 6: Differential Heat of Adsorption of Ar for natural and synthetic zeolites

extrapolated to zero coverage to determine q^0_{diff} (the heat of adsorption at zero coverage), representing the enthalpy change for the adsorption on these sites in the early stage of the adsorption, and presented in Table 2.

Table 2. Physical properties of the adsorbate gases

Adsorbate	Mol. Wt.	T_c (K)	Kinetic Diameter (\AA)	Polarizability ($\times 10^{-25} \text{cc}$)	Dipole ($\times 10^{-18} \text{esu}$)	Quadrupole ($\times 10^{-26} \text{esu-cm}^2$)
N_2	28	126	3.64	15.8	0	1.52
Ar	40	150.8	3.4	16.3	0	-
CO_2	44	304.2	3.30	26.5	0	4.30

Table 3: Heat of adsorption values of the zeolites at zero coverage, q^0_{diff}

Zeolites	Si/Al	q^0_{diff} [kJ/mol]		
		CO_2	N_2	Ar
NCW	4.04	80.39	9.10	3.96
C1-6h	5.25	38.54	0.83	1.52
C3-3h	6.08	37.52	4.98	6.03
C5-6h	8.4	55.99	3.92	1.39
P1	5.01	79.5	4.33	4.40
5A	0.98	83.08	7.31	9.86
13X	1.35	53.75	5.20	1.90

CONCLUSION

As a result of the calorimetric studies of CO_2 , N_2 and Ar gases with the natural and synthetic zeolites, the zero coverage heat of adsorption values of Ar and N_2 gases are comparable due to closer critical temperatures (126 and 150.8 K for N_2 and Ar respectively) which indicate that their nonspecific interactions with the zeolites are closer. However, CO_2 exhibits the highest zero coverage heat of adsorption values for all the zeolites because its polarizability, quadrupole moment, critical temperature are much greater than those of the other two gases.

The analysis of the differential heats of adsorption of probe molecules of different size as a function of the amount adsorbed showed that P1 zeolite treated with 1.1 M of H_3PO_4 solution has the highest heat of adsorption at zero coverage among the acid treated natural zeolites while washed natural zeolite (NCW) has a close adsorption heat with the P1 zeolite (approximately 80 kJ/mole). Besides, 5A zeolite has the highest heat of adsorption at zero coverage due to its lowest Si/Al ratio. The data obtained in this study show that calorimetrically measured heats of adsorption of a pure gas as functions of adsorbate loadings can be conveniently used to characterize the energetic behavior of the acid treated natural zeolite surface.

ACKNOWLEDGMENT

This research (IYTE 2002 #21) was supported by IYTE Research Foundation Grant.

REFERENCES

- [1] Ünveren E., Gündüz G., Özkan F., Chem. Eng. Com., 192 (3), 386-2005
- [2] Ackley M.W. , Yang. R.T., Ind. Eng. Chem. Res, 30 (1991) 2523-2530
- [3] Ertan A., Ms Thesis, Izmir Institute of Technology, Turkey, 2004
- [4] Auroux A., Topics in Catalysis, 4 (1997) 71-89
- [5] Guil J.M., Melon J.A., Carvalho M.B., Carvalho A.P., Pires J., Microporous and Mesoporous Materials, 51 (2002) 145-154
- [6] Bolis V., Broyer M., Barbaglia A., Busco C., Foddanu G.M., Ugliengo P., Journal of Molecular Catalysis A, 204-205 (2003) 561-569
- [7] Çakıcıoğlu Ö. F., Ulku S., Ads. Sci. and Tech., 21-4 (2003) 309
- [8] Becer M., (2003), Ms Thesis, Izmir Institute of Technology, Turkey
- [9] Solinas V., Ferino I., Catalysis Today, 41 (1998) 179-189
- [10] Auroux A., Topics in Catalysis, 19 (2002) 205-213
- [11] Rakic V., Dondur V., Hercigonja V., Thermochemica Acta, 379 (2001) 77-84
- [12] Gregg S.J., Sing K.S.W., Adsorption, Surface Area and Porosity, Second Ed, Academic Press, London 1982

Effect of Reaction Temperature on the Amount of Carbon Nanotubes by Chemical Vapor Deposition in Fluidized Bed

M. GURSOY¹, D.U. ZIRAMAN², Ö.M. DOĞAN² and B.Z UYSAL²

¹ Selcuk University, Konya/Turkey, mehmetgursoy@selcuk.edu.tr

² Gazi University, Ankara/Turkey

Abstract – In this study, carbon nanotubes were synthesized on Fe/Silica catalyst by chemical vapor deposition in a fluidized bed reactor. The mixture of CO and H₂ was fed into reactor. The purification experiments of carbon nanotubes were performed by multi-step method including oxidation and acid washing. After purification, carbon nanotubes were detected by high-resolution transmission electron microscopy. This study indicated that the reaction temperature is an important parameter determining the obtained amount of carbon nanotubes. At the same experimental conditions, carbon nanotubes were synthesized at three different reaction temperatures (700, 800 and 900°C). The largest amount of carbon nanotubes was produced at 800°C.

Keywords – Chemical vapor deposition, carbon nanotube, fluidized bed.

I. INTRODUCTION

SOLIDS of elemental carbon in sp² hybridization can form a variety of extraordinary structures, such as, fullerene (zero-dimensional), carbon nanotubes (one-dimensional), graphene (two-dimensional). Carbon nanotubes were discovered in 1991 by Sumio Iijima [1]. Carbon nanotubes are derived from rolled graphene sheets consisting solely of carbon atoms. Carbon nanotubes, with diameters of a few nanometers, but their length is in principle unrestricted, but ranges typically from tens to hundreds of micrometers [2].

Since the discovery of carbon nanotubes, they have attracted remarkable attention due to their unique physical, chemical, mechanical and electrical properties. The superior properties include high melting point, high tensile strength, and high thermal conductivity [4]. Carbon nanotubes have different potential applications, nano-electronic devices [5], hydrogen storage [6], buckypaper [7], transparent conductive film [8] and quantum wires [9]. They can be also used as a filler for preparing of composite materials.

So far, various synthesis methods have been developed for the production of carbon nanotubes. The most widely used methods are arc discharge method [10], laser furnace method [11], and chemical vapor deposition method [12]. Chemical vapor deposition method is the most popular and widely used because of its low set-up cost, relatively high production yield, lower reaction temperature, high purity, easy of control, and the good potential for large-scale production [13]. Chemical

vapor deposition of hydrocarbons over metal catalysts, Fe, Ni and Co (transition metals) on substrates such as alumina and silica is the most common way to produce carbon nanotubes [14]. The growth of carbon nanotubes has been reported to be better over Fe catalysts than over Co or Ni [15]. In this method, the most commonly used carbon sources are methane [16], ethanol [17], acetylene [18], ethylene [19] and carbon monoxide [20].

In this study, the mixture of CO+H₂ was used to produce carbon nanotubes using fluidized bed chemical vapor deposition method. In order to produce large amount and high quality carbon nanotubes, chemical vapor deposition parameters should be well determined. This study is focused on determining the effect of reaction temperature on the obtained amount of carbon nanotubes.

II. EXPERIMENTAL

Fe/Silica was prepared by impregnation method. In order to prepare catalyst, Fe(NO₃)₃.9(H₂O) was dissolved in 1.5 ml of water. Then, 100 μm of silica powders were added in the solution as a support material. The physical properties of silica powders were given in Table 1. After an hour, the mixture was heated at a temperature of 85°C. 0.25 g of Fe(NO₃)₃.9(H₂O) was again added to the silica particles and dissolved in 2 ml of water. After this process, the water of the solution was evaporated at 85°C temperature. Finally, catalyst materials were calcined at 750°C for 3 h to remove nitrogen oxides, then cooled to room temperature. Obtained catalyst was shown in Figure 1. The amount of iron in catalyst was analyzed by X-Ray Fluorescence.

Table 1: The physical properties of silica powders.

The physical properties of silica powders	
Bulk density	1488 kg/m ³
Particle density	2235 kg/m ³
Particle diameter	0.1 mm
Void ratio	0.334

Carbon nanotubes were produced using a custom-built fluidized bed chemical vapor deposition. The experimental system consisted of a 0.05 m inner diameter, 1-meter long vertical quartz reactor with a quartz disk sealed, a cyclone and

a gas-washing bottle. A vertical split tube furnace (Protherm, ASP 11/100/500) was used in chemical vapor deposition system. The fluidized bed chemical vapor deposition experimental system was schematically shown in Figure 2.



Figure 1: Fe/Silica catalyst.

75 g of Fe/Si catalyst was loaded into reactor. Before synthesis of carbon nanotubes, the system was purged with nitrogen (500 ml/min) and heated to the reaction temperature for 20 mins. During carbon nanotube synthesis, CO was used as a carbon source. Moreover, H₂ and N₂ were fed into reactor as reactant and carrier gases, respectively. The flow rate of CO, H₂ and N₂ were kept as 300, 300 and 1800 ml/min,

respectively, using mass flow controllers,

All experiments were carried out in atmospheric pressure. In order to determine the effect of reaction temperature on the obtained amount of carbon nanotubes, experiments were performed at three different reaction temperature conditions, 700, 800 and 900°C. Obtained carbon nanotubes contained impurities from catalyst and amorphous carbon. That's why, after production of carbon nanotubes, the purification was necessary

The purification experiments were performed by multi-step method, which includes ultrasonication and acid washing. First step was to remove amorphous carbon structures from samples by sonication in H₂O₂ solution for half an hour at 50°C. Following step was to remove metallic impurities using HCl solution and magnetic stirring at 70°C for 4 hours.

The morphologies of obtained carbon nanotubes were observed by using high-resolution transmission electron microscopy (HRTEM, JEOL JEM 2100F) at 200 kV.

III. RESULTS AND DISCUSSION

Based on XRF analysis results, 5.2 wt% Fe was founded in Fe/Silica catalyst.

Hydrogen peroxide treatment is highly effective method in removing amorphous carbon structures. However, oxidation treatment is not sufficient to remove residual metal catalyst impurities. That's why, in this study, apart from oxidation treatment, acid treatment was also applied.

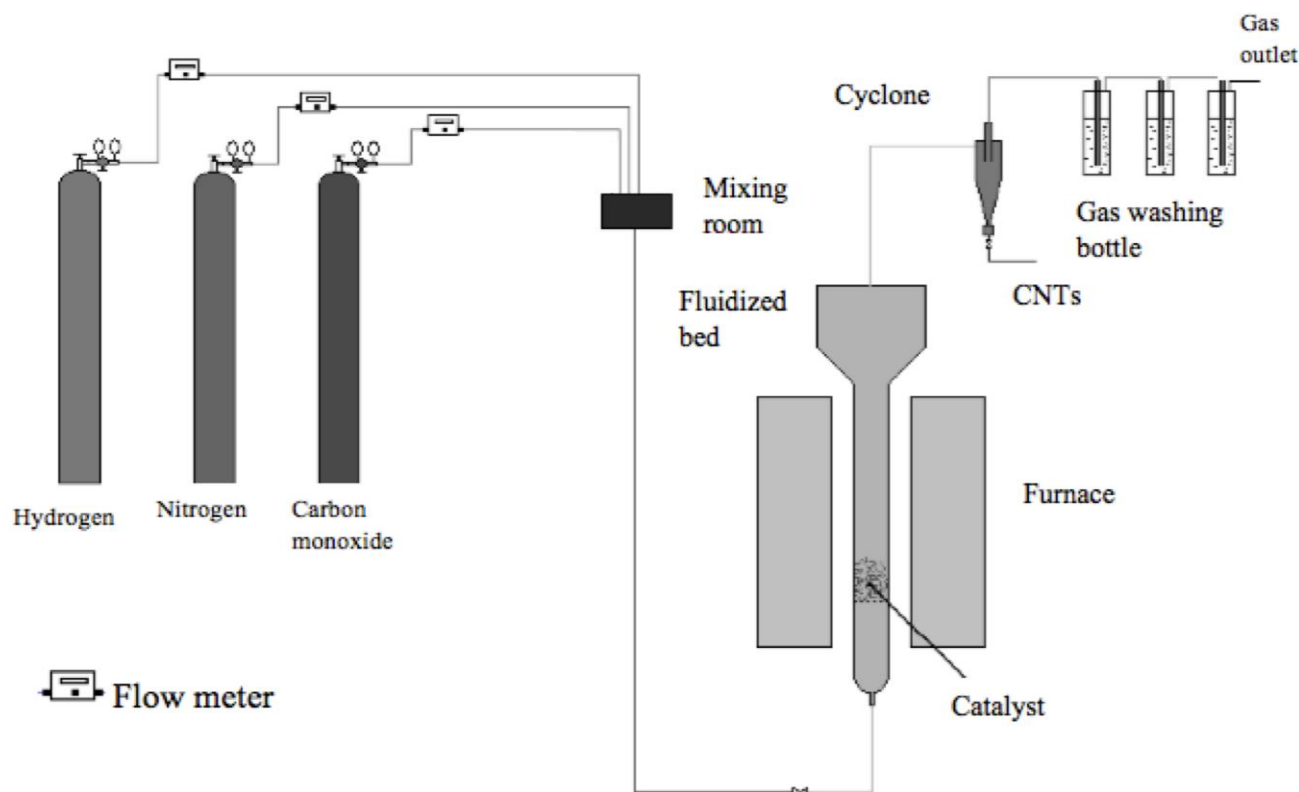


Figure 2: Fluidized bed chemical vapor deposition experimental system.

It is known that purification of carbon nanotube with acidic solvents (such as HCl, H₂SO₄, HNO₃) can cause some deformations on carbon nanotube surface structures [21]. The TEM image of obtained carbon nanotube was given in Figure 3. According to Figure 3, any defects on carbon nanotube surfaces were not observed. The purification method applied in this study can be considered as a successful and harmless approach to remove impurities from carbon nanotube surface. The obtained carbon nanotubes are with an average external diameter about 15 nm.

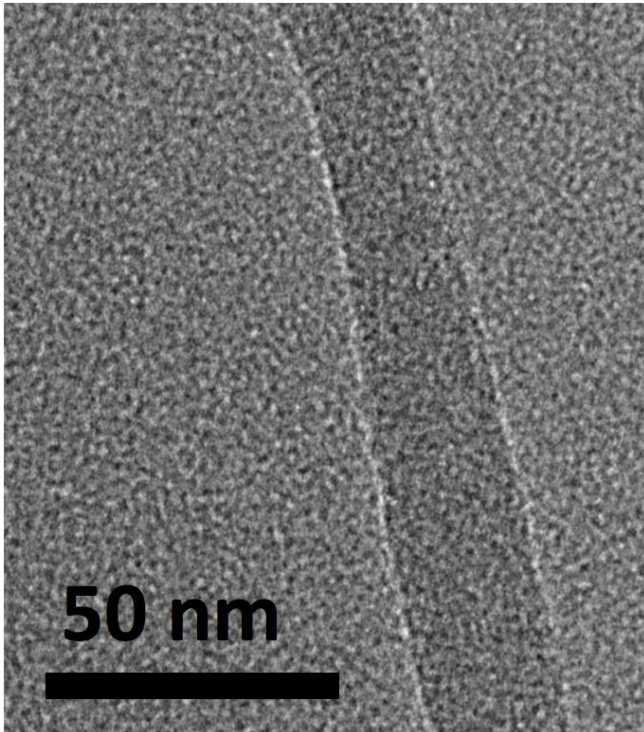


Figure 3: TEM image of carbon nanotube

The graph of carbon nanotube production amount at different reaction temperatures was given in Figure 4.

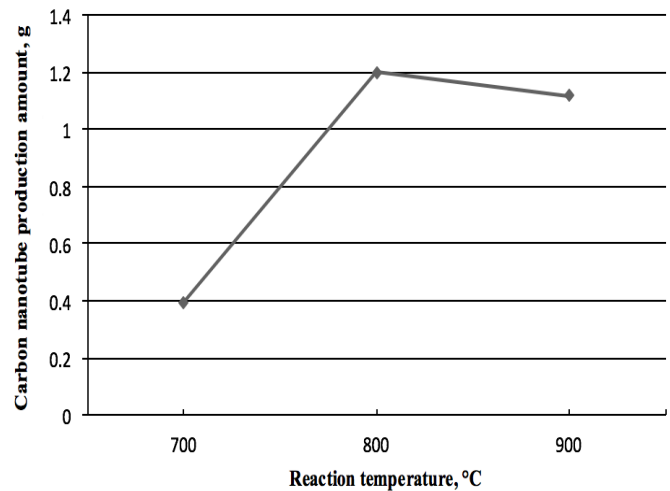


Figure 4: Carbon nanotube production amount at different reaction temperatures

According to Figure 4, it was observed that the obtained amount of carbon nanotubes increases with increasing applied reaction temperature from 700°C to 800°C. However, after heating up to 800°C, the obtained amount of carbon nanotube was decreased. The decrease in carbon nanotube amount can be attributed to the deformation of catalyst [22].

IV. CONCLUSION

This study has shown that fluidized bed reactor provided excellent mass and heat transfer for carbon nanotube growth, which could have led to high quality and yield carbon nanotube production.

It was found that reaction temperature is a significant parameter on the amount of carbon nanotubes.

ACKNOWLEDGMENT

This work was supported by Teknoprom, Gazi University BAP (06/2012-22) and Türkiye Kömür İşletmeleri (TKİ). The author M. Gürsoy was supported by The Scientific and Technological Research Council of Turkey (TÜBİTAK) – BİDEB

REFERENCES

- [1] S., Iijima, "Helical microtubules of graphitic carbon", *Nature*, 354, 56 (1991).
- [2] A., Köhler, C., Som, A., Helland and F., Gottschalk, "Studying the potential release of carbon nanotubes throughout the application life cycle", *Journal of Cleaner Production*, 16 (8-9):927-937, (2008).
- [3] S., Iijima and T., Ichihashi, "Single-shell carbon nanotubes of 1-nm diameter", *Nature*, 363, 603 (1993).
- [4] J., Fischer, in: Y., Gogotsi (Ed.), "Carbon Nanotubes: Structure and Properties", CRC Press, Boca Raton, (2006).
- [5] K., Tsukagoshi, N., Yoneya and S., Uryu, "Carbon nanotube devices for nanoelectronics", *Physica B*, 323, 107-114 (2002).

- [6] A.C., Dillon, K.M., Jones, T.A., Bekkedahl, C.H., Kiang, D.S., Bethune, and M.J., Heben, "Storage of hydrogen in single-walled carbon nanotubes," *Nature*, 386, 6623, 377–379 (1997).
- [7] M., Endo, H., Muramatsu, T., Hayashi, Y.A., Kim, M., Terrones and M.S., Dresselhaus, "Buckypaper from coaxial nanotubes", *Nature* 433, 476 (2005).
- [8] E.M., Doherty, S., De, P.E., Lyons, A., Shmeliov, P.N., Nirmalraj, V., Scardaci, J., Joimel, W.J., Blau, J.J., Boland and J.N., Coleman "The spatial uniformity and electromechanical stability of transparent, conductive films of single walled nanotubes" *Carbon*, 47, 2466–73 (2009).
- [9] S.J., Tans, M.H., Devoret, H., Dai, A., Thess, R.E., Smalley, L.J., Geerligs and C., Dekker, "Individual single-wall carbon nanotubes as quantum wires", *Nature*, 386, 474–477 (1997).
- [10] V.N., Popov, "Carbon nanotubes: properties and application", *Materials Science and Engineering*, 43, 61-102 (2004).
- [11] A., Thess, R., Lee, P., Nikolaev, H., Dai, P., Petit, R., Jerome, C., Xu, Y.H., Lee, S.G., Kim, A.G., Rinzler, D.T., Colbert, G.E., Scuseria, D., Tomanek, J.E., Fischer, and R.E., Smalley, "Crystalline ropes of metallic carbon nanotubes", *Science*, 273, 483-487 (1996).
- [12] M., José-Yacamán, M., Miki-Yoshida, L., Rendón, and J.G., Santiesteban, "Catalytic growth of carbon microtubules with fullerene structure", *Applied Physics Letters*, 62, 657-659 (1993).
- [13] F., Danafar, A., Fakhru'l-Razi, M.A.M., Salleh and D.R.A., Biak, "Fluidized bed catalytic chemical vapor deposition synthesis of carbon nanotubes—A review", *Chemical Engineering Journal*, 155, 37–48 (2009).
- [14] C.T., Hsieh, Y.T., Lin, W.Y., Chen and J.L., Wei, "Parameter setting on growth of carbon nanotubes over transition metal/alumina catalysts in a fluidized bed reactor", *Powder Technol.*, 192, 16–22 (2009).
- [15] K., Hernadi, A., Fonseca, J.B., Nagy, A., Siska and I., Kiricsi, "Production of carbon nanotubes by the catalytic decomposition of different carbon-containing compounds", *Appl. Catal. A*, 199, 245-255 (2000).
- [16] W., Qian, T., Liu, F., Wei, Z., Wang and Y., Li, "Enhanced production of carbon nanotubes: combination of catalyst reduction and methane decomposition", *Appl. Catal. A*, Gen. 258, 121–124, (2004).
- [17] G., Ortega-Cervantez, G., Rueda-Morales and J., Ortiz-López, "Catalytic CVD production of carbon nanotubes using ethanol", *Microelectronics Journal*, 36, 495-498 (2005).
- [18] M., Perez-Cabero, I., Rodriguez-Ramos and A., Guerrero-Ruiz, "Characterization of carbon nanotubes and carbon nanofibers prepared by catalytic decomposition of acetylene in a fluidized bed reactor", *J. Catal.*, 215 (2), 305-316 (2003).
- [19] M., Corrias, Y., Kihn, P., Kalck and P., Serp, "CVD from ethylene on cobalt ferrite catalysts: the effect of the support", *Carbon* 43, 2817–2833 (2005).
- [20] B., Kitiyanan, W.E., Alvarez, J.H., Harwell and D.E., Resasco, "Controlled production of single-wall carbon nanotubes by catalytic decomposition of CO on bimetallic Co–Mo catalysts", *Chem. Phys. Lett.*, 317, 497–503 (2000).
- [21] P.X., Hou, C., Liu and H.M., Cheng "Purification of carbon nanotubes", *Carbon*, 46(15), 2003-2025 (2008).
- [22] S.B., Sinnott, R., Andrews, D., Qian, A.M., Rao, Z., Mao, E.C., Dickey and F., Derbyshire, "Model of carbon nanotube growth through chemical vapor deposition", *Chem. Phys. Lett.*, 315: 25–30 (1999).

Estimation of Drinking Water Properties Filtered with Graphene Oxide: MATLAB-based Fuzzy Logic Modeling

Ö. BİLDİ CERAN¹, İ. SEVGİLİ², H. KORUCU¹, B. ŞİMŞEK¹ and O. N. ŞARA³

¹ Çankırı Karatekin University, Çankırı/Turkey, ozgebildi@karatekin.edu.tr

¹ Çankırı Karatekin University, Çankırı/Turkey, halukkorucu@karatekin.edu.tr

¹ Çankırı Karatekin University, Çankırı/Turkey, bsimsek@karatekin.edu.tr

² Çankırı Municipality, Water and Service Association, Çankırı/Turkey, inci_sevgili@hotmail.com

³Bursa Technical University, Bursa/Turkey, osman.sara@btu.edu.tr

Abstract – In this study, improvement rates of drinking water quality criteria were predicted using Matlab-based fuzzy toolbox. The data set were entered to the Matlab toolbox as fuzzy rules. The increase or decrease rates can be calculated for the water characteristics with the desired drinking water standard with the use Matlab fuzzy model. The amount of graphene oxide required for this desired improvement rate can be determined with the help of the expert system.

Keywords – Graphene oxide, water purification, fuzzy logic model, Matlab

I. INTRODUCTION

Clean water is one of the most fundamental elements for the life of living organisms. The processing cost of drinking water is constantly increasing due to the increasing energy cost, increasing population and environmental issues. That's why advanced water cleaning technologies are developed [1]. Environmental carbon-based nanotechnology is a promising area of research due to its application in water treatment [2, 3]. Recently, due to its remarkable physical properties, chemical stability and unique two-dimensional structures, graphene and graphene based nano materials have attracted attention as a new nano material in the field of drinking water treatment applications [1]. Graphene oxide (GO) is a more attractive material because it can be produced in large scale and it is more successful in drinking water treatment compared to reduced graphene oxide [4].

Chemical parameters of potable water quality are indicative of the acceptability of the water standard for human consumption, domestic consumption, agricultural and industrial consumption. In the evaluation of water quality, chemical parameters such as dissolved O₂ (DO), total organic carbon (TOC), total inorganic carbon (TIC), hardness (French hardness), turbidity and color should be considered [3, 5].

The most important stage of the water treatment process is to increase the efficiency of the process and to improve the system through optimization without increasing the cost. Since

the removal processes involve interactions of non-linear variables, it is very important to determine the optimum experimental conditions to obtain maximum efficiency. Traditional data processing methods are not sufficient enough to solve these problems, hence optimization techniques based on artificial intelligence approaches are considered as an effective solution in these processes in recent years [6]. In addition, artificial intelligence techniques based on existing data (which is created without extra experiments and cost) allows modeling and optimization studies [7, 8]. Artificial intelligence simulates human perception, learning and reasoning to solve problems. Artificial intelligence techniques can be listed mainly as knowledge-based systems (KBS), artificial neural networks (ANN), genetic algorithms (GA), fuzzy logic modelling (FL) [9]. In the last few years, many nonlinear models of artificial intelligence techniques have been used to predict drinking water parameters. Delpla at al. used the ANN model to determine the turbidity analysis of drinking water sources, Singh at al. also used the ANN model to determine the oxygen and biochemical oxygen demand levels [10, 11]. Vaidya used fuzzy logic method to analyze and compare measurement data of criteria such as pH, turbidity, conductivity, total dissolved solid and dissolved O₂ [12].

In this study, recovery rates of drinking water quality criteria such as dissolved O₂, turbidity, color, TIC, TOC, hardness were modeled with Matlab-based fuzzy tool. Thus, recovery rates in quality criteria can be estimated and how much graphene oxide can be used to achieve the desired recovery rate.

II. THEORETICAL BACKGROUND

A. Artificial Intelligence Technologies

Knowledge-based systems: KBSs are used to emulate a human expert who has extensive knowledge and experience about one specific area. These systems works very much like human experts in terms of solving an expertise problem. They use the same steps like answering the questions offering a solution and validating the results in solving a problem [13].

Artificial neural networks: ANN is based on our understanding of the brain and its associated nervous systems. An artificial cell model in artificial neural networks consists of five components, the input neuron (the information entering the cell), the weights, the coupling function, the activation function, and the output function (the values obtained). The biggest advantage of ANNs is their ability to model complex, nonlinear processes without having to take the form of the relationship between input and output variables [13].

Genetic algorithm: It is a successful way to solve optimization problems by simulating the principle of biological evolution [6]. GA is a search technique based on natural genetic mechanisms and biological processes. GA can be used as an optimization method to minimize or maximize an objective function. GAs have clearly demonstrated their ability to produce good solutions even in the case of highly complex, multi-parameter problems [13].

Fuzzy logic modelling: Fuzzy logic modeling (FL) use fuzzy sets to deal with inaccurate and missing data. In traditional set theory, an object is or is not a member of the cluster, but a fuzzy cluster receives a value between 0 and 1 [9]. An optimization problem is a formulation that maximizes or minimizes an object under a set of constraints, if the purpose or constraints are uncertain, then this is a fuzzy optimization problem [13].

B. Properties of Graphene Oxide

GO is a single atomic layered material containing carbon, hydrogen and oxygen molecules by oxidation of graphite crystals. GO is highly hydrophilic, water-dispersible and easily processable. GO can be produced using relatively cheap graphite as raw materials and using low cost chemical methods with high efficiency. Unlike other methods, it is less costly and the chemical method is the most preferred production method of graphene oxide [14]. The improved Hummers method is at the head of high-scale and relatively low cost graphene oxide production methods. The Hummers method is a more environmentally friendly production method than Brodie, and the synthesis method is summarized below. Graphite powder and phosphoric acid (H_3PO_4) are added to the reactor and mixed for 4 hours. Then potassium permanganate ($KMnO_4$) is slowly added to the mixture, mixture temperature is increased to $35^\circ C$ and mixed for 2 hours. The mixture is then heated to $95^\circ C$ and stirred for 2 hours again. After resting the mixture, H_2O_2 is added and the mixture is stirred for an additional 1 hours. The resulting mixture is filtered and washed with HCl. After centrifugation, it is dried in the oven [3, 15]

III. MATERIALS AND METHODS

A. Properties of drinking water

Turbidity is a parameter that measures the transparency of water based on the presence of aqueous particles. Living organisms and other suspended particles may decrease the effectiveness of chlorine or other disinfectant [11]. According to the World Health Organization, the acceptable limit for turbidity of drinking water is 5 NTU [16]. Hardness in water

originates from various dissolved metallic ions, mostly calcium and magnesium cations. It is usually expressed in milligrams per liter of calcium carbonate [16]. Drinking water should ideally contain no visible color. The color of drinking water depends on the presence of colored organic matter (mainly humic and fulvic acids). Color is strongly influenced by the presence of iron and other metals as natural impurities or corrosion products [16]. The dissolved O_2 content of water is affected by the source, raw water, treatment and chemical or biological processes involved in the distribution system. The depletion of dissolved O_2 in water sources can promote the reduction of nitrate to microbial nitrate and sulfate to sulfur [16]. Total dissolved solids arise from the presence of small amounts of organic matter and inorganic salts dissolved in water. The main ions contained in dissolved substances are carbonate, bicarbonate, chloride, sulfate, nitrate, sodium, potassium, calcium and magnesium. Dissolved substances affect the properties of water such as taste, hardness, corrosivity and encrustation potential [17].

B. Methodology

Three steps were performed to predict the improvement ratios of the drinking water quality and also an expert system based on Matlab fuzzy tool was built to estimate these ratios. Firstly, data collection stage from Şimşek et al.'s work was completed [3]. Eight experiment results were used for writing the rules and the fuzzy model was developed with the use of these experiments. Lastly, the improvement ratios of the drinking water quality such as dissolved O_2 , turbidity, color, TIC, TOC and hardness can be easily predict by the fuzzy model (figure 1).

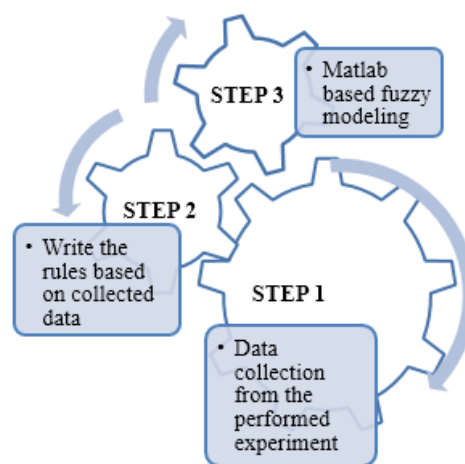


Figure 1: Propose methodology

IV. RESULTS AND DISCUSSIONS

Graphene oxide amount (v/v) was selected as input parameter and dissolved O_2 , turbidity, color, TIC, TOC and hardness were determined as output parameters. Graphene oxide amount (v/v) is divided into six numbers of subsets with triangular fuzzy membership functions and dissolved O_2 ,

turbidity, color, TIC, TOC and hardness is divided into three numbers of subsets with triangular fuzzy membership (Figure 2). Rules were written with the use of data set (Figure 3). Fuzzy model was developed using data set by Matlab fuzzy tool. (Figure 4)

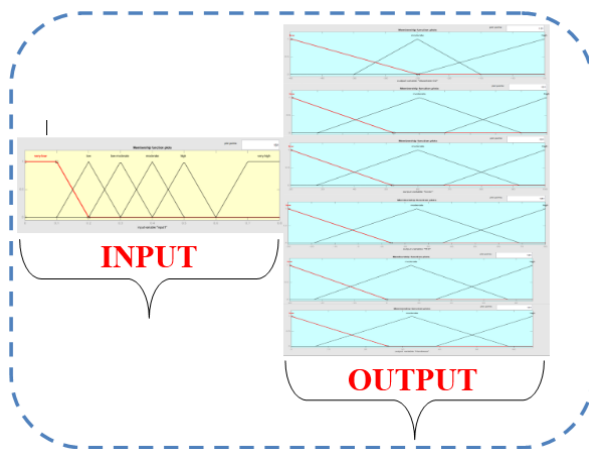


Figure 2: Membership functions for all parameters

```

1. If (Graphene-Oxide-Amount-(v/v) is very-low) then (dissolved-O2 is moderate)(Turbidity is high)(Color is low)(TIC is low)(TOC is moderate)(Hardness is low) (1)
2. If (Graphene-Oxide-Amount-(v/v) is low) then (dissolved-O2 is low)(Turbidity is high)(Color is low)(TIC is low)(TOC is low)(Hardness is moderate) (1)
3. If (Graphene-Oxide-Amount-(v/v) is low-moderate) then (dissolved-O2 is high)(Turbidity is high)(Color is moderate)(TIC is moderate)(TOC is high)(Hardness is moderate) (1)
4. If (Graphene-Oxide-Amount-(v/v) is low-moderate) then (dissolved-O2 is low)(Turbidity is high)(Color is moderate)(TIC is low)(TOC is moderate)(Hardness is moderate) (1)
5. If (Graphene-Oxide-Amount-(v/v) is moderate) then (dissolved-O2 is moderate)(Turbidity is high)(Color is moderate)(TIC is moderate)(TOC is high)(Hardness is moderate) (1)
6. If (Graphene-Oxide-Amount-(v/v) is high) then (dissolved-O2 is low)(Turbidity is moderate)(Color is moderate)(TIC is low)(TOC is high)(Hardness is moderate) (1)
7. If (Graphene-Oxide-Amount-(v/v) is high) then (dissolved-O2 is low)(Turbidity is high)(Color is high)(TIC is moderate)(TOC is high)(Hardness is high) (1)
8. If (Graphene-Oxide-Amount-(v/v) is very-high) then (dissolved-O2 is low)(Turbidity is high)(Color is high)(TIC is high)(TOC is high)(Hardness is high) (1)

```

Figure 3: Rules based on data set

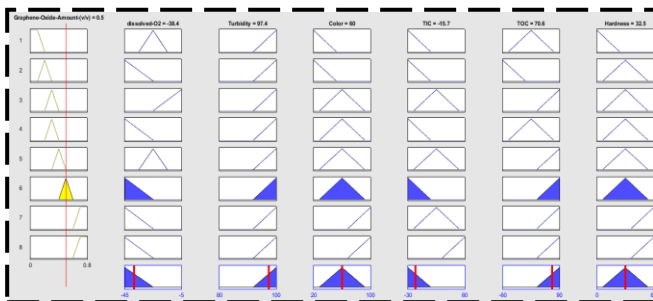


Figure 4: Fuzzy based expert model

The improvement rate belongs to amount of dissolved O_2 decreases with the amount of graphene oxide increasing. As the amount of graphene oxide used for drinking water filtration increases, the improvement rate belong to turbidity is increasing. The improvement rates belong to color, TIC, TOC and hardness increases with the amount of graphene oxide increasing (Figure 5).

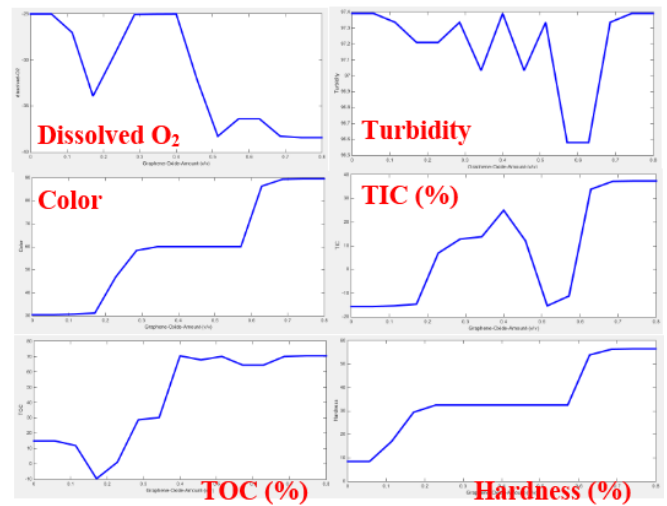


Figure 5: Improvement rates predicted by fuzzy model

V. CONCLUSIONS

In this study, improvement rates of drinking water quality criteria were modeled with the use of Matlab-based fuzzy tool. Results were obtained by the study was given as follows.

After obtaining the raw water values, the recovery rates can be calculated for the water characteristics with the desired drinking water standard. The amount of graphene oxide required for this recovery rate can be determined with the help of the expert system.

Much more data are needed to determine the much accurate utilization rates of nanomaterials. A much more successful expert system model can be created with much more data.

Artificial intelligence methods should be used for predicting, modeling, optimizing nano materials usage due to cost saving and experimental time reduction. Especially, genetic algorithm, fuzzy logic and neural network can be easily performed with the use of Matlab toolbox.

ACKNOWLEDGMENT

Authors thank to Çankırı Municipality, Water and Service Association.

REFERENCES

- [1] Lim, M.-Y., et al., *Cross-linked graphene oxide membrane having high ion selectivity and antibacterial activity prepared using tannic acid-functionalized graphene oxide and polyethyleneimine*. Journal of Membrane Science, 2017. **521**: p. 1-9.
- [2] Gurunathan, S., et al., *Oxidative stress-mediated antibacterial activity of graphene oxide and reduced graphene oxide in Pseudomonas aeruginosa*. International journal of nanomedicine, 2012. **7**: p. 5901.
- [3] Şimşek, B., et al., *Nanomaterials Based Drinking Water Purification: Comparative Study with a Conventional Water Purification Process*. Periodica Polytechnica Chemical Engineering, 2017.
- [4] Bildi C. Ö., S.İ., Şimşek B., Şara O. N. *Water Treatment with the Use of Reduced Graphene Oxide Filtration*. in *International Conference on Engineering Technologies (ICENTE'17)*. 2017. Konya, Turkey.
- [5] Salari, M., et al., *Quality assessment and artificial neural networks modeling for characterization of chemical and physical parameters of potable water*. Food and Chemical Toxicology, 2018. **118**: p. 212-219.

- [6] Cao, R., et al., *Artificial Intelligence Based Optimization for the Se (IV) Removal from Aqueous Solution by Reduced Graphene Oxide-Supported Nanoscale Zero-Valent Iron Composites*. Materials, 2018. **11**(3): p. 428.
- [7] Şimşek, B., et al., *Development of a graphical user interface for determining the optimal mixture parameters of normal weight concretes: A response surface methodology based quadratic programming approach*. Chemometrics and Intelligent Laboratory Systems, 2014. **136**: p. 1-9.
- [8] Şimşek, B., Y.T. İç, and E.H. Şimşek, *Hybridizing a fuzzy multi-response Taguchi optimization algorithm with artificial neural networks to solve standard ready-mixed concrete optimization problems*. International Journal of Computational Intelligence Systems, 2016. **9**(3): p. 525-543.
- [9] Chen, S.H., A.J. Jakeman, and J.P. Norton, *Artificial intelligence techniques: an introduction to their use for modelling environmental systems*. Mathematics and computers in simulation, 2008. **78**(2-3): p. 379-400.
- [10] Singh, K.P., et al., *Artificial neural network modeling of the river water quality—a case study*. Ecological Modelling, 2009. **220**(6): p. 888-895.
- [11] Delpla, I., M. Florea, and M.J. Rodriguez, *Drinking Water Source Monitoring Using Early Warning Systems Based on Data Mining Techniques*. Water Resources Management, 2018: p. 1-12.
- [12] Vaidya, B., *A Review On-Water Quality Measurement System Using Artificial Intelligence*. 2018.
- [13] Chau, K.-w., *A review on integration of artificial intelligence into water quality modelling*. Marine pollution bulletin, 2006. **52**(7): p. 726-733.
- [14] Ray, S.C., *Application and uses of graphene oxide and reduced graphene oxide*. Applications of Graphene and Graphene-Oxide Based Nanomaterials, 2015: p. 39-55.
- [15] Korucu, H., B. Şimşek, and A. Yartaşı, *A TOPSIS-Based Taguchi Design to Investigate Optimum Mixture Proportions of Graphene Oxide Powder Synthesized by Hummers Method*. Arabian Journal for Science and Engineering, 2018: p. 1-23.
- [16] Edition, F., *Guidelines for drinking-water quality*. WHO chronicle, 2011. **38**(4): p. 104-8.
- [17] Egemen, Ö. and U. Sunlu, *Su kalitesi*. Ege Üniv. Su Ürünleri Fak. Yayın, 1999(14).

Compressive Behavior of Glass-Carbon/Epoxy $\pm 55^\circ$ Filament Wound Hybrid Pipes Confined Composite Concrete with Expansive Cement

L.GEMİ¹, M. A. KÖROĞLU¹, M. ÇALIŞKAN¹

¹ Necmettin Erbakan University, Konya/Turkey, lgemi@konya.edu.tr

¹ Necmettin Erbakan University, Konya/Turkey, makoroglu@konya.edu.tr

¹ Necmettin Erbakan University, Konya/Turkey, mervecaliskan7094@gmail.com

Abstract - Today, a wide variety of modern composite materials and products found in the construction market offer many useful possibilities for using them in both structural and non-structural industrial building elements. The aim of this project; Investigation of the behavior under axial load of cylindrical columns produced using expanded concrete with cement water ratios of 0.4, 0.5 and 0.6 as reinforced with hybrid composite pipes with winding angle of $\pm 55^\circ$ produced by filament winding technique and investigating the effect of the columns on load capacity. Columns reinforced with composite pipes were tested and their behaviors were investigated by comparing cylindrical reference samples produced from expanded concrete with the same cement water ratio. As a result of the study, it was determined that there is a significant increase in load strength in the composite pipes strengthened girders compared to the reference specimens.

Keywords - Filament Winding, Composite Pipe, Expanding Cement, Damage Analysis, Confinement

I. INTRODUCTION

CORROSION of steel reinforcement due to harsh environments is a major cause of deterioration of performance and ductility of reinforced concrete columns. Various strengthening techniques have been developed to restore the column capacity and ductility, for example wrapping reinforced concrete columns by fibre reinforced polymer (FRP) jackets. However, in the last two decades, concrete filled FRP tube columns have been proposed as an alternative technique for protecting the internal steel against corrosion. In fact, FRP tubes not only preserve steel reinforcement from corrosion but also act as confining reinforcement in both axial and transverse directions.

For strengthening concrete members confining with FRP jackets externally has become a common method in construction industry. A significant number of experimental studies on compressive behaviour of FRP- confined concrete have been carried out over the past two decades [1-4]. However, the studies focused on FRP tubes are still limited [5-15]. Nevertheless, the high inelastic deformation capacity of FRP tubes with concrete has been a remarkable alternative for innovative high-performance columns [16].

FRP material has been popular in construction industry and not only to enhance the mechanical properties of concrete but also be used as reinforcement, beam or slab [17]. Nowadays, composite FRP piles have been an innovative solution for composite columns. On manufacturing composite pipes, filament wound winding angle is essential for damage mechanism. Filament wound winding angle configuration may develop load bearing capacity of pipe due to its position. Investigating development of damage in detail guides the selection of filament wound winding configuration for new pipes. There are a great number of experimental and analytical studies in the literature focusing on hoop stress behavior of glass/epoxy composites pipes [17].

The aim of this experimental study is to investigate the confinement effect of Glass/Epoxy $\pm 55^\circ$ Filament Wound Pipes on the capacity and ductility of short cylindrical pipes exposed to uniaxial compression for different types of concrete core. Additionally, after axial loading tests on concrete that evolved to hoop stress on the composite FRP pipe macro failure on pipes were investigated. And also to investigate the micro damage mechanisms on composite shell, selected specimens were studied under an electron microscope. Specimens produced both of composite concrete with low strength and concrete with expansive cement were examined and their behaviour has been collated. In order to accomplish a desirable composite behaviour, the interfacial contact between the pipe and concrete is essential. Therefore, ordinary Portland cement and expansive cement admixture were also studied. On account of examining the consolidation of fresh concrete, half of the specimens both with ordinary Portland cement and expansive cement were casted without fresh concrete vibration.

II. MATERIAL AND METHOD

Properties of Used Concrete; The ingredient proportions of cement, aggregate, sand, water and admixture proportions and the 28 days compressive strength of each mixture are shown in Table 1. CEM I 32.5 R type of cement was used to prepare the normal composite concrete (NCC) mixture and the other mixture was prepared using expansive cement (EC) instead of CEM I 32.5 R. For all specimens, nylon polymers (20 kg/m³;

0,83% by weight) were used in order to control shrinkage cracks and minimize settlement shrinkage. Nylon polymers, 100% virgin nylon fibrous monofilament, have 19 mm length and 966 MPa tensile strength. For all specimen series, 3 cubes with dimensions 100*100*100 mm are prepared and tested after 28 days. The average compressive strength of concrete cubes for each specimen is given in Table 1.

Table 1: Concrete mixing elements and their mechanical properties

Cement (kg/m ³)	Sand (kg/m ³)	Agregate (kg/m ³)	Water (kg/m ³)	W/C	28 days Strength (MPa)
975	1825	700	390	0,4	50,46
820	1680	800	410	0,5	45,07
750	1250	1500	450	0,6	32,57

The hybrid composite pipes used in this study were produced with filament winding technique in such a way that the winding angle is $(\pm 55^\circ)_3$ as shown in Figure 1. Stacking sequence configuration was set as Glass/Carbon/Glass [18]. The fibre material used in the pipes was Vetrotex 1200 tex E-glass with 17 μ m diameters and carbon 12K A-42 with 8 μ m diameters whereas the matrix material was Bisophenol A, Epoxy CY 225. After being manufactured, the pipes were, initially, cured in an oven at a temperature of 135°C for two hours and is, then, cured at 150°C temperature for another two hours. The length, inner diameter, and thickness of the pipes were 160 mm, 72 mm, and 2.4 ± 0.04 mm, respectively (Figure 1). The properties of the fibres and epoxy used are given in Table 2.

Table 2: Properties of the fibers and matrix used

	E (GPa)	σ_{TS} (MPa)	ρ (g/cm ³)	ϵ_r (%)
E-glass	73	2345	2,6	1,5-2
Carbon	230	3500	1,75	1,5
Epoxy	3,4	50-60	1,2	4-6

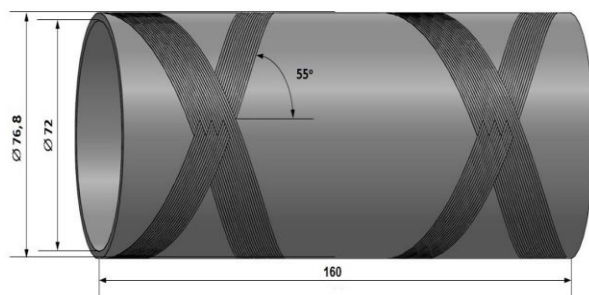


Figure 1: Geometry of hybrid composite pipe

III. EXPERIMENTAL STUDY RESULTS

The experimental results of the fracture damage of the specimens are shown in Figure 2. When the fracture modes were examined, it was seen that hybrid (HB) composite pipes showed ductile fracture.



Figure 2: Fracture damage of specimens after testing

When analyzed together with the results of the load-displacement graphs shown in Figure 3- Figure 4. HB-0.4 reached the load of 33 kN and when the load reached the load of 35 kN at the lower part, the matrix cracking sounds and cracks occurred in the direction of the fiber winding angle.

On the HB-0.5 spec, cracks were formed in the concrete under load of 32 kN and when the load went up to 35 kN, cracking on the concrete continued, and the cracks began to come from the sample. There was a load drop to 32 kN in the sample and there was severe damage in the fiber direction.

When load of 29 kN was reached at HB-0.6 specimen, the concrete strength was low and crushing occurred, and whitening occurred in the composite pipe, whitening all over the surface. When the load was 28 kN, the sample started to sound from the matrix material and the sample was broken in the fiber direction at 28 kN because of the low concrete strength. The reference specimens became unable to carry the broken load at approximately 20 kN. The best result is obtained from HB-0.4.

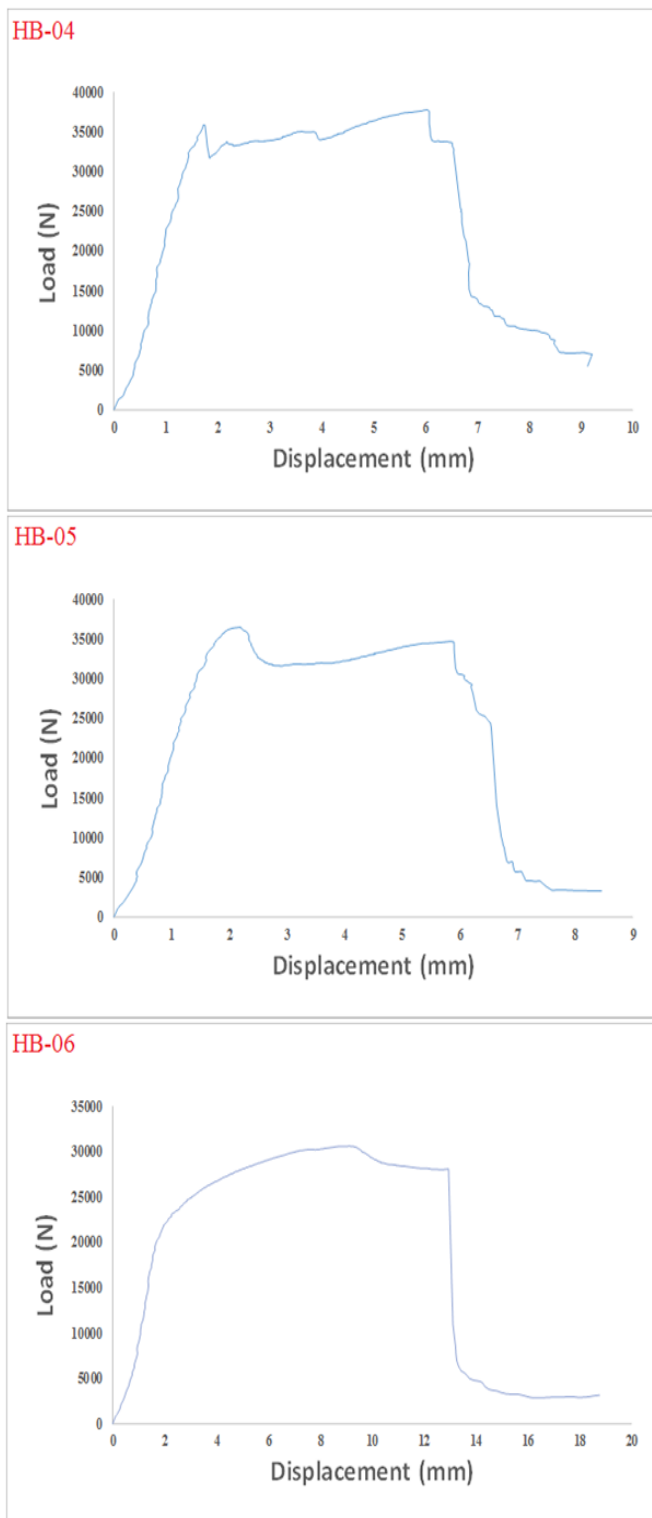


Figure 3: Load-displacement graphs of the samples

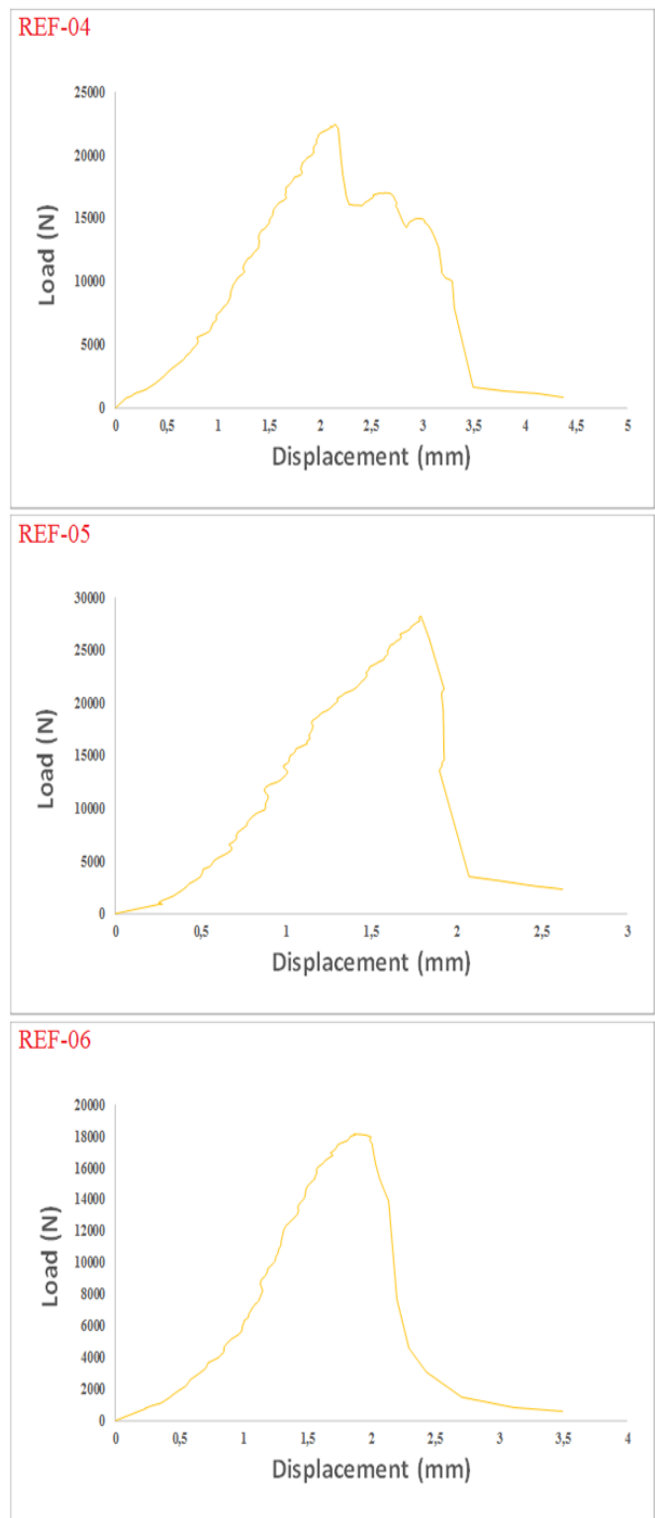


Figure 4: Load-displacement graphs of the samples (reference)

IV. CONCLUSION

The results obtained by applying the hybrid composite pipes with the cement water ratio of 0.4, 0.5 and 0.6 with a winding angle of $\pm 55^\circ$ and the reference specimens under the axial load test are given below.

- In the tests carried out, it was observed that the

breakage of the composite pipe, in which the fiber winding angle increased the strength of the composite pipe, was not suddenly broken, but increased in the direction of the fiber winding angle and increased fiber breakage.

- While the concrete specimen was fractured at 20 kN, it was observed that the hybrid pipe increased the load that the concrete could carry by the winding effect. The composite specimen was able to carry a load of 35 kN. It is seen that when the composite pipe is applied, the strength increases by two. According to the reference sample, more concrete load was carried on the composite specimens, and when the concrete load was released, the composite pipe continued to carry the load.
- It was observed that the resistance of concrete was decreased by increasing the water content of cement. The defects and voids that occur together with the increase of the cement water ratio in the inner structure of the concrete cause decrease of resistance. Because the concrete is more durable, it is damaged faster and the damage on the composite sample is faster.

ACKNOWLEDGMENT

The authors thank Necmettin Erbakan University Scientific Research Project Funding office (BAP-Project number: 181335001) for their financial support.

REFERENCES

- [1] T. Ozbakkaloglu, J. C. Lim, and T. Vincent, "FRP-confined concrete in circular sections: Review and assessment of stress-strain models," *Engineering Structures*, 49, 1068-1088, 2013.
- [2] B. Binici, "An analytical model for stress-strain behavior of confined concrete," *Engineering structures*, 27(7), 1040-1051, 2005.
- [3] A. Ilki, O. Peker, E. Karamuk, C. Demir, and N. Kumbasar, "FRP retrofit of low and medium strength circular and rectangular reinforced concrete columns," *Journal of Materials in Civil Engineering*, 20(2), 169-188, 2008.
- [4] V. Yazici, and M. N. Hadi, "Normalized confinement stiffness approach for modeling FRP-confined concrete," *Journal of composites for construction*, 16(5), 520-528, 2012.
- [5] M. A. Koroğlu, M. Ceylan, M. H. Arslan, and A. İlki, "Estimation of flexural capacity of quadrilateral FRP-confined RC columns using combined artificial neural network," *Engineering Structures*, 42, 23-32, 2012.
- [6] T. Ozbakkaloglu, "Compressive behavior of concrete-filled FRP tube columns: Assessment of critical column parameters," *Engineering Structures*, 51, 188-199, 2013.
- [7] T. Ozbakkaloglu, "Concrete-filled FRP tubes: Manufacture and testing of new forms designed for improved performance," *Journal of Composites for Construction*, 17(2), 280-291, 2012.
- [8] T. Vincent, and T. Ozbakkaloglu, "Influence of concrete strength and confinement method on axial compressive behavior of FRP confined high-and ultra high-strength concrete," *Composites Part B: Engineering*, 50, 413-428, 2013.
- [9] I. F. Kara, A. F. Ashour, and M. A. Koroğlu, "Flexural behavior of hybrid FRP/steel reinforced concrete beams," *Composite Structures*, 129, 111-121, 2015.
- [10] I. F. Kara, A. F. Ashour, and M. A. Koroğlu, "Flexural performance of reinforced concrete beams strengthened with prestressed near-surface-mounted FRP reinforcements," *Composites Part B: Engineering*, 91, 371-383, 2016.
- [11] I. F. Kara, M. A. Koroğlu, and A. F. Ashour, "Tests of continuous concrete slabs reinforced with basalt fibre reinforced plastic bars," *ACI Structural Journal*, 2017.
- [12] L. Gemi, M. Kayırcı, M. Uludağ, D. S. Gemi, and Ö. S. Şahin, "Experimental and statistical analysis of low velocity impact response of filament wound composite pipes," *Composites Part B: Engineering*, 149, 38-48, 2018.
- [13] O. S. Sahin, A. Akdemir, A. Avci, and L. Gemi, "Fatigue crack growth behavior of filament wound composite pipes in corrosive environment," *Journal of Reinforced Plastics and Composites*, 28(24), 2957-2970, 2009.
- [14] L. Gemi, M. Kara, and A. Avci, "Low velocity impact response of prestressed functionally graded hybrid pipes," *Composites Part B: Engineering*, 106, 154-163, 2016.
- [15] A. Castellano, P. Foti, A. Fraddosio, S. Marzano, and M. D. Piccioni, "Mechanical characterization of CFRP composites by ultrasonic immersion tests: Experimental and numerical approaches," *Composites Part B: Engineering*, 66, 299-310, 2014.
- [16] L. Gemi, Ö. S. Şahin, and A. Akdemir, "Experimental investigation of fatigue damage formation of hybrid pipes subjected to impact loading under internal pre-stress," *Composites Part B: Engineering*, 119, 196-205, 2017.
- [17] L. Gemi, M. A. Koroğlu, and A. Ashour, "Experimental study on compressive behavior and failure analysis of composite concrete confined by glass/epoxy±55° filament wound pipes," *Composite Structures*, 187, 157-168, 2018.
- [18] L. Gemi, "Investigation of the effect of stacking sequence on low velocity impact response and damage formation in hybrid composite pipes under internal pressure. A comparative study," *Composites Part B: Engineering*, 153, 217-232, 2018.

Experimental Investigation of Behavior of Hybrid (GFRP) Box Beam Sections

M. A. KÖROĞLU¹, L.GEMİ², M. YARIMOĞLU³

¹ Necmettin Erbakan University, Konya/Turkey, makoroglu@konya.edu.tr

² Necmettin Erbakan University, Konya/Turkey, lgemi@konya.edu.tr

³ Necmettin Erbakan University, Konya/Turkey, mehmetyarimoglu@gmail.com

Abstract - In this study, bending behavior of Glass Fiber Reinforced Polymer (GFRP) square box beams infilled by concrete and hybrid beams with steel reinforcements are investigated experimentally. Load displacement curves were investigated under four-point bending tests. Bending load capacity of (GFRP) square box beams was developed when compared to the bending load capacity of (GFRP) square box beams infilled with various concrete ratio after bending tests. Additionally, both bending load bearing capacity and ductility of beams were developed significantly when GFRP square box was used.

Keywords - Bending Test, FRP, GFRP, Hybrid, Beam, Composite

I. INTRODUCTION

TODAY the use of composite materials, in construction industry, as well as many technical areas are rapidly increasing and developing day by day. Within this development process, the construction industry is constantly struggling to find new ways to improve construction technologies and designs in engineering problems and to obtain economic solutions [1-3]. The new generation composites preferred in secondary structural elements which are not considered as carriers in the construction sector are now being used as carrier and main building element.

In particular, with the increase in mass production of FRP composites, the use of FRP materials which are light and nonmetallic has been started to be used more effectively for different purposes in strengthening, repairing and improving concrete structures [4]. In recent years, research and development studies have focused on hybrid systems, in which traditional building materials such as concrete, and FRP composite materials are used together [3]. A large number of studies have been conducted on hybrid FRP columns, which have been recently filled with concrete or that are formed of FRP pipes [5-8].

Based on scientific discussions, it is clear that the use of FRP composites in new structures in the near future will mainly focus on the use of hybrid structures [9]. As a result of many research results, the use of traditional materials, especially in concrete with FRP composites, has been shown to

be one of the key solution ways to overcome some disadvantages of FRP-produced structures [9, 10].

The aim of this study is to investigate the advantages of combining concrete which is the most basic building material with a long history as a hybrid with GFRP, also known as CTP (Glass Reinforced Plastic) box profiles. It is thought that GFRP profiles with many positive properties will develop in some physical and mechanical behaviors with the new synergy that will produce the new hybrid material produced by taking advantage of the positive properties of both component materials by combining these properties with concrete.

In this study, it is aimed to make contribution to each other by making use of the superior properties of both materials in the hybrid building material formed by GFRP with concrete.

II. MATERIAL AND METHOD

The GFRP box profiles used in the tests are box profiles produced in Turkey, with a section of 74x74 mm and 4 mm wall thickness (Figure 1). The physical and mechanical properties of these profiles, which are produced in the desired shape and size by polymer matrix and glass fiber reinforcement, are given in Table 1.

Table 1: Properties of GFRP box profile

Modulus of Elasticity	293000 kg/cm ²		
Tension Strength	5609 kg/cm ²		
Poisson ratio	0.34		
Unit weight	1.738 g/cm ³		
Specific weight	1.822		
Fiber volume percentage (%)	longitudinally	transverse	matrix
	41.59	8.76	49.64

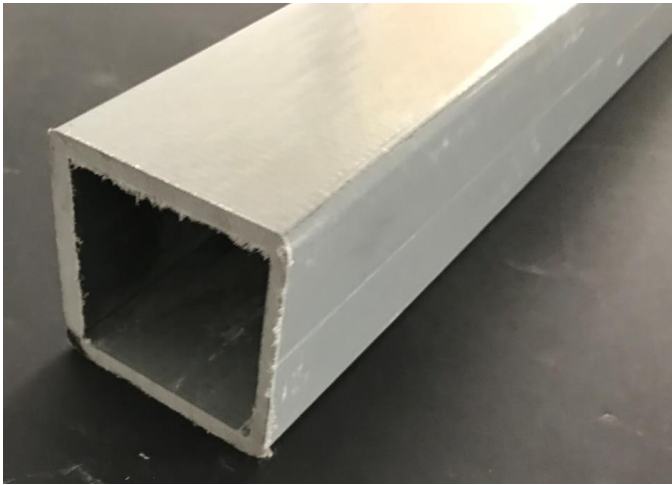


Figure 1: GFRP box profile

Weber.rep.grout mortar was used as the concrete filled into GFRP box profiles during the study. The material produced by Weber is manufactured in accordance with TS EN 1504-3 (Products and systems for protection and repair of concrete structures - Requirements, requirements, quality control and conformity assessment - Part 3: Structural and structural and non-structural repair). It has high adherence and high fluidity when applied with grouting mortar which is cement based high strength, high workability and does not shrink, waterproofing material. A mixture of 4.25 liters of clean water was applied on a 25 kg bag. The mixture was made in a laboratory environment with the help of a concrete mixer. The use of cementitious grout mortar in the study is that the material does not shrink. It is aimed to increase the adherence between the GFRP profile and the concrete by means of this non-shrinking mortar and work with GFRP box better together.

For the determination of tensile strength of the beams, 4-point bending tests were carried out. The 28-day average compressive strength of the concrete produced was found to be 53,75 MPa, the tensile strength 19 MPa and bending tensile strength 11 MPa.

In the bending tests, reinforced concrete beam specimens produced as hybrid beams were used. Beam-shaped materials with the same cross-section dimensions are prepared in various forms Experiments were carried out with a test specimen with a length of 150 cm having a width of 75x75 mm and a length of 120 cm from the support points. Subsequently, examination of the bending tests of the other specimens prepared was carried out. The bending test method and the GFRP box profile material used in the experiment are shown in detail in Figure 2.

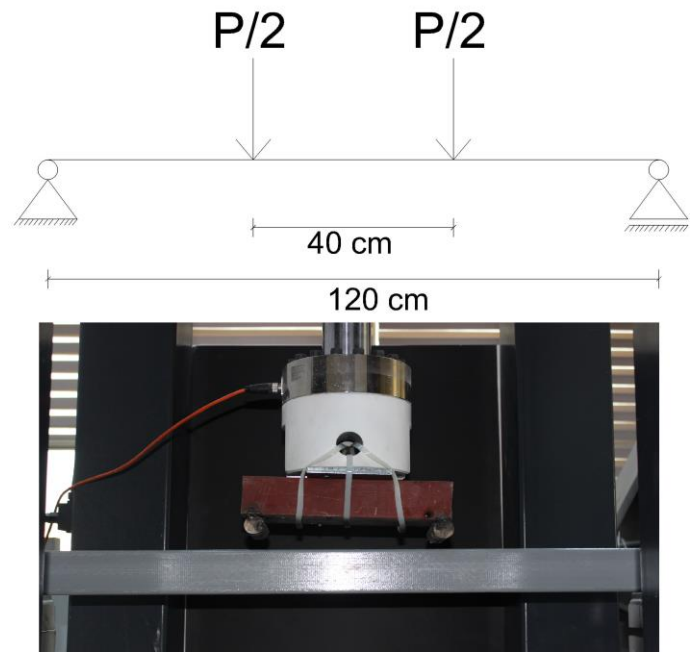


Figure 2: Test setup

III. EXPERIMENTAL STUDY RESULTS

Three beam was prepared for testing under 4 point bending tests. One specimen is concrete filled GFRP Box which is only filled with plain concrete called "s1". Second specimen is reinforced concrete filled GFRP Box which 4 steel bars with the diameter of 8 mm called "s2". And the last specimen is the reinforced concrete which has the same concrete and steel reinforcement with specimen 2 is called "s3" (Figure 3).

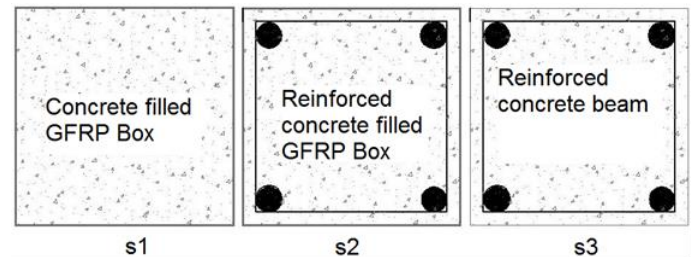


Figure 3: Specimen cross-sections

It was observed that there was a performance increase of 6% compared to the GFRP sample filled with reinforced concrete to GFRP sample filled with plain concrete. In the GFRP sample s1, damage was observed in the upper area, whereas in the sample with pressure-induced crushing on the front surfaces, cracks in the fiber direction were observed and a broken shear fracture was observed in the sample s2. In addition, as the preliminary surface and corner points were observed to be cracked in the sample s2. The cracking was spread over the surface and the front surface was separated from the bottom surface and the result damage was observed in the material.

A comparison of the maximum load-to-maximum deformation graphs using the data obtained after the bending tests of the samples is shown in Figure 4.

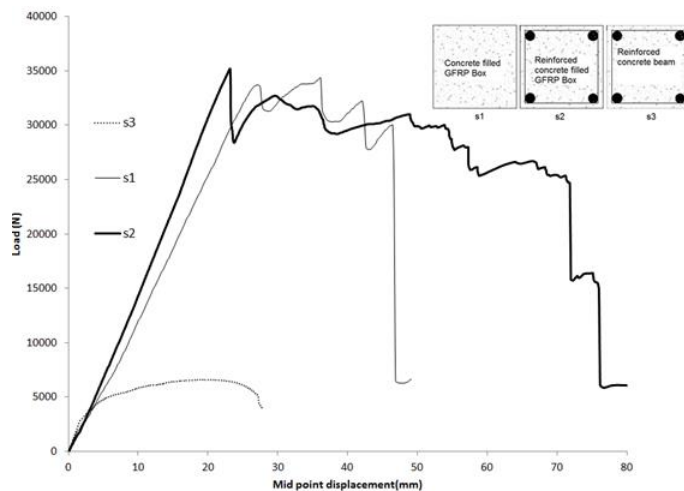


Figure 4: Load-Displacement curve

IV. CONCLUSION

The properties of GFRP and concrete were determined experimentally and the bending behaviors of hybrid structural elements were investigated in this study.

It is seen that GFRP materials have more advantageous in terms of lightness, corrosion and tensile strength compared to the basic materials used in the structures. Therefore, the use of GFRP materials as an active material especially in the construction sector is thought to be the solution to many problems encountered in the construction sector.

The concrete filled GFRP sections show a considerable strength and stiffness increase with 600% compared with the reinforced concrete section. Reinforced concrete filled GFRP box has higher strength and stiffness.

ACKNOWLEDGMENT

The authors thank Necmettin Erbakan University Scientific Research Project Funding office (BAP-Project number: 181319001) for their financial support.

REFERENCES

- [1] M. A. Koroğlu, M. Ceylan, M. H. Arslan, and A. İlki, "Estimation of flexural capacity of quadrilateral FRP-confined RC columns using combined artificial neural network," *Engineering Structures*, 42, 23-32, 2012.
- [2] I. F. Kara, A. F. Ashour, and M. A. Koroğlu, "Flexural behavior of hybrid FRP/steel reinforced concrete beams," *Composite Structures*, 129, 111-121, 2015.
- [3] I. F. Kara, A. F. Ashour, and M. A. Koroğlu, "Flexural performance of reinforced concrete beams strengthened with prestressed near-surface-mounted FRP reinforcements," *Composites Part B: Engineering*, 91, 371-383, 2016.
- [4] I. F. Kara, M. A. Koroğlu, and A. F. Ashour, "Tests of continuous concrete slabs reinforced with basalt fibre reinforced plastic bars," *ACI Structural Journal*, 2017.
- [5] L. Gemi, "Investigation of the effect of stacking sequence on low velocity impact response and damage formation in hybrid composite pipes under internal pressure. A comparative study," *Composites Part B: Engineering*, 153, 217-232, 2018.
- [6] O. S. Sahin, A. Akdemir, A. Avci, and L. Gemi, "Fatigue crack growth behavior of filament wound composite pipes in corrosive

environment," *Journal of Reinforced Plastics and Composites*, 28(24), 2957-2970, 2009.

- [7] L. Gemi, M. Kara, and A. Avci, "Low velocity impact response of prestressed functionally graded hybrid pipes," *Composites Part B: Engineering*, 106, 154-163, 2016.
- [8] O. S. Sahin, A. Akdemir, A. Avci, and L. Gemi, "Fatigue crack growth behavior of filament wound composite pipes in corrosive environment," *Journal of Reinforced Plastics and Composites*, 28(24), 2957-2970, 2009.
- [9] L. Gemi, M. A. Koroğlu, and A. Ashour, "Experimental study on compressive behavior and failure analysis of composite concrete confined by glass/epoxy $\pm 55^\circ$ filament wound pipes," *Composite Structures*, 187, 157-168, 2018.
- [10] L. Gemi, M. Kayrıcı, M. Uludağ, D. S. Gemi, and Ö. S. Şahin, "Experimental and statistical analysis of low velocity impact response of filament wound composite pipes," *Composites Part B: Engineering*, 149, 38-48, 2018.

Chemical recycling of polyethylene terephthalate (PET) bottle wastes with alcoholysis: transesterification of shredded PET with 2-ethylhexanol to produce dioctyl terephthalate (DOTP)

V. A. KÜÇÜK¹, B. ŞİMŞEK¹, T. UYGUNOĞLU², M. M. KOCAKERİM¹

¹ Çankırı Karatekin University, Çankırı/Turkey, barissimsek@karatekin.edu.tr

² Afyon Kocatepe University, Afyon/Turkey, uygunoglu@aku.edu.tr

Abstract – In this study, dioctyl terephthalate (DOTP) synthesis was performed by chemical recycling from shredded waste polyethylene terephthalate (PET) bottles. Alcoholysis of PET with 2-ethylhexanol was preferred for experiments to produce dioctyl terephthalate (DOTP) which is a commonly used plasticizer for PVC. The characterization of the synthesized samples was done by Fourier-transform infrared (FTIR) spectroscopy. When FTIR spectra were examined, it was determined that DOTP was obtained.

Keywords – polyethylene terephthalate, PET, waste PET, PET recycling, chemical recycling of PET, PET bottle waste, plasticizer, dioctyl terephthalate, DOTP, alcoholysis, solvolysis, transesterification, esterification

I. INTRODUCTION

The production of plastics on a commercial scale began at the beginning of the twentieth century. Since then, the interest in the use of plastics has been increasing day by day [1]. The most commonly produced commercial plastics in the world are polyethylene, polypropylene, polyethylene terephthalate [2]. Wide acceptance of the plastics lead to the excessive use and the disposal of plastic wastes became a serious problem [3, 4]. There are several options for plastics recycling. Mechanical recycling of plastic wastes and energy recovery from waste plastics are widely preferred options. However, chemical recycling such as hydrolysis, glycolysis solvolysis and alcoholysis may be more beneficial in terms of environmental and commercial aspects.

Plastics have superior physical properties. In order to alter physical properties several additives (UV durability improvers, fire retardants etc.) are used. Plasticizers are used to make the brittle polyvinyl chloride (PVC) flexible, which is one of the most widely used plastics. Flexible PVC is used in many

different products, some of which are medical devices, toys, food containers. Traditionally, phthalic acid-derived plasticizers are used in PVC. Most commonly used are dioctyl phthalate (DOP or DEHP), diisodecyl phthalate (DIDP) diisononyl phthalate (DINP). Plasticizers do not react chemically with PVC but they are included in the polymer matrix and change the physical properties of PVC [5] This causes plasticizers to separate from the polymer matrix in time [6] The use of non-phthalate plasticizers has become widespread due to the health risks of phthalic acid-derived plasticizers [7].

Dioctyl terephthalate (DOTP) is an important alternative to traditionally used phthalate based plasticizers. It is possible to produce dioctyl terephthalate by chemical recycling of waste PET. There are very few studies in the literature on this subject [8-10].

In this study, DOTP was synthesized by the alcoholysis of PET in 2-ethyl hexanol with zinc acetate catalyst.

II. MATERIALS AND METHOD

A. Materials

2-ethylhexanol (2EH) and Zinc acetate (ZAC) was supplied by Sigma Aldrich. Shredded polyethylene terephthalate (PET) water bottles (3mm x 3mm) were used for the reaction (Figure 1).

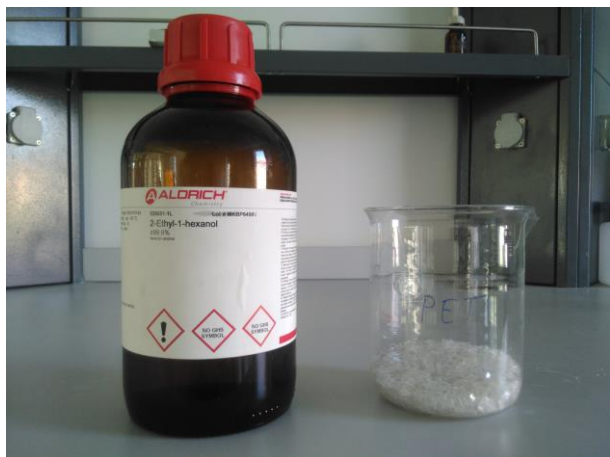


Figure 1: 2-ethylhexanol and shredded PET bottle

Reactions were took place in borosilicate flat bottom flask. Heating and stirring was made with a magnetic stirrer. In order to prevent solvent loss reaction was carried on with reflux apparatus (Figure 2).



Figure 2: Reactor and reflux apparatus

B. Method

Transesterification of PET with 2-ethylhexanol (2EH) was preferred for dioctyl terephthalate (DOTP) synthesis. With this approach it is possible to simplify the synthesis. Trials were carried out to determine amount of PET, 2-ethylhexanol and zinc acetate (ZAC). Experimental plan can be seen in Table 1.

Table 1: Experimental plan for reaction.

Exp. No.	2EH amount (g)	PET/2EH ratio	ZAC/PET ratio (%)
1	12	1:4	1.00
2	12	1:3	0.75
3	12	1:4	1.33
4	12	1:3	1.00
5	16	1:4	1.00
6	16	1:3	0.75
7	16	1:4	1.33
8	16	1:3	1.00

The procedure for the synthesis is as follows: 2-ethyl hexanol, PET and Zinc acetate catalyst were weighted and put into the reactor. Reactor was placed on to the hotplate. Reflux apparatus was installed. Mixing was made with magnetic stirrer. Reactor was heated up to the boiling point of the 2-ethyl hexanol (184-186 C). Reaction was carried on for 20-24 hours thus complete conversion of the PET could be achieved. After the reaction liquid contents are washed with water several times in order to separate water soluble content, namely ethylene glycol. Water phase and organic phase was separated with seperatory funnel. Organic phase was analyzed with Fourier-transform infrared spectroscopy (FTIR).

III. RESULTS AND DISCUSSION

Reference dioctyl terephthalate and 2-ethylhexanol was analyzed with Fourier-transform infrared spectroscopy (FTIR). Spectra of these compounds can be seen at Figure 3 and Figure 4 respectively.

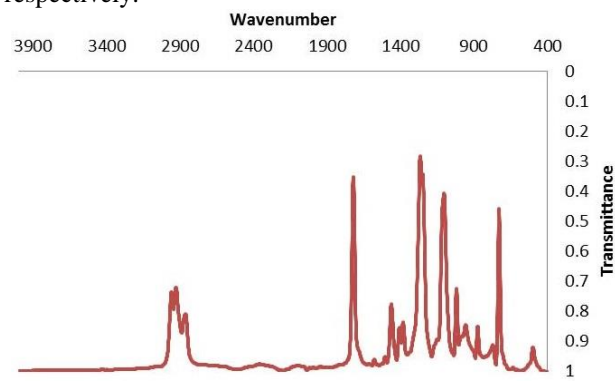


Figure 3: FTIR spectrum of reference dioctyl terephthalate.

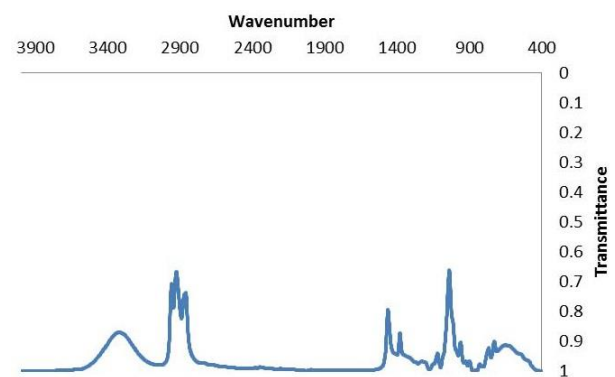


Figure 4: FTIR spectra of 2-ethylhexanol.

These spectra was used to evaluate the reaction products.

FTIR spectra of washed reaction products can be seen at Figure 5.

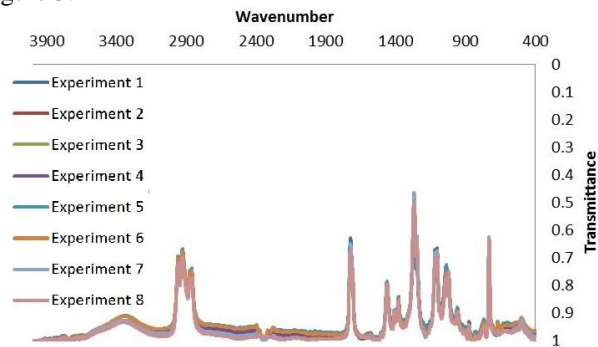


Figure 5: FTIR spectra of synthesized liquid.

It was concluded that all experiments yielded similar chemical composition. It can be clearly seen that esterification reaction between PET and 2-ethyl hexanol successfully driven and dioctyl terephthalate was formed according to the FTIR spectra. Reaction product is not only DOTP rather it is a mixture of 2-ethylhexanol and DOTP. Remaining 2-ethylhexanol can be separated with vacuum distillation thus DOTP can be obtained. This method can be an alternative an alternative method for DOTP production. Long reaction times can be rectified with the use of alternative catalysts and more favorable reaction conditions such as high temperature and high pressure.

ACKNOWLEDGMENT

This work was elaborated with the support of the Research Project (TUBITAK-MAG-217M274) funded by Turkish Scientific and Technical Research Institute. Authors thank to TUBITAK.

REFERENCES

- [1] Jambeck, J.R., et al., Plastic waste inputs from land into the ocean. *Science*, 2015. 347(6223): p. 768-771.
- [2] Geyer, R., J.R. Jambeck, and K.L. Law, Production, use, and fate of all plastics ever made. *Science advances*, 2017. 3(7): p. e1700782.
- [3] Ragaert, K., L. Delva, and K. Van Geem, Mechanical and chemical recycling of solid plastic waste. *Waste Management*, 2017.
- [4] Singh, N., et al., Recycling of plastic solid waste: A state of art review and future applications. *Composites Part B: Engineering*, 2017. 115: p. 409-422.
- [5] Lakeev, S., et al., Ester plasticizers for polyvinyl chloride. *Russian Journal of Applied Chemistry*, 2016. 89(1): p. 1-15.
- [6] Zygoura, P.D., E.K. Paleologos, and M.G. Kontominas, Migration levels of PVC plasticisers: Effect of ionising radiation treatment. *Food chemistry*, 2011. 128(1): p. 106-113.
- [7] Tickner, J.A., et al., Health risks posed by use of Di-2-ethylhexyl phthalate (DEHP) in PVC medical devices: A critical review. *American journal of industrial medicine*, 2001. 39(1): p. 100-111.
- [8] Dupont, L. and V. Gupta, Degradative transesterification of terephthalate polyesters to obtain DOTP plasticizer for flexible PVC. *Journal of Vinyl Technology*, 1993. 15(2): p. 100-104.

Theoretical Calculations on Structural Properties of 1,4-diaminobutane

Aysun GÖZÜTOK¹ and Akif ÖZBAY²

¹ Selçuk University, Konya/Turkey, gozutokaysun@gmail.com

² Gazi University, Ankara/Turkey, aozbay@gazi.edu.tr

Abstract – In this study, molecular structure parameters and vibrational frequencies of the 1,4-diaminobutane molecule were calculated in the most stable condition by Hartree-Fock (HF) and Density Functional theory (DFT) methods with Gaussian package program. Calculated results of bond angles and bond lengths were compared with Meng and Lin's study experimental values. Vibrational frequencies of the 1,4-diaminobutane molecule were compared with Sağlam et al.'s study experimental values.

Keywords – 1,4-diaminobutane, DFT, HF, vibrational frequency, molecular structure properties

I. INTRODUCTION

THE 1,4-diaminobutane has a fundamental carbon chain structure. So, it is used like synthesis molecule. This molecule is used as the ligand in the formation of Hofmann type host-guest compounds. Hofmann type host-guest compounds have two components. One of these components is the host molecule which forms the main lattice and the other is the guest molecule located in the spaces in the main lattice. The host molecule surrounds the guest molecule.

This molecule's geometry optimizations and vibrational frequencies were calculated using HF/6-31G(d), BLYP/6-31G(d) and B3LYP/6-31G(d) levels of theory with Gaussian program [1].

II. METHODS

Molecular structure and vibrational spectra of the most stable condition were calculated by HF/6-31G(d); BLYP/6-31G(d) and B3LYP/6-31G(d) levels of Density Functional theory (DFT) with using the Gaussian program [1].

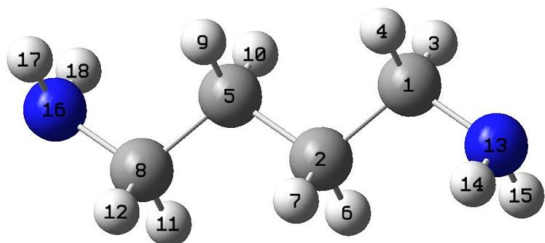


Figure 1: Optimized molecular structure and atom numbers of molecule (atom number 16 and 13 are N, atom number 1, 2, 5, 8 are C, others are H)

III. RESULT AND DISCUSSION

The molecule geometry of this molecule was optimized. The optimized molecular structure of this molecule is given in Figure 1. Theoretical calculation of the molecular structure parameters of this molecule were calculated with HF/6-31G(d), BLYP/6-31G(d) and B3LYP/6-31G(d) levels of theory.

The calculated molecular structure parameters were compared with Meng and Lin's study experimental values [2].

Table 1: Bond angles and bond lengths of the title molecule

Bond Lengths (Å)	Experimental [2]	HF/6-31G(d)	B3LYP/6-31G(d)	BLYP/6-31G(d)
N-H	0,90	1,00	1,01	1,03
C-H	0,97	1,08	1,09	1,10
N-C	1,48	1,45	1,46	1,48
C-C	1,51	1,53	1,53	1,55
Bond Angles (°)				
H-C-H	107,59	106,27	106,08	106,21
H-N-H	107,69	106,86	105,65	104,87
N-C-C	114,71	115,68	116,29	116,56
C-C-C	112,01	113,18	113,50	113,66

There is no published experimental data on the bond lengths and bond angles of the 1,4-diaminobutane, the calculated geometrical parameters of this molecule were compared with the experimental values of the geometrical parameters of the 1,6-diaminohexane molecule performed by X. G. Meng and Z.D. Lin [2].

The experimental values and the calculated geometrical parameters were compared in Table 1. It can be seen that in Table 1 in the B3LYP/6-31G(d) calculation method, the N-C-C (116,29°) bond angle is larger than C-C-C (113,50°), H-N-H (105,65°) and H-C-H (106,08°). The same situation is also obtained for HF/6-31G(d) and BLYP/6-31G(d) methods. In general, the N-C-C bond angles are larger than the C-C-C, H-C-H and H-N-H bond angles. This situation is also consistent

with the experimental results.

The bond length of C-C (1,53 Å) in the B3LYP/6-31G(d) method is greater than the bond lengths of N-C (1,46 Å), C-H (1,09 Å) and N-H (1,01 Å). The same situation for the calculation methods HF/6-31G(d) and BLYP/6-31G(d). In general, the C-C bond length is greater than the N-C, C-H and N-H bond lengths. This situation is also consistent with the experimental results.

In the calculations performed by the HF/6-31G(d) level, some bond lengths are calculated to be shorter than the experimental values. The N-C bond length was 1,48 Å experimentally and was calculated to be 1,45 Å in HF/6-31G(d) level.

The greatest difference in bond length between experimental values and calculated values appeared in BLYP/6-31G(d) method. This difference is approximately 0,13 Å. The biggest difference in the bond angle is BLYP/6-31G(d) method. This value was 2,82°.

The formula of the title molecule is C₄H₁₂N₂ and has 18 atoms in which the C and N atoms are planar and the H atoms are out of plane. This molecule belongs to the point group C_{2h}. For an N-atomic molecule the three Cartesian displacements of the N-atoms provide 3N inner modes. Since the title molecule is a non-linear molecule, there are 3N-6 = 48 vibration modes.

Table 2: Character table for the C_{2h} point group

C _{2h}	E	C ₂	i	σ _h	IR	Raman
A _g	1	1	1	1	R _z	x ² , y ² , z ² , xy
B _g	1	-1	1	-1	R _x , R _y	xz, yz
A _u	1	1	-1	-1	T _z	
B _u	1	-1	-1	1	T _x , T _y	
Γ _{3n}	54	0	0	18		

Table 3: The distribution according to the symmetry types of vibration modes of the molecule

Symmetry types	Vibrational modes
A _g	17
B _g	7
A _u	8
B _u	16

Since $\Gamma_{\text{Rot}}=A_g+2B_g$, $\Gamma_{\text{Trans}}=A_u+2B_u$, and $\Gamma_{\text{top}}=18 A_g + 9 B_g + 9 A_u + 18 B_u$, so we obtained $\Gamma_{\text{vib}}= \Gamma_{\text{top}} - (\Gamma_{\text{Rot}} + \Gamma_{\text{Trans}}) = 17 A_g + 7 B_g + 8 A_u + 16 B_u$ that as you can see in Table 3. That is the numbers of vibration modes for the title molecule.

The vibrational frequencies were calculated by the methods HF/6-31G(d), BLYP/6-31G(d) and B3LYP/6-31G(d). The vibration frequencies were multiplied by the scaling factors [4] and corrected. Then, calculation vibrational frequencies and experimental values [3] were compared, and were given in Table 4-6.

Table 4: Calculated and experimental vibrational frequencies of the title molecule in HF/6-31G(d) method

Normal Mode	HF/6-31G(d)					
	Calculated Frequencies ²	Scaling Frequencies ³	IR intensity	Raman intensity	Experimental ⁴	Assignment ¹
1	89,08	80,04	0,36	0,0		$\rho_r(\text{CH}_2)+\rho_r(\text{NH}_2)$
2	106,19	95,42	11,83	0,00		$\rho_r(\text{CH}_2)+\rho_r(\text{NH}_2)$
3	145,80	131,00	6,43	0,0		$\rho_w(\text{CH}_2)+\rho_w(\text{NH}_2)+\delta_s(\text{CCC})$
4	175,03	157,26	0,00	0,01		$\rho_r(\text{CH}_2)+\rho_r(\text{NH}_2)$
5	305,19	274,21	0,00	5,62		$\rho_r(\text{NH}_2)$
6	311,87	280,22	115,08	0,00		$\rho_r(\text{NH}_2)$
7	353,18	317,33	0,00	6,71		$\rho_w(\text{NH}_2)$
8	380,30	341,70	0,00	3,20		$\rho_w(\text{CH}_2)$
9	545,89	490,48	11,44	0,00		$\rho_w(\text{NH}_2)+\rho_w(\text{CH}_2)$
10	787,12	707,20	1,48	0,00	738 w	$\rho_r(\text{CH}_2)$
11	828,31	744,22	0,00	0,04	863 m,br	$\rho_r(\text{CH}_2)$
12	951,87	855,25	380,07	0,00		$\rho_w(\text{NH}_2)$
13	955,13	858,15	1,52	0,00	878 m,br	$\rho_r(\text{CH}_2)+\rho_w(\text{NH}_2)$
14	963,72	865,90	0,00	9,53		$\rho_w(\text{NH}_2)+\delta(\text{CCC})$
15	1091,67	980,89	144,66	0,00	954 w	$\rho_w(\text{NH}_2)$
16	1093,45	982,47	0,00	0,57		$\rho_r(\text{NH}_2)+\rho_r(\text{CH}_2)$
17	1112,02	999,15	0,00	3,04		$\nu(\text{CC})$
18	1159,57	1041,88	0,31	0,00		$\rho_r(\text{NH}_2)+\rho_r(\text{CH}_2)$
19	1161,51	1043,61	0,00	15,68		$\rho_w(\text{CH}_2)+\nu(\text{CC})$
20	1182,78	1062,74	35,38	0,00	1070 m	$\nu(\text{CN})$
21	1213,52	1090,34	0,00	9,59		$\rho_w(\text{NH}_2)+\rho_w(\text{CH}_2)$
22	1370,68	1231,57	0,00	0,10	1145 vw	$\rho_r(\text{NH}_2)$
23	1382,65	1242,31	17,19	0,00		$\rho_w(\text{CH}_2)$
24	1438,85	1292,85	0,00	0,00	1309 vw	$\rho_r(\text{CH}_2)$
25	1451,71	1304,36	0,00	27,96		$\rho_r(\text{CH}_2)$
26	1487,66	1336,66	0,00	1,30		$\rho_w(\text{CH}_2)$
27	1518,23	1364,13	0,89	0,00		$\rho_r(\text{NH}_2)+\rho_r(\text{CH}_2)$
28	1519,87	1365,60	0,00	15,08		$\rho_r(\text{NH}_2)+\rho_r(\text{CH}_2)$
29	1546,27	1389,35	32,32	0,00	1353 vw	$\rho_w(\text{CH}_2)$
30	1565,57	1406,69	0,00	0,32	1390 w	$\rho_w(\text{CH}_2)$
31	1632,40	1466,71	0,00	34,41		$\delta(\text{CH}_2)$
32	1633,51	1467,71	1,34	0,00		$\delta(\text{CH}_2)$
33	1646,05	1478,98	0,00	10,39		$\delta(\text{CH}_2)$
34	1655,97	1487,89	1,14	0,00		$\delta(\text{CH}_2)$
35	1838,78	1652,16	59,71	0,00	1497 s	$\delta(\text{NH}_2)$
36	1838,87	1652,25	0,00	13,05	1606 s	$\delta(\text{NH}_2)$
37	3172,79	2850,76	0,00	120,68	2853 vs	$\nu(\text{CH}_2)$
38	3174,30	2852,11	57,16	0,00		$\nu(\text{CH}_2)$
39	3189,71	2865,94	0,00	151,50	2926 vs	$\nu(\text{CH}_2)$

40	3207,69	2882,11	22,48	0,00		v (CH ₂)
41	3210,34	2884,49	0,00	188,55		v (CH ₂)
42	3211,47	2885,50	134,49	0,00		v (CH ₂)
43	3246,66	2917,13	0,00	88,36		v (CH ₂)
44	3253,77	2953,51	174,41	0,00		v (CH ₂)
45	3717,43	3340,08	0,68	0,00	3280 s	v (NH ₂)
46	3717,47	3340,14	0,00	167,63		v (NH ₂)
47	3801,13	3415,32	0,06	0,00		v (NH ₂)
48	3801,14	3415,28	0,00	112,22	3346 s	v (NH ₂)

¹ δ :Bending, ρ_t :Twisting, ρ_w :Wagging, δ_s :Scissoring, v:Stretching, ² Vibrational frequencies(cm⁻¹), ³ Scaling factor = 0,8985 [4], ⁴ sh (omuz), vw (very weak), w (weak), m (medium), s (strong), vs (very strong), br (broad) [3].

Table 5: Calculated and experimental vibrational frequencies of the title molecule in BLYP/6-31G(d) method

Normal Mode	BLYP/6-31G(d)						
	Vibrational Number	Calculated Frequencies ²	Scaling Frequencies ³	IR intensity	Raman intensity	Experimental ⁴	Assignment ¹
1	82,22	81,55	0,61	0,00			ρ_t (CH ₂) + ρ_t (NH ₂)
2	107,04	106,17	11,34	0,00			ρ_t (CH ₂) + ρ_t (NH ₂)
3	126,67	125,64	5,82	0,00			ρ_w (CH ₂) + ρ_w (NH ₂) + δ_s (CCC)
4	165,35	164,31	0,00	0,01			ρ_t (CH ₂) + ρ_t (NH ₂)
5	299,31	296,88	0,00	6,02			ρ_t (NH ₂)
6	307,70	305,21	95,89	0,00			ρ_t (NH ₂)
7	314,71	312,16	0,00	8,94			ρ_w (NH ₂)
8	338,27	335,53	0,00	5,06			ρ_w (CH ₂)
9	489,32	485,35	9,05	0,00			ρ_w (NH ₂) + ρ_w (CH ₂)
10	729,90	723,98	3,11	0,00	738 w		ρ_t (CH ₂)
11	760,35	754,24	0,00	0,04	863 m,br		ρ_t (CH ₂)
12	854,88	847,96	297,30	0,00			ρ_w (NH ₂)
13	870,67	863,62	0,94	0,00			ρ_t (CH ₂)
14	875,07	868,01	0,00	7,35	878 m,br		ρ_t (CH ₂) + ρ_w (NH ₂)
15	973,82	965,91	163,38	0,00	954 w		ρ_w (NH ₂)
16	996,31	988,24	0,00	1,98			ρ_t (NH ₂) + ρ_t (CH ₂)
17	999,50	991,40	0,00	1,00			v (CC)
18	1018,58	1010,33	0,00	9,73			ρ_t (NH ₂) + ρ_t (CH ₂)
19	1062,30	1053,69	5,73	0,00			ρ_w (CH ₂) + v (CC)
20	1063,27	1054,66	0,33	0,00			ρ_t (NH ₂) + ρ_t (CH ₂)
21	1101,37	1092,47	0,00	4,27	1070 m		v (CN)
22	1236,70	1226,68	0,00	0,56	1145 vw		ρ_t (NH ₂)
23	1246,06	1235,97	18,70	0,00			ρ_w (CH ₂)
24	1298,60	1288,08	0,19	0,00			ρ_t (NH ₂) + ρ_t (CH ₂)
25	1309,96	1299,38	0,00	27,13	1309 vw		ρ_t (CH ₂)

26	1332,93	1322,13	0,00	1,69			ρ_t (CH ₂)
27	1369,99	1358,90	0,00	5,13	1353 vw		ρ_w (CH ₂)
28	1373,73	1362,60	1,73	0,00			ρ_t (NH ₂) + ρ_t (CH ₂)
29	1373,75	1362,67	27,91	0,00	1390 w		ρ_w (CH ₂)
30	1375,61	1364,47	0,00	19,23			δ (CH ₂)
31	1472,39	1460,47	0,00	49,90			δ (CH ₂)
32	1473,11	1461,18	1,26	0,00			δ (CH ₂)
33	1486,84	1474,80	0,00	3,95			δ (CH ₂)
34	1501,62	1489,46	0,28	0,00			δ (CH ₂)
35	1658,85	1645,46	31,95	0,00	1497 s		δ (NH ₂)
36	1659,09	1645,66	0,00	22,67	1606 s		δ (NH ₂)
37	2923,58	2899,91	0,00	153,72	2853 vs		v (CH ₂)
38	2928,03	2904,31	34,64	0,00			v (CH ₂)
39	2945,11	2921,24	0,00	154,11	2926 vs		v (CH ₂)
40	2952,69	2928,78	0,00	167,62			v (CH ₂)
41	2955,14	2931,21	128,95	0,00			v (CH ₂)
42	2960,79	2936,80	11,90	0,00			v (CH ₂)
43	2990,48	2966,25	0,00	76,37			v (CH ₂)
44	2997,78	2973,50	144,69	0,00			v (CH ₂)
45	3316,51	3289,63	12,72	0,00	3280 s		v (NH ₂)
46	3316,57	3289,71	0,00	198,54			v (NH ₂)
47	3399,00	3371,45	0,00	116,32			v (NH ₂)
48	3399,01	3371,46	9,20	0,00	3346 s		v (NH ₂)

¹ δ :Bending, ρ_t :Twisting, ρ_w :Wagging, δ_s :Scissoring, v:Stretching, ² Vibrational frequencies(cm⁻¹), ³ Scaling factor = 0,9919 [4], ⁴ sh (omuz), vw (very weak), w (weak), m (medium), s (strong), vs (very strong), br (broad) [3].

Table 6: Calculated and experimental vibrational frequencies of the title molecule in B3LYP/6-31G(d) method

Normal Mode	B3LYP/6-31G(d)						
	Vibrational Number	Calculated Frequencies ²	Scaling Frequencies ³	IR intensity	Raman intensity	Experimental ⁴	Assignment ¹
1	84,41	81,05	0,58	0,00			ρ_t (CH ₂) + ρ_t (NH ₂)
2	107,00	102,75	12,22	0,00			ρ_t (CH ₂) + ρ_t (NH ₂)
3	131,57	126,34	6,09	0,00			ρ_w (CH ₂) + ρ_w (NH ₂) + δ_s (CCC)
4	169,13	162,42	0,00	0,01			ρ_t (CH ₂) + ρ_t (NH ₂)
5	298,18	286,35	0,00	5,86			ρ_t (NH ₂)
6	306,40	294,23	102,63	0,00			ρ_t (NH ₂)
7	326,42	313,46	0,00	7,10			ρ_w (NH ₂)
8	351,22	337,28	0,00	4,48			ρ_w (CH ₂)
9	506,32	486,22	11,01	0,00			ρ_w (NH ₂) + ρ_w (CH ₂)
10	744,95	715,42	3,10	0,00	738 w		ρ_t (CH ₂)
11	777,63	746,72	0,00	0,03	863 m,br		ρ_t (CH ₂)
12	881,56	846,57	350,02	0,00			ρ_w (NH ₂)
13	892,44	859,75	1,00	0,00	878 m,br		ρ_t (CH ₂) + ρ_w (NH ₂)
14	895,28	859,74	0,00	7,61			ρ_w (NH ₂) + δ_s (CCC)

15	1014,47	974,22	139,83	0,00	954 w	$\rho_w(\text{NH}_2)$
16	1023,57	982,93	0,00	0,85		$\rho_t(\text{NH}_2)+$ $\rho_t(\text{CH}_2)$
17	1041,50	1000,15	0,00	2,12		v (CC)
18	1071,88	1029,32	0,00	9,86		$\rho_t(\text{NH}_2)+$ $\rho_t(\text{CH}_2)$
19	1087,73	1044,55	0,31	0,00		$\rho_w(\text{CH}_2)+$ v (CC)
20	1104,12	1060,26	10,44	0,00	1070 m	v (CN)
21	1135,80	1090,71	0,00	4,95		$\rho_w(\text{NH}_2)+$ $\rho_w(\text{CH}_2)$
22	1270,75	1220,34	0,00	0,33	1145 vw	$\rho_t(\text{NH}_2)$
23	1278,71	1227,95	13,76	0,00		$\rho_w(\text{CH}_2)$
24	1333,88	1280,94	0,10	0,00	1309 vw	$\rho_t(\text{CH}_2)$
25	1345,18	1291,78	0,00	26,98		$\rho_t(\text{CH}_2)$
26	1371,23	1316,79	0,00	1,66		$\rho_w(\text{CH}_2)$
27	1409,33	1353,37	1,55	0,00		$\rho_t(\text{NH}_2)+$ $\rho_t(\text{CH}_2)$
28	1411,16	1355,13	17,48	0,00		$\rho_t(\text{NH}_2)+$ $\rho_t(\text{CH}_2)$
29	1417,20	1360,93	0,00	28,56	1353 vw	$\rho_w(\text{CH}_2)$
30	1420,72	1364,29	3,07	0,00	1390 w	$\rho_w(\text{CH}_2)$
31	1511,92	1451,90	0,00	44,65		$\delta(\text{CH}_2)$
32	1512,36	1452,32	1,20	0,00		$\delta(\text{CH}_2)$
33	1525,61	1465,04	0,00	5,072		$\delta(\text{CH}_2)$
34	1539,22	1478,12	1,04	0,00		$\delta(\text{CH}_2)$
35	1702,79	1635,19	41,55	0,00	1497 s	$\delta(\text{NH}_2)$
36	1702,99	1635,39	0,00	19,15	1606 s	$\delta(\text{NH}_2)$
37	3007,62	2888,19	0,00	148,94	2853 vs	v (CH ₂)
38	3011,80	2892,23	35,09	0,00		v (CH ₂)
39	3031,21	2910,86	0,00	152,68	2926 vs	v (CH ₂)
40	3037,37	2916,79	0,00	164,68		v (CH ₂)
41	3039,55	2918,88	122,18	0,00		v (CH ₂)
42	3047,09	2926,12	11,93	0,00		v (CH ₂)
43	3077,08	2954,92	0,00	74,96		v (CH ₂)
44	3084,03	2961,60	137,70	0,00		v (CH ₂)
45	3450,49	3315,51	4,73	0,00	3280 s	v (NH ₂)
46	3450,55	3318,56	0,00	185,96		v (NH ₂)
47	3534,21	3393,88	2,43	0,00		v (NH ₂)
48	3534,21	3393,89	0,00	112,37	3346 s	v (NH ₂)

¹ δ :Bending, ρ_t :Twisting, ρ_w :Wagging, δ_s :Scissoring, v:Stretching,
² Vibrational frequencies(cm^{-1}), ³ Scaling factor = 0,9603 [4], ⁴ sh (omuz), vw (very weak), w (weak), m (medium), s (strong), vs (very strong), br (broad) [3].

Comparisons of calculated and observed vibrational modes in different calculation methods of the title molecule are given in Table 4-6. There is no important difference between BLYP/6-31G(d) and B3LYP/6-31G(d), but it is observed that the calculated frequencies with B3LYP/6-31G(d) method are more consistent with experimental values. These methods are hybrid models developed instead of pure HF or pure DFT models and combining energy expressions of these models to

obtain a new total electronic energy expression. The B3LYP which denotes the hybrid functional [5], a linear combination of the gradient functionals proposed by Becke [6] and by Lee et al. [7] together with the HF local exchange function [8].

NOTES:

This paper is a part of Aysun Gözütok's master thesis.

REFERENCES

- [1] Frisch, M. J., Trucks, G. W., Schlegel, H. B., G. E. Scuseria, M. A. Robb, J. R. Cheeseman, V. G. Zakrzewski, J. A. Montgomery, Jr., R. E. Stratmann, J. C. Burant, S. Dapprich, J. M. Milliam, A. D. Daniels, K. N. Kudin, M. C. Strain, O. Farkas, J. Tomasi, V. Barone, M. Cossi, R. Cammi, B. Mennucci, C. Pomelli, C. Adamo, S. Clifford, J. Ochterski, G. A. Petersson, P. Y. Ayala, Q. Cui, K. Morokuma, D. K. Malick, A. D. Rabuck, K. Raghavachari, J. B. Foresman, J. Cioslowski, J. V. Ortiz, A. G. Baboul, B. B. Stefanov, G. Liu, A. Liashenko, P. Piskorz, I. Komaromi, R. Gomperts, R. L. Martin, D. J. Fox, T. Keith, M. A. Al-Laham, C. Y. Peng, A. Nanayakkara, M. Challacombe, P. M. W. Gill, B. Johnson, W. Chen, M. W. Wong, J. L. Andres, C. Gonzalez, M. Head-Gordon, E. S. Replogle, and J. A. Pople, Gaussian, Inc., Pittsburgh PA.
- [2] Meng, X. G. and Lin, Z. D., "catena-Poly[[tetraaquacadmium(II)- μ -hexane-1,6-diamine- $\kappa^2\text{N:N}'$] terephthalate dihydrate]", *Acta Cryst.*, E61: 263-264, 2005.
- [3] Sağlam, S., Sertbakan, T. R., Kasap, E., Kantarcı, Z., "Investigation of host-guest interactions in the Hofmann-dabn-type clathrates: $\text{M}(1,4\text{-diaminobutane})\text{Ni}(\text{CN})_4 \cdot 1.5\text{G}$ ($\text{M}=\text{Co}$ or Ni , $\text{G}=\text{benzene derivatives}$)", *J. Mol. Struct.*, 482-483, 69-74, 1999.
- [4] Scaling factor, <https://cccbdb.nist.gov/vibscalejust.asp>
- [5] Kohn, W., Sham, L. J., "Self-Consistent Equations Including Exchange and Correlation Effects", *Phys. Rev.*, vol. 140, 4A, 1133-1138, 1965.
- [6] Becke, A. D., "Density-functional exchange-energy approximation with correct asymptotic behavior", *Phys. Rev. A.*, vol. 38, 6, 3098-3100, 1988.
- [7] Lee, C., Yang, W., Parr, R. G., "Development of the Colle-Salvetti correlation-energy formula into a functional of the electron density", *Phys. Rev. B.*, vol. 37, 2, 785-789, 1988.
- [8] Karakaş, A., Karakaya, M., Taser, M., Ceylan, Y., Gözütok, A., Arof, A. K., El Kouari, Y., Sahraoui, B., "Computational studies on linear, second and third-order nonlinear optical properties of novel styrylquinolinium dyes", *Chemical Physics Letters*, 648, 47-52, 2016.

Theoretical Studies of N,N'-tetrachloro-1,4-diaminobutane and N,N'-tetrabromo-1,4-diaminobutane

Aysun GÖZÜTOK¹ and Akif ÖZBAY²

¹ Selçuk University, Konya/Turkey, gozutokaysun@gmail.com

² Gazi University, Ankara/Turkey, aobay@gazi.edu.tr

Abstract – In this paper, geometric parameters and vibrational frequencies of the title molecules were calculated Hartree-Fock (HF) method with Gaussian package program. Calculated results of bond angles and bond lengths were compared with the experimental values in literature. Also, vibrational frequencies were compared with the experimental frequencies in literature.

Keywords – HF, vibrational frequency, geometric parameters

I. INTRODUCTION

ADDING to nitrogen atoms bonded chlorine and bromine atoms in place of hydrogen atoms in the 1,4-diaminobutane molecule, the title molecules are formed. The geometrical parameters (bond angles and bond lengths) and vibration frequencies of N,N'-tetrachloro-1,4-diaminobutane (1) and N,N'-tetrabromo-1,4-diaminobutane (2) were investigated using HF/6-31G(d) in Gaussian program [1].

These molecule's geometry optimizations and vibrational frequencies were calculated using HF/6-31G(d) level of theory with Gaussian program [1].

II. METHODS

Molecular structure and vibrational spectra of the most stable condition of the title molecules were calculated by HF/6-31G(d) with using the Gaussian program [1].

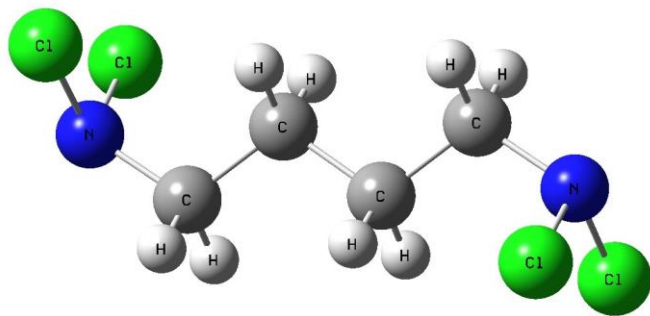


Figure 1: Optimized molecular structure of compound 1

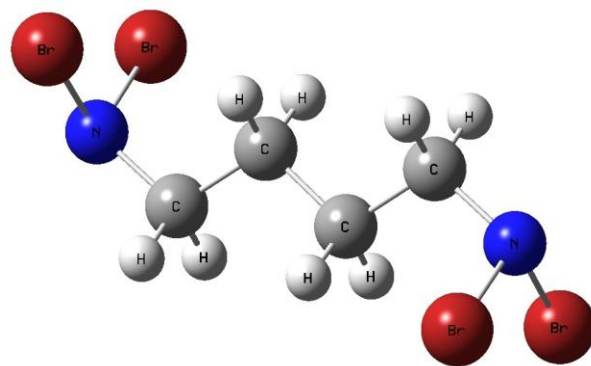


Figure 2: Optimized molecular structure of compound 2

III. RESULT AND DISCUSSION

The molecule geometries of these molecules were optimized firstly. The optimized molecular structures of these molecules are given in Figure 1. Theoretical calculation of the molecular structure parameters of these molecules were calculated with HF/6-31G(d) level of theory.

The calculated molecular structure parameters were compared with Meng and Lin's experimental values [2].

Table 1: Bond angles and bond lengths of compound1 and 2

Bond Length (Å)	Experiment al*	HF/6-31 G(d) ¹		HF/6-31 G(d) ²		HF/6-31 G(d) ³
N-H	0,90	1,00	N-Cl	1,72	N-Br	1,88
C-H	0,97	1,08	C-H	1,08	C-H	1,08
N-C	1,48	1,45	N-C	1,47	N-C	1,47
C-C	1,51	1,53	C-C	1,52	C-C	1,52

Bond Angles (°)	Experimental *	HF/6-31 G(d) ¹		HF/6-31 G(d) ²		HF/6-31 G(d) ³
H-C-H	107,59	106,27	H-C-H	107,65	H-C-H	107,74
H-N-H	107,69	106,86	Cl-N-Cl	110,17	Br-N-Br	110,41
N-C-C	114,71	115,68	N-C-C	117,98	N-C-C	117,97
C-C-C	112,01	113,18	C-C-C	110,62	C-C-C	110,93

¹1,4-diaminobutane, ²compound 1, ³compound 2, *Taken from Ref. [2]

There is no published experimental data on the bond lengths and bond angles of the 1,4-diaminobutane, the calculated geometrical parameters of compound 1 and 2 were compared with the experimental values of the geometrical parameters of the 1,6-diaminohexane molecule performed by X. G. Meng and Z.D. Lin [2].

The experimental values and the calculated geometrical parameters were compared in Table 1. The calculated bond length and bond angle values of compound 1 and 2, and the calculated bond length and bond angle values of the 1,4-diaminobutane molecule are shown to be closer to each other in the Table 1.

Correlation graphs were drawn to compare the geometrical parameters of compound 1 and 2 with the experimental values on the Table 1 (Figure 3-6).

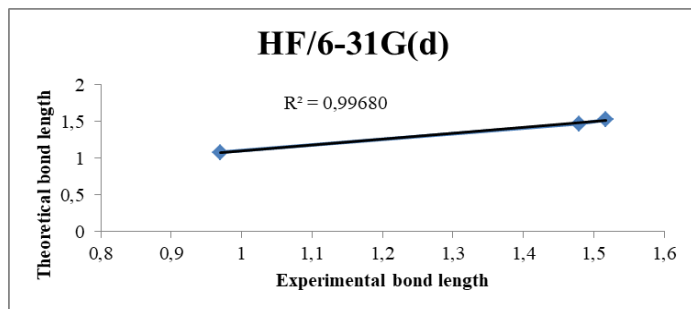


Figure 3: Correlation graph of bond lengths for compound 1

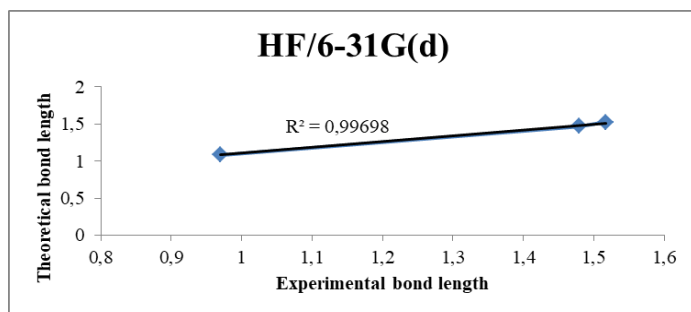


Figure 4: Correlation graph of bond lengths for compound 2

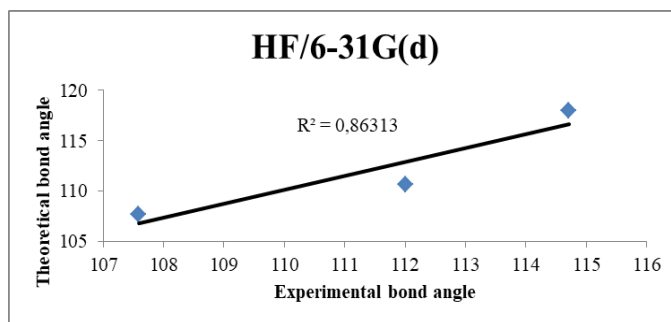


Figure 5: Correlation graph of bond angles for the compound 1

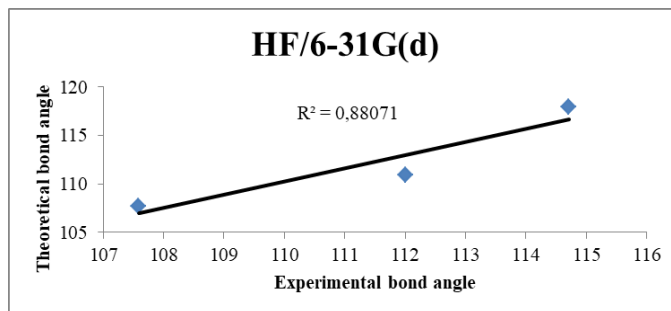


Figure 6: Correlation graph of bond angles for the compound 2

The vibrational frequencies of compound 1 and 2 were calculated at HF/6-31G(d) level. The vibration frequencies were multiplied by the scaling factors [4] and corrected. Experimental frequency values [3] were taken from the comparative values for the 1,4-diaminobutane molecule.

Correlated graphs were drawn to compare the calculated frequency values to the experimental frequency values [3] (Figure 7 and 8).

According to correlation graphs, the experimental and calculated values of bond lengths and bond angles for compound 2 are found to be closer each other at HF/6-31G(d) level (Figure 3-6).

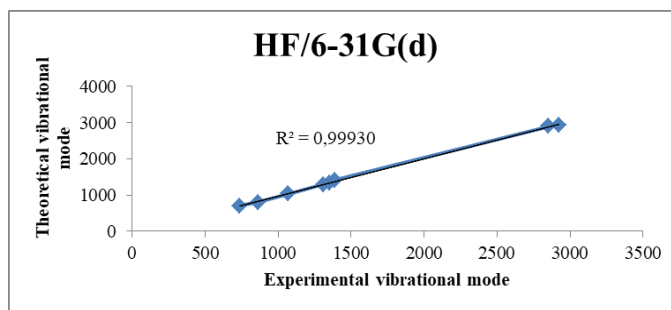


Figure 7: Correlation graph of vibrational frequencies for compound 1

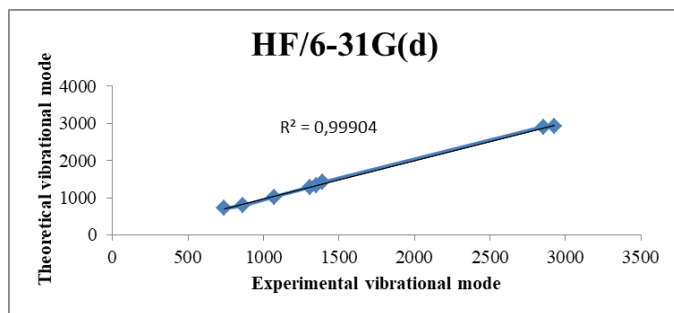


Figure 8: Correlation graph of vibrational frequencies for compound 2

The vibrational frequencies of compound 1 and 2 were calculated and correlation graphs were drawn with comparing the experimental frequency values (Figure 7 and 8). According to these graphs, the calculated values of compound 1 are more consistent with the experimental results than the compound 2.

NOTE:

This paper is a part of Aysun Gözütok's master thesis.

REFERENCES

- [1] Frisch, M. J., Trucks, G. W., Schlegel, H. B., G. E. Scuseria, M. A. Robb, J. R. Cheeseman, V. G. Zakrzewski, J. A. Montgomery, Jr., R. E. Stratmann, J. C. Burant, S. Dapprich, J. M. Milliam, A. D. Daniels, K. N. Kudin, M. C. Strain, O. Farkas, J. Tomasi, V. Barone, M. Cossi, R. Cammi, B. Mennucci, C. Pomelli, C. Adamo, S. Clifford, J. Ochterski, G. A. Petersson, P. Y. Ayala, Q. Cui, K. Morokuma, D. K. Malick, A. D. Rabuck, K. Raghavachari, J. B. Foresman, J. Cioslowski, J. V. Ortiz, A. G. Baboul, B. B. Stefanov, G. Liu, A. Liashenko, P. Piskorz, I. Komaromi, R. Gomperts, R. L. Martin, D. J. Fox, T. Keith, M. A. Al-Laham, C. Y. Peng, A. Nanayakkara, M. Challacombe, P. M. W. Gill, B. Johnson, W. Chen, M. W. Wong, J. L. Andres, C. Gonzalez, M. Head-Gordon, E. S. Replogle, and J. A. Pople, Gaussian, Inc., Pittsburgh PA.
- [2] Meng, X. G. and Lin, Z. D., "catena-Poly[[tetraaquacadmium(II)- μ -hexane-1,6-diamine- κ^2 N:N'] terephthalate dihydrate]", *Acta Cryst.*, E61: 263-264, 2005.
- [3] Sağlam, S., Sertbakan, T. R., Kasap, E., Kantarcı, Z., "Investigation of host-guest interactions in the Hofmann-dabn-type clathrates: $M(1,4\text{-diaminobutane})Ni(CN)_4 \cdot 1.5G$ ($M=Co$ or Ni , G =benzene derivatives)", *J. Mol. Struct.*, 482-483, 69-74, 1999.
- [4] Scaling factor, <https://cccbdb.nist.gov/vibscalejust.asp>

Evaluating the Stability and Heat Transfer Performance of Carbon-based Aqueous Nanofluids

T. FİDAN-ASLAN¹, A. TURGUT², M. Ö. SEYDİBEYOĞLU¹, E. ALYAMAÇ-SEYDİBEYOĞLU¹

¹Izmir Katip Celebi University, Izmir/Turkey, tugcefid@gmail.com

²Dokuz Eylul University, Izmir/Turkey, alpaslanturgut@gmail.com

¹Izmir Katip Celebi University, Izmir/Turkey, seydibey@gmail.com

¹Izmir Katip Celebi University, Izmir/Turkey, elifalyamac@gmail.com

Abstract – Due to its high thermal conductivity values, the use of carbon nanotubes in heat transfer fluids has recently become a popular research topic. Dispersion of carbon nanotubes in different base fluids is a challenging issue. The aim of this study is to prepare stable nanofluids and to increase their thermal conductivity. Aqueous dispersions of single-walled carbon nanotubes (SWCNT) were successfully prepared through ultrasound technology in the presence of polyethylene glycol-polyhedral oligomeric silsesquioxane (PEG-POSS) as a stabilizer. Stability evaluations were carried out by Ultraviolet-Visible (UV-Vis) spectrophotometry and zeta potential measuring device (Zetasizer Nano). Nanofluids which can remain stable for up to 60 days have been produced. Besides, 3ω method was used for determination of thermal conductivity of nanofluids. The results indicate that increase in nanoparticle and stabilizer concentration provided better stability of nanofluids.

Keywords – SWCNT, POSS, nanofluid, thermal conductivity

I. INTRODUCTION

The idea of increasing the thermal conductivity was first proposed by Maxwell in 1873, as the distribution of micrometers and millimeters size metal particles in the base fluid [1]. These large particles have collapsed very quickly, causing erosion and sudden pressure drops in the systems where they are used. With the development of nanotechnology, the idea of dispersing nano-sized particles (<100 nm) in the fluid has re-emerged. The term of “nanofluids” was first used by Choi in 1995, after the studies in the Argonne National Laboratory [2]. Further experimental and theoretical studies have been carried out by many researchers, with different nanofluids. A significant part of experimental results indicates that nanofluids have the potential to be used as new generation heat-transfer fluids [3]. Nano-sized metals, metal oxides and carbon materials are examples of particles commonly used in the base fluid to increase thermal conductivity. Although carbon nanoparticles have high thermal conductivity compared to metal and metal oxides, they are not effectively used in nanofluid production due to their stability problem. Additionally, the use of

surfactants to ensure stability leads to negative results in thermal conductivity. It is seen in the literature that water, ethylene glycol and various oils are frequently used as base fluids. Sodium dodecyl sulfate (SDS), sodium dodecyl benzene sulfonate (SDBS), cetrimonium bromide (CTAB), and Triton-X are examples of surfactants used in nanofluids [4, 8]. On the other hand, in many studies, the nanoparticles were functionalized by acid treatment and the stability of the nanofluids was tried to be increased [9,11].

As a result of previous experimental studies on thermal conductivity of nanofluids [12], it is stated that the increase in thermal conductivity of nanofluids cannot be explained by the traditional effective thermal conductivity models. Although there are various interpretations as to which factors this increase depends on, with every new theoretical study, possible reasons previously defended by a few research groups are rejected by some other researchers and disparate reasons are defended. Despite using transient hot wire technique (THW) in more than 50% of published articles [13], the experimental results obtained by different research groups show very important differences even in the same type of nanofluids [14, 15]. In the literature, it is stated that there is a chaos related to this subject, while some necessary criteria have been proposed for THW method accuracy [16].

In the scope of the study, method based on the principle of detection of the third harmonic (3ω method) using AC hot-wire and lock-in amplifier together, was used to measure the thermal conductivity of fluids. The thermal conductivity results measured by the 3ω method are more realistic, although they are lower than the data obtained from other methods. In many review articles, it is stated that the use of this method in the measurement of thermal conductivity is more valuable and realistic [17]. Although thermal conductivity studies have been conducted frequently, the stability of nanofluids has not yet been elucidated. Additionally, due to the dark and opaque structure of carbon-based nanofluids, zeta potential and UV-Vis spectrophotometry are challenging research topics.

II. MATERIALS AND METHODS

SWCNT (Tuball Matrix, Beta 302) was supplied from OcSiAl. PEG-POSS (PG1190) was purchased from Hybrid Plastics. All specifications of SWCNT and PEG-POSS are shown in Table 1. Ammonia (NH₃) anhydrous, ≥99.98% was purchased from Sigma-Aldrich.

Table 1: Material specifications of SWCNT and PEG-POSS.

SWCNT		PEG-POSS	
Appearance	Black powder	Appearance	Clear, colorless liquid
Carbon Content	> 75%	Molecular Weight	~5576 g/mol
Particle Diameter	< 2 nm	Viscosity (at 25 °C)	280 cP
Particle Length	5-10 μm	Thermal Stability	5 wt% loss at 250 °C
		Solvent Stability	Water, alcohols

A. Preparation of Nanofluids

For preparation of SWCNT nanofluids, distilled water was used as a base fluid. Ultrasonicator (UP400S, Hielscher Ultrasonics GmbH, Teltow, Germany) at a setting of cycle 0.5 and amplitude 50%, was used for aqueous SWCNT dispersions. Nanofluids having 0.05, 0.1, 0.5, 1.0, 1.5 and 2.0 wt% SWCNT concentration were sonicated for 10 min. before pH adjustment. The nanofluids including PEG-POSS were prepared by first sonicating distilled water and PEG-POSS together for 5 minutes, then SWCNTs were added into the solution and later, sonication was performed for extra 10 minutes.

Due to electrokinetic properties, the pH setting is a very critical stage to ensure stability [18]. 0.1 M NH₄OH solution was prepared and added into 10-min-sonicated dispersions. During addition of NH₄OH solutions, Innolab Multi 9310 pHmeter was used for pH measurements of all samples at around 25 °C. Initial and final pH values are given in Table 2, Table 3, and Table 4, for the dispersions without PEG-POSS, with 0.1 wt% PEG-POSS, and 0.2 wt% PEG-POSS, respectively. After pH adjustment, dispersions were sonicated for 50 minutes. To prevent overheating, ice bath was used during sonication. These all stages are given in Figure 1.

Table 2: The pH adjustments of PEG-POSS free dispersions.

SWCNT [wt%]	Initial pH	Final pH
0.05	7.55	8.37
0.10	7.38	8.06
0.50	>8.00	-
1.00	>8.00	-
1.50	>8.00	-
2.00	>8.00	-

Table 3: The pH adjustments of 0.1 wt% PEG-POSS dispersions.

SWCNT [wt%]	Initial pH	Final pH
0.05	7.21	8.06
0.10	6.95	8.08
0.50	7.46	8.26
1.00	>8.00	-
1.50	>8.00	-
2.00	>8.00	-

Table 4: The pH adjustments of 0.2 wt% PEG-POSS dispersion.

SWCNT [wt%]	Initial pH	Final pH
0.05	6.54	8.37
0.10	6.94	8.31
0.50	6.77	8.06
1.00	>8.00	-
1.50	>8.00	-
2.00	>8.00	-

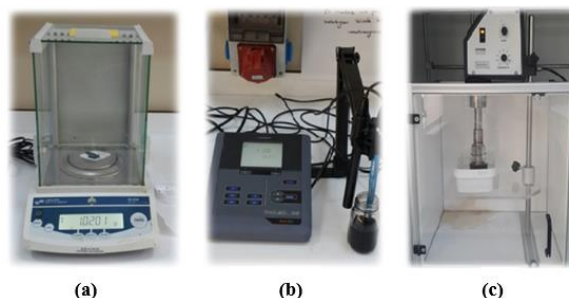


Figure 1: Weighing (a), pH adjustment (b) and ultrasonication (c) stages in the preparation of nanofluids.

III. RESULTS AND DISCUSSIONS

A. Stability of Nanofluids

In this study, nanofluid characterization can be classified as;

- Stability evaluations
- Thermal conductivity evaluations.

Zetasizer Nano (Malvern Instruments) and UV-Vis Spectrophotometer (Perkin Elmer Lambda) were used for the stability measurements.

The zeta potential is calculated based on the Smoluchowski equation given in Equation 1, depending on the electrophoretic mobility of the particles.

$$\xi = \frac{4\pi\eta\mu}{\varepsilon} \quad \text{Equation (1)}$$

$\mu = \nu/E$, μ and ν are mobility and velocity under an applied electric field E , respectively. η and ε are viscosity and electrical permittivity of nanofluid. The zeta potential (ξ) is the maximum value in the distribution generated by Zetasizer Nano [19].

The biggest problem encountered in the measurement of the zeta potential is the inability to take measurements due to the dark color of the carbon-based dispersions. As a result of further research, it has been observed that zeta potential

measurement can be made by diluting the dispersions in a certain ratio. However, since the pH adjustment was made in the dispersions prepared in this project, the dispersions were centrifuged for an average of 1.5 hours despite the ion balance deterioration of the dispersion in any dilution process. After centrifugation, dispersions in the upper part of the tube were drawn and zeta potential was measured for different concentrations.

Dispersions having an absolute value higher than 30 mV are regarded as stable [18]. As seen in Figure 2, the highest zeta potential value is -85.5 mV. The result means that 2.0 wt% SWCNT and 0.2 wt% PEG-POSS dispersion with the -85.5 mV have excellent stability. Obtaining these high values depends on both the use of PEG-POSS and the effect of pH adjustment, as well as the prolonged (50 minutes) ultrasonication.

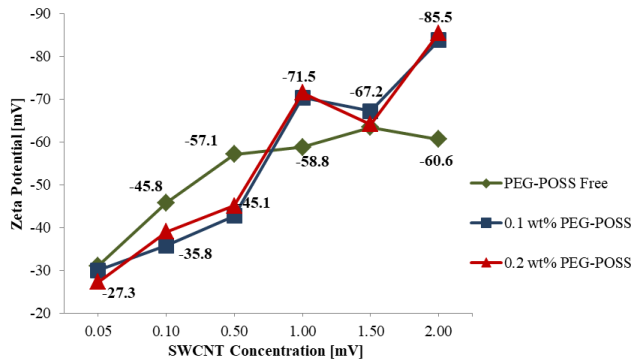


Figure 2: Zeta potential change with different SWCNT and PEG-POSS concentrations.

The purpose of the UV-Vis spectrophotometry measurement is to determine the concentration of nanofluids after a certain time (30th and 60th days) with the Beer Lambert Law given in Equation 2. Wavelength range during measurement is 590-200 nm [20].

$$A = -\log\left(\frac{I}{I_0}\right) = \epsilon bc \quad \text{Equation(2)}$$

In the specific beam path of light (b) and in the molar absorptivity (ϵ), the absorbance (A) and the particle concentration (c) are directly proportional to each other. First, samples were diluted with distilled water at 1:20 ratio [21, 22], then absorbance values of samples were measured. The UV-Vis spectra of without PEG-POSS, 0.1 and 0.2 wt% PEG-POSS dispersions are shown in Figures 3, 4, and 5, respectively.

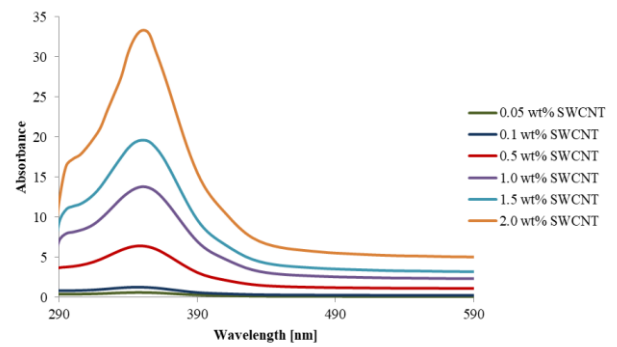


Figure 3: UV-Vis spectra of dispersions without PEG-POSS at different wavelength and different SWCNT concentrations.

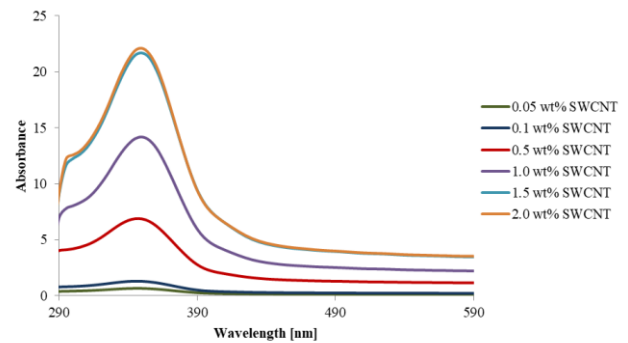


Figure 4: UV-Vis spectra of dispersions with 0.1 wt% PEG-POSS at different wavelength and different SWCNT concentrations.

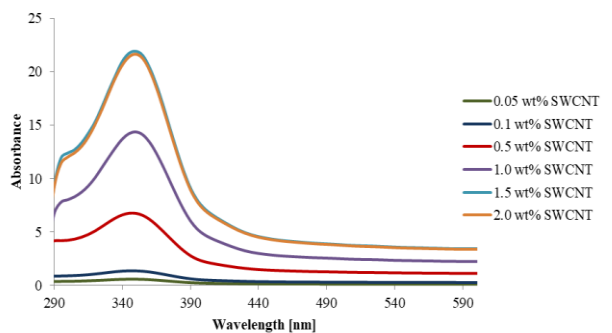


Figure 5: UV-Vis spectra of dispersions with 0.2 wt% PEG-POSS at different wavelength and different SWCNT concentrations.

The highest absorbance value was observed in the region between 345 and 350 nm. As time passes, a decrease in absorbance is expected to be recorded due to the sedimentation. Absorbance measurements of the dispersions prepared at different concentrations were performed at specific wavelength to determine sedimentation amount. Based Equation 2, at t_0 moment UV-Vis was measured in SWCNT dispersions and absorbance vs nanoparticle concentration graph was plotted. As shown in Figure 6, 7, and 8, the calibration curves fit the Beer-Lambert equation. It is seen that there is a good linear relation between absorbance values and concentration of dispersions. This is an indication that the nanoparticles were dispersed well in the base fluid [23].

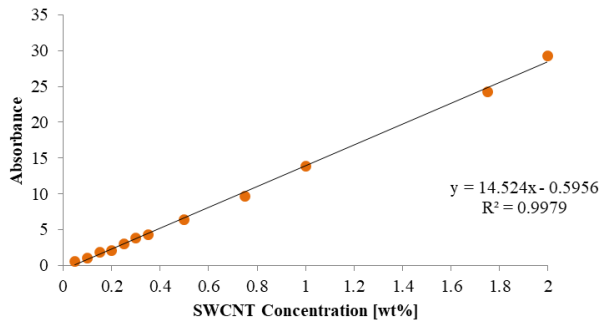


Figure 6: Absorption values of dispersions without PEG-POSS at different SWCNT concentrations.

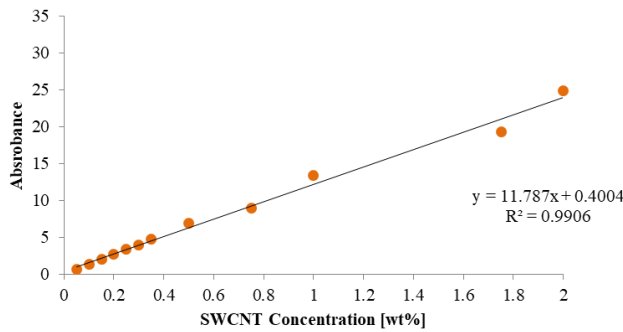


Figure 7: Absorption values of dispersions with 0.1 wt% PEG-POSS at different SWCNT concentrations.

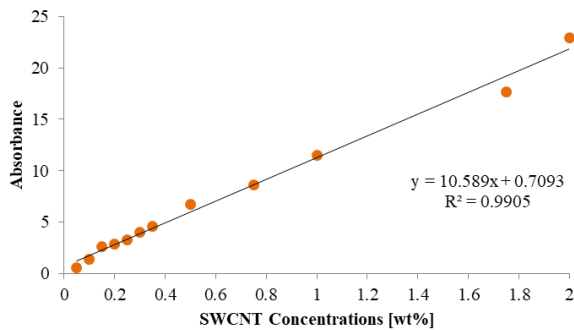


Figure 8: Absorption values of dispersions with 0.2 wt% PEG-POSS at different SWCNT concentrations.

The 60 days stability of SWCNTs dispersions of without PEG-POSS, 0.1 wt%, and 0.2 wt% PEG-POSS were shown in Figure 9, 10, and 11, respectively. By the increasing nanoparticle concentration, a slight decrease is seen at increased PEG-POSS concentration.

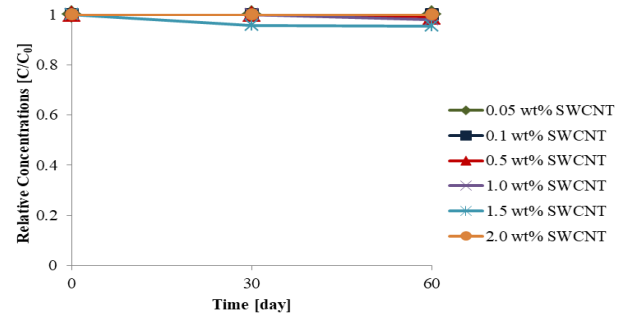


Figure 9: Relative concentration of dispersions without PEG-POSS vs sedimentation time.

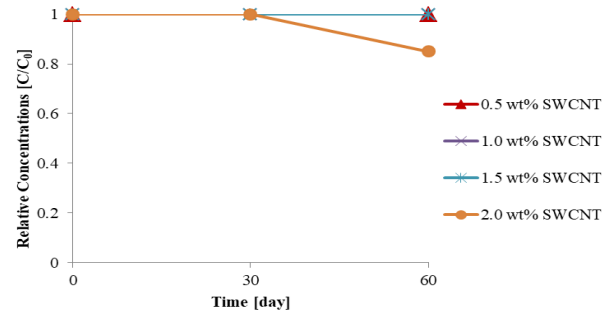


Figure 10: Relative concentration of dispersions with 0.1 wt% PEG-POSS vs sedimentation time.

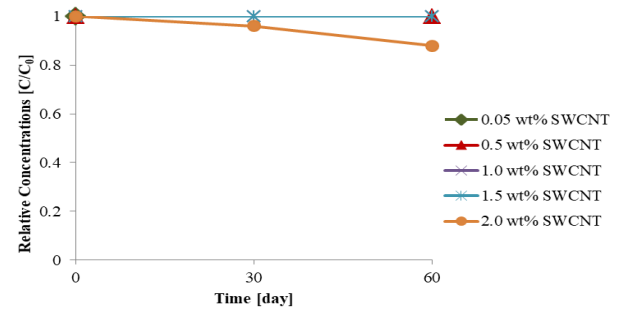


Figure 11: Relative concentration of dispersions with 0.2 wt% PEG-POSS vs sedimentation time.

B. Thermal Conductivity of Nanofluids

The 3ω method has proven to be reliable method for measuring the thermal conductivity of different type of materials [17]. In this research, a lab made setup was utilized for determining the thermal conductivity of the nanofluid based on an AC excited hot-wire with a 3ω lock-in detection technique. Turgut et al. [24] provided in details a full description of the theoretical background and the measurement procedures of the used setup. Nevertheless, a brief overview of this technique will be presented here. Briefly, a linear heater (very thin-wire) is excited by a sinusoidal current at an angular frequency ω . This, according to Ohms law, generates heat at 2ω which consequently resulting in both a temperature fluctuation in the wire also at the same frequency. The phase

and the amplitude of the temperature oscillation are mainly related to the properties of the heater and thermal characteristics of its surroundings. Thus, the thermal conductivity k of the surrounding medium (including nanofluid) can be determined by a developed model based on the resulted temperature oscillation. Sensing the temperature oscillation is very challenging and can be performed through sensing the resistance oscillation of the wire since these two parameters are related directly by β (temperature coefficient of the wire material resistance). The resistance fluctuation can be measured by measuring the induced voltage signal at 3ω , based on which the method obtained its name.

The schematic diagram of the used measurement setup, as shown in Figure 13, illustrates its main part. The employed thermal probe (ThP), which is made of a metallic wire (Nickel) of length $2l=19.0$ mm and diameter of $d=50$ μm , is totally immersed in the nanofluid sample. The wire of the ThP is acting simultaneously as a heater and a thermometer, as discussed above. The selection of the 3rd harmonic (3ω) from the differential voltage signal across the bridge is performed by a Stanford SR-850 lock-in amplifier. It is important to mention here that to achieve a good signal-to-noise ratio, the first harmonic 1ω must be cancelled by a Wheatstone bridge arrangement (Figure 12).

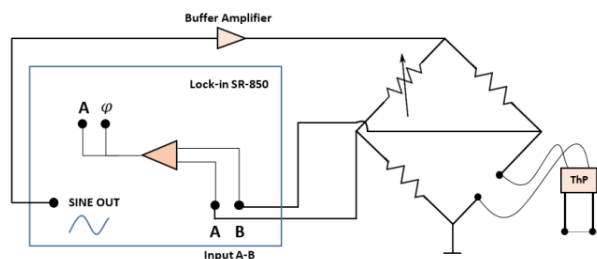


Figure 12: Schematic diagram of the experimental setup for 3ω hot-wire measurements (Thermal probe (ThP), Wheatstone bridge, lock-in amplifier, and buffer amplifier (ref. [25])).

Nanoparticle concentration is an important parameter in thermal conductivity measurements. It is a known fact that the thermal conductivity will increase with increasing concentration of nanoparticles. In this situation, the important criterion is to determine the optimum particle concentration. After a certain concentration, the particles will flocculate in the dispersion and tend to settling. This situation will negatively affect the increase in thermal conductivity. Particle size is also an important parameter in thermal conductivity measurements. As a result of some studies in the literature, it has been observed that thermal conductivity increases with decreasing particle size. This is theoretically explained by the Brownian motion of the particles and the presence of the base fluid layer formed around the particles. Otherwise, in some studies, it was noted that the reduction in particle size would decrease thermal conductivity as it would interrupt the connection between carbon atoms [26].

In the thermal conductivity part of this study, different

ultrasonication times such as 50 and 100 minutes and different PEG-POSS concentrations were studied to determine both the effect of particle size and PEG-POSS concentration. In Figure 13, thermal conductivity increases of 1.0 wt% and 2.0 wt% of SWCNT dispersions are given in different PEG-POSS concentrations, at 50 min and 100 min.

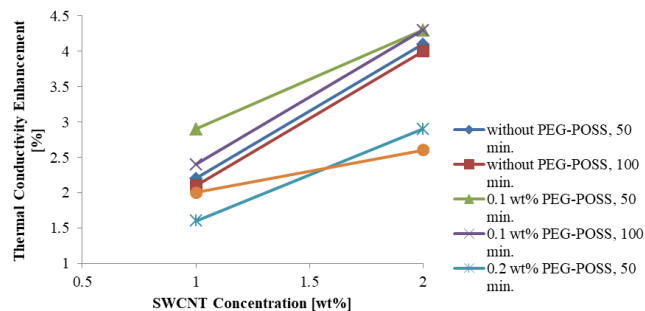


Figure 13: Thermal conductivity enhancement according to SWCNT concentration at different PEG-POSS concentrations and ultrasonication times.

As seen in the graph, the thermal conductivity values increased with the increase in nanoparticle concentration. The thermal conductivity increases for the 2.0 wt% SWCNT dispersion without PEG-POSS and with 0.1 wt% PEG-POSS are 4.1% and 4.3%, respectively. The PEG-POSS concentration from 0 to 0.1 wt% increases the thermal conductivity between 0.3% to 0.7% weight for the 1.0 wt% and 2.0 wt% SWCNT dispersions, respectively. When the PEG-POSS concentration is increased to 0.2% by mass, the thermal conductivity value for dispersion containing 2.0 wt% SWCNT is reduced to 2.9%. This is related to the fact that PEG-POSS forms a layer between the nanoparticles and reduces the thermal conductivity of this layer due to its organic structure. The maximum thermal conductivity increase was observed in the samples with 0.1 wt% PEG-POSS. This value is for 4.3%, 0.1 wt% PEG-POSS and 2.0 wt% for SWCNT.

IV. CONCLUSION

In this study, SWCNT/distilled water and SWCNT/PEG-POSS/distilled water nanofluids were successfully prepared, using ultrasound technology. For stability enhancement, pH was adjusted to the value (around 8), where the nanofluids would be expected to be stable. Thermal conductivity measurements and stability evaluations were performed using 3ω method, UV-Vis spectrophotometry, and zeta potential measuring device (Zetasizer Nano). Zeta potential analysis showed the highest value as -85.5 mV for 2.0 wt% SWCNT and 0.2 wt% PEG-POSS aqueous nanofluids. Increase in nanoparticle concentration provided better stability and thermal conductivity increment in nanofluids. The highest thermal conductivity enhancement was measured as 4.3%. Additionally, the nanofluids remain stable up to 60 days. Since the study has not yet been completed, further experimental work will be performed with ethylene glycol and mineral oil as

base fluids, along with some rheological measurements of nanofluids.

ACKNOWLEDGMENT

This study is supported by The Scientific and Technological Research Council of Turkey (TUBITAK) with the project no. 117M953.

REFERENCES

- [1] M. M. Tawfik, "Experimental studies of nanofluid thermal conductivity enhancement and application: A review," *Renew. Sust. Energ. Rev.*, vol. 75, pp. 1239–1253, 2017.
- [2] S. U. S. Choi, "Enhancing thermal conductivity of fluids with nanoparticles, developments and applications of non-newtonian flows," eds. D. A. Singer and H. P. Wang, *ASME*, vol. 231, pp. 99–105, 1995.
- [3] S. Shaikh, K. Lafdi, and R. Ponnappan, "Thermal conductivity improvement in carbon nanoparticle doped PAO oil: An experimental study," *J. Appl. Phys.*, vol. 101, 064302, 2007.
- [4] M. J. Assael, C-F. Chen, I. Metaxa, and W. A. Wakeham, "Thermal conductivity of carbon nanotube suspensions in water," *Int. J. Thermophys.*, vol. 25, pp. 971–985, 2004.
- [5] M. J. Assael, I. N. Metaxa, J. Arvanitidis, D. Christofilos, and C. Lioutas, "Thermal conductivity enhancement in aqueous suspensions of carbon multi-walled and double-walled nanotubes in the presence of two different dispersants," *Int. J. Thermophys.*, vol. 26, pp. 647–664, 2005.
- [6] M. J. Assael, I. N. Metaxa, K. Kakosimos, and D. Constantinou, "Thermal conductivity of nanofluids – experimental and theoretical," *Int. J. Thermophys.*, vol. 27, pp. 999–1016, 2006.
- [7] Y. J. Hwang, Y. C. Ahn, H. S. Shin, C. G. Lee, G. T. Kim, H. S. Park, and J. K. Lee, "Investigation on characteristics of thermal conductivity enhancement of nanofluids," *Curr. Appl. Phys.*, vol. 6, pp. 1068–1071, 2006.
- [8] Y. J. Hwang, H. S. Park, J. K. Lee, and W. H. Jung, "Thermal conductivity and lubrication characteristics of nanofluids," *Curr. Appl. Phys.*, vol. 6S1, pp. e67–e71, 2006.
- [9] J. Nanda, C. Maranville, S. C. Bollin, D. Sawall, H. Ohtani, J. T. Remillard, and J. M. Ginder, "Thermal conductivity of single-wall carbon nanotube dispersions: role of interfacial effects," *J Phys. Chem. C*, vol. 112, pp 654–658, 2008.
- [10] L. Chen, and H. Xie, "Silicon oil based multiwalled carbon nanotubes nanofluid with optimized thermal conductivity enhancement," *Colloids Surf. A Physicochem. Eng. Asp.*, vol. 352, pp. 136–140, 2009.
- [11] S. S. J. Aravind, P. Baskar, T. T. Baby, R. K. Sabareesh, S. Das, and S. Ramaprabhu, "Investigation of structural stability, dispersion, viscosity, and conductive heat transfer properties of functionalized carbon nanotube based nanofluids," *J. Phys. Chem. C*, vol. 115, pp. 16737–16744, 2011.
- [12] C. H. Chon, K. D. Kihm, S. P. Lee, and S. U. S. Choi, "Empirical correlation finding the role of temperature and particle size for nanofluid (Al₂O₃) thermal conductivity enhancement," *Appl. Phys. Lett.*, vol. 87, no. 15, 153107, 2005.
- [13] T. T. Loong, H. Salleh, "A review on measurement techniques of apparent thermal conductivity of nanofluids," *IOP Conf. Ser. Mater. Sci. Eng.*, vol. 226, 012146, 2017.
- [14] M. Kaszuba, J. Corbett, F. M. Watson, and A. Jones, "High-concentration zeta potential measurements using light-scattering techniques," *Philos. Trans. A Math. Phys. Eng. Sci.*, vol. 368, pp. 4439–4451, 2010.
- [15] S. M. S. Murshed, K. C. Leong, and C. Yang, "Thermophysical and electrokinetic properties of nanofluids - A critical review," *Appl. Therm. Eng.*, vol. 28, pp. 2109–2125, 2008.
- [16] K. D. Antoniadis, G. J. Tertsinidou, and W. A. Wakeham, "Necessary conditions for accurate, transient hot-wire measurements of the apparent thermal conductivity of nanofluids are seldom satisfied," *Int. J. Thermophys.*, vol. 37, no. 78, pp. 1–22, 2016.
- [17] C. Dames, and G. Chen, "1 ω , 2 ω and 3 ω methods for measurements of thermal properties," *Rev. Sci. Instrum.*, vol. 76, 124902, 2005.
- [18] V. Fuskele, and R. M. Sarviya, "Recent developments in nanoparticle synthesis, preparation and stability of nanofluids," *Mater. Today Proc.*, vol. 4, pp. 4049–4060, 2017.
- [19] R. D. Devre, M. B. Budhlall and C. F. Barry, "Enhancing the colloidal stability and electrical conductivity of single-walled carbon nanotubes dispersed in water," *Macromol. Chem. Phys.*, vol. 217, pp. 683–700, 2016.
- [20] W. Chamsa-ard, S. Brundavanam, C. C. Fung, D. Fawcett, and G. Poinern, "Nanofluid types, their synthesis, properties and incorporation indirect solar thermal collectors: A review," *Nanomaterials*, vol. 7, no. 6, pp. 1–31, 2017.
- [21] S. Sarsam, A. Amiri, M. N. M. Zubir, H. Yarmand, S. N. Kazi, and A. Badarudin, "Stability and thermophysical properties of water-based nanofluids containing triethanolamine-treated graphene nanoplatelets with different specific surface areas," *Colloids Surf. A Physicochem. Eng. Asp.*, vol. 500, pp. 17–31, 2016.
- [22] S. Sarsam, A. Amiri, S. N. Kazi, and A. Badarudin, "Stability and thermophysical properties of non-covalently functionalized graphene nanoplatelets nanofluids," *Energy Convers. Manag.*, vol. 116, pp. 101–111, 2016.
- [23] M. Mehrali, E. Sadeghinezhad, S. T. Latibari, S. N. Kazi, M. Mehrali, M. N. M. Zubir, and H. S. C. Metselaar, "Investigation of thermal conductivity and rheological properties of nanofluids containing graphene nanoplatelets," *Nanoscale Res. Lett.*, vol. 9, no. 15, pp. 1–12, 2014.
- [24] A. Turgut, C. Sauter, M. Chirtoc, J. F. Henry, S. Tavman, I. Tavman, and J. Pelzl, "AC hot wire measurement of thermophysical properties of nanofluids with 3 ω method," *Eur. Phys. J. Spec. Top.*, vol. 153, pp. 349–352, 2008.
- [25] A. Alasl, E. Evgin, and A. Turgut, "Re-dispersion ability of multi wall carbon nanotubes within low viscous mineral oil," *Colloids Surf. A*, vol. 538, pp. 219–228, 2018.
- [26] S. Özerinç, S. Kakaç, A. Güvenç Yazıcıoğlu, "Enhanced thermal conductivity of nanofluids: A state-of-art review," *Microfluid Nanofluid*, vol.8, pp. 145–170, 2010.

PtAu alloy nanoparticles as an electrochemical sensor for hydrogen peroxide

Ö. ŞAHİN

Konya Technical University, Department of Chemical Engineering, Konya/Turkey
Selcuk University, Department of Chemical Engineering, Konya/Turkey

gok.ozlem@hotmail.com

Abstract - PdAu/C, Pd/C and Au/C catalysts sensing activities for non-enzymatic hydrogen peroxide (H_2O_2) was investigated. The detection of H_2O_2 was performed with different electrochemical techniques such as cyclic voltammetry (CV) and chronoamperometry (CA). Electrochemical results revealed that PdAu/C catalyst showed perfect electrocatalytic activity in terms of electro-oxidation of H_2O_2 . PdAu/C catalyst showed a fast response of less than 5 s with a linear range of 7.0×10^{-3} - 6.5 mM and high sensitivity of 210.3 mA $\text{mM}^{-1} \text{cm}^{-2}$. PdAu/C catalyst exhibited great selectivity for detecting H_2O_2 in the existence of several hindering species such as uric acid and ascorbic acid.

Keywords - Platinum, gold, bimetallic nanocatalysts, hydrogen peroxide.

I. INTRODUCTION

H_2O_2 has found wide applications in pharmaceutical, clinical and food industries [1]. It is considered to be hazardous at high concentrations. Therefore, fast and accurate determination of H_2O_2 is very important. Various methods including spectrophotometry, chemiluminescence and titrimetry have been employed to detect H_2O_2 . Among these, electrochemical technique has attracted considerable interest due to its inherent advantages of simplicity, high sensitivity, fast response and low-cost. Recently, numerous enzymes modified electrodes have been widely employed for detecting H_2O_2 . Nevertheless, the relatively of high cost, limited lifetime and the critical operating situation limit enzyme-biosensor applicability. Therefore, electrochemical non-enzymatic detection has received significant attention, and has been an efficient approach to detect H_2O_2 with the advantages of high sensitivity and reliability, fast response, good selectivity, and low detection limit.

Platinum is one of the most studied noble metals in the field of sensors and catalysts. Pt-based materials, exhibit high electrocatalytic activity for the oxidation of some molecules (H_2O_2 , glucose, etc.) and are considered as potential building blocks for developing efficient enzyme-free sensors. However, these Pt-based electrodes often suffer from losing activity, because their active surfaces are easily poisoned by adsorbed intermediates, thus leading to low sensitivity and poor stability. However, the stability of Pt catalyst can be

significantly improved with the addition of Au [2].

In this study, electrochemical performance of various compositions of the PtAu/C catalysts towards H_2O_2 oxidation was investigated by cyclic voltammetry and then further studies performed by chronoamperometry for the optimized ratio catalyst.

II. EXPERIMENTAL

A. Preparation of catalysts

PtAu/C different ratio catalysts were prepared by microwave-assisted polyol process in polyol solution with $\text{H}_2\text{PtCl}_6 \cdot 6\text{H}_2\text{O}$ and AuCl as a precursor salt. In brief, carbon powder treated by 4.0 M HNO_3 (with the aim to increase the hydrophilic functional groups) was firstly impregnated with aqueous solutions of Pt and Au. Then, 4 mL of 0.12 M KBr was added. After ultrasonic treatment for 1 h, 5 mL of 0.05 M NaOH was added drop by drop under magnetic stirring. The beaker containing the solution was put into a domestic microwave oven (Electrolux Ems model 21400W, 2450 MHz, 800 W) and then heated for 2 min at 130 °C. Finally, the samples were filtered, washed with distilled water and ethanol and dried in a vacuum oven for 2 hours. Pt/C and Au/C catalysts were prepared in a similar way.

B. Electrochemical measurements

All the electrochemical measurements were conducted using CH Instruments 6043d potentiostat. The electrochemical experiments were carried out in an N_2 -purged NaOH solution and a standard three-electrode electrochemical cell. A Pt foil electrode and an Ag/AgCl served as the counter and reference electrode, respectively. Prior to each experiment GC electrode surface was polished with alumina powder until a mirror-like surface obtained. Then the electrode was washed thoroughly with acetone and distilled water.

The cyclic voltammetric experiments were executed in the potential range between 0.2 and 1.0 V vs. Ag/AgCl at a scan rate of 50 mV s^{-1} . A magnetic stirrer and a stirring bar provided convective transport during amperometric experiments. A desired amount of H_2O_2 was added into the

stirred phosphate buffer solution. Chronoamperometric measurements were performed at the desired working potential after reaching the steady-state current value. Freshly prepared solution was used in every measurement. All electrochemical experiments were carried out at room temperature and under nitrogen atmosphere.

III. RESULTS AND DISCUSSION

The electrochemical properties of PdAu/C, Pd/C and Au/C catalysts modified electrodes were studied in 0.1 M phosphate buffer solution, using cyclic voltammetry recorded between -0.25 to 1.0 V versus Ag/AgCl at scan rate of 50 mV s^{-1} . The oxidation peaks at an onset potential of 0.15 V vs. Ag/AgCl appeared with the addition of H_2O_2 (5 mM). The comparison of the sensitivity of catalysts (Figure 1) illustrated that PtAu/C catalyst show higher oxidation activity and improved sensitivity towards H_2O_2 compared with Pt/C and Au/C catalysts. This result showed that alloying Pt with Au improved the electrocatalytic performance towards H_2O_2 detection due to the synergistic effect between Pt and Au [3].

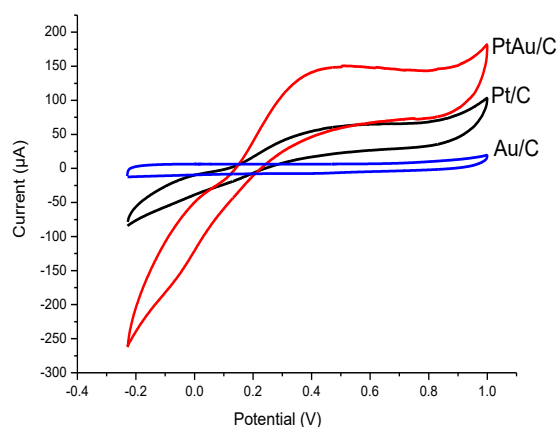


Figure 1: Cyclic voltammograms of PtAu/C, Pt/C, and Au/C catalysts to the addition of 5 mM H_2O_2 in N_2 saturated 0.1 M phosphate buffer solution at pH 7.4, scan rate: 50 mV/s .

The performance of the PtAu/C modified electrode was further evaluated by chronoamperometric method. Figure 2 shows the amperometric responses of PdAu/C, Pd/C and Au/C modified electrode for successive additions of H_2O_2 into the stirring phosphate buffer solution at 0.30 versus Ag/AgCl. The PdAu/C modified electrode responds rapidly (less than 5s) to the changes in H_2O_2 concentration. PdAu/C catalyst showed a fast response of less than 5 s with a linear range of 7.0×10^{-3} - 6.5 mM and high sensitivity of $210.3 \text{ mA mM}^{-1} \text{ cm}^{-2}$.

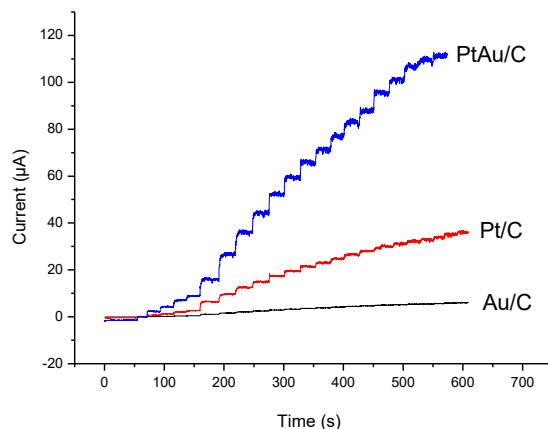


Figure 2: Amperometric response of the PtAu/C, Pt/C and Au/C for the successive addition of H_2O_2 into 0.1 M PBS, pH 7.4

In addition, the effect of interferents such as ascorbic acid (AA) and uric acid (UA) was investigated. The chronoamperometric measurements revealed that PtAu/C catalyst exhibited high electrocatalytic activity toward the oxidation of H_2O_2 (Figure 3).

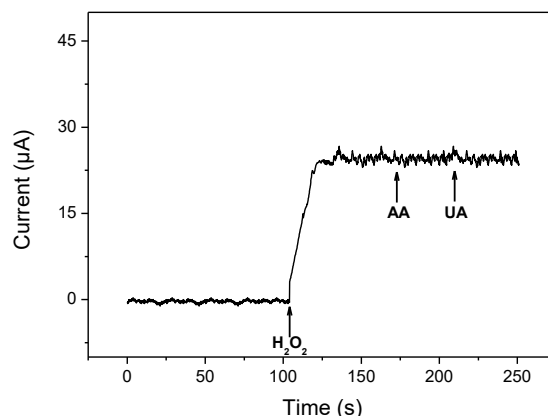


Figure 3: Amperometric response of PtAu/C to the successive addition of $1 \text{ mM H}_2\text{O}_2$, AA, UA.

Moreover, the long-term stability of the PtAu/C sensor was examined by measuring the response to $1.0 \text{ mM H}_2\text{O}_2$, as shown in Figure 4. The electrode was stored in 0.01 M phosphate buffer (pH 7.4) at room temperature when not in use. The response was found to remain at about 95% of its initial response after 4 weeks. PtAu/C modified electrode displayed good performance for H_2O_2 detection with simple electrode preparation procedure, low working potential, high sensitivity and selectivity, good reproducibility, acceptable long-term stability. In summary, the proposed H_2O_2 sensor with the above mentioned electrochemical performances could be also applied to the determination of H_2O_2 in various fields.

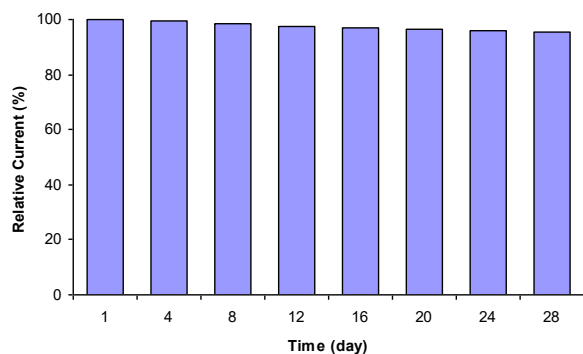


Figure 4: Long-term stability of the Pt₅Au₅/C at room temperature for 4 weeks.

IV. CONCLUSIONS

The new H₂O₂ sensors were constructed by modifying the surface of a GCE with PdAu/C, Pd/C and Au/C catalysts. Electrochemical studies of H₂O₂ oxidation reaction on those catalysts were investigated by different electrochemical techniques. Cyclic voltametric and chronoamperometric experiments indicated that the prepared PtAu/C catalyst displayed high performance for H₂O₂ detection with high sensitivity, selectivity and acceptable long-term stability. In summary, the constructed H₂O₂ sensor with the above mentioned electrochemical performances could be also applied to the determination of H₂O₂ in different fields.

ACKNOWLEDGMENT

CHI 6043d electrochemical workstation employed in electrochemical measurements was purchased from Selcuk University scientific research project (project number: 11401131). The author acknowledge to the Scientific Research Projects Coordination Unit (BAP) for the financial support.

REFERENCES

- [1] Chakraborty S, Raj C., Pt nanoparticle-based highly sensitive platform for the enzyme-free amperometric sensing of H₂O₂, *Biosensors & Bioelectronics*. 2009;24:3264-3268.
- [2] H. Zhu, Y. Liu, L. Shen, Y. Wei, Z. Guo, H. Wang, K. Han, Z. Chang, Microwave heated polyol synthesis of carbon supported PtAuSn/C nanoparticles for ethanol electrooxidation, *Int. J. Hydrogen Energ* 35 3125–3128, 2010.
- [3] A.Y. Vasil'kov, A.V. Naumkin, I.O. Volkov, V.L. Podshibikhin, G.V. Lisichkin, A.R.Khokhlov, XPS/TEM characterisation of Pt-Au/C cathode electrocatalysts prepared by metal vapour synthesis, *Surf. Interface Anal.* 42 559–563, 2010.

Effect of Process-Control Agent on the Characteristics of 316L Powders Prepared by Mechanical Alloying Route

C. NAZIK¹ and N. TARAKCIOGLU²

¹ Selcuk University, Konya/Turkey, cnazik@selcuk.edu.tr

²Selcuk University, Konya/Turkey, ntarakcioglu@selcuk.edu.tr

Abstract - 316L SS (stainless steel) powders were milled by adding direct and gradual methanol (as process control agent) different times as the first step. After the milling, characterization tests of them were investigated by SEM analysis (Scanning Electron Microscope) and particle size measurement. In the SEM analysis; it was observed that flake structured powders were formed at 5-hour and 10-hour milling when direct methanol was added. As a result, increase of milling time directly influenced on the characteristics of 316L SS powders.

Keywords – 316L, Flake powder metallurgy, Mechanical alloying, Particle size, Process control agent

I. INTRODUCTION

316L stainless steels (316L SS) have wide range of industrial application such as transportation, medical, automotive, marine and energy production due to their attractive corrosion resistance and mechanical properties [1]. These materials have been produced by such as forging, extrusion, casting and powder metallurgy methods (PM) [2-9]. Especially, powder metallurgy (PM) is a relatively new manufacturing method among them.

Many researchers have been used mechanical alloying (a powder metallurgy method) to obtain fine and homogenous microstructure in metal or composite powder [10-12].

Despite this advantage situation, many parameters, such as milling time, rotation speed, process control agent (PCA), ball diameter and ball-powder weight ratio etc., which are interconnected can cause complication in the expedient powder production [13]. For instance; it is well known that although the decrease in the crystal size with increasing the milling time is positive situation according to the Hall-Petch relationship [14]., irregular shape and increasing powder hardness due to plastic deformation has negatively affected compaction and sintering process [15-16].

Moreover, amount of PCA is very effective on the morphological and microstructural properties of the milled powders [17]. Therefore, researchers have developed new and simple “flake powder metallurgy (FPM)” method to obtain good sinterable powder which has high density as well as adequate deformation [18-21].

In this study, spherical 316L SS powder produced by the gas atomization method were milled in high energy ball milling machine at different times by adding methanol as PCA.

The aim of this paper is to investigate the effect of different milling time and PCA on the morphology and particle size of 316L SS powder.

II. EXPERIMENTAL

Gas-atomized 316L SS powder supplied by Vday Additive Manufacturing Technology Co., Ltd. (CN) was used in this study. The powder shape is spherical with particle size distribution ranging from 1 to 20 μm , having a mean particle size of $\sim 10 \mu\text{m}$ (Fig. 1). The chemical composition of 316L SS powder is pointed out in Table 1 and it has ≤ 600 ppm oxygen content.

Table 1: Chemical composition of 316L SS powder stated in this paper (wt%).

Cr	Ni	Mo	Mn	Si	P	C	S	Fe
16	10							
-	-	2 - 3	≤ 2	≤ 1	≤ 0.03	≤ 0.03	≤ 0.02	Bal.
18	14							

316L SS powders were milled at different times with PCA which was added directly and gradually within high energy ball milling machine (Retsch planetary type PM 100). The device was run for ten minutes and stopped for 5 minutes to prevent excessive heating of the vial during milling.

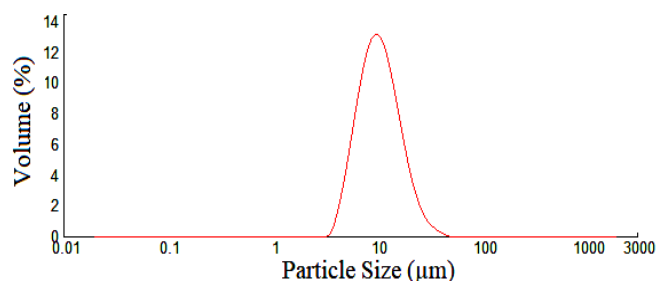


Figure 1: Average particle size of initial 316L SS powder

Vial and balls were made of tungsten carbide (WC). Ball-powder ratio, milling speed and PCA amount was chosen 10:1, 300 rpm and 3 wt% respectively.

Methanol was added directly and gradually as PCA at the same rate in milling process instead of adding different rate of it. Characterization of milled powder morphology was performed by Scanning Electron Microscope (SEM – Zeiss Evo LS 10). Mean particle size were measured by Malvern™ Mastersizer 2000 Laser particle size analyzer pursuant to Mie's theory using distilled water as a dispersant with ultrasonic mixer.

III. RESULTS AND DISCUSSION

A. Microstructure

The milling systems have been named as direct and gradual PCA during microstructural observations. Fig. 2 shows the initial stage of 316L SS powder before milling process.

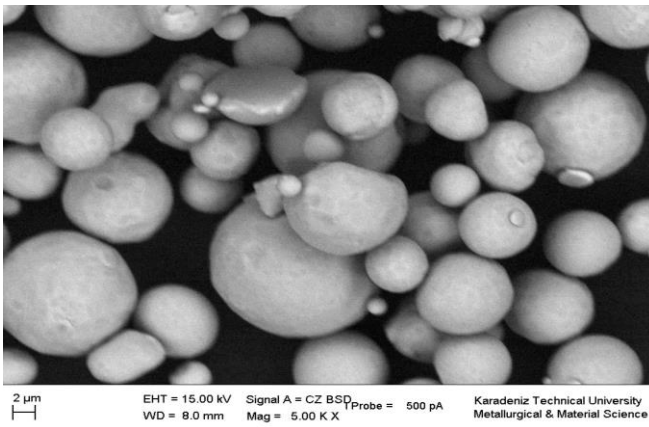


Figure 2: Initial morphologies of the gas atomized 316L SS powder.

➤ Morphologies of direct PCA system

Initial powders were milled (2-5-10 h) in vial with adding 3 wt% methanol directly. Fig. 3 (a-b-c) pointed out changing of their spherical form with increasing milling time.

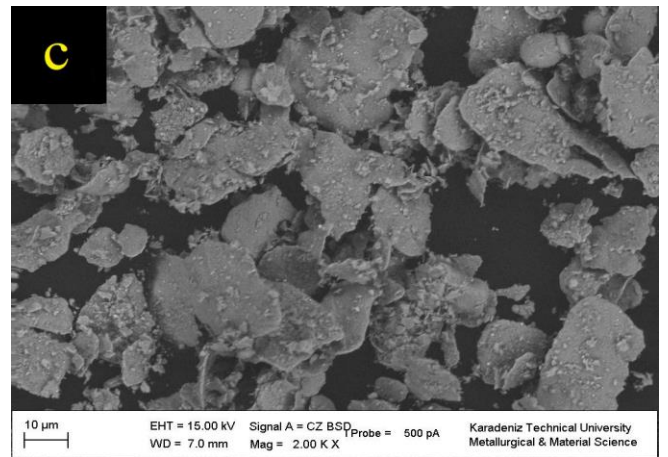
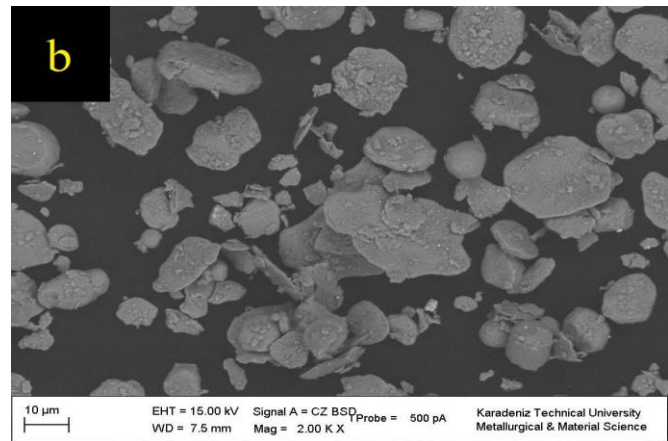
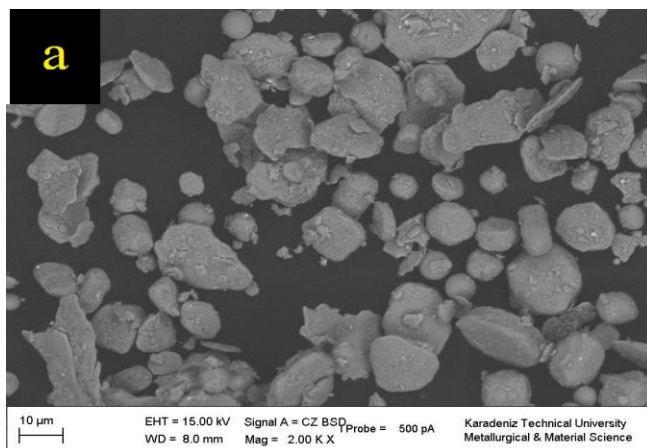


Figure 3: SEM images of milled 316L SS powder in direct system: (a) 2h milled, (b) 5h milled, (c) 10h milled

It was observed that the spherical powders turned into small amount of flake structure at the first stage of milling times (Fig 3-a).

Most of the powders were changed into flake structure and the fracture of powders based on ball impact is little at the second stage (Fig 3-b).

In the final stage of direct system, both nearly all of the powders have changed into the flake structure and number of small particles based on embrittlement increased due to excessive plastic deformation (Fig 3-c).

➤ Morphologies of gradual PCA system

Initial powders were milled (2-5-10 h) in the same way but $\frac{1}{4}$ of 3 wt% methanol was added into the powders every half hour until the 2h milling time.

After that, methanol was not added. Fig. 4 (i-ii-iii) indicate that morphological change of gradual PCA system powder with increasing milling time.

The first stage of the gradual system is almost identical to the first stage of the former (Fig 4-i).

However, in the 5h milling time, the powders were broken rapidly instead of the flake structure as in the direct system (Fig 4-ii).

In the final stage of gradual system, it is clearly seen that small particles were overlapped by means of cold welding. (Fig 4-iii).

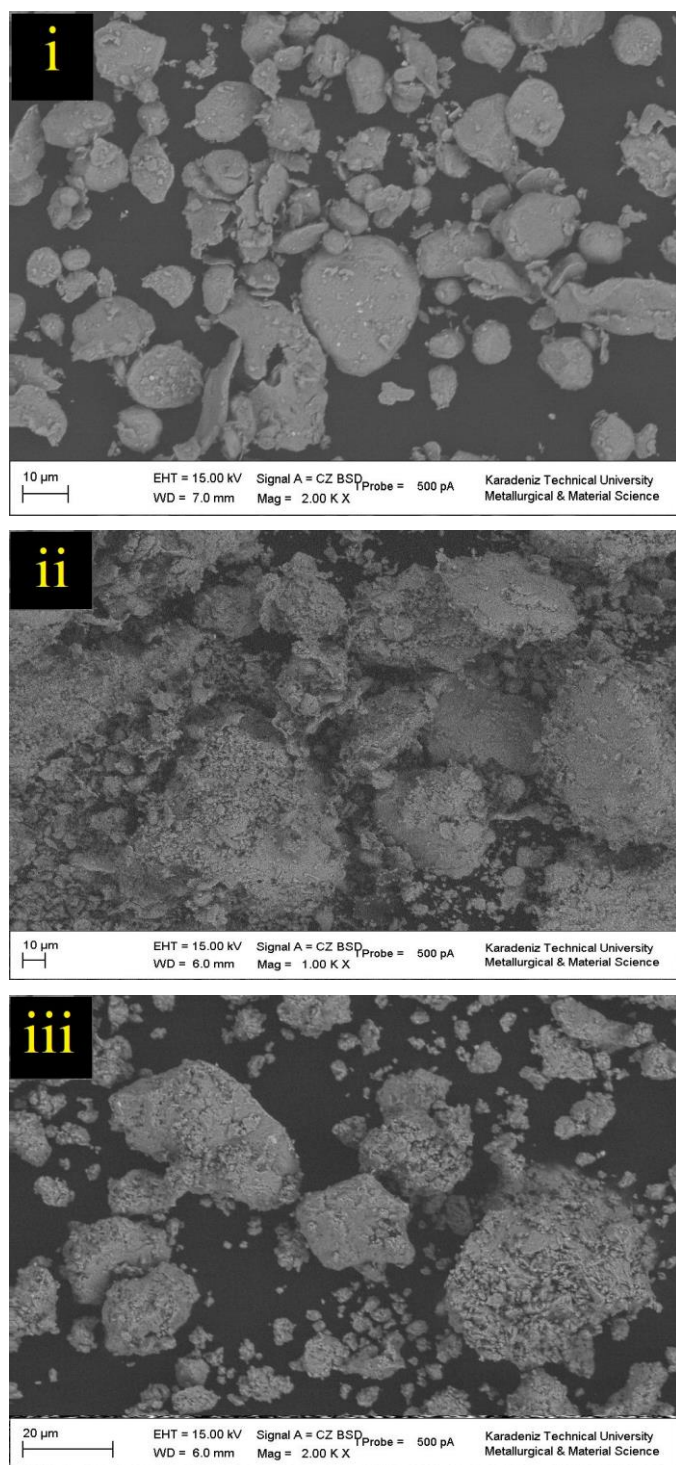


Figure 4: SEM images of milled 316L SS powder in gradual system: (i) 2h milled, (ii) 5h milled, (iii) 10h milled

It can be said that direct PCA system more effective than gradual system. 5h and 10h milling times are preferred in the direct PCA system to obtain flake structure contributed to increase of packing density.

Especially during the 10h milling time, both the flake powders and the decreasing particle size can contribute to increasing post-sintered density with adequate deformation.

B. Particle Size

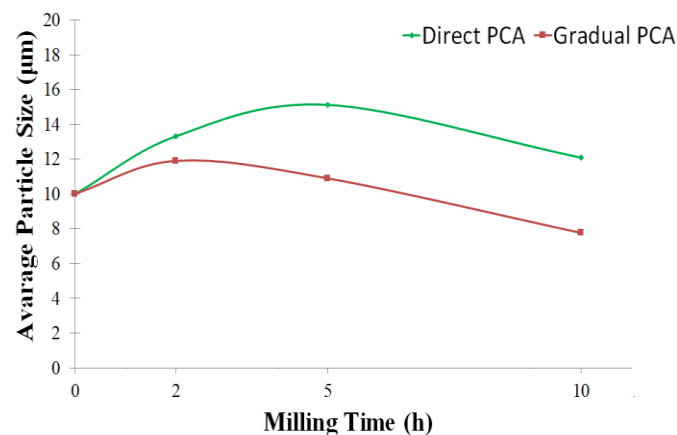


Fig. 5. Changing average particle size of 316L SS powders with increasing milling time

The average particle size of 316L SS powders increased with increasing milling time up to 2h milling time in both direct and gradual system.

Thereafter, in the direct system, the powder size increased for up to 5 hours, while in the graded system it was reduced. Because methanol formed effective film on the powders during milling process in direct PCA system.

On the other hand, the powders were broken rapidly without they were formed flake structure because of gradual PCA.

ACKNOWLEDGMENT

This paper was published as part of the PhD thesis supported by the Selcuk University Scientific Research Project Center (Project number: 17101007).

REFERENCES

- [1] Yusuf, S.M., et al., Microstructure and corrosion performance of 316L stainless steel fabricated by Selective Laser Melting and processed through high-pressure torsion. *Journal of Alloys and Compounds*, 2018. 763: p. 360-375.
- [2] Zhang, L.T. and J.Q. Wang, Effect of temperature and loading mode on environmentally assisted crack growth of a forged 316L SS in oxygenated high-temperature water. *Corrosion Science*, 2014. 87: p. 278-287.
- [3] Bartolomeu, F., et al., 316L stainless steel mechanical and tribological behavior-A comparison between selective laser melting, hot pressing and conventional casting. *Additive Manufacturing*, 2017. 16: p. 81-89.
- [4] Gulsoy, H.O., et al., Effect of Zr, Nb and Ti addition on injection molded 316L stainless steel for bio-applications: Mechanical, electrochemical and biocompatibility properties. *Journal of the Mechanical Behavior of Biomedical Materials*, 2015. 51: p. 215-224.
- [5] El-Hadad, S., W. Khalifa, and A. Nofal, Surface modification of investment cast-316L implants: Microstructure effects. *Materials Science & Engineering C-Materials for Biological Applications*, 2015. 48: p. 320-327.

- [6] Choi, J.P., et al., Sintering behavior of 316L stainless steel micro-nanopowder compact fabricated by powder injection molding. *Powder Technology*, 2015. 279: p. 196-202.
- [7] Pachla, W., et al., Nanostructurization of 316L type austenitic stainless steels by hydrostatic extrusion. *Materials Science and Engineering a-Structural Materials Properties Microstructure and Processing*, 2014. 615: p. 116-127.
- [8] Choi, J.P., et al., Investigation of the rheological behavior of 316L stainless steel micro-nano powder feedstock for micro powder injection molding. *Powder Technology*, 2014. 261: p. 201-209.
- [9] Li, S.B. and J.X. Xie, Fabrication of thin-walled 316L stainless steel seamless pipes by extrusion technology. *Journal of Materials Processing Technology*, 2007. 183(1): p. 57-61.
- [10] Wang, W.K., et al., Fabrication and Mechanical Properties of Tungsten Inert Gas Welding Ring Welded Joint of 7A05-T6/5A06-O Dissimilar Aluminum Alloy. *Materials*, 2018. 11(7).
- [11] Ozkaya, S. and A. Canakci, Effect of the B4C content and the milling time on the synthesis, consolidation and mechanical properties of AlCuMg-B4C nanocomposites synthesized by mechanical milling. *Powder Technology*, 2016. 297: p. 8-16.
- [12] Erdemir, F., A. Canakci, and T. Varol, Microstructural characterization and mechanical properties of functionally graded Al2024/SiC composites prepared by powder metallurgy techniques. *Transactions of Nonferrous Metals Society of China*, 2015. 25(11): p. 3569-3577.
- [13] Suryanarayana, C., Mechanical alloying and milling. *Progress in Materials Science*, 2001. 46(1-2): p. 1-184.
- [14] Huang, T.L., et al., Strengthening mechanisms and Hall-Petch stress of ultrafine grained Al-0.3%Cu. *Acta Materialia*, 2018. 156: p. 369-378.
- [15] Sharma, P., S. Sharma, and D. Khanduja, On the Use of Ball Milling for the Production of Ceramic Powders. *Materials and Manufacturing Processes*, 2015. 30(11): p. 1370-1376.
- [16] da Costa, F.A., et al., Effect of high energy milling and compaction pressure on density of a sintered Nb-20%Cu composite powder. *International Journal of Refractory Metals & Hard Materials*, 2015. 51: p. 207-211.
- [17] Canakci, A., T. Varol, and C. Nazik, Effects of amount of methanol on characteristics of mechanically alloyed Al-Al2O3 composite powders. *Materials Technology*, 2012. 27(4): p. 320-327.
- [18] Varol, T., A. Canakci, and E.D. Yalcin, Fabrication of NanoSiC-Reinforced Al2024 Matrix Composites by a Novel Production Method. *Arabian Journal for Science and Engineering*, 2017. 42(5): p. 1751-1764.
- [19] Trinh, P.V., et al., Microstructure, microhardness and thermal expansion of CNT/Al composites prepared by flake powder metallurgy. *Composites Part a-Applied Science and Manufacturing*, 2018. 105: p. 126-137.
- [20] Mereib, D., et al., Fabrication of biomimetic titanium laminated material using flakes powder metallurgy. *Journal of Materials Science*, 2018. 53(10): p. 7857-7868.
- [21] Chamroune, N., et al., Effect of flake powder metallurgy on thermal conductivity of graphite flakes reinforced aluminum matrix composites. *Journal of Materials Science*, 2018. 53(11): p. 8180-8192.

Effect of Milling Time on Properties of AA7075 Powders Enhanced by Mechanical Alloying Method

E.C. ARSLAN¹, N. TARAKCIOGLU², C. NAZIK³ and E. SALUR⁴

¹Selcuk University, Konya/Turkey, emrecn2626@gmail.com

²Selcuk University, Konya/Turkey, ntarakcioglu@selcuk.edu.tr

³Selcuk University, Konya/Turkey, cnazik@selcuk.edu.tr

⁴Selcuk University, Konya/Turkey, esalur@selcuk.edu.tr

Abstract – In this study, gas atomization technique was used to produce AA7075 powders. AA7075 powder was milled within planetary type ball milling machine by adding methanol. After the milling, characterization tests of the powders were investigated by SEM analysis (Scanning Electron Microscope), XRD analysis (X-Ray Diffraction) and particle size measurement. In the SEM analysis; it was observed that flake structured powders were formed at 2h milling time. The mean powder size decreased with increasing milling time and the powder hardness increased due to excessive deformation. It was also seen that the XRD peaks width increased with increase of milling time. As a result, the change in the milling time directly affected the particle size, crystallite size and morphology of AA7075 powders.

Keywords – AA7075, Flake Structure, Mechanical alloying, Methanol, Particle Size.

I. INTRODUCTION

Aluminium alloys are widely used in areas such as chemical, food, construction, automobile, fuse parts, missile parts, space-aerospace and defense industry thanks to lightweight, resistance to corrosion with protective oxide layer on the surface, low melting temperature and good thermal conductivity [1-7].

One of the aluminum alloys AA7075 is an Al-Zn-Mg-Cu alloy. 7075 aluminum alloys can be produced by casting, forging, cold forming, hot pressing, extrusion and powder metallurgy. Among these, powder metallurgy is seen as a new method [8-14].

Compared to other methods, more homogeneous microstructure, less impurities, good mechanical properties can be obtained via powder metallurgy [15-17]. Although these advantages, it is very difficult to control the milling parameters that are connected to each other, such as milling speed, milling time, process control agent (PCA), ball diameter, type of milling atmosphere, ball-powder ratio, type of milling jar and balls [18-21].

For example, the powder size decreases with the increase in the milling time but with the increasing plastic deformation, the irregularity of the powders shapes and the increased powder hardness cause the porosities to remain in the material during pressing and these porosities cannot be removed during sintering process [3].

Therefore, the milling time with the effect on the morphology and microstructural properties of the powders

have been researched to produce good sinterable powders with low deformation rate and high packing density.

In this study, nearly-spherical shape AA7075 powders produced by the gas atomization method milled different times by adding 4 wt% methanol gradually (25 % of methanol added into jar every 0.5h up to 2.0h) in different milling times in the planetary type milling machine. Jar and balls were made of tungsten carbide (WC). Milling speed and Ball-powder ratio was chosen 300 rpm and 10:1. The aim of this paper is to examine the effect of the different milling times on the properties of the AA7075 powders.

II. MATERIALS AND METHODS

AA7075 alloy powders produced by the gas atomization in Kütahya Dumlupınar University, Mechanical Engineering Research Laboratory (Turkey), particle size distribution ranging from 16 to 110 μm and mean particle size is 43.9 μm (Fig. 1).

Furthermore, alloy elements of AA7075 are pointed out Table I, experimental procedure is defined in Fig. 2. Morphology of the nearly-spherical AA7075 powder is indicated in Fig. 3.

Table 1: Alloy Elements of AA7075 Alloy powders

Cu	Mg	Mn	Fe	Si	Zn	Cr	Ti	Al
1,2	2,1	0,3	0,5	0,4	5,1	0,18	0,2	87,1
-	-	(max)	(max)	(max)	6,1	-	(max)	-
2	2,9					0,28		91,4

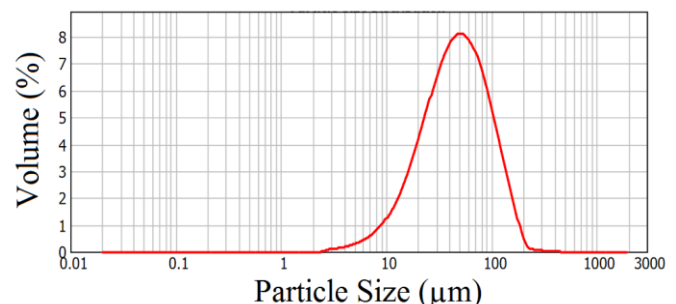


Fig. 1. Mean particle size of AA7075

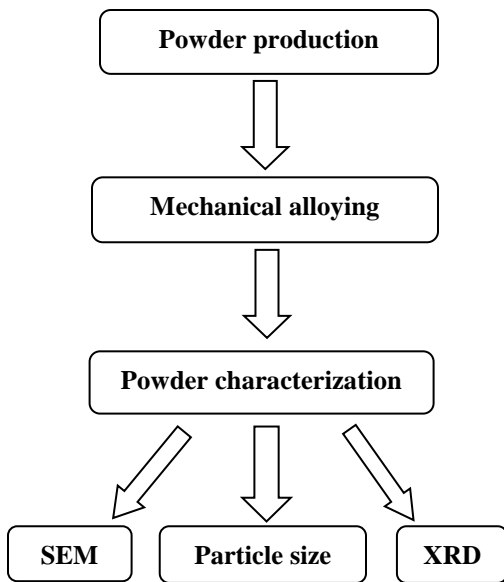


Fig. 2. Process of producing of the AA7075 powders

III. RESULTS AND DISCUSSION

A. Microstructure

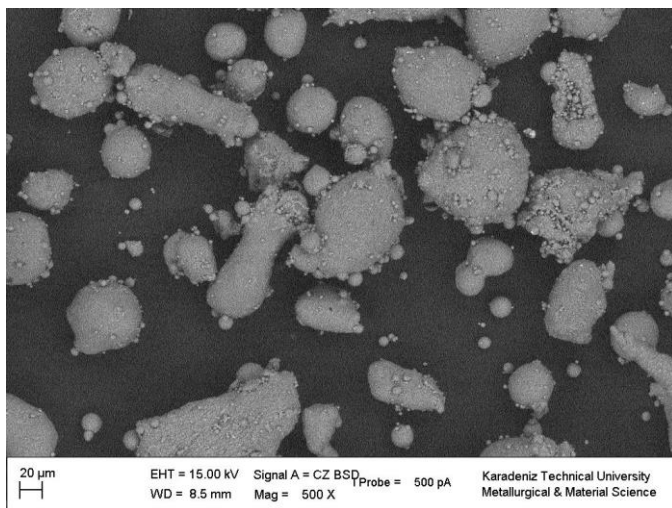
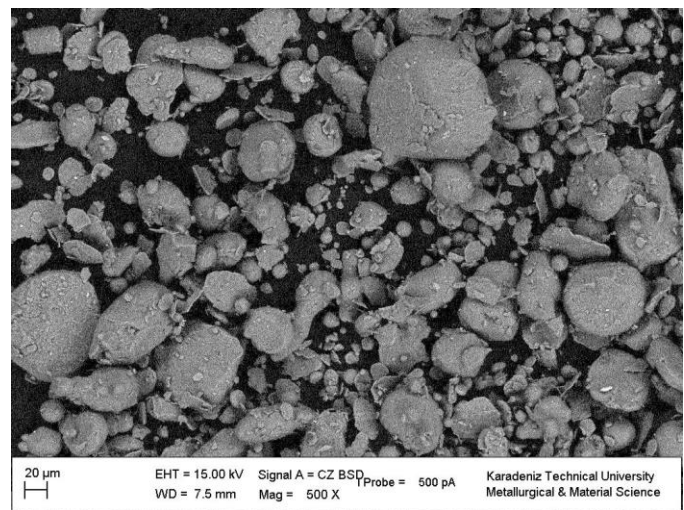
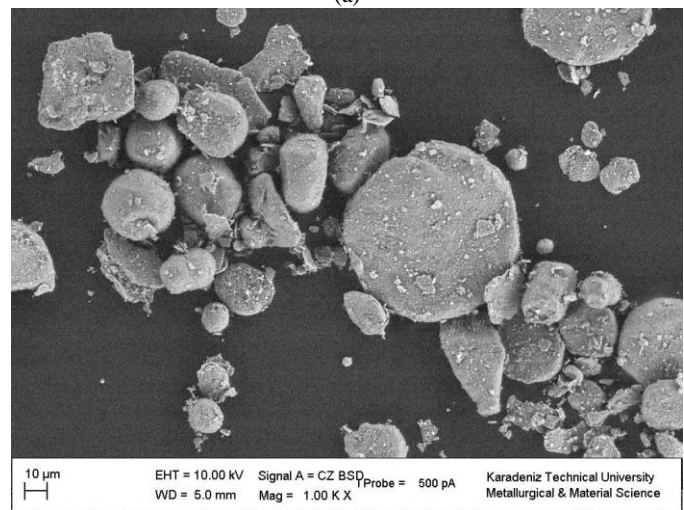


Fig. 3. Initial powder morphology of the AA7075

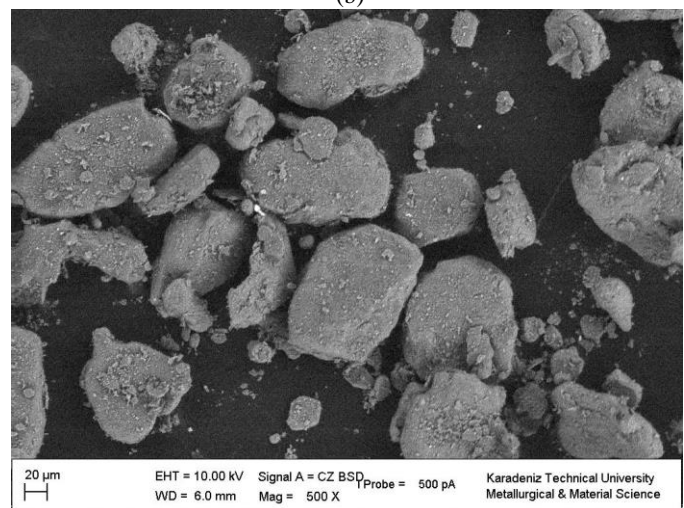
As can be seen from the SEM analysis in the Fig. 3, the initial phase morphology of the AA7075 powder is nearly-spherical shape.



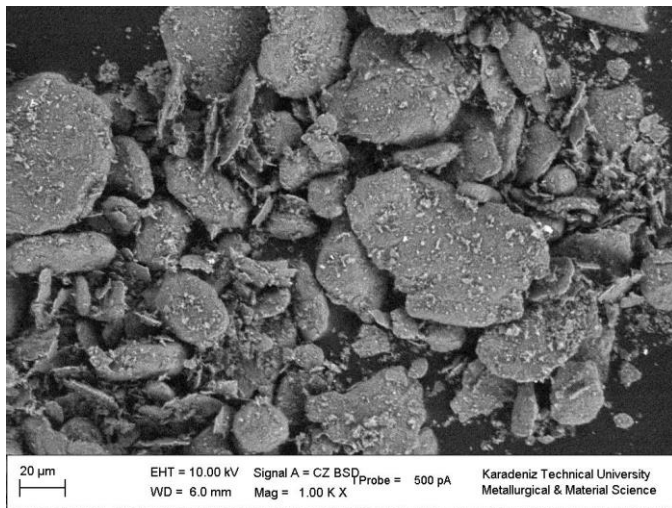
(a)



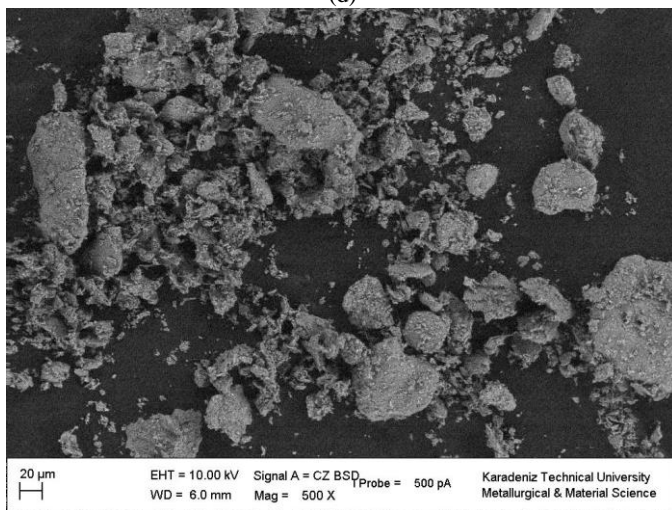
(b)



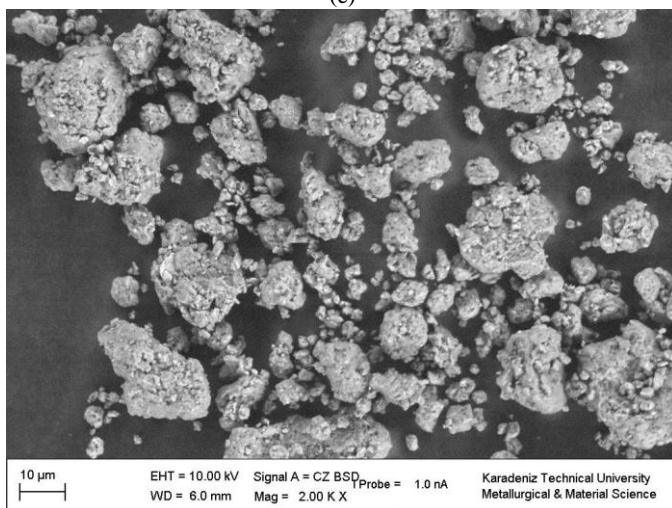
(c)



(d)



(e)



(f)

Fig. 4. (a) 0.5h (b) 1.0h (c) 1.5h (d) 2.0h (e) 3.0h (f) 5.0h milled AA7075 powders in planetary type milling machine with added gradually 4 wt% methanol

As can be seen from SEM figures in Fig. 4 (a-f), the AA7075 powders began to prolong in the first phases (0h -

1.5h) by the effect of plastic deformation and started to change to powder morphology called flake structure. At the end of 2.0h, it was seen that the quantity of flake structure powders increased but the small particles occurred in the structure because of sudden fracture with effect of methanol. At the end of 5.0h, it is seen that the powders have grown because of cold welding.

B. XRD analysis

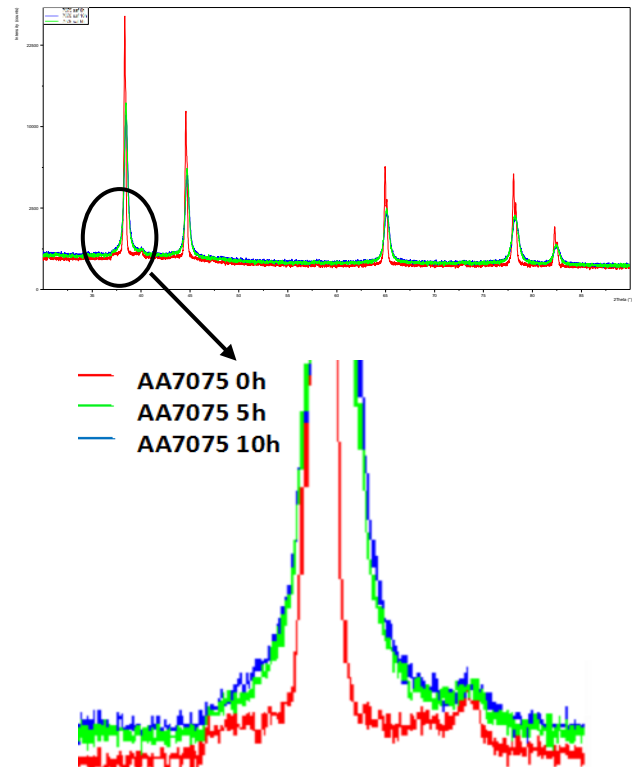


Fig. 5. 0h, 5h and 10h milled AA7075 powders XRD patterns

The expansion of the XRD peak indicates a decrease in crystallite size. In other words, increase in peak width at the end of 5h milling symbolizes the decrease of AA7075 powders crystallite size. At the end of 10h, the peak width has increased slightly, indicating that the crystallite size did not been reduced further (Fig. 5).

C. Powder Hardness

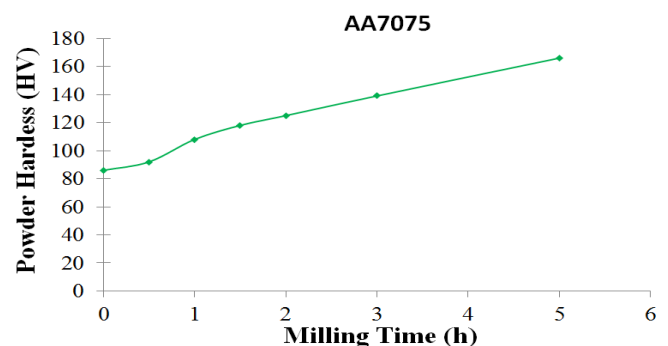


Fig. 6. Changing AA7075 powder hardness with milling time

Fig. 6 indicated that the hardness of the AA7075 powders increased due to the excessive plastic deformation that resulted in increased dislocation density.

D. Particle Size

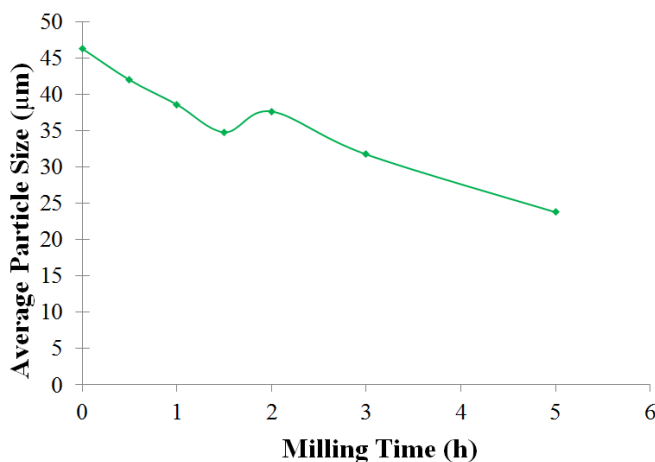


Fig. 7. Changing mean particle size of AA7075 powders with milling time

The mean particle size of AA7075 powders decreased with increasing milling time up to 1.5h milling time because of methanol effect which caused rapid fracture of powder but owing to acceleration of tendency to flake structure provoked increase of mean powder size up to 2h. Moreover, particle size decreased on account of the methanol effect becomes dominant again in the milling process (Fig. 7).

IV. CONCLUSIONS

With the increase of the milling time the powder hardness increased, however, the irregularity of the powder shapes and the high powder hardness caused the porosity based on negatively affected packaging density. Therefore, it is not hard to predict that decrease of mechanical properties of sintered AA7075 specimens.

Grain boundaries increase with the decrease of the powder size, and theoretically high strengthen samples can be produced, however, the presence of only small powders in the structure reduces the packaging density. This causes decrease of materials mechanical strength similarly as above mentioned.

ACKNOWLEDGMENT

This paper is a part of M.Sc. thesis supported by the Selcuk University Scientific Research Project Center (Project number 18201095).

REFERENCES

[1] Onur, A., Investigation of Machinability Depending on Aging Process of AA6XXX Series Aluminum Alloys. M. Sc. Thesis, Bilecik Seyh Edebali University, Bilecik, 2014: p. 69.

- [2] Cabeza, M., et al., Development of a high wear resistance aluminium matrix nanoreinforced composite. *Surface and Interface Analysis*, 2012. 44(8): p. 1005-1008.
- [3] Azimi, A., et al., Optimizing consolidation behavior of Al 7068–TiC nanocomposites using Taguchi statistical analysis. *Transactions of Nonferrous Metals Society of China*, 2015. 25(8): p. 2499-2508.
- [4] Azimi, A., A. Shokuhfar, and O. Nejadseyfi, Mechanically alloyed Al7075–TiC nanocomposite: Powder processing, consolidation and mechanical strength. *Materials & Design (1980-2015)*, 2015. 66: p. 137-141.
- [5] Arslan Ateş, E., Application of Aging Heat Treatment to AA2014-AL4C3 Systems Produced by Powder Metallurgy and Investigation of Their Microstructural Properties. M. Sc. Thesis, Gazi University, Ankara, 2012: p. 119.
- [6] Aoba, T., M. Kobayashi, and H. Miura, Effects of aging on mechanical properties and microstructure of multi-directionally forged 7075 aluminum alloy. *Materials Science and Engineering: A*, 2017. 700: p. 220-225.
- [7] Surya Sundara Rao, K. and K. Viswanath Allamraju, Effect on Micro-Hardness and Residual Stress in CNC Turning Of Aluminium 7075 Alloy. *Materials Today: Proceedings*, 2017. 4(2): p. 975-981.
- [8] Balaji, V., N. Sateesh, and M.M. Hussain, Manufacture of Aluminium Metal Matrix Composite (Al7075-SiC) by Stir Casting Technique. *Materials Today: Proceedings*, 2015. 2(4-5): p. 3403-3408.
- [9] Fang, G., J. Zhou, and J. Duszczczyk, Extrusion of 7075 aluminium alloy through double-pocket dies to manufacture a complex profile. *Journal of Materials Processing Technology*, 2009. 209(6): p. 3050-3059.
- [10] Flores-Campos, R., et al., Microstructure and mechanical properties of 7075 aluminum alloy nanostructured composites processed by mechanical milling and indirect hot extrusion. *Materials Characterization*, 2012. 63: p. 39-46.
- [11] Gökmeşe, H., Mold Modeling of Metallic Tension Bar in AA 7075 Aluminium Alloy Casting. *Mechanika*, 2018: p. 11.
- [12] Joshi, T.C., U. Prakash, and V.V. Dabhade, Microstructural development during hot forging of Al 7075 powder. *Journal of Alloys and Compounds*, 2015. 639: p. 123-130.
- [13] Kannan, C. and R. Ramanujam, Comparative study on the mechanical and microstructural characterisation of AA 7075 nano and hybrid nanocomposites produced by stir and squeeze casting. *J Adv Res*, 2017. 8(4): p. 309-319.
- [14] Pradeep Devaneyan, S., R. Ganesh, and T. Senthilvelan, On the Mechanical Properties of Hybrid Aluminium 7075 Matrix Composite Material Reinforced with SiC and TiC Produced by Powder Metallurgy Method. *Indian Journal of Materials Science*, 2017. 2017: p. 1-6.
- [15] Ozkaya, S. and A. Canakci, Effect of the B4C content and the milling time on the synthesis, consolidation and mechanical properties of AlCuMg-B4C nanocomposites synthesized by mechanical milling. *Powder Technology*, 2016. 297: p. 8-16.
- [16] Wang, W.K., et al., Fabrication and Mechanical Properties of Tungsten Inert Gas Welding Ring Welded Joint of 7A05-T6/5A06-O Dissimilar Aluminum Alloy. *Materials*, 2018. 11(7).
- [17] Erdemir, F., A. Canakci, and T. Varol, Microstructural characterization and mechanical properties of functionally graded Al2024/SiC composites prepared by powder metallurgy techniques. *Transactions of Nonferrous Metals Society of China*, 2015. 25(11): p. 3569-3577.
- [18] Abdellahi, M., H. Bahmanpour, and M. Bahmanpour, The best conditions for minimizing the synthesis time of nanocomposites during high energy ball milling: Modeling and optimizing. *Ceramics International*, 2014. 40(7): p. 9675-9692.
- [19] Abdellahi, M., M. Bhanpour, and M. Bahmanpour, Optimization of process parameters to maximize hardness of metal/ceramic nanocomposites produced by high energy ball milling. *Ceramics International*, 2014. 40(10): p. 16259-16272.
- [20] Nestler, D., et al., Beitrag zum Einfluss von Trennmitteln und Atmosphären zur Prozesskontrolle beim Hochenergie-Kugelmahlen bei der Herstellung von partikelverstärkten Aluminiummatrix-Verbundwerkstoffen. *Materialwissenschaft und Werkstofftechnik*, 2011. 42(7): p. 580-584.
- [21] Wu, Z., et al., Effect of Ball Milling Parameters on the Refinement of Tungsten Powder. *Metals*, 2018. 8(4).

INVESTIGATION OF LOW VELOCITY IMPACT BEHAVIOURS OF NANOSILICA FILLED AND BASALT FIBER REINFORCED NANOCOMPOSITES AT SEA WATER CORROSION CONDITION

İbrahim DEMİRCİ¹, Necati ATABERK², Mehmet Turan DEMİRCİ³,
Ahmet AVCI⁴

¹ Selcuk University, Konya/Turkey, ibrahim.demirci@selcuk.edu.tr

² Necmettin Erbakan University, Konya/Turkey, nataberk@konya.edu.tr

³ Selcuk University, Konya/Turkey, turandemirci@selcuk.edu.tr

⁴ Necmettin Erbakan University, Konya/Turkey, a.avci@konya.edu.tr

Abstract - In this study, the sea water exposed for 40 days and unexposed nano-silica filled and unfilled BFR/Epoxy composites were applied to the low velocity impact tests. The adding % weight ratio was determined as 4wt% on the basis of studies and literature searches. Low velocity impact tests were carried out at 10 j and 20 j energy levels according to ASTM D7136 / 7136M standard. As a result of experiments; the nanosilica addition into composites increased the maximum force for the corrosive and uncorrosive conditions. In addition sea water exposed all composites for 40 days corrosion period has reduced the maximum forces. It was found that the decreases of maximum forces with addition of nanosilica were lower than unfilled nanosilica at the end of 40 days of corrosion. At the same time, while increasing the bending stiffness by filling nanosilica, It has been found that at the end of the 40 days corrosion period, high rigidity values are shown according to the unfilled nanosilica BFR/Epoxy composites. It was determined that the addition of nanosilica decreased the displacement. In addition, at the end of 40 days of corrosion period, the displacement was increased for all of nanosilica filled and unfilled BFR/Epoxy composites but it was determined that the displacement for nanosilica filled composites was less than unfilled BFR/Epoxy composites.

Keywords - Basalt fibers, Nanocomposites, Nanosilica, Low velocity impact behavior, Seawater corrosion.

I. INTRODUCTION

Fiber reinforced composite materials have become widespread in the industry in recent years due to their high strength, rigidity and resistance to environmental conditions in many industrial areas.. Polymer matrix composites are the

most commonly used fibers are carbon and glass fiber. The recent studies show that basalt fibers may be an alternative to other fibers because of the high cost of carbon fibers and basalt fibers showing both natural and good mechanical properties [1,2]. No additives are made during the production of basalt fibers, so that the natural production of basalt fibers is both cost-effective and natural. [1, 2,3].

Nanoparticles have been studied by researchers to provide advantages such as polymeric matrix composites to improve electricity and heat insulation, improve mechanical properties, increase scratch resistance and corrosion resistance. The conducted studies were directed to SiO₂ as nanoparticles to improve the mechanical properties of the matrices and it has been observed improvement in the properties such as the elongation amounts of composite materials, energy absorption, and interface adhesion and corrosion resistance. [1,4].

Seawater corrosion in composite materials is effective and therefore seawater corrosion creates tensile stresses in composite materials.. This leads to surface cracks.[5] In polymer matrix composite materials, which are exposed in a seawater corrosion condition, the salts absorbed in the fiber and resin cause water pockets on the surfaces and ultimately cause the osmotic pressure to increase in the fiber matrix interface. Due to corrosion caused by these mechanisms in composite materials, it is important to conduct studies on losses in mechanical behavior in changing corrosion period. With the nanoparticles additive, there have not been enough studies to determine the level of losses in these mechanical behaviors. Therefore, the purpose of this study is to increase the corrosion resistance of the basalt fibers with SiO₂ nanoparticle additives.

II. MATERIAL AND METHOD

The SiO₂ nanoparticles used in the study were obtained from MKnano Canada by surface modification with silane. In the production of basalt fiber composite laminated plate, KamennyVek Advanced Basalt Fiber 12KV 400 tex basalt fibers which are in the range of 11-13 μm fiber diameter were used. DGEBA (MGS L160) medium viscosity epoxy was used as the matrix material. MGS 260S hardener was used as hardener. In unfilled BFR/Epoxy composites 100 mg of epoxy was added to 36% of hardeners and mechanically mixed for 15 minutes.

In order to produce SiO₂ filled Basalt / epoxy composite, SiO₂ was used at the weight ratio of 4%. The weighted additive rate, which provides the best mechanical strength, has been determined as 4%. 4% SiO₂ was added to the epoxy and mechanical mixing was carried out for 10 minutes. Then ultrasonic mixing was carried out for 1 hour at the tipped sonic device. After mixing is finished it was allowed to cool to room temperature. After cooling, 36% hardener was added and mechanically mixing for 10 minutes. With the prepared epoxy, the vacuum infusion method was produced with 6 layers of unfilled basalt fiber and filled composite materials. Samples produced according to ASTM D3039 / D3039M-08 standards were exposed in 0, 40 days seawater (Mediterranean) corrosion condition and low velocity impact tests were carried out at 10j and 20j energy levels.

III. EXPERIMENTAL METHODS

In this study low velocity impact tests were carried out in accordance with ASTM-D-7136 standard for 4% SiO₂ / BTP / Epoxy, and unfilled BTP / Epoxy composites at 10J and 20J energy levels. At the same time, 4% SiO₂ / BTP / Epoxy nano particles filled and unfilled BTP / Epoxy composites were expose in sea water conditions for 0 and 40 days and then low-speed impact tests were carried out at 10J and 20J energy levels.

In 0 day sea water corrosion condition, 4% SiO₂ / BTP / Epoxy and unfilled BTP / Epoxy composites are examined in the force-displacement graph, where the maximum force value is obtained in 4% SiO₂ / BTP / Epoxy composites at 10j and 20 j energy levels. This is shown in figure 1 and figure 3. When the displacement values were examined, it was observed that the displacement values of 4% SiO₂ / BTP / Epoxy composites were lower than that of unfilled BTP / Epoxy composites [1].

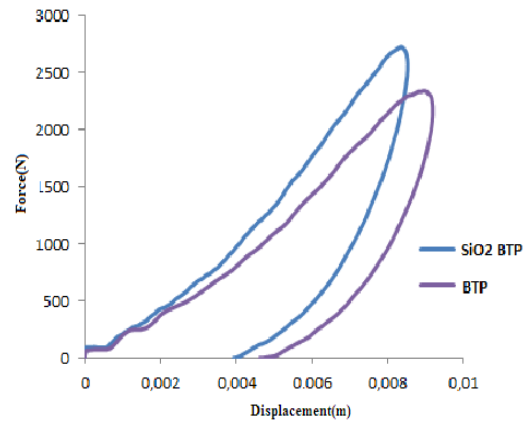


Figure 1: Force-displacement of 4% SiO₂ filled and unfilled BTP / Epoxy composites at 10J energy level [1].

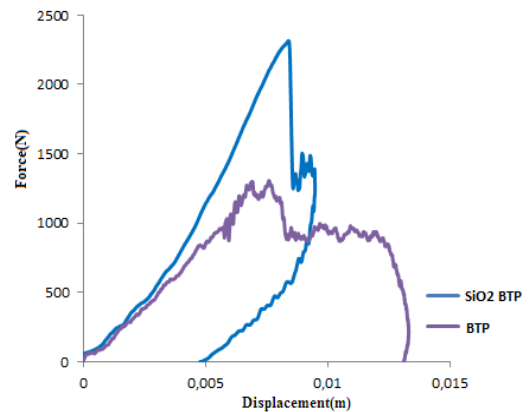


Figure 2: Force-displacement of 4% SiO₂ filled and unfilled BTP / Epoxy composites at 10J energy level in 40 days sea water corrosion condition [1]

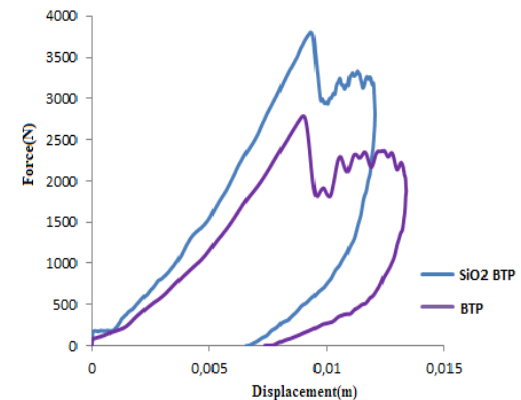


Figure 3: Force-displacement of 4% SiO₂ filled and unfilled BTP / Epoxy composites at 20J energy level [1]

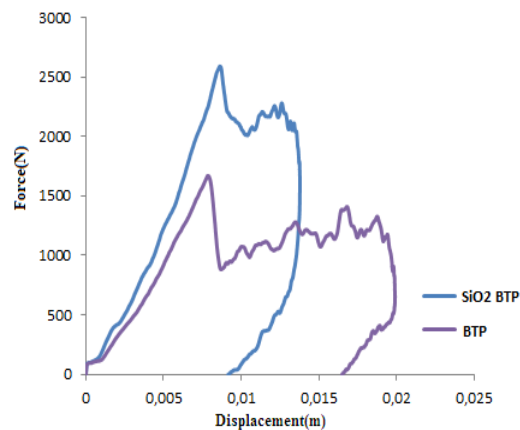


Figure 4: Force-displacement of 4% SiO₂ filled and unfilled BTP / Epoxy composites at 20J energy level in 40 days sea water corrosion condition [1]

40 days were determined to increase the amount of damage as a result of the corrosion period and the result of the displacement graph in the increase in the amount of displacement (collapse) has been a supporting result. It has been observed in the force-displacement graphs where the bending stiffness of BTP / Epoxy filled and unfilled BTP / Epoxy composites with 4% SiO₂ addition and 40 days corrosion time has been reduced. SiO₂ nanoparticles have a block effect in the entrance lines of the seawater composite layers and so it is thought that it prevents or decreases the entrance of the sea water and it increases the strength of the matrix / fiber interface.

IV. DISCUSSION AND CONCLUSION

4% SiO₂ filled BTP / Epoxy and unfilled BTP / Epoxy composites were produced by vacuum infusion method and exposed to sea water (Mediterranean) corrosion environment for 0 and 40 days. At the end of corrosion periods, low velocity impact tests were carried out at 10j and 20j energy levels. Results of the experiments were evaluated;

- It was determined that the maximum force and displacement values increased with the increase of energy level..
- It was determined that the maximum force value of BTP / Epoxy Composites increased and the displacement value decreased with SiO₂ nanoparticle addition.
- The corrosion time of SiO₂ nanoparticles filled and unfilled BTP / Epoxy composites was effective and caused an increase in the displacement values which caused a decrease in the maximum strength values.
- These decreases are reduced with nanoparticle filled and it is thought that nanoparticles create a block effect in the sea water entrances and at the same time increase the resistance of the fiber / matrix interface, cracking, crack guiding, fracture branching are

affected by the mechanisms of fracture to provide a healing effect in mechanical behaviors.

ACKNOWLEDGMENT

This study has been made by preparing from M. Sc. Thesis of Ibrahim DEMIRCI that was executed in The Graduate School of Natural and Applied Science of Selcuk University

REFERENCES

- [1] İ. Demirci, "Impact behaviors of carbon nanotubes and nano silica reinforced basalt/epoxy hybrid nanocomposites in corrosion environment", M.Sc. Thesis, Dept. Mechanical Engineering, Selcuk Univ, Konya, Turkey, 2017.
- [2] B. Wei, H. Cao, S. Song, "Degradation Of Basalt Fibre And Glass Fibre/Epoxy Resin Composites In Seawater", *Corrosion Science*, vol. 53,pp. 31-426, 2011.
- [3] S.Sferra, C.Ibarra-Castanedo, C.Santulli, A.Paoletti, D.Paoletti, F.Sarasini, A.Bendada, X. Maldague, "Falling weightim pacted glass and basalt fibre woven composites inspecte dusingnon destructive techniques", *Composites Part B*, vol. 45, pp. 8-601, 2013.
- [4] M.T. Demirci. "The effects of SiO₂ nanoparticle addition on the fatigue behaviors of surface cracked and uncracked basalt fiber reinforced composite pipes," Ph.D. Thesis, Dept. Metallurgical and Materials Engineering, Selcuk Univ, Konya, Turkey, 2015.
- [5] A. Apicella, C.Migliaresi, L.Nicodemo, L Nicolais, L. Iaccarino, S.Roccotelli, "Water sorptionand mechanical properties of a glass-reinforced polyester resin", *Composites*, vol. 13, pp. 10-406, 1982.
- [6] Ö.S. Şahin, " Corrosion fatigue behavior of filament wound pipes with surface crack," Ph.D. Thesis, Dept. Mechanical Engineering, Selcuk Univ, Konya, Turkey, 2004.

Removal of Phosphorus Using Mg-Al Layered Double Hydroxides

H.K.YESILTAS¹ and T.YILMAZ¹

¹ Cukurova University, Adana/Turkey, hkyesiltas@cu.edu.tr

¹ Cukurova University, Adana/Turkey, tyilmaz@cu.edu.tr

Abstract - In this study, phosphorus removal in synthetic wastewater was investigated by Mg-Al layered double hydroxides (LDH) synthesized in the laboratory by co-precipitation method. The Mg-Al LDHs synthesized were classified according to their particle diameters and all studies conducted in the laboratory were operated as batch systems. For the 600-850 μm particle class, which has the lowest grain diameter class, 90,56% removal efficiency was obtained and adsorption batch experiments results were well fitted when applied to Langmuir isotherm.

Keywords - Phosphorus Removal, Layered Double Hydroxides, Co-preparation Method, Adsorption, Synthesis, Adsorption Isotherms

I. INTRODUCTION

PHOSPHORUS is an important element for living things in addition many industrial factories uses in their applications. Discharge of domestic and industrial wastewater containing phosphorus to the receiving streams and water bodies causes eutrophication as an environmental problem [1,2]. As a result of eutrophication that occurs even at low phosphorus concentrations, it causes negative deterioration in the natural ecosystem, deaths in aquatic organisms and increasing cost of treatment in drinking water supply [2,3]. There are various methods for removing phosphorus, activated sludge from biological methods and chemical precipitation and adsorption from chemical methods are widely used [3-5]. Biological methods and chemical precipitation method are not effective at low concentrations at phosphorus that included wastewater [4,5]. In addition, the need for qualified operator during the application of these methods, the formation of sludge and the high operating costs of phosphorus removal are also seen as disadvantages of these methods [3,6]. Adsorption method is more economical than other methods and can be used effectively in low concentrations [4-7]. Various adsorbents such as red mud, fly ash, aluminum oxide, iron oxide, zirconium oxide and layered double hydroxides (hydrotalsite) are used in the removal of phosphorus from water and wastewater [7,8]. Layered double hydroxides can be used efficiently in phosphorus removal in terms of high anion exchange capacity, reusability as adsorbent, suitable to study under neutral pH conditions, high anion exchange capacity and recovery of phosphorus [7,9,10].

LDH's are classified as double layer nanostructured anionic

clays [8]. The anionic clays with crystal structure have an inner layer containing negatively charged water and anions between the positive charged metal hydroxide layers [11]. Figure 1 shows the typical structure of LDH. The general structural formula of LDHs is (1). Here are M^{+2} divalent cations (Mg^{+2} , Fe^{+2} , Co^{+2} etc.), M^{+3} trivalent cations (Al^{+3} , Cr^{+3} , Fe^{+3} etc.), the value of the anion in the inner layer n, (A^{-n}) the inner layer anions (CO_3^{-2} , Cl^- , SO_4^{-2} etc.), x is the molar ratio of value and takes value between 0,2-0,33 [9,12]. LDH's load density and ion exchange capacity can be controlled by changing the M^{+2}/M^{+3} ratio [13].

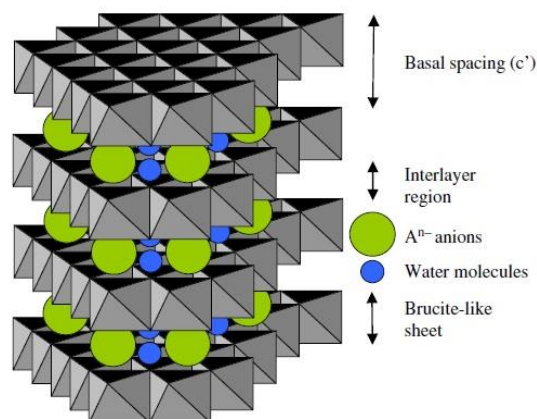
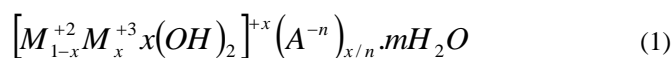


Figure 1: Typical structure of LDH (Here, the basal space (c') state the total thickness of the basal zone with the brucite-like layer) [11].



In this study, phosphorus removal from synthetic phosphorus solution was investigated with Mg-Al LDH synthesized in laboratory conditions. Synthesized LDH were classified according to their particle diameter distribution and batch adsorption applications were performed for each particle diameter class. In addition, the results of the analysis were used as data for the adsorption isotherm models and it was determined by Mg-Al LDH and phosphorus removal which adsorption isotherm model.

II. MATERIALS AND METHODS

Synthetic phosphorus solutions used in this study were prepared from potassium dihydrogen phosphate (KH_2PO_4 , Merck %96) salt. Phosphorus analyzes were performed using the Perkin Elmer TU-1880 model UV-VIS spectrophotometer with Standart Methods, 4500-P C [14] analysis method. pH measurements were made by using WTW 3110i pH meter calibrated according to Standart Methods, 4500-H+ B [14] method.

A. Preparation of LDH's

LDH synthesis was performed in two steps. The first step is the synthesis of double-layer hydroxides by the conventional co-precipitation method [12]. The second step is the preparation of Mg-Al LDH for the adsorption study.

Prior to synthesis, prepare 0.15 M 400 mL of sodium hydroxide (NaOH, Sigma %98) solution with deionized water. Subsequently, 4.16 g (20 mmol) of magnesium chloride ($\text{MgCl}_2 \cdot 6\text{H}_2\text{O}$) and 2.41 g (10 mmol) of aluminum chloride ($\text{AlCl}_3 \cdot 6\text{H}_2\text{O}$) salts are added slowly to the NaOH solution prepared at a stirring rate of 300 rpm at room temperature ($\cong 24^\circ\text{C}$). The pH suitable for the synthesis is between 10.5-11 and the pH value decreases during synthesis. Therefore, synthesis is continued by adjusting the pH during the mixing with NaOH. Stirring is continued by controlling the pH for 10 minutes. After 10 minutes, the pH is adjusted to 7 with hydrochloric acid (HCl, Merck %37) and the mixing process is completed. The resulting solid-liquid mixture is allowed to settle for 2 hours. Then, the liquid phase at the top is removed and the material is poured into the coarse filter paper and dried for 1 hour at ambient temperature.

In the second stage, LDH is dried for 24 hours in an oven set to 60°C . After drying, it is washed several times with deionized water and allowed to dry at room temperature ($\cong 24^\circ\text{C}$) for 24 hours. The LDHs synthesized after the drying process were subjected to sieve analysis and classified (three classes, 600-850 μm , 850-1000 μm and 1000 μm and above) according to particle size.

B. Adsorption Studies

For each class of LDHs, 0.1 g, 0.2 g, 0.3 g, 0.4 g and 0.5 g LDH were weighed and separately transferred to 100 mL volume reactors. Subsequently, 50 mL of a 1 L volume of synthetic phosphorus solution containing 108 mg / L PO_4^{3-}P was added to each reactor. The reactors were during for one hour at room temperature ($\cong 24^\circ\text{C}$) at a rinsing rate of 334 rpm and after 1 hour, the solutions in the reactor were transferred to separate glass vials. Finally, the solutions contained in the glass tubes were filtered using a vacuum apparatus (cellulose acetate filter, 0.45 μm) and phosphorus and pH analysis were performed in each filtrate water. After the study, phosphorus removal results for each LDH class were used as data in adsorption isotherm models (Freundlich, Langmuir, Temkin and Dubinin).

III. RESULT AND DISCUSSION

A. Phosphorus Removal of Mg-Al LDH's

The phosphorus removal concentrations determined by Mg-Al LDHs were found in Table 1. When the results of the analysis are examined, the amount of phosphorus is increased as the amount of LDH used increases. In addition, the amount of phosphorus increased as the particle size of the LDH decreased.

Table 1: Phosphorus (PO_4^{3-}P) concentrations after batch experiments

Quantity of LDH, g	600-850 μm , mg/L	850-1000 μm , mg/L	1000 μm and above mg/L
0,1	72,56	80,00	86,90
0,2	47,70	55,60	63,96
0,3	29,00	36,80	44,25
0,4	16,90	23,78	32,30
0,5	10,20	17,56	24,18

The maximum and smallest particle sizes of LDHs used in this study were determined as 77.61 % and 90.56 % phosphorous removal, respectively, using 1000 μm and above and 600-850 μm LDHs and 0.5 g of the largest LDH mass. (Figure 2).

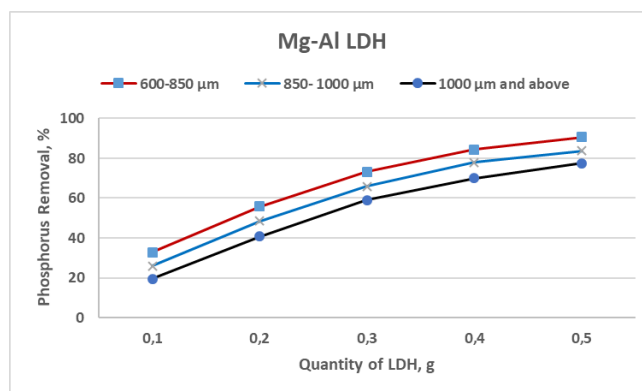


Figure 2: Mg-Al LDHs phosphorus removal efficiencies

After the phosphorus removal study, the reactors were examined and the LDH was precipitation in the bottom of the reactor and was ready for liquid-solid separation. As a result of this observation, it is thought that the separation of LDH after removal does not require an additional process and can be applied for column processes.

B. Solution of pH

The structure of LDHs includes hydroxyl and/or carbonate. Hydrogen and/or carbonate will be released to the aquatic environment by binding the phosphorus during ion exchange. As the hydroxyl and carbonate are alkaline species, the pH is expected to rise during phosphate removal. It is shown in Figure 3. that the amount of LDH in LDHs increased according to particle diameter distributions and increased in pH value.

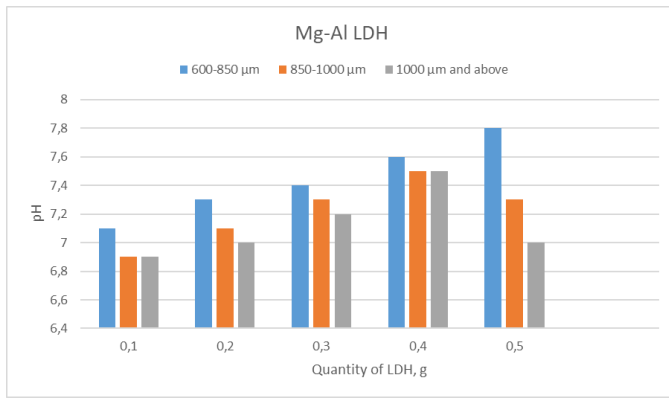


Figure 3. pH values of solutions after LDH removal

The distribution of phosphorus species in the aquatic environment can be determined by ionization of phosphoric acid, a weak acid with three ionisations as a function of pH [15]. The pH of the phosphate solution used in phosphorus removal was 6.5 and it was determined that the pH values changed between 6.9 and 7.8 after the phosphorus removal with Mg-Al LDHs. In this study, HPO_4^{2-} and $H_2PO_4^-$ forms are thought to be included in the phosphate forms used LDH.

Das et al [8], at the beginning of the synthesis of the Mg-Al molar ratio of 2: 1 as the expression of the LDH by using the pH range 3 to 11 phosphorus removal of the highest phosphorus removal at the pH 5 reported 91.7%. Drenkova-Tuhtan et al. [16] reported that they obtained 97.5% deposition with pH-Mg-Fe-Zr LDHs, they decreased the pH <3, and the pH value was decreased and the phosphorus removal increased with the decrease in pH value. As the pH value increases and the amount of OH^- will increase and the phosphate anions will compete to be incorporated into the LDH, it is recommended to remove the phosphate at neutral pH.

C. Adsorption Isotherms

Adsorption equilibrium isotherms are empirical equations describing the relationship between the volume adsorbent mass and the amount of adsorbed matter at constant temperature (2) [16]. The data obtained in this study were applied to the isotherms models of Freundlich, Langmuir, Temkin and Dubinin-Radushkevich. In this study, it was observed that batch adsorption data were fitted for Langmuir isotherm in phosphorus adsorption with Mg-Al LDHs (Figure 4-6).

$$q_e = \frac{x}{m} = \frac{C_0 - C_e}{m} \quad (2)$$

Where C_0 and C_e are initial ($t=0$) and effluent phosphorus concentration of reactor, respectively. q_e amount of adsorbed material per unit adsorbent and m quantity of adsorbent.

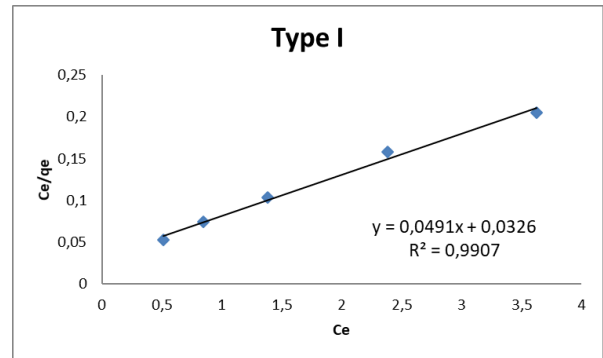


Figure 4. 600-850 µm particle size Langmuir isotherm graph.

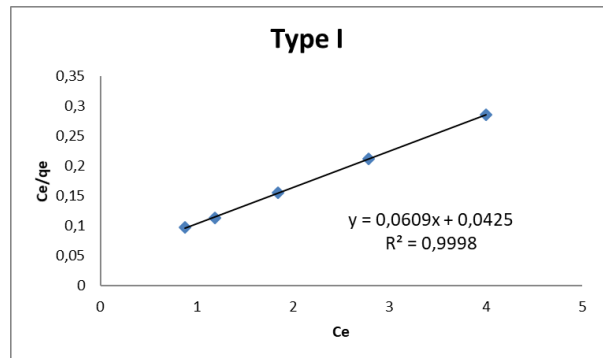


Figure 5. 850-1000 µm particle size Langmuir isotherm graph.

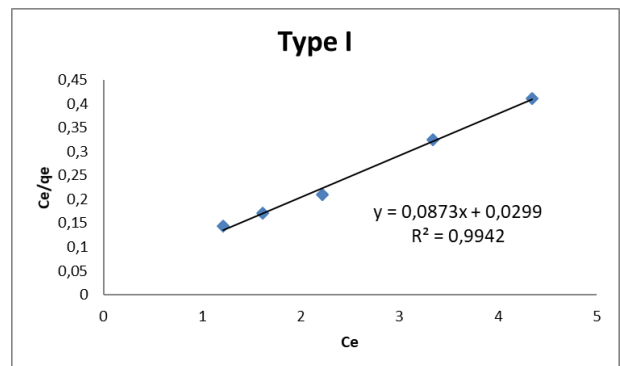


Figure 6. 1000 µm and above particle size Langmuir isotherm graph.

The Langmuir type I isotherm values for the three particle classes are given in R_L , q_m and K_L Table 2. The R_L value defines the separation factor that is of fundamental importance to the Langmuir isotherm. This value is used to determine whether the adsorption is reversible and irreversible. If R_L is equal to zero, the adsorption is irreversible. R_L 1 is preferred from 0 to 1 and is not preferred to be greater than 1.

Table 2. Constants of Langmuir Isotherm Type I

Particle size class	R_L	q_m , mg/g	K_L , 1/mg
600-850 µm	0,10	20,36	1,50
850-1000 µm	0,11	1,43	16,42
1000 µm and above	0,06	1,50	2,91

As seen in the calculated R_L values, it was determined that the Mg-Al LDHs were between 0-1 for all particle diameters and they were in the appropriate range for Langmuir isotherm.

Das et al. [8], 7 different types of initial molar ratios (4 kinds of Zn-Al-Zr and 3 kinds of Mg-Al-Zr) with LDH and chromase and selenate removal of the Langmuir isotherm and the maximum capacity values of 16-24 mg/g and 23-29 mg/g, Kuzawa et al. [7], (Tomita Pharmaceutical Co. Ltd., Japan) obtained from the synthetic Mg-Al hydrotalcite granular (0.5-1.7 mm particle diameter) and powder form using phosphorus removal to match the Langmuir isotherm, maximum capacity for granular hydrotalcite Drenkova-Tuhtan [17], converting the Mg-Al, Mg-Al-Zr, Mg-Fe-Zr and Mg-Fe hydrotalcite into superparamagnetic particles, and the maximum adsorption of phosphorus removal to the Langmuir isotherm. reported that the capacity value is 35 mg/g.

IV. CONCLUSION

This study showed that Mg-Al LDHs are used conveniently at neutral pH at phosphorus removal, they do not require qualified operators and they can be used effectively and efficiently even at low phosphorus concentrations.

This study was supported by the Scientific Research Projects Unit of Cukurova University. Project number FYL-2014-3201.

REFERENCES

- [1] K. Karageorgiu, M. Paschalis, G.N. Anastassakis, Removal of Phosphate Species from Solution by Adsorption onto Calcite Used as Natural Adsorbent. *Journal of Hazardous Materials*, 2007.
- [2] T. Nur, M.A.H. Johir, P. Loganathan, T. Nguyen, S. Vigneswaran, J. Kandasamy, Phosphate Removal from Water Using an Iron Oxide Impregnated Strong Base Anion Exchange Resin. *Journal of Industrial and Engineering Chemistry*, 2014.
- [3] J. Choi, S. Lee, K. Park, K. Lee, D. Kim, S. Lee, Investigation of Phosphorous Removal from Wastewater Through Ion Exchange of Mesosstructure Based on Inorganic Material. *Desalination*, 2011.
- [4] S. Zhong-liang, L. Fu-mei, Y. Shu-hua, Adsorptive Removal of Phosphate from Aqueous Solutions Using Activated Carbon Loaded with Fe(III) Oxide. *New Carbon Materials*, 2011.
- [5] J. Xie, Y. Lin, C. Li, D. Wu, H. Kong, Removal and Recovery of Phosphate from Water by Activated Aluminum Oxide and Lanthanum Oxide. *Powder Technology*, 2015.
- [6] P. Loganathan, S. Vigneswaran, J. Kandasamy, N.S. Bolan, Removal and Recovery of Phosphate from Water Using Sorption. *Critical Reviews in Environmental Science and Technology*, 2014.
- [7] K. Kuzawa, Y. Jung, Y. Kiso, T. Yamada, M. Nagai, T. Lee, Phosphate Removal and Recovery with a Synthetic Hydrotalcite as an Adsorbent. *Chemosphere*, 2006.
- [8] J. Das, B.S. Patra, N. Baliarsingh, K.M. Parida, Adsorption of Phosphate by Layered Double Hydroxides in Aqueous Solutions. *Applied Clay Science*, 2006.
- [9] C. Novillo, D. Guaya, A.A. Avendaño, C. Armijos, J.L. Cortina, I. Cota, Evaluation of Phosphate Removal Capacity of Mg/Al Layered Double Hydroxides from Aqueous Solution. *Fuel*, 2014.
- [10] H. Shin, N. Kim, S. Nam, H. Moon, Phosphorus Removal by Hydrotalcite-like Compounds (HTLcs). *Wat. Sci. Tech.*, 1996.
- [11] K. Goh, T. Lim, Z. Dong, Application of Layered Double Hydroxides for Removal of Oxyanions: A Review. *Water Research*, 2008.
- [12] F. Cavani, F. Trifirò, A. Vaccari, Hydrotalcite-type Anionic Clays: Preparation, Properties and Applications. *Catalysis Today*, 1991.
- [13] S.P. Newman, W. Jones, Synthesis, characterization and Applications of Layered Double Hydroxides Containing Organic Guests. *New J. Chem.*, 1998.
- [14] E.W. Rice, R.B. Baird, A.D. Eaton, L.S. Clesceri, *Standard Methods for the Examination of Water and Wastewater*. American Public Health Association, Washington, 2012.
- [15] R.H. Petrucci, F.G. Herring, J.D. Madura, C. Bissonnette, *General Chemistry: Principles and Modern Applications with Mastering Chemistry*. Pearson Education, USA, 2010.
- [16] A. Behnamfard, M.M. Salarirad, Equilibrium and kinetic studies on free cyanide adsorption from aqueous solution by activated carbon. *Journal of Hazardous Materials*, 2009.
- [17] A. Drenkova-Tuhtan, K. Mandel, A. Paulus, C. Meyer, F. Hutter, C. Gellermann, G. Sextl, M. Franzreb, H. Steinmetz, Phosphate recovery from wastewater using engineered superparamagnetic particles modified with layered double hydroxide ion exchangers. *Water Research*, 2013.

Modelling of Hardness Values of AISI 304 Austenitic Stainless Steels

N. F. YILMAZ¹, A. BILICI² and M. YILMAZ³

¹Gaziantep University, Gaziantep/Turkey, nfyilmaz@gantep.edu.tr

²Gaziantep University, Gaziantep/Turkey, aykutbilici@gantep.edu.tr

³Gaziantep University, Gaziantep/Turkey, msyilmaz@gantep.edu.tr

Abstract - Arc stud welding (ASW) is a process by which a metal stud is combined to a metal workpiece by heating both parts with an electric arc. Stud welding is a method of joining a bolt or specially formed nut to a workpiece generally in the form of sheet or plate. The arc stud welding process are affected from many factors and welding parameters such as welding time, welding current, plunge and lift. Each parameters has influence on the weld quality performance. In this study, using the Adaptive Neural Network Based Fuzzy Inference System (ANFIS), mathematical modeling of the complex relationship between the output parameters and the input parameters is formed and this model has been developed to estimate the hardness test results of stud welding in AISI 304 Austenitic Stainless Steels. This model will guide the users of the stud welding using AISI 304 austenitic stainless steels.

Keywords - Arc Stud Welding, Hardness, ANFIS.

I. INTRODUCTION

Manufacturing companies today aim to increase productivity while maintaining high quality of product. In the area of metal joining, arc stud welding is a method that answer both sides of this aim. Arc Stud Welding is a process which is used to join an entire cross section area of metallic studs to the sheet metals. The source of heat is an arc format between the metals to be welded (stud and sheet metals). The molten pool and the arc produced during welding operation are protected from atmospheric air contaminants by using either shielding gases or ceramic ferrule [1].

In comparison with the other welding methods, the arc stud welding method has many advantages especially in increasing the productivity, due to a short time of welding cycle, simplicity in the use of equipment, the possibility of the process to automate, the accuracy of stud location and cost efficiency. Another important advantage of stud welding method is that the accessibility to the other side of the welding plate is not necessary. In addition to that, stud welding shows high carrying capacities, while the process is robust and can easily be monitored by progress of stud movement, voltage and current [2]. In this process, welding elements are welded by an arc without additional material and no punching, drilling, bonding, thread cutting, riveting is required to fix the fastening element. In many application stud welding is the cheapest joining method for parts. Especially in thin plates, stud welding method is often the only technical solution.

Stud welding method includes the same thermal, metallurgical, mechanical and electrical principles as other welding method [3]. The arc stud welding process are affected from many factors such as materials, stud cross section area, surface condition, stud design, environmental conditions, base metal thickness, welding position and welding parameters; welding time, welding current, plunge and lift. Each parameters has influence on the weld quality performance [4].

Yılmaz and Hamza [5] revealed that arc stud welding can be successfully applied to AISI 304 austenitic stainless steel. They observed that welding time has the strongest effect on the mechanical property, followed by welding current, plunge and lift, respectively. They remarked that low welding current and welding time cause uncompleted fusion weld while selected high level of welding current and welding time causes burned weld (necking at the weld region) so in order to obtain good weld joint, welding current must be adjusted according to welding time.

In this study, the data obtained from the experimental studies [5] using the Arc Stud Welding Method are used and a user-friendly model has been developed which predicts the hardness values of the weld joint by Adaptive Neural Network Fuzzy Inference System (ANFIS) method. Welding parameters; current, time, lift, plunge and stud diameter are used as input parameters of the model. This model will be a guide for the selection of process parameters to users of stud welding in the industry.

II. EXPERIMENTAL WORK

There are many factors that affect the welding quality of the arc stud welding. In order to obtain robust weld joining, it is necessary to pay attention to the selection of the stud welding parameters. Each parameter has separate effect on the weld joining. In this study, important welding parameters; stud diameter (D), welding current (I), welding time (t), plunge (P) and lift (L) at different levels are presented in Table 1. Stud welding processes were performed using the welding machine shown in Figure 1. Soyer- BMK-16i type arc stud welding machine was used to join the stud and plate while Argon gas was used as a shielding gas with constant flow rate of (5 l/min).

Table 1: Welding Parameters and Levels

Parameters	Symbol	Unit	Stud Diameter (mm)	Levels			
Welding Current	I	Amp	6	300	400	500	600
			8	500	600	700	800
			10	600	700	800	9000
			12	700	800	900	1000
Welding Time	t	Sec	6, 8, 10, 12	0,1	0,2	0,3	0,4
Plunge	P	mm	6, 8, 10, 12	1	2	3	4
Lift	L	mm	6, 8, 10, 12	1,5	2	2,5	3

Within this work Taguchi method (L16 array) was used to design of experiment layout. Sixteen different welding condition experiments for each stud diameter were carried out according to the design of experiment layout.

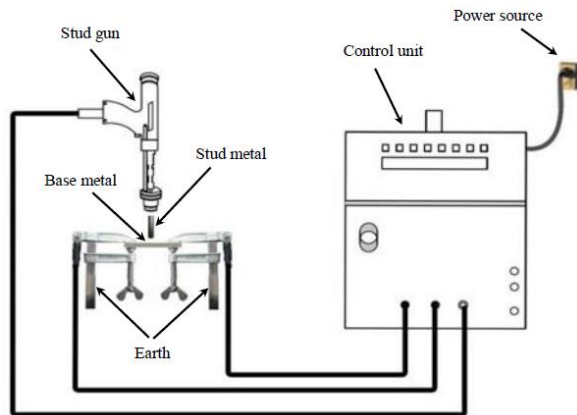


Figure 1: Arc Stud Welding Equipment [5]

In this work, used stud have a length of 60 mm, stud tip angle according to standard (ISO 14555) is 135° and base plate with dimensions of 60*50*5 mm, both of them are AISI 304 stainless steel. To obtain a good weldability, end surfaces of both metals were cleaned. Figure 2 shows the base plate and the stud metals which are prepared for welding operation in this work.

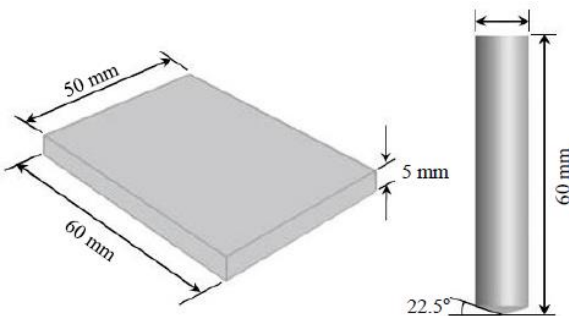


Figure 2: Represents the Stud and the Base Plate before Welding Operation [5]

The micro-hardness test have been developed for applications where the hardness of an important areas of the materials especially in a welded parts and thin materials [6]. In this study the Vickers micro-hardness method was used to measure the hardness of welding zone of the specimens. All prepared samples for micro-hardness test are tested according to the path shown in Figure 3 and hardness test values of each point were evaluated by averaging the results of 3 successive measurements in all samples.

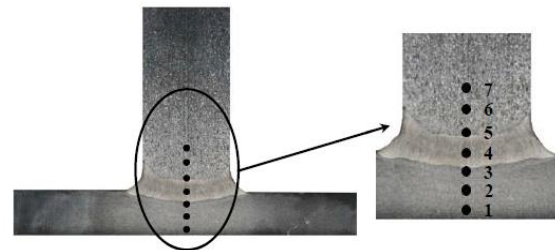


Figure 3: Illustration of Hardness Test Measurement [5]

III. ADAPTIVE NETWORK BASED FUZZY LOGIC INFERENCE SYSTEM (ANFIS)

Fuzzy logic and artificial neural networks are two different methods that can provide a suitable solution. The adaptive network based fuzzy logic inference system (ANFIS) is a hybrid model that occur with the combination of artificial neural network (ANN) and fuzzy logic [7]. In this way, there may be solutions to the wide range of problems of different areas [8, 9].

In this study, the ANFIS toolbox of MATLAB was used to construct the ANFIS model. In ANFIS models, 75% of the experimental data was randomly selected as the training data and 25% as the checking data (Table 2-3). According to this, 48 learning and 16 test data have been created to produce hardness model.

A model was created using stud diameter, welding current, welding time, plunge and lift as the input parameter and hardness values of welded samples as the output parameter. The results obtained from point 4 (welding zone) of the hardness value measurements given in Figure 3 were used for output parameter of ANFIS model.

Table 2: Training data

<i>Experimental Number</i>	<i>Welding Current</i>	<i>Welding Time</i>	<i>Plunge</i>	<i>Lift</i>	<i>Stud Diameter</i>	<i>Hardness Value</i>
1	300	0,1	1	1,50	6	229
2	300	0,2	2	2,00	6	228
3	300	0,3	3	2,50	6	226
4	400	0,1	2	2,50	6	228
5	400	0,3	4	1,50	6	225
6	400	0,4	3	2,00	6	223
7	500	0,1	3	3,00	6	227
8	500	0,3	1	2,00	6	224
9	500	0,4	2	1,50	6	222
10	600	0,1	4	2,00	6	225
11	600	0,3	2	3,00	6	221
12	600	0,4	1	2,50	6	218
13	500	0,2	2	2,00	8	226
14	500	0,3	3	2,50	8	224
15	500	0,4	4	3,00	8	222
16	600	0,1	2	2,50	8	226
17	600	0,2	1	3,00	8	224
18	600	0,4	3	2,00	8	221
19	700	0,1	3	3,00	8	225
20	700	0,2	4	2,50	8	223
21	700	0,4	2	1,50	8	220
22	800	0,1	4	2,00	8	223
23	800	0,2	3	1,50	8	221
24	800	0,4	1	2,50	8	218
25	600	0,1	1	1,50	10	226
26	600	0,2	2	2,00	10	225
27	600	0,4	4	3,00	10	221
28	700	0,1	2	2,50	10	225
29	700	0,2	1	3,00	10	224
30	700	0,4	3	2,00	10	218
31	800	0,1	3	3,00	10	223
32	800	0,2	4	2,50	10	221
33	800	0,3	1	2,00	10	220
34	900	0,1	4	2,00	10	220
35	900	0,2	3	1,50	10	218
36	900	0,3	2	3,00	10	217
37	700	0,1	1	1,50	12	224
38	700	0,2	2	2,00	12	223
39	700	0,4	4	3,00	12	220
40	800	0,2	1	3,00	12	222
41	800	0,3	4	1,50	12	221
42	800	0,4	3	2,00	12	218
43	900	0,1	3	3,00	12	222
44	900	0,2	4	2,50	12	220
45	900	0,4	2	1,50	12	215
46	1000	0,1	4	2,00	12	220
47	1000	0,3	2	3,00	12	215
48	1000	0,4	1	2,50	12	214

Table 3: Checking data

Experimental Number	Welding Current	Welding Time	Plunge	Lift	Stud Diameter	Hardness Value
1	300	0,4	4	3,00	6	223
2	400	0,2	1	3,00	6	227
3	500	0,2	4	2,50	6	225
4	600	0,2	3	1,50	6	223
5	500	0,1	1	1,50	8	227
6	600	0,3	4	1,50	8	223
7	700	0,3	1	2,00	8	222
8	800	0,3	2	3,00	8	220
9	600	0,3	3	2,50	10	223
10	700	0,3	4	1,50	10	221
11	800	0,4	2	1,50	10	218
12	900	0,4	1	2,50	10	215
13	700	0,3	3	2,50	12	222
14	800	0,1	2	2,50	12	224
15	900	0,3	1	2,00	12	217
16	1000	0,2	3	1,50	12	217

A. Performance Indicator

Determination coefficient (R^2) values were calculated to obtain prediction efficiency of the model. Determination coefficient (R^2) which is a number between 0 and +1 measures the degree of association between two variables [10]. Equation (3) are used for performance of models.

$$R^2 = 1 - \frac{\sum_{i=1}^n (O_i - P_i)^2}{\sum_{i=1}^n (O_i - O_{iave})^2} \quad (1)$$

In Equation (1), P_i , O_i and O_{iave} are the actual, predicted, and the average of the observed data, respectively.

IV. ANFIS MODELLING RESULTS

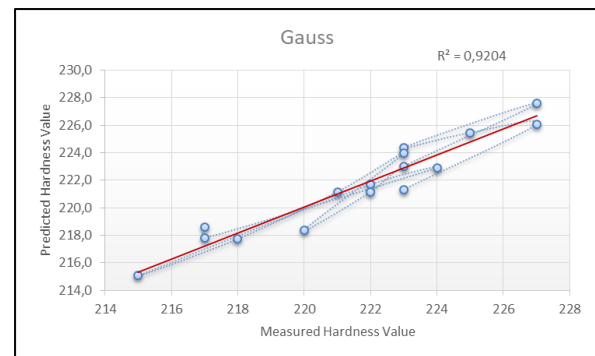
Although there are many different membership functions in the ANFIS toolbox; trimf, trapmf, gauss, and gbell are mostly used membership functions. In this study, it was seen that gauss and gbell membership functions give better results for the models. The number of membership functions was changed from 1-1-1-1-1 to 5-5-5-5-5 and many experiments were performed.

The best membership function types and ANFIS architecture obtained after trying all membership functions by trial and error method are presented in Table 4.

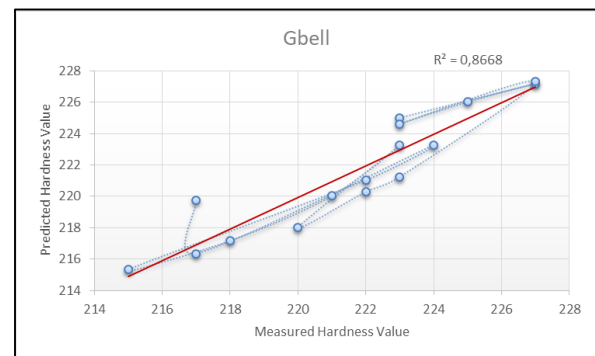
Table 4: ANFIS architecture of best two model

Number of Membership Functions (MF)	2 2 1 2 2	2 2 2 1 2
Membership function (MF) type	Gauss	Gbell
Number of nodes	58	58
Number of linear parameters	16	16
Number of non-linear parameters	18	18
Total number of parameters	34	34
Number of fuzzy rules	16	16

In order to estimate the performance of the models, the determination coefficients were calculated and the highest results were calculated as 0.92 and 0.87 respectively in the Gauss and Gbell membership function. The comparison of the estimation results and the experimental results of the models are given graphically for the best models in Figure 3.



a)



b)

Figure 3: Comparison of predicted hardness values and experimental hardness values a) Gauss model b) Gbell model

V. CONCLUSIONS

In this study, arc stud welding joints; 64 different experiments were performed by taking the stud diameter,

welding current, welding time, lift and plunge at different levels. Then, the data sets from experimental studies were used to develop adaptive network based fuzzy logic inference system (ANFIS) and this ANFIS models were created with MATLAB's toolbox. A lot of models were performed using different membership function types such as Trimf, Gaus and Gbell to create models. The accuracy of the models was evaluated according to the R^2 statistical data and the following results were obtained.

- The best model was obtained in the Gauss function type with the function number 2-2-1-2-2.
- Determination coefficient of the model with the best results is 0.7
- Determination coefficient of the model obtained with the trim function is not suitable because the R^2 value is below 0.7.
- The users of the arc stud welding can select the welding parameter set values that are suitable for the stud diameter, using the above models created with ANFIS to obtain a durable weld connection.

REFERENCES

- [1] Welding Handbook Committee. (2003). Ninth Edition. Welding Science and Technology. American Welding Society, Inc.
- [2] B. A. Behrens, D. Groß, & A. Jenicek, (2011). Stud welding within sheet metal working tools. *Production Engineering*, 5(3), 283-292.
- [3] J. Hildebrand, H. Soltanzadeh, A Review on Assessment of Fatigue Strength in Welded Studs. *International Journal of Steel Structures* June 2014. Vol 14. No 2. 421-438
- [4] A. A. Hamza, Investigation of the Effect of Parameters on Mechanical and Microstructural Properties of Arc Stud Welding. MSc thesis in Mechanical Engineering in Gaziantep University. 2014
- [5] N. F. Yilmaz, A. A. Hamza, Effect of Process Parameters on Mechanical and Microstructural Properties of Arc Stud Welds. *Materials Testing* 56 (2014) 10
- [6] H. Chandler, (1999). *Introduction to Hardness Testing*, 2nd Edition, United States: ASM International.
- [7] I. Samardzic, I. Kladaric, S. Klaric, 2009. The Influence of Welding Parameters on Weld Characteristics in Electric Arc Stud Welding. *Metalurgija* pp. 181-185
- [8] J.S.R. Jang, C.T. Sun, E. Mizutani, 1997. *Neuro-fuzzy and soft computing: a computational approach to learning and machine intelligence*. Prentice Hall, Inc.
- [9] J. Kim, N. Kasabov, 1999. ANFIS: Adaptive Neurofuzzy inference systems and their application to nonlinear dynamical systems. *Neural Networks*. pp. 1301-1319
- [10] K. P. Moustris, I. C. Ziomas, A. G. Paliatsos, 3-Day-Ahead Forecasting of Regional Pollution Index for the Pollutants NO_2 , CO, SO_2 , and O_3 Using Artificial Neural Network I Athens, Greece, *Water Air Soil Pollut* 2010, 209:29-43

Design and Dynamic Modelling of an Ankle-Foot Prosthesis for Transfemoral Amputees

S. AYDIN FANDAKLI¹, H. I. OKUMUS² and A. F. ERDEM³

¹ Karadeniz Technical University, Trabzon/Turkey, selinaydin@ktu.edu.tr

² Karadeniz Technical University, Trabzon/Turkey, okumus@ktu.edu.tr

³Gebze Technical University, Kocaeli, Turkey, ahmeterdem@gtu.edu.tr

Abstract - Today amputee people prefer low-cost and low-functioning passive prosthesis or costly active prosthesis with microcontroller. The aim of this study is the design and development of powered ankle-foot prosthesis that has low-cost, low-element, multi-functional for below-knee transfemoral amputees. For people who have lost their ankle and foot for various reasons, the system that carries out two controllable degrees of freedom, Dorsiflexion-Plantarflexion (DP) and Inversion-Eversion (IE) movements and can be controlled by EMG signals is proposed. Control using EMG signals will not be the subject of this paper, but will be touched upon that in future reports. A dynamic model of the main mechanism of the prosthesis has been established in order to be able to perform the system control.

Keywords - Ankle, Foot, Gait, Prosthesis, Amputee, Design

I. INTRODUCTION

AMPUTATION is a destructive operation that is cut off the limb that cannot be nourished, carries the disease and causes the loss of function. Factors such as trauma, infection, tumor and vascular diseases cause lower extremity amputations that reduce the vital activities such as walking, running, climbing stairs [1]. Studies have been accelerated to increase the functionality and aesthetics of lower extremity prostheses for the last two decades. The purpose of prosthetic studies is to create a device that will not feel the lack of the missing limb. Since the Second World War, work has been done to reuse artificial organs of limbs that have suffered body damage [2]. Until the 80s, passive prostheses including components such as spring was designed that cause asymmetry for amputee and require more energy than solid leg. Because of these problems experienced in passive prostheses, researchers have emphasized active prosthesis design studies [3].

According to a survey of lower extremity amputations, more than one million amputations occur annually in the world, and the most common is below knee amputation [4]. In the United States, more than 150,000 lower extremity amputations are performed each year [5].

Klute et al designed an active ankle-foot prosthesis driven by pneumatic McKibben actuators in 1998 [6]. Frank et. al

developed knee and ankle driven by double-action pneumatic actuators with power supply, which have two degrees of freedom action [7,8]. Rino and others designed a pneumatic actuated powered below knee prosthesis called the Pleated Pneumatic Artificial Muscle that can generate high torque and maintain the user's power during level-walking. This below knee prosthesis can perform two degrees of freedom dorsiflexion-plantar flexion and inversion-eversion movements and ensures that the ankle has sufficient range of motion. This prosthesis allows the ankle to have sufficient range of motion [9].

The use of pneumatic actuators is reduced due to control difficulties caused by increased size and noise of the prosthesis. At Arizona State University, a foot prosthesis called SPARKy 1 project, with a degree of freedom, actuated by a Series Elastic Actuator including powerful brushless DC motor and a ballscrew, was designed [10]. In the SPARKy 3 project, a second motor was added to the prototype to perform both dorsiflexion-plantarflexion and inversion-eversion movements [11]. The SPARKy 1 and SPARKy 3 projects are shown in Figure 1.

Herr et. al designed a powered ankle prosthesis with one-way spring parallel to the ankle in addition to the Series Elastic Actuator using the myoelectric inputs measured from the remaining muscles of the amputee. The parallel spring regulates both the impedance and the power output during dorsiflexion in the stance phase, increasing the peak force. In this study, a myoelectric-focused end-state controller was developed [12] as shown in Figure 2.

Zhu et al. [13] designed the ankle joint prosthesis with two Series Elastic Actuators, called as PANTOE 1, which controls the ankle joint and toe joint, including angle and force sensors. The sensor system allows the user to move more naturally and steadily following the position and moment of the joints in real time as given in Figure 3.

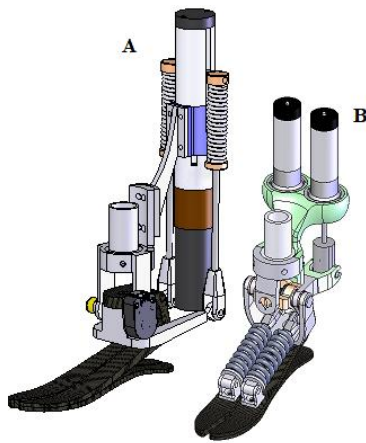


Fig 1. SPARKy project. In (A), the first design of the robotic ankle prosthesis of SPARKy project. In (B), SPARKy 3 with two degrees of freedom

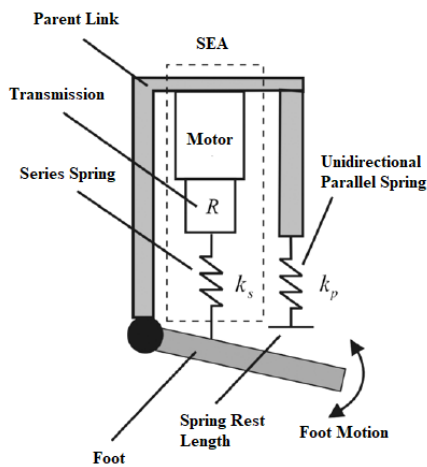


Fig 2. A schematic of the powered ankle-foot prosthesis.

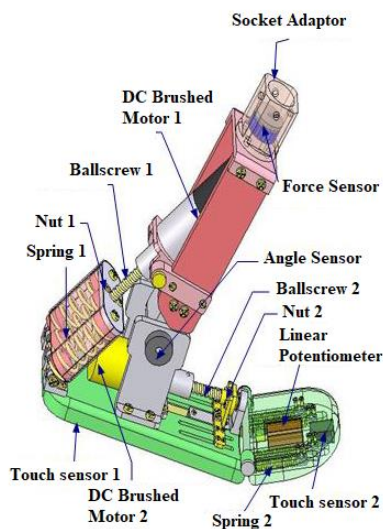


Fig3. The CAD model of PANTOE 1.

Brian and his colleagues proposed a finite-state controller for a transfemoral prosthesis that allows stairs to ascend and descend. This prosthesis, consisting of the load sensor, angle

sensor and inertia measurement unit, is actuated by two brushless DC motors [14].

Ficanha et. al have developed a two degrees of freedom mechanism that can perform dorsiflexion-plantarflexion and inversion-eversion movements. This cable-driven mechanism, which can follow trajectories like human ankle, is made up of two dc motors that make dorsiflexion-plantarflexion movements in the opposite direction, make inversion-eversion movements in the same direction [15].

Collins and Kuo developed a microprocessor-controlled artificial foot that stores the energy after the heel strike and release the energy at the end of the stance phase to minimize the metabolic energy expenditure. In addition, an ankle emulator was developed by Collins et al., who activated the ankle joint via Bowden cables in the DP and IE directions [16,17].

The aim of this study is to develop an ankle-foot prosthesis that can perform 2 degrees of freedom Dorsiflexion-Plantarflexion and Inversion-Eversion movements and controlled by EMG signals for people who are amputated under various circumstances. The first step in developing a 2-degrees-of-freedom prosthetic foot is to create a dynamic model for simulation and control design. The prosthesis to be developed will consist of commercial foot, actuators, controller, sensors, connectors and power unit. In addition to being compatible with human anatomy, it should have adequate degrees of freedom and range of motion. Actuators that provide the necessary force and moment for the movements to take place at the desired speed should be as small and light as possible. The control methods used in prosthesis application differ according to the input signals obtained from the prosthesis and the user. Force, pressure and EMG sensors, accelerometers, encoders etc. measurement devices provides the necessary input signals for the controller. Today, there are active actuators such as electrical, pneumatic and hydraulic actuators and passive actuators such as springs and dampers. The power unit must be used to provide power for the actuators and other electronic equipment. In this study, mechanical design was realized with Solidworks software.

II. THE CHARACTERISTICS OF THE ANKLE JOINT AND GAIT ANALYSIS

In order to determine how skeletal and muscular systems work under different conditions in humans, the biomechanics must first be examined. In order for a person to move, it is necessary to synchronize the skeletal and muscular system. All the bones that make up the skeleton are attached to the muscles. When the muscles contract, they pull the bones and allow them to move. Gait analysis is the first criterion in prosthetic foot design that allows a healthy individual to mimic foot movements. Kinematic data such as movement length of joints and kinetic data such as power and moment can be determined by gait analysis [18]. The cameras for kinematic measurements and force platforms for kinetic measurements are preferred today while direct measuring devices such as

potentiometers and electro goniometers have been used in the past [19,20].

Our body is divided into three planes: The sagittal plane divides the body into right and left, the frontal plane divides the body into front and rear and the transverse plane divides into the body down and up. The foot performs plantarflexion - dorsiflexion movements in the sagittal plane, inversion-eversion movements in the frontal plane, and abduction-adduction movements in the transverse plane. The foot and ankle is a complicated platform that allows the body to contact the ground and carries loads well above body weight. The ankle is the joint that provides the connection between the leg and foot by sending body weight to the foot and is responsible for the performance of the DP movements [22].

Gait is a reflexive cycle that is inherent in man. According to the gait parameters, the time of the foot is on the ground is called the stance phase (%60) and the time when the foot leaves the ground is called the swing phase (%40) [23,24].

III. MECHANICAL DESIGN

The mechanical design of the prosthetic foot is designed in the Solidworks program as shown in Figure 4 and 2 degree of freedom movement is provided.

The elements used in the designed mechanism are 1) body, 2) motor connection element, 3) L16-P linear motor, 4) Roadflexion foot connection element, 5) universal joint (1/2") and 6) universal joint (1/4"), respectively. The prototype of the designed prosthetic foot is given in Figure 5. In design, attention has been paid to the use of lightweight, low-cost and less element.

Roadflexion foot was used in our work. The roadflexion foot shown in the figure 6 consists of 3 main parts. The lower part 1 defines the calcaneus and forefoot, the rear part 2 defines the heel and acts as a damper. The upper part 3 defines the upper part of the foot and functions as an anterior tibialis muscle [25].

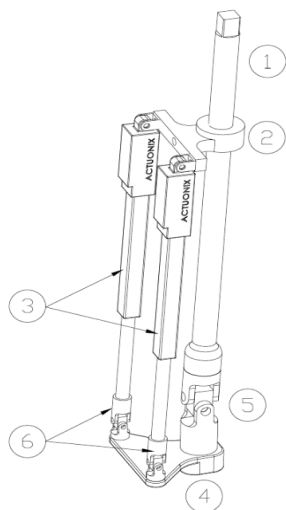


Fig 4. CAD model of ankle-foot prosthesis drive mechanism

As a motor, two linear motors are selected which can perform the DP movement when they move in the same direction and the IE movement when they move in opposite directions. The reason for not choosing cable-driven mechanism is to get rid of the cable losses and friction. The range of motion provided by the cable system was realized with universal joints.

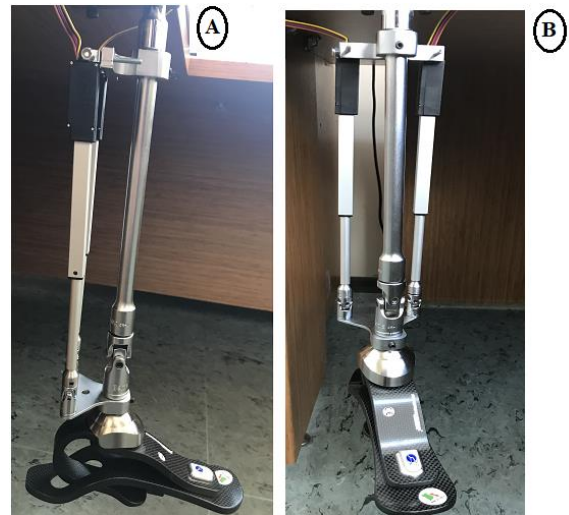


Fig 5. The prototype of two DOF ankle-foot mechanism A) side view B)front view.

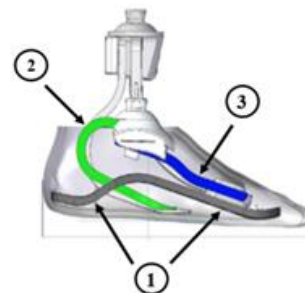


Fig 6. The parts of Roadflexion foot

With the development of technology in our constantly evolving and changing world, the need for equipment that moves rotational or linear motion in industrial devices is increasing steadily. Linear motion has become a field of choice for researchers increasingly diversified and practiced day by day due to their high reliability, high sensitivity in high-speed motion, and their ability to perform a job with minimum and simplest elements. Linear movements can be obtained by adding supplemental devices such as gear, belt-pulley system, worm screw etc. to the shaft of the electric motors producing rotational motion or by using pump, filter, valve, piston in hydraulic and pneumatic systems. The need for linear motors that can produce linear motion directly, do not require auxiliary elements and have less energy loss because of the fact that the linear motion acquisition method from the rotational motion generating devices requires too much maintenance, increases friction losses, weight, complexity and causes more failure [26].

A. Dynamic Model of Linear Motor

In a system, it is necessary to control this system in order to receive the signals instantly without disturbing the user and process them quickly and transfer them to the actuators. The dynamic model of the system must be determined in order to control [27]. Equivalent circuit of DC linear motor is given in Figure 7. There,

M_t : the total mass of the moving unit,

$\frac{dv(t)}{dt}$: acceleration,

$v(t)$: time dependent velocity,

F_e : electrically generated force,

$F_t + F_d$: forces generated in the opposite direction of movement,

e_b : the induced opposite electromotive force,

$R_b + R_f$: the armature resistance,

R_b : the resistance of the coil windings, and

L_b : the armature winding inductance.

Using the Newton and Kirchhoff laws, the differential equation of the moving part of the linear motor is given in Equation 1,2.

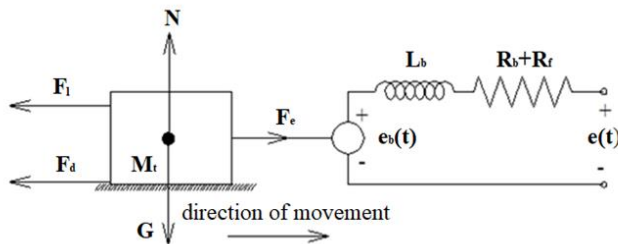


Fig 7. Equivalent circuit of DC linear motor

$$\frac{dv(t)}{dt} = \frac{K i_a(t)}{M_t} - \frac{\alpha v(t)}{M_t} - \frac{F_l}{M_t} \tag{1}$$

$$e(t) = R_a i_a(t) + L_b \frac{di_a(t)}{dt} + e_b(t) \tag{2}$$

The equation of state of the DC linear motor is given in Equation 3,4. There are two state variables, the motor speed ($v(t)$) and the armature current ($i_a(t)$).

$$\begin{bmatrix} \frac{dv(t)}{dt} \\ \frac{di_a(t)}{dt} \end{bmatrix} = \begin{bmatrix} -\frac{\alpha}{M_t} & \frac{K}{M_t} \\ -\frac{K}{L_b} & \frac{R_a}{L_b} \end{bmatrix} \begin{bmatrix} v(t) \\ i_a(t) \end{bmatrix} + \begin{bmatrix} 0 \\ \frac{1}{L_b} \end{bmatrix} e(t) + \begin{bmatrix} -\frac{1}{M_t} \\ 0 \end{bmatrix} F_l \tag{3}$$

$$v(t) = \begin{bmatrix} 1 & 0 \\ 0 & 1 \end{bmatrix} \begin{bmatrix} v(t) \\ i_a(t) \end{bmatrix} \tag{4}$$

The block diagram obtained from the transfer function of the motor is as given in Figure 8, 9.

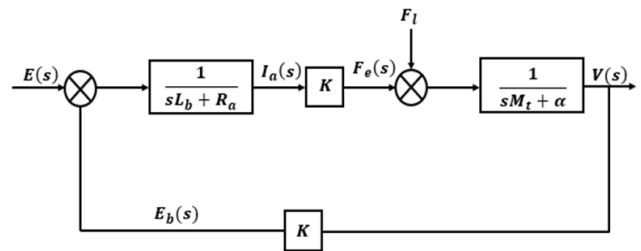


Fig 8. The block diagram of the DC Linear motor

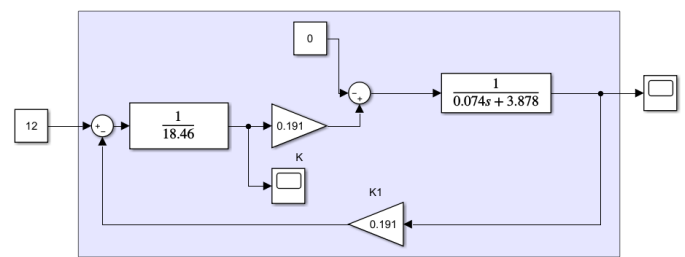


Fig. 9.The block diagram of simplified linear model of motor

Figures 10 and 11 show the speed response and motor current for the 12V input voltage, respectively. The results obtained match the values given in the motor datasheet.

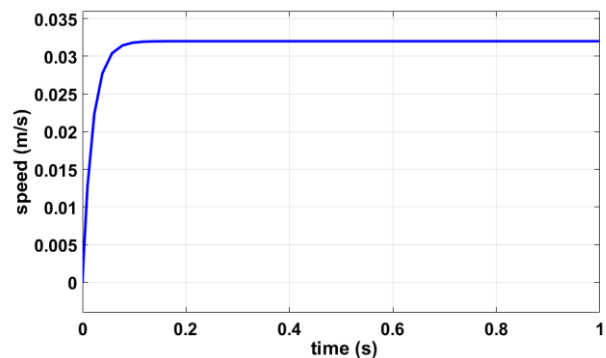


Fig 10. The velocity response of the DC Linear Motor (e(t)=12V)

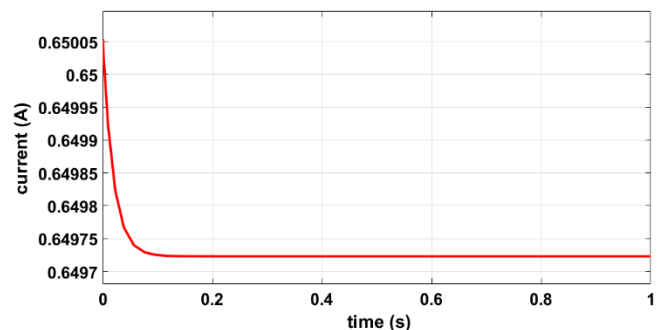


Fig 11. Time dependent change of motor current (e(t)=12V)

Table 1 gives the parameters of L16-P linear motor.

Table 1: L16P Specifications

Gearing Option	35:1
Stroke Option	100 mm
Mass	74g
Peak Power Point	50N @ 16 mm/s
Max speed (No load)	32 mm/s
Max Force	50N
Stall Current	650 mA @12V
Example column 1	Example column 2
Example text 1	Example text 2

The block diagram of the system with PID controller and the system output when the step response is applied to the system is given in Figure 12, 13, respectively.

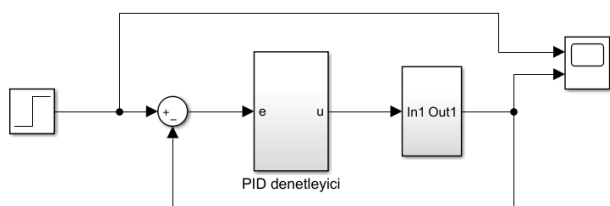


Fig 12. Block diagram of linear motor with PID controller

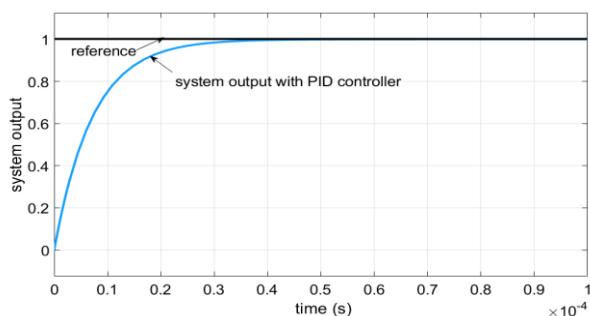


Fig. 13. PID for step response

When the step reference is applied to input for the uncontrolled system, system output is set to 2.66×10^{-3} . That shows the system needs a controller. PID is used as a controller in the system. When the step response is applied to the system, we assumed that the overlap is not available in the system output, the settling time is 2.8×10^{-5} seconds for PID. In this study the aim is to follow the reference as soon as possible, without overlap and without steady-state error.

IV. CONCLUSION

The two-degree-of-freedom DP and IE movement system was designed and prototyped. The block diagram of the system was created in MATLAB / Simulink and the speed response and motor current were investigated. Simulation results match the motor parameters. Our next aim is to control the system by adding a controller to the system first, then to change the input

signal, to use EMG signals received from the user as input signals.

ACKNOWLEDGMENT

The first author of the work was supported by the Scientific and Technological Research Council of Turkey (TÜBİTAK).

REFERENCES

- [1] R. Hoile, "Amputation: Surgical Practice and Patient Management," *British Medical Journal*, vol. 312, pp. 984-985, 1996.
- [2] Alderson, S., *The electric arm*, McGrawHill, NewYork, 1954.
- [3] G.R.Colborne, S. Naumann, P. E. Longmuir and D. Berbrayer, "Analysis of mechanical and metabolic factors in the gait of congenital below knee amputees: A comparison of the SACH and Seattle feet", *American Journal of Physical Medicine&Rehabilitation*,71(5), 272-278, 1992.
- [4] Eilenberg, M., Hartmut, G., and Hugh, H.: 'Control of a powered anklefoot prosthesis based on a neuromuscular model', *Trans. Neural Syst. Rehabil. Eng.*, 2010, 18, pp. 164–173.
- [5] Owings M, Kozak LJ, National Center for Health S. *Ambulatory and Inpatient Procedures in the United States, 1996*. Hyattsville, Md.: U.S. Dept. of Health and Human Services, Centers for Disease Control and Prevention, National Center for Health Statistics; 1998.
- [6] Klute, G.K., Czerniecki, J., Hannaford, B., "Development of Powered Prosthetic Lower Limb," *Proceedings of the First National Meeting, Veterans Affairs Rehabilitation Research and Development Service*, 1998.
- [7] F. Sup, A. Bohara, and M. Goldfarb, "Design and control of a powered knee and ankle prosthesis," *2007 IEEE International Conference on Robotics and Automation*, pp. 4134-4139, 2007.
- [8] F. Sup, A. Bohara, and M. Goldfarb, "Design and control of a powered transfemoral prosthesis," *The International Journal of Robotics Research*, 27(2), 263-273, 2008.
- [9] R. Versluis, A. Desomer, G. Lenaerts, M. Van Damme, and P. Beyl, "A pneumatically powered below-knee prosthesis: Design specifications and first experiments with an amputee," *2nd IEEE International Conference on Biomedical Robotics and Biomechanics*, pp. 372-377, 2008.
- [10] J. K. Hitt, T. G. Sugar, M. Holgate, and R. Bellman, "An active foot ankle prosthesis with biomechanical energy regeneration," *Journal of medical devices*, vol. 4, p. 011003, 2010.
- [11] R. D. Bellman, M. A. Holgate, and T. G. Sugar, "SPARKy 3: Design of an active robotic ankle prosthesis with two actuated degrees of freedom using regenerative kinetics," in *2008 2nd IEEE RAS & EMBS International Conference on Biomedical Robotics and Biomechanics*, 2008, pp. 511-516.
- [12] S. K. Au, J. Weber, and H. Herr, "Powered Ankle-Foot Prosthesis Improves Walking Metabolic Economy," *IEEE Transactions on Robotics*, vol. 25, pp. 51-66, 2009.
- [13] J. Zhu, Q. Wang, and L. Wang, "PANTOE 1: Biomechanical design of powered ankle-foot prosthesis with compliant joints and segmented foot," in *2010 IEEE/ASME International Conference on Advanced Intelligent Mechatronics*, 2010, pp. 31-36.
- [14] B. Lawson, H.A. Varol, A. Huff, E. Erdemir, and M. Goldfarb, "Control of stair ascent and descent with a powered transfemoral prosthesis," *IEEE Transactions on Neural Systems and Rehabilitation Engineering*, 21(3), 466-473, 2013.
- [15] E. M. Ficanha, M. Rastgaar, and K. R. Kaufman, "A two-axis cable driven ankle-foot mechanism," *Robotics and Biomimetics*, vol. 1, p. 1,2014.
- [16] S. H. Collins and A. D. Kuo, "Recycling energy to restore impaired ankle function during human walking," *PLoS One*, vol. 5, no. 2, 2010.
- [17] Collins, S. H., Kim, M., Chen, T., and Chen, T., 2015. "An ankle-foot prosthesis emulator with control of plantarflexion and inversion-eversion torque". In *IEEE International Conference on Robotics and Automation (ICRA)*, pp. 1210–1216.

- [18] Pfister, A., West, A. M., Bronner, S. and Noah J.A., Comparative abilities of Microsoft Kinect and Vicon 3D motion capture for gait analysis, *Journal of Medical Engineering and Technology*, Volume 38, 2014, Issue 5.
- [19] Blanc, Y., Vadi, P., An inexpensive but durable foot-switch for telemetered locomotion studies. *Biotelemetry and Patient Monitoring*, 8:240-245. 1981.
- [20] Chao, E.Y., Justification of triaxial goniometer for the measurement of joint rotation. *J Biomechanics*, a3:989-1006, 1980.
- [21] Sammarco, G. J., Hockenbury, R. T. (2001). Biomechanics of the Foot and Ankle. M. Nordin, V. H. Frankel (Ed.). *Basic Biomechanics of the Musculoskeletal System* (3 bs., c. 9, s. 222-225). USA: Lippincott Williams & Wilkins.
- [22] Wernick J., Volpe, G. R. (1996). Lower Extremity Function and Normal Mechanics. R. L. Valmassy (Ed.). *Clinical Biomechanics of the Lower Extremities* (1 bs., c. 1, s. 1-57). St. Louis: Mosby.
- [23] Perry, J. (1992). *Gait Analysis Normal and Pathological Function* (c. 4, s. 51-87). USA: SLACK.
- [24] Stauffer, R. N., Chao, E. Y., Brewster, R. C. (1977). Force and motion analysis of the normal, diseased, and prosthetic ankle joint. *Clinical orthopaedics and related research*, 127, 189-196.
- [25] <http://www.roadrunnerfoot.com/eng/prodotti/roadflexion.html>
- [26] Green, C.W. and Paul, R. J. (1969). Application of DC linear machines as short-stroke and static actuators. *Proceeding. IEEE*, 116(4), 597-604.
- [27] M. T. Tuncay, Sabit Mıknatıslı DC Lineer Motor Tasarımı ve Denetimi, Doktora Tezi, Gazi Üniversitesi, Fen Bilimleri Enstitüsü, 2016, Ankara.

Measurement of Wall Thickness of Extruded Pvc Profiles Using Image Processing Methods

M. AKDOĞAN¹ and S. YALDIZ²

¹Adil Karaagac Vocational and Technical Anatolian High School, Konya/Turkey, akdoganmurat@hotmail.com

²Selcuk University Technology Faculty, Mech. Eng. Department, Konya/Turkey, syaldiz@selcuk.edu.tr

Abstract— Today, machine vision systems are widely used in the mass production. The present work focuses on measurement of wall thickness of extruded pvc profiles through image processing technique. For this, a experimental setup has been prepared to hold digital camera in a fixed plane to capture the images of pvc profiles which help to get more accurate wall thickness results using image processing. This work has been done for measurement of up, down, left and right wall thickness of pvc profiles. The images are captured by using high resolution digital camera which are fixed in the experimental setup. OpenCV programming function was utilized in Python scripting language to perform image processing. So the high resolution captured images of profile are processed a sequential operations which are correcting defective images caused by working environment. And then developed image processing algorithms are applied to measurement of profile wall thickness. The acquiring results are compared with the results obtained by conventional systems. Dimension Control System decrease the non-standard profiles production and minimize the unnecessary consumption of raw materials.

Keywords— *Image Processing, Quality Control, Measurement.*

I. INTRODUCTION

Extruded profile part's wall thickness direct impact on profile quality so need a sampling inspection to determine its thickness between tolerances or not. It is generally used Vernier callipers measurement for profile wall thickness. Main shortcomings come out from contact measurement due to fact that worker, lack precision or not good calibrated measurement device. This paper introduces a kind of extruded profile thickness detection method based on image processing, and the result shows that it can well solve the wall thickness dimensions. To obtain images used high resolution image sensor (CCD). Profile boundaries fundamental importance in image processing so edge detection significantly reduces the amount of data and filters out useless information. Edge detection is in the forefront of image processing for object detection. In this paper firstly getting image from CCD and then some noise remove operations performed. Afterwards image thresholding applied to achieve interested image area. And then, segmentation of image algorithm, contours finding algorithm used. Lastly, improved algorithm used finished image and measured thickness of extruded profiles.

II. EXPERIMENTAL SETUP

In the experimental setup camera (Elp-Usb 8MP 5-50 mm varifocal lens, Sony IMX179 sensor) are placed at the end of the conveyor, in such a position takes a cross-section image of profile just some seconds before their cutting. An illuminator (30W 5600/3200K Dimmable 396 Led video light lamp) lights up the profile sections in order to increase image contrast. It can ensure image clearer and brighter in case of dark condition. For calibration used known references of profile's horizontal and vertical outer dimensions. Figure1. shows experimental setup.

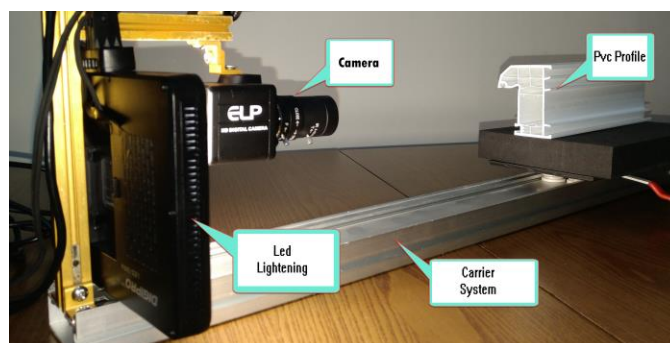


Figure 1: Experimental Setup

III. MEASUREMENT STEPS

The method includes three steps.

- Acquiring extruded profile image and pre-process.
- Extract the contour regions of profile.
- Using contours of profile measuring profile wall thickness via improved algorithm.

A. Acquiring extruded profile and pre-process

To find out useful information and data, this study getting image. Then, using some filters extract the noise removed images. This process is very important section before contour extracting step. Because, if wrong selected contour count of profile, next step is not success. In this step another important thing is lightening. Lightening is vital importance of well acquiring images.

1) *Image Thresholding*: Thresholding is the simplest method of image segmentation. From a grayscale image. Thresholding can be used to create binary images [1]. Figure 2. shows a thresholding view of profile image. For this operation used equation is shown (1).

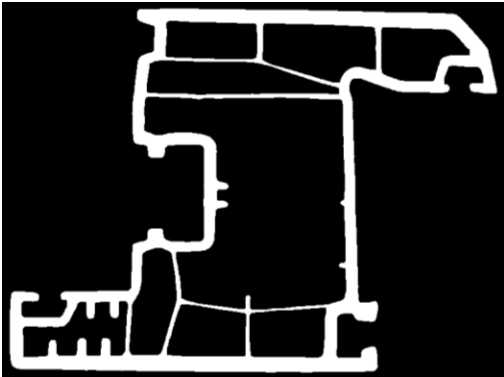


Figure 2: Threshed image of profile.

$$G_{x,y} = \begin{cases} 1, & f(x, y) \geq T(x, y) \\ 0, & f(x, y) < T(x, y) \end{cases} \quad (1)$$

2) *Median Filtering*: In image processing most suitable filter must be selected among the many filter [2]. Median filter is used some kind of noise reduction on an image. Median filtering is very widely used in digital image processing because, under certain conditions, it preserves edges while removing noise. Figure 3. (a) shows a not filtered view of profile image and Figure 3. (b) shows median filtered view of profile image.



(a) Not filtered image (b) Median filtered image

Figure 3: Median Filtering

3) *Gaussian Filtering*: Gaussian filtering is used to blur images and remove noise but in our image not good result so not used in our system. For this operation used equation is shown (2). Figure 4. shows a gaussian filtered view of profile image after thresholding.



Figure 4: Gaussian Filtering

$$G_{x,y} = \frac{1}{2\pi\sigma^2} \cdot \ell \frac{-(x^2+y^2)}{2\sigma^2} \quad (2)$$

4) *Edge Detection*: Edge detection is an image processing technique for finding the boundaries of objects within images. It works by detecting discontinuities in brightness. Edge detection is used for image segmentation and data extraction in areas. Canny edge detection algorithm is used in this study. For this operation used equation is shown (3) and (4). Figure 5. shows a Canny edge detection profile image after thresholding.

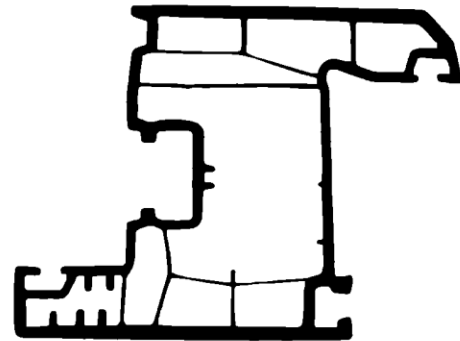


Figure 5: Canny edge detection image

$$G_x = \begin{bmatrix} -1 & 0 & 1 \\ -2 & 0 & 2 \\ -1 & 0 & 1 \end{bmatrix} G_y = \begin{bmatrix} -1 & -2 & -1 \\ 0 & 0 & 0 \\ 1 & 2 & 1 \end{bmatrix} \quad (3)$$

$$G = \sqrt{G_x^2 + G_y^2} \theta = \arctan\left(\frac{G_y}{G_x}\right) \quad (4)$$

B. Contour detection procedure via Suzuki Algorithm

The well-known edge-based segmentation algorithm proposed by Canny [3]. First a Gaussian low pass filtering is carried out. The algorithm then searches for those points (at the edges) where the gradient of the grey level is maximum, since these are expected to correspond to the contour points that are of interest. A binary image that contains the object of interest. Figure 6. shows real image of product.

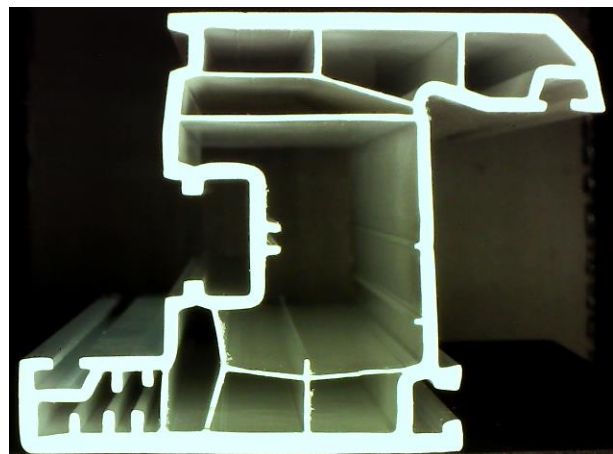


Figure 6: Real Image of Product

OpenCV uses the Suzuki algorithm to perform contour tracing [4]. In this algorithm, firstly the upper left contour pixel is found. Then, the neighborhood of the first pixel is checked in clockwise direction to find the next pixel of the contour. From now on, the search for the other pixels of the contour is done in anti-clockwise direction and ends when the first two pixels of the contour are found again. Polygonal representation performed and all contours described by a tree. This generates a collection of external contours.

OpenCV command; cv2.drawContours (image, contours, x, (0,0,255),2). x is contour number. Figure 7. shows image contours.

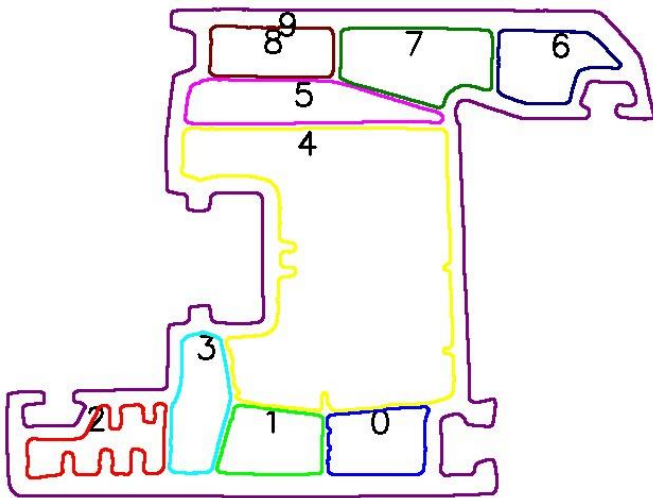


Figure 7: Image Contours

Figure 8. shows image based measurement result of test sample number 11.

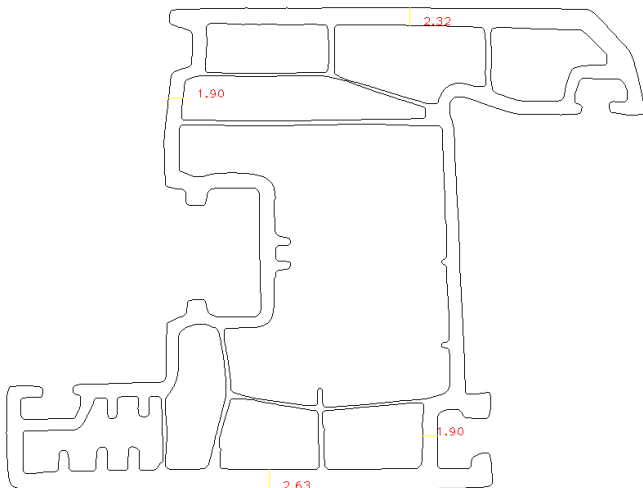


Figure 8: Measured image via image processing

Table 1. shows image based measurement result of test samples.

Table 2. shows error percentage between image based result and standard values.

Table 1: Wall Thickness Measurements via Image Processing

	Wall Thickness			
	Top	Bottom	Right	Left
Profile Samples	Std:2,50	Std:2,50	Std:2,00	Std:2,00
	Min:2,50	Min:2,50	Min:2,00	Min:2,00
	Max:----	Max:----	Max:----	Max:----
1	2,21	2,52	1,79	1,89
2	2,35	2,65	1,96	1,86
3	2,31	2,83	1,89	1,89
4	2,21	2,52	1,79	1,89
5	2,35	2,74	1,86	1,96
6	2,30	2,69	1,92	2,01
7	2,30	2,69	2,01	2,01
8	2,36	2,75	2,06	1,96
9	2,33	2,75	1,90	2,01
10	2,32	2,75	1,90	2,01
11	2,32	2,63	1,90	1,90
12	2,22	2,86	2,01	2,12

Table 2: Image Based Measurements - Standard Dimensions %Error

	Wall Thickness			
	Top	Bottom	Right	Left
Profile Samples	Std:2,50	Std:2,50	Std:2,00	Std:2,00
	Min:2,50	Min:2,50	Min:2,00	Min:2,00
	Max:----	Max:----	Max:----	Max:----
1	13,12	0,79	11,73	5,82
2	6,38	5,66	2,04	7,53
3	8,23	11,66	5,82	5,82
4	13,12	0,79	11,73	5,82
5	6,38	8,76	7,53	2,04
6	8,70	7,06	4,17	0,50
7	8,70	7,06	0,50	0,50
8	5,93	9,09	2,91	2,04
9	7,30	9,09	0,50	5,26
10	7,76	9,09	5,26	0,50
11	7,76	4,94	5,26	5,26
12	12,61	12,59	0,50	5,66

Figure 9. shows top wall thickness image based measurement error percentage.

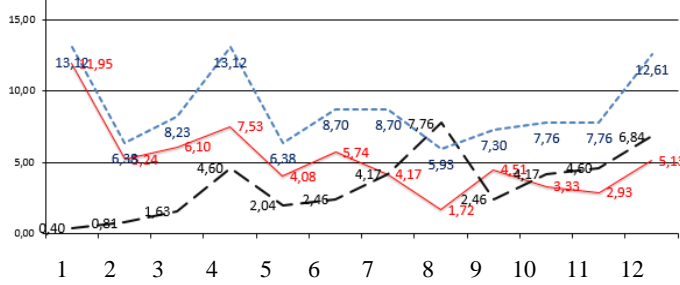


Figure 9: Top wall thickness

Figure 10. shows bottom wall thickness image based measurement error percentage.

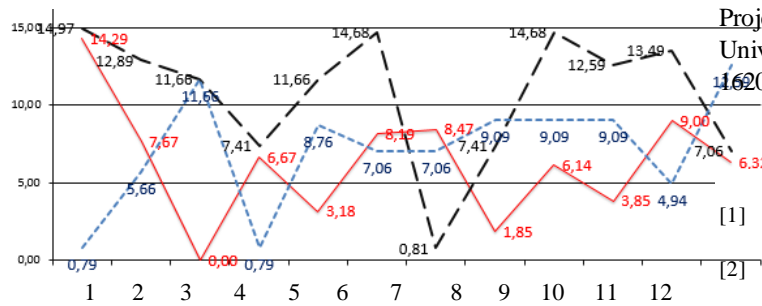


Figure 10: Bottom wall thickness

Figure 11. shows right wall thickness image based measurement error percentage.

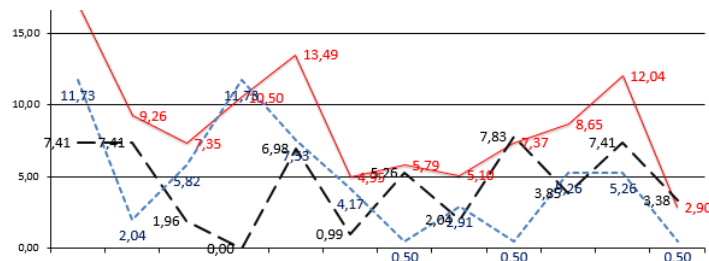


Figure 11: Right wall thickness

Figure 12. shows left wall thickness image based measurement error percentage.

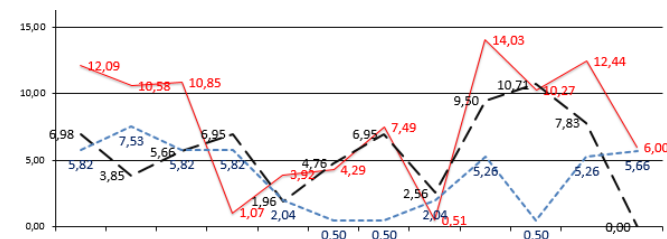


Figure 12: Left wall thickness

III. CONCLUSIONS

This study presents a extruded products wall thickness measurement method using image processing technics. The proposed method can measure wall thickness with a high accuracy. The experimental results show that the proposed measurement method is useful for wall thickness measurement of pvc profiles. The experimental results show the algorithm is fast and requires minimum user interaction. This work is easily applicable for the companies that produce extrusion pvc products. Future research focuses are concentrated on improve the more robust algorithm for profile which is different geometric shapes.

ACKNOWLEDGMENT

We are grateful to the Selcuk University Scientific Research Projects Coordinator. This work was supported by Selcuk University Scientific Research Projects Coordination Unit with 16201037 Doctora Thesis Project.

REFERENCES

- [1] Shapiro, Linda G. & Stockman, George C. (2002). "Computer Vision". Prentice Hall. ISBN 0-13-030796-3
- [2] Demigny D., On Optimal Linear Filtering for Edge Detection, IEEE Transactions On Image Processing, 2002, 11, 728-737
- [3] J.F. Canny, A computational approach to edge detection, IEEE Transactions on Pattern Analysis and Machine Intelligence PAMI-8 (6) (1986) 679-698.
- [4] Suzuki, S. and Abe, K., Topological Structural Analysis of Digitized Binary Images by Border Following. CVGIP 30 1, pp 32-46 (1985)
- [5] C. Liguori. A. Paolillo. A. Pietrosanto. "An on-line stereovision system for dimensional measurement of rubber extrusions". Measurement 35 (2004) 221-231

Numerical Investigation and Modelling of Confined Turbulent Recirculating Flows

T. KARASU¹

¹ Eskişehir Osmangazi University, Meşelik, 26480 Eskişehir/Turkey, tahirkarasu26@gmail.com

Abstract - This original paper presents the results of an extensive study of numerical investigation and modelling of steady, incompressible, and axisymmetric confined turbulent recirculating flows in circular-sectioned sudden expansion pipes at three different Reynolds numbers. Employing the finite-volume method with a hybrid scheme, a computer program based on the SIMPLE (Semi-Implicit Method for Pressure Linked Equations) algorithm has been developed. Numerical solution of the conservation equations of mass and momentum, together with the standard k-ε turbulence model, are obtained using an iterative numerical solution technique. Near the solid boundaries, wall-functions are employed. Numerical computations for radial profiles of axial velocity, turbulence kinetic energy, turbulence kinetic energy dissipation rate, effective viscosity, axial variation of center-line velocity, locus of flow reversal, wall static-pressure coefficient, wall-shear stress and friction coefficient distributions along top wall of the axisymmetric sudden expansion pipe flow geometry are presented and compared with experimental measurements. The results of numerical investigation show generally very good agreement with experimental data.

Keywords - Recirculating Flows, Turbulence, Computations.

I. INTRODUCTION

THE separated confined turbulent flow field downstream of an axisymmetric sudden expansion in a circular-sectioned pipe is a complex phenomenon characterized by flow separation, recirculation and reattachment. As illustrated in Figure 1, such a flow field may be divided by a dividing shear-layer surface into two main regions, one being the region of recirculating flow, the other being the region of main flow. The point at which the dividing shear-layer surface strikes the wall is called the reattachment point. In the recirculation region, the high adverse pressure gradient results in reverse flow and promotes instability and turbulence. Eddies generated in the recirculation region and in the vicinity of the reattachment point can be considered as a highly concentrated source of turbulence. The subsequent convection, diffusion, and decay of the turbulent eddies have a dominant influence on the characteristics of mean flow. Confined turbulent flow through an axisymmetric sudden expansion in a pipe is relevant to a large number of important engineering applications, such as hydraulic and fluidic devices, heat exchangers, combustors, mixing equipment and air conditioning ducts. Considerable experimental and theoretical works on confined turbulent flow through circular-sectioned

sudden expansions and pipes have been reported in the literature. Among the most interesting ones are the works of [1-43]. In the present numerical investigation, the experimental measurements of [3,10,15] have been used for comparison with the numerical computations. The main objective of this original investigation is to obtain numerical predictions for steady, incompressible, complex confined turbulent recirculating flow through circular-sectioned sudden expansion pipes using the standard k-ε turbulence model [44] with a wall-functions boundary condition, and to compare the results of numerical computations with available experimental measurements in the literature for validation.

II. MATHEMATICAL AND PHYSICAL MODEL

A. Governing Equations and Turbulence Model

With reference to Figure 1, the mathematical and physical model employed in the numerical investigation of steady, incompressible, complex confined turbulent recirculating flow through circular-sectioned sudden expansion pipes, requires the simultaneous solution of the governing equations, together with the turbulence model equations. The transport equations representing the conservation of mass, momentum, turbulence kinetic energy and its dissipation rate in steady state axisymmetric cylindrical coordinate system are cast into the following general form:

$$\frac{\partial}{\partial x}(\rho u \phi) + \frac{1}{r} \frac{\partial}{\partial r}(\rho r v \phi) - \frac{\partial}{\partial x} \left(\Gamma_{\phi} \frac{\partial \phi}{\partial x} \right) - \frac{1}{r} \frac{\partial}{\partial r} \left(r \Gamma_{\phi} \frac{\partial \phi}{\partial r} \right) = S_{\phi} \quad (1)$$

This equation represents a transport equation for a general variable ϕ . The variables u and v are the local time-averaged velocity components in the axial (x) and radial (r) directions, respectively, ρ is the fluid density and Γ_{ϕ} is the transport coefficient. The final term, S_{ϕ} , is the source term. The variables, ϕ , necessary in this numerical investigation are u , v , k and ϵ . Here, k and ϵ stand for the kinetic energy of turbulence and its dissipation rate, respectively. The turbulence model employed in the present study is the k-ε model of [44]. If ϕ is set equal to unity and Γ_{ϕ} and S_{ϕ} to zero, equation (1) reduces to the equation of continuity. Pressure is derived from the pressure correction equation [45,46]. The transport equations, coefficients and the source terms are summarised in Table 1.

Table 1: Transport equations, coefficients and source terms.

ϕ	Γ_ϕ	S_ϕ
1	0	0
u	$\mu_e = \mu + \mu_t$	$-\frac{\partial P}{\partial x} + \frac{\partial}{\partial x} \left(\mu_e \frac{\partial u}{\partial x} \right) + \frac{1}{r} \frac{\partial}{\partial r} \left(r \mu_e \frac{\partial v}{\partial r} \right)$
v	μ_e	$-\frac{\partial P}{\partial r} + \frac{\partial}{\partial x} \left(\mu_e \frac{\partial u}{\partial r} \right) + \frac{1}{r} \frac{\partial}{\partial r} \left(r \mu_e \frac{\partial v}{\partial r} \right) - 2 \mu_e \frac{v}{r^2}$
k	$\frac{\mu_e}{\sigma_k}$	$G - \rho \varepsilon$
ε	$\frac{\mu_e}{\sigma_\varepsilon}$	$\frac{\varepsilon}{k} (C_1 G - C_2 \rho \varepsilon)$

Note : 1. $\mu_t = C_\mu \rho k^2 / \varepsilon$

2. Turbulence model constants are assigned the following values (Lauder and Spalding, 1974) :

$$C_\mu = 0.09, C_1 = 1.44, C_2 = 1.92, \sigma_k = 1.0, \sigma_\varepsilon = 1.3$$

$$3. G = \mu_t \left\{ 2 \left[\left(\frac{\partial u}{\partial x} \right)^2 + \left(\frac{\partial v}{\partial r} \right)^2 + \left(\frac{v}{r} \right)^2 \right] + \left(\frac{\partial u}{\partial r} + \frac{\partial v}{\partial x} \right)^2 \right\}$$

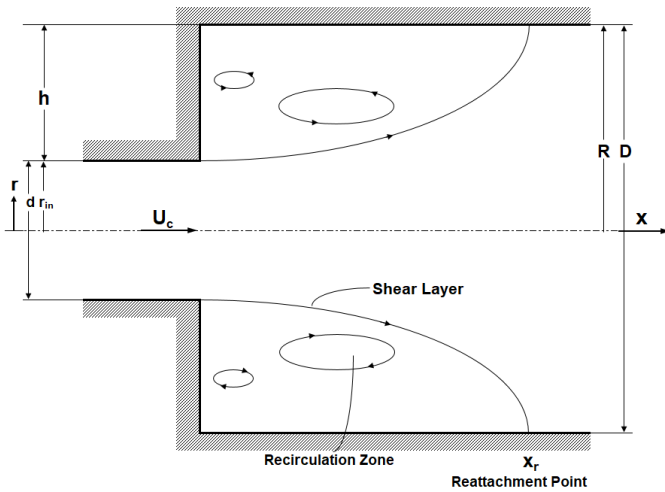


Figure 1: Axisymmetric cylindrical coordinate system and geometry of the sudden expansion pipe flow.

B. Boundary Conditions

With reference to Figure 1, the boundary conditions for steady, incompressible, complex confined turbulent recirculating flow through circular-sectioned sudden expansion pipes studied are given below. Four different boundary conditions were used: inlet plane, outlet plane, symmetry axis and solid walls. At the inlet to the sudden expansion pipe either axial radial velocity distribution or a uniform axial velocity distribution from the experimental measurements is specified, while the radial velocity is set equal to zero. If available, experimental radial turbulence kinetic energy distribution is specified at the inlet plane. If not, empirical

relationships are employed to assign uniform entrance values to turbulence quantities k and ε ; that is, $k = (0.002-0.005) u_b^2$ and $\varepsilon = (C_\mu k^{3/2} / 0.03R)$, where u_b is the bulk velocity in the smaller diameter pipe at the entrance of the larger one and R is the radius of the larger diameter pipe. The outlet plane was located sufficiently far away from the recirculation region so that fully-developed conditions could be assumed to prevail at the outlet; that is, all the axial gradients of the dependent variables vanish at the outlet plane and the radial velocity is assumed zero. At the sudden expansion pipe axis, symmetry is assumed: $(\partial\phi/\partial r) = v = 0$, where ϕ can be any of u , k or ε . At the top and step solid walls, velocity components u , v and turbulence quantities k and ε are set to zero. The values of k and ε at the near-wall grid points are calculated using the wall-functions of [44]. Initial field values throughout the computational domain were specified properly so as not to cause numerical divergence.

C. Numerical Solution Procedure

In this numerical investigation, employing the finite-volume approach, a computer program based on the SIMPLE algorithm of [45] has been developed. The partial differential equations (1) are discretised by a control-volume-based finite-difference method with a hybrid scheme. The finite-volume forms of the partial differential equations coupled with the boundary conditions are solved iteratively using a line-by-line solution procedure in conjunction with a tridiagonal matrix form [47].

D. Computational Details

The numerical computations were carried out on a Pentium 4 CPU 1.60 GHz personal computer. The computational grid distributions for all of the axisymmetric sudden expansion pipe flows studied are depicted in Figures 2, 13 and 24. All the computational grids employed were non-uniformly distributed with dense grid-line concentrations in the recirculation zone and near the walls of the axisymmetric sudden expansion pipe configuration. Staggered control volumes were used for axial and radial velocity components. All other quantities of interest were calculated at the grid points. The line-by-line method was used to obtain converged solutions iteratively. Underrelaxation factors were employed to procure numerical stability with values of 0.3, 0.3, 0.8, 0.8, 0.5 and 0.5 for u , v , k , ε , P and μ_e , respectively. The convergence criterion adopted in the present computations was that the summation of the absolute values of the mass residual in the entire computational domain be less than a prescribed value of 10^{-5} . Grid tests were performed with different grid sizes to obtain an optimum grid-independent solution for each flow case studied. All the computations presented in this study are grid-independent. Table 2 summarises details of computational requirements for all flow cases investigated. In this table, N is the number of iterations performed to obtain a converged solution, T is the time in cpu seconds, and T/N is the time per number of iterations.

Table 2: Flow case, Reynolds number, grid size, cpu time and number of iterations.

Flow case of	Re	Grid Size (x) × (r)	T, cpu time (secs)	N	T / N
S. A. Ahmed [10]	125 000	40 × 30	4.578125	357	0.0128238
Durrett et. al. [3]	84 000	40 × 30	7.046875	438	0.0160887
Poole and Escudier [15]	30 000	40 × 30	6.875	520	0.0132211

III. PRESENTATION AND DISCUSSION OF RESULTS

Numerical computations were carried out for complex confined turbulent recirculating flow in circular-sectioned sudden expansion pipes at three different Reynolds numbers, and the results of computations were compared with the experimental data of [3], [10], and [15]. With air used as the working fluid in the axisymmetric sudden expansion pipe, the experimental measurements of [10] are first selected as the comparison basis for this computational study. The axisymmetric sudden expansion pipe configuration has an expansion ratio of $D/d=1.5$. The Reynolds number of the flow at the inlet is $Re = 1.25 \times 10^5$ ($Re = u_{ref} d / \nu$, where u_{ref} is the centre-line velocity at inlet to the sudden expansion and d is the inlet pipe diameter). The computational domain is extended to an axial distance of $x=35h$ downstream from the inlet plane of the axisymmetric sudden expansion pipe. The numerical grid distribution for the axisymmetric sudden expansion pipe flow geometry of [10] is displayed in Figure 2. The predicted radial profiles of axial velocity along the sudden expansion pipe in dimensionless form u/u_{ref} , and radial distance r/R , at axial locations ranging from $x/h=0.38$ to 18 across the sudden expansion pipe have been compared with experimental measurements of [10] in Figure 3. As can be seen from the figure, there is a very good agreement between the predicted radial profiles of axial velocity and the corresponding measured ones. This figure also shows that how the predicted radial profiles of axial velocity develop along the sudden expansion pipe.

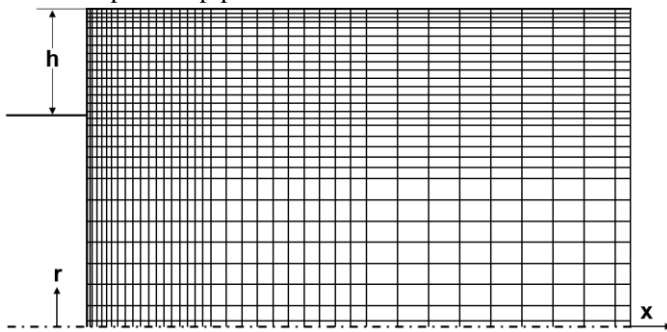


Figure 2: Numerical grid distribution for axisymmetric sudden expansion pipe flow of [10].

Figure 4 reveals a comparison between the predicted and experimental dimensionless centre-line velocity (u_c/u_{ref}) variation along the sudden expansion pipe axis, normalised to centre-line velocity (u_{ref}) at inlet and plotted as a function of downstream distance normalised to step height (h). As seen from the figure, the predicted axial variation of centre-line velocity is in good agreement with the experimental one.

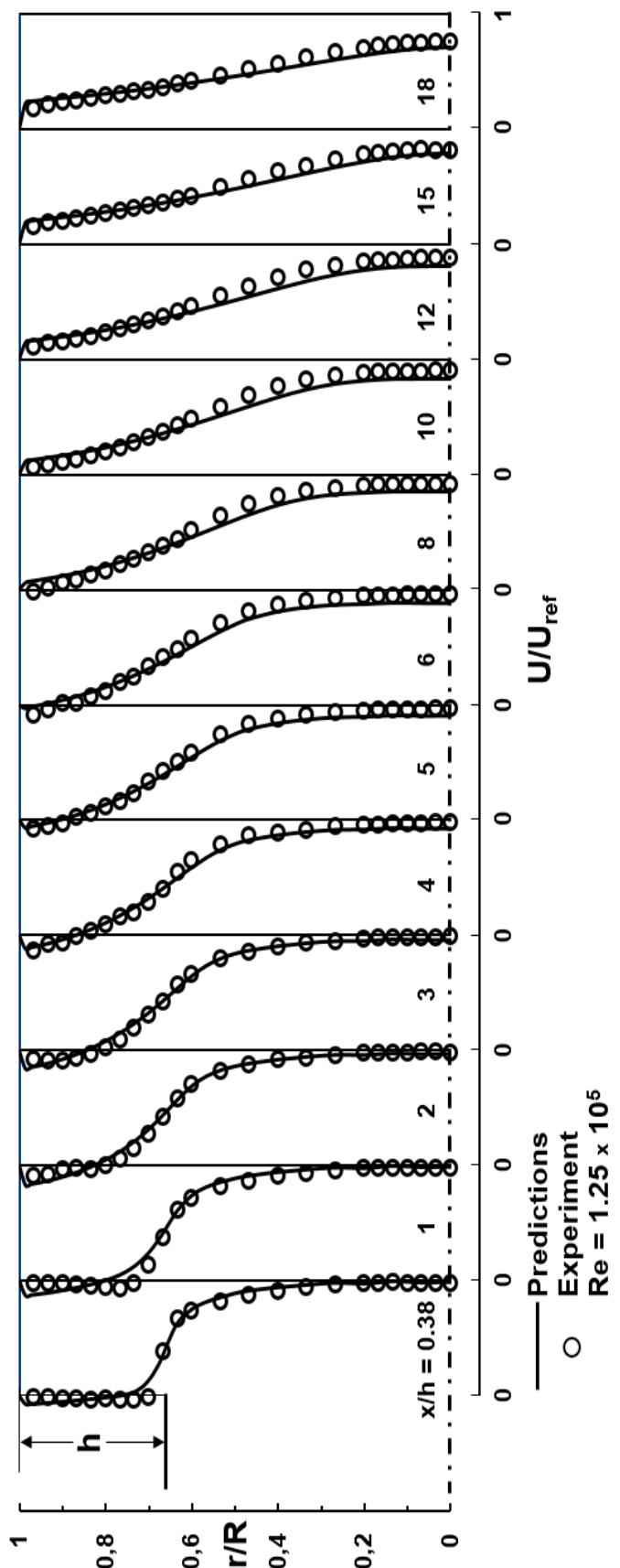


Figure 3: Comparison of predicted radial profiles of axial velocity along axisymmetric sudden expansion pipe flow with experimental data of [10].

In Figure 5, the predicted axial distribution of dimensionless turbulence kinetic energy $k^{0.5} / u_{ref}$ along symmetry axis of the sudden expansion pipe flow, as a function of downstream distance x/h , is compared with experimental measurements of [10]. As seen from the figure, the predictions indicate the same trend as the experimental measurements, and the agreement obtained is reasonable. The predicted locus of flow reversal ($u=0$) for the axisymmetric sudden expansion pipe flow is depicted in Figure 6. The normal distance y measured from the top wall is normalised to step height (h) and plotted as a function of downstream distance normalised to step height (x/h). In this figure, the axial velocity (u) is zero on the circles, positive above the circles and negative below the circles. As can be seen from the figure, the predicted flow reattachment length is found to occur at about $x_r/h=6.75$ downstream from the inlet plane, while the experimental flow reattachment length is reported to occur at $x_r/h=8$.

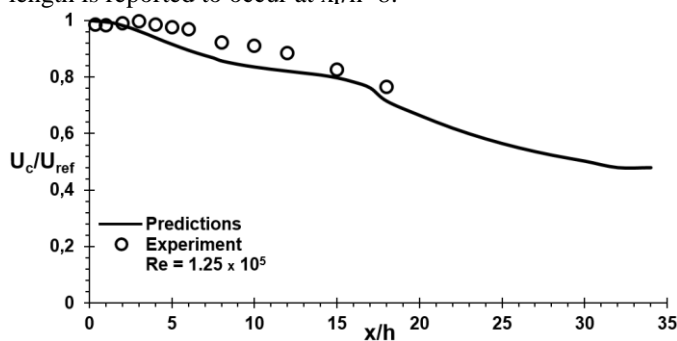


Figure 4: Comparison of predicted axial variation of dimensionless centre-line velocity along axisymmetric sudden expansion pipe flow symmetry axis with experimental data of [10].

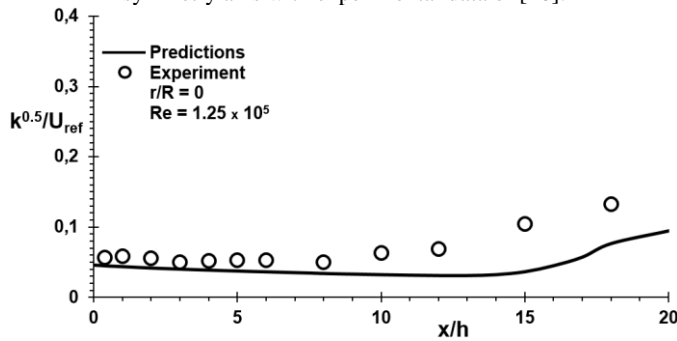


Figure 5: Comparison of predicted axial distribution of dimensionless turbulence kinetic energy along sudden expansion pipe symmetry axis with experimental data of [10].

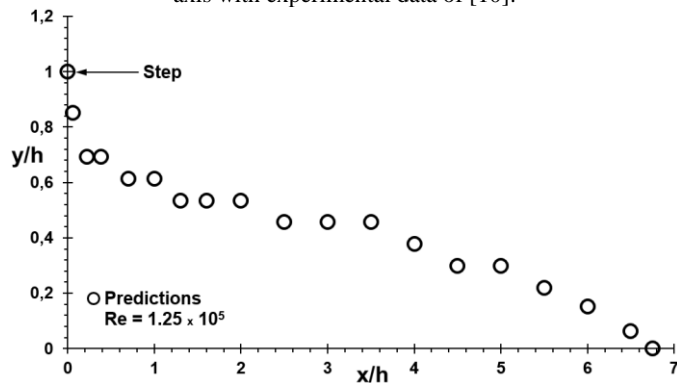


Figure 6: Predicted locus of flow reversal ($u=0$) for axisymmetric sudden expansion pipe flow of [10].

The predicted radial profiles of turbulence kinetic energy and their comparison with the experimental measurements of [10] in dimensionless form k/u_{ref}^2 and radial distance r/R , at 12 axial positions located at non-dimensional axial distances based on the step height of $x/h=0.38$ to 18, are presented in Figure 7. As seen from the figure, the agreement obtained between the predicted normalised turbulence kinetic energy profiles and the corresponding measured ones is quite good, although the measured ones are first slightly over predicted in the initial region of the recirculation zone and then under predicted at downstream axial locations from $x/h=10$ to 18. The reason for this is that the turbulence kinetic energy is produced in the shear layer but is not diffused radially toward the centre-line in the predicted flow field. Review of Figure 7 indicates that the radial distribution of turbulence kinetic energy diminishes as the flow develops along the sudden expansion duct. This event is also manifested by the predictions. Figures 8 and 9 show the predicted radial profiles of dissipation rate of turbulence kinetic energy and effective viscosity, respectively, along the sudden expansion pipe at the same downstream locations as in Figures 3 and 7. Here, the predicted profiles are normalised, respectively, with respect to maximum values of turbulence kinetic energy dissipation rate ϵ_{max} and effective viscosity $\mu_{e\ max}$ in the flow field. These figures indicate how the predicted dissipation rate of turbulence kinetic energy and effective viscosity profiles develop along the sudden expansion pipe flow configuration. In Figure 10, the predicted variation of wall-shear stress along the sudden expansion pipe top wall in dimensionless form of τ_w/τ_{wd} , as a function of downstream distance x/h , is given. Here, the wall-shear stress has been normalised with respect to its value at the outlet plane (τ_{wd}). As can be seen from the figure, starting from the inlet plane of the sudden expansion pipe until at about $x/h=6.75$ the wall-shear stress is negative. This is due to the negative axial velocities ($-u$) in the recirculation region. The top wall-shear stress, as it takes negative values, increases rapidly until it reaches its maximum negative value, and then decreases sharply to its zero value at about $x/h=6.75$, after which it takes positive values and increases until it attains its fully-developed value downstream at about $x/h=32$. The computed distribution of friction coefficient ($C_f = 2\tau_w/\rho u_{ref}^2$) along the sudden expansion pipe top wall, as a function of downstream distance x/h , is plotted in Figure 11. As seen from the figure, the top wall friction coefficient exhibits the same trend as the wall-shear stress shown in Figure 10. Finally, the predicted axial variation of wall static-pressure coefficient [$C_p=(P-P_{ref}) / 0.5 \rho u_{ref}^2$] along the sudden expansion pipe top wall, as a function of downstream distance x/h , is presented in Figure 12. As seen from the figure, the top wall static-pressure coefficient takes negative values just from the inlet plane of the sudden expansion pipe, and due to the recirculating flow, it increases continuously up to downstream location $x/h=30$. Beyond this location, it remains nearly constant.

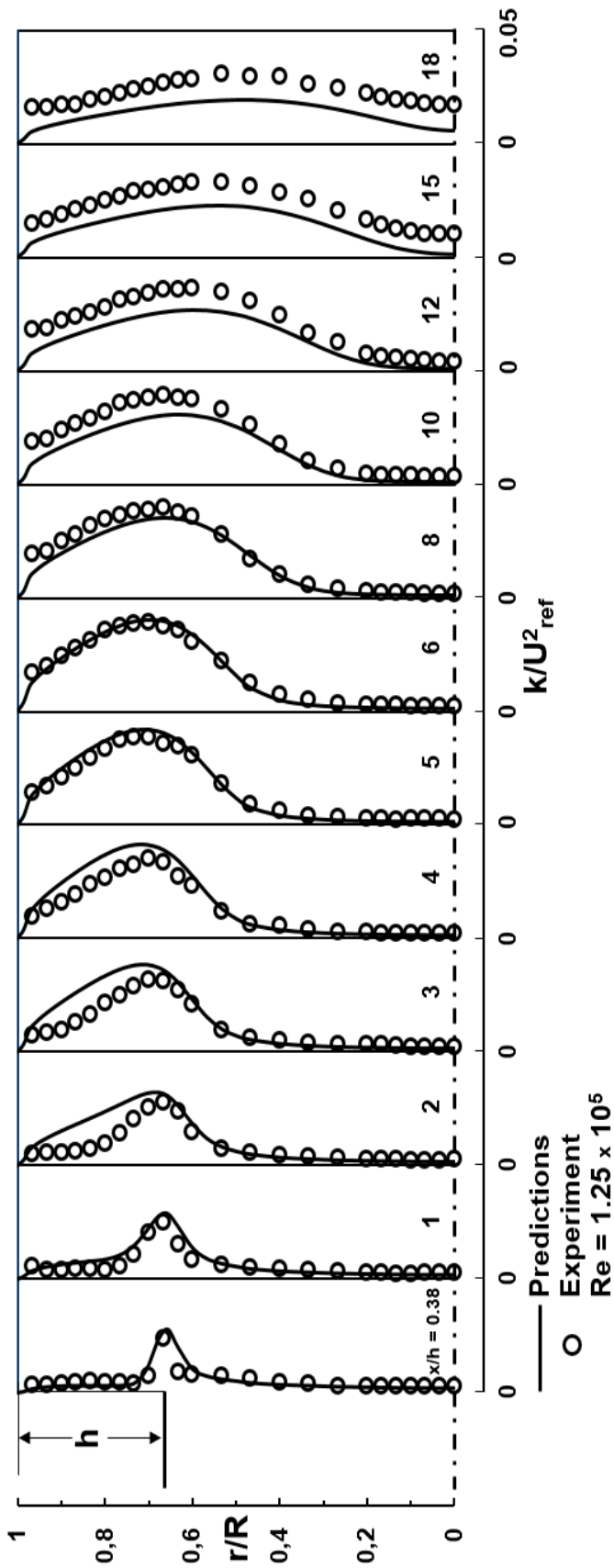


Figure 7: Comparison of predicted radial profiles of normalised turbulence kinetic energy along axisymmetric sudden expansion pipe flow with experimental data of [10].

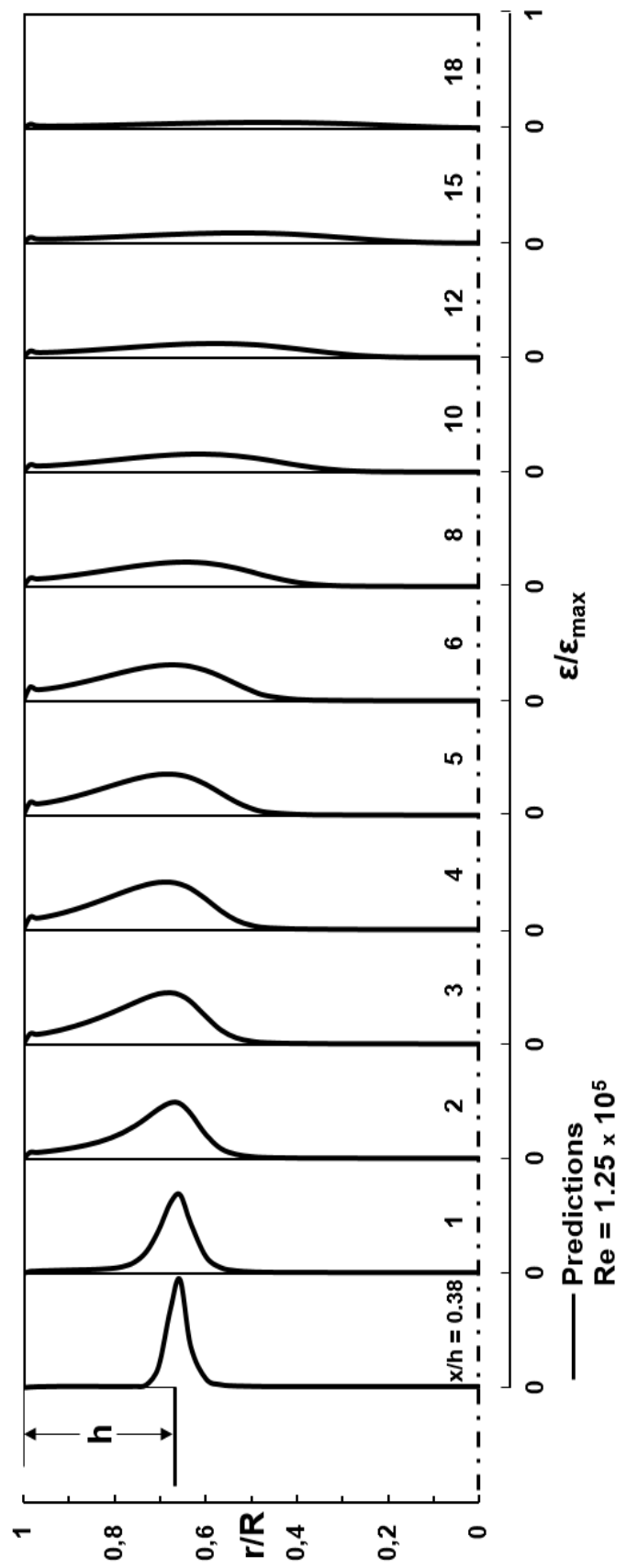


Figure 8: Predicted radial profiles of normalised turbulence kinetic energy dissipation rate along axisymmetric sudden expansion pipe flow of [10].

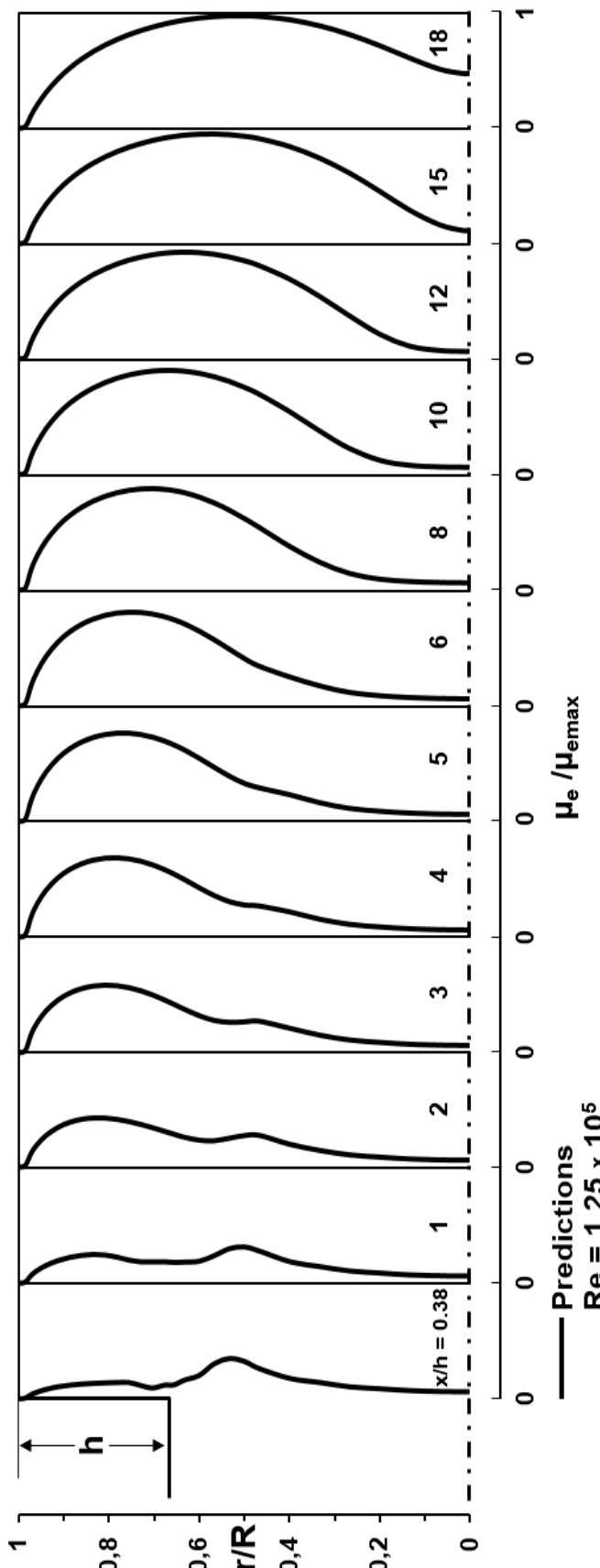


Figure 9: Predicted radial profiles of normalised effective viscosity along axisymmetric sudden expansion pipe flow of [10].

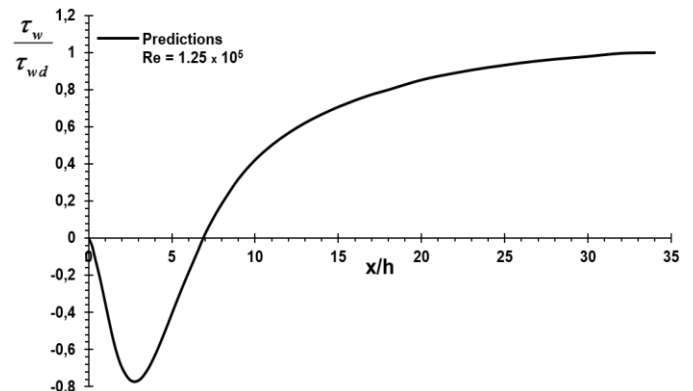


Figure 10: Predicted variation of dimensionless wall-shear stress along axisymmetric sudden expansion pipe top wall of [10].

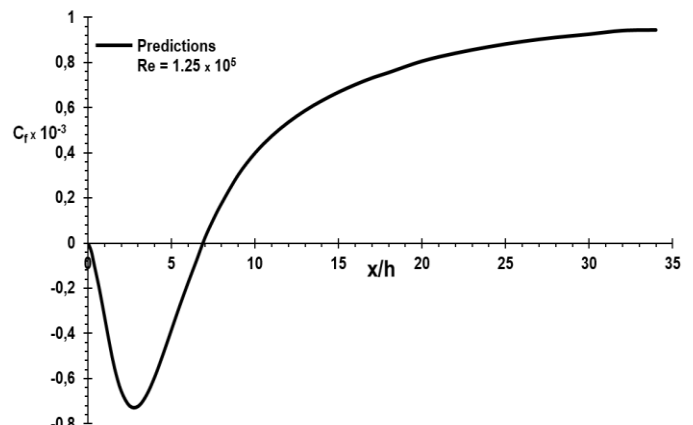


Figure 11: Computed distribution of friction coefficient along axisymmetric sudden expansion pipe top wall of [10].

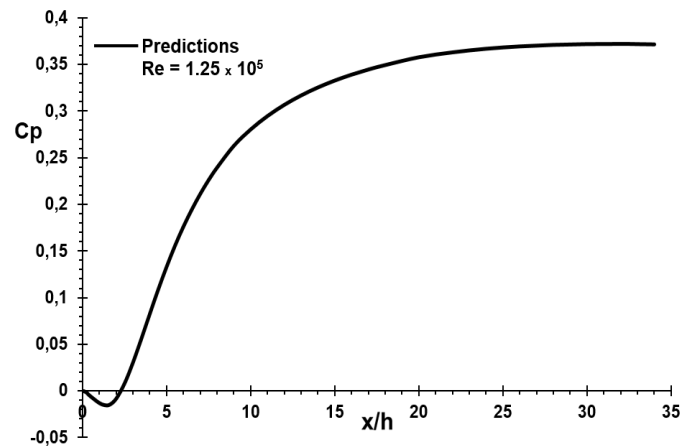


Figure 12: Predicted axial variation of wall static-pressure coefficient (C_p) along axisymmetric sudden expansion pipe top wall of [10].

The second flow configuration corresponds to the confined axisymmetric sudden expansion pipe flow experimental study of [3] with air used as the working fluid. The axisymmetric sudden expansion duct has an expansion ratio of $D/d=1.905$. The Reynolds number based on the inlet pipe diameter and centre-line velocity at the inlet plane is $Re = 8.4 \times 10^4$ ($Re = u_0 d / \nu$). For this flow situation, the calculation domain is extended to an axial distance of 40 step heights (h) downstream from the inlet plane of the sudden expansion pipe. The computational grid distribution for the axisymmetric

sudden expansion pipe flow of [3] is shown in Figure 13. The predicted radial profiles of axial velocity and their comparison with experimental measurements of [3] along the sudden expansion pipe in dimensionless form u/u_0 , and radial distance r/R , at axial positions ranging from $x/h=0.66$ to 38, are manifested in Figure 14. As can be seen from the figure, there is a very good agreement between the predicted axial velocity profiles and the corresponding measured ones. In addition, this figure also reveals how the predicted radial profiles of axial velocity develop along the sudden expansion duct. In Figure 15, the predicted axial variation of dimensionless centre-line velocity (u_c/u_0) along the sudden expansion pipe axis, as a function of downstream distance (x/h), is depicted. As seen from the figure, the predicted centre-line velocity decreases along the symmetry axis until it reaches its fully-developed value downstream at about $x/h=38$. In Figure 16, the predicted axial distribution of dimensionless turbulence kinetic energy $k^{0.5}/u_0$ along symmetry axis of sudden expansion pipe flow is given. As seen from the figure, the turbulence kinetic energy decreases until it attains its minimum value at $x/h=7.29$, and thereafter increases rapidly along the sudden expansion pipe axis until it reaches its maximum value at $x/h=14.58$, and then decreases again until $x/h=40$. The computed locus of flow reversal ($u=0$) for the sudden expansion pipe flow is presented in Figure 17. In this figure, the axial velocity (u) is zero on the circles, positive above the circles and negative below the circles. As seen from the figure, the predicted flow reattachment length is found to occur at about $x_r/h=7.65$ downstream from the inlet plane, whereas the experimental flow reattachment length is reported to occur at about $x_r/h=8.3$. The computed radial profiles of turbulence kinetic energy and their comparison with experimental data of [3] in dimensionless form k/u_0^2 and radial distance r/R , at 13 axial positions located at non-dimensional axial distances based on the step height of $x/h=0.66$ to 38, are displayed in Figure 18. As seen from the figure, the agreement obtained between the predicted normalised turbulence kinetic energy profiles and the corresponding measured ones is pretty good, although the measured ones are slightly over predicted in the initial region of the recirculation zone. Review of Figure 18 shows that the radial distribution of turbulence kinetic energy diminishes as the flow develops along the sudden enlargement pipe. This event is also demonstrated by the predictions.

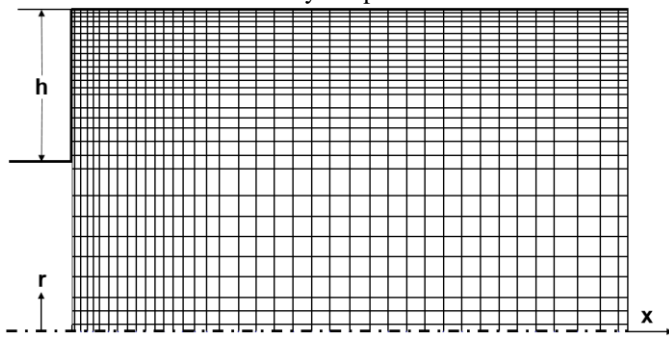


Figure 13: Computational grid distribution for axisymmetric sudden expansion pipe flow of [3].

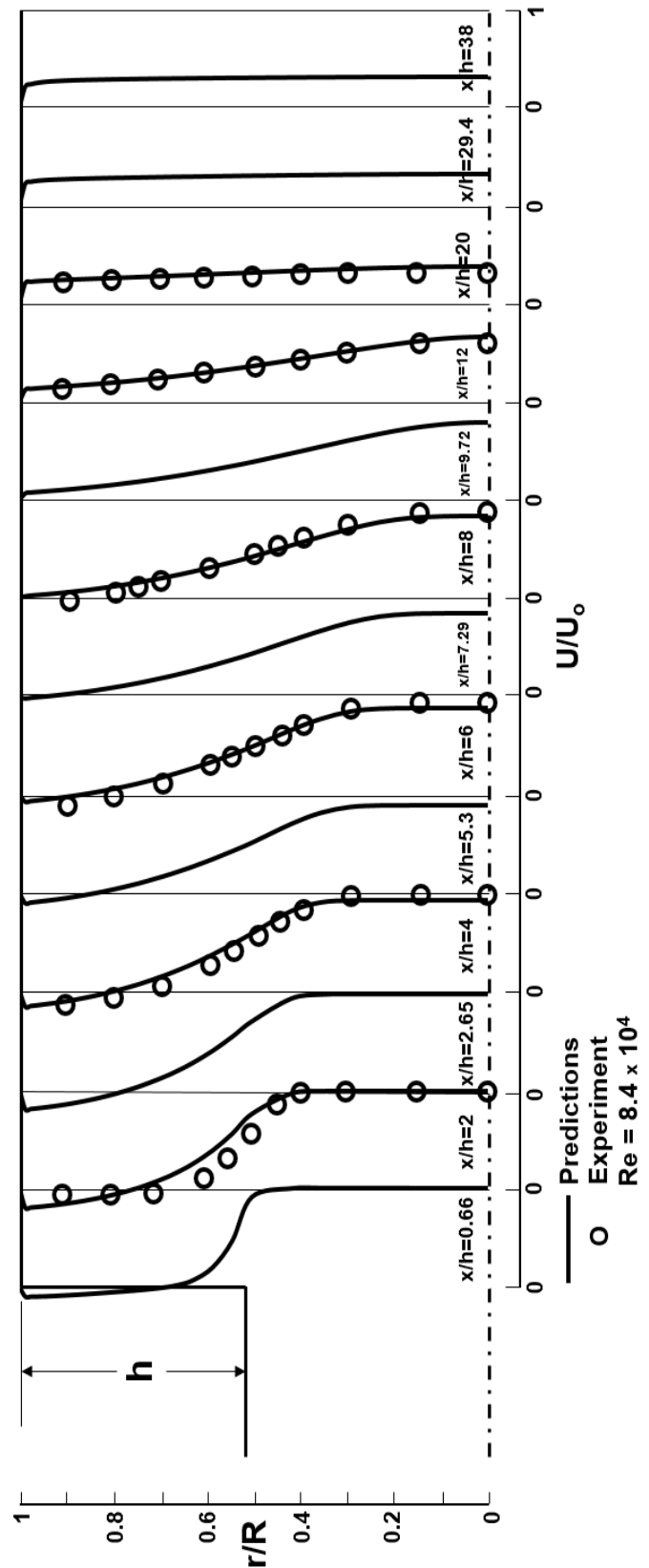


Figure 14: Comparison of predicted radial profiles of axial velocity along axisymmetric sudden expansion pipe flow with experimental data of [3].

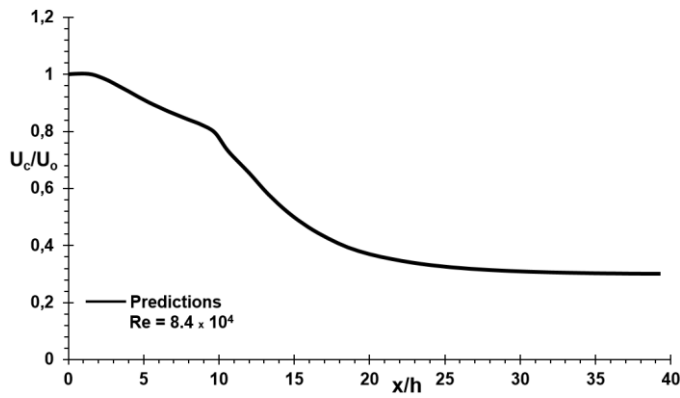


Figure 15: Predicted axial variation of dimensionless centre-line velocity along axisymmetric sudden expansion pipe flow symmetry axis of [3].

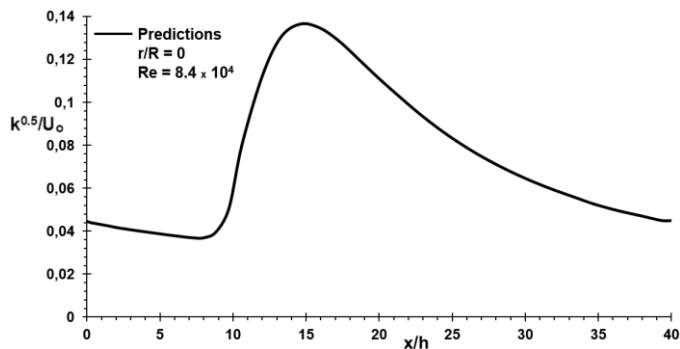


Figure 16: Predicted axial distribution of dimensionless turbulence kinetic energy along axisymmetric sudden expansion pipe flow symmetry axis of [3].

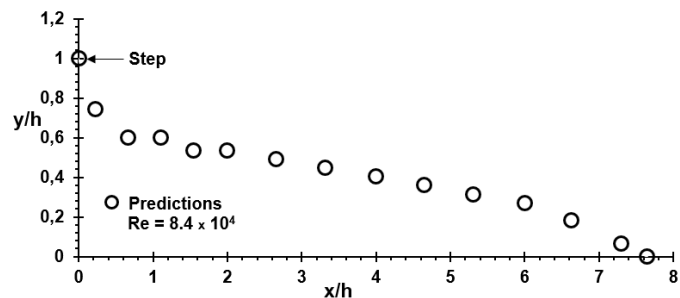


Figure 17: Computed locus of flow reversal ($u=0$) for axisymmetric sudden expansion pipe flow of [3].

Figures 19 and 20 exhibit the predicted radial profiles of dissipation rate of turbulence kinetic energy and effective viscosity, respectively, along the sudden expansion pipe at the same downstream locations as in Figures 14 and 18. Here, the predicted profiles are normalised, respectively, with respect to maximum values of turbulence kinetic energy dissipation rate ϵ_{max} and effective viscosity $\mu_{e max}$ in the flow field. These figures reveal how the predicted dissipation rate of turbulence kinetic energy and effective viscosity profiles develop along the sudden expansion pipe flow configuration.

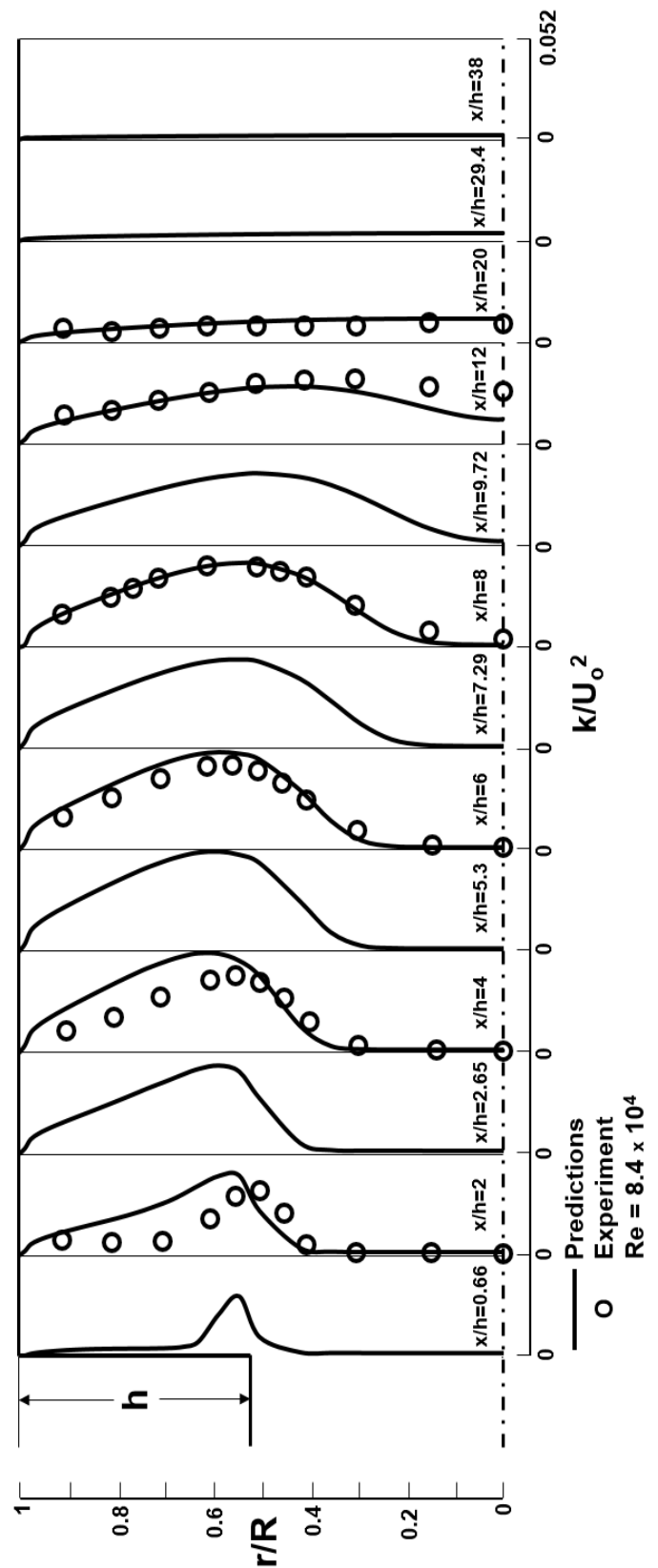


Figure 18: Comparison of predicted radial profiles of normalised turbulence kinetic energy along axisymmetric sudden expansion pipe flow with experimental data of [3].

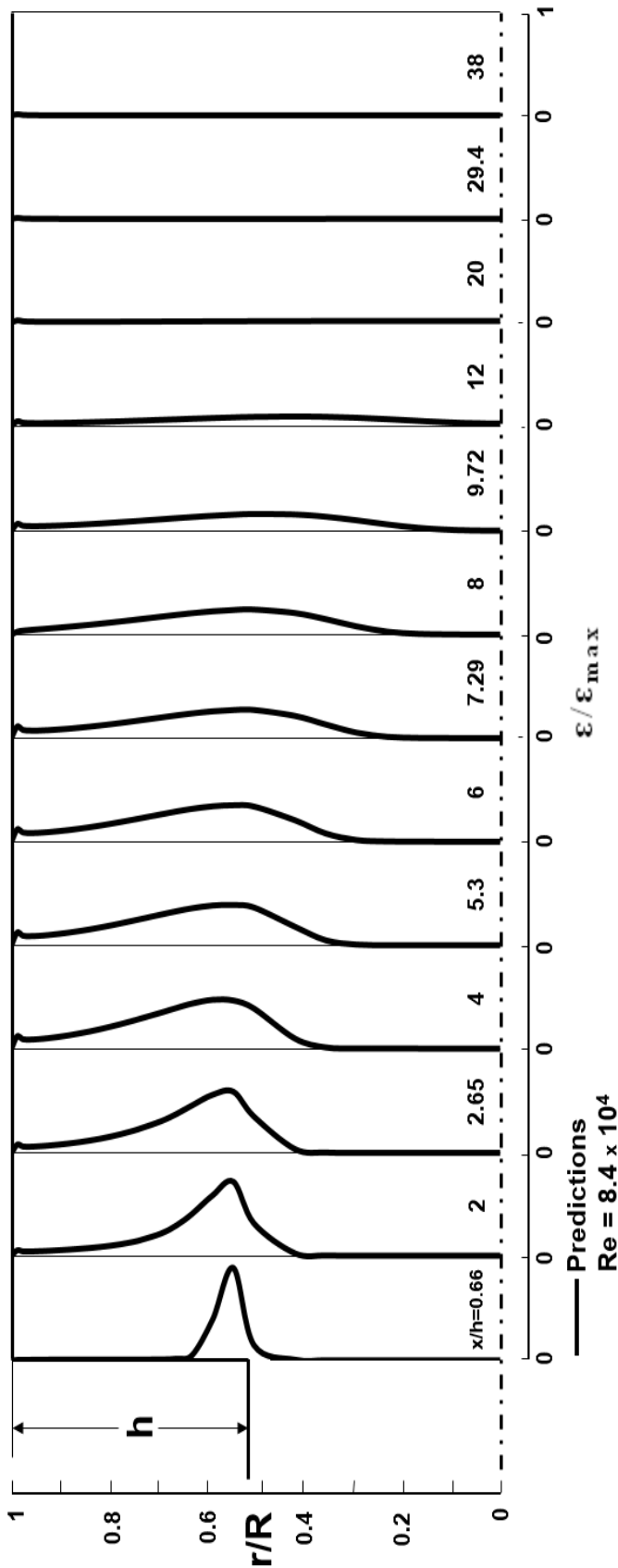


Figure 19: Predicted radial profiles of normalised turbulence kinetic energy dissipation rate along axisymmetric sudden expansion pipe flow of [3].

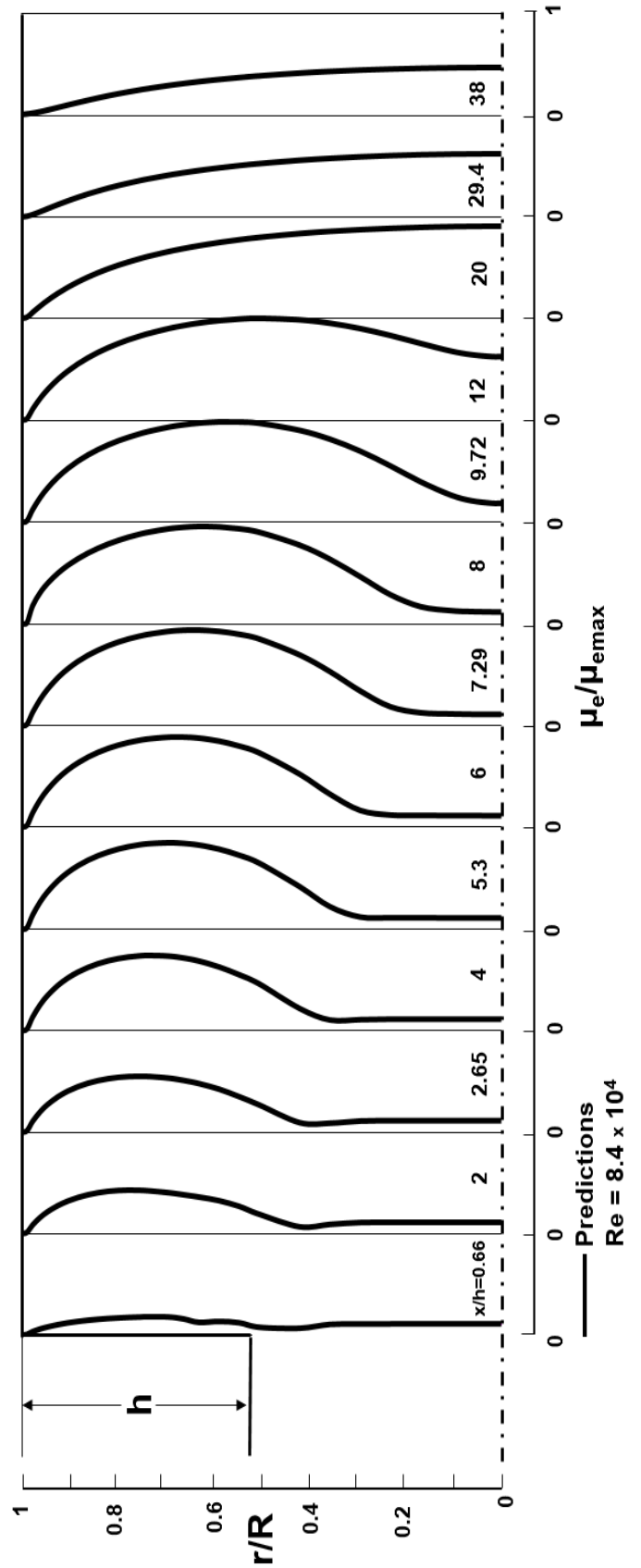


Figure 20: Predicted radial profiles of normalised effective viscosity along axisymmetric sudden expansion pipe flow of [3].

In Figure 21, the computed variation of wall-shear stress along the sudden expansion pipe top wall in dimensionless form τ_w/τ_{wd} , as a function of downstream distance x/h , is displayed. Here, the wall-shear stress is made dimensionless with respect to its value at the outlet plane (τ_{wd}). As can be seen from the figure, starting from the inlet plane of the sudden expansion pipe until at about $x/h=8$ the wall-shear stress is negative. This is due to the negative axial velocities (-u) in the recirculation zone. The top wall-shear stress, as it takes negative values, increases rapidly until it reaches its maximum negative value, and then decreases sharply to its zero value at about $x/h=8$, after which it takes positive values and increases until it attains its maximum positive value at about $x/h=23$, and thereafter decreases very slowly until $x/h=39$. The computed distribution of friction coefficient ($C_f = 2\tau_w/\rho u_o^2$) along the sudden expansion pipe top wall, as a function of downstream distance x/h , is plotted in Figure 22. As seen from the figure, the top wall friction coefficient indicates the same trend as the wall-shear stress shown in Figure 21. Finally, the computed axial variation of wall static-pressure coefficient [$C_p=(P-P_{ref}) / 0.5 \rho u_o^2$] along the sudden expansion pipe top wall, as a function of downstream distance x/h , is manifested in Figure 23. As seen from the figure, the top wall static-pressure coefficient takes negative values just from the inlet plane of the sudden expansion pipe, and due to the recirculating flow, it increases continuously up to downstream station $x/h=23$. Beyond this station, it remains nearly constant.

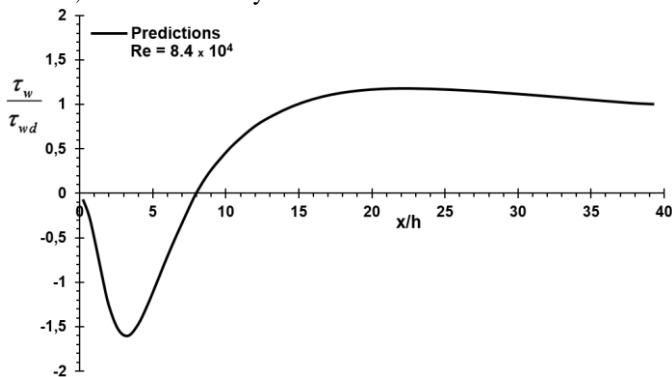


Figure 21: Computed variation of dimensionless wall-shear stress along axisymmetric sudden expansion pipe top wall of [3].

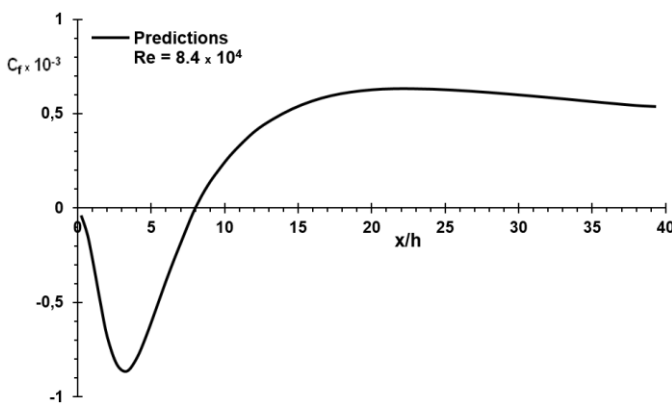


Figure 22: Computed distribution of friction coefficient along axisymmetric sudden expansion pipe top wall of [3].

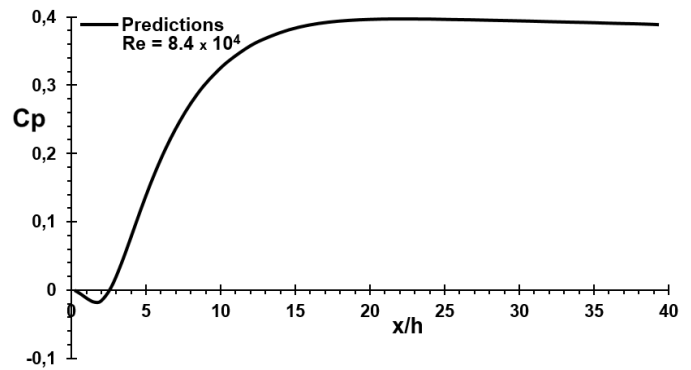


Figure 23: Computed axial variation of wall static-pressure coefficient (C_p) along sudden expansion pipe top wall of [3].

With water used as the working fluid in the confined axisymmetric sudden expansion pipe, the experimental study for turbulent flow conducted by [15] is thirdly selected as the test case for this computational study. The axisymmetric sudden expansion pipe configuration has an expansion ratio of $D/d=2$. The Reynolds number of the flow at the inlet is $Re = 3 \times 10^4$ ($Re = \rho u_b h / \mu$, where u_b is the bulk velocity at inlet to the sudden expansion and h is the step height). For this flow case, the computational domain is extended to an axial distance of 60 step heights (h) downstream from the inlet plane of the sudden expansion duct. The computational grid distribution for the axisymmetric sudden expansion pipe flow of [15] is depicted in Figure 24. The predicted radial profiles of axial velocity along the sudden expansion pipe in terms of u/u_b , and radial distance r/R , at axial locations ranging from $x/h=1$ to 20 across the sudden expansion pipe are compared with experimental data of [15] in Figure 25. As can be seen from the figure, there is a very good agreement between the predicted radial profiles of axial velocity and the corresponding measured ones. This figure also reveals that how the predicted radial profiles of axial velocity develop along the sudden expansion duct. The computed radial profile of axial velocity at $x/h=3$ is compared with the experimental measurements of [15] in Figure 26 separately, and a very good agreement is shown.

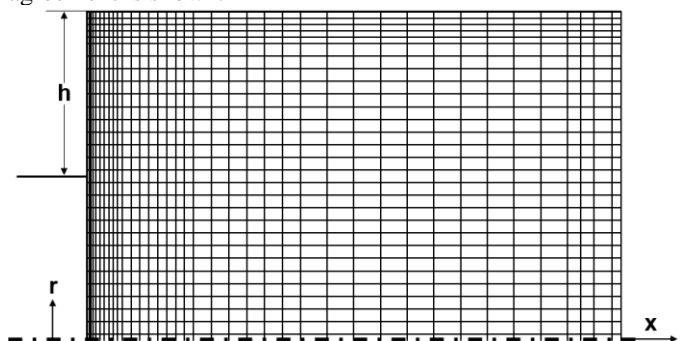


Figure 24: Computational grid distribution for axisymmetric sudden expansion pipe flow of [15].

Figure 27 demonstrates a comparison of the predicted and experimental centre-line velocity (u_c) variation along the sudden expansion pipe axis, normalised to bulk velocity (u_b) at inlet and plotted as a function of downstream distance normalised to step height (h). As seen from the figure, the

predicted axial variation of the centre-line velocity is faster in the initial region and slightly slower in the downstream region of the sudden enlargement pipe flow geometry. In general, however, there is a pretty good agreement between the predicted axial variation and the experimental one. In Figure 28, the predicted axial distribution of dimensionless turbulence kinetic energy $k^{0.5}/u_b$ along symmetry axis of the sudden expansion pipe flow is displayed. As seen from the figure, the turbulence kinetic energy decreases slowly until it attains its minimum value at $x_r/h=7$, and thereafter increases rapidly along the sudden expansion pipe axis until it reaches its maximum value at $x_r/h=14$, and then decreases again until $x_r/h=60$.

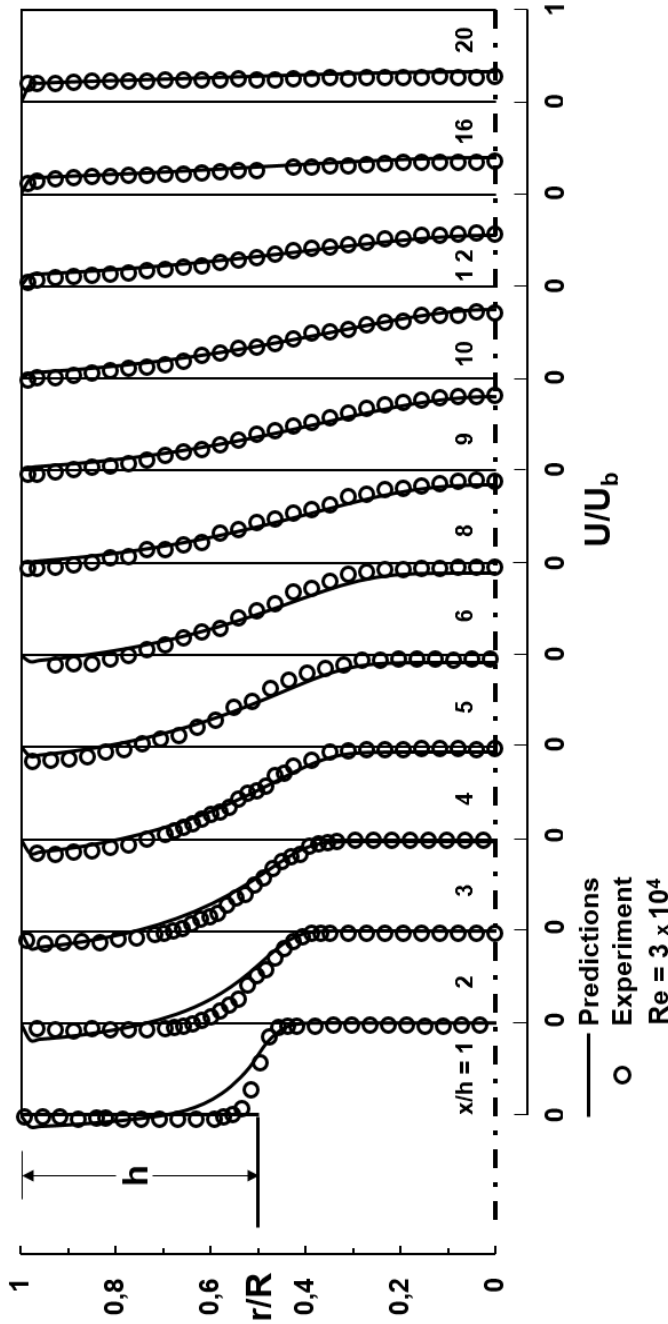


Figure 25: Comparison of predicted radial profiles of axial velocity along axisymmetric sudden expansion pipe flow with experimental data of [15].

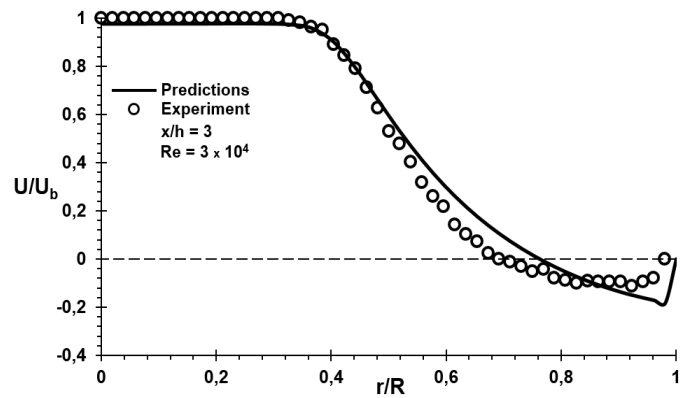


Figure 26: Comparison of computed radial profile of axial velocity at $x_r/h=3$ for axisymmetric sudden expansion pipe flow with experimental measurements of [15].

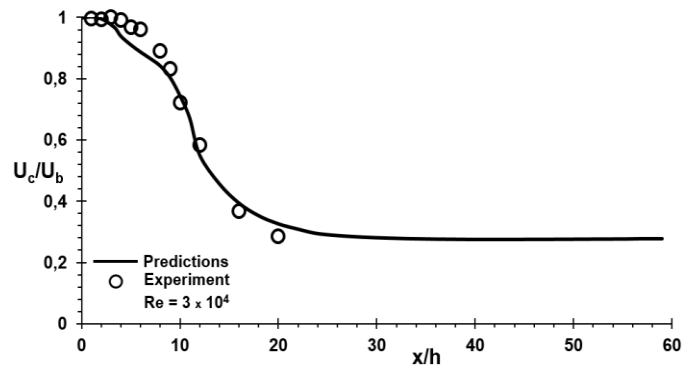


Figure 27: Comparison of predicted axial variation of dimensionless centre-line velocity along axisymmetric sudden expansion pipe flow symmetry axis with experimental measurements of [15].

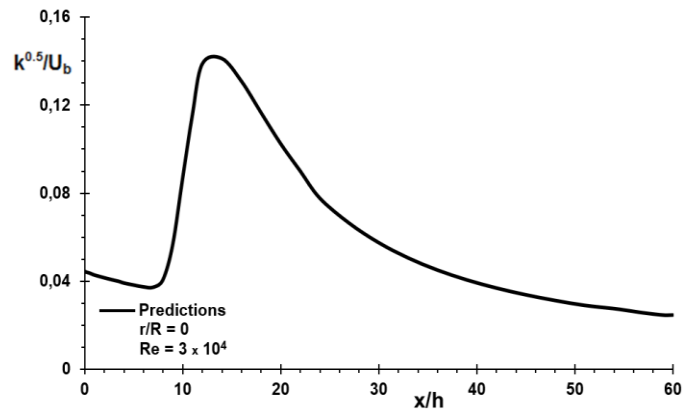


Figure 28: Predicted axial distribution of dimensionless turbulence kinetic energy along axisymmetric sudden expansion pipe flow symmetry axis of [15].

The predicted locus of flow reversal ($u=0$) for the axisymmetric sudden enlargement pipe flow is given in Figure 29. In this figure, the axial velocity (u) is zero on the circles, positive above the circles and negative below the circles. As can be seen from the figure, the predicted flow reattachment length is found to occur at about $x_r/h=7.5$ downstream from the inlet plane, while the measured flow reattachment length is reported to occur at $x_r/h=10$. The predicted radial profiles of turbulence kinetic energy and their comparison with experimental measurements of [15] in terms of k/u_b^2 and radial

distance r/R , at axial locations ranging from $x/h=1$ to 20, are indicated in Figure 30. As seen from the figure, the agreement obtained between the predicted normalised turbulence kinetic energy profiles and the corresponding experimental ones is quite good, although the experimental ones are first slightly over predicted in the initial region of the recirculation zone and then under predicted at downstream axial locations from $x/h=9$ to 12. The reason for this is that the turbulence kinetic energy is produced in the shear layer but is not diffused radially toward the centre-line in the predicted flow field. Review of Figure 30 shows that the radial distribution of turbulence kinetic energy diminishes as the flow develops along the sudden expansion duct. This event is also manifested by the predictions. Figures 31 and 32 show the predicted radial profiles of dissipation rate of turbulence kinetic energy and effective viscosity, respectively, along the axisymmetric sudden expansion pipe at the same downstream positions as in Figures 25 and 30. Here, the predicted profiles are made dimensionless, respectively, with respect to maximum values of turbulence kinetic energy dissipation rate ϵ_{max} and effective viscosity $\mu_{e\ max}$ in the flow field. These figures indicate how the predicted dissipation rate of turbulence kinetic energy and effective viscosity profiles develop along the axisymmetric sudden expansion pipe. In Figure 33, the computed variation of wall-shear stress along the axisymmetric sudden expansion pipe top wall in terms of τ_w/τ_{wd} , as a function of downstream distance x/h , is presented. Here, the wall-shear stress is made dimensionless with respect to its value at the outlet plane (τ_{wd}). As can be seen from the figure, starting from the inlet plane of the sudden expansion pipe until at about $x/h=8.5$ the wall-shear stress is negative. This is due to the negative axial velocities ($-u$) in the recirculation zone. The top wall-shear stress, as it takes negative values, increases rapidly until it reaches its maximum negative value, and then decreases sharply to its zero value at about $x/h=8.5$, after which it takes positive values and increases until it attains its maximum positive value at about $x/h=20$, and thereafter decreases slowly again until $x/h=59$. The predicted distribution of friction coefficient ($C_f = 2\tau_w/\rho u_b^2$) along the sudden expansion pipe top wall, as a function of downstream distance x/h , is plotted in Figure 34. As seen from the figure, the top wall friction coefficient reveals the same trend as the wall-shear stress shown in Figure 33. Finally, the predicted axial variation of wall static-pressure coefficient ($C_p = \Delta P/0.5\rho u_b^2$) along the axisymmetric sudden expansion pipe top wall with experimental measurements of [15], as a function of downstream distance x/h , is compared in Figure 35. The predicted shape of axial variation of wall static-pressure coefficient with experimental measurements is nearly identical, and the predicted static-pressure recovery occurs well downstream of flow reattachment length at about $x/h=22$.

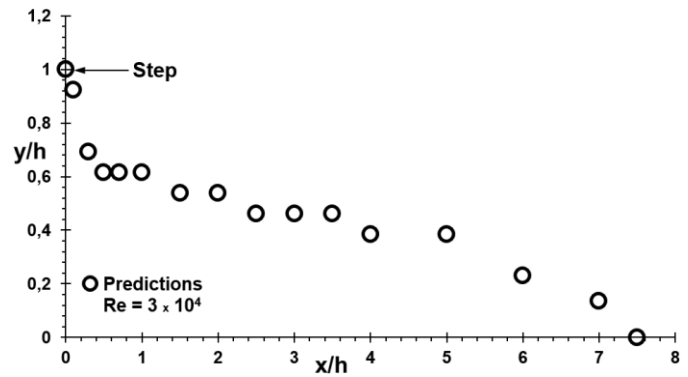


Figure 29: Predicted locus of flow reversal ($u=0$) for axisymmetric sudden expansion pipe flow of [15].

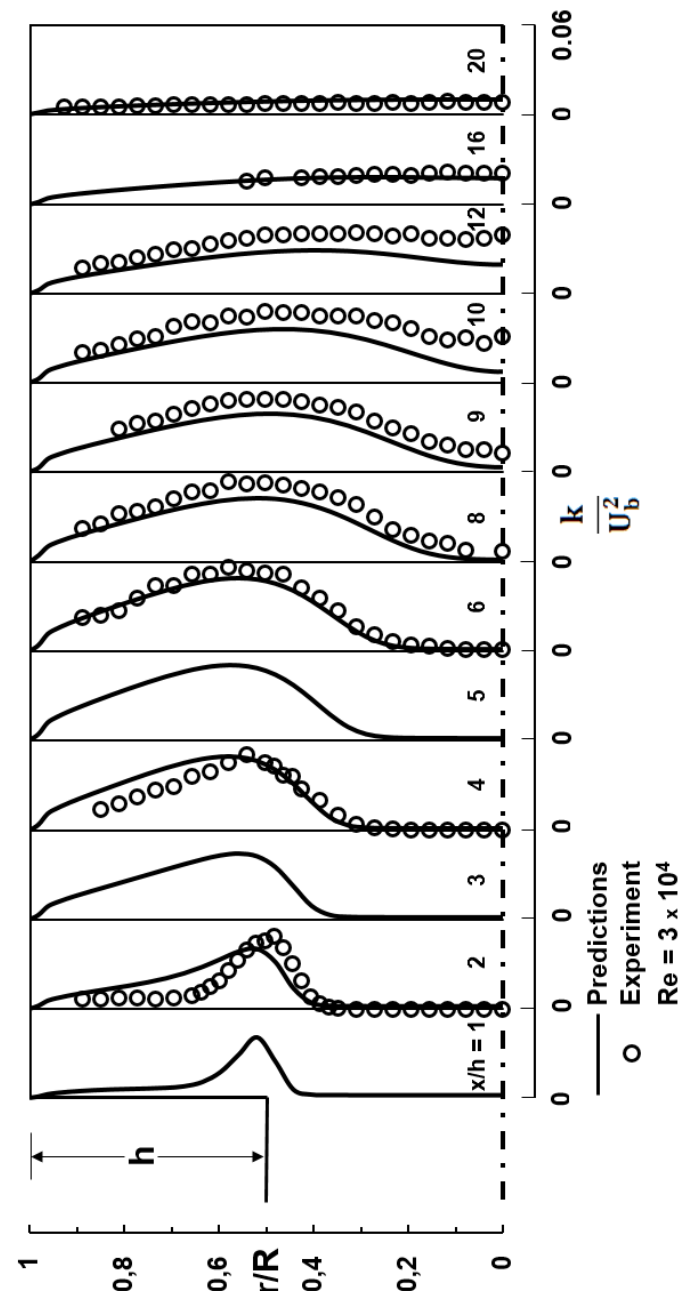


Figure 30: Comparison of predicted radial profiles of turbulence kinetic energy with experimental measurements of [15].

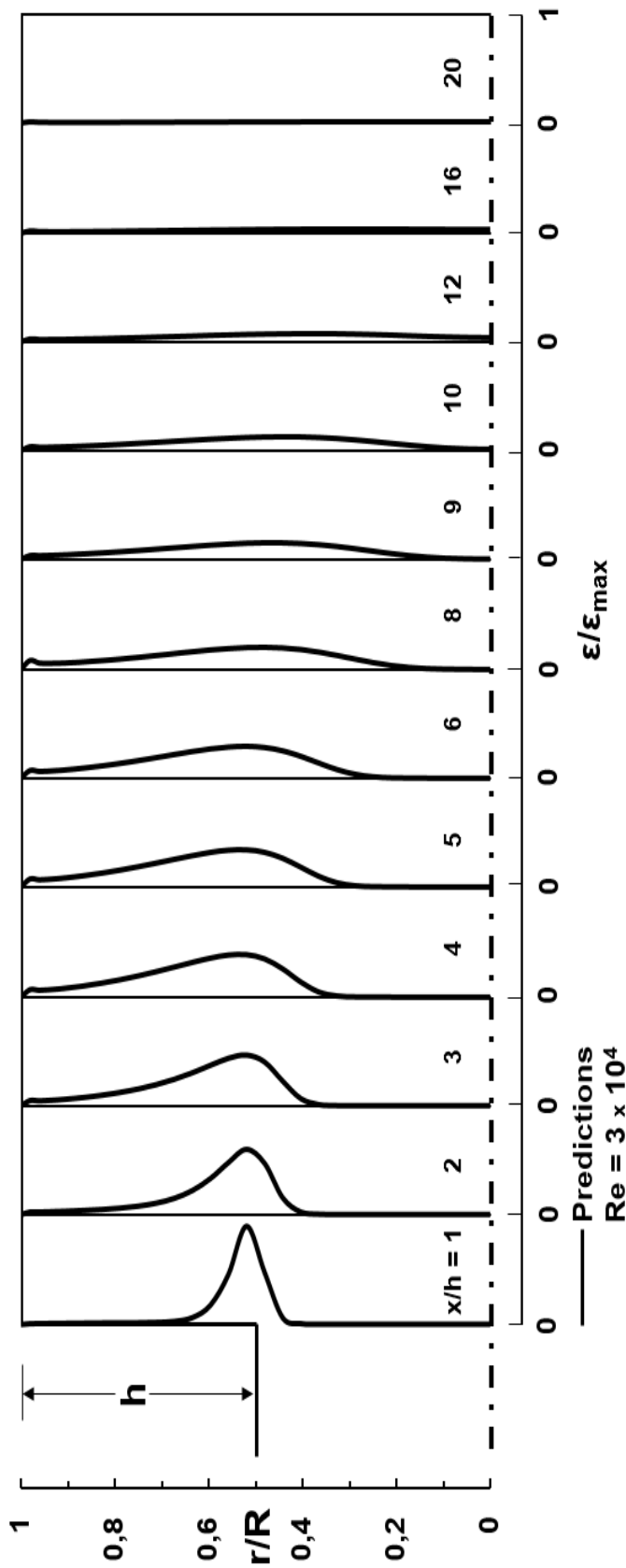


Figure 31: Predicted radial profiles of normalised turbulence kinetic energy dissipation rate along axisymmetric sudden expansion pipe flow of [15].

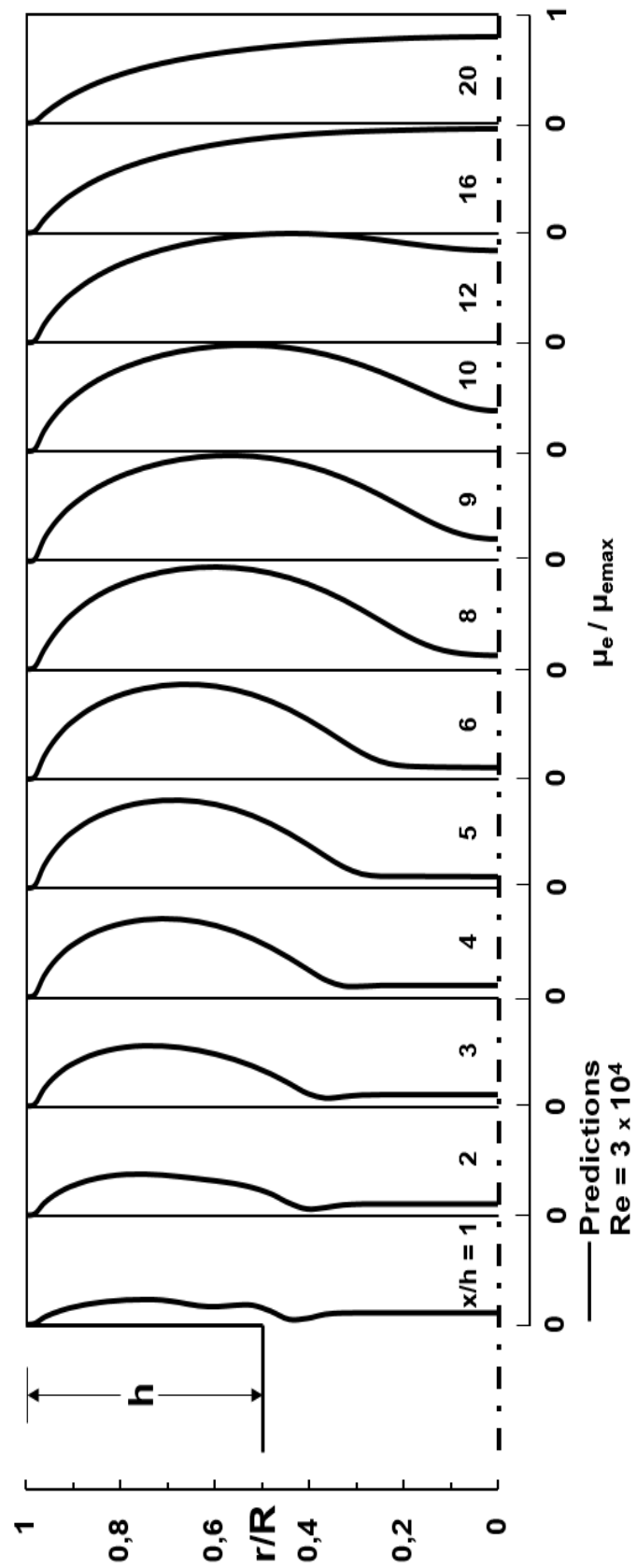


Figure 32: Predicted radial profiles of normalised effective viscosity along axisymmetric sudden expansion pipe flow of [15].

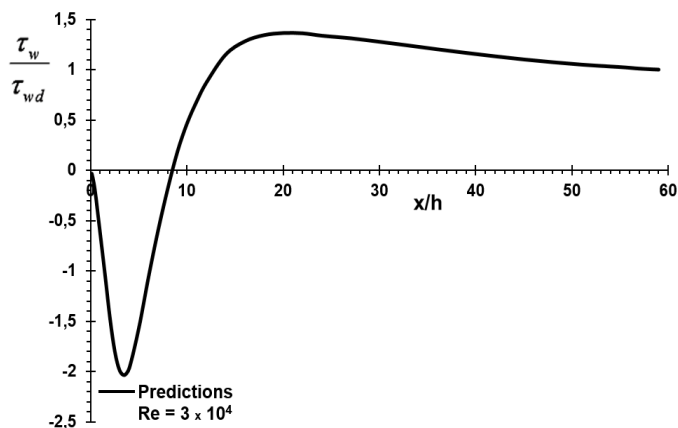


Figure 33: Computed variation of dimensionless wall-shear stress along axisymmetric sudden expansion pipe top wall of [15].

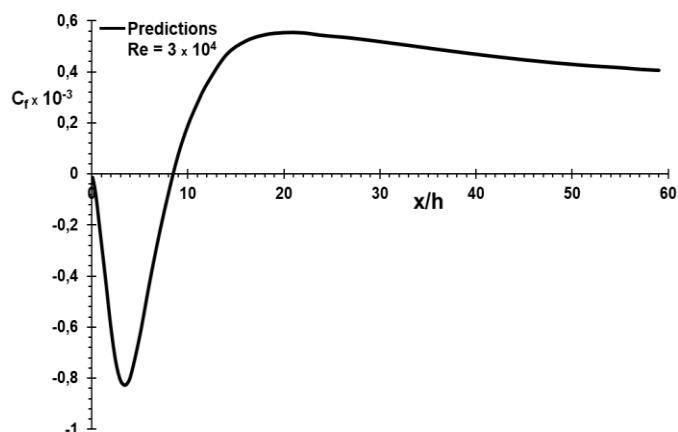


Figure 34: Computed distribution of friction coefficient along axisymmetric sudden expansion pipe top wall of [15].

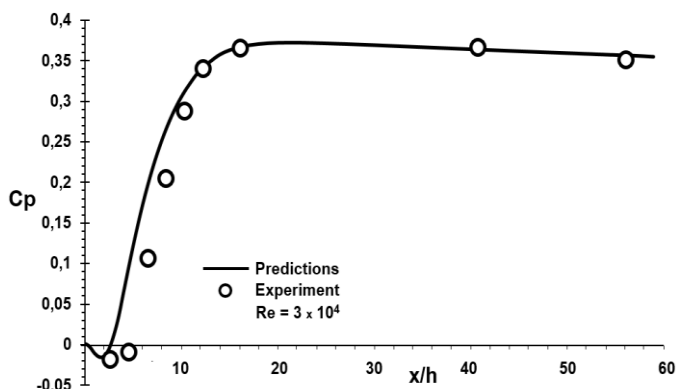


Figure 35: Comparison of predicted axial variation of wall static-pressure coefficient (C_p) along axisymmetric sudden expansion pipe top wall with experimental measurements of [15].

IV. CONCLUDING REMARKS

The main concluding remarks from the numerical investigation and modelling of the present original research work can be summarised as follows. Steady, incompressible, and axisymmetric separating and reattaching confined turbulent recirculating flows in circular-sectioned sudden expansion pipes at three different Reynolds numbers have been computed numerically employing the standard k- ϵ turbulence model. Using the finite-volume approach, a computer program based on the SIMPLE algorithm of Patankar [45] has been

developed. The performance of the standard k- ϵ turbulence model has been investigated for three different axisymmetric sudden expansion pipe flows. Numerical computations for radial profiles of axial velocity, turbulence kinetic energy, turbulence kinetic energy dissipation rate, effective viscosity, axial variation of centre-line velocity, locus of flow reversal, wall-shear stress, friction coefficient and wall static-pressure coefficient distributions along axisymmetric sudden expansion pipes are presented and, wherever available, compared with experimental measurements reported in the literature. The results of numerical investigation and modelling are generally in very good agreement with experimental measurements.

REFERENCES

- [1] R. D. Gould, W. H. Stevenson, and H. D. Thompson, "Investigation of turbulent transport in an axisymmetric sudden expansion," *AIAA Journal*, 28, pp. 276-283, 1990.
- [2] W. H. Stevenson, H. D. Thompson, and R. R. Craig, "Laser velocimeter measurements in highly turbulent recirculating flows," *ASME J. Fluids Eng.*, 106, pp. 173-180, 1984.
- [3] R. P. Durrett, W. H. Stevenson, and H. D. Thompson, "Radial and axial turbulent flow measurements with an LDV in an axisymmetric sudden expansion air flow," *ASME J. Fluids Eng.*, 110, pp. 367-372, 1988.
- [4] M. C. Chaturvedi, "Flow characteristics of axisymmetric expansions," *J. Hydraulics Div., Proc., ASCE*, 89, HY3, pp. 61-92, 1963.
- [5] L. F. Moon, and G. Rudinger, "Velocity distribution in an abruptly expanding circular duct," *ASME J. Fluids Eng.*, 99, pp. 226-230, 1977.
- [6] S. C. Favaloro, A. S. Nejad, and S. A. Ahmed, "Experimental and computational investigation of isothermal swirling flow in an axisymmetric dump combustor," *J. Propulsion, AIAA J.*, 7 (3), pp. 348-356, 1991.
- [7] A. S. Nejad, S. P. Vanka, S. C. Favaloro, M. Samimy, and C. Langenfeld, "Application of laser velocimetry for characterization of confined swirling flow," *ASME J. Eng. for Gas Turbines and Power*, 111, pp. 36-45, 1989.
- [8] S. A. Ahmed, and A. S. Nejad, "Premixed, turbulent combustion of axisymmetric sudden expansion flows," *Int. J. Heat and Fluid Flow*, 13 (1), pp. 15-21, 1992.
- [9] S. A. Ahmed, and A. S. Nejad, "Velocity measurements in a research combustor; part 1: isothermal swirling flow," *Exp. Ther. Fluid Science*, 5, pp. 162-174, 1992.
- [10] S. A. Ahmed, "ERCOFTAC Database: Isothermal dump combustor with swirl experiments," Retrieved, from the World Wide Web: <http://cfd.mace.manchester.ac.uk/ercoftac/classif.html>, 1992.
- [11] S. A. Ahmed, "Velocity measurements and turbulence statistics of a confined isothermal swirling flow," *Exp. Ther. Fluid Science*, 17, pp. 256-264, 1998.
- [12] A. S. Nejad, and S. A. Ahmed, "Flow field characteristics of an axisymmetric sudden expansion pipe flow with different initial swirl distribution," *Int. J. Heat and Fluid Flow*, 13 (4), pp. 314-321, 1992.
- [13] S. A. Ahmed, and K. B. Abidogun, "Measurements of turbulence statistics and energy budgets in a model combustor," *Energy*, 23, No.9, pp. 741-752, 1998.
- [14] S. A. Ahmed, and K. B. Abidogun, "An experimental investigation of turbulence statistics in an axisymmetric sudden expansion," *HTD-Vol. 346, National Heat Transfer Conference*, Vol. 8, pp. 101-110, ASME, 1997.
- [15] R. J. Poole, and M. P. Escudier, "Turbulent flow of viscoelastic liquids through an axisymmetric sudden expansion," *J. Non-Newtonian Fluid Mech.*, 117, pp. 25-46, 2004.
- [16] M. P. Escudier, and S. Smith, "Turbulent flow of newtonian and shear-thinning liquids through a sudden axisymmetric expansion," *Experiments in Fluids*, 27, pp. 427-434, 1999.
- [17] D. R. Cole, and M. N. Glauser, "Flying hot-wire measurements in an axisymmetric sudden expansion," *Experimental Thermal and Fluid Science*, 18, pp. 150-167, 1998.

- [18] D. R. Cole, and M. N. Glauser, "Applications of stochastic estimation in the axisymmetric sudden expansion," *Physics of Fluids*, 10, No.11, pp. 2941-2949, 1998.
- [19] C. E. Tinney, M. N. Glauser, E. L. Eaton, and J. A. Taylor, "Low dimensional azimuthal characteristics of suddenly expanding axisymmetric flows," *J. Fluid Mech*, 567, pp. 141-155, 2006.
- [20] W. J. Devenport, and E. P. Sutton, "An experimental study of two flows through an axisymmetric sudden expansion," *Experiments in Fluids*, 14, pp. 423-432, 1993.
- [21] N. Furuichi, Y. Takeda, and M. Kumada, "Spatial structure of the flow through an axisymmetric sudden expansion," *Experiments in Fluids*, 34, pp. 643-650, 2003.
- [22] H. Mak, and S. Balabani, "Near field characteristics of swirling flow past a sudden expansion," *Chemical Engineering Science*, 62, pp. 6726-6746, 2007.
- [23] D. H. Lee, and H. J. Sung, "Experimental study of turbulent axisymmetric cavity flow," *Experiments in Fluids*, 17, pp. 272-281, 1994.
- [24] T. Karasu, *Numerical prediction of incompressible turbulent swirling flows in circular-sectioned ducts and annuli*, Ph.D. Thesis, University of London, London, U.K., 1980.
- [25] T. Karasu, P. R. Choudhury, and M. Gerstein, "Prediction of some turbulent flows using upwind and hybrid discretisation schemes and the two-equation turbulence model," *Proc. 4th Miami international symposium on multi-phase transport and particulate phenomena*, Miami Beach, Florida, U.S.A., 5, pp. 105-124, 1988.
- [26] T. Karasu, "Prediction of turbulent flow with heat transfer in an annulus with rotating inner cylinder," *Proc. 8th Miami international conference on alternative energy sources*, Miami Beach, Florida, U.S.A., vol. 2, pp. 361-385, 1989.
- [27] T. Karasu, "Numerical prediction of turbulent swirling flows in circular-sectioned annuli," *Proc. 5th Miami international symposium on multi-phase transport and particulate phenomena*, Miami Beach, Florida, U.S.A., vol. 1, pp. 149-174, 1990.
- [28] T. Karasu, "Numerical study of turbulent flow in pipes," *Proc. 6th Miami international symposium on heat and mass transfer*, Miami, Florida, U.S.A., 1990.
- [29] T. Karasu, "Numerical prediction of turbulent recirculating flow through axisymmetric sudden expansions," *10th International Conference on Numerical Methods in Laminar and Turbulent Flow*, 21st -25th July 1997, Swansea, U.K., Proceedings Book, Vol. 10, pp. 357-368, 1997.
- [30] T. Karasu, "Numerical computation of turbulent flow in pipes," *Doğa-Tr. J. of Engineering and Environmental Sciences*, 17, pp. 29-38, 1993.
- [31] T. Karasu, "Numerical solution of turbulent flow with heat transfer in an annulus with rotating inner cylinder," *Turkish Journal of Engineering and Environmental Sciences*, Vol. 12, No. 3, pp. 250-272, 1988.
- [32] T. Karasu, "Numerical prediction of turbulent flow in circular pipes," *9th International Conference on Numerical Methods in Laminar and Turbulent Flow*, Atlanta, Georgia, U.S.A., Proceedings Book, Vol. 9, Part 2, pp. 1329-1339, 1995.
- [33] T. Karasu, "Kapalı türbülanslı akışların modellenmesi ve bilgisayarlı simülasyonu," *20. Ulusal Mekanik Kongresi*, 05-09 Eylül 2017, Uludağ Üniversitesi, Bursa, Türkiye. Bildiriler Kitabı, s. 1-12, 2017. ISBN 978-975561491-5.
- [34] T. Karasu, "Computational investigation of turbulent flow in pipes," *3rd International Conference on Advanced Technology and Sciences (ICAT'16)*, 01-03 September 2016, Selçuk University, Konya, Turkey, Proceedings Book, pp. 939-948, 2016.
- [35] T. Karasu, "Numerical computation of developing turbulent flow between two parallel plates," *21. Ulusal Isı Bilimi ve Tekniği Kongresi (ULIBTK'17)*, 13-16 Eylül 2017, Hitit Üniversitesi, Çorum, Türkiye, Bildiri Kitabı, ss. 11-20, 2017.
- [36] T. Karasu, "Numerical study of turbulent flow in circular-sectioned pipes," *8th Atmospheric Sciences Symposium (ATMOS'2017)*, 01-04 November 2017, Istanbul Technical University, Istanbul, Turkey, Proceedings Book, pp. 663-674, 2017. ISBN: 978-975-561-490-8.
- [37] T. Karasu, "Numerical investigation of turbulent recirculating flow through plane symmetric sudden expansions," *IV. Uluslararası Katılımlı Anadolu Enerji Sempozyumu (AES'2018)*, 18-20 Nisan 2018, Trakya Üniversitesi, Edirne, Türkiye, Bildiri Kitabı, part 3, ss. 2044-2056, 2018.
- [38] T. Karasu, "Numerical simulation of internal turbulent flows," *International Conference on Engineering Technologies (ICENTE'17)*, 07-09 December 2017, Selçuk University, Konya, Turkey, Proceedings Book, pp. 679-688, 2017.
- [39] T. Karasu, "Computer simulation and modelling of confined turbulent flows," *21. Ulusal Isı Bilimi ve Tekniği Kongresi (ULIBTK'17)*, 13-16 Eylül 2017, Hitit Üniversitesi, Çorum, Türkiye, Bildiri Kitabı, ss. 1-10, 2017.
- [40] T. Karasu, "Borularda türbülanslı akışların sayısal simülasyonu," *VIII. Ulusal Hidrolik Pnömatik Kongresi*, 22-25 Kasım 2017, İzmir. Bildiriler Kitabı, ss. 69-83, 2017. MMO Yayın No: E/MMO/678. ISBN 978-605-01-1088-3.
- [41] T. Karasu, "Paralel iki plaka arasında gelişen türbülanslı akışın sayısal araştırılması," *20. Ulusal Mekanik Kongresi*, 05-09 Eylül 2017, Uludağ Üniversitesi, Bursa, Türkiye. Bildiriler Kitabı, ss. 13-24, 2017. ISBN 978-975561491-5.
- [42] T. Karasu, "Computer simulation of turbulent recirculating flow through circular-sectioned sudden expansion pipes," *7th International Conference on Advanced Technologies (ICAT'18)*, April 28-May 1, 2018, Antalya, Turkey, Proceedings Book, pp. 752-763, 2018. E-ISBN: 978-605-68537-1-5.
- [43] T. Karasu, "Numerical investigation of turbulent recirculating flow in double-sided planar sudden expansions in channels," *7th International Conference on Advanced Technologies (ICAT'18)*, April 28-May 1, 2018, Antalya, Turkey, Proceedings Book, pp. 764-773, 2018. E-ISBN: 978-605-68537-1-5.
- [44] B. E. Launder, and D. B. Spalding, "The numerical computation of turbulent flows," *Comp. Meth. Appl. Mech. Engng*, 3, pp. 269-289, 1974.
- [45] S. V. Patankar, *Numerical heat transfer and fluid flow*, Hemisphere, McGraw-Hill, Washington, D.C., Chapters 5 and 6, 79-138, 1980.
- [46] S. V. Patankar, and D. B. Spalding, "A calculation procedure for heat, mass and momentum transfer in three-dimensional parabolic flows," *Int. J. Heat Mass Transfer*, 15, pp. 1787-1806, 1972.
- [47] D. B. Spalding, "A general-purpose computer program for multi-dimensional one-and-two phase flow," *Math. Comput. Simulation*, XXIII, pp. 267-276, 1981.

Dynamic analysis and controlling of a 2 DOF Robot Manipulator Using Fuzzy Logic Techniques

B.CIRAK¹,F.IRIM², S.ALKAN³

¹Karamanoglu Mehmetbey University, Karaman/Turkey, bcirak@kmu.edu.tr

²Konya Technical University, Konya/Turkey, fatih.irim@gmail.com

³Konya Technical University, Konya/Turkey, safa.alkan@gmail.com

Abstract - This paper reviews the literature on control of 2-DOF robot manipulator using fuzzy logic control (FLC). Different schemes of FLC laws are considered here. These are PID control, sliding mode control (SMC), and adaptive control. Importance of each control techniques with its advantages and disadvantages is discussed here. It is highlighted that the robustness of the system has improved considerably by using FLC than classical controller. System performance was evaluated by simulations of two degree of freedom robot arm.

Keywords - Robot manipulator, Control, Fuzzy Logic, Two-DOF, Dynamic Analysis

I. INTRODUCTION

Robots have the potential to play a large role in our world. They are currently widely used in industrial applications for labor-intensive operations that require a high level of precision and repetition. In addition, robots can be found in the entertainment industry in the form of toys and animatronics. The function of robots in society is constantly evolving and current research endeavors to bring them further into the realm of domestic assistance, medicine, military, search and rescue, and exploration. In many of these applications, the robot must perform only one specific task and thus can be designed to handle a single operation. However, as the potential use for robots grows, so does their need to interact with objects in their environment. Robots are defined as systems that perform location and direction change operations by programmed transport. Moving is a movement at a distance far from the body dimensions. Manipulator consists of multiple joints connected to each other. Movements of the joints are provided by the engine. The robot consists of mechanical parts, actuators and control units. The mechanical parts of the robot are classified as structural parts, power transmitting parts, bearings and coupling parts. The motors can also act as pneumatic or hydraulic as well as electrically. In modern robots, the control units are PC based and have advanced structures.

Today, the usage areas of robots are increased. Especially in industrial environments, a large number of robots are used for production assembly and similar works. Because the separation media properties change rapidly, in the real world robots are required to reach the desired target without hitting

the obstacles they encounter. The robots, the control technique used and the joint they contain according to their species. In terms of control technique it is possible to classify as adaptive robots, non-adaptive and intelligent robots. According to the joint types in the robots are grouped as rotary, prismatic, cylindrical, spherical and planar. In recent years, it is possible to find intelligent system applications on different stages of production.

These intelligent systems are an important part of industry, healthcare and automation sector. In this study, the dynamic behavior of the 2-axis industrial robot manipulator and the change of the robot arm configuration between the joints with time are examined and the articulated neural network model of the joints given mathematical kinematic models has been inspected.

II. MANIPULATOR KINEMATICS

Two linked or two degree of freedom manipulators are shown in Fig.1. It is assumed that the shaped O2 point is fixed. There are servo motors at O and O1 points. Manipulator consists of two rotating joints and two links. Basic and local coordinate systems are placed on the manipulator and kinematic calculation is started. The basic coordinate system at point O is considered fixed. Local coordinate systems are located at O1 and O2 points. The rotation of the joints is around the z-axis, perpendicular to the paper plane. By means of the transformation matrices expressing the relation between the neighboring links, the position and orientation in the robot arm are determined according to the basic coordinate system. Similarly, using the inverse of the transformation matrices, the values of θ_1 and θ_2 can be calculated when the robot hand is in any position. This process is called inverse kinematics. Kinematic parameters and transformation matrices are determined by the DenavitHartenberg method.

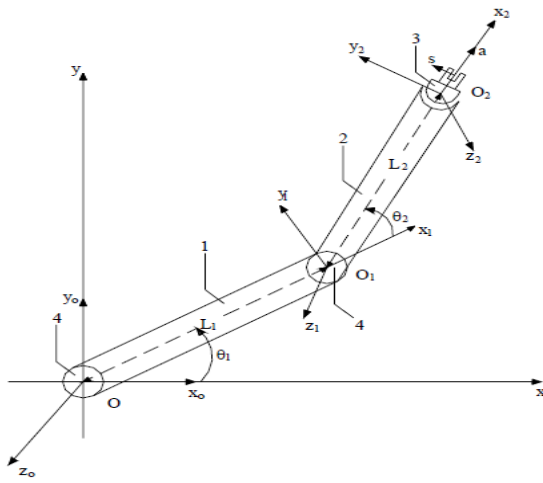


Figure1:Physical structure of the 2 DOF manipulator

Basic parameters of the manipulator; M1 and M2 are the mass of the first and second link. L1 and L2 are the lengths of the links. M1 = M2 = 6.5 kg, L1 = L2 = 0.75 m, gravity acceleration, g = 9.81 m / s²

III. MANIPULATOR DYNAMICS

The dynamic equation of a manipulator with n degrees of freedom is shown in equation 1.

$$T = D(q) \ddot{q} + h(q, \dot{q}) \dot{q} + c(q) \quad (1)$$

Where, the matrix T is n × 1 in size. Describes the generalized rotational moments that effect joints. The matrix D with dimension n × n shows the effect of accelerating inertia masses. The h matrix of size nx1 shows the centrifugal and Coriolis effect. The matrix c in n × 1 dimension shows the rotational moment acting on the joints due to gravity. q, which is defined as a generalized coordinate and is of dimension n × 1, shows the angular displacement of the joints. Therefore, \ddot{q} represents angular acceleration ($\ddot{\theta}$), and \dot{q} represents angular velocity ($\dot{\theta}$). The 2.equation expresses the dynamic model of the manipulator.

$$\begin{bmatrix} T_1 \\ T_2 \end{bmatrix} = \begin{bmatrix} D_{11} & D_{12} \\ D_{21} & D_{22} \end{bmatrix} \cdot \begin{bmatrix} \ddot{\theta}_1 \\ \ddot{\theta}_2 \end{bmatrix} + \begin{bmatrix} h_1 \\ h_2 \end{bmatrix} + \begin{bmatrix} c_1 \\ c_2 \end{bmatrix} \quad (2)$$

$$D_{11} = \frac{1}{3}L^2 (M_1 + 4M_2 + 3M_2 \cos\theta_2) \quad (3)$$

$$D_{12} = \frac{1}{3}M_2L^2 + \frac{1}{2}M_2L^2 \cos\theta_2 \quad (4)$$

$$D_{21} = \frac{1}{3}M_2L^2 + \frac{1}{2}M_2L^2 \cos\theta_2 \quad (5)$$

$$D_{22} = \frac{1}{3}M_2L^2 \quad (6)$$

$$h_1 = \frac{1}{2}L^2 \sin\theta_2 \cdot M_2 \dot{\theta}_2 (\dot{\theta}_2 + 2\dot{\theta}_1) \quad (7)$$

$$h_2 = \frac{1}{2}L^2 \sin\theta_2 \cdot M_2 \dot{\theta}_1 \dot{\theta}_1 \quad (8)$$

$$c_1 = \frac{1}{2}gL (M_1 \cos\theta_1 + M_2 \cos(\theta_1 + \theta_2) + 2M_2 \cos\theta_1) \quad (9)$$

$$c_2 = \frac{1}{2}gL M_2 \cos(\theta_1 + \theta_2) \quad (10)$$

Considering the problem of bringing the robot manipulator from a starting position to a target position within a fixed time interval. System kinematics can be used to calculate joint angles corresponding to the starting and target positions. What is desired here is to obtain a time-dependent $q(t)$ function for each joint between the starting position and the target position

at a constant time interval. There are many smooth functions that can be used for this study (Figure 2).

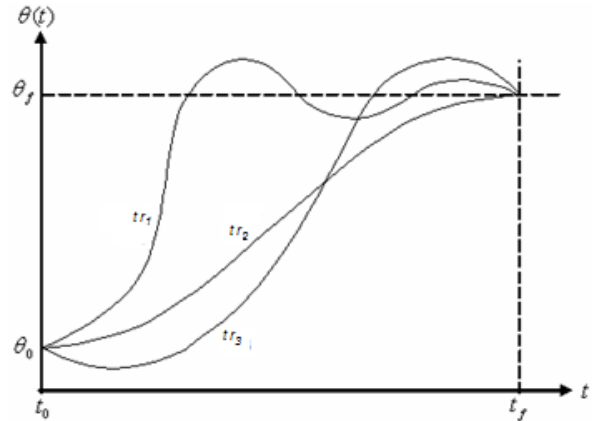


Figure 2:The trajectory for each joint

IV. FUZZY LOGIC CONTROL OF MANIPULATORS

Manipulators are constructed from open-chain link mechanism and nonlinear coupled system, which are difficult to control. PID controls are being used for their simplicity and satisfactory performance for the tracking of slow varying robot trajectories. When mass and inertia of the robot manipulators are not known accurately or if they vary in different operating condition, a conventional PID control may not work satisfactorily. However, operator can control these complexities based on their experiences. It is therefore necessary to design a control which can work on the experience of human operator, i.e., use of fuzzy control. Saturation of nonlinear PID regulator for industrial robot manipulators is discussed. However, PID control is also effective in controlling a highly nonlinear system with small tracking error given. first time, it has shown the concept to overcome the difficulty with the conventional PID controller, i.e., the use of fuzzy PID controller. A new hybrid control scheme (fuzzy + PID) is introduced to control inertial parameter changes for a direct drive 2-link manipulator. The motion control of the robot manipulator using the application of the fuzzy + PD logic control system. Fuzzy logic systems play the role of tuner for robot control gains. Control law used in PID control strategy is described as:

$$\tau_{PID} = K_D e + K_P e + K_I \int e dt \quad (1)$$

Where K_D , K_I , and K_P are the controller gain matrices, and τ_{PID} is the vector of joint torque. Block diagram of PID control of the robot manipulator with fuzzy logic is shown in Figure 3 and Figure 4. The fuzzy PID control algorithm designed in paper achieved the ideal control effect in the actual control. Conventional controllers include the following: simple PID, computed torque control, and feed forward inverse dynamics control, and intelligent control includes the following: fuzzy control, neural control, and neuro-fuzzy control. In fuzzy controller is combined with a conventional PID controller, to enhance the robustness of the PD-type

controller. Fuzzy self-tuning algorithm is presented to select P, I and D gains of the PID controller with respect to the actual state of the robot manipulator.

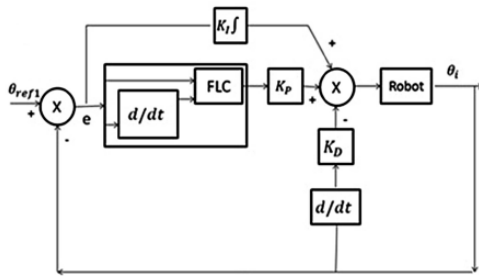


Figure 3: FLC Block Diagram

The configuration of fuzzy logic control (FLC) scheme is shown in Figure 4; it contains an equivalent control part and a two input single output FLC in which Mamdani's fuzzy inference method is used.

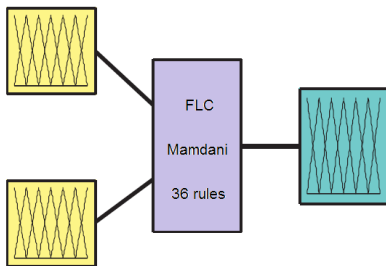


Figure 4: FLC control

V. SIMULATION

The success of the designed control system is due to the fact that the two degree of freedom manipulator answers were evaluated and evaluated. A software that updates the linearization coefficients and supervisor gains along the trajectory tracked by the manipulator is written in Matlab 14b. The parameters are updated 100 times over 10 seconds intervals. The desired maximum acceleration of the first joint of the manipulator in the orbital plane was set at 80 rad / sn² for the second joint and 45 rad/sn² for the second joint. The acceleration of the joints is by an accelerating acceleration, and the slowing and stopping of the joints are by a constant velocity and a decreasing acceleration. In simulations, the curves indicated by the dashed line are the reference or desired parameter value. The curves indicated by the straight line are the actual parameter values of the manipulator.

Parameter updates should be made more for the manipulator to be more sensitive and to reduce vibrations. Also, sudden changes in the currents of the articulating motors lead to increased system response vibrations and the need for powerful amplifiers. When a manipulator suddenly wants to be stopped after a sudden motion, the vibrations cause sudden stop and start of the manipulator. This situation delays the

system response. The system design should be done taking into account all these factors as well as the purpose and purpose of the manipulator. In the software, the structural parameters of the manipulator system, the parameters of the direct current motor, the parameter update frequency and the disturbing forces must be found directly and test simulations should be done.

In Figure 3, the desired reference angular acceleration-time graph of the first and second joints is shown. Figures 5-10 show the actual acceleration-time graphs of the first and second joints.

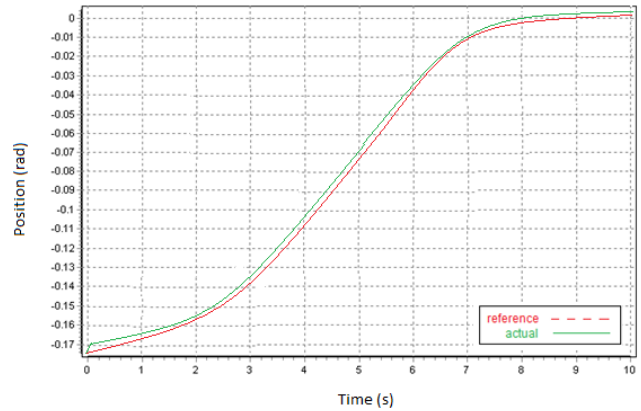


Figure 5: Position-time diagram for 1. Joint

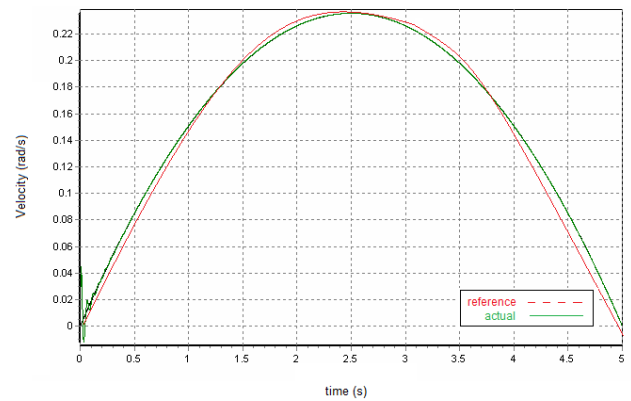


Figure 6: Velocity-time diagram for 1. Joint

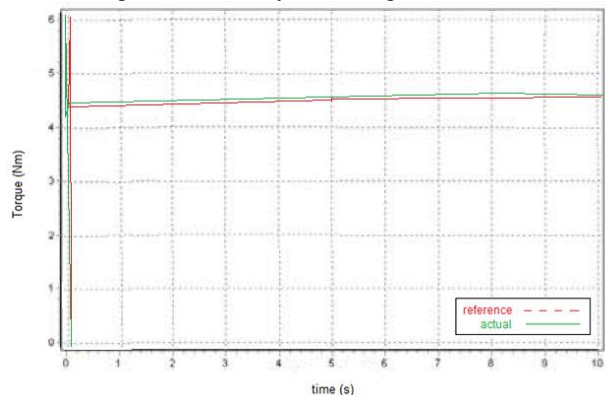


Figure 7: Torque-time diagram for 1. Joint

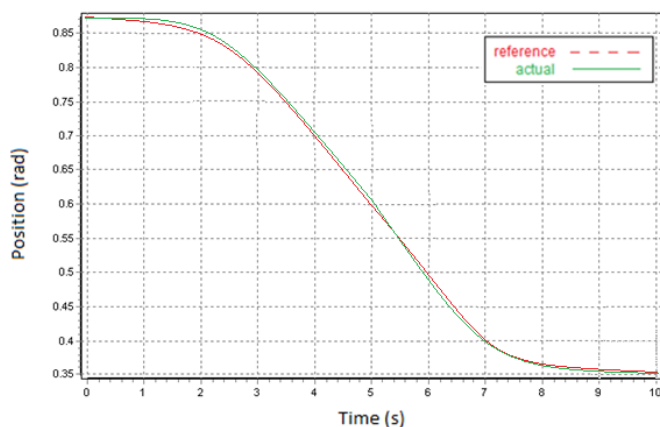


Figure 8: Position-time diagram for 2. joint

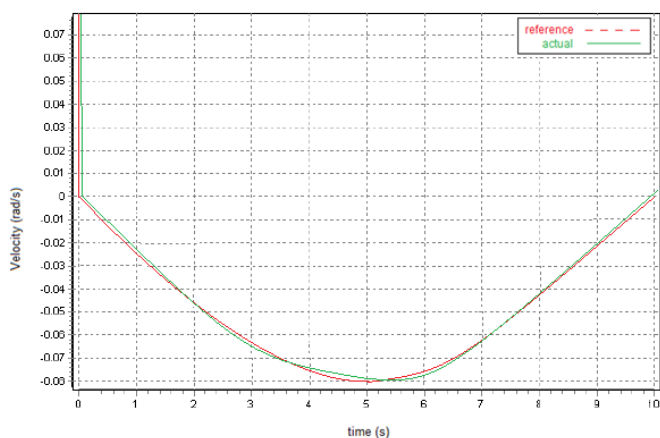


Figure 9: Velocity-time diagram for 2. joint

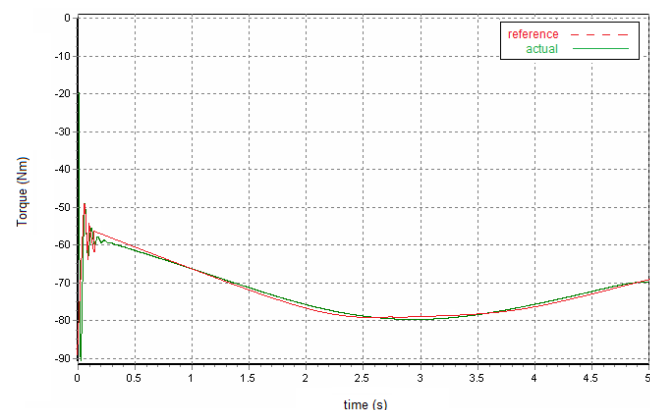


Figure 10: Torque-time diagram for 2. Jointmode power consumption was significantly reduced.

VI. CONCLUSION

Robot manipulator control, which is important for manipulator control, can move from any starting position of a robot manipulator end to a desired end position with minimum error. The fewer the squares of angular velocity errors of a joint, the less the robot manipulator shakes. Again, the smaller the angular misalignment of the joints, the farther the distal end of the robot manipulator to the target point is, the less the error

is. In the study, the independent joint control has been successfully carried out as a result of the reduction of the interaction between the joints. High resistance against external disturbing entrances. Since there is a feedback network, an inspection with a high resistance to decays has been carried out. No deterioration has been observed in system behavior at high acceleration movements (45 rad/s^2). Light and small motors can be used for manipulator design. Thus, the motions of joint motors can be reduced by limiting them. Equations follow the angular speed orbits with great accuracy. The angular speed deviations are mostly at the beginning of control and in the case of load drop. Simulation results show that the algorithms adapt themselves very quickly to the situation. These deviations are small enough to be neglected.

REFERENCES

- [1] Clarke, D. W., Zhang, L., Long-Range Predictive Control Using Weighting-Sequence Models, Proc. IEEE, 134, Pt. D(3): 187-195, 1987.
- [2] Soloway, D., Haley, P. J., Neural Generalized Predictive Control: A Newton-Raphson Implementation, Proceedings of the IEEE CCA/ISIC/CACSD, IEEE Paper No. ISIAC-TA5.2, Sept. 15-18, 1996.
- [3] Haley, P. J., Soloway, D., Gold, B., Real-Time Adaptive Control Using Neural Generalized Predictive Control, 1999 American Control Conference, San Diego, California, June 1999.
- [4] B. Armstrong, O. Khatib and J.Burdick, "The explicit dynamic model and inertial parameters of the PUMA 560 arm", IEEE Conf. on Robotics and Automation, pp. 510-518, April 1986.
- [5] Denavit, J., Hartenberg, R. S., A Kinematics Notation for Lower-Pair Mechanisms, J. Applied Mechanics, Vol. 22, pp. 215-221, 1955.
- [6] Bezine, H., Derbel, N., Alimi, A. M., Fuzzy control of robot manipulators : some issues on design and rule base size reduction, Engineering Applications of Artificial Intelligence, Volume 10, Issue 5, pp. 401-416, Sept. 2002.
- [7] Bezine, H., Derbel, N., Alimi, A. M., Fuzzy control of robot manipulators : some issues on design and rule base size reduction, Engineering Applications of Artificial Intelligence, Volume 15, Issue 5, pp. 401-416, Sept. 2002.
- [8] "ÜçEklemlı Bir Robot Kolunun NöroGenelleştirilmiş Öngörülü Kontrol İle Eklem Esaslı Yörünge Kontrolü", H. Temurtas, Doktora Tezi, 2004, Sakarya.
- [9] "The Operational Space Formulation Implementation to Aircraft Canopy Polishing Using a Mobile Manipulator", Rodrigo J., Marcelo H. Ang, Denny Oetomo, Oussama Khatib, Tao Ming Lim, SerYong Lim, International Conference on Robotics & Automation, May 2002, Washington D.C., p.p 400-4005.
- [10] Haley, P. J., Soloway, D., Gold, B., Real-Time Adaptive Control Using Neural Generalized Predictive Control, 1999 American Control Conference, San Diego, California, June 1999.
- [11] <http://www.rpautomation.com/Robotspecs/560spec.htm>
- [12] <http://www.rpautomation.com/Robotspecs/560spec.htm>

Usability of fuzzy logic control for performance of dual-axis solar tracking system

B.CIRAK¹, F.IRIM², S.ALKAN³

¹Karamanoglu Mehmetbey University, Karaman/Turkey, bcirak@kmu.edu.tr

²Konya Technical University, Konya/Turkey, fatih.irim@gmail.com

³Konya Technical University, Konya/Turkey, safa.alkan@gmail.com

Abstract - This paper describes fuzzy logic controller applied to a dual-axis sun tracking system. Sun tracker is the device that follows the position of the sun throughout the day to harness the output power. Sun tracking increases the output power production by keeping the panel parallel to the sun so that sun radiation makes 90° angle with panel. Solar tracking system is designed to optimize the operation of solar energy receivers. More solar energy is collected by the end of the day if solar receivers are installed with a tracker system. In this paper, a solar tracking system is modeled using Matlab/Simulink and a fuzzy logic control is designed for the control of this system. The generated controller was combined with the solar tracking system and the control was realized with the fuzzy logic controller in the Matlab/Simulink environment. Dual-axis solar tracking system with microcontrollers of fuzzy logic control was designed to increase the efficiency output obtained from solar energy and it was compared with the fixed system. In the moving system, mini PV panels are used as sensors to find the real position of the sun and that geared DC motors in the mechanism with PWM signals obtained from the fuzzy logic controllers were conducted in an intelligent way. All day long the electrical data obtained from fixed and tracking system was transferred to a computer online with the Arduino Due card. The voltage, current and power data of both systems were analysed through Matlab/Simulink software. When the data obtained from the designed prototypes was studied microcontroller-based solar tracking system was observed to have an 26.46% increase in efficiency according to the fixed system.

Keywords - Photovoltaic, Solar tracking, Fuzzy Logic Controller

I. INTRODUCTION

Renewable energy sources play an important role in electric power generation. There are various renewable sources which used for electric power generation, such as solar energy, wind energy, geothermal etc. Solar Energy is a good choice for electric power generation, since the solar energy is directly converted into electrical energy by solar photovoltaic modules. These modules are made up of silicon cells. When many such cells are connected in series we get a solar PV module. The current rating of the modules increases when the area of the individual cells is increased, and vice versa. When many such PV modules are connected in series and parallel combinations

we get a solar PV arrays, that suitable for obtaining higher power output. Solar energy is viewed as clean and renewable source of energy for the future. So the use of Photovoltaic systems has increased in many applications. That need to improve the materials and methods used to harness this power source. There are two major approaches; sun tracking and maximum power point tracking.

These two methods need efficient controllers. The controller may be conventional or intelligent such as Fuzzy Logic Controller (FLC). FLCs have the advantage to be relatively simple to design as they do not require the knowledge of the exact model and work well for nonlinear system. The applications for solar energy are increased, and that need to improve the materials and methods used to harness this power source. Main factors that affect the efficiency of the collection process are solar cell efficiency, intensity of source radiation and storage techniques. The efficiency of a solar cell is limited by materials used in solar cell manufacturing.

It is particularly difficult to make considerable improvements in the performance of the cell, and hence restricts the efficiency of the overall collection process. Therefore, the increase of the intensity of radiation received from the sun is the most attainable method of improving the performance of solar power. There are three major approaches for maximizing power extraction in solar systems. These methods needs controllers, may be intelligent such as fuzzy logic controller or conventional controller such as PID controller. The advantage of the fuzzy logic control is that it does not strictly need any mathematical model of the plant. It is based on plant operator experience, and it is very easy to apply. Hence, many complex systems can be controlled without knowing the exact mathematical model of the plant. In addition, fuzzy logic simplifies dealing with nonlinearities in systems. The nice thing about fuzzy logic control is that the linguistic system definition becomes the control algorithm [1-2].

Control theory has provided powerful regulator design tools for industrial processes. However, in many practical applications it is difficult to determine the controller parameters since the process and disturbance dynamics are

unknown. In this way, process parameters must be estimated. In addition, it is desirable to have a regulator that tunes its parameters in an online manner. Therefore, the designed controller must be composed of three parts: a parametric estimator, a linear controller and a block that determines the estimated process parameters used to calculate the controller parameters. The main reason for using an adaptive controller is when the process or its environment is continually changing as it is difficult to analyze such systems. To simplify the problem, one can assume that the process has unknown parameters. An important result of the self-adjusting regulator is that the controller parameters converge to the regulator that was designed even though the model structure is incorrect. In tracking control systems it is desirable for the controlled variable to follow the input signal. There are several types of systems for this purpose.

One can cite trajectory tracking of manipulating robots in which the robotic arm must follow a given trajectory; Solar thermal and photovoltaic tracker in which both the concentrated solar collector and the photovoltaic collector require the use of solar trackers to increase the area exposed directly by the sun. In photovoltaic systems the solar tracker maximizes energy production. Experimental results have shown that using trackers in PV modules has increased the annual energy production by more than 30 % compared to the same size and fixed slope photovoltaic systems. The controller type applied in this search is a self-tuning controller. This type of controller automatically adjusts its parameters to obtain the desired properties in closed loop. In several situations it is possible to reparametrize the process such that the model can be expressed in terms of the controller parameters. After realizing the system specifications in closed loop, the parameters of the plant are estimated taking into account these estimated parameters are treated as if they were the true parameters (principle of equivalence to certainty). These estimated parameters are used in the calculation of the control law. The article is organized into sections that present the proposed methodology, its development, the parametric estimator and adaptive algorithms, together with the results obtained [3-4].

In all photovoltaic systems, the increase in temperature has consequences such as shortening the life of solar panels, melting of cells by high temperatures and reduction of efficiency factors. If these drawbacks are brought to solar tracking systems, it can be noted that the efficiency at certain times can be virtually zero. Due to long exposure to radiation that would have a tracking system compared to a static system, the movement of the solar tracker would be totally inefficient. When considering these factors, it is observed that it is necessary that the system designed consider the monitoring of the sun taking into account both the incidence of solar radiation and the temperature that the panel has, in order to determine the ideal position. This work presents the design and implementation of a photovoltaic solar tracking system applying diffuse control in order to compare the efficiency of

this type of technologies in static mode and in constant movement [5].

II. THE EXPERIMENTAL SETUP

Photovoltaic (PV) Panel or Solar panels convert sunlight into electrical energy. When the sunlight hits the panels, direct current begins to be produced at the panels. Solar energy cells are connected according to the preferential power choices, either serial or parallel. The energy efficiency of a solar cell is measured with its yield. View of monocrystalline PV panel is given in Fig 1. The solar energy is a clean source of energy and the photo-voltaic (PV) solar panels convert the solar radiation into voltage. The sun tracking systems, in general, allow solar panels to collect up to 50 % more energy than that can be collected using stationary solar panels. In order to increase the power output from a PV panel, two different control schemes can be used, namely, the position feedback tracking and the optical feedback tracking. The mechanical setup of the sun tracker is shown in Fig. 1.

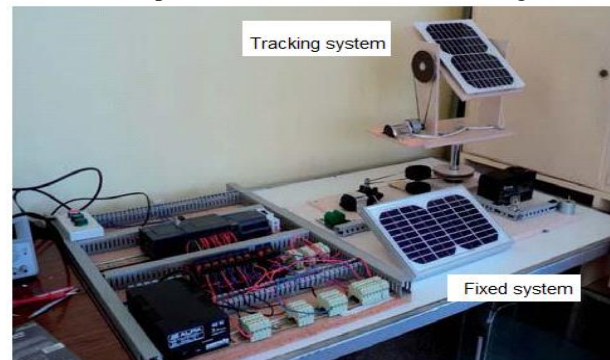


Figure 1: Experimental setup of tracking and fixed system

The main part of the setup is a circular turntable on top of which the solar panel and the optical sensors are mounted. The tracker rotates around the horizontal axis allowing for the East-West tracking of the sun. This structure is mounted on a frame which rotates around the azimuth axis allowing for the North-South tracking of the sun. Two dc motors are used to achieve these two directions of rotation. In this study, 4 mini PV panels were used to determine the position of the sun automatically to increase the efficiency of 20 watt electrical energy power obtained from solar panels. While ACS712 microcontroller current transducer supplies the current data of the panel, data of the voltage is provided with the trimpot of 100K Ω on the newly designed feeding card. Also the temperature of the panel is instantly checked with the PT100 temperature sensor. Linear actuator motors which provide the movement of the mechanical mechanism bearing the panel in two axis is controlled with MC33926 with motor driver and limit switches on actuator motors are used to prevent strain on mechanical parts. The data from sensors is collected in an online computer via the Arduino Due microcontroller. Fig 4 shows the correlation of the electrical and mechanical parts used in the system.

A. Fixed System

In fixed systems, solar cells are placed with a certain slope. Tilt angle will show variations according to regions and seasons. In the northern hemisphere PV systems are usually placed to the South with a particular point of view. To get the maximum yield from a fixed system the region's latitude angle ϕ and the sun's the position in the noon hours δ (north positive) should be taken in consideration. Accordingly, on 21 April 2018 the divergence angle of Karaman, where the PV system was established was obtained from the equation (1) and equation (2) was obtained from the angle PV module formed with the horizon [6-7].

$$\delta = 23.45 \sin \left(\frac{360(284+n)}{365} \right) \quad (1)$$

$$\theta = (\phi \pm \delta)^\circ \quad (2)$$

Where n is the day of the year and ϕ is the latitude angle of the region, "+" for winter and "-" for summer. The block diagram of the fixed system whose experimental study was done is provided in Fig 2. This system is generally, composed of solar panel, solar charge regulator, battery, measurement group, inverter and electronic load. Numeric data such as current, voltage and power of the electricity derived from solar panel in the fixed system, was recorded by Matlab software running on an online computer.

B. Tracking System

The solar tracking system whose prototype was produced has the capability to capture sun rays perpendicular to the panel from the sunrise to the sunset during the day. So by using sun rays in the most efficient way during the day it is possible to get the highest value from the solar energy. Solar tracking systems can be built with two axes just like single axis the system we designed has the ability to move along two axes to obtain full yield from the sun. System consists of the actuator motor, driver card, the Arduino microcontroller, 4 mini PV sensors determining the position of the sun, a computer which the data is recorded with Matlab/Simulink software, a battery, an inverter and an MPPT charging module. The block diagram of the system is given in Fig 2. Sensors were placed on the four corners of the solar PV Panel. The resulting electrical data obtained from sensors were used as input variables for the fuzzy logic unit used in Arduino Due. Here FLC processes data obtained from sensors in accordance with the base rule and sends the result obtained to motor driver card. Finally, actuator motors, solar PV panel are positioned to the position of the sun in the horizontal and vertical positions.

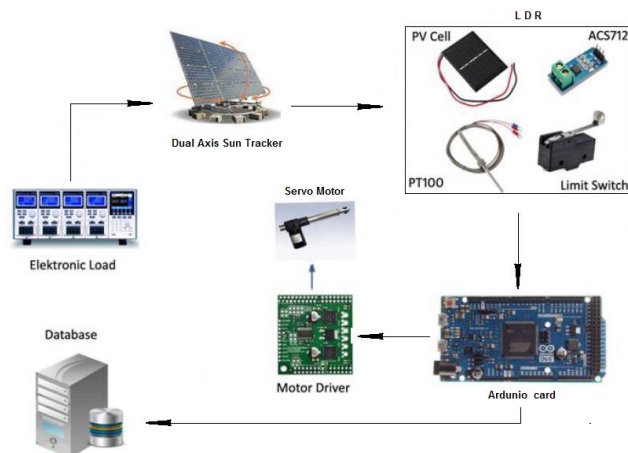


Figure 2: Parts of the dual-axis tracker

C. Servo Motor

The following elements are used for the operation of the servo motor used in the Sun tracker; 1. Servo motor, 2. Arduino card, 3. Breadboard, 4. Jumper cables. The circuit diagram of servo motor shows in Figure 3.

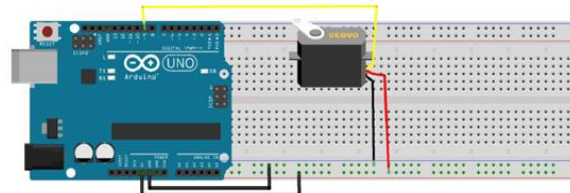


Figure 3: Sun tracker in Servo motor Arduino circuit diagram

The arduino program codes used for the servo motor are as follows;

```
#include <Servo.h> // include Servo library

Servo horizontal; // horizontal servo
int servoh = 90; // stand horizontal servo

Servo vertical; // vertical servo
int servov = 90; // stand vertical servo

// LDR pin connections
// name = analogpin;
int ldrlt = A0; //LDR top left
int ldr rt = A1; //LDR top right
int ldr ld = A2; //LDR down left
int ldr rd = A3; //ldr down right

void setup()
{
  Serial.begin(9600);
  // servo connections
  // name.attach(pin);
  horizontal.attach(9);
  vertical.attach(10);
}

void loop()
{
  int lt = analogRead(ldr lt); // top left
  int rt = analogRead(ldr rt); // top right
  int ld = analogRead(ldr ld); // down left
  int rd = analogRead(ldr rd); // down right

  int dtime = analogRead(A4)/20; // read
  potentiometers
  int tol = analogRead(A5)/4;
```

```

int avt = (lt + rt) / 2; // average value top
int avd = (ld + rd) / 2; // average value down
int avl = (lt + ld) / 2; // average value left
int avr = (rt + rd) / 2; // average value right

int dvert = avt - avd; // check the diffirence of up
and down
int dhoriz = avl - avr; // check the diffirence og
left and rigt

if (-1*tol > dvert || dvert > tol)
{
  if (avt > avd)
  {
    servov = ++servov;
    if (servov > 180)
    {
      servov = 180;
    }
  }
  else if (avt < avd)
  {
    servov = --servov;
    if (servov < 0)
    {
      servov = 0;
    }
  }
  vertical.write(servov);
}

if (-1*tol > dhoriz || dhoriz > tol)
{
  if (avl > avr)
  {
    servoh = --servoh;
    if (servoh < 0)
    {
      servoh = 0;
    }
  }
  else if (avl < avr)
  {
    servoh = ++servoh;
    if (servoh > 180)
    {
      servoh = 180;
    }
  }
  else if (avl == avr)
  {
    // nothing
  }
  horizontal.write(servoh);
}
delay(dtime);
}

```

D. LDR

In the PV panel following the sun with Arduino, LDR sensors are used. LDR light sensors are sensors that change resistance to light intensity. What need to do is to construct the algorithm according to the resistance values in the sunny environment and the shadow [8]. The dual axial sun tracker uses the following materials for the LDR; 1. LDR, 2. Led, 3. Resistor, 4. Arduino card, 5. Breadboard, 6. Jumper cables. The circuit diagram is as shown in Figure 4.

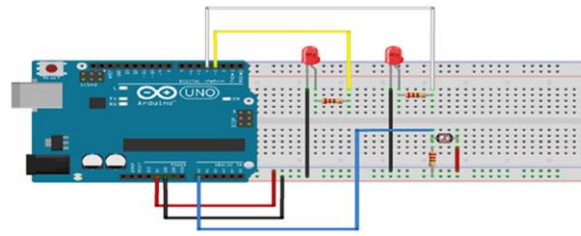


Figure 4: Sun tracker in LDR Arduino circuit diagram

In Fig. 5, horizontal and vertical rotations of the tracking system are shown by the sun angles [8].

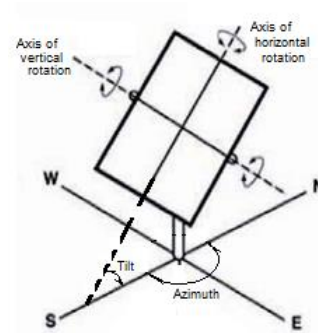


Figure 5: Rotation vertical axis, horizontal axis and sun angles in Tracker system

Where tilt angle is incline angle and azimuth angle is the angle that indicates the deviation of the sun's rays in the clockwise direction with respect to the north. For example, it is 180° at 12.00. The solar tracking system with arduino is the most accurate to use LDR sensors for experimental setup. LDR light sensors are sensors that change resistance by the intensity of light. It is necessary to construct the algorithm according to the values of the resistance in the sunny environment and the resistance in the shadow [9]. LDR positions of the sensor shown in Figure 6.

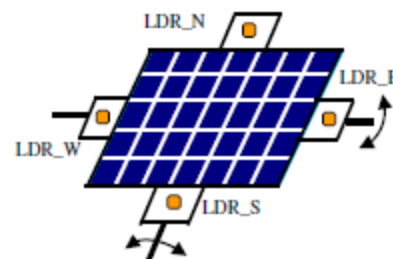


Figure 6: LDR positions

Servo motor is also used to provide rotation. Materials used in total or generally in the sun tracker:

1. Arduino card
2. 2 piece servo motor
3. 4 piece LDR sensor
4. 4 piece 10k resistor
5. 2 piece 10k potentiometer

The Sun tracker circuit diagram is shown in Figure 7 [10].

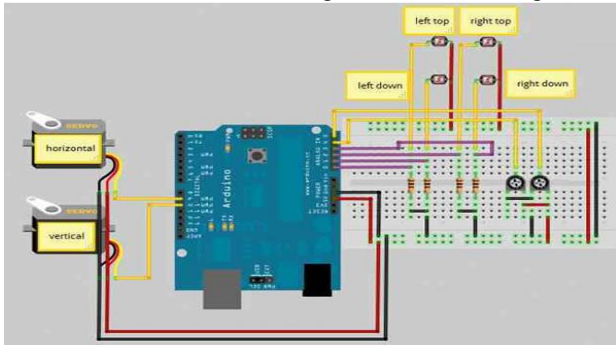


Figure 7: Sun tracker circuit diagram

III. THE FUZZY LOGIC CONTROL

The block diagram of the tracking system is given in Figure 8.

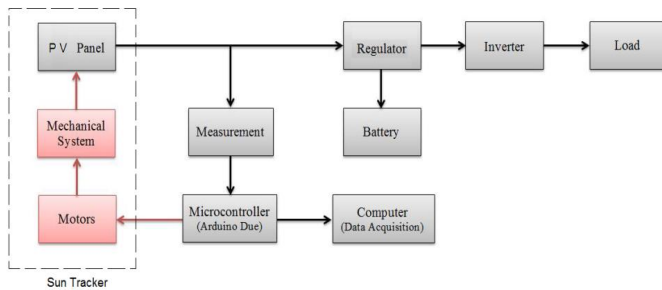


Figure 8: The block diagram tracking system.

In the position feedback tracking system, shown in Figure 9, the objective is to orient the solar panel such that it coincides with a reference direction θ_r . The inclination of the incident sun rays relative to the azimuth at any location (latitude and longitude lines) at any instant of time in any day of the year can be determined based on simple geometric calculations [11-12].

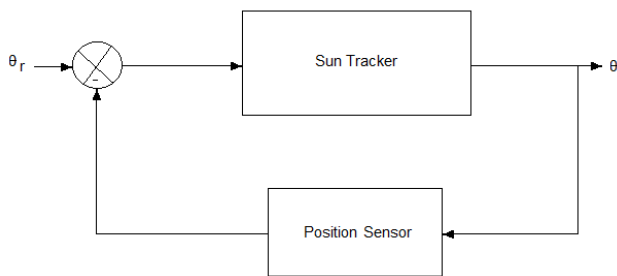


Figure 9: Position feedback tracking system

This inclination represents the reference direction. In this case the tracking system should be able to recognize and maintain the current inclination of the solar panel. The controller has to produce a correct action to rotate the panel from the current position such that the error ($\theta_r - \theta$) is minimized. The operation of this type of tracking is based on rotating the panel such that it is perpendicular to the incident sun rays. In this case, all the sensors are equally

illuminated with no shading effect. When the sun moves a fuzzy logic control algorithm for motion control systems expresses the knowledge of the system behavior in linguistic control rules and converts them into crisp control law. Therefore fuzzy logic control techniques can be applied to control complex nonlinear systems with unknown or unmodeled dynamics. The sun tracking system considered in this paper has unknown model and unknown parameters [13].

The system dynamics can be approximately modeled by four linearized differential equations, two of them represent the electric circuit of each motor and the other equations represent the mechanical equation in the East-West and North-South directions. The moment of inertia, friction coefficient and backlash of the rotating parts are unknown. However, the system behavior is fully understood and the motor voltages (control signal) can be related to the sensor voltages (input signal) in terms of linguistic if-then rules. Therefore, in order to avoid system modeling and parameter identification, a fuzzy logic-based control algorithm utilizing the knowledge of the system behavior is developed. Two fuzzy controllers are proposed for each motor to produce proper motor voltage in order to track the solar rays. A typical FLC includes three basic components, an input signal fuzzification, a fuzzy engine, and an output signal defuzzification [14-15].

The basic structure of a fuzzy logic controller (FLC) is shown in Figure 10.

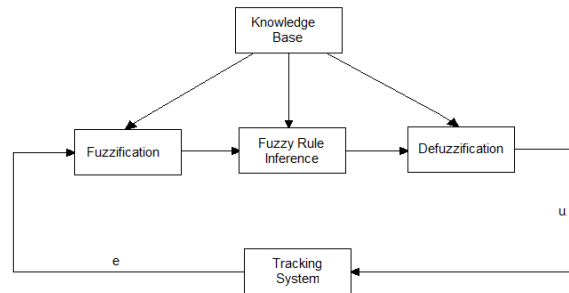


Figure 10: Structure of a FLC

In the fuzzification block, the continuous input signal is transformed into linguistic fuzzy variables. The fuzzy engine handles the rule inference where human experience can easily be injected through linguistic rules. The defuzzification module performs the mapping from a space of fuzzy control actions defined over an output universe of discourse into a space of crisp control actions that can be applied to the sun tracker. The design procedure of the fuzzy-logic controller is briefly described in the following subsections[16-17].

A. Fuzzification

In a fuzzy system fuzzy inference engine uses fuzzy sets and rule base instead of mathematical equations. In the fuzzy system two sources of information are taken in consideration as a combination,one being observation and measured values, and the other being the opinions of experts .This means that in addition to the numeric data base, existence of the verbal rule base is available. Expert opinions work to model out the uncertainties unknown in the system [18].

Fuzzy logic controller (FLC) based on Mamdani fuzzy inference system was designed to increase the efficiency of the energy obtained from track system and to obtain the desired quality power. The first of the two input signals is error signal $e(t)$ and the second one is $de(t)/d(t)$ the change of error signal according to time. Controller's output signal is PWM control signal that provides controls of dc motors to set the desired extent according to the position of the sun.In Figure 11 shows input and output of fuzzy logic controller.

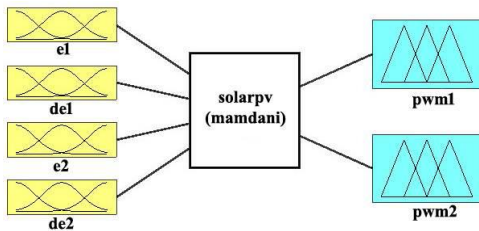


Figure 11: Input and Output of fuzzy logic controller

For each rule, holistic inference of inference system is calculated with the equation (3).

$$PWM = \frac{\sum_{i=1}^N w_i z_i}{\sum_{i=1}^N w_i} \tag{3}$$

Here, N; number of rules, W; the weight of rules, Z; output level. The error signal $e(t)$ from the input variables of FLC and change signal in the error $de(t)/d(t)$ are NB (negative big), NS (negative small), ZE (zero), PS (positive small) and PB (positive big) as linguistic variables. Triangle type the membership function was used in fuzzy inference system. When creating rule base" and " operator of logical operations is used. In Figure 11 a block diagram of fuzzy logic controller designed in the system with four entries and two output variables is given [19]. The input variables to the controller are defined as :

$$E_{SN} = E_1 - E_2 \tag{4}$$

$$E_{EW} = E_3 - E_4 \tag{5}$$

Where E_{SN} and E_{EW} are the voltage errors in the South-North and East-West directions respectively and E_1, E_2, E_3 and E_4 are the sensor output voltages. These variables are normalized using appropriate scaling factors and then converted to linguistic variables which may be viewed as

labels of fuzzy sets. Seven linguistic variables are used for the scaled inputs, namely, positive big (PB), positive medium (PM), positive small (PS), zero (Z), negative small (NS), negative medium (NM) and negative big (NB). A fuzzy set is defined by assigning the grade of membership values to each element in the universe of discourse. The choice of membership function is mainly dependent on the designer preference [20-21].

In this paper, triangular-shaped membership functions, shown in Figure 12 are used.

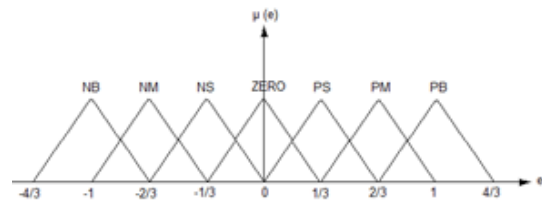


Figure 12: Membership function of the input variables

The FLC model in Matlab/Simulink software was used in the system. As seen in the block diagram of simulation given in Fig 13 data about the position of the sun provided by 4 sensors was read by 0, 1, 2, and 3 ADC input pins of Arduino Due microcontroller and after the difference was taken e_1 and e_2 error signals were obtained. These error signals and the change of error according to time were applied to FLC block. According to the rule base of FLC output PWM signals were obtained from the 13 and 14 pins and they were applied to MC33926 motor driver module.

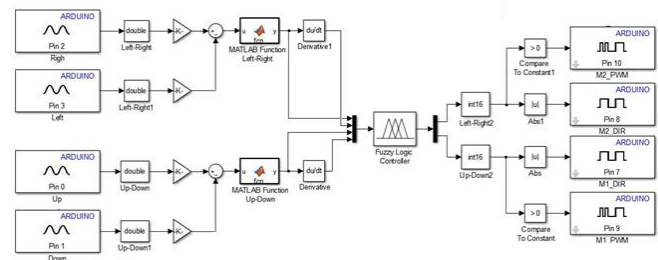


Figure 13: Simulation block diagrams of solar tracking system

As the system tracks the sun voltage and current data of the PV panel is multiplied and the power of the panel is calculated. With the blocks of the scope and workspace, voltage, current and power data of fixed and movable panels was recorded by Matlab and yield analysis was conducted. In Figure 14 connection blocks of Arduino Due microcontroller card of the fixed and movable panels can be seen.

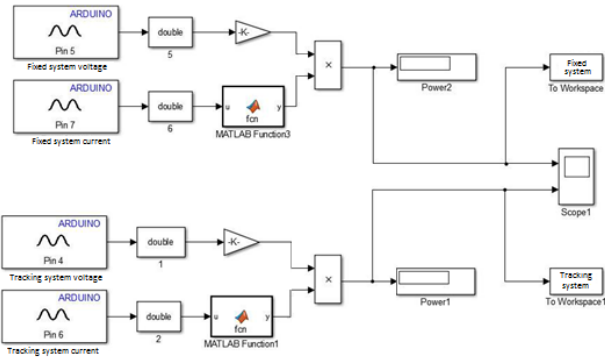


Figure 14: Model of the tracking system in Matlab/Simulink

IV. EXPERIMENTAL RESULTS

The efficiency of sunlight can show changes according to time and geographic structure. Turkey has favourable geographic coordinates, soithas the high solar energy potential. This experimental study was carried out in Karaman-City center / Turkey on a sunny day on 4 february 2018. The average temperature of the experiment day was try 11°Cand the average wind speed was 3 m/s.

The angle of the fixed solar panel with the horizon was computed using equations (4) and (5) and it read 60.54°. With the Sunrise (8:00) the system started to record the data and continued until (17:30) the sunset.Voltage, current and power data of both the solar tracking system and the fixed system was collected by an online computer all day. Some of this data can be seen in Table 1. When the data was analysed, the electrical output size of the solar tracking system, as expected, was higher than the fixed system. Where, U_T : voltage values of tracker system (Volt), I_T : current values of tracker system (Amper), P_T : power values of tracker system (Watt), U_F : voltage values of fixed system (Volt), I_F : current values of fixed system (Amper), P_F : power values of fixed system (Watt)

Table 1: Obtained by the data of solar systems

Time	Tracker system			Fixed system		
	U_T	I_T	P_T	U_F	I_F	P_F
08:00	0,053	0,069	0,00148	0,040	0,046	0,00088
08:30	0,292	0,383	0,09977	0,098	0,157	0,01047
09:00	1,198	0,634	0,72899	0,273	0,359	0,08963
09:30	1,641	0,694	1,11355	0,292	0,371	0,09469
10:00	3,740	0,991	3,63694	1,043	0,597	0,59034

15:00	6,289	1,290	7,97580	5,588	1,199	6,64522
16:30	3,734	0,998	3,63423	2,471	0,834	1,99197
17:00	0,392	0,433	0,15298	0,396	0,329	0,11739
17:30	0,066	0,098	0,00425	0,055	0,077	0,00199

In the chart of Figure 15 the voltage values of the both panels are compared during the time span from the sunrise to the sunset. When the graphics are examined voltage values between 12:00 – 15:00 are very close to each other but in the

early hours of the morning and the sun sets the gap between the voltages values are observed to increase.

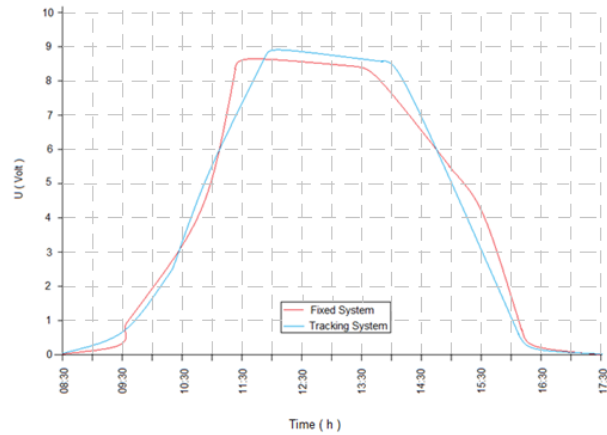


Figure 15: U_T and U_F values

When the chart in Figure 16 is examined tracking system provides much more current value with the load than the fixed system at noon hours. This value around 9:33 is decreased to 174 % and 4 % to around 12:45. Both panels' currents are nearly the same from 12:30 to 13:33 However, from 13:33 to sunset the current levels increase gradually from 8% to 51%. Tracking system proves to be much more advantageous than the fixed system.

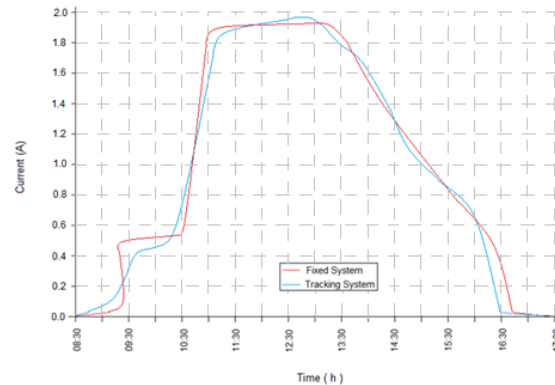


Figure 16: I_T and I_F values

When power data obtained from the fixed and moving panels in Figure 17 is calculated, the solar tracker has produced 31.52 % more power than the fixed system.

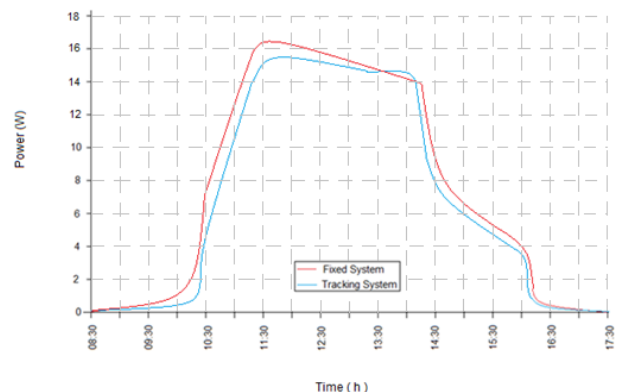


Figure 17: P_T and P_F values

V. CONCLUSION

With smart solar tracking based on fuzzy logic control system it is intended the Sun's irradiance can be followed with maximum density. This experimental work proved that the tracking system is more efficient than the fixed system. Solar energy has become one of the important types of alternative energy sources, such reasons as accessibility, cost efficient in production and low priced installation costs have made it favourable. But one of the problems of solar energy technology is that we should be able to increase the yield of solar panel output power by collecting as much sun rays as possible. The system we designed will contribute a solution to this problem. Clearly the tracking system we designed improved the output yield by 31.52 % when compared to the fixed panel. Besides actuator motors which enable the movement of the panel did not operate at maximum level and because it was controlled by the PWM modulation in smart mode power consumption was significantly reduced.

REFERENCES

- [1] Abdallah, S. "The effect of using Sun tracking systems on the voltage-current characteristics and power generation of at plate photovoltaics." *Energy Conversion and Management* 2004, 45 (11-12), 1671 -1679.
- [2] Ahmet Kaysal , The Design of Two Axis Solar Tracking System Based on Fuzzy Logic Control and Efficiency Analysis, *International Journal of Advanced Research in Electrical, Electronics and Instrumentation Engineering* Vol. 5, Issue 12, December 2016
- [3] Arian Bahrami; Chiemeka Onyeka Okoye; Ugur Atikol, Technical and economic assessment of fixed, single and dual-axis tracking PV panels in low latitude countries. *Renewable Energy* 2017, 113, 563-579.
- [4] A.Zakariah, J. J. Jamian and M. A. Yunus, Dual-Axis solar tracking system based on fuzzy logic control and light dependent resistors as feedback path elements, *IEEE Student Conference on Research and Development (SCORED)*, 2015, 139-144.
- [5] Bakhshi, R.; Sadeh, J.A. comprehensive economic analysis method for selecting the PV array structure in grid-connected photovoltaic systems. *Renewable Energy* 2016, 94, 524-536.
- [6] Chiesi, M.; Scarselli, E.F.; Guerrieri, R. Run-time detection and correction of heliostat tracking errors. *Renewable Energy* 2017, 105, 702-711.
- [7] Fathabadi, H. Novel high efficient offline sensorless dual-axis solar tracker for using in photovoltaic systems and solar concentrators. *Renewable Energy* 2016, 95, 485-494.
- [8] G.M. Tina, F. Arcidiacono and A. Gagliano, Intelligent sun-tracking system based on multiple photodiode sensors for maximization of photovoltaic energy production, *Mathematics and Computers in Simulation*, 91, 2013, 16-28.
- [9] J.A. Duffie and W.A. Beckman, *Solar engineering of thermal processes* (Canada: Wiley-Interscience Publication, 2013).
- [10] J.L. Diaz-Bernabe and A. Morales-Acevedo, Photovoltaic module simulator implemented in PICE and simulink, *12th International Conference on Electrical Engineering, Computing Science and Automatic Control (CCE)*, 2015, 1-5.
- [11] Lu, J.; Hajimirza, S. Optimizing sun-tracking angle for higher irradiance collection of PV panels using a particle-based dust accumulation model with gravity effect. *Solar Energy* 2017, 158, 71-82.
- [12] Natarajan, M.; Srinivas, T. Experimental and simulation studies on a novel gravity based passive tracking system for a linear solar concentrating collector. *Renewable Energy* 2017, 105, 312-323.
- [13] Mohammed S. EL-Moghany, Sun and Maximum Power Point Tracking in Solar Array systems Using Fuzzy Controllers Via FPGA, Master Thesis of Science in Electrical Engineering, The Islamic University Faculty of Engineering Electrical Engineering- 2011
- [14] Mousazadeh, H.; Keyhani, A.; Javadi, A.; Mobli, H.; Abrinia, K.; Sharifi, A. A review of principle and Sun-tracking methods for maximizing solar systems output. *Renewable and Sustainable Energy Reviews* 2009, 13(8), 1800 -1818.
- [15] Nuwayhid, R.Y.; Mrad, F.; Abu-Said, R. The realization of a simple solar tracking concentrator for the university research applications. *Renewable Energy* 2001, 24(2), 207-222.
- [16] Roth, P.; Georgiev, A.; Boudinov, H. Design and construction of a system for sun-tracking. *Renewable Energy* 2004, 29(3), 393-402.
- [17] Sharan, A.M.; Prateek, M. Automation of minimum torque-based accurate solar tracking systems using microprocessors. *Journal of Indian Institute of Science* 2006, 86(5), 415-437.
- [18] Soulayman, S. Comments on 'Optimum tilt angle for flat plate collectors all over the World – A declination dependence formula and comparisons of three solar radiation models' by Stanciu, C., Stanciu, D., *Energy Conversion and Management* 2015, 93, 448-449.
- [19] Stanciu, C.; Stanciu, D. Optimum tilt angle for flat plate collectors all over the World – A declination dependence formula and comparisons of three solar radiation models, *Energy Conversion and Management* 2014, 81 , 133-143.
- [20] Turkish State Meteorological Service, Republic of Turkey Ministry of Environment and Forestry
- [21] Z. Şen, Principles of Fuzzy Logic and Modeling, (İstanbul: Water Foundation Publication, 2009.

Investigation of Concrete Slab Crack When Placed Directly on Clay

H.CANAKCI¹ and A. ABDULLAH¹

¹ Gaziantep University, Gaziantep/Turkey, canakci@gantep.edu.tr

¹Gaziantep University, Gaziantep/Turkey, ahmed.gau88@yahoo.com

Abstract - In this study, Investigation of concrete slab cracks when placed directly on clay, ultrasonic pulse velocity, cracks depth, modulus of elasticity and compressive strength were investigated. A total of eight SSC mixtures were produced with 500 kg/m³ of total cementitious materials content and with a constant water/binder ratio of (0.55). each SSC mixture were casted over clay layer, each layer containing various water content, SSC samples were either cured by spraying at 23°C or maximum temperature of 28 days curing period. Test results revealed that 28-days compressive strength enhanced while leading to reduce in ultrasonic pulse velocity, it was found that the SSC mixtures that placed over high clay water content had higher compressive strength and lower dry shrinkage values compared to the samples that casted over low water content clay. However e-modulus of elasticity increased due to dry shrinkage.

Keywords - clay, ultrasonic pulse velocity, compressive strength, crack depth, dry shrinkage.

I. INTRODUCTION

In general, all the structures and buildings strength lies in its foundation which its main purpose is to hold and keep the structure upright and safely. Oppositely, a poor constructed foundation can cause damage and dangerous to human and neighborhood.

With the development of structure building these days, it is highly important to simulate the quality of foundation. The foundations have three major roles in the construction; support and distribute the load of the building, support the building and occupants of the building from the nature calamities such as earthquake, floods, and strong winds etc., also the foundation must be built such that it keeps protected from ground moisture in order not to leak out to the structure and causing weakness to the building.

In this study, tests had been carried out on a concrete foundation placed on clay soil with different water content ratio in order to estimate the water content that can carry the foundation safely and with minimum cracks.

The clay soil has a property that makes it consider as not an ideal choice to construct above without stabilization or treatment (Coduto 1999). The clay soil takes on significantly amount of water and expands which can cause the foundation to shift upward or downward (Grim, 1953; Das and Sobhan, 2013). Over time, this shifts can lead to a serious foundation cracking. The clayey soil performance very good at the optimum water content, when the amount of water rises above the optimum point the strength and the stiffness decrease noticeably (Dhakal, 2012). Studying the early age cracking

and the shrinkage behavior of concrete structure is very important, especially of that structures exposed to outdoor environmental and that that repeated heavy service load.

The soil properties is highly effected the reinforced concrete structures the random and nonlinear behavior of soil may lead to insufficient reliability levels (Kamel Bezih, 2015). The soil-structure interaction can cause reliable failure to the reinforced concrete structure especially when nonlinear behavior of soil is

considered •

II. LITERATURE REVIEW

R.R. Shakir, Jungao Zhu (2009) tested the simple shear of interface between clay and concrete. The samples were prepared at the same dry density and different water content ratio. They used two types of concrete, relatively smooth and relatively rough surface roughness. The results showed that the interface shear strength increases by increasing water content especially at the clay-rough concrete case. Also, two types of interface failure mechanism may change each other at different water content.

Canakci (2011) investigated the interface frictional resistance between organic soil and construction materials (concrete, wood, and metal). Direct shear test was performed to the samples of three fixed water content of the organic soil (0%, 25%, 50%, and 75%). Three different normal forces were used and maximum shear stress at 10% strain rate. The results indicated that the organic soil water content, surface roughness, and type of the material should be studied while investigation of interface friction angle of the organic soil-construction materials.

Chris Ramseyer (2015) studied behavior of concrete slab placed on ground at controlled environmental to understand the performance of the slab which is exposed to environment at the top and moisture ground at the bottom. They used different types of concrete (normal strength concrete, high strength concrete, concrete with shrinkage reducing, and concrete with calcium sulfoaluminate cement). Tests carried out to examine the joint movement, the effects and difference of temperature and humidity over the slab depth, and also the material characteristic tests. The results indicated that the normal strength concrete and high strength concrete show crack and continued with crack growth at over the age of 600 days. While the behavior of concrete using calcium

sulfoaluminate cement was very stable and showed no long term shrinkage, wrapping or cracking. The concrete with shrinkage reducing in its mixtures show minor impact at early age and limited effect on long term sectional stability. Boukhelkhal Djamil (2018) investigated the effect of adding admixtures such as limestone powder, granulated slag, natural pozzolana on the correlation factor (R^2) between compressive strength and pulse velocity of the self-compacted concrete (SCC) which is cured at 3, 7, 28, and 90 days. The results showed that it is possible to develop a good correlation factor for the relation between compressive strength and pulse velocity such as ($R^2 = 0.85$) in case of adding granulated slag and ($R^2 = 0.72$) by adding stone powder but lowest correlation ($R^2 = 0.69$) in case of adding pozzolana.

III. MATERIALS AND EXPERIMENTAL WORKS

A. Materials

1) Clayey soil

The soil used to treat in this study was collected from Gaziantep University campus (TURKEY). The soil classified according to ASTM D2487-2000 as CL. The particle size distribution of the soil is showing in Figure 1.

Table 1 showing some engineering properties that were obtained during the laboratory tests performed to the soil.

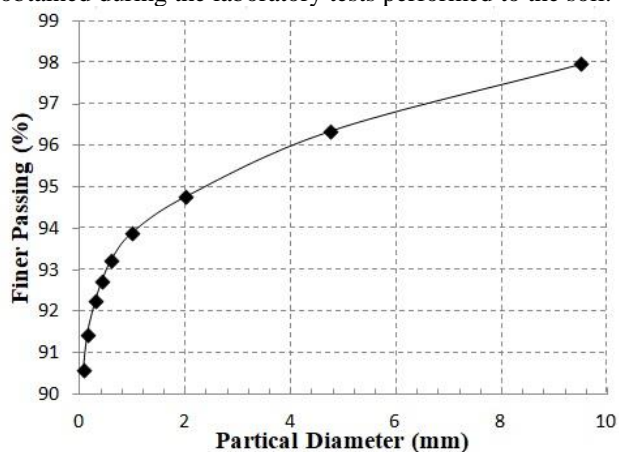


Figure 1: Particle size distribution of soil.

Table 1 Some engineering propertied of the untreated soil.

Properties of untreated soil	Results
Liquid limit (LL) %	41
Plastic limit (PL) %	25
Plasticity index (PI) %	16
Specific gravity, GS	2.77
Classification (USCS)	CL
Swelling potential %	3.58

2) Cement

Ordinary Portland cement (PC CEM, I 42.5R) conforming to the TS EN 197-1, which mainly based on the European EN

197-1, used in this study. It had a specific gravity of 3.15 g/cm³ and specific surface area of 326 m²/kg. It was utilized in the production of concrete. Physical and chemical properties of the cement are given in Table 2.

Table 2 Properties of plain Portland cement (CEM I 42.5R).

Composition	Percentage (%)
SiO ₂	19.79
Al ₂ O ₃	3.85
Fe ₂ O ₃	4.15
CaO	63.84
MgO	3.22
SO ₃	2.755
Na ₂ O	-
K ₂ O	-
Cl	0.0063
Insoluble residue	0.34
Loss on ignition	0.87
Free lime	1.28
Specific gravity (gr/cm ³)	3.12
Specific surface (cm ² /gr)	3349

3) Aggregate

River gravel with a greatest size of 16 mm was used as a coarse aggregate while the mixture of nature sand with a maximum size of 4 mm was as a fine aggregate. Nature sand and river gravel had the specific gravity of 2.66 and 2.72 and the fineness modulus of 2.79 and 5.68, respectively. The sieve analysis results of nature aggregates are presented in Figure 2 and Table 3.

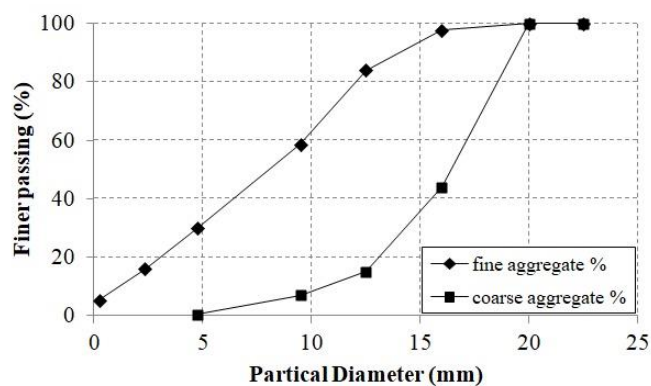


Figure 2: Particle size distribution of soil.

Table 3: Physical properties and sieve analysis of the aggregate.

Sieve size	Fine aggregate %	Coarse aggregate %
16	100	100
8	99.7	31.5
4	94.5	0.4
2	58.7	0
1	38.2	0
0.5	24.9	0
0.25	5.4	0
Fineness modulus	2.79	5.68
Specific gravity	2.66	2.72

B) Experimental works

1. Ultrasonic pulse velocity (UPV)

Non-destructive test has been applied to measure damage in structures. Common structures are assessed with the use of practical and easy application of ultrasonic pulse velocity (UPV). This study discusses the use of ultrasound with the time of flight to estimate the depth of surface opening cracks and S-P- waves Transducers. This technique is a very useful tool for practical applications. It is inexpensive, simple and easy to perform, giving a rapid indication of the extension of cracking.

2. Surface opening cracks by ultra-sonic method

Surface opening cracks often occurs in concrete they may appear as a consequence of several degradation mechanisms such as repeated loading, differential settlement and drying shrinkage Figure 3. While in some cases, surface cracks may only affect the aesthetics of the concrete surface, in most cases they are an indication of structural distress or decreased durability.

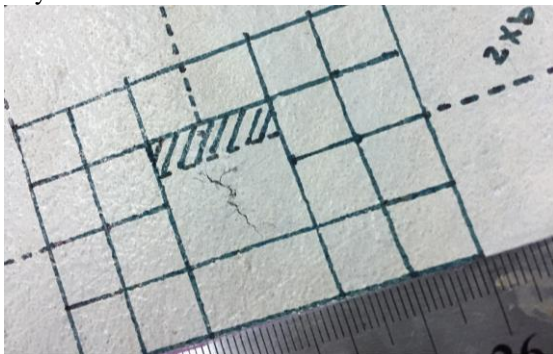


Figure 3: Open surface cracks that appeared after 28 days of curing.

In this study crack depth non-destructively determined by the time of flight diffraction technique BS 1881: Part 203. In this technique, stress waves are generated on one side of the crack, with wave arrival times monitored by a transducer placed on

the opposite side of the crack Figure 4 Stress waves can be generated by a mechanical pulse, such as given by ultrasound equipment's.

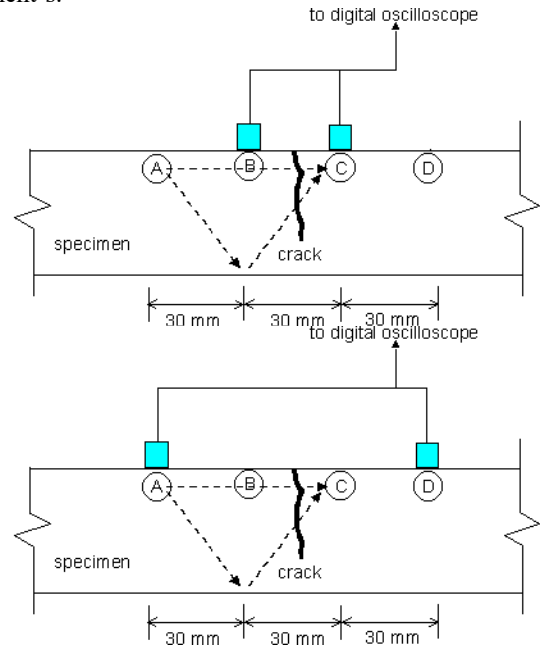


Figure 4: Crack depth measurement by ultra-sonic method.

3. S-P wave's measurement

We measured the P-wave velocity of concrete, V_P , according to BS 1881 using a pair of P-wave transducers (MK-954 transmitters and receivers) connected to a pulse-receiver (Ultrasonic-Pundit lab). The transmitter was driven by a 200V square pulse, generating a transverse (transmitter and receiver), and cross marks indicate the average P-wave velocity between two transducers. We acquired the transmitter and conditioned receiver signals using a high-speed (1MHz sampling rate) analog to digital data acquisition board. We developed a computer algorithm based on a fixed threshold level to determine the time of flight using the digitally acquired waveforms. Figure 5 presents a typical signal of the transmitter and receiver transducers.

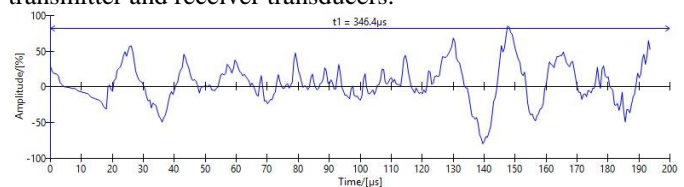


Figure 5: Typical signal of the transmitter and receiver transducers on computer.

For effective S-wave measurement we made a total of 20 direct S-wave measurements on each concrete slab using the same coordinate system as for the P-wave measurement. we labeled the gridlines along the width of the specimens as axes AB, CD, EF, and GH and those along the length of the

specimens as axes I, II, III, IV, and V. We carried out direct measurements at a single position because we used the pulse-echo method see Figure 6

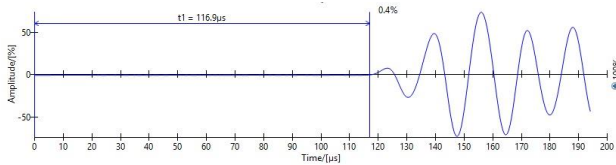


Figure 6: S-wave signal of the transmitter and receiver transducers on computer.

By measuring P-wave transmission time and as S-wave transmission time with Ultrasonic device we able to determine the P-wave modulus (M) and the shear modulus (G).

P-wave modulus (M):

$$M = \rho V_p^2$$

Where:

ρ = density of concrete

V_p = pulse velocity of the P-wave

Shear modulus (G):

$$G = \rho V_s^2$$

Where:

ρ = density of concrete

V_s = pulse velocity of the S-wave

4. Compressive Strength

For compressive strength measurement of SCCs, 150x150 mm cubes, 100x50 mm cylinders were tested according to ASTM C 39 by means of a 3000 KN capacity testing machine. The test was conducted on two 150x150 mm cubes, 100x50 mm cylinders for each mixture at the ages of 28 days. The compressive strength was computed from average of two cubes, cylinders at each testing age.

5. Crack width by microscope

A portable Microscope were used in this study for measuring open surface cracks width in concrete slabs after 28 days of curing. Specification of device listed in Table 4.

Table 4: Specification of the microscope device.

Magnification	X40
Power	1.5v battery for light source
Dimensions	Microscope:130mm high x 80mm x35mm
Weight	659g including case

I. RESULTS AND DISCUSSIONS

A) Ultrasonic Pulse Velocity (UPV)

Table 5 and Figure 7 shows the UPV values of the concrete specimens cured for 28 days. As expected, Figure 8 shows that the UPV increasing with specimens had low clay water content, (*Ultrasonics* 38, no. 1-8 (2000): 546-552). Used in this study. The relations between UPV and water content was obtained using:

$$c = 0.2 / (T_d - 0.6) \times 10^{-6}$$

Table 5: Results of UPV for each water content ratio.

Mix	UPV m/s
M1 0% CWC	8787
M2 5% CWC	8489
M3 10% CWC	6219
M4 15% CWC	5928
M5 20% CWC	4277
M6 25% CWC	4068
M7 30% CWC	3925
M8 35% CWC	3666

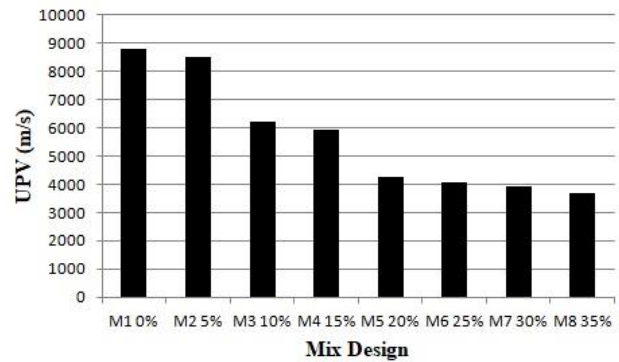


Figure 7: UPV values for concrete specimens cured for 28 days.

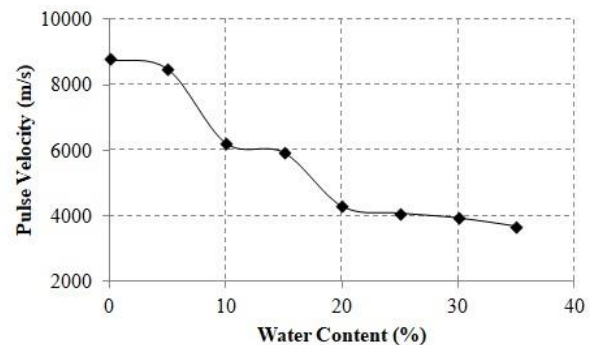


Figure 8: Relationship between UPV and water content of clay.

B) Compressive strength

Variations in the compressive strength of cubes and

cylinder core samples of concretes measured at 28 days, are tabulated Table 6 and presented in Figure 8 and 9. Two series of concrete having initial compressive strengths of about 22 and 30 MPa were achieved for 0% and 35% clay water content, respectively. It was observed that compressive strength decreased when concrete were placed over clay with low water content percentage this was due to loss of capillary water (Drying shrinkage). Contracting of hardened concrete mixture due to loss of capillary water is called Drying Shrinkage Figure 10. This shrinkage causes an increase in the tensile stress which is mean decrease in compressive strength. Several studies and investigations have demonstrated that adequate and proper curing of concrete is the most appropriate step to prevent shrinkages and developing a high degree of the desirable properties of concrete.

Table 6: Results of UPV for each water content ratio

Mix	UPV m/s
M1 0% CWC	8787
M2 5% CWC	8489
M3 10% CWC	6219
M4 15% CWC	5928
M5 20% CWC	4277
M6 25% CWC	4068
M7 30% CWC	3925
M8 35% CWC	3666

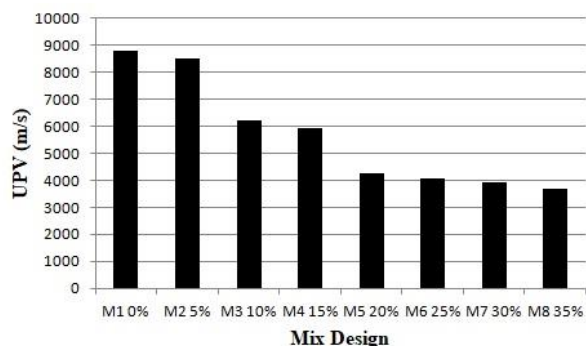


Figure 8: UPV values for concrete specimens cured for 28 days.

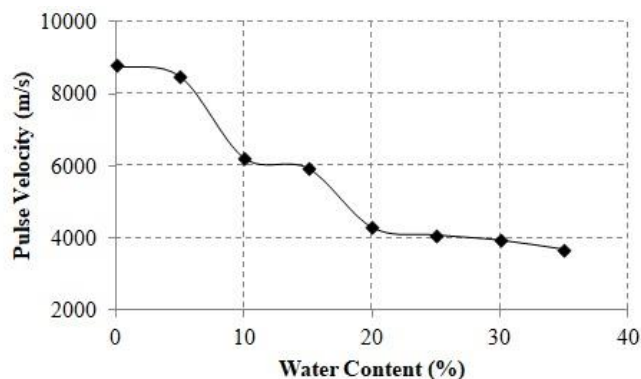


Figure 9: Relationship between UPV and water content of clay.

II. CONCLUSION

- 1- The changing in water content of the compacted clay effected the compressive strength of the concrete that placed directly above in a positive manner. The compressive strength recorded high at the high water content.
- 2- The shrinkage of concrete influenced inversely with the water content. The more water content of the clay, the less shrinkage of concrete.
- 3- The water content effected the ultrasonic pulse velocity (UPV). The UPV changed from 8787 m/s to 3666 m/s by changing the water content from 0% to 35%.
- 4- The relationship between the compressive strength and the UPV of the concrete considered to be linear relationship with a very good correlation factor ($R^2 = 0.96$).
- 5- E-modulus increases with the increasing of water content.
- 6- S-waves increased with the high water content while p-waves decreased with increasing water content.
- 7- Transmission time μs recorded its maximum value at water content of 10%.
- 8- Width of cracks decreased with increasing water content.

REFERENCES

- [1] Coduto, D. P. D. P. (1999). *Geotechnical Engineering: Principles and Practices*. (No. Sirsi) i9780135763803).
- [2] Grim, R. E. (1953). *Clay mineralogy*. McGraw-Hill Book Company, Inc; New York; Toronto; London.
- [3] Das, B. M., & Sobhan, K. (2013). *Principles of Geotechnical Engineering*. Cengage Learning.
- [4] Dhakal, S. K. (2012). Stabilization of very weak subgrade soil with cementitious stabilizers, MSc thesis, Louisiana State University, US.
- [5] Shakir, R. R., & Zhu, J. (2009). Behavior of compacted clay-concrete interface. *Frontiers of Architecture and Civil Engineering in China*, 3(1), 85-92.

- [6] Canakci, H., Yavuz, H. E., Celik, F., & Gullu, H. (2013, July). Interface friction between organic soil and construction materials. International Balkans Conference on Challenges of Civil Engineering.
- [7] Shadravan, S., Ramseyer, C., & Kang, T. H. K. (2015). A long term restrained shrinkage study of concrete slabs on ground. *Engineering Structures*, **102**, 258-265.
- [8] Demir, İ., Sevim, Ö., & Tekin, E. (2018). The effects of shrinkage-reducing admixtures used in self-compacting concrete on its strength and durability. *Construction and Building Materials*, **172**, 153-165.

Investigation of Wear Occurred in Dry Clutch Disk Working Under Various Torques and Rotation Speeds

İ. SEVİM¹, M. E. TOLU¹, N. GÜLTEKİN² and M. MAYDA¹

¹ Karamanoglu Mehmetbey University, Faculty of Engineering, Department of Mechanical Engineering, Karaman, Turkey

² Karamanoglu Mehmetbey University, Vocational High School of Technical Sciences, Department of Motor Vehicles and Transportation Technologies, Karaman, Turkey

Abstract - Effect of the friction factor observed in the mechanical systems is too much to deny. Friction causes wear that induces many serious problems in the system elements. Correct measurement and calculation of the wear between system elements that occurs because of the friction is extremely important to take precautions and keep system life, long. In this study, we aimed to observe and measure the wear caused by the friction of clutch disk that was operated at the conditions of 58, 78, 108, 148, 208 rotations per minute for totally 10 minutes and 42 Nm, 45 Nm, 48 Nm torque values for all rotation speed values. Weight of the clutch disk is 770,11 gr. before the experiments. Weight of the disk is measured after operating the clutch disk for 10 minutes, at all three different torque values and five different rotation speed values to evaluate the wear amount. Measured weight values are used to calculate the changes occurred at the weight loss, wear ratio and wear resistance. Obtained results are presented as tables and diagrams. The most appropriate and optimum working conditions determined and presented as conclusions.

Keywords – Dry clutch, wear, friction, rotation, torque.

I. INTRODUCTION

INTERNAL combustion motors can't work stable at the rotations speeds lower than the idle rotation speed. Because of this, clutch, gearbox and differential are important elements as moment converter internal mechanisms [1]. At this point, clutch has a great role at maintaining the continuity of vehicle velocity and driving comfort conditions. Clutch mechanism is used to stop the motion or transmit the motion of a rotating shaft to another shaft at the same direction. Clutch is a mechanism located between motor and gearbox that transmits the power of motor to the gearbox or stops the motion with the motion of clutch pedal. Clutch mechanism has to connect working motor to the gearbox smoothly and gradually, allow to shift gears when the vehicle is in motion and transmit the motion of motor to the gearbox without loss [2].

The important role at operating vehicles using internal combustion motors makes clutch mechanisms indispensable. Hence, clutch mechanisms are one of the main research areas for researchers who aim to investigate the working conditions of clutches to produce better quality clutch mechanisms. In this context, some of the important studies about clutch mechanisms are given below:

Khamlichi et al., made a study and modeled thermal characteristics of a dry clutch linings that was produced

according to the distributed winding procedure in 2013. They made the optimization of thermal characteristics proper to the material formulation of clutch linings and key parameters of manufacturing process [3].

Zhao et al., studied numerical simulation of the wear observed on the C/C composite multidisc clutch and investigated wear behaviors under simulated working conditions in 2009. On behalf of predicting the wearing process on the friction surfaces, they applied a modified Archard wear model that can be operated with an asymmetric finite elements model to the user subprogram. They presented wear process, wear rate over time and sliding distance values as Results [4].

Sfarni et al., investigated behaviors of the riveted clutch discs in 2011. Within the scope of their study, they modeled a clutch disk with finite elements method to predict the curve of the cushion clutch and presented obtained data as the results [5].

Fernandes et al., examined the effects of mild and severe wear conditions on the formation and stability of the friction film in 2013. Friction tests were carried out at two different rotation speeds such as 750 rpm and 1200 rpm and normal load values that are changing between 200 N and 450 N. Each test was maintained 3 hours at the room temperature. Friction material occurred at the disc surface was presented as results for both mild conditions and severe conditions. It was seen that at the severe friction regime, friction film was thinner and less durable. Therefore, it has been concluded that severity of the wear has great effect on the formation and stability of friction film [6].

Fernandes et al., made a study with a title of "Contribution on Understanding the Friction Film Development in the Performance of a Dry Automotive Clutch System" in 2015 and examined clutches for three different types of terrain. They simulated the wear mechanisms with the data obtained from the tests and as a result, they determined that obtained data from the tests and data obtained from the simulation of friction film show similar characteristic features [7].

Li et al., analyzed the wear of the friction lining of a wet clutch system in 2015 and they have reached the conclusion that both thermal degradation and mechanical effects have influence on wear mechanism. Model predictions were constituted according to the two-stage wear ratio phenomenon that is experimentally observed and added to the literature in the recent days [8].

Li et al., made a study in 2016 and presented an uncertainty measurement analysis for the wear process in a wet clutch on behalf of investigating the two-stage wear process of the paper-based friction lining in a wet clutch. Wear prediction data that were processed by computers were investigated by using Monte Carlo method for sensitivity analysis and model verification. Data based on extensive calculations were presented as results on the purpose of gaining insight about development of temperature and wear [9].

As it is seen from the literature survey, there is lack of research on this subject and this is the main motivation of this study. This study is organized as follows:

A general description and a literature survey about the subject are included in the introduction section. In the following section, information about the experiments and the

experimental setup is given. In the third section, results obtained after the experiments and the discussion on these results are presented. Finally, in the last section, conclusions about the study are given.

II. MATERIAL & METHOD

The experimental setup we need for investigation of weight losses due to wear that occurs in a dry clutch system when working under different rotation speeds and torque values has been established in the laboratory of our faculty as similar as possible to the clutch mechanism of a vehicle and all experiments have been carried out on this experimental system.



Figure 1: Dry clutch fixed to the experimental setup

Appropriate and various torque values were selected to provide the “half clutch” condition that occurs while operating a vehicle. Torque values were measured by torque meter. Firsthand dry clutch has been provided from the market and its first weight was measured by a precision balance that has 2 kg capacity and 10^{-2} sensitivity.



Figure 2: General image of a dry clutch

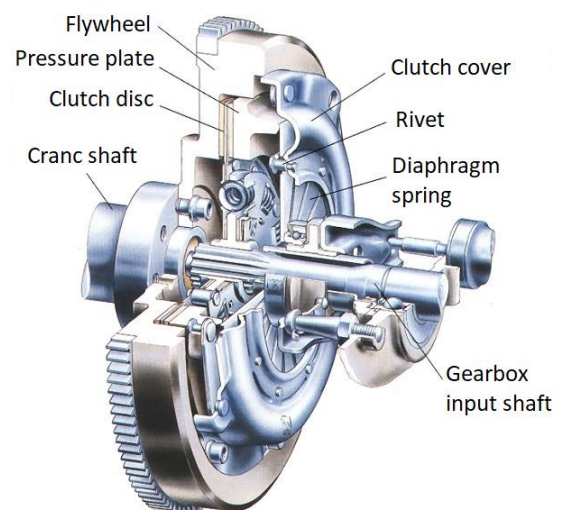


Figure 3: Main parts of a dry clutch mechanism

Dry clutch system that has a first weight of 770,11 grams was operated at the rotation speeds of 58 rpm, 78 rpm, 108 rpm, 148 rpm, 208 rpm and at the torque values of 42 Nm, 45

Nm, 48 Nm for each rotation speed. Operating time was set to 10 minutes for each experiment and experiments were carried out at room temperature, under normal circumstances.



Figure 4: Torque measurements of the dry clutch fixed to the experimental system

In an attempt to understand the wear occurred under different working conditions, the weight of the dry clutch that has a first weight of 770,11 grams was measured after each experiment by precision balance that has 2 kg capacity and 10^{-2} sensitivity. Weight loss ratios and changes in the wear resistance were determined by using the data obtained from the experiments.

III. RESULTS

A. Effects of Various Torques and Rotation Speeds to the Weight Loss

Dry clutch system was operated at the torques of 42 Nm, 45

Nm, 48 Nm and at the rotation speeds of 58 rpm, 78 rpm, 108 rpm, 148 rpm, 208 rpm respectively for each torque. Under these circumstances, weight losses were measured, weight loss ratios and wear resistances were calculated.

Obtained data were presented as tables and Table 1 and Figure 5. With the data in hand, it was concluded that for each specific torque, the weight loss increases with the increase of rotation speed and for each rotation speed, temperature increase rises parallel to the increasing of torque values.

Table 1: Weight loss of the dry clutch operating at the 42 Nm, 45 Nm, 48 Nm torques and 58, 78, 108, 148, 208 rpms

Rotation Speed (rpm)	Torque (Nm)	Weight Loss (gr)	Torque (Nm)	Weight Loss (gr)	Torque (Nm)	Weight Loss (gr)
58	42	0,02	45	1,02	48	1,51
78		0,08		1,15		1,56
108		0,35		1,24		1,65
148		0,58		1,34		1,73
208		0,97		1,46		1,89

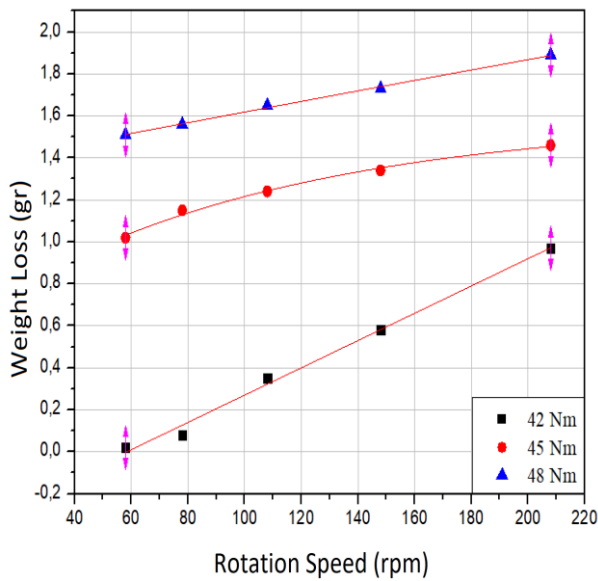


Figure 5: Graphical display of weight loss of the dry clutch operating at the 42 Nm, 45 Nm, 48 Nm torques and 58, 78, 108, 148, 208 rpms

B. Effects of Various Torques and Rotation Speeds to the Wear

Weight losses were calculated by using the data obtained from experiments and with the information of weight losses, wear rates were calculated. These data obtained after the

calculations were presented in Table 2 and Figure 6. Investigation of the calculated data shows that when the clutch system operated at the various rotation speeds for a specific torque, weight loss increases parallel to the increase of the rotation speed.

As a result of calculations, clutch disk operated at 42 Nm torque and 208 rpm lost 48,5 times more weight than the clutch disc operated at 42 Nm torque and 58 rpm. Near that, clutch disk operated at 45 Nm torque and 208 rpm lost 1,4 times more weight than the clutch disc operated at 45 Nm torque and 58 rpm and clutch disk operated at 48 Nm torque and 208 rpm lost 1,25 times more weight than the clutch disc operated at 48 Nm torque and 58 rpm. According to these results, it can be seen that higher torques mean higher wear rates and with the increasing torque values, accrual of wear rate decreases for different rotation speeds. This means that as the torque value rises, the effect of the increase of rotation speed to the wear rate decreases. The difference between the weight loss of the clutch disk operated at the lowest torque and rotation speed and the weight loss of the clutch disc operated at the highest torque and rotation speed is calculated as nearly 100 times. As a result of all these experiments and calculations, it can be said that torque and rotation speed values have a great effect on weight loss and wear.

Table 2: Wear rate of the dry clutch with a first weight of 770,11 grams, operated at the 42 Nm, 45 Nm, 48 Nm torques and 58, 78, 108, 148, 208 rpms

Rotation Speed (rpm)	Torque (Nm)	Weight (gr)	Wear Rate (%)	Torque (Nm)	Weight (gr)	Wear Rate (%)	Torque (Nm)	Weight (gr)	Wear Rate (%)
58	42	770,09	0,002597	45	769,09	0,132449	48	768,60	0,196076
78		770,03	0,002597		768,96	0,149329		768,55	0,202568
108		769,76	0,045448		768,87	0,161016		768,46	0,214255
148		769,53	0,075314		768,77	0,174001		768,38	0,224643
208		769,14	0,125956		768,65	0,189583		768,22	0,245419

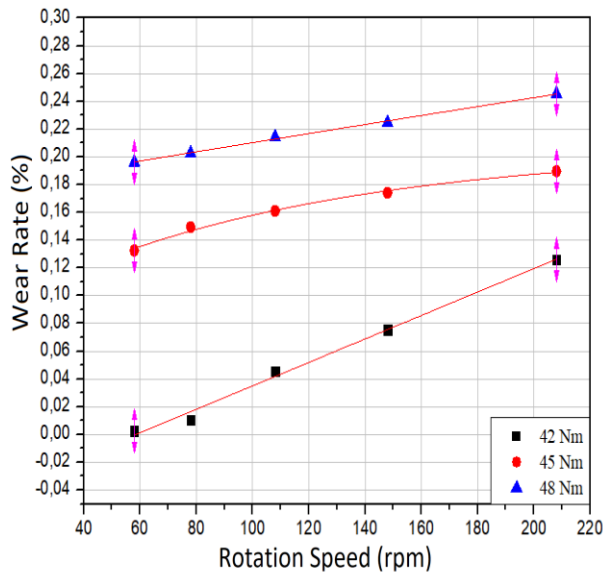


Figure 6: Graphical display of the wear rate of dry clutch with a first weight of 770,11 grams, operated at the 42 Nm, 45 Nm, 48 Nm torques and 58, 78, 108, 148, 208 rpms

C. Effect of Various Rotation Speeds on Wear Resistance for Each Torque Value

Wear resistance values are calculated for each torque and rotation speed by using the weight loss values which were determined previously and the data obtained with these calculations are presented in Table 3 and Figure 7. Figure 7 consists of three different diagrams for three different torque values.

With the data in hand, it can be seen that for a fixed torque value, wear resistance of the dry clutch system decreases in consequence of the increase of the rotation speed. For each torque values it was observed that wear resistance decreases with the increase of torque values.

Table 3. Changes observed at the wear resistance of the dry clutch operated at the 42 Nm, 45 Nm, 48 Nm torques and 58, 78, 108, 148, 208 rpms

Rotation Speed (rpm)	Torque (Nm)	Wear Resistance	Torque (Nm)	Wear Resistance	Torque (Nm)	Wear Resistance
58	42	50	45	0,98	48	0,662
78		12,5		0,87		0,641
108		2,857		0,806		0,606
148		1,724		0,746		0,578
208		1,031		0,685		0,53

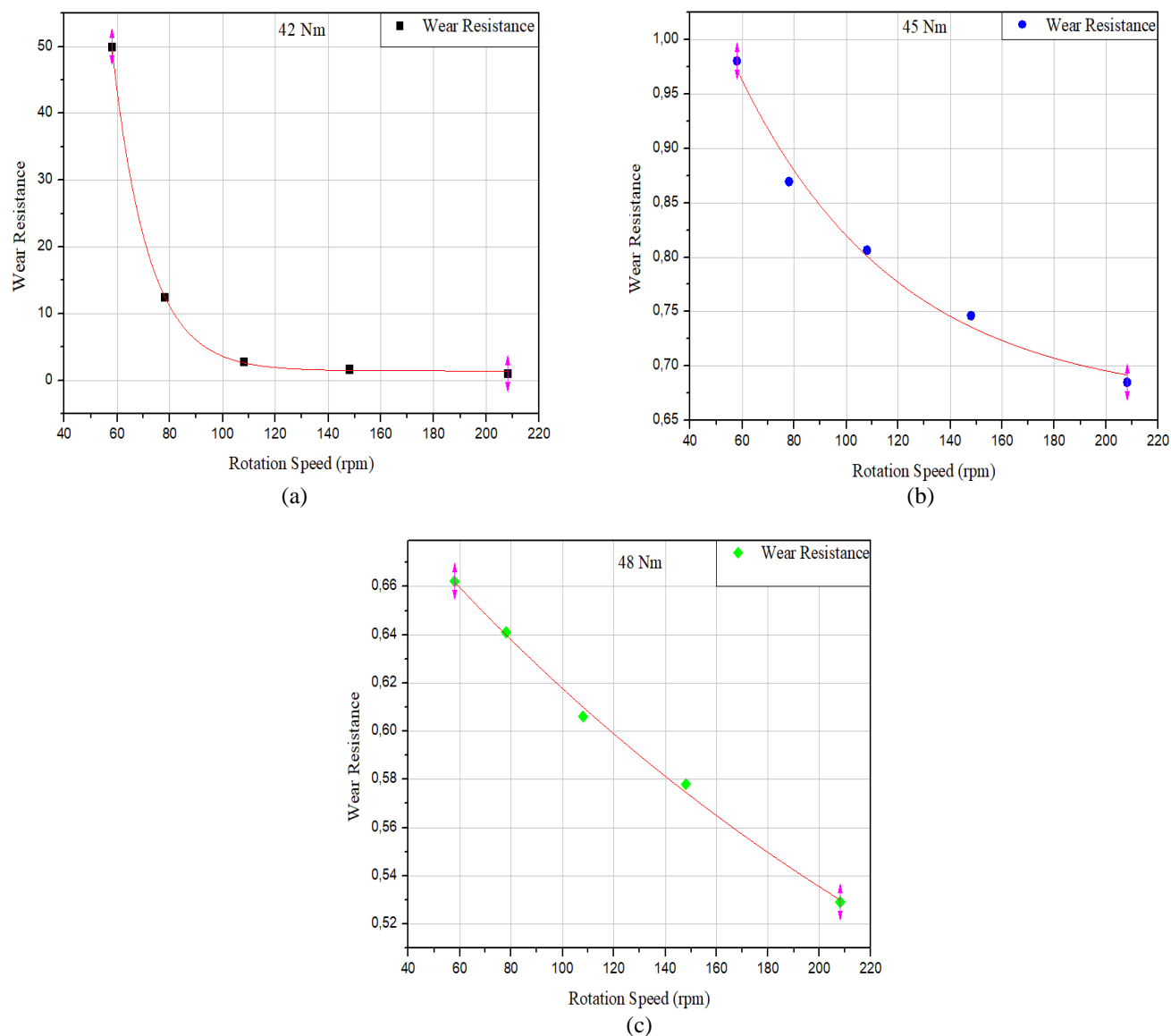


Figure 7: Graphical display of the changes observed at the wear resistance of the dry clutch operated at the 42 Nm (a), 45 Nm (b), 48 Nm (c) torques and 58, 78, 108, 148, 208 rpms

IV. CONCLUSION

In this study weight losses of a dry clutch system operating under the torques of 42 Nm, 45 Nm and 48 Nm and rotation speeds of 58, 78, 108, 148, 208 rpms were measured by using a precision balance that has a sensitivity of 10⁻². The obtained data were used to calculate the wear rates and wear resistances. All results obtained after the experiments and calculations were presented as tables and graphs. After this study, following conclusions were made:

- After the investigation of the effects of various torque and rotation speed values on the weight loss, it was concluded that, with the increase of the torque and rotation speed values, weight loss and the wear increases.
- Clutch systems have a big role on vehicle mechanism and they are essential parts of a vehicle to provide driving comfort. Hence, clutch systems are needed to be longlife mechanisms. This study, investigated the effects of various operating conditions on the lifetime of clutch systems.
- As a result of this research, it has been detected that wear rate of the dry clutch increases and according to this, wear resistance and life of the dry clutch system decreases if the vehicle is used under various operating conditions (half clutch position).
- Therefore, it can be seen that, developing new applications and mechanisms to decrease the wear rate and increase the lifetime of a clutch system is essentially important.

REFERENCES

- [1] A. Boyalı, “Hibrid Elektrikli Yol Taşıtlarının Modellenmesi ve Kontrolü”, Doktora Tezi, İstanbul Teknik Üniversitesi, Fen Bilimleri Enstitüsü, 2008.
- [2] M. J. Nunney, *Light and Heavy Vehicle Technology*. Routledge, 2007.
- [3] A. Khamlichi, M. Bezzazi and M. P. Vera, “Optimizing the thermal properties of clutch facings”, *Journal of Materials Processing Technology*, vol. 142(3), pp. 634-642, December 10, 2003.
- [4] S. Zhao, G. E. Hilmas, L. R. Dharani, “Numerical simulation of wear in a C/C composite multidisc clutch”, *Carbon*, vol. 47(9), pp. 2219-2225, August, 2009.
- [5] S. Sfarni, E. Bellenger, J. Fortin, M. Malley, “Numerical and experimental study of automotive riveted clutch discs with contact pressure analysis for the prediction of facing wear”, *Finite Elements in Analysis and Design*, vol. 47(2), pp. 129-141, May, 2011.
- [6] G. P. Fernandes, P. S. Zanotto, A. Sinatora, “Contribution on understanding the friction film development in the performance of a dry automotive clutch system”, *Wear*, vol. 342-343, pp. 364-376, November 15, 2015.
- [7] G. P. Fernandes, Jr. W. Haertel, P. S. Zanotto, A. Sinatora, “Influence of mild and severe wear condition in the formation and stability of friction film in clutch system”, *Wear*, vol. 302(1-2), pp. 1384-1391, April-May, 2013.
- [8] M. Li, M. M. Khonsari, N. Lingesten, P. Marklund, D. M. C. McCarthy, J. Lundin, “Model validation and uncertainty analysis in the wear prediction of a wet clutch”, *Wear*, vol. 364-365, pp. 112-121, October, 2016.
- [9] M. Li, M. M. Khonsari, D. M. C. McCarthy, J. Lundin, “On the wear prediction of the paper-based friction material in a wet clutch”, *Wear*, vol. 334-335, pp. 56-66, July 15, 2015.

Energy Consumption Optimization for Heat Pump Domestic Heater

E. SAGLICAN¹ and O. AGRA²

¹Yildiz Technical University, Istanbul/Turkey, esaglican@gmail.com

²Yildiz Technical University, Istanbul/Turkey, oagra@yildiz.edu.tr

Abstract - Nowadays, usage of heat pump systems as home appliances has become increasingly common in order to reduce the increased energy consumption. In this study, charge amount and compressor speed on the energy consumption (EC) and heat pump operation time ($t_{operation}$) were investigated experimentally. Water is heated from $15^{\circ}\text{C} \pm 2^{\circ}\text{C}$ to 52°C by the heat pump system. R600a is used as the refrigerant. The air source evaporator uses the ambient heat. Experiments have been carried out at different compressor speeds with 30 g, 35 g and 40 g refrigerant charges. According to results, energy consumption has been found to be optimum between 2600 rpm and 3500 rpm compressor speed in 35 g charge amount.

Keywords - Heat pump, Charge amount, Compressor speed, Energy consumption, Operation time.

I. INTRODUCTION

Problems such as the effects of global warming and reduction of natural resources have been increasing day by day. With the increase of human population, need for energy and natural resources have also increased. For these reasons, efforts of consume less energy and less natural resources with current resources.

Electricity energy is converted to heat energy by resistance type heaters. By using a heat pump system, more heating capacity can be obtained by using less energy. Thus, energy saving can be achieved by consuming less energy.

Bengtsson, P., Berghel, J., Renström, R. (2014) have studied to reduce total energy consumption by using heat pump system in the domestic heater machine. In this system, process water is heated by heat pump system instead of electric element. Parameters of compressor cylinder volume, compressor operating time are investigated. The evaporator, which is placed in a water tank, takes heat of water. As a result of this study, the less energy consumption is obtained 6 cm³ compressor cylinder volume and 70 minutes compressor run time. Using heat pump system, the energy consumption value reduced by 24% according to the electric element system. [1]

Bengtsson, P., Eikevik, T. (2016) have studied on using hydrocarbon refrigerant as R290 and R600a instead of R134a heat pump system. Global warming potential (GWP) value of R134a refrigerant is 1300. But GWP of R290 and R600a refrigerants are 3. So, using hydrocarbons are very important to reduce global warming. In this study comparisons were

made R134a cycle, R290 cycle and R600a cycle according to the electrical heater. [2]

Bengtsson, P., Berghel, J. (2016) have investigated the influence of capillary tube length on energy consumption in a domestic heater heat pump system. R600a refrigerant is used in system. The capillary tube outer diameter is 0.9 mm. Compressor speed is 4000 rpm. In this study, the effect of different capillary tube lengths on the different charge amounts was investigated. Between 22°C and 40°C machine internal temperatures, the energy consumption of compressor is related to the capillary tube length. The less energy consumption is 0.098 kWh for 0.68 m capillary tube length with 60 g charge amount. [3]

Kim, D., H., Park, H., S., ve Kim, M., S. (2013) were studied the optimization of charge amount in a double stage steam compression refrigeration cycle. Optimum subcool degrees of both the R410A single-stage cycle and the R134a/R410A cascaded cycle have been determined with experimentally and numerically. For the single-stage cycle, ambient air temperatures were set to -15°C , -7°C and 7°C . Charge amounts were set between 1.0 and 1.6 kg. As a result of experimental and numerical studies, the maximum heating capacity for the single stage cycle was observed at the maximum charge amount. However maximum COP value was observed in subcool degrees between 3 and 7 K. As a result of reduced ambient temperature, the degree of subcool has decreased. For cascade cycle, maximum heating capacity was observed at maximum charge amount. Optimum COP value was observed in degree of subcool between 4 and 8 K for R134a cycle and in degree of subcool between 5 and 6 K for R410A cycle. [4]

Zhang, J., Wang, R., Z. ve Wu, J., Y. (2006) have studied an optimization for an air-source heat pump system used for heating the water. Experimental studied have used R22 refrigerant. In this study, the amount of charge was determined for less energy consumption. The maximum COP value was observed at the 1.5 kg charge amount. [5]

Kerpiççi, H., Poyraz, O., Aynur, T., N., Teke, İ. (2012) have investigated the effect of evaporation temperature and air flow rate on total energy consumption in a 90 liter freezer cabinet. The air flow rate value was normalized and the optimum energy consumption was found to be normalized air flow rate value 1 and -26°C evaporation temperature. [6]

In this study, unlike other studies in the literature, the effect

of different parameters on the energy consumption in a heat pump domestic heater using R600a refrigerant was investigated experimentally. Experiments have been carried out at different compressor speeds with 30 g, 35 g and 40 g refrigerant charges.

II. MATERIAL AND METHODS

In this study, the process water is heated by the heat pump system. For this study experimental setup is shown in Figure 1.

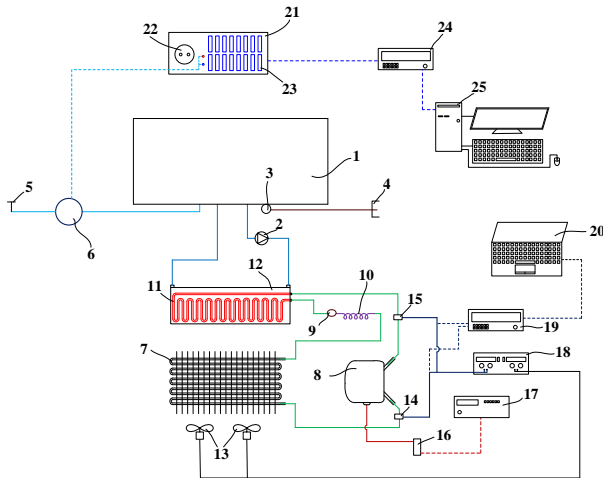


Figure 1: Experimental setup.

In the experimental setup of Figure 1; number 1 refers to the process tank, number 2 refers to the circulation pump, number 3 refers to the discharge pump, number 4 refers to the discharge open, number 5 refers to the fresh water tap, number 6 refers to the flowmeter, number 7 refers to the evaporator, number 8 refers to the compressor, number 9 refers to the dryer, number 10 refers to the capillary, number 11 refers to the condenser, number 12 refers to the condenser water tank, number 13 refers to the evaporator fans, number 14 refers to the low pressure transducer, number 15 refers to the high pressure transducer, number 16 refers to the compressor inverter card, number 17 refers to the compressor signal driver, number 18 refers to the power supply, number 19 refers to the first data logger, number 20 refers to the notebook, number 21 refers to the data collect station, number 22 refers to the electric supply station, number 23 refers to the thermocouple station, number 24 refers to the second data logger, number 25 refers to the PC.

The experimental setup consists of 3 cycles. The first cycle is the heat pump cycle in which the R600a refrigerant flows; the second cycle is open cycle in which evaporator takes the heat of ambient air; the third cycle is closed water cycle in which the water is heated by the condenser.

The experimental studies were performed under standard laboratory conditions ($22^{\circ}\text{C} \pm 0.5^{\circ}\text{C}$ and $55\% \text{ Rh} \pm 5\%$). At $15^{\circ}\text{C} \pm 0.5$, 4.2 liters of water to be heated is taken to the process tank of the domestic heater. The water is heated by

heat pump system to 52°C .

In the experimental studies, the effect of the charge amount and compressor speed to total energy consumption and heat pump operation time. The matrix of experiments is shown Table 1.

Table 1: The matrix of experiments

Charge amount	Compressor speeds
30 g	3200, 3500 and 3700 rpm
35 g	2300, 2600, 2900, 3200, 3500 and 3600 rpm
40 g	2300, 2600, 2900, 3200, and 3500 rpm

Firstly, experiments were made carried out at 2300, 2600, 2900, 3200, 3500 and 3600 rpm compressor speeds and the optimum region was determined for the 35 g charge amount. Then, experiments were carried out at 2300, 2600, 2900, 3200 and 3500 rpm compressor speeds for 40 g charge amount and optimum location for this charge amount was determined. For the 30 g charge amount experiments were carried out at 3200, 3500 and 3700 rpm compressor speeds and optimum location was determined according to the experimental results of 35 g and 40 g charge amount.

III. EXPERIMENT RESULTS

In experiments with different compressor speeds at 30 g, 35 g and 40 g charge amounts, the total energy consumption and heat pump operation time of domestic heater are shown normalized values in the graphs below. The value to be normalized in the experimental studies ($\beta_{parameter}$) is divided by the maximum value in the experimental work ($\beta_{max, parameter}$). Normalized value ($\lambda_{normalized}$) is found by the formula in equation (1).

$$\lambda_{normalized} = \frac{\beta_{parameter}}{\beta_{max, parameter}} \quad (1)$$

Total energy consumption variation was shown in Figure 2. Total energy consumption (EC) is normalized by the formula in equation (1).

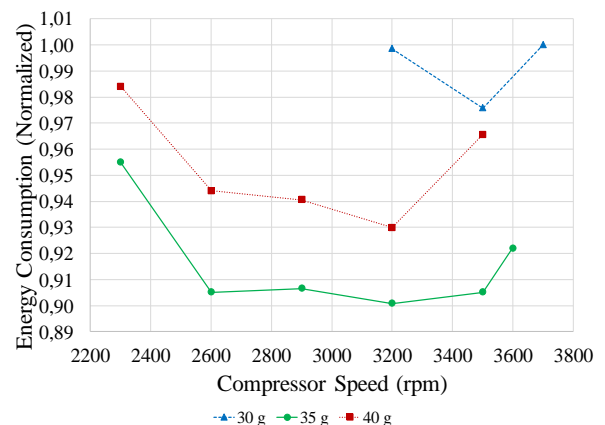


Figure 2: Total energy consumption variation related to

compressor speed at different charge amounts.

As seen in Figure 2, the energy consumption at 35 g charge amount is found to be less than the energy consumptions at 30 g and 40 g charge amounts. At the 35g charge amount, energy consumption is lowest between 2600 rpm compressor speed and 3500 rpm compressor speed.

Operating time variation was provided in Figure 3. Operating time is normalized by the formula in equation (1).

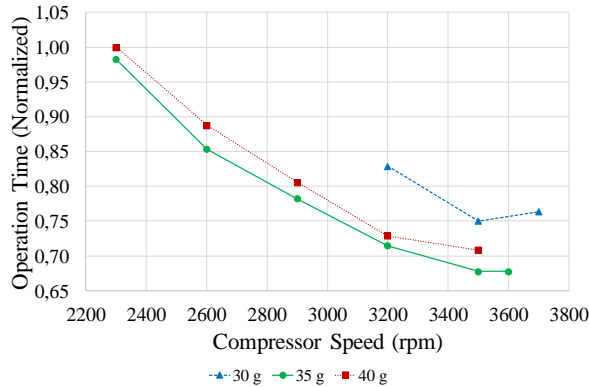


Figure 3: Heat pump operation time variation related to compressor speed at different charge amounts.

As seen in Figure 3, the operation time at 35 g charge amount is found to be less than the operation times at 30 g and 40 g charge amounts. In addition, as the compressor speed increases, the operation time decreases.

During the heating of the process water in the heat pump system, the evaporator fans blows the ambient air to the evaporator and the circulation pump directs the process water to the condenser tank. When calculating total energy consumption (ΣEC), power of circulation pump (\dot{W}_{pump}) and power of evaporator fans (\dot{W}_{fan}) as well as the compressor power ($\dot{W}_{compressor}$) are also included in this calculation. Total energy consumption is calculated by the formula in equation (2).

$$\Sigma EC = t_{operation} \times (\dot{W}_{compressor} + \dot{W}_{pump} + \dot{W}_{fan}) \tag{2}$$

During the experimental study, an integral area calculation method is performed to obtain the average of all experimental data. For example, a formula that changes the time-dependent power is obtained. From the beginning to the end of the experiment, the time-dependent power function is integrated. The ratio of this integrated function to time which is from the beginning to the end of the experiment gives the average power consumption. Total average power consumption is calculated by the formula in equation (3).

$$\frac{\left(\int f(x) \right)}{(t_2 - t_1)}$$

(3)

In Figure 4 the variation of the average total power values according to charge amount and the compressor speeds is provided. Average total power is normalized by the formula in equation (1).

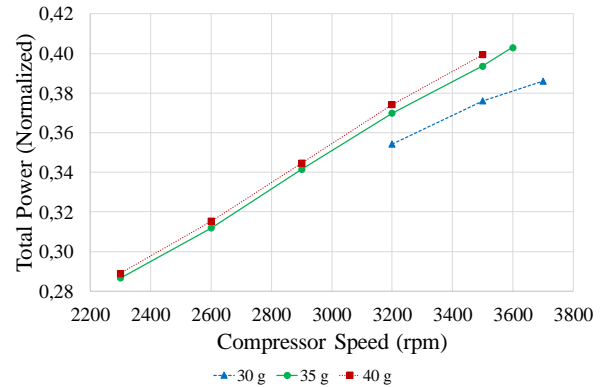


Figure 4: Total power consumption variation related to compressor speed at different charge amounts.

As shown in Figure 4, the total power consumption is increased by increasing the charge amount. It is also seen that total power consumption value is increased with the increasing of the compressor speed in each charge amount.

Figure 5 shows the variation of the average compressor power values according to charge amount and the compressor speeds. Average compressor power is normalized by the formula in equation (1).

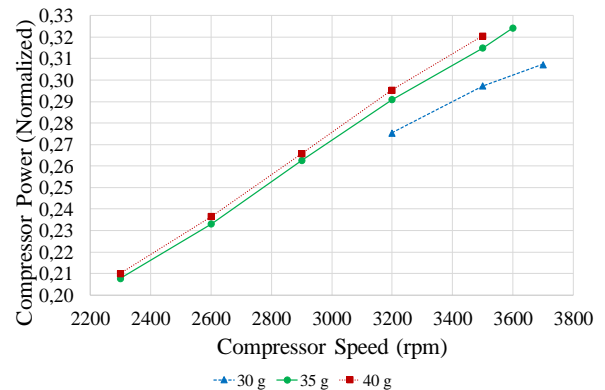


Figure 5: Compressor power consumption changing related to compressor speed at different charge amounts.

As a shown in Figure 5, the compressor power consumption has same trend as the total power consumption. Compressor work is calculated by in equation (4). The compressor power is determined by the ratio of the compressor work ($\dot{W}_{compressor, work}$) to compressor efficiency. Compressor efficiency is assumed to be 0.7. Compressor work is related to refrigerant flow rate and enthalpy difference. Number 1 refers to the compressor input point (h_1), while number 2 refers to the compressor output (h_2). The refrigerant flow rate is expressed in (\dot{m}_{ref}).

$$\dot{W}_{\text{compressor,work}} = \dot{m}_{\text{ref}} \times (h_2 - h_1) \quad (4)$$

Figure 6 shows the refrigerant flow rate variation related to compressor speed at the 30 g, 35 g and 40g charge amounts.

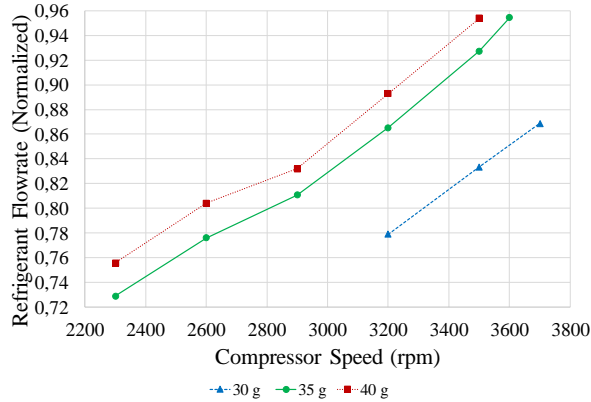


Figure 6: Refrigerant flowrate variation related to compressor speed at different charge amounts.

As shown in Figure 6, the refrigerant flowrate is increased by increasing the charge amount. It is also seen that the refrigerant flowrate is increased with the increase of the compressor speed in each charge amount. The charge amount is calculated by the formula in equation (5). The refrigerant density is demonstrated by (ρ_{ref}), velocity is demonstrated by (V_{ref}). The area of the cross-section through which the refrigerant passes is shown by A_{section} .

$$\dot{m}_{\text{ref}} = \rho_{\text{ref}} \times A_{\text{section}} \times V_{\text{ref}} \quad (5)$$

In the heat pump systems, the volume of compressor is constant and the density in the unit volume increases with the increase of charge amount. The increase in density leads to a higher refrigerant flow.

Figure 7 shows the variation of evaporation and condensation temperatures due to compressor speed at different charge amount.

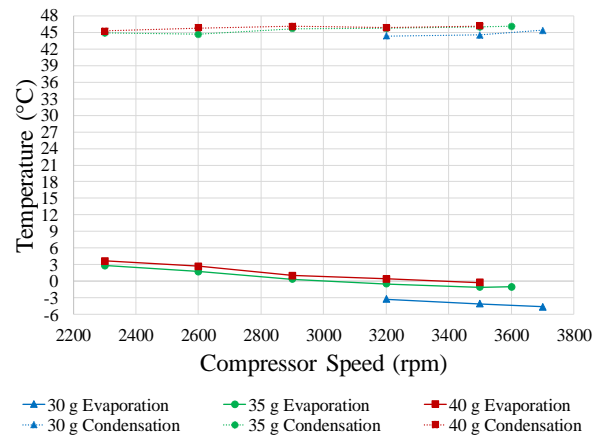


Figure 7: Variation of evaporation and condensation temperatures related to compressor speed at different charge amounts.

As the amount of charge increases, the pressure of the refrigerant in the evaporator increases. The evaporation temperature increases with the increasing evaporation pressure. At the same charge amount, the evaporation pressure decreases with the compressor speed increases. Because the velocity of the refrigerant passing through the capillary tube increases and the pressure drop increases as the result of the increased velocity. The evaporation temperature decreases as the compressor speed increases, depending on the evaporation pressure.

As a result, increased refrigerant flowrate, compressor power has increased.

Figure 8 shows the variation of the average heat extraction capacities according to charge amount and the compressor speed. Capacities are normalized by the formula in equation (1).

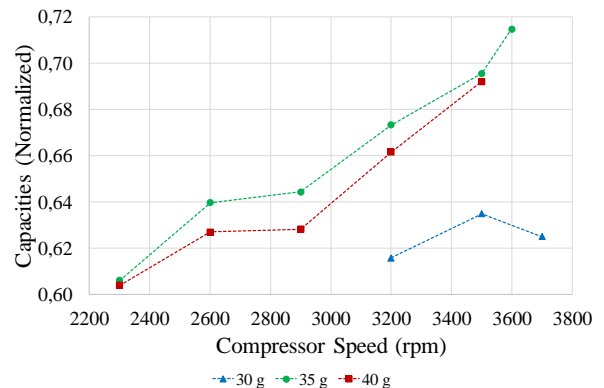


Figure 8: Variation of heat extraction capacities related to compressor speed at different charge amounts.

As seen in Figure 8, the heat extraction capacity at the 35 g charge amount is higher than other charge amounts.

The evaporation temperature of 35 g charge amount is higher than the evaporation temperature of 30 g charge amount. The evaporation temperature of 40 g charge amount is higher than the evaporation temperature of 35 g charge amount (Figure 7). However, the heat extraction capacity is higher in the 35 g charge amount. This situation may be explained by

the gradual decrease in the temperature difference between the ambient air and the refrigerant passing through in the evaporator. Therefore, the heat extraction capacity at 35 g charge amount is the highest.

As a shown in Figure 8, at 30 g charge amount the heat extraction capacity at 3500 rpm compressor speed is higher than the heat extraction capacity at other compressor speeds while the heat extraction capacity increases with increasing compressor speed at 30 g and 40 g charge amounts.

As a seen in Figure 7, the evaporation temperatures at 30 g charge amount below 0°C at all compressor speeds. At 3700 rpm compressor speed the evaporation temperatures is the less all compressor speeds. As a result of this situation, ambient air condenses faster on the evaporator surfaces of the air and the rate and amount of snow on the evaporator surfaces increase. As a result of the snow, the air flow rate which passing through the evaporator surfaces decreased and the heat transfer rate decreased.

The heat extraction capacity is calculated by the calculation on the side of the refrigerant, due to the amount of snow and the change of air flow rate.

With the increase of the compressor speed, heat extraction capacity of the evaporator increased because the temperature difference between the refrigerant flow and the ambient air increased and the refrigerant flowrate increased. The heating capacity increased with increasing heat extraction capacity.

The heat extraction capacity ($\dot{Q}_{\text{heat,extraction}}$) related to the refrigerant flow rate and enthalpy difference is calculated by in equation (6). Number 1 refers to the compressor input or evaporator output point (h_1), while number 4 refers to the capillary tube output or evaporator input (h_4).

$$\dot{Q}_{\text{heatextraction}} = \dot{m}_{\text{ref}} \times (h_1 - h_4) \quad (6)$$

Figure 9 shows the variation of the average heating capacities according to the charge amount and the compressor speeds. Capacities are normalized by the formula in equation (1).

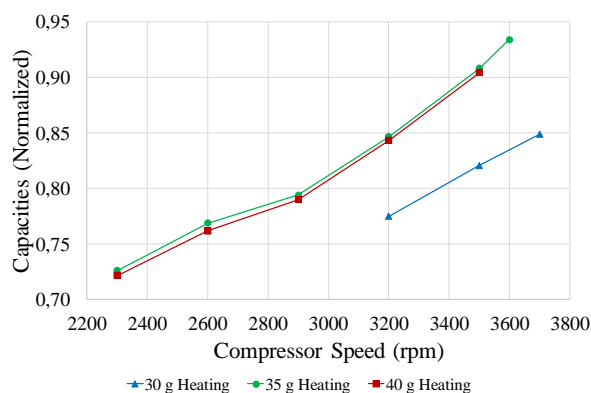


Figure 9: Variation of heating capacities related to compressor speed at different charge amounts.

As shown in Figure 9, the heating capacity and the heat extraction capacity variations have similar trends. As the heating capacity at the 35 g charge amount is higher than the heating capacities of other charge amounts, the process water heats up faster at the 35 g charge amount. Therefore, the working time is least at 35 g. The same situation is also seen with the increase of compressor speed. Therefore, the heat pump operation time is reduced with the increase of the compressor speed at the same charge amount.

The heating capacity (\dot{Q}_{heating}) is calculated by in equation (7). The heating capacity is related to the refrigerant flow rate and enthalpy difference. Number 2 refers to the compressor output or condenser input point (h_2), while number 3 refers to the condenser output or capillary tube input (h_3).

$$\dot{Q}_{\text{heating}} = \dot{m}_{\text{ref}} \times (h_2 - h_3) \quad (7)$$

Increasing the charge amount from 30 g to 35 g increases the average total power consumption by %4.4, while decreasing the operating time by 13.8% at the 3200 rpm compressor speed.

Comparing the experimental results of 2300 rpm compressor speed and 2600 rpm compressor speed at 35 g charge amount shows that the energy consumption at 2600 rpm compressor speed is 5.2% less than the compressor speed of 2300 rpm. While the total power consumption value at 2600 rpm compressor speed increased by 8.8% compared to the total power consumption value at 2300 rpm compressor speed. The operation time at 2600 rpm compressor speed was increased by 13.1% compared to the operation time at 2300 rpm compressor speed. The total energy consumption is lower at 2600 rpm compressor speed, as the increasing of the operation time is greater than the increasing of the power consumption.

The energy consumption values between 2600 rpm compressor speed and 3500 rpm compressor speed are very close to each other at the 35 g charge amount. According to the 2600 rpm compressor speed:

- At the 2900 rpm compressor speed, the power consumption value is 9.5% higher, while the operating time is 8.4% less and the energy consumption value is 0.2% higher.
- At the 3200 rpm compressor speed, the power consumption value is 18.6% higher, while the operating time is 16.3% less and the energy consumption value is 0.5% less.
- At the 3500 rpm compressor speed, the power consumption value is 26.2% higher, while the operating time is 20.6% less and the energy consumption value is 0.002% less.

According to 3500 rpm compressor speed the total power consumption is increased but the operating time did not change at 3600 rpm compressor speed. According to 3500 rpm compressor speed, the energy consumption value increased by

1.86% at 3600 rpm compressor speed. Total power consumption increased 2.4%, while operating time increased by 0.4%. Because of these factors, total energy consumption value has increased.

IV. CONCLUSION

Energy consumption and operating time for various compressor speeds at 30g, 35g and 40g charge amounts were investigated experimentally.

- The lowest energy consumptions at each charge amounts are;
 - 30 g charge amount: 3500 rpm compressor speed,
 - 35 g charge amount: 3200 rpm compressor speed,
 - 40 g charge amount: 3200 rpm compressor speed.
- Energy consumption value at 35 charge amount and 3200 rpm compressor speed is:
 - 7.7% less than the energy consumption value at 30 g charge amount and 3500 rpm compressor speed.
 - 3.1% less than the energy consumption value at 40 g charge amount and 3200 rpm compressor speed.
- At 35 g charge amount, operating points between 2600 rpm and 3500 rpm compressor speeds are the optimum area when considering energy consumption values.

ACKNOWLEDGMENT

The authors are encouraged to make experimental works possible and to ensure that all contributions are made to Arçelik A.S. Research and Development Center Directorate.

REFERENCES

- [1] Bengtsson, P., Berghel, J. & Renström, R., "A Household Dishwasher Heated by A Heat Pump System Using an Energy Storage Unit with Water as The Heat Source", *International Journal of Refrigeration*, vol. 49, pp. 19-27, 2015.
- [2] Bengtsson, P., Eikevik, T., "Reducing the Global Warming Impact of a Household Heat Pump Dishwasher Using Hydrocarbon Refrigerants", *Applied Thermal Engineering*, vol. 99, pp. 1295-1302, 2016.
- [3] Bengtsson, P., Berghel, J., "Study of Using a Capillary Tube in A Heat Pump Dishwasher with Transient Heating", *International Journal of Refrigeration*, vol. 67, pp. 1-9, 2016.
- [4] Kim, D. H., Park, H. S. & Kim, M. S., "The Effect of the Refrigerant Charge Amount on Single and Cascade Cycle Heat Pump Systems", *International Journal of Refrigeration*, vol. 40, pp. 254-268, 2014.
- [5] Zhang, J., Wang, R. Z. & Wu, J. Y., "System Optimization and Experimental Research on Air Source Heat Pump Water Heater", *Applied Thermal Engineering*, vol. 27, pp. 1029-1305, 2007.
- [6] Kerpiçi, H., Poyraz, O., Aynur, T., N & Teke, L., "Investigation of The System Parameters Affecting the Runtime of a Freezer Compartment", *Proceedings of the ASME 2012 International Mechanical Engineering Congress & Exposition*, Houston, Texas, USA, 2012

Investigation Of The Effects Of Walnut Biodiesel On A Diesel Engine Exhaust Emissions

A.E. ÖZÇELİK¹ H. AYDOĞAN¹ and M. ACAROĞLU¹

¹ Selcuk University, Mechanical Engineering, Konya/Turkey, eozececik@selcuk.edu.tr

¹ Selcuk University, Mechanical Engineering, Konya/Turkey, haydogan@selcuk.edu.tr

¹ Selcuk University, Mechanical Engineering, Konya/Turkey, acaroglu@selcuk.edu.tr

Abstract - Diesel engines are the most efficient thermal machines capable of reaching up to approximately 40% of thermal efficiency. Different studies are carried out to increase the efficiency of diesel engines and also to reduce environmental pollution. The studies aimed at improving the combustion process constitute the most important part of them. As is known, with the improvement of combustion process; Besides increasing the efficiency of the engine, environmental pollution is also reduced. For this reason, in recent years to improve combustion process in diesel engines; Both structural (conconstructive) studies and fuel-related studies are underway. Structural works include exhaust manifold designs, improving the shape of the combustion chamber, increasing the valve count and Valve section area, regulations and improvements in the spraying system, the expansion of the turbocharger application, etc. Located. In the studies related to fuels; More economical use of existing fuels and studies on different alternative fuels can be given as examples.

In this study, Biodiesel was produced from walnut oil by transesterification method. The walnut biodiesel is then mixed with the Eurodiesel fuel, which will be 7% (B7) and 10% (B10) by volume. Eurodiesel fuel was accepted as comparison fuel. Diesel engines with common-rail fuel system were used in the experiments. The results of the tests were compared with the emission values of CO, CO₂, HC, O₂, smoke and NOx with Eurodiesel fuel values.

Keyword - Walnut, biodiesel, engine, emissions

I. INTRODUCTION

Because biodiesel is chemically similar to diesel fuel, you can incorporate biodiesel directly into the fuel tank of any diesel vehicle [1]. There are many advantages to using biodiesel as a vehicle fuel. Biodiesel is found to be less emissions, produced with its own country resources without external dependence, does not affect the performance of the engine and is obtained from plants. Biodiesel can be defined as solar-powered liquid fuels as plants grow with solar energy[2,3].

Biodiesel thermal value is very close to the thermal value of the engine and the number of Biodiesel Cetane is higher than the number of the array[4]. With the use of biodiesel, the engine operates with less of a hit, while the specific fuel

consumption, power and torque values close to the string are achieved. The biodiesel engine has better lubrication characteristics than power-reducing deposits and diesel[5].

Biodiesel is a good solvent. It can solve some paints in contact with painted surfaces. Due to the ability to solve biodiesel, the insulating elements used in diesel engine should be replaced and used with substances that biodiesel cannot solve[6].

Walnut is a versatile plant that can grow naturally in our country, fruit can be evaluated at the same time as timber, leaf and green shells. Turkey walnut (*Juglans regia* L.) is one of the country home of the plant. It is reported that the existence of walnut trees in Anatolia and its production are based on at least 3000 years ago and even transported them to other growing areas in the world [7]. In many parts of our country, walnut trees are considered as great and festivals are organized on behalf of them. Walnut is a long-lived plant that can grow in every region of our country. Unlike other fruit varieties, the ability to produce fruit without the necessity of hanging is the main reason for walnut being a widely grown fruit. In addition, the valuable form of timber was also a factor in widespread walnut breeding in Anatolia[8,9].

In this study, a four-stroke, common-rail fuel system, a water-cooled, 4-cylinder diesel engine, the effects of biodiesel engines on engine emissions were investigated. The results were evaluated by comparison.

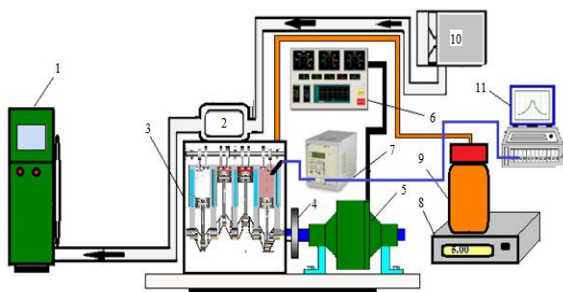
II. MATERIAL AND METHOD

Biodiesel was produced from walnut oil used in this study using transesterification method. Two mixtures are considered in the volumetric mixture. These;

1. 100% Diesel (witness fuel)
- 2.% 7 Biodiesel +% 93 Eurodiesel
- 3.% 10 Biodiesel +% 90 Eurodiesel

Experiments were carried out on the engine with common rail fuel system with these prepared mixtures. The work on biodiesel blends in engines with common-rail fuel systems is quite new. If it is related to walnut biodiesel, the work done is very few.

The experiments used a diesel engine with a four-stroke, four-cylinder, electronic fuel injection system with a common-rail fuel system. The test setup used in the study is shown in Figure 1. Technical specifications of the engine used in the survey Table 1 shows the characteristics of the engine dynamometer Table 2 and Table 3 show the specifications of the exhaust emission device.



- | | | |
|--------------------|--------------------------|---------------------------------|
| 1. Emission Device | 5. Hydraulic Dynamometer | 9. Fuel Tank |
| 2. Turbocharger | 6. Control Panel | 10. Orefiz Plate |
| 3. Test Engine | 7. Charging Amplifier | 11. AVL Cylinder pressure gauge |
| 4. Mesh | 8. Precision Balance | |

Figure 1: Schematic view of the test set

Table 1: Technical specifications of the engine used in the study

Motor	1.9 Multijet
Number of cylinders and layout	4, a single row of the front transverse
Cubic capacity (cc)	1910
Compression ratio	5.18: 1
Maximum power hp - d / d	105 - 4000
Maximum torque Nm (kgm) - d/d	200 - 1750
Fuel	diesel
Fuel supply	Electronically controlled Common Rail type MultiJet direct injection, turbocharger and intercooler
Ignition	compressional
Bore x Stroke (mm)	82 x 90.4

Table 2: Technical specifications of the engine dynamometer

Model	BT-190 FR
Capacity	100 kW
Maximum speed	6000 rpm
Maximum torque	750 Nm

A Bosch BEA 350 emission device was used to measure emissions of exhaust gases. Technical specifications of the emission device are given in Table 3.

Table 3: Technical specifications of the exhaust emission device

Parameters	Measurement Range	Precision
HC	0-20.000 ppm	1 ppm
CO ₂	0-20%	0.1%
CO	0-15%	0.001%
O ₂	0-21.7%	0.01%
NO _x	0-5000 ppm	1 ppm

The engine is heated to the operating temperature before starting the measurements. The experiments were performed at a full throttle position in different engine cycles. First, the experiment was performed using Eurodiesel fuel. Then the other fuels in volume were used in the B7 and B10 mixtures respectively.

III. RESULTS AND DISCUSSION

The main reason for the presence of CO among combustion products is the inadequacy of oxygen or the absence of complete combustion. Figure 2 shows the variation of % CO in the exhaust gases with respect to engine dynamics in the use of biodiesel-Eurodiesel fuels mixtures. When the figure is examined, it is seen that the amount of CO increases a little as the cycle increases. B10 fuel use seems to have decreased by more than 28% in CO values. This reduction is due to the presence of oxygen in the content of biodiesel.

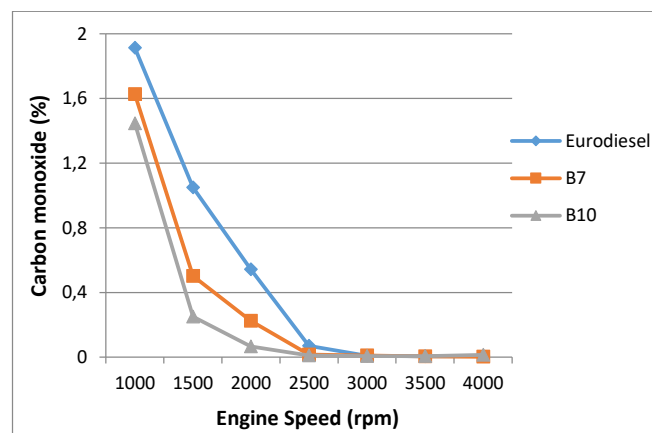


Figure 2: CO change according to engine speed

The variation of CO₂ values in the exhaust gases with respect to engine dynamics is shown in Figure 3. The increase in the amount of CO₂ in the exhaust gases shows a good combustion. With the use of biodiesel and Eurodiesel mixtures, CO₂ emissions have been reduced by up to 14%. This decrease can be explained by the impoverishment of the mixture due to the presence of O₂ in the content of biodiesel.

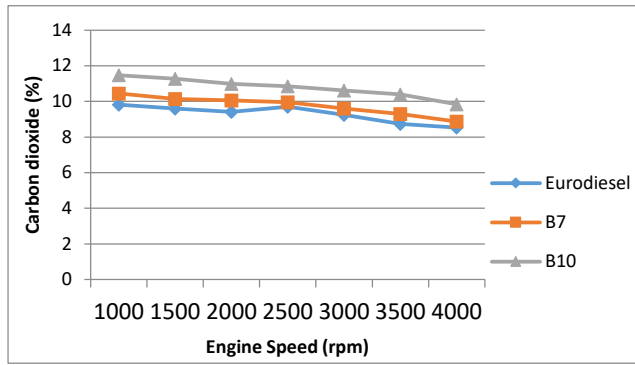


Figure 3: Change of CO₂ according to engine speed

HC means unburned fuel. The use of biodiesel-Eurodiesel mixtures in Figure 4 shows a change in HC values according to different engine revolutions. The lowest HC value was measured in the use of B7-B10 fuel. In the use of Eurodiesel fuel, HC values decreased by more than 50%. This situation suggests that combustion is better.

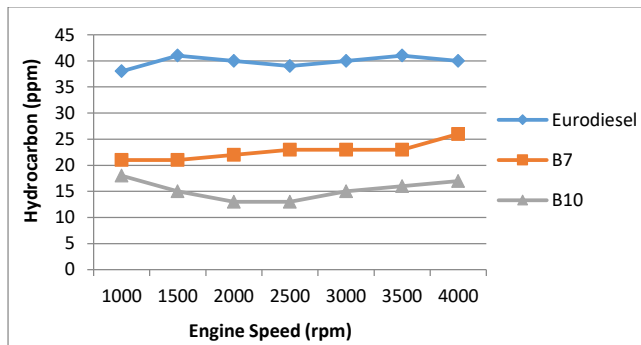


Figure 4: HC change according to engine speed

Oxygen values (O₂) change in exhaust gas according to engine rpm has given in Figure 5. At 1000 rpm lowest O₂ values recorded on Eurodiesel, and highest recorded on B10. Increasing engine speeds caused a little drop in O₂ until engine reached 2000 rpm but after engine speed passed 2000 rpm O₂ level started to increase. Since biodiesel contains more O₂ compared to eurodiesel, it shows higher O₂ values on biodiesel mixture fuels.

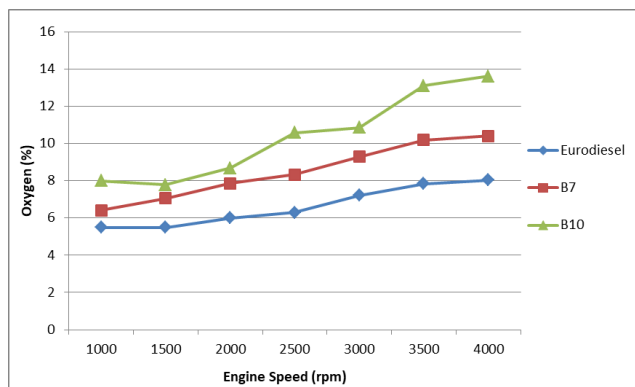


Figure 5: O₂ (%) value

In Figure 6, the use of bioethanol-unleaded gasoline mixtures shows a change in NO_x values relative to different engine revolutions. The highest NO_x value was measured in the use of B7-B10 fuel. The use of this fuel has shown that NO_x values increase by more than 10%. This is expected because of the presence of oxygen in the biodiesel.

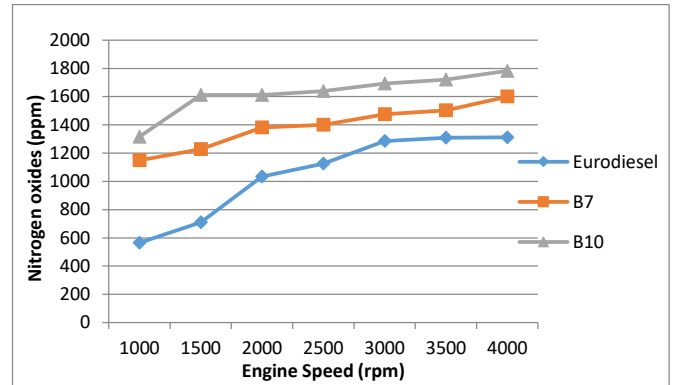


Figure 6: NO_x change according to engine speed

Change in smoke emission values is given in Figure 7. If reviewed, highest exhaust gas smoke emissions recorded on 1000 rpm. Smoke emissions decrease with the increase of engine rpm. The lowest emissions recorded on B10 fuel. Smoke emission decreases according to biodiesel percentage increase in fuel mixtures.

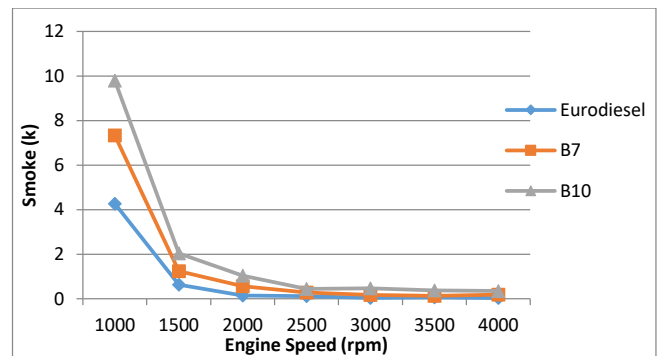


Figure 7: Smoke emission value of fuel

IV. RESULTS

This study was done with, eurodiesel and safflower oil product biodiesel mixtures. This fuels are Eurodiesel B7, B10 mixtures. This mixture was used on a diesel engine with common-rail fuel system and emission values of these fuels reviewed. So, the result are:

1. Lowest CO values recorded with B10 which is 28% lower than Eurodiesel.
2. Highest CO₂ values recorded with B100 which is 14% higher than Eurodiesel.

3. Lowest HC values recorded with Eurodiesel and highest recorded in B10.
4. Lowest O2 values recorded with B0 fuel and the highest O2 value recorded with B10 which is 30% higher than Eurodiesel.
5. Highest NOx value recorded with B10 which is 40% higher than Eurodiesel.
6. Increase in biodiesel percentage of mixtures leads to smoke emission to diminish.

This study shows that biodiesel fuel on diesel engine reduces NOx emissions every other. Adding more biodiesel to eurodiesel fuel, highly affects vehicle emissions is the most important polluter of the world, so show us the importance of cleaner fuels sharper.

V. RESOURCES

- [1] Agarwal, A.K. and Rajamanoharan, K., Experimental Investigations Of Performance And Emissions Of Karanja Oil And Its Blends In A Single Cylinder Agricultural Dize Engine, *Applied Energy*, 86, 106-112, 2009
- [2] López, I., Quintana, C.E., Ruiz, J.J., Cruz-Peragón, F., Dorado, M.P., Effect of the use of olive-pomace oil biodiesel/diesel fuel blends in a compression ignition engine: Preliminary exergy analysis, *Energy Conversion and Management*, Volume 85 , Pages 227–233, 2014
- [3] Allen, C., Toulson, E., Tepe, D., Schock, H., Miller, D., Lee, T., Characterization of the effect of fatty ester composition on the ignition behavior of biodiesel fuel sprays, *Fuel*, Volume 111, Pages 659–669, 2013
- [4] Aleksandra Sander, Mihael Antonije Koscak, Dominik Kosir, Nikola Milosavljevic, Jelena Parlov Vukovic, Lana Magic, The influence of animal fat type and purification conditions on biodiesel quality, *Renewable Energy*, 118, pp.752-760, 2018
- [5] Koukouch, A., Idlimam, A., Asbik, M., Sarh, B., Izrar, B., Bostyn, S., Bah, A., Ansari, O., Zegaoui, O., Amine, A., 2017, Experimental determination of the effective moisture diffusivity and activation energy during convective solar drying of olive pomace waste, *Renewable Energy*, Volume 101, Pages 565-574, 2017
- [6] Özçelik, A.E., “Aspir Biyodizelinin ve Motorinle Karışımlarının Tek Silindirli Bir Dizel Motorda Yağlama Yağına Etkilerinin Belirlenmesi”, Doktora Tezi, *Selçuk Üniversitesi Fen Bilimleri Enstitüsü*, Konya, 2011
- [7] BR Moser, B.R., Preparation of fatty acid methyl esters from hazelnut, high-oleic peanut and walnut oils and evaluation as biodiesel, *Fuel*, 2012
- [8] Aytaç, Ş., Küçük Güçlü Bir Dizel Motorunda Motorin ve Bitkisel Yağların Oransal Karışımlarının Yakıt Olarak Kullanılmasında Bazı Performans Değerlerinin Saptanması Üzerine Bir Araştırma, Doktora Tezi, *Trakya Üniversitesi Fen Bilimleri Enstitüsü*, Edirne, 1997
- [9] Nilva R. Uliana, Andre Polloni, Marshall Paliga, Josamaique G. Veneral Marintho B. Quadri, J. Vladimir Oliveira, Acidity reduction of enzymatic biodiesel using alkaline washing, *Renewable Energy*, 113, pp.393-396, 2017

Heat Recovery Optimization

C.KOCABAŞ¹ and A.F. SAVAŞ²

¹ Bilecik Şeyh Edebali University, Bilecik/Turkey, ceyda.pak@bilecik.edu.tr

² Bilecik Şeyh Edebali University, Bilecik /Turkey, ahmetfevzi.savas@bilecik.edu.tr

Abstract - In this study, changes in the heat recovery performance of the system under different operating conditions are investigated. A waste heat recovery device was installed for the experimental setup. A cross-flow plate heat exchanger made from cellulosic material is placed and thus heat transfer is ensured. Three different operating parameters were determined. Optimum conditions were determined by giving different values to these parameters. Statistical design of experiment (DOE) method was used for analyzes. As a result of the study, the values to be set for each parameter are explained in order to maximize the thermal effectiveness.

Keywords – Design of experiment, Plate heat exchanger, Cellulosic, Waste heat recovery, Thermal effectiveness.

I. INTRODUCTION

The rapid development of industry leads to the depletion of natural resources. For this reason, the *sustainability* of energy resources is very important. While meeting today's energy needs, on the one hand, resources to be transferred to future generations should be kept as much as possible.

Industrial systems that use very high amounts of energy have large heat recovery potential. With energy savings to be made in such systems, it will be possible to realize an environmentally sensitive production and to contribute to the country's economy. Waste energy can be reused by means of various equipments and one of the most preferred equipment for heat recovery is the plate heat exchanger. In this type of exchanger, hot air passes from one side of the plates while cold air is sent from the other side. At this point, some of the heat in the hot air is transferred to the cold air.

It is desirable that the heat exchanger plates are manufactured from materials having a high heat transfer coefficient. Therefore, aluminum is one of the most preferred materials in plate manufacturing. However, it is exposed to corrosion effects, especially in moist and chemical environments. For this reason, companies have turned to alternative materials. In recent years, materials such as polymers, ceramics, and cellulose have been used for this purpose. In this way, we can benefit from the positive properties of these different materials. For example; when micropore polymeric membranes or processed paper with moisture retention characteristics are used, latent heat transfer as well as sensible heat can be obtained and highest efficiency achieved [1, 2].

When we review the literature, studies on heat exchangers produced from paper or cellulose materials are very limited. Nasif et al. have experimentally evaluated the thermal performance of the heat transfer surface using a heat exchanger made of kraft paper [3]. Kocabas and Savaş, compared the waste heat recovery performance of a plate heat exchanger made of three different materials, aluminum, polymer and cellulosic [4].

In this study, different from the literature; the recovery performance of air to air waste heat was statistically investigated using a heat exchanger consisting of cellulosic plates. The purpose of this study is to reveal the best working parameters for waste heat recovery using the statistical design of experiment method.

II. MATERIAL AND METHODS

The present experiment simulates the process of transferring the heat contained in the exhaust air to the fresh air before the exhaust air is directed to the outer atmosphere. For this simulation; a system consisting of two fans to generate hot and cold air currents, resistors to generate hot air and a compressor to generate cold air is designed. In order to obtain exhaust air and fresh air at different temperature values, temperature thermostats which can set the desired value are used. In addition, a single-phase speed controller is preferred to control the speed of air supplied to the system [2].

A cross-flow plate heat exchanger is used in the system where heat transfer from air to air will be ensured. This system prevents dirty and clean air from mixing with each other. The heat exchanger consisting of cellulosic plates used in the experiment is given in Fig 1.



Figure 1: Cellulosic heat exchanger used in the experiment.

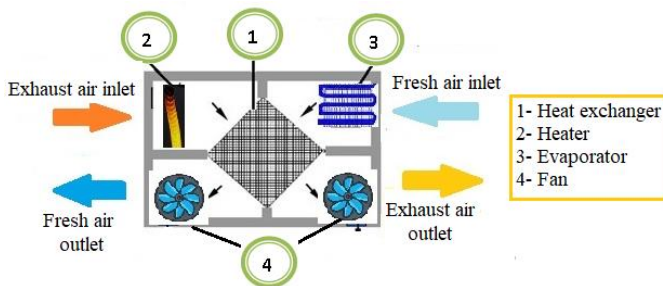


Figure 2: Schematic diagram of the heat recovery system.

The operating principle of the system is as follows: When exhaust air is sent from one side of the plate, fresh air passes by the other side. The fan is used to provide this air flow. The heat flow is synchronous. Fresh air and exhaust air do not come into contact with each other during heat transfer. Thus, the only heat transfer takes place. When the system is operated in winter conditions; warmer air is sent instead of cold fresh air towards the interior. So, by providing heat recovery; we have improved both thermal effectiveness and got energy saving [4].

Design of experiment; it is defined as experiments in which the input factors are intentionally changed in order to detect changes in output of a process. Variations in the output of the experiment are observed by giving various values to the factors. It is observed at which value the factors reach the target output. This method is very useful for determining the best or optimum operating conditions, estimating the individual effects of the factors, estimating the output values under optimal conditions, and so on [2, 5].

In order to implement the design of experiment method, quality variable, factors and levels should be determined. Therefore, in this study; thermal effectiveness is chosen as quality variable and it was aimed to maximize the thermal effectiveness value. Three factors have been identified: air flow rate, fresh air and exhaust air inlet temperatures. It is planned to use two levels of these factors. The factors represented by the letters A, B and C and their levels are shown in Table 1.

In the design of the experiment, ready tables which can be selected according to the factor and level numbers are used. By using these tables, we can perform experiments in a certain logic order and explain the results statistically. In the current study, $2 * 2 * 2 = 8$ experiments should be performed to test all combinations of factors and levels since there are 3 factors and 2 levels. The ready L8 (2^3) test plan is given in Table 2. The "-" sign on the table indicates the first level and the "+" sign indicates the second level [2].

Table 1: Factors and levels.

Symbol	Factors	Level 1	Level 2
A	Fresh air inlet temperature	0 °C	10 °C
B	Air flow rate	1.2 m/s	2 m/s
C	Exhaust air inlet temperature	28°C	40°C

Table 2: Ready L8 test plan [5].

Fresh air inlet temp.	Air flow rate	Exhaust air inlet temp.	Results
-	-	-	
-	-	+	
-	+	-	
-	+	+	
+	-	-	
+	-	+	
+	+	-	
+	+	+	

III. RESULTS

All experiments were carried out in accordance with the L8 test plan given in Table 2. Using fresh and exhaust air inlet and outlet temperatures, thermal effectiveness are calculated as we explained in our previous studies [2, 4]. Factors, levels and calculated effectiveness values are shown in Table 3.

To find out how much each factor affects the result of the experiment, all the results should be grouped four by four according to two different levels of each factor. The first group is the first four values of the factor corresponding to the first level and the other group is the last four values of the factor corresponding to the second level. To determine the effect of the relevant factor on the test result, it is necessary to take the average of the first four values and compare them to the average of the second four values. For example, when we select the fresh air inlet temperature, which is one of the factors, the effect of the factor is calculated as:

First group average = $(62,8+64,4+60,9+62,1) / 4 = 62,55$

Second group average = $(62,4+63,7+59,5+61,5) / 4 = 61,78$

Effect of factor = Second group average - first group average = $(61,78 - 62,55) = -0,77$ (values taken from table 3)

According to the calculation, the transition from the first level to the second level caused the effectiveness to fall from 62,55 to 61,78. In this case, the effect of this factor is -0.77 which is the difference between the two averages. The meaning of the "-" sign is that changing the factor from level 1 to level 2, reduces the result of the experiment. The effects of all other factors can be found in the same way.

Table 3: Effectiveness results in accordance with L8 test plan [2].

Factors			Effectiveness (%)
Fresh air inlet temp. (°C)	Air flow rate (m/s)	Exhaust air inlet temp. (°C)	
0	1.2	28	62,8
0	1.2	40	64,4
0	2	28	60,9
0	2	40	62,1
10	1.2	28	62,4
10	1.2	40	63,7
10	2	28	59,5
10	2	40	61,5

Table 4: Experimental results show in excel L8 table [2].

Experiment Results	A		B		C		AB		AC		BC		ABC	
	1. Level	2. Level	1. Level	2. Level										
62,8	62,8		62,8		62,8		62,8		62,8		62,8		62,8	
64,4	64,4		64,4			64,4		64,4	64,4		64,4			64,4
60,9	60,9			60,9	60,9		60,9			60,9	60,9			60,9
62,1	62,1			62,1		62,1	0.621		0.621			0.621	0.621	
62,4		62,4	0.624		0.624		62,1		62,1			62,1		62,1
63,7		63,7	63,7			63,7	63,7			63,7	63,7			63,7
59,5		59,5		59,5	59,5			59,5	59,5		59,5			59,5
61,5		61,5		61,5		61,5		61,5		61,5		61,5		61,5
Average	62,55	61,78	63,33	61,00	61,40	62,93	62,28	62,05	62,10	62,23	62,13	62,20	62,03	62,30
Effect	-0,77		-2,33		1,53		-0,23		0,12		0,08		0,27	

The excel table prepared in order to facilitate the above calculation is shown in Table 4. This table is used in practice for the analysis of test results as follows: First, the experiment result column is filled. All values in the row of this column are copied to the empty cells in that row. The averages of all columns are calculated and then saved on the "Average" row. Finally, the column averages of level 1 are subtracted from the average of the columns of each level 2 and the results are recorded in the "Effect" row [5].

The AB, BC, AC, and ABC columns indicate the interaction between factors. If we accept the first level of each factor as "-" and the value of the second level as "+" as we defined in Table 2, these signs are multiplied to create the sign of the interaction. For example, to find the sign of the first cell in the AC interaction column; The sign (-) on the first cell of A and the sign (-) on the first cell of C are multiplied. Since the multiplication result is "+", the sign of the first cell of the AC column becomes "+" and is saved as the 2nd level. The same method is followed to find the signs of other interactions. In this way; we can find the effects of all factors and interactions. The factor with the higher absolute value in the effect row has a much higher effect. According to this; factor B has the greatest effect, followed by factors C and A respectively.

Minitab program was used to visualize the data in the "Effect" row. The normal probability line showing the statistically significant effects is given in Figure 3. Confidence level was taken as 0.05 in statistical calculations. When the normal plot is examined, the significant points are found in the lower left corner of the graph or in the upper right part of the graph. The points near the normal probability line are statistically insignificant. Accordingly; points A, B, and C, which are directly distant, have been identified as significant; the AB, AC, BC and ABC interactions are considered to be insignificant since they are close to the line. The points on the left side of the line have a negative effect. This means that passing from the first level to the second level causes the result of the experiment to fall. Conversely, the points on the right side of the line have a positive effect on the end of result [2].

The Pareto graph showing the order of the points according to their significance levels is given in Figure 4. According to the Pareto graph; B is the factor with the greatest impact, followed by Factors C and A, respectively. If it is desired to improve effectiveness, the focus should first be on the B factor. As we can see in Figure 3, factor B has the (-) effect. Therefore; for the factor B, the first level, 1.2 m / s, should be selected.

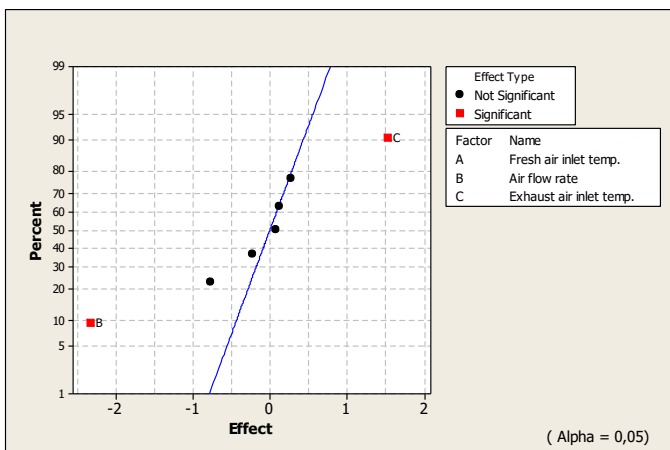


Figure 3: Normal plot of the effects.

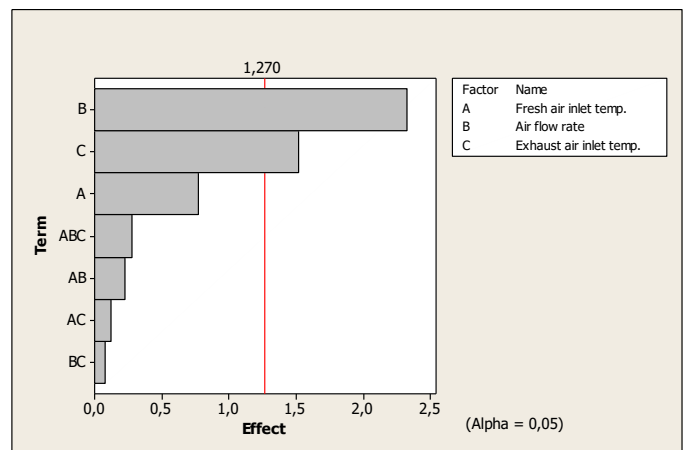


Figure 4: Pareto chart.

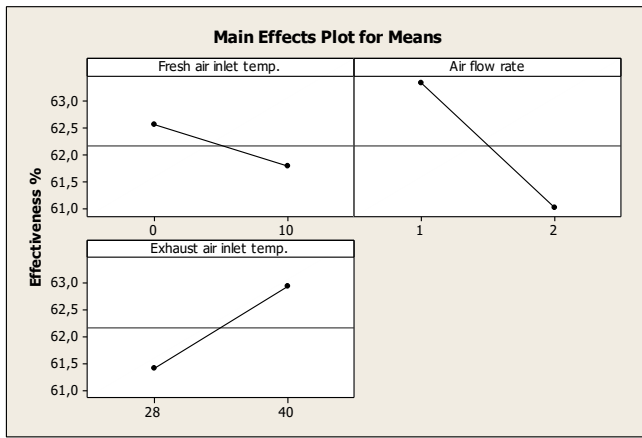


Figure 5: The effect of factors [2].

The change in the effect of bringing factors from the first level to the second level on the effectiveness is shown in Figure 5. The following comments can be made from this figure:

- 1) For Factor A: Increasing the fresh air inlet temperature from 0 ° C to 10 ° C will reduce effectiveness. This can be explained by the reduction in temperature difference between hot and cold air. The amount of the reduction is given in Table 4 as approximately 0,77%.
- 2) For factor B: Increasing the air flow rate from 1.2 m/s to 2 m/s led to a rapid fall in effectiveness. This is because there is not enough time for heat transfer when the air flow rate increases. The amount of fall is given in Table 4 as approximately 2,33%.
- 3) For factor C: Increasing the exhaust air inlet temperature from 28 ° C to 40 ° C will cause the effectiveness to rise slightly. This is due to the increase in temperature difference between hot and cold air. The amount of the increase is given in Table 4 as approximately 1,53%.
- 4) Air flow rate, represented by the factor "B" has the highest degree of effect on effectiveness. Then the factors "C" and "A" respectively.

IV. CONCLUSION

In this study, the effect ratios of factors affecting thermal effectiveness in a waste heat recovery system are investigated using full factorial design method L8 (2^3). A plan is created for two different levels of each factor. In analyzes where Minitab's statistical software program is preferred, air flow rate is the most effective factor. This is followed by exhaust air inlet temperature and fresh air inlet temperature, respectively.

These results show that higher effectiveness can be achieved at a low air flow rate, low fresh air inlet temperature and high exhaust air inlet temperature. In this respect, the most suitable working parameters for the system specified in the existing conditions; 0 ° C for fresh air inlet temperature, 1.2 m/s for air flow rate and 40 ° C for exhaust air inlet temperature. Moreover, this study shows that the experiment design method can be used easily in analyzing and optimizing the waste heat recovery performance.

REFERENCES

- [1] M. S. Owen, *Isıtma, Havalandırma ve İklimlendirme Uygulamaları*. İstanbul: ASHRAE -Türk Tesisat Mühendisleri Derneği, 2007.
- [2] C. Kocabaş, "Farklı malzemelerden imal edilmiş plakalı ısı değiştiricilerinin atık ısı geri kazanım performanslarının deneysel analizi", Master Thesis, Institute of Science and Technology, Bilecik Şeyh Edebali Üniversitesi, 2014.
- [3] M. S. Nasif, R. Al-Waked, M. Behnia, M. and G. Morrison, "Modeling of air to air enthalpy heat exchanger," *Heat Transfer Engineering*, vol. 33, pp. 1010-1023, 2012.
- [4] C. Kocabaş and A.F. Savaş, "Comparison of waste heat recovery performances of plate-fin heat exchangers produced from different materials," *Contemporary Engineering Sciences*," vol. 8(11), pp. 453 - 466, 2015.
- [5] M. Şirvancı, *Kalite İçin Deney Tasarımı Taguchi Yaklaşımı*. İstanbul: Literatür Yayınları, 1997.

Dynamic Characterization of the Torsional Vibration Damper using Quasi-static Torque Loading Test

A. ERKEÇ¹, Ö. F. ÜNAL¹, C. KAPLAN¹, Y. ÇETİNKAYA¹ and T. KARAÇAY¹

¹Kentpar Automotive, Konya/Turkey, anil.erkeç@kentpar.com.tr

¹Kentpar Automotive, Konya/Turkey, omer.unal@kentpar.com.tr

¹Kentpar Automotive, Konya/Turkey, cihangir.kaplan@kentpar.com.tr

¹Kentpar Automotive, Konya/Turkey, yuksel.cetinkaya@kentpar.com.tr

¹Gazi University, Ankara/Turkey, karacay@gazi.edu.tr

Abstract – Torsional vibration occurs in the crankshaft of an internal combustion engine due to the sudden burst in the firing orders. The torsional vibration dampers (TVD) are used to reduce these torsional vibrations. TVD's although it has different types, consist of a pulley, inertia ring and vulcanized rubber that connects the two parts to the hub, it works as dynamic absorber. Therefore, the design and determination of dynamic characteristic of TVD is critical for proper operations. Experimentally, the dynamic characteristic of a TVD could be determined by modal testing either using impact hammer or sweep test using a modal exciter. In this study, the dynamic characteristic of a TVD is determined using the quasi-static torque test data. Combining these data with the mechanical properties of the pulley and hub, the dynamic torsional characteristic of a TVD is obtained and the results are compared with the modal testing which is conducted by impact test.

Keywords - Torsional vibration damper, quasi-static torque test, torsional stiffness

I. INTRODUCTION

In internal combustion engines, sudden bursts and inertia forces in the firing order cause vibrations in the crankshaft. The most critical of these vibrations is the torsional vibration. Torsional vibrations lead to fatigue problems and failures in the crankshaft [1, 2].

Torsional vibration dampers are used to reduce torsional vibrations in the crankshaft. There are many different types of TVD with evolving technology. In general, TVD types are as follows:

- Frictional dampers
- Rubber dampers,
- Viscous damper,
- Spring damper.

These torsional vibration dampers are the dynamic components using inertia force and damping elements (dry friction, silicon oil and rubber) to reduce the torsional vibration. Despite being the same common name, these TVDs differ not only in design solutions but also in their operating characteristics [3]. The operating characteristics of different TVDs are as follows.

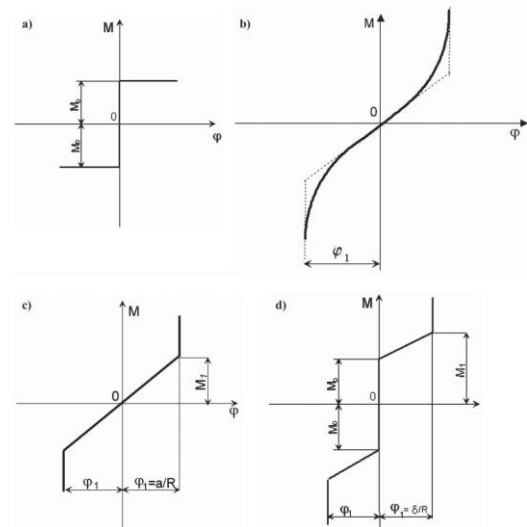


Figure 1: Operational characteristics of dampers [3]

In the automotive industry, the torsional vibration rubber damper (TVRD) is commonly used in internal combustion engines. TVRD is assembled on the front-end of the engine and transfers power to air conditioner pulley, alternator and pulley for water circulation pump. There are basically two types of TVRDs: single-mode TVRD and multi-mode TVRD. Single-mode TVRD consists of the following parts: inertia ring (pulley), rubber ring, and hub. Multi-mode TVRD consists of the following parts: pulley + hub with vulcanized rubber and inertia ring with rubber (Fig.3).

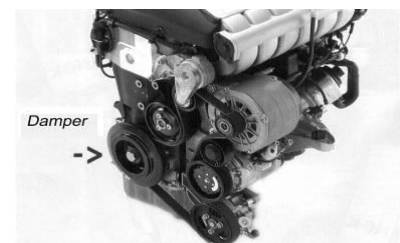


Figure 2: Internal combustion engine with torsional vibration dampers [4]



(a) Single mode TVRD



(b) Multi-mode TVRD

Figure 3: Torsional vibration rubber dampers

TVRDs operate as dynamic absorbers. The torsional natural frequency of TVRD is adjusted to the critical resonance frequency of the crankshaft. Thus, torsional vibration damper reduce torsional vibration of the crankshaft by means of rubber. Because of the internal friction of the deformation, the rubber exerts energy as heat during operation [4]. The elasticity of the rubber allows relative movement between the hub and the inertia ring.

Since TVRD is a dynamic absorber, it is critical to determine the dynamic characteristic in the design phase. The dynamic characteristic of the damper could be determined by modal tests. Modal test could be conducted either by impact test or sweep test using modal exciter, and these two tests have advantages and disadvantages relative to each other [5]. In the modal impact hammer test, in addition to triggering the torsional mode, bending modes can also triggered and this mode is observed in the frequency response analysis. These modes could be identified by the dynamic simulation of the TVD or especially, in the design phase, it is easier to calculate torsional stiffness from the torque test.

In this study, a quasi-static torque test data are used to determine the dynamic characteristics of a pulley + hub of the multi-mode TVRD. Torsional stiffness and torsional natural frequency of pulley + hub of TVRD has been calculated from the obtained results while mechanical properties of the pulley and hub obtained from CAD data. The accuracy of the results is discussed.

II. DYNAMIC CHARACTERISTIC OF TORSIONAL VIBRATION RUBBER DAMPER

Determination of dynamic characteristics of TVD is critical especially in the design phase. Therefore, test procedures must be planned precisely to determine dynamic characterization.

The dynamic characteristic of a TVD has its torsional natural frequency, damping and damping ratio. No damping ratio is included in the scope of this work. The torsional natural frequency of any system equals:

$$f = \frac{1}{2\pi} \sqrt{\frac{I}{k_t}} \text{ (Hz)} \quad (1)$$

Where; I : inertia moment, k_t : Torsional stiffness, f : natural frequency.

How the torsional natural frequency of the TVD is determined will be explained in detail in the next section. In addition, the torsional natural frequency of TVD and frequency response of the system is calculated using the mathematical model of TVD in numeric analysis. Extraction of a multimodal torsional vibration rubber damper mathematical model, finding the torsional natural frequency and evaluate the system frequency response is the subject of these studies, which is not in the scope of this work [6 - 9].

Although TVD do the same task - reducing the torsional vibration of the crankshaft - the dynamic characterization of different designs is self-evident. A multimode TVD has been used in this study. The component that determined dynamic characteristic of the TVRD is rubber. Rubber is a nonlinear material with viscoelastic characteristic. The correlation between rubber exposed torque load and its angular displacement is indicated by a hysterical curve. This hysterical loop is caused by the relaxation of the rubber. The torsion stiffness of the rubber has a non-linear characteristic. If the operation range of the TVD is determined correctly, the specified region can be linearized. Thus, a torsional stiffness is obtained and torsion stiffness equals:

$$k_t = \frac{T}{\theta} \text{ (Nm / rad)} \quad (2)$$

The torsional stiffness of the TVD can be determined by a quasi-static torque test which will be explained in the following section.

III. TESTS, RESULTS AND INTERPRETATIONS

A. Modal Impact Hammer Test

The dynamic characteristic of torsional vibration rubber damper is determined by modal hammer impact test and sweeps test using modal exciter. In this study, the torsional natural frequency of pulley + hub of TVD has been determined by the modal impact hammer test. Modal impact hammer test TVD is applied in the following way: The pulley + hub is rigidly assembled to the rigid frame. A small aluminum piece is tangentially bonded to the direction of rotation of the TVD. The excitation is applied via this small part with modal impact hammer. Thereby the torsional mode of TVD is excited. The response of TVD is measured by an accelerometer tangential to the direction of rotation of the damper (Fig.4). The measured response is applied to the FFT analysis and displayed the response in frequency domain.

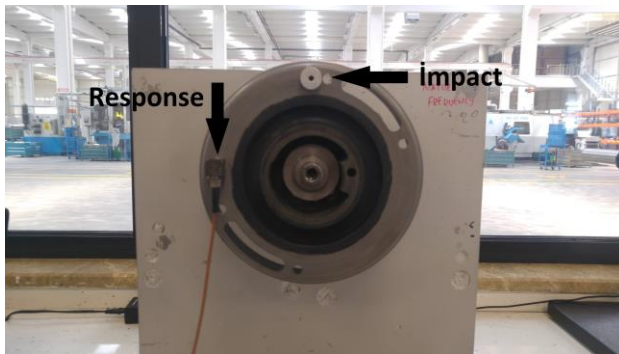


Figure 4: Modal impact test setup

In this study, used DJB IH-05, 1mV/N sensitivity modal hammer. Signal processing has been performed with Dewesoft Sirius 8 channel data acquisition system. To measure the response of the TVD, DJB AT/14 200 mV/g sensitivity three-axis accelerometer has been used. The test result is given in (Fig.5).

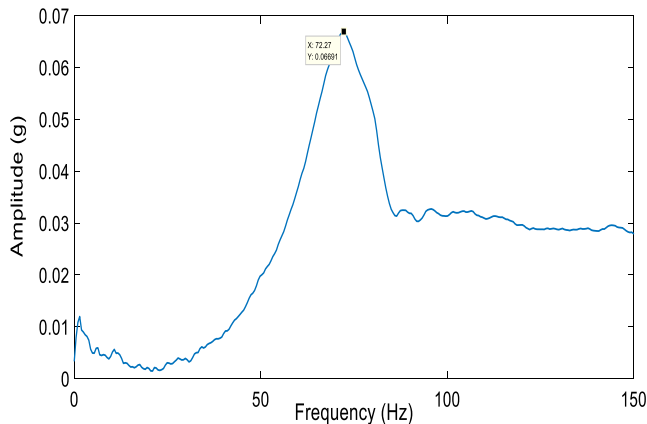


Figure 5: Torsional natural frequency of pulley + hub

According to the test result, the torsional natural frequency of the pulley + hub is 72.27 Hz. The moment of inertia obtained from the CAD data is used in Equation 1 and the torsional stiffness is calculated as 707.2 Nm/rad.

B. Quasi-static Torque Test

Quasi-static term refers the load applied slowly. For example, torsional loading of TVD in the 0-1 Hz range is quasi-static loading. With a torsional fatigue test bench, TVD can be torsional loading at the specific angle. The test bench displays the torque excited the torsional angle with aid of load cell. By this way, the excitation torque values for each angle are known. With these values, the angle-torque curve is drawn. The torsional fatigue test bench is shown in Fig.6.



Figure 6: Quasi-static torque test setup

The most important point in this result is that the curve is nonlinear. Therefore, the nonlinear curve must be linearized. The slope of the linear curve gives the torsional stiffness. What should be noted is the determination of the operating range of the torsional angle properly because of the slope changes due to the linearization of the different regions of the nonlinear curve. The acceptable torsional amplitude in the automotive industry is 0.4-0.5 degrees. In this study, TVD has been twisted from 1° to 7° at interval of 1° by torsional loading test instrument. The angle-torque curve has been drawn using the quasi-static torque test data. The obtained curve is linearized and the equation of the linear curve is shown as $y = ax + b$. In this equation, the coefficient “a” equal the torsional stiffness. The angle-torque graph is shown in Fig 7.

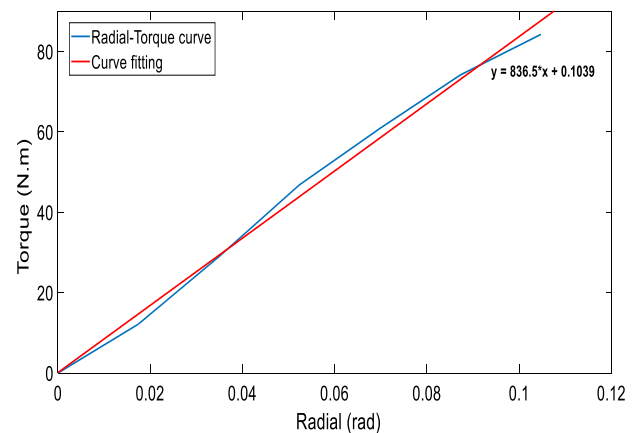


Figure 7: Nonlinear and linearized curves for first 7 degrees

According to the quasi-static torque test results, the torsional stiffness is 836.5 Nm/rad. The torsional natural frequency obtained from the torsional stiffness determined from quasi-static test is found to be 78.5 Hz. The inertia moment of the pulley + hub part is obtained from the CAD data. Inertia moment I is 0,0034342 kg.m². The results of both tests are shown in Table 1. According to the results, the error rate between the frequency obtained from the modal impact test and the frequency obtained from the quasi-static test is 0.08%.

Table 1: Torsional natural frequency and torsional stiffness obtained from two test method

Test Methods	Frequency	Torsional stiffness	Error
Modal Impact Hammer Test	72,27 Hz	707,2 Nm/rad	-
Quasi-static Torque Test	78,58 Hz	836,5 Nm/rad	%0,08

The results show that the torsional natural frequency of pulley + hub of TVD can be detected by quasi-static torque test with a low error rate. In addition, the reason the torsional natural frequency obtained by the modal impact hammer test is lower than the torsional natural frequency obtained by the quasi-static torque test is due to accelerometer and aluminum piece for using excitation increase moment of inertia. It is important to linearize which region of the non-linear curve formed in the quasi-static torque test result. If linearization is applied to the operation range properly, the error rate between the measured natural frequency and the natural frequency will be lower.

IV. CONCLUSION

In the design phase of a TVD, a quick and efficient method is need to determine the torsional dynamic characteristic of the TVD. The torque-loading test widely used in the TVD test and combining these data with the mechanical properties of the TVD obtained from CAD data could be easily used to determine the dynamic characteristic of the TVD easily with an acceptable accuracy.

ACKNOWLEDGMENT

This study was carried out within Kentpar Automotive R&D Center. The authors would like to thank to Kentpar Automotive R&D Center for its support in using of the test instruments and conduction of the tests.

REFERENCES

- [1] A. Londhe, V. Yadav, "Design and Optimization of Crankshaft Torsional Vibration Damper for a 4-Cylinder 4-Stroke Engine," SAE Technical Paper 2008-01-1213, 2008
- [2] P. Deuzskiewicz, J. Pankiewicz, "Nonlinear model of rubber torsional vibration damper," *Vibroengineering PROCEDIA*, Vol. 6, 2015, p. 13-17.
- [3] W. Homik, "Diagnostics, maintenance and regeneration of torsional vibration dampers for crankshafts of ship diesel engines," *POLISH MARITIME RESEARCH* 1(64) 2010 Vol 17; pp. 62-68
- [4] W. Homik, "Influence of temperature changes on torsional rigidity and damping coefficient of rubber torsional vibration damper," *Transport Problems*, Volume 6, Number 1, 2011, pp. 129-135(7)
- [5] Ö. F. Ünal, A. Erkeç, T. Karaçay "Krank Kasnağı Dinamik Karakteristiğinin Belirlenmesi," 9th International Automotive Technologies Congress, OTEKON 2018, p. 878-884
- [6] T. Matyja, B. Lazarz, "Selection of torsional vibration damper based on the results of simulation," *Journal of Vibroengineering*, Vol. 17, Issue 8, 2015, p. 4069-4077.
- [7] Z. Dabrowski, B. Chilinski, "Identification of a model of the crankshaft with a damper of torsional vibrations," *Journal of Vibroengineering*, Vol. 19, Issue 1, 2017, p. 539-548.

- [8] P. Deuzskiewicz, J. Pankiewicz, "Nonlinear model of rubber torsional vibration damper," *Vibroengineering PROCEDIA*, Vol. 6, 2015, p. 13-17.
- [9] W. Homik, P. Grzybowski, "The simulation model of small-dimension rubbery torsional vibration damper," *Vibroengineering PROCEDIA*, Vol. 6, 2015, p. 78-82.

Emission Characteristics of Biodiesel Blends in Common Rail Diesel Engine

H. AYDOĞAN¹, A.E. ÖZÇELİK¹ and M. ACAROĞLU¹

¹ Selcuk University, Mechanical Engineering, Konya/Turkey, haydogan@selcuk.edu.tr

¹ Selcuk University, Mechanical Engineering, Konya/Turkey, ozcelik@selcuk.edu.tr

¹ Selcuk University, Mechanical Engineering, Konya/Turkey, acaroglu@selcuk.edu.tr

Abstract - As a renewable, sustainable and alternative fuel for compression ignition engines, biodiesel instead of diesel has been increasingly fueled to study its effects on engine performances and emissions in the recent 10 years. Biodiesel is easily produced from the transesterification of vegetable oils (both edible and non-edible), animal fats, used cooking oil, and algae oil. Hence, biodiesel is a renewable, biodegradable, nontoxic and environmentally friendly biofuel. For example, biodiesel can be derived from palm oil, which is an edible oil; *Jatropha*, which is a non-food plant growing in dry and marginal land; or used cooking oil, which reduces the health risk from the repetitive re-use of oil. In the present study, the effects of 60% canola, 20% sunflower and 20% safflower oils blends biodiesel fuels obtained through transesterification on engine emissions of these fuels compared to diesel fuel were determined particularly focusing on new blend ratios of B7 and B20.

Keyword - Biodiesel, engine emissions, common rail engine

I. INTRODUCTION

Conventional transportation fuels from petroleum are one of the primary sources of greenhouse gas (GHG) emissions that promote global warming. Renewable fuels including ethanol, biodiesel, and jet fuel are practical and effective alternative energy sources [1-3].

Biodiesel production is an important area of research due to the increasing petroleum prices and the environmental advantages of biofuels. Biodiesel, a low-emission renewable fuel made from biomass resources, has recently attracted great interest as one of the best substitutes for diesel fuel [2, 4].

Among the various alternative fuels, biodiesel fuels have significant advantages and benefits such as renewable, sustainable, domestic, environmentally friendly, clean, high cetane number, non-toxic, superior flash point, high biodegradable, better inherent lubricity characteristics [3, 5, 6]. Moreover, the biodiesel has the minimal aromatic hydrocarbon and sulfur content. There is approximately 10e12% oxygen content by weight contained in the biodiesel structure. Additionally, the biodiesel can be operated in the diesel engine without modification because it can be used in both the neat and in the blended forms [7-11].

Biodiesel can have beneficial impacts on engine emissions. Many reports show a reduction of particulate matter emissions with biodiesel blends [e.g., [7, 10-14]]. Typically, the soluble organic fraction (SOF) of the particulate increases and the mutagenicity of the particulate SOF decreases. However, emissions of oxides of nitrogen (NOx) increase by 2–4% for B20 (i.e., 20 vol.% biodiesel blended with conventional diesel), and as much 10% for B100 (i.e., 100 vol.% biodiesel) [13-18]. The NOx increase has primarily been demonstrated in pump-line-nozzle (PLN) fuel injection systems [e.g., [5, 19]], but recent reports show that even in engines with common rail fuel systems the NOx increase is observed [20, 21].

In this study, a four-stroke, common-rail fuel system, a water-cooled, 4-cylinder diesel engine, the effects of biodiesel engines on engine emissions were investigated. The results were evaluated by comparison.

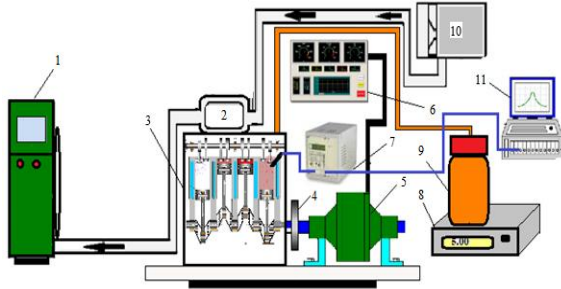
II. MATERIAL AND METHOD

Biodiesel was produced from 60% canola, 20% sunflower and 20% safflower oils blends used in this study using transesterification method. Two mixtures are considered in the volumetric mixture. These;

1. % 100 Eurodiesel
2. 7% Biodiesel +% 93 Eurodiesel
3. 20% Biodiesel +% 80 Eurodiesel

Experiments were carried out on the engine with common rail fuel system with these prepared mixtures. The work on biodiesel blends in engines with common-rail fuel systems is quite new. If it is related to walnut biodiesel, the work done is very few.

The experiments used a diesel engine with a four-stroke, four-cylinder, electronic fuel injection system with a common-rail fuel system. The test setup used in the study is shown in Figure 1 Technical specifications of the engine used in the survey Table 1 shows the characteristics of the engine dynamometer Table 2 and Table 3 show the specifications of the exhaust emission device.



- | | | |
|--------------------|--------------------------|---------------------------------|
| 1. Emission Device | 5. Hydraulic Dynamometer | 9. Fuel Tank |
| 2. Turbocharger | 6. Control Panel | 10. Orefiz Plate |
| 3. Test Engine | 7. Charging Amplifier | 11. AVL Cylinder pressure gauge |
| 4. Mesh | 8. Precision Balance | |

Figure 1: Schematic view of the test set

Table 1: Technical specifications of the engine used in the study

Motor	1.9 Multijet
Number of cylinders and layout	4, a single row of the front transverse
Cubic capacity (cc)	1910
Compression ratio	5.18: 1
Maximum power hp - d / d	105 - 4000
Maximum torque Nm (kgm) - d/d	200 - 1750
Fuel	diesel
Fuel supply	Electronically controlled Common Rail type MultiJet direct injection, turbocharger and intercooler compressional
Ignition	
Bore x Stroke (mm)	82 x 90.4

Table 2: Technical specifications of the engine dynamometer

Model	BT-190 FR
Capacity	100 kW
Maximum speed	6000 rpm
Maximum torque	750 Nm

A Bosch BEA 350 emission device was used to measure emissions of exhaust gases. Technical specifications of the emission device are given in Table 3.

Table 3: Technical specifications of the exhaust emission device

Parameters	Measurement Range	Precision
HC	0-20.000 ppm	1 ppm
CO ₂	0-20%	0.1%
CO	0-15%	0.001%
O ₂	0-21.7%	0.01%
NO _x	0-5000 ppm	1 ppm

The engine is heated to the operating temperature before starting the measurements. The experiments were performed at a full throttle position in different engine speeds. First, the experiment was performed using Eurodiesel fuel. Then the other blend fuels in volume were used in the B7 and B20 mixtures respectively.

III. RESULTS AND DISCUSSION

The main reason for the presence of CO among combustion products is the inadequacy of oxygen or the absence of complete combustion [22]. Figure 2 shows the variation of % CO in the exhaust gases with respect to engine dynamics in the use of biodiesel-eurodiesel fuels mixtures. When the figure is examined, it is seen that the amount of CO decreases a little as the cycle increases. B20 fuel use seems to have decreased by more than 37% in CO values. This reduction is due to the presence of oxygen in the content of biodiesel [23].

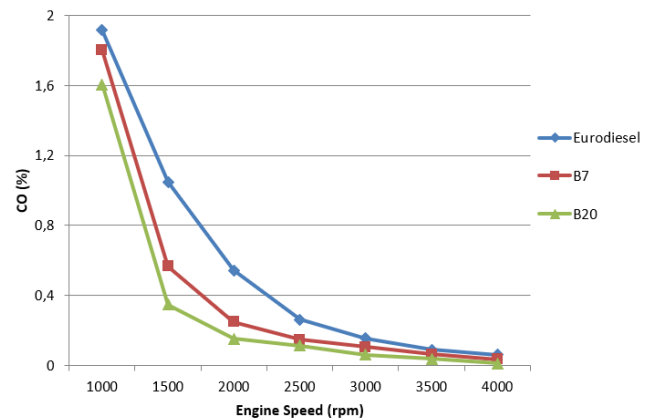


Figure 2: CO change according to engine speed

The variation of CO₂ values in the exhaust gases with respect to engine dynamics is shown in Figure 3. The increase in the amount of CO₂ in the exhaust gases shows a good combustion. With the use of biodiesel and eurodiesel mixtures, CO₂ emissions have been reduced by up to 20%. This decrease can be explained by the impoverishment of the mixture due to the presence of O₂ in the content of biodiesel.

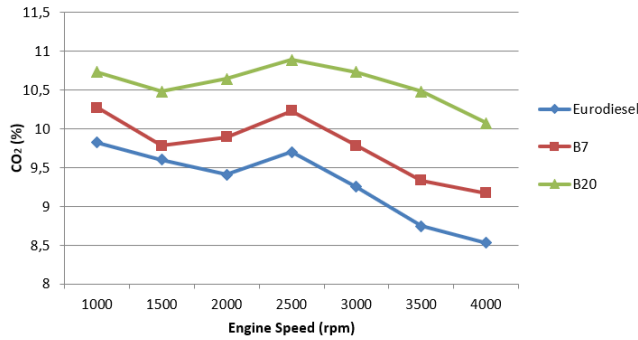


Figure 3: Change of CO₂ according to engine speed

HC means unburned fuel [1]. The use of biodiesel-eurodiesel mixtures in Figure 4 shows a change in HC values according to different engine speeds. The lowest HC value was measured in the use of B20 fuel. In the use of eurodiesel fuel, HC values decreased by more than 80%. This situation suggests that combustion is better [10].

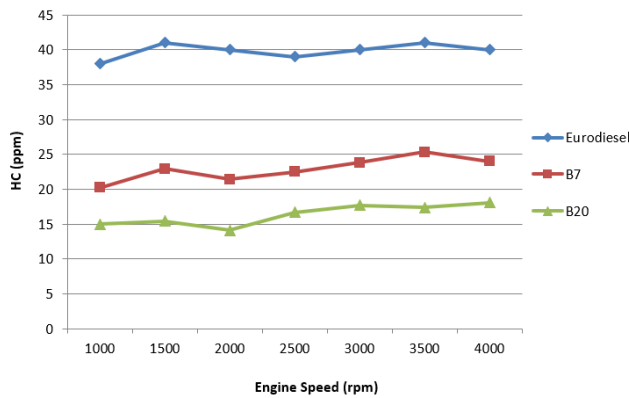


Figure 4: HC change according to engine speed

Oxygen values (O₂) change in exhaust gas according to engine rpm has given in Figure 5. At 1000 rpm lowest O₂ values recorded on eurodiesel, and highest recorded on B20. Increasing engine speeds caused a little drop in O₂ until engine reached 2000 rpm but after engine speed passed 2000 rpm O₂ level started to increase. Since biodiesel contains more O₂ compared to eurodiesel, it shows higher O₂ values on biodiesel mixture fuels.

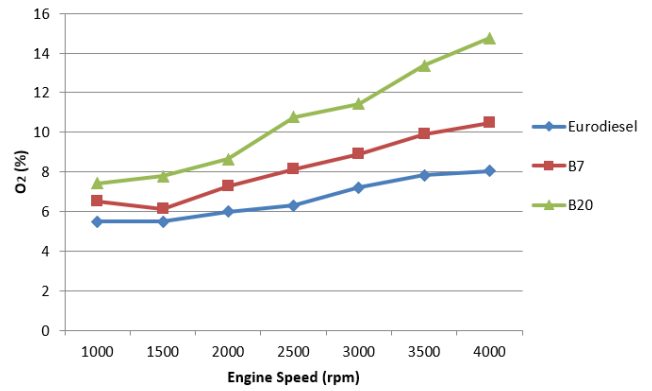


Figure 5: O₂ (%) value

In Figure 6, the use of biodiesel-eurodiesel blends shows a change in NO_x values relative to different engine speeds. The highest NO_x value was measured in the use of B20 fuel. The use of this fuel has shown that NO_x values increased by more than 10%. This is expected because of the presence of oxygen in the biodiesel.

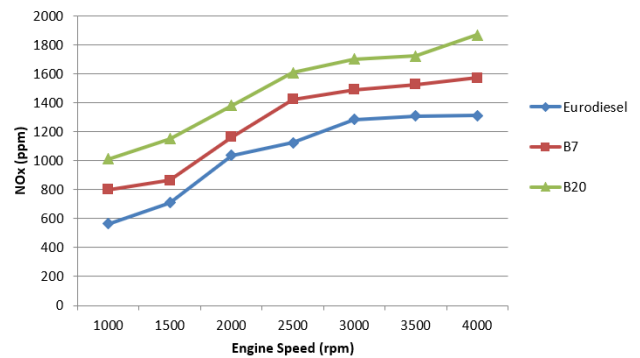


Figure 6: NO_x changes according to engine speed

Change in smoke emission values is given in Figure 6. If reviewed, highest exhaust gas smoke emissions recorded on 1000 rpm. Smoke emissions decrease with the increase of engine speed. The lowest emissions recorded on B20 fuel. Smoke emission decreases according to biodiesel percentage increase in fuel mixtures.

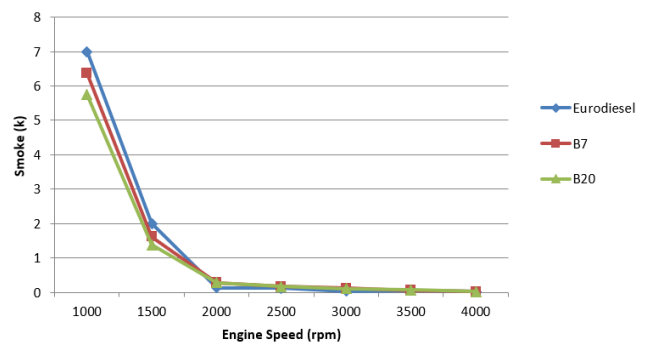


Figure 7: Smoke emission value of fuel

IV. RESULTS

This study was done with, eurodiesel and 60% canola, 20% sunflower and 20% safflower oil product biodiesel mixtures. This fuels are Eurodiesel, B7, B20 blends. This blends were used on a diesel engine with common-rail fuel system and emission values of these fuels reviewed. So, the result are:

1. Lowest CO values recorded with B20 which is 37% lower than eurodiesel.
2. Highest CO₂ values recorded with B20 which is 20% higher than eurodiesel.
3. Lowest HC values recorded with B20 and highest recorded in eurodiesel.
4. Lowest O₂ values recorded with eurodiesel fuel and the highest O₂ value recorded with B20 fuel blend.
5. Highest NO_x value recorded with B20 which is 10% higher than Eurodiesel.
6. Increase in biodiesel percentage of mixtures leads to smoke emission to decreased.

This study shows that biodiesel fuel on diesel engine increases NO_x emissions every other. Adding more biodiesel to eurodiesel fuel, highly affects vehicle emissions is the most important polluter of the world, so show us the importance of cleaner fuels sharper.

V. RESOURCES

1. Özçelik, A.E., H. Aydoğan, and M. Acaroğlu, *Determining the performance, emission and combustion properties of camelina biodiesel blends*. Energy Conversion and Management, 2015. **96**: p. 47-57.
2. Arunkumar, M., M. Kannan, and G. Murali, *Experimental studies on engine performance and emission characteristics using castor biodiesel as fuel in CI engine*. Renewable Energy, 2019. **131**: p. 737-744.
3. Atmanli, A. and N. Yilmaz, *A comparative analysis of n-butanol/diesel and 1-pentanol/diesel blends in a compression ignition engine*. Fuel, 2018. **234**: p. 161-169.
4. Dueso, C., et al., *Performance and emissions of a diesel engine using sunflower biodiesel with a renewable antioxidant additive from bio-oil*. Fuel, 2018. **234**: p. 276-285.
5. J.P. Szybist, A.L.B., *Behavior of a diesel injection system with biodiesel fuel*. Society of Automotive Engineers, 2003. **2003-01-1039**.
6. Lapuerta, M., O. Armas, and J. Rodriguezfernandez, *Effect of biodiesel fuels on diesel engine emissions*. Progress in Energy and Combustion Science, 2008. **34**(2): p. 198-223.
7. C.A. Sharp, S.A.H., J. Jobe, *The effect of biodiesel fuels on transient emissions from modern diesel engines, part 1 regulated emissions and performance*. Society of Automotive Engineers, Technical Paper, 2002. **2002-01-1967**.
8. Örs, I., et al., *The effects on performance, combustion and emission characteristics of DICl engine fuelled with TiO₂ nanoparticles addition in diesel/biodiesel/n-butanol blends*. Fuel, 2018. **234**: p. 177-188.
9. P. Szybist, A.L.B., R.L. McCormick, J.D. , *Evaluation of formulation strategies to eliminate the biodiesel NO_x effect*. Fuel Processing Technology 2005. **86**(10): p. 1109-1126.
10. Perumal, V. and M. Ilangkumaran, *The influence of copper oxide nano particle added pongamia methyl ester biodiesel on the performance, combustion and emission of a diesel engine*. Fuel, 2018. **232**: p. 791-802.
11. Sandouqa, A., Z. Al-Hamamre, and J. Asfar, *Preparation and performance investigation of a lignin-based solid acid catalyst manufactured from olive cake for biodiesel production*. Renewable Energy, 2019. **132**: p. 667-682.
12. R.L. McCormick, M.R., L. Moens, R. Lawrence, *Factors affecting the stability of biodiesel sold in the United States*. Preprint of Papers-American Chemical Society Division Fuel Chemistry 2006. **51**(1): p. 14-15.
13. Sathiyamoorthi, R., et al., *Experimental investigation on performance, combustion and emission characteristics of a single cylinder diesel engine fuelled by biodiesel derived from Cymbopogon Martinii*. Renewable Energy, 2019. **132**: p. 394-415.
14. Suthisripok, T. and P. Semsamran, *The impact of biodiesel B100 on a small agricultural diesel engine*. Tribology International, 2018. **128**: p. 397-409.
15. M.S. Graboski, R.L.M., *Combustion of fat and vegetable oil derived fuels in diesel engines*. Progress in Energy and Combustion Science, 1998. **24** (2): p. 125-164.
16. Szybist, J.P., et al., *Biodiesel combustion, emissions and emission control*. Fuel Processing Technology, 2007. **88**(7): p. 679-691.
17. Vardast, N., M. Haghighi, and S. Dehghani, *Sono-dispersion of calcium over Al-MCM-41 used as a nanocatalyst for biodiesel production from sunflower oil: Influence of ultrasound irradiation and calcium content on catalytic properties and performance*. Renewable Energy, 2019. **132**: p. 979-988.
18. Xue, J., T.E. Grift, and A.C. Hansen, *Effect of biodiesel on engine performances and emissions*. Renewable and Sustainable Energy Reviews, 2011. **15**(2): p. 1098-1116.
19. M.E. Tat, J.H.V.G., S. Soylu, M. Canakci, A. Monyem, S. Wormley, *The speed of sound and isentropic bulk modulus of biodiesel at 21 degrees C from atmospheric pressure to 35 MPa*. Journal of the American Oil Chemists Society, 2000. **77**(3): p. 285-289.
20. Cheng, A.S., Upatnieks, A. and Mueller, C.K., , *Investigation of the impact of biodiesel fueling on NO_x emissions using an optical DI diesel engine*. International Journal of Engine Research, 2006.
21. Yesilyurt, M.K., *The effects of the fuel injection pressure on the performance and emission characteristics of a diesel engine fuelled with waste cooking oil biodiesel-diesel blends*. Renewable Energy, 2019. **132**: p. 649-666.
22. Manigandan, S., et al., *Emission and injection characteristics of corn biodiesel blends in diesel engine*. Fuel, 2019. **235**: p. 723-735.
23. Nabi, M.N. and M.G. Rasul, *Influence of second generation biodiesel on engine performance, emissions, energy and exergy parameters*. Energy Conversion and Management, 2018. **169**: p. 326-333.

Tool Wear Based Surface Roughness Prediction via Neural Network in Face Milling

H. SAĞLAM¹ and M. KUNTOĞLU²

¹Selcuk University, Konya/Turkey, hsaglam@selcuk.edu.tr

²Selcuk University, Konya/Turkey, mkuntoglu@selcuk.edu.tr

Abstract - Actually, face milling is most widely used to generate flat surfaces in manufacturing industry. The quality of machined surface is evaluated in terms of surface roughness parameters as Ra and Rt and surface geometry as flatness. The estimation of surface roughness has closely dependent on flank wear- V_B as tool wear-and also the monitoring of tool wear is very important for optimisation of cutting parameters and performing the automated manufacturing as reliable as possible. The machined surface reflects the rate of tool wear and the plot of surface provides reliable information about tool condition. At the beginning of cutting, the tool insert is sharp that surface roughness is higher, and then decrease with increased tool wear after that increase with exceeded tool wear. Therefore the tool life is limited by required surface quality. In this paper the quality of surface parameters defined depend on tool wear is estimated by artificial neural network (ANN). Multilayer perceptron (MLP) neural networks (NN) trained by backpropagation are used for estimating surface roughness with four input parameters as three component of cutting forces and tool wear- V_B into account. Also the effects of input parameters on surface roughness are also evaluated. Since metal machining is shown a nonlinear character, ANN with parallel computation ability and having high success solving nonlinear equation systems the estimated results are very close to the experimental results.

Keywords - Surface Roughness, Tool Wear, Tool Condition Monitoring, Artificial Neural Network

I. INTRODUCTION

In principle, face milling is most widely used machining operations of metal cutting for the generation of flat surfaces of workpiece. According to the international standards, the quality of machined surface is measured in terms of surface roughness, Ra/Rt. Surface roughness has in various papers [1, 2, 3] been shown to increase with increased flank wear of face mill teeth. Workpiece specifications will usually detail the maximum roughness value that has to be machined. As the worn surface of the cutting edge increases, the cutting edge of the replaceable indexable inserts must therefore be changed, before the maximum surface roughness is reached [4, 5, 6].

Many researchers have developed surface roughness prediction models in face milling using Artificial Intelligence (AI). Benardos and Vosniakos [7] introduced the neural network modelling approach to predict surface roughness, Ra, in Computer Numerical Control (CNC) machine face milling. Saglam and Unuvar [8] suggested the use of a multilayer neural network for status monitoring and the estimation of flank wear and surface roughness in face milling. Selaimia et al. [9] modelled the output responses, namely: surface

roughness (Ra), cutting force, cutting power, specific cutting force and metal removal rate during the face milling of the austenitic stainless steel.

The cutting force system in face milling has been extensively studied both analytically and empirically. A more empirical approach to modelling a face milling system has been popular and well developed [10,11]. He also introduced the notion that the average undeformed chip thickness could be used in establishing a relationship between the condition of the cut and specific cutting pressure required. Koenigsberger and Sabberwal [12] studied tangential force in detail in both slab and face milling. They confirmed that specific cutting pressure is only a function of instantaneous chip thickness disregarding the workpiece material, the shape of the cutter, helix and chip cross-section. Advances in dynamometry and other instrumentation and computer technology have led through the work of several investigators [13,14] to our present knowledge of the milling operation.

Due to discontinuous nature of the cutting and chip geometry changing continuously during milling, cutting forces must be analysed as detailed. The cutting forces, temperature, vibration and acoustic emission signals occurring during cutting are source of information about the basic mechanic of chip formation and/or tool condition. From these, cutting force has been a primary measurement in a majority of previous studies in milling for sensing surface roughness and tool wear [15]. Since the chip thickness varies throughout each cutting cycle, this generates varying tool forces and contact conditions at the tool surface. During cutting, chips sometimes adhere or weld onto the cutting edge and are carried into the next cut and cause a build-up edge and consequently increase on cutting forces. As the milling cutter is multi-edged tool and more than one-edge joins to cut, the oscillating happens on cutting forces.

It is known that cutting forces is an important criterion on tool condition monitoring they are taken as reference to decide output parameters such as tool wear, surface roughness and tool life. In this paper an indirect method as ANN will be used prediction of surface roughness employing cutting forces and tool wear (V_B) into account. Therefore, a tool condition monitoring system that defining surface roughness generate a signal to keep the surface roughness in desired range.

A. Cutting Force Generation and Measurement in Face Milling

Milling can be classified as peripheral and face milling. Face milling can be examined as up and down-cut milling too depends on tool diameter, the position of workpiece according to the tool and the direction of feed. In face milling the chips are cut by the periphery of the cutter. The cutter edges produce very little contact to the workpiece surface and so high degree of flatness can be obtained. Due to the long-undeformed chip length the torque at the arbour is quite smooth [16].

The cutting forces generated in face milling can be analysed as seen in Fig. 1. Since the dynamometer actually measures the normal (F_Y) and feed forces (F_X) on the workpiece, radial forces (F_R) and tangential forces (F_T) based on (F_Y) and (F_X) can be calculated as a function of instantaneous position angle (θ) of the cutting edge [17].

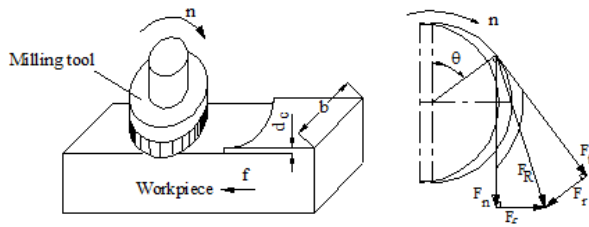


Fig. 1 Cutting forces in peripheral milling

$$F_T = F_X \cos\theta - F_Y \sin\theta \quad (1)$$

$$F_R = F_X \sin\theta + F_Y \cos\theta \quad (2)$$

The tangential forces are assumed to be proportional to the instantaneous chip thickness while the radial force is expressed as a fraction of tangential force by neglecting effects of tool geometry (rake and lead angles).

$$F_T = k_s d_c f_i \sin\theta$$

$$F_R = F_T k_r$$

Therefore, a simple but good approximation to the instantaneous chip loads of the tooth, C_i , at angular position θ_i , is ($F_T \sin\theta_i$) [11]. The instantaneous chip cross-sectional area can, therefore, be approximated accurately as ($F_T \sin\theta_i d$), where;

k_s : specific cutting pressure (N/mm^2),

k_r : a constant relating radial force to tangential force,

f_i : feedrate per tooth

d_c : axial depth of cut

In face milling system, axial forces coincide with Z-forces while X-forces and Y-forces can be obtained by decomposing tangential and radial forces that are measured by the dynamometer as follow. In multi-tooth face milling, there may be more than one tooth cutting simultaneously. Therefore, to obtain forces on the cutter at any instant (angle of cutter rotation), component forces acting on each tooth that is engaged with the workpiece must be summed.

II. TOOL WEAR AND SURFACE ROUGHNESS

Tool wear is a natural fact as a result of interaction of tool-work-piece couple and machining conditions. The amount of initial wear is dependent on cutting conditions. Since friction has been occurred on interface of tool-chip and tool-work-piece, wear is developed on the different locations: nose, flank and notch. Temperature is also an accelerated factor in this process. Following the primary stage, the tool progressively wears at almost constant rate until it reaches the final stage at which wear develops at an increasing rate leading to a tool failure [18]. Some tool wear mechanisms such as plastic deformation, abrasive wear, diffusion, oxidation, fatigue and adhesion wear are dominant on tool wear. During cutting, three faces of tool participate cutting and the main tool wear types such as flank wear (V_B) crater wear (KT), nose wear and also notch wear at the end of depth of cut occur. The cutting parameters such as cutting speed, feed rate and depth of cut are effective on tool wear while the dominant factor is cutting speed.

The surface roughness is one of the widely known measurable surface quality parameters. Cutting parameters should be determined correctly in order to obtain ideal surface roughness values. Surface roughness affects the work piece properties such as tribological, sealing, hydrodynamic, electrical conduction and thermal conduction. Improving the values of surface roughness depend on the factors that by reducing depth of cut, low feed rate, high cutting speed, increased delivery of cutting fluid, higher nose radius, and rake angles [19, 20]. The provided models that predicting surface quality in advance will lead about determining cutting parameters increase operation efficiency.

During machining progressed tool wear increases cutting force components at different levels (Fig. 2). In addition, at the beginning of machining with new cutting insert surface roughness is higher and then it is decreased with increased tool wear (Fig. 3).

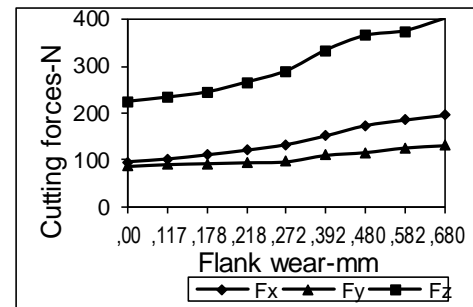


Fig. 2 Graph of wear-cutting forces

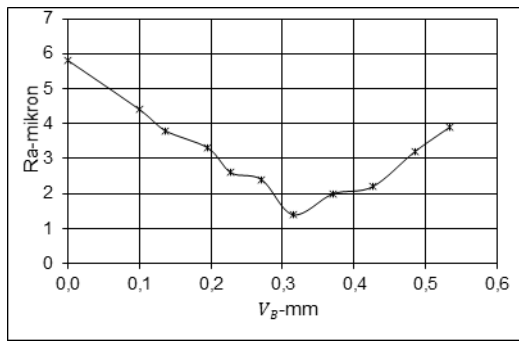


Fig. 3 Graph of wear-surface roughness ($v=140$ m/min; $f=0.088$ mm/tooth; $d=1.5$ mm)

The cutting inserts of milling tool have to be changed before desired surface quality value is exceeded. It is possible to manage the process of changing surface roughness directly by controlling the amount of tool wear through dimensional wear.

III. ESTIMATION OF SURFACE ROUGHNESS

A. Artificial Neural Network

Automated machining systems require reliable on-line monitoring processes. In this paper, the application of multi-layered neural network for TCM in face milling was introduced and evaluated on cutting force data. The present work uses the with back-propagation (BP) algorithm for training neural network of $4 \times 8 \times 1$ architecture. ANN's have been used for feature selection in order to estimate surface roughness (Ra) during milling operation. The relationship of cutting parameters with V_B and Ra are established. The sensor selection using statistical methods based on the experimental data helps in determining average effect of each factor on the performance of NN model. This model with cutting speed, feed rate, depth of cut and three cutting forces components (feed force, radial force and vertical-Z-axis force) presents close matching for estimation of Ra . Therefore, the NN with parallel computation ability provides possibility for setting up intelligent sensor systems. Thus, the purpose of this study is to set up a model for predicting the surface roughness in a complex correlation between tool wear and cutting forces using ANN in online monitoring of manufacturing.

IV. MATERIAL AND METHOD

A. Experimental Procedure

Experimental face milling was performed, in order to predict the roughness of based on the flank wear three components of cutting forces. To do so, experimental sample manufactured from Ç1040 (similar to AISI 1040) steel and hardened at 40 HRc and with the dimensions $150 \text{ mm} \times 65 \text{ mm} \times 40 \text{ mm}$ was machined on the milling machine. The milling process is carried out at dry conditions using the non-coated cutting inserts of Mitsubishi SPMW 12 04 08 SBF (HW) P15-P30. The cutting parameters employed for the face milling operations are specified in Table 1.

Table 1. Cutting parameters

Cutting speed (m/min)	Feed rate (mm/min)	Depth of cut (mm)
113	200	1
140	250	1,5
178	315	2,5
226	400	3,5

The cutting force components were measured by force dynamometer [21]. Meanwhile the flank wear land of the inserts placed on mill tooth was measured periodically by tool maker (Fowler-Sylvac 25) while surface roughness is measured by surf test profilometer (Taylor-Hobson Mitutoyo) as Ra from the three locations on machined surfaces and averaged for analyse. According to full factorial design for four levelled three variables ($4^3=64$) experiments were needed but instead of that orthogonal array developed by Taguchi [22] the outputs of 16 experiments were considered.

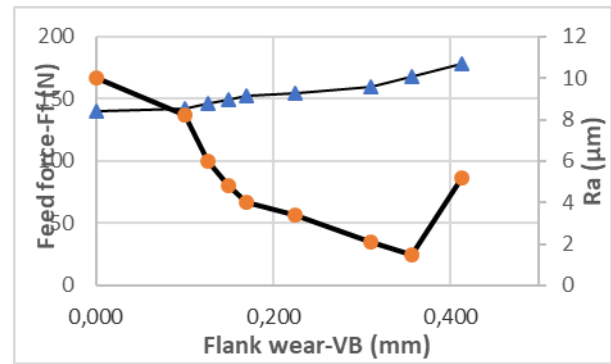
B. Modelling of Neural Network

For modelling surface roughness, multi-layered neural networks were used in the present work. The activation function in the NN is sigmoid function, which is a non-linear function. The NN have to be trained as off-line with BB type training algorithm [12] and then can be tested on-line with feed-forward method. In the case of MLPs, three parameters are tuned: momentum, learning rate, and number of neurons in the hidden layer. The most common ANN typologies are considered as standards in the prediction of surface roughness in machining processes [23]. MLPs use a back-propagation algorithm to calculate the weights for each connection between neurons [24]. When determining training models for the network, 12 cutting pass were taken as a reference. The input and output values are normalized between 0-1 to fit to the sigmoid function. So the selected training models for 16 experiment combinations are given in Table 2.

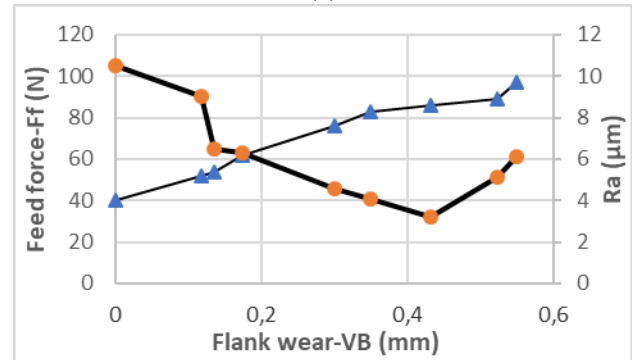
The graphs (a-d) of the average experimental values of the surface roughness as a function of flank wear and feed force values selected are shown in Fig. 4. At the beginning of the tests, the flank wear is zero, cutting force components starts to increase but the surface roughness is higher at first passes then down to minimum value, after that increases again till the cutting tool reach the catastrophic tool failure. Increased feed rate also causes increment especially on feed force (F_f) and surface roughness since risen feed force is a function of feed rate (Fig. 4). Feed rate, on the other hand feed force and also cutting tip radius are more effective on surface roughness. As a result of progressive tool wear, tool tip radius is to be greater gradually and instead of ideal cutting chatter will be dominant because of tool vibration, so surface roughness increases after minimum point. Therefore, in order to control of surface roughness the change in flank wear as periodically and feed force as continuously can be monitored.

Table 2. Training patterns for ANN

Test No..	Inputs							Output
	v	f	d	F_x	F_y	F_z	VB	
1	113	200	1,0	87	115	225	0,383	1,3
2	226	400	3,5	234	341	550	0,544	3,2
3	140	250	3,5	222	220	518	0,291	2,0
4	178	315	1,0	110	112	222	0,542	2,6
5	178	200	3,5	140	142	351	0,202	1,1
6	140	400	1,0	97	124	306	0,548	3,8
7	226	250	1,0	76	84	208	0,491	2,2
8	113	315	3,5	211	270	590	0,247	3,7
9	226	315	1,5	92	107	240	0,467	2,1
10	113	250	2,5	170	199	500	0,217	1,8
11	178	400	2,5	150	216	380	0,454	3,3
12	140	200	1,5	76	106	205	0,228	1,2
13	140	315	2,5	160	190	430	0,310	2,9
14	178	250	1,5	88	120	250	0,305	2,1
15	113	400	1,5	121	215	345	0,385	4,2
16	226	200	2,5	132	96	290	0,272	1,0

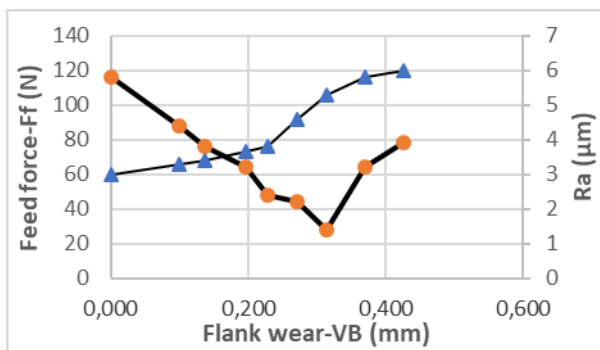


(c) $(v=140 \text{ m/min}, f=315 \text{ mm/min}, d=2.5)$

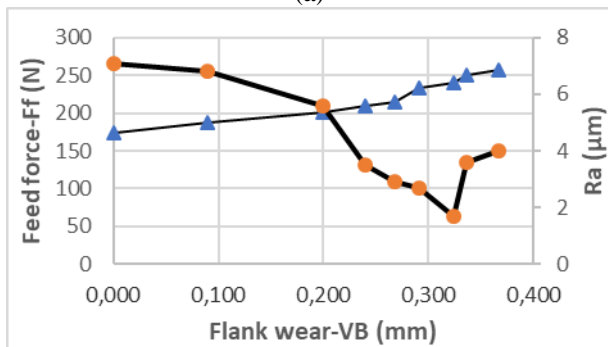


(d) $(v=140 \text{ m/min}, f=250 \text{ mm/min}, d=1)$

Fig. 4 Variation of surface roughness depends on tool wear and feed force



(a) $(v=140 \text{ m/min}, f=200 \text{ mm/min}, d=1.5)$



(b) $(v=140 \text{ m/min}, f=250 \text{ mm/min}, d=3.5)$

Multilayer perceptron (MLP) neural networks trained by backpropagation are used for estimating surface roughness with four input parameters as three component of cutting forces and tool wear (V_B) into account. Also the effects of input parameters on surface roughness are also evaluated. The network configuration for training and test patterns are arranged in Fig. 5.

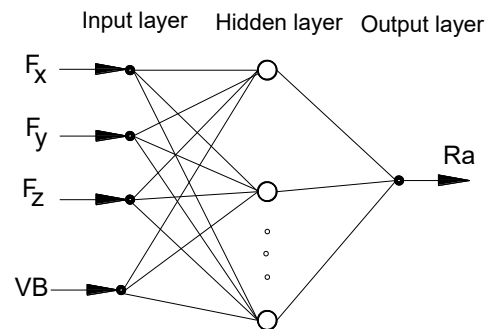


Fig. 5 Neural network configuration used for training

In this study, experimental results were modelled to predict surface roughness using ANN architecture by means of NN toolbox in MATLAB. In order to carry out the performance of ANN the results of five patterns were used as a test patterns given in Table 3. In the architecture one hidden layer and 8 neurons in the hidden layer were used. The results of ANN for

test patterns are also given in last column of Table 3. The obtained regression coefficient of R_a is 0,8719.

Table 3. The ANN and Experimental Results for Test Patterns

Test No.	Inputs							Output (R_a)	
	v	f	d	F_x	F_y	F_z	VB	Exp.	ANN
1	113	315	3,5	211	270	590	0,247	3,7	3,293
2	226	200	2,5	132	96	290	0,272	1,0	1,1054
3	140	400	1,0	97	124	306	0,548	3,8	4,1995
4	178	400	2,5	150	216	380	0,454	3,3	3,7457
5	178	250	1,5	88	120	250	0,305	2,1	1,3479

The results of the comparison of surface roughness values estimated by ANN in test patterns (Table 3) showed very close similarities to the experimental results. So that, reliance or reliability of applicability of ANN in modelling and having done study has been observed and proved in Fig. 6.

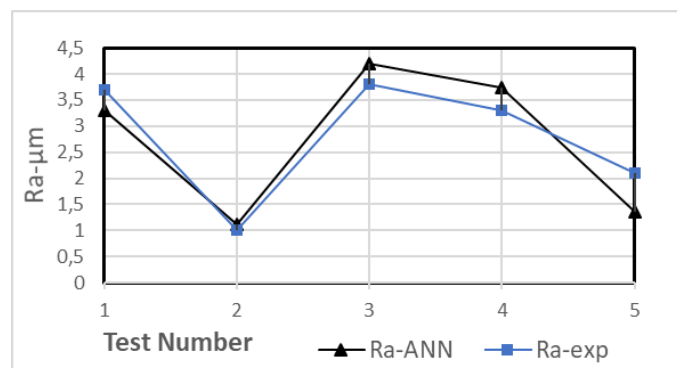


Fig. 6 Comparison of roughness estimated by ANN and measured values

V. CONCLUSIONS

The aim of the study is to develop an ANN model to estimate surface roughness based on tool wear and the cutting force components in dry conditions. The model developed can be used to define the quality of surface finish in tool condition monitoring systems. The system developed was found accurate enough to predict surface roughness in the trained range although metal cutting processes present non-linear characteristic. It was found that the ANN results are very close to the experimental results. In this case, in order to obtain prediction of surface roughness the flank wear is evaluated, the cutting forces, especially feed force are monitored and the machining process is stopped when the desired surface roughness is achieved. If the values of both feed force and flank wear are low, the roughness may remain at low values. However, if either of these two parameter values exceeds a certain threshold, surface roughness levels will increase dramatically.

As a result, since cutting tool wear and feed force signals are source of reliable information about tool condition, they can be used as primary input prediction of surface quality in tool condition monitoring systems.

REFERENCES

- [1] A. Fernández-Valdivielso, L. López De Lacalle, N. Urbikain, G. A. Rodriguez, "Detecting the key geometrical features and grades of carbide inserts for the turning of nickel-based alloys concerning surface integrity", *Proceedings of the Institution of Mechanical Engineers, Part C: Journal of Mechanical Engineering Science*, vol. 230(20), pp. 3725–3742, 2016
- [2] D. Y. Pimenov, "Geometric model of height of micro roughness on machined surface taking into account wear of face mill teeth", *Journal of Friction and Wear*, vol. 34(4), pp. 290–293, 2013.
- [3] D. Y. Pimenov, "Experimental research of face mill wear effect to flat surface roughness" *Journal of Friction and Wear*", vol. 35(3), pp. 250–254, 2014.
- [4] F. Gong, J. Zhao, Y. Jiang, H. Tao, Z. Li, J. Zang, "Fatigue failure of coated carbide tool and its influence on cutting performance in face milling SKD11 hardened steel", *International Journal of Refractory Metals and Hard Materials*, vol. 64, pp. 27–34, 2017.
- [5] T. Mikołajczyk, K. Nowicki, A., Kłodowski, D. Y. Pimenov, "Neural network approach for automatic image analysis of cutting edge wear", *Mechanical Systems and Signal Processing*, vol. 88, pp. 100–110, 2017.
- [6] T. Mikołajczyk, K. Nowicki, A. Bustillo, D. Y. Pimenov, "Predicting tool life in turning operations using neural networks and image processing", *Mechanical Systems and Signal Processing*, vol. 104, pp. 503–513, 2018.
- [7] P. G. Benardos, G. C. Vosniakos, "Prediction of surface roughness in CNC face milling using neural networks and Taguchi's design of experiments", *Robotics and Computer-Integrated Manufacturing*, vol.18(5–6), pp. 343–354, 2002.
- [8] H. Saglam, A. Unuvar, "Tool condition monitoring in milling based on cutting forces by a neural network", *International Journal of Production Research*, vol. 41(7), pp. 1519–1532, 2003.
- [9] A. A. Selaimia, M. A. Yaltese, H. Bensouilah, I. Meddour, R. Khattabi, T. Mabrouki, "Modeling and optimization in dry face milling of X2CrNi18-9 austenitic stainless steel using RMS and desirability approach", *Measurement: Journal of the International Measurement Confederation*, vol. 107, pp. 53–67, 2017.
- [10] M. E. Martellotti, "An analysis of the milling process", *ASME Transactions*, vol. 63, pp. 677-700 1941.
- [11] M. E. Martellotti, "An analysis of the milling process, Part II: Down Milling", *ASME Transactions*, vol. 67, 1, pp. 233-251, 1945.
- [12] F. Koengsberger, A. J. P. Sabberwal, "An investigation into the cutting force pulsations during milling operations", *Int. J. of Machine Tool Des. and Research*, vol. 1, pp. 15-33, 1961.
- [13] J. Tlustý, P. MacNeil, "Dynamics of cutting forces in end milling", *Annals of CIRP*, pp. 20-25, 1975.
- [14] J. Tlustý, F. Ismail, "Special aspects of chatter in milling", *ASME Journal of Vibration*, vol. 105, pp. 24-32, 1983.
- [15] H. Victor, "Computer-aided measurement of cutting forces applied to the wear of an end milling cutter", *Wear*, vol. 62, pp. 185-195, 1980
- [16] H. Saglam, A. Unuvar, "Three-component, strain gage based milling dynamometer design and manufacturing", *Transaction of the SDPS*, vol. 5, pp. 95-109, 2001.
- [17] M. C. Shaw, "Metal Cutting Principles Oxford Sci. Public", England, 1984.
- [18] S. E. Oraby, D. R. Hayhurst, "Development of models for tool wear force relationships in metal cutting", *International Journal of Mechanical Sciences*, vol. 33, pp. 125–138, 1991.
- [19] C. M. Cakir, C. Ensrioglu, I. Demirayak, "Mathematical modelling of surface roughness for evaluating the effects of cutting parameters and coating material", *J Mater Process Tech.* vol. 209 pp. 102–109, 2009.
- [20] O. Colak, C. Kurbanoglu, M. C. Kayacan, "Milling surface roughness prediction using evolutionary programming methods" *Materials & Design*, vol. 28 pp. 657–666, 2007.
- [21] H. Sađlam, A. Unuvar, "Multi-purpose dynamometer design and manufacturing", vol. 97/42, Selcuk University, Research Funding, 1997.
- [22] P. J. Ross, "Taguchi Techniques for Quality Engineering", *McGraw-Hill*, New York, 1989.
- [23] P. G. Benardos, G. C. Vosniakos, "Predicting surface roughness in machining: A review", *International Journal of Machine Tools and Manufacture*, vol. 43(8), pp. 833–844, 2003.
- [24] C. M. Bishop, "Neural networks for pattern recognition", New York, NY: *Oxford University Press, Inc.* 1995.

CFD Case Study on a Nozzle Flow: Literature Review, Theoretical Framework, Tools and Educational Aspects

A.H. ABDULKAREEM¹, E. CANLI² and A. ATES³

¹Kirkuk University, Kirkuk/Iraq, alihuseyin81@yahoo.com

²Selcuk University, Konya/Turkey, ecanli@selcuk.edu.tr

³Selcuk University, Konya/Turkey, aates@selcuk.edu.tr

Abstract - State of art engineering involves lots of software types and numbers. The theoretical framework on a vocation is not sufficient for today's undergraduates to integrate into the industry. Therefore, engineering programs are implementing courses on related software types. This work focuses on particular and widespread Computational Fluid Dynamics software in respect of mechanical engineering education. A case was determined which involved a nozzle flow analysis. Particular attention was paid on recent works for the case and for the related education studies. After a theoretical framework section containing governing equations of the physical phenomena, a section is dedicated on the used software tool. Subsequently, a results section is provided on case results and this section also includes evaluation of the results in terms of undergraduate education of mechanical engineering. Finally some concluding remarks are listed. As a major conclusion, skills on using software and skills on understanding and evaluating results in respect of engineering should be separated from each other and should be subject of different courses. The two dimensional CFD analysis results show that the analysis is in agreement with real world physics. The static pressure values ranged between -88120 Pa gauge pressure and 286200 Pa gauge pressure while Mach Number ranged between 0.15 to 2.85.

Keywords - CFD, Engineering Education, Fluid Mechanics, Mach, Nozzle.

I. INTRODUCTION

THE undergraduate education in engineering is being distinguished from past. While basic theory still depending on the known references, vocational education include professional and commercial software programs more. Although this can be seen as an advantage for application ease and faster processes, the increasing amount of data and information can be a problem for inexperienced applicants. The abundant data makes decision making, assessment and evaluation difficult. Certain outcomes cannot be easily identified by inexperienced applicants. In order to realize this phenomenon, an undergraduate application is examined. The literature survey and results are reviewed by the authors of the present report while the evaluations are compared to the points identified by the applicant student.

Some literature papers were provided to applicant as guides for the work to be done. Therefore a literature survey was done prior to providing these references to the applicant. The surveyed works are briefly summarized below. The first work is from 2013 by Najar et al. [1]. Authors used two different turbulence models, namely $k-\epsilon$ and Spalart-Allmaras, in order to investigate a compressible flow in a converging diverging nozzle by a 2D axisymmetric geometrical model. While the solution is 2D axisymmetric, results are mirrored to provide a better sight. To compose a smooth wall boundary for the nozzle throat, authors used 27 points and their coordinates. They provided very details of their CFD software case setup configuration. However, as it will be shown in the following sections, it is understood that the student (applicant) couldn't use this scientific paper sufficiently and instead, referred to internet tutorials. This conclusion is based on the differences between the setup of the applicant and this reference. Narayana and Reddy [2], compared five different mesh structures while investigating a converging diverging nozzle using CFD software. The first mesh is an unstructured mesh while the other four are structured meshes. Meshes are different from each other by their finer dimensions. The nozzle geometry is similar to the one in the undergraduate work. The medium mesh is seen to be convenience for the tradeoff between computational cost and accuracy of the results. However the applicant ignored this mesh independency study too and used one mesh configuration. Sudhakar et al. [3] reported a CFD simulation of a converging diverging nozzle while they compared their CFD results with analytical results. Their findings are consistent with the analytical ones.

It is seen that similar papers in the literature provides detailed information about the case setup of CFD software. However it can be said that there is a lack of standard for the information to be given for the method part of the papers.

In this report, a case study that was done by an undergraduate student applicant is examined and evaluated in respect of the advantages and disadvantages of engineering software on the engineering education. Applicant was provided some related literature, CFD software and a flow problem

including a converging diverging nozzle. The simulation and evaluation of the results were expected. The results of the simulation are evaluated by the current authors and compared to the report of the applicant. Some conclusions and remarks are given at the end of the paper.

II. THEORETICAL BASIS AND METHOD

The engineering problem to be investigated and solved as an undergraduate study was selected as a converging diverging nozzle. The aim is to lead to skills for solid geometrical modeling, using software interface, arrangements for commercial computational fluid dynamics (CFD), assessing and evaluating obtained results. Therefore a geometrical nozzle model is used for a flow analysis in commercial CFD software (ANSYS FLUENT). The dimensions were determined as:

- Total length of nozzle = 75 mm
- Inlet diameter= 25 mm
- Throat diameter= 10 mm
- Outlet diameter = 35 mm
- Convergent angle=35°
- Divergent angle =12°

During the interview between the applicant and the supervisor (instructor), it was decided to take the nozzle limits and boundaries as the computational domain boundaries. Therefore the inlet boundary condition exists at the nozzle inlet and outlet boundary condition is the outlet of the nozzle. Inlet pressure boundary condition was determined as 3 bar and inlet temperature boundary condition was selected as 300 K.

The applicant first surveyed the theory and literature. Some of the basic isometric relations for the properties i.e. pressure, temperature and velocity at throat are find out by the following relations:

$$\frac{P_t}{P_o} = \left[\frac{2}{(\gamma + 1)} \right]^{\frac{\gamma}{\gamma - 1}} \quad (1)$$

$$\frac{T}{T_o} = \left[\frac{2}{(\gamma + 1)} \right] \quad (2)$$

$$V_t = \sqrt{\frac{2\gamma}{\gamma + 1} RT_o} = \sqrt{\gamma RT_t} \quad (3)$$

Velocity and temperature values at different cross sections are by the following formulae. The continuity equation is:

$$A_x V_x \rho_x = \rho_t V_t A_t \quad (4)$$

The steady flow energy equation is as follows:

$$\frac{Q - W}{m} = \left(h + \frac{V^2}{2} + gz \right)_t - \left(h + \frac{V^2}{2} + gz \right)_x \quad (5)$$

Above equations were not directly used during CFD simulations however viewing them enhances understanding and evaluating the results.

The geometrical model after a structured mesh is applied can be seen in Figure 1.

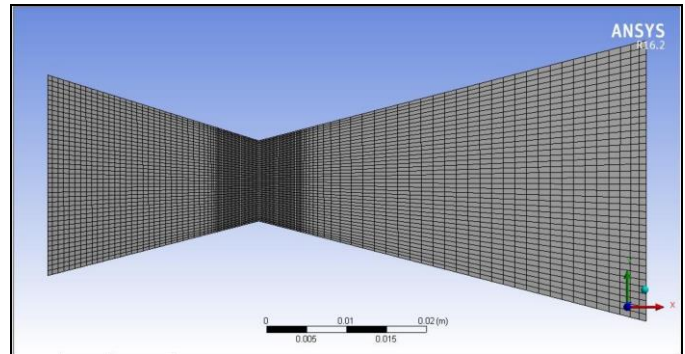


Figure 1: The geometry with structured mesh

10^{-3} was arranged for the residuals. With these residuals, the computation was completed about 300 iterations. The solution was a steady solution.

The method can be criticized since the 2D analysis should be conducted as an axially symmetrical case. This would impose cylindrical geometry effect on the results. However the 2D planar simulation is missing this effect. Nevertheless results are presented in the following section.

III. RESULTS

The first result to be presented is given as static pressure contours in Figure 2. Static pressure contours revealed a shock at the throat of the nozzle. Therefore the upstream has substantial high values of pressure while the downstream has values very close to atmospheric pressure. There are also some locations in the downstream having a pressure value in the vacuum region according to the atmospheric pressure. With these pressure values in the downstream, the nozzle can be used as a mixing device for other phases such as solids or liquids. The applicant of the undergraduate work identifies the shock wave at the throat section. Also the gradient from inlet towards outlet is mentioned in the report of the graduate work. There are no other comments by the applicants on the static pressure.

The second result provided is the temperature distribution throughout the nozzle in Figure 3. The main reason of this temperature difference is the phase change of the fluid due to the decreasing pressure after the throat. It can be justified by the similarity between static pressure contours and temperature contours. However this event couldn't be identified by the applicant. The applicant only gives the maximum temperature which is actually the inlet boundary condition and mentioned about the temperature gradient.

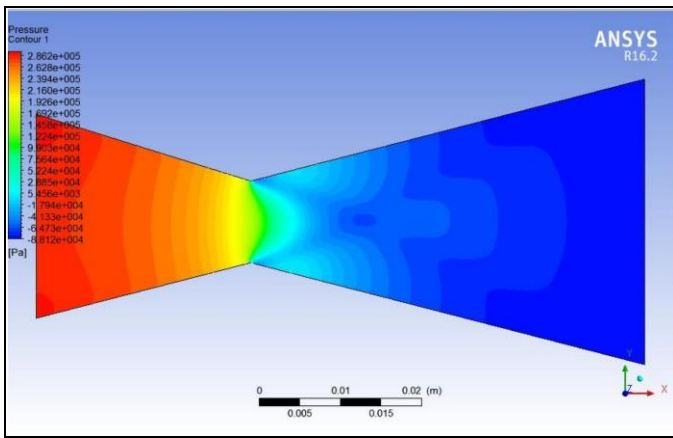


Figure 2: Total pressure contours in Pascal

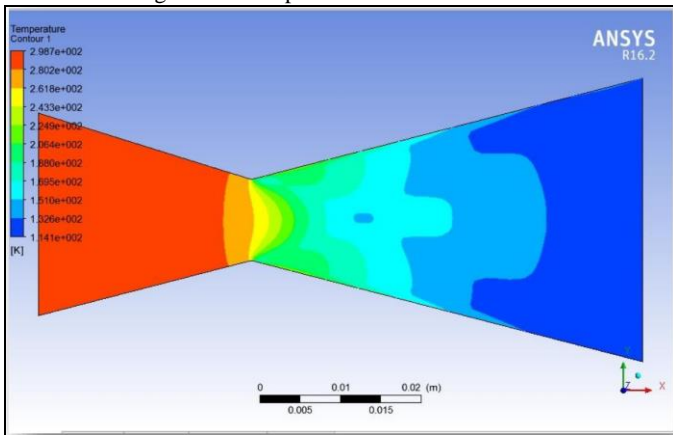


Figure 3: Temperature distribution

The velocity result is given in Figure 4. The applicant identified the choked flow at the nozzle throat and could calculate the dimensionless local Mach numbers. The inlet, outlet and throat Mach numbers are also reported and identified as subsonic, choked and supersonic by the applicant. However the relation between the static pressure values and the velocity is missing. It should be mentioned that the main mechanism effecting on the velocity is the decrease of static pressure due to the divergence and therefore the decreased part of the pressure is converted into speed.

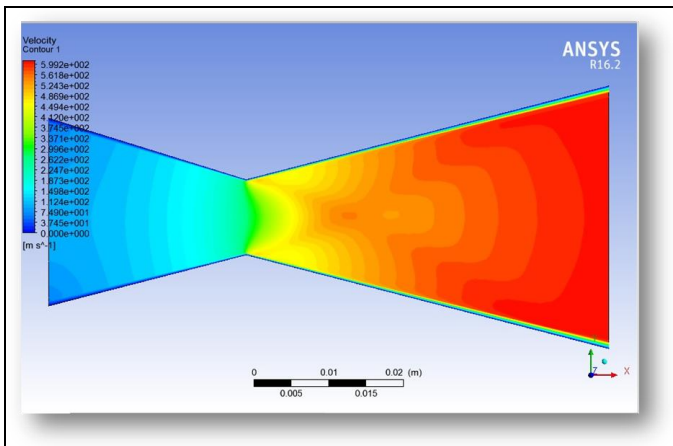


Figure 4: Velocity distribution

The 2D plots of the static pressure, Mach number and temperature at the nozzle walls are also provided in Figure 5, 6 and 7 respectively. These plots are easier to view the quantitative results. Static pressure decreases starting from the inlet linearly till 20 mm distance due to the viscosity and then decrease sharply towards the nozzle throat at the “0” position of the plot in Figure 5. This sharp decrease is due to the choking flow at the throat because of the shock. The static pressure is converted into kinetic energy/velocity by the converging boundaries. When flow passes the throat, there exist small wakes increasing the static pressure for a short distance. As diverging boundaries increases the velocity further, static pressure decreases more. Same trends are viewable for temperature and Mach number indicating that these results are correlated. However, evaluation and examination of these physical events are missing in the report of the applicant.

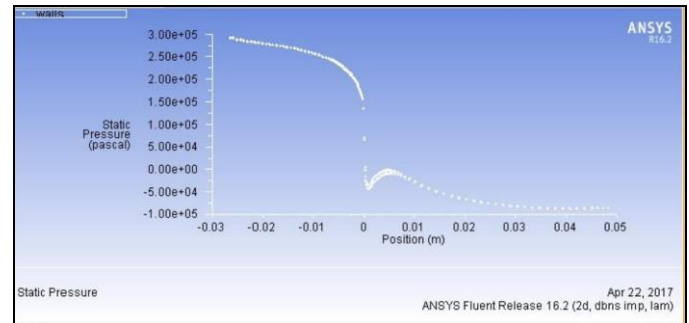


Figure 5: Static pressure plot on walls

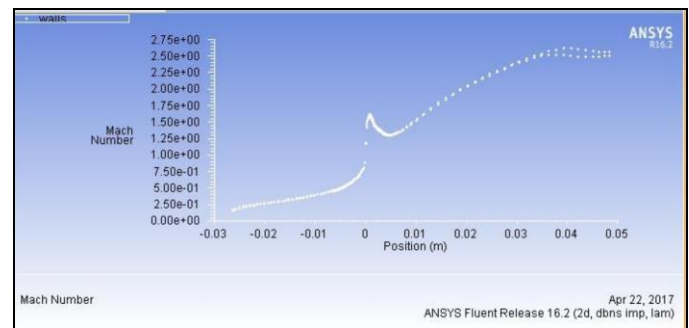


Figure 6: Mach number plot on walls

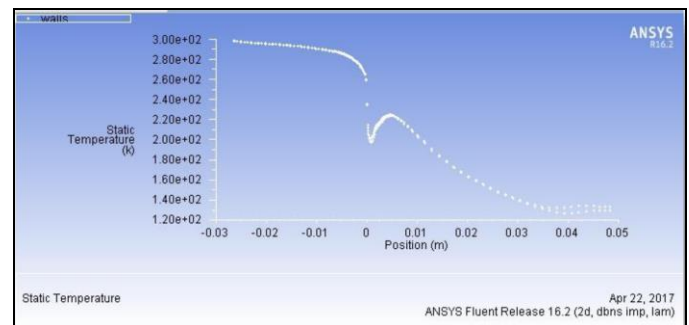


Figure 7: Static temperature plot on walls

IV. CONCLUSION

The recent software tools for engineering provide ease,

flexibility and comprehensive information about engineering systems. Their interfaces are becoming more user-friendly. However these advantages may be cumbersome for inexperienced engineers or engineer candidates without necessary knowledge and field experience. This phenomenon can be observed in applied studies of undergraduate engineering programs. Such a report from 2017 is examined and evaluated here in respect of the engineering education. Following drawings and remarks can be stated.

- With the presence of abundant tutorials, web materials and examples, undergraduate student can apply simulation software to a certain problem. Even the post-processing can be done with viewable and meaningful information.
- It is observed that applicant of such a work sees enough of giving the simulation results and doesn't wonder the physical phenomena underlying it.
- Only small portion of mechanisms and outcomes of the simulation is identified by the applicant.
- The method used for the simulation and calculation is explained by the applicant by a brief and closely manner. It is thought that the main reason for this behavior is due to the abundant web material that makes the applicant to think that most of the information about the method is not worth to mention.
- The authors of the present report suggest that applied engineering projects should clearly indicate the main motivation and reason of the work for the students. The connection between engineering profession and the results by the software should be identified by the advisors prior to the assignment of the project/application to the applicant.
- Engineering software can yield results even if the setup is not correct and adequate.
- Students tend to give the results and skip evaluating it and thinking on it.
- Even the results can be modified or changed by the student if the case files are not investigated by the instructor.
- Engineering software applications without step by step lectures and careful inspections can lead to unachieved goal of the application.
- Unsuccessful applications not only short on achieving the training goal but also reduce the qualification of the students. Instructors should not ignore this fact.

APPENDIX

P	–	Pressure	(Pa)
T	-	Temperature	(K)
V	–	Velocity	(m/s)
g	–	Gravitational Acceleration	(m/s ²)

z	–	Height	(m)
A	–	Area	(m ²)
C _p	–	Specific heat at constant pressure	(J/Kg·K)
C _v	–	Specific heat at constant volume	(J/Kg·K)
γ	-	Adiabatic Index	(C _p /C _v)
h	–	Enthalpy	(J)
R	–	Specific gas constant	(J/Kg·K)
ρ	–	Density	(Kg/m ³)
Q	–	Heat input to the system	(J)
W	–	Work done by the system	(J)
m _o	–	Mass flow rate	(Kg/s).

ACKNOWLEDGMENT

This report is prepared based on a survey with an undergraduate student in University of Kirkuk, College of Engineering, Mechanical Engineering Department. The main purpose of the report is assessing global software products on engineering education.

REFERENCES

- [1] N.A. Najar, D. Dandotiya, and F.A. Najar, "Comparative Analysis of K-ε and Spalart-Allmaras Turbulence Models for Compressible Flow through a Convergent-Divergent Nozzle," *The International Journal Of Engineering And Science*, vol. 2, iss. 8, pp. 08–17, 2013.
- [2] K.P.S.S. Narayana and K.S. Reddy, "Simulation of Convergent Divergent Rocket Nozzle using CFD Analysis," *IOSR Journal of Mechanical and Civil Engineering*, vol. 13, iss. 4, pp. 58–65, 2016.
- [3] B.V.V.N. Sudhakar, B.P.C. Sekhar, P.N. Mohan, M.D.T. Ahmad, "Modeling and simulation of Convergent-Divergent Nozzle Using Computational Fluid Dynamics," *International Research Journal of Engineering and Technology*, vol. 3, iss. 8, pp. 346-350, 2016.

STRENGTH AND COMPACTION CHARACTERISTICS OF RECYCLED CONCRETE AGGREGATES

E.B. TOKA¹ and M. OLGUN¹

¹ Konya Technical University, Konya/Turkey, ebtoka@selcuk.edu.tr

¹Konya Technical University, Konya/Turkey, molgun@selcuk.edu.tr

Abstract - Every year, a large amount of construction and demolition wastes are produced worldwide. The use of these wastes in the granular road base (GRB) and granular road subbase (GRSB) layers contributes to sustainability. In Turkey, the necessary attention should be given to the reuse of these materials. In this study, compaction and strength properties of recycled concrete aggregates (RCA) obtained from 3 different building demolitions, one natural aggregate (NA) and one crushed aggregate (CA) from Konya City/Turkey were investigated comparatively. For this purpose, Modified Proctor and unsoaked California Bearing Ratio (CBR) tests were performed on the pure forms of these 5 different aggregates and the mixtures of 25% - 75%, 50% -50%, 75%- 25% ratios of RCAs with CA and NA. As a result of the Modified Proctor tests, it was found that the optimum moisture content of RCAs compared to NA and CA were high due to high water absorption of RCAs and the maximum dry unit weights were low due to low specific gravities of RCAs. As a result of the CBR tests, the CBR values of the RCAs were high enough to be compared to the CA; however, in the mixtures, a decrease in CBR values was observed. The results showed that the RCA in Turkey has some sufficient mechanical properties to be used in GRB and GRSB; however, further studies must be done.

Keywords – Recycled concrete aggregate, Granular road base, Granular road subbase, California bearing ratio, Modified Proctor

I. INTRODUCTION

An excessive amount of construction and demolition waste emerges every year. These wastes must be landfilled in order to avoid environmental pollution. As the cost of landfilling is high, it is known that waste materials in the landfill areas may pollute the environment if adequate precautions are not taken. For this reason, it was thought that construction and demolition wastes could be reused and studies were carried out. Some of these studies were to investigate the usability of RCAs obtained from construction and demolition wastes as a GRB and GRSB material in geotechnical and transportation engineering.

Poon and Chan [1] found that when 100% RCA was used as the subbase material, it increased the optimum moisture content and decreased the maximum dry density, and the soaked CBR values were lower than those with natural aggregates; however, these CBR values were above 30%,

which was the minimum strength requirement in Hong Kong. Jimenez et al.[2] conducted some tests with 7 different recycled aggregates, they found that RCA and CA can be more susceptible to moisture changes as a result of the Modified Proctor test and the high CBR values of RCA have an acceptable bearing. Gabr and Cameron [3] observed that although RCAs have less density than CAs, due to their residual cement mortar; can have more CBR values if they are treated adequate curing. Haider et al. [4] found that the CBR tests performed in the NA and the RCAs from 2 different plants and RCAs had a CBR value of 2.18 to 1.67 times more than the NA. Arulrajah et al. [5] conducted dynamic triaxial tests on 3 different recycled construction and demolition materials and found that recycled materials had greater resilient modulus and lower permanent deformation than conventional GRSB material. In order to investigate the self-cementing properties of RCAs, Jitsangiam et al. [6] conducted tests of strength and resilient modulus on samples subjected to different curing times and found that self-cementing occurs in RCAs obtained from structures with high strength concrete and this increases the material strength. In their study of the mechanical properties of the RCAs, Bestgen et al. [7] found that the CBR values were relatively high in RCAs and that the increase in cure time could lead to a further increase in CBR due to the unhydrated adherent cement mortar initiating cementation. Most data from literature studies have shown that RCAs can be used in unbound road layers as compared to CA [8].

In this study, the strength and compaction properties of RCAs were compared experimentally with CA and NA. For this purpose, CBR and Modified Proctor tests were performed on the pure forms of each material and on the mixtures of RCAs with NA and CA in certain proportions.

II. MATERIAL AND METHOD

In this study, 3 different RCAs obtained from Meram region of Konya city and CA and NA obtained from Egribayat Region were used. RCAs are shown as RCA1, RCA2, and RCA3. Some physical properties of each aggregate are shown in Table 1.

Table 1: Some physical properties of the materials.

Material	Specific Gravity	Los Angeles Abrasion, %	Water Absorption, % (Coarse Aggregate)
CA	2.645	31.1	0.625
NA	2.632	33.8	2.489
RCA1	2.515	46.7	4.626
RCA2	2.556	40.4	2.882
RCA3	2.576	45.1	3.559

After the recycled aggregates were brought from the debris area, they were adjusted to the appropriate gradation for GRB and GRSB that are determined in the Technical Specification of Highway [9]. Laboratory jaw crusher was used for this purpose. The results of the sieve analysis of each material are shown in Figure 1.

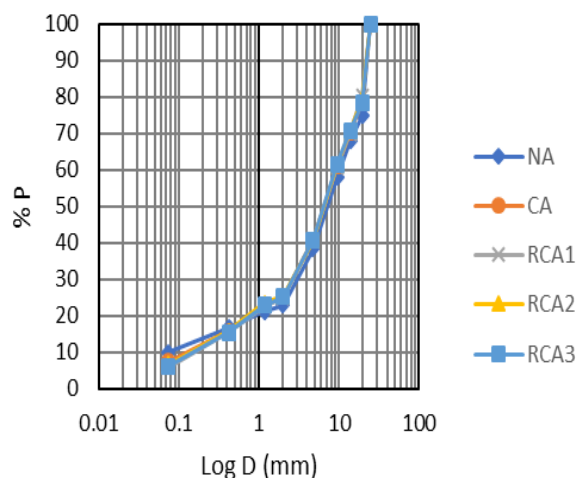


Figure 1: Sieve analysis results of the materials.

The compaction characteristics of the GRB and GRSB materials must be measured by the Modified Proctor test according to the Technical Specification of Highway [9]. For this reason, Modified Proctor tests were carried out following TS 1900-1 [10] procedure. The optimum moisture content and maximum dry unit weights that are the compaction characteristics were obtained by Modified Proctor tests.

The strength of GRB and GRSB material is evaluated by CBR tests. Unsoaked CBR tests were performed in this study according to TS 1900-2[11]. CBR values are obtained from these tests, which are based on the comparison of the strength of the standard crushed material with the strength of the material subject to testing and are expressed as "percent".

Designs have been created to investigate the usability of recycled materials in GRSB and GRB. In Table 2 these designs are shown. These designs consist of mixtures of materials and these materials in pure form. In the mixtures, each RCA was used with NA and CA in 50% -50% and 75-25% ratios. For example; 25 CA 75 RCA1 means that 25% CA and 75% RCA1 exist in this mixture.

Table 2: Designs of the materials.

Design No	Design Name
1	100 CA
2	100 NA
3	100 RCA1
4	100 RCA2
5	100 RCA3
6	75 CA 25 RCA1
7	75 CA 25 RCA2
8	75 CA 25 RCA3
9	50 CA 50 RCA1
10	50 CA 50 RCA2
11	50 CA 50 RCA3
12	25 CA 75 RCA1
13	25 CA 75 RCA2
14	25 CA 75 RCA3
15	75 NA 25 RCA1
16	75 NA 25 RCA2
17	75 NA 25 RCA3
18	50 NA 50 RCA1
19	50 NA 50 RCA2
20	50 NA 50 RCA3
21	25 NA 75 RCA1
22	25 NA 75 RCA2
23	25 NA 75 RCA3

III. RESULTS AND DISCUSSION

The Modified Proctor test results in Table 3 show that the optimum moisture content increased as the RCA content increased.

Table 3: Modified Proctor test results.

Design	Optimum moisture content (w_{opt}), %	Maximum dry unit weight (γ_{kmax}), kN/m ³
100 CA	5.35	21.97
100 NA	4.40	22.22
100 RCA1	9.75	19.48
100 RCA2	8.60	19.69
100 RCA3	9.60	19.70
75 CA 25 RCA1	6.40	21.62
75 CA 25 RCA2	6.20	21.78
75 CA 25 RCA3	6.47	21.64
50 CA 50 RCA1	7.20	20.73
50 CA 50 RCA2	6.60	21.14
50 CA 50 RCA3	6.60	21.26
25 CA 75 RCA1	7.75	20.38
25 CA 75 RCA2	7.30	20.58
25 CA 75 RCA3	9.20	20.24
75 NA 25 RCA1	6.42	21.76
75 NA 25 RCA2	6.95	21.49
75 NA 25 RCA3	5.40	21.71
50 NA 50 RCA1	7.50	20.99
50 NA 50 RCA2	7.40	21.33
50 NA 50 RCA3	8.35	20.96
25 NA 75 RCA1	7.23	20.42
25 NA 75 RCA2	7.80	20.64
25 NA 75 RCA3	7.10	20.52

The highest optimum moisture content was obtained in 100 RCA1 with 9.75% and the lowest optimum moisture contents were obtained in 100 CA and 100 NA with 5.35% and 4.40%, respectively. The optimum moisture content generally increases as the presence of fines increases or the interaction of these fines with water increases. In RCAs, the fine material consists of both aggregate and cement mortar from the parent concrete. This cement mortar which is present in RCAs, also leads to high water absorption capacity, thus increasing the optimum moisture content.

Table 3 shows the maximum dry unit weights. The maximum dry unit weights, which are indicative of good compaction, decreased with increasing RCA. Maximum dry unit weights were achieved in 100 NA with 22.22 kN/m³ and in 100 CA with 21.97 kN/m³; but the lowest values of maximum dry unit weights were observed in RCA1, RCA2, and RCA3. When the specific gravity of the materials shown in Table 1 is examined, it is seen that the specific gravity of RCAs is lower than NA and CA. As a result, low specific gravity resulted in a reduction in the weight of the material filling the same volume. The low specific gravity of RCAs was caused by the cement mortar they contain, which means that the cement mortar reduced the specific gravity and indirectly affected the maximum dry unit weights.

When the results in Table 4 are analyzed, it is seen that the CBR values of the materials were highest in the CA with %152.210. This can be explained by the fact that the CA material has a higher intrinsic strength.

Table 4: CBR test results.

Design	CBR (%)
100 CA	152.210
100 NA	79.153
100 RCA1	115.720
100 RCA2	122.590
100 RCA3	127.358
75 CA 25 RCA1	109.730
75 CA 25 RCA2	105.350
75 CA 25 RCA3	104.299
50 CA 50 RCA1	92.600
50 CA 50 RCA2	100.630
50 CA 50 RCA3	96.370
25 CA 75 RCA1	122.926
25 CA 75 RCA2	115.735
25 CA 75 RCA3	117.770
75 NA 25 RCA1	58.530
75 NA 25 RCA2	55.647
75 NA 25 RCA3	67.410
50 NA 50 RCA1	41.291
50 NA 50 RCA2	41.074
50 NA 50 RCA3	34.292
25 NA 75 RCA1	85.980
25 NA 75 RCA2	82.580
25 NA 75 RCA3	94.359

The lowest CBR values were obtained after RCA mixtures of NA, followed by the CBR value of the NA. RCAs had lower CBR values than CBR value of the CA; these can be explained

by the fact that they have been obtained in old structures and therefore have a lower strength that has been exposed to bad environmental conditions for a long time.

It should be noted that these materials long waited at the location of debris which means that the RCA had been constantly exposed to rain, heat, freeze-thaw etc. CBR values of the mixtures were generally lower than the CBR values of the pure materials. This may have been caused by materials with varying grain sizes, structures and gradations resulting in poor grain packing when they are mixed and this poor packing caused irregular formation and lower CBR values. However, when the RCAs in RCA mixtures of NA were 75%, higher CBR values were obtained in these mixtures than pure NA. This is due to the fact that the intrinsic strength of pure RCAs is greater than that of pure NA, which in turn increases the overall strength of the mixture and therefore the CBR. In Figure 2, change and comparison of the CBR values of the designs are shown.

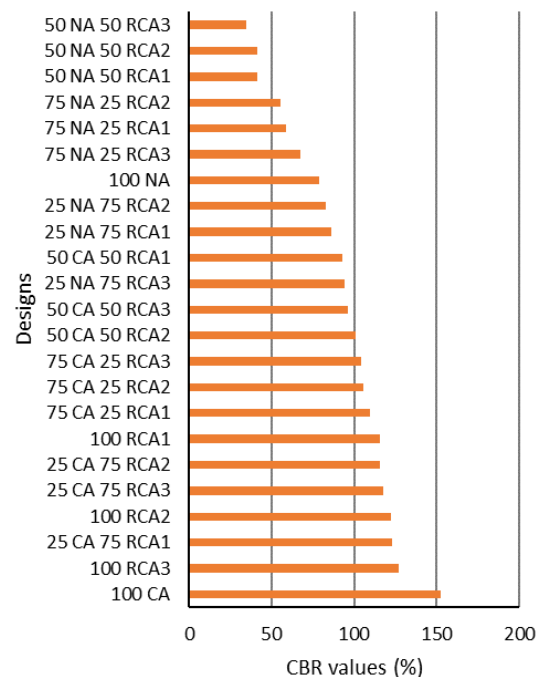


Figure 2: Comparison of the CBR values.

IV. CONCLUSION

In this study, unsoaked CBR and Modified Proctor tests were performed on pure samples and mixtures consisting of RCA, NA, and CA. As a result of the tests, the following inferences can be made.

- The optimum moisture content values of RCAs have increased due to the cement it contains. Whereas The maximum dry unit weight was decreased because of the low specific gravity of RCAs.

- The highest CBR values were obtained in the CA and then in the RCAs and in the RCA mixtures of the CA, because of intrinsic strengths of these materials.
- Since CBR is a strength indicator, the materials with the lowest strength were NA and NA mixtures.
- For further investigation of the usability of RCAs for GRB and GRSB, carrying out additional tests such as resilient modulus, permeability, and soaked CBR would be appropriate.

ACKNOWLEDGMENT

This paper is in scope of “Experimental Investigation of The Usability of Recycled Concrete Aggregate in Road Superstructure” Master’s Thesis Project and “Investigation of the Usability of Recycled Concrete Aggregate Obtained from Urban Transformation Applications in Road Base and Subbase Layer” TUBITAK Project (**Project Number: 217M969**). This study is supported by TUBITAK. The authors are grateful to Selcuk University and TUBITAK for their support.

REFERENCES

- [1] C. S. Poon and D. Chan, “Feasible use of recycled concrete aggregates and crushed clay brick as unbound road sub-base” *Construction and Building Materials*, vol. 20, pp. 578-585, October 2006.
- [2] J. R. Jimenez, J. Ayuso, F. Agrela, M. Lopez, and A. P. Galvin, “Utilisation of unbound recycled aggregates from selected CDW in unpaved rural roads” *Resources, Conservation and Recycling*, vol. 58, pp. 88-97, January 2012.
- [3] A. R. Gabr and D. A. Cameron, “Properties of recycled concrete aggregate for unbound pavement construction” *Journal of Materials in Civil Engineering*, vol. 24, pp. 754-764, June 2006.
- [4] I. Haider, B. Cetin, Z. Kaya, M. Hatipoglu, A. Cetin, and A. H. Aydilek, “Evaluation of the mechanical performance of recycled concrete aggregates used in highway base layers” *2014 Geo-Congress 2014*.
- [5] A. Arulrajah, J. Piratheepan, M. M. Y. Ali, and M. W. Bo, “Geotechnical properties of recycled concrete aggregate in pavement sub-base applications” *Geotechnical Testing Journal*, vol. 35, pp. 743-751, September 2012.
- [6] P. Jitsangiam, K. Boonserm, T. Phenrat, S. Chummuneerat, P. Chindaprasirt, and H. Nikraz, “Recycled concrete aggregates in roadways: laboratory examination of self-cementing characteristics” *Journal of Materials in Civil Engineering*, vol. 27, 2015.
- [7] J. O. Bestgen, M. Hatipoglu, B. Cetin, and A. H. Aydilek, “Mechanical and environmental suitability of recycled concrete aggregate as a highway base material” *Journal of Materials in Civil Engineering*, vol. 28, 2016.
- [8] R. Cardoso, R. V. Silva, J. D. Brito, and R. Dhir, “Use of recycled aggregates from construction and demolition waste in geotechnical applications: a literature review”, *Waste Management*, vol. 49, pp. 131-145, March 2016.
- [9] Technical Specification of Highway, 2013, *General Directorate of Highways*, Ankara, Turkey.
- [10] TS 1900-1, 2006, “Methods of testing soils for civil engineering purposes in the laboratory – Part 2: Determination of physical properties”, *Turkish Standards Institution*, Ankara, Turkey.
- [11] TS 1900-2, 2006, “Methods of testing soils for civil engineering purposes in the laboratory - Part 2: Determination of mechanical properties” *Turkish Standards Institution*, Ankara, Turkey.

A Computational Study for Plain Circular Pipe Flow

A.H. ABDULKAREEM¹, E. CANLI² and A. ATES³

¹Kirkuk University, Kirkuk/Iraq, alihuseyin81@yahoo.com

²Selcuk University, Konya/Turkey, ecanli@selcuk.edu.tr

³Selcuk University, Konya/Turkey, aates@selcuk.edu.tr

Abstract - Although much has been said on Newtonian flow in a circular conduit, emerging computational fluid dynamics codes are still of interest to capture the real world physics as close as possible. There are studies going on in terms of methods, tools, models and validation. According to the recent literature in this work, Direct Numerical Solution is especially seen more frequently. Nano particles as two phase flows for heat transfer research, non-Newtonian flows and secondary flows in big diameter pipes at the radial plane are the other topics that are recently encountered. Also, emerging software tools are another point to be emphasized. In order to draw a theoretical framework, a common Computational Fluid Dynamics code was also utilized for the work and described in detail. While 0.0005 m/s uniform velocity inlet boundary condition was selected, flow remained in the development region due to the laminar flow considering the 4 m axial length of the pipe. Results are in accordance with the known velocity profiles. Future needs are addressed and the topic is also evaluated in terms of mechanical engineering education.

Keywords - Circular, Newtonian Flow, CFD, Review.

I. INTRODUCTION

THE flow in a circular conduit or pipe is a well known phenomenon yet it is still being investigated by researchers and engineers because the developing technology imposes new problems. To raise skilled people for the field, common cases are used as training tools. The common cases are attractive because they are easy to be validated. Therefore training process can be evaluated and there are plenty of explanations for the physical events.

Currently plain circular pipes related flow studies focuses on various problems. Some of them are listed below:

- Calculating flow quantities across the flow domain without modeling (Direct Numerical Solution – DNS)
- Multiphase pipe flow including nano-scale particle addition
- Secondary flows related to inclination angles and big pipe diameters
- Non-Newtonian flows
- Super-critical points of gases such as CO₂ and hydrogen
- Body forces such as magnetism

Among those, DNS studies have cases relatively simple in order to assess and develop the method. Since the flow domain is divided into very fine volumes and the time steps are so small, there is a huge computational cost. So care is paid on the method and cases are selected as they have validations and simple geometries. The remaining topics usually necessitate mathematical models and modifications in governing equations to represent their special conditions. For instance, secondary flows due to pipe diameter and inclination need gravity to be accounted while super-critical flows need additional equations of state to be calculated.

Some recent literature examples are given in the following. Sambit investigated flow in a straight pipe by means of experiments, analytical equations, empirical correlations and CFD simulations for pipeline application in India [1]. He used four different fluids in the simulations which are water, liquid ammonia, diesel and crude oil. The simulations are on default settings of ANSYS Fluent and the mesh is very coarse. Still the simulation results are not deviated much from the experimental ones. Canli et al. reported a comparison of turbulence models for flow in a plain pipe [2]. $k-\omega$ turbulence model provides more information near the wall while $k-\epsilon$ turbulence model leads to more turbulence information near to pipe axis. In the hydraulic entrance length of the pipe, it is interesting to find out that viscous flow model for laminar flow gives very similar radial velocity profile to turbulence models. It is also detected that the convergence criteria for the residuals plays a significant role on pressure-velocity coupling since SIMPLE and COUPLED schemes yielded different results with same convergence criteria. Canli et al. also used the model for a conjugate heat transfer problem by adding thick wall boundaries [3]. In that report, trends are said to be similar if the quantities are ignored when the thermodynamic and physical properties of the fluid are taken constant independent from the temperature boundary condition. It is also said that the COUPLED scheme yielded better results for the same residual convergence criteria.

The remaining of this report contains a CFD simulation of a pipe flow. Method is explained in the next section and results section follows it. Concluding remarks are about the new

aspects of the related field.

II. THEORETICAL BASIS AND METHOD

The geometry and its dimensions prior to meshing are given in Figure 1. It is a surface geometry and it represents a huge diameter with 10 hydraulic diameter axial lengths.

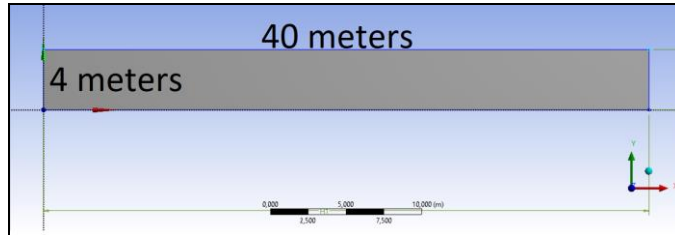


Figure 1: Geometry of the flow domain

A homogenous uniform rectangular mesh was arranged for the domain. The view of the mesh and mesh statistics are given in Figure 2. Although the curvature feature was selected, the geometry in general is rectangular and therefore rectangular elements were obtained. Element sizes were left as default and those values are about 6 mm for minimum element size. There are 7616 elements and 7917 nodes.

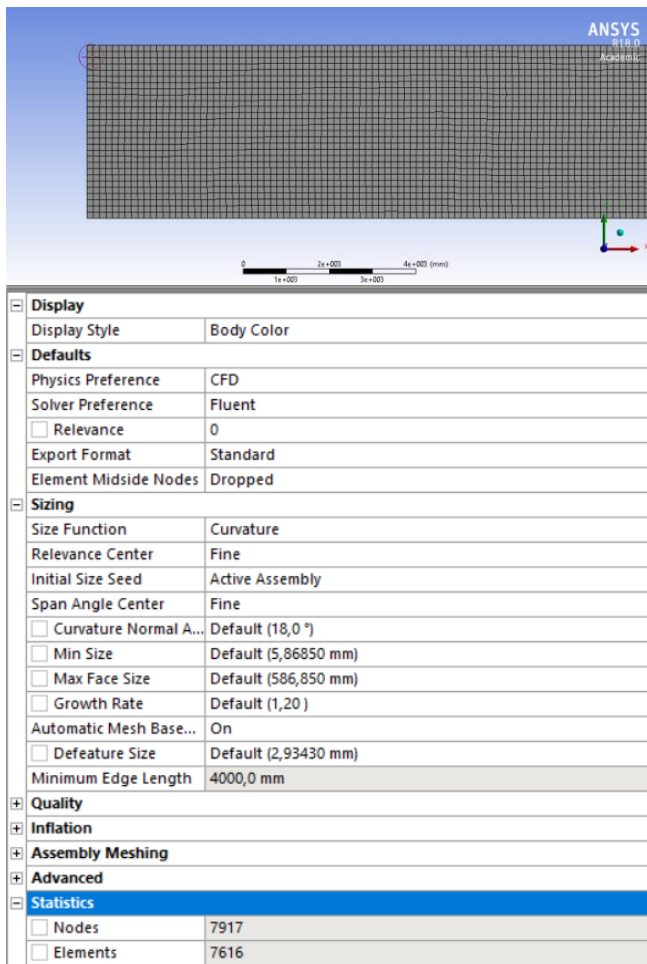


Figure 2: Mesh view and statistics

Pressure based solver was selected. Steady 2D planar setup and absolute velocity formation were arranged. Viscous flow model for laminar flow was used for the flow model. The fluid was selected as water. 0.0005 m/s was the velocity inlet boundary condition while outlet boundary condition was selected as outflow. SIMPLE scheme was used for pressure-velocity coupling. The spatial discretization configuration was Least Squares – Cell Based for Gradient; Second Order Pressure; Second Order Upwind Momentum. Relaxation factors and residual limits were left as default.

III. RESULTS

Figure 3 shows the static pressure distribution at the inlet of the flow domain. As flow approaches to stagnation at the boundaries, static gauge pressure approaches as its maximum value near to the value of 0 Pa. Since flow accelerates at pipe center, static pressure has its lowest value as about -1.4×10^{-5} Pa gauge value which means a lesser value from atmospheric pressure. The trend of the line seems like an inverse Poiseuille flow curve which means that flow will develop in a distant axial length similar to this curve but in inverse direction.

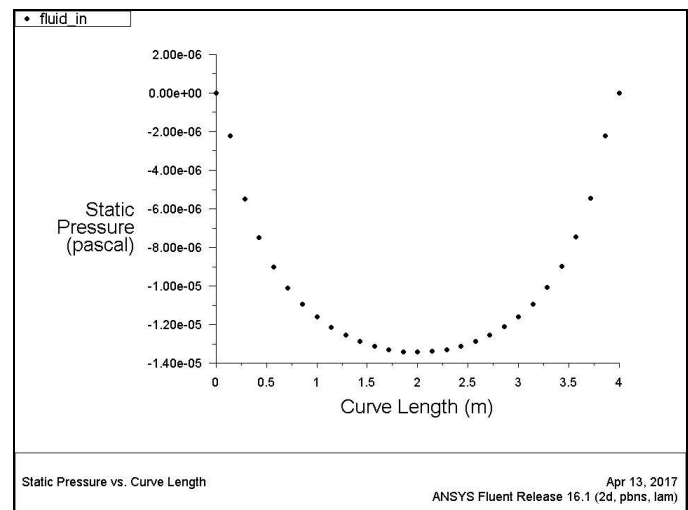


Figure 3: Inlet static pressure

The static pressure distribution at the outlet exhibits an unfavorable pressure gradient at the bottom wall corner due to computational problems as it can be seen in Figure 4. This occurs as reversal flow warning in the software. Outlet boundary condition can be modified in order to overcome this warning and correct the outlet surface.

Figure 5 is given for the hydraulic development of the flow. It is seen that flow is still developing although laminar flow is at stake. One can think or conclude that flow is turbulent looking to the figure; however, it is still developing. More pipe length is necessary to obtain a developed laminar flow. The 0 velocity value shows the location of the walls. Maximum velocity reaches to 6×10^{-4} m/s at the pipe axis and will increase if the pipe will be longer. Velocity boundaries are forming near the walls and radial velocities are forming.

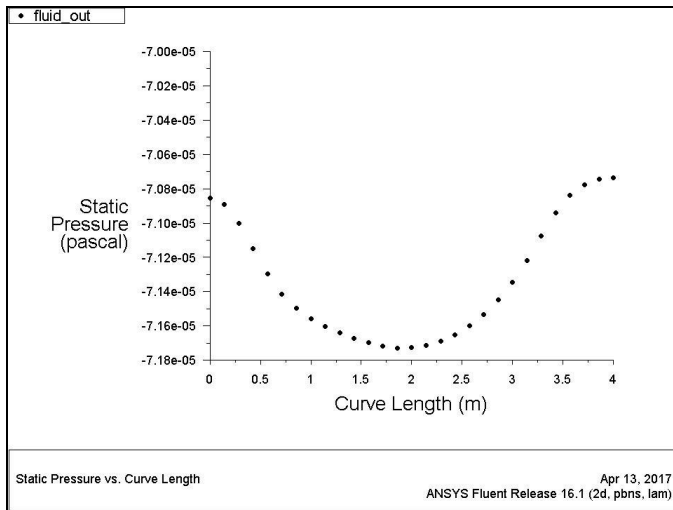


Figure 4: Outlet static pressure

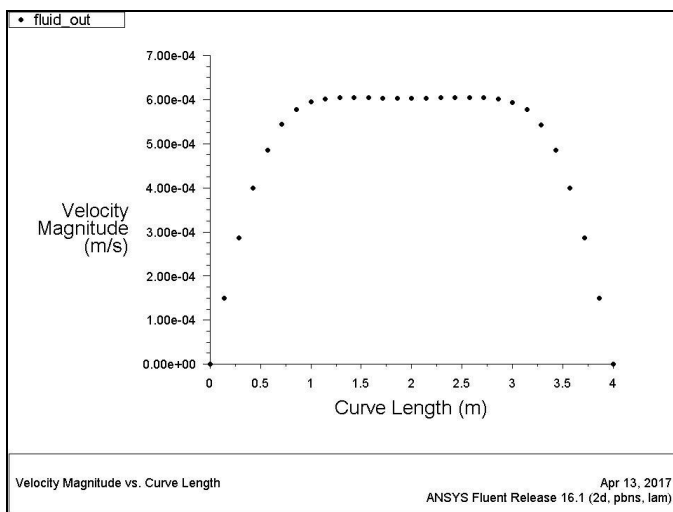


Figure 5: Outlet velocity

Since a plain pipe is at stake, static pressure is expected to decrease linearly and Figure 6 shows this. At the near proximity of the inlet, the slope is steeper while it gets moderate values as it gets further in axial direction. Only 8 Pa pressure drop is visible since there is no flow disturbances and there is relatively a short distance in axial direction comparing to the pipe diameter.

The axial velocity profiles are given in Figure 7. There are 8 curves in axial direction. The lowest value curve is at the walls and the highest value curve is at the pipe axis. Curves in the boundary flow decreases while the curve at the pipe axis slightly increases indicating the mass flow conservation. The figure can be regarded as a common graphic for laminar flow cases in plain pipes when gravity is not considered.

Wall shear stress is due to the viscosity of the fluid. As velocity has higher values, more stress is acting on the walls. As velocity has lower values, the shear stress has lower values proportionally. The wall shear stress values at the walls in axial direction are given in Figure 8. As flow develops and

boundary flow velocities decrease, wall shear stress decreases.

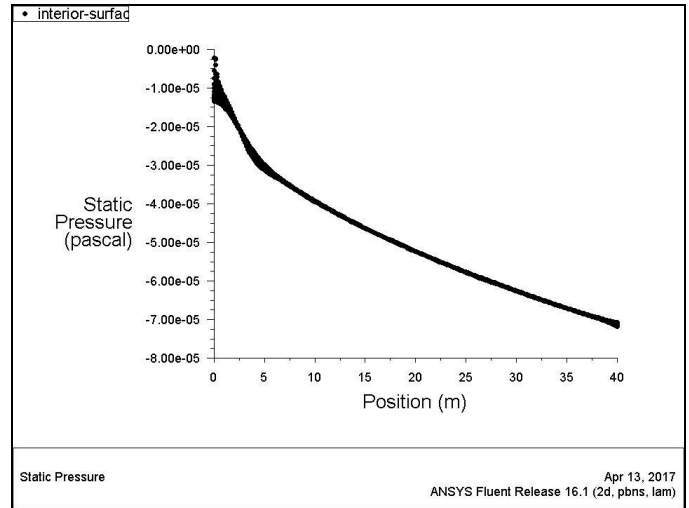


Figure 6: Axial static pressure

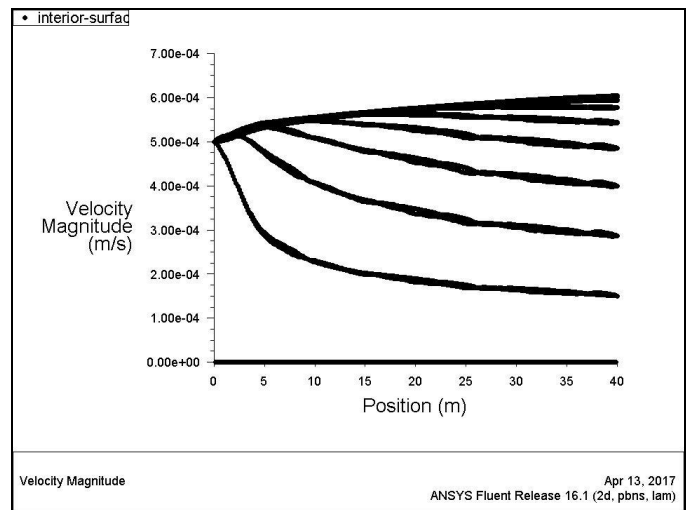


Figure 7: Axial velocity

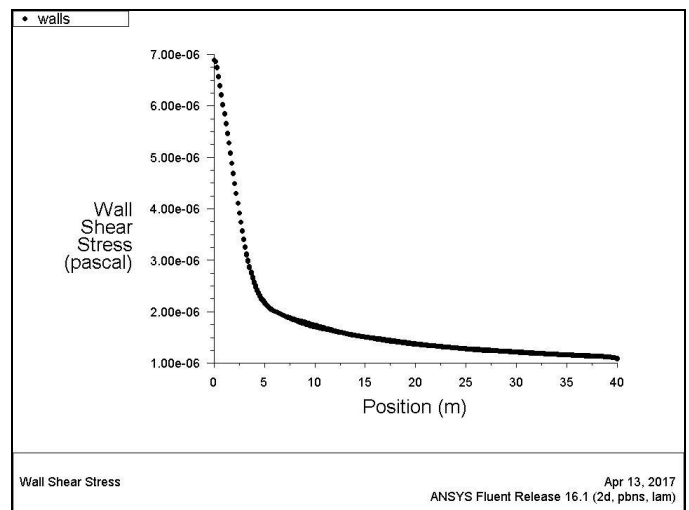


Figure 8: Wall shear stress

The developing x velocity is given in contour graphics in

Figure 9 while the radial velocity contours is given in Figure 10. The negative values of radial velocities are indicating the direction. The positive radial velocities are directing towards upper wall and negative radial velocities are directing towards bottom wall. The pipe entrance has the highest radial velocity values because of the instant effect of the walls on x velocity. As flow develops, more homogenous radial velocity distribution occurs.

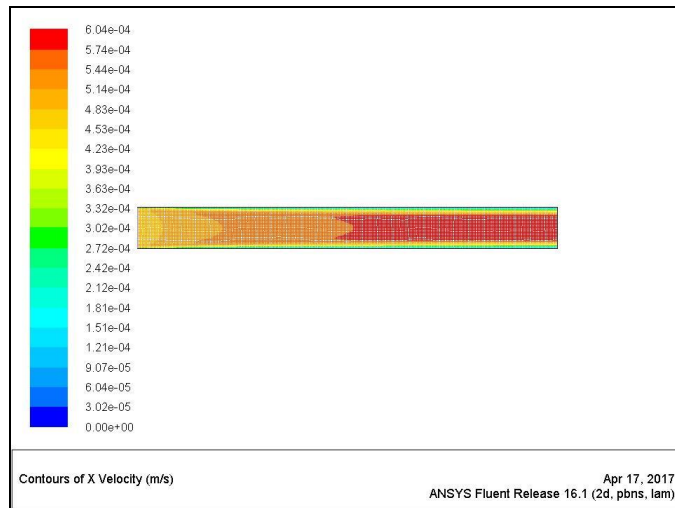


Figure 9: Axial velocity contours

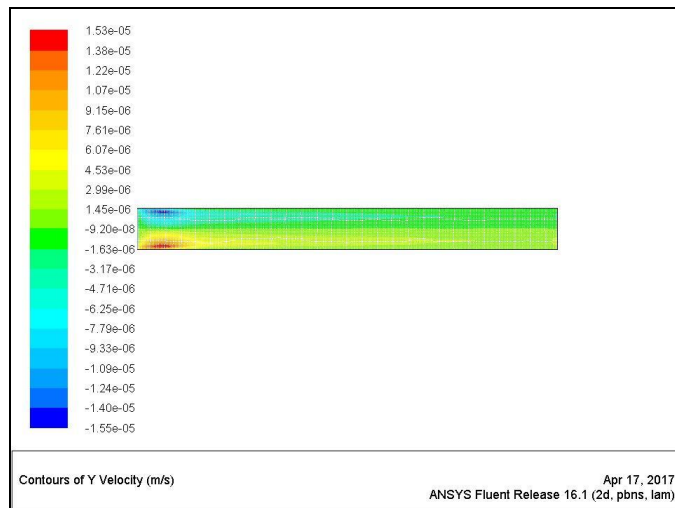


Figure 10: Radial velocity contours

IV. CONCLUSION

Pipe flow is still an attractive topic for two main reasons: First the common cases are an ideal way of engineering training due to their validation opportunities and vast amount of theoretical explanations. Second, the technological advancement of engineering imposes new cases for pipe flow. Following remarks are given for future studies.

- By considering the advancement in computer technology, Direct Numerical Solution (DNS) offers very reliable results that can be regarded as

accurate results as experimental ones. However the main focus is on the developments of the method and the cases are mostly selected as simple cases due to the low computer costs and high validation opportunities.

- Some trending topics in the field are; Multiphase pipe flow including nano-scale particle addition; Secondary flows related to inclination angles and big pipe diameters; Non-Newtonian flows; Super-critical points of gases such as CO₂ and hydrogen; Body forces such as magnetism. All are for pipe flows.
- The common and simpler pipe flow cases for CFD training are used for providing insight of computational and numerical methods such as finite volumes, discretization schemes, turbulence modeling and post processing for derivative results.

ACKNOWLEDGMENT

This report is prepared based on a CFD simulation done for a undergraduate study in University of Kirkuk, College of Engineering, Mechanical Engineering Department under the guidance of Dr. Ali Hussein Abdulkareem.

REFERENCES

- [1] S. Sambit, "Simulation and flow analysis through a straight pipe," Bachelor of Technology In Civil Engineering, Department Of Civil Engineering National Institute Of Technology, Rourkela, 2017.
- [2] E. Canli, A. Ates, and S. Bilir, "Comparison of turbulence models and CFD solution options for a plain pipe," *EPJ Web of Conferences*, vol. 180, pp. 02013, 2018. <https://doi.org/10.1051/epjconf/201818002013>
- [3] E. Canli, A. Ates, and S. Bilir, "Conjugate heat transfer for turbulent flow in a thick walled plain pipe," *EPJ Web of Conferences*, vol. 180, pp. 02014, 2018. <https://doi.org/10.1051/epjconf/201818002014>

The Relationship between Tire Mechanics and Energy

E. CANLI¹, S. EKINCI²

¹Selcuk University, Konya/Turkey, ecanli@selcuk.edu.tr

²Selcuk University, Konya/Turkey, sekinci@selcuk.edu.tr

Abstract – Tire mechanics are a field of study for academia and engineering due to its complex responses to operational conditions and due to the probabilities of material parameters. A lot of works have been conducted on characterizing the tire behavior under various loads. However there is a relationship between tire behavior, especially rolling resistance and friction factor with vehicle energy consumption since some of the consumed energy is spent on rolling resistance cost while some of the consumed energy is regarded as waste energy because of the slippage. In this work, some examples in the literature dealing with the relation between tire mechanics and energy are surveyed and some analytical and empirical relations are examined. It is seen that tire mechanics are directly related with energy consumption of the vehicles. Rolling resistance is also interdependent with tire slippage, leading to efficient utilization of the consumed energy. However there is an optimum and this is subjected to research and design studies. In the last part of the paper, some remarks are provided for the future work.

Keywords – Energy, Mechanics, Rolling Resistance, Slippage, Tire.

I. INTRODUCTION

THE energy for work of vehicle first stored in the vehicle by various means. The most common way is to store the energy in vehicles in the form of chemical energy potential by loading a fuel in a depot. Continuing on this instance in order to exemplify the energy conversion process, fuel is then sent to the engine in order to convert the chemical energy to mechanical energy by means of combustion. The combustion is a chemical reaction in which oxygen reacts with carbon and hydrogen while releasing heat. This heat increases the temperature in the combustion chamber leading to an expansion. The expansion is a form of mechanical energy and mechanisms are used to convert it into different types of motion. Engine, in general, converts this mechanical energy to rotational motion or in other words another type of mechanical energy. This mechanical energy is a high quality energy type since it is also regarded as work. Auxiliary and additional mechanisms and equipment are used to distribute this work for various purposes. One of them is the motion of the vehicle via its wheels. In undergraduate training, wheels can be thought as rigid objects that can be used to obtain movement of the vehicle, without any slippage. However in reality, the interface between ground and the tire is subjected to slippage. In other words, the rotational length of the tire or wheel for a unit time

is not equal to the vehicles distance from its initial position. When slippage occurs, a portion of the energy spent for turning wheels is converted in to waste energy by means of mechanisms such as friction leading to heat and wear, soil compaction and etc. Contact area of the tire with the ground can be increased in order to avoid slippage or torque acting on the wheel should be controlled in order to be lower than the value of torque that leads to the slippage. The torque control is rather a control issue and can be regarded in the field of electronics and vehicle dynamics. It is contact area that involves the tire mechanics. Unloaded tire is a circular shape while the shape changes under loads. The contact line of the wheel becomes the contact area of the tire. Although the friction coefficient is independent from the tire contact area, the contact area determines the traction force. For a given contact area value under a given static load, traction force without any slippage may not enough to move the vehicle in desired speed due to its weight. Therefore either traction force should be increase even though there is slippage or the contact area should be increased to avoid slippage. And increasing contact area is not feasible always. Decreasing inflation pressure of the tire increases the contact area of the tire to a point but there will be a tradeoff and it is called rolling resistance. Rolling resistance is actually the cost for elastic shape change of the tire. Since only a portion of tire significantly changes its shape, and it is depending on the angular position of the wheel, this work is done continuously as the wheel turns. It is unavoidable with common vehicle tires due to the load. Designers use this shape change for increased contact area of the tire. However there is a tradeoff between contact area and the rolling resistance because the cost of the rolling resistance can exceed the cost of the slippage. The ultimate solution is the highest contact area with the lowest rolling resistance. An example to this is the military armored vehicle tracks. The wheels can be regarded as rigid objects while track contact surface is relatively huge. But this again has controversies due to the inertia of the system and again has a tradeoff in energy consumption. And there is also higher soil compaction due to the weight. Considering the material parameters, this decision making is an optimization work.

II. SOME EXAMPLES FROM LITERATURE

There is a directly related work of Ekinici et al. in 2015 by a journal which's scope is on the energy topics [1]. It is said that

about 20% of the fuel consumption is spent on rolling resistance of the tire. Although the relation between tires and energy efficiency is mentioned verbally in the text, the work is mostly about predicting traction by using experimental data. Analytical relations between energy and tire mechanics are missing. Their experimental setup is capable of measuring the torque applied on the wheel and slippage by calculations from the travel reduction using peripheral speed of the wheel and the travel distance. The report reveals that there are other independent variables effecting on the traction efficiency via the rolling resistance, slippage and inertia. Those are tire inflation pressure which's higher values makes tire to behave a more rigid manner and makes contact area smaller; tire lug height which is affecting surface area and friction coefficient proportionally, dynamic axle load which affects rolling resistance and tire contact area. It is also seen that traction efficiency is measured against the changes of independent variables such as lug height, inflation pressure and dynamic axle loads, however interdependent variables are not presented quantitatively.

The relation between tire deflection and tire contact area can be regarded as an indicator for the relation between rolling resistance and contact area. Ekinici et al. conducted experiments and measured tire deflection values and contact area values [2]. They concluded that there is a significant relation between tire deflection and the contact area and increasing deflection is found to be increasing contact area. They also suggested that deflection increases rolling resistance. Therefore, contact area increase means higher traction force while also increases energy to consume on the rolling resistance. They measured the static deflection and dynamic deflection by means of a linear displacement transducer and detect the contact area of the tire by using a dye and paper method. The difference between static and dynamic deflection is what causes additional rolling resistance. The linear curve fitting of their results yielded a slope of 20 and 0.91 R^2 which indicates that higher deflection increases contact area and rolling resistance linearly. A view of contact area determination is given in Figure 1.



Figure 1. Different contact areas due to inflation pressures and loads acting on the tire [2]

In the report of Ekinici and Carman, it is stressed that tire types such as radial or bias and soil type play an important role on traction efficiency [3]. Therefore, experimentation with a single tire type or soil type cannot represent other types. In

other words, independent variables should be assessed and interdependent variables should be calculated for tire and soil types. Another point in the report is the relation between contact area and load distribution. Authors suggest that increasing contact area due to the use of broad or twin tires and the correct setting of the inflation pressure, not just the floor loading but also the rolling resistance is reduced and this reduces fuel consumption. They also categorized rolling resistance as internal and external rolling resistances. The internal resistance is defined as the dissipated energy within the tire that is mainly dependant on the hysteresis of the material used and therefore the tire deformation. The external rolling resistance, however, results due to the floor compaction caused by the tire and the so-called bulldozing effect. Here it should be said that the internal rolling resistance is lower than the external one.

In the paper of Ekinici and Carman [4], not only 20% to 55% of the energy transferred to traction wheels is lost without utilization as transmission losses but also it makes soil to be more compact. Therefore environmental effects are also in question.

All details in the above references are from a PhD work [5]. The relationship between energy consumption and tire mechanics is emphasized in the various parts of the work. The slippage and wasted energy are proposed to be linearly and directly proportional by means of a linear curve fit with a 0.99 R^2 value. It is said that total agriculture energy consumption has a portion of 20% spent in tractors while about 20% to 55% of this 20% is lost through tire mechanics. There are also environmental issues such as soil compaction.

Simikic et al. suggest to measure drawbar power and calculate a ratio of drawbar power over engine power in order to evaluate the tractive efficiency [6]. They propose that traction force by the wheel or tire not always represent the best option for tractive efficiency as there are other factors playing a role on the traction force through the drawbar such as transmission losses. After a comprehensive experimental work for an oblique drawbar, they marked optimum points for drawbar force and wheel slippage in order to obtain best tractor power delivery efficiency and concluded that this also leads to the best tractive efficiency. Still their conclusion is thought to be arguable by the authors of the present report since the power delivery efficiency of the tractor is highly depending on the tractor sub systems and can be misleading for tires.

Battiato and Diserens conducted a simulation for calculating tractor traction performance by using software called TASC which was developed by Diserens [7]. They claim that the software is proper for practical agricultural purposes unlike the scientific models in the literature. In their work, the simulation results are undergone a comprehensive experimental validation. The schematic drawing of the tire and soil contact in their work is given in Figure 2. The energy requirement is claimed to be calculated prior to the experimentation.

However, their software is commercially available and should be paid for access.

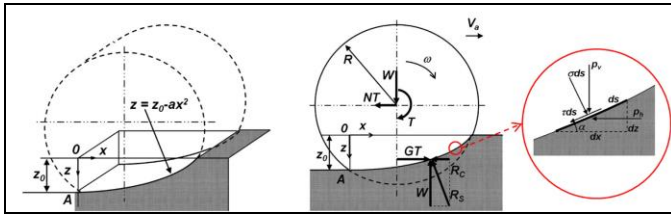


Figure 2. Tire and soil contact [7]

Fuel consumption of a tractor that takes tire inflation pressures and kinematic mismatch as parameters is reported by Janulevicius and Damanauskas [8]. They suggest that the tractor fuel consumption can be minimized by making the kinematic mismatch factor close to 1 while regulating the inflation pressures. They emphasized the over speed of the leading smaller wheels in practice and its importance that can cause several problems if not appropriately handled. They tried to obtain the lowest possible inflation pressure and ballast weights while ensuring the correct kinematic mismatch for the lowest fuel consumption. The fuel consumption graphic in their work shows an optimum inflation pressure point for rear and front tires.

III. RELATIONS BETWEEN TIRE MECHANICS AND ENERGY

Equations that are relating tire mechanics and energy are given here. The symbols are explained in the Appendix section as they appear in the text. The first equation to be presented is the slippage. It is given in equation 1. However, it is just an indicator of a ratio of the travel opportunity that is lost. The direct indicator of energy loss is given in terms of tractive efficiency as in equation 4. Prior to that, drawbar power in equation 2 and axle power in equation 3 are given. As it can be seen from the equations 1-4, traction efficiency is the ratio of drawbar power to the power delivered by the axle. Slippage affects the value of the actual velocity while contact area determines the force of traction. Force of traction is what is left from the torque acting on the wheel after costs of rolling resistance and inertia. This and the tradeoffs between tire mechanics are shown in Figure 3 schematically.

$$S = \left(1 - \frac{V_A}{V_T}\right) \cdot 100 \tag{1}$$

$$P_D = F_D \cdot V_A \tag{2}$$

$$P_{Ax} = \frac{T \cdot n}{9549} \tag{3}$$

$$\eta = \frac{P_D}{P_{Ax}} \tag{4}$$

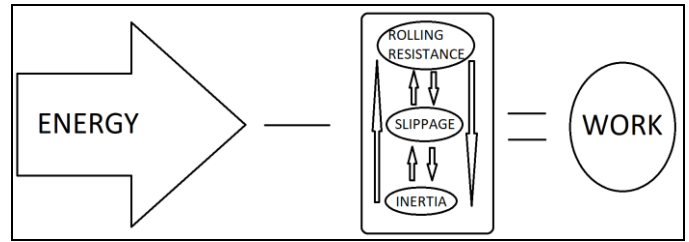


Figure 3. The schematic representation of the tradeoffs between energy losses due to the tire mechanics

The rolling resistance is given schematically in Figure 4. When tire changes its shape due to the load acting on it and due to the rolling, the reaction force of the tire soil interface shifts towards the movement direction of the vehicle. The physical magnitudes in Figure 4 are explained by the following analytical relations.

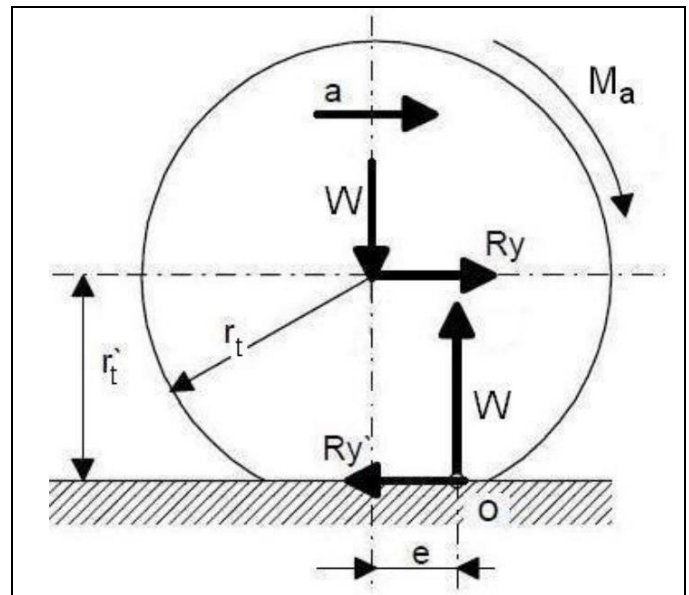


Figure 4. The schematic representation of the tradeoffs between energy losses due to the tire mechanics [5]

$$M_a = F_t \cdot r_t \tag{5}$$

$$M_a - W \cdot e = F_t \cdot r_t - R_y \cdot r'_t \tag{6}$$

$$R_y = \frac{W \cdot e}{r'_t} \tag{7}$$

$$f = \frac{e}{r'_t} \tag{8}$$

IV. CONCLUSION

It is desired to relate the tire mechanics and energy efficiency in the present work. The independent variables such as lug height, inflation pressure and loads; interdependent variables such as rolling resistance, slippage and inertia; and

the final outcome as energy efficiency are tried to be identified. Following remarks and conclusions are given.

- Total agriculture energy consumption has a portion of 20% spent in tractors while about 20% to 55% of this 20% is lost through tire mechanics. There are also environmental issues of soil compaction.
- The traction efficiency can be experimentally measured by changing independent variables such as lug height, tire inflation pressure, dynamic axle loads. However those results are for a specific tire design. The design and material composition cannot be changed for those results because material and mechanical studies for developing better tire materials rely on mechanical experiments and comparison should be done with mechanical results such as rolling resistance, contact area, inertia etc.
- For conventional tires, the only variable that can be changed during operation seems to be the inflation pressure to acquire better energy efficiency. When the optimum point in respect of rolling resistance, slippage and inertia tradeoffs is known, tire inflation pressure can be changed to get to a better position according to the optimization map. The inflation control can be done by means of a change on the rims; such that can inflate or deflate the tire for desired pressures.
- Although almost all related works in the literature mention about the relationship between tire mechanics and energy consumption, no study giving any quantitative data or a direct mathematical relations for calculating energy loss or fuel consumption by using tire parameters. The only work close to this remark is the report about the simulation tool named TASC in [7].

T	Theoretical
D	Drawbar
Ax	Axle
y	Rolling
t	Tire
a	Vehicle

REFERENCES

- [1] S. Ekinci, K. Çarman, and H. Kahramanlı, "Investigation and modeling of the tractive performance of radial tires using off-road vehicles," *Energy*, vol. 93, pp. 1953-1963 (2015).
- [2] S. Ekinci, K. Carman, M. Tasyurek, and M. Mirik, "Relationship between Deflection and Contact Area of Drive Tire," *International Journal of Materials, Mechanics and Manufacturing*, vol. 4, no. 3, pp. 179-182 (2016).
- [3] S. Ekinci, and K. Çarman, "Effects on Tire Contact Area of Tire Structural and Operational Parameters," *6th International Advanced Technologies Symposium (IATS'11)*, 16-18 May 2011, Elazig, Turkey.
- [4] S. Ekinci, and K. Çarman, "Experimental Setups Designed for Tractive Performance Tests of Drive Tires," *Selçuk Tarım ve Gıda Bilimleri Dergisi*, vol. 27, no. 1, pp. 63-73 (2013).
- [5] S. Ekinci, "Effects to traction performance of structural and working characteristics of some drive tires using in horticulture tractors," PhD Thesis, *Selçuk University Natural and Applied Sciences Institution*, Konya, Turkey, (2011).
- [6] M. Simikic, N. Dedovic, L. Savin, M. Tomic, O. Ponjican, "Power delivery efficiency of a wheeled tractor at oblique drawbar force," *Soil & Tillage Research*, vol. 141, pp. 32-43 (2014).
- [7] A. Battiato, E. Diserens, "Tractor traction performance simulation on differently textured soils and validation: A basic study to make traction and energy requirements accessible to the practice," *Soil & Tillage Research*, vol. 166, pp. 18-32 (2017).
- [8] A. Janulevicius and V. Damanauskas, "How to select air pressures in the tires of MFWD (mechanical front-wheel drive) tractor to minimize fuel consumption for the case of reasonable wheel slip," *Energy*, vol. 90, pp. 691-700 (2015).

APPENDIX

S	Slippage	(%)
V	Velocity	(m/s)
P	Power	(kW)
F	Force	(kN)
T	Torque	(kN·m)
n	Revolution	(rev/min)
e	reaction force shift distance	(m)
W	Weight	(kN)
R	Resistance force	(kN)
r	Radius	(m)
r'	Radius after deflection	(m)
M	Moment	(kN·m)
a	Velocity of the vehicle	(m/s)
f	Rolling resistance factor	

Subscripts

A – Actual

The Design Optimization of a Gripper Mechanism Using the Bees' Algorithm

Osman ACAR^{1*}, Mete KALYONCU², Alaa HASSAN^{2,3}

¹Selcuk University, Konya/Turkey, osmanacar@selcuk.edu.tr

²Konya Technical University, Konya/Turkey, mkalyoncu@selcuk.edu.tr

³University of Lorraine, Nancy/France, alaa.hassan@univ-lorraine.fr

Abstract - Mechanisms are used for a specific objective. The objective of a mechanism may be following a trajectory or transmitting force. For a gripper mechanism, several objectives can be written. Performing the objectives with success requires optimized link lengths of the mechanism. There are several methods for optimization nowadays. Heuristic optimization methods are advantageous for problems with multivariable objective functions. One of the heuristic and population-based optimization method, the bees' algorithm searches optimal points in a wide space of solution of the objective function. In this paper, a gripper mechanism was optimized by using the bees' algorithm and compared with non-dominated sorting genetic algorithm version II (NSGA-II).

Keywords - Optimization, Heuristic Optimization, The bees' Algorithm, Gripper Mechanism, NSGA II.

I. INTRODUCTION

AS the robotic researches increase, gripper mechanisms for robotic applications have been intensively studied for longer than last two decades[1]. Designing a gripper mechanism needs an optimization process to determine link lengths of mechanism by forming an objective [2]. An optimization problem of gripper mechanism has multiple and conflicting objectives with complex search space. Therefore, solution of the problem is highly difficult with conventional optimization methods. The intelligent optimization methods are generally used for gripper mechanism optimization problems.

The paper consists of five sections. In section 1, a literature search was proposed. In section 2, the mechanism, objectives, constraints and parameters were briefly presented. In section 3, the bees' algorithm was shortly mentioned. In section 4, results were illustrated. The conclusions were given in section 5.

An evolutionary search algorithm for a gripper optimization problem of six objectives, eight variables and eleven constraints was used by [3]. In the study, parameters of a gripper B02 made by Global Modular Gripper were optimized. The parameters of the gripper were successfully optimized. Between 110-135 mm distances of gripper ends, the change of the force in the ends of gripper were 50N.

A proposition to solve a gripper optimization problem with five objectives, nine constraints and seven variables by using Multi-objective Genetic Algorithm (MOGA), Elitist Non-dominated Sorting Genetic Algorithm (NSGA-II) and Multi-

objective Differential Evolution (MODE) was carried out in [4]. The process had three stages. From these three stages, a Pareto optimal front were generated. Best values were selected. As a consequence of comparison between the three algorithms, MODE was found as the best in terms of minimum effort, solution spread measure and algorithm effort. But NSGA-II performed the best number of solution with high value of ratio of non-dominated individuals. Therefore, NSGA-II was best for several solutions demanded problem.

A study regarding optimization and demonstration on the behavior of a tendon-driven robotic gripper performing fingertip and enveloping grasps was executed [5]. The gripper consists of two fingers, each with two links, and is actuated using a single active tendon. The optimization problem for the gripper design was derived. The optimization was performed using a combination of random search and gradient descent with numerical gradient computation.

A four-bar slider-crank mechanism for a gripper was modeled in terms of geometrical, kinematical and dynamical[6]. So that, the force in the end of the gripper mechanism and the dimensional parameters were derived. Force transmission ratio and the difference between F_{max} and F_{min} along the actuating distance were determined as objective functions. Nine geometrical inequality constraints and six variables were generated. NSGA-II was used to optimize objectives and parameters. Ultimately, two of the parameters were found the most effective on objective functions.

An optimal design of an under-actuated tendon-driven robotic gripper with two 3-phalange fingers and a geometric design optimization method to achieve a stable grasp performance was presented [7]. The problem has twenty-two design variables. The genetic algorithm is applied to addressing the optimization problem. Practical experiments are performed as well to validate the proposed approach.

A newly developed polar bear optimization algorithm was presented and analyzed [13]. They targeted to imitate adaptation talent of polar bears to harsh winter condition as an advantage for local and global search, while birth and death mechanism controls the population. Experimental results and analysis with various parameters showed rapid recognition of the area by the relevant population and efficient birth and death mechanism to improve global and local search within the solution space. However, there is not application.

In this study, we targeted to contribute an application of Bees Algorithm (BA) on gripper design and comparison

between NSGA II and BA. There is also no application of constrained BA in literature. The BA is commonly compared with genetic algorithm[8]. BA is characterized by its simplicity, low computational cost, the ability to solve different types of problems and the ease of adoption of the algorithm to suit problems [9].

II. THE MECHANISM AND THE OBJECTIVE FUNCTIONS

The gripping mechanism compose of two symmetrical four-bar slider-crank mechanism. Therefore, half of the whole gripping mechanism is enough to scrutinize for optimization. The mechanism is basically composed of link 2, link 3 and link 4 whose dimensions are symbolized as d_2 , d_3 and d_4 shown in Fig. 1.

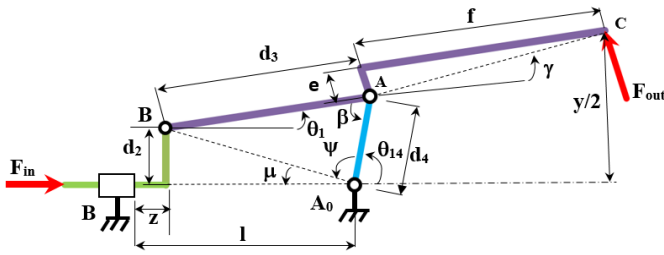


Figure 1: Force distribution, design and geometrical dependency variables of the gripper mechanism [6].

Parameterization of the mechanism for optimization requires geometrical, kinematical and dynamical modelling [6]. For details of modelling, derivations can be referenced to [6]. For the geometrical modelling joints of gripping mechanism were illustrated with the frame as in Fig. 1. In geometrical modelling, location vector of the end-effector and the joint coordinate vector are evaluated. For this study, it is found simpler to model the mechanism by analysis of static equilibrium as in Fig. 2.

The optimization process requires design parameterization and problem formulation. The design parameterization supply design variables $x = (d_2, d_3, d_4, l, e, f)$ for a proper gripper. The design variables and the problem formulation are derived from the modelling process. The geometrical dependencies of the model with design variables are given in Eq.(1-5). The design variables and geometrical dependencies of gripper mechanism are shown in Fig. 1.

$$\mu = \arctan\left(\frac{d_2}{(l-z)}\right) \quad (1)$$

$$\Phi = \pi - \mu \quad (2)$$

$$\Psi = \arccos\left(\frac{q^2 + d_4^2 - d_3^2}{2qd_4}\right) \quad (3)$$

$$\beta = \arccos\left(\frac{d_4^2 + d_3^2 - q^2}{2d_4d_3}\right), q = \sqrt{d_2^2 + (l-z)^2} \quad (4)$$

$$\theta_{14} = \Phi - \Psi, \theta_{13} = \theta_{14} - \beta \quad (5)$$

The optimization problem is formed by using the force in

the end-effector. The formulation may be derived from the static force equilibrium on the links of mechanism in terms of design and geometric dependency variables as in Fig. 2

The coupler link of the mechanism is under effects of three forces and assumed in static equilibrium. Two of the forces direction are known. The force (F_{out}) which is effective for gripping process, is vertical to the coupler link. The force exerted by link 4 to link 3 is in the direction of link 4. So that the direction of the force exerted by link 2 to link 3 can be found by intersecting two former forces as shown in Fig. 2. The moment in slider was neglected due to no moment in horizontal axes which is useful for calculation of F_{32} .

From the static equilibrium analysis of link 2, the magnitude of unknown force (F_{23}) on coupler link can be found from Eq. (6) which is force equilibrium on the horizontal axes by the help of known F_{in} . Finally, F_{out} can be found from equilibrium of moment on the joint A as in Eq. (7).

$$F_{32} = F_{23} = \frac{P}{2\cos(\theta_{13} + \alpha)} \quad (6)$$

$$F_{out} = \frac{F_{23} d_2 \sin(-\alpha)}{f} \quad (7)$$

where

$$\alpha = \arccos\left(\frac{n^2 + d_3^2 - m^2}{2nd_3}\right)$$

The first objective in Eq. (8) is the difference between the values of F_{out} in the range of the end-effector displacement. Minimization of this difference is the objective of the optimization problem.

$$f_1(x) = \max_z F_{out}(x, z) - \min_z F_{out}(x, z) \quad (8)$$

The second objective in Eq.(9) comprises of the transmission ratio, between F_{in} and F_{out} for Z_{max} . The maximization of transmission ration is the second objective of the optimization problem.

$$f_2(x) = P / \max_z F_{out}(x, z) \quad (9)$$

The constraints of the optimization problem are generated from the geometrical limits of the gripper mechanism. Therefore, the displacement of gripper end is formulated depend on the actuating distance in Eq.(9).

$$y(x, z) = 2(d_2 + d_3 \sin(\theta_{13}) + c \sin(\theta_{13})) \quad (10)$$

Where

$$c = \sqrt{f^2 + e^2}$$

$$\gamma = \arctan(e/f)$$

The geometric and force parameters are assumed as

$$Z_{max} = 25 \text{ mm}, Y_{max} = 70 \text{ mm},$$

$$Y_{min} = 30 \text{ mm}, Y_G = 100 \text{ mm} P = 95 \text{ N}$$

1. The minimum displacement between the ends of gripper should be less than the minimum dimension of the gripped object,

$$g_1(x): Y_{min} - y(x, Z_{max}) > 0 \quad (11)$$

2. The distance between the gripper ends at the maximum actuating distance should be greater than zero,

$$g_2(x): y(x, Z_{max}) > 0 \quad (12)$$

3. The maximum distance between the gripper ends at the no actuating distance should be greater than maximum dimension of gripped object.

$$g_3(x): y(x, 0) - Y_{max} > 0 \quad (13)$$

4. The maximum distance between the gripper ends should be greater than or equal to the distance between the gripper ends at the minimum actuating distance.

$$g_4(x): Y_G - y(x, 0) \geq 0 \quad (14)$$

5. The maximum actuating distance should be smaller than the design variable l .

$$g_5(x): l - Z_{max} > 0 \quad (15)$$

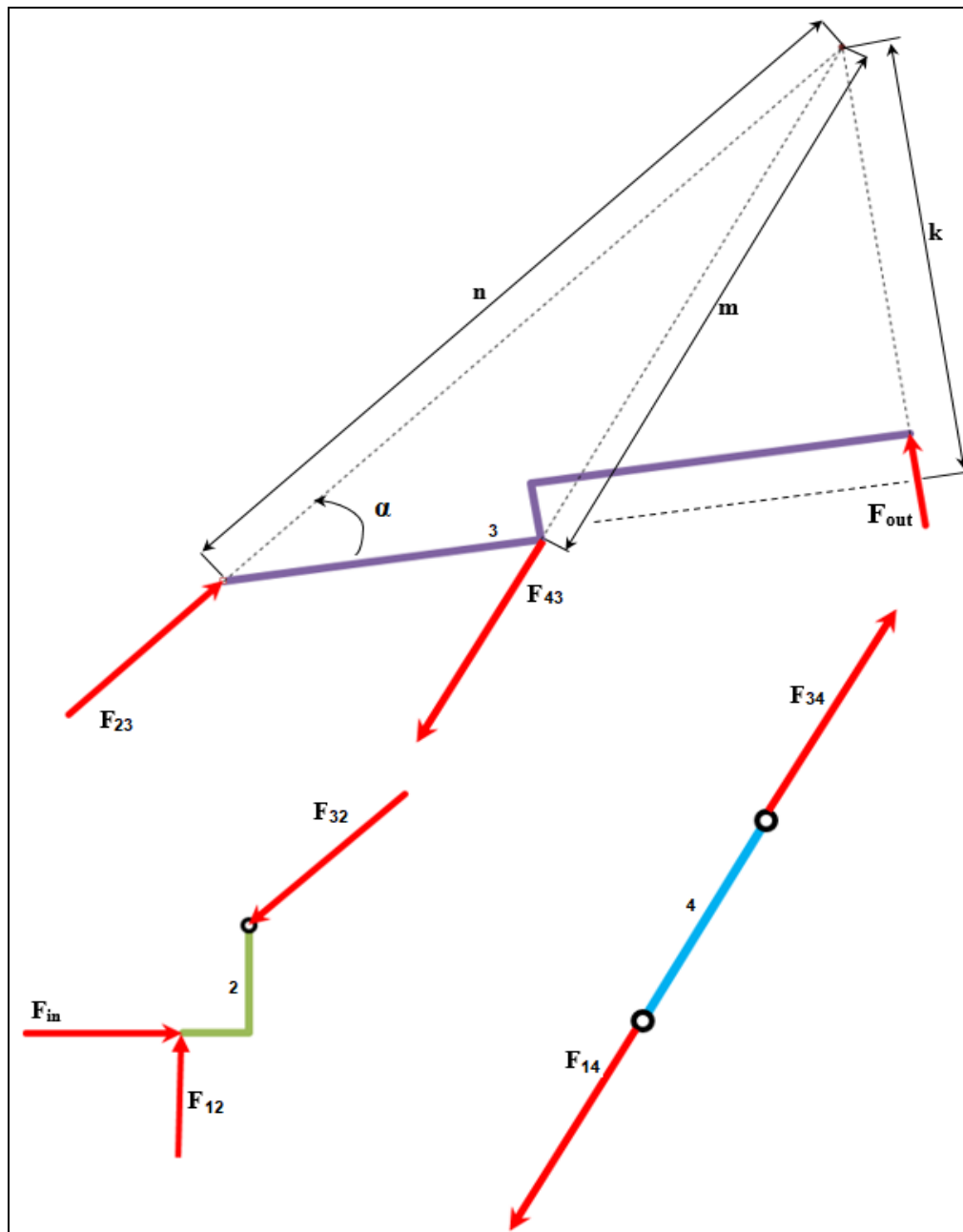


Figure 2. Static force equilibrium on mechanism links.

6. For permanent motion of the output link of the mechanism in the clockwise direction, the angle β should be smaller than $\pi/2$ at the minimum actuating distance.

$$g_6(x): \beta(z=0) < \pi/2 \quad (16)$$

7. A stable gripping process requires the absolute value of declination angle α smaller than $\pi/36$.

$$g_7(x): |\alpha| < \pi/36 \quad (17)$$

8. The input of arccos function in Eq.(4) should be smaller than one. For verification of triangle condition in ΔOAB .

$$\left| \frac{g^2 + d_4^2 - d_2^2}{2gd_4} \right| < 1 \quad (18)$$

After simplification and substitution of g , and rearrangement,

$$g_8(x): d_2^2 + (l - Z_{max})^2 - (d_4 - d_2)^2 > 0 \quad (19)$$

$$g_9(x): (d_3 + d_4)^2 - d_4^2 + l^2 > 0 \quad (20)$$

9. The geometric bounds of link lengths, or design variables, (in mm), are

$$10 \leq d_2 \leq 50, 10 \leq d_3 \leq 60, 10 \leq d_4 \leq 50, 10 \leq l \leq 50 \\ 5 \leq e \leq 15, 50 \leq f \leq 100$$

Briefly, the optimization can be expressed as

$$x^* = (d_2^*, d_4^*, d_5^*, l^*, e^*, f^*) \text{ which can satisfy}$$

$$f(x^*) = \min[f_1(x), F(x, Z_{max})]$$

III. THE BEE'S ALGORITHM

The BA is an intelligent swarm-based optimization tool that is inspired by the food foraging behavior of honey bees[10]. Regarding the algorithm, the parameters to be set, namely: number of scout bees (n), number of sites selected out of n visited sites (m), number of best sites out of m selected sites (e), number of bees recruited for best e sites (nep), number of bees recruited for the other ($m-e$) selected sites (nsp), initial size of patches (ngh) which includes site and its neighborhood and stopping criterion[11].

The algorithm starts with the determination of algorithm parameters. " n " number of design variables are placed randomly in the determined range. Differently in this study, the design variables are controlled if they fits the geometrical constraints after each random design variable production. The value of the objective functions calculated from randomly placed design variables are increasingly sequenced. The sequence is investigated within the three following processes[12].

The first " e " number of sequence are chosen for neighborhood search. The neighborhood search is executed by randomly generated " nep " number of neighbor with the " ngh " criterion from the elected design variables. The values of objective functions for neighbors are sequenced incrementally. Among the neighbors, the best " e " values are selected[12].

The ($m-e$) number of the sequence are selected for neighborhood search. The previous process is similarly repeated with " nsp " number of neighbors. Among the neighbors, the best " $m-e$ " values are selected. The rest of the " n " number sequenced values are randomly searched, sequenced as in Fig.3. This process repeats until iteration ends[12].

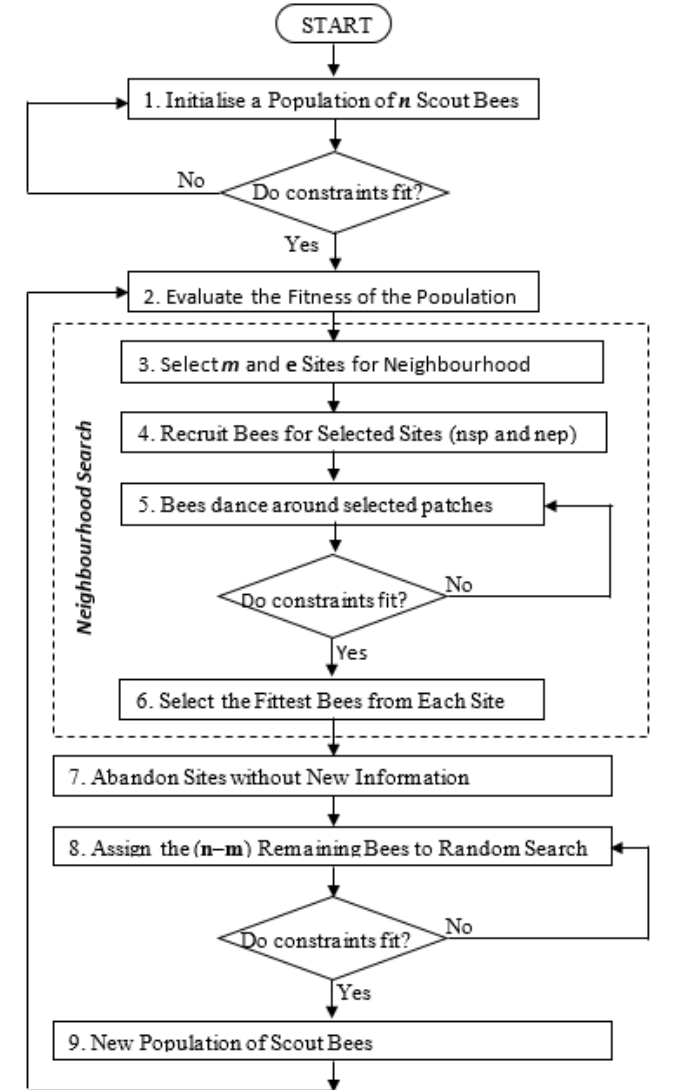


Figure. 3. Pseudo code of the constrained bees' algorithm

IV. THE RESULTS

The BA gives a set of convergence to the optimal solutions as shown in Fig. 5. Contrary to NSGA-II [6], the BA searches very distant variable spaces and selects the best of the local space as in Table 1. Therefore, it has fluctuating graph in the result of second objective. The BA can give high number of Pareto optimum if population and iteration is set properly. But It takes longer time. In this study, the BA has few Pareto optimum solutions with very high values in Table 1. The three results of design variables (A,B,C) for f_2 and f_1 values were given as in Table 1. The values of B are selected as the best

among. The optimization parameters were tuned by the help of literature (Hussein, Sahran et al. 2017) regarding elapsed time (6,43 s), minimum iteration to the converged value as $itr=50$, $n=20$, $nsp=10$, $ngh=0.1$, $m=10$, $nep=20$, $e=5$.

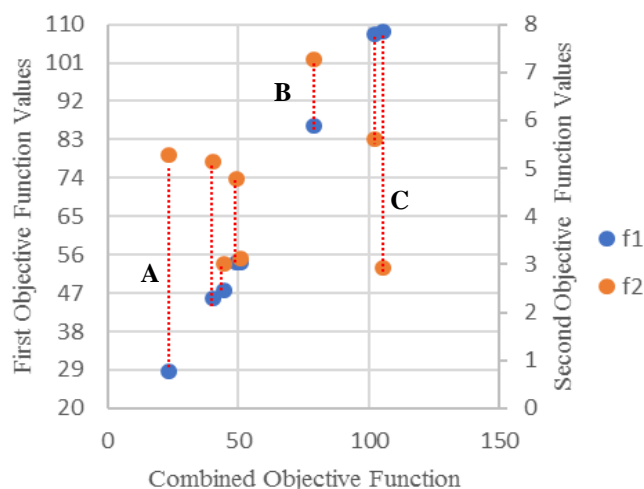


Figure 4. Set of optimal solutions obtained using the bees' algorithm

Table 1

The best three converged values of the bees' algorithm.

	f_2	f_1	d_2	d_3	d_4	l	e	f
A	5,27	28,55	36,44	59,72	42,91	42,62	5,07	71,34
B	7,26	86,21	20,69	44,30	29,26	39,9	7,65	55,12
C	2,92	108,44	47,48	50,32	39,70	40,71	10,62	65,16

Table 2

The three selected values from Pareto front of NSGA-II[6].

	f_2	f_1	d_3	d_4	d_5	l	e	f
A	6,64	93,81	32,92	19,08	54,73	49,85	5,00	50,00
B	6,25	138,9	30,89	18,88	52,31	49,74	5,00	50,00
C	6,09	184,2	29,69	18,80	51,28	49,71	5,00	50,00

When compared with the results of NSGA-II in Table 2 (Hassan and Abomoharam 2017), The bees algorithm found bigger transmission ratio and lower differences between forces of actuating distances. The two algorithms performed under a PC specifications Intel® Core™ 2 Due @ 2.53GHz, RAM: 2048MB, Windows 7 Ultimate 64-bit. Consequently, as the bee's algorithm takes 6,43 seconds, NSGA-II takes 30 minutes for optimization process. As mentioned in previous sections, the objective of the optimization is minimization of the difference between the forces in the end-effector at non-actuated and maximum actuated distances. Related to this objective, the second objective is the maximization of transmission ratio. To optimize these converse objectives, they are multiplied with weight numbers and combined.

V.CONCLUSION

This study has proposed a comparison between bees'

algorithm and NSGA-II for optimization of a mechanism dimensions. The modelling stage, constraints and objectives are briefly mentioned. The algorithm is illustrated by a flow chart. Finally, the results are compared. The goal of this paper was to scrutinize the superiority of searching method of the bees' algorithm. The results verified that the bees' algorithm has outstanding feature for searching optimal points.

The oncoming work on the study may be to use a harmonic bees' algorithm for mechanism optimization. The sensitivity analysis of design variables also can be executed.

REFERENCES

- [1] Andreas Wolf, R. S., Henrik Shunk (2005). Grippers in Motion. Italy.
- [2] Garet J. Monkman, S. H., Ralf Steinmann, Henrik Schunk (2007). Robot Grippers. Germany, WILEY-VCH.
- [3] Krenich, S. (2004). Multicriteria design optimization of robot gripper mechanisms. IUTAM Symposium on Evolutionary Methods in Mechanics, Springer.
- [4] Saravanan, R., S. Ramabalan, N. G. R. Ebenezer and C. Dharmaraja (2009). "Evolutionary multi criteria design optimization of robot grippers." *Applied Soft Computing* 9(1): 159-172.
- [5] Ciocarlie, M., F. M. Hicks and S. Stanford (2013). Kinetic and dimensional optimization for a tendon-driven gripper. Robotics and Automation (ICRA), 2013 IEEE International Conference on, IEEE.
- [6] Hassan, A. and M. Abomoharam (2017). "Modeling and design optimization of a robot gripper mechanism." *Robotics and Computer-Integrated Manufacturing* 46: 94-103.
- [7] Dong, H., E. Asadi, C. Qiu, J. Dai and I.-M. Chen (2018). "Geometric design optimization of an under-actuated tendon-driven robotic gripper." *Robotics and Computer-Integrated Manufacturing* 50: 80-89.
- [8] Arif Şen, M., M. Tinkir and M. Kalyoncu (2018). "Optimisation of a PID controller for a two-floor structure under earthquake excitation based on the bees algorithm." *Journal of Low Frequency Noise, Vibration and Active Control*: 1461348418757906.
- [9] Haj Darwish, A., A. Joukhadar and M. Kashkash (2018). "Using the bees algorithm for wheeled mobile robot path planning in an indoor dynamic environment." *Cogent Engineering*(just-accepted): 1426539.
- [10] Pham, D., A. Ghanbarzadeh, E. Koc, S. Otri, S. Rahim and M. Zaidi (2011). The bees algorithm-A novel tool for complex optimisation. *Intelligent Production Machines and Systems-2nd I* PROMS Virtual International Conference* (3-14 July 2006), sn.
- [11] Pham, D. T. and M. Castellani (2015). "A comparative study of the Bees Algorithm as a tool for function optimisation." *Cogent Engineering* 2(1): 1091540.
- [12] Pham, D. and M. Kalyoncu (2009). *Optimisation of a fuzzy logic controller for a flexible single-link robot arm using the Bees Algorithm*. *Industrial Informatics, 2009. INDIN 2009. 7th IEEE International Conference on, IEEE*.
- [13] Polap, D. (2017). "Polar Bear Optimization Algorithm: Meta-Heuristic with Fast Population Movement and Dynamic Birth and Death Mechanism." *Symmetry* 9(10): 203.

Comparison of Empirical and Experimental Results of Temperature on Cutting Tool Hardness During Rough Turning

M.KUNTOĞLU¹ and H. SAĞLAM²

¹ Selcuk University, Konya/Turkey, mkuntoglu@selcuk.edu.tr

² Selcuk University, Konya/Turkey, hsaglam@selcuk.edu.tr

Abstract – The temperature variation on cutting tool during machining informs about the tool wear improvement indirectly. Rough turning operation requires maximum material removal rate in minimum machining time. Higher machining parameters generate high temperatures and reduce tool life. Because of this, cutting temperatures should be optimized and considered as a function of tool life. For minimization of experimental work and production cost, prediction-based approaches have increased attention in last years. This study investigates the cutting tool temperatures on the rough turning of AISI 1050 material with different type of cutting tools in dry cutting conditions. Depth of cut was kept constant and cutting speed (135-194-207 m/min), feed rate (0,171-0,214-0,256 mm/rev) and hardness of cutting tool (P10-P25-P35) were chosen as variables. The research is performed with both experimental and empirical approaches and comparison curves showed that two results seem compatible. Experiments were committed based on full factorial design principle and empirical analysis was performed with orthogonal cutting conditions. Analysis of variance (ANOVA) showed that cutting tool hardness (45%) and cutting speed (44%) have dominant effect on cutting tool temperature. Empirically provided data show promising results to investigate the orthogonal process in future studies.

Keywords – Temperature, Variation of Tool Hardness, AISI 1050, Rough Turning, Empirical Calculation, Analysis of Variance,

I. INTRODUCTION

Increasing the productivity of machining operations require proper selection of tool and workpiece material, tool geometry, cutting conditions, monitoring the operation and predicting results with several methods such as Empirical, Artificial Intelligence. Especially for the rough turning operation, material removal rate is approved as a success criterion and gives data for productivity. Higher material removal rates cause several results as high cutting forces, cutting temperatures because of the high cutting parameters. High cutting temperatures deform the material structure and make easier wear development. The interaction between these parameters should be considered to understand the machining process for the optimization.

Cutting temperature variates depend on tool geometry, workpiece material, cutting forces and cutting parameters.

The temperature on cutting tool increases with positive rake angles and shear angles. Besides, insufficient clearance angle cause increasing of the friction of tool and workpiece and lead to higher temperatures. For higher production rates, the basic cutting parameters namely cutting speed, feed rate and depth of cut should have optimum values. Increasing of cutting speed enable the removal of the chips from the cutting area rapidly and produce high rate of heat. Also, the tool wear and surface quality have important effects on production cost, aforementioned parameters should be adjusted for these outputs. The effect of the cutting speed and feed rate on cutting temperature were studied by many researchers as far [1-11]. The temperature values always show increasing trend with higher cutting speeds. But the increasing in feed rate affects temperatures in decreasing [1,4] or increasing [6,11] trend.

Empirical or analytical calculations provides the prediction the required process parameter under different cutting conditions. The predicted results can be used for prevention of excessive heat rise and sudden tool breakage with the help of adaptive control applications. Some researchers have found promising results using both experimental and empirical approaches [1,4,12]. They found a similar trend between experimental and calculated results with a fluctuating error rate. The relationship can be characterized with a dynamic coefficient using an equation between two results. For obtaining a reliable result, sensor-based measurement should be performed but the prediction with empirical approach provides information for understanding the effect of cutting conditions on temperature variations [1].

This study aims to investigate the effect of the cutting tool hardness, cutting speed and feed rate variation on tool temperatures. A statistical evaluation was carried out using ANOVA for better understanding of the effects of inputs and their optimal values. In addition to that, measured results were compared with the calculated values which is based on empirical approach considering orthogonal conditions. 27 experiments were executed on a lathe and temperature measurements were performed with a radiation sensor mounted on the tool holder. Measurement of tool temperature provides promising results to show the tool wear indirectly

and provided results empirically can be used for the prediction of temperature values for future studies. This study focuses on the evaluation of cutting tool temperatures and effective parameters during rough turning of AISI 1050 material by means of empirical and statistical methods.

II. EXPERIMENTAL SETUP

A. Machine Tool and Radiation Sensor

Experiments were performed on a CNC lathe and adaptation of radiation sensor was set up with mechanical connection devices to fix the position of sensor in order to obtain temperature data reliable and robust way. The sensor connection on the machine tool is shown in Fig. 1a and 1b as schematical and real respectively.

The temperature on cutting tool is measured by In Ga As radiation sensor (TelC DKM2000B1). A compact system was designed for the reliable and robust measurement of temperature which is demonstrated on Fig. 1a. The devised system has connection equipments for the best settlement of radiation sensor. The position of the sensor is adjusted as 90 mm far from the tool. The sensor is capable of measuring of 300-800 °C temperature range and 1 mm around the tool. During measuring, 10 data in a second were transferred directly to a PC for the evaluation of temperature signals. A software XKM by TelC was used for on-line monitoring and storage of signals.

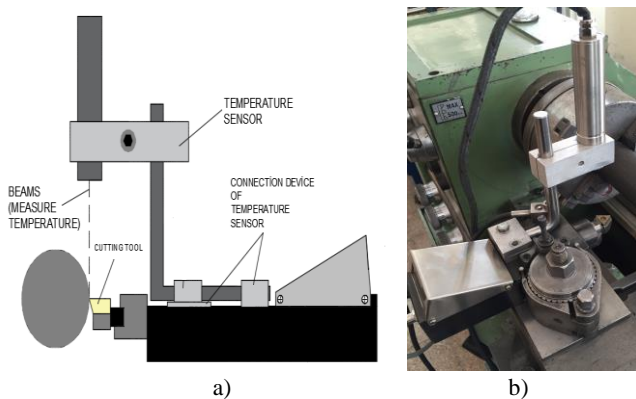


Figure 1. a) The Measurement Technique of Radiation Sensor
b) Experimental Setup Constituted on a Lathe

B. Cutting Tool, Tool Holder and Workpiece Material

The workpiece material was chosen as AISI 1050 high carbon steel because of having the widely usage in industrial applications as vehicle, machine, engine, device, shaft and gear manufacturing. Steel bars were cut to the Ø50x400 mm in length for experiments. Before the experimental work was started, oxide layered surface on the material was removed for better machining and enhancing the accuracy of measurement. The chemical composition of AISI 1050 material is given in Table 1.

Tool holder (Takımsaş R/L 140 0 20 16) which has 60° approaching angle and cutting tools (Bohler TCMT 16T304) were selected as tooling equipments.

Table 1: Chemical Composition of AISI 1050

Fe	C	Mn	Pmax	Smax
98,46-98,92	0,45-0,55	0,6-0,9	0,035	0,035

C. Experimental Design and Cutting Conditions

The selection of cutting parameters was performed according to tool-workpiece combination with the help of tool manufacturer and the operating ranges of machine tool. The variables were chosen as 135, 194 and 207 m/min for cutting speed, 0.171, 0.214, 0.256 mm/rev for feed rate and P10, P25 and P35 for tool hardness (Table 2).

Table 2: Experimental Variables

Cutting Variable / Level	Cutting Speed	Feed Rate	Hardness of Tool
1	135	0,171	P10
2	194	0,214	P25
3	207	0,256	P35

Depth of cut was kept constant as 2 mm for better understanding and analyzing the rough turning operation. 27 experiments based on full factorial design principle were performed at dry cutting conditions for better comparison with studies in the past. Each test sample was performed with a new cutting tool and workpiece material for eliminating the variations. Experimental design and temperature results were given in Table 3.

Table 3: Experimental Design and Results

Experiment Number	Cutting Speed (m/min) (V)	Feed (mm/rev) (f)	Tool Hardness (T)	Temperature (°C)
1	135	0,171	P35	395,5
2	135	0,214	P35	408,75
3	135	0,256	P35	397,75
4	194	0,171	P35	398,75
5	194	0,214	P35	404,5
6	194	0,256	P35	391,75
7	207	0,171	P35	400,5
8	207	0,214	P35	392,25
9	207	0,256	P35	396,25
10	135	0,171	P25	403,5
11	135	0,214	P25	403
12	135	0,256	P25	413,5
13	194	0,171	P25	413
14	194	0,214	P25	400
15	194	0,256	P25	403,25
16	207	0,171	P25	397,25
17	207	0,214	P25	413
18	207	0,256	P25	404
19	135	0,171	P10	385,5
20	135	0,214	P10	386,75
21	135	0,256	P10	395,25

22	194	0,171	P10	391,75
23	194	0,214	P10	389,75
24	194	0,256	P10	403,5
25	207	0,171	P10	441
26	207	0,214	P10	395,75
27	207	0,256	P10	410,75

III. EMPIRICAL APPROACH

A. Main Purpose of the Research

Experimental approaches provide information with real applications that requires time, cost and labour but finally, reliable and robust data can be obtained. Because of the existence of high number of parameters in machining operations, the relation between cutting conditions and quality characteristics can be hard to understand. Extensive information should be obtained from manufacturers and similar studies from literature for machining of each workpiece material. The requirement of high quality of product and low machining time pushes the researchers and industries for new methods to increase the productivity. Meeting these demands highly depends on the usage of artificial intelligence methods for predicting the uncertainties. By this way, undesirable results can be prevented and excessive cost and time losses can be avoided. The success of the operation is rely on these aforementioned items. For the optimized parameters and desired results, cutting mechanism needs to be understood and experimental work should be minimized. This paper purposes to better understanding of temperature dependent variations during turning of AISI 1050 material. Thus, empirical approach was carried out to calculate temperatures between tool-chip interface under different cutting conditions. Temperature deviations according to different variables were evaluated and compared with the experimental results. Additionally, the effects of cutting variables on cutting tool temperature were investigated with statistical analysis.

B. Calculation of Temperature Rise and Shear Plane Temperatures at Tool-Chip Interface

Metal cutting process is performed under high pressure and high speed leading excessive heat generation at cutting area. As a result of energy conversion, generated mechanical energy converts to heat and increases temperature at tool and workpiece. The heat transferred to the chip as possible as maximum heat is preferred to prevent the tool and workpiece being exposed to excessive heat. Accelerated tool wear and deformed material surface can be the result of undesired heat distribution. The adjustment of tool geometry and selection of cutting conditions according to the operation type will be the significant factors to prevent over-transferring of heat to the tool and workpiece. Despite the hard to define structure of cutting area because of the much number of parameters, the prediction of cutting temperatures provide information for the determination of cutting parameters before experimental work. The average temperature can be calculated with following formula defined by Oxley [13]

$$T_s = T_r + \lambda_h * (1 - \lambda_s) * P_s / m_c * c_s \quad (1)$$

where T_r is the room temperature considered as 20 °C and λ_h identifies the performed plastic work considered as 0.7 for carbon steel [14], λ_s identifies the rate of the transferred heat to the workpiece. P_s defines the friction power on tool-chip interface and calculated as

$$P_s = F_c * \sin\alpha_r + F_f \cos\alpha_r * v_c \quad (2)$$

where F_c is main cutting force, F_f is feed cutting force. m_c (kg/s) is material removal rate, c_s specific coefficient of heat of workpiece and considered as 470 Nm/kg°C. m_c is calculated with following equation

$$m_c = \rho * b * h * v \quad (3)$$

where ρ (kg/m³) is specific weight of workpiece, b (mm) is depth of cut, V (m/min) is cutting speed and h is undeformed chip thickness. λ_s is formulated with following equations [15]

$$\lambda_s = 0.5 - 0.35 \log(R_T * \tan \phi_c) \text{ for } 0.04 \leq (R_T \tan \phi_c) \leq 10 \quad (4)$$

$$\lambda_s = 0.3 - 0.15 \log(R_T * \tan \phi_c) \text{ for } (R_T * \tan \phi_c) \geq 10 \quad (5)$$

where ϕ_c is shear angle and R_T is a non-dimensional number and formulated as

$$R_T = \rho * c_s * v * h / c_t \quad (6)$$

where, c_t is thermal conductivity of workpiece and considered as 29 W/(m°C). The defined equations (1-6) can be used to calculate the tool temperatures during turning operation empirically. Some of the predicted results are demonstrated comparatively with experimental results in Fig. 3.

IV. RESULTS AND DISCUSSION

A. ANOVA Results and the Effects of the Input Parameters

Statistical analysis provides an important point of view in terms of finding out the contribution rate of a parameter on an output or quality characteristic. This refers to the understanding of the effectiveness of a parameter on a variable. Besides, the second and third order (or how many parameters including in the experimental design) inputs can be obtained for forward analyzing. After learning of the level of importance of inputs, each of input should be arrayed depends on how many level contains. By this way, to optimize of any variable, dominant parameters can be found out. ANOVA (Analysis of Variance) was preferred by many author in machining studies for years [16,17]. The provided results show that ANOVA can be considered as useful and reliable method to analyze for this kind of studies.

In this study, cutting speed, feed rate and tool hardness were used as cutting parameters rate conditions to investigate the rate of contribution on cutting tool temperature. In the

following tables, the most effective parameters are demonstrated. According to Table 4, tool hardness and cutting speed have dominant effects on temperature with 44% and 45% contribution rates. On the other hand feed rate has no more important effect to be considered. Percent contribution (PC) states the effectiveness and calculated with sum square (SS) values for each parameter to divide the parameter value to the total sum square value.

Table 4: ANOVA Results for S/N Ratios

Source	Dof	SS	MS	F	P	PC
Cutting Speed	2	0,096158	0,048079	5,47	0,154	0,44
Feed Rate	2	0,003696	0,001848	0,21	0,826	0,01
Tool Hardness	2	0,098076	0,049038	5,58	0,152	0,45
Error	2	0,017566	0,008783	-	-	-
Total	8	0,215496	-	-	-	-

Because of the higher temperatures soften the cutting tool and accelerate tool wear, also have a negative effect on machined surface, should be kept minimum as far as possible. Table 5 shows the best option of cutting parameters for obtaining the best/minimum temperature results. 135 m/min for cutting speed, 0,171 mm/rev for feed rate and P35 for tool should be considered as optimum parameters that can be symbolized by T1, v1, f1.

Table 5: Response Table for S/N Ratios

Level	Cutting Speed	Feed Rate	Tool Hardness
1	-51,94	-52,03	-51,93
2	-52,19	-52,06	-52,18
3	-52,04	-52,08	-52,06
Delta	0,25	0,05	0,26
Rank	2	3	1

The temperature variation with the combined effect of cutting speed and feed rate for each of tool hardness are shown in Figure 2. The graphs were constituted using program of Statistica version 12.0. Individually evaluation for every tool were preferred for better analyzing and to see the temperature ranges during turning with different hardness.

In Fig. 2a, variation in temperature for P10 cutting tool namely hard tool can be seen. When the cutting speed increases, tool temperature increases. However, the change in feed rate is not affected considerably on temperature and the second order feed rate seems giving the best results. For the P25 tool, a linear surface model develops contrary to P10 tool. Increasing in cutting speed increases the temperature similar with P10 tool. While the effect of feed rate variation seems unimportant for high cutting speed, towards to low cutting speeds, increasing feed rate increases the temperature. In Fig. 2c, except from a little area which belongs to high cutting conditions, the surface demonstrates that P35 tool is inconvenient for turning of this steel at determined cutting conditions. Temperature values appear in a small range and

variations in cutting speed and feed rate barely affects the temperature.

Hard tools generate higher temperatures especially for boundary conditions and causes enlarging of the temperature range. But the general temperature map is considered, for P10 tool have a larger reasonable area for the selection of turning AISI 1050 under designed conditions.

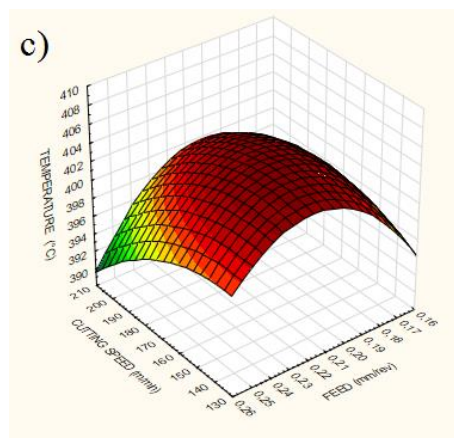
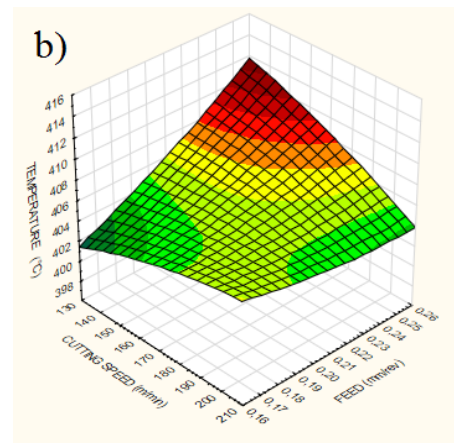
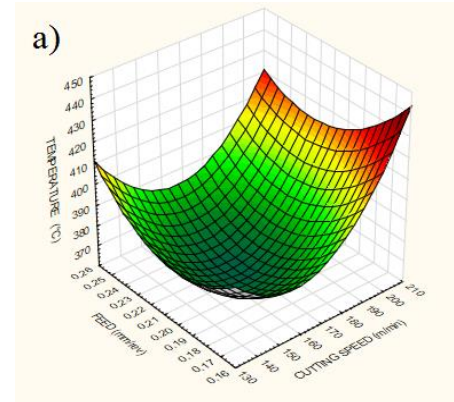


Figure 2: Temperature Variation with Combination of Cutting Speed and Feed Rate for Different Tool Hardness a) P10 b) P25 c) P35

B. Comparison of the Empirical and Experimental Results

Accordingly, the graph for $v=194$ m/min and P25 tool and for $v=207$ m/min and P10 tool for different feed rates and also for $v=194$ m/min and $f=0,256$ mm/rev for different cutting tool is shown in Fig. 3a, 3b and 3c respectively. The samples were selected to represent the differences and trends when considering the real and artificial conditions. The two lines show same trend with changing conditions with some temperature difference. The authors think that the difference between two results arise from the noise factors existing in real. Besides, some factors as developing tool wear, disorders in material and vibrations in machine tool affect the temperature progress which absent in empirical calculations.

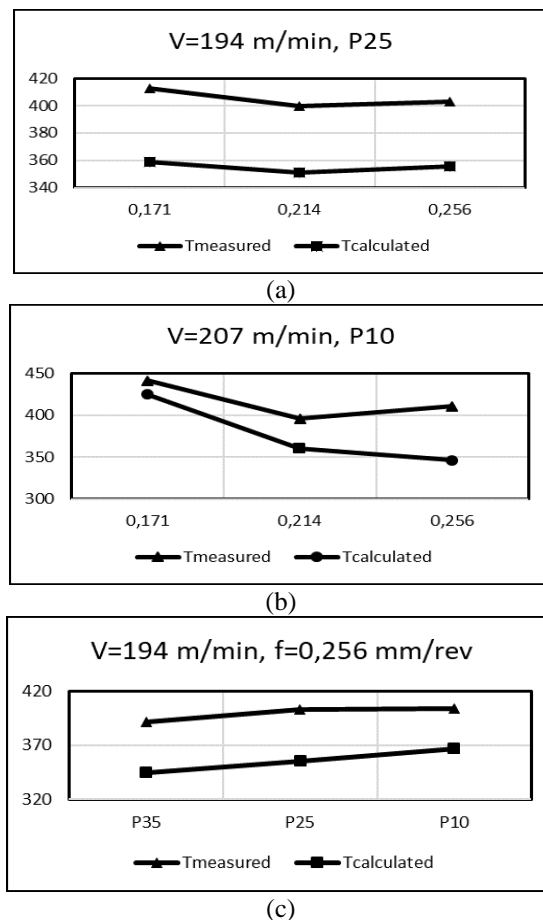


Figure 3. Comparison of Measured and Calculated Temperature Values

V. CONCLUSION

During turning of AISI 1050 material in dry cutting conditions, the effect of 3 different input parameters on cutting temperature were investigated and also empirical calculations were carried out additionally for comparing with experiments. The following deductions can be obtained from the paper:

1. When the calculated and measured results were compared, both line/slope show similar trends in different temperature ranges. The difference between two results derive from the microstructural disorders and

material properties resulting from during the manufacturing process. Also, because of the cutting conditions depend on the stiffness of machine tool, measured results demonstrate fluctuating pattern. On the other hand, calculated results show linear variation due to the lack of deteriorating effects existing in real applications.

2. As a novel approach, the tool hardness was considered as an input for investigating the effect on cutting tool temperature. According to ANOVA results, tool hardness has same effect on temperature with cutting speed. After all, feed rate has nonsignificant effect compared to other two parameters. (45% for tool hardness, 44% for cutting speed, 1% for feed rate obtained from S/N ratios).

3. For the P10 cutting tool, temperature increases with the increasing of cutting speed and reaches the maximum degrees with lower feed rate values. In order to obtain low temperatures, feed rate and cutting speed values for the optimized cutting conditions should be selected from the medium range as it can be seen in Fig. 2a. When the general temperature map is considered, P10 tool is the best option for this study.

4. The optimum temperature values for P25 tool can be obtained at lower feed rate and cutting speeds. Besides, low feed rate values during variation of cutting speed show no important increase at temperature. Despite the high temperature values seem in some areas especially for low cutting speeds, the usage of P25 tool can be preferred generally.

5. On the contrary of P10 cutting tool, P35 tool reaches maximum temperatures at medium cutting conditions. With the easy changing structure, P35 type tool causes high temperatures for all cutting conditions. Usage of this cutting tool seem inconvenient for turning of AISI 1050, considering the cutting tool temperatures.

6. The temperature surfaces in graphs (Fig. 2) demonstrate different characteristics depend on the cutting tool hardness. The combined effect of two important parameters which are cutting speed and tool hardness, reveals different shapes and temperature ranges. This situation results from the wear formation occurring on the tool surface. Chipping and breakages occur during turning with P10 tools. But, build up edge comes about especially for P35 tools. For P25 tools, flank wear and chipping which comprises at the tip of the tool occur. By this way, high cutting temperatures appear at the tools which possess chipping or breakage and observed for P10 during cutting.

7. As a result of feed rate-cutting speed-temperature graphs and ANOVA, cutting speed has a dominant effect on temperature and indirectly on tool wear. Despite feed rate seems has no important effect on temperature according to statistical results, temperature ranges at different feed rate values show significant variation for all cutting tool.

8. During experimental design procedure, manufacturers need to know about the effects of cutting parameters on

quality characteristics. By this way, optimal parameters can be chosen and productivity dependent items can be optimized. Tool temperatures affect tool wear and can cause sudden tool breakages. To obtain the best temperature result for maximum tool life, statistical analysis results show that first order of cutting speed, feed rate and cutting tool values which are $v_1=135$ m/min, $f_1=0,171$ mm/rev and $T_1=P35$ should be selected.

As a final suggestion, because of the tough structure of P35 tool and high wear resistance of AISI 1050 material, deformation proceeds rapidly. The tough structure of P35 tool is forced to machine the hard steel and cause increasing of temperatures. Since the temperature increase is accepted as a sign of tool wear and deformation rate, high temperatures refer to rapid changes of tool geometry. On the other hand, with hard to deform structure of P10 tool hardness generates low temperatures except from the high cutting speeds. If an increased tool life is required, harder tools should be preferred. Finally, although the empirical approaches give promising results for the evaluation of cutting mechanism and prediction of some variables, experiments should be performed in order to obtain real results and make the comparison with simulations and calculations.

For the next studies, the authors recommend to include the depth of cut as an input in addition to cutting conditions comprised in this study. The effectiveness on temperature of an important cutting parameter, depth of cut, can be investigated by this experimental design.

ACKNOWLEDGEMENTS

This paper was supported by Coordinatorship of Scientific Research Projects of Selcuk University with 15401125 project number. The authors would like to thank to Coordinatorship of Scientific Research Projects for funding our project and following papers.

VI. REFERENCES

- [1] H. Saglam, F. Unsacar, S. Yaldiz, "Investigation of the effect of rake angle and approaching angle on main cutting force and tool tip temperature," *Machine Tools and Manufacture*, vol. 46, pp. 132-141, 2006.
- [2] M. Vasu, H. N. Shivananda, "Investigation of cutting force tool tip temperature and surface roughness during dry machining of spring steel," *Materials Today: Proceedings*, vol. 5, pp. 7141-7149, 2018.
- [3] J. C. Heigel, E. Whinton, B. Lane, M. A. Donmez, V. Madvahan, W. Moscoso-Kingsley, "Infrared measurement of the temperature at the tool-chip interface while machining Ti-6Al-4V," *Journal of Materials Processing Technology*, vol. 243, pp. 123-130, 2017.
- [4] H. Saglam, S. Yaldiz, F. Unsacar, "The effect of tool geometry and cutting speed on main cutting force and tool tip temperature," *Materials & Design*, vol. 28, pp. 101-111, 2007.
- [5] G. K. Dosbaeva, M. A. El Hakim, M. A. Shalaby, J. E. Krzanowski, S. C. Veldhuis, "Cutting temperature effect on PCBN and CVD coated carbide tools in hard turning of D2 tool steel," *Int. Journal of Refractory Metals and Hard Materials*, vol. 50, pp. 1-8, 2015.
- [6] R. M. Saoubi, H. Chandrasekaran, "Investigation of the effects of tool micro-geometry and coating on tool temperature during orthogonal turning of quenched and tempered steel," *International Journal of Machine Tools & Manufacture* vol. 44, pp. 213-224, 2004.

- [7] P. B. Asha, C. R. P. Rao, R. Kiran, D. V. Ravi Kumar, "Effect Of Machining Parameters On Cutting Tool Temperature And Tool Life While Turning EN24 And Hcher Grade Alloy Steel," *Materials Today: Proceedings*, vol. 5, pp. 11819-11826, 2018.
- [8] N. R. Dhar, M. W. Islam, S. Islam, M. A. H. Mithu, "The influence of minimum quantity of lubrication (MQL) on cutting temperature, chip and dimensional accuracy in turning AISI-1040 steel," *Journal of Materials Processing Technology*, vol. 171, pp. 93-99, 2006.
- [9] G. Sutter, L. Faure, A. Molinari, N. Ranc, V. Pina, "An experimental technique for the measurement of temperature fields for the orthogonal cutting in high speed machining," *International Journal of Machine Tools & Manufacture*, vol. 43, pp. 671-678, 2003.
- [10] D. Jin, Z. Jingjie, W. Ligu, "Heat partition and rake face temperature in the machining of H13 steel with coated cutting tools," *Int J Adv Manuf Technol*, vol. 94, pp. 3691-3702, 2018.
- [11] M. Kamruzzaman, S. S. Rahman, Z. I. Ashraf, "Modeling of chip-tool interface temperature using response surface methodology and artificial neural network in HPC-assisted turning and tool life investigation," *Int J Adv Manuf Technol*, vol. 90, pp. 1547-1568, 2017.
- [12] M. Lazard, P. Corvisier, "Modelling of a tool during turning Analytical prediction of the temperature and of the heat flux at the tools tip," *Applied Thermal Engineering*, vol. 24, pp. 839-849, 2004.
- [13] P.L.B. Oxley, *The Mechanics of Machining*, Ellis Horwood Limited, Chichester, 1989.
- [14] A.O. Tay, M.G. Stevenson, G. De Vahl Davis, P.L.B. Oxley, A numerical method for calculating temperature distributions in machining, from force and shear angle measurements, *International Journal Machine Tool Design and Research* 16 (1976) 335-349.
- [15] U. Seker, A. Kurt, I. Ciftci, The effect of feedrates on the cutting forces when machining with linear motion, *Journal of Materials Processing Technology* 146 (3) (2004) 403-407.
- [16] S. R. Das, R. P. Nayak, D. Dhupal, "Optimization of cutting parameters on tool wear and workpiece surface temperature in turning of aisi d2 steel", *Lean Thinking*, vol. 3, pp. 140-156, 2012.
- [17] S. B. Chikalthankar, R. B. Kakade, V. M. Nandedkar, "Investigation and optimization of tool tip temperature in turning of ohns", *International Journal of Engineering Research & Technology*, vol. 3, pp. 1039-1044, 2014.

Analysis of Exergy Destruction Rates in the Components of the ORC System Using N-Pentane Fluid

A.KAHRAMAN¹, R. ŞAHİN² and S.ATA²

¹ Necmettin Erbakan University, Konya/Turkey, akahraman@konya.edu.tr

² KTO Karatay University, Konya/Turkey, remzi.sahin@karatay.edu.tr

² KTO Karatay University, Konya/Turkey, sadik.ata@karatay.edu.tr

Abstract - In this study, exergy analysis of ORC model designed using n-pentane fluid was performed. The effect of evaporation pressure and superheating temperature on system performance was determined. MATLAB and EES (Engineering Equation Solver) program was used in this study. In the simple ORC model, the exergy loss caused by the change in the evaporation pressure of n-pentane fluid between 250 kPa and 400 kPa was investigated. The exergy destruction in the pump, evaporator, turbine and condenser is determined comparatively. In addition, the effect of superheating temperature on the efficiency of the system has been investigated. Three different models were created for this. These are the system with no superheating temperature, a system with a superheating temperature of 10 °C and 20 °C. The effect of evaporation pressure and superheating temperature change on energy and exergy efficiency was determined in three different models. The percentage of exergy destruction occurring in system components within the total irreversibility value was determined. In which case it is indicated which component should be improved.

Keywords - Organic Rankine Cycle (ORC), n-pentane, Exergy, Exergy Destruction

I. INTRODUCTION

WHAT makes ORC systems different from other Rankine cycles is the type of fluid used in the system, not the system equipment. In the Organic Rankine Cycle, the organic working fluid has a lower boiling point and a higher vapor pressure than the water in the traditional rankine cycle. Since this fundamental difference increases the efficiency of the cycle, the lower the boiling point of the working fluid to be selected and the higher the vapor pressure, the greater the energy obtained from the turbine [1].

The main characteristic of the work fluids used in ORC is their ability to evaporate at low temperatures. In this way, it is possible to produce electricity without the need for high temperature heat sources needed by the water. Fluids are examined in three groups as wet, dry and isentropic according to the slope of the saturated steam curve.

In the studies, it was stated that it is more appropriate to use dry and isentropic fluids in ORC systems. In the case of wet

fluids, the expansion of the turbine at the end of the turbine flows into the wet vapor phase, which damages the turbine. In order to prevent this, superheating should be carried out in systems where wet fluids are used. However, in dry or isentropic fluids, the process of expansion of the turbine during the expansion process does not occur. Thus, since both the superheating process does not need to be done and the fluid can enter the turbine in the saturated vapor phase, the dry and isentropic fluids at the same heat source temperature enter the turbine with higher pressure than the wet fluids. As a result, the system efficiency will be higher as the pressure difference between the maximum pressure in the system and the minimum pressure will be higher if the superheating process is not done. Because of the dryness of dry fluids, even after the expansion rate is high, it is one of the most important elements of the cycle and prevents damage to the turbine which can be damaged very quickly by water droplets [2].

In this study, it is investigated how superheating temperature affects an ORC system using dry fluid. In addition, some studies on the determination of ORC performance by literature review are summarized below. Velez et al. [3], for the analysis of the ORC system, they worked on different fluids such as water, some hydrocarbons and refrigerants at a maximum temperature of 150 °C. System performance under different turbine inlet temperature and inlet pressure were evaluated. The thermodynamic analysis of ORC was carried out with the help of Aspen HYSYS software. In their study, they stated that system efficiency increased with pressure ratio and an increase of turbine inlet temperature. They have reached a maximum efficiency of 9%. Cataldo et al. [4], in the ORC system, they have done optimization by using the genetic algorithm method for selecting suitable fluid. Organic fluid, evaporation temperature and condensation temperature were determined as performance parameters. At the end of the study, they recommended the selection of Novec649, RE347mcc and R245fa with a low critical temperature. Tumen Özdil et al. [5], performed the thermodynamic analysis of the simple ORC system using the EES software. In the study, the effect of water in different phase states on the efficiency of the system was investigated. They stated that the water reached maximum

energy (9.96%) and exergy efficiency (47.22%) in the saturated liquid phase. They emphasized that the evaporator component has a significant effect on the determination of system performance. Rahbar et al. [6], studied the parametric analysis and optimization of small-scale radial turbines in ORC. Small-scale radial turbine performance was examined using eight organic fluids. The R152a fluid has reached maximum efficiency under a superheating temperature of 7°C. Wang et al. [7], studied the thermodynamic analysis of the ORC system designed using hydrofluoroethers. They used the EES program. The HFE7000, HFE7100 and HFE7500 organic fluids were compared with the change of turbine inlet temperature in terms of first-second law efficiency, net power and turbine size factor. In their study, they stated that the best thermodynamic performance is in HFE7000 fluid.

In this study, the effect of evaporation pressure (P_{eva}) and superheating temperature (T_{sup}) on the cycle performance was determined in simple ORC system. As the organic fluid, n-pentane fluid which is widely used in today's geothermal ORC systems has been chosen. First, the effect of the change in pressure at the turbine inlet on the exergy destruction of the system components was determined. At the same time, the energy and exergy efficiency of the system was examined. The effect of the superheating temperature on the system efficiency was determined for the n-pentane fluid of the dry fluid class. Then, the performance of the system with four different pressure values (250 kPa-300 kPa-350 kPa-400 kPa) under different superheating temperatures (0 °C-10 °C-20 °C) was investigated. The percentage distribution of the exergy losses occurring in the system components in the total irreversibility was determined. The main aim of this study is to determine the effect of n-pentane fluid used in the field of geothermal ORC application on exergy analysis of the system with the changes in evaporation pressure and superheating temperature.

II. MATERIALS AND METHODS

The working principle of the Organic Rankine Cycle and the T-s diagram are given in Figure 1. According to this figure; 1-2: Isentropic compression in the pump, 2-3: Heat input at constant pressure in the evaporator, 3-4: Isentropic expansion in the turbine, 4-1: Heat output at constant pressure in the condenser

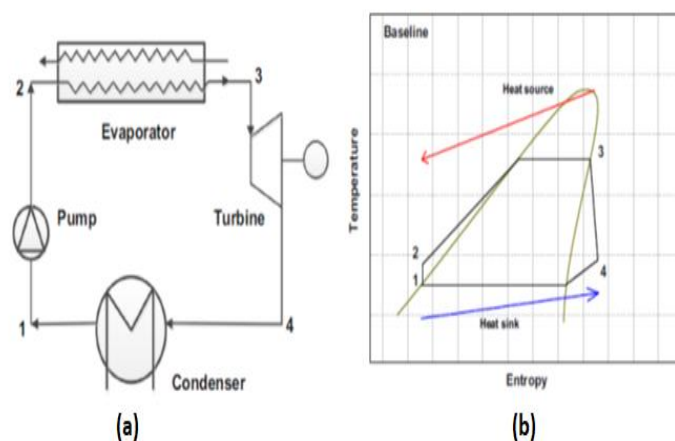


Figure 1: ORC Working principle and T-s diagram [8]

The physical and environmental properties of the n-pentane fluid determined in the study are given in Table 1. It is noteworthy that it has a low boiling temperature and that ODP value which is important from environmental care is 0.

Table 1: Physical and environmental properties n-pentane used in design [9]

Properties	n-pentane
ds/dT	Dry fluid
Molecular Mass (g/mol)	72.15
Normal Boiling Point (°C)	36.1
Critical Temperature (°C)	196.6
Critical Pressure (MPa)	3.37
ASHRAE 34 safety group	A3
ODP	0
GWP	20

When the slope of the saturation curves in the T-s diagrams of the fluids is positive, it is called the dry fluid. The T-s diagram of the n-pentane fluid which is a dry fluid is given in Figure 2.

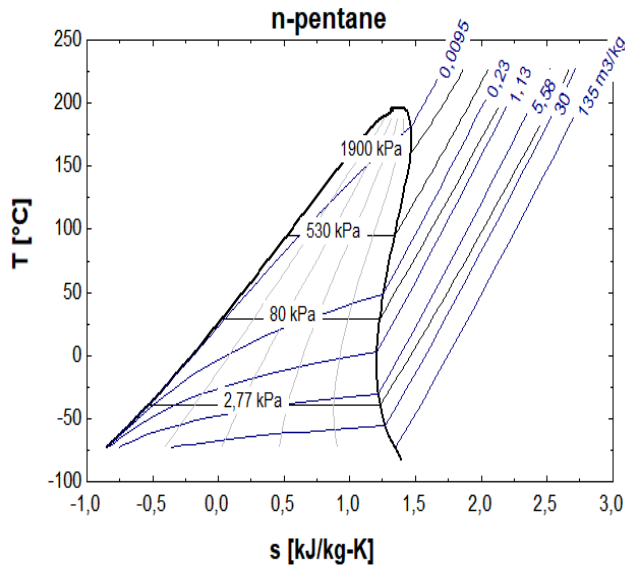


Figure 2: T-s diagram of n-pentane fluid

The constant values and independent variables used in the thermodynamic design model prepared with the aid of MATLAB and EES are given in Table 2.

Table 2: Fixed values and independent variables for the thermodynamic design model

Constant Values	Turbine Isentropic Eff.	85%
	Pump Isentropic Eff.	85%
	Heat Source Temp.	120 °C
	Sink Temperature	17 °C
	Condenser Outlet Temp.	20 °C
Independent Variables	Organic Fluid	n-pentane
	Evaporation Press. Range	250 kPa-400 kPa
	Superheating degree	0 °C – 10 °C – 20 °C

In this study, it is aimed to indicate the importance of evaporation pressure on system performance in simple ORC system using n-pentane fluid. At the same time, the effect of superheating temperature application on exergy loss was determined. Exergy losses in all components are determined and it is stated on which component should be improved.

III. RESULTS AND DISCUSSIONS

Figures 3-5 show the effect of evaporation pressure change on the exergy loss of the components for systems with different superheating temperatures. For $T_{sup} = 0^\circ\text{C}$; The component where the exergy loss occurs most is evaporator and then continues as turbine, condenser and pump. With the

increase of evaporation pressure, it was determined that the exergy loss in the evaporator decreased but increased in the condenser and turbine. Exergy loss in the pump was not affected by the increase in evaporation pressure. As the evaporation pressure increased and the difference between the heat source temperature and the evaporation temperature decreased, the exergy loss in the evaporator decreased. In addition, the maximum exergy loss was 71.79 kJ/kg for the non-superheating system and it was determined that this value increased to 75.25 kJ/kg and 78.84 kJ/kg by applying 10 °C and 20 °C superheating respectively. The turbine outlet temperature has increased with the increase of superheating temperature. Therefore, the loss of exergy in the condenser is increased.

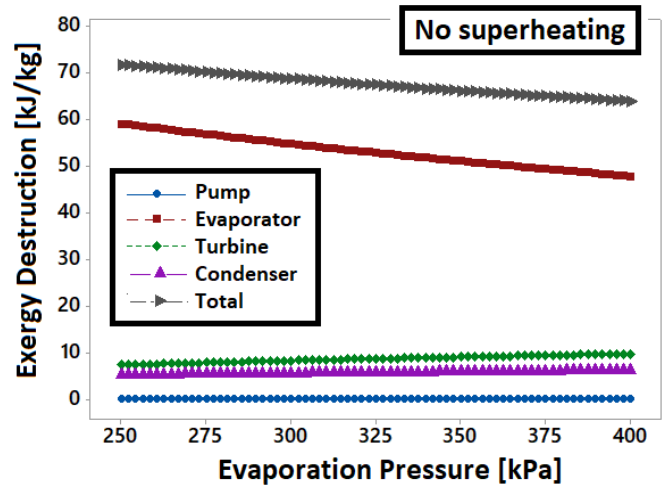


Figure 3: Effect of evaporation pressure change on exergy destruction in system components for $T_{sup}=0^\circ\text{C}$

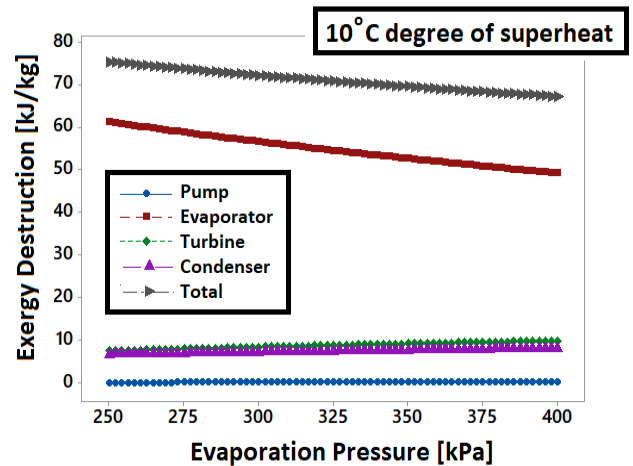


Figure 4: Effect of evaporation pressure change on exergy destruction in system components for $T_{sup}=10^\circ\text{C}$

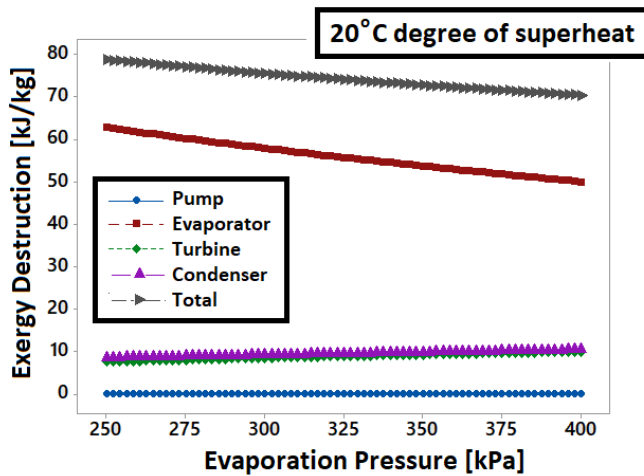


Figure 5: Effect of evaporation pressure change on exergy destruction in system components for $T_{sup}=20\text{ }^{\circ}\text{C}$

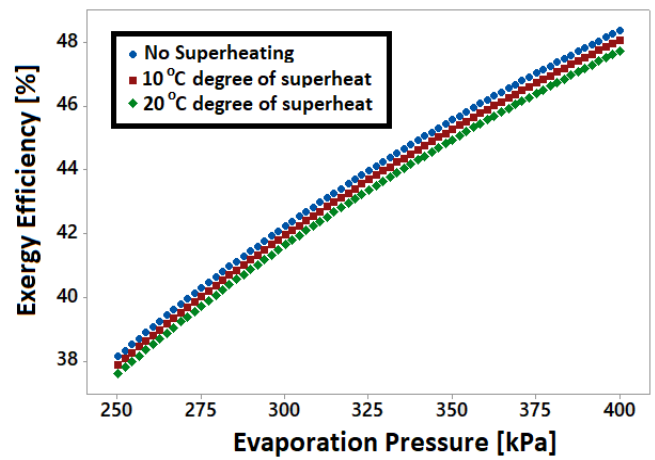


Figure 7: Effect of evaporation pressure on exergy efficiency under different superheating temperatures.

Figure 6-7 shows the effect of evaporation pressure change on thermal efficiency and exergy efficiency for models with different superheating temperatures. It is seen from the efficiency graphs that there is no need for application of superheating temperature in dry fluids. In case the superheating temperature is not applied, the fluid can pass into the superheated vapor phase. Therefore, energy and exergy efficiency decreased when 10 °C and 20 °C superheating temperature was applied. In the case of a constant evaporation pressure of 400 kPa, a system that does not apply superheating and a system with a superheating temperature of 20 °C are compared; energy efficiency from 12.59% to 12.42%; exergy efficiency decreased from 48.37% to 47.72%.

Figure 8-11 shows the effect of superheating temperature on the exergy destruction of the components for four different evaporation pressure values. The performance of the system with four different pressure values (250 kPa-300 kPa-350 kPa-400 kPa) under different superheating temperatures (0 °C-10 °C-20 °C) was investigated. Twelve different models were prepared for this. For each model prepared, the percentage of exergy destruction occurring in the components in the total exergy destruction is indicated. Although the exergy loss in the evaporator increased with the increase of the superheating temperature at all pressure values, the percentage of total irreversibility decreased. Exergy destruction occurs in the evaporator at 82.3% of the total irreversibility for 250 kPa and $T_{sup} = 0\text{ }^{\circ}\text{C}$. In the case of 20 °C superheating temperature, this value decreased to 79.6%. With increasing evaporation pressure, it was determined that the percentage of exergy loss occurs in the turbine and condenser increased and the evaporator decreased in all superheating temperature conditions. The decrease in the percentage of exergy loss occurring in the evaporator with the increase of superheating temperature was observed at a maximum evaporation pressure of 400 kPa.

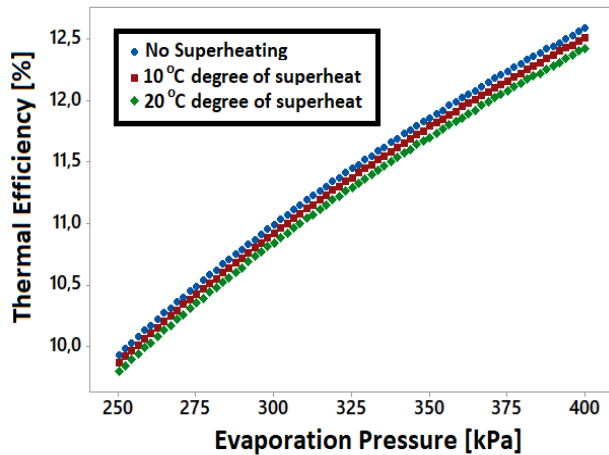


Figure 6: Effect of evaporation pressure on thermal efficiency under different superheating temperatures

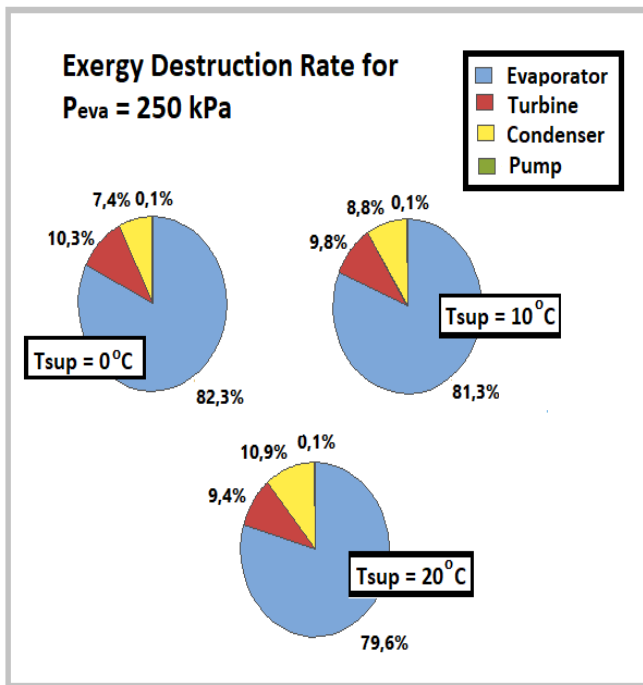


Figure 8: Exergy destruction rates in components in the case of three different superheating temperatures for 250 kPa evaporation pressure

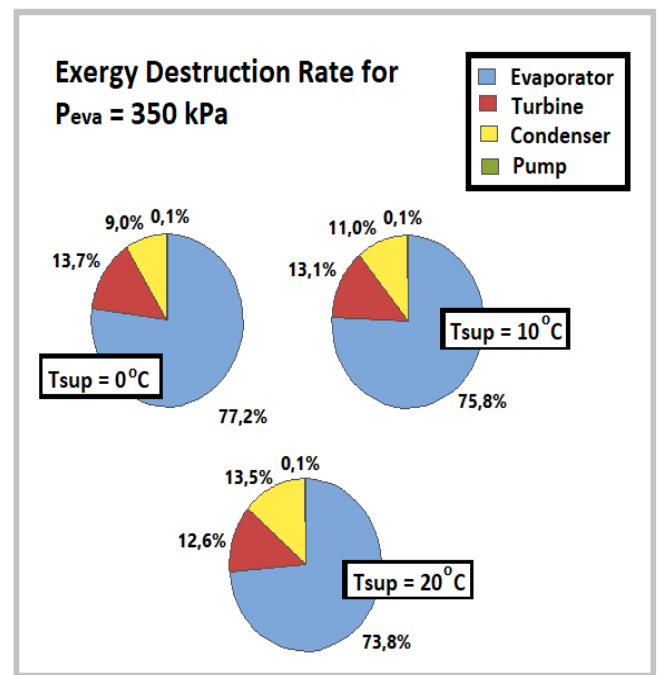


Figure 10: Exergy destruction rates in components in the case of three different superheating temperatures for 350 kPa evaporation pressure

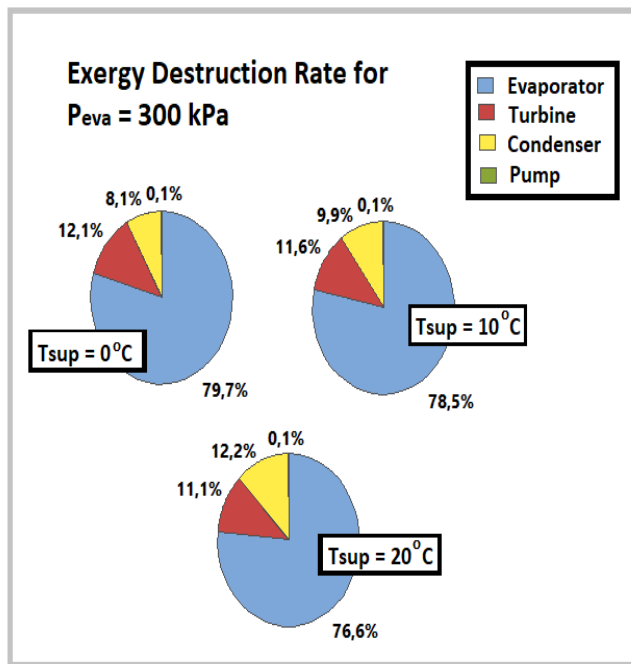


Figure 9: Exergy destruction rates in components in the case of three different superheating temperatures for 300 kPa evaporation pressure

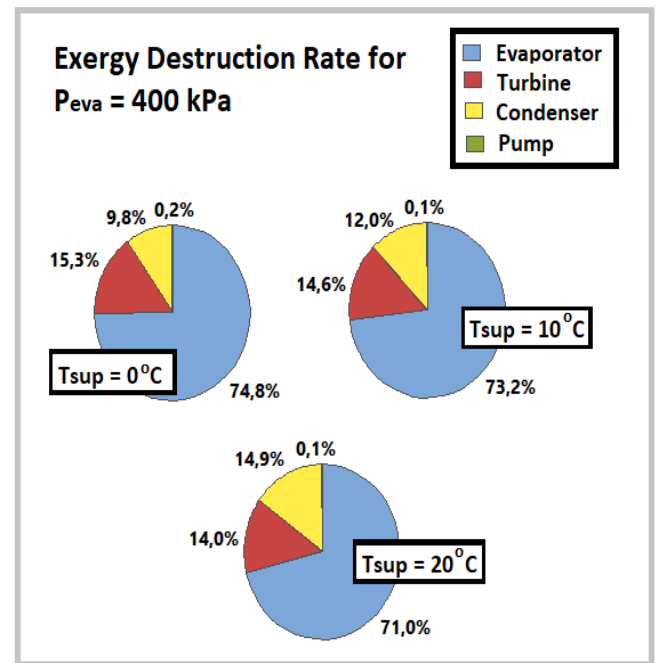


Figure 11: Exergy destruction rates in components in the case of three different superheating temperatures for 400 kPa evaporation pressure

IV. CONCLUSIONS

In this study, exergy analysis of the simple ORC system working with n-pentane fluid used in geothermal ORC application was performed. The performance parameters are defined as evaporation pressure and superheating temperature. Exergy destruction values, total irreversibility value of the system, energy and exergy efficiency of the system were determined by changing these parameters. The important parameters obtained in the study are given below.

- It has been stated that increasing the superheating temperature under constant pressure decreases the system efficiency at a small rate. In the absence of superheating at 250 kPa evaporation pressure, the exergy efficiency of the system is 38.14% and this value decreases to 37.6% at 20 °C superheating temperature.
- Exergy efficiency of the system increased with increasing evaporation pressure. Exergy efficiency increased by 26% as the evaporation pressure increased from 250 kPa to 400 kPa.
- With the increase of turbine inlet pressure, the loss of exergy in the turbine due to an increase in the pressure ratio has increased. As a result of evaporation pressure increased from 250 kPa to 400 kPa, exergy loss in the turbine increased by 32%.
- Exergy destruction rates for evaporator, turbine and condenser were determined as 79.6%, 9.4% and 10.9% respectively for evaporation pressure of 250 kPa and $T_{sup}= 20$ °C. As a result of evaporation pressure increased to 400 kPa with same superheating value, the rate of exergy loss in the evaporator decreased to 71% and increased to 14% and 14.9% for turbine and condenser respectively.
- Increased evaporation pressure positively affects system efficiency but increases the loss of exergy occurring in the turbine and condenser.

As a result, it has been stated that the largest share of exergy destruction values is in the evaporator for all cases examined. Therefore, it has been determined that the parameters such as heat source temperature, evaporation temperature and superheating temperature have a significant effect on the exergy loss occurring in the evaporator. It has been stated that selecting and analyzing these parameters in design and experimental studies will improve the system performance.

REFERENCES

- [1] M. Pelit, "Biyokütle Kaynaklı Organik Rankine Çevrimli Güç Ünitesinin Termoeconomik Analizi," Yüksek Lisans Tezi, Karabük Üniversitesi Fen Bilimleri Enstitüsü, Karabük, 2015.
- [2] İ. Günaydın, "1,5 kW Gücünde Organik Rankine Çevriminin Parametrik Tasarımı Termodinamik Analizi Prototip İmalatı ve Testi," Yüksek Lisans Tezi, Kırıkkale Üniversitesi Fen Bilimleri Enstitüsü, Kırıkkale, 2016.
- [3] F. Vélez, et al., "Comparative study of working fluids for a Rankine cycle operating at low temperature," *Fuel Processing Technology*, vol. 103, pp. 71-77, 2012.
- [4] F. Cataldo, et al., "Fluid selection of Organic Rankine Cycle for low-temperature waste heat recovery based on thermal optimization," *Energy*, vol. 72, pp. 159-167, 2014.
- [5] N.F. Tumen Ozdil, et al., "Thermodynamic analysis of an Organic Rankine Cycle (ORC) based on industrial data," *Applied Thermal Engineering*, vol. 91, pp. 43-52, 2015.
- [6] K. Rahbar, et al., "Parametric analysis and optimization of a small-scale radial turbine for Organic Rankine Cycle," *Energy*, vol. 83, pp. 696-711, 2015.
- [7] H. Wang, et al., "Thermodynamic Analysis of Organic Rankine Cycle with Hydrofluoroethers as working fluids," *Energy Procedia*, vol. 105, pp. 1889-1894, 2017.
- [8] G. Li, "Organic Rankine cycle performance evaluation and thermoeconomic assessment with various applications part I: Energy and exergy performance evaluation," *Renewable and Sustainable Energy Reviews*, vol. 53, pp. 477-499, 2016.
- [9] J.M. Calm and G.C. Hourahan, "Refrigerant Data Update," *Heating/Piping/Air Conditioning Engineering*, vol. 79(1), pp.50-64, 2007.

Potential Evaluation of Scaling and Similarity for Tractor Tires

E. CANLI¹, S. EKINCI²

¹Selcuk University, Konya/Turkey, ecanli@selcuk.edu.tr

²Selcuk University, Konya/Turkey, sekinci@selcuk.edu.tr

Abstract – The common exercise in investigations and industrial applications for tires and specifically tractor tires is experimenting. However there are difficulties which will be detailed in the text. Similar issues are encountered in fluid mechanics but fluid mechanics studies sometimes involves scaled models and uses similarity approaches to overcome some of the difficulties. However only one significant study has been encountered in the literature about tire scaling and no study is encountered about tractor tires. In this report, scaling, similarity and dimensionless analyses are introduced first. Then the work about tire scaling is viewed. Points for scaling tractor tires are proposed. Some concluding remarks and propositions are made for future work.

Keywords – Scaling, Similarity, Tire, Tractor.

I. INTRODUCTION

THE studies on tires of vehicles in general depends on three main approaches. The first one is experimentation and empirical tools such as correlations and tabular data are included in this approach. The second one is mathematical modeling by analytical analysis. The third approach uses the computational and numerical methods. There is a tradeoff between these approaches in terms of financial cost and labor cost. In other words, an approach that is easier to apply has higher financial cost. A cheaper approach is more likely to be harder to realize in terms of work load. Nevertheless these aforementioned approaches work on full scale tires. For instance, tires at full scale are tested on a real ground with a real vehicle. Although results of those studies are very reliable, there are certain difficulties which can be listed as below:

- Safety issues: Working with full scale instrumentation imposes some safety risks on the operator/tester. Inertia of the system, hazardous effects, emissions, sharp machine elements and such are composing the risks.
- Applicability: It is not always possible to test full scale equipment.
- Work load: Establishing a facility, maintenance, monitoring, need of several disciplines other than the discipline of the investigation, hygiene duties and test operations compose a real work load.
- Financial cost: Experimentation is sometimes quite expensive. The instruments for measuring physical

quantities add on the cost of the equipment to be tested.

- Limitations due to technique and technology: Recent technology is sometimes incapable of measuring the physical quantity. The temperature distribution in a material or stresses is normally calculated from measured magnitudes. Therefore theoretical knowledge cannot be always validated by experiments directly. Another thing about limitations of the technique and technology is due to the sizes of the full scale systems.
- Time cost: Another cost of the experimentation is time cost. Realizing a procedure depends on time and parameter combinations can lead to high numbers of tests.
- Hardness: Due to all above reasons for working with full scale equipment, there is a motivation issue of working with full scale systems. This perception of hardness is another fact to be considered for those studies.

Although tire studies are based on full scale, other disciplines such as fluid mechanics use scaling. By inspiration from fluid mechanics, it is thought to use scaling in tire mechanics. Since there is sufficient validation data, results of scaled tire investigations can be validated easily. Hence deciding and planning the procedure is what is left. The next section gives information about scaling, similarity and dimensionless systems. After that section, an example of scaled tire testing is given. The plans for scaling tractor tires are presented consequently. Finally, in the last section of conclusion, concluding remarks and proposition for future studies are given.

II. SCALING, SIMILARITY AND DIMENSIONLESS ANALYSIS

Scaling is actually a geometrical concept. It means reproducing the geometry in a different size while satisfying a scale ratio. If a length of geometry is reduced in “x” times, other lengths of the geometry should satisfy this scale. By this way, geometrical similarity is attained. Geometrical similarity is tried to be explained by Figure 1.

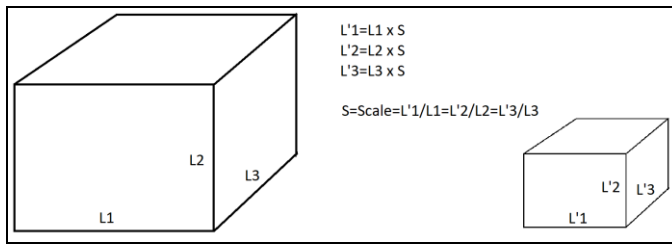


Figure 1. Schematic state of scaling and geometrical similarity

Geometric similarity is not enough for investigating and examining physical systems because there are structures, thermodynamic and physical properties like density, irregularities, forces, stresses and other environmental effects such as gravity, magnetism, etc. Another cause is for the search of a low cost material and/or easy to handle material for scaling. When material is changed, simple scale is not enough. The other similarities for studying physical systems are static similarity, kinematic similarity and dynamic similarity. If the system is investigated for a static load, static similarity should be satisfied. If a moving system is analyzed in terms of velocity only, then kinematic similarity should be satisfied. If all the physical effects on a moving system are investigated, then dynamic similarity should be satisfied. In order to satisfy these similarities, geometrical scale is not enough.

If Figure 1 is examined again, there is only one physical reference dimension which is length. For a system in which other dimensions are exist such as time, mass, temperature, etc., more scales are needed and the number is at least the number of the dimensions. This is obviously difficulty and leads to complexity. The dimensions can be related with each other and they may have a cumulative effect on the result to be investigated. Also parameters having different dimensions can be related with each other by combining dimensions. Therefore there is a technique in which parameters having different dimensions are put in mathematical relations in order to get a dimensionless scale. By this way, dimensionless scales include the relationships between parameters and dimensions leading to less number of scales. For instance, Reynolds number is a dimensionless scale for kinematic viscosity while there are a lot of parameters and dimensions. A small object in a wind channel for a given Reynolds number can do the kinematic representation of a big object in a real road. For a dynamic representation, additional dimensionless scales are needed but still the total of the scales are less and application is easier. Nevertheless, obtaining a dimensionless scale is not a very easy task. A very common way of using dimensionless scales or numbers are looking to the literature and using readily presented numbers. In some rare cases, dimensionless numbers can be derived special to the case. Buckingham Pi theorem is a well known method to obtain such dimensionless numbers.

Buckingham Pi theorem is a procedure to obtain the necessary dimensionless numbers or sometimes it is used for deciding to select the dimensionless number to be used. For instance, $1/Re$ can be found as a result of Buckingham pi theorem; however

the applicant can select Re as the dimensionless scale as the proper number.

In the Pi theorem, n number of parameters with dimensions can be reduced into $n-r$ number independent dimensionless variables where r is the number of reference dimensions. Mathematically;

$$p_1 = f(p_2, p_3, \dots, p_n) \quad (1)$$

$$\Pi_1 = f(\Pi_1, \Pi_2, \dots, \Pi_{n-r}) \quad (2)$$

By means of dimensionless analysis and dimensionless numbers as scales, similarities can be attained and following advantages can be achieved.

- Low cost
- Ease in handling
- Safety
- High number of experiments in unit time
- More control with less personnel

There are plenty of scaling examples but it can be said that there are almost no example of tire scaling except one work. It is mentioned in the next section.

III. TIRE SCALING

Tire scaling hadn't been encountered in scientific works till 2003. So a comprehensive Master Dissertation dedicated to the details of scaled tire testing is reported in 2003 [1]. Scientific reports can also be found originating from that thesis in 2004 [2] and 2006 [3]. The only references that are encountered in the literature so far are those reports. In this section, those reports are evaluated and summarized.

The specific motivation of the mentioned study (references given above) is said that scaling vehicle studies are done only the interval of linear region of tire steady state response. In other words, the tires in the modeled vehicle cannot represent the nonlinear or transient responses of a real tire. Therefore some of the scaled vehicle tests are restricted for a response interval of substitute tires which are not properly scaled and physically similar [1].

Tire testers, whether they are for a full scale test or scaled test, are explained to have some properties for arranging testing conditions and to be able to measure some quantities. Those properties are slip angle, camber angle, caster angle, speed, percent slip, normal load, bouncing frequency, etc. Those quantities to be measured are moments along each tire axis, temperature, inflation, wear, deformation and geometry [1].

The author emphasized that scaled tire testing necessitates lesser amount of forces. Therefore stationary experimental setups become attractive. Another important point against

mobilized test setups is that environmental effects on the measurements would be higher since the quantities are smaller in the scaled tests. So author established a stationary tire testing setup. The solid model and a picture of the setup are given in Figure 2.

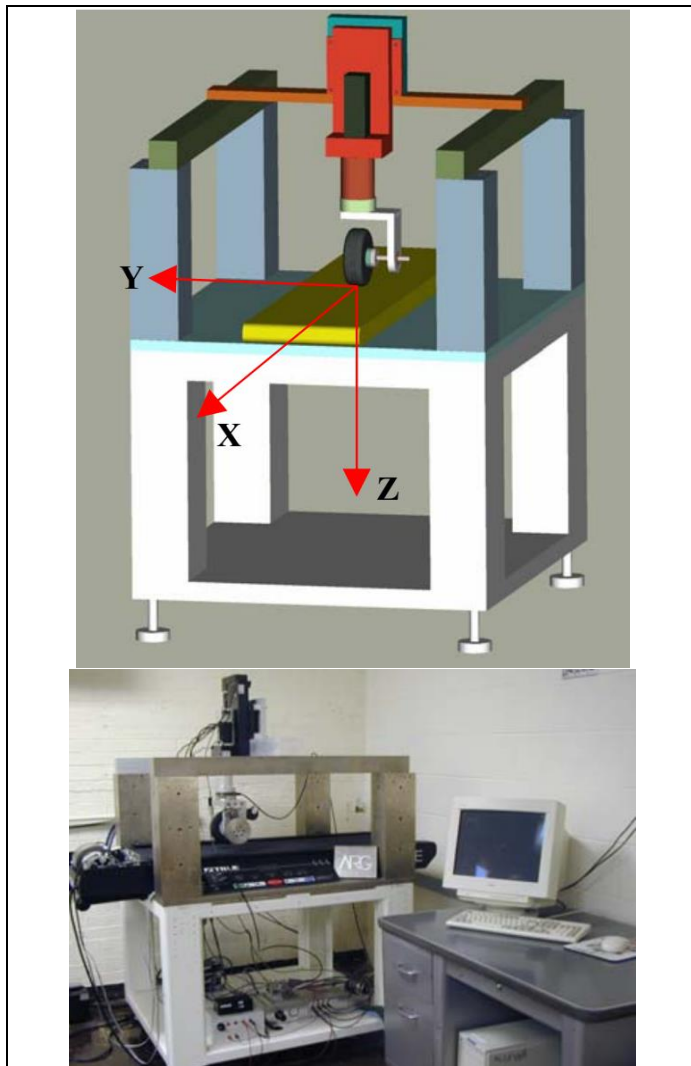


Figure 2. Stationary scaled tire test setup [1]

About the tires, it is explained that the full size vehicle tires are limited to an interval in such way that the smallest sizes cannot be used in scaled tire testing. Therefore new tires should be manufactured specifically to the testing but this imposes financial costs. The last option is to use a tire from a different application. Finally, it is stated that a proper small tire could only be found in remote control air plane market. The tires that are used for scaling are shown in Figure 3 and comparison of those tires with full scale ones are given in Figure 4.

Differences of the scaled tires from full size tires are listed as;

- Tread patterns

- Internal linings
- Belts and plies

which are completely missing in the scaled tires. However it is still proposed that the scaled tires can be used for testing since the experimentation of full sized tires represents tire response plus the missing properties above specifically to the tire. The tire response is assumed to be the common part.



Figure 3. Remote control air plane tires for scaling [1]



Figure 4. Comparison of scaled tires and full scale tires [1]

An image from the experiments is given in Figure 5. A comparison of scaled tire results and full scale tire results are given in Figure 6. As it can be seen from the figures, a scaled pneumatic tire can be put into test for nonlinear steady responses. The results of the test bench is not equal in quantity for scaled and full sized tires but the trends have similar and suggest that results can be used for assessment after a dimensionless conversion is made. The critical point here is calculating dimensionless result in order to use the outcomes of the scaled tire testing.

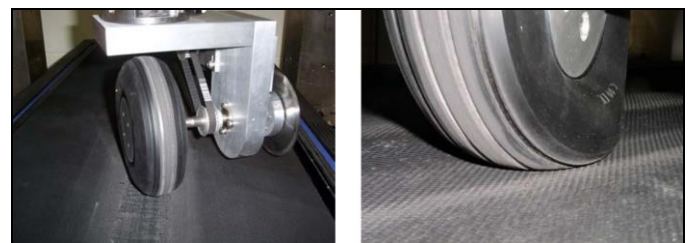


Figure 5. An instance from the experiments [1]

As a conclusion, it is understood that scaled tire testing is suitable for steady non-linear tire response. But there is no work for scaled tires for tire mechanics.

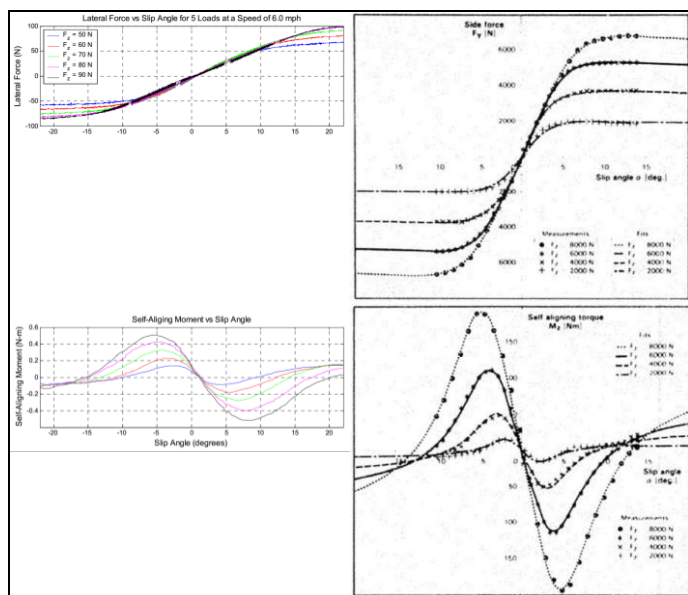


Figure 6. Comparison of scaled and full sized tire results [1]

IV. SCALING TRACTOR TIRES

Scaled tires for tire mechanics and scaled tractor tire testing has not been encountered in the literature. Tractor tires are a key point for the industry and have an enormous impact on energy consumption and soil compaction. However working with full sized tires is really hard because of the big loads acting on them and much diversified soil types. It can be clearly suggested that scaled tire testing has a potential for tractor tires.

The plan for such testing is given in bullet points below:

- The parameters (whether independent or dependent) should be decided for investigation.
- The reference dimensions of the parameters should be determined.
- Pi theorem should be applied to determine the dimensionless numbers/parameters.
- Scaled tires should be manufactured/produced.
- A proper design of test setup for the scaled tractor tires should be developed and implemented.
- Results of the tests should be compared to full sized tractor tires by using results with dimensions and dimensionless results.
- After validation is done by the comparison, extreme cases or cases that have not been tested can be investigated.

The point to be emphasized here is details of scaling for complete similarity. Soil, for instance, could not be used for scaled tests. Instead, wheat flour, concrete powder and finer grains would be used. The sensors would have higher sensitivity due to smaller magnitudes.

Here, a reference in the literature will be given in order to

have some inspiration though the tire is not scaled. Ekinci reported a rigid wheel that was made of metal and metal tire lugs can be mounted on it with different mounting angle [4]. It is very interesting to see such work in respect of two points; 1st, the rigid wheel has a geometrical similarity although it is not responding as the rubber tire does; and 2nd, tire lugs are found to have a significant role in traction performance. The study that is examined in the previous section mentioned that treads and patterns have a lesser effects on the tire performance because it focuses on the passenger vehicles. However this study reveals that tire lugs should be scaled too. And another outcome of this paper is that logs can be separately scaled and can be separately investigated.

In the last section, as conclusion, it is tried to summarize the observations and evaluation on the topic.

V. CONCLUSION

Scaling for acquiring similarity in order to make scientific investigations is a well known technique, especially in fluid mechanics. Dimensionless analysis and numbers are tools of the technique. Although research about tire mechanics can benefit from such technique, only a single work has been encountered in the literature so far. And no work has been encountered about scaled tractor tires. Following remarks are given for future work.

- Graduate studies can be dedicated to develop a plan and strategy in order to facilitate a scaled tractor tire and its test setup.
- The proposed setup and research is not only for commercial companies but it has a potential for agriculture since a huge diversity of soil types can be tested and strategies can be developed in two key issues; soil compaction and fuel consumption.
- The scaled tractor tire testing is much suitable than the full sized equipment for academia.

REFERENCES

- [1] M.S. Polley, "Size effects on steady state pneumatic tire behavior: an experimental study," Master of Science in Mechanical Engineering in the Graduate College of the University of Illinois at Urbana-Champaign, 2003.
- [2] M. Polley and A.G. Alleyne, "Dimensionless Analysis of Tire Characteristics for Vehicle Dynamics Studies," Proceeding of the 2004 American Control Conference Boston, Massachusetts June 30 - July 2, 2004
- [3] M. Polley, A. Alleyne, and E. De Vries, "Scaled vehicle tire characteristics: dimensionless analysis," *Vehicle System Dynamics*, vol. 44, no. 2, pp. 87-105, 2006.
- [4] S. Ekinci, "Effect Of Lug Angles Of Rigid Wheel On The Tractive Performance On Hard Soil Terrain", *Journal of Agricultural Faculty of Gaziosmanpasa University*, vol. 34, no. 3, pp. 278-229, (2017)

Mathematical Modeling of Thermoelectric Generator by Regression Analysis

A.C. AĞAÇAYAK¹, H. TERZİOĞLU², S. NEŞELİ³ and G. YALÇIN⁴

¹ Konya Technical University, Konya/Turkey, cemagacayak@selcuk.edu.tr

² Konya Technical University, Konya/Turkey, hterzioglu@selcuk.edu.tr

³ Selcuk University, Konya/Turkey, sneseli@selcuk.edu.tr

⁴ Konya Technical University, Konya/Turkey, yalcin@selcuk.edu.tr

Abstract - As countries grow, their need and demand for energy grow as well. The development of the technology and industry, which come to exist due to the growth of the country, a brings about a rise in energy consumption, as well as increasing the damage to the environment. Therefore, as the environmental and energy-related issues started to emerge more and more, we have seen an increase in the number of studies on energy production and its effects on the environment. Such studies highlight the renewable energy sources among the non-polluting alternative energy sources. Geothermal energy, particularly, shines out among the other renewable energy sources. It is a clean energy source that has been sustained since the Earth was formed. This study focuses on the design of a device named thermoelectric generator (TEG) that converts a renewable energy source, geothermal energy, directly into electric energy. Hence, we ran a simulation of a regression analysis and mathematical model on the thermoelectric modules TEC1-12706 and TEC1-12710, which can easily be found on the market, and then crosschecked the simulation results of different temperature, pressure, and water flow with experiments. The values for current, voltage, power, hot and cold surface temperatures, and the temperature difference between hot and cold surfaces were constantly monitored and recorded. The results of the experiment were compared using the regression analysis method. For the device TEC1-12706, error percentage of 9 experiments was 16.52% while it was 9.70% for TEC1-12710. At 90°C temperature difference, for TEC1-12706, output voltage was $V_{max} = 2.03V$, output power $P_{max} = 2.17W$, and efficiency 32.15%. For TEC1-12710, output voltage was $V_{max} = 2.11V$, output power $P_{max} = 3.42W$, and efficiency 38.53% [19,21].

Keywords - Geothermal energy, thermoelectric generator (TEG), modeling, regression analysis

I. INTRODUCTION

IN our current decade, where energy preservation gained such importance, especially the developed countries form their energy policies so that at least 10% of their energy demand can be provided using renewable energy sources. As the environment and energy-related issues increase worldwide in the recent years, the number of studies focusing on energy consumption and its effects on the environment have also increased. For this reason, many countries started to favor the geothermal energy sources among renewable sources. Geothermal energy have existed for a really long time, and it provides a clean and cheap energy source. Every year, new

geothermal energy sources are detected all over the world and the use of this energy source also increases rapidly. Since we need devices to produce megawatts of electricity and we need to import the solar panels and wind turbines needed from developed countries, this ends up being very costly for Turkey. Thanks to the studies and investments on the subject, it is apparent that the power deficit resulting from ever growing demand for power can be quenched using the residual heat from energy conversion. If we look back in time, we can see that we have used our energy sources inefficiently. We need to rethink the necessity of energy usage in many industries to fix this[10,11,12]. As the thermoelectric modules (TEM) have many advantages such as being durable, not requiring maintenance, being quiet, not having moving parts, and having a simple structure, the importance of these modules and the thermoelectric (TE) semiconductors have increased swiftly ever since the production of electric energy using residual heat energy became more popular[6,8,13,15,16].

This study focuses on the design of a thermoelectric generator (TEG) that converts a renewable energy source, geothermal energy, directly into electric energy. We used common thermoelectric modules that can easily be found on the market. During the experiments, the thermal liquid in TEGs was operated at different temperature, pressure and speed options. Upon conducting the experiments, we did a TEG modeling using the data we have collected. This paper inspects the small power TEG design model. As we have aimed to build bigger systems in the future, we designed the prototype so that it would be similar to the bigger systems within the bounds of possibility.

II. MATERIALS AND METHODOLOGY

We put the common thermoelectric coolers in copper blocks that had water tunnels inside.

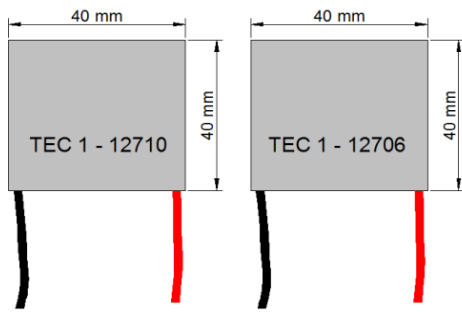


Figure 1: TEC1-12706 and TEC1-12710 Thermoelectric Coolers.

As can be seen from figure 1, TECs can be purchased from the market in a square shape with the size of 40x40 mm. When negative and positive DC voltage is applied to the black and red cables of the module, they work in a peltier way. During this process, the PNP and NPN semiconductive materials inside go through electron movements. When these electrons move from one place to another, the temperature of the surfaces change according to the movement direction of the electrons. While one of the surfaces get cold, the other one gets warm and this allows the device to cool small areas such as vehicle refrigerators or mini refrigerators. There are studies still underway to use this method in human clothing, shoes, car seats, etc. [3,17].

If you apply high temperature to one of the ceramic surfaces and low temperature to the other one instead of applying DC energy to the cables, the electrons in PNP and NPN series semi conductors, which are thermally parallel and electrically series with copper sticks, will start moving and you will receive DC voltage from the red and black cable ends of the module. This process is called thermoelectric generator (TEG) practice. To generate energy from temperature difference in the system, two different TECs coded as TEC1-12706 and TEC1-12710 with size of 40*40*3,8 mm were used. The parameters for the used TECs are listed in Table 1 [3,12].

Table 1. TEC1-12706 and TEC1-12710 specifications

Performance characteristics	TEC1-12706		TEC1-12710	
	25°C	50°C	25°C	50°C
Hot Side Temperature (°C)	25°C	50°C	25°C	50°C
Qmax (Watt)	50	57	85	96
ΔTmax (°C)	66	75	66	75
Imax (Ampere)	6,4	6,4	10,5	10,5
Vmax (Voltage)	14,4	16,4	15,2	17,4
Modul Resistance (Ohm)	1,98	2,30	1,08	1,24

As can be seen from Figure 2, TECs are placed between plates that have water tunnels inside.

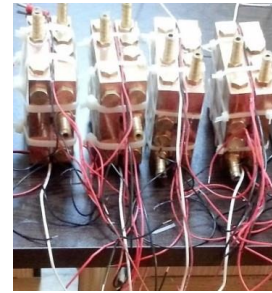


Figure 2: Placement of TEC1-12706 and TEC1-12710 in Thermoelectric Cooling Blocks

The TECs that are placed in copper blocks are connected electrically as shown in Figure 3.

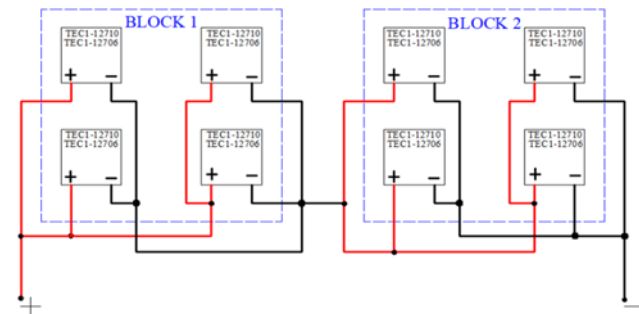


Figure 3: Electrical Wiring of TEC1-12706 and TEC1-12710 in Thermoelectric Cooling Blocks.

Different temperatures are applied to the thermoelectric modules' surfaces by running hot or cold water through water tunnels as shown in Figure 4 [14].

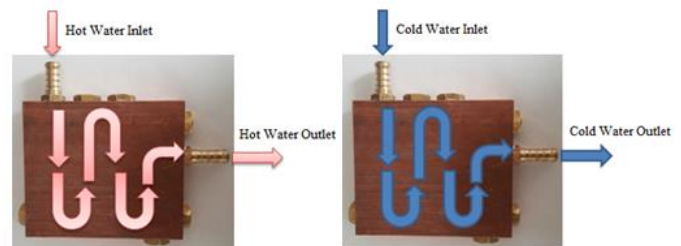


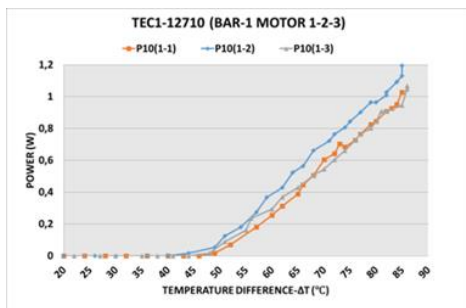
Figure 4: Hot and Cold Water Running Through the Copper Blocks.

In the experimental setup, we built two independent close systems so that cold and hot water can run separately. We flushed cold and hot water in the closed systems and set the pressure between 1 and 3.5. We conducted several experiments with different pressures. The temperature of the inbound water and the temperature of the outbound water along with the pressure levels are monitored constantly using sensors. We also measured the temperature and the amount of electricity generated using the measuring devices on the blocks or on the cables of TEGs. Since most of the geothermal sources in Turkey have a lower temperature and the heat resistance level of the TECs were 120°C at max, we stopped the experiments when we reached 85-90°C difference.

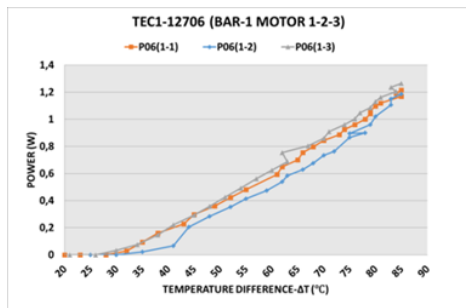
III. RESULTS AND DISCUSSION

We conducted experiments with 3 different pressure and 3 different water levels, then monitored the amount of energy and power generated. We conducted 9 experiments for each of the machines, using different bar pressures (1, 2.5 and 3.5 bar) and water pump power options (at 1st, 2nd and 3rd option).

In experiments conducted at 1 bar pressure and 3 different water levels, in TEC1-12706 TEMs produced more power when the water levels increased, as can be seen in Figure 5. TEC1-12710, however, worked better at medium water level. In all three experiments, TEC1-12706 TEMs generated more power than TEC1-12710 TEMs at lower temperatures, and throughout the experiment, TEC1-12706 TEMs continued generating more power than TEC1-12710 TEMs.



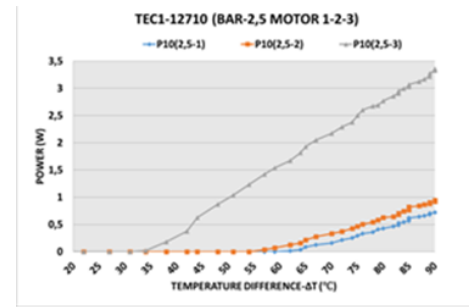
(a)



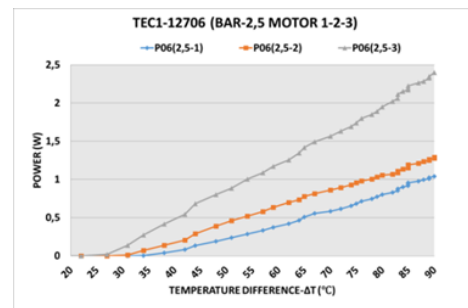
(b)

Figure 5: The power generated by TEC1-12710 (a) and TEC1-12706 (b) at 1 bar pressure and with 3 different water levels.

In experiments with 2.5 bar pressure and 3 different water levels, if the water levels rise, the amount of power generated also increase. Moreover, as the water level increased, they produced more power at temperatures at which they started to generate power. In all three experiments, TEC1-12706 TEMs started generating power at lower temperatures compared to TEC1-12710s. This can be seen in Figure 6 in a graph.



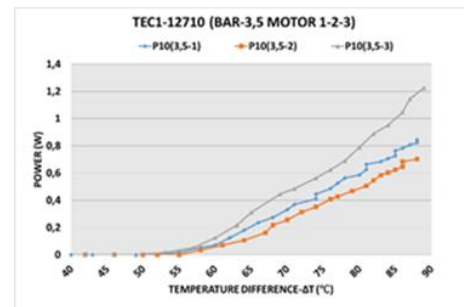
(a)



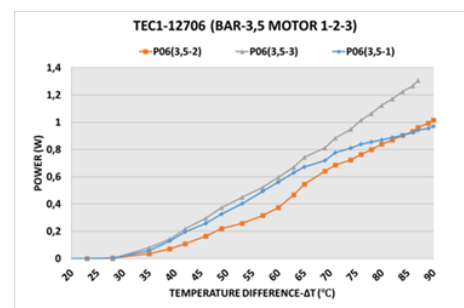
(b)

Figure 6: The power generated by TEC1-12710 (a) and TEC1-12706 (b) at 2.5 bar pressure and with 3 different water levels.

In experiments at 3.5 bar pressure and with 3 different water levels, if the water pressure is constant, the amount of power generated increases proportionately to the water levels. Moreover, as the water levels increased, they started producing more power at lower temperatures. This can be seen in Figure 7 in a graph.



(a)



(b)

Figure 7: The power generated by TEC1-12710 (a) and TEC1-12706 (b) at 3.5 bar pressure and with 3 different water levels.

A. Accuracy of TEG Modeling

Accuracy denotes how close the calculated data was to the measured data. Equation 1 is used for every data value to determine the error percentage between the calculated value and the measured value.

$$\delta_i = \frac{|R_a - R_a^0|}{R_a} * 100 \tag{1}$$

In this equation, δ_i : each value's error, R_a : estimated results, R_a^0 : experiment results, and i denotes data value.

To calculate the total error rate of the whole model, we use Equation 2.

$$\Delta = \frac{1}{n} \sum_i \delta_i \tag{2}$$

In this equation Δ : estimated accuracy of the model and n : number of values.

We used Equation 1 and Equation 2 to determine the accuracy of the three recommended methods to model the induction change in segmental ARMs.

Table 2: Mathematical Modeling and ANOVA Table.

Regression Statistics		Parameters			
Multi-R	0.915	Constant	0.897		
R Squared	0.837	Engine Speed	0.022		
Adjustable R Squared	0.836	Pressure	0.160		
Standart Hata	0.233	Temperature Difference	0.021		
Observation	321.000				
ANOVA					
	<i>df</i>	<i>SS</i>	<i>MS</i>	<i>F</i>	<i>Significance F</i>
Regression	3	88.291	29.43	544.081	0.000
Difference	317	17.147	0.054		
Total	320	105.438			

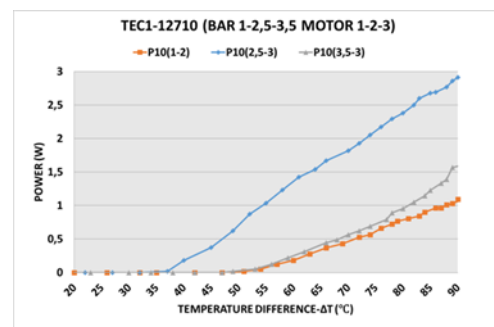
Error rates between the voltage values obtained from the 9 experiments and the regression analysis can be seen in Table 3.

Table 3: Error rates in voltage values in experiments

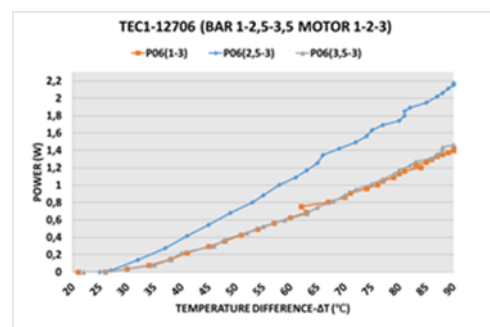
TEC1-12706				TEC1-12710			
Flow (rev/m)	32.3	49.5	64.2	Flow (rev/m)	32.3	49.5	64.2
Press. (bar)	%			Press. (bar)	%		
1	16.4	14.2	16.0	1	7.7	9.3	9.6
2.5	20.2	15.3	15.6	2.5	7.1	8.0	20.3
3.5	17.5	18.5	15.2	3.5	7.7	6.9	10.4
Average	%16.52			Average	%9.70		

IV. RESULTS

This study distinctively analyzed the TECs, different pressure settings, and different water levels using only one experiment setup. We designed a system where using hot-cold water level, pressure and temperature difference we could generate cheap, clean and easy electric energy.



(a)



(b)

Figure 8: Comparison of the best power generation levels of TEC1-12710 (a) and TEC1-12706 (b) TEMs at 1, 2.5 and 3.5 bar pressures and three different water levels

If we take into account the 9 experiments we've conducted, we can say that TEMs work the most efficiently at high pressure and with high water level. Their efficiency is pretty low at low pressure and with low water level. As can be seen from Figure 8, water level has a bigger effect on the efficiency than the pressure[3,4,5].

In thermoelectric modules, TEC1-12706 generates faster current and voltage at lower temperatures. In most of the

experiments, TEC1-12706 generated more power than TEC1-12710. However, at high pressure and with high water levels, TEC1-12710 thermoelectric modules generated more power than TEC1-12706. This shows that while picking out the thermoelectric module, we should bear in mind the water level and the temperature difference in the water. Additionally, the data collected in these experiments were supported with mathematical modeling. Regression analysis shows that for voltage, TEC1-12706 has an error percentage of 16.52% in 9 experiments while TEC1-12710 has an error percentage of 9.70%. When TEC1-12706 thermoelectric modules are used as TEG, efficiency level for 9 experiments is 32.15%, while it is 38.53% for TEC1-12710[19,21].

In future studies, the number of TEGs should be increased and the experiments should be conducted at higher temperatures. The experiments should also be conducted at one of the energy conversion systems in Turkey by building an experiment setup and should be supported with real practices on-site.

REFERENCES

- [1] R. Ahıskas, H. Mamur and M. Uliş, "Modelling and Experimental Study of Thermoelectric," *J. Fac. Eng. Arch. Gazi Univ.*, Vol.26, pp.889-896, 2011.
- [2] A.C. Ağaayak, H. Teziöglü, H. Çimen, S. Neşeli, G. Yalçın, (2018). "The Effects of Speed and Flow Rate on Power in Thermoelectric Generators," *International Journal of Intelligent Systems and Applications in Engineering*, Vol.6, pp.65-71, 2018.
- [3] A.C. Ağaayak, "Investigation of The Factors Affecting The Electric Energy Production of Thermoelectric Generators by Using Geothermal Energy," Post Graduate, Institute of Science, Afyon Kocatepe Univ., Afyon, Turkey, 2017.
- [4] A.C. Ağaayak, H. Çimen, S. Neşeli, G. Yalçın, "Electric Power Generation with Thermoelectric Generator," *In UMYOS 6th International Vocational School Symposium*, Vol:2, pp.541-549, Saray Bosna, 2017.
- [5] A.C. Ağaayak, S. Neşeli, G. Yalçın and H. Teziöglü, "The Impact of Different Electric Connection Types in Thermoelectric Generator Modules on Power," *International Journal of Engineering Research & Science (IJOER)*, Vol.3, pp.2395-6992, 2017.
- [6] T.Y. Kim and J. Kim, (2018). "Assessment of the energy recovery potential of a thermoelectric generator system for passenger vehicles under various drive cycles," *Energy*, Vol.143, pp.363-371, 2018.
- [7] M. Kotsur, "Optimal Control of Distributed Parameter Systems with Application to Transient Thermoelectric Cooling", *Advances in Electrical and Computer Engineering*, Vol.15, pp.117-122, 2015.
- [8] T.Z. Kowalski, "Gas gain in low pressures proportional counters filled with TEG mixtures," *Radiation Measurements*, Vol.108, pp.1-19, 2018.
- [9] T.H. Kwan, W. Xiaofeng and Y. Qinghe, "Multi-objective genetic optimization of the thermoelectric system for thermal management of proton exchange membrane fuel cells," *Applied Energy*, Vol.217, pp.314-327, 2018.
- [10] S. Miyata, Y. Yoshiwara, H. Watanabe, K. Yamauchi, K. Makino and S. Yamaguchi, "Evaluation of Thermoelectric Performance of Peltier Current Leads Designed for Superconducting Direct-Current Transmission Cable Systems," *IEEE Transactions on Applied Superconductivity*, Vol.26, pp.1-4, 2016.
- [11] P. Moteiei, M. Yaghoubi, E. Goshtashbirad and A. Vadiiee, "Two-dimensional unsteady state performance analysis of a hybrid photovoltaic-thermoelectric generator," *Renewable Energy*, Vol.119, pp.551-565, 2018.
- [12] S. Neşeli, H. Terziöglü, A.C. Ağaayak and G. Yalçın, (2017). "Electrical Power Generation by Thermoelectric Generator Using Geothermal energy and The Low-Power Dc-Dc Buck_Boost Converter Application," *In Graduate School of Natural and Applied Sciences*, Selçuk University, Konya, Turkey, 2017.
- [13] K. Nithyanandam and R.L. Mahajan, "Evaluation of metal foam based thermoelectric generators for automobile waste heat recovery," *International Journal of Heat and Mass Transfer*, Vol.122, pp.877-883, 2018.
- [14] G. Yalçın, M. Selek and H. Terziöglü, "A Plate Design to Produce Maximum Energy by Thermoelectric Generators," *In UMYOS 5th International Vocational School Symposium*, Vol.1, pp.909-916, Prizren, 2016.
- [15] C. Zhang, K. Li, J. Deng and S. Song, "Improved Realtime State-of-Charge Estimation of LiFePO4 Battery Based on a Novel Thermoelectric Model," *IEEE Transactions on Industrial Electronics*, Vol.64, pp.654-663, 2017.
- [16] H. Zhang, T. Xu, S. Hashimoto and T. Watanabe, "The possibility of mW/cm²-class on-chip power generation using ultrasmall Si nanowire-based thermoelectric generators," *IEEE Transactions on Electron Devices*, Vol.65, pp.2016-223, 2018.
- [17] S. Qing, A. Rezanian, L.A. Rosendahl and X. Gou, "Design of flexible thermoelectric generator as human body sensor", *Materials Today: Proceedings*, Vol.5, pp.10338-10346, 2018.
- [18] H. Çimen, A.C. Ağaayak, S. Neşeli, and G. Yalçın, (2017, December). Comparison of Two Different Peltiers Running as Thermoelectric Generator at Different Temperatures. In 2017 International Renewable and Sustainable Energy Conference (IRSEC). pp. 1-6. *IEEE*. Available: <https://ieeexplore.ieee.org/abstract/document/8477309>
- [19] A.C. Ağaayak and H. Teziöglü, "Analysis of Thermoelectric Cooler Used to Produce Electrical Energy in terms of Efficiency," *Academic Studies in Engineering*, Gece Publishing, pp. 111-120, 2018.
- [20] A.C. Ağaayak, H. Teziöglü, S. Neşeli and G. Yalçın, "Small Power Wind Turbine Design," *Academic Studies in Engineering*, Gece Publishing, pp. 121-130, 2018.
- [21] H. Teziöglü, S. Servi and A.C. Ağaayak, "An Overview of Thermoelectric Generators and Mathematical Modeling," *Academic Studies in Engineering*, Gece Publishing, pp. 133-148, 2018.
- [22] H. Teziöglü, S. Neşeli and G. Yalçın, "An Overview of Thermoelectric Generators and Their Applications," *Academic Studies in Engineering*, Gece Publishing, pp. 149-160, 2018.

Intern Engineering: Application & Statistics

E. CANLI¹ and A.A. SERTKAYA²

¹Selcuk University, Konya/Turkey, ecanli@selcuk.edu.tr

²Selcuk University, Konya/Turkey, asertkaya@selcuk.edu.tr

Abstract – Internship is a common tool for undergraduate education. Although engineering faculties in Turkey has internship applications, most of them are restricted for a limited period of time; about 60 days and usually it is done in summer semester. By the advancement of technology, conventional education and internship have become insufficient as their content can be short for recent technique. In the last decade, 17 technology faculties were established for engineering training and they have an internship program that can be regarded as a novel application. This new internship program involves private sector as the field of application and students spend almost 4 months, which should be normally spent in classes, in one of the winter semesters in the private sector companies. The impact of this application should be measured and assessed in order to aid decision making of the remaining engineering training facilities in Turkey and may be in the world. This work describes the experience of Selcuk University Technology Faculty Intern Engineer Program. It is also a preliminary step towards a comprehensive impact measurement. Some statistics such as student numbers, semesters, company numbers are provided. Some projections are given in the last part of the paper.

Keywords - Engineer, Impact Assessment, Intern, Internship, Private Sector.

I. INTRODUCTION

THE engineering vocation is an old expertise though its format has been developing for about two centuries. Training hours, training tools, training environment and content are changing according to the needs of industry and society. This change depends on time. In the last decades, technological developments gain acceleration and it is a very hard task to compose an up to date curriculum and plan for engineering training. The work load is not the only problem but engineering training needs recent equipment that is always expensive. Furthermore it should be updated. The only solution seems that giving principle theory and basic applied training in schools while leaving the technological and application skills to business life. Actually this seems indispensable considering the dynamics of modern world. However there is a competition among students for better job opportunities. And they seek better application skills from schools. An intermediate solution can be a long term internship in private sector while the training continues. By this way, the cost (both money and time) is shared between private sector and schools. Private sector emphasis here can be alienated by some readers however it should be known that undergraduate education in Turkey is undertaken by the government itself. Only exceptions are universities established by foundations

however they cannot make profit of it. It is under regulation. Therefore the support of the private sector should be encouraged by some means of incentives and promotions. There is a long term internship program in technology faculties, which is the focus of the present paper, in Turkey but before proceeding further, some information about technology faculties should be given.

Technology faculties established in the last decade, between 2009-2012, can be considered as a step forward to increased applied training. There were national meetings starting from 2008 for their establishment. The “Technical Education Faculties” (TEF) were closed and their infrastructure is used for technology faculties. The “Technical Education Faculties” (TEF) that were established for training teachers for vocational high schools had no equivalent programs in abroad. Engineers are hired for vocational education around the globe. Since there were enough engineering programs at that time, TEF were planned to be closed. There were also additional problems including graduates from the TEF who could not be hired in vocational schools because of their vast number and insufficient positions. The graduates had hard times in working industries because their titles were teacher. So the question of what to be done to the infrastructure of TEF was raised. Vocational education starting from the high schools is problematic in Turkey. There is a lack of “skilled” technical personnel including engineers. It should be emphasized that the number of the technical personnel is sufficient; the insufficient thing is the technical personnel who has application skills. These application skills can be listed but not limited to: reading and drawing technical drawings; handling tools; conducting measurements; conducting comprehensive calculations; management and such. The situation between 2008 and 2012 was the same. The laboratory and workshop infrastructure of the universities in Turkey are weak in general. Educational and training programs are mostly theoretical. The technological and technical development is too fast that schools cannot keep up with it. Most of the equipments in schools are too old for industry. And industry itself has the newest technology. The communication and cooperation between industry and schools are weak. Graduates are lacking in self-confidence in their profession. Turkey is still regarded as a developing country and mostly relies on works in workshops. Considering these points, “Technology Faculties” (TF) with specialized programs were established on the infrastructures of TEF. In the meetings for planning the TFs, it

was decided principally that one semester of the TFs would be devoted for industrial application in private sector. The curriculums of the TFs would be designed so that graduates would gain detailed instructions on specialized application field. And the curriculum design details were left to individual faculties. In other words, these TFs were given freedom to develop unique features in order to enhance applied training. For instance, a report was published by Unsacar et al. (2013) in order to explain new applications of Selcuk University Technology Faculty for applied training [1]. However, long term internship of engineering students in one of the winter semesters was mandated for TFs.

The long term internship of engineering students in TFs got a name in time; Intern Engineering Program (IEP). IEP aims to divide the excess load and cost of the applied training between schools and private sector. By this way, schools can focus on principal theory and applications with limited equipment; students have self confidence prior to the business life; private sector members can assess engineer candidates before involving a contract. The insurance of the students against industrial accidents and occupational illnesses are granted by the government. There is a study going on in order to give a wage that is to be paid to the students by government. It is not mandatory but companies usually decide to pay extra wages to the IEP students.

In this paper, literature about IEP, its application details, some statistics in Selcuk University Technology Faculty (SUTF) and some concluding remarks are given respectively. The aim is to start an assessment about the impacts of the application. Future work will contribute to improvement of IEP.

II. LITERATURE

Gunay (2010) published a presentation about configuration and formatting of TFs [2]. A diagram of Gunay is given below in Figure 1. Author suggests that TFs are located at the intersection between engineering and engineering technology. This implies better application skills alongside of the theoretical education in a balanced manner.

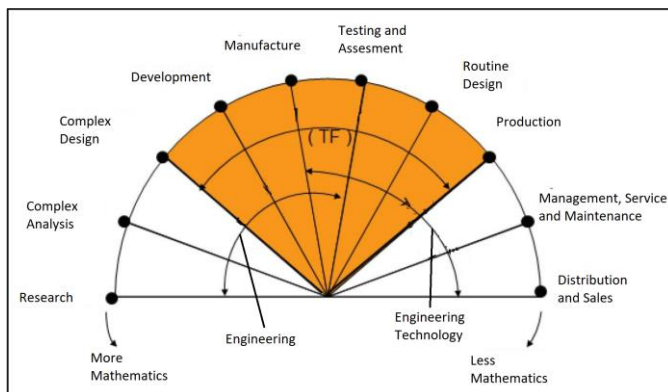


Figure 1. The diagram showing the intersection of the Engineering and Technology and the Technology Faculties (TFs) [2]

Unsacar et al. [1] have a paper in the Third Industry Council of Turkey, presenting novel suggestions that can be put into use in TFs. One of them is the IEP. Authors not only make suggestions but also emphasized the possible advantages.

In the University Industry Cooperation (USIMP) gathering in 2015, Salan et al. again presented SUTF applications about applied training and one of them was IEP [3].

Canli and Ates [4] gives information about an open test field of SUTF for renewable energy systems while considering the applied engineering training topic. They also reviewed literature for applied training of engineering.

Canli [5] stressed the relationship between applied training of engineering and equipment infrastructure. The author gives details of process and operation of an open field facility for renewable energy systems of SUTF. The literature of applied training for engineering also surveyed in the paper.

Although above list of references mention the IEP in different way of approaches, almost no direct reference has been encountered in the literature. The only direct reference is given in [6]. However it is not directly assess the impact and effectiveness of the application but it measures the effectiveness of the application in respect of cooperation between universities and industry. In the first half of the paper, tools for promoting cooperation between universities and industry in Turkey are introduced. In the second part of the paper, IEP is assessed in respect of the cooperation between universities and industry in Turkey by surveying opinions of graduates of Suleyman Demirel University in Isparta, who realized IEP before their graduation. Authors interviewed 289 graduates out of 340, which corresponds to 85% ratio. Total graduate number is 340, total company number is 233, total supervisor faculty member number is 27 and total company member who was assigned as intermediate between the company and the student is 159. They achieved 69% confidence rate for their evaluations. General response of the surveyed opinions suggests that IEP is found appropriate. An interesting outcome of that work is that almost half of the responses are indicating IEP helps them to determine their work field. Another important suggestion of the paper is the business culture in a positive manner. It is understood from the survey that IEP applicants having problems for using technologically advanced devices in companies. Some of the IEP students had hard times for establishing a common communication ground with the company members. It can be said that universities in campuses are relatively isolated from real life and when students experience real life and business life, they may face a culture shock. A common language is not always possible between company members and students. By saying common language, it is not literally mentioned; the cultural sharing is implied. Although supervision of the faculty members is found "very good" according to the responses of the students, this result should be validated by some other measures since it is a very hard thing for students to give negative responses for that question. The information about

how many graduates are working in the same company that they were done their IEP is missing in the work. So it can be said that the data during and just after the IEP of theirs are exist but long term data is missing.

IEP should be assessed carefully to measure its impacts and effectiveness. This paper is aiming to raise awareness for the necessity on such work and it can be regarded as a preliminary step forward.

III. APPLICATION

IEP in SUTF has been applying since 2016 (the winter semesters between 2016-2017 transition). Currently, the length of the application is one semester which corresponds to 14 to 16 weeks. Total working hours in a week is between 40 and 45 hours. The realization has changed from its initiation to date. Therefore it is desired to mention all details including past and present.

In the past, at first, SUTF assigned a mission of its personnel (3 to 5 person approximately) in order to give industry members information about IEP prior to the first application. A passenger vehicle of the SUTF was used, a driver was assigned and a route was determined. However, determining that route which meant determining target companies in other words was not an easy task. The diversity of company specification and the vast number of companies are confusions for decision makers. Therefore, Konya Chamber of Industry (KSO) was invited and met in order to establish cooperation in deciding companies to be met. A protocol was signed between SUTF and KSO. KSO undertook the preliminary introduction of IEP and collected information of volunteer companies. Then personnel of SUTF visited each company and told them the details of IEP. Regulation documentation was prepared according to the meetings with companies and national regulatory documents. A protocol contract between SUTF and companies and a work contract between student, SUTF and company were prepared as guide documents. An office in SUTF was established named as Career Planning and Monitoring Office (CPMO or KPTO in Turkish). The KPTO page can be viewed in [7]. KPTO recorded protocols, contracts and some information about students and companies. Students were matched with companies by KPTO. It is tried to match students only with Konya companies because Konya is the city of SUTF. Otherwise, supervisor faculty members would be sent outside of Konya bearing more cost and work load. At that time, it was not clear how to make the insurance against industrial accidents and occupational illnesses. So it was concluded to make special insurances from private sector and the premiums were decided to be paid by companies. A faculty member was assigned for each student to supervise the process during IEP. Guides and templates were prepared. Online reporting system was established. And first IEP students were sent to the companies.

With the initiation of IEP, some problems emerged. They

are given below but not limited to:

- Students having more wages from companies were admired by other students that had less or no wages from companies. Some of the students tried to change their companies to the admired ones.
- Companies had hard times for assigning jobs and tasks to IEP students.
- A couple of accidents were happened.
- Some of the IEP students couldn't decide how to report their works.
- Some of the students that were matched with companies faced problems such that companies said that they didn't have any information about the study of the student. This indicated that agreements between SUTF and companies were not sufficiently dealt by companies. There were also incidents that companies didn't adhere to the agreements. Because, there wasn't any sanction other than not sending students anymore.
- Students had hard times adhering to the deadlines and keeping up with announcements. This was particularly due to the absence of their experience in an application very different from school life.
- Departments of the SUTF evaluated some parts of the application differently from each other. This indicated that regulatory documents have unclear points or in other words they were open to comments.
- Since students had no business life experience at the beginning of the application, some of them felt terrible facing the work and tried to change the company at the first challenge. It was understood that possible challenges should be explained to the students prior to the application. It was also realized that there should be sanctions for the students to prevent company changing due to unnecessary reasons because company resource was limited.
- The matching of students with companies imposed a real work load on SUTF.
- Supervising students in cities other than Konya would bear a high cost for SUTF.

After above experiences, there were changes in the application of IEP. These changes are listed below but not limited to:

- Criteria for companies were left to departments of SUTF.
- Matching students with companies were left to departments of SUTF.
- The format and the method of evaluation and assessment of the IEP for each student were left to departments of SUTF.

- Update in protocols and new protocols were induced on students.
- By a governmental regulation, insurances were undertaken by universities.
- Preparations and preparation process for IEP became more similar to conventional internship applications.
- Online report submission and tracking was quitted.
- Cities other than Konya were allowed for IEP. Students doing IEP in cities other than Konya were supervised by online camera interviews and only one site visit might be done considering the distance and convenience.
- Mechanical Engineering Department, especially, put some additional criteria for companies outside Konya such as being a company having strategically important to the country or being in the first 500 companies in Turkey according to its gross income.

Recently, IEP is arranged in such a way that it can only be done in spring semester. Applications of the departments are becoming more different from each other. The graduates from SUTF are not monitored. So it is convenient to say that there is an urgent need for a research focusing on the development and impact of IEP.

IV. STATISTICS

In this section, it should be noted prior to the numbers that statistics are coming from two main sources. The first one is KPTO and the second one is Mechanical Engineering Department (MED). It should also be noted that there is no direct source of statistics due to several reasons. Instead, numbers are compiled from different recordings. It should be admitted that records can be better. Although papers such as protocols, contracts, etc. are stored, extracting data from them needs more time and labor which are not possible for the recent report. Hence, the data from existing recordings in computer files are used. But half of the 2017 and information about 2018 are missing for SUTF. Only MED data are complete from the beginning to date.

From 2016 (2016-2017) to the first semester of 2017 (2017-2018) following numbers are acquired for SUTF (Table 1). It is seen that 1.5 times more students in 2016 and 2 times more students in 2017 joined IEP for EED comparing to other departments. This is due to the fact that more students acquired prerequisites for IEP from EED. Those prerequisites are at least 1.8 General Credit Weighed Average Score of Education (GANO) and having no class from previous years with attendance clause. Looking to the company numbers, it can be said that EED students are more crowded in a company than CED and MED respectively. This is due to the fact that most of the companies in Konya are working in the field of mechanical engineering while the number of companies and

varieties in electronics and computer fields are lesser. In other words, MED students have more options in terms of companies. Totally 93 Konya companies are listed in the file from what these figures are taken.

Table 1. 2016 and half of 2017 in respect of student and company distribution

Year	2016			2017		
	MED	CED	EED	MED	CED	EED
Students	45	46	67	18	16	31
Companies	27	18	27	11	10	17

* MED=Mechanical Engineering Department, CED=Computer Engineering Department, EED= Electric&Electonic Engineering Department

In a different figure in the archives of KPTO is given in Table 2; in the same format of Table 1.

Table 2. Another version of 2016 and half of 2017

Year	2016			2017		
	MED	CED	EED	MED	CED	EED
Students	57	78	72	32	32	40
Companies	40	45	33	27	26	27

According to Table 2, Table 1 comments can be kept same for company distribution while CED seems equal to EED in terms of prerequisites and student numbers.

In 2017, KPTO recorded companies distributed according to departments. 57 companies for MED, 30 companies for CED and 40 companies for EED are visible. All of them were from Konya. 17 new companies were added as new protocols. 32 companies were negotiated but almost all of them rejected the offer. Four companies were marked to be cancelled due to their relations with the students of SUTF. 28 companies outside of the Konya are visible in the computer files of KPTO. 17 of them hosted CED students, only a single company hosted EED and 10 companies hosted MED.

In 2016 spring semester, 35 CED students, 32 EED students and 17 MED students were sent to companies. The distributions between normal education and secondary education (evening education) were 19 to 16 for CED, 22 to 10 for EED and 8 to 9 for MED. 70 companies were from Konya, 1 was from Samsun, 10 was from Ankara, 1 was from Bursa, 1 was from Cizre and 1 was from İstanbul. In the fall semester, there were 36 MED students, 44 CED students, 41 EED students and their distribution in normal education and evening education were 16 to 15 for MED, 23 to 21 for CED and 26 to 15 in EED. 9 students out of 36 completed IEP outside of Konya for MED, 15 students out of 44 completed IEP outside of Konya for CED and only 1 of 41 students done its IEP outside of Konya for EED.

103 students are visible in 2017 fall semester for all departments and 11 of them made their IEP outside of Konya. Among them, Ankara is the most common city. In the spring semester of 2017, which is absent in above tables and

numbers, 45 students are visible for MED and 6 of them completed IEP outside of Konya. 4 of them were in Ankara. 41 students were from CED and 13 of them were outside of Konya. The city distribution except Konya doesn't indicate a specific city. But they are the biggest and industrial cities of Turkey. 45 students were from EED and 5 of them were outside of Konya. 3 were in Ankara.

In 2018, MED list shows that 41 students are doing IEP in fall semester and 61 will do in spring semester. Spring students haven't determined and applied companies however 4 of the fall semester students are outside of Konya.

The conclusions are given according to above information in the next section.

V. CONCLUSION

Intern Engineering Program is introduced in this paper. Its advantages, drawbacks, experienced problems and some statistics are shared. It is desired to outline a future comprehensive work in order to assess and monitor its impact and effectiveness. Following remarks should be considered for the future work.

- The readily existing data in tabular form from KPTO lacks consistency. Documentation in the archives on paper should be carefully viewed and data should be extracted.
- There is a need of time and labor for extracting data from archive documents such as protocols, student contracts and archives of the departments. These should be undertaken in other technology faculties too.
- There is a need of future work in a comprehensive manner for assessment and long term monitoring of the impacts and effectiveness of the IEP.
- There should be a class at least one semester before the IEP that can prepare students for the challenges of IEP.
- Faculty members and companies should have a common vision and plan. The communication between faculty members and companies seems insufficient.
- Ankara is the most common city among students having their IEP outside of Konya. It is thought that the reason is being one of the largest cities of Turkey while it is very close to Konya.
- There is no calculated cost of the application. A financial and time cost calculation should be done for the university, for the private sector and for the students.

ACKNOWLEDGMENT

Authors acknowledge the cooperation of Selcuk University

Technology Faculty for their knowledge on Intern Engineering application. Ilhan Seyfi Turker, in particular, should be mentioned here.

REFERENCES

- [1] F. Unsacar, S. Alan, and E. Canli, "Selcuk University Technology Faculty Example as a Model Proposal for Institutionalizing University Industry Cooperation", T.C. Bilim Sanayi ve Teknoloji Bakanlığı 3. Sanayi Şurası Tebliği, 216-227, Ankara, Turkey (2013) (in Turkish)
- [2] D. Gunay, "Configuration of Technology Faculties (Teknoloji Fakültelerinin Yapılandırılması)", Ankara, (2010) (in Turkish)
- [3] S. Alan, E. Canli, and F. Unsacar, Selcuk University Technology Faculty Applications of University Industry Cooperation (Selcuk Üniversitesi Teknoloji Fakültesi Üniversite Sanayi İşbirliği Uygulamaları)," 8. Üniversite Sanayi İşbirliği Kongresi 9 - 10 June (2015)
- [4] E. Canli and A. Ates, "A test and illustration chamber for renewables: design and application," 2nd International Energy & Engineering Conference, pp. 719-727, 12-13 October 2017, Gaziantep, Turkey
- [5] E. Canli, "A field setup of demonstration for renewable energy generation systems," Uluslararası Yeşil Başkentler Kongresi, pp. 965-982, 8-11 May 2018 / Konya, Turkey
- [6] M.N. Dikmen and H. Baysal, "Research on faculty of technology of workplace training model in the scope of university-industry cooperation," *International Journal of Sustainable Engineering and Technology*, vol. 1, no. 1, pp. 35-46, (2017).
- [7] <http://tf.selcuk.edu.tr/index.php?lang=tr&birim=033&page=1393>

VARIATION OF FRACTURE TOUGHNESS OF RESISTANCE ON SPOT WELDED SHEET STEELS WITH HARDNESS

İ. SEVİM¹, M. E. TOLU²

Karamanoglu Mehmetbey University, Faculty of Engineering, Department of Mechanical Engineering, Karaman, Turkey

¹isevim@kmu.edu.tr, ²metolu@kmu.edu.tr

Abstract - In order to estimate the fatigue life of resistance on a spot welded joint one needs to know fracture toughness, strain energy release rate, and critical crack length. The weld bead of a welded pair has been investigated under tensile-shear condition to impose a welding zone shear stress. Both the fracture toughness and the strain energy release rate depend on the shear stress.

In this study, we investigated the variation of fracture toughness, strain energy release rate and crack length with the hardness of the spot welding bead. We used the tensile-shear force obtained from the data for Mod II fracture to determine the variations in fracture toughness and the stain energy release rate with hardness of the welding zone for Mod I fracture. The fracture toughness and stain energy release rate for spot welded steel sheets are calculated by using the formula given in literature. The results are compared with the literature.

The results show that the fracture toughness, KIIC and strain energy release rate GIIC, decrease as the hardness, H, increases, the critical crack length aIIC increases to critical value of fracture toughness, and the stress intensity factors KI, KII, can be estimated for spot-welded joints, for any one of the modes I or II.

Keywords – Resistance spot welding, fracture toughness, strain energy release rate, Vickers Hardness, critical crack length.

I. INTRODUCTION

Resistance spot welding is widely used in joining metal sheets. This technique is commonly used in the automotive industry and for the manufacturing of house appliances because of its high efficiency in manufacturing components made from thin steel sheets. A wide variety of metal sheets of up to 3 mm thickness can be handled by the resistance spot welding method.

Resistance spot welded materials may be exposed to different forces. Factors such as shear stress at the weld zone, sheet thickness, multi-spot welding and the width of the welding zone are important parameters that affect the fatigue life. The fatigue life for resistance spot welding is often expressed in terms of the stress density, or fracture toughness. These quantities are used to predict the fatigue life of resistance spot welded components. In order to determine the fracture parameters, such as, the notch stress on spot welded joints, fracture toughness, and potential energy discharge rate, fracture mechanics can be employed. In his review on spot welding Davidson [1] quotes work on stress density performed by Kan [2], and Wilson and Fine [3]. Kan [2], used the finite

element method to obtain the stress density at the elastic-plastic stress zone under the influence of variable shear loads. Wilson and Fine [3] defined the stress density around the spot weld by relating the stress density to the fatigue of the smooth sheet welded samples using in Neuber analysis. Darwish et al. [4], investigated the variation of welding current, electrode force, and weld application time with failure rate. Chang et al. [5], investigated the hardness of the metal, heat affected zone, weld metal and the adhesive layer for lap joint welding. For resistance spot welded joints, the linear fracture mechanical approach is used [6]. In fracture mechanics, the fracture toughness at the tip of a sharp crack is expressed through fracture toughness.

The focus of this study is to investigate the variation of fracture toughness, strain energy release rate and crack length with the hardness of the spot welding bead.

In this paper, we first discuss fracture mechanics briefly. The next section, describe the experimental work. Then the experimental data are applied and discussed in Section 4. The last section is devoted to the conclusions.

II. FRACTURE MECHANICS APPROACH

The fracture of a material is studied in terms of three different modes [7]. These are opening mode, K_I , sliding mode, K_{II} , and tearing mode, K_{III} , (Fig. 1) where K_I , K_{II} , K_{III} are fracture toughness for the opening, sliding and tearing modes, respectively. The fracture toughness, K_{IIC} , of spot welded joints is related to these three modes. The computational burden is high, especially for the tearing mode.

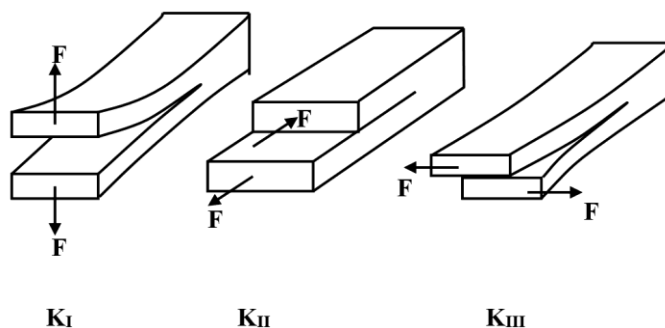


Figure 1: The three modes of fracture: KI, opening mode; KII, sliding mode; KIII, tearing mode [4].

Little work has been done in establishing stress-intensity expressions for spot-welded sheets. The most widely used method was recommended by Pook [8]. He developed the following fracture toughness equations for spot welding using the equations for elliptical relations given below [9, 10]:

$$K_I = \tau \cdot \left(\pi \cdot \frac{D}{2} \right)^{1/2} \cdot \left(0.605 \left(\frac{D}{t} \right)^{0.397} \right) \quad (1)$$

$$K_{II} = \tau \cdot \left(\pi \cdot \frac{D}{2} \right)^{1/2} \cdot \left(0.5 + 0.287 \left(\frac{D}{t} \right)^{0.710} \right) \quad (2)$$

where τ is the shear stress, D is the weld bead diameter, and t is the sheet thickness.

For resistance spot welded joints, the strain energy release rates, G_I and G_{II} for Mode I and Mode II are given by the following equations [11]:

$$G_I = \frac{K_I^2 (1 - \nu^2)}{E} \quad (3)$$

$$G_{II} = \frac{K_{II}^2 (1 - \nu^2)}{E} \quad (4)$$

where ν is Poisson's ratio which is approximately 0.3, and E is the Young's modulus.

III. EXPERIMENTAL WORK

Resistance spot welded joints may be exposed to stress under shear conditions. The experiments were designed to determine for Mod II fracture, the relationships of the fracture toughness, K_{IIc} , the strain energy release rate, G_{IIc} , and the computed crack length, a , with the hardness, H , of the welding zone.

Furthermore, we used the data for rupture force of Mode II to determine the fracture toughness, K_{IIc} , and the strain energy release rate, G_{IIc} , for Mode I. The graphs for K_{IIc} , and G_{IIc} are generated accordingly. The results are compared with those given in the literature.

A. Materials

Grades 1010, 1030, 1040, 1050 and 50CrV4 in the form of steel sheet of 3 mm thickness were used in the experiments. The chemical properties of these steels are listed in Table 1.

Table 1: The chemical compositions of the steel used in the (wt. %)

Alloys	C	Si	Mn	P	S	Cr	Mo	Ni	Al	Cu	Ti	V
	(%)	(%)	(%)	(%)	(%)	(%)	(%)	(%)	(%)	(%)	(%)	(%)
1010	0.107	0.11	0.413	0.019	0.025		0.003		0.032	0.031	0.002	
1030	0.328	0.069	0.673	0.015	0.019		0.001			0.037	0.002	0.005
1040	0.402	0.247	0.82	0.012	0.028	0.025	0.001	0.003	0.014	0.032	0.001	0.003
1050	0.506	0.252	0.654	0.014	0.006	0.251	0.002		0.006	0.017	0.002	0.006
50CrV4	0.523	0.394	0.915	0.021	0.027	0.917	0.025	0.034		0.183		0.095

B. Shape and Dimensions of a Weld-Bonded Lap Joint

Resistance spot welding was carried out on 3 mm thick 1010, 1030, 1040, 1050 and 50CrV4 steel sheets. The dimensions of the metal sheets and the position of the spot weld are shown in Figure 2 (DIN 50124 DVS 29.2). These dimensions were selected to minimize the edge effects and produce fracture in the weld zone under tensile-shear conditions [11, 12].

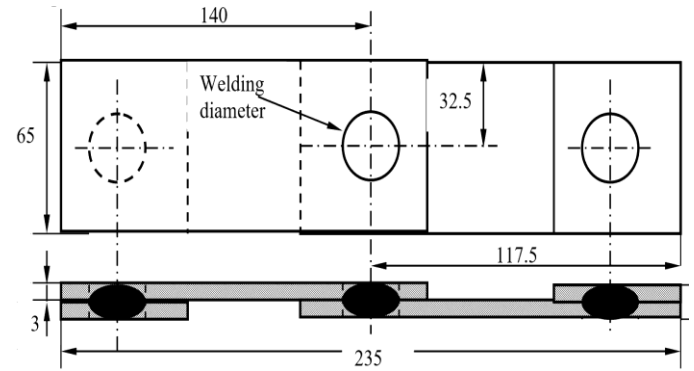


Figure 2: The spot welded sample prepared for testing under Mode II fracture

C. Spot-Welding Machine

A 180-kV spot welding machine was used in the experiment. The electrodes are made of a copper alloy with a spherical tip of 16 mm diameter. The electrode for resistance spot welding machine was loaded with a constant 7500 N force in the same direction of the electrode. Welding currents were measured to be 13 kA and 18 kA. The welding process was performed for 30 welding cycles. The spot diameter changed in the range 8-13 mm due to changes in the welding current and the properties of the material.

D. Instron Testing Machine

The resistance spot welded parts were tested to determine the tensile strength of the joint, as shown in Figure 3. The tensile strength was calculated from the maximum rupture force value read on the testing machine scale. During the tensile experiments, a constant cross-head speed of 7 mm per minute was used. The weld bead chemical compositions are given in Table 2.

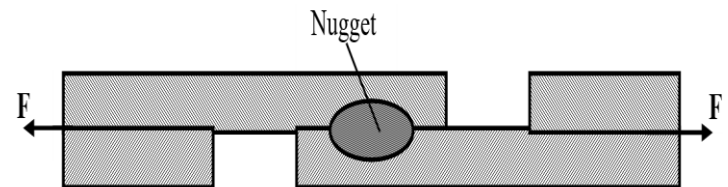


Figure 3: The tensile-shear force loading of electrical resistance spot welded samples

Table 2: The chemical compositions of the weld beads (wt. %)

Alloys	C (%)	Si (%)	Mn (%)	P (%)	S (%)	Cr (%)	Mo (%)	Ni (%)	Al (%)	Cu (%)	Ti (%)	V (%)
50CrV4-1010	0.315	0.252	0.665	0.020	0.026	0.458	0.014	0.017	0.016	0.10	0.001	0.05
50CrV4-1030	0.425	0.231	0.794	0.018	0.023	0.458	0.013	0.017		0.11	0.001	0.05
50CrV4-1040	0.463	0.321	0.868	0.017	0.028	0.471	0.013	0.019	0.007	0.108	0.004	0.049
50CrV4-1050	0.514	0.323	0.784	0.018	0.017	0.584	0.014	0.017	0.003	0.1	0.001	0.050

E. The Calculation Fracture Toughness for Welded Parts

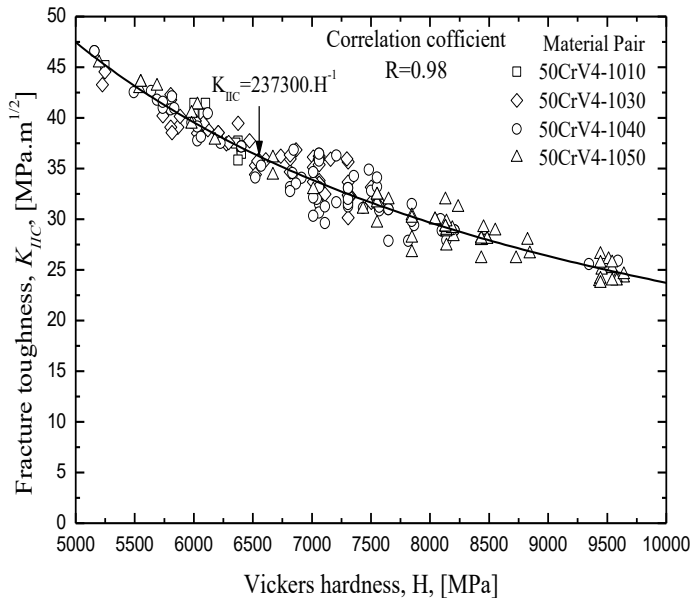
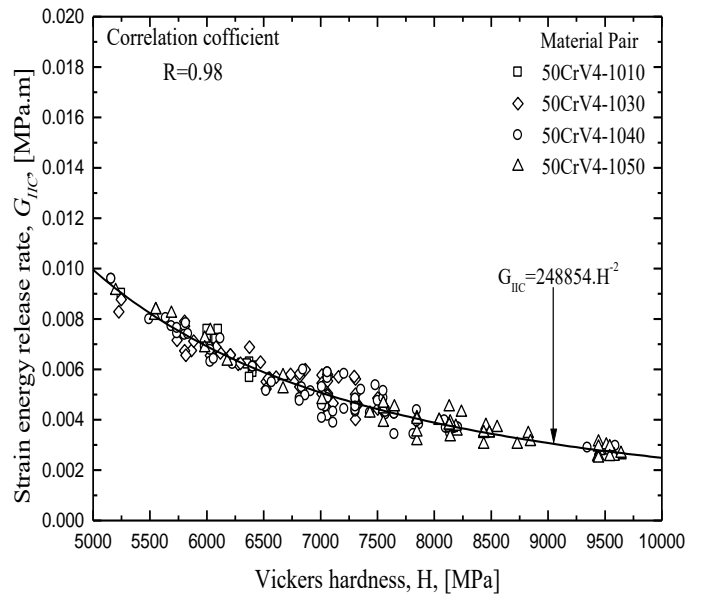
The rupture force for the welded parts was determined from the data from the tensile force experiment. The weld bead diameters were measured from the weld zones of the ruptured parts. The diameters were measured three times and the arithmetical mean of these three measurements is taken as the weld bead diameter. For the case in Figure 3, equations (2) and (4) were used to calculate the fracture toughness, K_{IIc} and the strain energy release rate, G_{IIc} according to Mode II fracture.

F. Hardness Analysis of the Weld Bead

The weld zones were polished using abrasive papers of 80-1200 mesh, and then 0.3 mm diamond paste. The Vickers hardness of the surface was measured at 0.5 mm interval under a load of 10 kg (98.0665 N). The standard deviations and arithmetic means of the measured data were computed, and the results were combined to obtain hardness values for the ruptured samples.

IV. RESULTS AND DISCUSSION

The fracture toughness, K_{IIc} , value and strain energy release rate, G_{IIc} , were computed for spot welded sheets applying the equations (2) and (4) respectively. The variation of K_{IIc} and G_{IIc} with the Vickers hardness (HV) is given in Fig. 4 and 5.

Figure 4: Fracture toughness, K_{IIc} , versus Vickers hardness, H Figure 5: Strain energy release rate, G_{IIc} versus Vickers hardness, H

In this work, the relation between the fracture toughness, K_{IIc} , strain energy release rate, G_{IIc} , for welded pair and the hardness, H , is found to be;

$$K_{IIc} = 237300 H^{-1} \quad (5)$$

$$G_{IIc} = 248845 H^{-2} \quad (6)$$

where K_{IIc} is fracture toughness for Mod II ($\text{MPa m}^{1/2}$) and H is Vickers hardness (MPa).

The effect of cracks can be expressed by the inequality;

$$K_{II} \geq K_{IIc} \quad (7)$$

Equation for K_{II} can be written as;

$$K_{II} = \tau \sqrt{\pi a_{IIc}} \quad (8)$$

where τ , is the applied shear stress, a_{IIc} the critical crack length?

Due to fracture, the plastic deformation can be expressed as;

$$\tau \cong \tau_{yield} \quad (9)$$

The shear yield stress, τ_{yield} (MPa), can be expressed in terms of the Vickers hardness, H (MPa), as [13];

$$\tau_{yield} \cong H / 10. \quad (10)$$

By substituting the equations (9) and (10) into equation (8), the relation between K_{II} and H is obtained as;

$$K_{II} = (H / 10) \sqrt{\pi a_{IIc}} \quad (11)$$

Substituting from (5) and (11) in (7), the effect of fracture can be expressed as;

$$H \sqrt{\pi a_{IIc}} \geq 237300 H^{-1} \quad (12)$$

Rearranging (12), the critical crack length, a_{IIc} , can be expressed as;

$$a_{IIc} \geq \frac{1}{\pi} \left(\frac{2373000}{H^2} \right)^2 \quad (13)$$

Figures 6 and 7 respectively show the variation of fracture toughness, K_{IIc} , and the potential energy discharge rate, G_{IIc} , of the spot welded pair, with the computed crack length a_{IIc} . The computed crack length a_{IIc} , increases with both K_{IIc} and G_{IIc} .

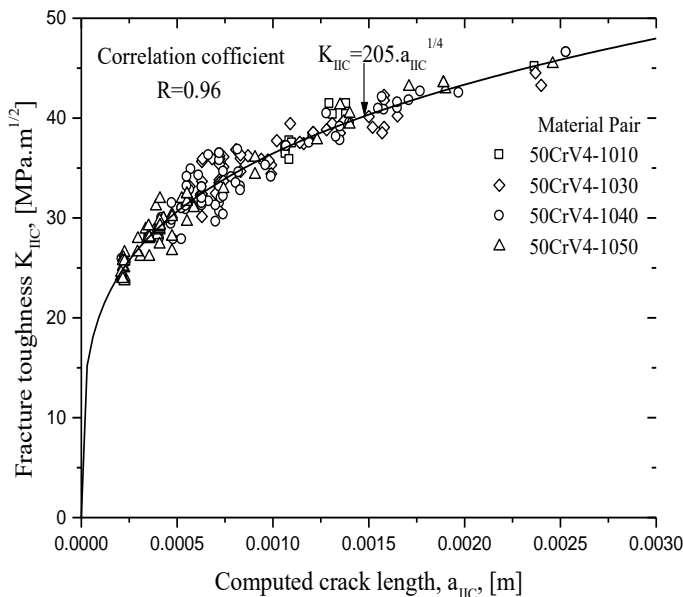


Figure 6: Fracture toughness, K_{IIc} versus computed crack length, a_{IIc}

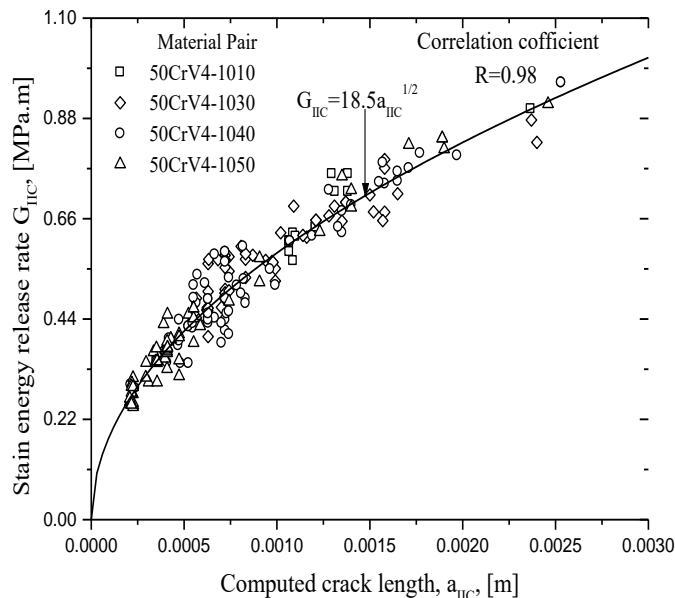


Figure 7: Computed crack length a_{IIc} versus strain energy release rate G_{IIc}

The all solid lines in Figure 4-9 are obtained from the least squares method [14]. The correlation coefficients for each graph are shown in Figure 4-9. Figure 4 shows that the fracture toughness is inversely proportional with hardness for spot welds. The variables that affect the microstructure of the

welding zone are welding current, the cycle of the current, holding time, the chemical composition of the steel sheets, and the cooling rate of the weld zone. Different microstructures occur depending on these parameters. In the resistance spot weld zone, the material gains the features of a cast metal due to melting at the welding zone. The fracture toughness of the spot welding structure depends on the cast structure of the welding zone. For a brittle and hard spot welded structure, even a small crack is sufficient to initiate fast fracture (Fig. 6). From Figure 4, for a high carbon percentage in the welded material, the fracture toughness, K_{IIc} , decreases and the hardness, H , increases so that the crack length a_{IIc} , becomes very small. Inclusions, incoherent particles and grain boundaries are probable crack initiation sites. They could also aid crack propagation and eventually lead to failure in spot welded joints. Zum Gahr [15] shows that the fracture toughness decreases while the hardness increases. Radaj [16] using Pook's [8] equation, showed that the following equations are valid for spot-welded joints of steels under shear-tensile stress;

$$\left(\frac{K_I}{K_{II}} \right) = 0.82 \quad (14)$$

In this study we found these ratios using equation (1), and (2) to be better since they are in good agreement with those of Radaj [16].

$$\left(\frac{K_I}{K_{II}} \right) = 0.831 \quad (15)$$

The correlation coefficient for that calculation is $R=0.98$ (see Fig.8). Therefore, any stress intensity factor for a given mode can be easily computed by using equations (15) provided that the stress intensity factor is valid for a specific mode. For example, if K_I is known, then it is a simple matter to compute K_{II} .

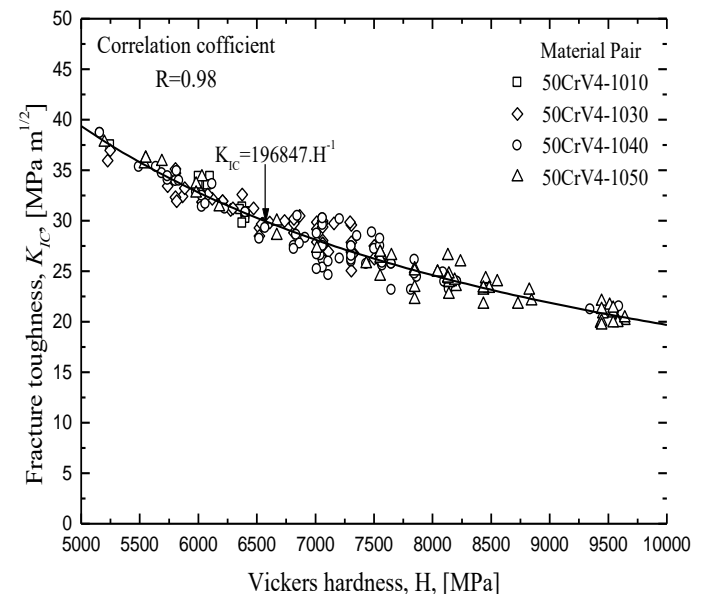


Figure 8: Fracture toughness, K_{IIc} , versus Vickers hardness, H

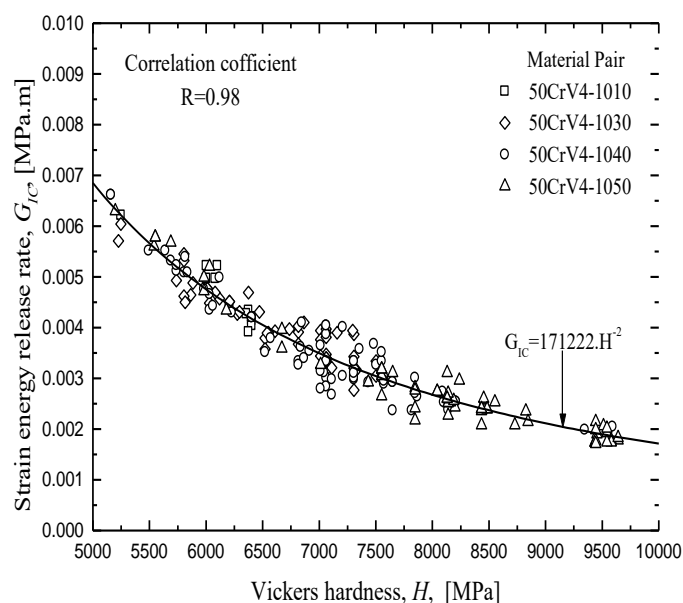


Figure 9: Strain energy release rate, G_{IC} , versus Vickers hardness H

V. CONCLUSION

The following results have been obtained for spot weld joints made of sheet samples when the experimental data are applied as in Fig. 2:

- The fracture toughness, K_{IIC} , and strain energy release rate, G_{IIC} , decrease as the hardness, H , increases. The decrease is proportional to H^{-1} and H^{-2} for fracture toughness values and strain energy release rate, respectively.

- The hardness at the welding zone is higher than that of unaffected areas, which is probably due to the microstructure being altered during welding.

- The critical crack length a_{IIC} , decreases as the hardness H , increases. a_{IIC} is the critical crack length that corresponds to critical value of fracture toughness. The increase in critical crack length is proportional to the square of strain energy release rate.

- To estimate the stress intensity factors K_I , K_{II} , for spot-welded joints, for any one of the modes I or II , at least one of them has to be obtained experimentally.

- The fracture toughness of spot weld is not only dependent on the nugget diameter D , but it also depends on sheet thickness t , tensile rupture force and the hardness H .

ACKNOWLEDGEMENT

The authors thank the Faculty of Mechanical Engineering, Istanbul Technical University for allowing them to use the Tool and Die Laboratory, the Engineering Workshop and Materials Testing Laboratory.

REFERENCES

- [1] J. A. Davidson, "A Review of the fatigue properties of spot welded sheet steels", *SAE Transactions*, vol. 92, pp. 35-47, 1983.
- [2] Y. R. Kan, "Fatigue resistance of spot welds- An analytical study", *Metals Engineering*, pp. 26-36, November, 1976.
- [3] R. B. Wilson, T. E. Fine, "Fatigue behavior of spot welded high strength steel joints", *SAE Transactions*, pp. 810354, 1981.
- [4] S. M. Darwish, M. S. Soliman, A. M. Al-Fahead, "Manufacturing and characteristics of brass damping sheets", *Journal of Materials Processing Technology*, vol. 79, pp 66-71, 1998.
- [5] B. Chang, Y. Shi, L. Lu, "Studies on the stress distribution and fatigue behavior of weld-bonded lap shear joints", *Journal of Materials Processing Technology*, vol. 108, pp. 307-313, 2001.
- [6] P.C. Paris, F. Erdoğan, "A critical analysis of crack propagation laws", *Journal of Basic Engineering*, vol. 85, pp. 528-533, 1963.
- [7] B. Lawn, "Fracture of brittle solids", *Cambridge University Press*, Second Edition, 1993.
- [8] L. P. Pook, "Fracture mechanics analysis of the fatigue behaviour of spot welds", *International Journal of Fracture*, vol.11, pp.173-176, 1975.
- [9] P. C. Paris, G. C. Sih, "Stress analysis of cracks", *Symposium On Fracture Toughness Testing and Its Applications*, ASTM STP 381, pp. 30-83, 1965.
- [10] M. K. Kassir, G. C. Sih, "External elliptical crack in elastic solid", *International Journal of Fracture Mechanics*, vol.4, pp.347-356, 1968.
- [11] I. Sevim, "Effect of abrasive particle size on wear resistance for abrasive wear of steels", Ph.D. Thesis, I.T.U., Graduate Institute of Science, ISTANBUL, 1998.
- [12] B. I. Eryurek, "Study of contact resistance at electrical resistance spot weld", Ph.D. Thesis, I.T.U., Faculty of Mechanical Engineering, Istanbul, 1976.
- [13] J. B. Cahoon, W. H. Broughton, A.R. Kutzak, "The determination of yield strength from hardness measurements", *Metallurgical Transactions*, vol. 2, pp. 1979-1983, 1971.
- [14] B. A. Köksal, *İstatistik-Analiz Metodları*, Çağlayan Kitabevi, ISTANBUL, 1995.
- [15] K. H. Zum Gahr, "Microstructure and wear of materials", *Elsevier*, vol. 10, 1987.
- [16] D. Radaj, "Strength assesment for spot-welded joints on the local stresses", *Schweissen & Schneiden*, Weld Cut, 1, 10-14.

Effect of Red Mud as a Nanofluid on Cooling Performance

A.A. SERTKAYA¹ and E. CANLI²

¹Selcuk University, Konya/Turkey, asertkaya@selcuk.edu.tr

²Selcuk University, Konya/Turkey, ecanli@selcuk.edu.tr

Abstract – Fluids such as water, oil, glycerin and ethylene glycol are conventional heat transfer fluids that are used in heat exchangers. Improving heat transfer and effectiveness of heat exchangers by means of fluids is one of the principle topics. A type of improvement works is adding solid materials that have high thermal capacity and conductivity into the fluid. Al_2O_3 , CuO , TiO_2 , SiC , TiC , Ag , Au_2 , Cu_2 and Fe are the most common materials as solid particles that are used for enhancing heat transfer of fluids. Early on, macro scaled additives were tried; however desired outcomes couldn't be obtained due to fouling, blockage and sedimentation. Recently, studies on ability to be enhanced and improved in terms of heat transfer and hence heat exchangers with high effectiveness by the addition of nano-particles to fluid have become intensive. It is known that precious elements such as Al_2O_3 , SiO_2 , Fe_2O_3 , TiO_2 , Na_2O , CaO , P_2O_5 are contained in the body of red mud that is a disposal material coming from the process of producing aluminum from bauxite. Thermal capacity and thermal conductivity of these matters are very high. Effects of nano scale red mud added into heat transfer fluid on the cooling performance are investigated in this work.

Keywords - Enhancement, Heat exchanger, Heat transfer, Nano fluid, Red mud

I. INTRODUCTION

Energy need constantly increases depending on the increasing population and advancing technology in our day. In return, limited energy sources, restrictions that are brought by environmental problems in energy supply and usage makes more efficient utilization of energy sources alongside with searching new sources indispensable. The most important topic in transferring heat energy from a medium to another one is realizing heat transfer by consuming the least possible power and in the least possible time; in other words, by the most efficient way. One of the most important elements about energy and heat transfer in most of the industrial practices is heat exchangers. Among the important parameters of heat exchangers that affect heat transfer performance and energy efficiency of heat exchangers, on the other hand, the thermal conductivity of the heat transfer fluid is very essential. Thermal performances of fluids such as water, mineral oils and ethylene glycol that are commonly used in heat exchangers currently are limited. Changes are observed in properties of fluids such as thermal conductivity, viscosity by adding solid metal particles and various matters which have higher thermal capacity than the fluid in order to increase the thermal conductivity capacity of the fluid. Struggles for improving heat

transfer properties of the fluids by adding solid particles into the fluids are a method that was previously tried. However, desired results cannot be acquired due to reasons such as sedimentation of the particles, wearing of the system components and pressure drop while big scale solid particles improves thermal properties only by slightly with only by high volumetric rates. By the advancement of the technology, studies for enhancing and improving thermal properties of the heat transfer fluids are reconsidered and are continuing with an increasing trend by the realization of the production at nano scale. Constituting a suspension mixture by adding particles at nano scales to the conventional fluids is called nanofluids. Solid metal particles that have high thermal conductivity and that are most commonly used are defined as; copper, aluminum, silver, gold and iron while alloys are; aluminum oxide (Al_2O_3), copper oxide (CuO), TiO_2 , ZnO , SiO_2 . Enhancing thermal conductivity of nanofluids is depending on sizes of nano particles and rates of nano-particles. Some of the studies on nanofluids are given in [1,2] and below.

Saidur et al. have compiled and reviewed a comprehensive literature on the applications and challenges of nanofluids [3]. Specific applications of nanofluids in engine cooling, solar water heating, cooling of electronics, cooling of transformer oil, improving diesel generator efficiency, cooling of heat exchanging devices, improving heat transfer efficiency of chillers, domestic refrigerator-freezers, cooling in machining, in nuclear reactors, defense and space have been reviewed and presented by them [3]. Akbarinia et al. investigated forced convection Al_2O_3 - water nanofluid flowing in two-dimensional rectangular micro-channels for heat transfer enhancement by addition of the nano-particles to the base fluid at low Reynolds number [4]. It is said that constant Reynolds number studies of nanofluids are not an adequate approach to evaluate the heat transfer and the skin friction factor for the nanofluids they used [4]. Liu and Li have reviewed and summarized the research done on heat pipes using nanofluids as working fluids, recently. The effect of characteristics and mass concentrations of nano-particles on the thermal performance in various kinds of heat pipes with different base fluids under various operating conditions were explored. As a result, they show that nanofluids have great application prospects in various heat pipes [5]. Mahian et al. investigated the nanofluids' applications in solar thermal engineering systems. It was found that the effects of nanofluids on the performance of solar collectors and solar water heaters are satisfactory from the efficiency, economic and environmental considerations

viewpoints by them [6]. Fang et al. investigated flow boiling heat transfer of nanofluids, with an emphasis on the heat transfer coefficient (HTC), critical heat flux (CHF), pressure drop, nanofluid stability, flow and heat transfer mechanism, and flow pattern and bubble dynamics. The important achievements, inconsistency, and contradictions of the existing research results are identified, and several topics worthy of attention for future investigations are identified [7]. Hemmat Esfe et al. researched an experimental study of Fe–water nanofluids to investigate the effective thermal conductivities and dynamic viscosity of water-based nanofluids containing Fe nano-particles [8]. Li et al. examined the thermal conductivity and viscosity of ethylene glycol based ZnO nanofluids. They find out that thermal conductivity increased slightly by the increasing temperature from 15 to 55 °C and it is dependent strongly on particle concentration and increased nonlinearly with the concentration within the range studied. Moreover, they found that viscosity increased with concentration as usual for ZnO nano-particles and decreased with temperature [9]. Shafahi et al. investigated the thermal performance of a cylindrical heat pipe utilizing nanofluids with using the most common nano-particles (Al_2O_3 , CuO , and TiO). When using a nanofluid, they found a substantial change in the heat pipe thermal resistance, temperature distribution, and maximum capillary heat transfer of the heat pipe [10].

Red mud is a disposal material that comes during the Bayer process for producing alumina from bauxite. Approximately 40 to 45% ratios of the bauxite ore that is used for producing aluminum leave the process as red mud. The red mud obtained during the production of aluminum from bauxite as a by-product contains valuable materials such as Fe, Al, Na, V, Ti etc. Red mud can be utilized in limited fields such as chemical industry, construction business and obtaining some elements inside it. But recycling has a high cost [11].

II. EXPERIMENTAL SETUP

A radiator of 4 cylinder vehicle engine was utilized as the heat exchanger in the experimental work. A big portion of the heat generated by the engine in vehicles is transferred to air by means of natural or forced convection through radiator. Normally, the fluid that is circulated between the engine body and the radiator elements by means of a pump transfers the heat to the ambient by natural convection from the outside of the radiator when the engine is in stationary position. However, a fan is used for increasing heat transfer rate for the circumstances where natural convection is insufficient. The heat carrying capacity of the fluid here is an important factor. Generally a mix of distilled water and antifreeze solution is used as engine cooling liquid in vehicles. In this work, red mud is added to the distilled water with the rates of 3, 6 and 9% wt. in order to increase the thermal convection coefficient of the fluid. Before red mud-water mixture was poured into the system, it was put into reaction with Triton X 100 (about 0.3 wt.%) which is a surface activating matter. An ultrasonic vibrator generating ultrasonic pulses of 200 W and 36 kHz was used for dispersing a specified amount of red mud nano-particles in distilled water. The nanofluids were kept under ultrasonic vibrator continuously for 12 h. Tests were repeated

first using distilled water only and then using the mixture of distilled water and red mud with previously mentioned ratios. Temperatures that were measured from different locations are recorded by means of a data logger. The schematic cooling system of the engine in the experimental setup is given in Figure 1.

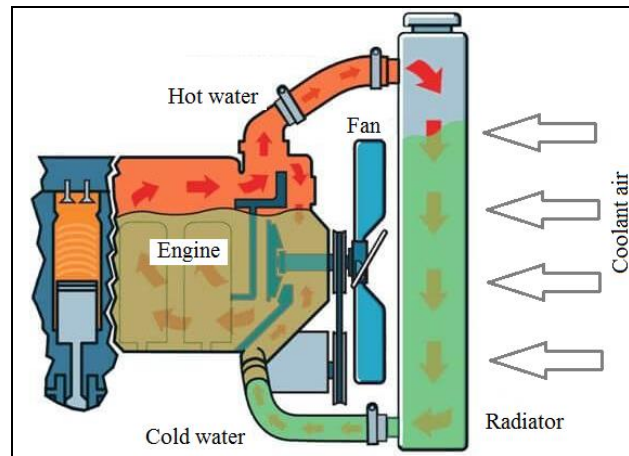


Fig. 1 Schematic motor cooling system

Precious elements such as Al_2O_3 , SiO_2 , Fe_2O_3 , TiO_2 , Na_2O , CaO , P_2O_5 are contained in the body of red mud as a disposal in the process of producing aluminum from bauxite. The chemical composition of the red mud that was used in the experiments is given in Table 1 while the dispersion of nano-particle sizes is given in Figure 2.

Table 1. Chemical composition of red mud

Component	%
Al_2O_3	19.61
Fe_2O_3	39.01
TiO_2	5.90
Na_2O	7.86
CaO	4.47
SiO_2	13.62
Al	8,43
Other	1,10

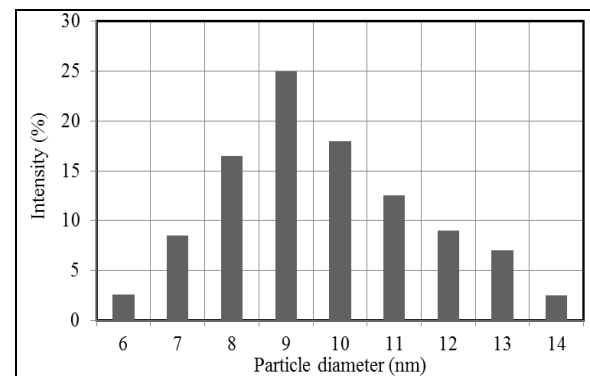


Fig. 2. Size distribution of the nano-particles

The grain size of red mud was mostly (>90%) less than 12 nm. The red mud-water mixture is showed in Figure 3.

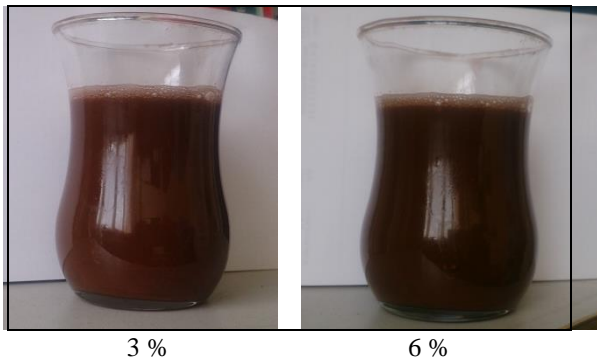


Fig. 3 Red mud-water mixture with 3% and 6% concentration

III. THEORETICAL ANALYSIS

Heat load of hot fluid (\dot{Q}_h) is calculated by the following formula.

$$\dot{Q}_h = \dot{m}_h c_{p,h} (T_{h,in} - T_{h,out}) \quad (1)$$

Where \dot{m}_h is the mass flow of hot fluid, $c_{p,h}$ is the specific heat of hot fluid, $T_{h,in}$ is the inlet temperature of hot fluid and $T_{h,out}$ is the outlet temperature of hot fluid.

Transferred heat from the hot fluid to cold fluid in the radiator;

$$\dot{Q}_c = \dot{m}_c c_{p,c} (T_{c,out} - T_{c,in}) \quad (2)$$

is calculated with the formula. Where \dot{m}_c is the mass flow rate of cold fluid, $c_{p,c}$ is the specific heat of cold fluid, $T_{c,out}$ is the outlet temperature of cold fluid and $T_{c,in}$ is the input temperature of cold fluid.

Taken heat from radiator is equal to given heat to the environment.

$$\dot{Q}_h = \dot{Q}_c \quad (3)$$

Heat transferred from radiator to environment can be given as follows;

$$\dot{Q} = hA\Delta T_{lm} \quad (4)$$

Where h is the convective heat transfer coefficient between the fluid and the radiator, A is the area of the heat transfer of radiator.

As seen in Eq.4, ΔT_{lm} is the logarithmic mean temperature difference between the environment and the surface radiator.

$$\Delta T_{lm} = \frac{\Delta T_{in} - \Delta T_{out}}{\ln\left(\frac{\Delta T_{in}}{\Delta T_{out}}\right)} \quad (5)$$

IV. RESULTS AND DISCUSSION

The difference between inlet and outlet temperatures of the radiator that was used as heat exchanger in the experimental setup gives idea about the cooling performance of the fluid. The temperatures of the radiators should be in control and regulated. This is done by thermostats. The thermostat in the experimental setup turns on the fan at 93°C and turns off the fan at 84°C. Natural convection is at stake between 84°C and 93°C when temperature is rising. Forced convection is applied between 93°C and 84°C when temperature is decreasing. Figure 4 is given in order to show in how much time a test fluid lowers the radiator temperature from 93°C to 84°C. This means that, a coolant trend with the shortest time in the figure has a better cooling performance.

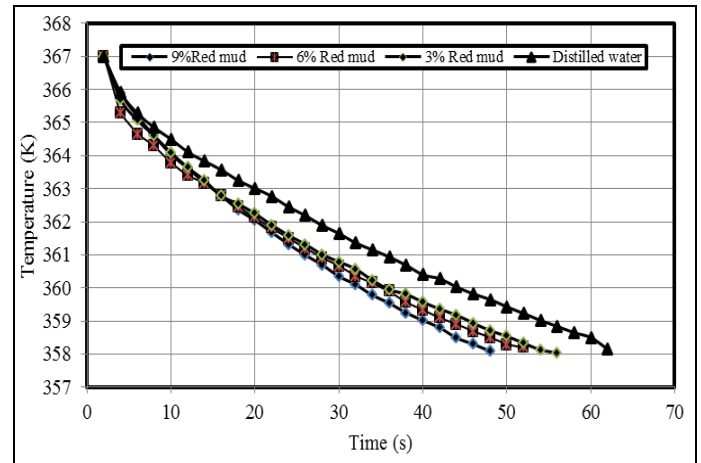


Fig.4 Temperature-Time change

The heat transfer capacity of the coolant fluid is higher for shorter times passing for reaching minimum temperature. The cooling period can be shortened about 14 seconds by using 9% wt. red mud in the distilled water. The percentage of the red mud in the distilled water seems directly proportional with the shortened time.

Four different coolants are used in this work. They are distilled water and distilled water-red mud mixtures with 3, 6 and 9% wt. ratios. Following conclusions are drawn:

- Heat transfer is enhanced by means of red mud-distilled water mixtures in every tested condition comparing to the distilled water only test.
- The reduction in time for the closure of the fan by thermostat is 10% for 3% wt. red mud; 16% for 6% wt. red mud; and 24% for 9% wt. red mud.
- The abundance of (Fe_2O_3) that has a high intensity in the red mud makes sedimentation faster. It is observed that nano particles in the red mud settled down after about 5 days.
- On the other hand, it was observed that red mud forms resident residues on the surfaces.

As a general conclusion, it is detected that red mud increases thermal conductivity and found as a positive factor in respect of heat transfer. However, the sedimentation in relatively short periods and the residues on the surfaces due to the red mud are

the disadvantages. Additionally, the load on the circulation pump, imposed by the existence of the red mud, should be investigated theoretically and experimentally in the future.

REFERENCES

- [1] A. Ghadimi, R. Saidur, H.S.C. Metselaar, "A review of nanofluid stability properties and characterization in stationary conditions", *International Journal of Heat and Mass Transfer*, vol.54, pp. 4051–4068, 2011.
- [2] K.H. Solangi, S.N. Kazi, M.R. Luhur, A. Badarudin, A. Amiri, Rad Sadri, M.N.M. Zubir, S. Gharehkhani, K.H. Teng, "A comprehensive review of thermo-physical properties and convective heat transfer to nanofluids", *Energy*, vol.89, pp. 1065-1086, 2011.
- [3] R.Saidur, K.Y.Leong, H.A. Mohammad, "A review on applications and challenges of nanofluids", *Renewable and Sustainable Energy Reviews*, vol. 15, pp. 1646–1668, 2011.
- [4] A. Akbarinia, M. Abdolzadeh, R. Laur, "Critical investigation of heat transfer enhancement using nanofluids in microchannels with slip and non-slip flow regimes", *Applied Thermal Engineering*, vol. 31, pp. 556-565, 2011.
- [5] Z.-H. Liu, Y.-Y. Li, "A new frontier of nanofluid research – Application of nanofluids in heat pipes", *International Journal of Heat and Mass Transfer*, vol. 55, pp. 6786–6797, 2012.
- [6] O. Mahian, A. Kianifar, S.A. Kalogirou, I. Pop, S. Wongwises, "A review of the applications of nanofluids in solar energy", *International Journal of Heat and Mass Transfer*, vol. 57, pp. 582–594, 2013.
- [7] X. Fang, R. Wang, W. Chen, H. Zhang, C. Ma, "A review of flow boiling heat transfer of nanofluids", *Applied Thermal Engineering*, vol. 91, pp. 1003-1017, 2015.
- [8] M.H. Esfe, S. Saedodin, S. Wongwises, D. Toghraie, "An experimental study on the effect of diameter on thermal conductivity and dynamic viscosity of Fe/water nanofluids", *J Therm Anal Calorim*, vol. 119, pp. 1817–1824, 2015.
- [9] H. Li, L. Wang, Y. He, Y. Hu, J. Zhu, B. Jiang, "Experimental investigation of thermal conductivity and viscosity of ethylene glycol based ZnO nanofluids", *Applied Thermal Engineering*, vol. 88, pp. 363-368, 2015.
- [10] M. Shafahi, V. Bianco, K. Vafai, O. Manca, "An investigation of the thermal performance of cylindrical heat pipes using nanofluids", *International Journal of Heat and Mass Transfer*, vol. 53, pp. 376–383, 2010.
- [11] Y. Çengelöglu, "Kırmızı Çamurun Değerlendirilmesi (Utilizing Red Mud)" PhD Thesis, Selcuk University Natural and Applied Sciences Institute, Konya, Turkey, 1991. (in Turkish)

Criticism on Applied Training Reviews: Renewable Energy Field Case

E. CANLI¹ and S. ALAN²

¹Selcuk University, Konya/Turkey, ecanli@selcuk.edu.tr

²Selcuk University, Konya/Turkey, salan@selcuk.edu.tr

Abstract – The rapid advancement in technology weakens effectiveness of conventional technical education. New fields of earnings are emerging and there is a decreasing tendency towards technical departments. Skilled technical professionals are sought. A practical solution seems to be short trainings of existing professionals and recent graduates. A significant field that can exemplify the issue is the renewable energy (renewables) sector with its intrinsic characteristics. There is a struggle towards promoting renewable energy conversion systems. However it is a relatively new field and there is a need of skilled man power. Some researchers focused on the studies for training professionals and they try to assess various approaches and try to measure their impact. Because, there is diversity in training approaches and a common application is hard to be mentioned. In this report, some references from literature are reviewed while conceptual and principal criticisms are made for some of the methods and evaluations in terms of assessment of the effectiveness of applied training. In a general manner, selected quantities for grounding qualitative conclusions seem not adequate or sufficient. Most of the comments are based on subjective responses. Monitoring practical skills on applications is missing. Long term monitoring of new professionals haven't been encountered in the literature. Significant examples on applied training on a specific application are hard to find. Therefore, some propositions are made for better assessment of the applied training.

Keywords – Applied training, Assessment, Qualitative, Quantitative, Renewable Energy, Review.

I. INTRODUCTION

EDUCATION is one of the most common term in the world. It should not be argued that it has utmost importance, yet one cannot mention a single universal model. It is actively studied and it is continuing to change. Modern technology has a high impact on this change. New fields of education emerge frequently. Those new field requires new techniques, new tools, new approaches for education. Engineering vocation, on the other hand, is an old expertise though its format has been developing for about two centuries. It is a relatively difficult field. It is understood that less students tend to prefer engineering departments for undergraduate education. Starting from the mid 2000s, it is tried to lower class hours and homework in engineering education while adding classes out of the discipline, i.e. social contents. But this reduces the applied skills. For developing countries such as Turkey, applied skills are very important.

When it comes to applied education, it is sometimes referred as training because it involves human motor skills, sensation, muscles. Muscle memory is at stake for a huge part of it. Unlikely to the theoretical, applied training is a bodily experience. You can theoretically teach an engineer how to run a turning machine in manufacture field but operating that machine imposes vibration, noise, heat, etc. on the operator which cannot be experienced in the theoretical education. One cannot think for each step but do it almost automatically. It is more like driving a car. Developing countries involve and need skills that should be trained more. Therefore, applied training is still a serious topic to be studied.

Professionals in the industry need to keep up with technology and new applications. Lifelong learning and vocational retraining (in service training) are trending topics for awhile and nowadays. Authorities are trying to formulate some ways to aid industry in this manner. However it is hard to talk about a universally accepted practice. Different practices exist and they are continuously assessed in order to measure their impact.

Assessment of a training method can be done by two activities; (1) measuring student skills and (2) long term monitoring. These two activities have vital importance. Without them, resources would be wasted, which would lead to not only ineffective training but also long term negative effects. Training can sometimes be seen as an unnecessary procedure for obtaining a license by the students and when students pose a pressure on the system with their so called sense about being unnecessary of the procedure, measurement of the skills could become a nonfunctional thing on paper. Without long term monitoring, it would be very difficult to detect such error. It is feared that some fields of applied training in Turkey may have this trouble.

Renewable energy is relatively a new field, not only for Turkey, but also for the world. And skilled professionals are sought by the private sector. The departments in universities have been forming or emerging since mid 2000s. Hence it is a trending topic and it is easier to find assessment studies in literature about applied training on renewables.

In this paper, literature about applied training on renewables

is surveyed and some explanatory samples are mentioned below. It is aimed not only to speak about their content but also criticize some common points that appear a lot in the papers. Some propositions for better assessment of applied training studies are provided in the following section. It is hoped that this work is a preliminary step forward to a comprehensive evaluation on how to form a procedure for applied training, especially for engineering.

II. LITERATURE

There are four papers in this section and all of them are from Renewable Energy Journal [1]. This is a Scientific Citation Index (SCI) journal with 4.9 impact factor. The research topics of the journal, or scope in other words, are; Biomass Conversion, Photovoltaic Technology Conversion, Solar Thermal Applications, Wind Energy Technology, Desalination, Solar and Low Energy Architecture, Climatology and Meteorology, Geothermal Technology, Wave, Tide and Ocean Thermal Energies, Hydro Power, Hydrogen Production Technology and Fuel Cells, Socio-economic and Policy Issues. However, surveys on applied training for renewable energy are quite common in the journal. This can be related to the Socio-economic and Policy Issues topics.

The first paper is from 1999. It is the paper of Kandpal and Garg [2]. It is a relatively short paper on issues relating to the renewable energy education and proposed curricula for certificate and license level programs. Renewable energy is related with the development of developing countries. The current level of renewables, as it hasn't taken the place of primary sources, is attributed to lack of a structured framework for renewables education or energy education. Authors claimed that instruments and equipments for renewables exist however after-sale services such as maintenance, trouble shooting, and repair are insufficient due to the low number of skilled professionals. At this point, a reference is needed for numbers showing that how many failures have been dealt late due to lack of personnel. Because authors comments on lack of personnel can be an individual estimation or subjective presume. As it is more likely to find out that there is no reference for asked statistics, then various means can be used to report one. These means can be but not limited to; energy transparency platforms of governments; domestic energy providers that buys energy from individual providers; after-sale services and customer relations; complaint platforms on the internet. Authors suggest development of courses in industry and university mediums. Additionally, vocational retraining and promoting public awareness are emphasized. Authors mention about Industrial Training Institutes (ITI) and Diploma level Courses as a must for renewables. However, it is thought that theoretical principles of renewable energy conversion systems are very deep and wide. Graduates of a program cannot deal with the whole field. Instead, the idea of the present paper is to locate the applied training to a position after basic engineering curricula or license. While Kandpal and Garg list several point to be in the renewable education, almost all of them are related with management and awareness

issues. One can expect more technical content. Nevertheless, the last part of their paper stresses the technical skills. They also underlined the need for specialized text books. Their ITI level content consists of almost all renewables. However, present paper proposes programs specific to a single type of system. By this way, expert and professional skilled individuals can occur for a specific application. Their proposition for diploma level course curriculum is too general and is seen not proper to form a vocation other than a generally aware person on renewables.

The second work is from ten years later; in 2009. It is the paper of Jennings [3]. It is found more mature in content since ten years had passed. In general, author underlines two types of education; (1) technical training; and (2) promoting public awareness. And the author emphasizes distance/online learning as a key tool/element for both education types. Author also gives examples of experiences and responses in order to prove the idea about distance learning applications. However, this type of learning is more suitable for management and awareness issues. Practical skills cannot be trained or suffer the absence of the advantages of conventional applied training as it is stated by the author. The reason for studies on renewable energy education is proposed by the author as a sudden rush towards renewables. When the rush to commercial renewables equipment was realized, lack of professionals was surfaced. A part in the paper supports this proposition. It is said that government in Australia put 2% mandatory renewable energy utilization target which in turn yielded positions in companies for renewables. Another interesting fact that the author underlines is that professionals of common engineering fields are trained for harnessing sources and producing work while they were not thought almost anything about sustainability. For instance, a mechanical engineer can design a HVAC system with the lowest cost and highest effectiveness while ensuring that the HVAC system meets the thermal comfort demands. However he/she almost never puts constraints to the design due to environmental concerns or takes additional measures for sustainability of the system. Common engineering professions are aware of regulations but they see them as limits/conditions for their design. Therefore author suggest that additional education for raising awareness of engineers as a necessity. Another instance of engineers and their low perception on sustainability can be given as that engineers except a few ones are not aware of carbon emission market. They build renewables but most of them have no idea to sell the carbon emission quota that becomes available by the new renewable system to developed countries. An engineer might not have knowledge about particular market properties of a certain type of renewables. Characteristics of various firms and their technologies can be realized either by experience or additional education. About public awareness, author mention past negative experiences; disappointment of people after aggressive marketing and sales while there were absence of trained personnel for the after sale services in the field. As a solid proof, it is said that only two thirds of remote area power supply systems were operational due to bad after sale service, which can be attributed to lack of skilled

professionals. In order to cure negative public impression on renewables, which can be listed but not limited to; unreliable; easy to be broken; low power output; bad service; expensive; money trap; etc., author requests global and domestic education for all people. However, this seems as a wish rather than a solution proposition. Although above opinions of the author suggest an education very different from applied training, author stresses that renewables should be handled by skilled technical personnel who had training on a technical field previously and then received an applied training on renewables. Nevertheless, as a criticism, most of the paper highlights distance education and awareness issues rather than applied training. Applied training is mentioned as a must but its details do not exist in the paper. The parts relating to applied training evoke advertisements because they refer to certain institutes and contain very few details. Another thing to be criticized of the paper is the suggestion of the author that electrical engineers of yesterday are not needed but a new breed of engineering disciplines should be trained with a much wider content including social, economic and environmental issues. However modern world imposes multidisciplinary works including a lot of people who specialized in a narrow field with high knowledge. Broader range of information including very different fields is only necessary for management of a whole project and everyone is aware that very few people are involved for that kind of management. There is a very subjective conclusion in which author suggests that companies having a part of their investment dedicated towards educational tools for their personnel and customers are thrived. Author also suggests that companies which didn't do the same failed. This strong conclusion is not supported by any instance or number or a reference. The points given in the paper as needs for education are far too general to be used for an educational program. Nevertheless, author's suggestions about the re-training of existing engineers and technical persons for technical skills are in parallel with the opinions of the present paper. Short courses are highlighted such as distance learning. Short courses are important because it applies to almost any engineering field or technical skill. "Picture book" is given as an example, which shows the pictures of class activities to persons who cannot attend the class or who decided to take distance learning options. However, it is thought that practices such as picture book cannot fill the gap by the absence of applied training. Appropriate accreditation procedures for training are also underlined by the author.

The work of Karabulut et al. is published in 2011 [4]. They formed a questionnaire and claim that they highlight the renewable energy education in Turkey. However this claim seems too strong considering the content of the paper. It is rather a survey on limited institutes and people for mostly measuring awareness issues about renewables. There are some numbers indicating student numbers, instructor levels in academia, number of scientific researches and laboratories/workshops. However, drawing a conclusion from them about renewable education in Turkey is quite difficult. Authors suggest that finding experts for renewables seems

difficult but they ground this proposition on the absence of a specialized training program on renewables in Turkish universities rather than numbers and statistics from the market. These types of inferences make assessment of the situation harder and blurry. An undergraduate degree program that is specialized for renewables should be too wide and heavy to form an expert since it includes several disciplines. Vocational re-training and short courses are better solutions since they provide training for professionals who already have a background on technical issues and various disciplines. Currently there are some undergraduate degree programs in Turkey named "Energy Systems Engineering" and they are out of students or very few students comparing to their quota because no one preferred them [5]. Students of programs with a very specific field, in other words, restricted to a specific work field are subjected to limited job opportunities. Moreover, their curriculum contains knowledge from very different disciplines that makes the depth of knowledge shallow. So, common engineering programs such as mechanical engineering, electrical engineering, etc. have advantages over them in terms of finding a job. The evaluation of the authors which is suggesting that renewable energy education in Turkey is at encyclopedia level, supports the idea of shallow knowledge. Applied training should be provided to common engineering professions after graduation as a better solution. In Table 13 of the reference, it is seen that less than 10% in average of the education is done by applied training with equipments. The only renewable energy system that has 23.9% applied training is the hydraulic energy which can be considered as a conventional one and most probably it is using the infrastructure of mechanical and civil engineering departments. Authors mentioned that education plays a role at three different levels in the field of science and technology but they only give two of them in the conclusion section. Although this part seems irrelevant with the conclusion section, authors add that equipments for applied training are insufficient for education. About the questionnaire, the number of the questions is found low and there isn't any cross-examination question. The reasons of the questions are not explained. Statistical measures are missing. The outcomes seem subjective and they should be supported by solid proofs. The method section in the paper is too confined. There is a repetitive text in the first two paragraphs of results section. Authors suggest that the selected universities have pioneering studies in renewables and refer to Table 1 but Table 1 contains only the names of the universities. Authors suggest that education of renewables initiate at master level however Table 3 in their paper 3500 undergraduate students received education about renewables. Geothermal energy topic is significantly found more common in the classes of the surveyed universities in terms of class hours. Table 7 shows that renewables education is done in engineering faculties. This information seems unnecessary since only members of these faculties were responded to the questionnaire most probably. As a general opinion about the paper and the work; this questionnaire could give better results if it would be additionally applied to industry and consumers with some additional questions. It can be questioned that how a student or

a faculty member decide the order and the weight of renewables topics without the information from the market.

The last paper is also from 2011 by Acikgoz [6]. Paper claims that it analysis and classifies renewable energy sources, how to find their origins, how to motivate students on renewables, development of competencies for trainers in the abstract section. These strong promises are very difficult to be fulfilled with a four page paper. Actually, there seems to be a confusion of the author between education for awareness and training for skilled professionals. They are quite different concepts. Author informs that almost one hundred studies on energy education between 70s and 2008 exist. Still, it is concluded in the paper that the conducted studies are limited. Promoting awareness and training professionals are considered together throughout the paper. Solution proposals are too general. They are like using mass media, initiating courses at undergraduate degree and graduate levels, etc. Although the paper is about the energy education, only incentives about energy sector in Turkey are mentioned and any incentive on energy education is missing. The opinion of the author about short courses for professionals and in service training are shared and acknowledged. The names of computer files as examples of tools in digital media are unnecessary in the text. It is hard to find a significant solution in the conclusion section. The ones that are found in this section are confined and too general.

III. PROPOSITION

The debate on applied training and engineering education in general can continue further but a fact here should be stressed out; content and form of the training and education are not the only responsible ones about the problems but social life and public sensation constitute a prejudgment against technical vocations. Marketing of private sector and various media types produce contents that incite people to impossible lifestyles and lower the prestige of technical vocations because of the market concerns. Market driven policies are not sustainable. It is obvious that a technical vocation can find job in almost anywhere in the world while there are hard restrictions for an unqualified person across borders. It should not be forgotten that having a vocation as a qualification promotes self confidence.

The following points are proposed for the assessment of applied training:

- The qualifications should be determined according to the needs of the industry and market. For instance, proper clothing, use of tools, dealing with disposals in battery maintenance should be determined in guidance of a battery provider.
- Governmental institutions should publish standards for training applied skills after receiving qualification needs from private sector members.
- Short courses on very specific applications such as

aligning solar panels, erecting wind turbine posts, etc., should be accredited according to aforementioned standards.

- Trainee should perform a task more than one time to train their muscles and form a muscle memory.
- Test and assessment of a certain skill training should be done on commercial products and products should be checked according to quality control procedures.
- Training should focus on a specific task. Wider theoretical knowledge and long classes should be skipped considering the background of the applicant. The applicant can be tested prior to the training for their theoretical backgrounds as a qualification for the training.
- Education for promoting awareness is different than training for technical skills. Contents of the applied training should focus on techniques, not the reasons.
- Assessment should yield quantitative results. Linguistic scores are inadequate and insufficient. For instance, a welding practice should be scored with strength measurements of the test specimens. And the strength measurement scores should exceed a limit value. A linguistic score such as “well”, “mediocre”, etc. are not proper for technical jobs.

IV. CONCLUSION

This paper is a preliminary step forward to a comprehensive study on assessment of applied training for promoting and increasing technical skills. An example field as renewables was selected in order to survey some reports. Not only their contents are summarized but also some criticism are made on assessment of the education. Following drawings are listed below.

- Experiences around the globe in applied training should be compiled in order to form a comprehensive guide for new attempts/institutions. They should be in the form of comprehensive reports internationally published by governmental institutions.
- In order to address problems relating to applied training issue, statistical and quantitative data is needed from sectors and industry. Studies for collecting data are anticipated.
- Although literature suggest that undergraduate degree programs, certificate and diploma programs should be initiated for promoting new and specific engineering fields, present paper suggest that these applied training programs should be realized based on and after common engineering programs such as mechanical engineering, etc.
- Short specific courses seem indispensable for

graduates and professionals in the market. They should be rather short and focused on a single skill. An instance can be given as aligning photovoltaic panels according to domestic sun orbit or maintenance batteries, etc.

- Long term monitoring seems an overlooked tool for assessment of applied training. Online platforms are necessary that cooperating with databases of governmental bodies. An example of such databases is SGK.
- In order to mark lack of skilled professionals, certain statistics from governmental and private sector bodies are needed. As an instance, these means can be but not limited to; energy transparency platforms of governments; domestic energy providers that buys energy from individual providers; after-sale services and customer relations; complaint platforms on the internet for renewables.
- Most of the propositions in the literature for education related topics of engineering are awareness and management related issues rather than technical skills.
- It is an obvious fact that applied training is expensive. Innovative solutions such as Intern Engineering Program [7] are needed.
- Accreditation of applied training programs is important to proceed towards a globally uniform application.
- Showing a workshop application to a trainee by videos or pictures are not equivalent of making that trainee do the task by itself.
- Publications without numerical data about applied training makes finding a scale or measure with numbers harder. Because they increase the number of papers to be viewed.
- Undergraduate degree programs with specific field such as plant engineering restrict job opportunities while programs containing several disciplines such as energy systems engineering makes provided knowledge too shallow. Therefore, common engineering programs for target audience of applied training for technical skills are a better solution.

- [6] C. Acikgoz, "Renewable energy education in Turkey", *Renewable Energy*, vol. 36, pp. 608-611, (2011)
- [7] <http://tf.selcuk.edu.tr/index.php?lang=tr&birim=033&page=1394>

REFERENCES

- [1] <https://www.journals.elsevier.com/renewable-energy> ISSN: 0960-1481
- [2] T.C. Kandpal and H.P. Garg, "Renewable energy education for technicians/mechanics", *Renewable Energy*, vol. 16, pp. 1220-1224, (1999)
- [3] P. Jennings, "New directions in renewable energy education", *Renewable Energy*, vol. 34, pp. 435-439, (2009)
- [4] A. Karabulut, E. Gedik, A. Kecebas, M.A. Alkan, "An investigation on renewable energy education at the university level in Turkey", *Renewable Energy*, vol. 36, pp. 1293-1297, (2011)
- [5] <http://www.osym.gov.tr/TR,13046/2017.html>

Strength and Modal Analysis of 8 Membered Walking Mechanism

A. FEYZULLAH¹ and K. KAVLAK¹

¹ Konya Technical University, Konya/Turkey, alifeyzullah@hotmail.com

¹ Konya Technical University, Konya/Turkey koray.kavlak@konyateknik.edu.tr

Abstract - Different designs have been made and various control systems have been developed for the application of walking motion to robots. One of these designs is the one degree of freedom walking mechanisms. One degree of freedom walking mechanisms have some important advantages, such as wheeled and tracked robots, which are easier and more stable to move in uneven terrain. In this study, the design of an 8-link mechanism developed from 4 bar mechanism to use in the robot was made by the geometric analysis program (Cinderella) and the length of the links was optimized. The strength and modal analysis of the three dimensional modeled mechanism were performed with Solidworks.

Keywords - Walking mechanism, legged robot, coupler point curve, strength analysis, modal analysis.

I. INTRODUCTION

Although many single degree of freedom walking mechanisms have been designed, almost all have some common points in terms of design. Some of the qualifications required in walking mechanisms are:

- The mechanism should be able to provide the basic walking curve.
- The linear velocity must be constant when the foot is in contact with the ground.
- The foot that does not touch the ground must reach the start of task zone of this curve before the other foot reaches the end of the task curve.
- The height from the ground of the mechanism must remain constant.
- The input torque of the mechanism must be constant.
- The weight of the mechanism should be low. Increasing the number of links, low transmission angles (as this will increase the link cross-sectional area) effect increasing the weight of the mechanism.
- The center of gravity should be inside the support area.
- The mechanism must be able to move in the forward and reverse direction [1].

To fulfill these requirements, the Russian Mathematician Pafnuty Chebyshev (1821-1894) 's Plantigrade mechanism was one of the first studies on this subject. The mechanism is has four links and is called the Lambda mechanism [2]. The walking mechanism derived from it consists of two feet with a phase difference between them. In order to ensure walking, the number of conjugate mechanisms must be 2 or more [3].

In 1990, the Dutch artist Theo Jansen, who deals with kinetic sculptures and works, developed a mechanism driven by breeze winds made of PVC, wood and fabric and called it Strandbeest. The mechanism consists of 8 links and requires at least 4 replications of the mechanism (the number of feet that tracks the same locus) to enable walking [4]. Later on, many academic studies and thesis were formed about Strandbeest and in 2016, NASA announced that this mechanism would be used as a concept for the discovery rover to be used in Venus under the AREE Project [5].

The widely used 6-link Klann Mechanism as a walking mechanism was designed by Joe Klann in 1994 for port cranes and patented in 2001 [6]. Since the main purpose of the port cranes is to move at only constant altitude after the lifting of the load, the linearity of the movement in the cranes is similar to the walking mechanism.

The walking mechanism of Amanda Ghassaei from MIT Cambridge is similarly 8 links [7]. Although it is a design that meets the criteria for velocity, robot altitude and torque stability on the planar ground, it has a significant disadvantage in exceeding the discontinuities in the ground such as obstacles, due to having wide leg. As the Strandbeest and Klann Mechanism, this mechanism is symmetrical with respect to an vertical line that cuts off the drive point. The symmetrical design allows the robot to exhibit the same motion characteristics when moving forward or backward.

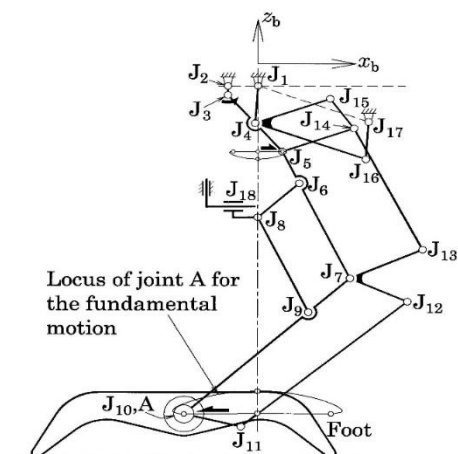


Figure 1: General view of walking chair design [9]

Funabashi H., Takeda, Y., Kawabuchi I. and Higuchi M., from the Tokyo Institute of Technology, has designed a walking chair that could move on a flat surface, climb uphill and stairs for walking disabled people. Simplicity, reliability, smoothness in motion and lightness are greater importance as the field of application is directly concerned about humans [8]. The mechanism structure of the walking chair can be seen in Figure 1. Although the mechanism normally has one degree of freedom, the degree of freedom is increased by level ascending or descending, and adjusting the step length levers of the chair.

The Trotbot Mechanism was created by modeling the galloping horse [10]. Therefore, the foot member of the mechanism tracks a like rectangular locus. Although it can be moved on not only flat surfaces but also uneven terrain, its efficiency is relatively low considering shape of coupler curve of the legs. On the other hand, the rectangular structure of the coupler curve makes the mechanism successful in exceeding obstacles. Knock and vibration in the movement can be prevented by adding heel and finger mechanism etc. to the foot member.

In this study, the design principles of a one-degree of freedom 8-link walking mechanism are mentioned and as a result of the study, optimization of the links lengths was made and strength and vibration were analyzed by output data.

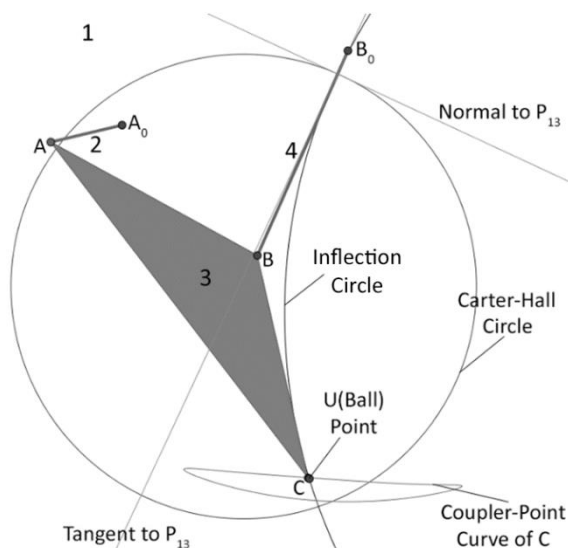


Figure 2: Creating of walking locus by 4 bar mechanisms

The walking mechanism in the study consists of a parallelogram mechanism connected to a 4 bar mechanism (1, 2, 3 and 4 links as shown in Figure 2) providing the basic walking locus. The point P_{13} in the figure shows the instantaneous point of rotation of the 3rd link. A_0 and B_0 are the center of curvature of A and B. P_{13} (the pole), normal and tangent of it, Carter-Hall Circle, inflection circle are also needed to find Ball Point. The mechanism was drawn in Cinderella software and the C point has been traced to the planar trajectory by fixing Ball Point of 3rd link to itself in 4

bar mechanism formed by 1st, 2nd, 3rd and 4th links [11].

In order to increase the number of parameters that can be controlled after the desired walking movement is achieved, a parallelogram mechanism is connected to C point on the member 3 so that the symmetry of this movement is also obtained in the foot member.

The entire mechanism is shown in Figure 3. As mentioned, the coupler curve of J is symmetrical and magnified of the coupler curve of E using the Ball Point.

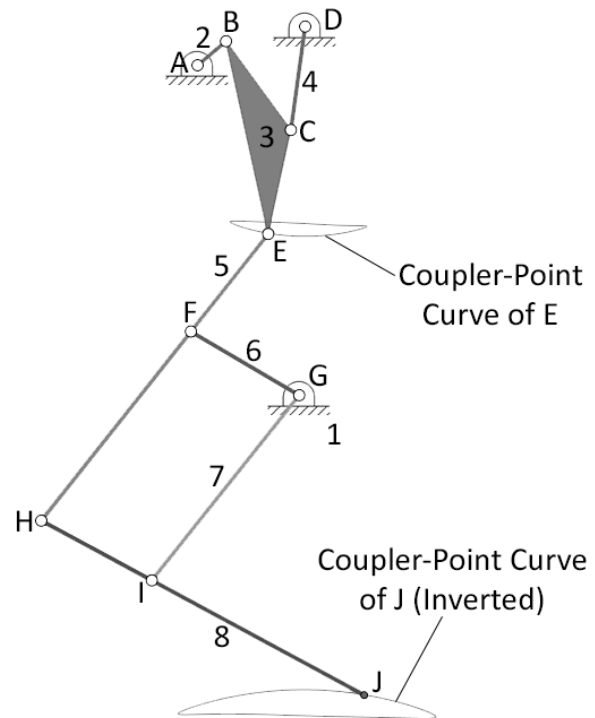


Figure 3: 8 Link Walking Mechanism

As a result of the analysis, the mechanism link lengths for ideal walking mechanism are obtained as follows:

- $AB = 23.5 \text{ mm}$**
- $BC = 69.4 \text{ mm}$**
- $CD = 66 \text{ mm}$**
- $AD = 72.1 \text{ mm}$**
- $BE = 124.7 \text{ mm}$**
- $CE = 67.3 \text{ mm}$**
- $AG = 218.2 \text{ mm}$**
- $DG = 233.1 \text{ mm}$**
- $EF = 78.6 \text{ mm}$**
- $FG = 79.3 \text{ mm}$**
- $FH = 151.4 \text{ mm}$**
- $HI = 79.3 \text{ mm}$**
- $GI = 149.5 \text{ mm}$**
- $IJ = 152.4 \text{ mm}$**

The main result from obtaining the mechanism is; not the length value, but the length ratio to each other. In this way, the

lengths can be reduced or increased by multiplying by a coefficient.

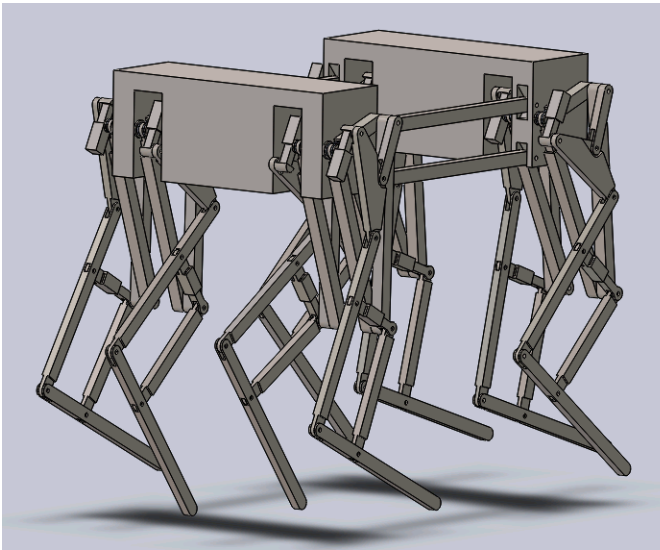


Figure 4: 8-legged robot with one-degree of freedom walking mechanism

II. DESIGN

Solidworks software was used to draw the robot with the one-degree of freedom walking mechanism. In order to ensure continuous movement in the zone where the robot contact to the ground, there must be at least two identical mechanisms. Thus, since there are four contact zones in order to ensure balance in three dimensions, eight walking mechanisms are required.

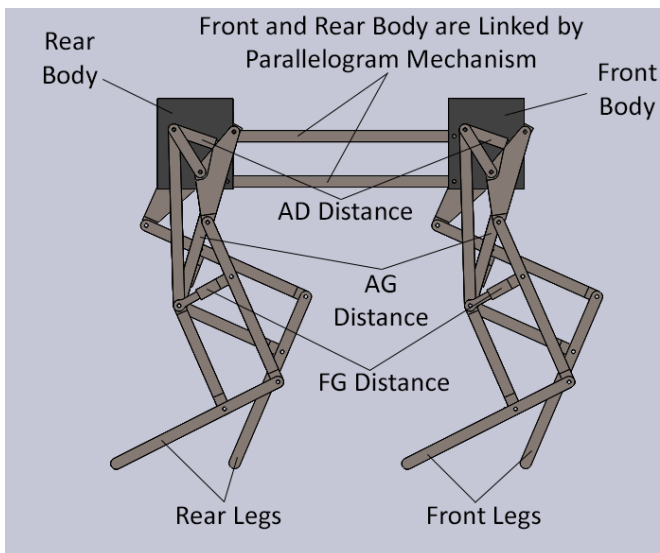


Figure 5: Front view of robot

Figure 4 shows the whole simplified state of the robot consisting of the right and left parts. While the side legs connected to the front and rear body move simultaneously, the center legs move with the 180 degree crank angle phase difference compared to the side legs. If all the members were in the same plane, all types of stresses would be tensile and

compression, like in the two dimensional cage system. This is not possible while the member 2 makes full rotation. However, as the distance of parallel member planes increases, combined stresses will occur instead of simple stresses. Therefore this state was considered when drawing the robot.

Figure 5 shows a simplified front view of the robot. The front and rear body connection allow the bodies to move in parallel with each other.

III. STRENGTH ANALYSIS

The forces affecting on the static analysis of the design only arise from the forces on the body and on the part weights. The members of the mechanism of the robot are made of alloy steel and the each body part is made of high density PE. As shown in the Figure 6, the red arrow shows the gravitational force acting on the center of gravity (approximately 23.8 kgf) and the purple arrows indicate the external load that placed on the robot. The value of the external load acting on each body is 25 kgf.

In the analysis, the robot was examined while in rest and 8 feet were simultaneously contacting the ground. It is seen in stress distribution in Figure 6 that the maximum von Mises stress (σ) occurs in the anterior and posterior legs. The von Mises stress, also known as the maximum distortion energy criterion, has been used because it gives sensitive results for ductile materials [12]. The maximum stress value is in the I support colored green (the supports are shown in Figure 3) and the value is 3.45 MPa.

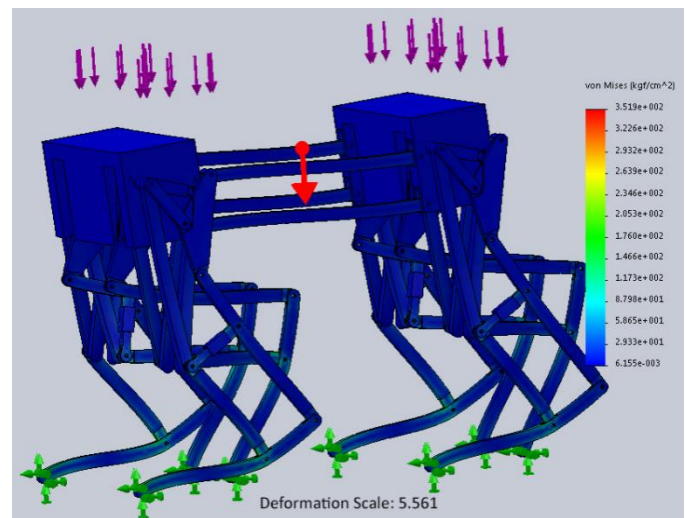


Figure 6: Stress analysis of 8-link walking robot

The deformation (δ) occurring under the same conditions is also seen in Figure 7. The largest deformation as a part occurs in the member 8 as seen in the previous results. However, because of the robot's contact with the ground, the deformation is interpolated and the greatest deformation is seen in the upper part of the robot and its value is 1.34 mm.

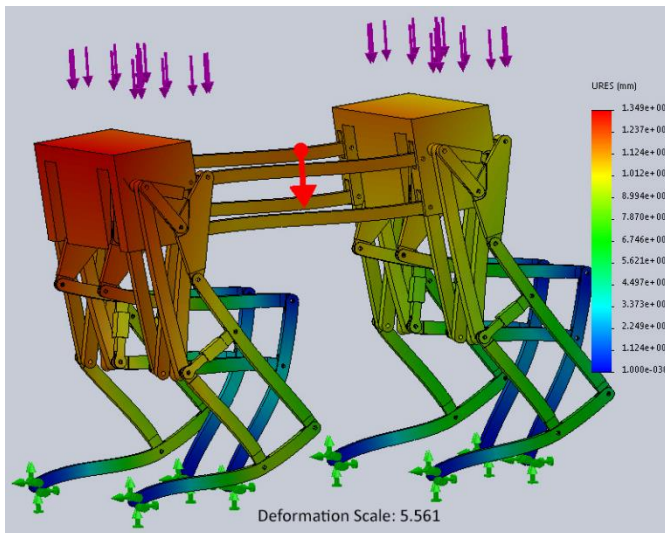


Figure 7: Deformation of the 8-link walking robot

The strain (ϵ) is seen in Figure 8. As expected, the strain takes its maximum value when the stress is highest. Therefore Figure 8 is a great similarity between Figure 7. The maximum value in the strain analysis is 1.94×10^{-2} (approximately 2%).

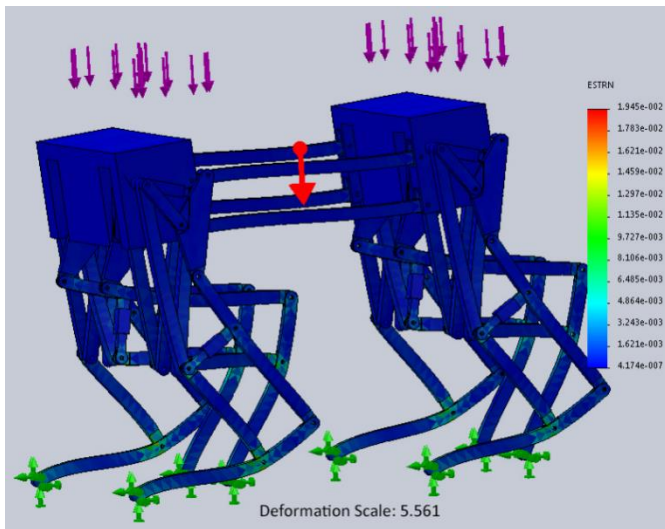


Figure 8: 8 Strain of the 8-link walking robot

IV. MODAL ANALYSIS

The natural frequency of the design determines the range of component frequencies added on the robot. These components are the drive motor and other external equipment. Natural frequencies are seen in Figure 9. Accordingly, 27.31 Hz, 31.24 Hz, 37.52 Hz, 77.69 Hz, 117.69 Hz are the resonance frequencies for the first 5 mode shapes. Critical rotational speeds of the motor are obtained by multiplying these values by 60 (1 min = 60 sec) and results are 1638 rpm, 1874 rpm, 2251 rpm, 4461 rpm and 7020 rpm.

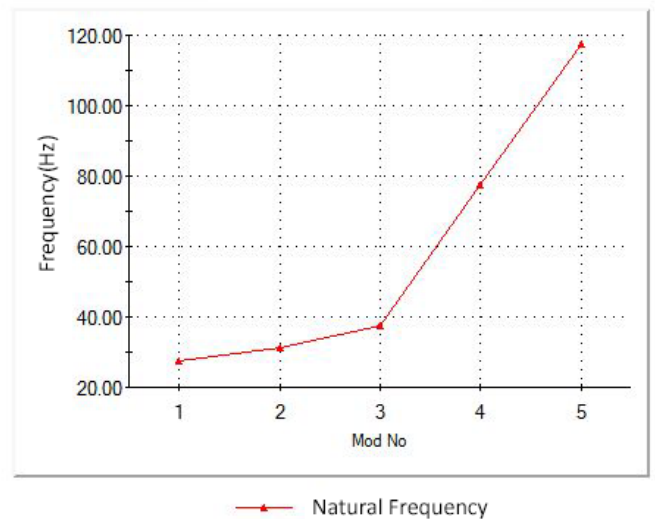


Figure 9: Natural frequency graph of the 8-link walking mechanism

There are higher rotational speeds for other mode shapes (greater than 5). As the motor speed is 600 rpm, it is not necessary to adjust the design.

The mod shapes corresponding to natural frequencies in Figure 9 are shown in Figures 10 to 14. The feature of the mode shapes gives information on which type of loadings are to be made or to be avoided. Mode shape 1 is generated by the vibration of the robot to the right and left (horizontal axis in top view).

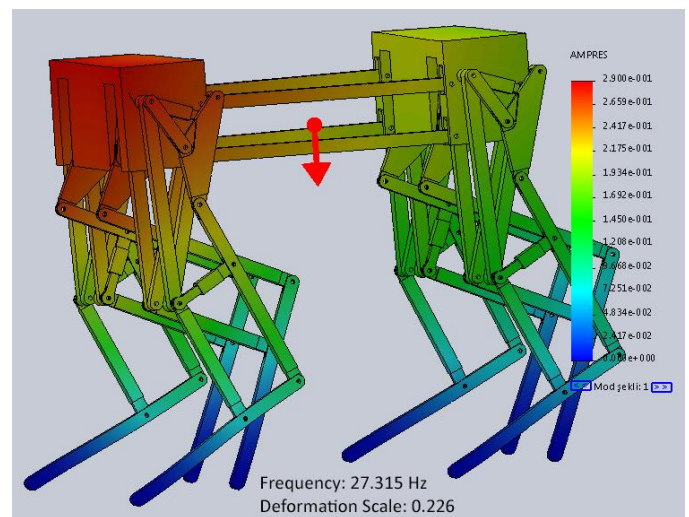


Figure 10: Mod shape 1 of the robot

The mode shape 2 is in the form of forward and backward tilting of the robot. During the progress of the robot, acceleration and deceleration at the fixed frequency occurs and this acts in the same as mode 1.

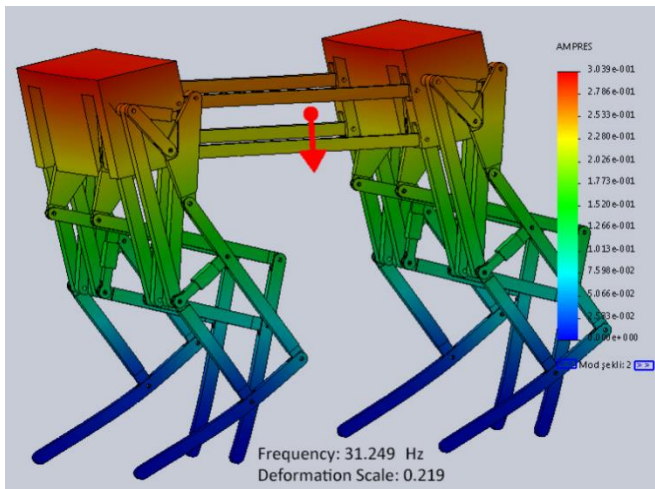


Figure 11: Mod shape 2 of the robot

Mode 3 is like the rotation of the robot in the top plane (yaw rotation). The vibration that occurs when the robot rotates to the right and left while the robot is moving is similar to the mode 3 shape shown in Figure 12.

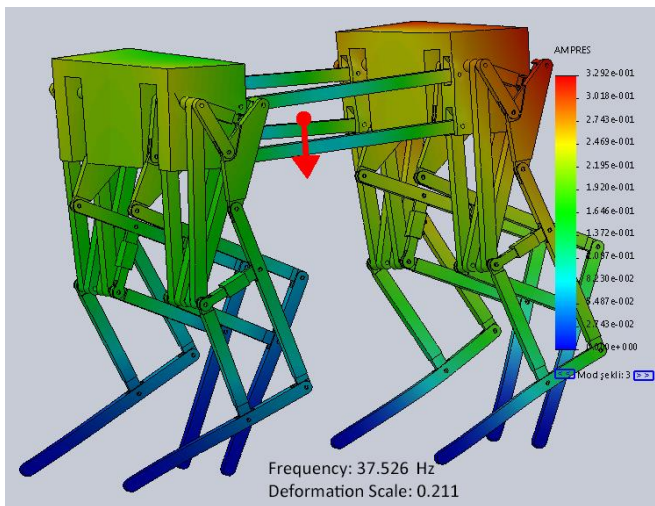


Figure 12: Mod shape 3 of the robot

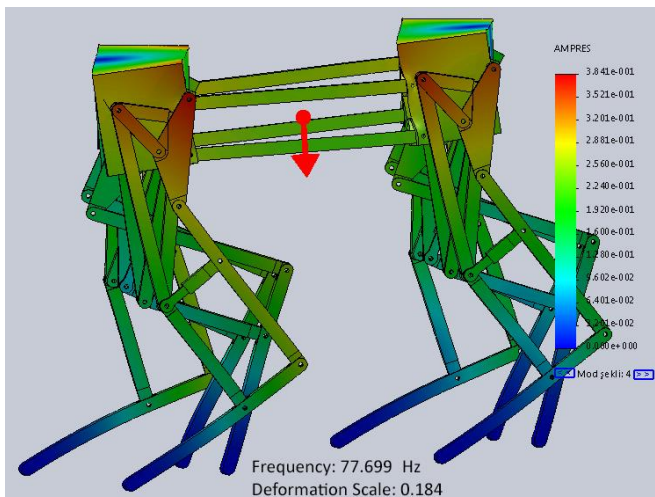


Figure 13: Mod shape 4 of the robot

Mode 4 shape is in the form of the yaw movement of each body. In normal conditions, external forces rarely cause this kind of vibration.

Mode 5 is the shape of the displacement caused by weight (vertical axis in front view - Z axis). The vibration caused by the sudden altitude differences in the ground on which the robot is moving causes a similar effect to mode 5.

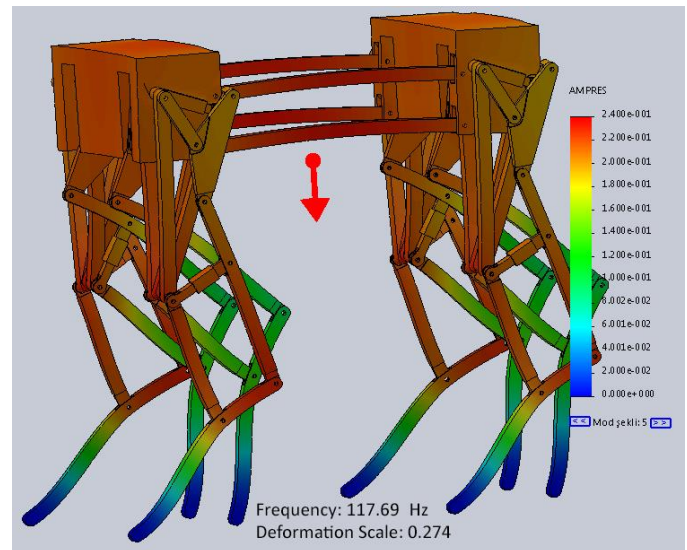


Figure 14: Mod shape 5 of the robot

V. CONCLUSION

Excessive deformation will be observed in legs as called member 8 that is weakest member of the robot when it is subjected to loading on the forces more than applied on the analysis. In order to prevent this, the cross-sectional area can be increased or the new designs can be made for this member.

The modal analysis was based on the unloaded mass of the robot and the critical frequencies were out of the operating range, so there was no need for any arrangement. However, it may be necessary to recalculate for safety because the equipment added to the robot will increase the mass and reduce the natural frequency value[13].

VI. REFERENCES

- [1] J. E. Shigley, *The Mechanics of Walking Vehicles, Land Locomotion Laboratory Research Division Research and Engineering Directorate*, September 1960.
- [2] P. Tchebysheva, *Theory of Machines*, Academy of Sciences of the Union of Soviet Socialist Republics, Moscow Published in 1984 (Теория Механизмов, Пчебышева П., Академия Наук союза ССР, Москва, 1948).
- [3] A. Sato, M. Beuhler, "A Planar Hopping Robot with One Actuator: Design, Simulation and Experimental Results", *2004 IEEE/RSJ International Conference, January 2004*.

- [4] S. A. Burns, "Four-Legged Theo Jansen "Strandbeest" Walking Mechanism", January 16, 2015.
- [5] J. Sauder, E. Hilgemann, M. Johnson, A. Parness, B. Bienstock, J. Hall, "Automaton Rover For Extreme Environments", California Institute of Technology, 2017.
- [6] United States Patent and Trademark Office Patent No: US 6,260,862 B1, Date of Patent: Jul. 17, 2001.
- [7] Ghassaei, Amanda, "The Design and Optimization of a Crank-Based Leg Mechanism", Pomona College Department of Physics and Astronomy, April 20, 2011.
- [8] H. Funabashi, Y. Takeda, I. Kawabuchi, M. Higuchi, Development of a walking chair with a self-attitude-adjusting mechanism for stable walking on uneven terrain. 10th World Congress on the Theory of Machines and Mechanisms. Oulu, Finland, June 20–24, 1999.
- [9] Figure was taken from <https://www.jsme.or.jp/english/documents/jsme-news/the-japan-society-of-mechanical-engineers-vol-12-no-2-december-2001>
- [10] W. Chun-Yung, H. June-Hao, Analysis and Applications of Theo Jansen's Linkage Mechanism, Graduate Institute of Architecture, National Chiao Tung University, Hsinchu, Taiwan, 2018.
- [11] L. R. Yin, J. Y. Han, J. Huang, T. Yang, A General Method for Synthesizing Straight-Line Linkage with Ball and Burmester Points, November 2012.
- [12] F. Beer, E. R. Johnson, *Mechanics of Materials*, 7th Edition, Mc Graw Hill, 2015.
- [13] S. S. Rao, University of Miami, *Mechanical Vibrations*, 5th Edition, Pearson 2010.

Numerical Simulation of the Coalescing Oil/Water Separator

Sedat Yayla¹ and Mehmet Oruç¹,

¹VAN YuzuncuYil University/Mechanical Engineering Department, Van-Turkey; mehmetoruc@yyu.edu.tr

¹VAN YuzuncuYil University/Mechanical Engineering Department, Van-Turkey; sedyayla@yahoo.com

Abstract - During the production of oil, a large amount of contaminated water is produced which has a harmful effect on the environment. In this research, the separation of the fluid mixture at a certain velocity between the plates was investigated by using the 3D computational fluid dynamics (CFD) program. As a result of the researches, it was observed that the distance between the combined plates is inversely proportional to the decomposition efficiency and at the same time the rate of introduction of the mixture

into the system is proportional to the dissociation efficiency and sweat. It has also been found that the best separation efficiency is in the plates with a cylindrical shape having a hole diameter of 15 mm. It was found to be. The separation efficiency results ranged from 38% to 98% depending on the different speed values used and the distance between the plates.

Keywords: *CFD, two-phase flow, oil-water separation efficiency, coalescing plate*

I. INTRODUCTION

Well fluids taken from the ground are generally mixtures of gas, oil and water. This fluid mixture needs to be separated, so that each of the separated products can be used for a particular application. One of the easiest ways to separate oil and water from one another is to take advantage of the law of gravity to provide separation. Thus water; While the oil is lighter than water, the oil is collected on the surface of the water. Separated crude oil can also be sent to reservoir tanks for processing. As a result, the oil-water mixture must be separated before being transported to the pipelines (Algifri et al., 1988). In oil industry, various problems can arise in the process of separating oil from water. To increase oil production, gas and oil companies are constantly looking for more efficient ways to reduce the amount of water in the mixture. Since the eighteenth century it has been produced as a mixture of water, water and oil. Decomposing companies have always tried to develop new methods to achieve a higher separation efficiency. Once the separation tank is separated from oil and gassed liquids, the remaining water will flow from the water treatment plant for further processing (Escobar, 2005).

product produced as a volumetric ratio in the oil production process (Razi et al., 2009; Razi et al., 2010; Hashim et al., 2009). The process of producing crude oil or gas depends on the composition of the fluid mixture. A mixture of hydrocarbons, gas and water extracted from the ground is usually found in the hydrocarbon mixture which is dissolved or insoluble in solids or solids (John et al., 2004). Due to the level of solubility of high toxicity in decomposed or produced water, great environmental risks arise for all humanity (Zhaohui et al., 2003). According to the US environmental protection agency, there is serious evidence that these mixtures can lead to various types of cancer and other serious diseases. (Agency U.S.E.P., 1998). For this reason, it is essential to protect the sea and human life, which will be done to better decompose these mixtures (Reusser and Field, 2002).

Water produced with natural gas and crude oil is treated as polluted water and cannot be used for drinking or irrigation. Water is the largest waste

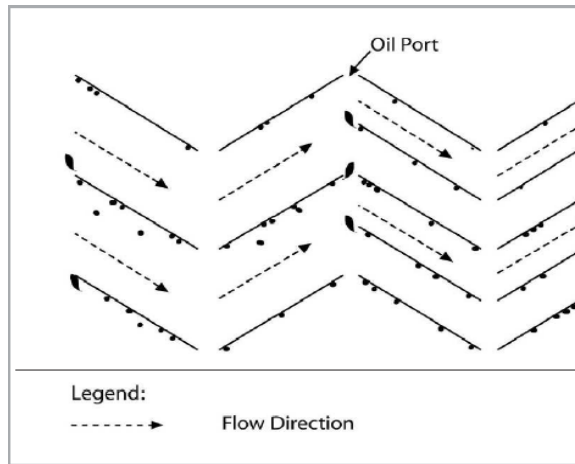


Figure 1: Oil-water separation mechanism in coalescing plates (Ling et al., 2006)

Ling et al., (2006), describe the use of multiple angled and parallel bonded plates to separate emulsified and free oils in contaminated water as shown in Figure 1. They also showed that the horizontal and parallel placement of the assembled plates mounted in the system yielded a higher separation efficiency in the oil-water separation.

Tadros, (2009); Sztukowski et al., (2003); Frising et al., (2006), the process of thinning and disintegration of the liquid layers between the globules and the process of separation between the separation of the globular process can be called as a limitation. The process called merger is carried out in several stages as follows:

- Approach of oil droplets to each other.
- Deformation and pitting for shaping a planar interface between the planar area and the globules in which the pile phase is drained.
- The bridge between the oil droplets results in an irreversible bond in almost a single globular.

In this study, a series of simulation studies for a horizontal oil-water mixer is shown using the Euler model. With this method, a two-phase flow (oil-water) behavior can be shown by means of a horizontal separator, and separation efficiency is found for various input speeds and distances between the coalescing plates.

II. MATERIAL AND METHOD

Computational Fluid Dynamics (CFD) is a numerical technique that facilitates research and decomposition with the help of fluid dynamics. Using the CFD program helps to create a computational model representing a device or system to be examined. In this program, the

physical and chemical properties of the fluid are typically applied, and the program solves the management equations to provide the output parameters for the fluid dynamics and associated physical phenomena. Therefore, the CFD program can also be seen as a complex calculation-based analysis and analysis procedure (Nowakowski et al., 2004). The program provides the ability to mimic gas and liquid flow, moving objects, chemical reaction, multiphase physics, heat and mass transfer, structure fluid interface and acoustics within the computer system. Applying this program can help create a practical model of the system that needs to be analyzed. The software will provide pictures and facts that await the characteristics of this system (Ansys fluent theory, 2009)

Table 1: Shows mesh independent test

Number of element	Separation efficiency	% difference
825000	85.8	(95.92-85.8)/95.92=0.1055
932000	87.85	(95.92-87.85)/95.92=0.0841
1145000	92.61	(95.92-92.61)/95.92=0.0345
2229000	93.7	(95.92-93.7)/95.92=0.0231
4954440	95.92	(95.92-95.92)/95.92=0.00

When oil and water flow along channels or pipes, the viscosity of the mixture is higher than the viscosity of each substance or phase in the mixture. The viscosity of the oil-water mixture is influenced by many factors such as the mixing speed and interface tension (explained in the equation (Fritz and Russ, 2001; Awad 2012; Ansys flow theory, 2009).

As seen in Table 1, the number of mesh used in the flow model is made independent of the mesh number so that it does not affect the separation efficiency. The decomposition efficiency obtained by this preliminary study has become generalizable.

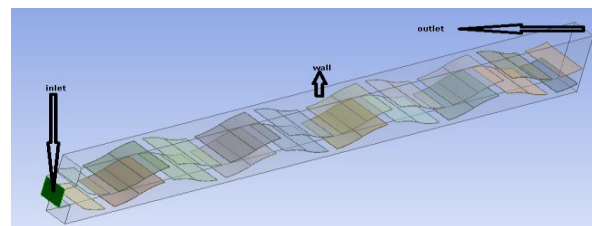


Figure 2a: Show the geometry and boundary inlet, wall, outlet

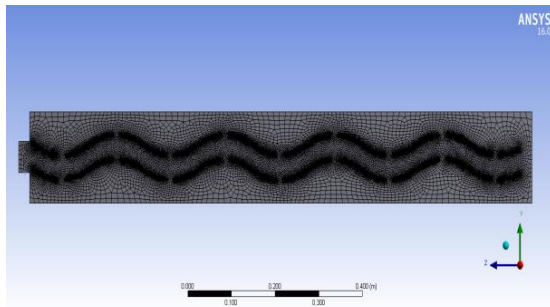


Figure 2b: Show meshing size of the separator

Figures 2 (2a and 2b) show boundary entry, wall and outlet conditions. In this study, separate solvent and covered formulation were chosen. The gravity vector is related to the magnitude of the zero-axis direction due to the flat-flow flow. A multiphase 3D plane shape, the axle is not symmetrical. The VOF model is models to simulate the properties of the two-phase flow. In this case the pressure-based solvent is used because the density can be changed. Steady state calculation is possible. The application equation for a pressure-based solvent is time-independent terms when calculating steady state (Ansys fluent theory, 2009). Since the initial conditions of the solution are independent and have separate flux boundaries for single phases, the VOF calculation in stable state is logical. For example, in the meantime, the shape of the free surface in a rotating container is based on the initial level of the liquid; Such a subject should be solved using the time-dependent formulation. Alternatively, the water flow in a channel with a top air zone and a separate air inlet can be resolved by the steady-state formulation (Ansys fluent theory, 2009)

III. RESULTS AND DISCUSSION

Problems during oil and water decomposition require the solution of two-phase flow and separation problems that must be used in a multi-phase model. The model used has the following characteristics: fluid volume (VOF), mixture, Euler and discrete phase model (DPM).

In this section, three factors that influence the effectiveness of the fusion separation have been investigated: the input flow rate of the gluing plate, the data of the results, the accuracy of the simulation and the high efficiency of the bi-directional wave plate separator. Furthermore, the merger mechanism was supported and analyzed by data. The effect of the input flow on the coalescence separation efficiency was performed on the flow condition of the laboratory in combination with the available data according to the process conditions of the field experiments. Figure 3 shows the oil phase contours of an axial cross-section of Z-O when the input oil phase concentration was 68% under different inlet flow rates.

In Fig. 3, it is more intuitive to see that the combining effect of the disintegrant is very different under various flow rates. The figure shows that the oil phase concentration can reach 92% or more at the bottom. At the same time, the dissociation separator may provide an output concentration of up to 98% at a flow rate of 1900 L / h. However, when the flow rate was greater than 2300 L / s, the concentration was significantly reduced. The comparison of oil phase cloud charts appears to be a disintegrant that can be used in practical applications where the highest oil phase concentration is not clear, the main difference reflected in the thickness changes of the oil layer, transition layer and water layer is particularly important for inclusion. The results of this study are in agreement (Wang et al., 2017).

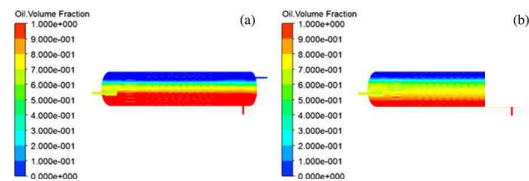


Figure 3: Contour of volume fraction under feed's oil concentration of 68%. (a) Inlet flow 1100 L/h (b) inlet flow 2300 L/h.

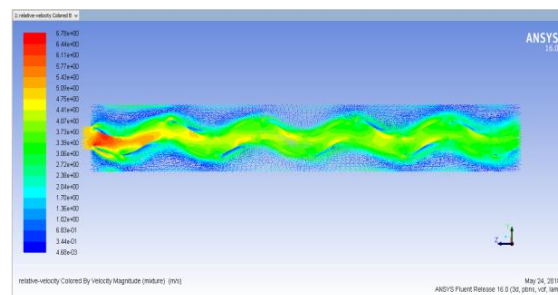


Figure 4: Relative Velocity Magnitude of velocity when $h = 8$ mm and velocity = 5 m/sec

Figure 4 shows that the speed at which the mixture enters the separation system is 5 m / s and the distance between the plates is 8 mm and the velocity magnitude increases to 6.78 m / s. This change in speed results in a connection plate. It is important that the speed magnitude is higher than the speed of the mixing flow input. The results of this study are in agreement (Ivanenko et al., 2010).

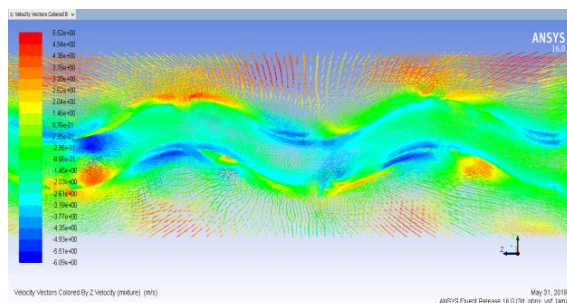


Figure 5: Velocity vector when $h=15$ mm and velocity 5 m/sec

Figure 5 shows that the velocity vector increases to 5.52 m/s when the input speed to the system is 5 m/s and the distance between the combined plates is 15 mm. This is due to the deterioration of the speed vector on the connecting plate. It is important to note that in each case the velocity vector is higher than the speed of the mixed flow input, which is very important for decomposition. This is consistent with the outcome of the study (Ivanenko et al., 2010).

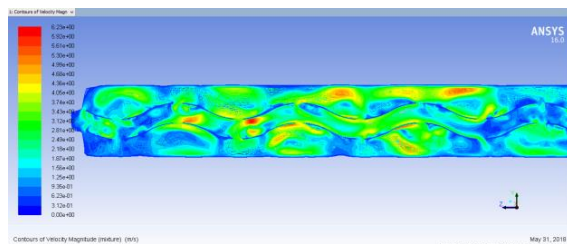


Figure 6: Contours of Velocity Magnitude $h = 24$ mm and velocity = 5 m/sec

Figure 6 shows that when the speed of the mixing inlet is 5 m/s and the distance between the plates is 24 mm, the velocity magnitude increases to 6.23 m/s. This change in speed allows the separation plate to perform the separation process. The speed magnitude is higher than the speed of the mixture flow inlet. In this case the separation efficiency is inefficient because the speed mixture inlet is equal to 5 m/s and the distance between the plates is 24 mm. It is in agreement with the findings of this study (Ivanenko et al., 2010).

IV. CONCLUSIONS

In this study, research is carried out to obtain information on the oil-water two-phase flow phenomena in joint or corrugated plate separators. In order to obtain the benefit of a CFD and a selected volume of liquid (VOF) oil-water phase model, ANSYS FLUENT presents a draft using commercially available CFD simulation software.

The purpose of this article is to review the CFD numerical simulation to study the process conditions of the two-way wave plate unified plate separator. This study investigates the most appropriate process conditions; verify the actual decomposition efficiency of the parser; and it is important to analyze the coupling mechanism at the same time.

The two-way wave plate is loaded into the three-dimensional model of the combined plate separator. When the fluid dynamics is combined with the numerical simulation method, the Euler model is selected which includes wall adhesion for the effect of surface modification for better examination of the process parameters and for the separation efficiency. The highest concentration and two-phase layer thickness were used to characterize the separation effect. The simulation results showed that the simulation values could be a good match in experimental values and error intervals. The composition and flow rate have an interaction effect in separation. In the case of different flow composition, the optimal selection of the input flow range is given. As a result of the studies conducted, it was observed that the maximum decomposition efficiency was obtained when the mixing speed of the mixture was 5 m/s and the distance between the combined plants was 15 mm.

Since the oil droplets are caught by the perforated plate at the top of the plates, they become larger and become larger and accelerate their upward movement. The speed will be higher than the speed of the mixture. The vertical velocity (y-axis) of the fat globules should be less than the x-velocity, higher than the velocity input called v-velocity or transverse velocity. The rising droplet will produce another x speed at horizontal speed or u-speed on top. The most important part is that the x-velocity should be higher than the speed of the mixture flow input. X-velocity and y-velocity were found to be negatively correlated with the separation efficiency.

References

- [1] Agency USEP (1998). National Center for Environmental Assessment–Washington Office of Research and Development. Carcinogenic Effects of Benzene: An Update, Washington, DC, p57.
- [2] Algifri AH, Bhardwaj RK, Rao YVN (1988). Turbulence measurements in decaying Swirl Flow in a Pipe. Applied Scientific Research, January 1988, Vol. 45, and pp. 233-250.
- [3] Ansys fluent guide (ANSYS FLUENT), theory and guide in 2009.
- [4] Escobar OM (2005). The graduate school performance evaluation of modified liquid-liquid cylindrical cyclone. Petroleum Engineering The Graduate School The University of Tulsa.

- [5] Frising T, Noik C, Dalmazzone C (2006).The Liquid-Liquid Sedimentation Process: From Droplet Coalescence to Technologically Enhanced Water/Oil Emulsion Gravity Separators: A Review, *Journal of Dispersion Science and Technology*, 27:1035–1057.
- [6] Hashim R, Abdolhamid, Al-baghdadi MARS, El hinshiri AK (2009). Evaluation of bio-surfactants enhancement on bioremediation process efficiency for crude oil contaminated soil at oilfield. *Strategic study* 20: p. 25-30.
- [7] Ivanenko A, Yablokova YU, Petrov SI (2010).Simulation of the Separation of Emulsified Oil Products from Water in an Apparatus with Sinusoidal Profiled Oleophilic Plates. *Theoretical Foundations of Chemical Engineering*, Vol. 44, No. 5, pp. 729–741.
- [8] John AV, Markus GP, Deborah E, Jr RRJ (2004). Argonne National Library a White Paper Describing Produced Water from Production of Crude Oil, Natural Gas, and Coal Bed Methane. Prepared for: U.S Department of Energy National Energy Technology Laboratory.
- [9] Ling LP, Hei NL, Kuok WK, Pgn AAR, Yusuf H(2006).development and performance tests of a separator for removal of psychically emulsified and free oils from waste waters. Department of Civil Engineering, University Malaysia Sarawak, 94300 Kota Samarahan, Sarawak,June.
- [10] Nowakowski AF, Cullivan JC, Williams RA, Dyakowski T (2004). This a realizable option or still a research challenge. Application of CFD to modeling of the flow in hydrocyclones. *Journal of Minerals Engineering*, Vol. 17, pp. 661-669.
- [11] Razi FA, Alireza P, Zainal AZ, Chuah AL, Awang BDA, Siavash MS (2010). Application of membrane-coupled sequencing batch reactor for oilfield produced water recycle and beneficial re-use .*Bio resource technology*, 101(18): p. 6942-6949.
- [12] Razi FA, Pendashteh A, Abdullah LC, Biak DRA, Madaeni SS, Abidin ZZ (2009). Review of technologies for oil and gas produced water treatment. *Journal of hazardous materials*, 170(2–3): p. 530-551.
- [13] Reusser DE, Field JA (2002). Determination of benzyl succinicacid in gasoline-contaminated ground water by solid-phase extraction coupled with gas chromatography. *Mass spectrometry*. 953, 215-225.
- [14] Sztukowski, DM, Jafari M, Alboudwarej H, Yarranton HW (2003).Asphaltene Self Association and Water-in-Hydrocarbon Emulsions. *Journal of Colloid and Interface Science*, 265 (1), 179-186, 2003.
- [15] Tadros TF (2009).*Emulsion Science and Technology*. Wiley-VCH Verlag GmbH & Co.KGaA.
- [16] Zhaohui X, Ashok M, Wilfred C (2003).Detection of Benzene, Toluene, EthylBenzene, and Xylenes (BTEX) Using Toluene Dioxygenase-Peroxidase Coupling Reactions. *Biotechnology Progress*, 19(6): p. 1812-1815.
- [17] Xiaojing Wang, Yangyang Yan, Zhongzheng Xu(2017). Application Experiment and Numerical Simulation Analysis of Oil-Water Separator With Two-Oriented Corrugated Coalescence Plate. *Journal of Dispersion Science and Technology*, 38 (10) : p. 1509-1515.

ELECTRICAL ENERGY HARVESTING WITH PIEZOELECTRIC

Mehmet Oruç¹, Sedat Yayla¹

¹VAN YuzuncuYil University/Mechanical Engineering Department, Van-Turkey; mehmetoruc@yyu.edu.tr

¹VAN YuzuncuYil University/Mechanical Engineering Department, Van-Turkey; sedyayla@yahoo.com

Abstract - Fossil fuels are used in industrial plants, automobiles and machines, and they have negative effects on human health with their gas and fossil particles. In order to meet the energy we need, instead of this renewable energy source, we need to turn to energy sources that can use the natural processes for energy production and that can be produced more rapidly than the exhaustion time of the energy resources used. Within the scope of the studies, vortex producer plates with different angles and diameters

have been designed in order to obtain electrical energy from the renewable energy source hydraulic energy. Within the scope of this study, studies on renewable energy have been mentioned.

Keywords: Piezoelectric material, renewable energy, vortex generator plate

I. INTRODUCTION

The advancement of technology and science, the need for energy increases day by day in parallel with the increasing population and the level of prosperity. In order to meet this energy need, which has become a big problem, alternative solutions are used. Many problems, especially air, water and environmental pollution, arise with energy needs. With renewable energy sources and clean energy sources, solutions should be sought without damaging the nature. Most of the increasing demand for energy needs is met by fossil fuels and leads to greenhouse gas. (Khojasteh et al. (2018) are fossil fuels such as natural gas, petroleum and coal, which are also known as mineral fuels, which are not renewable natural energy sources. At the same time, fossil fuels are used in industrial facilities, automobiles and machines, and they have negative effects on human health with the gas and fossil particles that are spreading around it. We need to focus on energy resources that can be produced more quickly than the period of exhaustion and that can renew itself. approach is required for Koçer et al. (2016).

With the help of developing technology, the tendency towards functional energy converting systems is increasing. In order to manufacture multi-functional devices (including mechanical, optical, electrical and magnetic properties),

ferroelectric-metal composites have been studied in recent years. Studies are carried out on materials to enrich ferroelectric and piezoelectric properties in Yudong et al. (2017). It is aimed to increase the gain in energy by these development methods made on the materials. The piezoelectric material, which is one of the materials used in energy converting systems, makes it possible to return the current energy produced by manpower, such as dynamic pressure, sound wave, water wave, to natural energy. There are many studies to obtain electrical energy by using piezoelectric material and energy harvesting method.

II. HARDWARE WITH PIEZOELECTRIC IN ELECTRICITY

II. I Renewable Energy

In order to meet the energy we need, instead of the renewable energy source, we need to turn to energy sources that can use the natural processes for energy production and can be produced more rapidly than the exhaustion time of the energy resources used. These sources can be listed as wind, solar, hydraulic (hydroelectric), geothermal, biomass (biogas), hydrogen, tidal and wave energy. Many applications are made to generate energy with renewable energy sources.

The idea of using solar panels that convert sunlight into electrical energy to generate electricity, generating wind power by generating electricity, wind turbines, converting the energy generated by the water flow into electrical energy by means of hydraulic power plants and the dependence on fossil fuels that cannot be renewed and consumed can be prevented. The solar energy, which we regard as a renewable energy source 'may become more widely available towards the end of the first 25 years of the two thousand years (Çobanoğlu, 1997) Yen. Considering the applications of solar energy in the world's electric and thermal fields, it is seen that economical and technologically efficient investments are made. It is observed that the wind energy usage, which is another renewable energy source, has existed for 5500 years. Moving ships with energy from the wind can be shown as an example of the use of wind energy for many years. Hizmet The systems that produce electricity from wind energy started to be installed in the beginning of this century and facilities that can produce 5 to 25 kW of power have been put into service until 1910 (Altaş, 1998) .

The rapid increase in energy consumption starts with the industrial revolution and cannot be expected to become stagnant. It is estimated that the cumulative energy consumption of the world will be at least 82500 EJ between 2000 and 2000. (Koç, 2012) tüketim It is necessary to avoid the compulsory tendency of fossil fuels in order to meet the energy we need. In the long term, the use of renewable energy sources is more advantageous than the use of non-renewable energy sources. Fossil fuels, an irreplaceable energy source, are the cause of serious health problems as well as their long term depletion. Combustion and distillation of coal, the most widely used fossil fuel type in the world, tar and hydrocarbons cause skin and liver cancer.

II. I. I. Hydraulic Energy

The energy that allows the electricity to be obtained by using water as well as the operation of the machines with this water is called hydraulic energy. The term hydroelectric energy means obtaining electric energy from rivers.

As it is tried to obtain electricity with the water flowing in the experimental setup used within the scope of the project, we can say that the type of renewable energy used is hydroelectric energy.

II. II. Energy Transducer Systems

Different devices are used for applications with innovative and original organic / inorganic materials used as energy converters (microsystem based energy harvesting methods such as piezo-

electric, piezo-resistive, electromagnetic) and improvements are made on these devices.

Jabbar et al. (2017) propose a stepped piezoelectric energy converting material with a two-way inductorless half-bridge circuit that operates under zero-voltage switching conditions as a new approach to the piezo-electric energy harvesting method as shown in Figure 1.

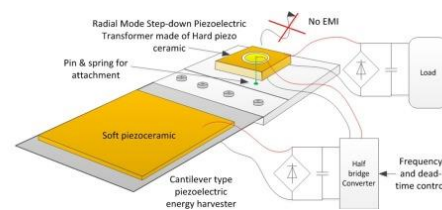


Figure 1: A typical system for impedance matching and power conversion from a piezoelectric energy harvester (Jabbar et al. (2017).

Sasmal et al. (2016) studied the change in the potential drop under the cyclic loading regime in a study to detect damages in the cement by piezo-resistive sensors, and attempted to prevent damage in the event of any damage started.

Hamid et al. (2017) propose a new energy collection system by combining electrical and electromagnetic energy harvesting in a single unit to create an electrical energy source as energy harvesting method.

Energy converter devices (WEC; Wave Energy Converter); Piezoelectric Energy Harvesting (PEH) Method is an example. Piezoelectric Energy Harvesting (PEH) method to obtain electrical energy is available in many studies. The piezoelectric material makes it possible to convert the existing energy produced by natural power, such as dynamic pressure, sound wave, water wave, to natural energy. There are many studies on the development of wave energy transducer (WEC; Wave Energy Converter) devices by using the water wave obtained by the wave energy which is one of the renewable energy sources. Energy converting devices; Piezoelectric Energy Harvesting (PEH) Method is an example. Piezoelectric Energy Harvesting (PEH) method to obtain electrical energy is available in many studies. The piezoelectric material makes it possible to convert the existing energy produced by natural power, such as dynamic pressure, sound wave, water wave, to natural energy.

II. II. I. Piezoelectric Materials and Properties

The piezoelectric effect comes from the word piezin, which is known as tourmaline crystal and discovered in transparent stones of different colors and whose name is in the sense of Greek pressure. The electrical charge caused by the pressure effect creates the piezoelectric effect.

Piezoelectric materials have a reversible property, making piezoelectric materials more useful and expanding their use. Piezoelectric materials produce electrical current with a force applied depending on their crystal structure and they change their shape in the electric field as a result of electric current.

Piezoelectric ceramic materials; Lead is produced by applying the most modern methods of titanium and lead zirconium. One of their main advantages; zirconium and titanium ratio can be adjusted in desired ratio and material properties can be optimized for desired application. Piezoelectric ceramics are hard, do not show chemical activity, and are not affected by moisture or other atmospheric conditions. These materials are produced by methods similar to other ceramic insulators whose mechanical properties are better known. Piezoelectric components are ideal for all types of electromechanical transducers (Koç, 2002).

II.II.I.I. Use of Piezoelectric Materials in Energy Production

Elhalwagy et al. (2017) carried out a study on the benefits of electrical energy to be obtained by harvesting energy by making a case study for future applications of energy that can be achieved by pressure and vibration from the piezoelectric energy collection mechanisms that can be established in the interiors of buildings.

Piezoelectric materials are used in many places for energy harvesting. The fields of use can be listed as follows:

- Sensors
- Generators
- They actuators
- Transducers

Xu et al. (2017) wanted to obtain energy harvest by embedding the energy generated by the vibration generated by the vehicles traveling on the road by embedding the equipment they have obtained by integrating the piezoelectric transducers into the packaging boxes. They aimed to cover the energy harvested by the traffic signs and traffic lights on the roads, along with the energy harvests they built by burying the boxes on the road. They have worked on long-lasting piezoelectric equipment and aimed to fill these boxes with high-strength materials to prevent any damage to the road

between the packaging boxes and the pavement. They used the Albert Pouring Glue, which is extremely durable as a solution to resistance and water damage.

Yang et al. (2017) Energy harvesting by means of energy gathering to convert energy into energy by means of energy collection by means of pressure generated by vehicles using polymer based piezoelectric material on highways in order to obtain electrical energy, which is one of the energies obtained by transformation of energies obtained from renewable energy sources. machine have been worked on.

Jung et al. (2017) In order to convert the mechanical energy generated by the vehicles to the electrical energy on the highways, the strong friction and fatigue resistance of the PVDF polymer based piezoelectric material has been taken to increase the resistance to the bending cycles created by the vehicles and they have worked on the energy harvesting machine. .

Wong and his colleagues (2017), using real rain water, rain drops on the design of the beams, the energy produced by the force of the piezoelectric material they have worked to convert the electrical energy they have worked with. In this study, the parameters such as rainfall rate, depth, precipitation type, number of drops, droplet size were examined. It was observed that the collected energy rate depends on the rainfall and that the impact force of the raindrop depends on the diameter of the rain drop. It has been proposed that further raindrop drops can be made on the designed beam and that a rechargeable battery can be added as an energy source to the energy collection system when there is low voltage. The fact that it can only be used on rainy days is seen as a disadvantage for this system and the idea that this system, which is designed with other energy harvesting machines such as wind and sun, can be obtained even when it is not raining.

II.II.I.II Harvest Method of Energy Obtained by Vibration

Hu et al. (2018) performed experimental and numerical studies on piezoelectric transducer modeling with vibration due to swirl oscillation. As shown in figure 2, for the experiment setup, it is aimed to obtain a cylindrical flow channel, flow meter, centrifugal pump, digital storage oscilloscope, resistance box, magnet, flow regulating honeycomb bodies and electrical energy harvesting from the piezoelectric material by using bimorph structure to obtain the voltage from the generated vibration.

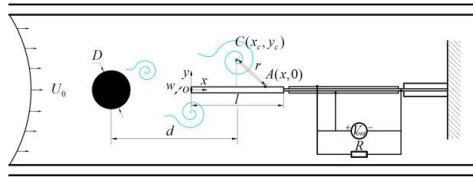


Figure 2: Schematic representation of the VSIV type piezoelectric energy harvesting machine proposed by Hu et al.

Hu et al. (2018) Discussed the positioning of the materials used in the experiments. They will work on electromechanical connections and damping in future studies.

Mutsuda et al. (2017) used a piezoelectric material with a high strength PFED structure for extreme bending and weather conditions caused by waves and currents to obtain electrical energy from the wave energy in the oceans.

Watanabe et al. (2013) are highly flexible and adaptable to collect energy from various forces in order to prevent damage to the ocean wave on the piezoelectric material, and the FPED material can be customized to the demanding size and electricity demand. They carried out a study in order to convert the energy generated by the fluctuation movements into electrical energy.

Xie et al. (2013) as shown in figure 3 discussed the factors affecting the energy collection efficiency of the transformer part produced for energy harvesting from the water wave in the seas and the factors affecting energy collection efficiency such as waveform, wave height and sea depth. a study was carried out to ensure.

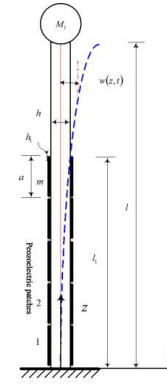


Figure 3: Energy harvester designed by Xie et al.

Wang et al. (2017) studied an energy harvesting machine for collecting and harvesting wave energy from the ocean wave, made of composite piezoelectric material. They carried out a mathematical study on this model by developing a group of conical shaped piezoelectric cubicles and a buoy-shaped prototype with a magnetic brick of the same dimensions. The energy converter prototype design they make is shown in Figure 4.

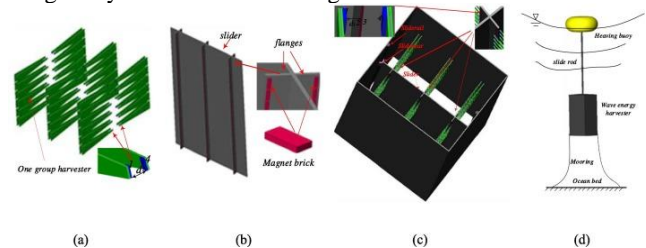


Figure 4: The energy harvester designed by Wang et al.

References

- [1] Çengel, Y., Cimbala, J., 2006. Akışkanlar mekaniği temelleri ve uygulamaları.
- [2] Çobanoğlu, Z., 1997. Enerji ve Çevre, Ankara.
- [3] Elhalwagy, A., Ghoneem, M., Elhadidi, M., 2017. Feasibility study for using piezoelectric energy harvesting floor in building interior spaces ,İspanya.
- [4] Hamid, R., Yuce, M., 2017. A wearable energy harvester unit using piezoelectric–electromagnetic hybrid technique
- [5] Hu, Y., Yang, B., Chen, X., Wang, X., Liu, J., 2018. Modeling and experimental study of a piezoelectric

energy harvester from vortex shedding-induced vibration, Çin.

- [6] Jabbar, H., Jung, H., Chen, N., Cho, D., Sung, T., 2017. Piezoelectric energy harvester impedance matching using apiezoelectric transformer
- [7] Jung, I., Shin, Y., Kim, S., Choi, J., Kang, C., 2017. Flexible piezoelectric polymer-based energy harvesting system for roadway applications
- [8] Karadağ, E., 2012. Matlab portföy eniyileştirme aracı ve örnek uygulamaların matlab platformundan bağımsız (standalone) halde hazırlanması, Kocaeli.
- [9] Khojasteh, D., Khojasteh, D., Kamali R., Beyene, A., Iglesias, G., 2018. Assessment of renewable energy resources in Iran; with a focus on wave and tidal energy .
- [10] Koç, M., 2002. Yenilenebilir enerji kaynaklarının Türkiye’de yaz ve kış klimasında uygulama alanlarının belirlenmesi, İstanbul.

- [11] Koçer, A. Öztürk, M., 2016. Elektrik ve hidrojen üretimi için entegre sisteminin termodinamik analizi, Mühendis ve Makine cilt57, sayı 681, s.25-44.
- [12] Mutsuda, H., Tanaka, Y., Patel, R., Doi, Y., Moriyama, Y., 2017. A painting type of flexible piezoelectric device for ocean energy harvesting.
- [13] Nielsen, P., 2011. 3D CFD-analysis of conceptual bow wings
- [14] Pınarbaşı, A., Güleren, K., 2001. İki boyutlu geometrik cisimlerin üzerindeki farklı türbülans model yaklaşımları, 13. Ulusal Isı Bilimi ve Tekniği Kongresi, Konya.
- [15] Sasmal, S., Ravivarman, N., Sindu, B., 2016. Synthesis, characterisation and performance of piezo-resistive cementitious nanocomposites
- [16] Wang, Q., Xie, X., 2017. A study on an ocean wave energy harvester made of a composite piezoelectric buoy structure, Hong Kong.
- [17] Watanabe, R., Doi, Y., Tanaka, Y., Azuma, S., Mutsuda, H., 2013. Ocean power generator using flexible piezoelectric device, Fransa.
- [18] Wong, V., Ho, J., Chai, A., 2017. Performance of a piezoelectric energy harvester in actual rain, Malezya.
- [19] Xie, X., Wang, Q., Wu, N., 2014. Potential of a piezoelectric energy harvester from sea waves , Çin.
- [20] Xu, X., Cao, D., Yang, H., He, M., 2017. Application of piezoelectric transducer in energy harvesting in pavement, Çin.
- [21] Yang, H., Wang, L., Zhou, B., Wei, Y., Zhao, Q., 2017. A preliminary study on the highway piezoelectric power supply system, Çin.
- [22] Zheng, M., Hou, Y., Zhu, M., Yan, H., 2017. Nanodomains in metal/ferroelectric 0-3 type composites: On the origin of the strong piezoelectric effect, Çin

Fatigue Tester Design and Frame Analysis for Estimation of Fatigue life of Helical Compression Springs

G. YALÇIN¹, S. NEŞELİ^{2*}, H. TERZIOĞLU³ and A.C. AĞAÇAYAK³

¹ Konya Teknik University, Konya/Turkey, yalcin@selcuk.edu.tr

² Selcuk University, Konya/Turkey, neseli@selcuk.edu.tr

³ Konya Teknik University, Konya/Turkey, hterzioglu@selcuk.edu.tr, cemagacayak@selcuk.edu.tr

Abstract - The springs sometimes break suddenly due to the loads under dynamic operating conditions. For this purpose, the determination of the fatigue strength of the helical thrust springs in the working environment requires the use of specially designed devices, especially in the case of high frequency vibration. In this study, a test device is designed to measure the fatigue limit of helical compression springs. The design is made by taking 5 helical pressure springs with 5 windings and 30 mm free length. The building is then thought to be a test unit body and a control panel unit. The movement from the horizontally positioned motor in the test section is transferred to the springs to be tested in groups by means of the eccentric drive device. In order to increase occupational safety and health, the test part has been designed as closed and 360 degree security has been taken into consideration. In addition, thanks to the enclosed environment, fatigue strength is measured to be isolated from environmental conditions. In addition, the deflection performed by the forces performed during the study was carried out by FEM analysis. It is concluded that the chassis formed by the analysis carries the forces formed safely.

Keywords - Fatigue test device, Helical compression springs, Displacement analysis.

I. INTRODUCTION

Each machine tool used in engineering exhibits spring behavior depending on the elasticity limits in the case of dynamic loads. However, there is a need for machine elements that maintain the load in the form of energy by using a wider range of harmonic motion energy, depending on the location of use. There are many types of springs available in the industry for this purpose. Since the deformation and loading characteristics of springs subjected to dynamic loading affect working efficiency, the determination of fatigue life for the detection of efficient use has been the subject of researchers for many years. The determination of the life of the springs can be done by applying certain experiments under different conditions. In these experiments, the aim is to determine how soon the springs will break under repeated loads, or loosen by losing the spring property. In the experiments, the same

springs, which are wrapped in the same material and have the same characteristics, are operated under the same conditions and their fatigue values are determined. In this process the loading frequency is very important [1]. It is recommended that test speeds be between 200 and 500 rpm in ASTM and DIN international standards [2].

A spring fracture process can be thought of as three stages; The initial fatigue damage that caused the crack to begin is that the remaining section of the crack progressively weakens to the point where it can not carry the applied loads, and the remaining section breaks suddenly. Kailas (2015) [3] investigated the phases in which the formation of fatigue occurred as a malfunction. Berger and Kaiser (2006) [4] investigated fatigue behavior with a machine that could test 160 of the helical compression springs at the same time, and the results of this research have experienced fatigue behavior in a very high cyclic regime. It has been emphasized that the fatigue strength begins to decrease in the fatigue test from 10^7 reckons to 10^8 reckons and above and that these limit values should be paid attention. Pyttel et al. (2013) [5] can be described as the continuation of the research carried out by Berger and Kaiser in 2006. In this study, helical spring compression tests were carried out at 40 Hz. This study compares the fatigue lives of springs in various spring sizes, variable materials and variable compression conditions, and shows that the ideal parameters are $d = 1,6$ mm and $d = 3$ mm for $P_s = 98\%$ (probability of strength). Gönen et al. (2008) [6] designed and fabricated a mechanical spring fatigue tester for fatigue analysis to determine the life span of metallic springs. The most important feature of the device is that it allows fatigue analysis at two different compression ratios at the same time. With this feature, the determination of two different points at the drawing of the stress-life diagram is time-consuming. In this system, a compressor applying 8 bar pressure was used and the fatigue tests of the springs between 20 and 200 mm were made as prestressed and prestressed.

In this study, a horizontal axis 3-phase asynchronous motor and PLC-controlled eccentric test machine designed to perform fatigue test of the same type and same type of helical printing at the desired frequency range was designed. In this case helical pressure emission fatigue test and analysis which

* Corresponding author. Tel.: +90-332 2233344

E-mail address: neseli@selcuk.edu.tr (Suleyman Neseli).

can be designed according to the variability of working conditions (frequency and load) was possible

II. MATERIAL AND METHOD

In order to test the spring life, details such as the load to be loaded on the spring, the operating temperature of the spring to be tested, the frequency of the spring, the frequency and the loading status have been taken into consideration. A maximum of 5 helical prints can be tested in a single test. The most critical information in making a mechanical design is the determination of the load state. The safe operation of the system according to dynamic or static loading conditions is possible by designing the appropriate frame and components to be mounted on it. For this purpose; 1) the optimum frame design has been achieved, 2) the mechanical system and the drive train, and finally 3) the control unit assembly has been designed. The fatigue tester designed in Fig. 1 is shown schematically.

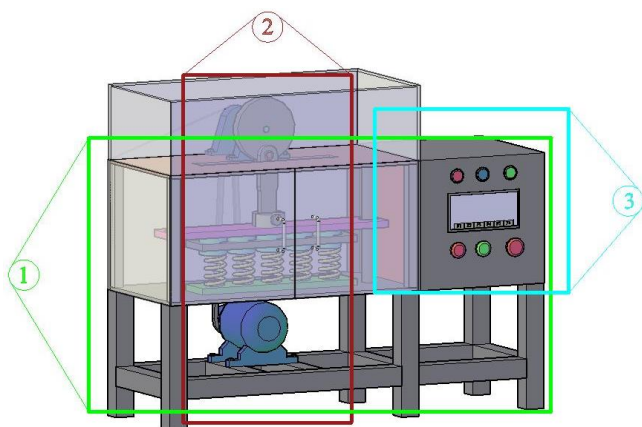


Figure 1. Designed fatigue tester

A. Frame and Mechanical System

The frame subsystem is 40x40x2 mm and the frame upper system is formed by cutting and welding at appropriate dimensions using 20x20x1 mm square profiles. The 10 mm plates in the upper and intermediate sections were welded together by welding to form a fixed joint. In order to prevent undesired vibrations during the operation of the electric motor used as the drive system, the mechanical system was positioned near the center of the center of gravity and the connections on the frame were bolted. The motion taken by the motorcycle has been conveyed to the belt cam system, which is articulated with bolted connection to the frame. It is ensured that the springs to be tested are supported by the inner bill formed by considering the spring inner diameter on the plate (fixed) on the bottom of the rigidity spring and the inner bill formed by considering the spring outer diameter on the top plate (movable). The linear movement of the upper plate, which will print on the springs to be tested by the effect of eccentric motion, is provided with columns from both sides. A

bushing is used between the fixed columns and the movable top plate. Oxy carbon graphite materials were preferred as the bushing material (see Figure 2).

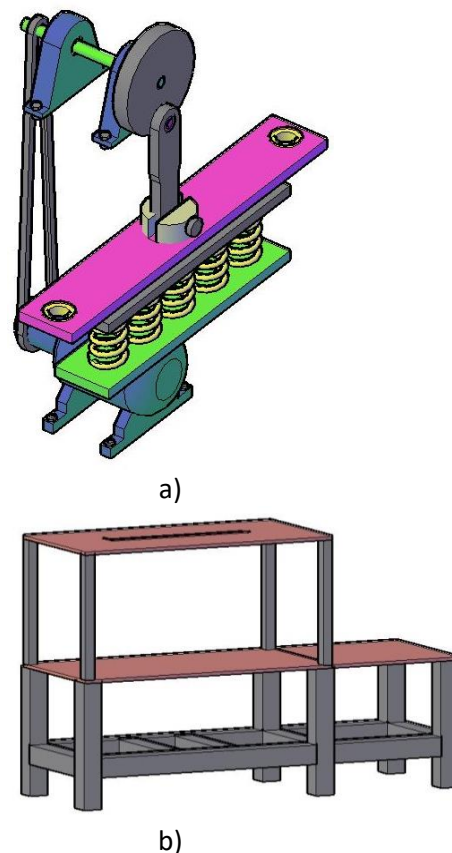


Figure 2. a) Mechanical system, b) Chassis

B. Electronic Data Collection and PLC System

In this system, 3-phase asynchronous motor is used. Siemens speed controller is used for speed control of asynchronous motor. PLC and operator panel are used to determine the desired speed of the asynchronous motor in the control panel created for system control. Depending on the reference speed determined from the operator panel, the speed controller operates the ASM at the desired speed. Motor speed, drawn current, operating frequency and power values are displayed on the operator panel.

The schematic view of the designed electronic data acquisition and PLC system is shown in Fig 3

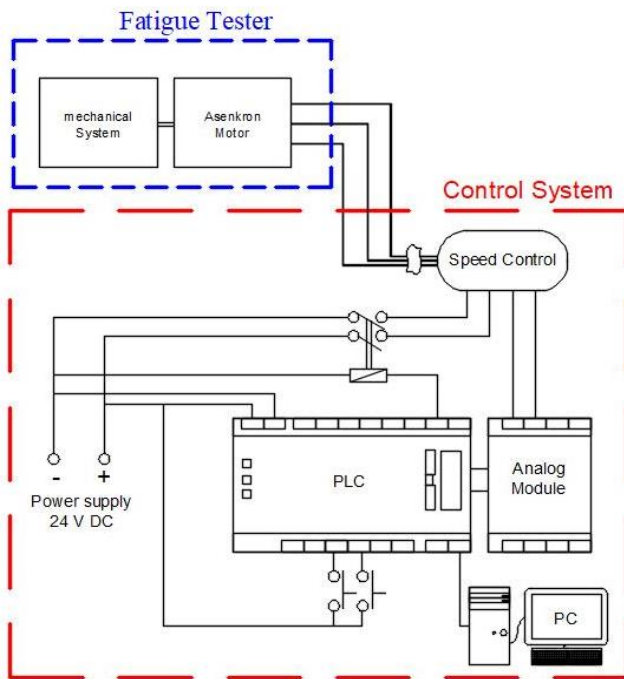


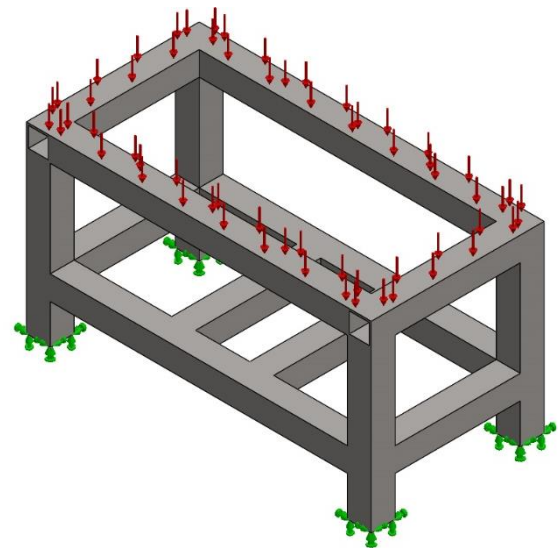
Figure 3. The schematic view of the designed electronic data acquisition and PLC system

III. WORKING PRINCIPLE AND DISPLACEMENT ANALYSIS

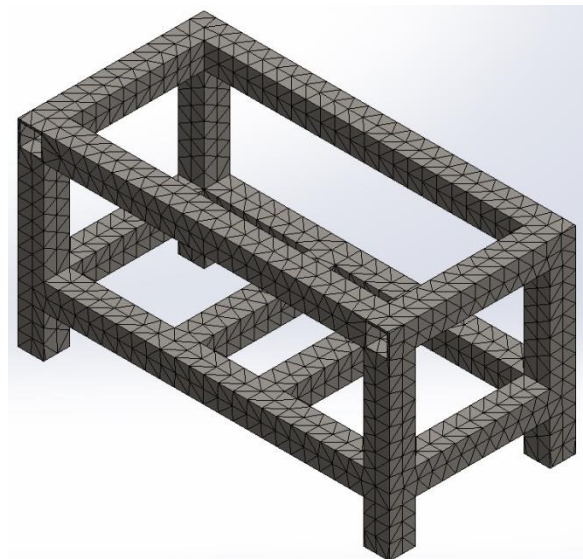
It is recommended that an helical spring fatigue test be performed at speeds of 200 - 500 rpm in the international standards of the American Society for Testing and Materials (ASTM) and the Deutschland Industrial Norm (DIN) [2]. Accordingly, the standards mentioned in the design of the test equipment made in the scope of this study are taken into consideration.

This fatigue testing machine is working with electrical power and controlled with PLC. Fatigue test carry out according to determined loading force which graphically entered into the PLC operation system before. The loading force has different shapes such as trapeze, triangle, rectangular or square. All obtained data from fatigue test has recorded in PLC system.

By using the designed device finite element method (SolidWorks program Analysis part), the resistance of the device is determined by the dynamic behavior of the device. All materials used in the design are defined as steel (AISI 1020). Installation status and model network structure is given in Figure 4. Hexahedral, oval, chamfered, etc. In the complex parts, tetrahedral network structure was used.



a)



b)

Figure 4. a)Loading status, b)Mesh design

As seen in Figure 5, when the frequency is 69.52 Hz, a displacement of about 1.45 mm occurs. However, it is seen that the design is suitable even if only mode 1 is examined. Because the engine speed is 1250 rpm and the applied force is $F_y = 1270$ N. In this analysis, the force is taken as $F_{maks} = 3000$ N considering the unforeseen conditions.

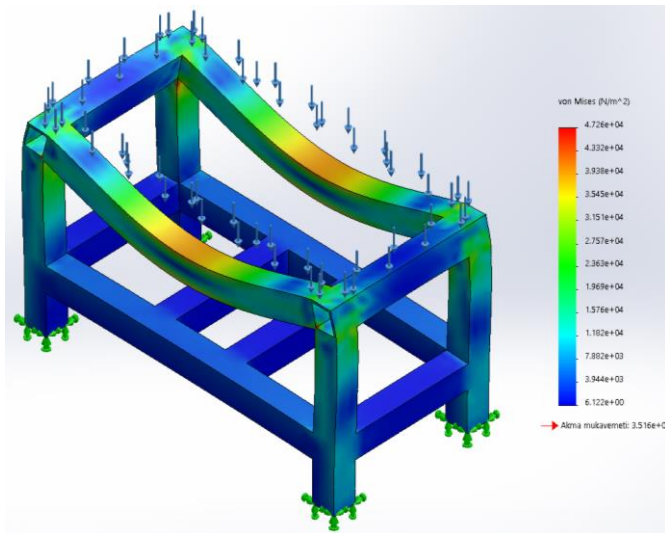


Figure 5. Displacement shape of main frame

IV. CONCLUSION

The importance of testing machine in investigation and production is indisputable. The testing machine is to provide much knowledge about the mechanical properties mentioned above.

In this study, a test device designed to measure the fatigue lives of helical compression springs was designed. Lifetime analysis of helical compression springs with 5 spindles and 30 mm of free length will be possible. all the desired data can be recorded by means of the designed PLC software.

If requested, the system can be revised for different springs and experiments can be conducted for the specified parametric conditions

REFERENCES

- [1] K. Çavdar, T.G. Yılmaz, "Kalıp Yayları İçin Yorulma Test Cihazı Tasarımı ve Analizi", *Uludağ Üniversitesi Mühendislik Fakültesi Dergisi*, Cilt 22, Sayı 3, 2017
- [2] H. Pıhtılı, L. Özler, "Yay Tellerinde Yorulma ve Yorulma Deneylerinde İzlenecek Temel Esaslar", *Mühendis ve Makine*, 38 (445), 38-41, 1997
- [3] S.V. Kailas, (2015). Chapter 8: Failure. Available: http://engineering108.com/Data/Engineering/Mechanical/Material_Science/Module8.pdf
- [4] C. Berger, B. Kaiser, "Fatigue Behavior of Technical Springs", *Materialwissenschaft und Werkstofftechnik*, 36(11), 685-696, 2005
- [5] B. Pyttel, I. Brunner, C. Berger, B. Kaiser, M. Mahendran, "Fatigue Behavior of Helical Compression Springs at a Very High Number of Cycles", *International Journal of Fatigue*, 60, 101-109, 2013.
- [6] D. Gönen, A. Oral, C.M. Cakır, "Çift Sıkıştırma Oranlı Yay Yorulma Test Cihazı Tasarım ve İmalatı", *BAÜ FBE Dergisi*, 10(1), 98-108, 2008

Determination of Basic Construction Parameters of Knitting Machines

D. ERDEM¹ and G. ABDULLA²

¹ Selcuk University, Konya/Turkey, duygu.erdem@selcuk.edu.tr

²Suleyman Demirel University (Retired), Isparta/Turkey, gabilabdulla@sdu.edu.tr

Abstract - To obtain a knitted structure, many elements should work together in a harmony in a knitting machine. However, each element is produced in some certain production limits and that makes them harder to work compatible with each other. To overcome this situation lots of equations should be derived and the most appropriate one should be chosen. In this study, the most basic design parameters were determined, and their relations were studied.

Keywords – Knitting machines, knitting elements, machine design.

I. INTRODUCTION

Although the concept of weaving has appeared first in the textile industry, knitting became more important than the weaving after knitting process was automated. Since, people prefer knitted products, which are softer and more comfortable, than woven products. Knitted products are frequently used in many different fields from underwear to outerwear.

Hand knitting was used to produce wool socks, headgears, etc. until the 16th century. Knitted products became widespread after the invention of the mechanical knitting machine. The rapid increase in demand for the knitted products in the 16th century has been a driving force for mechanization of the knitting process. After the Second World War, the reflections of the developments in mechanical and electronic fields began to be seen in knitting technology. Circular knitting machines have experienced a series of improvements that increase production performance and product variety. The knitted fabric production and improvements in knitting machines began to increase gradually in the 1950s and 1960s. Developments in knitting machines have progressed at a dizzying pace in parallel with developments in the electronics sector in the 20th century.

Today, fully electronically controlled knitting machines have infinite pattern capacity and high production speed. Furthermore, fully fashioned garments could be produced with special knitting machines and time loss in the clothing industry could be pretended.

To obtain a knitted structure, many elements should work together in a harmony in a knitting machine. However, each element is produced in some certain production limits and that makes them harder to work compatible with each other. To

overcome this situation lots of equations should be derived and the most appropriate one should be chosen. In this study, the most basic design parameters were determined, and their relations were studied.

II. MATERIAL AND METHOD

The basic construction parameters of knitting machines are machine gauge, needle type, yarn count, needle hook thickness and sinker thickness. These parameters determine technologic purpose of the machine.

A. Machine Gauge

Machine gauge is defined as the number of needles per unit length and represented with notation “E”. Most popularly, inch is used as the unit length in Europe and consequently in Turkey [1]. Machine gauge directly influences the yarn count and yarn twist, machine speed, knitting structure, fabric width and shrinkage in width. Finer, smoother and more stable structures can be produced with finer gauge machines [2].

Nowadays, a wide range of machines with different gauges are produced to accommodate the wide range of yarns available in the market. All yarns cannot be used in every machine. As machine gauge increases, finer yarns need to be used. For instance, lower gauge machines are used with handspun and bulkier weight yarns, when fine gauges are used with lace weight yarns [3].

B. Selection of Needle Type

The needle is a hooked metal element which gives loop formation to the thread in knitting machines. Firstly, the needle type must be determined to specify the parameters related to the needle. Three types of needles are used in modern machines: latch needle, bearded needle, bi-partite compound needle. Same knitting structure can be produced by all of these needles, however most appropriate needle must be selected to obtain the optimum results in terms of design [2, 4, 5].

Main factors affecting the selection of needle type are machine gauge, the simplicity of the machine construction and productivity. In recent years, bearded needles can be produced as thin as latch needles. Therefore, it is also possible to use latch needles in fine gauge knitting machines. Bi-partite compound needles are mostly used in warp knitting machines. Besides, on the contrary of bi-partite compound needles,

nonuse of a presser while using latch needles and bearded needles greatly simplifies the construction of the knitting machine. It is recommended to use latch needles for simplicity of machine construction. Lastly, when needle types were examined in terms of productivity, it is seen that needle displacement is the key factor. On equal terms, needle displacement is minimum for bi-partite compound needles and maximum for latch needles because of the requirement of additional time for closing the latch. Based on this information, it can be said that bi-partite compound needles are more advantageous than the other needle types [5].

C. Determination of Yarn Count and Yarn Twist

Yarn count is a numerical expression which indicates the thickness of a yarn and determined by its mass per unit length. An important consideration in the determination of a yarn count is machine gauge. As it is seen in the previous chapters, the finer the machine gauge, the finer required the yarn count. Choice of yarn count is also restricted by the type of the knitting machine and the knitting construction and determinant for designating the thickness of the needle hook and sinkers [4,5].

Another important issue when choosing a yarn for knitting processes is yarn twist. The aim of twisting is to strengthen the yarn. Yarn twist is directly related with twist coefficient. As is known, yarn strength increases when the twist coefficient increases by a certain value. On the above values, a decrease in strength is observed. Additionally, it is known yarn twist factor is the most important variable influencing fabric spirality [5, 6]. Chen et al. indicated that when the twist factor of single yarns has no significant effect on spirality, correlation between angle of spirality and twist factor of ply yarn is quite strong. Also, it is pointed out that a fabric knitted with a highly twisted yarn will have higher spirality [6].

D. Needle Hook Thickness and Sinker Thickness

Correlations between needle hook thickness, sinker thickness and yarn count are the essential values which define minimum distances between knitting elements. Needle cylinder undertakes the role of sinker in sinkerless knitting machines. Under these circumstances, two yarns are located between cylinder teeth at the same time. One of them is the yarn which will form the new loop and the other one is the yarn which forms the legs of the previous loop. In this position, new yarn is exposed to tension between teeth while the former yarn is released. When one of these two yarns is on top of another, it is possible to ignore yarn of the previous loop in the calculation of the distances between the teeth. The same situation is acceptable for double cylinder knitting machines.

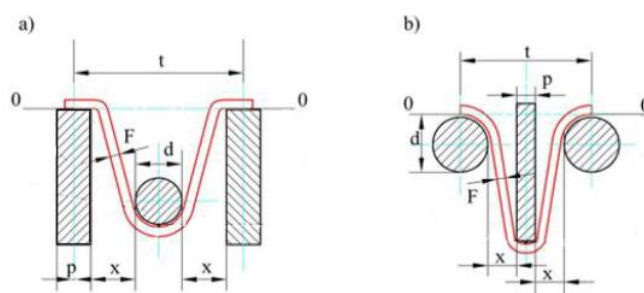


Figure 1: Knitting element and yarn positions for a) needle hook and b) sinker (t: amount of the needle movement, F: yarn count, d: needle hook thickness, p: sinker thickness, x: minimum distance between needle and sinker)

Figure 1.a shows the yarn forming process using the needle hook and Figure 1.b shows the yarn forming process using sinker. As seen in the figure, the amount of the needle movement is calculated using the equation (1) for both cases:

$$t=d+p+2x \quad (1)$$

In the equation, t, d, p and x represents amount of the needle movement, needle hook thickness, sinker thickness and minimum distance between needle and sinker, respectively.

It is understood from the Figure 1 and equation (1) that yarn count must be smaller than minimum distance between needle and sinker to avoid the yarn to be squeezed. Therefore, needle hook thickness and sinker thickness are determined as certain values according to machine gauge and yarn count. Relations between these four parameters are resulted in experience.

When the correlations between needle hook thickness (d), sinker thickness (p), and minimum distance between needle and sinker (x) were examined for different knitting machines, it is seen that rates can be chosen the same for machines in similar gages. Accordingly, in the process of designing a new machine, needle hook thickness (d) and sinker thickness (p) parameters can be chosen according to a similar machine whose parameters are known [5].

III. RESULTS AND DISCUSSION

In this study, basic construction parameters of knitting machines are examined, and they are listed as machine gauge, needle type, yarn count, needle hook thickness and sinker thickness. Each parameter is highly important to design a new machine and they are entirely related to each other. Here, all these parameters and their relations are summarized in Table 1.

Table 1: Relations between machine gauge (E), needle hook thickness (d), sinker thickness (p), yarn count (F) and minimum distance between needle and sinker (x) for different machines [5]

Machine type	Machine gauge	d/E	p/E	x/E	x/F
Circular knitting machine with latch needle	3-10	0,20	0,17	0,315	1,50
	10-16	0,25	0,17	0,290	
	16-28	0,30	0,17	0,265	
Socks knitting apparatus	6-10	0,18	0,17	0,325	2,25
	10-22	0,25	0,17	0,290	
	22-34	0,32	0,17	0,245	
Flat knitting machine	All gauges	0,20	0,20	0,300	2,25
Warp knitting machines with bearded needle		0,34	0,20	0,230	1,69
Fully fashioned knitting machines	15-36	0,30	0,17	0,265	1,50

IV. CONCLUSION

Although Turkey is in a good place of producing textile products, it is not possible to tell the same for textile machinery production. In the future, to have a right to say in the textile industry, textile machines should be produced in our country. For designing the textile machines, design parameters should be determined at first. When previous researches were examined, it is seen that there is not much work to be done in this regard.

According to this information, in this study it is studied to determine the basic construction parameters and relations between them. It is concluded that the most basic parameters are machine gauge, yarn count, needle hook thickness, sinker thickness, and minimum distance between needle and sinker. The features of other parts must be taken into consideration in designing and selecting the elements and the design should be taken as an integral part.

V. REFERENCES

1. S. C. Ray, *Fundamentals and Advances in Knitting Technology*. WPI Publishing, 2012.
2. A. Bayazit Marmaralı, *Atkı Örmeciliğine Giriş*, İzmir: E.Ü. Tekstil ve Konfeksiyon Araştırma-Uygulama Merkezi, 2004.
3. M. A. Islam and A. N. M. A Haque, "Selection of suitable machine gauge by considering the GSM, shrinkage and spirality of single jersey knit fabric", *Research Journal of Science and IT Management*, 3(3), pp. 50-55, 2014.
4. D. J. Spencer, *Knitting Technology: A Comprehensive Handbook and Practical Guide (Third Edition)*. Cambridge, England: Woodhead Publishing Limited, 2001.
5. V. N. Garbaruk, *Proektirovanie Trikotazhnykh Mashin [Design of Knitting Machines]*, Leningrad: Masiostoenie, 1980.
6. Q. H., Chen, K. F., Au, C. W. M., Yuen, and K. W. Yeung, "Effects of yarn and knitting parameters on the spirality of plain knitted wool fabrics", *Textile Research Journal*, 73(5), pp.421-426, 200

Investigation of the Energy Profile of Karaman

Bekir Cirak¹, Mehmet Onur Ogulata¹,

Sezgin Eser¹, Yasin Unuvar²

¹ Karamanoğlu Mehmetbey University, Engineering Faculty, Mechanical Engineering Department, Yunus Emre Campuses, Karaman / TURKEY

² Karamanoğlu Mehmetbey University, Graduate School of Natural and Applied Sciences, Advanced Technologies Master Science, Yunus Emre Campus, Karaman / TURKEY

Abstract – In recent years, the energy demand has increased rapidly due to increasing population, industrialization, urbanization and developing technologies. Also, the troubles in production and consumption of this necessity once again show the importance of effective and efficient use of energy resources. For this reason, it is very important to know the energy resources potential in our country and to use them effectively. In this study, Karaman province energy profile which is one of the most important energy potential areas of Turkey has been studied. Renewable energy sources such as sun, wind, biomass, geothermal energy sources and non-renewable energy sources, fossil energy sources and natural gases shined out in Karaman..

Keywords - : Renewable energy, Solar Energy, Wind, Biomass, Geothermal energy, Oil

I. INTRODUCTION

NOWADAYS, the negative effects of the residual gases that are released by burning of fossil fuels to the environment has led the governments and scientists to seek alternative energy sources. Especially in big cities, pollutant emissions from the vehicles pollute the whole atmosphere and cause an increasing danger called greenhouse effect. In addition, the energy crisis caused by the depletion of fossil fuel sources had an impact on the attempt to use alternative energy sources. For this purpose, various researches, laboratory experiments have been performed and alternative sources have been found as fuel in vehicles. Alternative fuel types such as hydrogen, methanol, ethanol and LPG have been used in vehicles and some of them are still in use. There are some problems in the use of these resources and the development of this sources is still in process. For example, storage problems have occurred in the use of hydrogen as fuel. There is a high-volume problem for the storage of hydrogen as a pressurized gas or as a metal hybrid and also there are problems such as high cost and evaporation losses for storage in liquid form. Because of such problems researchers focus on solar energy in their researches.

Table 1. The Use Of Alternative Energy Sources

	Alternative energy	Source
1	Nuclear Energy	Uranium
2	Solar Energy	Sun
3	Wind Energy	Wind
4	Wave Energy	Oceans and seas

5	Natural Gas	Underground sources
6	Geo-Thermal Energy	Underground Waters
7	Hydraulic potential	Rivers
8	Hydrogen	Water & Hydroxides
9	Bio-mass, bio-diesel, bio-gas	Biological waste, Oils

It is necessary to investigate the usability of alternative clean energy sources (renewable energy sources: solar, geothermal, wind)

- The use of other alternative fuels considered suitable for use in the regulation for heating purposes should be encouraged.
- Renewable energy, practically unlimited, is the energy that can be used continuously and repeatedly.
- Nonrenewable energy is defined as energy that is used and does not regenerate in a short time interval. Lifetime of the nonrenewable sources are about; 40 years for oil, 62 years for natural gas and 240 years for coal.

II. KARAMAN AND ENERGY

The demand for natural resources and energy are increased because of population increase, urbanization, industrialization and trade opportunities because of globalization. Turkey is the country with the fastest increase in demand for energy in place of the OECD countries for last decades. Turkey, after China, is the second largest economy with demand for electricity and natural gases since 2002. Studies show that this trend will continue in the medium and long term. Turkey's energy-related strategy and policy are based on energy efficiency, energy supply security, alternative energy sources, sustainability and the acquisition of domestic resources into the economy. For this reason, it is important to utilize domestic and renewable energy resources as a priority. Within the framework of the energy policies of our country, the share of renewable energy resources in general energy consumption will be increased to at least %20 in 2023 and the share of renewable energy resources in total electricity production will be increased to at least %30. In this context, it is aimed to maximize the potential of the country by extending the use of solar energy for electric energy production. Turkey follows the latest technological developments in the use of solar energy in electricity production. It is aimed that in 2023, solar power capacity will be reached to 5000 MW (including unlicensed projects).

Regarding energy saving in the city; studies on illegal use of electricity, compensation and digital meter usage are carried

out. The region has the potential to produce solar energy, wind energy, biogas and micro and small-scale HPPs. According to the solar energy atlas based in Karaman, Ayrancı district is the most advantageous district in terms of total solar radiation values.

A. Solar Energy

Karaman has the highest solar radiation value in Turkey. According to the Potential Atlas of Solar Energy (GEPA); Turkey's average annual total solar radiation is about 500 thousand kWh / m² year, the total daily radiation intensity is 4,17 KWatt /hour per square meter. Karaman has radiant intensity of annual 700 000 KWh/m², and this value is above average of Turkey. In this respect, it is very convenient in terms of heat and electricity production from solar energy. Karaman is one of the most suitable cities to obtain solar energy because of its solar radiation, hours of sunshine, geographical position, lack of a mountain block the sunlight sunrise and sunset time, low amount of precipitation (especially snow), low average temperature, low moisture content etc. Due to these features in electricity generation, 67 companies established 80 measuring stations to Karaman in order to be able to produce licensed electricity to city,

Within the scope of the 38 MW Solar Energy Generation License announced by the Energy Market Regulatory Authority (EMRA); there was a high level of participation over demand and also 699 unlicensed electricity generation applications were made for 607859kWatts

Karaman has the capacity of 530,7 MW HEPP and RES. Furthermore, the electricity potential has been diversified by signing additional agreements. Thus, Karaman produces 2.2% of Turkey's energy production. It is planned to increase this rate to 10% within 5 years. According to the Karaman district-based solar energy atlas, Ayrancı district is the most advantageous district on the basis of total solar radiation values. In Karaman, solar energy is utilized by obtaining hot water through panels placed on the roof of buildings.

Table 2. Operating Solar Power Plants in Karaman

	Power Plant	City, District	Company	Power
1)	Konar Enerji Ayrancı GES	Karaman, Ayrancı	Konar Enerji	3,00 MW
2)	Emrullah Er GES	Karaman, Kazımkarabekir		1,00 MW
3)	Cerrahi Eğitim İnşaat GES	Karaman, Kazımkarabekir	Cerrahi Eğitim İnşaat	1,00 MW
4)	Eksun Enerji Güneş Santrali	Karaman, Ayrancı	Eksun Enerji Üretim	0,99 MW
5)	Halis Cem Enerji Güneş Enerji Santrali	Karaman, Ayrancı	Halis Cem Enerji	0,99 MW
6)	Karaman Belediyesi GES	Karaman, Merkez	Karaman Belediyesi	0,99 MW
7)	Onurlu Karaman Güneş Enerjisi Santrali	Karaman, Merkez		0,50 MW
8)	Karaman İl Özel	Karaman,	Karaman	0,50

	İdaresi Güneş Enerji Santrali	Merkez	İl Özel İdaresi	MW
9)	KMU Güneş Enerjisi Santrali	Karaman, Merkez	KMÜ	0,46 MW
10)	Çavsa Güneş Enerjisi Santrali	Karaman, Merkez		0,30 MW
11)	Hacı Hasan Armutlu GES	Karaman, Merkez		0,12 MW
12)	Ermenek Hükümet Konağı GES Tesisi	Karaman, Ermenek	Ermenek Hükümet Konağı	0,040 MW

Table 3. Under Construction Solar Power Plants

	Power Plant	City, District	Company	Power
1)	Ermenek Güneş Enerji Santrali	Karaman, Ermenek		9,00 MW
2)	Konar Enerji Ayrancı GES	Karaman, Ayrancı	Konar Enerji	3,00 MW
3)	Cereyan Karaman Güneş Enerji Santrali	Karaman, Merkez	Solar Cereyan	2,97 MW
4)	3E Ermenek GES	Karaman, Ermenek		1,00 MW

Table 3. Pre-licence GES

	Power Plant	City, District	Company	Power
1)	Mümine Hatun Güneş Enerji Santrali	Karaman	Teknar Enerji	4,88 MW

Table 4. Planned Solar Power Plants

	Power Plant	City, District	Company	Power
1)	Teksin Enerji Güneş Enerji Santrali	Karaman	Teksin Enerji	33 MW

Existing power generation is capable of meeting only 50% of the amount of energy will be needed in 40 years. For this reason, in Turkey and other countries have felt the necessity of obtaining energy from sunlight. Ayrancı, has an annual average 2230 hours of exposing sunshine and this is beyond Turkey and Europe average.

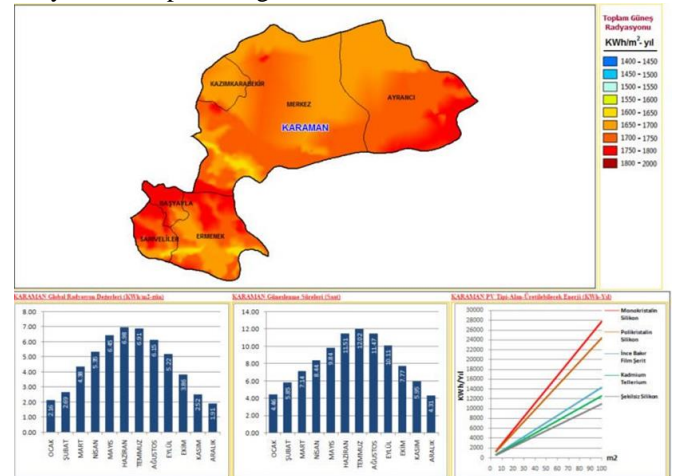


Figure 1. Karaman Solar Energy

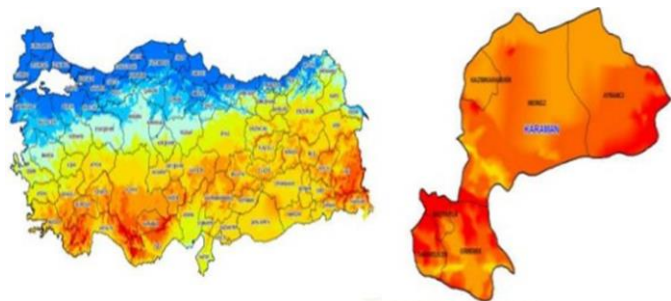


Figure 2. Solar Energy Potential

In Ermenek, a power plant was established on an area of 217000m² which could meet the electricity needs of 10 thousand houses annually. Located in the Taseli plateau and with an altitude of 1300 meters, the district is surrounded by high mountains and hills.



Figure 3. Ermenek Power Plant

Farming, orcharding and lignite mining are the main livelihoods of people live in Ermenek (approximately 30000 people). A solar power plant was established by a private company in the area of 217000m² in the Arpakırı in the north of the city, because of the solar potential of Arpakırı. The plant is able to meet the electricity needs of 10 thousand houses annually.

B. Wind Energy

Borusan EnBW Energy also commissioned two important wind power plants, Harmanlık WPP and Koru RES, which have completed the investment together with the "Mut Wind Energy Plant" WPP, which was established within the boundaries of the village of Gökçetaş in the Mut District of Mersin and Karaman Merkez Medreselik. General as having 90 meters in height and length of 60 meters wings established in Mut wind power plant, each of the 16 windmill is to produce 3 MW electric power, is scheduled to make a significant contribution to Turkey's energy production through wind power plant and the environment.

On 5 June 2015, the 5 phase of the second phase of the 16.8 MW Mut Wind Power Plant, which was commissioned by the first phase of the 19.8 MW Mut Wind Power Plant, was commissioned. It is known that the power plant works at full

capacity.

Karaman has a wind potential suitable for wind energy production. Wind Speed Distribution 50 M for economic WPP investment, wind speed of 7 m/s or above is required. Capacity Factor Distribution 50M For economic WPP investment, a capacity factor of 35% or more is required. The power capacity of the wind power plant that can be installed in Karaman province is shown below.

Table 5. Power Plants in Karaman

	Project Name	Type	Power (Mw)	Project Phase
1.	Merkezi Mut	Rüzgar	50,00	Operating
2.	Mut	Rüzgar	50,00	Project
3.	Akyel-1-2 (40+10 MW)	Rüzgar	50,00	Project
4.	Hilal-2	Rüzgar	7,00	Project
5.	Yellibel	Rüzgar	50,00	Project
Genel Toplam:			157,00	

Table 6. Operating Wnd Power Plant

	Power Plant	City, District	Company	Power
1	Hilal 2 RES	Karaman, MERKEZ	Sanko Enerji	7,00 MW

Table 7. Licenced Wind Power Plant

	Power Plant	City, District	Company	Power
1)	Akyel 1 Rüzgar Enerji Santrali	Karaman, MERKEZ	Akyel RES Elektrik Üretim	40 MW

Karaman is generally a region with wind energy potential. Due to the development of tribune technology that can generate electricity at different wind speeds, the region (TR-52) has the possibility of generating electricity from wind energy in southern districts such as Ermenek, Sarıveliler and Başyayla, which have moderate wind presence. The total installed capacity of the wind power plant for Karaman is 1,860,08 MW

Table 8. The capacity of hydroelectric power that can be installed according to the provinces in Turkey

City	Total Area	Power (MW)	City	Total Area	Power (MW)
Balıkesir	2765,47	13827,36	Kütahya	38,03	190,16
Çanakkale	2602,51	13012,56	Giresun	32,1	160,48
İzmir	2370,86	11854,32	Çorum	31,23	156,16
Manisa	1060,46	5302,32	Bolu	23,42	117,12
Samsun	1044,50	5222,48	Kocaeli	15,57	77,84
Muğla	1034,19	5170,96	Karabük	14,67	73,36
Tekirdağ	925,33	4626,64	Niğde	12,42	62,08
İstanbul	835,39	4176,96	Bartın	12,32	61,6
Bursa	776,24	3881,68	Bingöl	12,29	61,44
Mersin	706,24	3531,20	Burdur	11,63	58,16
Edirne	694,02	3470,08	Eskişehir	8,22	41,12
Hatay	682,8	3414	Hakkari	5,89	29,44
Kırklareli	615,87	3079,36	Bitlis	4,42	22,08

Tokat	600,5	3079,36	Van	3,88	19,36
Aydın	504,75	2523,76	Erzurum	3,55	17,76
Ordu	455,15	2275,76	Trabzon	3,38	16,88
Kahramanmaraş	414,48	2072,40	Siirt	3,01	15,14
Kayseri	377,06	1885,28	Tunceli	2,62	1312
Konya	372,02	1860,08	Artvin	1,96	9,76
Sivas	328,5	1642,48	Uşak	1,86	9,28
Isparta	284,62	1423,12	Nevşehir	1,65	8,24
Malatya	279,01	1395,04	Batman	1,58	7,92
Amasya	239,9	1199,52	Kars	0,67	3,36
Adıyaman	239,39	1196,88	Sakarya	0,4	2
Antalya	234,08	1170,40	Iğdır	0,35	1,76
Yozgat	215,3	1076,48	Gümüşhane	0,21	1,04
Elazığ	205,68	1028,40	Ağrı	0,05	0,25
Karaman	186,72	933,6	Şanlıurfa	0,05	0,24
Adana	179,74	898,72	Aksaray	0	0
Afyon	172,05	860,24	Ankara	0	0
Osmaniye	143,62	718,08	Bayburt	0	0
Diyarbakır	127,01	635,04	Düzce	0	0
Yalova	106,62	533,12	Kilis	0	0
Kastamonu	102,98	514,88	Kırıkkale	0	0
Mardin	101,78	508,88	Kırşehir	0	0
Erzincan	76,54	382,72	Muş	0	0

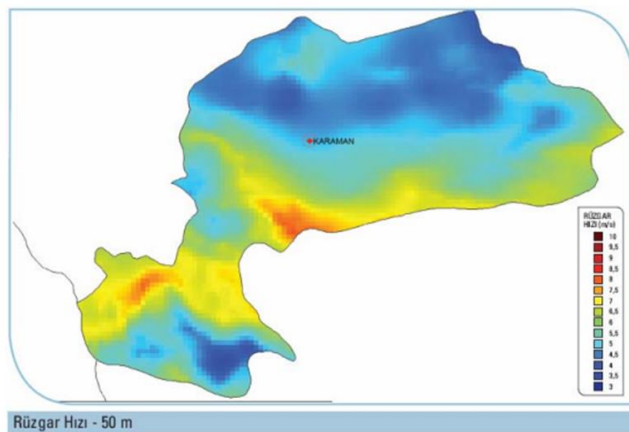


Figure 4. Wind speed distribution (50m)

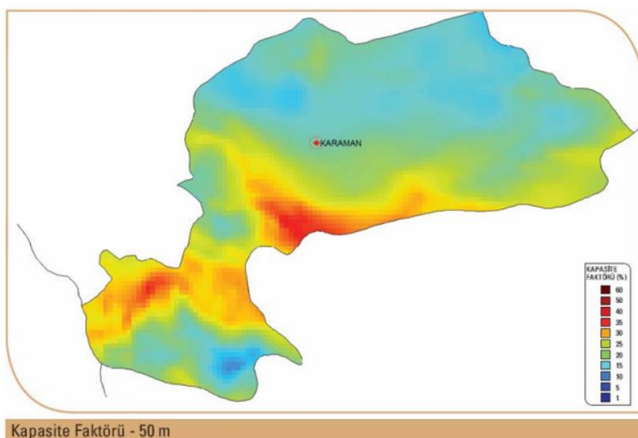


Figure 5. Capacity Factor Distribution

According to REPA, the wind energy potential of Karaman is 1860,08MW. Considering the 50m wind atlas prepared for Turkey it was observed that the average of the atlas was matched with the measurement was made KMU. There are some factors that hinder the establishment of the wind power plant. These are; higher than 1,500 m high altitude, more than 50 m deep, lakes, sea-like parts and settlements and their relatives. It is accepted that wind power plants can be installed in regions with a capacity factor of 25 percent or more.

It is assumed that the Wind Power Plant cannot be installed in gray areas. 7m / s or more wind speeds are required in economic wind power plant areas, and these areas are the Karaman city center and Ermenek, Mut, Başyayla and Sartavul regions. The capacity factor map is composed of annual wind data at a height of 50 m and a turbine with a power of 1.5-2.0 MW. In the calculation, 250-300 m between the turbines and 500 m between the turbine rows were taken. It is determined that 6 turbines can be placed on an area of 1 km².

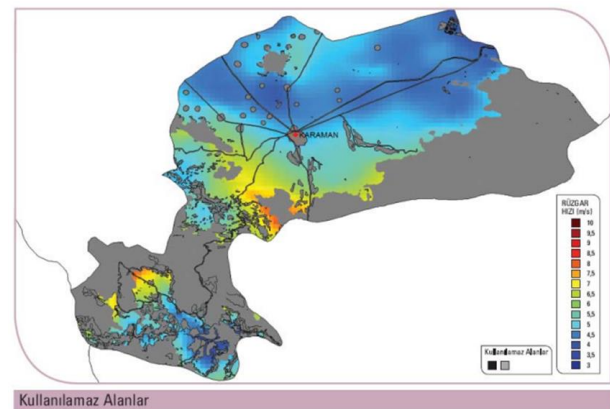


Figure 6. Wind Power Plant Installable Areas

For an installed capacity of 1 MW, the approximate cost of the wind farm is 1 - 1.2 million Euro. However, one of the important points that wind power plant investors should pay attention to is the possibility of connecting the project to the interconnected system. TEİAŞ has limited the installed power of the wind projects to 5% of the short circuit power of the substation to be connected. This means that no matter how much the project's wind potential is, the installed power is limited by the interconnected system connection. In fact, it can be seen that most of the projects with high wind potential are not connected to the system. Investors need to know the potential of the region along with the wind potential.

Table 9. 50m Wind Energy Potential

50 m Wind Power (W/m ²)	50 m Speed of Wind (m/s)	Area (km ²)	Total Installed Power (MW)
300 –400	6.8 –7.5	153,50	767,52
400 –500	7.5 –8.1	24,21	121,04
500 –600	8.1 –8.6	8,86	44,32
600 –800	8.6 -9.5	0,14	0,72
> 800	> 9.5	0	0
		933,60	186,72

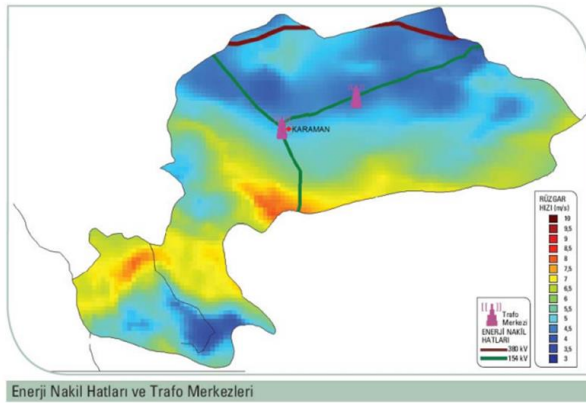


Figure 6. Substations and Power Transmission Lines

For economic WPP investment, wind speed must be at least 7 m/s. For an economic RES investment, the capacity factor must be at least 35%. For this reason, areas with a capacity factor of over 35% appear only in limited regions. The contours on the given map were obtained by the estimation methods. The potential determination measurements shall be repeated with at least one-year period in accordance with the core diameter of the turbine intended for further analysis.

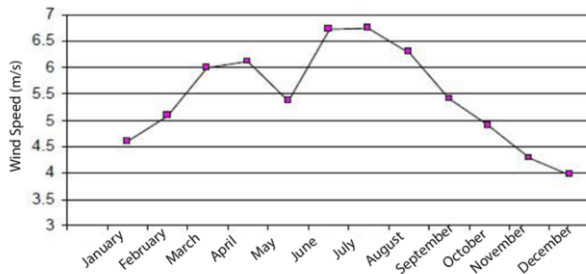
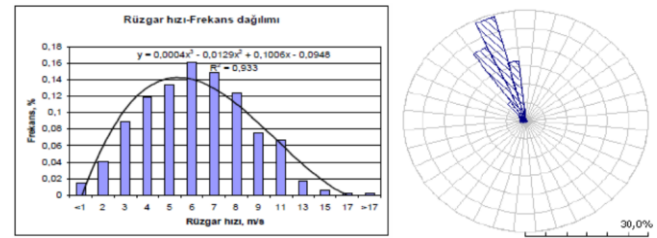


Figure 7 Wind Speed Change Graph

The monthly average wind velocities obtained from the measurements made with a 40-meter-high measurement system at the Karamanoğlu Mehmetbey University Yunus Emre Campus are given in the figure above for 2017. It is noteworthy that the wind speed value for Karaman wind values is higher in the summer months. This shows that wind energy can be used easily in Karaman for agricultural irrigation and energy needs. Because the need for energy in agriculture is higher in summer and lower in other months. The analysis of the wind data shows that the unit wind power on a 40-meter-high tower was 308 W / m² for 2005, the annual average wind speed was 6.01 m / s and for 2006 it was 295 W / m² and 5.87 m / s respectively. Wind speed values may fluctuate by $\pm 10\%$ per year.



The turbulence density, which is defined as the ratio of the standard deviation amount of the average wind speed data to the average velocity value (V_m) of this data, has been calculated. When the data from 2005 were analyzed, the average speed standard deviation was 0.75, the average turbulence density was 0.12, and the standard deviation of the direction was 10.30 and 2006 data were accepted to be in accordance with the standards as 0.65, 0.12 and 11.20, respectively. It is recommended to install a wind power plant in areas where turbulence density is greater than 0.25. In some areas of Karaman region, it has been calculated that the power plant payback period is approximately 4 to 8 years. As the wind speed rises, the payback period decreases very quickly.

C. Water

The existing water resources in the city are used for agriculture and irrigation purposes. The city does not have a seashore.

D. Wood

The wood is used as fuel and about 20-25 thousand sten firewood is obtained annually from the forest.

E. Natural Gas

There is no information on natural gas reserves within the provincial boundaries.

F. Biomass (Biogas, Wood, Turf)

Biomass sources are wood, animal and plant residues. These sources are used in place of fossil fuels used in boilers. The steam generated by the combustion of wood or waste is used in conventional steam power plants. Biogas production is carried out when the animal manure reacts in a closed environment without oxygen. Biogas, colorless, odorless, lighter than air, with a bright blue flame and the combination of organic matter in the composition depending on the composition; It is a mixture of 40-70% methane, 30-60% carbon dioxide, 0-3% hydrogen sulfide and a mixture of nitrogen and hydrogen.

The garbage of metropolitan cities is also a good thermal resource. Garbage gas obtained as a result of storage of waste is an important energy source containing 60% methane. This resource is evaluated with the facilities established in many countries of Europe. Istanbul Metropolitan Municipality produces electricity using the city's garbage. Another thermal source is biodiesel. Biodiesel; It is a product that is released as a result of the reaction of oils or animal fats obtained from oilseed plants such as rapeseed (canola), sunflower, soy, safflower or animal oils with a short chain alcohol (methanol or ethanol) in the presence of a catalyst. Domestic frying oils and animal fats can also be used as biodiesel raw materials.

There is no use and consumption of biogas within the provincial boundaries. In rural areas, the dike is also used as fuel.

As a result of the expansion of biofuel production, national resources will be evaluated and energy imports will be reduced. While an increase in national income will be achieved, employment will be provided with a new business area. In addition, the use of environmentally friendly fuel, with the EU legal requirements and regulations in accordance with the processing of organic waste, environmental pollution control will be realized

G. Petroleum

There is no petroleum reserve within the provincial borders.

H. Geothermal Fiels

There is no geothermal energy reserve within the provincial boundaries.

I. Thermal Energy and Coal

Table 10. Coal Potential

No	Project Name	Type	Power (Mw)	Project Phase
1.	Komet DGÇS	DG+Solarş	1.080	Under Construction
2.	Bio Kütile	Biogas	1,44	Under Construction
3.	Ayrancı Kömür Santrali	Coal	5.000	Fisibility
Total :			6.081,44	

Type	Country	Location	Quality	Reserve
Coal	Ermenek	Halimiye	AID 4.063 Kcal/kg	Apperent 2.000.000 t. Possible 3.900.000 t.
Coal	Ermenek	Boyalık	AID 3.262 Kcal/kg	Possible 1.700.000 t.
Coal	Ermenek	Muzvadi	AID 5.500 Kcal/kg	
Coal	Ayrancı	Ayrancı Dokuzyol Akçaşehir		1.800. Milion t.

J. Hydrogen Energy

Since hydrogen is a compound, it is not a natural source of energy. The most well-known compound of hydrogen is water. However, hydrogen is produced from primary raw materials with different energy sources and conversion processes are used in its production. Therefore, it is an energy carrier developed almost a century after electricity and interpreted as an alternative source of the future. Hydrogen is a fuel suitable for flameless combustion on catalytic surfaces as well as direct

use in internal combustion engines. However, the subject of fuel cells is the main field for researches about hydrogen energy. Fuel cells are energy conversion technology that does not harm the environment. Without the use of a steam boiler or turbine, fuel cells produces electrical energy only by the chemical reactions.

Hydrogen energy system is new, but hydrogen production dates back to earlier times. 500 billion m³ of hydrogen is produced, stored, transported and used in the world every year. Because of hydrogen does not contain carbon, it does not cause environmental problems like fossil fuels does.

K. Hydraulic Energy

The potential and kinetic energy of the water is collected in the reservoirs of the reservoirs. Seas, lakes and rivers form hydraulic resources. Hydraulic resources are inexhaustible and cheapest energy sources. Although thermal sources such as coal, oil and natural gas can be exhausted, hydraulic resources are inexhaustible (renewable) potential sources of energy. 17% of the world electricity production is produced by using hydro power.

Table 11. Hydro Power Plants

NO	Project Name	Installed Power (MW)	Stage of Project
1	Kepezkaya	28	Operating
2	Damlapınar	16,4	Operating
3	BalkusanHES	38,8	Operating
4	Günder HES	28,8	Operating
5	Ermenek HES	300	Operating
6	Daran HES	68,7	Operating
Total:		480,7	
7	Bucakkışla HES	33,50	Under Construction
8	Gökdere HES	30,53	Under Construction
9	Zeyve HES	3,720	Under Construction
10	Yalnızardıç Barajı ve Berat HES	21,190	Project
11	Ballık HES	23,70	Project
12	Güneyyaka HES	6,63	Project
13	Yalman II HES	2,90	Project
14	Efsun HES	9,00	Fisibility
15	Ketir HES	29,29	Fisibility
16	Yalman HES	1,00	Fisibility
17	İncekaya HES	21,00	Fisibility
Hydroelectric Plant Total:		663,16	

L. Nuclear Energy

A very large amount of energy is released as a result of the fission of heavy radioactive atoms (such as uranium) into smaller atoms by the attack of a neutron (fission) or by the fusion of light radioactive atoms to form heavier atoms (fusion). This is called nuclear energy. No research has been conducted on whether or not radioactive resource reserves exist in the province.

M. Mine

The investment potential of Karaman raw mineral deposits is also very high.

Table 12. Mine Reserves of Karaman

Type	Country	Location	Quality	Reserve
Aluminum	Ayrancı	Gerdekkirse	SiO ₂ :%2,2 Fe ₂ O ₃ :%31 TiO ₂ :%3,4	Appearance 1.000.000 t. Possible 2.000.000 t.
Iron	Ermenek	Kazancı Sarıvadi		
Iron	Ermenek	Kazancı	Fe:%3-50	Apperent 60.000 t.
Zinc-lead	Ermenek	Göktepe Mevliat mezar	Pb: %3,85 Cd: %0,01	
Barit	Merkez	Ağaçobaköyü	BaO: %62	Appearance
Bentonit Kaolen	Ermenek	Esentepe Köyü		
Meerschaum	Kazımkarabekir	Sodur (Sinci) Deveyatağı Kızılkırtepe Gökuyataktepe	MgO: %46,6 SiO ₂ : %1,68 CaO: %1,35	Appearance 197.500 t. Possible 3.480.000 t.
Meerschaum	Kazımkarabekir	Erentepe (Sodur)	MgO: %46,6 SiO ₂ : %1,68 CaO: %1,35	Appearance 316.700 t. Possible 4.640.000 t.



III. RESULTS AND RECOMMENDATIONS

According to 2017 data, non-renewable energy resources in Turkey is dependent on foreign by 73.8%, and for electricity generation this value is 55% percent. This dependency has a great negative in terms of security of supply and economic development. Turkey's dependence on foreign energy decreased slightly in terms of the extent of the use of domestic resources. According to the analyzes and the data collected, Karaman is rich in energy resources. Due to its geographical location, Karaman province should make more use of renewable energy sources (especially solar energy) than its current situation. In addition, it should benefit more from biomass energy that can be obtained from the recycling of agriculture and domestic waste.

The energy source of the Karaman province has the highest ratio and the energy source hydro power has a power of approximately 250 MW. Although it has a potential on average in terms of solar energy, Karaman is not used sufficiently. It has a potential of about 1580 kWh / m². Karaman province has a 7.92 MW wind energy potential as of the current situation. However, there are no facilities for wind energy. The biomass energy, which is another renewable energy source, has an energy source of 69.618,95 TEP / year, but there is no facility. A similar situation applies to the geothermal energy source. There is no active geothermal power plant in Batman province.

As a result, Karaman province has renewable energy sources as well as non-renewable energy resources. It should make more use of renewable and clean energy resources. It needs to make more use of solar energy due to its geographical location. On the other hand, hydroelectric energy potential should be used more efficiently. Biomass energy should be considered as effective by taking the cheapest energy recovered energy principle. Karaman province, renewable,

fossil (traditional, conventional) renewable, alternative energy sources, by reducing coal from fossil fuels, ash, water, sulfur to reduce the rate, calorific (thermal) to increase the value of the process (to increase the thermal value of the fuel, to minimize pollution If necessary, it can be used for direct heating to minimize air pollution, environmental pollution and solid waste risks by blending with imported top quality coal, improving, enriching and fertilizing processes, and can be focused on energy production through thermal power plants by selecting environmentally friendly, high technologies.

From renewable energy sources (RES), starting from Mugla, Turkey, Antalya, Karaman, Adıyaman, Karaman, et al It is an opportunity for Karaman to be in the belt of efficient solar energy potential, which is exposed to the maximum sunshine duration, including our South-East provinces. Alternative renewable energy sources such as solar power plants (GES), geothermal power plants (JES), organic origin waste or materials (vegetable-fruit, park-garden, slaughterhouse waste, offal, whole-winged and small, large-scale animal fertilizers, shelf life is completed, stale and dairy products anaerobic (airless) in the environment with metanization of biogas plants (BIGS) "recovery" within the framework of evaluating the methane gas generated by burning the cogeneration system twice by burning energy, the remaining aqueous pulp 100% organic can be used as fertilizer in agriculture, park-gardens, smooth, environmentally friendly, clean, alternative, renewable energy resources can be started.

I would like to thank Karamanoğlu Mehmetbey University, which was established in 2008, and the faculty members of the Faculty of Engineering Energy Systems Engineering Department.

REFERENCES

- [1] .Karaman İli Çevre Durum Raporu, Karaman Valiliği İl Çevre ve Orman Müdürlüğü, 2017.
- [2] Çevre Bakanlığı, Çevre Referans Laboratuvarı analiz sonuçları, 2017.
- [3] TEDAŞ Müessese Müdürlüğü, Karaman.
- [4] Karaman MTA Bölge Müdürlüğü Tarafından Önerilen ve Yürütülen Projeler, Jeotermal Enerji
- [5] *MEVKA Ön Bölgesel Raporu, 2017.*
- [6] Türkiye Çevre Atlası, T.C. Çevre ve Orman Bakanlığı
- [7] Yenilenebilir Enerji, <http://www.bugday.org/article.php?ID=79>
- [8] T.C. Enerji ve Tabii Kaynaklar Bakanlığı Yenilenebilir Enerji Genel Müdürlüğü verileri
- [9] http://www.obitet.gazi.edu.tr/obitet/alternatif_enerji/yenilenebilen_enerji_kaynaklari.htm
- [10] www.karaman.org
- [11] http://www.yegm.gov.tr/YEKrepa/REPA-duyuru_01.html
- [12] <http://www.enerjiatlas.com/ruzgar-enerjisi-haritasi/karaman>

APPLICATIONS OF 3D PRINTING TECHNOLOGY IN DENTISTRY

B. CIRAK¹ and M.O. OGULATA² and S.ESER³ and Y. UNUVAR⁴

¹ Karamanoglu Mehmetbey University, Karaman/Turkey, bcirak@kmu.edu.tr

² Karamanoglu Mehmetbey University, Karaman/Turkey, onurogulata@kmu.edu.tr

³ Karamanoglu Mehmetbey University, Karaman/Turkey, sezgineser@kmu.edu.tr

⁴ Karamanoglu Mehmetbey University, *Graduate School of Natural and Applied Sciences, Advanced Technologies Master Science*, Karaman/Turkey, yasininuvar70@hotmail.com

Abstract - In this study, applications of 3D printing techniques in dentistry sector are explained. In 3D applications, there are single tooth coating, bridge, implant tooth making, partial and prosthetic tooth making studies. These applications, which are made with 3d instead of manual according to the mouth of the patient, are longer lasting and useful. Therefore, 3d printing technology has started to be important and necessary in dentistry. It is preferred to use an abrasion resistant plastic material and porcelain material. The important point here is that a carcinogenic material should not be used as it is a study of oral and dental health. Such a study should be done by health and chemistry society.

Keywords - Teeth; Dentistry; 3D Printer; Design

I. INTRODUCTION

THE 3D printer, known as the technology of the future, is a machine that models an imaginary part in a computer environment and transforms it into tangible concrete objects in a short time. In usually, the 3D dental models (including 3D single tooth) used in CAD/CAM dentistry system are mostly obtained by optical digitizers, which is typically represented by using a watertight triangular mesh. The 3D dental model is an integral model without obvious blending boundary between the single-tooth and the soft tissues. Two adjoining teeth sometimes are fused together and without obvious tooth gap, due to teeth overlapping, lower measurement precision, and limited resolution triangulating methods during digitizing step. In order to satisfy the prerequisites of manufacturing the dental restorations and assessing the virtual dental behaviors, the teeth have to be independent of each other and keep the original shape of the real tooth. The accurate single-tooth shape restoration and extraction techniques for the 3D dental model play a vital role in CAD/CAM dentistry system [1].

The use of 3D CAD models in dentistry has great advantages over conventional physical models. Many dental and maxillofacial surgery applications such as endodontic procedures, treatment of malocclusion problems [2] and treatment simulations require an accurate knowledge of the 3D shape of teeth. Physical models require physical space for

storage, adding financial and logistic burdens, while virtual models are stored electronically.

Model retrieval is greatly facilitated, communication with other dental specialties is improved, and the traditional duplicating of plaster casts, handling, and shipping becomes obsolete. Several companies now offer virtual study models. Proprietary software for virtual model analysis is provided by the companies, giving the clinician valuable tools for almost any application. The ability of 3D virtual models to represent the patient's dentition accurately and the validity and reproducibility of measurements on these models, have been extensively studied [4]. Because it is less time consuming, easier to use, and cost effective at comparable levels of clinical accuracy, a strong argument can be made for the routine application of computer-based 3D models [2].

II. 3D PRINT

3D printing technology began in the 1980s. However, after 2010, the name has become more pronounced and has become more widely used today. The reason for this is that more and more entrepreneurial firms invest in this technology, the interest of academia, the advantages and advantages of technology in many areas, and the reduction of production costs. The first 3D was produced in 1984 by Chuck Hull of 3D Systems. The fields where 3D printer is used and applied are shown in Fig.1 Accordingly, it is understood that the medical and dental area 3D printers are used in a significant amount in these areas. Printing prosthetic parts, organs, medical models, synthetic skin, etc. [3].

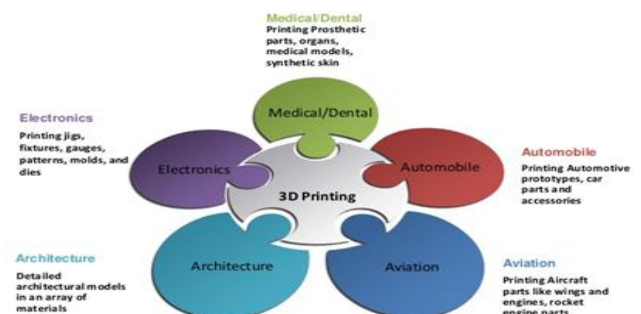


Fig.1. 3D Printing using fields [7]

A. 3D Print Methods

The printing process starts in the computer environment and is completed by the printing of the printer. Some 3D can print by reading the design file on the memory card without the need for a computer connection. 3D design files are sliced through computer software and converted into three-dimensional printable file format. These files are in STL file format. This file contains information about all the movements of the 3D during printing and when it will start to cast raw materials. The resolution of the printer depends on the thickness of the layer and the motion sensitivity on the x-y axes. Typically the print thickness is 100 μm (250 DPI). But some printers can print at a much higher resolution. 16 μm (1,600 DPI). Printing time varies according to printer and printing design. Fig. 2. Shows a key mascot 3d printing steps [4].

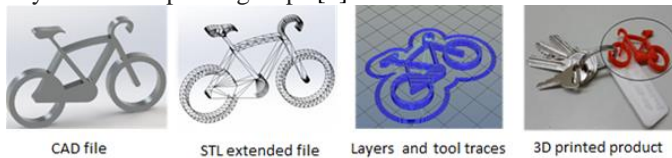


Fig. 2. A key mascot 3d printing steps [6]

B. FDM (Layer Accumulation Modeling) Technology

The most widely known and used in the world is FDM technology (Fused Deposition Modeling) or stacking layer technology by combination. This technique uses thermoformable thermoplastic (PLA, ABS) materials. Materials Using in FDM Technology; ABS, PLA, PET, Nylon 3B Filament, Metal-looking 3D Filament, Ceramic 3D, Filament, Wooden 3D Filament, 3D Shining Filament in the Dark, Carbon Fiber PLA, Polycarbonate ABS, UV Sensitive ABS. FDM 3D Printing shown in Fig. 3.

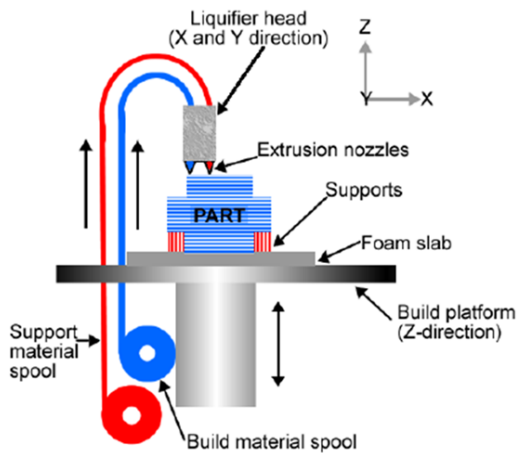


Fig. 3. FDM 3D Printer [8]

III. 3D PRINTER APPLICATIONS USED IN DENSITY

The dental benefits of 3D printer application are; High accuracy positioning of implants, Obtaining the prosthesis or corn coating parts, which cannot be obtained with CNC (Computer Numerical Controlling) or conventional methods with a more precise 3D printer, High

process speeds, Zero waste and low cost, Since the workflow process is digitalized, the least error, Possibility to work with biocompatible materials of dental materials (Resins). Intra oral digital scanner is used to scan the tooth structure or appearance of the patient's mouth. The model of the desired tooth structure according to the scanned image is modeled by drawing in the CAD (Computer Aided Design) program. The modeled tooth is sent to the 3D printer. The crown coating (metal or acrylic) made from a 3D printer is attached to the mouth of the patient as shown in Fig. 4. DMLS method is preferred as a 3D printer process in Crown coatings [5].

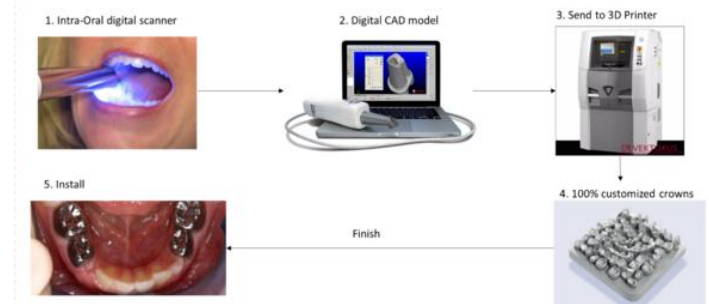


Fig. 4. A product levels of crown teeth in patient mouth [9]

A. Bridge

3D printer technology is important in plant construction. Today it is used effectively. As seen in the above, bridge production is done. The term bridge dent means the group used in dentistry. These teeth are the production options that are produced before the prosthesis. 1-2-3-4 as in members. The total prosthesis production option is approached as the number of members increases in these groups. In the classical system, pre and robust teeth are used as bridge supporting legs. But now bridge legs are made as implant instead of solid teeth. Bridge group teeth are also produced in 3d printer. Fig 5 shows fixed partial denture (bridge) [6]. In other words, a 3-member bridge with an implanted foot is seen in Figure 6.

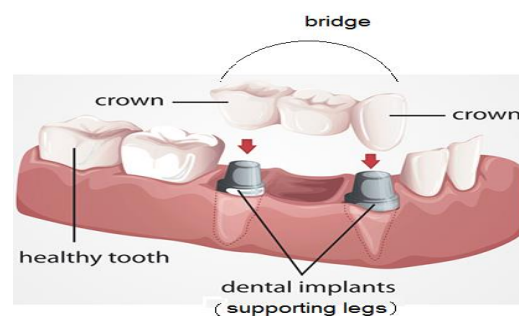


Fig. 5. Three members of crown and implant [9]

The 4 and 5 member 3D printed bridges are shown in Figure 6.



Bridge (5 members) Bridge (4 members)
 Fig .6. Bridge of five and four members [9]

B. Crown

Crowns are protective coatings that are glued to teeth to protect teeth that have not been drawn, decayed, and for a longer period of time. They are fixed by sticking on the main tooth. The skins of the covering are glued in such a way that they do not get air and water and are leak proofed. The patient's skin to be covered is first subjected to retention and smoothing. Then it is glued with the adhesive called cement. These are illustrated in Figures 7 and 8. DMLS method is preferred as a 3 D printer process in Crown coatings [7].

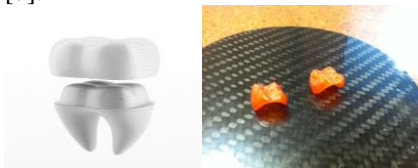


Fig. 7. Crowns [9]

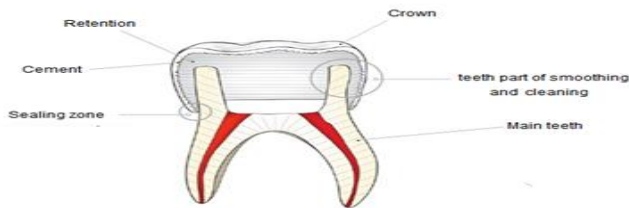


Fig. 8. Cementing of crown [10]

C. Total and Partial Prosthesis

In total and partial prosthesis, SLA method is generally used as 3D printer method. Figure 9 shows the state of the total prosthesis on the 3D printer.

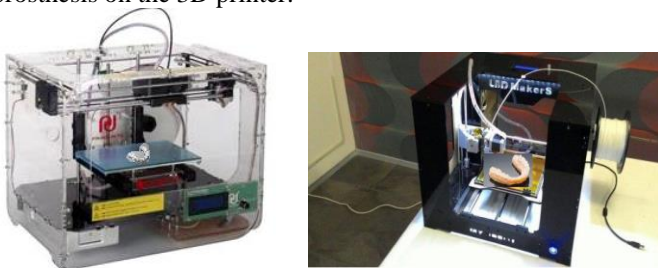


Fig. 9. Total prosthesis and 3D Printer [10]

If the partial prosthesis is metal, the DMLS method is used. The waxy state (proof color) and the finished state (metal state) of a partial prosthesis are shown in Fig.10



Fig.10. 3d printed state of a partial prosthesis model [7]

Total prosthesis are seen in Figure 11. Protective and transparent prostheses are esthetically preferred prostheses. In addition, the denture-based dentures are not aesthetic but are made in 3D printers to protect the teeth and mouth structure of the athlete in box matches [8].



Fig.11. 3d printed state of a total prosthesis model [7]

D. IMPLANT

The concept of implantation, which means implanting a non-female tooth at birth into the mouth of the patient, has recently become important in terms of oral health. In discussing the effect of metal screws used at implantation on the jawbone, it is more prevalent than bridging and crowning methods. If they endure an economic outcome, sometimes they use the choice of implanting all oral teeth totally. Figure 12 shows the implant crown coating. The implant screw is also shown. The disadvantage of Crown coating is shudder; besides the dental decay to be covered, the intact parts must also be shaved. Because the crown does not sit completely in the tooth. This leveling made in consideration of the adhesion, damages the toothy areas especially the enamel layer. If carcinogenic and economical disadvantages are not taken into account, the implant method is preferred over crowns [9].

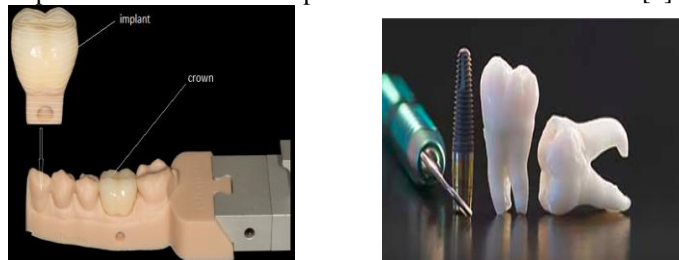


Fig.12. Single members of crown and implant with screw [8]

Figure 13. shows the relationship between the implant and the jawbone. The implant, called dental implantation or grafting to the jawbone, is secured to the female bone by means of a screw. There is a special task here for jawbone cells. Because of the impact of the operation and to break the fractures are required.

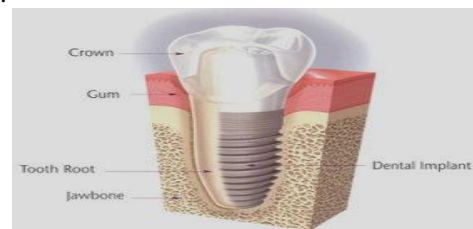


Fig.13.The jawbone and implant with screw [8]

E. Single and Array product in 3D printers

In dentistry, dental production is done as a single, as in multi or array dental production. The bridge includes the meaning of a jacket worn over the model. In the 3 D printer, Acrylic material is solved from the filament and layered on the model sprue. This occurs due to the melting of the nozzle in acrylic material. Figure 14 shows the production of a small molar crown coating with a 3 D printer alone [10].

3.5.1 Single product in 3D printers.

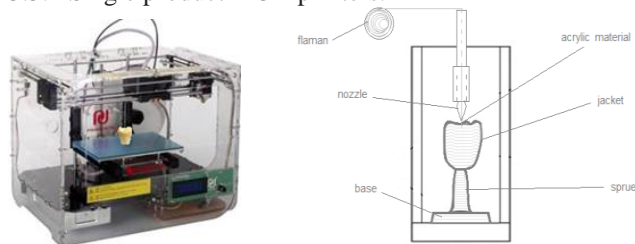


Fig. 14. Application 3D printer for small molar teeth [9]

Figure 15 shows the teeth made in 3D printer as single small and big molar. These teeth are the teeth to be used for implant application or crown coating application.



Fig. 15. Applied of small and big molar teeth [9]

3.5.2 Array Product in 3D Printers

Array of temporary crowns printed in E-dent material on EnvisionTEC 3D Printing system. Multiple crowns and full dental production can be done in 3 D printers as arrays. There is a need for a pre-architectural design and layout model for this production. Because, the more optimal design is made, the more the optimum number and quantity of arrays arise. In other words, production capacity and capability increase. Figure 16 shows the application of the molar teeth for implant and 3D print [11].



Fig. 16. Applied of Design of molar teeth for implant and 3D print [10]

Applied of arch models built in plaster like material on 3D Printing system shown in Figure 17.



Fig. 17. Applied of Arch models built in plaster like material on 3D Printing system [10]

IV. CONCLUSION AND 3D PRINTER TECHNOLOGY IN FUTURE

Children will have the chance to make their own game with a three-dimensional toy data downloaded from the internet. If any part of the home appliance is broken, it is enough to pay only for the necessary geometry and material information, rather than bringing it directly from the factory. In the field of medicine, the production of special titanium bone fragments, materials and dentures suitable for orthodontic uses will become widespread. At Oxford University, scientists have succeeded in producing human stem cells with 3D printers, which will be used to create organs in the future. This means that in the near future, the organs that people need can be produced in a 3D compatible with the human body. With 3D printing technology, purchased products will have all the features that are required. For example, shoes suitable for the foot structure of a person or clothes suitable for their expectations can be produced easily. From new car designs to a wide range of interior design to home furnishings will accelerate, so the acceleration of innovation will also increase.

A possible mistake made with 3D Printers is that the product will be noticed and can be fixed at the design stage. For example, if a part of a machine imported from abroad is required, it may be difficult to obtain this part by conventional methods, in terms of cost and time. With 3D data sharing of only the required part of the computer, this part can be produced in individual systems or in Digital Services. 3D printers will also increase the number of parts used for aerospace and the weight of parts, thereby boosting efficiency. European giant aircraft maker Airbus has begun to produce more than 1000 pieces of aircraft in industrial 3D printers. This also signaled in the future that an entire aircraft could be produced with industrial 3D printers. The jet engine, produced by the world's first three-dimensional printing technology, has been exhibited at the Australian International Air Show 2015 [12].

ACKNOWLEDGMENT

This study was partially supported by Automation and Mechatronic Department of Industrial Vocational School in Karaman / Turkey

REFERENCES

- [1] Ausiello, P., Franciosa, P., Martorelli, M., Watts, D.C.: Mechanical behavior of post-restored upper canine teeth: A 3D FEA .Dental Mater. **27**(12), 1285–1294 (2011). ISSN: 0109-5641
- [2] Hirogaki, Y., Sohmura, T., Satoh, H., Takahashi, J., Takada, K.: Complete 3-D reconstruction of dental cast shape using perceptual grouping. IEEE Trans. Med. Imag.**20**(10), 1093–1101 (2001)
- [3] Bell, A., Ayoub, A.F., Siebert, P.: Assessment of the accuracy of a three-dimensional imaging system for archiving dental study models. J. Orthod. **30**, 219–223 (2003)
- [4] Quimby, M.L., Vig, K.W.L., Rashid, R.G., Firestone, A.R.: The accuracy and reliability of measurements made on computer-based digital models. Angle Orthod. **74**, 298–303 (2004)
- [5] Garino, F., Garino, G.B.: Comparison of dental arch measurements between stone and digital dental casts. World J. Orthod. **3**, 250– 254 (2002)
- [6] Life of 3D Printer, Power point demo, Karabük University Department of Industrial Design Engineering- 2015
- [7] <https://www.youtube.com/watch?v=XLaeOQa0APw>
- [8] http://3dprintturkey.org/imp_dates.html
- [9] <https://www.google.com.tr/search?q=teeth+produce+with+3d+printer>
- [10] <https://3dprintingindustry.com/news/roland-dg-releases-new-dental-3d-printer-dgshape-subsiary-106869/>

Comparison of Various Machine Learning Methods on Wart Treatment Performance of Cryotherapy

K. SABANCI¹, M. KOKLU² and M.F. UNLERSSEN³

¹ Karamanoglu Mehmetbey University, Karaman/Turkey, kadirsabanci@kmu.edu.tr

² Selcuk University, Konya/Turkey, mkoklu@selcuk.edu.tr

³ Necmettin Erbakan University, Konya/Turkey, mfunlersen@konya.edu.tr

Abstract – Warts are skin growths that are caused by the human papillomavirus (HPV). HPV stimulates quick growth of cells on the skin's outer layer. Most common warts go away without treatment, though it may take a year or two and new ones may develop nearby. It is more comfortable to perform wart treatment under a professional supervision because of the reasons that the treatment does not give results at home, the warts are aesthetically and physically disturbing and prone to spread. The goals of treatment are to destroy the wart. There are various methods of wart treatment. These treatments can be listed in basic concepts like Stronger peeling medicine (salicylic acid), Freezing (cryotherapy), other acids, Minor surgery, and Laser treatment. Although the treatment method decision depends on the doctor's opinion, a system that presents the treatment success rate by using the basic characteristics of the patient and the wart can be useful for doctors. In this study, a success rate calculation system of cryotherapy treatment on warts is performed. For this purpose various machine learning methods are investigated and the most effective results are presented. The results present that the best performance of treatment result estimation is achieved as %91.24.

Keywords - Machine Learning Methods, MLP, Knn, KStar, Wart Treatment.

I. INTRODUCTION

WARTS are a skin infection created by the human papillomavirus (HPV). The virus penetrates the body through a tear in the skin, such as a cut. It then constitutes a harsh plump on the surface of the skin. Warts are benign growths [1].

Warts may go away on their own after a certain amount of time because of the struggle which is occurred by the immune system with the virus that causes them. However, since warts can be embarrassing, and can become irritated or painful, they may be wanted to have treated [1]–[3].

Wart treatment can be divided into two groups as home wart treatment and medical wart treatment.

In the "home wart treatment" (also called "over-the-counter treatments"), salicylic acid which is an over-the-counter product, is used to treat warts. It comes in a gel or liquid, or as a patch. Formulations with a higher percentage of salicylic acid are more effective. These treatments work better if the thick

skin of the wart is pared down before application. To treat a wart successfully, it needs at least a month and need to be applied for the topical (on the skin) medicines every day [3].

Medical treatment options can be as follow:

- **Cryotherapy:** This treatment destroys the wart by freezing it with liquid nitrogen. Cryotherapy causes a blister to form; when the blister peels off, all or part of the wart peels off.
- **Topical treatment:** Topical medicines work by stripping away layers of the wart.
- **Other:** Other options to treat plantar warts include laser therapy, surgery, and immunotherapy. However, because these treatments are expensive, can be painful and cause scarring and other side effects, they are used less often [3].

Additionally, there are various studies about wart treatments in the literature.

Phillips et.al proposes Candida Antigen injection method for wart treatment. This method is investigated on 104 patients. And a survey is applied to the patients. The results show that 76% is "very happy", 10% is "happy", 12% is "unhappy" and 2% is "very unhappy". 82% would repeat the treatment if needed [4].

Mohamed et.al in 2018, compares the performance of intralesional bleomycin injection and micro needling-assisted topical bleomycin spraying in the treatment of plantar warts. The results revealed complete clearance of warts in 70% of patients who were treated by intralesional (IL) bleomycin and 83.3% of patients who were treated by spraying of bleomycin following microneedle [5].

Khozeimeh et.al identify the appropriate treatment for two common types of warts and to predict the responses of two of the best methods to the treatment. It is reported that the prediction accuracy of immunotherapy and cryotherapy methods was 83.33% and 80.7%, respectively [6].

Zandi et.al determine the therapeutic effect of topical application of HD tablets on dermal warts in their study. It is reported that while treatment of dermal warts has more complications, the HD treatment would be more cost-effective with fewer complications [7].

Gaillard et.al extend knowledge of bio field therapy to another area of medicine such as dermatology and to propose complementary or alternative practices to improve patient well-being. The main strength of the study is that it is a randomized, single-blind, assessor-blind, placebo-controlled study. As a result, it is reported that data derived from trials on salicylic acid and cryotherapy show only a moderate therapeutic effect. Other therapies are anecdotal and could not be recommended. It may become a first-line therapy because it is less invasive than conventional treatments [8].

In this study, a machine learning methods based treatment method selector is proposed.

II. MATERIAL AND METHODS

An advisory system about the selection of wart treatment method is presented for professionals who treat patients. This system is based on machine learning methods.

A dataset created by collecting in the dermatology clinic of Ghaem Hospital in Mashhad from January 2013 to February 2015 is used for training and testing. The dataset is obtained from the University of California Irvine machine learning repository. The data were collected from patients, with plantar and common warts, who had referred to the dermatology clinic [6]. There are seven attributes and a class in the dataset. These attributes are presented in Table 1.

Table 1: The attributes and class of dataset.

Name	Value Range	Mean±SD
Gender (Count)	1 - Female (49) 2 - Male (41)	
Age [year]	15 – 56	31.04±12.17
Time elapsed before treatment [month]	0 – 12	7.23±3.08
The number of warts	1 – 19	6.14±4.19
Types of wart (Count)	1– Common (47) 2– Plantar (22) 3– Both (21)	
Surface area of the warts [mm ²]	6 – 900	95.7±135.85
Induration diameter of initial test [mm]	5 - 70	14.33±17.12
Response to treatment	1 – Yes 2 – No	

The dataset consisted of 90 records. For training and testing operations two individual dataset is created. These are obtained

by division of the main dataset by %66 and %34 for training and testing respectively. The selection of records for training or testing is random. But none of the records exists simultaneously in both datasets.

In this study various machine learning methods are investigated. First one is the *k-Nearest Neighbor Algorithm* (k-NN). The k-NN is a supervised learning algorithm that solves classification problems. The important point is the determination of the features of each category in advance. The most important optimization problems in the k-NN method are the identification of the number of neighbors and the method of distance calculation algorithm [9]. In the study, the identification of the optimum k number is performed with experiments, and the Euclidean Distance Calculations method is used as a distance calculation method.

The next one is *Multilayer Perceptron*. It is a feed forward type artificial neural network model which maps input sets onto appropriate output sets. A multilayer perceptron (MLP) is composed of multiple layers of nodes where each layer is connected to the next. Each node is a processing element or a neuron that has a nonlinear activation function except the input nodes. It uses a supervised learning technique named back propagation and it is used for training the network. The alteration of the standard linear perceptron, MLP is capable of distinguishing data which are not linearly separable [10].

Another machine learning method, *Naïve Bayes Classifiers* used in the study, are a family of simple probabilistic classifiers based on applying Bayes' theorem with strong (naive) independence assumptions between the features. The advantage of these classifiers is that they require small number of training data for estimating the parameters necessary for classification. When the symptoms are given, the network can calculate the probabilities of the existence of various diseases [11]–[13].

Random Forest is a supervised learning algorithm. It creates a forest and makes it somehow random. The random forest algorithm is used in a lot of different fields, like Banking, Stock Market, Medicine and E-Commerce [14], [15].

Locally Weighted Learning is a class of function approximation techniques, where a prediction is done by using an approximated local model around the current point of interest. The goal of function approximation and regression is to find the underlying relationship between input and output. In a supervised learning problem training data, where each input is associated to one output, is used to create a model that predicts values which come close to the true function. All of these models use complete training data to derive global function. However, a disadvantage of global methods is that sometimes no parameter values can provide a sufficient good approximation. Also the computational costs are also very high in such cases [16].

K-star or K* is an instance-based classifier. The class of a test example is attributed to the training samples similar to it, as specified by some similarity function. In terms of using an entropy-based distance function, it differs from other instance-based learners [17].

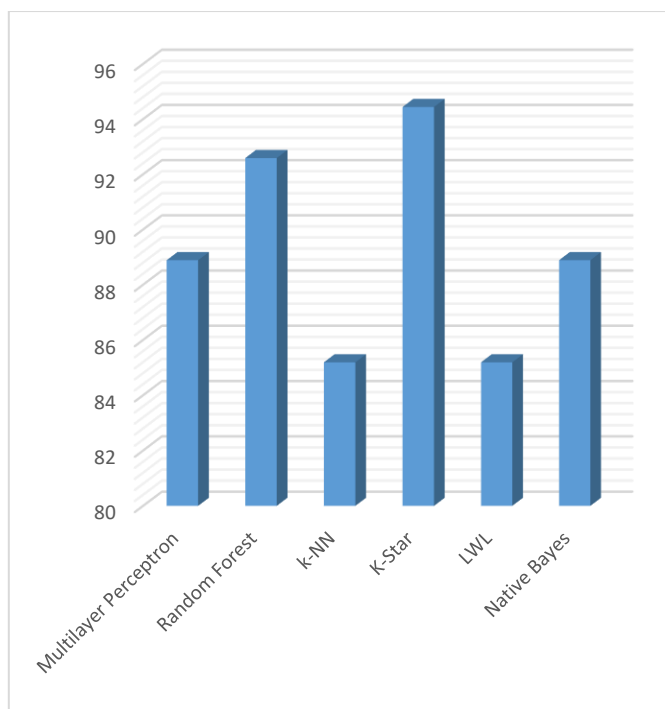
III. RESULTS

To determine the machine learning method with the best performance in finding if Cryotherapy is going to be possible to succeed, various machine learning methods are investigated. For this purpose, the main dataset is divided into two groups as training dataset and testing dataset with the percentage of 66% and 34% respectively. Each machine learning methods is trained and tested by the datasets. The estimation success rates of mentioned methods are presented in Table 2.

Table 1: The results of machine learning methods.

Machine Learning Method	Success Rate %
Multilayer Perceptron	88.89
Random Forest	92.59
k-NN	85.19
K-Star	94.44
LWL	85.19
Native Bayes	87.78

In success ability estimation of wart treatment of cryotherapy, the best performance can be achieved is 94.44% with K-Star method. The graphical representation of the machine learning methods presented in Table 1 is presented in Figure 1.



IV. CONCLUSION

In this study, a model is designed to advisory if wart treatment of cryotherapy is going to be success or not. The best performance can be achieved is 94.44% with K-Star method. The second and third performances are Random Forest and Multilayer Perceptron with success rates of 92.59% and 88.89% respectively. The treatment of a wart is always a troublesome period. In order to achieve high patient satisfaction, it is important to start treatment with the right method. So this method will be made patient more comfortable and less troublesome during wart treatment.

REFERENCES

- [1] M. H. Bunney, *Viral Warts: Their Biology and Treatment*. USA: Oxford University Press, 1982.
- [2] I. Ahmed, S. Agarwal, A. Ilchyshyn, S. Charles-Holmes, and J. Berth-Jones, "Liquid nitrogen cryotherapy of common warts: cryo-spray vs. cotton wool bud," *Br. J. Dermatol.*, vol. 144, no. 5, pp. 1006–1009, May 2001.
- [3] "Warts Management and Treatment | Cleveland Clinic," *Cleveland Clinic*, 2016. [Online]. Available: <https://my.clevelandclinic.org/health/diseases/15045-warts/management-and-treatment>. [Accessed: 05-Oct-2018].
- [4] R. Phillips, R. TS, P. JL, and G. MR, "Treatment of warts with candida antigen injection," *Arch. Dermatol.*, vol. 136, no. 10, pp. 1274–1275, Oct. 2000.
- [5] M. R. Al-Naggar, A. S. Al-Adl, A. R. Rabie, M. R. Abdelkhalik, and M. L. Elsaie, "Intralesional bleomycin injection vs microneedling-assisted topical bleomycin spraying in treatment of plantar warts," *J. Cosmet. Dermatol.*, Apr. 2018.
- [6] F. Khozeimeh, R. Alizadehsani, M. Roshanzamir, A. Khosravi, P. Layegh, and S. Nahavandi, "An expert system for selecting wart treatment method," *Comput. Biol. Med.*, vol. 81, pp. 167–175, Feb. 2017.
- [7] S. Zandi, R. Ahmad Zadeh, S. R. Yousefi, and F. Gharibi, "Promising New Wart Treatment: A Randomized, Placebo-Controlled, Clinical Trial," *Iran. Red Crescent Med. J.*, vol. 18, no. 8, p. e19650, Aug. 2016.
- [8] C. Gaillard *et al.*, "Real versus sham proximal biofield therapy in the treatment of warts of the hands and feet in adults: study protocol for a randomized controlled trial (MAGNETIK study)," *Trials*, vol. 18, no. 1, p. 263, Dec. 2017.
- [9] M. F. Unlensen, K. Sabanci, and M. Ozcan, "Determining Cervical Cancer Possibility by Using Machine Learning Methods," *Int. J. Latest Res. Eng. Technol.*, vol. 3, no. 12, p. 6, 2017.
- [10] M. W. Gardner and S. R. Dorling, "Artificial neural networks (the multilayer perceptron)—a review of applications in the atmospheric sciences," *Atmos. Environ.*, vol. 32, no. 14, pp. 2627–2636, 1998.
- [11] E. Frank, M. A. Hall, and I. H. Witten, *The WEKA Workbench. Online Appendix for "Data Mining: Practical Machine Learning Tools and Techniques"*, Fourth. 2016.
- [12] S. J. (Stuart J. Russell, P. Norvig, and E. Davis, *Artificial intelligence: a modern approach*. Prentice Hall, 2010.
- [13] J. D. M. Rennie, J. D. M. Rennie, L. Shih, J. Teevan, and D. R. Karger, "Tackling the Poor Assumptions of Naive Bayes Text Classifiers," *Proc. Twent. Int. Conf. Mach. Learn.*, pp. 616–623, 2003.
- [14] N. Donges, "The Random Forest Algorithm," *SAP Mach. Learn. Found.*, vol. 5, pp. 18–22, 2018.
- [15] S. Dreiseitl and L. Ohno-Machado, "Logistic regression and artificial neural network classification models: a methodology review," *J. Biomed. Inform.*, vol. 35, no. 5–6, pp. 352–359, Oct. 2002.
- [16] P. Englert, "Locally Weighted Learning."
- [17] M. KOKLU, K. SABANCI, and M. F. UNLERSEN, "Classification of Heuristic Information by Using Machine Learning Algorithms," *Int. J. Intell. Syst. Appl. Eng.*, vol. 4, no. Special Issue-1, pp. 252–254, Dec. 2016.

Flame Retardant Finish For Cotton Fabric Using Boron Hybrid Silica Sol

E. GELGEÇ¹, S. ARAS, F.F. YILDIRIM, P. KOPTUR, Ş. YUMRU, M. ÇÖREKÇİOĞLU

¹ Ozanteks Tekstil Tic. ve San. A.Ş. R&D Center, DENİZLİ, TURKEY
esra@ozanteks.com.tr

Abstract - In this study, the flame retardant properties of boric acid in a 100% cotton fabrics were examined. The boron compound was implemented to fabrics using various combinations of sol-gel method. Duration of inflammation, amount of combustion, spectrophotometer and stiffness the results are compared with the reference fabric and the cotton fabric which is treated with commercial flame retardant product. As a result, the flame retardant sol-gel system containing Silica Boron (S-B) was found to be as successful as the commercial product in the combustion test. The treated fabrics exhibited some changes in color and stiffness relative to the reference fabric. Although the stiffness values of the fabrics have increased, the colors of the treated samples have become lighter.

Keywords – Cotton, Flame retardancy, Boron hybrid, Sol-gel, washing durability

I. INTRODUCTION

COTTON is one of the excellent natural materials with large application areas. Additionally, cotton fiber made of C, H, O are flammable [1, 2, 3]. Cellulose textiles (carpets, curtains, home textiles, wall paper, etc.) used in various areas easily ignite [4]. When solid materials are heated, some chemical and physical changes can occur at certain temperatures depending on the chemical structure of these materials. Thermoplastic polymers soften and then melt. At some higher temperature both non-thermoplastic and thermoplastic solids are chemically degraded (pyrolyze) (Fig 1). Chemical changes begin and then continue throughout the burning temperature when combustion occurs [21, 22]. Combustion is an exothermic reaction that requires heat, oxygen and appropriate fuel components. When remaining conditions are ignored, the combustion is self-catalyzed and continues until oxygen, fuel, or heats are consumed [5].

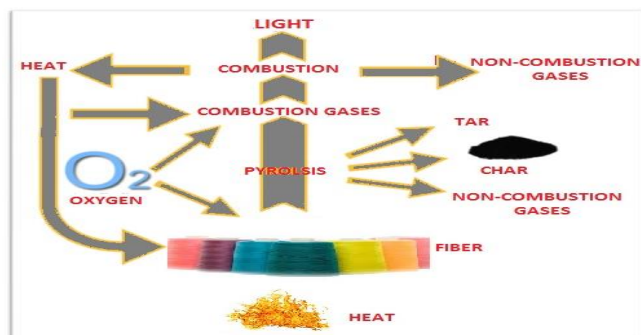


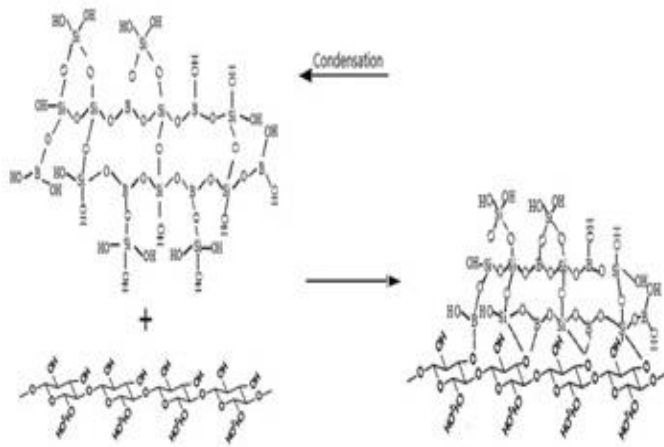
Figure 1. Combustion cycle of textile fibers (5,21,22)

Today, with increasing industrialization, collective settlement areas and developing technology, the fire risk increases and the use of flame retardant textiles become necessity. Conventional flame retardants used for cotton fabrics contain phosphorus and halogen. Flame retardants provide the best flame retardancy to cotton. However, during thermal decomposition some toxic and corrosive gases such as HBr and HCl are formed [6, 7, 8].

Today, textile safety regulations and measurement for flame retardants have become tighter [9, 10]. For this reason, environmentally friendly, non-toxic and formaldehyde-free flame retardants are investigated by industrial and academic researchers. Silicon, nitrogen and boron compounds are becoming a focus of interest as flame retardants due to their environmental friendly structure [11, 12]. Turkey has 73.2% of the world's boron rezerviv. Boron has features such as, high ignition temperature, easily transferable product transfer, and emissions do not pollute the environment. The flame retardant effect of the boron has been the subject of many researchers. The sol-gel method has been applied in textile products in recent years and has received considerable attention. The sol-gel method enables effective confinement of organic and inorganic compounds to different textile surfaces without disturbing the structure of the material and can be applied in mild processing conditions [13]. The sol-gel is a versatile synthetic route based on a two-step reaction (hydrolysis and condensation), starting from (semi) metal alkoxides (usually tetraethoxysilane tetramethoxysilane, titanium tetraisopropoxide, aluminium isopropoxide) and then this leads the formation of completely inorganic or hybrid organic-inorganic coatings at or near room temperature[20].

Alongi [14] found that sol gel treatments are able to modify the thermal and combustion behavior of cellulose because of the shield effect of SiO₂ network as an insulator barrier at high temperature. S.A. Chapple et al.[15] in 2006, urea and ammonium dihydrogen phosphate in the silica sol system were used to provide flame retardancy for cotton [15]. In this study, strength, handle and flame retardancy properties of the treated samples were evaluated. Cireli et al.[18] were synthesized phosphorus-doped silica thin films by sol-gel method to increase the flame retardancy properties of the cotton. These films showed increasing flame retardancy properties. Yaman [19] investigated the effect of sol-gel phosphate-based flame retardant coating on flammability, stiffness and strength on polyacrylonitrile fabrics [19].

In this study, a boron-doped silica solution was prepared and then the fabric was implemented by the sol-gel method. The treated fabrics were compared with both the reference fabric



Scheme 2. Crosslinking of cotton fabric with boron-silica sol

The resulting sol-gel formulation is thought to form a covalent bond in Scheme 1 and Scheme 2 [23].

C.1 Colour Properties

The color measurements of the fabric coated by the sol-gel method were compared with the commercial product treated fabric and reference fabric. In addition, two flame retardancy methods were compared among themselves. For each step, the CIE Lab values (L *, a *, b *, C *, and ho) of the samples were evaluated.

The CIELAB values and appearance of the treated samples are given in Table 2 In addition, the color properties of flame retardant cotton fabrics are shown in Figures 2-4.

Table 2: Spectrometer Measurement Results

Samples	L	a*	b*	C*	h	dE*
A0	31,719	0,384	1,466	1,490	73,990	
A1	32,571	0,334	0,848	0,912	51,05	1,337
A2	29,185	0,386	0,128	0,407	18,30	2,851
A3	31,441	0,408	0,635	0,755	57,31	0,880
A4	32,696	2,314	2,640	3,511	48,771	2,529

observed in the commercial product treated flame retardant cotton sample.

It was observed that there was no significant differences among the* and b* values of the samples. The highest result was obtained from the A3 coded sample.

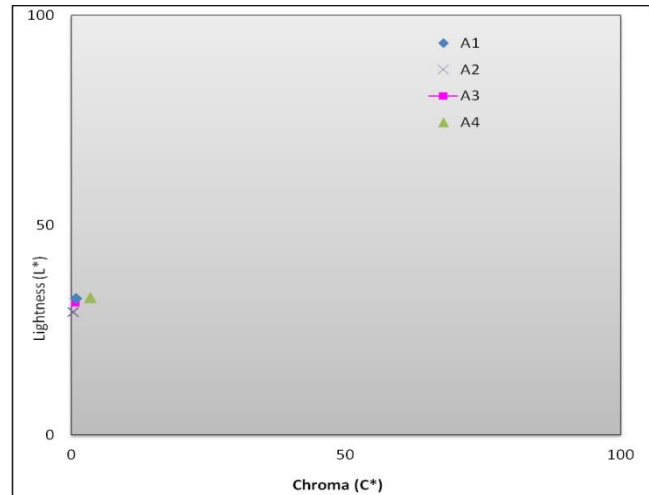


Figure 3. L* (Lightness)-C*(Chroma) values of samples

In Figure 3 and Table 2, the sol-gel coated sample exhibited similar colorimetric values. It was observed that increasing the amount of boric acid did not affect the L values.

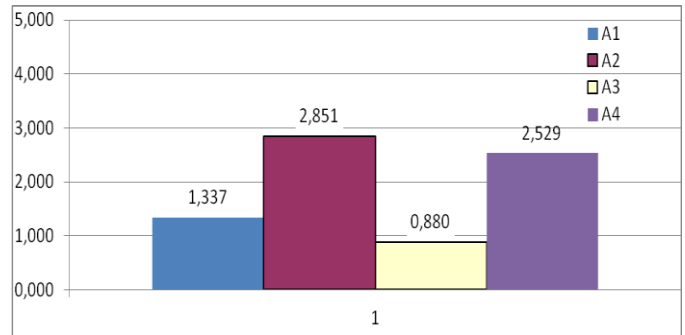


Figure 4. Color differences (ΔE) values of samples

In Figure 4, it was observed that amount differences of boric acid in sol-gel coated fabrics did not affect ΔE values. The maximum color difference was observed in A4 coded sample which is treated with phosphorous based flame retardant product.

As a result, A1, A2, A3 samples showed the least deviation in color. A maximum deviation was observed in A4 code sample.

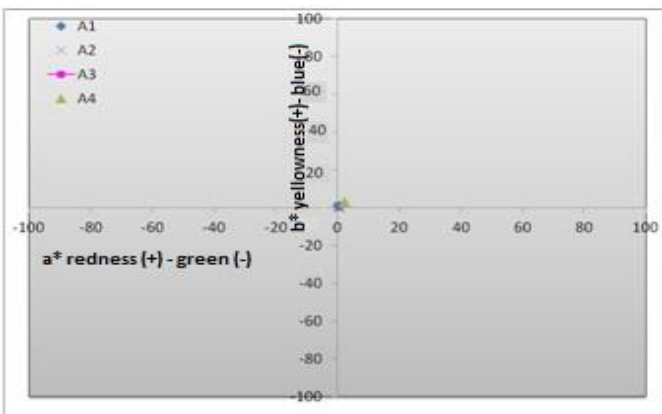


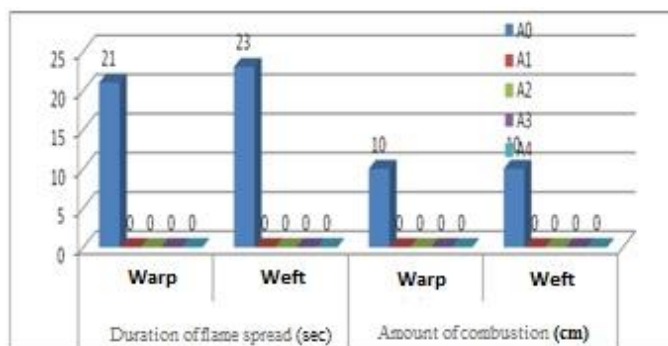
Figure 2. a* (redness)-b*(yellowness) values of samples

As seen on Figure 2, the a* and b* values of the samples exhibited similar values. The maximum deviation was

C.2 Combustion Test

Table 3: Combustion test results

Fabric name	Flammability time (sec)		Duration of flame spread (sec)		Amount of combustion (cm)	
	Warp	Weft	Warp	Weft	Warp	Weft
A0	3	3	21	23	10	10
A1	5	5	0	0	0	0
A2	5	5	0	0	0	0
A3	5	5	0	0	0	0
A4	0	3	0	0	0	0

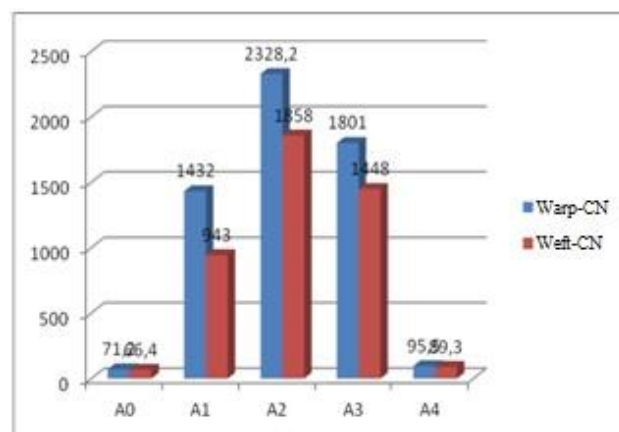
**Figure 5.** Duration of flame spread (sec), Amount of combustion (cm)

As seen on Table 3 and Figure 5, A1, A2, A3, A4 samples were exposed to flame for 5 seconds. The duration of the flame and spread was examined. The A0 code sample was burned in 3 seconds. It was observed that the boric acid treated samples and the commercial product treated samples exhibited excellent results.

C.3 Stiffness (Stiffness-Softness) Test

Table 4: Stiffness Test Results

Fabric Name	Warp-CN	Weft-CN
A0	71,2	66,4
A1	1432	943
A2	2328,2	1858
A3	1801	1448
A4	95,5	89,3

**Figure 6.** : Stiffness Test Results of Fabric Samples

As shown on Table 4 and Figure 6, the stiffness of the fabrics was determined according to ASTM D4032. It was seen that the stiffness values were increased significantly as the amount of boric acid increased.

It was observed that the sol-gel treated fabrics were exhibited stiffer fabrics compared to the commercial product treated fabric and the reference fabric.

IV. CONCLUSION

In this paper, highly homogeneous boron hybrid silica sol was prepared successfully through sol gel method using the tetraethoxysilane (TEOS) and boric acid (H_3BO_3) as starting reactants when boric acid sol-gel treated cotton fabric exposed to the flame was observed that fabric did not ignite for 5 seconds. However, the results show that the commercial product treated fabrics and sol-gel coated fabrics were exhibited good flame retardancy. Stiffness test showed that the sol-gel coated cotton fabrics were stiffer than the commercial product treated fabrics. There was no significant deviation in color. It's thought that the color differences in the samples may be caused by silica.

ACKNOWLEDGMENT

This work has been partly supported by Ozanteks R&D center in frame of the Project 17U03.

REFERENCES

- [1] Hou, A., & Sun, G. (2013). Multifunctional finishing of cotton fabrics with 3,3,4,4- benzophenone tetracarboxylic dianhydride: Reaction mechanism. *Carbohydrate Polymers*, 95, 768.
- [2] Hou, A., Zhang, C., & Wang, Y. (2012). Preparation and UV-protective properties of functional cellulose fabrics based on reactive azobenzene Schiff base derivative. *Carbohydrate Polymers*, 87, 284–288.
- [3] Abou-Okeil, A., Ei-Sawy, S. M., & Abdel-Mohdy, F. A. (2013). Flame retardant cotton fabrics treated with organophosphorus polymer. *Carbohydrate Polymers*, 92, 2293–2298.
- [4] Horrocks, A. R., Kandola, B. K., Davies, P. J., Zhang, S., & Padburg, S. A. (2005). Developments in flame retardant textiles—A review. *Polymer Degradation and Stability*, 88, 3–12.
- [5] Omerogullari, Z., & Dilek, K. U. T. (2012). "Tekstilde Güç Tutuşurluk".
- [6] Wu, W., & Yang, C. Q. (2007). Comparison of different reactive organophosphorus flame retardant agents for cotton. Part II: Fabric

- flame resistant performance and physical properties. *Polymer Degradation and Stability*, 92, 363–369.
- [7] Alongi, J., Ciobanu, M., & Malucelli, G. (2011). Novel flame retardant finishing systems for cotton fabrics based on phosphorus-containing compounds and silica derived from sol–gel processes. *Carbohydrate Polymers*, 85, 599–689.
- [8] Lu, S., & Ian, H. (2002). Recent developments in the chemistry of halogen-free flame retardant polymers. *Progress in Polymer Science*, 27, 1661–1712.
- [9] Guan, J.P., Yang, C.Q., Chen, G.C. (2009). Formaldehyde-free flame retardant finishing of silk using a hydroxyl-functional organophosphorus oligomer. *Polym. Degrad. Sta.*, 94, 450–455.
- [10] Chaiwong, C., Tunma, S., Sangprasert, W., Nimmanpipug, P., Boonyawan, D. (2010). Graft polymerization of flame-retardant compound onto silk via plasma jet, *Surf. Coat. Technol.*, 204, 2991–2995.
- [11] Xie, K., Gao, A., Zhang, Y. (2013). Flame retardant finishing of cotton fabric based on synergistic compounds containing boron and nitrogen, *Carbohydr. Polym.*, 98, 706–710.
- [12] Dogan, M., Yilmaz, A., & Bayramli, E. (2010). Synergistic effect of boron containing substances on flame retardancy and thermal stability of intumescent polypropylene composites. *Polymer Degradation and Stability*, 95, 2584–2588.
- [13] Ren Y., Zhang Y., Zhao J., Wang X., Zeng, Q., Gu, Y. (2017). Phosphorus-doped organic–inorganic hybrid silicon coating for improving fire retardancy of polyacrylonitrile fabric, *J. Sol-Gel Sci. Tech.*, 82 (1), 280-288.
- [14] Alongi, J., Ciobanu, M., Tata, J., Carosio, F., Malucelli, G. (2011). Thermal stability and flame retardancy of polyester, cotton, and relative blend textile fabrics subjected to sol–gel treatments, *J. Appl. Polym. Sci.* 119, 1961–1969.
- [15] Chapple, S.A., Ferg, E. Influence of precursor ratios on the properties of cotton coated with a sol-gel flame retardant, (2006). *AATCC Rev.* 11,36–40.
- [16] Gürsoy, N.Ç., 2010. Hauser, P. Yeni Katyonik Ağartma Aktivatörleri Kullanılarak Ağartılmış Pamuklu Örme Kumaşların Boyama Özelliklerinin İncelenmesi. *Tekstil ve Konfeksiyon Dergisi* (2): 155-161
- [17] ASTM D 4032-94, 2001. “Standard Test Method for Stiffness of Fabric by the Circular Bend Procedure”, American Society for Testing and Materials, Pennsylvania.
- [18] Cireli, A., Onar, N., Ebeouglugil, M. F., Kayatekin, I., Kutlu, B., Culha, O., et al. (2007). Development of flame retardancy properties of new halogen-free phosphorus doped SiO₂ films on fabrics. *Journal of Applied Polymer Science*, 105, 3747–3756.
- [19] Yaman, N. (2009). Preparation and flammability properties of hybrid materials containing phosphorous compounds via sol–gel process. *Fibers and Polymers*, 10, 413–418.
- [20] Sakka,(2003). *Sol-gel Science and Technology. Topics and Fundamental Research and Applications*, Kluwer Academic Publishers, Norwell,
- [21] Tomasino C., (1992) “Chemistry And Technology Of Fabric Preparation And Finishing”, Department Of Textile Engineering, Chemistry And Science College Of Textiles North Carolina State University
- [22] Schindler, W. D., & Hauser, P. J. (2004). *Chemical finishing of textiles*. Elsevier
- [23] Zhang, Q.H., Gu, J.L., Chen, G.Q., Xing, T.L. (2016). Durable flame retardant finish for silk fabric using boron hybrid silica sol, *Appl. Surf. Sci.* 387, 446–453.



ICENTE'18

INTERNATIONAL CONFERENCE
ON ENGINEERING TECHNOLOGIES

October 26-28, 2018

Konya/TURKEY



<http://icente.selcuk.edu.tr>